

REPORT DOCUMENTATION PAGE

AFRL-SR-AR-TR-03-

0077

Public Reporting burden for this collection of information is estimated to average 1 hour per response, including the time for reviewing existing information, gathering material and reviewing the collection of information. Send comment regarding this burden estimate or any other aspect of this collection of information, including suggestions for reducing this burden, to Washington Headquarters Services, Directorate for Information Operations and Reports, 1215 Jefferson Davis Highway, Suite 1204, Arlington, VA 22202-4302, and to the Office of Management and Budget, Paperwork Reduction Project (0704-0188), Washington, DC 20503.

1. AGENCY USE ONLY (Leave Blank)		2. REPORT DATE 19 Feb 2003		3. REPORT TYPE AND DATES COVERED Final Technical Report 01-SEP-1999 - 31-AUG-2002	
4. TITLE AND SUBTITLE Optoelectronics Research Center				5. FUNDING NUMBERS F49620-99-1-0330	
6. AUTHOR(S) S. R. J. Brueck, et al					
7. PERFORMING ORGANIZATION NAME(S) AND ADDRESS(ES) The University of New Mexico Center for High Technology Materials, 1313 Goddard SE Albuquerque, NM 87106				8. PERFORMING ORGANIZATION REPORT NUMBER FT31523X	
9. SPONSORING / MONITORING AGENCY NAME(S) AND ADDRESS(ES) AFOSR/NE 4015 Wilson Blvd. Rm 713 Arlington, VA 22203-1954				10. SPONSORING / MONITORING AGENCY REPORT NUMBER	
11. SUPPLEMENTARY NOTES The views, opinions and/or findings contained in this report are those of the author(s) and should not be construed as an official Air Force Office of Scientific Research position, policy or decision, unless so designated by other documentation.					
12 a. DISTRIBUTION / AVAILABILITY STATEMENT Approved for public release; distribution unlimited.				12 b. DISTRIBUTION CODE	
13. ABSTRACT (Maximum 200 words) The AFOSR Optoelectronics Research Center has maintained a broadly based program at the forefront of optoelectronics with efforts in linear and nonlinear materials, device processing, device design, and in device integration. Examples of materials and structures are quantum dots, superlattices, digital alloys, and strained-layer semiconductors, and new nonlinear materials. Processing developments relate to smaller dimensions and improved techniques for the selective deposition, modification and removal of materials. Improved devices, based both on semiconductors and on fibers, have also resulted from increased understanding of the underlying device and material physics and from innovative approaches to device design and synthesis.					
14. SUBJECT TERMS Quantum Dot, Lasers, Nanoheteroepitaxy, Interferometric Lithography, Optoelectronics, MBE, MOCVD				15. NUMBER OF PAGES 128 + Appendices	
				16. PRICE CODE NSP	
17. SECURITY CLASSIFICATION OR REPORT UNCLASSIFIED	18. SECURITY CLASSIFICATION ON THIS PAGE UNCLASSIFIED	19. SECURITY CLASSIFICATION OF ABSTRACT UNCLASSIFIED	20. LIMITATION OF ABSTRACT UL		

NSN 7540-01-280-5500

Standard Form 298 (Rev.2-89)
Prescribed by ANSI Z39-18

20030319 015

AFOSR FINAL TECHNICAL REPORT
Optoelectronics Research Center

PRINCIPAL INVESTIGATOR:

Dr. Steven R. J. Brueck
Center for High Technology Materials
University of New Mexico
MSC04 2710
1313 Goddard, SE
Albuquerque, NM 87106
OFFICE: (505) 272-7800
e-mail address: Brueck@chtm.unm.edu

GRANT NUMBER: F49620-99-1-0330

REPORT PERIOD Final Technical Report 01-SEP-1999 – 31- AUG-2002

AFOSR PROGRAM MANAGER:

Dr. Howard Schlossberg
AFOSR/NE
4015 Wilson Blvd. Room 713
Arlington, Virginia, 20332
703-696-7549
howard.schlossberg@afosr.af.mil

SUBMITTED BY:



NAME: Steven R. J. Brueck DATE:
TITLE: Professor, EECE/Physics and Astronomy

Abstract	3
I. Introduction	4
A. Quantum Dot and Antimonide Based Diode Lasers	4
B. Vertical Cavity Surface Emitting Lasers (VCSELs) and Subsystem Applications	4
C. Mid-IR Fiber Laser and Advanced Fiber Optic Devices	5
D. Nanoheteroepitaxy.....	5
II. Detail Description of Technical Results	5
A. Antimonide Based Diode Lasers	5
B. Extremely Low Room-Temperature Threshold Current Density Diode Lasers Using InAs Dots in an In _{0.15} Ga _{0.85} As Quantum Well	7
C. High Performance Surface-Emitting Lasers and Integrated VCSEL Arrays	11
D. Mid-IR Fiber Laser and Advanced Fiber Optic Devices	12
E. Advanced Fiber Optic Devices	17
F. Electrically -tunable fiber Bragg gratings.....	18
G. Nanoheteroepitaxy: A Revolutionary Approach to Lattice-Mismatched Heterostructure Growth	20
H. Influence of the Microstructure on Transport Properties of p-type GaN:Mg.....	25
I. High-Power Diode-Pumped Mid-IR Fiber Lasers	26
J. Inductive and capacitive grids for 2-5 μm spectral regime	30
K. Nanoheteroepitaxy of GaN and GaAs on Si.....	33
L. Nanoscale Molecular Beam Epitaxy	36
M. Fabrication of quantum dot DFB lasers	40
N. Development of Ordered, Nanostructured Thin Films for Electrical and Optical Applications	43
O. InNAs – a New Optoelectronic Material	48
P. Fabrication of a DFB laser by Interferometric Lithography	52
Q. Study of grating fields in presence of negative index materials	55
R. Nanostructured detector	66
S. Nanoheteroepitaxy Integration of Highly Mismatched Semiconductor Materials	67
T. Application of Interferometric Lithography to Nanoscale Faceting and Lateral Growth by Molecular Beam Epitaxy	73
III. End of Program Summary	83
A. MBE-Grown Mid-IR Lasers	83
B. MOCVD Grown Micro-Optical Devices and Nanoheteroepitaxy for the Integration of Highly Mismatched Semiconductors.	85
C. Quantum Dot Lasers and Detectors	89
D. Quantum Dot Lasers	91
E. Vertical Cavity Surface-Emitting Lasers	98
F. Free-Space Optical Communications	103
G. Development of Artificial Dielectrics for Optical and Electrical Applications.....	105
Appendix 1 – Faculty Biographies	107
S. R. J. BRUECK.....	108
STEPHEN D. HERSEE	110
RAVINDER K. JAIN	111
SANJAY KRISHNA	112
LUKE F. LESTER.....	114

KEVIN J. MALLOY	115
MAREK OSINSKI	118
Appendix 2 – Publications (unpaginated)	122
Appendix 3 – Document References (Endnotes)	123

Abstract

The AFOSR Optoelectronics Research Center has maintained a broadly based program at the forefront of optoelectronics with efforts in linear and nonlinear materials, device processing, device design, and in device integration. Examples of materials and structures are quantum dots, superlattices, digital alloys, and strained-layer semiconductors, and new nonlinear materials. Processing developments relate to smaller dimensions and improved techniques for the selective deposition, modification and removal of materials. Improved devices, based both on semiconductors and on fibers, have also resulted from increased understanding of the underlying device and material physics and from innovative approaches to device design and synthesis.

I. Introduction

The *Optoelectronics Research Center* (OERC) at the University of New Mexico that was begun in FY87 under the auspices of the Air Force Office of Scientific Research, has functioned in conjunction with the *Center for High Technology Materials* (CHTM), which in turn is being supported by the State and University of New Mexico, and with the *Optoelectronic Materials Center*, which is funded by DARPA. CHTM is an interdisciplinary research organization with faculty and research representation from three departments: Electrical Engineering, Physics, and Chemistry. Since its inception, the AFOSR OERC has become a leading university optoelectronics program with substantial impact on the development of the field.

The goal of the AFOSR OERC is to continue to be at the forefront of advances in optoelectronics. The coupling and increasing merger of optics and electronics has already had important consequences, but the major advances which will occur over the next decade will dwarf those seen to date. These will result from advances in linear and nonlinear materials, device processing, device design, and in device integration. Examples of materials and structures are quantum dots, superlattices, digital alloys, and strained-layer semiconductors, and new nonlinear materials. Processing developments relate to smaller dimensions and improved techniques for the selective deposition, modification and removal of materials. Improved devices also result from increased understanding of the underlying device and material physics and from innovative approaches to device design and synthesis.

Major accomplishments are highlighted below. Section II includes more detailed descriptions. Section III provides end-of-program summaries, including publication lists. Finally the appendices contain biographies of the investigators, and reprints of publications and conference presentations which provide a detailed account of our results.

Major accomplishments include:

A. Quantum Dot and Antimonide Based Diode Lasers

- 2- μm wavelength AlGaAsSb/GaInAsSb multiple quantum well lasers with 140K characteristic temperature.
- 1.25- μm quantum dot lasers with ultra-low linewidth enhancement factor (0.1) and threshold current density (16 A/cm²).
- Studies of the dependence of bandedge emission and electron-hole overlap in type III GaSb/InAs heterojunctions.

B. Vertical Cavity Surface Emitting Lasers (VCSELs) and Subsystem Applications

- Developed a new and reliable technique for achieving quasi-planar oxide-confined microcavity lasers with micron-sized apertures and submilliampere threshold currents.
- Achieved high-performance microcavity VCSELs with different active area geometries and a higher packing density using the etched-trench oxidation technology.
- Achieved high speed oxide-confined VCSELs with low parasitics and a maximum modulation bandwidth of up to 16 Ghz.

- Achieved efficient (>32%), low-power dissipation (0.2 mW at threshold) cryogenic VCSELs optimized for low temperature operation (6K to 200 K) using an oxide-confined design with double intracavity contacts, with low operating voltage (<1.5V), submilliampere threshold current (~ 0.15 mA) and high slope efficiency (70 %).
- Achieved long-wavelength semiconductor lasers emitting in the 1.1 μm wavelength region) using multiple InGaAsN/GaAs quantum wells grown on a GaAs substrate by MOCVD. Efficient cw lasing was achieved at temperatures up to 60°C, with high power (>25 mW per facet) and high slope efficiency (25% per facet) at room temperature, and a large characteristic temperature (125 K).
- Efficient, continuous-wave lasing operation of narrow-stripe, oxide-confined, long-wavelength InAs quantum dot lasers in the ground state ($\lambda \approx 1.28 \mu\text{m}$) has been achieved at temperatures up to 100°C, with a very low threshold current density ($J_{\text{th}} = 24 \text{ A/cm}^2$) and high differential quantum efficiency (55%).

C. Mid-IR Fiber Laser and Advanced Fiber Optic Devices

- Demonstrated an efficient and novel depopulation mechanisms for the lower laser level via cross-relaxation (#1) of Er ions at high doping densities and energy transfer to co-doped Pr ions.
- Reported the first observation of passive Q-switching (7 μs pulsewidth, 35 kHz repetition rate) of a mid-IR Er-ZBLAN fiber laser
- Passive Q-switching was achieved by using a liquid gallium mirror as a saturable absorber.
- Demonstrated electro-optic tuning of a FBG fabricated in a thermally-poled fiber. 40 pm of tuning was achieved, corresponding to an electro-optic coefficient of 0.25 pm/V.
- First demonstration of an 2x2 all-fiber electrooptic switch.

D. Nanoheteroepitaxy

- Invented Nanoheteroepitaxy for the elimination of defects in highly mismatched heterostructures
- Developed original theory of Nanoheteroepitaxy
- Demonstrated experimentally many of the predictions of Nanoheteroepitaxy for GaN on Si heterostructures.

II. Detail Description of Technical Results

A. Antimodide Based Diode Lasers

The effect of doping on wave-function overlap and band-edge energy in type III InAs/GaSb structures has been analyzed in this project within the grant. By varying the dopant concentration in type III InAs/GaSb quantum wells, an order of magnitude increase in electron-hole wave function overlap and a significant band edge shift are demonstrated using a self-consistent Schrödinger-Poisson solver. InAs/GaSb type III quantum well structures are of current interest as active regions for mid-IR semiconductor lasers because of their relative simplicity in crystal growth compared to quantum cascade, "W", or type-II interband cascade lasers. InAs/GaSb type III structures, however, rely on spatially-indirect overlap of electron and hole wave functions,

which can be weak in non-optimized designs. Unintentionally-doped InAs/GaSb heterojunctions provide little band bending leaving the holes in the GaSb far away from the InAs/GaSb interface. In this case, a modest overlap can only be achieved by growing very thin layers of InAs, providing substantial gain only for near-IR wavelengths. By intentionally doping an InAs/GaSb structure, band-bending can be substantially increased and the holes brought closer to the interface providing a substantial increase in the wave function overlap between the electrons and heavy holes. The large overlap of valence subbands makes intervalence band absorption a concern in these structures, but these resonances occur mostly in the far-IR. This makes the InAs/GaSb system a good candidate for mid-IR applications.

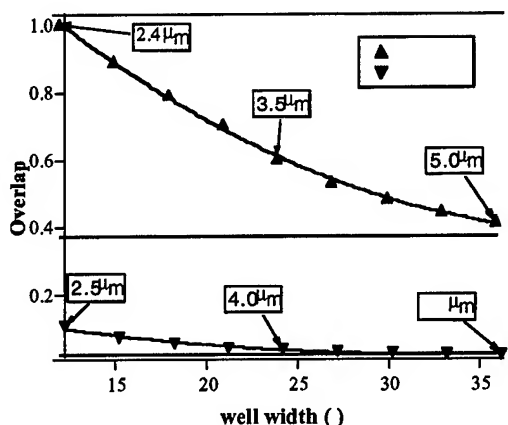


Fig. 1. The calculated wave-function overlap for InAs/GaSb multiple quantum well structures with different InAs well thicknesses for undoped and intentionally doped cases.

The baseline structure to be modeled consists of a narrow InAs well sandwiched between GaSb layers grown on a GaSb substrate. Using a self-consistent Schrödinger-Poisson solver, Fig. 1 shows the inner product (overlap) of the electron state in the InAs well with the first heavy hole subbands in the GaSb layers as a function of InAs well width. The undoped case, for which GaSb is usually unintentionally p-type and the InAs n-type, shows a very small overlap. The unintentional doping concentrations are 10^{17} cm^{-3} . The doped example has an order of magnitude larger overlap even at very long wavelengths. In this instance, both the InAs and GaSb are n-type with a concentration of 10^{17} cm^{-3} . The asymptotic overlap for both cases is shown by the dashed lines, and several emission wavelengths are tagged. With the significant increase in overlap, a substantial decrease in the lasing threshold is expected for all wavelengths.

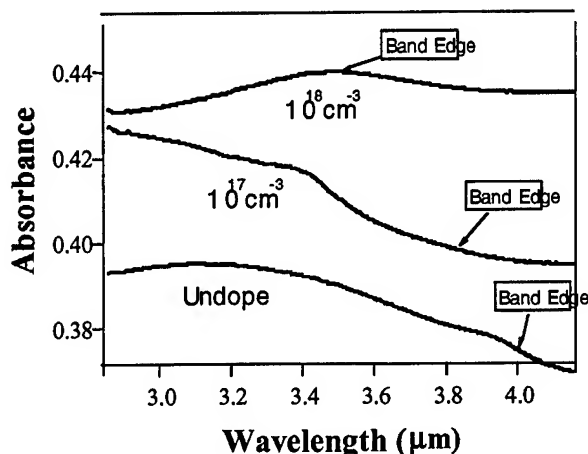


Fig. 2. FTIR absorption spectra measured at 300K for undoped and n-type doped InAs/GaSb superlattices

To monitor the shift in band edge with doping, three test structures were grown by molecular beam epitaxy on GaSb substrates with a 20 period superlattice composed of 24Å of InAs and 400Å of GaSb. Two of the samples were doped n-type with tellurium to a concentration of 10^{17} cm^{-3} and 10^{18} cm^{-3} , and the third wafer was left undoped. Room temperature FTIR data was taken from the samples and is plotted in Fig. 2 along with the calculated band edge. A clear shift in the band edge is evident, and the theoretical and experimental data agree reasonably well. The ability to tailor the wavelength by shifting the heavy hole energies with doping is of particular importance for this system because then the strained InAs well thickness can be optimized to avoid relaxation and doping can be used to tailor the operating wavelength.

In conclusion, it has been shown that doping has a profound effect on the overlap and band edge energy in type III InAs/GaSb quantum wells. Auger recombination should not be substantially increased in these structures because the doping is necessary only in the immediate vicinity of the heterojunction.

B. Extremely Low Room-Temperature Threshold Current Density Diode Lasers Using InAs Dots in an $\text{In}_{0.15}\text{Ga}_{0.85}\text{As}$ Quantum Well

It has been predicted that the threshold current density of quantum dot lasers should be lower than that of quantum well lasers due to the reduction of density of states.¹ In particular, efforts have been made in the past few years to reduce the threshold current density of quantum dot lasers on GaAs substrates.^{2,3} A recently developed approach is to put the InAs dots in a strained $\text{In}_{0.2}\text{Ga}_{0.8}\text{As}$ quantum well.^{iii,4} This "dot in a well" (DWELL) design not only improves carrier capture by the dots, but also increases the density of quantum dots (to $7 \times 10^{10} \text{ cm}^{-2}$) over growth on GaAs directly. Consequently, ground state lasing from a single layer of dots is possible at reasonable cavity lengths. While competition with radiative quantum well transitions was suggested as a concern,⁵ quantum well transitions were not observed in previous workⁱⁱⁱ or in this study. In this letter, further improvements have been made by putting a single layer of InAs quantum dots into a strained $\text{In}_{0.15}\text{Ga}_{0.85}\text{As}$ quantum well. An extremely low threshold current

density of 26 A cm^{-2} has been achieved for a 7.8 mm cavity length, cleaved facet laser. Other operating characteristics of these DWELL lasers are described below.

Device Structures and Growth

The laser structure was grown by solid-source molecular beam epitaxy (MBE) on a $\langle 100 \rangle$ n⁺-GaAs substrate. The laser structure was the same as reported in Ref. ⁱⁱⁱ except that $\text{In}_{0.15}\text{Ga}_{0.85}\text{As}$ was used as the quantum well. The epitaxial structure consists of an n-type (10^{18} cm^{-3}) 300 nm thick GaAs buffer, a 2 μm n-type (10^{17} cm^{-3}) lower $\text{Al}_{0.7}\text{Ga}_{0.3}\text{As}$ cladding layer, a 230 nm thick GaAs waveguide surrounding the laser active region, a 2 μm p-type (10^{17} cm^{-3}) upper cladding layer, and a p⁺-doped ($3 \times 10^{19} \text{ cm}^{-3}$) 60 nm thick GaAs cap. This cavity was a low-loss design following Ref. ⁶. In the center of the waveguide, an equivalent coverage of 2.4 monolayers of InAs results in quantum dots grown approximately in the middle of the 100 Å $\text{In}_{0.15}\text{Ga}_{0.85}\text{As}$ quantum well. The quantum dots and quantum well were grown at 510 °C, and all other layers were grown at 610 °C, as measured by an optical pyrometer.

Room temperature photoluminescence (PL) result is shown in Fig.3. The PL linewidth is 37 meV and has been reduced compared with Ref. ⁱⁱⁱ. No emission from the quantum well is observed, providing clear proof of minimal competition from quantum well radiative transitions. This implies that the relaxation time from the quantum well to the quantum dots is much faster than the spontaneous lifetime of the quantum well.

Results

Broad area lasers with 100 μm stripe widths were fabricated from this structure. The wafer was then cleaved into 7.8 mm long laser bars. All devices were tested with the epi-side up on a thermoelectric cooler using pulsed excitation. The pulse width was 300 ns with a duty cycle of 0.5%. The temperature of the thermoelectric cooler was set to be 20 °C. The single facet output L-I curve from a typical bar is shown in Fig.4. The lasing threshold current is 200 mA, which corresponds to a threshold current density of 26 A cm^{-2} . The external quantum efficiency is 31%. The lowest previously reported threshold current densities for quantum wells lasers were around 50 A cm^{-2} .^{7,8} The near-threshold lasing spectrum at three different injection current levels, $0.90 I_{\text{th}}$ (180mA), $0.95 I_{\text{th}}$ (190mA) and I_{th} (200mA) was measured by an optical spectrum analyzer (OSA) and is shown in Fig. 5. The lasing wavelength is 1.25 μm . Clear spectral narrowing can be observed at $0.95 I_{\text{th}}$ (190mA). A much broader spectrum was also taken at five times the threshold current and is shown in Fig. 6. No emission from the quantum well layer is observed, again suggesting the lack of radiative competition from the quantum well and the rapid capture of carriers by the dots from the well. The dependence of the threshold current on temperature was also measured and is shown in Fig. 7. The characteristic temperature, T_0 , is 60 K between 10 °C and 50 °C, and decreases significantly to 34.5 K between 50 °C and 80 °C. Carrier heating out of the quantum well may be one reason the T_0 value of this laser is smaller than predicted T_0 values for quantum dot lasers.¹

Conclusion

We have demonstrated an extremely low threshold current density DWELL laser with a single layer of InAs quantum dots in an $\text{In}_{0.15}\text{Ga}_{0.85}\text{As}$ quantum well. This is the first time that the threshold current density performance of quantum dot lasers surpasses that of quantum well lasers. Experimental evidence suggests that the relaxation time from the quantum well to the quantum

dots is much shorter than the spontaneous lifetime of the quantum well. The T_0 value for these DWELL lasers is 60 K between 10 °C and 50 °C.

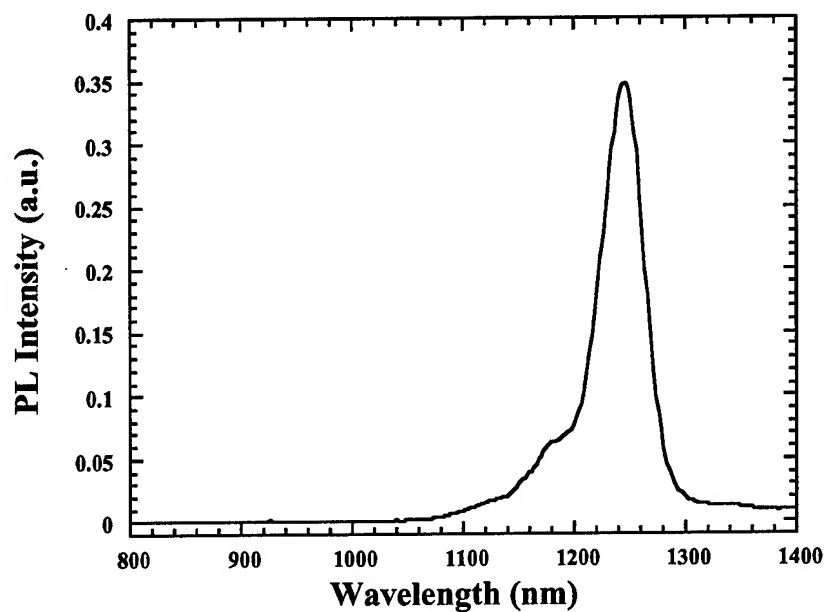


Fig. 3: Photoluminescence spectrum of the laser wafer. No emission from the quantum well is observed. The FWHM is 37 meV.

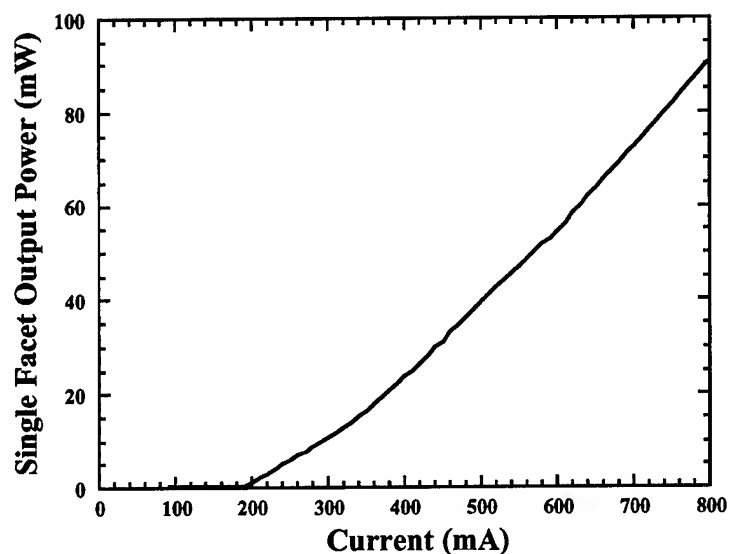


Fig. 4: Single facet output L-I curve of a 7.8 mm cavity length laser. The threshold current density is 26 A cm^{-2} . The external efficiency is 31%.

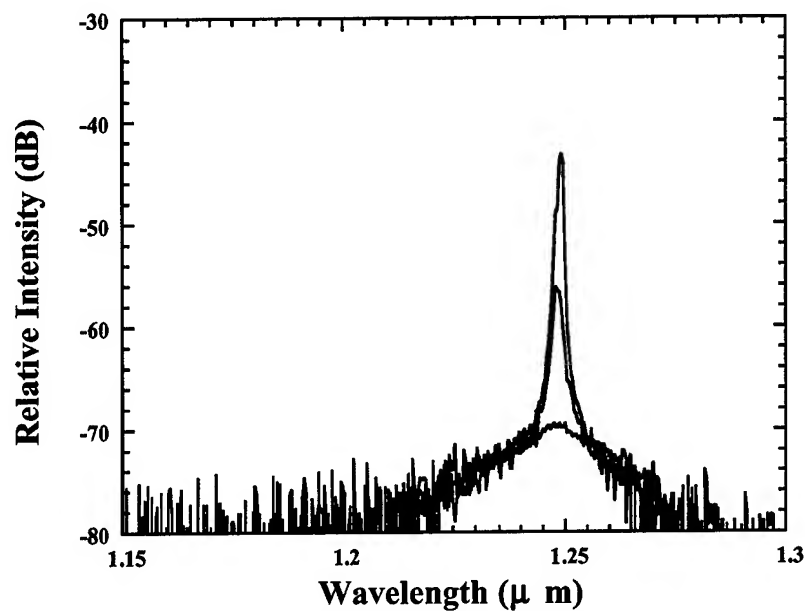


Fig. 5: Lasing spectrum at $0.90 I_{th}$ (180 mA), $0.95 I_{th}$ (190 mA), and I_{th} (200 mA).

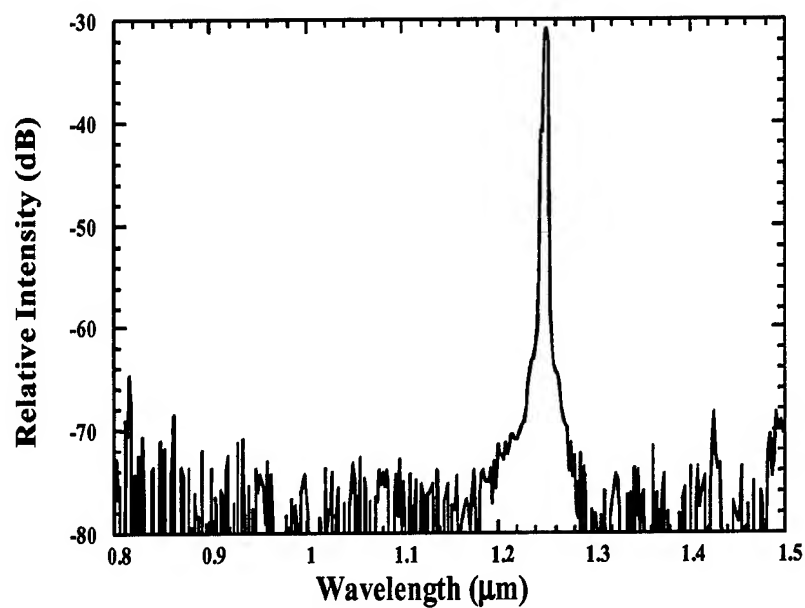


Fig. 6: Lasing spectrum at five times the threshold current density. No emission from the well is observed.

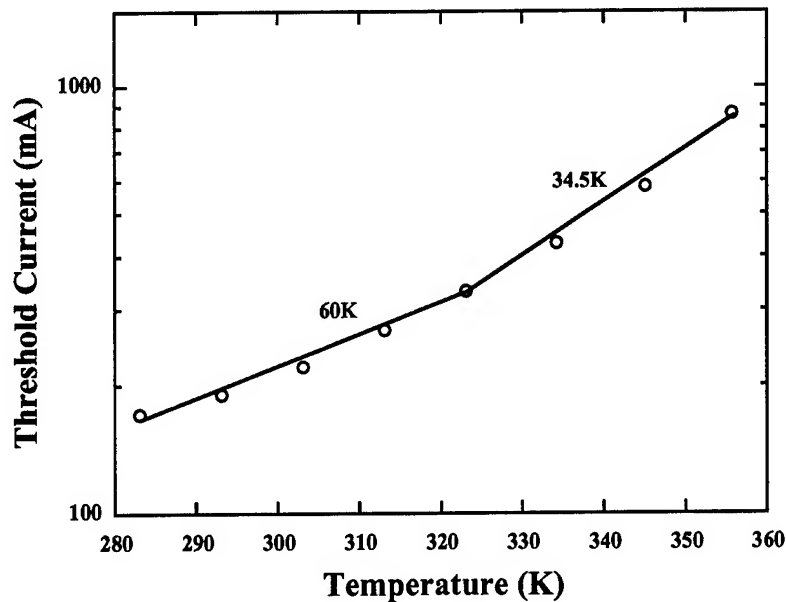


Fig. 7: The threshold current and T_0 as a function of temperature for the 7.8 mm cavity length device.

C. High Performance Surface-Emitting Lasers and Integrated VCSEL Arrays

For the monolithic integration of large VCSEL arrays, power dissipation is a critical limiting factor for dense array operation, and individual VCSELs must have a very low current density. In order to reduce the power dissipation, we need to reduce the lasing threshold to a submilliampere, almost threshold-less level. This requires a combination of more effective current confinement, a smaller lasing volume, and better mode control through index guiding. Novel VCSEL structures have been investigated to achieve these objectives. The achievement of VCSEL arrays with low power dissipation is described below.

Efficient, Low-Power-Dissipation VCSELs:

Planarity is desirable for the monolithic integration of VCSELs, and low power dissipation is required for dense arrays. To minimize power dissipation, oxide-confined VCSELs with small active areas and low operating currents have been developed. In conventional (non-planar) oxide-confined VCSELs, the active area is defined by the lateral wet oxidation of the high aluminum content layers from the periphery of an etched mesa, with a typical oxidation length that is $\sim 10\text{-}20\ \mu\text{m}$. Minimizing the thermal and electrical resistances dictate a large mesa size, which requires a longer oxidation time and greater uncertainty in the final aperture size. The oxidation time and uncertainty can be reduced without sacrificing planarity or increasing the mesa size by using a novel technique that uses local oxidation centers from which multiple oxidation fronts can proceed to define an active aperture.

We have developed a quasi-planar technology that facilitates the monolithic integration of oxide-confined VCSELs with very small active area apertures, in which a continuous oxidation front of arbitrary geometry is defined by concatenating the oxidation fronts emanating from a number of

crescent-shaped trenches. This approach preserves planarity while providing improved dimensional control and increased accuracy in the production of devices with very small oxide apertures (2-4 μm). The electrical and lasing characteristics of oxide-confined VCSELs fabricated using the quasi-planar etched-trench (ET) technique are in many ways comparable to those of conventional etched mesa (EM) VCSELs. However the dc lasing characteristics of the ET VCSEL arrays show greater uniformity and superior dimension control for devices as small as 2 μm . They also have higher output power and reduced thermal roll-over. Another advantage of the new ET VCSELs is the preservation of planarity without increasing device parasitics. The optical modulation response shows a -3dB bandwidth of more than 12 GHz at $10 \times I_{\text{th}}$. A maximum modulation bandwidth of up to 16 GHz has been observed.

Efficient VCSEL Arrays with Very Low Threshold and Low Power Dissipation for Cryogenic Applications

VCSELs operating at cryogenic temperatures offer the promise of superior lasing performance as a result of a higher differential gain coefficient, a higher quantum efficiency, lower losses, and lower noise, resulting in a higher modulation bandwidth, lower power dissipation, and a higher power conversion efficiency. High efficiency and low power dissipation make cryo-VCSELs particularly appealing for use as a non-invasive, power-efficient optical means for transferring high-speed image data from infrared sensor arrays housed in a cryogenic environment to external electronic signal processors that may be situated locally or at some distance away. An optical link can provide both electrical and thermal isolation, as well as a larger bandwidth and a longer link span between the imaging array and the external processing electronics.

An efficient cryogenic link requires VCSELs with low operating currents and voltages that are compatible with on-board cryogenic CMOS drive circuits (≤ 2 mA and 3.3 V, respectively). The efficient cw lasing operation of InGaAs/GaAs VCSELs with low threshold voltage and low power dissipation has been achieved over a wide range of cryogenic temperatures (77K to 250K) using an oxide-confinement design that employed double intracavity contacts and undoped DBRs, along with proper alignment of the cavity mode and the gain peak at low temperatures. Low operating voltages were obtained by routing current through two intra-cavity contacts to bypass both distributed Bragg reflector (DBR) mirrors, while lower optical losses were achieved by using undoped DBR mirrors with abrupt heterointerfaces. This resulted in devices with a low operating voltage (< 1.5 V), submilliampere threshold current ($I_{\text{th}} \sim 0.15$ mA) and low current density ($J_{\text{th}} = 600$ A/cm²), high slope efficiency (70 %), low power dissipation ((0.2 mW at threshold, 0.81 mW for $P_{\text{out}} = 0.2$ mW) and a high power conversion efficiency ($\eta_{\text{eff}} = 31\%$).

D. Mid-IR Fiber Laser and Advanced Fiber Optic Devices

Mid-IR Fiber Laser

Goal: Research and development of diode-pumped compact, high-power CW and pulsed, tunable mid-IR fiber lasers.

Background: The 2.7 μm transition in Er-ZBLAN is particularly attractive for the design of compact, high-power mid-IR fiber lasers of excellent beam quality as needed for applications ranging from laser surgery to countermeasures and spectroscopic monitoring. The problem with

the 2.7 μm laser transition in Er (Fig. 8a) is the fact that the natural lifetime of the lower laser level (9.4 ms) is longer than that of the upper laser level (7.5 ms), leading to a population bottleneck that inhibits efficient steady-state (CW) lasing in Er:ZBLAN fiber lasers.

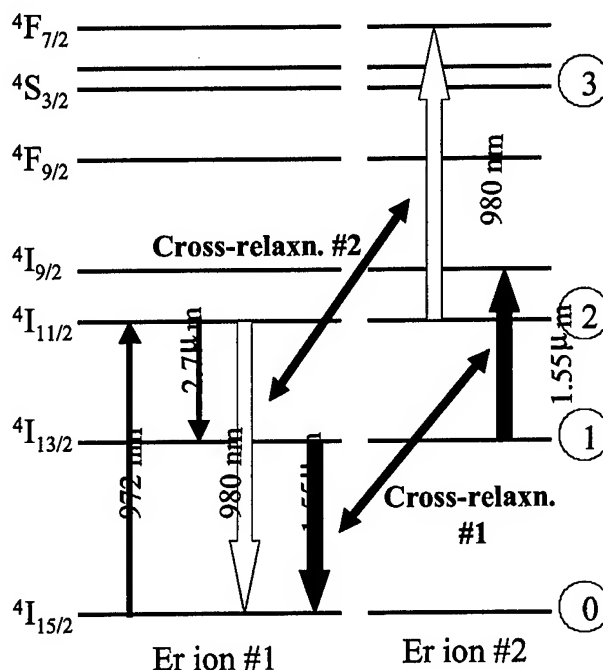


Fig. 8(a): Energy level diagram of Er showing dominant cross-relaxation

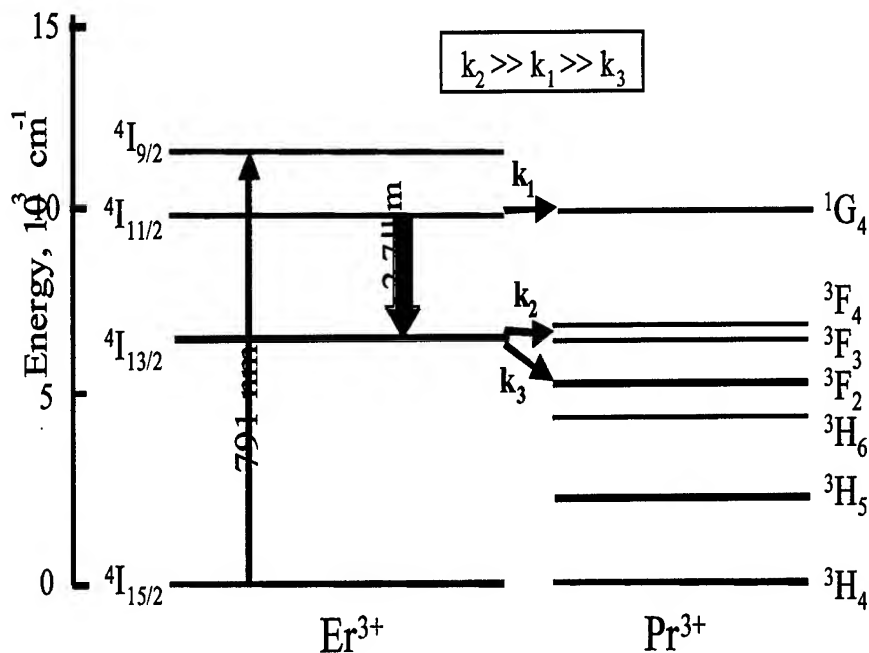


Fig. 8(b): Dominant energy transfer pathways between laser levels in Er and resonantly-matched energy levels in Pr.

Diode-pumped high-power CW mid-IR fiber lasers using cross-relaxation and energy transfer processes:

We have proposed and demonstrated an efficient and novel depopulation mechanisms for the lower laser level via cross-relaxation (#1) of Er ions at high doping densities (Fig. 8a) and energy transfer to co-doped Pr ions (Fig. 8b).

Ion clustering at high doping densities:

The cross-relaxation process in Er shown in Fig. 8a was believed to be significant only at concentrations of >150,000 ppm in bulk glasses. Such concentrations however lead to high intrinsic losses in fibers. On the other hand, our studies show significant percentage of ions in clusters even at concentrations of 10,000 ppm in fibers, thereby facilitating the cross-relaxation process to depopulate the lower laser level of the 2.7 μm transition in Er.

Key Accomplishments:

We performed a precise quantification of the percentage of ion clusters in Er-ZBLAN fibers via measurement of non-saturable optical absorption and fitting of the data to a simple theoretical model for ions in clusters (Fig. 9).

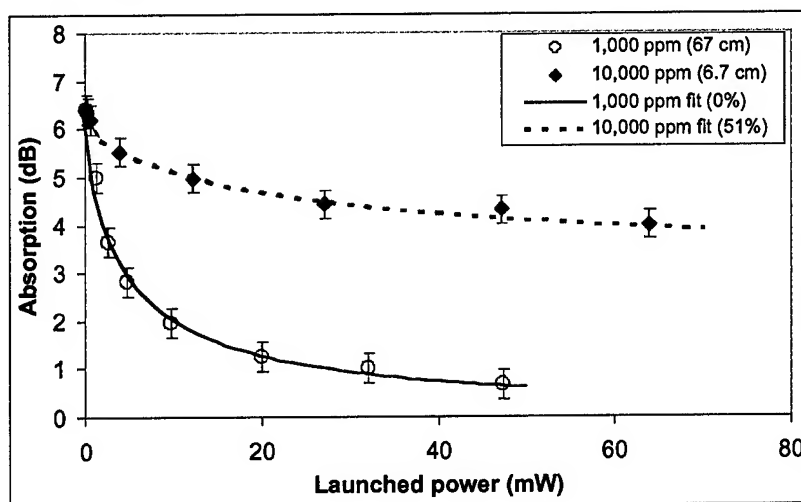


Fig. 9: Plot of the measured and calculated values of the absorption at 972 nm radiation as a function of launched power in two fibers corresponding to significantly dif-

We have demonstrated the presence of 51% ions in clusters for fibers with an average doping density of 10,000 ppm, whereas a similar fiber with an average doping density of 1,000 ppm shows negligible effects of clustering.

Single transverse mode diode pumping at 980 nm :

Key Accomplishments:

We have demonstrated a relatively efficient power-scalable 2.7 μm 10,000 ppm Er-ZBLAN fiber laser pumped by readily available 1W 980 nm laser diodes.

The 12 mW CW power levels and 6.7% slope efficiency reported are significantly higher than those reported previously for any diode-pumped mid-IR fiber laser.

The linearity of the output power even at high pump powers used indicates that this laser can be further optimized to yield much higher output powers.

Diode array pumping at 795 nm:

Key Accomplishments:

We have utilized the enhanced inter-ion cross-relaxation in 20,000 ppm double clad Er-ZBLAN fibers for the realization of high-power (400 mW) diode-pumped 2.7 μm mid-IR lasers.

The fiber laser was demonstrated with a slope efficiency of 12% with respect to the absorbed power and a threshold of 250 mW.

Diode-pumped high-power CW mid-IR fiber lasers using cross-relaxation and energy transfer processes:

Key Accomplishments:

We have utilized energy transfer to Pr ions along with enhanced inter-ion cross-relaxation to depopulate the lower laser level more efficiently.

We have demonstrated a high power (660 mW) CW operation of a diode-pumped 20,000 ppm/5,000 ppm Er/Pr:ZBLAN 2.7 μm fiber laser with a slope efficiency of 13% with respect to the absorbed power (Fig. 10). The linearity of the plot clearly indicates scalability to multi-Watt power levels using high pump powers or more efficient pump coupling and pump absorption techniques.

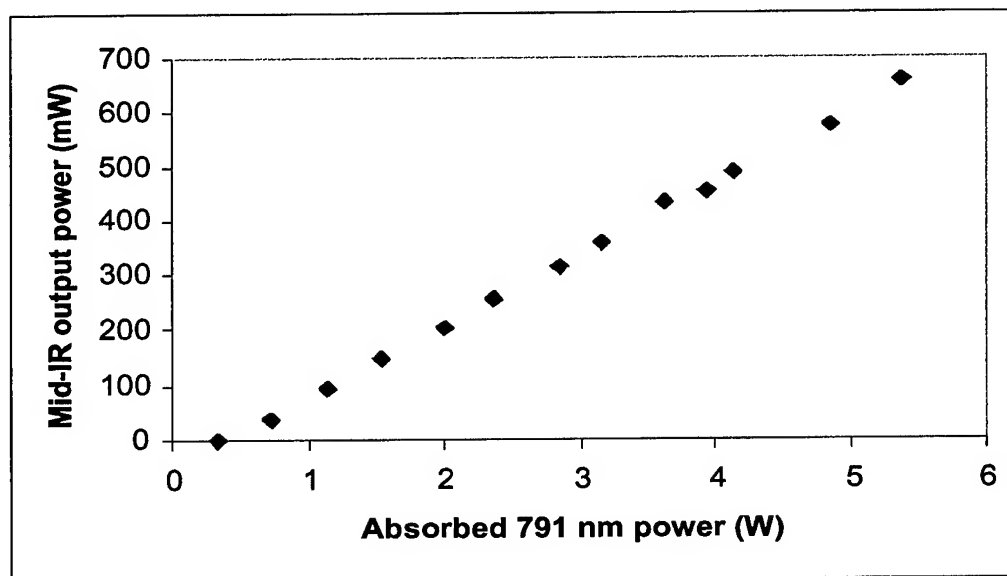


Fig. 10: CW 2.7 μm output power vs. absorbed 791 nm pump power

Passive Q-switching of mid-IR fiber laser:

Compact mid-IR pulsed laser sources with emission wavelengths in the vicinity of 3 μm mid-IR water absorption peak are needed for a number of medical applications.

Key Accomplishments:

We recently reported the first observation of passive Q-switching (7 μ s pulsewidth, 35 kHz repetition rate) of a mid-IR Er-ZBLAN fiber laser (Fig. 11). Passive Q-switching was achieved by using a liquid gallium mirror as a saturable absorber⁹

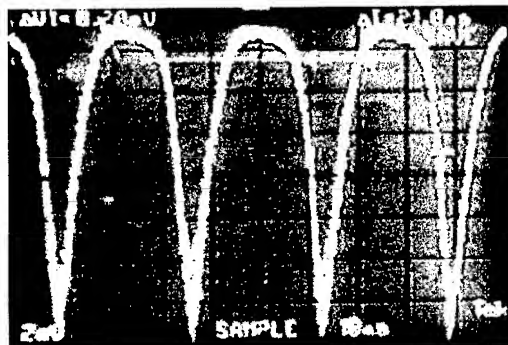


Fig. 11: Pulsed operation of a passively Q-switched Er:ZBLAN 2.8 μ m fiber laser

Wavelength tunable mid-IR fiber laser:

Tunable operation of a diode-pumped mid-IR Er-ZBLAN fiber laser in the vicinity of 2.8 μ m is needed for high sensitivity spectroscopic detection of important trace gases such as HF, NO, water vapor.

Key Accomplishments:

We recently reported tunable operation of a diode-pumped mid IR Er-doped ZBLAN fiber laser using a bulk grating in the Littrow configuration.

The output wavelengths were tunable from 2.71 μ m – 2.83 μ m with powers varying from 1 mW – 30 mW (Fig. 12). The tendency of the laser to shift to longer wavelengths at higher pump powers is presumably due to re-absorption effects and saturation of the lower energy levels of the $^4I_{13/2}$ manifold.

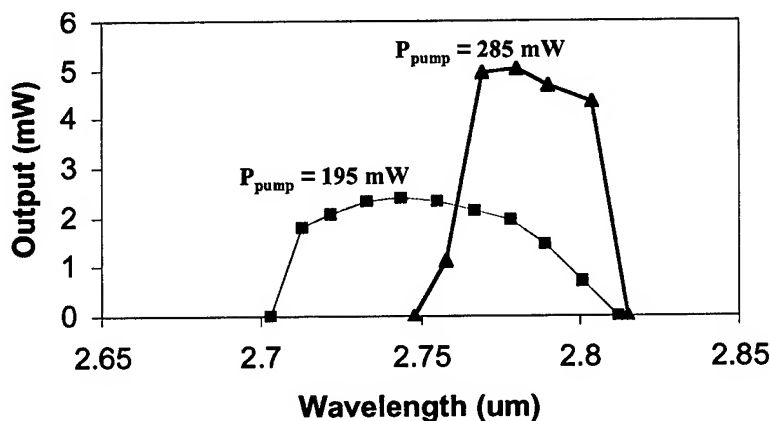


Fig. 12: Tuning curves for diode pumped Er:ZBLAN fiber laser at two different 790 nm

E. Advanced Fiber Optic Devices

Goal: Research and development of manufacturable, high-performance all-fiber modulators and all-fiber tunable filters for reconfigurable fiber interconnects and "smart" fiber networks.

Thermally stable fiber Bragg gratings (FBGs):

Goal: To improve the thermal stability of FBGs.

Background: The focus of our work is to improve the stability of "fixed FBGs" (to be used subsequently as tunable filters). In particular, we studied several key issues regarding the thermal stability of FBGs, as elaborated below. The thermal stability of FBGs is an important issue for the fabrication of electro-optically tunable FBGs since the as-fabricated FBGs are subjected to temperatures of $\sim 300^\circ\text{C}$ during the thermal poling process (used to make such FBGs electro-optically tunable).

The high-contrast UV interference patterns used to fabricate FBGs are believed to create an index modulation in the fiber via a light-induced distribution of defects. The defects are distributed in shallow trap sites (low activation energy, E_a) and deep trap sites (higher E_a). Upon annealing at elevated temperatures, the lower E_a trap sites and the corresponding index components vanish, leaving behind only $<20\%$ of the original index modulation. If the fiber is illuminated by supplementary uniform UV radiation, shallow defects are also formed in the nulls of the interference pattern, reducing the amount of subsequent redistribution from the peaks of the interference pattern, resulting in a more stable "permanent" refractive index modulation. Such a stabilization technique has been demonstrated by Salik et al¹⁰ for weak ($\Delta n \sim 10^{-5}$) Bragg gratings fabricated in non-hydrogen-loaded fibers.

Key Accomplishments:

We have demonstrated a technique (similar to Salik et al) for fabricating thermally-stable strong ($>10^{-3}$) FBGs in hydrogen-loaded fibers by using a phase mask that transmitted $\sim 20\%$ of the zero order. Fig. 13 shows the superior stability of an FBG fabricated by the above-described method when compared to an FBG fabricated in a similar fiber¹¹ using a holographic method (in which the zero order transmission was suppressed). The higher mean activation energy, $E_a = 2.9$ eV, for trap sites in our work relative to the $E_a = 1.6$ eV inferred for trap sites in Patrick et al. (Fig. 14) is

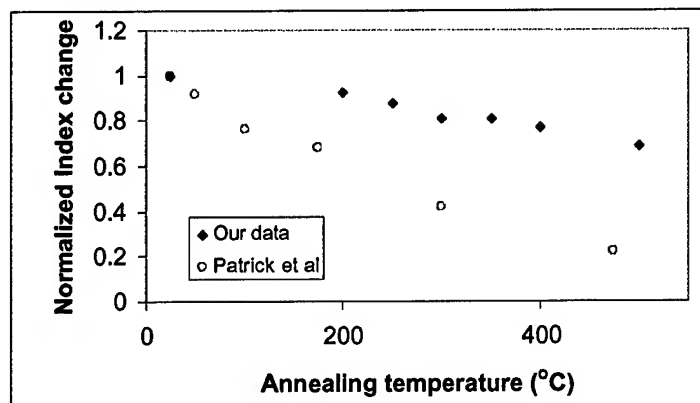


Fig. 13: Results of annealing studies illustrating the superior stability of FBGs fabricated using our technique when compared to the high-

further confirmation of the superiority of our FBG fabrication technique in hydrogen-loaded fibers. We also observe that the defects responsible for the FBG fabricated in 5% GeO_2 -doped fiber have higher mean activation energy (Fig. 15, 3.2 eV vs. 2.4 eV for higher GeO_2 conc.). Such an observation indicates that the FBGs fabricated in fibers with relatively low GeO_2 concentration exhibit superior thermal stability.

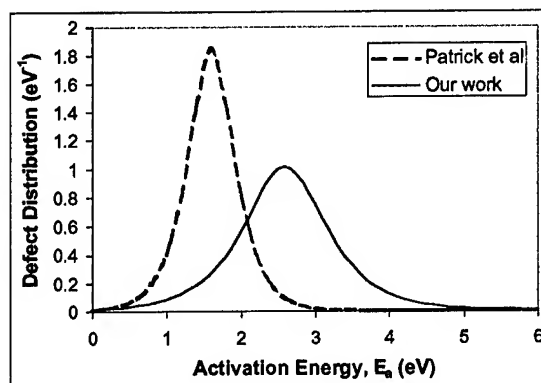


Fig. 14: Plot of the estimated defect distributions (obtained using the model of Erdogan et al. as a function of the activation energy, E_a , for our data as well as that of Patrick et al.¹¹

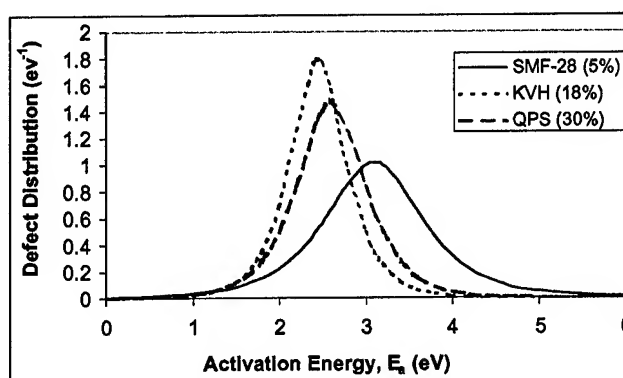


Fig. 15: Distribution of defect activation energies for FBGs fabricated under similar conditions in fibers with three different GeO_2 concentrations.

F. Electrically—tunable fiber Bragg gratings

Goal: To fabricate Bragg gratings at 1550 nm in D-shaped fibers, to pole the fiber Bragg grating, and to demonstrate tunability of 10 GHz (80 pm) using voltages of the order of 100 V.

Key Accomplishments:

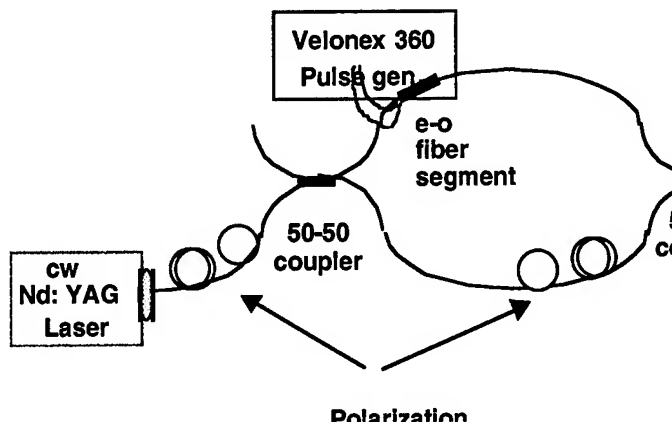
We have demonstrated electro-optic tuning of a FBG fabricated in a thermally-poled fiber. 40 pm of tuning was achieved, corresponding to an electro-optic coefficient of 0.25 pm/V.

To eliminate the possibility of the observed tuning due to thermal or piezo-electric effects, we observed the tuning of FBG as a function of reversed polarities. The tuning in opposite directions corresponding to the reversed polarities confirms the electro-optic tuning mechanism.

2x2 All-Fiber Electrooptic Switch

Recently, we demonstrated an all-fiber switch employing a poled electrooptic fiber segment. A Mach-Zehnder interferometer with a poled electrooptic fiber segment in one arm is formed using commercial 2x2 fiber directional couplers. In the preliminary experiments reported there, the poled segment was fabricated independently, in Andrew Corp. D-fiber, then butt-coupled to pigtails, resulting in an undesirable 5 dB loss that we compensated with a following fiber amplifier. The switch speed was around 2 Mhz with 2 kV switching voltage.

Here, we report an improved result with further iterations in the fabrication process. As illustrated in Figure 17, a Mach-Zehnder interferometer is formed using commercial 2x2 fiber



directional couplers. Two mechanical controllers, one in the reference arm, one in the input port, were used to adjust the polarization state. A cw YAG laser at $1.06\ \mu\text{m}$ provided the optical source.

An RF metal strip line, defined using standard lithography techniques, was deposited atop a 6-cm long D-side of the fiber for high voltage poling and high speed modulation. After the metal line was deposited on the fiber, the fiber was affixed, D-side down, to a silicon wafer using a thin layer of polyimide. Additional layers of polyimide were spun on and cured until the fiber was totally surrounded by polyimide. The total fiber thickness was then polished down to $20\ \mu\text{m}$. Finally, the fiber was inverted and remounted on a silica glass plate with a blanket deposited metal film and layers of polyimide were spun on and cured. The fiber was poled by applying a high voltage (3 kV) between the top microstrip line electrode and the bottom metal-film ground electrode with the fiber heated to 250°C . After a ten minute poling time, the fiber was allowed to cool with the voltage applied. Additional segments of Andrew e fiber were subsequently butt-coupled to either end. These were spliced to Flexcore 1060 segments, to match the 3dB couplers forming the interferometer.

Figure 18 shows the switching voltage to be 1.4 kV. The measured extinction is $\sim 15\ \text{dB}$, this low extinction ratio may be caused from poor balance of light intensity in the two arms. Figure 19 shows an expanded view of the rise time, the optical signal risetime of 30 ns (solid line) is indistinguishable from the rise time of the applied voltage (dotted line). The measured total capacitance C is 16 pF, including the capacitance between the metal RF strip line and ground electrode and the capacitance between connection pads. The electrical resistance R of the RF strip line is $150\ \Omega$, giving an RC rise time of 5.3 ns, consistent with the measurement. The measurement puts a lower bound of 150 Mhz on the bandwidth of the poled fiber switch.

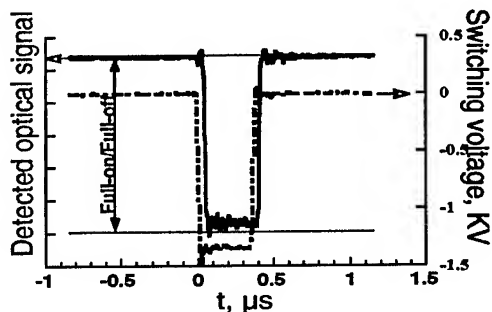


Fig. 18: Detected signal and applied voltage pulse.

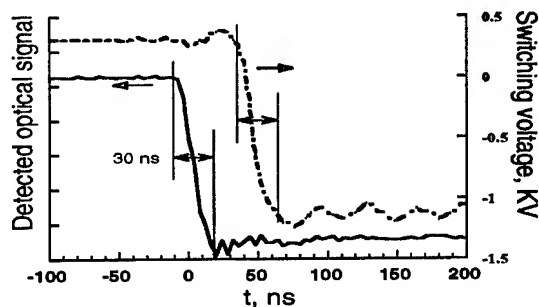


Fig. 19: Expanded view of rise times of both signals. The switch turn on time is limited by the applied voltage pulse.

G. Nanoheteroepitaxy: A Revolutionary Approach to Lattice-Mismatched Heterostructure Growth

During this program we have developed the theory and practice of a new technology for the elimination of mismatch defects in lattice-mismatched heterostructures. We call this approach Nanoheteroepitaxy (NHE).¹² NHE combines three-dimensional stress relief mechanisms, that are uniquely available in nanoscale (< 100 nm) islands, with strain partitioning between the epitaxial layer and the substrate, to achieve a dramatic reduction in the stored strain energy and associated defect density.

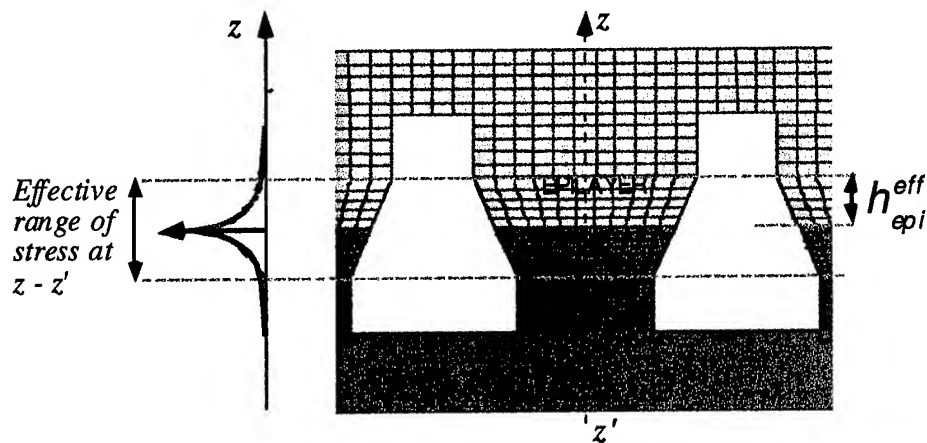


Fig.20: A generic nanoheteroepitaxy sample showing partitioning of mismatch strain between the epilayer and substrate. The exponential decay of strain away from the heterointerface results from 3-D stress relief mechanisms that are unique to NHE.

In the generic NHE approach (Fig. 20), a single crystal substrate is patterned into nanoscale islands separated by a selective growth mask. Selective epitaxy nucleates the epilayer only on top

of the islands. As the layer grows it is able to deform in 3D because it is so small¹³, and the mismatch stress decays exponentially on either side of the heterointerface. Once the epilayer thickness exceeds the stress decay length, it is no longer strained and further growth does not increase the stored strain energy. The creation of mismatch defects, e.g., dislocations or stacking faults, requires a minimum strain energy. In the NHE approach this strain energy is dramatically reduced and for many highly mismatched materials it remains too low to form mismatch defects.

Once the epilayer thickness exceeds the effective stress range, the epitaxial growth conditions are modified to promote lateral growth and coalescence as shown at the top of Fig.20. As the effective range of strain is very small in NHE samples (typically < 50 nm) this coalescence can be accomplished when the epilayer is typically ~ 100-nm thick, where it is still compliant. Thus in NHE, we anticipate that coalescence can also be achieved without defect formation. Coalescence in NHE is very different than in the recently developed lateral epitaxial overgrowth techniques.^{14,15} In the latter, coalescence occurs for layers that are already several- μm thick and generally results in a highly defected region. XTEM investigation of the coalescence of OMVPE-grown, GaN on SOI, NHE islands (see Fig. 21) supports our expectation and indicates that the coalescence boundary has the potential to be defect free.

NHE is a generic approach applicable to a wide range of important semiconductor materials including: AlGaInAs/Si; AlGaInN/Si; GaInAsSb/Si; and SiGe/Si. In each case the large lattice mismatch between the constituent materials has previously placed severe limits either on the thickness of films or on the minimum achievable defect concentration. Our NHE theory^{ix} predicts that these limitations can be relaxed significantly, if not eliminated, using the NHE approach.

Initial Results for NHE GaN/Si

NHE is itself enabled by CHTM's advanced interferometric lithography capability for nanoscale patterning and the availability of this unique capability has allowed us to experimentally test the NHE theory for the extremely mismatched combination of GaN on Si (20 % lattice mismatch.). We have used our established capability in GaN OMVPE growth^{16,17} and developed a novel sample structure specifically for GaN on Si (fig 2.)

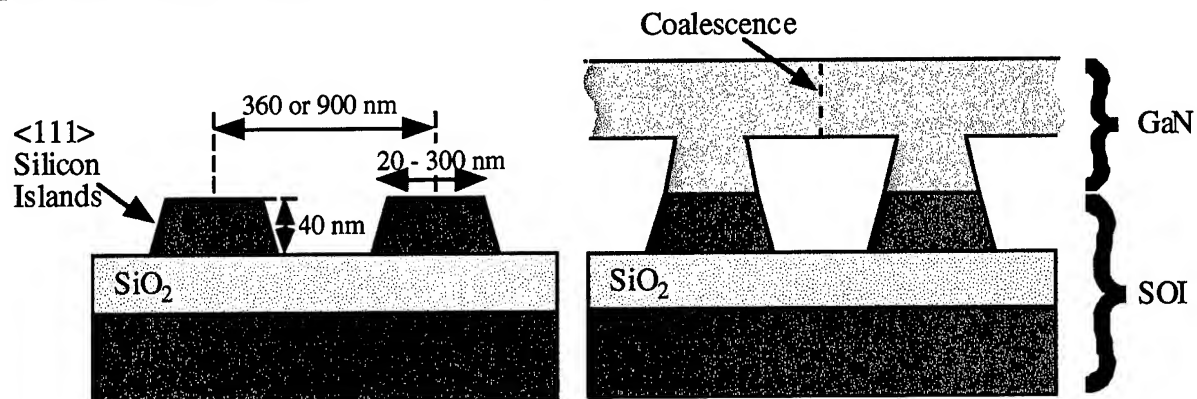
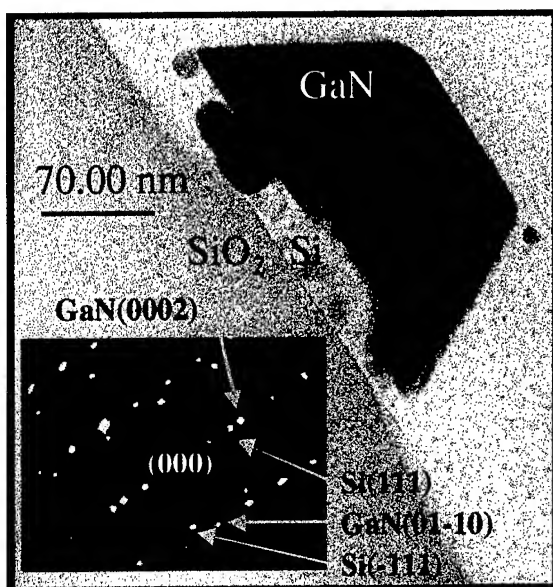
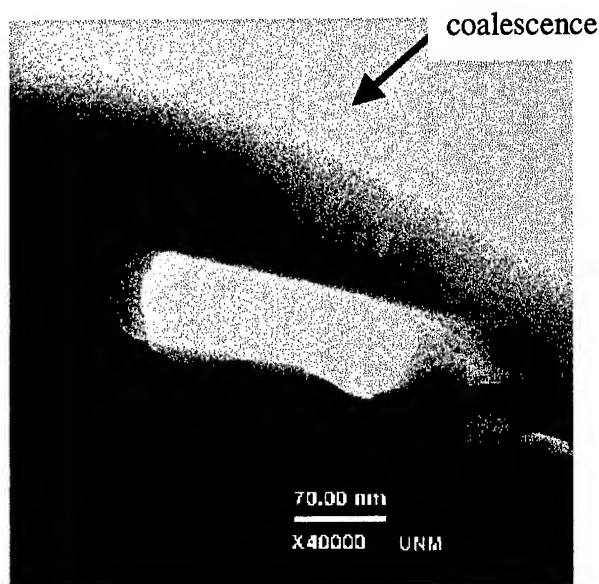


Figure 21: Schematic representation of NHE <111> SOI substrate (left) and GaN film growth stages showing island nucleation and coalescence.

The SIMOX SOI wafers were patterned using interferometric lithography and reactive ion etching to form a 2-dimensional array of $\langle 111 \rangle$ silicon islands on top of a field of SiO_2 . The height of the islands is 40 nm and diameters in the range 20 to 300-nm are being investigated. The array period of present NHE samples is 360 or 900 nm. GaN is selectively nucleated on the silicon islands using a three step sequence consisting of; an *in-situ* cleaning at a temperature of 878°C for 5 min. in hydrogen, a low temperature (543°C) nucleating layer deposition and, finally, main epilayer growth at high temperature (1031°C). This yields a GaN island thickness of approximately 100 nm prior to coalescence. The exposed SiO_2 layer in the SOI serves as a convenient mask for the selective nucleation of GaN.



A. (b)



B) Coalescence of two GaN islands

Fig. 22: a) Individual GaN/Si nanoisland.

Figure 22a shows GaN growth on a 70-nm diameter Si island. A defected region is observed near the heterointerface. Beyond this region, the decaying strain field (as predicted by NHE theory) is clearly observed. The inset in Fig. 22a is an electron diffraction micrograph taken at the heterointerface and showing the epitaxial alignment of the $\langle 111 \rangle$ Si and $\langle 0001 \rangle$ GaN directions. Figure 22b shows the coalescence region between two GaN on Si islands. The GaN in this region contains localized defects, possibly nanopipes, but these defects do not propagate in the growth direction. Thus it appears that in the case of a highly mismatched system such as GaN/Si (20% mismatch) the mismatch defects remain localized at the heterointerface.

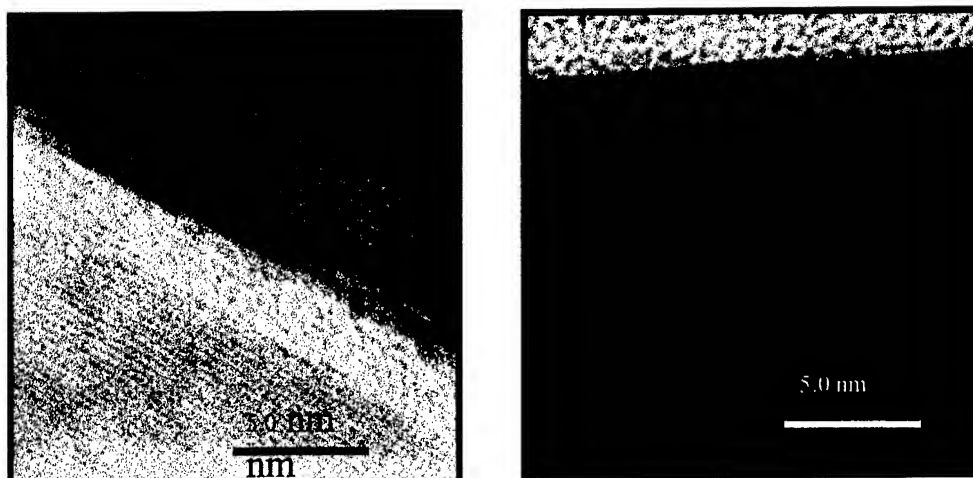


Fig. 23: High resolution TEM reveals defects are located close to the hetero-interface (left). The top surface of the GaN (right) is undefected.

Figure 23 shows high-resolution XTEM micrographs of a GaN nanos island grown on a 300-nm diameter Si island. The defects formed at the interface (left) are in-plane, stacking-fault type defects indicating that defect formation in the NHE sample is also very different to defect formation in the normal planar sample. It is often the case that the closest free surface plays an integral role in the formation of crystalline defects. In the NHE sample the closest surface is generally the edge of the nanos island (rather than the epilayer surface) and this might well be a cause of the unusual orientation and nature of the defect structures seen in our NHE GaN/Si samples. These defects should be contrasted with those formed during conventional planar growth of GaN on sapphire or on silicon, where the mismatch defects are frequently edge type dislocations that propagate vertically in the $\langle 0001 \rangle$ direction.¹⁸ This figure also shows that the majority of the mismatch defects appear to be in the Si side of the heterointerface, verifying the NHE hypothesis that the Si nanos island will be highly compliant. Away from the interface (Fig. 23, right) the GaN is defect free and unstrained as predicted by NHE theory.

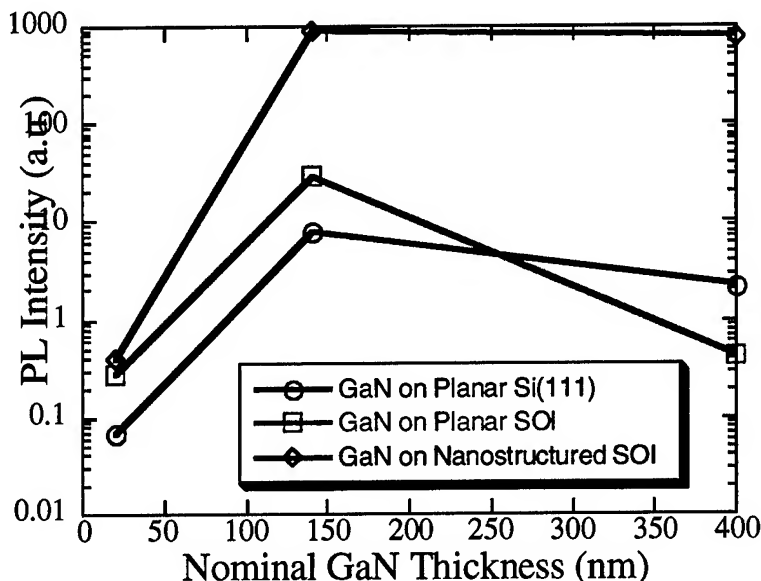


Fig. 24: PL intensity in the NHE sample is much higher and is sustained for thicker layers indicating no new defect formation as layer thickness grows.

Photoluminescence measurements on NHE GaN on Si (Fig 24) show a dramatic increase in intensity compared to PL on GaN grown on planar Si. Figure 24 shows the band-edge (360 nm) PL intensity (300K) for three samples. The highest intensity was measured for the NHE sample and importantly this high intensity is sustained as the GaN layer is grown thicker. For the planar samples (GaN grown on SOI (compliant substrate) and GaN grown on Si) the intensity is lower and falls for epilayer thickness > 150 nm, possibly indicating additional defect formation.

Conclusions

Our experimental results for GaN on Si using the NHE approach are very encouraging. Many of the predictions of the NHE theory have been confirmed (the decaying strain field (Figure 20a), the super compliance of Si-nanoislands (Figure 22a), the unusual defect structure (Figure 13) and the dramatically enhanced PL intensity (Fig. 24). While GaN on Si, with a lattice mismatch of 20%, is an extreme example of mismatched heteroepitaxy; these results give us confidence that less strained materials, such as GaAs on Si, will also follow the predictions of NHE theory. In fact our theory predicts that GaAs on Si can be grown defect free if the nanoisland diameter is reduced to 40 nm. This is within the range of our interferometric nanostructuring capability and will be attempted in future studies.

Our published NHE model^{ix} lays out a solid framework for calculating the strain energy at the heteroepitaxial interface for the NHE structure. While our experimental work with the highly mismatched GaN on Si system has confirmed many of the predictions of the NHE theory, it also suggests that the actual strain energy is less than predicted by the model. Furthermore, preliminary studies of coalesced GaN (Fig. 11) indicate that even when defects are formed at the heterointerface, they can be localized at this interface and may not affect the performance of devices grown in the epilayer above them. Part of the overestimate of strain energy by the NHE theory

stems from our conservative approach. For example, we sum the strain energy in the epilayer and the strain energy in the substrate and assume that the total strain energy acts at only at the heterointerface. Furthermore, we calculate the total strain energy at the center of the nano-nucleus, where the strain energy per unit area is a maximum. In practice there will be a decrease of strain energy per unit area towards the edge of the nucleus, which will mean that the average value of this quantity will be lower than the maximum value at the nucleus center. However, a more significant source of disagreement between theory and experiment, that is especially relevant to GaN on Si, is the phenomenon that we have recently identified¹⁹ and we call "active compliance". Clearly, much work remains to be done in improving the accuracy of the NHE model and in the experimental application of NHE to other mismatched heterostructures.

H. Influence of the Microstructure on Transport Properties of p-type GaN:Mg

We have presented an analysis of the hole transport in p-type Mg-doped GaN grown on sapphire substrates by metal-organic-chemical vapor deposition (MOCVD). We found that the experimental Hall mobility cannot be explained solely by traditional extended state scattering mechanisms. Not only are the mobilities not accurately modeled by numerically solving the Boltzmann transport equation (BTE), but the calculated results do not even reflect the trend in experimental mobility values between the investigated samples. We attributed these discrepancies to the microstructure of GaN:Mg grown on sapphire. A microstructure-oriented transport model was presented for an interpretation of the transport of holes in p-type GaN:Mg grown on sapphire. The microstructure-oriented model provides a simplified picture of the microstructure, consisting of two distinct microstructural phases in GaN on sapphire. Using this model for the experimental mobility, the extracted parameters from hole transport measurements were shown to be positively correlated with microstructural parameters determined from x-ray diffraction (XRD) measurements. The experimental mobility of p-type GaN:Mg grown on sapphire can be described as dependent upon the acceptor doping, impurity compensation, and microstructure, including dislocation density, columnar grain size, and grain boundaries.

With improved growth of GaN, the material will approach ideal single crystal quality. In these cases the mobility of p-type GaN:Mg should be well described by traditional extended state scattering mechanisms. The calculated mobility for crystalline p-type GaN:Mg with an activation energy of 150 meV and compensation ratio of $K = 0.1$ is constant with a value of ~ 120 cm²/Vs for substitutional Mg doping less than 1×10^{18} cm⁻³ at 300 K. The calculated conductivity shows an upper limit of 10 (Ω cm)⁻¹ at 300 K and 30 (Ω cm)⁻¹ at 500 K. These results imply that as the growth of p-type GaN:Mg improves, GaN devices that include p-type GaN:Mg will still possess a high spreading resistance.

In addition, we investigated the noise properties of p-type Mg-doped GaN using low frequency noise spectroscopy. The epitaxial GaN:Mg films were grown on a sapphire substrate by metal-organic chemical vapor deposition (MOCVD) in different laboratories. Generation-recombination (g-r) noise and $1/f$ noise were observed for temperatures above 250 K. The magnitude of the $1/f$ noise exceeds the g-r noise magnitude for frequencies less than 30 Hz, and the $1/f$ noise level was characterized by high values of the Hooge parameter, $\alpha \approx 1 - 150$, indicating a high level of structural imperfection. In addition, the integrated noise power spectral density divided by the voltage squared in the frequency range of 1 Hz to 30 Hz, correlated strongly with

the structural imperfection of the sample as measured from the asymmetric rocking curve (ω -scan) FWHM. The generation-recombination noise was related to a high concentration trap level with an activation energy of $120 \text{ meV} \pm 25 \text{ meV}$ and a repulsive barrier that is possibly associated with the Mg dopant.

I. High-Power Diode-Pumped Mid-IR Fiber Lasers

Summary:

We developed innovative high concentration Er:ZBLAN material designs in the first half of the program culminating in mid-infrared fiber lasers with Watt-type CW output power levels. Based on these innovative materials, we continued with work on diode-pumped tunable and pulsed mid-infrared fiber lasers. Widely tunable ($\sim 140 \text{ nm}$) mid-IR laser sources were demonstrated and progress towards compact monolithic fiber Bragg grating -tunable laser sources was shown. Active and passive mid-IR pulsed laser sources were also demonstrated using a custom designed acousto-optic modulator and a novel saturable absorber. These mid-IR pulsed lasers hold promise as compact diode-pumped master oscillators in future MOPA (Master Oscillator Power Amplifier) pulsed mid-IR source designs.

Development of High-Concentration Er:ZBLAN fibers for Efficient High-Power Lasers:

Goal: To design Er:ZBLAN fiber materials with more favorable lifetime ratios leading to more efficient diode-pumped high power mid-IR sources.

The $2.7 \mu\text{m}$ transition in Er-ZBLAN is particularly attractive for the design of compact, high-power mid-IR fiber lasers of excellent beam quality as needed for applications ranging from laser surgery to countermeasures and spectroscopic monitoring.

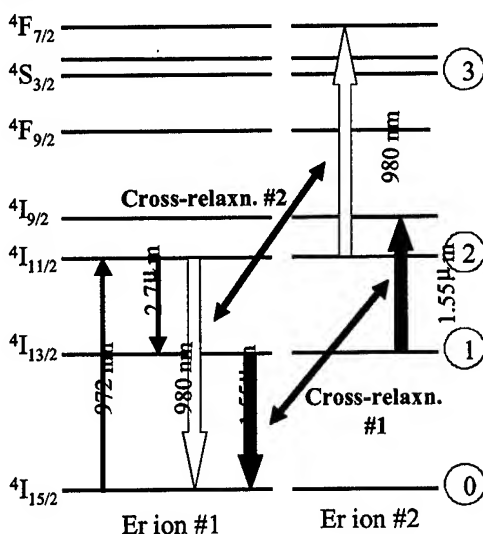


Fig. 1: Energy level diagram of Er showing dominant cross-relaxation

The problem with the $2.7 \mu\text{m}$ laser transition in Er is the fact that the natural lifetime of the lower laser level (9.4 ms) is longer than that of the upper laser level (7.5 ms), leading to a population bottleneck that inhibits efficient steady-state (CW) lasing in Er:ZBLAN fiber lasers.

Our laser material designs rely on the cross-relaxation process in Er shown in Fig. 1a, this was believed to be significant only at concentrations of $>150,000 \text{ ppm}$ in bulk glasses. Such concentrations however lead to high intrinsic losses in fibers. On the other hand, our studies showed significant percentage of ions in clusters even at concentrations of $10,000 \text{ ppm}$ in fibers, thereby facilitating the cross-relaxation process to depopulate the lower laser level of the $2.7 \mu\text{m}$ transition in Er.

- We proposed and demonstrated efficient and novel depopulation mechanisms for the lower laser level via cross-relaxation (#1) of Er ions at high doping densities (Fig. 1) and energy transfer to co-doped Pr ions (Fig. 2).

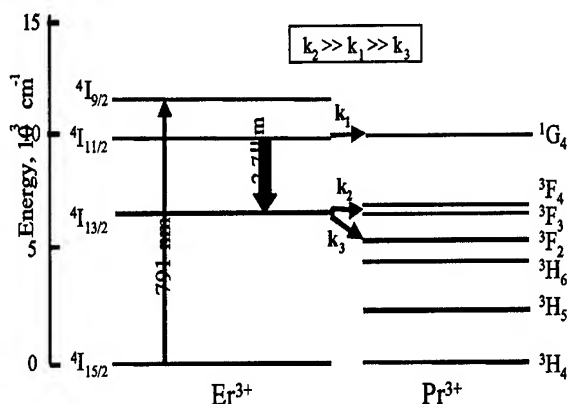


Fig. 2: Dominant energy transfer pathways between laser levels in Er

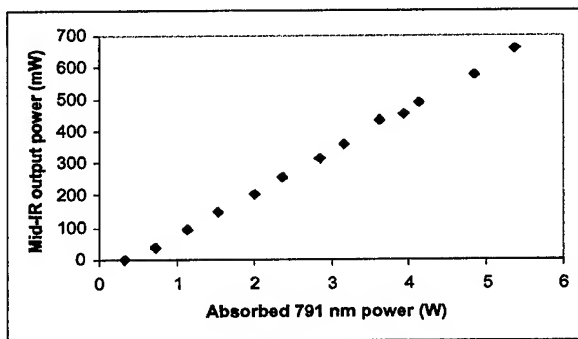


Fig. 3: CW 2.7 μ m output power vs. absorbed 791 nm

sorption techniques.

- We performed a precise quantification of the percentage of ion clusters in Er-ZBLAN fibers via measurement of non-saturable optical absorption and fitting of the data to a simple theoretical model for ions in clusters. We measured and calculated values of the absorption at 972 nm radiation as a function of launched power in fibers corresponding to significantly different mean Er concentrations. Our results implied the presence of 51% ions in clusters for fibers with an average doping densities $> 10,000$ ppm, whereas similar fibers with average doping densities of 1,000 ppm showed clustering.

- We utilized energy transfer to Pr ions along with enhanced inter-ion cross-relaxation to depopulate the lower laser level more efficiently. Using such high-Er-concentration Pr co-doped materials, we demonstrated high power (660 mW) CW operation of a diode-pumped 20,000 ppm/5,000 ppm Er/Pr:ZBLAN 2.7 μ m fiber laser with a slope efficiency of 13% with respect to the absorbed power (Fig. 3). The linearity of the plot clearly indicates scalability to multi-Watt power levels using high pump powers or more efficient pump coupling and pump ab-

Demonstration of Tunable Mid-Infrared Fiber Laser:

Goal: To demonstrate a compact diode pumped wavelength tunable mid-infrared fiber laser. Such lasers have applications which include ultra-sensitive mid-IR spectroscopy (ie. OH detection in glass preforms, ppt water vapor detection in semiconductor manuf. processes), and optical pumping of molecular gas -based THz radiation sources.

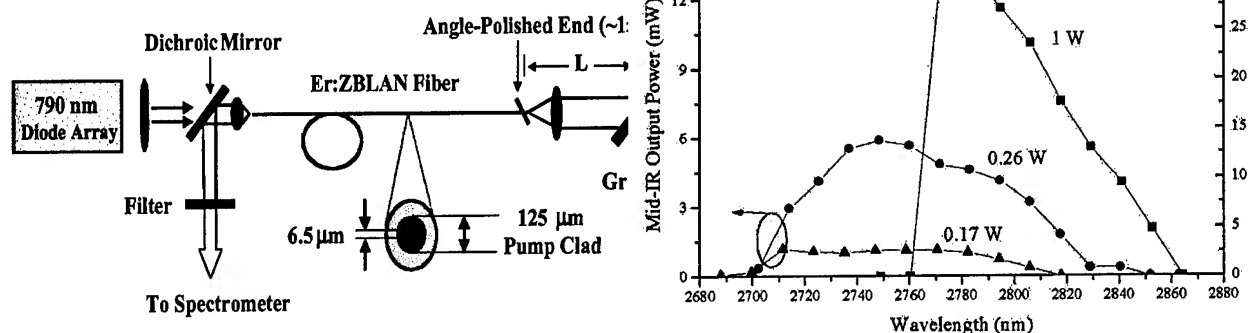


Fig. 4 (a) Schematic of tunable diode pumped laser (b) Tuning curves at various P_{pump} values

- We demonstrated a wavelength-tunable fiber laser (Fig 4a) using innovative high-concentration (20,000 ppm mean doping density) Er-doped fluoride fibers. The fibers were custom designed for high power diode pumping via the use of double clad fiber geometries.
- Output powers (Fig. 4b) greater than 1 mW were achieved over a 140 nm (2.71 μm - 2.85 μm) tuning range, with maximum output powers as high as 30 mW. The emission linewidths were less than 0.1 nm (resolution-limited). The laser is seen to operate more efficiently at longer wavelengths with increased pump power. This tendency for the laser spectra to shift to longer wavelengths at high pump powers has been observed before even in erbium-doped bulk glass and fiber lasers without any intracavity tuning elements. This is presumably due to increased dominance of the gain for the emission from the more heavily populated lower Stark levels of the $^4I_{11/2}$ manifold, and the spectral dependence of the inter-ionic cross-relaxation processes that depopulate the $^4I_{13/2}$ lower lasing level and repopulate the ground state.

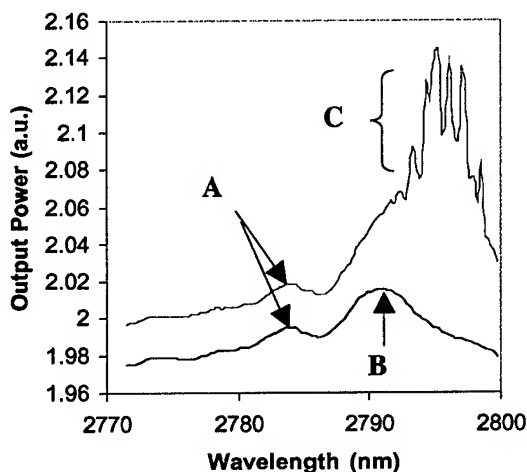


Fig. 5. Fluorescence spectra at two 790 nm launched pump powers: 0.7 W & 1 W. Feature A corresponds to FBG peak reflection.

- A phase mask was designed and procured for UV-photoinscription of silica fiber Bragg gratings (FBGs) with reflective peaks at 2.8 μm. In Fig 5 we show indirect evidence of UV-written fiber Bragg gratings (FBG) in the mid-infrared. The FBGs

were mechanically spliced to a broadband mid-IR source optically pumped below threshold. Fluorescence features (B and C) were observed to shift to longer wavelengths at high absorbed pump powers, as is consistent with our tunable laser results, while fluorescence peak A stays constant at the design wavelength for the FBG peak ($\sim 2.785 \mu\text{m}$). When the FBG is removed from the setup, this fluorescence feature (peak A) was not observed. Several FBGs were fabricated and further efforts are currently underway to directly characterize the devices (i.e. via transmission experiments and visible light diffraction experiments), to reduce mechanical splice losses between ZBLAN and silica, and to strain-tune the gratings for application in all-fiber mid-infrared laser sources.

J. Inductive and capacitive grids for 2-5 μm spectral regime

Introduction

Metallic inductive and capacitive grids have long been used in the microwave regime as filters. With the advent of microlithography techniques (interferometric lithography, being one important example) it is now possible to make these devices for the near infrared and optical wavelengths. The importance of these structures is underscored by recent research, which has shown that sub-wavelength inductive grids display²⁰ interesting physical properties in the visible and may be used to make novel optoelectronic devices²¹. In addition, these subwavelength devices have the potential for behaving as composite materials having values of permittivity and permeability not normally found in nature²².

Here we present our experimental and numerical work on sub-wavelength metallic inductive and capacitive grids for 2-5 μm spectral range. These biperiodic gratings are made on a silicon substrate using interferometric lithography; a technique well suited to the periodic nature of these structures. The transmission spectra of these metallic grids are characterized using Fourier transform infrared spectroscopy (FTIR).

RCWA Modeling

Given that the size of these grids is comparable to or smaller than the illuminating wavelength, we use a rigorous electromagnetic model. One of the simplest and perhaps the most versatile such model uses a Fourier basis to represent the electromagnetic fields, and is variously known as Fourier modal method or rigorous coupled wave analysis (RCWA). We have developed this model to characterize structures having two-dimensional periodicities such as metallic grids as well as structures having three-dimensional periodicities. The focus of this report however will be restricted to modeling and characterization of two-dimensional subwavelength metallic inductive and capacitive grids.

Figure 1a shows the experimental transmittance spectrum and numerical modeling (using RCWA) for one of our capacitive grids. Although the model depicts the important features of the transmittance spectrum there is a quantitative difference in the transmittance as obtained experimentally and the numerical model. This difference is attributed to the fact that we are taking the silicon substrate to be infinite in the numerical model. This is typical in modeling diffraction from periodic structures but becomes inappropriate when the substrate is essentially transparent in the wavelength range of interest and has a high refractive index ($n \sim 4$) leading to large reflected beams and multiple reflections within the substrate.

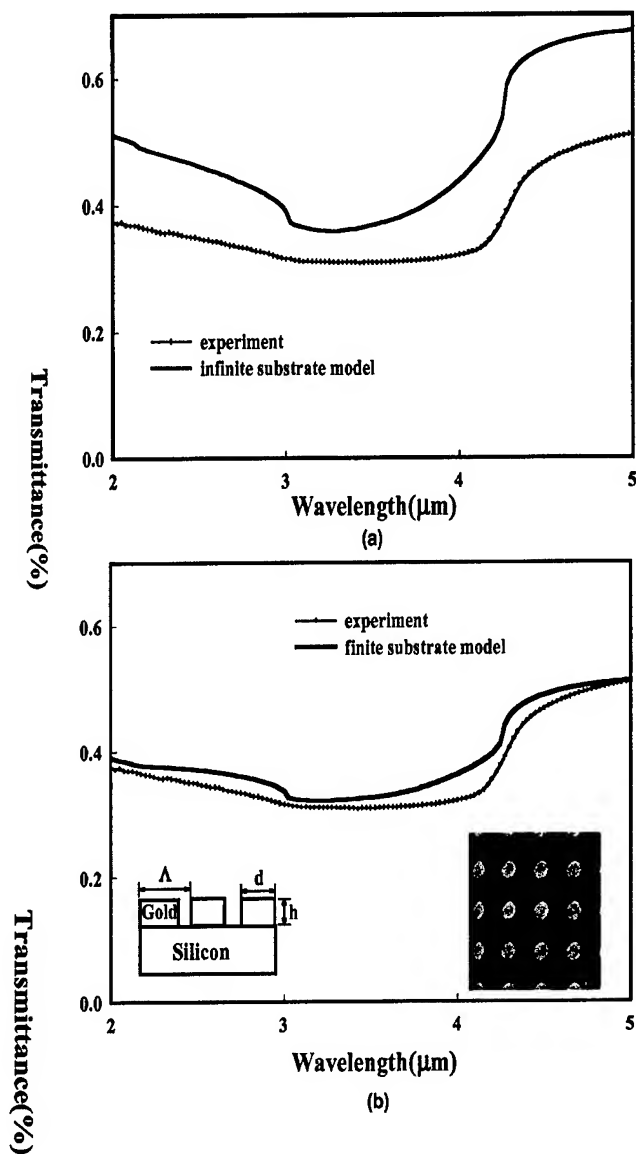


Figure 1: Experimental and rigorous modeling results for transmittance through a capacitive grid of circular gold scatterers on a silicon substrate. Referring to the inset in the figure $\Lambda = 1.24 \mu\text{m}$, $h = 0.1 \mu\text{m}$ and diameter of the gold scatterers obtained from SEM measurement is $0.54 \mu\text{m}$ and from mean square fitting of the numerical model to experimental data is $0.50 \mu\text{m}$. The wavelength resolution for numerical model is $0.025 \mu\text{m}$. Part (a) shows the numerical modeling taking the silicon substrate to be infinite, while part (b) takes the silicon substrate to be finite.

For our chosen experimental conditions the thickness of the silicon substrate is much larger than

the coherence length of the incident light. Therefore the suitable way to model the effect of finite substrate is to do an incoherent addition of the diffracted orders inside the substrate. Figure 1b shows the results of the modified numerical model and experiment. The capacitive grid has the same parameters as in figure 1a. As may be seen from the figure we obtain a very good quantitative match between the finite substrate model and experiment.

In order to understand the physics of metallic grids we complement our rigorous modeling with the more intuitive surface plasma wave approach. Previous work has used this approach to analyze subwavelength inductive grids. Our experimental and numerical work illustrates that surface plasma wave coupling may also be used to examine the behavior of capacitive grids. The details of this work are presented in a recent submission to JOSA A²³ also included in the Appendix of this report.

Future Work

Given the current interest in periodic structures with their potential applications as optoelectronic devices²¹, "photonic crystals"²⁴ and composite materials having novel properties²⁵, we believe that subwavelength metallic grids (inductive and capacitive) will play an increasingly important role. Accordingly our future work will focus on the following aspects of these devices.

- Study the effects of various grids parameters (in particular the effect of substrate index) on the transmittance spectrum of subwavelength grids.
- Improving the computational efficiency of the vector diffraction model
- Potential of subwavelength grids to provide novel constitutive parameters on a macroscopic scale.

K. Nanoheteroepitaxy of GaN and GaAs on Si.

Introduction

Heterogeneous integration of III-V materials and devices onto Si substrates and with Si integrated circuits is a long sought goal that, if achieved, would have a major impact on the functionality of integrated circuits by combining improved speed, noise and optical performance with the massive density available from Si circuits. Even without achieving complete integration, the development of high-performance III-V devices on Si substrates, which are now available in 300 mm diameters with exceptional quality, would have a dramatic impact.

Any heterogeneous integration strategy must cope with and significantly reduce the defect density in the epitaxy, by addressing the large lattice and thermal expansion mismatches between III-V materials such as GaAs (~ 4% lattice mismatch or misfit) or GaN (~ 20% misfit) and Si. By far the dominant issue for GaAs on planar and μm -scale patterned silicon substrates has been the formation and propagation of large densities of line and areal defects, principally dislocations, stacking faults, and cracks²⁶. To date, achievable defect densities are incompatible with high performance (especially high power) III-V devices. For example, high frequency GaAs based transistors fabricated on these high defect density epitaxial layers have shown poor performance characteristics, including high noise figures, current drift due to traps, and hysteretic I-V curves²⁷. These characteristics make them undesirable for high performance low-noise or power amplifiers and these types of defects are prohibitive for many optoelectronic device applications.

Recently developed heterogeneous integration strategies such as compliant substrates^{28,29} and epitaxial lateral overgrowth^{30,31} have resulted in a renewed research emphasis towards these challenging goals. Nanoheteroepitaxy (NHE) is a fundamentally new, heterogeneous-integration approach that we believe offers an attractive alternative to existing integration schemes^{32,33}.

Traditionally, epitaxial growth has been explored on large substrate areas where the substrate is effectively infinite in extent and any mismatch strain must be accommodated along the growth direction in the film. Strain energy builds up linearly with film thickness, and the accumulated strain ultimately leads to defects which limit the device capabilities of heterogeneous materials with thicknesses greater than h_c , the critical thickness.

Nanoheteroepitaxy

In contrast, NHE growth begins on a dense array of nanosize (diameter $d \lesssim 10h_c$) nuclei for which both the substrate and the film are able to deform in three-dimensions in response to the lattice mismatch strain. Strain free material is achieved after only 10's of nanometers of material have been deposited. In further growth, lateral extent is encouraged and the epilayer is coalesced to form a complete layer. Theory and experiment show that strain energy is dramatically reduced and in many cases can be below the energy required to form crystallographic defects for lithographically achievable nanostructure dimensions. In particular, NHE theory indicates that for lattice mismatches up to 4.5 % (this range includes many of the important III-V on Si combinations including GaAs) this approach can **completely eliminate** mismatch defects. Even in more highly misfit systems, such as GaN on Si, the local presence of free surfaces in the novel NHE growth regime impacts the character of the defects that do form and leads to improved material quality.

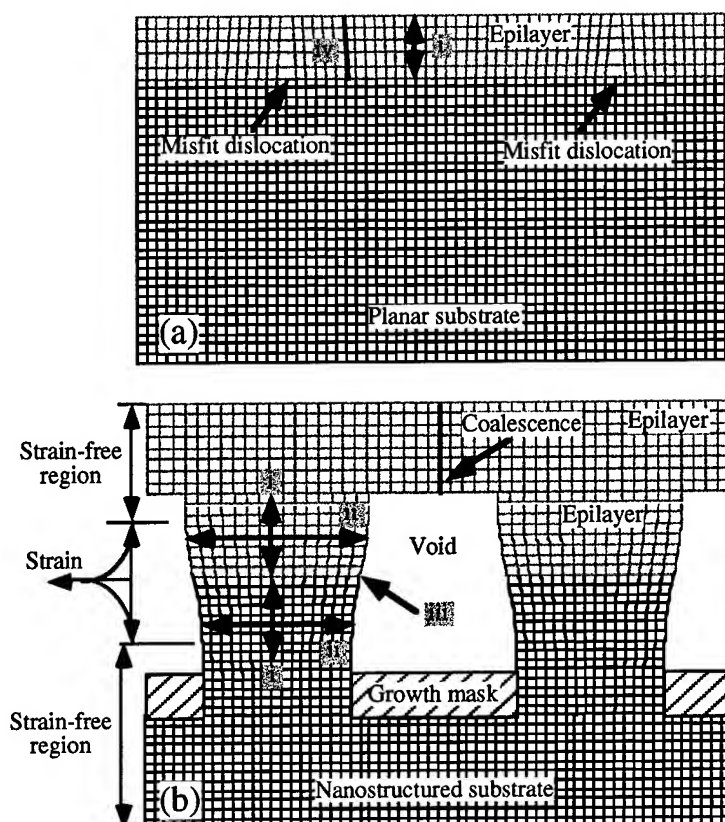


Figure 1: Schematic comparison of conventional large substrate area growth and nanoheteroepitaxy. The nanoscale area seed and the presence of free surface near the growth interface at the early stages of growth strongly changes the growth kinetics.

The nanoheteroepitaxy concept is shown schematically in Fig. 1.

GaN on Si

A cross section TEM of a GaN on Si island is shown in Figure 2. The crystal quality appears to be very high without any observable stacking faults. More details are provided in the reprints from Applied Physics Letters³³ and from the Journal of Vacuum Science and Technology³⁴ included in the Appendix

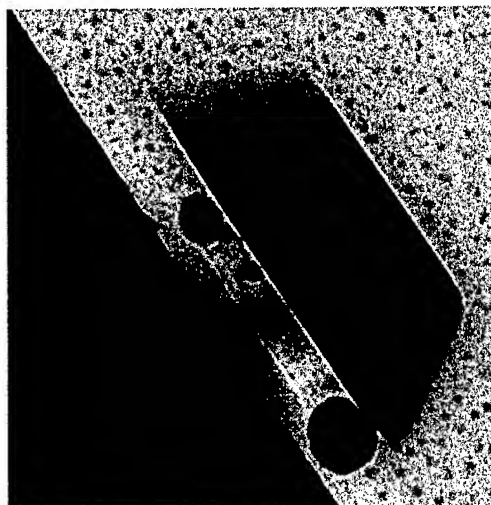


Figure 2: Cross Section TEM of a GaN on Si island showing the absence of any stacking faults. The tParticles under the island are artifacts of the TEM preparation

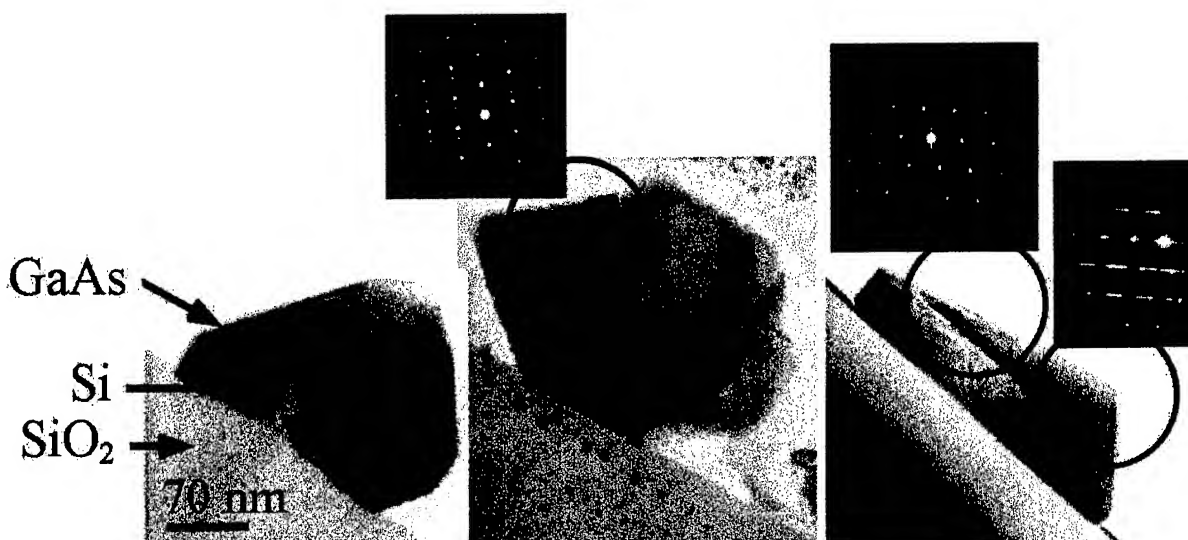


Figure 3: Examples of GaAs on Si nanoheteroepitaxy. Cross-section diffraction-contrast images of GaAs/Si heterostructures after 100 nm of GaAs deposition at 605 °C during the lateral growth stage but with a growth initiation temperature of (a) 433 °C, (b) 519 °C, and (c) 605 °C. Inset diffraction patterns in (b) and (c) were taken from the areas indicated by circles. All scale

L. Nanoscale Molecular Beam Epitaxy

Introduction

Self-assembled QDs have significant potential for many device applications. In many cases, additional control of the size and positional distribution of the dots over that possible so far with self-assembled growth would be desirable. Recently, there have been several attempts to control the nucleation of self-assembled quantum dots (QDs) with patterned substrates³⁶. Most of these have concentrated on growth of InAs or $\text{In}_x\text{Ga}_{1-x}\text{As}$ self-assembled QDs on a GaAs or a InP substrate using optical or electron-beam lithography for patterning either an overlayer mask or the substrate³⁷⁻⁴¹ or have exploited facet-dependent migration.^{37,42-48} In spite of the advantages resulting from the self-assembled formation mechanism, the inherent size fluctuation and random spatial distribution are critical issues that are not yet adequately controlled. Several attempts relying on patterned growth have been reported to attack these problems.²⁻⁹ Most of these have employed formation of steps or particular facets, to enable orientation-dependent migration and incorporation (ODMI) of In atoms.²⁻⁷ Control of sites for QD formation through circular or square patterns transferred onto substrates with chemical or dry etching to utilize a self-assembling mechanism also have been reported.^{6,8,9}

Our recent progress in lithographic technologies has expanded the regime of accessible mask/substrate patterning into the nanoscale. A pattern for which the scale approaches the lateral dimension of typical self-assembled QDs strongly suggests the capability to grow QDs on a limited area of a substrate with better controllability in both size and spatial distribution. This so-called nanoscale patterned growth basically requires a highly uniform pattern and a selective growth mode.

MBE growth on nanopatterned substrates

We have made substantial progress in applying this lithographic technology to MBE growth in the InGa/GaAs system over the past year. Accomplishments include: 1) homoepitaxial growth of GaAs on GaAs with a nanoscale SiO_2 growth mask. This was the first demonstration⁴⁹ of selective growth in MBE achieved by reducing the pattern size to the range of the surface diffusion length of Ga-adatoms on the SiO_2 surface of ~ 100 nm. 2) Extension of this work to growth of InAs dots on a GaAs surface with a nanoscale SiO_2 mask⁵⁰. A transition between an artificial Vollmer-Weber (layer-by-layer) growth for small dots ~ 50 - to 100 -nm diameter to Stranski-Krastanov (self-assembled dots) growth for larger dots, ~ 150 nm diameter, is observed. 3) Finally using one-dimensional patterning, we have demonstrated a novel integration of top-down lithographic patterning and bottom-up self assembly to form rows of single dots confined in $\langle 100 \rangle$ face trenches between $\langle 111\text{A} \rangle$ GaAs sidewalls.⁵¹ This opens for the first time the possibility of studying transport between dots as well as the properties of the uncoupled dots. In addition, the dot size distribution is more controlled than for the case of 2D self-assembly. Only brief highlights of this work are included here, details are found in the appendix.

Figure 1 shows the sequence for homoepitaxial growth of GaAs on GaAs. The top left panel is a ~ 200 nm pitch pattern in the photoresist. The bottom left panel is the hole pattern transferred into the oxide. The top right is the pattern after growth of the GaAs. Note that the growth is only in the holes and no growth is apparent atop the oxide. The lower right panel is the result of stripping the oxide leaving only the GaAs growth regions.

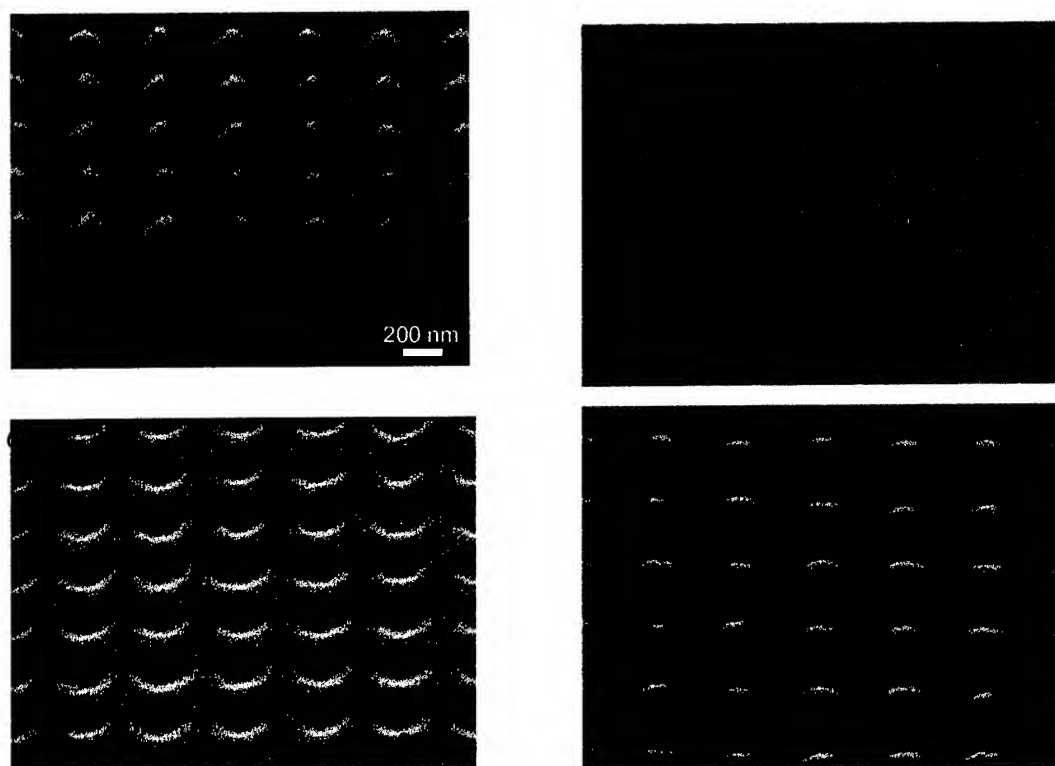


Figure 1: Homoepitaxial growth of GaAs on GaAs. See text for details.

Figure 2 shows a similar sequence for InAs growth. Again top left is the photoresist pattern, this time at a 185-nm pitch, close to the air-exposure limit for a 355 nm laser source. The bottom left shows the pattern transferred into the oxide. The hole size is reduced to less than 100 nm in the etch process. The top right shows the InAs dots inside the oxide mask and the bottom right is the result after stripping the mask. Because the lithography and pattern transfer is at the limit, there is significant dot-to-dot size variation in this result. This will be improved as we master both aspects of nanoscale fabrication as detailed in many other sections of this report.

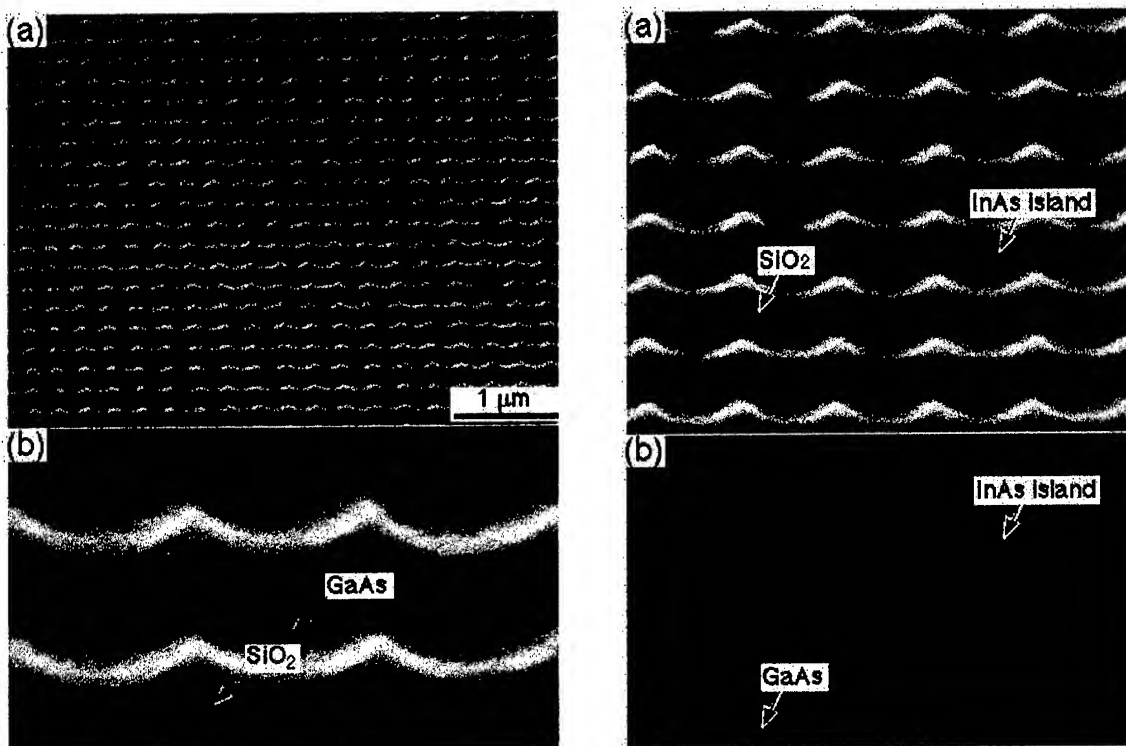


Figure 2: Heteroepitaxial growth of InAs on nanopatterned GaAs. See text for details.

The final example is a different approach that combines in a unique way top down lithographic capabilities and bottom up self assembly approaches. Figure 3 shows the general concept. A 1D oxide pattern oriented along a 110 direction, width ~ 40 nm, is produced by interferometric lithography and etching. In a first growth step, homoepitaxial growth of GaAs is performed. Because of the restricted growth dimensions, $\langle 111 \rangle$ facets develop in this growth. The oxide is then stripped and an InAs layer is regrown. The In sticking coefficient is facet dependent and the growth occurs only on the $\langle 100 \rangle$ facets of the original substrate. Control of the width of this facet allows for the growth of a single dot wide row of dots.

Figure 4 shows the intermediate substrate (b of fig. 3) after the GaAs growth. Figure 5 shows the final growth result. More details are provided in the appendix.

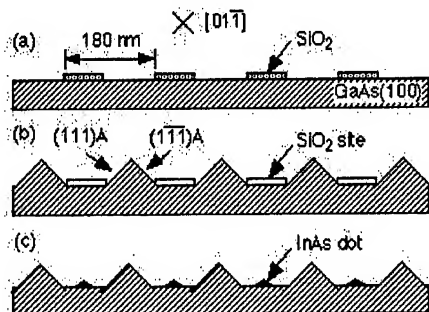


Fig. 3: Growth and fabrication sequence for growth of 1D rows of quantum dots. A) initial substrate has patterned SiO_2 stripes; b) growth of GaAs forms (111) faces; strip SiO_2 ; c) growth of InAs forms self-assembled dots.

We are clearly at the beginning of exploring a large parameter space. Goals for the next year include further exploratory growth runs and initial device studies based on this unique growth modality.

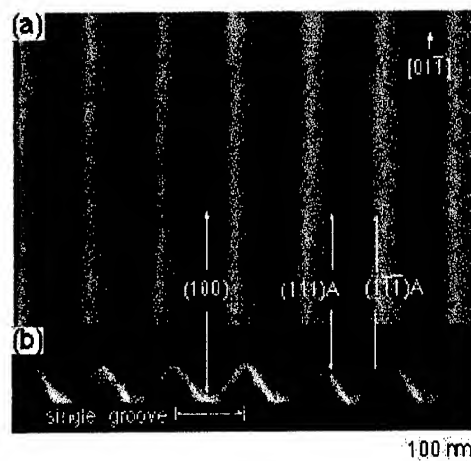


Fig. 4 (a) a 45°-tilted and (b) a cross-sectional SEM image of a nanopatterned GaAs (100) substrate prepared by selective growth.

Future Work

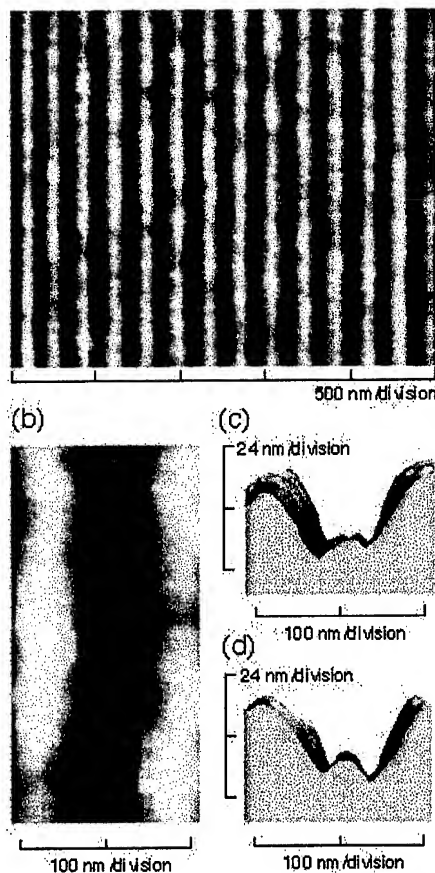


Fig. 5 AFM images of aligned QDs (a) with 2.5 μm scan range, and (b) with its 5x magnification. Side views of the AFM image of (b) seen from (c) the top and (d) the bottom.

M. Fabrication of quantum dot DFB lasers

Introduction

Single longitudinal mode semiconductor lasers are very important for high speed optical communications because of their very narrow spectra. There are two approaches to reach single longitudinal mode, either DFB (distributed feedback) configuration in which gratings are everywhere along the active region or DBR (distributed Bragg reflector) configuration in which gratings only exist at the two ends of the active region. In DFB and DBR, gratings are used to couple the forward propagating and backward propagating beams and must satisfy the Bragg condition

$$d = \frac{m\lambda}{2\bar{n}} \quad (1)$$

where m is an integer denoting the order of grating and \bar{n} is the effective index of the waveguide.

A first order grating ($m = 1$) gives the strongest coupling and eliminates radiation loss. For a DFB laser operating around $1.3 \mu\text{m}$, the period of first order grating is about $0.2 \mu\text{m}$, which is difficult to make by optical lithography because it approaches the diffraction limit of current I-line light source ($\sim 365 \text{ nm}$). Most of the gratings for DFB lasers have been made by electron beam lithography which can not be used for manufacture. In our approach, interferometric lithography is used for first order grating which combines flexibility, precision, high efficiency, and good repeatability.

Quantum dots lasers are very good for DFB fabrication because:

- quantum dots laser has a wide gain spectrum due to fluctuating dot size which is good for fabrication of lasers of different wavelengths on the same wafer.
- The gain peak of quantum dot layer changes very slowly with temperature, which is crucial for DFB laser operating across a wide temperature range.

Fabrication of first order gratings for index coupled quantum dot DFB with regrowth

Recently, some work has been done on quantum dot DFB lasers without regrowth,^{52,53} all of them require electron beam lithography. None of the work has been done on quantum dot DFB laser with regrowth yet, the efficiency of production would be increased greatly if we can combine interferometric lithography with a regrowth step. For index coupled DFB lasers with regrowth, a grating is formed along the interface of the upper core and cladding. The periodic fluctuation of effective index gives the mode selection. A regrowth step follows grating formation in order to complete the laser structure. This requires very careful sample cleaning before regrowth, and it is even more difficult for GaAs based materials system due to high Al concentration in the upper cladding. However, the step of making gratings is relatively easy owing to the planar topology when grating is formed. The follows are the details of the fabrication of gratings.

Material: InGaAs/AlGaAs quantum dot gain material

Wavelength: $\sim 1.3 \mu\text{m}$

Pitch of first order grating: $\lambda/2n \sim 0.2 \mu\text{m}$

Procedure for grating fabrication:

- deposit ARC (70 nm) on substrate
- spin on PR (100 nm)
- pattern PR into 0.2 μm pitch gratings with UV (355 nm) beam
- etch through ARC using oxygen reactive ion etch (RIE)
- Transfer pattern into substrate by inductively coupled plasma etch (ICP).

For very small features, standing waves are a serious problem, so ARC is used to remove standing waves. After etching through the ARC, the gratings get narrower, which is not good for DFB because 50% duty cycle gives the best coupling effect. Our next step is to try different ICP etching conditions to get an optimal pattern transfer into the substrate.

Fabrication of second order gratings for laterally gain(loss) coupled DFB without regrowth

For index coupled lasers, there are two degenerate modes on both sides of the DFB stop band, which makes the yield for a given wavelength quite low. The introduction of modulated gain(or loss) greatly increases the single mode yield. A gain coupled laser is almost impossible to make by conventional method due to difficulties in regrowth step. To avoid regrowth, laterally coupled DFB laser has been extensively studied recently.⁵²⁻⁵⁶ Usually in a laterally gain(loss) coupled DFB laser, metal gratings are deposited on both side of the narrow ridge to couple with the evanescent field of the guided mode.⁵² Although the confinement factor of the grating is very low, the strong absorption of the chosen metal (Cr) can compensate. Due to non-planar topology and very small periods, gratings are all made by electron beam lithography, which is expensive and gives very low yield. In the following part we discuss a new method we are developing to fabricate second order gratings with interferometric lithography.

Material: InGaAs/AlGaAs quantum dots laser

Wavelength: $\sim 1.3 \mu\text{m}$

Pitch of second order grating: $\lambda/n \sim 0.4 \mu\text{m}$

Procedure for fabrication:

- Define the ridge with photoresist (2 μm wide)
- transfer the ridge into substrate (1.6 μm deep)
- spin on ARC($\sim 300 \text{ nm}$) and PR ($\sim 250 \text{ nm}$)
- pattern grating in PR

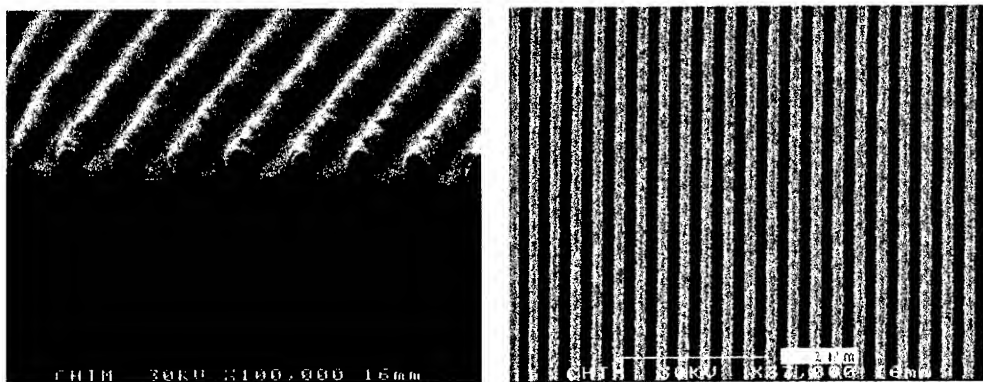


Figure 1. Cross section view and top view of the 0.2- μm period pattern in

- etch pattern through ARC

- Lift-off process, deposit Cr on the substrate
- Use plasma line to clean the ARC, leaving Cr grating on substrate

Etching through ARC is the most crucial part in this process. Due to the constraint of current etching system, we can only fabricate second order grating. In the future, a better etching system is needed for the fabrication of first order grating.

VI.1.4. Application of WIDE(wet etchable ARC) to fabrication of DFB

In many cases during the fabrication of DFB lasers, etching very small patterns through ARC deteriorates the quality of gratings. WIDE, a new type of ARC, can be etched by the developer at the same time as the photoresist, so there is no need for further plasma etching. Because the etching process by developer is totally isotropic, control of the development time is crucial, especially for small lines. For the same exposure time, different development times are tried in making 0.4- μm -pitch gratings. From the FEM pictures, at 90 second development, the WIDE is barely etched through, and at 110 second, the lines collapse due to surface strain. The development time window is quite narrow. We will improve our etching system (switch from RIE to

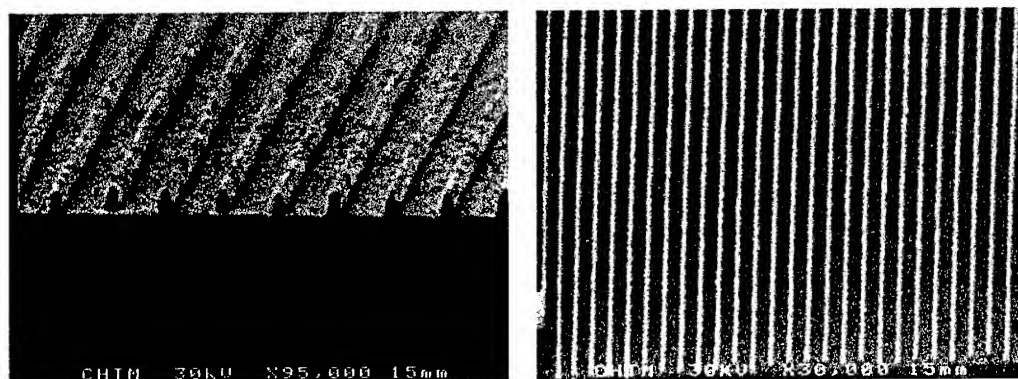


Figure 2: Pattern remaining after 85 sec oxygen plasma RIE to remove ARC

TCP system), try to make first order gratings for the laterally coupled DFB lasers. Switch from I-line laser source (355 nm) to deep UV (213 nm) to fabricate gratings with smaller pitch for DFB lasers operating at shorter wavelength.

N. Development of Ordered, Nanostructured Thin Films for Electrical and Optical Applications

Introduction

We describe a multi-year effort aimed at furthering our understanding, and developing applications for a new class of nanostructured thin films. These films allow using chemical synthesis techniques for fabricating *ordered* superlattices of metal and semiconductor quantum dots. Such ordered nanostructured composites allow tuning of the optical, electrical, and potentially the magnetic properties, of the composite materials through chemical control of the nano-particle size, loading and interparticle spacing. This provides possibilities of coupling both classical and quantum effects into a single thin film layer. A unique aspect of our program rests on the ability to fabricate such systems in essentially *carbon-free* silica sol-gel films, allowing direct incorporation into standard semiconductor device processes.

Introduction

Nanostructured composite materials fabricated using chemical synthesis techniques for the self-assembly of metal and semiconductor nanocrystals into a host substrate/film have rapidly evolved during the last several years. This has been enabled to some degree by advances in the chemical processes allowing the production of controlled, narrow size distributions of the nanocrystal particles. However, incorporation of nanometer-size particles into electronic devices requires the preparation of uniform thin films with narrow sized distributions of the nanocrystals, in itself a nontrivial process. Furthermore, in order to control the wave function overlap between adjacent particles, precise control of the interparticle spacing is required. This aspect is extremely important when attempting to tune the electronic and optical properties of these materials. Present approaches that use self-assembly of the nanocrystals into a host material experience difficulty controlling the interparticle spacing and hence the tuning of the material properties. Various schemes have been used to create ordered films of metal nanocrystals, however, they are based on the compression of Langmuir monolayers using metal cores passivated with linear alkyl thiol on the surface. Such approaches, while of interest for the investigation of limited number of film properties, do not lend themselves to macroscopic device fabrication techniques, also these films have carbon incorporated into the film.

Our effort is unique in that it employs a nanocomposite formation scheme that not only produces ordered arrays of nanocrystals in the host film, but produces those arrays in silica (carbon free) based films. These films are easily spun onto substrates using standard semiconductor processing equipment. Relatively straightforward processes are used to adjust both nanocrystal size and spacing. The use of silica based host films allows the nanocrystals to be incorporated into insulating layers. Furthermore, the films are based on standard silica sols co-assembled with a surfactant for templating. Since the films are based on materials commonly used in semiconductor processing (spin-on-oxides) their incorporation into standard device fabrication processing is relatively straightforward.

Experimental Results to Date-

Film fabrication

Nanostructured nanocrystals/silica films are prepared by spin-coating precursor solutions onto silicon wafers of selected resistivity and carrier type. The wafers have previously been

coated with a thin film of aluminum on the backside for electrical contact to the substrate. Precursor solutions are prepared containing tetraethyl orthosilicate (TEOS), HCl (0.6N HCl aq.), surfactant (CTAB; $\text{CH}_3(\text{CH}_2)_{15}\text{N}^+(\text{CH}_3)_3\text{Br}^-$), H_2O , and gold nanocrystals. The weight percentages are: 7.7% TEOS, 4.1% HCl, 2.9% CTAB, 82.8% H_2O , 0.6-2.4% gold nanocrystals. The films are coated using spin speeds of 300-500 rpm in air with 10-20% relative humidity at 25°C. Surfactant molecules, like detergents, usually have hydrophobic tail and hydrophilic head groups. These molecules form a spherical structure in water with hydrophobic tails inside the sphere or core and hydrophilic head groups outside or on the surface of the sphere. In Fig. 1 we show a cartoon of the self-assembly process while in Fig. 2 we show plan view TEM of an ordered Au nanocrystal array contained in a silica based film. Following formation and spinning onto the substrate the films are cured in vacuum at 50°C for 12 hrs.

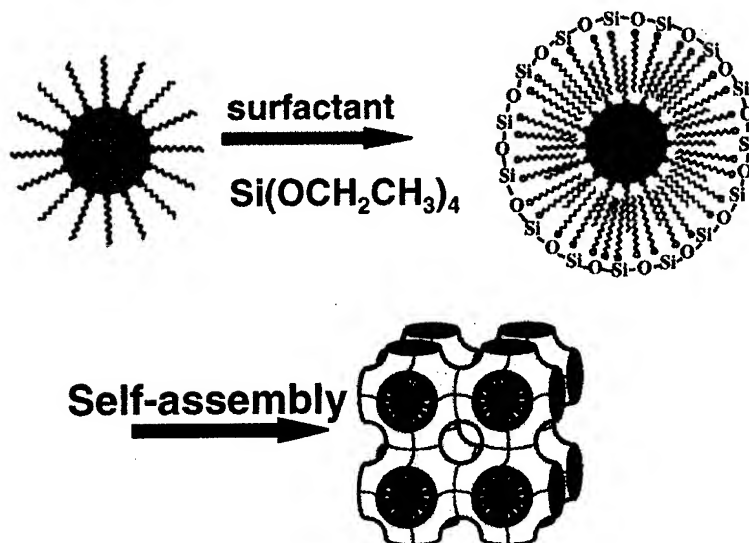


Figure 1 Cartoon showing the process flow for formation of an Au nanocrystal array.

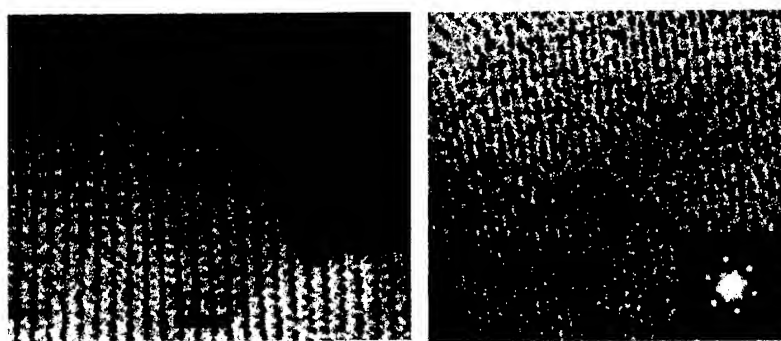


Figure 2 Plan view TEM of an Au nanocrystal array formed in a silica thin film.

Typical film thicknesses are approximately 100 to 130nm.

MOS capacitor fabrication

Films prepared in the previously described manner were then used to fabricate MOS capacitors. Silicon (100) *p*-type wafers of approximately 10^{15} cm^{-3} doping were used for the substrate material. Backside contact is provided using $\sim 420\text{nm}$ of e-beam evaporated Al, followed by a 450°C forming gas anneal for 25 minutes. The nanocomposite films were then spun onto the wa-

fers. The capacitor structures were formed using e-beam evaporated Al films of $\sim 400\text{nm}$ through a shadow mask. The finished wafers are then annealed in N_2 at 300°C for 5 hrs to further stabilize the layers and drive out unwanted solvents. Control samples are fabricated using the nanocomposite films fabricated without Au nanocrystals. Before the capacitor structures are defined the relative dielectric constant (K) of the films are measured using standard ellipsometry techniques. Typical values are ~ 2 for the films with Au and ~ 2 for the films without Au. Following the above fabrication steps I - V and C - V measurements were then performed on both sets of films.

I - V measurements

D - C current vs. voltage measurements were made on several devices both with and without Au nanocrystals using a Hewlett Packard 4140B picoammeter. The measurements are performed at several temperatures ranging from 12 to 75°C . The samples are biased at zero volts during the temperature stabilization period, and then scanned from $+2$ to -2 volts in a period of ~ 1 second. In Fig. 3a and b we show representative I - V measurements for samples without Au nanocrystals (Fig. 3a) and with Au nanocrystals (Fig. 3b). Two features are immediately obvious from this figure, *i.*) the film containing Au exhibits a higher conductivity than that without Au, and *ii.*) the temperature dependence of the I - V data reverses between the films. Also, a rectifying like behavior is exhibited in the data that is centered roughly near the expected flatband voltage for the devices. Since these capacitors were fabricated on p -type Si, accumulation of the Si surface occurs at negative voltages while inversion occurs at positive. In the next section we briefly mention a simple model we have developed that qualitatively explains this behavior.

C - V measurements

We have been able to attain high frequency capacitance voltage (C - V) measurements on both sets of devices. We use either a SULA Technologies DLTS Spectrometer driven by a Stanford Research DS345 function generator or a Keithley System 82-WIN C - V analyzer. For this discussion all measurements have been taken with the devices at room temperature unless otherwise indicated in zero light conditions. Samples without Au nanocrystals exhibit standard high frequency C - V plots uncorrected, for the oxide leakage effects. There appears to be highly mobile charged ions in the films that result in flat band shifts occurring during the actual time of the measurement, therefore the measurement time is important. An example of this is shown in Fig.

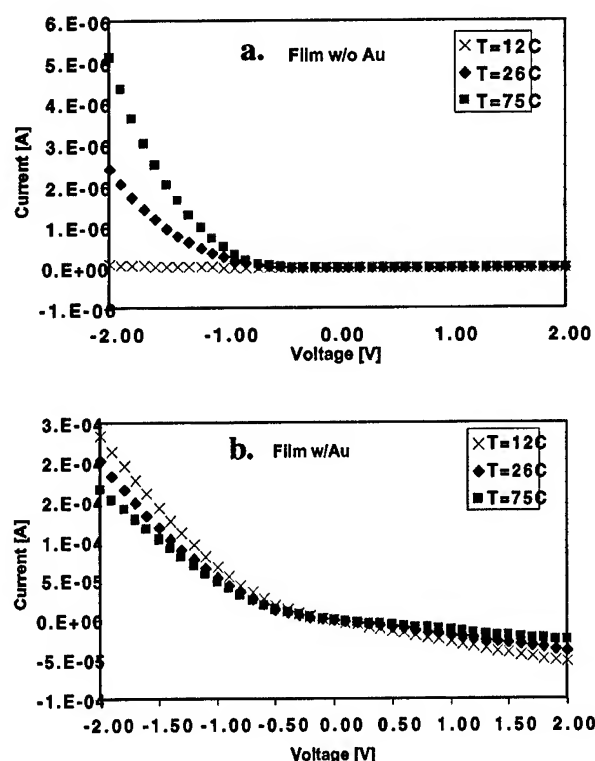


Figure 3 a.) I - V measurements for samples without Au nanocrystals, and b.) with Au nanocrystals. Data for several measurement temperatures are shown.

4 where a Au free device is shown for a voltage sweep going from negative to positive and then from positive to negative voltages. Calculated values of flatband voltage for the structures allow us to determine the *net* sign and concentration of this mobile charge.

The results are somewhat different for the Au nanocrystal loaded films. One reason for this is the measurement error caused by the higher leakage current in the film. Another is charge carrier communication between the Si substrate and the Au level in the oxide film. Films with Au nanocrystals also exhibit significant charge retention when biased in accumulation (-0.5V in Fig. 5) a further indication that communication between the substrate and Au level in the oxide is occurring. This is seen directly in Fig. 6 where we have plotted the normalized charge on the capacitors vs. time. For this measurement the sample is initially biased a $-V_f$ and then switched to $+V_f$ ($V_f = 1\text{V}$) and the current is integrated coming out of the capacitor. The sample without Au exhibits a rapid drop in charge vs. time when compared to the sample with Au.

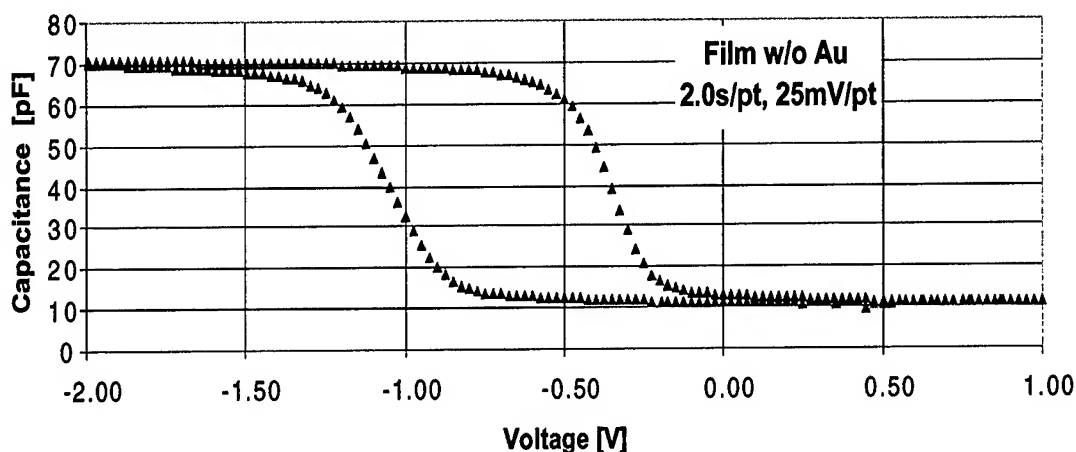


Figure 4 100 kHz C-V results for a sample w/o Au loading. The shift in the two curves is a result of mobile ions moving in the film with bias voltage.

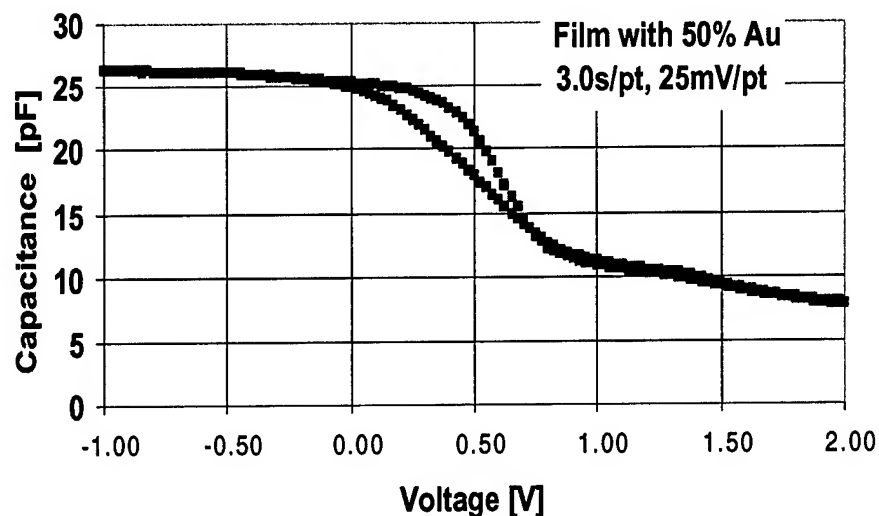


Figure 5 100 kHz C - V results for a sample with 50% Au loading. The deviation from the standard C - V curve in the range from flatband to inversion is a result of communication between the Au states in the oxide with the semiconductor surface.

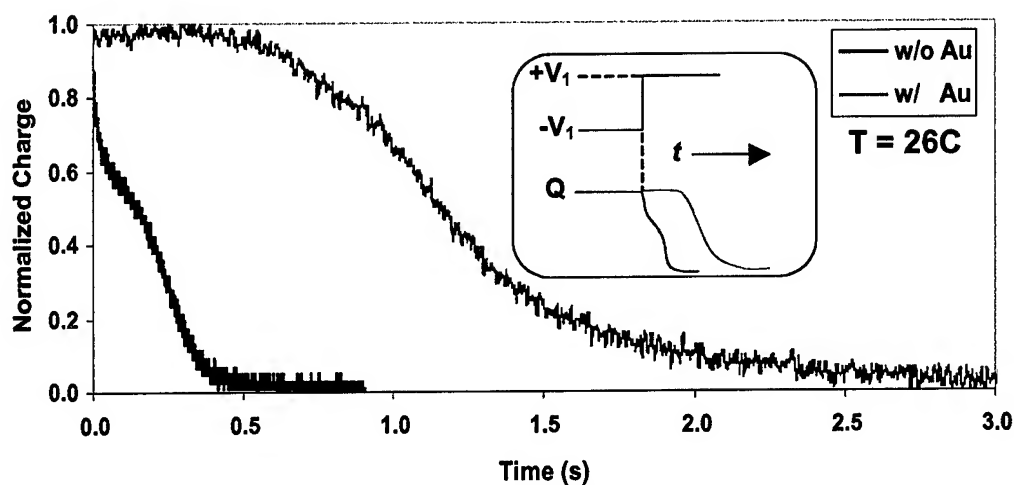


Figure 6 Normalized charge vs. time for samples with and without Au loading. It is seen that the charge decays quickly from the sample without Au nanocrystals, whereas the Au loaded sample retains the initial charge for several seconds.

O. InNAs — a New Optoelectronic Material

Semiconductor lasers and detectors operating in the mid-infrared (2-8 μm) wavelength range are ideal for a variety of commercial and military applications. For example, lasers emitting at 4- μm are needed as Band IV sources in advanced countermeasures applications. Mid-IR sources are needed for remote detection of chemical vapors and liquids, environmental sensing, and trace gas monitoring. In material processing, a higher brightness source allows thermal processes to be performed at higher speeds. Many of these applications may require *low cost* solutions and operation over *wide temperature range*, ranging from cryogenic to room temperature, or at the very least, to an operation temperature consistent with *thermoelectric cooling* (greater than ~ 240 K). In all these applications, due to their compactness, ruggedness, reliability, and high efficiency, semiconductor lasers are by far preferred over any other types of lasers.

So far, most of the work on mid-IR diode laser emitters focused on using *group-III-antimonide-based materials*. Unfortunately, due to small band offset in this material system, operation of antimonide-based mid-IR diode lasers has been limited to *cryogenic temperatures*. While non-cryogenic operation up to 290 K is achievable with *optical pumping*⁵⁷, the maximum cw operation temperature of electrically pumped devices⁵⁸ is only 195 K. An alternative approach, relying on intersubband transitions in GaAs/AlGaAs *quantum cascade lasers*⁵⁹, requires very complicated multilayer structures with very stringent requirements of epitaxial growth precision, which results in high cost of these devices and makes it practically impossible to reach high output power levels. Moreover, even though the *cw operation of quantum cascade lasers at room temperature* has been reported very recently⁶⁰, the optical *output power* is still very *small* (3 mW at 312 K), and the *output wavelength* is very *long* (9.1 μm), longer than required for most mid-IR applications.

These results are based on *our recent breakthrough in MOCVD growth of novel active-region material, InNAs, that can be grown on GaAs substrates*⁶¹. The $\text{In}_x\text{As}_{1-x}$ alloy is a very promising and yet still unexplored material for mid-infrared (2-8 μm) emitters and detectors. As with other dilute nitrides, the bandgap of $\text{In}_x\text{As}_{1-x}$ was predicted to shrink with increasing nitrogen content x , although prior to our recent work this had been confirmed experimentally⁶² only for compositions $x < 6\%$. Our recent results extend this range considerably to $x \approx 18\%$.

The $\text{In}_x\text{As}_{1-x}$ alloy can be lattice-matched to GaAs when $x = 38\%$. The *large band offset* between InNAs and GaAs barriers makes it particularly attractive for *increasing the maximum temperature of cw operation and reducing temperature sensitivity of mid-IR lasers*. If needed, even larger barriers can be obtained in the *InNAs/AlGaAs system* lattice-matched to GaAs. Most importantly, the use of GaAs/AlGaAs materials for the substrate and cladding layers makes it possible to use *mature, proven technology* that is very promising for achieving new *record levels of mid-IR diode laser performance*.

MOCVD growth and characterization of InNAs on GaAs

With a single exception of recently reported MOCVD growth of InNAs using plasma cracked ammonia source⁶³, all studies of InNAs growth utilized plasma-source MBE and related techniques, such as gas-source MBE. Recently, we have succeeded in growing InNAs by MOCVD, using for the first time the dimethylhydrazine (DMHy) as nitrogen source⁶⁴.

InNAs/GaAs multiple-quantum-well (MQW) samples were grown on (100) GaAs at 500 °C and 60 Torr using trimethylindium, trimethylgallium, arsine, and DMHy. The wells were grown using tertiarybutylarsine with 95-97.5% nitrogen in the vapor phase.

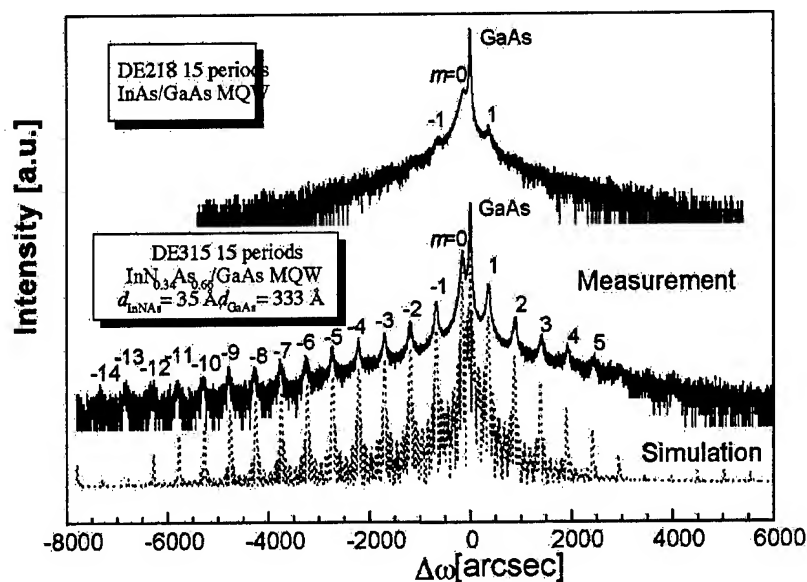


Fig. 2. ω -2 θ scans of (004) reflections for 15-period MQW samples with InAs wells (top scan) and InNAs wells (middle scan). Dotted scan represents a simulated HRXRD spectrum. The FWHM of the $m = 0$ InNAs peak (middle scan) is 43 arcsec, which together with a clearly resolved spectrum displaying up to 14 diffraction orders indicates high crystalline quality of the sample. The FWHM of the $m = -3$ satellite peak of sample DE315 is only 47 arcsec. The satellite peaks wash out in the case of InAs/GaAs MQWs (top scan), revealing poorer interface flatness and partial relaxation.

We have investigated crystalline quality, composition, and thicknesses of grown layers using high-resolution x-ray diffraction (HRXRD). Fig. 2 shows HRXRD spectra for two MQW structures grown under otherwise identical conditions, except for the presence of DMHy during the well layer growth. Sample DE218 (top scan) contained InAs/GaAs well layers, while sample DE315 (middle scan) contained InNAs/GaAs MQWs. Comparison of the two scans clearly reveals great improvement in quality of the nitrogen-containing sample, which we attribute to a *reduced lattice-constant mismatch* between InNAs and GaAs. High quality of InNAs/GaAs MQWs is also confirmed by cross-sectional TEM measurements, illustrated in Fig. 3.

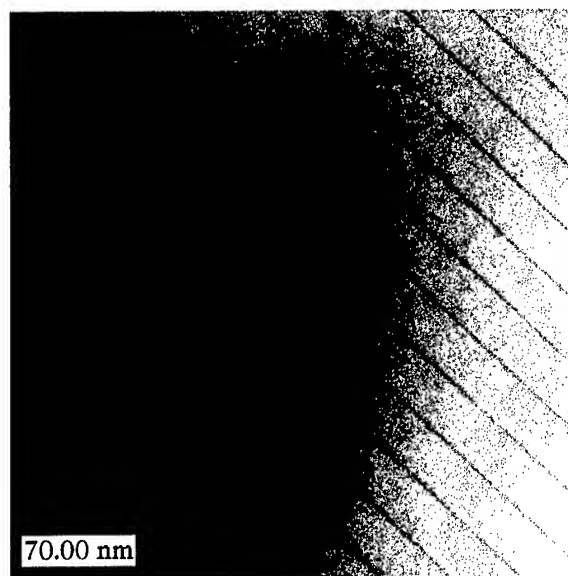


Fig. 3. Cross-sectional TEM of 15-period InNAs/GaAs MQW sample DE315.

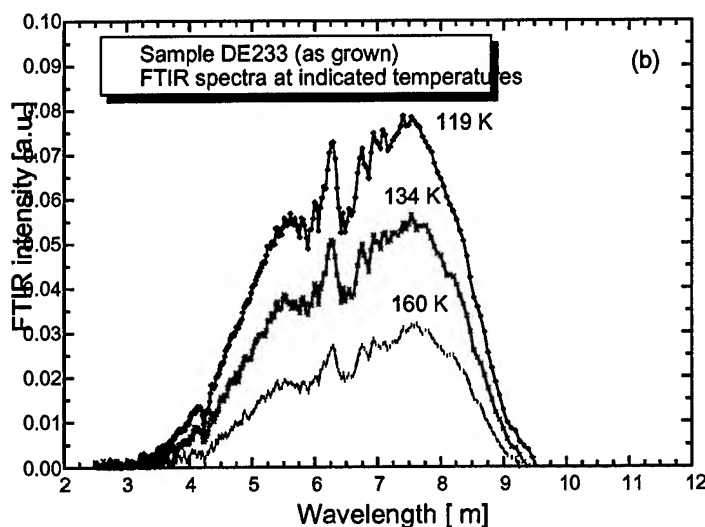


Fig. 4. Photoluminescence spectra of sample DE233 containing a triple-quantum-well 5-nm $\text{In}_{0.72}\text{N}_{0.18}\text{As}$ /37.5-nm GaAs structure. The dip at 4.26 μm is due to CO_2 absorption, while the broad minima near 5.9 and 6.5 μm are caused by water vapor absorption in the ambient atmosphere. The maximum at 6.3 μm coincides with water vapor transmission window. Note that these results represent the *longest-wavelength emission ever observed from InNAs*.

Figure 4 shows the measured PL spectra for sample temperatures ranging from 119 to 160 K. The PL setup included a 7.5-W Ar-ion laser pumping a tunable Ti:sapphire laser, and an FTIR spectrometer. The output power from the Ti:sapphire laser tuned to 890 nm was 320 mW, illuminating a spot with ~ 1 mm diameter. Rather than relying on temperature-controller readings, we used a bulk InSb sample for *in-situ* temperature calibration of illuminated sample. The temperatures indicated in Fig. 4 are actual sample temperatures determined by using the Varshni formula for PL emission peak from a bulk InSb sample placed in the cryostat, determining

Varshni parameters for InNAs, and extrapolating beyond InSb emission temperatures. The sample temperature during measurements was varied from 30 K to 160 K. At 30 K, the peak emission wavelength was $\sim 6.5 \mu\text{m}$ (190 meV), and the FWHM of the PL spectrum was $\sim 3.5 \mu\text{m}$ (110 meV). Clear PL signals $\sim 7 \mu\text{m}$, with FWHM narrowing down to $\sim 2 \mu\text{m}$ (~ 65 meV), were observed up to 160 K.

Recently, InNAs band structure calculations were reported⁶⁵ [Tit 2000], considering various possible arrangements of group-V atoms around an In atom. For 17.6% nitrogen content, bandgaps ranging from 8 meV for maximally nitrogen-rich clusters to 251 meV for maximally As-rich clusters were predicted. This wide bandgap range is consistent with our observation of broad PL emission spectra (Fig. 4). It is also very promising for *widely tunable mid-IR lasers*.

While the results we obtained so far are very encouraging, more investigations are needed in order to (i) explore properties of InNAs/GaAs quantum wells; (ii) determine optimal growth conditions for efficient PL; and (iii) modify the quantum well design with the goal of increasing the maximum PL emission temperature to at least 240 K. We also plan to perform analytical material studies of the InNAs/GaAs quantum wells, including elemental mapping using UNM's HRTEM facility, and SIMS using the services of Charles Evans and Associates, Inc.

P. Fabrication of a DFB laser by Interferometric Lithography

Collaborators: Don Wortman and John Bruno, Maxion

Leveraging Support: Maxion, Inc. (Phase II SBIR from AF)

Introduction

DFB lasers are important for optical communication and mid-IR gas detection due to their narrow line-width and high modulation bandwidth. Interferometric lithography is a rapid and cost effective way to fabricate gratings on DFB laser compared to other more conventional techniques such as electron beam lithography.

In the interferometric lithography process, the third harmonic of a single frequency YAG laser was used as source (~ 355 nm) along with a mirror to deflect half of the beam at a certain angle onto the wafer, with the other half of beam directly on the wafer. The angle between the two interfering beams, which determines the pitch of the grating, can easily be tuned by rotating the mirror with respect to incoming beam. The duty cycle of the grating is determined by the exposure and development times.

Mid-IR interband cascade (IR) DFB laser

Single-longitudinal mode Interband Cascade (IC) DFB lasers have been fabricated with a core which consists of 18 cascaded active regions separated by n -type injection regions based on the InAs/GaSb/AlSb material system. The core is sandwiched between an n -type InAs/AlSb strained-layer-superlattice (SLS) and a $0.3\text{-}\mu\text{m}$ deep, p -type GaSb separate-confinement/electrical contact layer (figure 1). A 465-nm pitch grating was transferred onto the surface to a 40-nm depth using interferometric lithography followed by ICP etching with boron trichloride gas (Fig.2). Then a narrow ridge was formed using a wet etching process.

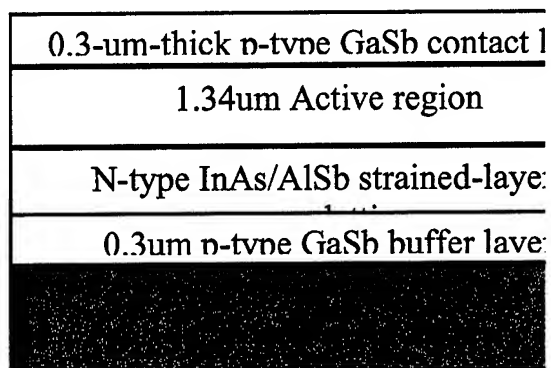


Figure 1. layer structure of IR laser

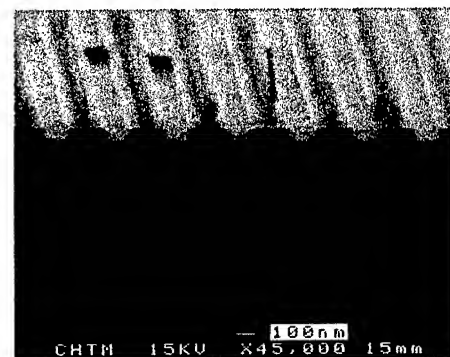


Figure 2 SEM of grating

The performance of the lasers with and without DFB gratings is compared in figures 3 and 4. For the laser without DFB grating, multiple longitudinal modes exist due to the Fabry-Perot cavity.

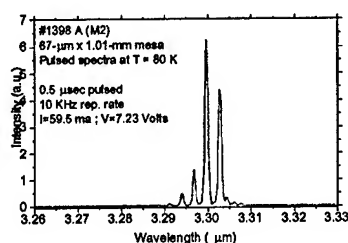


Figure 3. spectrum of laser without grating

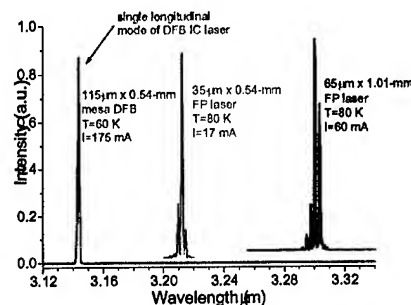


Figure 4. Spectrum of DFB laser

Single longitudinal mode output was achieved by the coupling of grating with optical mode and the suppression ratio was better than 30dB (figure 5).

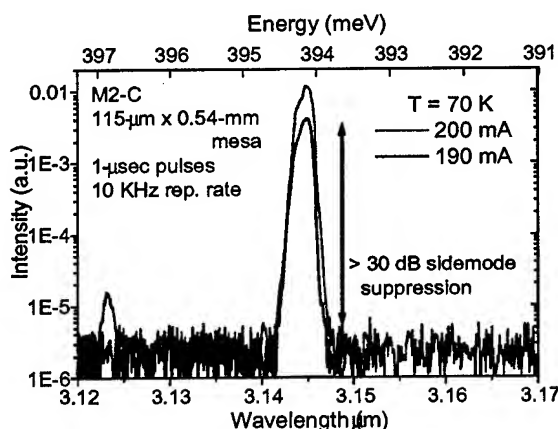


Figure 5. Detailed

Laterally loss coupled DFB laser at 1.3 μm and 1.55 μm

Recently, gain coupled DFB lasers have attracted a great deal of attention because of their superior mode selection performance compared to DFBs with conventional or phase-shifted index modulated gratings⁶⁶. Lateral coupling has become an important way to fabricate gain coupled DFB laser because it obviates the need of regrowth step⁶⁷. To date, all the gratings in laterally loss coupled DFB lasers have been fabricated using electron beam lithography, which is slow and expensive and not suitable for commercial production. In our approach, we combined optical interferometric lithography and liftoff processes to fabricate second order chromium grating down at the corner of the ridge, which couples with the evanescent field to achieve mode selection (figure 6).

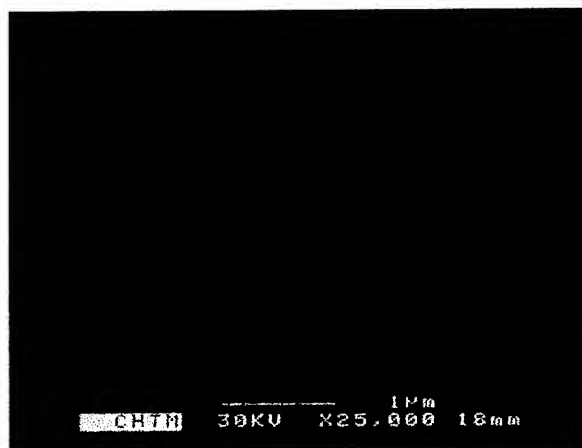


Figure 6. FEM of Cr grating at corner of ridge

The height of ridge was about $1.6\text{ }\mu\text{m}$ and the corresponding pitches of the second order grating were ~ 0.4 and $\sim 0.46\text{ }\mu\text{m}$ for the lasers emitting at 1.3- and $1.55\text{-}\mu\text{m}$, respectively.

Future Plans

In the case of mid-IR index coupled DFB laser, we have a plan to put a $\lambda/4$ phase shift at the center of device to improve the mode selection. For laterally loss coupled DFB lasers, so far, we only have fabricated grating structure on test samples. In the near future, we will extend our work to InAs quantum dot and quantum dash laser for 1.3- and $1.55\text{-}\mu\text{m}$ emission. We also have plans to push the DFB grating to 1st order, which is more efficient and does not suffer from radiation losses. These period ranges are accessible at 355 nm , using very high incidence angles or at 244 and 213 nm at more modest angles.

Q. Study of grating fields in presence of negative index materials

Introduction

Recently, there has been a great deal of interest in materials with simultaneously negative ϵ and μ ,^{68,69} variously known as left-handed materials, meta-materials or negative index materials. Several, novel applications of such materials have been suggested⁶⁸⁻⁷¹. Among them is that special configurations of such materials may be used to achieve 'perfect' imaging. Pendry⁶⁹ has shown that a slab of negative index material can behave as a 'perfect lens' for the special case of $\epsilon = -1$, $\mu = -1$. Extrapolating from that he has also demonstrated that in the quasi-static approximation, a slab of silver can also be used to significantly improve the near field image. All his calculations are done for the case of homogeneous slab.

In this report⁷², we first verify Pendry calculations by carrying out vector diffraction modeling of metallic subwavelength grating in the presence of a homogeneous slab having $\epsilon < 0$, $\mu < 0$. We modify rigorous coupled wave analysis⁷³ (RCWA) to study the field of metallic grating and show using Maxwell equations and appropriate boundary conditions that the grating field can indeed be 'perfectly imaged' by negative index slab. We extend Pendry results to show that the values of ϵ and $\mu = -1$ is a special case of a more general situation. In order to gain further insight into the behavior of electromagnetic fields in presence of negative index materials, we first study the evanescent fields in a two-layered structure, as the real part of ϵ and μ is varied in all the four quadrants. This analysis is done for TE as well as TM polarization. Our study of evanescent fields for $\epsilon < 0$, $\mu > 0$ (imaginary parts are taken to be zero, unless otherwise stated) for TM polarization indicates the excitation of surface plasma waves (SPW), this is a well-known result⁷⁴, and is the basis of Pendry observation, that a metallic film can be used to enhance the near field of an object. We observe similar results for TE case, and as expected the roles of ϵ and μ are reversed in this situation. After analyzing the layered configuration, we consider the situation where a grating (simulating as an 'object' whose image we are interested in) is placed on this structure, and study the fields in the 'image plane', (which is still in the near field region). For this initial study, the well-known criterion of visibility is used to study the image contrast in the near field. Our results indicate a remarkable improvement in the visibility for the case of $\epsilon < 0$, $\mu > 0$ (TM polarization) and $\epsilon > 0$, $\mu < 0$ (TE polarization). The case of TM polarization is clearly more useful, as materials having $\epsilon < 0$, $\mu > 0$ (metals) are readily available. Therefore, we analyze a practical configuration of chrome grating placed on a glass slab, whose backside is coated with silver film. This configuration is similar to that used by Pendry, our results indicate that although the losses in silver does attenuate the fields, the visibility is still significantly improved in the presence of silver films. Therefore the use of metallic films to improve near fields merits further study.

The remaining part of the report provides the details of our study and is divided as follows. Section 1.1 presents the 'proof' that gratings fields can be propagated without change in the presence of negative index materials. Section 1.2 analyzes the evanescent fields in a two-layered structure as ϵ and μ are varied in all the four quadrants. Finally, section 1.3 extends the analysis to grating fields placed on top of this two-layered structure.

A 'proof' that the grating fields may be transmitted without change in presence of left-handed medium

This 'proof' is shown for incident illumination being TE polarized (although similar results will exist for TM polarized light too). It is also assumed that the constitutive parameters (ϵ_r , μ_r) of homogeneous and transmitted media are real. With reference to figure 1 the fields in the transmitted and homogeneous media are given as follows:

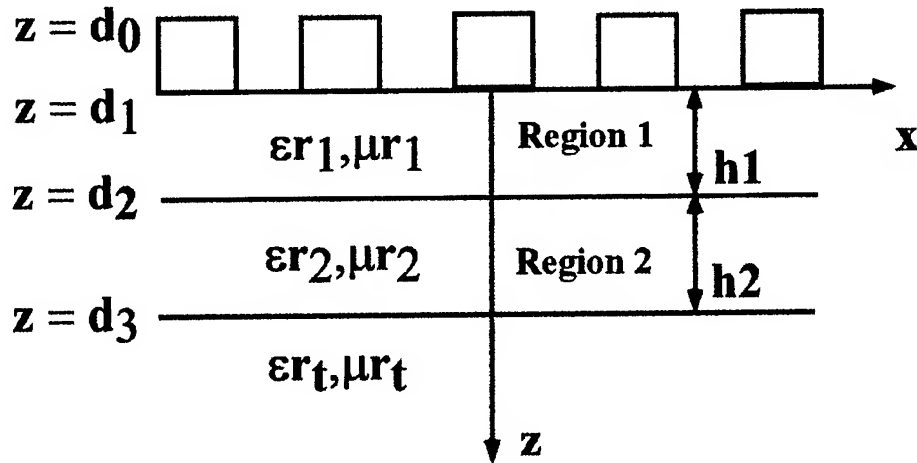


Figure 1: Geometry of the structure, region 2 can have $\epsilon < 0$, $\mu < 0$.

1. Homogeneous layer (ϵ_r, μ_r), $d_1 \leq z \leq d_2$

$$E_y(x, z) = \sum_n [f_n \exp(-jk_{zn}^{(1)}(z - d_1)) + b_n \exp(jk_{zn}^{(1)}(z - d_2))] \exp(-jk_{xn}x)$$

$$H_x(x, z) = \frac{1}{j\omega\mu_0\mu_r} \partial_z E_y(x, z) =$$

$$\frac{1}{\omega\mu_0\mu_r} \sum_n k_{zn}^{(1)} [-f_n \exp(-jk_{zn}^{(1)}(z - d_1)) + b_n \exp(jk_{zn}^{(1)}(z - d_2))] \exp(-jk_{xn}x) \quad (1)$$

Here

$$k_{xn} = k_{x0} - \frac{n2\pi}{d}$$

$$k_{zn}^{(1)} = \sqrt{\epsilon_r} \sqrt{\mu_r} \sqrt{k_0^2 - \frac{k_{xn}^2}{\epsilon_r \mu_r}} \quad \text{for} \quad k_0^2 \geq \frac{k_{xn}^2}{\epsilon_r \mu_r} \quad (2)$$

$$k_{zn}^{(1)} = -j \sqrt{\epsilon_r} \sqrt{\mu_r} \sqrt{k_0^2 - \frac{k_{xn}^2}{\epsilon_r \mu_r}} \quad \text{for} \quad k_0^2 < \frac{k_{xn}^2}{\epsilon_r \mu_r}$$

2. Homogeneous layer (ϵ_r, μ_r), $d_2 \leq z \leq d_3$

$$\begin{aligned}
 E_y(x, z) &= \sum_n [f_{n_2} \exp(-jk_{zn}^{(2)}(z - d_2)) + b_{n_2} \exp(jk_{zn}^{(2)}(z - d_3))] \exp(-jk_{xn}x) \\
 H_x(x, z) &= \frac{1}{\omega \mu_0 \mu_{r_2}} \sum_n k_{zn}^{(2)} [-f_{n_2} \exp(-jk_{zn}^{(2)}(z - d_2)) + b_{n_2} \exp(jk_{zn}^{(2)}(z - d_3))] \exp(-jk_{xn}x)
 \end{aligned} \tag{3}$$

3. Transmitted region ($\epsilon_{r_i} > 0, \mu_{r_i} > 0$), $z \geq d_3$

$$\begin{aligned}
 E_y(x, z) &= \sum_n t_n \exp(-jk_{zn}^{(i)}(z - d_3)) \exp(-jk_{xn}x) \\
 H_x(x, z) &= -\frac{1}{\omega \mu_0 \mu_{r_i}} \sum_n k_{zn}^{(i)} t_n \exp(-jk_{zn}^{(i)}(z - d_3)) \exp(-jk_{xn}x)
 \end{aligned} \tag{4}$$

4. Boundary Conditions at $z = d_3$

Matching the tangential electric and magnetic fields at $z = d_3$, and comparing the Fourier series coefficients, we get for any n ,

$$f_{n_2} \exp(-jk_{zn}^{(2)}h_2) + b_{n_2} = t_n \tag{5}$$

$$\frac{1}{\mu_{r_2}} k_{zn}^{(2)} (-f_{n_2} \exp(-jk_{zn}^{(2)}h_2) + b_{n_2}) = -\frac{1}{\mu_{r_2}} k_{zn}^{(i)} t_n$$

Here $d_3 - d_2 = h_2$, now if the homogeneous medium is left-handed, with $\mu_{r_2} = -|\mu_{r_i}|$ and $\epsilon_{r_2} = -|\epsilon_{r_i}|$, then from equation (2), $k_{zn}^{(2)} = -k_{zn}^{(i)}$, and equation (5) will become

$$f_{n_2} \exp(-jk_{zn}^{(2)}h_2) + b_{n_2} = t_n \tag{6}$$

$$-f_{n_2} \exp(-jk_{zn}^{(2)}h_2) + b_{n_2} = -t_n$$

From equation (6) it is evident that $b_{n_2} = 0$, $f_{n_2} \exp(-jk_{zn}^{(2)}h_2) = t_n$ (7)

4. Boundary conditions at $z = d_2$

$$f_{n_1} \exp(-jk_{zn}^{(1)}h_1) + b_{n_1} = f_{n_2} + b_{n_2} \exp(-jk_{zn}^{(2)}h_2) \tag{8}$$

$$\frac{k_{zn}^{(1)}}{\mu_{r_1}} (-f_{n_1} \exp(-jk_{zn}^{(1)}h_1) + b_{n_1}) = \frac{k_{zn}^{(2)}}{\mu_{r_2}} (-f_{n_2} + b_{n_2} \exp(-jk_{zn}^{(2)}h_2))$$

Here $d_2 - d_1 = h_1$, and for the special case when $\mu_{r_2} = -|\mu_{r_1}|$ and $\epsilon_{r_2} = -|\epsilon_{r_1}|$, we will have $k_{zn}^{(2)} = -k_{zn}^{(1)}$, so equation (8) will become

$$f_{n_1} \exp(-jk_{zn}^{(1)} h_1) + b_{n_1} = f_{n_2} \quad (9)$$

$$-f_{n_1} \exp(-jk_{zn}^{(1)} h_1) + b_{n_1} = -f_{n_2}$$

Here $b_{n_2} = 0$, as noted from equation (7). From equation (9) it is evident that $b_{n_1} = 0$, and $f_{n_1} \exp(-jk_{zn}^{(1)} h_1) = f_{n_2}$. Using these results, we get for t_n as

$$t_n = f_{n_1} \exp(-jk_{zn}^{(1)} (h_1 - h_2)) \quad (10)$$

From equation (10) it may be shown that we can make the phase shift equal to zero at any desired place in the transmitted region for $h_2 \geq h_1$. Also, the above equation shows that for the grating fields to be transmitted unchanged the following relationships need to hold between the constitutive parameters and thickness of the layered structure.

$$\epsilon_{r_2} = -|\epsilon_{r_1}| = -|\epsilon_{r_1}|$$

$$\mu_{r_2} = -|\mu_{r_1}| = -|\mu_{r_1}|$$

$$h_1 = h_3 = \frac{h_2}{2}$$

Study of slab fields in all the four quadrants

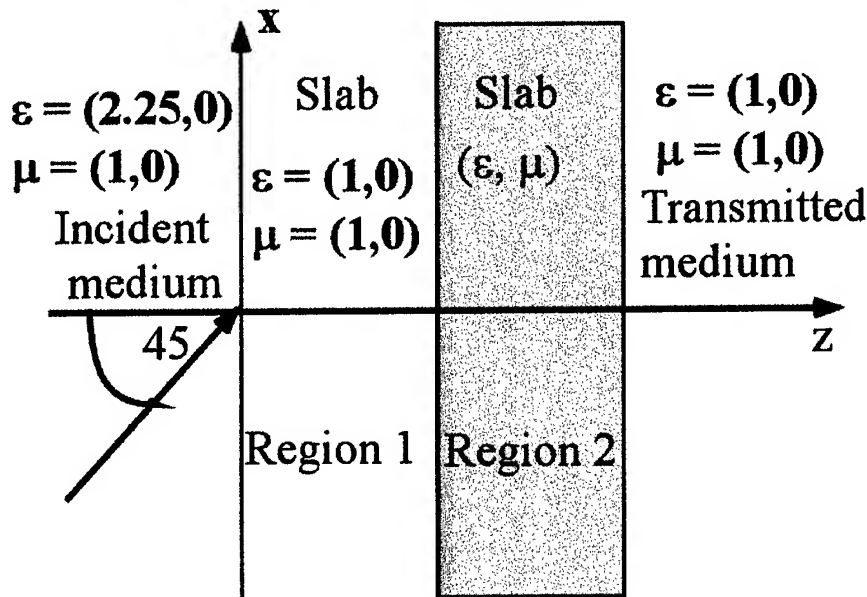


Figure 2: Layered configuration for studying evanescent fields, incident illumination is TE or TM polarized plane wave, obliquely incident at greater than critical angle, to generate evanescent wave in region 1. The illumination wavelength is $\lambda = 1 \mu\text{m}$ for TE case and $\lambda = 0.36 \mu\text{m}$ for TM case.

The two layered configuration is shown in the figure2, where we are obliquely incident from the glass medium to generate evanescent wave in region 1, the fields for TE and TM situations are analyzed as follows.

TE case.

The results are shown in the figure 3, and as noted earlier, the case of $\epsilon = -1, \mu = -1$, gives exactly the same value of the field at $z/\lambda = 0$ and $z/\lambda = 2$. It may be noted that this is a special case, as evanescent fields change significantly once we move away from the 'symmetric' configuration of ϵ and $\mu = -1$, this is shown in figure 4. Also shown in the figure is the case of $\epsilon > 0, \mu < 0$ for different values of μ . It may be noted that amplitude of the evanescent field is increased on the surface of region 2 as we increase μ , this situation is similar to that of excitation of SPW in TM case.

TM case

The results are shown in figure 5, the practical case of $\epsilon < 0, \mu > 0$ shows the excitation of SPW. In figure 6 we show the behavior of evanescent fields as magnitude of ϵ is increased. Figure 6 also shows the effect of 'small' losses on the strength of the evanescent fields. It may be noted that for the purpose of this study the electric field tangential to the interfaces is shown, clearly the total time averaged field given as $|E|^2 = |E_x|^2 + |E_z|^2$ will be greater.

Study of grating fields placed on a two layered slab

The configuration under study is shown in figure 7, and again we study the TE and TM polarization as follows.

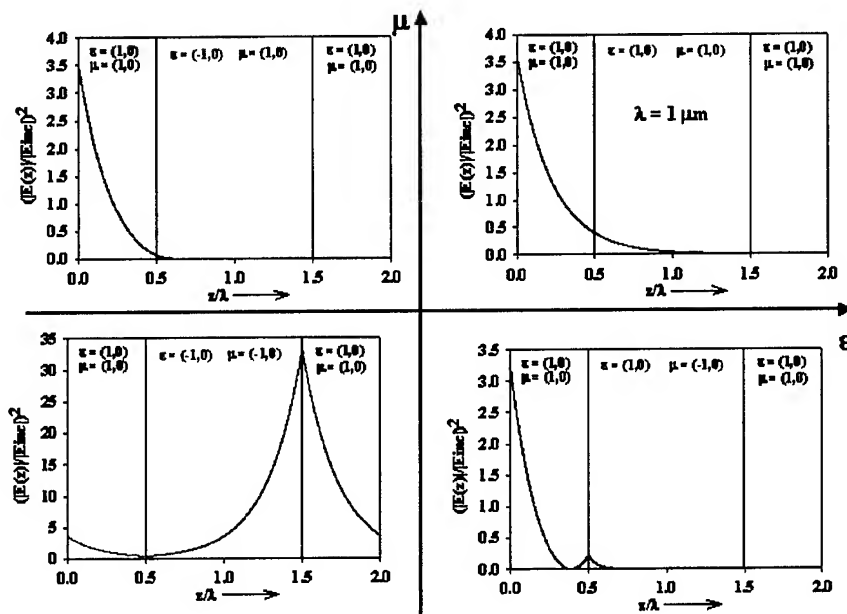


Figure 3: Behavior of evanescent field as the constitutive parameters are varied in four quadrants. The magnitude of ϵ and μ remains the same in each case.

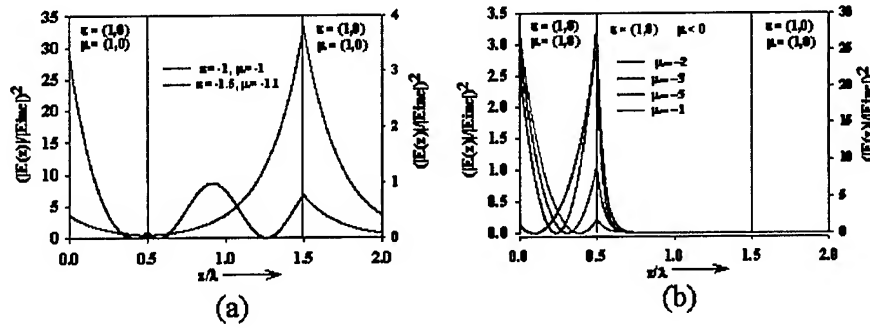


Figure 4: Part (a) of the figure shows that the evanescent field is 'distorted' for ϵ and $\mu \neq 1$. Part (b) shows the case of $\epsilon > 0, \mu < 0$; the strength of evanescent field increases as we increase the magnitude of μ .

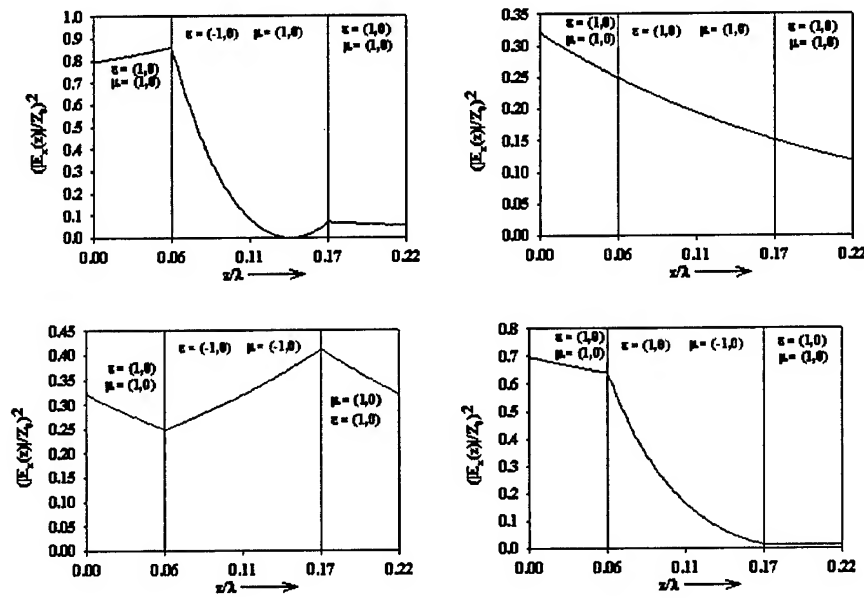


Figure 5: Study of evanescent fields for TM case, only the tangential component of the electric field (normalized with respect to the free space impedance) is shown.

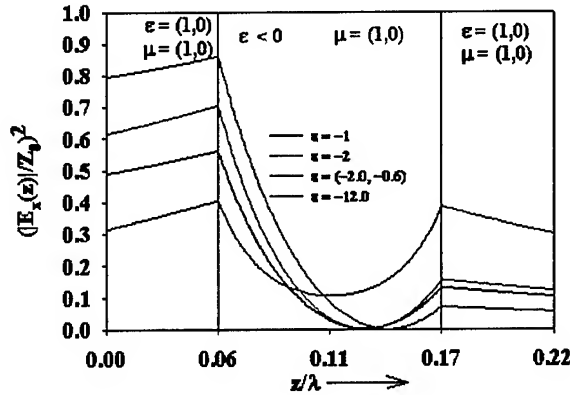


Figure 6: Behavior of evanescent fields, as the magnitude of ϵ for region 2 is increased. Figure also shows that introducing losses (i.e. making ϵ complex) in the material reduces the evanescent field significantly.

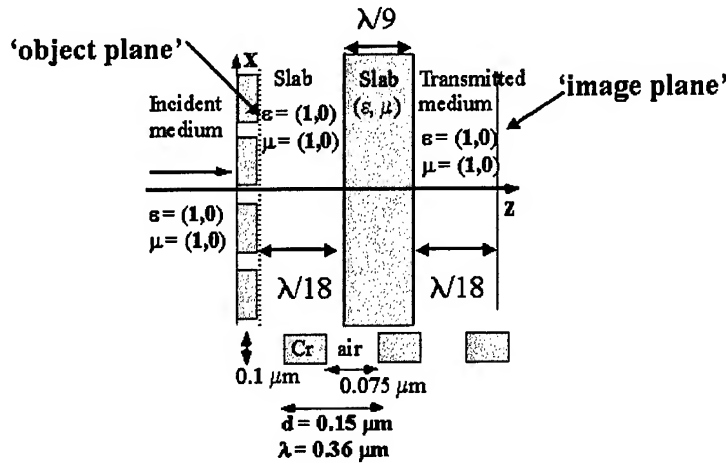


Figure 7: Figure shows the parameters of the grating and definitions of 'object' and 'image' plane. The 'object' plane is defined to be the back surface of the grating and the 'image' plane is in transmitted medium. The shaded region is the homogeneous slab (region 2), whose constitutive parameters are varied.

TE polarization

The four-quadrant study is shown in the figure 8, here the magnitude of ϵ and μ is 1 in all the four quadrants. Again the interesting cases are $\epsilon < 0$, $\mu < 0$, and $\epsilon > 0$, $\mu < 0$. We notice a significant improvement in visibility for the latter case, due to excitation of surface waves. Figure 9 shows the transverse and longitudinal variations in the electric field. From figure 9 it may be noted that rapid variations of the electric field in the z direction at the interfaces of region 2 is due to setting up of surface waves.

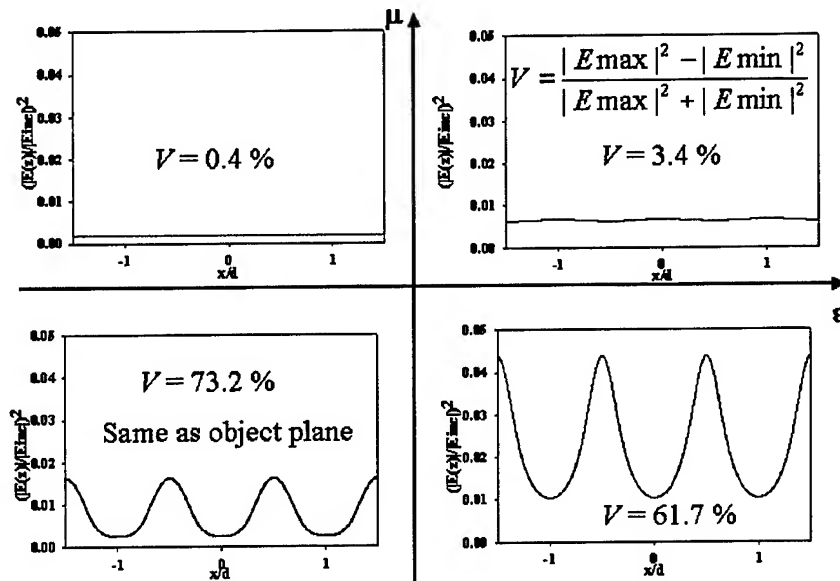


Figure 8: Variation of visibility in the 'image plane' as the constitutive parameters of region 2 are varied in the four quadrants. The normally incident illumination is TE polarized.

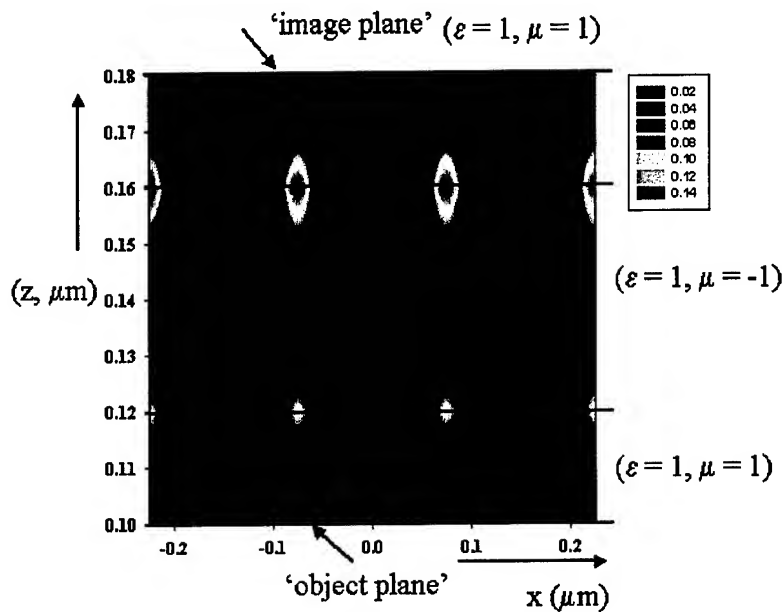


Figure 9: Variation in $|E_y(x,z)|^2$, the 'hot spots' at the boundaries and along the direction of propagation (z axis) are due to excitation of surface waves.

TM polarization

This further divided into two cases.

Case 1: The configuration is the same as for TE case. The case of $\epsilon < 0$, $\mu > 0$, shown in figure 10 displays remarkably high visibility. Also, we observe higher order harmonics in the field; one reason for this may be that we are plotting only part of the total field. Figure 11 shows the two-dimensional variations of the electric field. Again we notice the excitation of surface waves at the interfaces of region 2, also the field is plotted $0.01 \mu\text{m}$ away from the grating back surface, as the magnitude of field intensity on the grating surface is very high due to excitation of SPW⁷⁵. Figure 11 also shows more 'hot spots' on the back interface of region 2, this is due to presence of higher order harmonics as already noted in figure 10.

Case 2: This is the more practical configuration shown in figure 12, and it may be realizable using interferometric lithography. Again we notice a significant improvement in the visibility in the 'image' plane as displayed in figure 13.

It may be noted that the above observations are valid when the diffracted fields can be classified as either TE or TM; further investigation is needed for the general case of diffraction from two-dimensional objects.

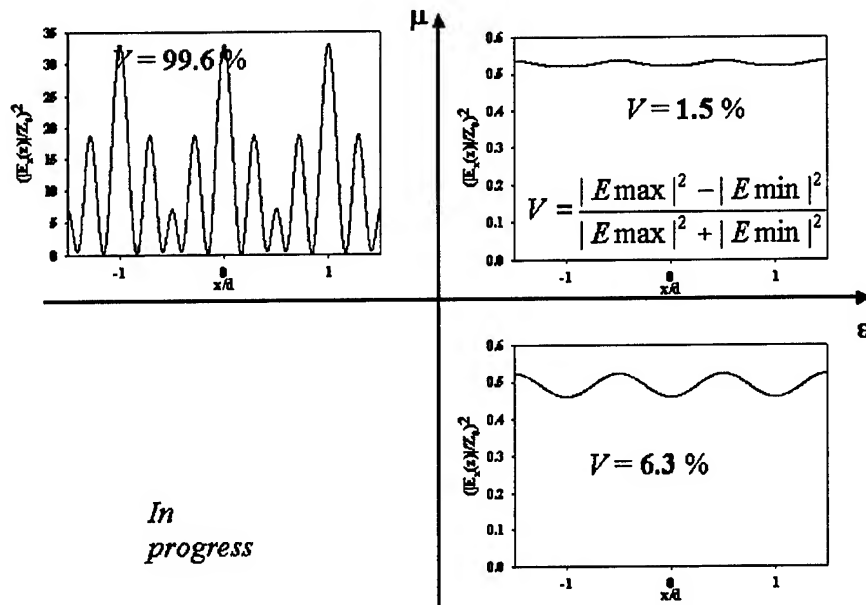


Figure 10: Variation of visibility in the 'image plane' as the constitutive parameters of region are varied in the four quadrants. The normally incident illumination is TM polarized.

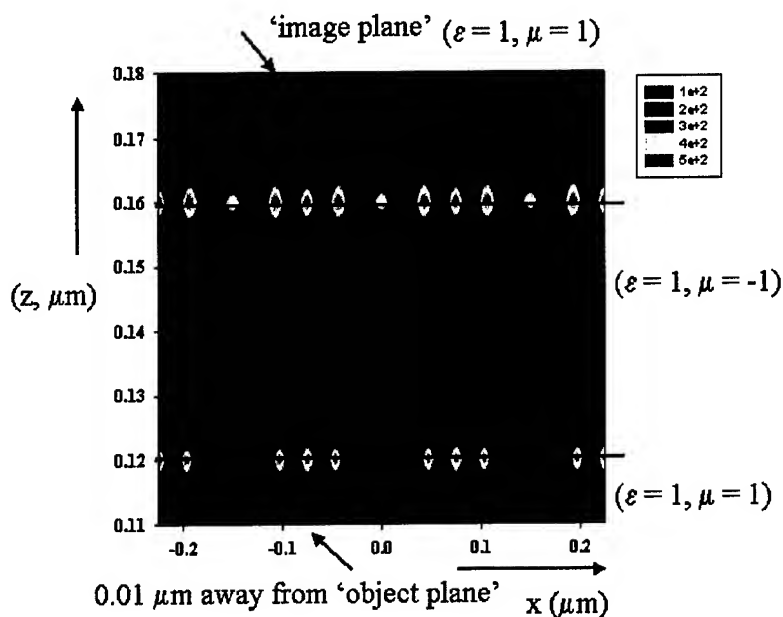


Figure 11: Two-dimensional variation of the tangential electric field for TM polarization. Notice the presence of extra field variations on the back interface of region.

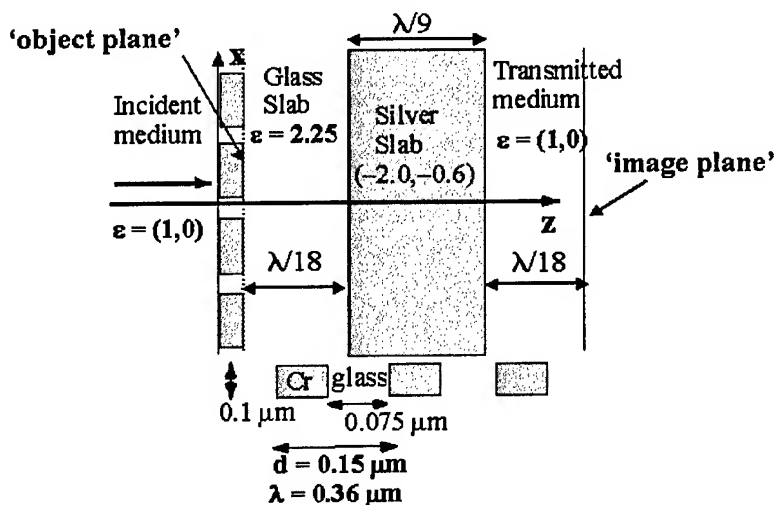


Figure 12: A 'practical' configuration for improving the near field of the grating.

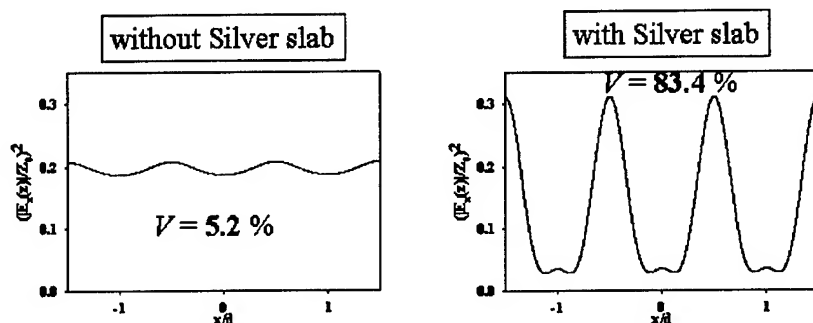


Figure 13: Figure shows the improvement in visibility in the grating near field due to presence of silver film.

Conclusions

A preliminary study of grating fields in the presence of negative index materials shows the potential of these materials in making 'perfect lens'. Furthermore, the more physically realizable situation of $\epsilon < 0$, $\mu > 0$ (TM polarization) demonstrate that excitation of SPW using thin metallic films can significantly improve the near field image quality.

R. Nanostructured detector

We report an experimental evaluation of the performance of silicon (Si) photodetectors incorporating one-dimensional (1-D) arrays of rectangular and triangular-shaped nanoscale structures within their active regions. A significant ($\sim 2\times$) enhancement in photoresponse is achieved in these devices across the 400- to 900-nm spectral region due to the modification of optical absorption properties that results from structuring the Si surface on physical optics scales smaller than the wavelength, which both reduces the reflectivity and concentrates the optical field closer to the surface. Both patterned (triangular and rectangular lineshape) and planar Ni-Si back-to-back Schottky barrier metal-semiconductor-metal (MSM) photodetectors on n-type ($\sim 5 \times 10^{14} \text{ cm}^{-3}$) bulk Si were studied. One-dimensional, ~ 50 - 250 nm linewidth, ~ 1000 nm depth, grating structures were fabricated by a combination of interferometric lithography and dry etching. The nanoscale grating structures significantly modify the absorption, reflectance, and transmission characteristics of the semiconductor: air interface. These changes result in improved electrical response leading to increased external quantum efficiency (from $\sim 44\%$ for planar to $\sim 81\%$ for structured devices at $\lambda=700$ nm). In addition, a faster time constant (~ 1700 ps for planar to ~ 600 ps for structured at $\lambda=900$ nm) is achieved by increasing the absorption near the surface where the carriers can be rapidly collected. Experimental quantum efficiency and photocurrents results are compared with a theoretical photocurrent model based on rigorous coupled wave analysis (RWCA) of nanostructured gratings. A paper on this work will be published in the December, 2002 issue of the IEEE Journal of Quantum Electronics.

S. Nanoheteroepitaxy Integration of Highly Mismatched Semiconductor Materials

The nanopatterning capability being developed under this MURI is a critical enabling technology for CHTM's revolutionary nanoheteroepitaxy (NHE) approach, which addresses the integration of highly lattice-mismatched semiconductor materials. NHE is a generic approach that has application in a wide range of materials systems (e.g. GaN/Si, GaN/SiC, GaN/Al₂O₃, SiGe/Si) and which holds promise for achieving two strategically important objectives:

- Reducing the defect density and thermal mismatch stress in III-N epitaxial structures and significantly enhancing the performance of III-N based devices.
- Increasing the functionality and performance of Si-CMOS integrated circuits by combining III-V and Si-based devices on the same substrate.

Defect reduction is vital for all III-N devices as defects increase leakage current⁷⁶, reduce avalanche breakdown voltage, and reduce minority carrier lifetime due to enhanced recombination and trapping. While some of these processes appear to be less severe in the III-Nitrides, recent results⁷⁷ indicate that defects must be eliminated for optimum device longevity. For GaN this represents a formidable challenge as previous work⁷⁸ shows that a high density of mismatch defects is typically present in the epitaxial layer. For GaN/SiC, where the lattice mismatch is 3.5%, the defect density is typically within the range 10^8 to 10^9 cm⁻². For GaN/Si, where the lattice mismatch is 22%, the defect density is typically within the range 10^{10} to 10^{12} cm⁻².

The basic concept of NHE (nanoheteroepitaxy) is shown in figure 1, which compares strain in the growth of two lattice-mismatched materials for the conventional (planar) case (fig. 1a) and for a nanoscale growth nucleus (fig. 1b). In conventional growth (fig. 1a) strain can only occur in the vertical direction and remains constant while the epitaxial layer is coherent (i.e., the material is strained but no defects have formed). The strain energy associated with this layer grows linearly with layer thickness (fig. 2, curve A) and at some critical value of layer thickness this strain energy becomes large enough to result in a defect.

By contrast, in a nanoscale growth nucleus (fig. 1b) it has been predicted theoretically⁷⁹ and demonstrated experimentally⁸⁰, that strain occurs in all 3 dimensions. This leads to a stress and strain field that decays exponentially away from the heterointerface with a characteristic decay length that is of the same order as the growth nucleus diameter. Integrating the exponentially decaying strain yields a strain energy that saturates after a thin layer has been grown (curve B in fig. 2). If this "saturated" strain energy is below the energy needed to create a defect then NHE theory predicts that an infinite epilayer thickness can be grown without defect formation.

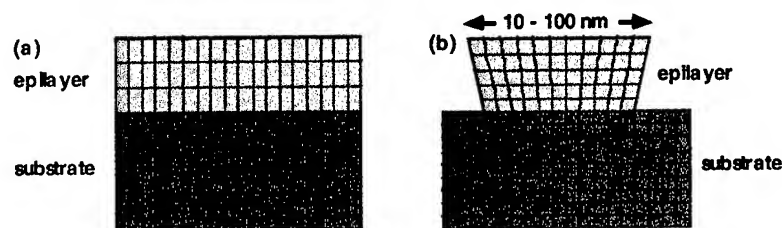


Figure 1: Comparison of strain in (a) planar growth and (b) nanoscale growth

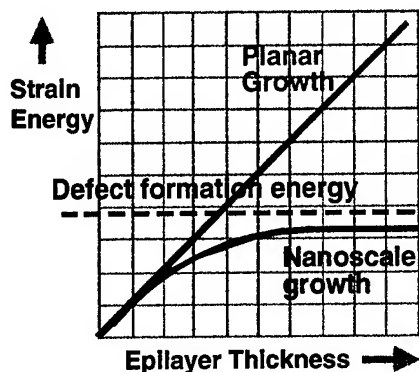


Figure 2: Comparison of strain energy accumulated during planar growth (curve A) and nanoscale growth (curve B)

The NHE approach exploits this enhanced compliance of nanoscale objects by connecting two lattice-mismatched crystals via an interface region that consists of an array of highly compliant, crystalline, nanoscale connections (figure 3). In the first part of the process the nanoscale growth islands are grown just thick enough to ensure that they are terminated by strain free material. The islands are then coalesced, while the epilayer is still very thin, to form a continuous film.

Research on patterned substrates on the scale $\geq 1\text{-}\mu\text{m}$ has been extensively reported in the literature but recent theoretical and experimental results^{81,82} have shown that novel strain relief mechanisms are available when the substrate is patterned at the nanoscale.

These mechanisms, active when the scale of the nanostructures approaches the critical thickness, offer new approaches for dealing with the stress associated with lattice and thermal mismatches⁸³.

This report summarizes progress in our ongoing study of nanoheteroepitaxy (NHE), which exploits the three dimensional strain relief mechanisms that are available to nanoscale nuclei, in a practical and Scalable technology.

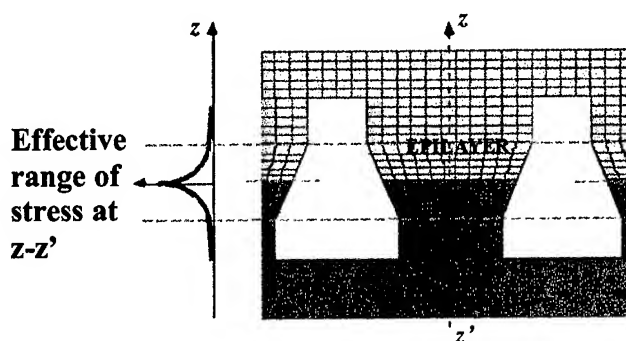


Figure 3: Schematic of NHE showing highly strained growth island and coalescence after strain has decayed.

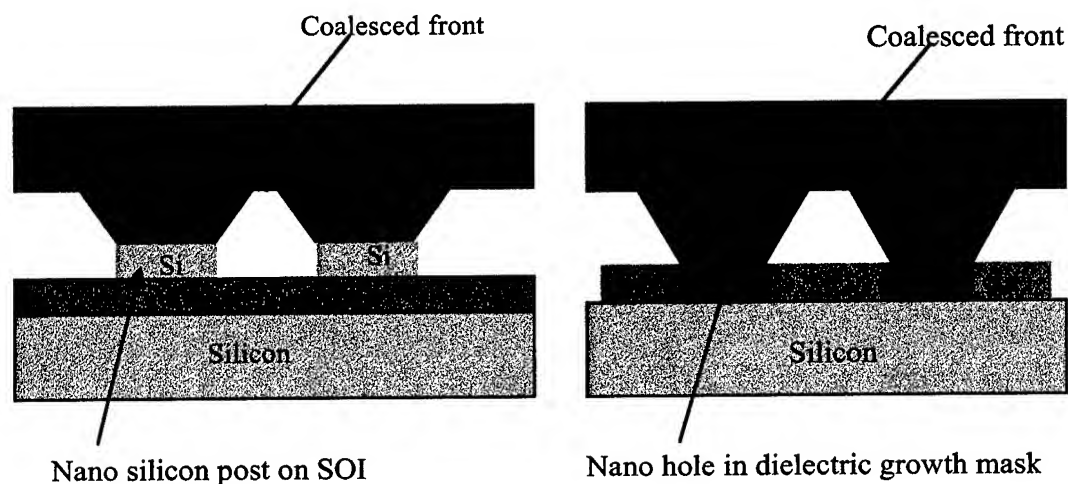


Figure 4: NHE Ideal and alternative substrates

NHE Substrate preparation

A facile large-area nanopatterning technique is required to fabricate nanoscale growth templates for NHE. Interferometric lithography⁸⁴ has been developed as a unique technique to form periodic arrays of nanoscale structures on the surface of a substrate. Nanoscale features (as small as 10 nm and densities of 10^{11} cm^{-2} over areas of $> 10 \text{ cm}^2$) with an immense flexibility in the pattern characteristics (size, density, array, and nanoelement symmetry, area, etc.) are easily achievable by interferometric lithography. The nanoscale features explored to date for nanoheteroepitaxy range from 40- to 100-nm with pattern pitch in the range 360- to 500-nm. Different substrate patterns have been explored to study NHE of GaAs and GaN on different substrates.

The ideal NHE substrates were developed from a SOI wafer (usually $\langle 111 \rangle$ for GaN and $\langle 100 \rangle$ for GaAs) where the top silicon layer is etched to form nanoscale silicon islands on a bed of silicon dioxide. These substrates provide unique three-dimensional stress relief mechanisms and also are compliant enough to accommodate a substantial part of the heterojunction strain. Due to the unavailability of good quality SOI $\langle 111 \rangle$ compared to planar silicon $\langle 111 \rangle$ wafers, alternative substrate schemes with nanoholes in

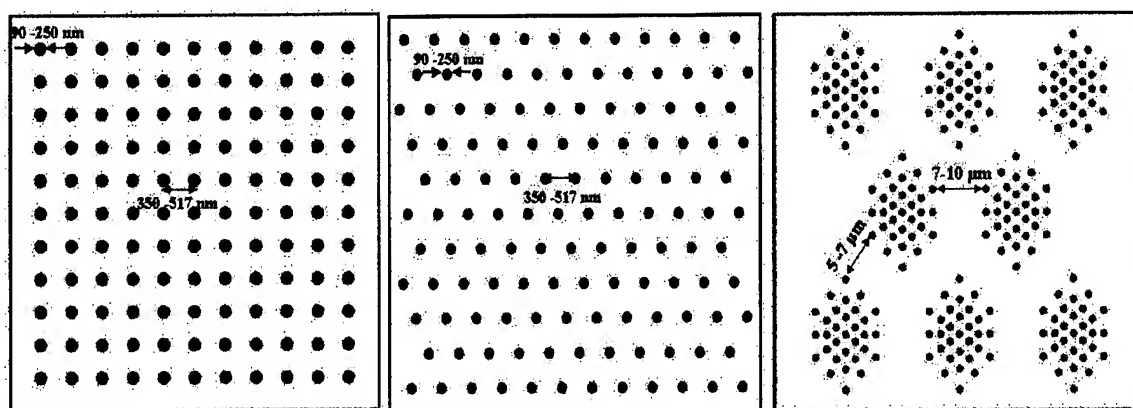


Figure 5: Schematics of 2-D patterns: (a) square array, (b) hexagonal array and (c) moiré

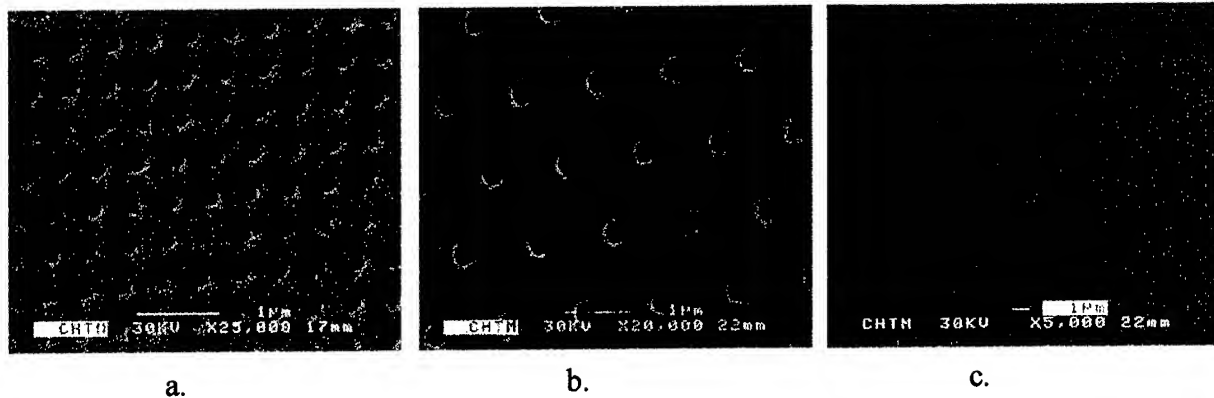


Figure 6 (b): Plan view SEM images of 2-D square array, Hexagonal array and moiré patterns created by Interferometric Lithography

a dielectric mask reaching the substrate instead of nanoposts have been fabricated to study NHE of different materials. Though these substrates are not sufficiently compliant to completely accommodate the strain, we have seen that stress free material can be grown on these substrates provided the dimensions of the holes meet the NHE size requirements. Harnessing the potential capabilities of Interferometric lithography patterns with different geometry can be fabricated. A schematic representation of the NHE substrate schemes is seen in Figure 4.

Different patterns have been generated with the alternative substrate scheme by means of interferometric lithography. Ordered arrays of 2 -dimensional holes on a square grid, hexagonal grid and also isolated areas of patterns from moiré techniques have also been fabricated on silicon and silicon carbide substrates to study NHE of GaN. Schematic views of different patterns generated by Interferometric lithography for NHE can be seen in Figures 5(a), (b) and (c). Plan-view, scanning electron microscope images of these patterns are shown in Figures 6(a),(b)and(c).

Nanoheteroepitaxy of GaN/Si and GaN/SiC

Metal organic chemical vapor deposition (MOCVD) has been employed to grow GaN on the nanopatterned silicon and silicon carbide substrates. The mismatch in these material systems is 20% and 3.5% respectively. Very good coalesced films with low stress measured on GaN/Si and almost stress free GaN pyramids grown on Silicon carbide substrates have been obtained. GaN grown on the square array and moiré pattern substrates of silicon have shown very good coales-

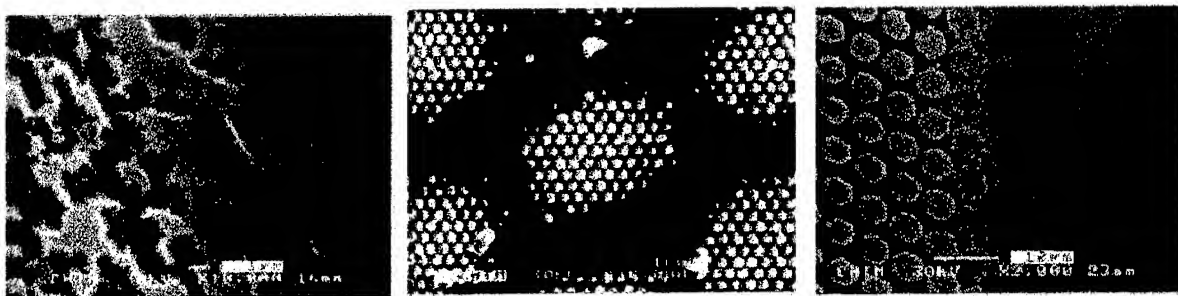


Figure 7: SEM images of (a) Coalescing GaN film on a square 2-D array hole pattern on Si (b) selective GaN growth on moiré patterns on Si followed by (c) coalescing film of GaN on moiré patterned Si substrate.

cence (Fig 7).

Micro Raman spectroscopy measurements performed on these films have shown the least stress of -0.09 GPa tensile stress on the partially coalesced (left side of fig. 7c) compared to -0.51 GPa and -0.56 GPa on coalesced square array (fig. 7a) and the coalesced film on moiré pattern (right hand edge of fig. 7c) samples. These values were found to be lower than the stress observed in GaN grown on planar silicon. The lower stress shown on the NHE substrates suggests that the grouped NHE samples may be a viable route for higher quality GaN-on-Si.

Transmission electron microscope measurements performed on these samples have shown that there is a significant reduction in the c-oriented threading dislocations, which appear to transform into in-plane defects that are localized to the hetero interface. (Figs 8(a) and (b).)

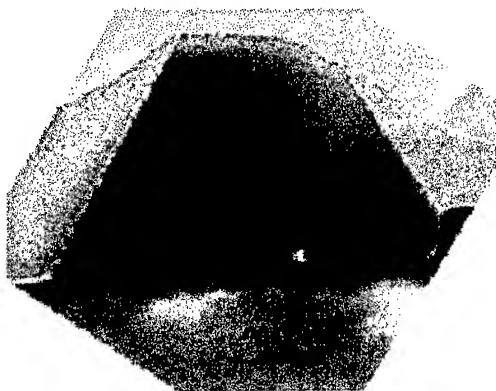


Fig 8 (a)

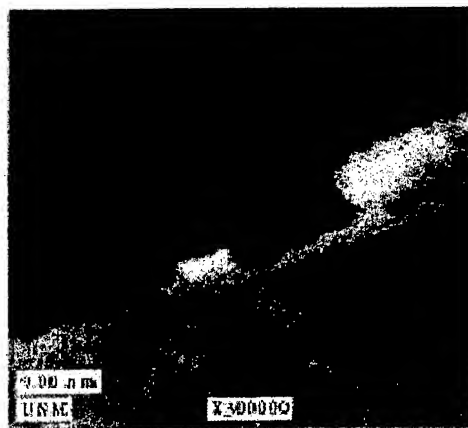


Fig 8 (b)

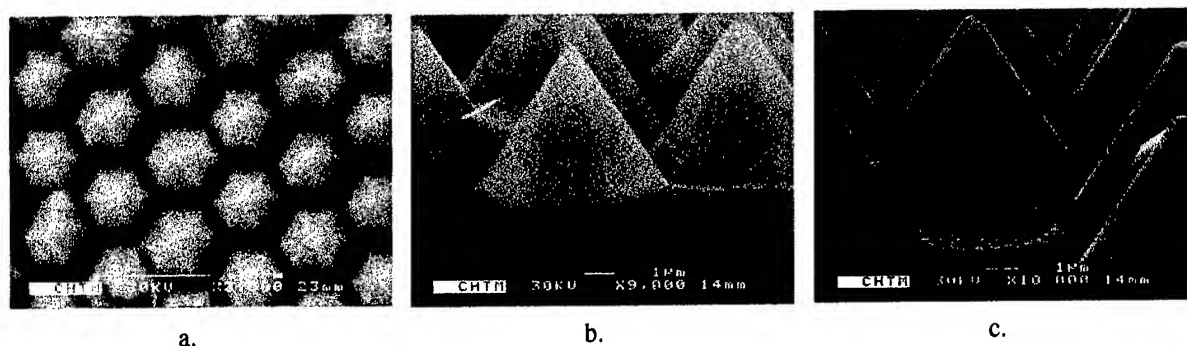


Figure 9: (a) selectively grown pyramids (b) smooth hexagonal facets of a GaN pyramid and (c) Underlying pattern of a pyramid lifted off during cleavage of the substrate.

GaN has been grown on moiré patterned silicon carbide substrates with silicon nitride as the growth mask. As a demonstration of the excellent coalescence that can be achieved, GaN pyramids with very smooth hexagonal facets, were grown shown in figure 9. Each of these pyramids is formed by the coalescence of approximately 80 small GaN nuclei that are each individually grown from one hole. The underlying pattern of the grouped holes can be seen in Figure 9(c).

Cross-sectional transmission electron microscope measurements have been made on the GaN pyramids and the selected area diffraction pattern has revealed a single crystalline behavior of the GaN pyramids (Figure 10.) Raman stress measurements made on the GaN pyramids have shown a least stress value of +0.008 and +0.003GPa that can be considered as stress free.

A close inspection of bright field cross sectional transmission electron microscopy measurements of the GaN periods have shown bending of c-oriented threading dislocations to the edges of the pyramids as shown in Figure 10(b) in contrast the vertical propagation found in large-area growth. More detailed study in this direction is underway and further research should yield information towards the progress of NHE.

Summary of Nanoheteroepitaxy Results

This brief description of the nanoheteroepitaxy project shows that it has great promise for achieving its challenging goal of combining highly mismatched materials. The importance of interferometric lithography in fabricating nanoscale patterns with flexible geometries for NHE substrates has been presented. A synopsis of NHE performed on GaN/Si and GaN/SiC has been illustrated with results pointing to the growth of stress free material with different lattice mismatches. Cross sectional TEM measurements have been shown to illustrate the mitigation of defects into the epilayer and further study on bending of dislocations has been emphasized. Nanoheteroepitaxy, enabled by interferometric lithography, has been shown to be a viable route for heterogeneous integration of materials for the future technologies.

We are also pleased to report that the positive progress in the NHE program has led to additional funding in NHE materials research (ARO/MURI, DARPA and ARO) and in the development of low-defect devices structures (ONR – Nitride based HBTS, DARPA – UV Emitters)

Figure 8: XTEM of (a) GaN/Si nucleus showing absence of c-oriented threading dislocations (b) High resolution XTEM showing stacking faults at interface

T. Application of Interferometric Lithography to Nanoscale Faceting and Lateral Growth by Molecular Beam Epitaxy

Introduction

Interferometric lithography (IL) has been applied to nanoscale faceting and nanoscale lateral growth (NLG) by molecular beam epitaxy (MBE). Control of nanoscale faceting along the boundary between a SiO₂ mask and an open GaAs surface provides a powerful new approach to the formation of nanopatterned surfaces that avoids many of the damage and crystal disruption issues associated with subtractive (etching) preparation of nanopatterned substrates. Nanoscale faceting accompanied by selective growth mode has many important applications in MBE. Several different facets generated on a substrate surface redistributes incident atoms along their preference of incorporation sites and results in composition/thickness modulation in heteroepitaxy. We report growth of InAs quantum dots (QDs) aligned on a nanoscale periodic faceted GaAs substrate.

It has been known that lateral growth is unavailable in MBE. With nanopatterned growth, however, we realized NLG associated with selective growth and faceting for the first time^{85,86}. NLG has strong applications and one of them is for strained heteroepitaxy of large lattice-mismatched material systems such as GaAs on Si or GaN on GaAs or Si. Lateral growth and coalescence over the SiO₂ mask between adjacent epilayers which are locally grown on nanoscale open surfaces patterned substrate result in a strain-reduced structure near the epilayer/substrate interface and can be used as a strain buffer suppressing generation of misfit dislocations.

For nanoscale faceting and NLG, two types of nanoscale SiO₂ patterns were prepared on GaAs(100) by IL: a 180- and 265 nm period 1 dimensional (1D) stripe pattern and a 350-nm period 2 dimensional (2D) circular hole pattern. The width of a SiO₂ stripe and the hole diameter were controlled in sub-100nm (15- to 80 nm) and 120 - 200 nm range, respectively. On these nanopatterned GaAs substrates, we investigate 1D and 2D nanoscale faceting and NLG with growth of GaAs by MBE. Also, we report growth of InAs QDs aligned on a 180-nm period 1D (100)-(311) nanoscale faceted GaAs substrate.

Fabrication of nanoscale SiO₂-patterned substrates

The critical steps for fabrication of a SiO₂ pattern on GaAs(100) are to prepare a 1D or 2D photoresist (PR) pattern by IL and to transfer it onto a SiO₂ film. The process begins with the exposure of a PR film and a SiO₂ film stacked on GaAs(100) to an ultraviolet (UV) light by IL. A single longitudinal and transverse mode, frequency-tripled YAG laser at a 355-nm wavelength was the UV light source. The direction of 1D pattern was along $[01\bar{1}]$. In Fig. 1(a), the parameters used in this report are summarized. Development, pattern transfer of the PR pattern onto the SiO₂ film by dry etching with CF₄ plasma, and removal of the residual PR film from the SiO₂ surface result in a SiO₂-stripe-patterned GaAs(100).

A 45°-tilted scanning electron microscopy (SEM) image of 1D 25-nm-thick SiO₂ stripe patterns oriented along $[0\bar{1}1]$ on a GaAs(100) substrate is shown in Fig. 1(b). Two different period 1D SiO₂-patterned substrates were used : a 180 period with the width of an open GaAs surface, w_{GaAs} , ~ 120 -130 nm and the width of SiO₂ stripe, w_{SiO_2} , ~ 50 - 60 nm and a 265-nm period with w_{GaAs} ~ 180 - 250 nm and w_{SiO_2} ~ 15 - 80 nm. In the latter, w_{SiO_2} was controlled by dry etch time with a mechanical mask to define different regions with varying w_{SiO_2} . Figure 1(c)

shows a top-view SEM image of 350-nm period 2D SiO_2 pattern generated on GaAs(100). The hole diameter, d , is in the range of 120 - 200 nm.

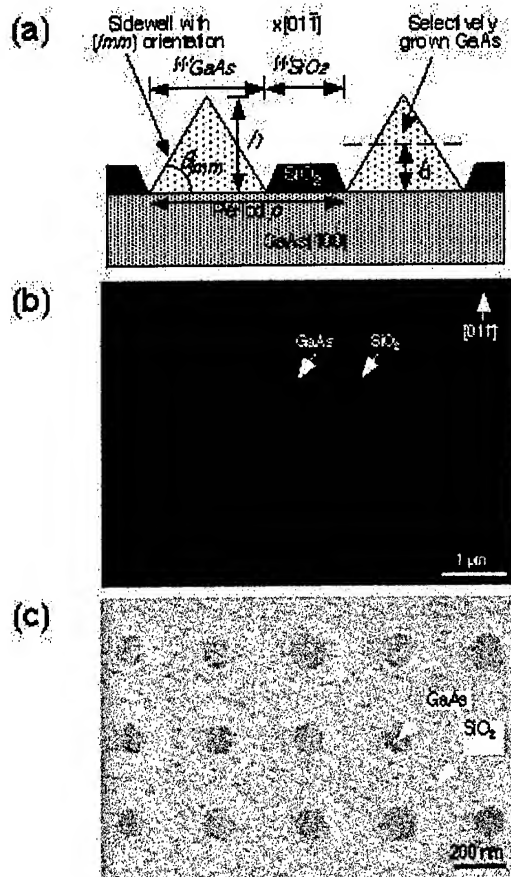


Figure 1 (a) A schematic illustration of a cross-sectional view of an as-grown sample with the parameters used in this work. SiO_2 stripe masks in every sample shown in subsequent figures were removed by HF treatment after growth. (b) A 45°-tilted SEM image of a 180-nm period 1D stripe PR pattern. (c) A top-view SEM image of a 355-nm period 2D circular hole pattern.

MBE growth

Growth of GaAs was performed at 610° – 630°C with growth rate of about 0.1 ML/s. Under these conditions, the sticking coefficient of a Ga atom on a SiO_2 surface is very low and selective growth is realized⁸⁶. Figure 1(a) is a schematic illustration of a cross-sectional view of an as-grown sample of which each sidewall consists of a single facet. As indicated by the dashed line in Fig. 1(a), deposition thickness, t_d , was determined from growth time multiplied by growth rate and refers to the thickness of GaAs deposited on an unpatterned wide-area GaAs(100) surface under the same growth condition. Growth of InAs QDs was performed at 510°C with nominally a 2.5 monolayer (ML) deposition.

Nanoscale faceting

Figure 2 shows cross sectional SEM images taken from a single growth run on a sample with regions of different periods and w_{GaAs} 's between SiO_2 stripes. The deposition thickness, t_d , is

about 46 nm. Phenomenologically, the faceting observed in Fig. 2 can be understood as follows. At the initial stage of growth, a (311) facet begins to appear on an open GaAs surface near the boundary between SiO₂ mask and open substrate surface. For $w_{GaAs} = 340$ nm [Fig. 2(c)], a (111) facet has just begun to form at the edges of the open GaAs surface. For $w_{GaAs} = 170$ nm [Fig. 2(b)], the (111) facet boundary is closer to the apex of the growth, and finally for $w_{GaAs} = 130$ nm [Fig. 2(a)], the (311) facets are gone entirely and the (111) facets completely fill the open area. For the same t_d , therefore, (311) facets are gradually replaced by (111) facets as w_{GaAs} decreases. Facet replacement similar to Fig. 2 is also observed for a given w_{GaAs} with continued deposition.

Initial faceting of Fig. 2 is consistent with minimization of surface free energy, E , if (311) facets are more stable or have lower surface free energy than (111) facets. Although there has been no absolute comparison of surface free energies between different orientations of GaAs, Scheffler and his coworkers have evaluated the surface free energy of several GaAs surfaces with density-functional theory, and suggest that a (311) surface has a surface free energy comparable with other lower index surfaces^{87,88}. According to their calculation, a (311) facet has surface free energy of 47 meV/Å² compared to 51 - 54 meV/Å² for a (111) facet in an As-rich environment which is similar to our growth conditions. Although surface free energy depends on surface reconstruction which is also effected by growth temperature and As-environment, their calculation is consistent with our experimental findings.

Faceting shown in Fig. 2 suggests a very important application: control of facet formation by a pattern period or a deposition thickness. Control of nanoscale faceting can be utilized for composition modulation in lattice-mismatched heteroepitaxy. Growth of InAs quantum dots (QDs) aligned on a periodic (100)-(111) nanofaceted GaAs substrate will be presented below.

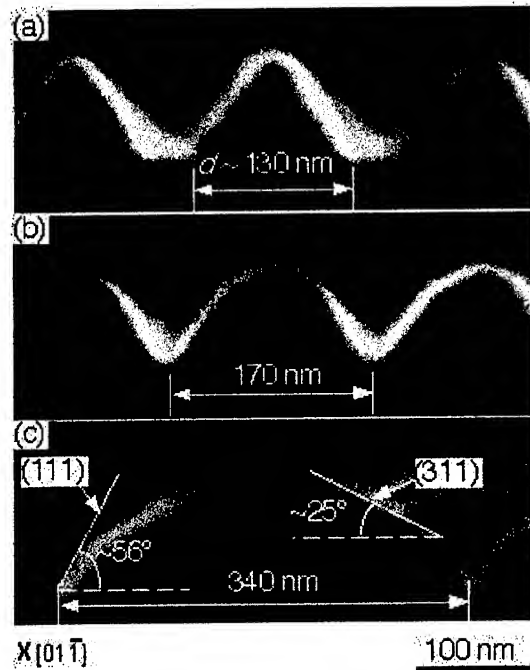


Fig. 2. Cross sectional SEM images for $w_{\text{GaAs}} = 130$ nm (a), 170 nm (b) and 340 nm (c) SiO_2 -patterned substrate after GaAs growth of $t_d = 46$ nm.

Nanoscale lateral growth

1D NLG

We explored the possibility of lateral growth through continued growth over the faceted surface. For this purpose, we employed 265-nm period, 25-nm-thick SiO_2 patterns providing better resolution. Figure 3 presents a cross section SEM images after deposition of $t_d = 200$ nm of GaAs for $w_{\text{GaAs}} \sim 180 - 250$ nm. Adjacent triangular cross sectioned GaAs stripes undergo coalescence as the growth proceeds. The coalescence is non-uniform as a result of variations in w_{GaAs} and w_{SiO_2} associated with process limitations at this sub-100-nm scale. If the SiO_2 pattern were uniform, simultaneous overall coalescence might have occurred although the edge definition is intrinsically limited at this nm-scale by the discrete atomic nature of the interfaces. Once initial coalescence occurs at some point over SiO_2 mask which is generally around a small- w_{SiO_2} region, growth partly proceeds along the $[0\bar{1}1]$ direction, onto the plane of the cross sections, as well as filling in the V-groove between the (111) faces. The coalescence shown in Fig. 3 results in growth of single crystalline GaAs over the SiO_2 mask.



Fig. 3. 45°-tilted [(a) and (b)] and cross section [(c)] SEM images of a 265-nm period SiO_2 -patterned substrate after GaAs growth of $r_2 = 200$ nm.

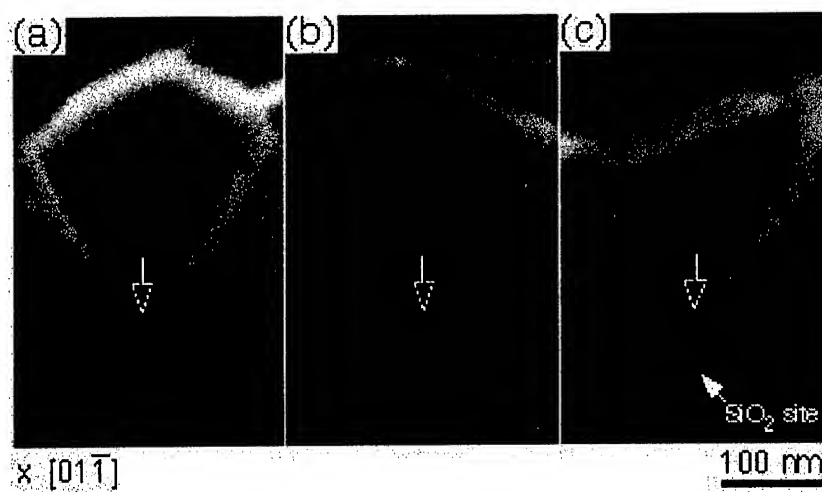


Fig. 4. Cross sectional SEM images of a 265-nm period SiO_2 -patterned substrate having different w_{SiO_2} (~ 15 - 80 nm) after GaAs growth of $r_2 = 200$ nm.

Magnified views of NLG and coalescence regions are shown in Fig. 4 for different w_{SiO_2} values ranging from ~15- to 80-nm. These images correspond to different regions of the sample prepared with differing etch times to vary w_{SiO_2} , but with a single growth to ensure identical growth conditions. Coalescence depends on w_{SiO_2} . In Fig. 4, NLG over the SiO_2 mask is clearly revealed as w_{SiO_2} is increased. In this figure, NLG retains (111) sidewall facets. The mask used in this work is only 20- to 30-nm thick and does not have vertical sidewalls. These slanted SiO_2 sidewalls may allow extension of the (111) facets over SiO_2 mask. If extension of existing facets over the SiO_2 mask were energetically more favorable than creation of the next-highest-surface-free-energy facet, epitaxial growth would keep its minimum E by facet-extension. This interpretation can be applied to the replacement of (311) by (111) of Fig. 2. Lateral growth is thus accompanied by over-growth filling out the space bounded by open GaAs (100) surface and slanted sidewalls of SiO_2 mask.

2D LNG

Figure 5(a) shows a 45°-tilted SEM image of a 2D patterned as-grown sample viewed from $[01\bar{1}]$. Figure 5(b) and 5(c) show 80°- and 0°-tilted (top view) SEM images of one section of the same sample after stripping off the SiO_2 mask in diluted HF. These images were taken along $[001]$ as indicated in the figure. In Figure 1, d varied from 120- to 200-nm. The uniformity of d is limited by the process techniques employed in this work. For convenience, we refer to the individual GaAs epilayer regions as epitaxially grown GaAs islands (or epi-islands). In some epi-islands, labeled E through I in Fig. 5(b), faceting and nonuniform lateral growth over the SiO_2 mask is observed. While an epi-island close to circular shape (label B) was formed in some small- d holes, rectangular (label E) and multiple-sided (label G) islands with rounded corners are also observed. These are very striking shapes previously unobserved in μm -scale patterned MBE.

Figure 5(b) and 5(c) reveal various faceting states with different shapes and a large volume fluctuation amongst the epi-islands. These variations are partly due to nonuniformity of initial hole diameter. Unlike the observation for 1D NLG, faceting significantly affects overall shape of GaAs islands. Since diameter fluctuation and perimeter irregularities of the holes are major factors of initial faceting, every epi-island does not undergo the same faceting and lateral growth in our patterned growth.

We intensively examined the epi-island labeled A in Fig. 5(b) which belongs to the mid-sized islands in volume. Figure 6 presents various SEM images taken from island A tilted from 80° to 0° (top view) in three different orientations indicated in the figure for top view. A 45°-tilted SEM image taken along $[010]$ clearly shows the faceted surface of island A. In top-view SEM of Fig. 6, island A has a rectangular shape close to a square. It should be noted that the original open GaAs surface provided by nanoscale patterning has the circular shape indicated by a dashed circle in Fig. 6,. In Fig. 6, 80°-tilted SEM reveals entirely different images changing with orientation. This is crucial in understanding selective growth accompanied by faceting and associated lateral growth. Viewed along a $[01\bar{1}]$ direction, island A shows a profile close to triangular with slanted sidewalls consisting of two different facets. On the other hand, it has sidewalls closer to (011) type planes viewed along $[011]$. In these two directions, no lateral growth was observed. However, lateral growth over SiO_2 mask clearly occurs in the view along $[010]$, as indicated by the arrows in the 80°-tilted SEM image (top image in middle column).

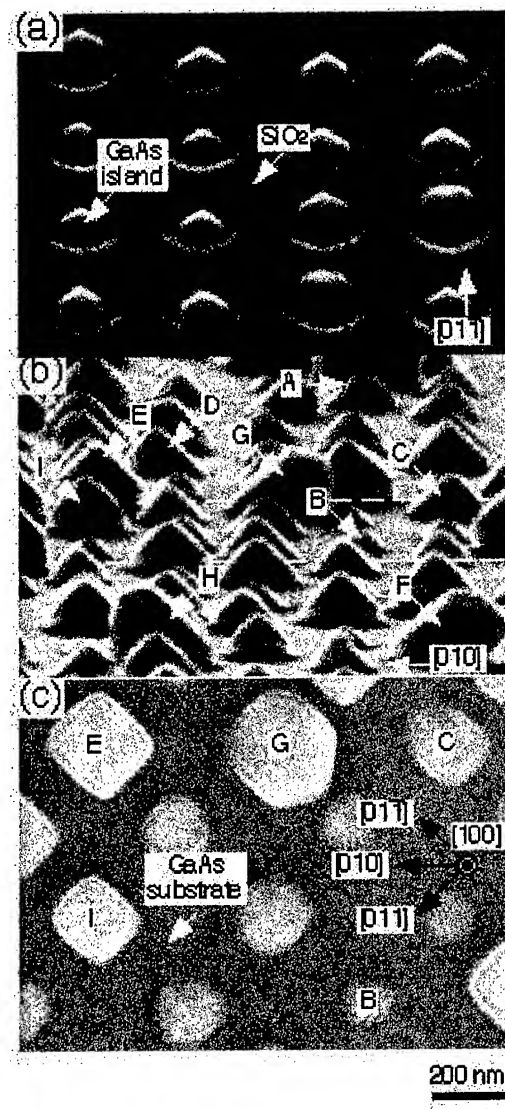


Fig. 5 (a) a 45°-tilted SEM image of an as-grown sample viewed along a $[011]$ direction. (b) 80°-tilted and (c) 0°-tilted (top-view) SEM images of the as-grown sample after removing the SiO₂ mask, taken along a $[010]$ direction. Labeled GaAs islands in (b) and (c) are the same; the area covered in (c) corresponds to the dashed rectangle in (b).

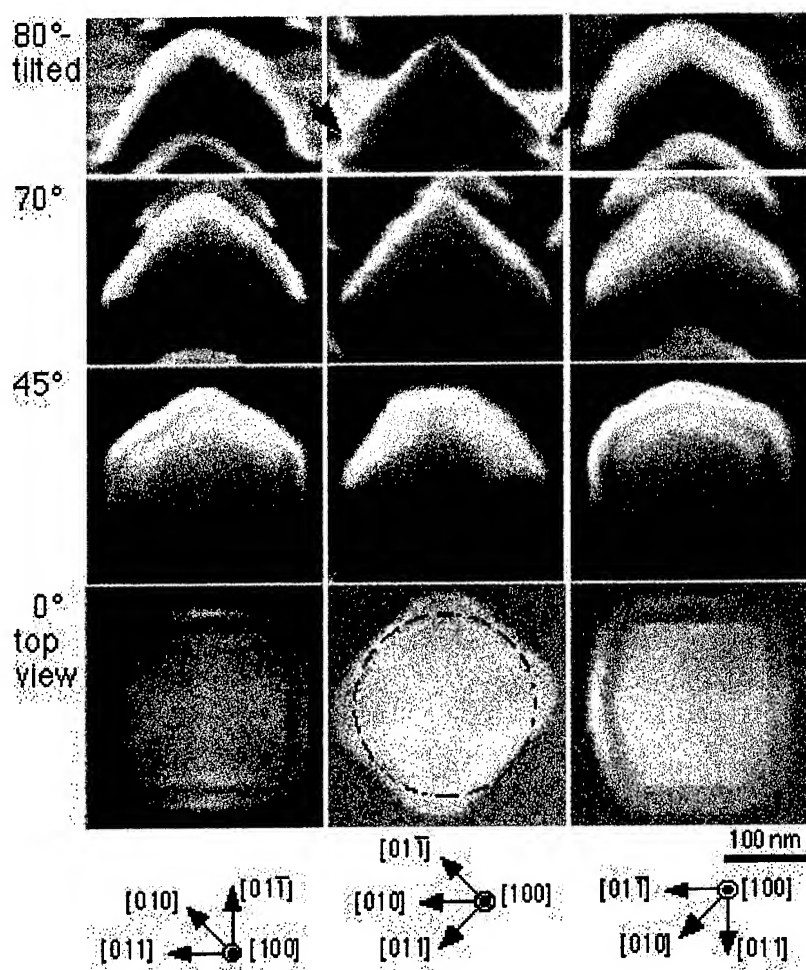


Fig. 6 SEM images taken from the island labeled A in Fig. 5 tilted from 80° to 0° (top view) from three different directions. The orientations indicated below the images are for the top view. In top view, some bended sides may be due to slight deviation of the sample from 0°.

The thickness and sidewall slope of the SiO_2 mask probably affect the initial faceting and lateral growth like 1D NLG. Even though the initial faceting may be random because of an imperfect circular pattern, lateral growth of Fig. 5 and 6 is apparently a characteristic growth mode. The directions of lateral growth of Fig. 6 are also different from those of 1D NLG which has fewer degrees of freedom in the faceting and incorporation of migrating Ga atoms, compared with relatively complicated 2D cases. Further investigation is required to understand both 1D and 2D NLG. Lateral growth in the $[010]$ and $[001]$ directions could be an expansion of facets initially generated on sidewalls in $\langle 011 \rangle$. The order of generation/disappearance of facets and their expansion/contraction in shape evolution can be an indirect index for the hierarchy of surface free energies between different orientations.

Application of nanoscale faceting on heteroepitaxy - Growth of InAs QDs aligned on a 180-nm period (100)-(311) nanofaceted GaAs substrate

Figure 7 shows an atomic force microscopy image of InAs QDs aligned on nanoscale (100)-(311) faceted GaAs(100) along $[01\bar{1}]$. Growth temperature was 510°C and deposition thickness was ~ 2.5 ML. One of the major mechanisms of QD alignment is orientation-dependent migration and incorporation (ODMI) that is mass transport during growth from one facet to another one caused by different adsorption kinetics corresponding to alternative surface bonding configurations. This results in composition/thickness modulation in the direction perpendicular to the pattern orientation. As mentioned in Section I, control of nanofaceting can provide a periodic (100)-(311) faceted substrate where In atoms preferentially migrate from a (311) to an adjacent (100) facet. In Fig. 7, the formation of InAs QDs is localized to the bottom of each groove and typical QD size is about 15 - 20 nm. From the profile shown at the bottom of Fig. 7, the height of InAs QDs are about 3 - 4 nm. The dot density of Fig. 7 is about $2 \times 10^{10} \text{ cm}^{-2}$ which is almost 60 - 70% of the dot density obtained from an unpatterned wide-area GaAs(100) at the same growth conditions. Figure 7 show the possibility of customization of shape, size, spacing, density and area coverage of InAs QDs in deep sub-100 nm lithography which is very important in device applications.

Summary and future work

We have reported the fabrication of nanoscale 1 and 2 dimensional SiO_2 patterns on GaAs(100) and nanoscale faceting and NLG by molecular beam epitaxy. Growth of aligned InAs QDs and realization of NLG are very promising for the improvement of size fluctuation of QDs and strain-reduction of large lattice mismatched heteroepitaxy. Composition/thickness modulation assisted by ODMI on nanoscale faceted surface suggests another strong potential of its application to optoelectronic devices. For further research and real device application such as high density QDs and surface planarization, the reduction of pattern period is very important. Also, the improvement of pattern uniformity is required. Currently, 244- and 213-nm UV light sources are available and a 118-nm light source is being developed.

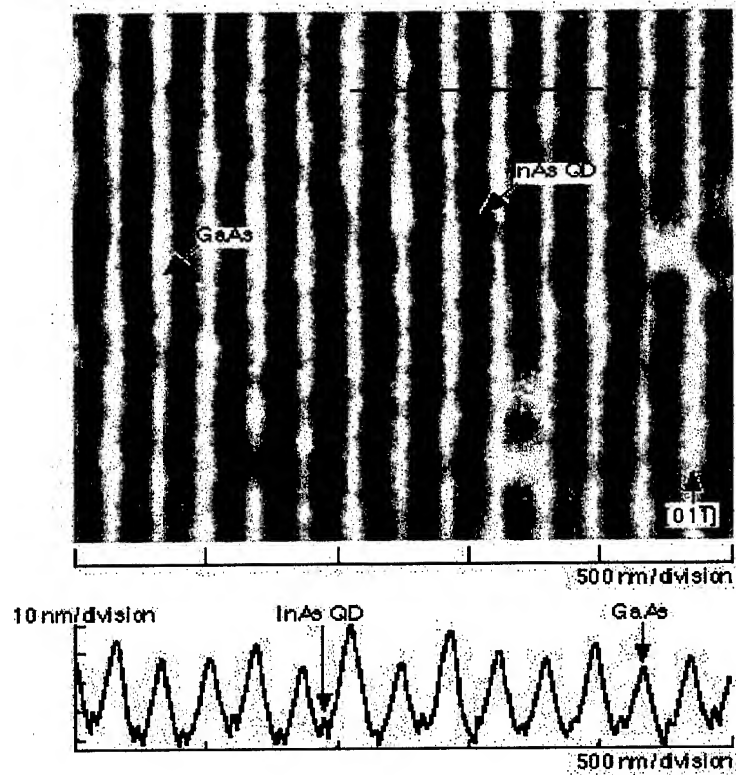


Fig 7. An AFM image of self-aligned InAs QDs on (100)-(311) nanofaceted GaAs surface with 2.5 μm scan range. The profile at the bottom corresponds to dashed line in the top image.

III. End of Program Summary

A. MBE-Grown Mid-IR Lasers

Due to the wide scope of optoelectronic devices desired for high speed optical interconnects, electronic counter measures, ladar applications, and trace gas sensors, there is an ongoing need to provide a suitable growth platform for semiconductor alloys for which no lattice matched substrate is readily available. Many interesting and potentially high performance device structures have been identified but not fabricated due to the lack of a suitable substrate on which to grow them. For the III-V compound semiconductors the substrates available in reasonable quantity with high metallurgical quality at affordable cost are limited to a few of the binary materials, including GaAs, InP, InAs, InSb, GaSb, and GaP. To date, no high quality substrates of any of the ternary III-V alloys are commercially available. For this program we have addressed the need for flexibility in the lattice constant of the substrate material by using appropriate metamorphic (strain-relaxed) buffer layers in various forms. These metamorphic layers are grown on a binary III-V substrate in such a way that they relax to a lattice constant suitable for the epitaxial growth of the desired device structure. Thus we achieve a ternary (or quaternary) alloy substrate, not by bulk growth, but by epitaxial processes. The greatest challenge for this approach is to maintain planarity and metallurgical quality in the metamorphic layers in spite of the high degree of lattice mismatch. During this program we have used this technique to grow high quality metamorphic buffer layers in two III-V alloy systems, in one case for lattice constants about mid way between that of GaAs and InP, and the other about mid way between that of GaSb and InSb. In both cases we have used these buffer layers as growth platforms for the fabrication of high quality novel device structures with very promising performance.

The first application is motivated by the desire to extend the emission wavelength of InAs quantum dot lasers grown on GaAs substrates to $1.55\ \mu\text{m}$. The nucleation of InAs quantum dots is caused by the large lattice mismatch ($\sim 6.5\%$) between the InAs nucleation layer and the GaAs substrate (or the $\text{In}_2\text{Ga}_8\text{As}$ quantum well layer for the dots-in-a-well [DWELL] structure). The large mismatch causes dots to form at nucleation layer thickness that limits the size of the quantum dots. The small dot size, combined with the large residual strain in the dots limits the emission wavelength to $\sim 1.35\ \mu\text{m}$, well short of the desired $1.55\ \mu\text{m}$. We have used a step-graded $\text{Al}_{0.5}\text{Ga}_{0.5}\text{As}_{1-x}\text{Sb}_x$ metamorphic buffer structure with 8 layers having increments of $\Delta x = .03$ to a final $x = .24$ to provide a substrate with substantially larger lattice constant than that of GaAs. This buffer structure also serves as the bottom cladding layer for the laser. Using this as a growth platform, the decrease in mismatch between substrate and InAs results in the growth of larger InAs dots with decreased residual strain. We have demonstrated buffer structures whose terminating layer shows no threading dislocations in cross sectional TEM images. Quantum dot structures without top cladding layers show strong PL intensity at $1.49\ \mu\text{m}$, demonstrating the movement of the ground state to longer wavelength. Electrically injected full laser structures emit at $1.27\ \mu\text{m}$ (not in the ground state) with $J_{\text{th}} = 1400\ \text{A/cm}^2$ at RT.

Two issues have been identified in these buffer structures. First, they exhibit noticeable cross-hatching as observed with Nomarski microscopy. Second, the top layer is not completely strain relaxed ($\sim 85\%$). It is likely that the failure of laser emission to occur in the ground state is the result of loss associated with the lack of planarity of the active region, in turn due to the non-planarity of the buffer layer. To improve the planarity a different approach has been used for the growth of the individual $\text{Al}_{0.5}\text{Ga}_{0.5}\text{As}_{1-x}\text{Sb}_x$ layers. Instead of using a homogeneous bulk-like layer with a constant value of x , we have used a digital alloy approach. In place of each hom o-

geneous layer we have substituted many alternating pairs of thin (tens of \AA) layers of $\text{Al}_{0.5}\text{Ga}_{0.5}\text{As}$ and $\text{Al}_{0.5}\text{Ga}_{0.5}\text{As}_{0.76}\text{Sb}_{0.24}$ with the thickness of each layer chosen to give the desired average Sb composition. After a suitable number of periods, the thickness ratio of the layers is changed to simulate a larger average Sb composition, and so on until the final composition of 24% Sb is obtained. The additional strain concentration at the many interfaces of the digital alloy structure is beneficial for both the generation of dislocations necessary to achieve complete relaxation, and the filtering of those dislocations by bending in the strain field of the interfaces. Buffer layers grown by the digital alloy technique are much smoother and demonstrate relaxation in excess of 95%. Using these buffer layers, quantum dot PL structures show strong emission at $1.62\text{ }\mu\text{m}$, a longer wavelength than any InAs quantum dot laser grown on GaAs published to date. Laser structures using the digital alloy buffers have not been functional due to complications in the doping capability of the MBE system. Modifications have been made to the growth system and properly doped laser structures will be grown soon.

The second application is motivated by the desire to achieve type I band offset structures for mid-IR emitters and detectors. Most structures presently in use are grown on GaSb and require use of both As and Sb in the alloys to achieve lattice match to the substrate. This usually results in type II band alignments with little or no confinement of holes due to valence band offsets. In contrast, As-free alloy combinations, such as $\text{AlGaInSb}/\text{GaInSb}$ have type I offsets with substantial offset (confinement) in both the conduction and valence bands. However, these structures are not lattice matched to GaSb. We have overcome this obstacle by using digital alloy metamorphic buffer structures composed of thin layers of $\text{Al}_{1-x}\text{In}_x\text{Sb}$ and $\text{Al}_{1-y}\text{In}_y\text{Sb}$. The values of x and y as well as the thickness of the layers are adjusted to give the desired average In content of each component of the buffer layer. Using this technique in much the same fashion as the previous AlGaAsSb example, we grade the In composition in steps of 9% to final values as large as 54%. Cross sectional TEM images are dislocation free for In content as high as 45%. A wide range of multi-quantum well laser structures using AlGaInSb barriers and GaInSb wells has been fabricated on buffer structures with final In content of 0.27, 0.36, 0.45, and 0.54. In these optically pumped structures CW stimulated emission is observed at wavelengths of $2.58 - 3.45\text{ }\mu\text{m}$ with power as high as 0.5 W/facet . Maximum CW operating temperature is as high as 370 K and T_0 is as high as 119 K . These results are extremely encouraging. To our knowledge, these are the only As-free mid-IR lasers reported. Further work could focus on achieving sufficient electrical conductivity in the buffer and cladding layers to allow electrical injection.

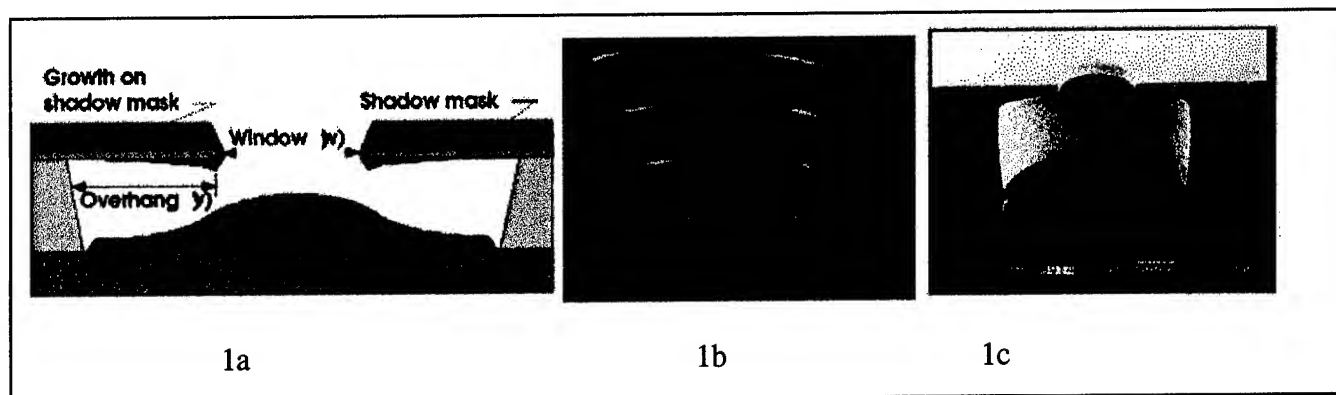
Accomplishments:

1. MBE growth and characterization of very high quality metamorphic $\text{Al}_{0.5}\text{Ga}_{0.5}\text{As}_{0.76}\text{Sb}_{0.24}$ buffer layers on GaAs substrates.
2. MBE growth and fabrication of InAs quantum dot laser structures on $\text{Al}_{0.5}\text{Ga}_{0.5}\text{As}_{0.76}\text{Sb}_{0.24}$ buffer layers with ground state PL emission at $1.49\text{ }\mu\text{m}$ and laser emission at $1.27\text{ }\mu\text{m}$ with $J_{\text{th}} = 1400\text{ A/cm}^2$.
3. MBE growth and characterization of very high quality metamorphic AlInSb buffer layers on GaSb substrates.
4. Design, growth, and fabrication of first As-free (type I offset) mid-IR lasers, with wavelength as large as $3.45\text{ }\mu\text{m}$, output power as high as 0.5 W/facet , CW operating temperature as high as 370 K , and T_0 as high as 119 K .

B. MOCVD Grown Micro-Optical Devices and Nanoheteroepitaxy for the Integration of Highly Mismatched Semiconductors.

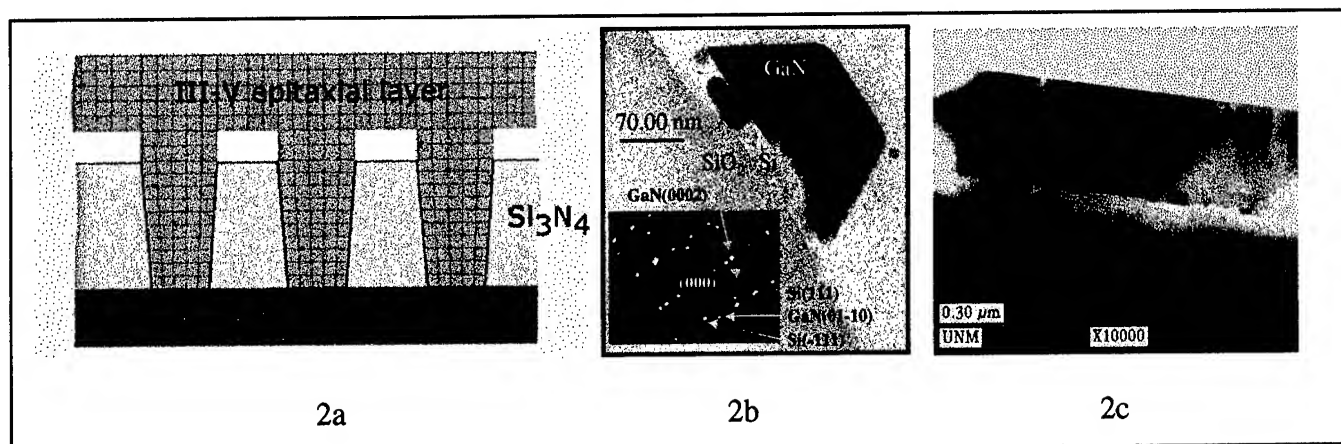
1: MOCVD grown micro-optical devices

We discovered that when MOCVD growth is performed through a shadow mask, a unique growth behavior occurs inside the shadow mask and it is possible to grow 3D crystalline objects (for example in GaAs) with smoothly curving surfaces and **no facetting** (figure 1a). We demonstrated that the detailed shape of the 3D object could be readily controlled by the shadow mask geometry (window width (w), overhang distance (y) and spacer height (h)). Arrays of high quality GaAs microlenses (figure 1b) were fabricated with apertures in the range $5\text{ }\mu\text{m}$ to $500\text{ }\mu\text{m}$ and with focal lengths as small as $40\text{ }\mu\text{m}$. Convex, concave and cylindrical micro-optical devices were demonstrated. We also developed a deep-RIE, silicon mask technology (figure 1c) that allowed the shadow mask to be reused in subsequent growths. A key application envisaged for these microlenses is as collimating lenses for small-area, low threshold VCSELs as required for optical interconnects. This work resulted in 4 papers, one Ph.D thesis and the award of two patents.



2: Nanoheteroepitaxy for the Integration of Highly Mismatched Semiconductors.

In collaboration with Dr. Brueck's group we have invented and experimentally demonstrated a new approach for combining highly mismatched semiconductors that we call Nanoheteroepitaxy or NHE. NHE uses a highly compliant, crystalline interface layer, that is composed of nanoscale bridges, to connect two highly mismatched semiconductor crystals (figure 2a). This new paradigm in heteroepitaxy is quite generic and has relevance to many strategically important materials systems. We have demonstrated the NHE approach in GaAs/Si, GaN/Si and GaN/SiC. Figure 2b is a TEM sample showing the growth of GaN onto a 70 nm Si feature that was patterned by interferometric lithography. The mismatch in this case is 22% yet the GaN crystal is free of threading defects. The electron diffraction pattern (inset) indicates that the Si $\langle 111 \rangle$ and the GaN $\langle 0002 \rangle$ directions are perfectly aligned and that this small island has acted as an epitaxial template. Figure 2c shows a GaN on Si film after coalescence. It appears that in addition to reducing the strain energy and therefore the mismatch defect density, the NHE approach also allows threading defects to terminate at the nucleus sidewall. In NHE structures we therefore consistently observe that the majority of the defects are in the growth plane where they will often have little impact on device behavior.



This work resulted in 11 papers, one Ph.D thesis and a patent awarded is anticipated based on this technology.

Accomplishments

- Demonstrated a viable technology for the fabrication of micro-optical devices using shadow masked MOCVD (2 patents awarded)
- Developed and experimentally demonstrated Nanoheteroepitaxy
 - Successfully applied Nanoheteroepitaxy to GaAs/Si, GaN/SiC, GaN/Si
 - Demonstrated 2 practical NHE sample structures
 - Demonstrated 3 defect reduction mechanisms active in NHE.
 - Demonstrated that thermal mismatch effects can also be controlled by using an appropriate NHE pattern geometry
 - Demonstrated high quality coalescence
 - Showed that NHE GaN films have reduced defect density, higher PL intensity and increased minority carrier lifetime.

Publications

1. "Nanoheteroepitaxy: A New Approach to the Heteroepitaxy of Mismatched Semiconductor Materials", D. Zubia* and S.D. Hersee, J. Appl. Phys., **85** (1999) 6492-6496
2. "Properties of GaN epilayers grown on misoriented sapphire substrates", Carol Trager-Cowan, S. McArthur, P. G. Middleton, K. P. O'Donnell D. Zubia*, S.D. Hersee, MRS Journal of Internet, accepted Oct 1998: (<http://nsr.mij.mrs.org/3/36/>)
3. "Micromachined, Reusable Shadow Mask for Integrated Optical Elements Grown by MOCVD", G.M. Peake*, L. Zhang, N.Y. Li, A.M. Sarangan, C.G. Willison, R.J. Shul and S. D. Hersee, J. Vac. Sci. and Technol., B **17** (1999) 2070 - 2073

4. "A Micromachined, Shadow-Mask Technology for the OMVPE Fabrication of Integrated Optical Structures", G.M. Peake*, L. Zhang, N.Y. Li, A.M. Sarangan, C.G. Willison, R.J. Shul and S. D. Hersee, *Journal of Electronic Materials*, 29 (2000) 86-90
5. "Nanoheteroepitaxial Growth of GaN on Si by OMVPE", D. Zubia*, S.H. Zaidi, S.R.J. Brueck, S.D. Hersee, *Appl. Phys. Lett.* 76 (2000) 858
6. "Chemical Vapor Deposition of $B_{12}As_2$ Thin Films on 6H-SiC", R.H.Wang*, D. Zubia*¹, T. O'Neil*¹, D. Emin², T. Aselage³, W. Zhang³, and S.D. Hersee, *J. Electronic Matls*, 29(11) (2000) 1304-1306
7. "Probing Nitride Thin Films in 3D Using a Variable Energy Electron Beam", Carol Trager-Cowan, K. P. O'Donnell, W. Van der Stricht, I. Moerman, P. Demeester, M.F. Wu, A. Vantomme, D. Zubia*, S.D. Hersee, published in *Proceedings of MRS 1999 Fall Symposium*.
8. "Nanoheteroepitaxy - A Nanofabrication Route to Improved Epitaxial Growth", D. Zubia, S.H. Zaidi, S.D. Hersee, S.R.J. Brueck, *JVST B* 18(6), Nov/Dec (2000) 3514-3520
9. "Initial Nanoheteroepitaxial Growth of GaAs on Si(100) by OMVPE", D. Zubia, S. Zhang, R. Bommena, X. Sun, S.R.J. Brueck, S.D. Hersee, *Journal of Electronic Materials*, 30 (2001) 812-816
10. "Strain Partitioning in Compliant Heterostructures", D. Zubia, S.D. Hersee, T. Khraishi, *Appl. Phys. Lett.*, 80 (2002) 740-420
11. **Invited** "Nanoheteroepitaxy for the Integration of Highly Mismatched Semiconductor Materials", S.D. Hersee, D.Zubia, X. Sun, R. Bommena, M. Fairchild, S. Zhang, D. Burckel, A. Frauenglass, S.R.J. Brueck, *J. Quantum Electronics*, 38 (2002) 1017-1028

Conference Presentations

- "Auger and Electrical Analysis of Pt/Au and Ni/Au Contacts to p-GaN", D.J. King, L. Zhang, J.C. Ramer, A. Rice, K.J. MALLOY, S.D.HERSEE, L.F. LESTER, paper ThF5 at *LEOS '98 (IEEE Lasers and Electro-Optics Society 1998 Annual Meeting)*, Orlando, Florida, Dec 1998.
- "Integrated Optical Structure Grown by Shadow Masked MOCVD", G.M. Peake, A.M. Sarangan and S.D. HERSEE, paper FQ3 at *LEOS '98 (IEEE Lasers and Electro-Optics Society 1998 Annual Meeting)*, Orlando, Florida, Dec 1998.
- "Shadow Masked OMVPE for Integrated Optical Structures Using a Micromachined Silicon Mask", G.M. Peake*, L. Zhang, N. Li, A.M Sarangan, S.D. Hersee, *Ninth Biennial Workshop on Organometallic VPE*, 23-27 May, 1999, Ponte Vedra Beach, FL.
- "Nanoheteroepitaxy: Selective MOCVD Growth of GaN on Compliant ,Nanostructured Silicon", D. Zubia, S. Zaidi, S.R.J. Brueck, *Ninth Biennial Workshop on Organometallic VPE*, 23-27 May, 1999, Ponte Vedra Beach, FL.
- "Application of Nanoheteroepitaxy (NHE) to the OMVPE Growth of GaN on Silicon", S.D.Hersee, D.Zubia, S.H. Zaidi, S.R.J. Brueck, *Lateral Epitaxial Overgrowth Workshop*, 2-6 Aug, 1999, Juneau, Alaska.
- "Nanostructured SOI Compliant Structures", D.Zubia*, S.H. Zaidi, T. O'Neil*, S. Jaffer, S.R.J. Brueck, S.D.Hersee, *First International Conference on Compliant and Alternative Substrate Technology*, Buena Vista, FL, Sept. 19-23, 1999
- "Nanoheteroepitaxy for the Integration of III-V Devices on Silicon", S.D. Hersee, D. Zubia*, R. Bommena*, X. Sun*, presented at *ONR (Office of Naval research) Workshop on "Challenges in Porous and Amorphous Wide Gap Semiconductors"*, June 2001, Newfoundland, Canada. – (received "Best Paper of Workshop Award")

- "Nanoheteroepitaxial Growth of GaN on Silicon", S.D. Hersee, R. Bommena*, X. Sun*, D. Burckel, S.R.J. Brueck, presented at "*7th Wide Bandgap III-Nitride Workshop*", Richmond, Virginia, March 2002.

Patents Awarded

1. G.M. Peake, S.D. Hersee, "Non-Planar Micro-Optical Structures, Patent No. 6,122,109, (2000)
2. G.M. Peake, S.D. Hersee, "Method of Making Non-Planar Micro-Optical Structures Patent No. 6,363,237 (2002)

Theses related to this program (with Hersee as advisor)

G.M. Peake — Ph.D 2000. Shadow Masked OMVPE for Advanced Micro-Optical Structures .
D. Zubia — Ph D. 2001. "Nanoheteroepitaxy: Theory and Application to GaN on Silicon"

C. Quantum Dot Lasers and Detectors

Novel InAs/InGaAs Quantum Dot in a Well (DWELL) Detectors

InAs/InGaAs quantum dot detector structures were designed, grown, fabricated and characterized in Prof. Krishna's group at CHTM. Normal incidence detectors with peak responsivity of $\sim 1\text{A/W}$ ($V_b = -1\text{V}$) and peak detectivity ($2 \times 10^9 \text{ cmHz}^{1/2}/\text{W}$) were reported at 78K. These detectors had the largest responsivity reported so far in any QD detectors. The detectors were characterized in collaboration with researchers from Army Research Laboratory and Air-Force Research Laboratory.

Two Color Quantum Dot Detectors

Recently, we have obtained a two-color response ($\lambda_{1\text{peak}} \sim 4\mu\text{m}$ and $\lambda_{2\text{peak}} \sim 8\mu\text{m}$) from the InAs/InGaAs QD detectors by appropriate heterostructure engineering of the detectors. Two color detectors are in great need for thermal vision and remote sensing applications as the fusion of images obtained in two different wavelength bands improves the signal to noise ratio.

Adaptive Quantum Dot Detectors

We have observed quantum confined Stark shift in the QD detectors that we have fabricated so far. Thus the spectral response changes as a function of the applied bias. We are presently undertaking modeling of the bandstructure to explain this empirically obtained shift. In collaboration with Prof. Hayat and Prof. Tyo of the EECE department at the University of New Mexico, we have developed a projection algorithm, which can be applied to our detectors to give rise to a tunable response from 5-8 μm . This could prove very beneficial for next generation "smart" focal plane arrays where the applied bias would determine the spectral response.

Room Temperature InGaSb $3\mu\text{m}$ Photovoltaic Detectors

Using a novel growth technique, we have fabricated room temperature "Arsenic Free" InGaSb photovoltaic detectors with $\lambda_{\text{cut-off}} \sim 3.2 \mu\text{m}$ on GaSb substrates. In this technique, graded InAlSb layers are grown using a digital alloying technique that removes the lattice matching conditions. Transmission electron microscopy images reveal very few dislocations at the top of metamorphic buffer layer.

InAs/InGaSb Strain Layer Superlattices

The structural and optical properties of InAs/InGaSb strain layer superlattices have been investigated for mid wave infrared and long wave infrared detectors. Using X-ray crystallography, the strain in the system was determined. Absorption close to 10 μm has been observed. Detectors are being fabricated using this material system.

Accomplishments

- Design, growth, fabrication and characterization of novel InAs/InGaAs quantum dot in a Well (DWELL) Detectors
- Demonstration of two color operation ($\lambda_{1\text{peak}} \sim 4\mu\text{m}$ and $\lambda_{2\text{peak}} \sim 8\mu\text{m}$) of quantum dot detectors
- Observation of quantum confined Stark effect in QD detectors
- Demonstration of bias dependent tunable response of QD detectors for "Adaptive" focal plane arrays
- Design, growth, fabrication and characterization of room temperature InGaSb $3\mu\text{m}$ photovoltaic detectors using graded digital alloy buffer layer
- Growth and characterization of InAs/InGaSb strain layer superlattices for MWIR and LWIR detection.

Publications

1. E. A. Pease, L. R. Dawson, A. L. Gray, L. F. Lester, D. M. Gianardi, *Proc. IEEE/LEOS Ann. Meeting*, 1, 201, 2001.
2. 2.3 – 3.5 mm Optically Pumped GaInSb/AlGaInSb Multiple Quantum Well Lasers Grown on AlInSb Metamorphic Buffer Layers, E. A. Pease, L. R. Dawson, L. G. Vaughn, P. Rotella, and L. F. Lester, *Journal of Quantum Electronics*, in press.

D. Quantum Dot Lasers

UNM Partial List of Achievements

- Invented the dots-in-a-well or DWELL design that is instrumental in increasing the dot density and gain in the active region of practical quantum dot laser diodes.
- Developed the lowest threshold current density room-temperature semiconductor laser at 10 A/cm^2 .
- Demonstrated the one of the widest tuning ranges of any semiconductor laser at 200 nm.
- Measured the lowest linewidth enhancement factor of any semiconductor laser, 0.1, demonstrating the potential for feedback insensitivity and ultra-low chirp.

Quantum Dot Lasers

(I) Ultra-low threshold injection current density. The reduced density of states and the smaller physical volume of the active material means that fewer carriers are necessary in order to invert the quantum dots, resulting in extremely low threshold current densities. UNM has demonstrated a significant difference in threshold current between an InAs/In_{0.15}Ga_{0.85}As QD laser (DWELL structure) and an In_{0.15}Ga_{0.85}As QW laser [Liu00]. The two lasers are identical except for the fact that the active region of the QW laser does not include the InAs quantum dot layer. As shown in Figure 1, the threshold current density of a 7.8-mm-long QD laser is 26 A/cm^2 , which is over 7 times lower than that of the identical length QW laser with $J_{th} = 188 \text{ A/cm}^2$. The slope efficiency (mW/mA) is also improved in the QD laser due to lower internal loss of the waveguide cavity

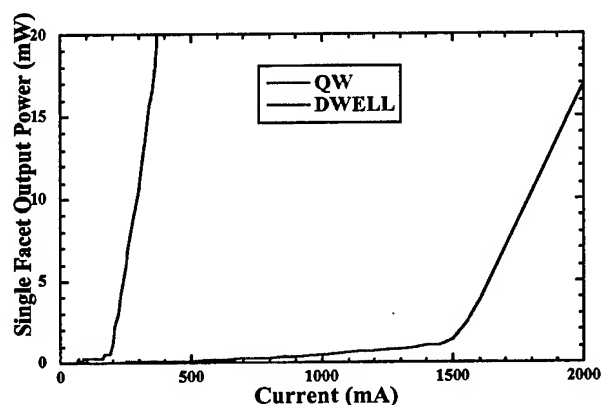


Figure 1. Comparison of threshold current density between a QD laser (DWELL structure) and a QW laser, identical in all aspects except for the layer of quantum dots.

(II) Extremely broad gain spectrum at low injection current density. The low density of states and the small physical volume of the active region in QD lasers yield a low threshold current density and a small ground state saturated gain. As a result, the higher-order confined energy states of the quantum dots can easily become populated by carriers. Therefore, QD lasers exhibit a very broad gain spectrum (larger than 250 nm) at a low injection current density on the order of

1-2 kA/cm². The extent of the gain spectrum increases with the optical losses of the QD laser, which in turn shifts the lasing wavelength toward shorter wavelengths. This is explained by the fact that higher optical losses require a larger threshold current density in order to populate the higher-order energy states of the quantum dots, which due to their larger gain can overcome the increased losses of the laser.

UNM has demonstrated the broad spectral gain of first-generation QD lasers [Varangis00], [Li00]. Figure 2(b) shows the free-running amplified spontaneous emission (ASE) spectrum, which is the measure of the extent of the gain spectrum, and the lasing spectrum of a 1.7-mm-long ridge waveguide InAs/ In_{0.15}Ga_{0.85}As QD laser with a single-DWELL structure. Just below threshold, the QD laser exhibits an almost 300-nm-wide gain spectrum (*red curve*) at an injection current density of 3.2 kA/cm². Comparison of Figures 2(a) and (b) also demonstrates the increase in the extent of the gain spectrum with the judicious increase of the optical losses of the Fabry-Perot laser, by modifying the laser cavity length.

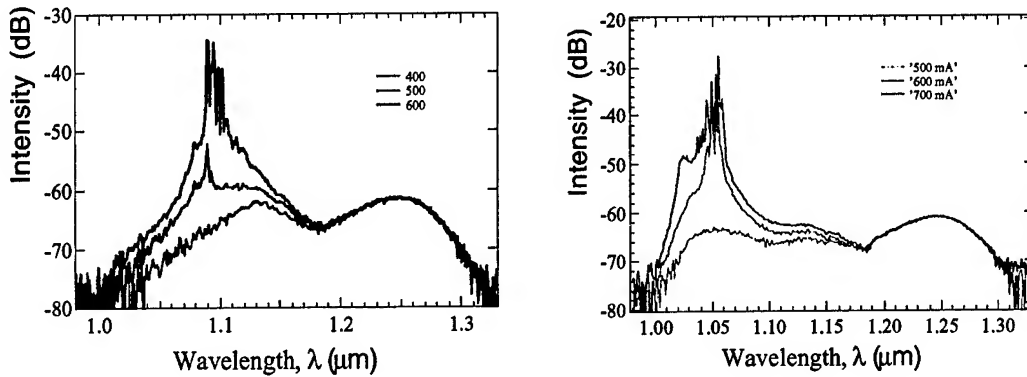


Figure 2. Free-running amplified spontaneous emission (ASE) and lasing spectra of ridge-waveguide InAs/ In_{0.15}Ga_{0.85}As QD lasers with a single-DWELL structure (**a-left**) $L = 2.0$ mm, and (**b-right**) $L = 1.7$ mm cavity length. The two lasers are identical in all aspects except for the cavity length L . The longer-cavity laser has lower optical losses. The threshold injection current density J_{th} of the two QD lasers is 2.83 kA/cm² and 3.46 kA/cm², respectively. The ASE spectrum is the measure of the extent of the gain spectrum of the QD laser (red curve).

(III) Continuous lasing coverage of the available gain spectrum. The ease of populating the excited states by carriers leads to lasing at the short wavelength excited state as well as the long wavelength ground state. However, due to the energy separation between the discrete ground and excited states, lasing at intermediate levels should not necessarily occur. Yet, UNM researchers have shown that continuous lasing from below the ground state to high energy excited states does take place [Varangis00], [Li00].

The physical phenomena underlying this trait are inhomogeneous and homogeneous gain broadening mechanisms. The inhomogeneous gain broadening is due to variations in the size of the dot and their spatial isolation. This variation leads to a distribution in QD energy levels, which means that the gain profile is substantially broadened. Homogeneous gain broadening is attrib-

uted to the scattering processes to exchange electrons between the ground state and the excited states, including the wetting layers. Under homogeneous broadening, lasing-mode photons receive gain not only from the energetically resonant dots but also from other non-resonant dots that lie within the extent of its influence. Measurements have demonstrated that the homogeneous and inhomogeneous gain broadening are comparable. The combination of these two processes results in both an emission spectrum with narrow linewidth, and continuous coverage of the gain spectrum of the QD laser. This is shown in Figure 3.3. The single-DWELL InAs/In_{0.15}Ga_{0.85}As QD laser shown in Figure 3.2(b), when incorporated in an external-cavity configuration, has been continuously tuned across 201-nm at a maximum injection current density of 2.87 kA/cm², which is approximately ten times less than the bias required for comparable tuning of QW lasers.

Therefore, the dot-size variation, which is normally undesirable for low-threshold operation, can be exploited, through the homogeneous broadening, to vary the emission wavelength of the laser. The emission wavelength of the QD laser can thus be selected in order to fit the requirements of a specific application and can be varied either by external means (i.e. diffraction grating in an external-cavity configuration) or by the appropriate design of the laser device (i.e. cavity length, etched grating periodicity in DFB or DBR lasers).

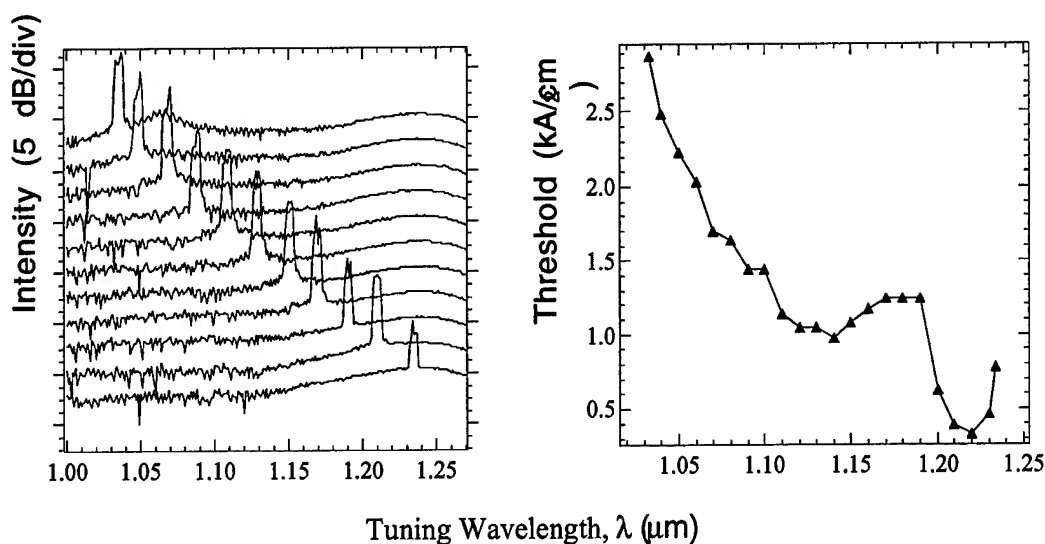


Figure 3. (a-left) Lasing spectra, and **(b-right)** threshold current density as a function of the emission wavelength across the 1033 nm – 1234 nm tuning range, of a grating-coupled external-cavity single-DWELL InAs/ In_{0.15}Ga_{0.85}As QD laser with 9- μm -wide ridge waveguide and 1.7-mm internal FP cavity length.

(IV) Record low linewidth enhancement factor. Due to their symmetric gain spectrum, QD lasers possess a linewidth enhancement factor α [Agrawal93] with an extremely small value. UNM researchers have measured record-low α -values ($\alpha = 0.1$) in DWELL lasers [Newell99]. Large values of α can lead to antiguiding in narrow stripe lasers, self-focusing and filamentation in broad-area emitters, and chirp under high-speed modulation. For strained InGaAs single QW

lasers operating near 980 nm, the value of α is typically 2 or higher at carrier densities corresponding to threshold. At the communication wavelengths of 1.3 μm and 1.55 μm , α is usually much higher unless modulation doping or a large number of quantum wells is employed.

(V) **Reduced temperature sensitivity.** The wavelength of the peak gain point in QD lasers exhibits a smaller shift with temperature when compared to the gain peak of QW lasers. For simple broad area lasers, i.e. edge emitters with a 100-200 μm wide lasing stripe, 1.5 μm QW lasers fabricated by UNM have demonstrated 0.6 nm/ $^{\circ}\text{K}$ wavelength shift while 1.58 μm QD lasers have exhibited only 0.3 nm/ $^{\circ}\text{K}$. This existing red-shift depends predominantly on the corresponding shift of the bandgap of the active region, which is an intrinsic property of III-V semiconductors. The slower gain shift is critical for the high-temperature operation of the DFB laser emitters in WDM systems, especially in reduced-cost low-channel-count uncooled WDM systems. Other investigators have observed that the gain shift is approximately 80% larger in $\lambda \sim 1 \mu\text{m}$ QW lasers compared to quantum dot lasers, that is, 0.33 nm/ $^{\circ}\text{K}$ versus 0.17 nm/ $^{\circ}\text{K}$, respectively [Kamp99].

[Agrawal93] G. P. Agrawal and N. K. Dutta, "Semiconductor Lasers," published by Van Nostrand Reinhold, New York, 2nd ed. 1993.

[Stintz00] A. Stintz, G.T. Liu, A.L. Gray, R. Spillers, S.M. Delgado and K.J. Malloy, *Characterization of InAs quantum dots in strained In_xGa_{1-x}As quantum wells*, Journal of Vacuum Science and Technology B, vol. 18(3), pp. 1496-1501 (2000).

[Liu00] G. T. Liu, A. Stintz, H. Li, T. C. Newell, A. L. Gray, P. M. Varangis, K. J. Malloy, and L. F. Lester, "The Influence of Quantum Well Composition on the Performance of Quantum Dot Lasers Using InAs/InGaAs Dots-in-a-Well (DWELL) Structures", accepted for publication in the IEEE Journal of Quantum Electronics (2000).

[Varangis00] P. M. Varangis, H. Li, G. T. Liu, T. C. Newell, A. Stintz, B. Fuchs, K. J. Malloy, and L. F. Lester, "Low-Threshold Quantum Dot Lasers with a 201-nm Tuning Range", Electronics Letters, Vol. 36(18), pp. 1544-1545 (2000).

[Lester99] L. F. Lester, A. Stintz, H. Li, T. C. Newell, E. A. Pease, B. A. Fuchs, and K. J. Malloy, "Optical Characteristics of 1.24- μm InAs Quantum-Dot Laser Diodes", IEEE Photonics Technology Letters, Vol. 11 (8), pp. 931-933 (1999).

[Li00] H. Li, G. T. Liu, P. M. Varangis, T. C. Newell, A. Stintz, B. Fuchs, K. J. Malloy, and L. F. Lester, "150 nm Tuning Range in a Grating-Coupled External Cavity Quantum Dot Laser", IEEE Photonics Technology Letters, Vol. 12 (7), pp. 759-761 (2000).

[Newell99] T. C. Newell, D. J. Bossert, A. Stintz, B. Fuchs, K. J. Malloy, and L. F. Lester, "Gain and Linewidth Enhancement Factor in InAs Quantum-Dot Laser Diodes", IEEE Photonics Technology Letters, Vol. 11(12), pp. 1527-1529 (1999).

[Kamp99] M. Kamp, M. Schmitt, J. Hofmann, F. Schafer, J.P. Reithmaier, and A. Forchel, "In-GaAs/AlGaAs Quantum Dot DFB Lasers Operating up to 213° C", *Electronics Letters*, Vol. 35 (23), pp. 2036-2037 (1999).

Conference and Journal Publications

1. Wang, R.H.; Stintz, A.; Rotter, T.J.; Malloy, K.J.; Lester, L.F.; Gray, A.L.; Newell, T.C.; Varangis, P.M. "Low threshold oxide-confined InAs quantum dash ridge waveguide lasers on InP substrates", *LEOS 2001. 14th Annual Meeting of the IEEE Lasers and Electro-Optics Society*, 12-13 Nov. 2001, San Diego, CA, USA.
2. Xiaodong Huang; Stintz, A.; Hua Li; Lester, L.F.; Cheng, J.; Malloy, K.J. "Demonstration of passive Q-switching and passive mode-locking in 1.3 μm , two-section InAs quantum dot lasers", *CLEO 2001. Technical Digest. Summaries of papers presented at the Conference on Lasers and Electro-Optics. Postconference Technical Digest*, 6-11 May 2001, Baltimore, MD, USA
3. Ronghua Wang; Stintz, A.; Varangis, P.M.; Newell, T.C.; Li, H.; Lester, L.F.; Malloy, K.J. "1.6 μm single and multiple-stack room temperature quantum dash lasers on InP", *CLEO 2001. Technical Digest. Summaries of papers presented at the Conference on Lasers and Electro-Optics. Postconference Technical Digest*, 6-11 May 2001, Baltimore, MD, USA
4. Lester, L.F. "Materials growth and device characterization of InAs quantum dot lasers", *LEOS 2000. 2000 IEEE Annual Meeting Conference Proceedings*, 13-16 Nov. 2000, Rio Grande, Puerto Rico
5. Li, H.; Newell, T.C.; Liu, G.T.; Stintz, A.; Malloy, K.; Lester, L.F. "Carrier lifetime and radiative recombination in quantum dot LEDs", *LEOS 2000. 2000 IEEE Annual Meeting Conference Proceedings*, 13-16 Nov. 2000, Rio Grande, Puerto Rico
6. Newell, T.C.; Varangis, P.M.; Pease, E.; Stintz, A.; Liu, G.T.; Malloy, K.J.; Lester, L.F. "High-power 1.52- μm AlGaInAs strained multi-quantum well lasers", *Digest. 2000 Conference on Lasers and Electro-Optics Europe*, 10-15 Sept. 2000, Nice, France
7. Newell, T.C.; Li, H.; Eliseev, P.; Liu, G.T.; Stintz, A.; Malloy, K.J.; Lester, L.F. "Broadening mechanisms, gain, and low linewidth enhancement factor in InAs quantum-dot lasers", *CLEO 2000 Technical Digest. Postconference Edition. TOPS Vol.39*, 7-12 May 2000, San Francisco, CA, USA
8. Liu, G.T.; Li, H.; Stintz, A.; Newell, T.C.; Lester, L.F.; Malloy, K.J. "Modal gain and T_0 value improvements in quantum dot lasers using dots-in-a-well (DWELL) structure", *Digest. 2000 IEEE 17th International Semiconductor Laser Conference*, 25-28 Sept. 2000, Monterey, CA, USA
9. Newell, T.; Gray, A.L.; Lee, H.; Dorato, S.; Lester, L.F. "Improved efficiency in 2 μm broadened waveguide GaInAsSb/AlGaAsSb multiple quantum well lasers", *LEOS'98. 11th Annual Meeting. IEEE Lasers and Electro-Optics Society 1998 Annual Meeting*, 1-4 Dec. 1998, Orlando, FL, USA
10. Liu, G.T.; Stintz, A.; Pease, E.A.; Newell, T.C.; Malloy, K.J.; Lester, L.F. "1.59 μm lattice-matched AlGaInAs-InGaAs-InP lasers with digital alloy barrier and waveguide

- layers", *LEOS'98. 11th Annual Meeting. IEEE Lasers and Electro-Optics Society 1998 Annual Meeting, 1-4 Dec. 1998, Orlando, FL, USA*
11. Gray, A.L.; Dawson, L.R.; Lin, Y.; Stintz, A.; Xin, Y.-C.; Garza, A.A.; Lester, L.F. "InAs quantum dots grown on an AlGaAsSb strain-relief buffer", *Semiconductor Quantum Dots II. Symposium, 27-30 Nov. 2000, Boston, MA, USA*
 12. Pease, E.A.; Dawson, L.R.; Gray, A.L.; Lester, L.F.; Gianardi, D.M. "AlGaInSb/GaInSb multiple quantum well mid-infrared lasers", *LEOS 2001. 14th Annual Meeting of the IEEE Lasers and Electro-Optics Society, 12-13 Nov. 2001, San Diego, CA, USA*
 13. Li, H.; Liu, G.T.; Mvarangis, P.; Newell, T.C.; Stintz, A.; Fuchs, B.; Malloy, K.J.; Lester, L.F. "150 nm tuning in a grating-coupled external cavity quantum dot laser", *Digest. 2000 Conference on Lasers and Electro-Optics Europe, 10-15 Sept. 2000, Nice, France*
 14. Liu, G.T.; Stintz, A.; Li, H.; Newell, T.C.; Varangis, P.; Malloy, K.J.; Lester, L.F. "One and three-stack quantum dot lasers with very low threshold current density", *Conference: on Lasers and Electro-Optics (CLEO 2000). Technical Digest. Postconference Edition. TOPS Vol.39, 7-12 May 2000, San Francisco, CA, USA*
 15. Varangis, P.M.; Li, H.; Liu, G.T.; Newell, T.C.; Stintz, A.; Fuchs, B.; Malloy, K.J.; Lester, L.F. "183 nm tuning range in a grating-coupled external-cavity quantum dot laser", *Digest. 2000 IEEE 17th International Semiconductor Laser Conference, 25-28 Sept. 2000, Monterey, CA, USA*
 16. Eliseev, P.G.; Li, H.; Liu, G.T.; Stintz, A.; Newell, T.C.; Lester, L.F.; Malloy, K.J. "Gain in ultra-low-threshold InAs/InGaAs quantum dot lasers", *Digest. 2000 IEEE 17th International Semiconductor Laser Conference, 25-28 Sept. 2000, Monterey, CA, USA*
 17. Newell, T.C.; Li, H.; Stintz, A.; Bossert, D.; Fuchs, B.; Malloy, K.J.; Lester, L.F. "Optical characteristics and low linewidth enhancement factor in 1.2 μm quantum dot lasers", *1999 IEEE LEOS Annual Meeting Conference Proceedings. LEOS'99. 12th Annual Meeting, 8-11 Nov. 1999, San Francisco, CA, USA*
 18. Liu, G.T.; Stintz, A.; Li, H.; Newell, T.C.; Lester, L.F.; Malloy, K.J. "Very low room-temperature threshold current density dots in a well (DWELL) lasers", *1999 IEEE LEOS Annual Meeting Conference Proceedings. LEOS'99. 12th Annual Meeting, 8-11 Nov. 1999, San Francisco, CA, USA*
 19. Liu, G.T.; Stintz, A.; Li, H.; Malloy, K.J.; Lester, L.F. "1.25 μm low threshold current density dots-in-a-well (DWELL) lasers", *1999 Digest of the LEOS Summer Topical Meetings, 26-30 July 1999, San Diego, CA, USA.*
 20. Qiu, Y.; Gogna, P.; Forouhar, S.; Stintz, A.; Lester, L.F. "High-performance InAs quantum dot lasers near 1.3 μm ", *Applied Physics Letters; 26 Nov. 2001; vol.79, no.22, p.3570-2.*
 21. Eliseev, P.G.; Li, H.; Liu, T.; Newell, T.C.; Lester, L.F.; Malloy, K.J. "Ground-state emission and gain in ultralow-threshold InAs-InGaAs quantum dot lasers", *IEEE Journal of Selected Topics in Quantum Electronics; March-April 2001; vol.7, no.2, p.135-42.*
 22. Varangis, P.M.; Li, H.; Liu, G.T.; Newell, T.C.; Stintz, A.; Fuchs, B.; Malloy, K.J.; Lester, L.F. "Low-threshold quantum dot lasers with 201 nm tuning range", *Electronics Letters; 31 Aug. 2000; vol.36, no.18, p.1544-5.*

23. Eliseev, P.G.; Li, H.; Stintz, A.; Liu, G.T.; Newell, T.C.; Malloy, J.; Lester, L.F. "Transition dipole moment of InAs/InGaAs quantum dots from experiments on ultralow-threshold laser diodes", *Applied Physics Letters*; 10 July 2000; vol.77, no.2, p.262-4.
24. Newell, T.C.; Varangis, P.M.; Pease, E.; Stintz, A.; Liu, G.T.; Malloy, K.J.; Lester, L.F. "High-power AlGaInAs strained multiquantum well lasers operating at 1.52 μm ", *Electronics Letters*; 25 May 2000; vol.36, no.11, p.955-6.
25. Newell, T.C.; Bossert, D.J.; Stintz, A.; Fuchs, B.; Malloy, K.J.; Lester, L.F. "Gain and linewidth enhancement factor in InAs quantum-dot laser diodes", *IEEE Photonics Technology Letters*; Dec. 1999; vol.11, no.12, p.1527-9.
26. Lester, L.F.; Stintz, A.; Li, H.; Newell, T.C.; Pease, E.A.; Fuchs, B.A.; Malloy, K.J. "Optical characteristics of 1.24 μm InAs quantum-dot laser diodes", *IEEE Photonics Technology Letters*; Aug. 1999; vol.11, no.8, p.931-3.
27. Liu, G.; Stintz, A.; Li, H.; Malloy, K.J.; Lester, L.F. "Extremely low room-temperature threshold current density diode lasers using InAs dots in $\text{In}_{0.15}\text{Ga}_{0.85}\text{As}$ quantum well", *Electronics Letters*; 8 July 1999; vol.35, no.14, p.1163-5.
28. Yarotski, D.A.; Averitt, R.D.; Negre, N.; Crooker, S.A.; Taylor, A.J.; Donati, G.P.; Stintz, A.; Lester, L.F.; Malloy, K.J. "Ultrafast carrier-relaxation dynamics in self-assembled InAs/GaAs quantum dots", *Journal of the Optical Society of America B (Optical Physics)*; June 2002; vol.19, no.6, p.1480-4.
29. Wang, R.H.; Stintz, A.; Varangis, P.M.; Newell, T.C.; Li, H.; Malloy, K.J.; Lester, L.F. "Room-temperature operation of InAs quantum-dash lasers on InP (001)", *IEEE Photonics Technology Letters*; Aug. 2001; vol.13, no.8, p.767-9.
30. Xiaodong Huang; Stintz, A.; Hua Li; Lester, L.F.; Julian Cheng; Malloy, K.J. "Passive mode-locking in 1.3 μm two-section InAs quantum dot lasers", *Applied Physics Letters*; 7 May 2001; vol.78, no.19, p.2825-7.
31. Liu, G.T.; Stintz, A.; Li, H.; Lester, L.F.; Malloy, K.J. "Ultra-low threshold current density quantum dot lasers using the dots-in-a-well (DWELL) structure", *Proceedings of the SPIE - The International Society for Optical Engineering*; 2000; vol.3944, pt.1-2, p.814-22.
32. Liu, G.T.; Stintz, A.; Li, H.; Newell, T.C.; Gray, A.L.; Varangis, P.M.; Malloy, K.J.; Lester, L.F. "The influence of quantum-well composition on the performance of quantum dot lasers using InAs-InGaAs dots-in-a-well (DWELL) structures", *IEEE Journal of Quantum Electronics*; Nov. 2000; vol.36, no.11, p.1272-9.
33. Li, H.; Liu, G.T.; Varangis, P.M.; Newell, T.C.; Stintz, A.; Fuchs, B.; Malloy, K.J.; Lester, L.F. "150-nm tuning range in a grating-coupled external cavity quantum-dot laser", *IEEE Photonics Technology Letters*; July 2000; vol.12, no.7, p.759-61.
34. Stintz, A.; Liu, G.T.; Li, H.; Lester, L.F.; Malloy, K.J. "Low-threshold current density 1.3 μm InAs quantum-dot lasers with the dots-in-a-well (DWELL) structure", *IEEE Photonics Technology Letters*; June 2000; vol.12, no.6, p.591-3.
35. Liu, G.T.; Stintz, A.; Pease, E.A.; Newell, T.C.; Malloy, K.J.; Lester, L.F. "1.58 μm lattice-matched and strained digital alloy AlGaInAs-InP multiple-quantum-well lasers", *IEEE Photonics Letters*; Jan. 2000; vol.12, no.1, p.4-6.
36. Varangis, P.M.; Gavrielides, A.; Kovanis, V.; Lester, L.F. "Linewidth broadening across a dynamical instability", *Physics Letters A*; 21 Dec. 1998; vol.250, no.1-3, p.117-22.

37. Varangis, P.M.; Gavrielides, A.; Kovanis, V.; Emeux, T.; Lester, L.F. "All-optical double-sideband suppressed-carrier modulation of semiconductor lasers", *Journal of Applied Physics*; 15 June 1998; vol.83, no.12, p.8071-3.

E. Vertical Cavity Surface-Emitting Lasers

Main accomplishments:

- Invention of "*Broad area semiconductor laser with grating-induced, laterally anisotropic waveguide*" for high-power single-mode operation (United States Patent number 6,421,363, issued on 16 July 2002) (Marek Osinski, Alexander P. Bogatov, William Thompson)
- Analysis of vector LP modes in vertical-cavity surface-emitting lasers using the effective frequency method (Gennady A. Smolyakov, Petr G. Eliseev, Marek Osinski)

The effective frequency method (EFM) has been generalized to the case of vector analysis of LP modes in VCSELs and applied to proton-implanted and oxide-confined VCSEL structures. Resonant wavelengths and mode profiles of a number of vector LP modes have been calculated for different values of active region radius. The vectorial EFM has been shown to provide important information about the vertical and radial components of the energy flux inside the laser structure. The maximum values for "weak" E_z and "strong" E_x components of the electrical field within the laser structure have been calculated. Their intensity ratio in the "near-cutoff" situation has been suggested as a quantitative verification of weak-guiding assumption in VCSELs, on which the derivation of the EFM was based.

- Design of InGaN /GaN/AlGaIn vertical-cavity surface-emitting lasers using electrical-thermal-optical simulation (Marek Osinski, Vladimir A. Smagley, Gennady A. Smolyakov, Petr. G. Eliseev)

3D electrical-thermal-optical numerical simulator has been developed and applied to model group-III-nitride-based intracavity-contacted VCSELs with InGaIn multi-quantum-well active region. The optical model based on the effective frequency method has been combined with electrical-thermal simulator using the control volume method. Isothermal (pulsed regime imitation) and CW modes of operation have been calculated over a range of voltages, covering sub-threshold spontaneous emission and lasing emission. Effects of current crowding at the active-region periphery have been examined, and in particular an impact on mode profiles of spatial hole burning superimposed on nonuniform gain distribution has been studied. In order to reduce the current crowding and provide more uniform gain distribution within the active region, a semitransparent p -side contact design has been proposed.

- Analysis of resonant mode coupling in InGaIn/AlGaIn/GaN edge-emitting lasers (Gennady A. Smolyakov, Petr G. Eliseev, Marek Osinski)

Many diode laser structures, including those based on group-III nitride system, contain passive waveguide layers of higher refractive index than in the adjacent layers. Modes of such passive

waveguides ("passive" modes) can interact with an active layer mode ("active" mode), giving rise to two kinds of normal modes or "supermodes" of a laser structure. Away from resonance, one of them is localized predominantly in the active region ("lasing" mode), while the other ones are located mostly in passive waveguides ("ghost" modes). The *lasing* mode is the mode at which laser generation occurs. The lossy *ghost* modes are parasitic modes of a laser structure that can consume energy from the active region. Resonant coupling occurs when the lasing mode and a ghost mode are in phase synchronism. In this paper, the concept of ghost modes is applied to InGaN-based diode lasers. The values for critical thickness are calculated for *p*-GaN cap layer and for *n*-GaN buffer/substrate layer for a particular multilayer laser structure. The typical thickness of 0.5 μm of AlGaIn-cladding layer is found to be insufficient to prevent rather strong coupling between the modes. Under the resonant coupling conditions, the modal gain is shown to be strongly suppressed, allowing no lasing at all.

- Studies of high-power laser ablation of wide-bandgap group-III nitride semiconductors (Marek Osinski, Petr G. Eliseev, Andrei A. Ionin, Yuri M. Klimachev, Dimitri V. Sinitsyn, Jinhyun Lee)

We have studied laser annealing, laser surface processing, and laser lift-off procedure as applied to semiconductor nitride-based structures (GaN films and InGaIn/GaN optoelectronic device structures grown on sapphire substrates). Ablation rate was investigated under subpicosecond laser pulses and under long-pulse irradiation in the IR range (wavelengths of 5.0-5.8 and 9.6 μm). The cleanest pattern of ablation has been obtained with sub-picosecond pulse irradiation.

- Studies of operator ordering of a position-dependent effective-mass Hamiltonian in lattice-matched semiconductor superlattices and quantum wells. (Marek Osinski, Vladimir A. Smagley, Mohammad Mojahedi)

The position-dependent effective mass Hamiltonian $H = (\hbar^2/2)[m(z)]^\alpha \nabla [m(z)]^\beta \nabla [m(z)]^\alpha + V(z)$ with $2\alpha + \beta = -1$ is applied to the problem of periodic heterostructure with abrupt interfaces and discontinuous mass distribution. In order to determine the most suitable operator ordering, numerical results for interband and intersubband transition energies are compared with experimental data for various GaAs/Al_xGa_{1-x}As superlattices and quantum wells. The ordering-related energy shift as a function of structural parameters (well thickness, barrier thickness and height) is investigated. We find that variation of kinetic energy operator ordering can cause transition energy shift exceeding 40 meV. The model with $\alpha = 0$ and $\beta = -1$ consistently produces the best fit to experimental results.

- MOCVD growth of InN_xAs_{1-x} on GaAs using dimethylhydrazine (Marek Osinski, Abdel-Rahman A. El-Emawy, Hongjun Cao, Noppadon Nuntawong, Edward Zhmayev, Jinhyun Lee, David Zubia)

InNAs/GaAs multiple-quantum-well samples were grown by MOCVD on (100) *n*⁺-GaAs substrates at 500 °C and 60 Torr using uncracked dimethylhydrazine (DMHy). Quantum well layers were grown using trimethylindium, tertiarybutylarsine, and 95-97.5% of DMHy in the vapor phase, while GaAs buffer, barrier, and cap layers were grown using trimethylgallium and

arsine. The crystalline quality and solid phase composition were evaluated using high-resolution x-ray diffraction analysis. Nitrogen content in InNAs wells was determined to be 18%. Surface morphology was investigated by atomic force microscopy (AFM) and field emission microscopy (FEM). Photoluminescence measurements confirm that the bandgap energy of InNAs is significantly lower than that of InAs. The peak emission wavelength of ~ 6.5 μm at 10 K is the longest reported so far for dilute nitride semiconductors.

- Analysis of resonant mode coupling and ghost modes in group-III nitride lasers (Gennady A. Smolyakov, Petr G. Eliseev, Marek Osinski)

Modes of passive waveguides in certain laser diode chips can interact with an active layer mode, giving rise to two kinds of normal modes or supermodes of a laser structure. Away from resonance, one of them is localized predominantly in the active region, while the other ones are mostly in passive waveguides (ghost modes). The active-region mode is the mode at which laser generation occurs. The lossy ghost modes are parasitic modes of a laser structure that can consume energy from the active region. Resonant coupling between the lasing mode and a ghost one occurs when an active mode and a passive one are in phase synchronism. We have applied the concept of ghost modes to InGaN-based laser diodes. The values for critical thickness have been calculated for p -GaN cap layer and for n -GaN substrate layer for a particular multilayer laser structure. The typical thickness of 0.5 μm of AlGaIn-cladding layer has been found to be insufficient to prevent rather strong coupling between the modes. The modal gain has been shown to be strongly suppressed under the resonant coupling conditions, allowing no lasing at all.

Bullet list of main accomplishments

- Invention of "*Broad area semiconductor laser with grating-induced, laterally anisotropic waveguide*" for high-power single-mode operation (United States Patent number 6,421,363, issued on 16 July 2002) (Marek Osinski, Alexander P. Bogatov, William Thompson)
- Analysis of vector LP modes in vertical-cavity surface-emitting lasers using the effective frequency method (Gennady A. Smolyakov, Petr G. Eliseev, Marek Osinski)
- Design of InGaIn/GaN/AlGaIn vertical-cavity surface-emitting lasers using electrical-thermal-optical simulation (Marek Osinski, Vladimir A. Smagley, Gennady A. Smolyakov, Petr. G. Eliseev)
- Analysis of resonant mode coupling in InGaIn/AlGaIn/GaN edge-emitting lasers (Gennady A. Smolyakov, Petr G. Eliseev, Marek Osinski)
- Studies of high-power laser ablation of wide-bandgap group-III nitride semiconductors (Marek Osinski, Petr G. Eliseev, Andrei A. Ionin, Yuri M. Klimachev, Dimitri V. Sinitsyn, Jinhyun Lee)

- Studies of operator ordering of a position-dependent effective-mass Hamiltonian in lattice-matched semiconductor superlattices and quantum wells. (Marek Osiński, Vladimir A. Smagley, Mohammad Mojahedi)
- MOCVD growth of $\text{InN}_x\text{As}_{1-x}$ on GaAs using dimethylhydrazine (Marek Osinski, Abdel-Rahman A. El-Emawy, Hongjun Cao, Noppadon Nuntawong, Edward Zhmayev, Jinhyun Lee, David Zubia)
- Analysis of resonant mode coupling and ghost modes in group-III nitride lasers (Gennady A. Smolyakov, Petr G. Eliseev, Marek Osinski)

Publications acknowledging AFOSR ORC support:

1. W. Nakwaski and M. Osiński, "*Thermal properties of vertical-cavity surface-emitting semiconductor lasers*", Progress in Optics XXXVIII (E. Wolf, Ed.), North-Holland, ISBN 0-444-82907-5, Ch. III, pp. 165-262, 1998.
2. J. Wang, R. S. Q. Fareed, M. Hao, S. Mahanty, S. Tottori, Y. Ishikawa, T. Sugahara, Y. Morishima, K. Nishino, M. Osiński, and S. Sakai, "*Lateral overgrowth mechanisms and microstructural characteristics of bulk-like GaN layers grown by sublimation method*", J. Applied Physics **85** (#3), pp. 1895-1899 (1 Feb. 1999).
3. G. A. Smolyakov, P. G. Eliseev, and M. Osiński, "*Design limitations for InGaN/AlGaIn/GaN lasers imposed by resonant mode coupling*", Techn. Digest, Nineteenth Annual Conf. on Lasers and Electro-Optics CLEO '99, Baltimore, MD, 23-28 May 1999, Paper CtuU5, p. 203.
4. P. G. Eliseev, G. A. Smolyakov, and M. Osiński, "'Ghost' modes and resonant effects in Al-GaN/InGaIn/GaN lasers", IEEE J. Selected Topics in Quantum Electronics **5** (#3), pp. 771-779, May/June 1999.
5. M. Osinski, "*Green, blue, and beyond - current status and future prospects for short-wavelength diode laser development*", Invited Paper, Proc. of 8th International Plastic Optical Fibers (POF) Conf., Makuhari Messe, Chiba, Japan, 14-16 July, 1999, pp. 78-84.
6. M. Osinski, V. A. Smagley, C. Fu, G. A. Smolyakov, and P. G. Eliseev, "*Design of In-GaN/GaN/AlGaIn vertical-cavity surface-emitting lasers using electrical-thermal-optical simulation*", Physics and Simulation of Optoelectronic Devices VIII (R. Binder, P. Blood, and M. Osinski, Eds.), San Jose, CA, 24-28 Jan. 2000, Proc. of SPIE, Vol. **3944**, pp. 40-55.
7. M. Osinski and G. A. Smolyakov, "*Design of InGaIn/GaN/AlGaIn VCSELs using the effective frequency method*", Invited Paper, International Symp. on Ultra-Parallel Optoelectronics, Kawasaki, Japan, 3-4 Feb. 2000.

8. P. G. Eliseev, M. Osinski, J. Lee, T. Sugahara, and S. Sakai, "*Band-tail model and temperature-induced blue-shift in photoluminescence spectra of $\text{In}_x\text{Ga}_{1-x}\text{N}$ grown on sapphire*", J. of Electronic Materials **29** (#3), pp. 332-341, March 2000.
9. G. A. Smolyakov, P. G. Eliseev, and M. Osinski, "*Analysis of vector LP modes in VCSELs using the effective frequency method*", Physics and Simulation of Optoelectronic Devices IX (Y. Arakawa, P. Blood, and M. Osinski, Eds.), San Jose, CA, 22-26 Jan. 2001, Proc. of SPIE, Vol. **4283**, pp. 113-128.
10. M. Osinski, V. A. Smagley, G. A. Smolyakov, and P. G. Eliseev, "*Design of InGaN/GaN/AlGaIn vertical-cavity surface-emitting lasers using electrical-thermal-optical simulation*", IEEE J. Selected Topics in Quantum Electronics **7** (#2), pp. 270-279, March/April 2001.
11. A. A. El-Emawy, H.-J. Cao, E. Zhmayev, J.-H. Lee, D. Zubia, and M. Osinski, "*MOCVD growth of $\text{InN}_x\text{As}_{1-x}$ on GaAs using dimethylhydrazine*", Physica Status Solidi (b) **228** (#1), pp. 263-267, 5 Nov. 2001.
12. V. A. Smagley, M. Mojahedi, and M. Osinski, "*Operator ordering of a position-dependent effective-mass Hamiltonian in lattice-matched semiconductor superlattices and quantum wells*", Physics and Simulation of Optoelectronic Devices X (P. Blood, M. Osinski, and Y. Arakawa, Eds.), SPIE International Symp. on Optoelectronics 2002, San Jose, CA, 21-25 Jan. 2002, Proc. SPIE, Vol. **4646**, pp. 258-270.
13. G. A. Smolyakov, P. G. Eliseev, and M. Osinski, "*Effects of resonant mode coupling on near- and far-field characteristics of InGaIn-based lasers*", Physics and Simulation of Optoelectronic Devices X (P. Blood, M. Osinski, and Y. Arakawa, Eds.), SPIE International Symp. on Optoelectronics 2002, San Jose, CA, 21-25 Jan. 2002, Proc. SPIE, Vol. **4646**, pp. 563-573.
14. P. G. Eliseev, A. A. Ionin, Yu. M. Klimachev, D. V. Sinitsyn, J.-H. Lee, and M. Osinski, "*Applications of high-power laser technology to wide-bandgap nitride semiconductor processing (Invited Paper)*", High-Power Laser Ablation IV (C. R. Phipps, Ed.), Taos, NM, 21-26 April 2002, Proc. SPIE, Vol. **4760**, pp. 143-155.
15. H.-J. Cao, N. Nuntawong, A. A. El-Emawy, and M. Osinski, "*Characterization of MOCVD-grown InNAs/GaAs quantum wells*", Techn. Digest, 23rd Annual Conf. on Lasers and Electro-Optics CLEO 2002, Long Beach, CA, 19-24 May 2002, Paper CFG2, pp. 653-654.

F. Free-Space Optical Communications

At CHTM we have are assembling the optical beam director for a 22-km optical communications test range. The range originates at CHTM and terminates at the top of Sandia mountain. The optical transmitter and receiver hardware is located in CHTM laboratory 171-A. This method allows us to use ordinary laboratory equipment for field experiments. Thus we are able to avoid the engineering costs associated with field qualified hardware and yet we can still measure the atmospheric channel effects on optical communications. The transmitter assembly is designed to provide up to 8 spatially diverse transmit beams. The use of several transmit beams that are separated by more than the Fried radius has been shown to effectively average effects of scintillation, thereby reducing the magnitude of the scintillation fluctuations by $1/(\text{number of beams})^{1/2}$. The same mounting structure supported the transmit beam mirrors and the return beam collection mirror. All of the mirrors are pointed together. The optical communications beam director and the retro-reflection mirror located on the top of Sandia mountain will allow us to perform optical channel characterization experiments with almost all of the flexibility of laboratory experiments. This system will be used in the experiments planned for next year.

In high data-rate optical communications a significant source of loss is coupling from the receiving telescope to the photo-receiver. Fast photodetectors have small areas while the receiving aperture is generally many orders of magnitude larger than the detector aperture. The lowest coupling loss for a high data-rate terrestrial free-space optical communications link has been demonstrated by Lucent. They were only able to reduce the loss to 8-dB loss in spite of the fact that they used a custom designed receiving telescope with custom aspheric lenses. For their application they were only collecting the light with a 0.2-m diameter telescope, while for the ground to Low-earth-orbit experiments that we are planning our possible receiving apertures range from 0.6-m to 1.6-m. If these larger apertures are to be efficiently used then a novel system needs to be designed for that application. We examined the limitations and challenges presented by conventional optical systems and determined that a new approach was warranted, we designed a novel nonimaging optical concentrator that out performs conventional optical systems in terms of optical throughput into a small area photodetector and even allows the signal collected by a 1.2-m diameter telescope to be coupled to a 50- μm diameter graded index fiber with less than 0.2-dB of loss. In addition, our design is 2 orders of magnitude less sensitive to longitudinal displacements than the best conventional systems. Our novel dielectric compound conical angular transformer or DCCAT is 8-cm long and can be molded from high optical quality glass or plastic and hence should be inexpensive to manufacture. The DCCAT reduces the loss by nearly 8-dB. We are in the process of preparing a journal article on the design and characterization of the DCCAT. We plan to build and test a DCCAT for use in our ground-to-low-earth-orbit laser communications experiments.

Accomplishments

- The beam director for our 22-km optical communications atmospheric test range designed and is being assembled.
- A novel nonimaging optical receiver that increases the coupling efficiency by almost 8-dB was designed and simulated.

Presentations

1. "Full-Duplex Communication on Single Laser Beam," T. M. Shay, J. MacCannell, D. A. Hazzard, G. Lee, C. D. Garrett, J. A. Payne, N. Dahlstrom, and S. Horan, Solid State Diode Laser Technology Review 2002, Albuquerque, NM, June 3-6, 2002.
2. "Theoretical Model for a Cloudy-Channel Laser Communications Experiment," T. M. Shay, M. Enoch and R. Ewart, IEEE MILCOM 2002, Anaheim, CA, Oct. 7-10, 2002.

Masters Thesis

"Design and Simulation of 3D-Nonimaging Angular Transformer to Improve Power Coupling Efficiencies in a Free-Space Optical Communications System," Vanessa S. Berg, Nov. 2002, submitted in partial fulfillment of the MS in Optics degree.

G. Development of Artificial Dielectrics for Optical and Electrical Applications

Summary

Film fabrication

Artificial dielectric films are prepared by spin-coating precursor solutions onto silicon wafers of selected resistivity and carrier type. The wafers have previously been coated with a thin film of aluminum on the backside for electrical contact to the substrate. Precursor solutions are prepared containing tetraethyl orthosilicate (TEOS), HCl (0.6N HCl aq.), surfactant (CTAB; $\text{CH}_3(\text{CH}_2)_{15}\text{N}^+(\text{CH}_3)_3\text{Br}^-$), H_2O , and gold particles. The weight percentages are: 7.7% TEOS, 4.1% HCl, 2.9% CTAB, 82.8% H_2O , 0.6-2.4% gold. The films are coated using spin speeds of 300-500 rpm in air with 10-20% relative humidity at 25°C. Surfactant molecules, like detergents, usually have hydrophobic tail and hydrophilic head groups. These molecules form a spherical structure in water with hydrophobic tails inside the sphere or core and hydrophilic head groups outside or on the surface of the sphere. In Fig. 1 we show plan view TEM of an ordered artificial dielectric film. Following formation and spinning onto the substrate the films are cured in vacuum at 50°C for 12 hrs. Typical film thicknesses are approximately 100 to 130nm.

MOS capacitor fabrication

Films prepared in the previously described manner were then used to fabricate MOS capacitors. Silicon (100) *p*-type wafers of approximately 10^{15} cm^{-3} doping were used for the substrate material. Backside contact is provided using $\sim 420\text{nm}$ of e-beam evaporated Al, followed by a 450°C forming gas anneal for 25 minutes. The dielectric films were then spun onto the wafers. The finished wafers are then annealed in N_2 at 300°C for 5 hrs to further stabilize the layers and drive out unwanted solvents. Capacitor structures are formed using e-beam evaporated Al

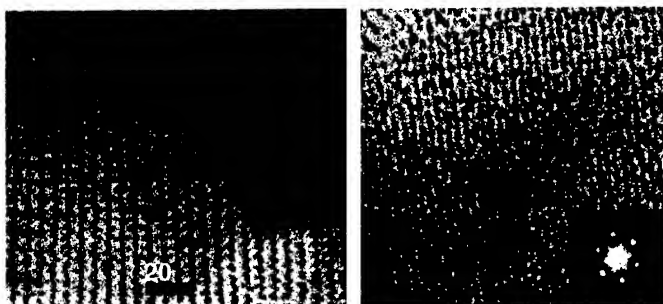


Fig. 1 Plan view TEM of an artificial dielectric array formed in a silica thin film.

films of $\sim 400\text{nm}$ through a shadow mask. Control samples are fabricated using films fabricated without Au particles. Before the capacitor structures are defined the index of refraction of the films are measured

using standard ellipsometry techniques. Typical values are ~ 2 for the films with Au and 1.7 for the films without Au. Following the above fabrication steps and *C-V* measurements were then performed on both sets of films. Figure 2 illustrates charge storage observed in these films.

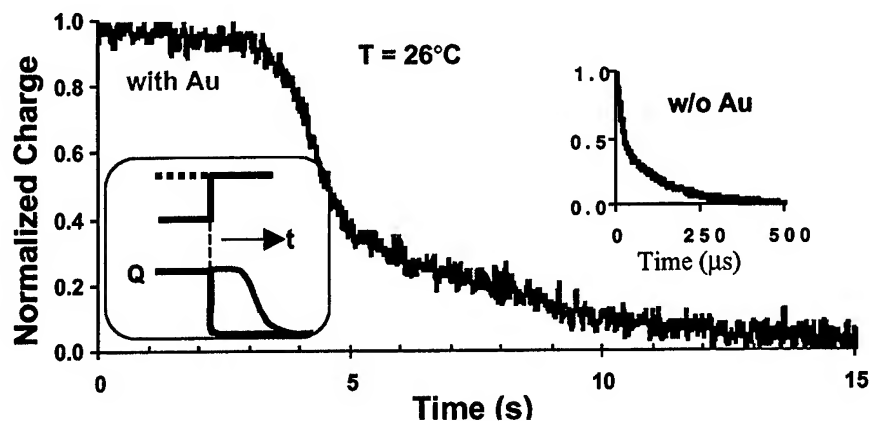


Fig. 2 Illustration of charge storage in artificial dielectric thin film.

Accomplishments:

- Demonstration of thin films of self-assembled ordered metal nanocrystal arrays
- Fabrication of thin film structures of such arrays
- Unique electrical properties of arrays (charge storage) observed

Publications:

Manuscript in preparation

Appendix 1 — Faculty Biographies

S. R. J. BRUECK

Professional Employment History:

Director, Center for High Technology Materials Professor of Electrical and Computer Engineering and Professor of Physics University of New Mexico	1985 - present
Staff Member Quantum Electronics Group M.I.T. Lincoln Laboratory	1971 - 1985

Education:

Doctor of Philosophy in Electrical Engineering
Massachusetts Institute of Technology 1971
Thesis: *Spontaneous and Stimulated Spin-Flip Raman Scattering in InSb*
Master of Science in Electrical Engineering
Massachusetts Institute of Technology 1967
Thesis: *Microwave Acoustic Instabilities in Semiconductors in a Magnetic Field*
Bachelor of Science in Electrical Engineering
Columbia University 1965

Experience: Extensive experimental and theoretical research in many aspects of optics and laser spectroscopy. Material systems investigated include semiconductors, molecular gases, simple molecular liquids, and plasmas used for semiconductor processing. Major current areas of interest include: nonlinear optics of amorphous glasses, imaging interferometric lithography for nanoscale fabrication, optical and electronic properties of Si nanostructures, and optoelectronic diagnostics for semiconductor manufacturing.

Technical and administrative leadership have been major aspects of my position as director of the Center for High Technology Materials (CHTM). CHTM was initiated by the state of New Mexico with mandates to: establish a major research and education center at UNM; encourage interactions among the federal laboratories, industry and the university; and contribute to economic development of New Mexico. During my tenure, CHTM has become a well established, internationally recognized center for optoelectronics and microelectronics research.

Professional Society Affiliations:

American Association for the Advancement of Science
American Physical Society
Institute of Electrical and Electronics Engineers (fellow)
Materials Research Society
Optical Society of America (fellow)
International Society of Optical Engineering (SPIE)

Professional Activities: Involved in numerous professional society activities including conference committees, society governing boards, and editorial offices. Editor of the IEEE *Journal of Quantum Electronics* (1988-1994). Founding editor of IEEE *Journal of Selected Topics in Quantum Electronics* (1995). Program Co-Chair of CLEO'98; General Co-Chair of CLEO'00

Publications / Patents: 156 refereed publications, 6 books edited, 16 patents awarded, 5 pending

L. RALPH DAWSON

Education: Ph. D., Electrical Engineering, *Univ. of Southern California*, 1968; M. S., Electrical Engineering, *Univ. of Southern California*, 1965; B. S., Electrical Engineering, *California Inst. of Technology*, 1962.

Professional Experience: Research Professor, EECE Dept., Center for High Technology Materials, *University of New Mexico*, 1997- present. Distinguished Member of Technical Staff, Sandia National Laboratories, Albuquerque, NM, 1976-1997. Member of Technical Staff, Bell Laboratories, Murray Hill, NJ, 1969-1976.

Current Research Interests: MBE growth of III-V arsenides and antimonides for IR emitters and detectors; monolithic integration of Silicon and III-V device structures; MBE growth of highly mismatched materials.

Honors and Society Offices: 1985 DOE Basic Energy Sciences Award for Sustained Outstanding Research (Strained-layer Superlattices); 1993 DOE Basic Energy Sciences Award for Sustained Outstanding Research (Artificially Structured Materials); 1990-1996 Distinguished UNM-Sandia Labs Professor; Electronic Materials Committee (TMS), member for 21 years, chairman for two years, Electronic Materials Conference Chair for two years; International Symposium on Compound Semiconductors, member, International Advisory Committee, Conference Chair in 1991; Narrow Gap Semiconductor Conference, member, International Advisory Committee, Conference Chair in 1995; Materials Research Society, organizer of 4 symposia, former chair of education and short course committee, instructor of 14 short courses.

Principal Accomplishments: First MBE growth of strained layer superlattices (SLSs); MBE growth of first pseudomorphic HEMT devices, first strained quantum well lasers; MBE growth of InAsSb/InSb SLSs for 8-12 mm detectors; MBE growth of InAs/InAsSb SLS for mid IR lasers; MBE growth of AlAsSb/GaAsSb Bragg reflectors; LPE growth of high efficiency AlGaAs light emitting diodes, laser diodes, and GaP light emitting diodes.

Publications and Patents: 185 journal publications, 160 conference presentations, editor of 6 proceedings volumes, 12 patents.

STEPHEN D. HERSEE

shersee@chtm.unm.edu, www.chtm.unm.edu/hersee

Education

Brighton Polytechnic (UK)	Applied Physics	B.Sc.	1972
Brighton Polytechnic (UK)	Applied Physics	Ph.D.	1975

Appointments

Professor, Elect. and Computer Engineering, University of New Mexico	1996 – present
Assoc. Professor, Elect. and Computer Engineering, University of New Mexico.	1991 - 1996
Senior Materials Engineer, General Electric Co.	1986 - 1991
Ingenieur IIIA, Thomson CSF (France).	1980 - 1986
Principal Scientist, Plessey Research Caswell Ltd. (UK).	1975 - 1980

Research Activities

Dr. Hersee has published and presented over 120 peer reviewed papers and holds three patents with five invention disclosures. He has graduated 1 MS and 8 Ph.D students while at UNM. Dr. Hersee has contributed extensively in the area of semiconductor materials and devices during the last 25 years: the identification of failure mechanisms in GaAs high radiance LEDs (1977); the first growth of quantum-well lasers by MOCVD and the achievement of world-record, quantum-well laser performance (1982); the first demonstration of the orientation dependence of MOCVD (1986); state of the art MOMBE grown AlGaAs (1990); demonstration of record levels of coherent power from novel unstable-resonator semiconductor lasers (1992 -1997). Since 1993 his research has covered the materials science and device applications of III-N wide-gap semiconductors and since 1995, the development of nanoheteroepitaxy for the integration of lattice mismatched materials and devices.

Professional Activity

- Senior Member IEEE
- Conference Chair: "*Ninth International OMVPE Workshop*", May 1999,
- Member of Organizing Committee for *International OMVPE Workshop*, 1995 - present
- Co-editor for special issue of *Journal Electronic Materials* 1995
- Conference chair, SPIE: "*Sources and Detectors for Fiber Communications*", Boston, 1992

RAVINDER K. JAIN

Education: Ph.D., EECE, *Univ. of Calif., Berkeley*, 1974; M.S., EECS, *Univ. of Calif., Berkeley* 1972; A.B, Physics and B.S., EE, *Santa Barbara*, 1970

Professional Experience: Professor, EECE & Physics, *Univ. of New Mexico* (Jan. 1992 – present); Assoc. Director, Alliance for Photonic Technology (Jan. 1992 - present); Senior Res. Scientist & Group Leader, Physical Technology Deptt, *Amoco Technol. Co.* (1984 - 1991); Senior Scientist, Optical Physics Deptt, *Hughes Research Labs* (1978 - 1984); Member of Technical Staff, *Bell Labs* (1975 – 1978).

Current Research Interests: Reconfigurable optical interconnects and OADMs; Reconfigurable optical networks; Glass waveguide and fiberoptic switches; Fiber sensors & fiber lasers; Tunable FBGs.

Honors and Society Offices: Fellow, IEEE; Fellow, SPIE; Fellow, OSA; Harold E. Edgerton Award, SPIE, 1992, Special Achievement Award, Amoco Technol. Co, 1990, Outstanding Paper of the Year Award, Hughes Research Labs, 1983, Member, Sigma Xi, 1974, Member, Phi Beta Kappa, JRD Tata Scholar. Member, Membership & Education Council, OSA (1994-1996); Chair, LEOS Technical Committee on Ultrafast Optics and Electronics (1991-1994); Member, IEEE LEOS Quantum Electronics Award Committee (1992-1993); Member, LEOS Board of Governors (1991-92); Member, OSA Publications Committee (1989-90); Member, OSA Publications Council (1991); Member, OSA Fellows and Honorary Members Committee (1990); Chair and Committee Member on numerous conferences.

Principal Accomplishments: Development of commercializable electro-optic sampling systems and fiber amplifiers; Invention and development of electrooptically tunable FBGs, fiber Raman lasers, high-power mid-IR fiber lasers, and regeneratively pulsed diode lasers; First demonstration of cw mode-locked Ti:S laser; Discovery and use of the plasmon-photon interaction in tunnel junctions; Discovery and use of nonlinearities caused by nanocrystallites in semiconductor-doped glasses; Invention and development of commercializable synchronously mode-locked dye lasers and diode-pumped solid state lasers.

Publications & Patents: Over 75 publications, 10 U.S. and 20 foreign patents.

SANJAY KRISHNA

EDUCATION

DOCTOR OF PHILOSOPHY (APPLIED PHYSICS) University of Michigan, 2001
 MASTER OF SCIENCE (ELECTRICAL ENGINEERING) University of Michigan, 1999
 MASTER OF SCIENCE (PHYSICS) Indian Institute of Technology, Madras, 1996
 BACHELOR OF SCIENCE, B.SC. (HON. PHYSICS.) S.S.S.I.H.L, Bangalore, 1994

EXPERIENCE

Assistant Professor, (EECE Dept, 07/01-Present) University of New Mexico, Albuquerque
 Graduate Student Research Assistant (05/98- 06/01), University of Michigan. Ann Arbor
 Graduate Student Instructor (09/97- 05/98), University of Michigan, Ann Arbor.
 Visiting Student Researcher (05/95-07/95), Tata Inst. of Fundamental Research, India.

RESEARCH EXPERTISE

Epitaxial Growth

Extensive molecular beam epitaxial growth of InGaAs/GaAs/AlGaAs heterostructure materials and self-assembled quantum dot heterostructures for lasers, MIR detectors and transistors.

Device Fabrication and Characterization

Fabrication of state-of-the-art quantum dot interband and intersubband lasers, vertical and lateral quantum dot detectors in class-100 clean room equipped with facilities for metallization with optical lithography, wet and dry etching, wire bonding, substrate thinning and packaging.

Fundamental Physics Studies

Carrier dynamics and scattering mechanisms are studied in novel material systems using pump-probe spectroscopy and Fourier transform infrared spectroscopy.

AWARDS AND HONORS

- Oak Ridge Associated Universities Ralph E. Powe Junior Faculty Enhancement Award
- Nomination for the Rackham Distinguished Doctoral Thesis Award by University of Michigan
- Gold Medal from the Indian Institute of Technology, Madras for the best academic performance in the Master's program in Physics 1996.
- Best Student Paper Award at the 16th North American Molecular Beam Epitaxy Conference in Banff, Canada, 1999.
- Fellowship, Department of Physics, University of Michigan 1997-1998.
- First in the Graduate School of Physics at Tata Institute of Fundamental Research, Mumbai in Fall 1996 and Spring 1997.
- Prof. Chilukuri Ramasastry Memorial for the best academic performance by a first year student at the Indian Institute of Technology, Madras, 1995.
- Merit Scholarship for academic excellence during study at IIT, Madras, 1995-1996.
- Second rank in the University in the undergraduate honors program in Physics (1994)

SIGNIFICANT ACHIEVEMENTS

- **Demonstration of MWIR QD detector with highest operating temperature** In collaboration with ARL, we demonstrated a normal incidence QD detector operating at 4 mm at $T=150\text{K}$. This is the highest temperature reported so far for normal incidence mid-IR QD detectors.
- **Strain patterning of growth front to achieve uniform QDs**
 Using a layer of buried InAlAs stressor dots, InAs QDs with very low size fluctuations (PL linewidth = 19 meV at $T=17\text{K}$) and increased areal density ($\sim 2 \times 10^{11} \text{cm}^{-2}$) were grown on a GaAs substrate.

- **Demonstration of the first quantum dot laser grown on a Si substrate** Using a thermally cycled buffer layer, we demonstrated the first InGaAs QD laser grown on a silicon substrate. The large lattice and thermal mismatch between GaAs and Si created many dislocations and an optimized buffer layer was designed to filter these dislocations.
- **First demonstration of intersubband emission from QDs**
Demonstration of the first quantum dot intersubband LED and first demonstration of intraband gain, stimulated emission, and lasing from self organized quantum dots at *13 mm*.
- **Demonstration of LWIR QD detector with large responsivity and detectivity**
Recently, in collaboration with ARL and AFRL, we have demonstrated a normal incidence QD detector operating at $\lambda = 7.2$ mm (spectral width $\sim 35\%$) with a large responsivity ($R_{\text{peak}} = 3.58$ A/W at $T = 78$ K) and a large detectivity ($D_{\text{peak}}^* = 2.7 \times 10^9 \text{ cmHz}^{1/2}/\text{W}$, $T = 78$ K). *We believe this is the highest responsivity and detectivity reported in a LWIR QDIP at 78K.*

LUKE F. LESTER**EDUCATION**

Ph.D. in Electrical Engineering from Cornell University, May 1992.

Advisor: Lester F. Eastman

WORK EXPERIENCE

Associate Professor of Electrical and Computer Engineering, University of New Mexico (2000 to present). Research projects and interests include quantum dot semiconductor lasers, mid-IR lasers, tunable laser diodes, and process technology for III-V semiconductors.

Assistant Professor of Electrical and Computer Engineering, University of New Mexico (1994-2000). Research projects included group-III nitride devices and tunable lasers. Faculty supervisor of the Center for High Technology Materials cleanroom. Microelectronics and Optoelectronics graduate program chairman.

Senior Process Engineer, General Electric Electronics Laboratory (1992-1994). Project leader in the fabrication, design, and testing of microwave/millimeter-wave optoelectronic devices and circuits. Also responsible for development of millimeter-wave power HEMT transistors and sub-micron electron beam lithography.

Process Engineer, GE Electronics Laboratory (February 1985 to May 1992). Developed process technology for 0.25 μm low-noise HEMTs including e-beam gate lithography, ohmic contact, via-hole, passivation, and air-bridge techniques. Initiated development of 0.15 μm mushroom gate process to improve noise and frequency performance. Designed and fabricated state-of-the-art millimeter-wave power HEMTs.

AWARDS AND HONORS

- Awarded UNM's School of Engineering Junior Faculty Research Excellence Award in 1998.
- National Science Foundation CAREER Grant (1995-2000)
- Martin-Marietta Corp. Manager's Award for tripling MMIC yield.

KEVIN J. MALLOY
malloy@chtm.unm.edu

EDUCATION

Stanford University

Ph.D., January 1984
 Electrical Engineering

University of Notre Dame

B.S., May, 1978
 Electrical Engineering

EXPERIENCE

January 1990
 to Present

Associate (since June 1994) Professor of Electrical and Computer Engineering, The University of New Mexico. Member of the Center for High Technology Materials. I teach and conduct research on optoelectronic devices and materials.

November 1988
 to January 1990

Visiting Associate Research Engineer, The University of California - Berkeley. Worked with Professors Shyh Wang and Eicke Weber on semiconductor lasers and defects.

October 1983
 to October 1988

USAF Captain and Program Manager for Electronic Materials, The Air Force Office of Scientific Research, Washington, DC. Responsible for implementing and managing \$6 million in basic research funding and coordinating Air Force-wide research.

May 1978
 to September 1978

Electronic Technician, Air Force Avionics Laboratory. Brought one of the nation's first commercial MBE machines on line

HONORS

Air Force Commendation Medal for participation in Project Forecast II
 Air Force Meritorious Service Medal for exceptional service.
 UNM School of Engineering Outstanding Researcher Award - Junior Faculty
 UNM School of Engineering Outstanding Teacher Award - Junior Faculty

PROFESSIONAL ACTIVITIES

Member of the IEEE, MRS, AVS and APS

Advisory Board for Critical Reviews in Solid State and Materials Science.

Member of several NSF review committees, most recent 1997

Reviewer for Applied Physics Letters, Journal of Applied Physics, IEEE Photonics Technology Letters, IEEE Journal Quantum Electronics, IEEE Transactions on Microwave Theory and Techniques and others.

External Reviewer, University of Arizona MURI on Thin Film Science

External Reviewer, Arizona State University MURI on Spatial Light Modulators

Organizer and Co-Chair "Workshop on Quantum Electronic Devices," Atlanta Georgia

Organizer and Chair "Workshop the Mechanical Properties of Materials: Semiconductors and Beyond," Dayton Ohio

Panel member for several Accelerated Research Thrust programs at ONR.

Panel Chairman, ONR/NSF workshop on "Monitoring Foreign Science and Technology for Enhanced International Competitiveness: Defining U.S. Needs."

I participated in several National Research Council panels including "Artificially Structured Materials" and "Photonics."

I contributed to the Office of Technology Assessment's study on "Microelectronics Research and Development"

I served as session chairman at several Materials Research Society Symposia and American Vacuum Society sessions, primarily between 1984-1988

Advisory Committee for the Conference on the Physics and Chemistry of Semiconductor Interfaces (1985-1988)

Session Chair for NATO ASI (#139) "Emerging Technologies for In-Situ Processing," Cargese, Corsica (1989)

Advisory Committee for the International Conference on Hot Carriers in Semiconductors (1987)

OTHER SERVICE ACTIVITIES

Area Chair for Optoelectronics (1991-1997). I counseled graduate students, managed course offerings and ran the PhD qualifying exam for the optoelectronic graduate students.

Member, EECE Graduate Committee (1991-1997).

Chair, EECE Search Committee (1997).

Member, EECE Chair Search Committee (1998).

Chair, EECE Search Committee (1999).

Member, University Research Policy Committee (1999).

From 1995-1999, I supervised four high school students from Sandia Prep in various projects for the New Mexico Supercomputer Challenge. The team

finished in third-place (statewide) for the past two years.

I instruct 2nd through 5th graders at Chelwood Elementary school in various topics in science once a week (I am substituting for Professor Kendall during his sabbatical)

MAREK OSINSKI

Present Position: Professor of Electrical and Computer Engineering, Professor of Physics and Astronomy, and Professor of Computer Science, Center for High Technology Materials, Univ. of New Mexico

Education: Ph.D., Physical Sciences, Institute of Physics, Polish Academy of Sciences, 1979
M.Sc., Physics, University of Warsaw, 1971

Professional Experience:

July 1999 - present, Professor, Univ. of New Mexico; Jan. 1997 - Jan. 1998: Visiting Professor, Department of Electrical and Electronic Engineering and Satellite Venture Business Laboratory, Univ. of Tokushima, Japan; 1988-1989: NTT Visiting Professor in Telecommunications, Univ. of Tokyo, Japan; 1987-1999: Associate Professor, Univ. of New Mexico; 1985 - 1987: Visiting Associate Professor, Univ. of New Mexico; 1984-1985: British Telecom Senior Associate of Research in Coherent Optical Communication at Cambridge Univ., England; 1980-1984: Visiting Research Fellow at Southampton Univ., England; 1971-1980: Research Assistant and Senior Research Associate, Inst. of Physics, Polish Academy of Sciences, Warsaw

Professional Activities:

- Member of OSA, LEOS, SPIE, MRS, Senior Member of IEEE
- Conference Co-Chairman, *Physics and Simulation of Optoelectronic Devices II-X*, SPIE Photonics West 1994-2002
 - Optoelectronics Technical Committee Member, Technical Program Committee, *IEEE International Reliability Physics Symposium*, 1995-1998
- Program Committee Member, *Photonics for Space Environments IV-VII*, SPIE Annual Meeting, 1996-2000
- Program Committee Member, *2nd International Symp. on Blue Laser and Light Emitting Diodes (2nd ISBLLED)*, Chiba, Japan, 29 Sept. - 2 Oct., 1998
- Steering Committee Member, *SPIE/Laser Society of Japan International Forum on High Power Lasers and Applications AHPLA '99*, Osaka, Japan, 1-5 Nov. 1999
- Conference Chairman, *Advanced High-Power Lasers*, Osaka, Japan, 1-5 Nov. 1999
- Conference Chairman, *Design, Fabrication, and Characterization of Photonic Devices, SPIE International Symposium on Photonics and Applications ISPA '99*, Singapore, 30 Nov. - 3 Dec. 1999
- Symposium Chairman, *Symposium on Optoelectronic Integrated Devices and Applications*, SPIE Photonics West, San Jose, CA, Jan. 1998-2001

Honors and Society Offices: Editor, *Progress in Quantum Electronics* (1991-present)
Member, *Optoelectronics Best Paper Award Committee*, SPIE Photonics West 1998-2001

Areas of Current Research Interest: Optoelectronic materials and devices (especially based on group-III nitrides); high power semiconductor lasers; VCSELs and 2D arrays; comprehensive semiconductor laser simulation; thermal effects in semiconductor lasers; life testing, reliability and failure analysis of optoelectronic devices; effects of radiation on optoelectronic devices; unipolar optoelectronic devices, position sensing detectors, quantum-well intermixing, semiconductor laser gyros, tunable diode lasers.

Principal Accomplishments: Co-inventor of resonant-periodic-gain (RPG) surface-emitting lasers; Demonstration of optical chaos in multiterminal semiconductor lasers; Invention and first demonstration of distributed-feedback RPG surface-emitting lasers; First self-consistent comprehensive studies of thermal properties of VCSELs and 2D arrays; Determination of defect-related degradation mechanism in AlGaIn/InGaIn/GaN optoelectronic devices driven at high current densities; Formulation of criterion for estimating the strength of current self-distribution effect in diode lasers; First thermal-electrical simulation study of cryogenic VCSELs and intracavity-contacted VCSELs; Invention of integrated semiconductor ring laser gyro; Co-inventor of high-brightness broad-area semiconductor lasers with tilted-gratings.

Publications and Patents: Over 320 publications, 11 edited books of proceedings, 4 book chapters, 2 awarded and 3 pending patents.

Thomas W. Sigmon

Education

Texas Technological College	Engineering. Physics	BSc 1962
Stanford University	Electrical Engineering	MSc 1964
Stanford University	Electrical Engineering	PhD 1970

Professional Experience.

Jul. 2000 to present:	Professor of Electrical Engineering, University of New Mexico
Jun. 1995 to Jun. 2000:	Program Manager, Lawrence Livermore National Laboratory
Jan. 1994 to May 1995:	Visiting Professor of Electrical Engineering, Arizona State University
Jan. 1992 to Dec. 1993:	Professor of Applied Physics and Electrical Engineering and Department Head, Oregon Graduate Institute
Aug. 1982 to Aug., 1993:	Professor of Electrical Engineering, Research Department of Electrical Engineering, Stanford University
Jul. 1978 to Aug. 1982:	Senior Research Associate, Department of Electrical Engineering, Stanford University
Dec. 1976 to June 1978:	Associate Professor, Electrical and Computer Engineering, Oregon State University
Spring 1975 and 1976:	Lecturer in Applied Physics, California Institute of Technology
Jun. 1970 to Nov. 1977:	Member Technical Staff, Hewlett-Packard Laboratories

Research Interests.

Laser materials interactions, ion beam analysis and processing of materials, non-equilibrium MBE growth of magnetic semiconductors and development of novel device concepts.

Publications Relevant to Proposed Research.

- D. Toet and T. W. Sigmon, "Process for Direct Integration of a Thin-Film Silicon p - n Junction Diode with a Magnetic Tunnel Junction", Lawrence Livermore National Laboratory Patent Application #IL-10609 in US and Foreign Filing (Dec., 2001).
- Y. Chang, S. Y. Chou, T. W. Sigmon, A. F. Marshall, and K. H. Weiner, "Formation of $\text{In}_x\text{Ga}_{1-x}\text{As}/\text{GaAs}$ Heteroepitaxial Layers Using a Pulsed Laser Driven Rapid Melt-Solidification Process", *Appl Phys. Lett.* **56**(19), pp. 1844-1846, (May 1990).
- T. Zhang and T. W. Sigmon, "Defect Induced Schottky Barrier Height Modification by Pulsed Laser Melting of GaAs", *Appl Phys. Lett.* **55** (6), pp. 580-582, (August 1989).
- K.-J. Kramer, S. Talwar, and T.W. Sigmon, "Heteroepitaxial $\text{Si}/\text{Si}_{1-x}\text{Ge}_x/\text{Si}$ structures produced using pulsed uv -laser processing," *Appl. Phys. Lett.* **65** (13), pp. 1709-1711, (Sept. 26, 1994).
- K.-J. Kramer, S. Talwar, T.W. Sigmon, and K.H. Weiner, "Crystallinity, strain, and thermal stability of heteroepitaxial $\text{Si}_{1-x}\text{Ge}_x/\text{Si}$ (100) layers created using pulsed laser induced epitaxy", *Appl. Phys. Lett.* **61** (7), pp. 769-771 (Aug., 17 1992).

Significant Publications- Unrelated.

- G. K. Giust and T. W. Sigmon, "High-performance thin-film transistors fabricated using excimer laser processing and grain engineering", *IEEE Trans. Elect. Dev.* **45** (4), pp 925-932, (April, 1998).

- P. M. Smith, P. G. Carey, and T. W. Sigmon, "Excimer Laser Crystallization and Doping of Silicon Films on Plastic Substrates," *Appl. Phys. Lett.* **70**(3), pp. 342-4, (Jan. 20, 1997).
- R. Anholt and T. W. Sigmon, "Substrate-Impurities Effects on GaAs MESFETs", *Jour. of Electr. Matls.* **17**, No. 1 (March 1988).
- L. Csepregi, E. F. Kennedy, J. W. Mayer and T. W. Sigmon, "Substrate-Orientation Dependence of the Epitaxial Regrowth Rate from Si Implanted Amorphous Si", *J. Appl. Phys.* **49**, pp. 3906-3911 (January 1978).
- T. W. Sigmon and R. M. Swanson, "MOS Threshold Shifting by Ion Implantation", *Solid-State Elec.* **16**, pp. 1217-1232 (March 1973).

Recent Professional Activities:

Conference Co-Chairman, "Quantum Computing and Information," SPIE International Symposium Optoelectronics 2002, Jan. 2002, San Jose, CA.

Honors and Awards

- Fellow of the IEEE, 1998
- 2000 IEEE Millennium Award

Collaborators

G. K. Giust	Present Affiliation:	LSI Logic, Santa Clara, CA.
D. Toet	Present Affiliation:	FlexICs Milpitas, CA
M. O. Thompson	Present Affiliation:	Cornell University, Dept. Materials Science
P. M. Smith	Present Affiliation:	FlexICs Milpitas, CA
P. G. Carey	Present Affiliation:	FlexICs Milpitas, CA

Graduate Advisor

J. F. Gibbons	Present Affiliation:	Stanford University, Dept. of Electrical Engr.
---------------	----------------------	--

Thesis Advisor (last 5 years)

G. K. Guist	Present Affiliation:	LSI Logic, Santa Clara, CA.
In-Cha Hsieh	Present Affiliation:	HannStar Display, Taiwan, R.O.C.

Post Doctoral Advisor (last 5 years)

D. Toet	Present Affiliation:	FlexICs Milpitas, CA
S. Theiss	Present Affiliation:	3M Corp. Mpls. MN

Total PhD Advisor **18s**

Total Post Doctoral Advisor **4**

Appendix 2 — Publications (unpaginated)

Reprinted from

PROGRESS IN OPTICS

VOLUME XXXVIII

EDITED BY

E. WOLF

University of Rochester, N.Y., U.S.A.

Contributors

S. DUTTA GUPTA, P. HELLO, J.L. HORNER, J. JAHNS, B. JAVIDI,
A.W. LOHMANN, D. MENDLOVIC, W. NAKWASKI, M. OSIŃSKI, Z. ZALEVSKY



1998

ELSEVIER

AMSTERDAM · LAUSANNE · NEW YORK · OXFORD · SHANNON · SINGAPORE · TOKYO

E. WOLF, PROGRESS IN OPTICS XXXVIII
© 1998 ELSEVIER SCIENCE B.V.
ALL RIGHTS RESERVED

III

**THERMAL PROPERTIES OF VERTICAL-CAVITY
SURFACE-EMITTING SEMICONDUCTOR LASERS**

BY

WŁODZIMIERZ NAKWASKI*

Institute of Physics, Technical University of Łódź, ul. Wólczańska 219, 93005 Łódź, Poland

MAREK OSIŃSKI**

*Center for High Technology Materials, University of New Mexico,
1313 Goddard SE, Albuquerque, NM 87131, USA*

* Also with the Department of Electrical and Computer Engineering, University of New Mexico, Albuquerque, NM 87131, USA.

** Also with the Department of Electrical and Computer Engineering, and the Department of Physics and Astronomy, University of New Mexico, Albuquerque, NM 87131-6081, USA.

CONTENTS

	PAGE
§ 1. INTRODUCTION	167
§ 2. COMPARISON OF VERTICAL-CAVITY SURFACE-EMITTING AND EDGE-EMITTING DIODE LASERS.	168
§ 3. EFFECTS OF TEMPERATURE ON VCSEL OPERATION . .	182
§ 4. FUNDAMENTALS OF THERMAL MODELING OF VCSELs .	205
§ 5. COMPREHENSIVE THERMAL MODELS OF VCSELs . . .	218
§ 6. CONCLUSIONS	254
ACKNOWLEDGMENTS	255
REFERENCES	256

§ 1. Introduction

Vertical-cavity surface-emitting lasers (VCSELs) generate considerable interest due to their unique features which distinguish them from conventional edge-emitting lasers (EELs): narrow low-divergence circular non-astigmatic output beam, inherent dynamic single-longitudinal-mode operation, geometry suitable for integration into two-dimensional (2D) arrays or for monolithic integration with electronic devices, compatibility with vertical-stacking architectures, and so on. Rarely, the paramount role of thermal effects in VCSELs is listed among those features, perhaps because it usually represents an obstacle rather than an advantage. Ever since the inception of VCSELs, thermal problems have plagued their development (Iga, Koyama and Kinoshita [1988], Geels and Coldren [1991], Hasnain, Tai, Dutta, Wang, Wynn, Weir and Cho [1991]), and to this date they represent a major hurdle that must be overcome if massive integration into 2D arrays is ever to be realized (Osiński and Nakwaski [1995a]).

Compared to EELs, VCSELs have a number of unique features which make them potentially more immune to damage caused or accelerated by external ambient. These include complete isolation of the active region from the external medium, a very small active-region volume, the potential for temperature-insensitive operation, and high internal optical power density (low radiative carrier lifetime). These properties make VCSELs attractive for applications in harsh environments.

In spite of the remarkable progress achieved over the last several years (e.g., Iga [1992a,b], Coldren, Geels, Corzine and Scott [1992], Iga and Koyama [1993], Huffaker, Deppe, Kumar and Rogers [1994], Morgan [1994], Chang-Hasnain [1994], Morgan, Lehman, Liu, Hibbs-Brenner and Bristow [1997], Coldren, Hegblom, Strzelecka, Ko, Akulova and Thibeault [1997], Morgan [1997], the continuous wave (CW) performance and integration scale of VCSELs are still seriously limited by their thermal behavior. To this day, closely packed VCSEL arrays can be operated only if the array elements are excited sequentially, one at a time. Average heat-flux densities generated inside the active regions of VCSELs are often extremely high ($\sim 300 \text{ W/mm}^2$ in $10\text{-}\mu\text{m}$ diameter etched-well VCSELs (Nakwaski and Osiński [1991a]), compared to $\sim 30 \text{ W/mm}^2$ in $15\text{-}\mu\text{m}$ wide stripe-geometry edge-emitting lasers (Nakwaski [1984]), both

evaluated at CW currents 2 times higher than the pulsed threshold). This leads to a substantial increase in temperature, accompanied by a corresponding increase in the threshold current density, a shift in the emission wavelength, and a reduction of the optical output power. Efficient heat dissipation, along with an ultra-low threshold, is therefore critical for large-scale integration into 2D arrays. In addition, since the operating lifetime of semiconductor lasers usually decreases exponentially with temperature, it is essential to design lasers with consistently low self-heating.

In this chapter, we give a comprehensive review of temperature-dependent phenomena in VCSELs, followed by a discussion of various comprehensive approaches used so far to model thermal properties of VCSELs. The chapter is organized as follows. In § 2, the main differences between properties of VCSELs and EELs are highlighted. In § 3, we discuss in more detail the experimental data on various device characteristics affected by temperature. The basics of thermal VCSEL modeling are formulated in § 4. In § 5, we describe comprehensive analytical and numerical thermal models of VCSELs. Such models are especially important if device design needs to be optimized.

§ 2. Comparison of Vertical-Cavity Surface-Emitting and Edge-Emitting Diode Lasers

The main structure difference between edge-emitting diode lasers (EELs) and vertical-cavity surface-emitting diode lasers (VCSELs), reflected in their very names, is illustrated in fig. 1. In EELs, stimulated radiation traveling between resonator mirrors propagates in the plane parallel to the p-n junction, remaining all the time within the active region. In VCSELs, the lasing radiation travels in the direction perpendicular to the p-n junction plane and is amplified inside the active region only during a small fraction of each round trip.

Several important consequences follow from the vertical-cavity configuration. First of all, the coupling between the optical field and the gain medium is much weaker in VCSELs than in EELs, therefore a much higher gain would normally be required in VCSELs to achieve a lasing threshold comparable to that of EELs. The high gain requirement can be mitigated to some extent by reducing the radiation losses, which is accomplished mainly by utilizing VCSEL resonator mirrors of much higher reflectivity (very close to unity) than in standard EELs. This, however, causes an increase in densities of both internal stimulated and spontaneous radiation within the VCSEL resonator and a decrease in the differential quantum efficiency. Consequently, the design of high performance

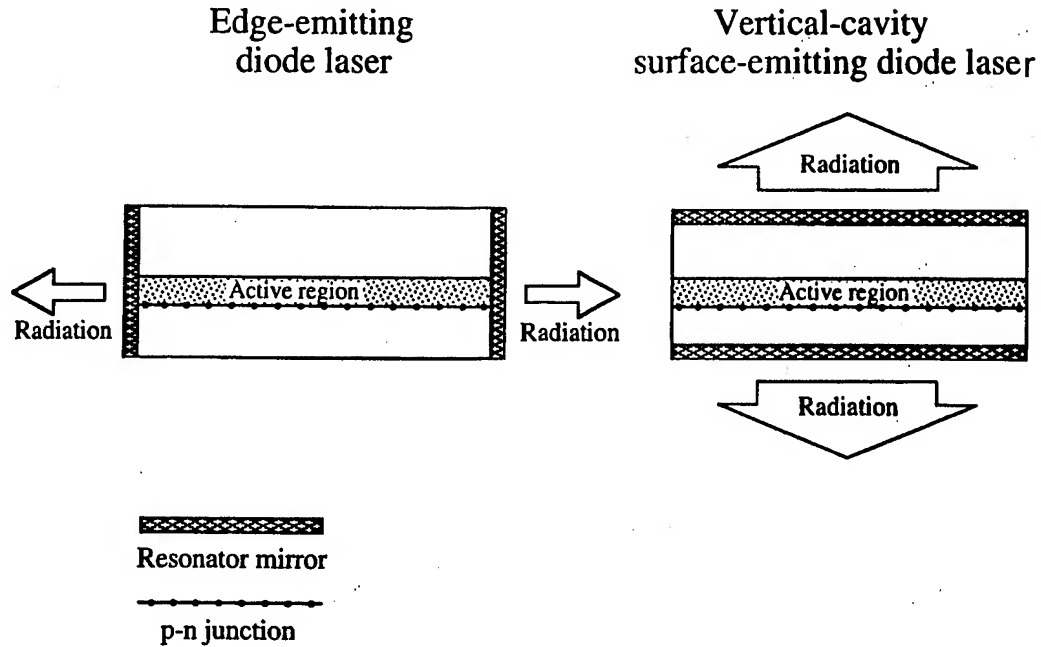


Fig. 1. Schematic configuration of edge-emitting diode lasers (EELs) and vertical-cavity surface-emitting diode lasers (VCSELS).

VCSELS involves a compromise between low-threshold and high-efficiency requirements. Low-threshold VCSELS should have smaller active regions, fewer quantum wells, and mirrors of reflectivities as high as possible, whereas highly efficient VCSELS should have larger emitting areas, more quantum wells, and lower-reflectivity mirrors (cf. Scott, Geels, Corzine and Coldren [1993]).

Another important consequence of vertical-cavity configuration is the very small magnitude of the cavity length L . While in EELs L is typically between $100\text{ }\mu\text{m}$ and $500\text{ }\mu\text{m}$, the effective length of VCSEL resonators (cf. eq. 7, below) is usually in the range of as little as about $1\text{ }\mu\text{m}$ (Hasnain, Tai, Yang, Wang, Fischer, Wynn, Weir, Dutta and Cho [1991], Taylor and Evaldson [1994]) to several micrometers (Iga, Koyama and Kinoshita [1988]). The *longitudinal-mode spacing* $\Delta\lambda_{\text{FP}}$ for the Fabry-Perot (FP) resonator can be approximately written as (Young [1993]):

$$\Delta\lambda_{\text{FP}} = \frac{\lambda^2}{2n_G L}, \quad (1)$$

where n_G is the group refractive index (eq. 4) and λ is the radiation wavelength. Taking $\lambda = 0.85\text{ }\mu\text{m}$ and $n_G = 4.3$ for GaAs (see table 3, p. 183) gives $\Delta\lambda_{\text{FP}} = 4.2\text{ }\text{\AA}$ for EELs with cavity length $L = 200\text{ }\mu\text{m}$, compared to $\Delta\lambda_{\text{FP}}$ as large as $840\text{ }\text{\AA}$ for VCSELS with effective cavity length $L_{\text{eff}} = 1\text{ }\mu\text{m}$. For that reason, usually several longitudinal modes are close to the gain peak in EELs, resulting in multimode

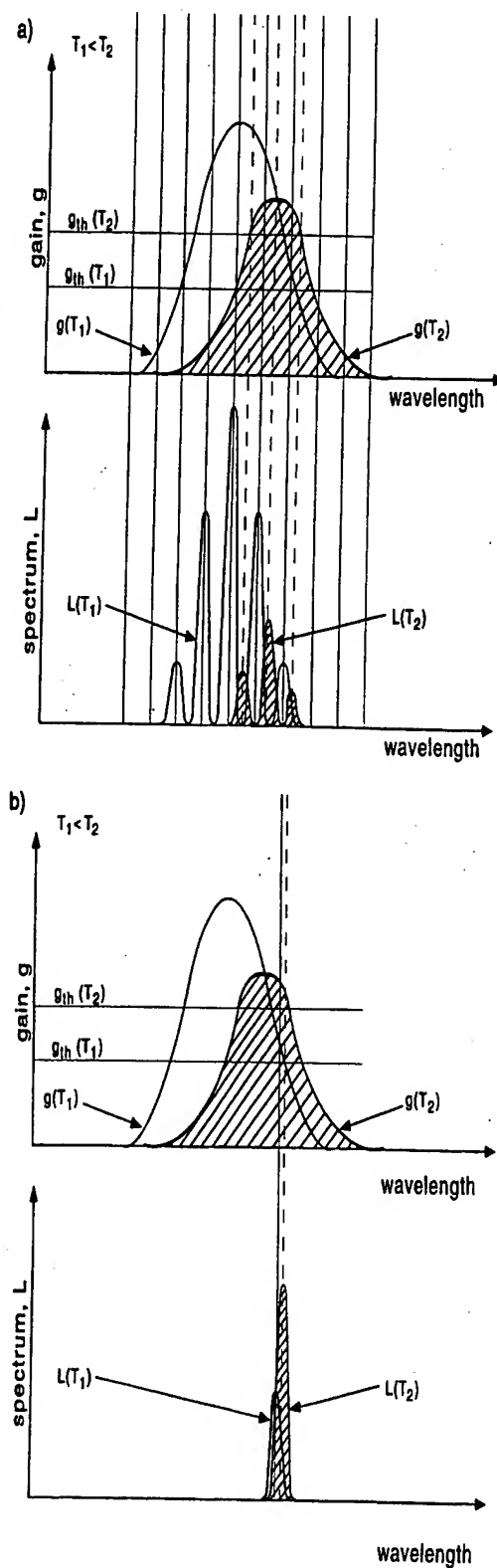


Fig. 2. Illustration of different reactions of output spectra from (a) EELs and (b) VCSELs to an increase in their active-region temperature.

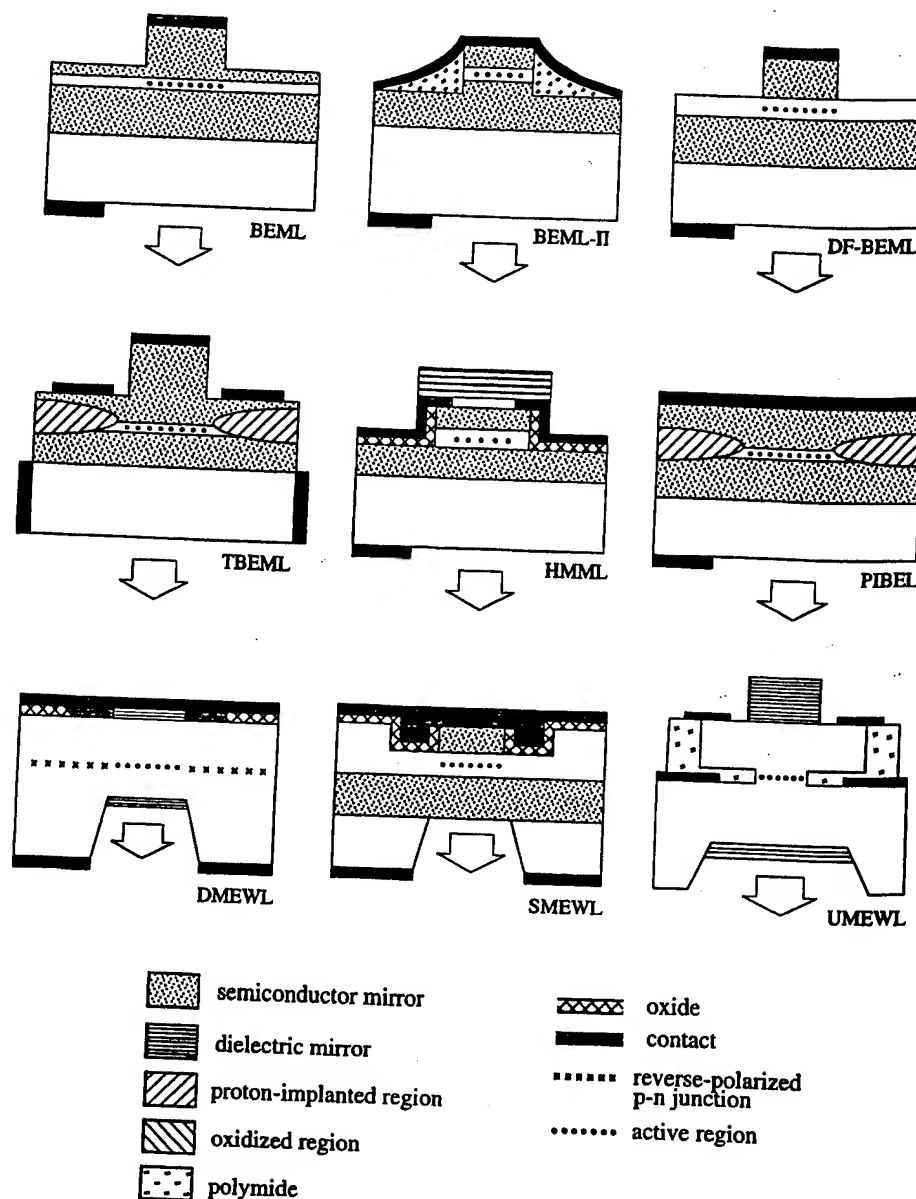


Fig. 3a. Schematic illustration of bottom-emitting VCSELs. See table 1 for abbreviations.

spectral characteristics (see fig. 2a). In contrast, only one (if any) longitudinal mode is within the spectral gain bandwidth in VCSELs (fig. 2b); therefore, they always lase a single longitudinal mode. Inherently, VCSELs operate in a single longitudinal mode even under modulation conditions, which is one of their most important advantages.

Over the last few years, numerous VCSEL structures of different designs were studied. Figure 3 presents schematic structures of some of these devices

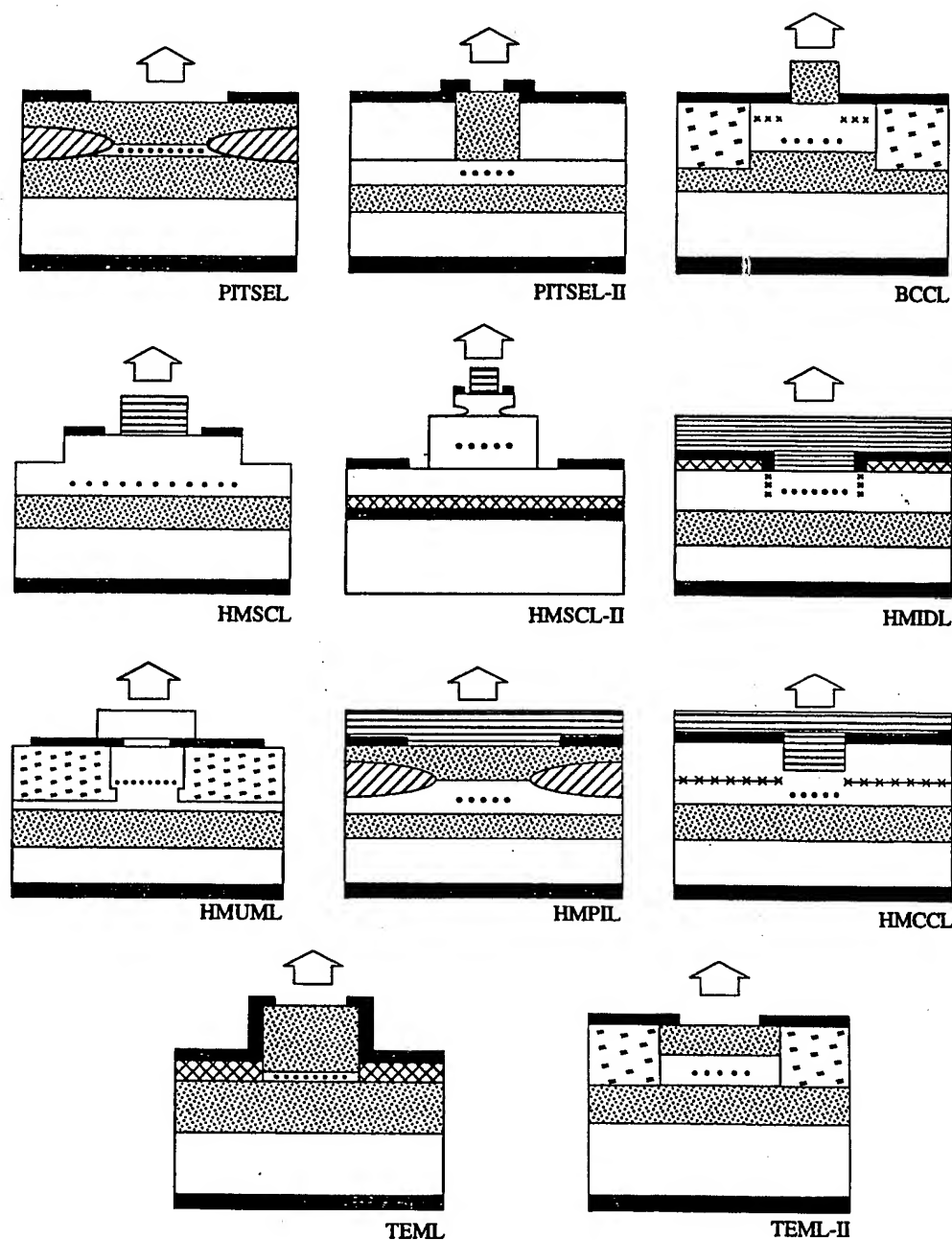


Fig. 3b. Schematic illustration of top-emitting VCSELs.

referred to in this chapter, together with designated abbreviations by which they are identified. Table 1 contains a summary of key features of these devices.

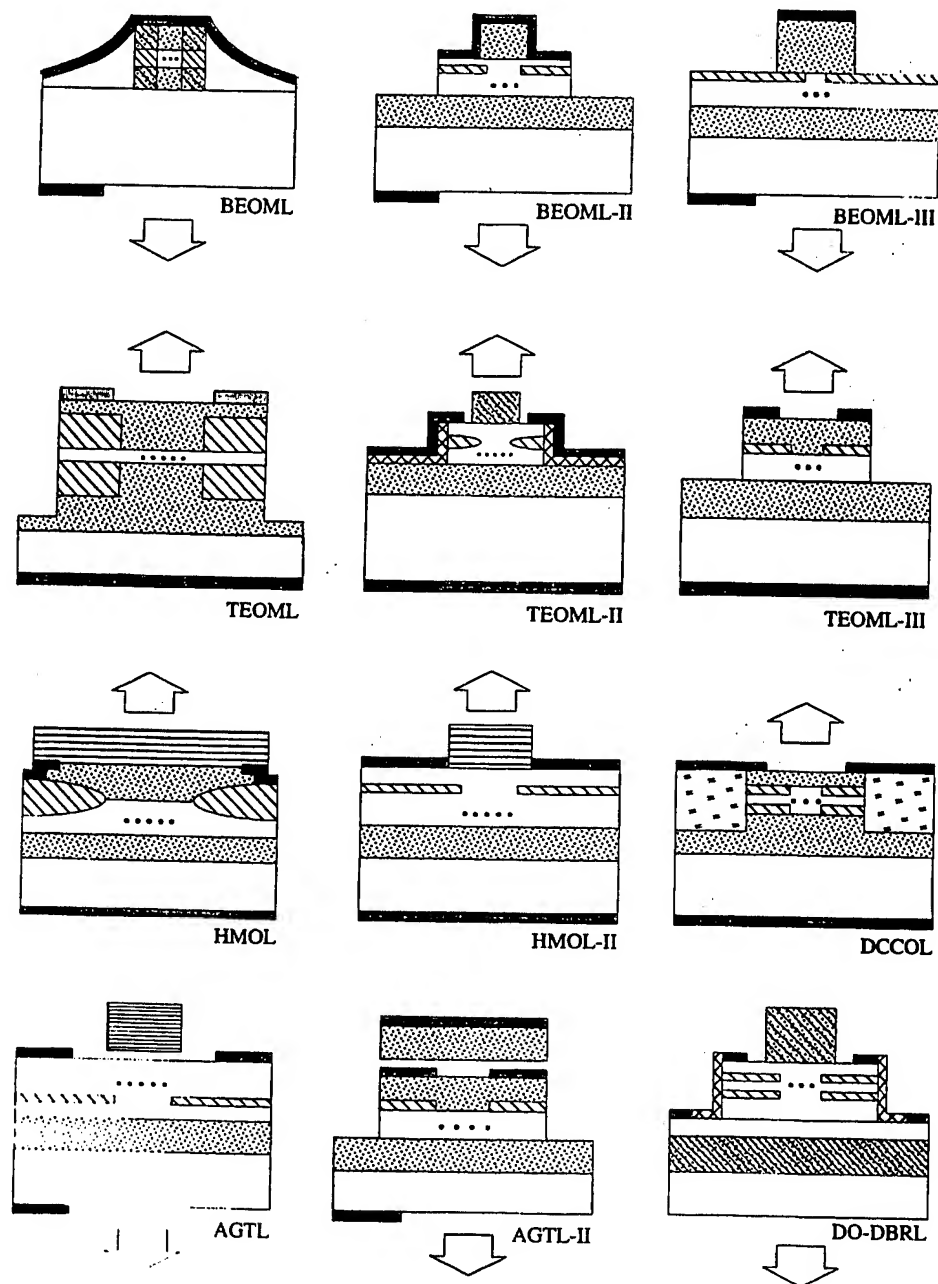


Fig. 3c. Schematic illustration of oxidized VCSELs.

Table 1
Vertical-cavity surface-emitting laser structures

Abbreviation	Active region	Spacer cavity	Bottom reflector	Top reflector	Reference
PITSEL-ATT-A	4 × 10 nm GaAs/Al _{0.2} Ga _{0.8} As MQW	GRIN Al _x Ga _{1-x} As 0.3 ≤ x ≤ 0.6 2 waves	30.5 periods AlAs/Al _{0.15} Ga _{0.85} As stair-case barriers	20 periods AlAs/Al _{0.15} Ga _{0.85} As stair-case barriers	Hasnain, Tai, Dutta, Wang, Wynn, Weir and Cho [1991]; Hasnain, Tai, Yang, Wang, Fischer, Wynn, Weir, Dutta and Cho [1991]
PITSEL-ATT-B	4 × 10 nm GaAs/Al _{0.3} Ga _{0.7} As MQW	GRIN Al _x Ga _{1-x} As 0.3 ≤ x ≤ 0.6 2 waves	29.5 periods AlAs/Al _{0.14} Ga _{0.86} As stair-case barriers	20 periods AlAs/Al _{0.14} Ga _{0.86} As stair-case barriers	Tu, Wang, Schubert, Weir, Zydzik and Cho [1991]
PITSEL-UNM	4 × 8 nm GaAs/Al _{0.15} Ga _{0.85} As MQW	GRIN Al _x Ga _{1-x} As 0.15 ≤ x ≤ 1.0 1 wave	43.5 periods AlAs/Al _{0.15} Ga _{0.85} As graded barriers	24 periods AlAs/Al _{0.15} Ga _{0.85} As graded barriers	Zhou, Cheng, Schaus, Sun, Zheng, Armour, Hains, Hsin, Myers and Vawter [1991]
PITSEL-SNL	3 × 8 nm Ga _{0.46} In _{0.54} P/ (Al _{0.5} Ga _{0.5}) _{0.5} In _{0.5} P MQW	Al _{0.5} In _{0.5} P 2 × 3 waves	55.5 periods AlAs/Al _{0.5} Ga _{0.5} As parabolic-graded barriers	36 periods AlAs/Al _{0.5} Ga _{0.5} As parabolic-graded barriers	Schneider, Choquette, Lott, Lear, Figiel and Malloy [1994]
PITSEL-II-UU	3 InGaAs/GaAs MQW	Al _{0.3} Ga _{0.7} As 1 wave	30.5 periods Al _{0.7} Ga _{0.3} As/GaAs	28 periods Al _{0.7} Ga _{0.3} As/GaAs graded and δ-doped barriers	Zeeb, Reiner, Ries, Möller and Ebeling [1995]
HMIDL-SFIT	1 μm GaAs DH	Al _{0.15} Ga _{0.85} As >1 μm	20.5 periods AlAs/Al _{0.15} Ga _{0.85} As	7 periods SiO ₂ /TiO ₂	Wüthrich, James, Ganière and Reinhart [1990]

continued on next page

Table 1, *continued*

Abbreviation	Active region	Spacer cavity	Bottom reflector	Top reflector	Reference
HMUML-UCSB	0.3 μm InGaAsP DH ($\lambda_g = 1.3 \mu\text{m}$)	InP/InGaAsP 1.4 μm	27 periods AlAs/GaAs digital alloy grading + λ GaAs	4 periods Si/SiO ₂	Dudley, Babic, Mirin, Yang, Miller, Ram, Reynolds, Hu and Bowers [1994]
HMSCL-RIT	9 \times 7 nm InGaAsP/InGaAsP MQW	InP/InGaAsP 5 waves	50 periods InGaAsP/InP	5 periods Si/SiO ₂	Streubel, Rapp, André and Wallin [1996]
HMSCL-II-CU	30 \times 6 nm InGaAsP/InGaAs strain-compensated MQW	1.42 μm InP + 0.44 μm InGaAsP	SiO ₂ /Al	4 periods Si/SiO ₂	Chua, Zhu, Lo, Bhat and Hong [1995]
HMPIL-HTC	3 \times 7 nm GaAs MQW	Al _{0.6} Ga _{0.4} As 1 wave	30.5 periods AlAs/Al _{0.16} Ga _{0.84} As graded barriers	8 periods AlAs/Al _{0.16} Ga _{0.84} As graded barriers + 5.5 periods SiO ₂ /TiO ₂	Morgan, Hibbs-Brenner, Lehman, Kalweit, Walters, Marta and Akinwande [1995]
HMCCL-BTL	1.55 μm InGaAsP ($\lambda_g = 1.4 \mu\text{m}$)	InP 1 wave	45 periods InP/InGaAsP ($\lambda_g = 1.4 \mu\text{m}$)	4 periods Si/Al ₂ O ₃	Fisher, Huang, Dann, Elton, Harlow, Perrin, Reed, Reid and Adams [1995]
BCCL-TUM	3 \times 8 nm In _{0.18} Ga _{0.82} As/GaAs MQW	In _{0.35} Ga _{0.65} As 860 nm	27 periods AlAs/GaAs	18 periods AlAs/GaAs	Rochus, Hauser, Röhr, Kratzer, Boehm, Klein, Traenke and Weimann [1995]

continued on next page

Table 1, continued

Abbreviation	Active region	Spacer cavity	Bottom reflector	Top reflector	Reference
TEML-UCB	3 × 8 nm In _{0.2} Ga _{0.8} As/GaAs MQW	Al _{0.33} Ga _{0.67} As 2 × 1500 Å	33.5 periods Al _{0.9} Ga _{0.1} As/GaAs superlattice barriers	7 periods Al _{0.9} Ga _{0.1} As/GaAs superlattice barriers + external cavity	Hadley, Wilson, Lau and Smith [1993]
TEML-II-NTT	6 GaAs/Al _{0.2} Ga _{0.8} As MQW	Al _{0.3} Ga _{0.7} As 1 wave	34.5 periods Al _{0.15} Ga _{0.85} As/AlAs	20 periods Al _{0.15} Ga _{0.85} As/ Al _{0.5} Ga _{0.5} As/AlAs	Ohiso, Kohama and Kurokawa [1995]
BEML-UCSB	3 × 8 nm In _{0.2} Ga _{0.8} As/GaAs MQW	Al _{0.2} Ga _{0.8} As 1 wave	18.5 periods AlAs/GaAs graded barriers + Au contact	16 periods AlAs/GaAs graded barriers	Geels, Thibeault, Corzine, Scott and Coldren [1993]
BEML-II-TIT	3 × 8 nm In _{0.2} Ga _{0.8} As/GaAs MQW	Al _{0.4} Ga _{0.6} As 1 wave	22 periods AlAs/GaAs graded barriers	25 periods AlAs/GaAs graded barriers + metalization	Mukaihara, Hayashi, Hatori, Ohnoki, Matsutani, Koyama and Iga [1995]
DF-BEML-UCSB	7 × 7 nm InGaAsP MQW	InGaAsP 5.2 waves	25.5 periods AlAs/GaAs graded barriers	24 periods AlAs/GaAs graded barriers	Babic, Dudley, Streubel, Mirin, Bowers and Hu [1995]; Babic, Streubel, Mirin, Margalit, Bowers and Hu [1995]
TBEML-UU	3 × 8 nm In _{0.2} Ga _{0.8} As/GaAs MQW	Al _{0.4} Ga _{0.6} As 1 wave	24.5 periods AlAs/GaAs stair-case barriers	20 periods AlAs/GaAs stair-case barriers + metalization	Wipiejewski, Panzlaff, Zeeb and Ebeling [1994]

continued on next page

Table 1, continued

Abbreviation	Active region	Spacer cavity	Bottom reflector	Top reflector	Reference
AGTL-SU	2×6 nm In _{0.21} Ga _{0.79} As/GaAs MQW	AlAs/Al _{0.31} Ga _{0.69} As/ GaAs 2 waves	22.5 periods GaAs/AlAs	2×SiO ₂ /SiN _x H _y /SiO _x + λ/4 GaAs + metalization + air gap + 7 periods InP/InGaAsP + 5 periods SiO ₂ /TiO ₂ 4.5 periods + air gap + 22.5 periods + Au metalization	Sugihwo, Larson and Harris [1997] Vail, Li, Yuen and Chang-Hasnain [1996] Uchiyama and Iga [1984] Koyama, Kinoshita and Iga [1989]
AGTL-II-UCB	3 GaAs MQW	AlAs 1 wave	24 periods		
DMEWL-TIT-A	2 μm InGaAsP DH (λ _g = 1.3 μm)	InP 5.8 μm	SiO ₂ /Au/Zn/Au	λ/4-SiO ₂ /Au	
DMEWL-TIT-B	2.5 μm GaAs DH	Al _{0.3} Ga _{0.7} As (2.7 μm) Al _{0.1} Ga _{0.9} As (0.3 μm)	5 periods SiO ₂ /TiO ₂	Au/SiO ₂ /TiO ₂ /SiO ₂	
DMEWL-OFL	12×4 nm InGaAsP/InGaAsP (λ _g = 1.1 μm) MQW	InP 5 μm	8.5 periods Si/Al ₂ O ₃ + Au metalization	6 periods Si/SiO ₂	Uchiyama and Kashiwa [1995]; Uchiyama, Yokouchi and Ninomiya [1997]
SMEWL-ATT	0.5 μm GaAs DH	Al _{0.3} Ga _{0.7} As 300 nm	5 periods Al _{0.1} Ga _{0.9} As/ Al _{0.7} Ga _{0.3} As	22 periods AlAs/Al _{0.1} Ga _{0.9} As	Tai, Fischer, Seabury, Olsson, Huo, Ota and Cho [1989]

continued on next page

Table 1, continued

Abbreviation	Active region	Spacer cavity	Bottom reflector	Top reflector	Reference
UMEWL-UCSB	0.5 μm InGaAsP DH ($\lambda_g = 1.3 \mu\text{m}$)	InP 4 μm	5 periods Si ₃ N ₄ /Si	5 periods Si ₃ N ₄ /Si	Wada, Babic, Crawford, Reynolds, Dudley, Bowers, Hu, Merz, Miller, Koren and Young [1991]
HMML-NTT	9 \times 1%-compressibly strained InGaAsP/InGaAsP MQW	InGaAsP ($\lambda_g = 1.2 \mu\text{m}$)	25 periods GaAs/AlAs + 10.5 periods InP/InGaAsP	7 periods InP/InGaAsP + 5 periods SiO ₂ /TiO ₂	Ohiso, Amano, Itoh, Tateno, Tadokoro, Takenouchi and Kurokawa [1996]
PIBEL-ATT	3 \times 8 nm In _{0.2} Ga _{0.8} As/GaAs MQW	GaAs 1 wave	20 periods AlAs/GaAs	14 periods AlAs/GaAs	Jewell, Scherer, McCall, Lee, Walker, Harbison and Florez [1989]
BEOML-TIT	3 \times 8 nm In _{0.2} Ga _{0.8} As/GaAs MQW		22.5 periods AlAs/GaAs	20 periods AlAs/GaAs graded barriers + metalization	Hayashi, Mukaiharu, Hatori, Ohnoki, Matsutani, Koyama and Iga [1995]
BEOML-II-UCSB	3 \times 8 nm In _{0.17} Ga _{0.83} As/GaAs MQW	Al _{0.3} Ga _{0.7} As 1 wave	18.5 periods AlAs/GaAs digital alloy grading	21 periods Al _{0.9} Ga _{0.1} As/GaAs Au metalization	Thibeault, Bertilsson, Hegblom, Strzelecka, Floyd, Naone and Coldren [1997]
BEOML-III-UCSB	3 \times 8 nm In _{0.174} Ga _{0.826} As/ GaAs MQW	Al _{0.5} Ga _{0.5} As 0.24 μm	18.5 periods AlAs/GaAs graded barriers	26 periods Al _{0.75} Ga _{0.25} As/GaAs + 1 period GaAs/AlAs graded and δ -doped barriers	Floyd, Thibeault, Coldren and Merz [1996]

continued on next page

Table 1. *continued*

Abbreviation	Active region	Spacer cavity	Bottom reflector	Top reflector	Reference
TEOML-SNL-A	1.6 nm In _{0.5} Ga _{0.5} P	AlGaInP 1 wave	55.5 periods AlAs/Al _{0.5} Ga _{0.5} As parabolically graded barriers	34 periods AlAs/Al _{0.5} Ga _{0.5} As parabolically graded barriers	Crawford and Schneider [1995]; Choquette, Schneider, Crawford, Geib and Figiel [1995]
	1.6 nm Al _{0.5} Ga _{0.5} P = In _{0.5} P MQW				
TEOML-SNL-B	3.0 nm InGaAs	AlGaAs 1 wave	38 periods Al _{0.96} Ga _{0.04} As/GaAs uniparabolically graded barriers	25 periods Al _{0.96} Ga _{0.04} As/GaAs uniparabolically graded barriers	Lear, Schneider, Choquette, Kilcoyne, Figiel and Zolper [1994]; Choquette, Schneider, Lear and Geib [1994]; Lear, Choquette, Schneider and Kilcoyne [1995]
	MQW				
TEOML-II-USC	3 × 6 nm In _{0.15} Ga _{0.85} As/GaAs	Al _{0.5} Ga _{0.5} As 1 wave	30 periods AlAs/GaAs	4 periods AlAs oxide/GaAs	MacDougal, Dapkus, Pudikov, Zhao and Yang [1995]; Yang, MacDougal and Dapkus [1995]
	MQW				
TEOML-III- KAIST	4 × 8 nm Al _{0.11} Ga _{0.89} As/ Al _{0.3} Ga _{0.7} As	AlGaAs 1 wave	40 periods Al _{0.3} Ga _{0.7} As/ Al _{0.9} Ga _{0.1} As linearly graded barriers	26 periods Al _{0.3} Ga _{0.7} As/ Al _{0.9} Ga _{0.1} As linearly graded barriers	Shin, Ju, Shin, Ser, Kim, Lee, Kim and Lee [1996]
	MQW				
TEOML-III-UU	3 × 8 nm GaAs/Al _{0.2} Ga _{0.8} As MQW	Al _{0.5} Ga _{0.5} As 1 wave	30.5 periods AlAs/Al _{0.2} Ga _{0.8} As	26 periods Al _{0.9} Ga _{0.1} As/ Al _{0.2} Ga _{0.8} As step-graded and δ-doped barriers	Schnitzer, Fiedler, Grabherr, Jung, Reiner, Zick and Ebeling [1996]; Jäger, Grabherr, Jung, Michalzik, Reiner, Weigl and Ebeling [1997]

continued on next page

Table 1, continued

Abbreviation	Active region	Spacer cavity	Bottom reflector	Top reflector	Reference
HMOL-UTA	3 × 6 nm In _{0.2} Ga _{0.8} As/GaAs MQW	GaAs 1 wave	26 periods AlAs/GaAs	1 period AlAs/GaAs + 4–6 periods ZnSe/CaF ₂	Huffaker, Deppe and Rogers [1994]; Huffaker, Shin, Deng, Lin, Deppe and Streetman [1994]
HMOL-II-UTA	8 nm In _{0.2} Ga _{0.8} As/ GaAs SQW	Al _{0.96} Ga _{0.04} As + Al _{0.75} Ga _{0.25} As/ GaAs superlattice + 1/2 wave GRIN AlGaAs	26 periods AlAs/GaAs	5–7 periods MgF/ZnSe	Huffaker, Graham, Deng and Deppe [1996]
DCCOL-SNL	3 × 8 nm In _{0.2} Ga _{0.8} As MQW	GRIN AlGaAs 1 wave	38 periods GaAs/Al _{0.92} Ga _{0.08} As uniparabolically graded barriers	18 periods GaAs/Al _{0.92} Ga _{0.08} As uniparabolically graded barriers	Lear, Mar, Choquette, Kilcoyne, Schneider and Geib [1996]; Choquette, Chow, Crawford, Geib and Schneider [1996]
DO-DBRL-USC	2 × 6.5 nm In _{0.2} Ga _{0.8} As (λ _g = 0.99 μm) GaAs MQW	AlGaAs–GaAs– InGaAs 1 wave	7 periods AlAs oxide/GaAs	5 periods AlAs oxide/GaAs	MacDougall, Yang, Bond, Lin, Tishinin and Dapkus [1996]

continued on next page

Table 1, notes

Abbreviations			
PITSEL, proton-implanted top-surface-emitting laser	ATT, AT&T Bell Laboratories	MQW, multiple quantum well	
HMIDL, hybrid-mirrors in-diffused laser	UNM, University of New Mexico	SQW, single quantum well	
HMUML, hybrid-mirrors undercut-mesa laser	SNL, Sandia National Laboratories	DH, double heterostructure	
HMSCL, hybrid-mirrors strain-compensated laser	UU, University of Ulm	GRIN, graded index	
HMPIL, hybrid-mirrors proton-implanted laser	CU, Cornell University	λ_g , bandgap wavelength	
HMCCL, hybrid-mirrors current-confinement laser	SFIT, Swiss Federal Institute of Technology		
BCCL, buried current-confinement laser	UCSB, University of California at Santa Barbara		
TEML, top-emitting mesa laser	RIT, Royal Institute of Technology		
BEML, bottom-emitting mesa laser	HTC, Honeywell Technology Center		
DF, double-fused	BTL, BT Laboratories		
TBEML, tunable bottom-emitting mesa laser	TUM, Technische Universität, München		
AGTL, air-gap tunable laser	UCB, University of California at Berkeley		
DMEWL, dielectric-mirrors etched-well laser	NTT, NTT Opto-electronics Laboratories		
SMEWL, semiconducting-mirrors etched-well laser	TTT, Tokyo Institute of Technology		
UMEWL, undercut-mesa etched-well laser	SU, Stanford University		
HMML, hybrid-mirrors mesa laser	OFL, Optoelectronics Furukawa Laboratory		
PIBEL, proton-implanted bottom-emitting laser	USC, University of Southern California		
BEOML, bottom-emitting oxidized mesa laser	UTA, University of Texas at Austin		
TEOML, top-emitting oxidized mesa laser	KAIST, Korean Advanced Institute of Science and Technology		
HMOL, hybrid-mirrors oxidized laser			
DCCOL, double-current-confinement oxidized laser			
DO-DBRL, double-oxide DBR laser			

§ 3. Effects of Temperature on VCSEL Operation

In this section, temperature-related effects on VCSEL performance are presented, including the temperature dependence of the longitudinal mode spectra, the transverse-mode structure, the threshold current, and the output power.

3.1. TEMPERATURE DEPENDENCE OF THE LONGITUDINAL MODE SPECTRA

In a resonant cavity of length L , filled with a homogeneous material of refractive index n_R , the wavelength λ_M of a longitudinal mode M is given approximately by (neglecting phase shifts at the cavity boundaries):

$$\lambda_M = \frac{2n_R L}{M}. \quad (2)$$

The rate of longitudinal mode wavelength change with temperature is determined by the temperature sensitivity of the refractive index and by the thermal expansion of the cavity length (Mroziewicz, Bugajski and Nakwaski [1991], p. 151):

$$\frac{d\lambda_M}{dT} = \frac{\lambda_M}{n_G} \left[\left(\frac{\partial n_R}{\partial T} \right) \Big|_{\lambda} + n_R \alpha_T \right], \quad (3)$$

where α_T is the linear thermal expansion coefficient, and n_G is the group index,

$$n_G = n_R - \lambda_M \left(\frac{\partial n_R}{\partial \lambda} \right) \Big|_T. \quad (4)$$

The partial derivatives $(\partial n_R / \partial T)|_{\lambda}$ and $(\partial n_R / \partial \lambda)|_T$ in eqs. (3) and (4) are to be evaluated at constant wavelength and temperature, respectively. The refractive index in semiconducting materials changes approximately linearly with temperature. Near the lasing wavelength of $0.85 \mu\text{m}$, a value of $(\partial n_R / \partial T)|_{\lambda} = 4 \times 10^{-4} \text{ K}^{-1}$ can be extracted from the data of Marple [1964] for GaAs, and $1 \times 10^{-4} \text{ K}^{-1}$ can be extracted from the data of Grimmeiss and Monemar [1971] for AlAs. For InP, a similar value of $3 \times 10^{-4} \text{ K}^{-1}$ near the bandgap can be obtained from the data of Pettit and Turner [1965]. The latter value has been also assumed by Bissessur, Ettinger, Fernandez and Davies [1993] for the quaternary InGaAsP materials. These values are about an order of magnitude higher than the product of the group index and the linear expansion coefficient, listed in tables 2 and 3. Hence, the longitudinal mode wavelength shift is determined primarily by the temperature dependence of the refractive index.

Table 2
Thermal expansion coefficient α_T near 300 K

Material	α_T [$10^{-6}/^\circ\text{C}$]	Reference(s)
GaAs	6.4–6.9	Swaminathan and Macrander [1991]; Adachi [1985]
AlAs	4.9–5.2	Swaminathan and Macrander [1991]; Adachi [1985]
$\text{Al}_x\text{Ga}_{1-x}\text{As}$	$6.4 - 1.2x$	Adachi [1985]
InP	4.56	Adachi [1992]
$\text{In}_{1-x}\text{Ga}_x\text{As}_y\text{P}_{1-y}$ ^a	$4.56 + 1.18y$	Adachi [1992]

^a Lattice-matched to InP, with $x = 0.4527y/(1 - 0.0311y)$.

Table 3
Group index n_G near 300 K

Material	Wavelength	n_G	Reference
GaAs	0.85 μm	4.3	Buus [1983]
$\text{Al}_{0.2}\text{Ga}_{0.8}\text{As}$	0.85 μm	4.2	Determined from data given by Casey and Panish [1978]
$\text{In}_{0.73}\text{Ga}_{0.27}\text{As}_{0.6}\text{P}_{0.4}$ ^a	1.30 μm	4.3	Buus and Adams [1979]
$\text{In}_{0.6}\text{Ga}_{0.4}\text{As}_{0.85}\text{P}_{0.15}$ ^b	1.55 μm	4.6	Buus and Adams [1979]

^a Bandgap wavelength $\lambda_g = 1.3 \mu\text{m}$.

^b Bandgap wavelength $\lambda_g = 1.55 \mu\text{m}$.

The diode laser cavity is not homogeneous; hence, except for devices where the optical field is very well confined within the active region, eqs. (2) and (3) only approximately describe the actual situation. For EELs, the refractive index n_R should be replaced with the effective index n_{eff} , which averages the refractive indices of the active region and the claddings with proper weights determined by field penetration into the claddings (Thompson [1980], p. 118).

Rather than employing discrete mirrors, most VCSEL designs incorporate distributed Bragg reflectors (DBRs). For a DBR consisting of alternating quarter-wave layers of thicknesses and refractive indices d_L , n_L , and d_H , n_H , respectively, the center wavelength of its reflectivity spectrum is determined by the optical thickness of the DBR period:

$$\lambda_{\text{DBR}} = 2(n_L d_L + n_H d_H). \quad (5)$$

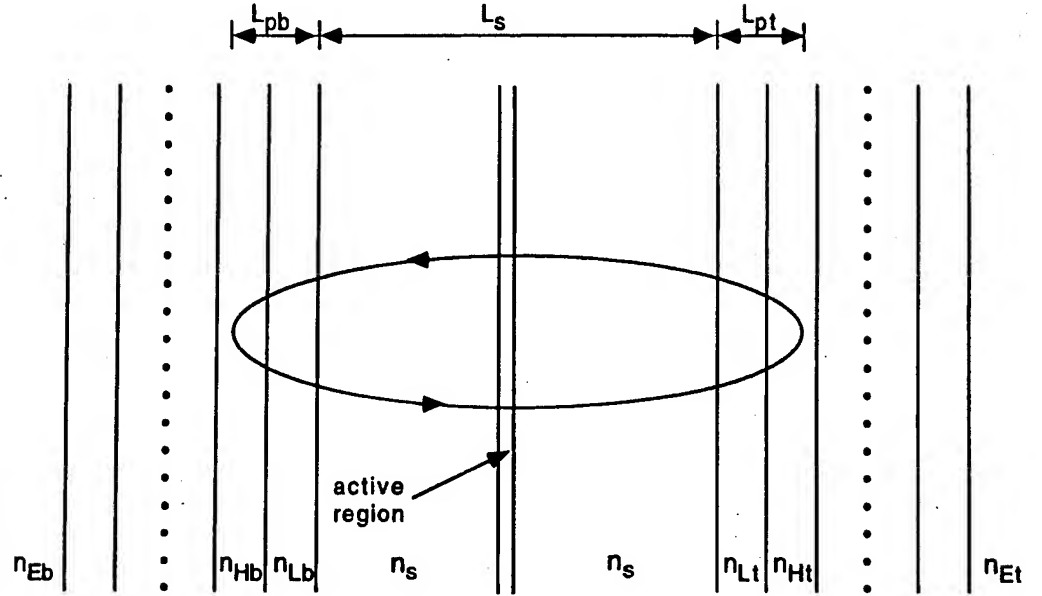


Fig. 4. Schematic structure of a typical VCSEL cavity, showing the refractive indices of the bottom exit medium (n_{Eb}), high- and low-index layers of the bottom DBR (n_{Hb} , n_{Lb}), spacer medium (n_s), low- and high-index layers of the top DBR (n_{Lt} , n_{Ht}), and the top exit medium (n_{Et}), as well as bottom and top phase penetration depths (L_{pb} , L_{pt}) and the spacer thickness L_s .

The temperature variation of the Bragg wavelength, λ_{DBR} , is then described by a formula analogous to eq. (3) (Dudley, Crawford and Bowers [1992]):

$$\frac{d\lambda_{DBR}}{dT} = \frac{n_L d_L \alpha_{T,L} + n_H d_H \alpha_{T,H} + d_L \left(\frac{\partial n_L}{\partial T} \right) \Big|_{\lambda} + d_H \left(\frac{\partial n_H}{\partial T} \right) \Big|_{\lambda}}{\frac{1}{2} - d_L \left(\frac{\partial n_L}{\partial \lambda} \right) \Big|_T - d_H \left(\frac{\partial n_H}{\partial \lambda} \right) \Big|_T}, \quad (6)$$

where $\alpha_{T,L}$ and $\alpha_{T,H}$ are thermal expansion coefficients of the low- and high-index material, respectively. Again, the terms containing $\alpha_{T,L}$ and $\alpha_{T,H}$ are much smaller than those containing the variation of the refractive index with temperature, and the dispersion terms are much smaller than $\frac{1}{2}$. Experimentally, $d\lambda_{DBR}/dT$ was determined to be $0.87 \text{ \AA}/^\circ\text{C}$ for a GaAs/AlAs mirror centered at $0.98 \mu\text{m}$, and $1.1 \text{ \AA}/^\circ\text{C}$ for an InP/InGaAsP (bandgap wavelength $\lambda_g = 1.15 \mu\text{m}$) mirror centered at $1.32 \mu\text{m}$ (Dudley, Crawford and Bowers [1992]).

A typical VCSEL cavity, shown schematically in fig. 4, consists of two DBRs separated by a spacer region which incorporates the active region. The spacer thickness L_s (including the optically equivalent active-region thickness) and the phase penetration depths of the top and bottom DBRs L_{pt} , L_{pb} , respectively, combine into an *effective VCSEL cavity length* L_{eff} :

$$L_{eff} = L_s + L_{pt} + L_{pb}, \quad (7)$$

where (Babic and Corzine [1992])

$$L_{pa} = \frac{\lambda_{\text{DBR},a}}{4n_s} \left[\frac{q_a}{1-p_a} \frac{(1-s_a^2 p_a^{N_a-1})(1-p_a^{N_a})}{1-q_a^2 s_a^2 p_a^{2N_a-2}} \right] \quad \alpha = t, b, \quad (8)$$

with

$$q_a = \frac{n_{\text{IL}a}}{n_{\text{IH}a}}, \quad (9)$$

$$p_a = \frac{n_{\text{L}a}}{n_{\text{H}a}}, \quad (10)$$

$$s_a = \frac{n_{\text{EL}a}}{n_{\text{EH}a}}. \quad (11)$$

Here, $\lambda_{\text{DBR},a}$ ($\alpha=t, b$) is the center wavelength of the top (t) or bottom (b) DBR, N_a is the total number of quarter-wave layers, n_s is the refractive index of the spacer region (assumed to be homogeneous), and q_a , p_a , and s_a are, respectively, the ratios of the lower to higher refractive indices at the interfaces of the incident (I) medium and the DBR, the Bragg mirror layers, and the DBR/exit (E) medium. For a top-emitting VCSEL, the exit medium for the top reflector is normally the air, and for the bottom reflector it is the substrate. For a bottom-emitting VCSEL, the top exit medium is usually the metallic contact, and the bottom exit medium is the air.

The longitudinal modes in a VCSEL cavity can be found by considering the round-trip phase condition that takes into account propagation in the cavity of the effective length L_{eff} given by eqs. (7)–(11) and the detuning between the mode wavelength, λ_M , and the center wavelengths of the two DBRs, $\lambda_{\text{DBR},t}$ and $\lambda_{\text{DBR},b}$. Assuming a homogeneous spacer medium, we obtain the following *longitudinal mode resonant condition*:

$$\lambda_M = \frac{2n_s L_{\text{eff}}}{M + 2n_s \left[\left(\frac{L_{\text{pt}}}{\lambda_{\text{DBR},t}} \right) + \left(\frac{L_{\text{pb}}}{\lambda_{\text{DBR},b}} \right) \right]}. \quad (12)$$

In an ideal VCSEL cavity with a thin (quantum well) active layer and two Bragg mirrors of identical center wavelength, λ_{DBR} , the thickness of the spacer region should be chosen such as to select $\lambda_M = \lambda_{\text{DBR}}$. In this case, eq. (12) simplifies to an expression fully analogous to eq. (2):

$$\lambda_M = \frac{2n_s L_s}{M}. \quad (13)$$

Note that because of the $\lambda_M = \lambda_{\text{DBR}}$ condition, only one longitudinal mode can be supported by an ideal VCSEL cavity. In addition, the effective cavity length,

L_{eff} , no longer appears in the resonance condition (13). We see that the optical thickness of the spacer must be an integer multiple of the half-wave $\lambda_{\text{DBR}}/2$. In VCSELS with quantum-well active regions, the additional requirement for the maximum of the standing wave intensity pattern to occur at the center of the spacer limits M to even numbers; i.e., $n_s L_s$ must be equal to an integer multiple of λ_{DBR} . The control of the spacer thickness is less critical in VCSELS with bulk active regions (over 400 Å thick), since the standing-wave intensity maximum will always be located somewhere within the active layer.

The mode wavelength shift with temperature in an ideal VCSEL cavity is still given by eq. (3) with the spacer index n_s , provided that the spacer material satisfies the following *thermal dispersion matching condition*:

$$\frac{(\partial n_s / \partial T)|_{\lambda}}{n_s} = d_L \frac{(\partial n_L / \partial T)|_{\lambda} + d_H (\partial n_H / \partial T)|_{\lambda}}{n_L d_L + n_H d_H} \quad (14)$$

Equation (14) was derived by neglecting the thermal expansion and wavelength dispersion terms in eqs. (3) and (6).

Measurements of the temperature variation of the lasing wavelength in GaAs/AlGaAs-based VCSELS give the *mode shifts* near room temperature in the range of 0.56–0.90 Å/°C (e.g., Van der Ziel, Deppe, Chand, Zydzik and Chu [1990], Hasnain, Tai, Yang, Wang, Fischer, Wynn, Weir, Dutta and Cho [1991], Tell, Leibenguth, Brown-Goebeler and Livescu [1992], Wipiejewski, Panzlaff, Zeeb and Ebeling [1993], Catchmark, Morgan, Kojima, Leibenguth, Asom, Guth, Focht, Luther, Przybylek, Mullay and Christodoulides [1993], Geels, Thibeault, Corzine, Scott and Coldren [1993], Norris, Chen and Tien [1994]) for both pulsed and CW operation. Most of the reported values are very close to the measured center wavelength shift of 0.87 Å/°C in the GaAs/AlAs DBR mirrors (Dudley, Crawford and Bowers [1992]), indicating that condition (14) seems to be satisfied in GaAs/AlGaAs devices. They are also comparable to mode shift rates in GaAs/AlGaAs Fabry–Pérot EELs, which are typically about 0.50 Å/°C (Mroziwicz, Bugajski and Nakwaski [1991], p. 151). Because of the higher thermal resistance of VCSELS (see table 4), the VCSEL active region heats up with the ambient temperature at a faster rate than in edge emitting lasers. Hence, the observed wavelength shift should be somewhat larger than in edge-emitters. This is indeed the case, which confirms that eq. (3) describes well the mode wavelength shift in VCSELS.

Figure 5 illustrates the lasing wavelength shift with temperature under both pulsed and CW conditions for two PITSELS with the active-region diameter of 16 μm and with different room-temperature values of λ_M . It is clear that under pulsed conditions, $\lambda_M(T)$ dependence can remain linear over a wide temperature

Table 4
Thermal resistance R_{TH}

R_{TH} (K/W)	Size (μm)	Structure ^a	Reference
300 ^b	6×6	HMIDL-SFIT	Wüthrich, James, Ganière and Reinhart [1990]
1788	15 Ø	PITSEL-ATT-A	Hasnain, Tai, Yang, Wang, Fischer, Wynn, Weir, Dutta and Cho [1991]
1250	10×10	deep-etched BEML-UCSB	Coldren, Geels, Corzine and Scott [1992]
1000	10×10	shallow-etched BEML-UCSB	Geels, Thibeault, Corzine, Scott and Coldren [1993]
800	15 Ø	PITSEL-ATT-A	Wu, Tai and Huang [1993]
920	16 Ø	PITSEL-UNM	Lu, Zhou, Cheng and Malloy [1994]
2100	16 Ø	PITSEL-UNM	Lu, Zhou, Cheng, Malloy and Zolper [1994]
3000 ^b	11 Ø	wafer-fused HMUML-UCSB	Dudley, Babic, Mirin, Yang, Miller, Ram, Reynolds, Hu and Bowers [1994]
233–345 ^c	60 Ø	TEML-UCB	Norris, Chen and Tien [1994]
274–384 ^c	60 Ø	TEML-UCB	Chen, Hadley and Smith [1994]
2500	7×7	TEOML-SNL	Choquette, Schneider, Lear and Geib [1994]
613	21 Ø	Au-plated BEML-UCSB	Wipiejewski, Young, Peters, Thibeault and Coldren [1995]
4221	4.5 Ø	Au-plated BEML-UCSB	Wipiejewski, Young, Peters, Thibeault and Coldren [1995]
800	20 Ø	BEML-II-TIT	Mukaihara, Hayashi, Hatori, Ohnoki, Matsutani, Koyama and Iga [1995]
1300	10 Ø	BEML-II-TIT	Mukaihara, Hayashi, Hatori, Ohnoki, Matsutani, Koyama and Iga [1995]
3000	6 Ø	BEML-II-TIT	Mukaihara, Hayashi, Hatori, Ohnoki, Matsutani, Koyama and Iga [1995]
800	20 Ø	PITSEL-ATT-A	Morgan, Hibbs-Brenner, Marta, Walterson, Bounnak, Kalweit and Lehman [1995]
1210	16 Ø	TEML-II-NTT	Ohiso, Tateno, Kohama, Wakatsuki, Tsunetsugu and Kurokawa [1996]
660	26 Ø	TEML-II-NTT	Ohiso, Tateno, Kohama, Wakatsuki, Tsunetsugu and Kurokawa [1996]
2550	2×2	HMOL-UTA with SQW	Huffaker and Deppe [1996]
2280	3.5×3.5	HMOL-UTA with SQW	Huffaker and Deppe [1996]

continued on next page

Table 4, *continued*

R_{TH} (K/W)	Size (μm)	Structure ^a	Reference
1615	5.4 \emptyset	BEOML-II-UCSB with SQW	Akulova, Thibeault, Ko and Coldren [1997]

^a For an explanation of the abbreviations see table 1.

^b Pulsed operation.

^c For current range from $I_{th,cw}$ to $3I_{th,cw}$, where $I_{th,cw}$ is the threshold current for CW operation.

range, although different regimes characterized by different values of $d\lambda_M/dT$ may exist. For example, the slope of $\lambda_M(T)$ changes at 300 K for the “865 nm mode” device. Under the CW conditions, $\lambda_M(T)$ deviates significantly from a linear behavior, mostly because of varying degree of heating occurring at the CW threshold current, at which the data were taken (cf. § 3.2).

Knowledge of the wavelength shift rate with temperature can be used

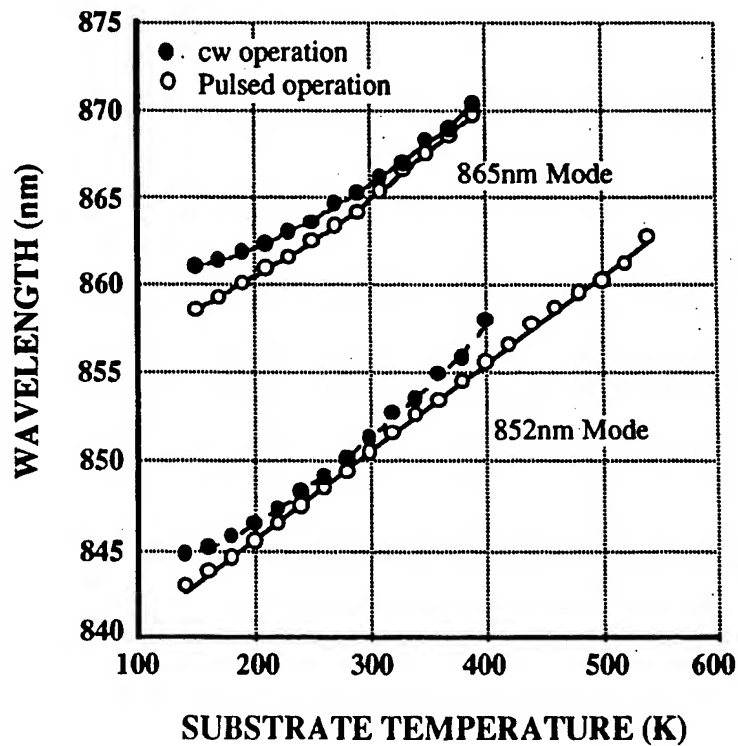


Fig. 5. Wavelength shift with temperature for two 16 μm PITSELs with different lasing mode positions relative to a common gain peak (847 nm at 300 K), measured under pulsed (100 ns, 0.1% duty cycle) and CW conditions (after Lu, Zhou, Cheng, Malloy and Zolper [1994]). The devices were placed on a temperature-controlled stage and the substrate temperature is assumed to be equal to the stage temperature.

conveniently to estimate the average active-region temperature, necessary to evaluate the thermal resistance of the device (defined by eq. 49, below). This approach has been employed widely, giving the estimates of thermal resistance in various VCSELs between 233 and 4221 K/W (see table 4). These values are much higher than typical thermal resistances of EELs, ranging between 20 and 50 K/W (e.g., Joyce and Dixon [1975], Manning [1981], Hughes, Gilbert and Hawrylo [1985]).

3.2. TEMPERATURE DEPENDENCE OF THE THRESHOLD CURRENT

The lasing threshold in all diode lasers is determined by the balance between optical gain and losses. With increasing temperature, two main effects take place: the energy gap in III-V semiconductors shrinks (see table 5), and the carrier density distribution within each band broadens, with its peak shifting further into the band. The bandgap shrinkage is dominant, and the net result of these two opposing effects is that the gain-peak shifts towards the longer wavelengths. In addition, the gain peak is lowered at a given carrier concentration. Thus, even if the optical losses were to remain unchanged, the threshold current would have increased with temperature, since higher current density is required to maintain the same gain level. In addition, optical losses do increase with temperature, since the higher density of carriers necessary to maintain the required gain level results in increased free-carrier absorption in the active region. Somewhat less important, at least at room temperature and above, is an increase in free-carrier absorption that can occur in passive layers, caused by temperature-dependent impurity ionization.

These considerations assume implicitly that all current flowing through the diode laser results in radiative transitions. However, only a fraction of electron-hole pairs recombines radiatively. Nonradiative processes can also be temperature dependent, either directly, or indirectly via increased carrier density necessary to balance the optical loss. An example of such a process is Auger recombination that increases rapidly with carrier density. Another mechanism of carrier loss is leakage along a shunt path away from the active region or straight over the quantum-well active region. The current density associated with the latter process can be described using a simple expression, analogous to the standard current-voltage equation for a p-n junction (Scott, Corzine, Young and Coldren [1993]):

$$j_{\text{leak}} = j_0 \exp \left[-\frac{E_{\text{gB}} - \Delta F_{\text{cv}}}{k_B T_A} \right], \quad (15)$$

Table 5
Temperature dependence of bandgap E_g and peak gain g_{\max}

Material	$-\partial E_g/\partial T$ [10^{-4} eV/°C]	$-(\partial g_{\max}/\partial T)_N$ ($\text{cm}^{-1}/^\circ\text{C}$)
GaAs ^a	3.9–4.6 ^{e,f,g}	1.4 ^k
AlAs	5.1–5.2 ^{e,f}	
$\text{Al}_x\text{Ga}_{1-x}\text{As}$	$3.95 + 1.15x$ ^f	
InP	3.3–4.0 ^{h,i}	
$\text{In}_{0.73}\text{Ga}_{0.27}\text{As}_{0.6}\text{P}_{0.4}$ ^b	3.25–3.82 ^{ij}	1.48 ^l
$\text{In}_{0.6}\text{Ga}_{0.4}\text{As}_{0.85}\text{P}_{0.15}$ ^c	3.75 ⁱ	1.22 ^l
$\text{In}_{1-x}\text{Ga}_x\text{As}_y\text{P}_{1-y}$ ^d	4.0–0.3 ^y ⁱ	

^a The values of $\partial E_g/\partial T$ are not independent of temperature. Using the results of Thurmond [1975] for GaAs, we obtain $\partial E_g/\partial T = -5.405 \times 10^{-4} T(T + 408)/(T + 204)^2$ eV/°C.

^b Bandgap wavelength $\lambda_g = 1.3$ μm .

^c Bandgap wavelength $\lambda_g = 1.55$ μm .

^d Lattice-matched to InP, with $x = 0.4527/(1 - 0.0311y)$.

^e Swaminathan and Macrander [1991], p. 16.

^f Adachi [1985].

^g Yan and Coldren [1990].

^h Lautenschlager, Garriga and Cardona [1987].

ⁱ Adachi [1992].

^j Dutta and Nelson [1982].

^k Extracted from theoretical curves reported by Stern [1973].

^l Extracted from theoretical curves reported by Dutta and Nelson [1982].

where E_{gB} is the local bandgap energy in the cladding (barrier) region (dependent on temperature), ΔF_{cv} is the local separation of quasi-Fermi levels in the active region (dependent on both carrier concentration and temperature), k_B is the Boltzmann constant, and T_A is the local active-region temperature. For index-guided bottom-emitting mesa lasers, deeply etched just through the active region, the parameter j_0 was fitted to 8×10^3 kA/cm² (Scott, Corzine, Young and Coldren [1993]).

Another implicit assumption is that the laser operates at the gain-peak wavelength, and that the lasing wavelength follows the gain-peak shifts with temperature. This is true only when the spacing between the longitudinal modes in the lasing cavity is small, as in conventional Fabry–Pérot lasers. If the spacing is large or if some additional frequency-selective elements are used, the gain-peak wavelength will not coincide with the lasing wavelength. This situation occurs in distributed-feedback (DFB) and distributed-Bragg-reflector (DBR) EELs, and is characteristic of all VCSELs. Depending then on the sign of the

initial detuning from the gain peak at room temperature, the lasing wavelength can approach the gain peak or depart from it. In the former case, which takes place when the room-temperature lasing wavelength is offset from the gain peak towards the longer wavelengths, the increase in threshold current described in the first paragraph is partially compensated by the simultaneous shift of the lasing wavelength towards the gain peak. Conversely, if the room-temperature lasing wavelength is on the short-wavelength side of the gain peak, temperature variation of the threshold current will be accelerated.

According to Chow, Corzine, Young and Coldren [1995], many-body Coulomb interactions between carriers are not canceled completely by plasma screening. This leads to a decrease in the wavelength dependence of the threshold carrier concentration and consequently, a greater tolerance to the changes in the resonance/gain overlap with temperature on the low-temperature side of the threshold minimum.

It is clear that the complex interplay between all these mechanisms can result in a variety of different patterns of threshold current evolution with temperature. Yet, it is a common practice to describe the temperature dependence of the threshold current using the *Arrhenius-type relation*,

$$I_{\text{th}}(T) = I_{\text{th}}(300 \text{ K}) \exp\left(\frac{T - 300 \text{ K}}{T_0}\right), \quad (16)$$

with T in Kelvin and the *characteristic temperature* T_0 used as a measure of temperature sensitivity of the threshold current. With T_0 constant, eq. (16) usually approximates the actual threshold variation within a certain temperature interval. More generally, T_0 is itself a function of temperature, and for an arbitrary $I_{\text{th}}(T)$ dependence it can be defined simply as

$$T_0(T) = \frac{d\left\{\ln\left[\frac{I_{\text{th}}(T)}{I_{\text{th}}(300 \text{ K})}\right]\right\}}{dT}. \quad (17)$$

In spite of its limited applicability to VCSELs, eq. (16) is the only analytical form in which the temperature dependence of the VCSEL threshold current was reported. Not surprisingly, measured values of T_0 for VCSELs are scattered widely and sensitive to device structure (see tables 6a,b). They range from very high (practically infinite) values in devices where the threshold current remains practically constant within a certain temperature range (cf. Geels, Thibeault, Corzine, Scott and Coldren [1993]), through moderate values of 130–150 K, (see, e.g., Uchiyama, Ohmae, Shimizu and Iga [1986] and Iga, Koyama and

Table 6a
Characteristic temperature T_0 for pulsed operation

T_0 (K)	Range (K)	Size (μm)	Structure	Reference
200	100–220	20–30 \emptyset	DMEWL-TIT-A	Uchiyama, Ohmae, Shimizu and Iga [1986]
70	220–263	20–30 \emptyset	DMEWL-TIT-A	Uchiyama, Ohmae, Shimizu and Iga [1986]
210	283–363	15 \emptyset	PITSEL-ATT-A	Hasnain, Tai, Yang, Wang, Fischer, Wynn, Weir, Dutta and Cho [1991]
47.5	223–253	8 \times 8	UMEWL-UCSB	Wada, Babic, Crawford, Reynolds, Dudley, Bowers, Hu, Merz, Miller, Koren and Young [1991]
26.8	253–339	8 \times 8	UMEWL-UCSB	Wada, Babic, Crawford, Reynolds, Dudley, Bowers, Hu, Merz, Miller, Koren and Young [1991]
24	203–253	20 \times 20	wafer-fused HMUML-UCSB	Wada, Babic, Ishikawa and Bowers [1992]
47	203–298	8 \times 8	wafer-fused HMUML-UCSB	Wada, Babic, Ishikawa and Bowers [1992]
67	200–300	11 \emptyset	wafer-fused HMUML-UCSB	Dudley, Babic, Mirin, Yang, Miller, Ram, Reynolds, Hu and Bowers [1994]

Kinoshita [1988]), to negative values in devices that are detuned towards the longer wavelengths (cf. fig. 8).

Thus, in stark contrast to Fabry–Perot-type EELs, the T_0 parameter in VCSELs becomes more of a design parameter (Tell, Brown-Goebeler, Leibenguth, Baez and Lee [1992]), than a material- or structure-related characteristic. Since the arbitrary temperature sensitivity of a VCSEL threshold current can be obtained in principle, this opens up a possibility of designing *temperature-insensitive VCSELs*, with infinitely large T_0 . Some interesting examples of such constructions were demonstrated not only for ambient room temperatures (Young, Scott, F.H. Peters, Thibeault, Corzine, M.G. Peters, Lee and Coldren [1993], Kajita, Kawakami, Nido, Kimura, Yoshikawa, Kurihara, Sugimoto and Kasahara [1995]), but also for cryogenic conditions (Lu, Luo, Hains, Cheng, Schneider, Choquette, Lear, Kilcoyne and Zolper [1995], Ortiz, Hains, Lu, Sun, Cheng and Zolper [1996], Goncher, Lu, Luo, Cheng, Hersee, Sun, Schneider and Zolper [1996]), and elevated temperatures (Dudley, Ishikawa, Babic, Miller, Mirin, Jiang, Bowers and Hu [1993], Catchmark, Morgan, Kojima, Leibenguth,

Table 6b
Characteristic temperature T_0 for CW operation

T_0 (K)	Range (K)	Size (μm)	Structure	Reference
115	288–323	15 \emptyset	SMEWL-ATT	Tai, Fischer, Seabury, Olsson, Huo, Ota and Cho [1989]
120	250–300	10 \emptyset	DMEWL-TIT-B	Extracted from data reported by Koyama, Kinoshita and Iga [1989]
210	293–363	15 \emptyset	PITSEL-ATT-A	Hasnain, Tai, Dutta, Wang, Wynn, Weir and Cho [1991]
130	283–323	15 \emptyset	PITSEL-ATT-A	Hasnain, Tai, Yang, Wang, Fischer, Wynn, Weir, Dutta and Cho [1991]
330	273–298	10 \emptyset	PITSEL-ATT-B	Tu, Wang, Schubert, Weir, Zydzik and Cho [1991]
80	328–348	10 \emptyset	PITSEL-ATT-B	Tu, Wang, Schubert, Weir, Zydzik and Cho [1991]
40	283–353	20 \times 20	PIBEL-ATT	Von Lehmen, Banwell, Carrion, Stoffel, Florez and Harbison [1992]
60 ^a	328–393	10 \times 10	shallow-etched BEML-UCSB	Geels, Thibeault, Corzine, Scott and Coldren [1993]
156	293–318	10 \emptyset	PITSEL-SNL	Schneider, Choquette, Lott, Lear, Figiel and Malloy [1994]

^a Determined using the active-region temperature.

Asom, Guth, Focht, Luther, Przybylek, Mullay and Christodoulides [1993], Shoji, Otsubo, Matsuda and Ishikawa [1994], Lu, Zhou, Cheng, Malloy and Zolper [1994], Morgan, Hibbs-Brenner, Marta, Walterson, Bounnak, Kalweit and Lehman [1995], Ohiso, Tatenno, Kohama, Wakatsuki, Tsunetsugu and Kurokawa [1996]).

It should be emphasized that the temperature T usually used in eq. (17) in experimental determination of T_0 , is the ambient (stage or heat sink) temperature (cf. § 4.2). Under low-duty-cycle pulsed conditions, it coincides with the active-region temperature. The pulsed and CW values of T_0 should be very similar if the active-region temperature is used instead of the ambient temperature, except for weakly guiding or weakly antiguiding VCSEL structures (cf. § 3.3) in which lateral nonuniformity of CW temperature profiles plays an important role.

It should be noted that the temperature sensitivity of the threshold current depends on the size of the active region. Larger devices usually exhibit lower values of the characteristic temperature T_0 , which results from poorer overlap

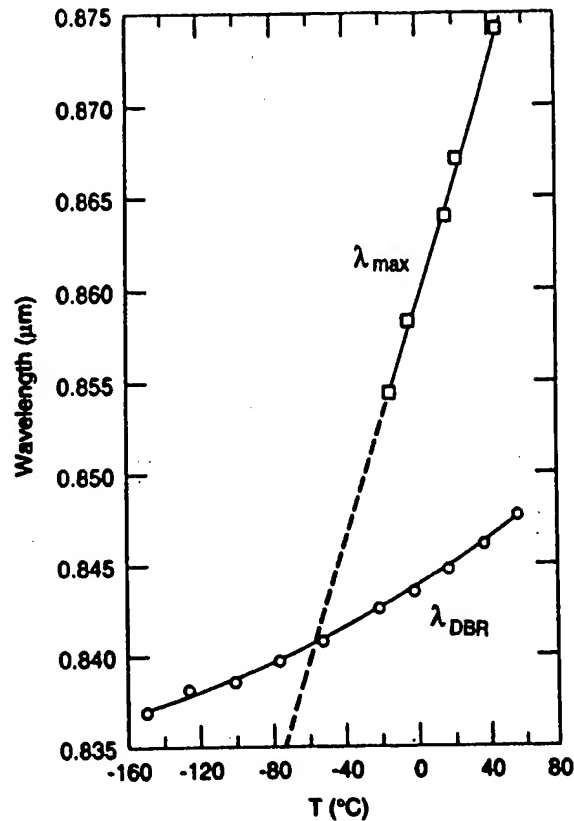


Fig. 6. Temperature effects on the gain-peak wavelength λ_{\max} and the vertical-cavity mode wavelength λ_{DBR} in a PITSEL. The $\lambda_{\max} = \lambda_{\text{DBR}}$ point corresponds to the minimum threshold current. T_0 is negative in the region when λ_{DBR} is offset towards longer wavelengths relative to λ_{\max} . After Tell, Brown-Goebeler, Leibenguth, Baez and Lee [1992].

between the gain and photon density profiles (Wada, Babic, Ishikawa and Bowers [1992]) as well as from worsening thermal properties, with increasingly one-dimensional heat flow.

The shift of the gain spectrum in VCSEL structures can be determined experimentally by fabricating Fabry-Pérot EELs from VCSEL wafers and measuring the lasing wavelength shift with temperature. Typical measured values of $d\lambda_{\max}/dT$ for GaAs/AlGaAs VCSELS are (3.2–3.4) Å/°C (e.g., Geels, Thibeault, Corzine, Scott and Coldren [1993], Tell, Brown-Goebeler, Leibenguth, Baez and Lee [1992], Scott, Corzine, Young and Coldren [1993]), which is greater than the analogous value of ~2.5 Å/°C in conventional EELs. The accelerated shift of gain-peak wavelength is probably caused by heating associated with higher series resistance of multilayer EELs incorporating horizontal Bragg reflectors and by reabsorption of amplified spontaneous emission in the vertical direction, enhanced by high-reflectivity horizontal Bragg

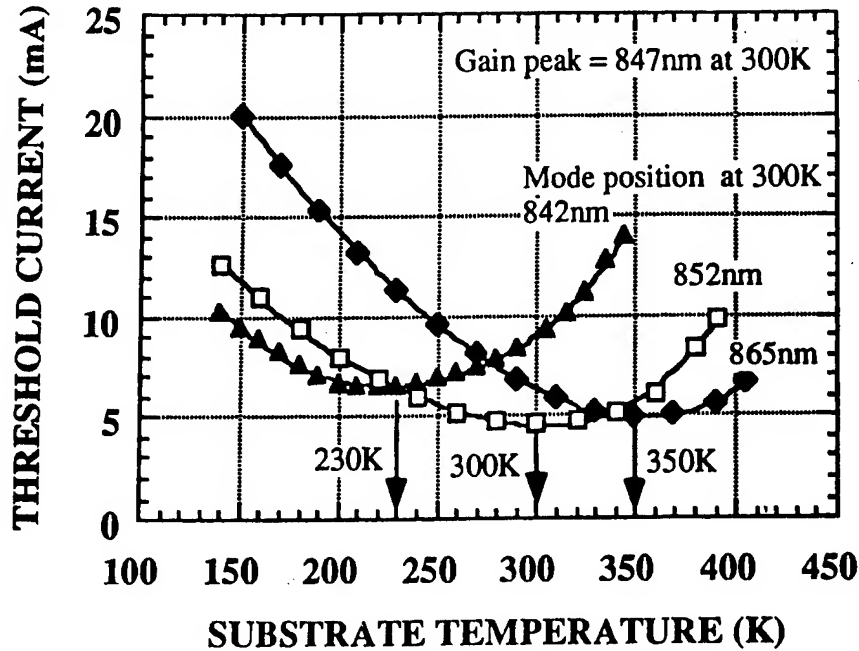


Fig. 7. Temperature dependence of the CW lasing threshold currents for three 16 μm PITSELs with different lasing mode positions relative to a common gain peak (847 nm at 300 K). The minimum threshold current occurs close to the temperature where the gain peak and lasing mode wavelengths coincide (after Lu, Zhou, Cheng, Malloy and Zolper [1994]).

mirrors. On the other hand, as illustrated in fig. 6, the observed mode wavelength shift (cf. § 3.1) is 4–5 times slower than the gain-peak wavelength shift.

For each VCSEL design there exists an optimal temperature, for which an ideal alignment between the gain spectrum and the vertical-cavity resonant mode takes place. This usually coincides with the condition for minimum $I_{th}(T)$, provided optical and electrical losses are not changing drastically around this temperature. Figure 7 presents typical $I_{th}(T)$ curves for three PITSELs with different lasing mode positions at 300 K (Lu, Zhou, Cheng, Malloy and Zolper [1994]). The larger the room-temperature detuning of λ_{DBR} towards the longer wavelengths, the higher the temperature at which the threshold current reaches minimum.

Figure 8 shows the temperature dependence of T_0 extracted from the data of fig. 7 using eq. (17). It is clear that T_0 can be considered constant only over a very limited range of temperatures, away from the vertical asymptote. The asymptotes in fig. 8 correspond to the minima of $I_{th}(T)$ curves in fig. 7.

The temperature dependence of the threshold current in VCSELs, with a minimum occurring near the temperature at which λ_{DBR} and λ_{max} are aligned, resembles that of frequency-selective EELs, such as DFB or DBR lasers. In edge-emitting DFB lasers, however, $I_{th}(T)$ characteristics may be more complicated,

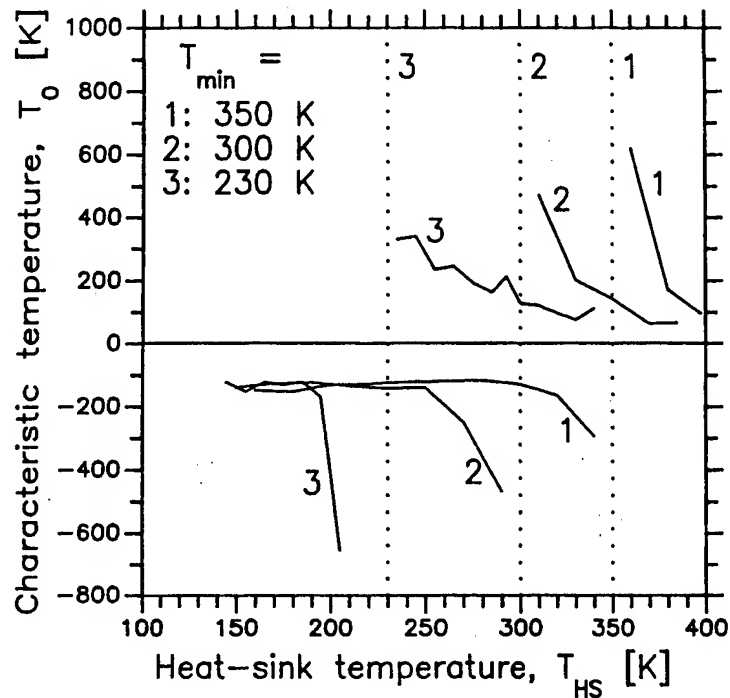


Fig. 8. Temperature dependence of the characteristic temperature T_0 extracted from the data of fig. 7.

with multiple minima corresponding to various transverse modes (cf. Aiki, Nakamura and Umeda [1976]).

3.3. TEMPERATURE DEPENDENCE OF TRANSVERSE-MODE PROPERTIES

Compared to EELs, transverse-mode properties of VCSELS are considerably more complex. Transverse modes in VCSELS are determined by an intricate interplay of gain profile, absorption, diffraction, reflection, spatial filtering, built-in index waveguiding, and temperature distribution (Scott, Young, Thibeault, Peters and Coldren [1995], Michalzick and Ebeling [1995]). Depending on the particular VCSEL structure, some of these effects can be more important than others, but rarely can a single mechanism be identified as the dominant one. In addition, VCSEL cavities can usually support many transverse modes (Valle, Sarma and Shore [1995a]), especially in large-diameter ($\geq 20 \mu\text{m}$) devices or in strongly index-guided structures. Hence, mode competition and single-transverse-mode control are important problems, even though the device operates in a single longitudinal mode.

The difficulties with transverse mode control are best illustrated by the small value (4.4 mW) of the fundamental-mode CW output power achieved so far (Lear, Schneider, Choquette, Kilcoyne, Figiel and Zolper [1994]). Coupling to an

external cavity, which is a proven technique for increasing the single-mode output power in EELs, has until now resulted in single-mode CW powers of only 2–2.4 mW (Hadley, Wilson, Lau and Smith [1993], Wilson, Hadley, Smith and Lau [1993]). Spatial filtering with the aid of a graded-index lens has recently extended this value to only 4.5 mW (Koch, Leger, Gopinath, Wang and Morgan [1997]). This contrasts with significantly larger single-mode powers of 36–100 mW in the same external-cavity VCSELs injected with 100 ns pulses at 0.1% duty cycle (Hadley, Wilson, Lau and Smith [1993], Wilson, Hadley, Smith and Lau [1993]). The large difference between the pulsed and CW results clearly illustrates the strong effect of heating on the transverse mode structure.

One of distinct features of VCSELs is that their threshold currents for pulsed and CW operations are often very similar to each other and that the CW threshold can sometimes be even lower than the pulsed one (e.g., Hasnain, Tai, Yang, Wang, Fischer, Wynn, Weir, Dutta and Cho [1991]). This is caused by the so-called *thermal lensing effect*, which focuses the radiation in regions of higher temperature because of temperature-dependent refractive index.

Thermal lensing can strongly influence the transverse mode structure in so-called gain-guided (or carrier-guided) diode lasers without a built-in waveguide in the p–n junction plane, where lateral confinement of the optical field occurs via a combination of gain guiding and index antiguiding (e.g., Nash [1973], Cook and Nash [1975], Thompson [1980] (chapter 6.4.1.), Hadley, Hohimer and Owyong [1987], Cherng and Osinski [1991]). A similar situation takes place in VCSELs with no built-in lateral waveguide, for example in PITSELs (e.g., Hasnain, Tai, Yang, Wang, Fischer, Wynn, Weir, Dutta and Cho [1991], Chang-Hasnain, Harbison, Hasnain, Von Lehmen, Florez and Stoffel [1991], Zeeb, Möller, Reiner, Ries, Hackbarth and Ebeling [1995]), and, partially, in TBEMs (Michalzik and Ebeling [1993]). In low-duty-cycle short-pulse operation, when thermal effects are negligible, the confinement of the optical field in the radial direction occurs via a combination of gain guiding, carrier antiguiding, absorption, diffraction (Babic, Chung, Dagli and Bowers [1993], Jansen van Doorn, van Exter and Woerdman [1995]), and spatial filtering at the top contact. Carrier antiguiding tends to defocus the optical field, which leads to large diffraction losses (Hasnain, Tai, Yang, Wang, Fischer, Wynn, Weir, Dutta and Cho [1991], Dutta, Tu, Hasnain, Zydzik, Wang and Cho [1991]). Under CW conditions, the active-region heating results in a non-uniform, bell-shaped temperature distribution which peaks in the active region and falls off in the radial direction (cf. fig. 16 in § 5.1.1). Since $(\partial n_R / \partial T)_\lambda$ is positive (see § 3.1), the thermal contribution to the refractive index also peaks in the active region, causing the thermal lensing effect. Nonuniformity of the temperature distribution

becomes more pronounced with increasing pumping current, to the point where real-index guiding associated with temperature profile may become dominant, resulting in tighter focusing of the optical field. Experimental observations of narrowing near-field patterns of the bell-shaped fundamental transverse mode with increasing current in PITSELS (Chang-Hasnain, Harbison, Florez and Stoffel [1991], Chang-Hasnain, Harbison, Hasnain, Von Lehmen, Florez and Stoffel [1991]) have been confirmed by the calculations of Michalzik and Ebeling [1993]. Thermally-induced waveguiding improves the overlap between the optical field and the gain region and reduces the diffraction loss.

In the intermediate regime of relatively long pulses (over 100 ns long), the build-up of thermal waveguide leads sometimes to anomalously long time delays in lasing. When the pulse amplitude is only slightly larger than the CW threshold current, the time delay before the onset of lasing can be as long as several μs (Hasnain, Tai, Yang, Wang, Fischer, Wynn, Weir, Dutta and Cho [1991]). The time delay rapidly decreases with increasing current and reaches the "normal" level of 25 ns when the pumping current amplitude exceeds the pulsed threshold value.

A quantitative analysis of the thermal lensing and its effects on the time delay in PITSELS is given by Dutta, Tu, Hasnain, Zydzik, Wang and Cho [1991]. At the beginning of a low-amplitude pulse, threshold losses are higher than the modal gain, and therefore lasing action cannot start. As the device starts to heat up, thermal lensing begins to play a more and more important role, steadily reducing diffraction losses. The observed time delay is simply equal to the time necessary to create a sufficiently strong thermally-induced waveguide. A similar phenomenon has been observed by Prince, Patel, Kasemset and Hong [1983] in carrier-guided stripe-geometry EELs and was explained in terms of thermally-controlled dynamic evolution of waveguide properties.

While a thermally-induced waveguide is beneficial from the point of view of lowering the CW threshold current, it can at the same time facilitate excitation of higher-order transverse modes. At higher currents, a stronger real-index thermal waveguide supports a larger number of high-order modes which can then compete with the fundamental mode. Therefore, the dynamic switch-on response of VCSELS initially contains sometimes a single-lobe profile (the fundamental transverse mode), and after the time (dependent on pumping conditions) necessary for the thermal waveguide to build up transforms into a double-lobe profile (the first-order transverse mode) (Yu and Lo [1996], Buccafusca, Chilla, Rocca, Feld, Wilmsen, Morozov and Leibenguth [1996]). Once the thermal waveguide is established, the main mode competition mechanism switches to *spatial hole burning* (e.g., Vakhshoori, Wynn, Zydzik, Leibenguth, Asom,

Kojima and Morgan [1993], Scott, Geels, Corzine and Coldren [1993], Scott, Young, Thibeault, Peters and Coldren [1995], Valle, Sarma and Shore [1995b], Law and Agrawal [1997]). The fundamental transverse mode is localized in the central part of the active region, therefore the stimulated recombination associated with this mode takes place primarily in this area. This depresses the local carrier density and the gain in the central part of the laser cavity, reducing the modal gain for the fundamental mode, while allowing the carriers to build-up near the edges of the active region and increasing the modal gain of higher-order doughnut-shaped transverse modes. Eventually, the laser ends up operating in multiple transverse modes.

In VCSELs with no built-in lateral waveguide or with weak index-guiding, spatial hole burning can cause a positive-feedback phenomenon known as *self focusing*, which further reinforces the real-index thermal waveguide (see Wilson, Kuchta, Walker and Smith [1994]). A depression in the carrier concentration produces a local increase in the refractive index which can further intensify the stimulated emission, locally reducing the carrier concentration, and so on. A similar effect can also arise from thermal lensing via absorption of the emitted light within the core of thermal waveguide.

A depression in carrier density, similar to that caused by the spatial hole burning, can also be caused by *nonuniformity of current injection* in devices with annular contacts (see Osiński, Nakwaski and Varangis [1994]). The two effects can be distinguished by observing the spontaneous emission profile, which is proportional to carrier density distribution. Nonuniformity due to current spreading should also manifest itself below the lasing threshold, while spatial hole burning can occur only above threshold. The only experiments reported so far by Vakhshoori, Wynn, Zydzik, Leibenguth, Asom, Kojima and Morgan [1993] and by Wilson, Kuchta, Walker and Smith [1994], involving measurements of the spontaneous emission profile above threshold, indicate that at moderate currents the spontaneous emission profile has a doughnut shape. Further above threshold, when higher-order transverse modes become excited, the carrier density profile is sensitive to details of the laser structure. For example, smooth profiles were observed by Wilson, Kuchta, Walker and Smith [1994] in their bottom-emitting VCSELs with circular top contacts, indicating that spatial hole burning was the dominant effect. In contrast, Vakhshoori, Wynn, Zydzik, Leibenguth, Asom, Kojima and Morgan [1993] observed dark spot near the center of the spontaneous emission profile even high above threshold, which suggests that nonuniform injection was the main effect in their top-emitting devices with annular contacts.

Nonuniform current injection, with current crowding near the edges of the

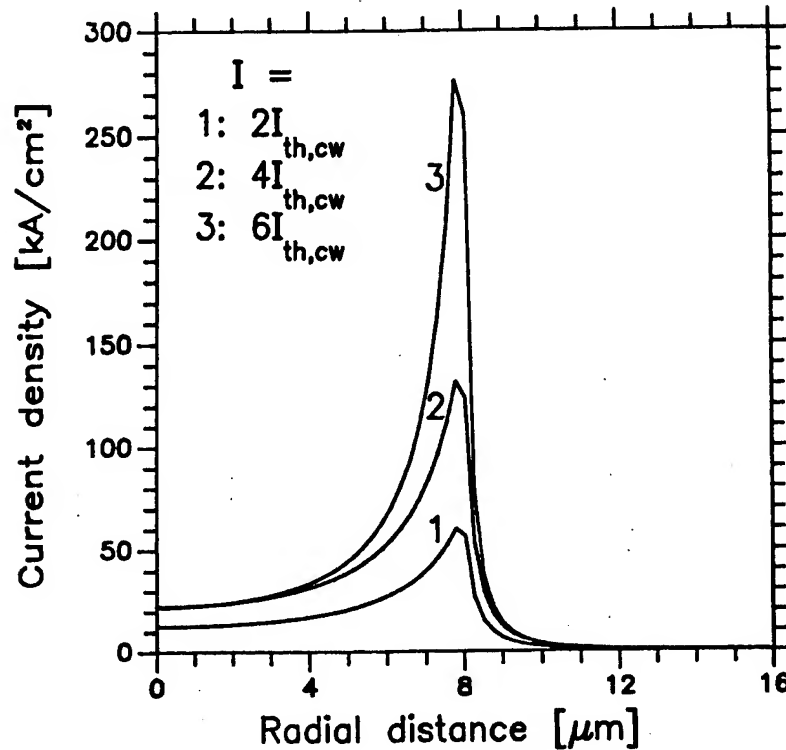


Fig. 9. Current density profiles in the p-n junction plane for a 16 μm etched-well GaAs/AlGaAs VCSEL (structure DMEWL-TIT-B) with parameters given by Nakwaski and Osiński [1993].

active region in VCSELs with annular contacts (e.g., Nakwaski and Osiński [1991b], Nakwaski, Osiński and Cheng [1992], Wada, Babic, Ishikawa and Bowers [1992], Scott, Geels, Corzine and Coldren [1993]), also favors excitation of higher-order transverse modes. To some extent, the nonuniform injection is counterbalanced by the ambipolar radial diffusion of carriers prior to their recombination (Sarzała and Nakwaski [1997]), which makes the local gain distribution more uniform than the current-density distribution (e.g., Wada, Babic, Ishikawa and Bowers [1992], Chong and Sarma [1993], Sarzała, Nakwaski and Osiński [1995]). Nevertheless, the gain profile still has an on-axis minimum and is better matched to the higher-order transverse modes than to the fundamental one. This effect is usually not strong enough to suppress the fundamental mode near threshold, but gains in importance with increasing pumping level, as the current crowding becomes more and more intense (see fig. 9). The better overlap of the gain profile with the optical field of the higher-order modes may then become sufficient to overcome the higher diffraction loss suffered by these modes.

Nonuniformity of the current density in devices with annular contacts can be largely leveled out if the heterointerfaces between the alternating layers of

Bragg mirrors are not graded (Michalzik and Ebeling [1993]). This, however, increases the series resistance (the specific heteroresistance between p-GaAs and p-AlAs layers can be as high as $2.5 \times 10^{-4} \Omega \text{cm}^2$) and results in more intense Joule heating.

Built-in index antiguiding can be used as a mechanism for extending the single-transverse mode operation range, since the higher-order modes suffer a higher diffraction loss penalty than the fundamental mode (e.g., Chang-Hasnain, Wu, Li, Hasnain, Choquette, Caneau and Florez [1993], Wu, Chang-Hasnain and Nabiev [1994], Wu, Li, Nabiev, Choquette, Caneau and Chang-Hasnain [1995], Yoo, Chu, Park, Park and Lee [1996]). The negative index step between an equivalent index of the DBR reflector and the surrounding high-index medium can be made as large as 0.18 (Wu, Chang-Hasnain and Nabiev [1993]), hence the antiguide cannot be affected significantly by the much smaller (one-two orders of magnitude) positive index step due to radial temperature profile. So far, however, this approach has had only limited success. While the near-field intensity profiles in bottom-emitting passive-antiguiding-region InGaAs/AlGaAs VCSELs show no symptoms of thermal lensing, spatial hole burning or self-focusing, the maximum single-transverse-mode power is still limited to only 1.2 mW (Wu, Chang-Hasnain and Nabiev [1993], Wu, Li, Nabiev, Choquette, Caneau and Chang-Hasnain [1995]). Introducing higher doping at the active region perimeter to increase free-carrier losses and using low-reflectivity ring contacts on the top VCSEL reflector were other mode selection methods postulated by Morgan, Guth, Focht, Asom, Kojima, Rogers and Callis [1993].

Another class of temperature-insensitive waveguide involves *strong index guiding* (Jewell, Scherer, McCall, Lee, Walker, Harbison and Florez [1989], Geels, Corzine, Scott, Young and Coldren [1990], Geels and Coldren [1990,1991], Shimizu, Babic, Dudley, Jiang and Bowers [1993], Dudley, Babic, Mirin, Yang, Miller, Ram, Reynolds, Hu and Bowers [1994], Young, Kapila, Scott, Malhotra and Coldren [1994], Yoffe, van der Vleuten, Leys, Karouta and Wolter [1994], Yoo, Park and Lee [1994]). Compared to strongly antiguiding VCSELs, index-guiding structures have a serious disadvantage of lowering the threshold of higher-order-mode excitation (Chang-Hasnain, Orenstein, Von Lehmen, Florez, Harbison and Stoffel [1990], Schröder, Grothe and Harth [1996]). Consequently, fundamental-transverse-mode operation can be maintained only over a very limited current range near threshold.

3.4. TEMPERATURE DEPENDENCE OF THE OUTPUT POWER

Because of the thermal lensing effect (see § 3.3), the threshold current for

the CW operation in PITSELS is often distinctly lower than for the pulsed one. The external differential quantum efficiency, which is the laser parameter proportional to the slope of the light-current characteristic above the threshold current, is, however, much higher for the pulsed operation (Hasnain, Tai, Yang, Wang, Fischer, Wynn, Weir, Dutta and Cho [1991]). Similarly, maximum available output power and the operating current range are enhanced under pulsed conditions.

From fig. 7, we may conclude that in order to obtain efficient CW high-power operation of VCSELS at room temperature, their cavity-mode positions at this temperature should be on the long-wavelength side of the gain spectrum. Although such lasers may have higher threshold currents for pulsed operation than those with aligned cavity-mode and gain-peak positions, nevertheless their CW threshold currents will be lower because of the *active-region heating* (provided the cavity-mode and gain-peak wavelengths are matched at the active-region temperature). However, since the active-region temperature depends on the driving current, the conditions for minimum threshold current would in general be different from the conditions for maximum output power. This is illustrated in fig. 10, showing the temperature dependence of light-current (L - I) characteristics of a PITSEL device with a room-temperature detuning of the cavity mode by 18 nm towards the longer wavelengths. The CW lasing threshold for this device, shown also in fig. 7, has a minimum at 350 K. All L - I characteristics display a typical thermal roll-off behavior, indicating that over the wide temperature range of 90 K–400 K, the output power P_{out} is thermally limited. The maximum output power is determined primarily by the temperature variation of the peak gain (see table 5) and by changes in the external *differential quantum efficiency* η_d . The latter can be extracted from fig. 10 using the following formula (Agrawal and Dutta [1993]):

$$\eta_d(T) = \frac{e\lambda(T)}{hc} \frac{dP_{\text{out}}}{dI}, \quad (18)$$

where e is the electron charge, h is Planck's constant, and c is the speed of light. Equation (18) implies that all output power from a top-emitting VCSEL is collected through the top mirror.

Figure 11 shows the temperature dependence of η_d , calculated by applying eq. (18) for the device of fig. 10. The raising part of L - I curves, not too far above threshold, is used to determine η_d . $\lambda(T)$ is obtained from the data of fig. 5, taking the CW lasing wavelength for the "865 nm mode" and extrapolating down to 90 K. In any case, the wavelength variation represents only a very small correction to η_d determined from the slope efficiency dP_{out}/dI with a constant

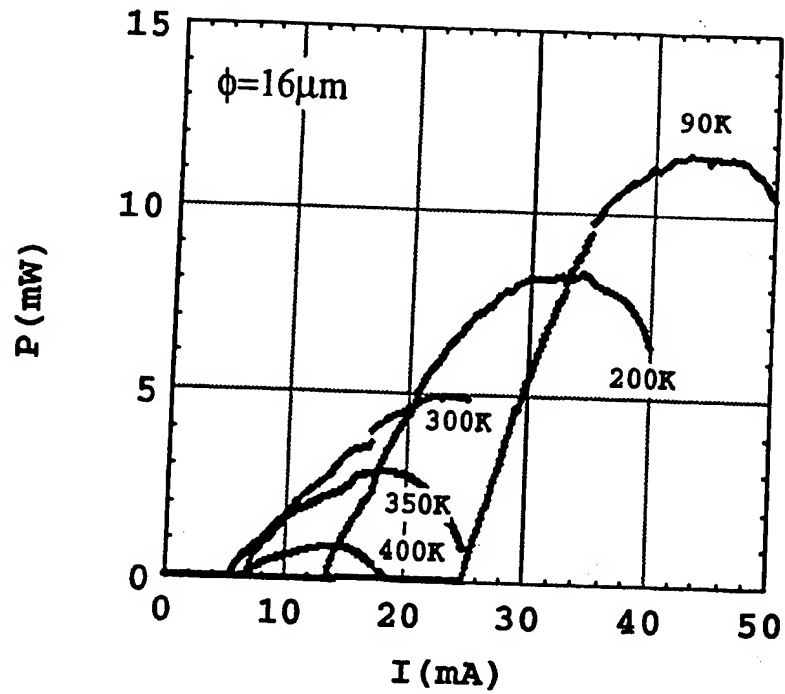


Fig. 10. Temperature evolution of the light-current characteristics for a $16\mu\text{m}$ PITSEL shown in fig. 7 as having minimum CW threshold at 350 K (mode wavelength 865 nm at 300 K) (after Lu, Zhou, Cheng and Malloy [1994]).

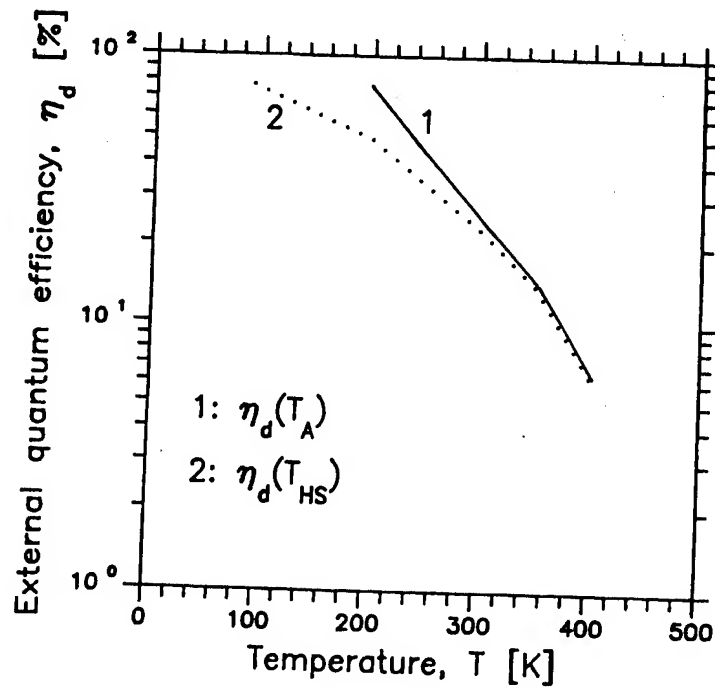


Fig. 11. Temperature dependence of the differential quantum efficiency η_d for the device in fig. 10, using either the stage temperature T_{HS} (dotted line) or the active-region temperature T_A (solid line) as the argument in $\eta_d(T)$.

wavelength. The logarithmic scale in fig. 11 is chosen to verify whether an exponential formula analogous to eq. (16),

$$\eta_d(T) = \eta_d(300 \text{ K}) \exp \left(\frac{T - 300 \text{ K}}{T_\eta} \right), \quad (19)$$

with a constant characteristic temperature T_η , would hold for VCSELS, as it does for EELs (e.g., Papannareddy, Ferguson and Butler [1987]). Note that sometimes a simpler approximation is used (Wipiejewski, Peters, Thibeault, Young and Coldren [1996]): $\eta_d(T) = \eta_{\max}(1 - \Delta T/T_{\max})$, where T_{\max} is the characteristic roll-over temperature of the laser. The two curves in fig. 11 correspond to results obtained using either the stage temperature T_{HS} (dotted line) or the active-region temperature T_A (solid line) as the argument in $\eta_d(T)$. T_A is estimated using the wavelength shift between the CW and pulsed operation shown in fig. 5, again extrapolating down to 90 K. Under pulsed conditions, the "865 nm mode" device has two clear regimes of linear wavelength shift, characterized by $\partial\lambda_M/\partial T = 0.41 \text{ Å/°C}$ for $90 \leq T_{\text{HS}} < 300 \text{ K}$, and $\partial\lambda_M/\partial T = 0.59 \text{ Å/°C}$ for $300 \leq T_{\text{HS}} < 400 \text{ K}$. The deviation of the CW wavelength from the pulsed one gives then the following estimates of the active-region temperature at CW threshold: $T_A = 198 \text{ K}$ at $T_{\text{HS}} = 90 \text{ K}$, $T_A = 239 \text{ K}$ at $T_{\text{HS}} = 200 \text{ K}$, $T_A = 310 \text{ K}$ at $T_{\text{HS}} = 300 \text{ K}$, $T_A = 354 \text{ K}$ at $T_{\text{HS}} = 350 \text{ K}$, and $T_A = 403 \text{ K}$ at $T_{\text{HS}} = 400 \text{ K}$.

If the stage temperature T_{HS} is used (dotted curve in fig. 11), T_η decreases steadily with T_{HS} ($T_\eta = 241 \text{ K}$ for $90 \leq T_{\text{HS}} < 200 \text{ K}$, $T_\eta = 129 \text{ K}$ for $200 \leq T_{\text{HS}} < 300 \text{ K}$, $T_\eta = 104 \text{ K}$ for $300 \leq T_{\text{HS}} < 350 \text{ K}$, and $T_\eta = 63 \text{ K}$ for $350 \leq T_{\text{HS}} < 400 \text{ K}$). Hence, it is clear that if T_{HS} is used as an argument in $\eta_d(T)$, eq. (19) can be used only over a very small temperature range. Conversely, using the active-region temperature T_A (solid curve in fig. 11), produces two regimes of behavior ($T_\eta = 91 \text{ K}$ for $198 \leq T_A < 310 \text{ K}$, and $T_\eta = 62 \text{ K}$ for $310 \leq T_A < 403 \text{ K}$) that coincide with the two regions of constant pulsed-wavelength shift rate (cf. fig. 5).

It is interesting to note that the value of $T_\eta = 91 \text{ K}$ agrees very well with $T_{\text{sp}} = 93 \text{ K}$ (valid for $300 \text{ K} \leq T_A \leq 440 \text{ K}$) determined experimentally by Chen, Hadley and Smith [1994], where T_{sp} is the characteristic temperature for the spontaneous emission efficiency variation with temperature. This indicates that reduction of internal quantum efficiency, rather than changes in optical losses, is the main effect responsible for the temperature variation of the external quantum efficiency η_d .

The increase in slope of $\partial\lambda_M/\partial T$ and the reduction in T_η from 91 K to 62 K around $T_A = 310 \text{ K}$ is most likely caused by the onset of carrier leakage over the heterobarriers (cf. eq. 15). In EELs, opening of an additional current

leakage path would have unavoidably reduced the value of T_0 . In VCSELS, this process is obscured by strong variations of $I_{th}(T)$ caused by the detuning between the gain peak and the cavity mode (cf. § 3.2). Nevertheless, fig. 7 does display an asymmetry between the low- and high-temperature branches of $I_{th}(T)$, indicating a faster growth at high temperatures. Additional corroborating evidence is provided by fig. 8, where, compared with low-temperature behavior, T_0 reaches lower values on the high-temperature side of the asymptotes. While T_0 for the “865 nm mode” device (curve 3 in fig. 8) continues to fall at 400 K, the “852 nm mode” device (curve 2 in fig. 8) reaches a floor of $T_0 = 62\text{--}65$ K. Although more studies of this subject are needed to eliminate the possibility of a serendipitous coincidence, the close matching of the high-temperature values of T_0 and T_η for the same device is remarkable. Moreover, a T_η of 62 K is very close to the high-temperature value of $T_0 = 60$ K reported by Geels, Thibeault, Corzine, Scott and Coldren [1993] for a BEML, indicating that the phenomenon responsible for the low T_0 values at high temperatures may be the same in different VCSEL structures. Carrier leakage over heterobarriers could indeed represent such common mechanism, since both PITSELS and BEMLs incorporate quantum-well active-regions.

§ 4. Fundamentals of Thermal Modeling of VCSELS

Thermal modeling of VCSELS is a very involved task because of:

- (i) a multilayer structure (sometimes containing over a hundred layers), often of nonplanar or buried-type designs, with many heterojunctions, graded layers, strained layers, single or multiple quantum wells, superlattices, oxide and oxidized layers, barriers, etched wells or mesas, etc. (cf. fig. 3); and
- (ii) the necessity of taking into account many mutual nonlinear interactions between particular physical phenomena; i.e., thermal, electrical, optical and sometimes also mechanical and photochemical processes, taking place during laser operation (cf. fig. 15, below).

In analytical modeling of VCSELS, their complex structure imposes the necessity of solving the equations describing their operation separately for each homogeneous region. Mutual correlation of those partial solutions, with the aid of proper boundary conditions (see, e.g., Nakwaski and Osiński [1994]), should then be carried out. This method is very time-consuming, and therefore simplified approaches are sometimes adopted, transforming the inhomogeneous laser structure made of isotropic materials into an equivalent homogeneous, but anisotropic medium (see, e.g., Osiński and Nakwaski [1993a], Osiński, Nakwaski

and Varangis [1994], Osiński, Nakwaski and Leal [1994], Sarzała, Nakwaski and Osiński [1995]).

The second of the above mentioned factors, i.e., mutual interactions between individual physical processes occurring during a diode laser operation, whose incomplete review will be presented in fig. 15, obliges us to use a self-consistent approach. A flow chart of a typical self-consistent diode laser simulation will be presented in fig. 14.

4.1. HEAT CONDUCTION EQUATION

For the transient-state condition, the heat conduction equation in a medium of cylindrical symmetry is of the following form (Oezisik [1980]):

$$\nabla \{k[r, z, T(r, z)] \nabla T(r, z)\} = \frac{k}{\kappa} \frac{\partial T}{\partial t} - g(r, z), \quad (20)$$

which for a uniform medium with temperature-independent k , κ , and g may be reduced to

$$\frac{\partial^2 T}{\partial r^2} + \frac{1}{r} \frac{\partial T}{\partial r} + \frac{\partial^2 T}{\partial z^2} = \frac{1}{\kappa} \frac{\partial T}{\partial t} - \frac{1}{k} g(r, z). \quad (21)$$

In the above equations, k and κ stand for the thermal conductivity and the thermal diffusivity, respectively, and $g(r, z)$ is the distribution of the volume density of heat generation (in W/cm^3). In the steady-state case, the first term of the right-hand-side of eqs. (20) and (21) vanishes. Examples of room-temperature values of thermal conductivities for several semiconductor materials commonly used in VCSEL structures are listed in table 7.

To solve the thermal conduction equation (20) (or 21), it is necessary to formulate an appropriate set of *boundary conditions*. VCSEL structures are usually axially symmetric, so the first boundary condition is written as follows (cf. fig. 12):

$$\left. \frac{\partial T}{\partial r} \right|_{r=0} = 0. \quad (22)$$

In a typical packaging scheme, the outer surfaces of VCSELs are exposed to interaction with an external ambient medium (usually air). In principle, this may result in heat transfer to the external ambient medium via the direct contact of air particles with the laser walls and subsequent diffusion and convection processes. In natural convection, the flux of heat from the surface

Table 7
Thermal conductivity k

Material	k (W/mK)	Reference
GaAs	44	Adachi [1985]
AlAs	91	Adachi [1985]
$\text{Al}_x\text{Ga}_{1-x}\text{As}$	$100/(2.27 + 28.83x - 30.0x^2)$	Adachi [1985]
InP	68	Kudman and Steigmeier [1964]
$\text{In}_{0.73}\text{Ga}_{0.27}\text{As}_{0.6}\text{P}_{0.4}$ ^a	5.5	Nakwaski [1988]
$\text{In}_{0.63}\text{Ga}_{0.37}\text{As}_{0.79}\text{P}_{0.21}$ ^b	5.15	Nakwaski [1988]
$\text{In}_{0.6}\text{Ga}_{0.4}\text{As}_{0.85}\text{P}_{0.15}$ ^c	5.1	Nakwaski [1988]

^a Bandgap wavelength $\lambda_g = 1.3 \mu\text{m}$.

^c Bandgap wavelength $\lambda_g = 1.55 \mu\text{m}$.

^b Bandgap wavelength $\lambda_g = 1.45 \mu\text{m}$.

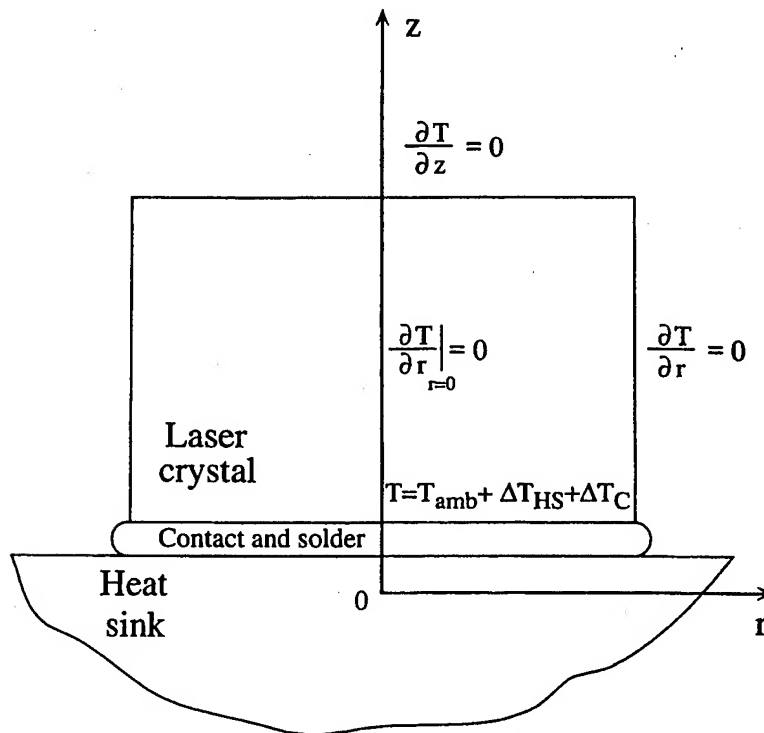


Fig. 12. Boundary conditions of the thermal conduction equation for VCSELS.

is approximately proportional to the 5/4 power of the difference between the surface temperature and the ambient temperature (Carslaw and Jaeger [1988], p. 21). In VCSELS, however, considerable temperature increase occurs only in

the vicinity of the active region, buried deep inside the device. The temperature at the outer surfaces is usually only slightly higher than that of the surrounding medium. Thus, heat transfer through the surfaces is very small compared to a very efficient heat conduction through the laser heat sink and can be neglected completely. Consequently, the outer surfaces of the VCSEL chip can be assumed to be adiabatic (cf. fig. 12):

$$\left. \frac{\partial T}{\partial r} \right|_{\text{side walls}} = 0, \quad (23)$$

$$\left. \frac{\partial T}{\partial z} \right|_{\text{upper walls}} = 0. \quad (24)$$

Heat flux conduction through the VCSEL base (see fig. 12) produces a temperature increase inside the contact and solder layers (ΔT_C) as well as inside the heat sink (ΔT_{HS}). The corresponding boundary condition can be written as follows:

$$T|_{\text{bottom walls}} = T_{\text{amb}} + \Delta T_{HS} + \Delta T_C, \quad (25)$$

where T_{amb} stands for the temperature of the ambient and ΔT_{HS} and ΔT_C are to be determined and will be analyzed in the next section.

4.2. HEAT-SINK AND CONTACT/SOLDER-LAYER TEMPERATURE INCREASE

Exact determination of the temperature increase ΔT_{HS} in the heat sink usually requires an involved three-dimensional thermal analysis. An estimate of ΔT_{HS} can, however, be made using the concept of the *effective diameter*, D_E , for the heat flux entering the heat sink from the device, as proposed by Nakwaski and Kontkiewicz [1985] for cylindrically symmetric devices. This approach is based on an assumption that a uniform heat flux entering the heat sink through an effective circular thermal contact of diameter D_E will cause exactly the same average temperature increase ΔT_{HS} in the heat sink as the actual nonuniform heat flow. D_E can be determined using the following expression:

$$D_E = 2 \lim_{\Delta d_a \rightarrow 0} \left(\pi k_a \frac{\Delta R_{TH}}{\Delta d_a} \right)^{-1/2}, \quad (26)$$

where R_{TH} is the laser thermal resistance (defined by eq. 49) and Δd_a is the thickness of a hypothetical additional layer (of a thermal conductivity k_a) between the heat sink and the device.

Once D_E is determined, the average temperature increase ΔT_{HS} inside the heat sink can be found using the following formula (Carslaw and Jaeger [1988], p. 216):

$$\Delta T_{HS} = \frac{16Q_T}{3\pi^2 D_E k_{HS}}, \quad (27)$$

where Q_T stands for the total power of the heat flux entering the heat sink, and k_{HS} is the thermal conductivity of its material. In the derivation of eq. (27), the heat sink is assumed to be much larger than the laser chip.

To determine ΔT_C , the thicknesses of all the intermediate layers between the laser chip and the heat sink (i.e., contact and solder layers, and for some VCSEL structures also oxide layers) should be averaged over the effective diameter D_E . The average temperature increase within these layers ΔT_C can then be expressed as

$$\Delta T_C = \frac{4Q_T}{\pi D_E^2} \sum_i \frac{d_{i,av}}{k_i}, \quad (28)$$

where the summation should be carried out over the intermediate layers, $d_{i,av}$ are their averaged thicknesses and k_i are their thermal conductivities.

4.3. HEAT SOURCES

Diode lasers are supplied with the electric power which, in processes of current spreading, carrier recombination as well as emission and absorption of radiation, is transformed into output power and heat in a way illustrated in fig. 13.

In VCSELS, the following heat generation mechanisms should be taken into consideration: volume and barrier Joule heating, nonradiative recombination of carriers, absorption of spontaneous radiation, and absorption of laser radiation. Distributions of these heat sources are directly associated with distributions of carrier concentration, current density, and spontaneous and stimulated radiation intensities, hence they are influenced by current spreading, carrier diffusion and waveguiding mechanisms. Their magnitudes are influenced in turn by such device and material parameters as internal quantum efficiency, threshold current density, threshold carrier concentration, absorption coefficients, electrical resistivities – all nonlinearly dependent on temperature.

The *power balance in a semiconductor laser* may be presented in the following form:

$$P = UI = (U_{pn} + IR_S)I$$

$$\begin{aligned}
= & I^2 R_S && \text{Joule heating} \\
& + U_{pn} I_{th} (1 - \eta_{sp}) && \text{nonradiative recombination} \\
& && \text{at threshold} \\
& + U_{pn} I_{th} \eta_{sp} (1 - f_T) && \text{absorption of spontaneous} \\
& && \text{radiation inside the active} \\
& && \text{region at threshold} \\
& + U_{pn} I_{th} \eta_{sp} f_T && \text{escape spontaneous radiation} \\
& && \text{at threshold} \\
& + U_{pn} (I - I_{th}) (1 - \eta_i) && \text{nonradiative recombination} \\
& (1 - \eta_{sp}) && \text{for } I > I_{th} \quad (29) \\
& + U_{pn} (I - I_{th}) (1 - \eta_i) \eta_{sp} && \text{absorption of spontaneous} \\
& (1 - f_T) && \text{radiation inside the active} \\
& && \text{region for } I > I_{th} \\
& + U_{pn} (I - I_{th}) (1 - \eta_i) \eta_{sp} f_T && \text{escape spontaneous radiation} \\
& && \text{for } I > I_{th} \\
& + U_{pn} (I - I_{th}) (\eta_i - \eta_d) && \text{absorption of stimulated} \\
& && \text{radiation outside the active} \\
& && \text{region} \\
& + U_{pn} (I - I_{th}) \eta_d && \text{laser output power.}
\end{aligned}$$

In the above equations, P is the electric power supplied to the laser, U is the total voltage drop inside the device, U_{pn} is the voltage drop at the p-n junction, I and I_{th} are the operation current and the threshold current, respectively, η_{sp} , η_i , and η_d are the quantum efficiencies: internal for spontaneous emission and for lasing radiation as well as differential external for lasing, respectively, and f_T is the radiative transfer coefficient for spontaneous emission (cf. § 4.3.1).

All heat sources in semiconductor lasers are associated with current densities, carrier concentrations or radiation intensities, which are nonuniform. Therefore these heat generation processes are nonuniform not only along the z axis (because of different structure layers of different heat yields) but also along the r axis inside all homogeneous layers.

With the exception of the Joule barrier heating, all heat generation processes represent volume heat sources. They are, however, often treated as flat (planar) heat sources located in the middle of their generation regions. Such approximation can deteriorate the accuracy of the calculated temperature profiles, especially in the close vicinity of the heat source, so it may be used only when the heat sources are relatively thin.

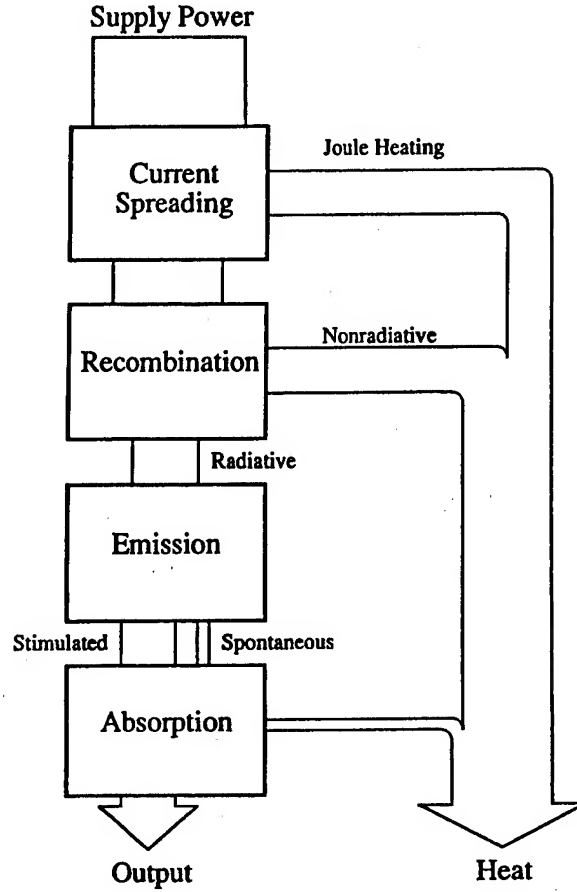


Fig. 13. Power balance in diode lasers.

4.3.1. Active-region heating

Nonradiative recombination of carriers takes place within the active region, where carriers of both kinds (electrons and holes) can meet each other. This process is associated with the *efficiency of radiative recombination*, which for an ideal injection is simply equal to the *internal quantum efficiency*.

Below the threshold, i.e., for $j < j_{th}$, where j and j_{th} stand for the operation current density and the threshold current density, respectively, most of the electric power supplied to the active region is transformed into heat because the internal quantum efficiency for the spontaneous emission η_{sp} is much less than unity. Then the volume density g_A (in W/cm^3) of active-region heat generation may be expressed as

$$g_A = \frac{U_{pn}j(1 - \eta_{sp})}{d_A} \quad j \leq j_{th}, \quad (30)$$

where d_A stands for the active region thickness (cumulative thickness in the case of multi-quantum-well active regions). This expression should be modified slightly if we take into account absorption of some part of spontaneous radiation in the active region and radiative transfer of the remaining part out of this region:

$$g_A = \frac{U_{pn}j(1 - \eta_{sp}f_T)}{d_A} \quad j \leq j_{th}, \quad (31)$$

where f_T stands for the radiative transfer coefficient (Kobayashi and Furukawa [1975], Nakwaski [1979]):

$$f_T = 2\sin^2\left(\frac{\alpha_{cr}}{2}\right), \quad (32)$$

with

$$\alpha_{cr} = \arctan\left(\frac{n_{R1}}{\sqrt{n_{R2}^2 - n_{R1}^2}}\right), \quad (33)$$

and where n_{R1} and n_{R2} are the refractive indices of the cladding and the active-region materials, respectively.

Above the laser threshold, an analogous equation reads as follows (Kobayashi and Furukawa [1975], Nakwaski [1979]):

$$g_A = \frac{U_{pn}(1 - \eta_{sp}f_T)[j_{th} + (j - j_{th})(1 - \eta_i)]}{d_A} \quad j > j_{th}, \quad (34)$$

where η_i is the internal quantum efficiency of the stimulated emission.

Whenever intense heating takes place, it is important to remember that the threshold current density j_{th} is not a constant device parameter, but is itself temperature dependent. As the pumping current density j increases, so does the active-region temperature, and therefore j_{th} is also current dependent. To emphasize this, Scott, Geels, Corzine and Coldren [1993] have introduced the concept of a current-dependent *effective threshold current density* $j_{th,e} \equiv j_{th}(j)$. Alternatively, we could write $j_{th} \equiv j_{th}(T_A)$, where T_A is the average active-region temperature.

For high reliability, the quality of semiconductor laser materials must be very good. Consequently, in most cases the internal quantum efficiency for stimulated emission η_i is very close to unity (Petermann [1991]). Thus, eq. (34) reduces to:

$$g_A = \frac{U_{pn}j_{th,e}(j)(1 - \eta_{sp}f_T)}{d_A} \quad j > j_{th,e}. \quad (35)$$

In the case of proton-bombarded VCSELS, e.g., in PITSELS, this part of the spontaneous radiation, which is leaving the active region, is mainly absorbed in the closest vicinity of the active region; i.e., in surrounding it highly absorbing (of high absorption coefficient α) areas exposed during their fabrication to a stream of protons. Thicknesses ($=\alpha^{-1}$) of these new heat sources are very low. Therefore, it is quite a good approximation to assume that these absorption events take place also inside the active region. Then, the radiative transfer coefficient f_T should be put equal to zero in all the above expressions.

Saturation of the voltage drop $U_{pn}(r)$ at the p-n junction above the lasing threshold (e.g., Sommers [1971], Paoli [1973]) should also be taken into account. It does not simply mean that $U_{pn}(r)$ is taken as a constant distribution for all currents above the threshold, because an increase in the pumping is followed by an increase in the active-region temperature, which results in an increase in the threshold current. Therefore, for a given value of the pumping current, the saturated profile of the voltage drop at the p-n junction should correspond to an actual active-region temperature increase.

In laser structures, where diffusion of minority carriers within the active region before their recombination (radiative or nonradiative) plays an important role, i.e., in lasers without radial carrier confinement mechanisms, it is more justified to associate the above heat generation with carrier concentration distribution rather than with a current density profile. Each act of nonradiative recombination is followed by heat generation of energy equal to about $h\nu$, where h is the Planck constant, and ν is the laser radiation frequency. Generally, especially in lasers with quantum-well active regions, this energy may be different than the energy eU_{pn} , where e is the unit charge. Then this heat generation consists of two processes – carrier thermalization and carrier recombination, whose sum must give the supply energy eU_{pn} . Even if they are separated in space, they both occur inside or very close to the active region. Therefore we may neglect their separation. Equation (35) will be then modified to the following form:

$$g_A = \frac{P_A}{N_{A,e}} n_{th,e}(j)(1 - \eta_{sp} f_T) \quad j > j_{th,e}, \quad (36)$$

where P_A stands for the total effective threshold power generated (mainly nonradiatively) inside the active region, defined as

$$P_A = 2\pi \int_0^{r_s} U_{pn}(r) j_{th,e}(r) r dr \quad [\text{W}], \quad (37)$$

and $N_{A,e}$ is the total carrier number composing the effective threshold within the active region:

$$N_{A,e} = 2\pi d_A \int_0^{r_s} n_{th,e}(r) r dr, \quad (38)$$

with r_s the structure radius and $n_{th,e}$ the threshold effective carrier concentration (associated with $j_{th,e}$). In the above, we assume that all the heat generation inside the active region is distributed uniformly over $N_{A,e}$ recombining carriers.

4.3.2. Absorption of laser radiation

Absorption of laser radiation is associated with generation of heat of a volume density g_{abs} :

$$g_{abs} = p_{int} \alpha \quad [W/cm^3], \quad (39)$$

where α is the absorption coefficient (different in various layers) for the laser radiation and p_{int} is its internal density inside the resonator:

$$p_{int}(r) = U_{pn}(r) [j(r) - j_{th,e}(r)] \quad [W/cm^2]. \quad (40)$$

Note that according to the suggestions of Petermann [1991], the internal quantum efficiency for stimulated emission is taken equal to unity in the above equations.

4.3.3. Absorption of spontaneous radiation

In contrast to a stimulated radiation, spontaneous radiation is always emitted isotropically in all directions. Some part of its vertical component is reflected at boundaries between the active region and the cladding layers as well as from the resonator mirrors and is effectively absorbed within the active region, which was already taken into account in § 4.3.1. The in-plane emission, on the other hand, can be amplified significantly by stimulated processes within the active region (Onischenko and Sarma [1997]).

Spontaneous radiation reaches sometimes distant regions of the laser. Its absorption may, therefore, occur in many different places. For that reason, a distribution of heat generation associated with this absorption is usually difficult to determine, unless the active region is surrounded by highly absorptive areas, as in PITSELS (§ 4.3.1).

4.3.4. Joule heating

In all layers, a current flow is followed by generation of the volume Joule heating g_J :

$$g_J = j^2 \rho \quad [\text{W/cm}^3], \quad (41)$$

where ρ stands for the electrical resistivity (in Ωcm).

A current flow through a potential barrier as contacts and heterobarriers is in turn followed by a generation of the Joule heat of a surface density q_B :

$$q_B = j^2 R_B \quad [\text{W/cm}^2], \quad (42)$$

where R_B is the specific contact resistance (in Ωcm^2) of the barrier.

4.4. SELF-CONSISTENT APPROACHES

The thermal conductivity, k , of a semiconductor material is a temperature-dependent parameter. This dependence is especially important for relatively high temperature increases because of its strong nonlinear behavior. It may be easily taken into account with the aid of the Kirchhoff transformation (Carslaw and Jaeger [1988], p. 11):

$$\Theta = \frac{1}{k(T_R)} \int_{T_R}^T k(T) dT. \quad (43)$$

Then all of the calculations are carried out for the transformed temperature Θ ; i.e., as if the thermal conductivity were constant. These temperature profiles should afterwards be recalculated for the temperature-dependent thermal conductivity case, using the inverse transformation. In eq. (43), T_R stands for the reference temperature. Usually we assume it to be equal to the lowest temperature inside a semiconductor medium; i.e.,

$$T_R = T_{\text{amb}} + \Delta T_{\text{HS}} + \Delta T_C. \quad (44)$$

The detailed form of the reverse transformation depends on a functional dependence $k(T)$ in a temperature range of interest. At temperatures around and

over room temperature, for example, the thermal conductivity of GaAs may be expressed as (Amith, Kudman and Steigmeier [1965]):

$$k_{\text{GaAs}}(T) = 0.44 \cdot (300/T)^{1.25} \quad [\text{W/cm K}], \quad (45)$$

and that of InP as

$$k_{\text{InP}}(T) = \left[\frac{1.47 + (T - 300)}{117} \right]^{-1} \quad [\text{W/cm K}]. \quad (46)$$

Equation (46) was obtained on the basis of fig. 1, published by Kudman and Steigmeier [1964]. Introducing successively eqs. (45) and (46) to eq. (43), we get the inverse transformation formula for GaAs in the following form:

$$T = T_R \left[1 - \frac{k_{\text{GaAs}}(T_R) \Theta}{528} \left(\frac{T_R}{300} \right)^4 \right]^{-1/4} = T_R \left[1 - \frac{\Theta}{1200} \left(\frac{T_R}{300} \right)^{11/4} \right]^{-1/4}, \quad (47)$$

and that of InP as

$$T = 128 + (T_R - 128) \exp \left[\frac{k_{\text{InP}}(T_R) \Theta}{11\,700} \right]. \quad (48)$$

In all the above equations, temperature should be put in Kelvin.

Thermal diffusivities κ of semiconductor materials are also dependent on temperature. It is not, however, possible to take into consideration at the same time the temperature dependencies of both these thermal material parameters; i.e., $k(T)$ and $\kappa(T)$, using a transformation analogous to that presented above. Therefore, in detailed analytical transient thermal analyses, i.e., when both the above parameters should be included, another method of calculation, namely the so-called staircase approach, is recommended. For each time step, Δt , temperature profiles are determined using values of k and κ found in a previous calculation step, starting from an initial temperature of the entire structure equal to that of the ambient (T_{amb}).

There is still another temperature-dependent term in the thermal conduction equation (20) – including the volume power density of a heat generation; i.e., g . This is because many material parameters (such as electrical resistivities, refractive indices, absorption coefficients) and device parameters (such as threshold current and quantum efficiencies), which influence the heat generation, are strongly dependent on temperature. The above may be included in the model using the self-consistent approach, when in successive iteration loops of the

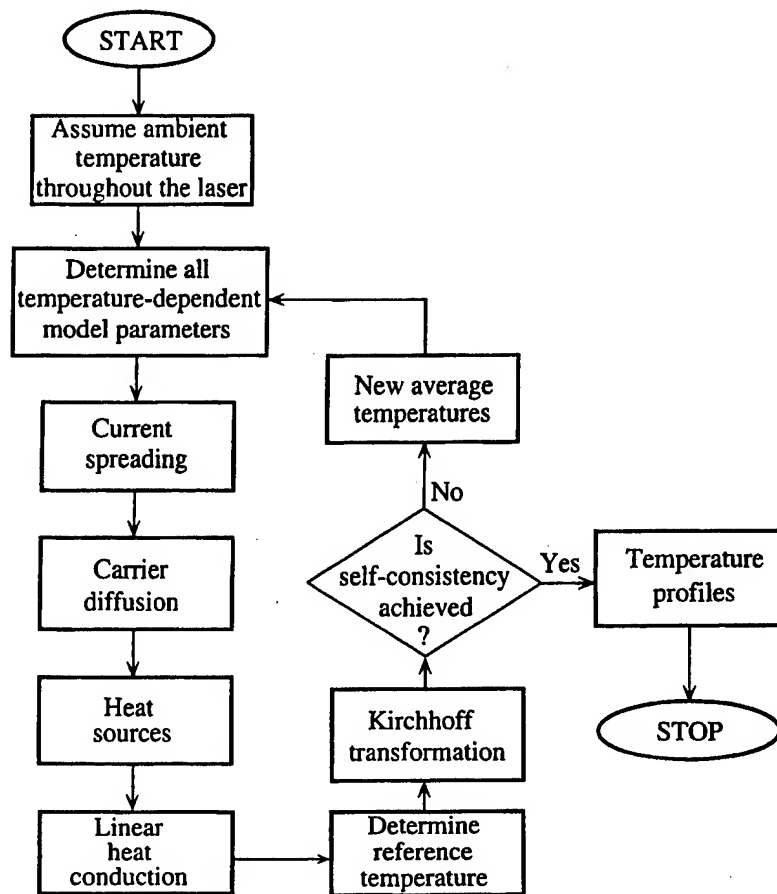


Fig. 14. Flow chart of the thermal-electrical self-consistent calculations in VCSELS.

calculation values of the above parameters determined in the previous loop are used. Self-consistency is assumed to be reached when differences between results of calculations obtained in two consecutive loops are below given limits.

Strictly speaking, not only material and device parameters but also distributions of current densities and carrier concentrations within the whole laser structure are dependent on current temperature profiles. This is because the current spreading and the carrier diffusion phenomena are temperature-dependent processes. Therefore in more exact thermal analyses of VCSELS, the thermal-electrical self-consistent procedure is recommended (fig. 14), in which mutual interactions between thermal and electrical processes in the laser are included.

Even more exact is the thermal-electrical-optical self-consistent approach in which optical processes, with their mutual interactions with both the thermal and electrical processes, are also taken into consideration. The full picture of mutual

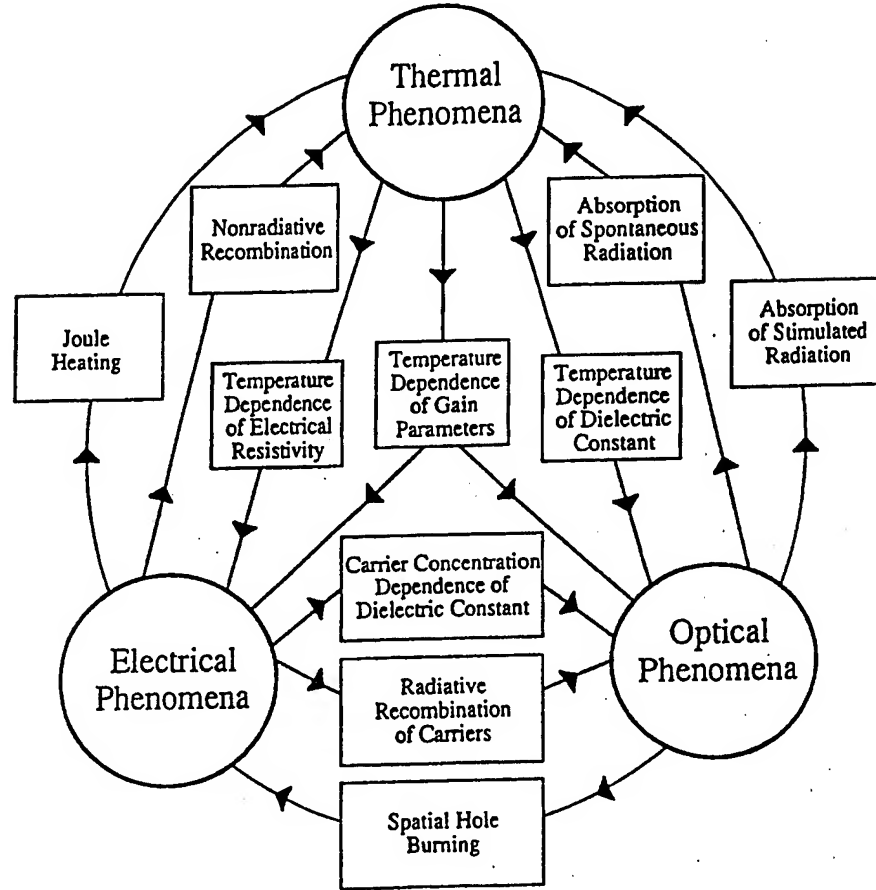


Fig. 15. Mutual interactions between thermal, electrical, and optical processes in semiconductor lasers.

interactions between all these processes is shown in fig. 15. In VCSELS with strained active regions, additionally mechanical processes should be included.

§ 5. Comprehensive Thermal Models of VCSELS

The key parameter used in all simplified treatments of steady-state thermal problems in diode lasers is the thermal resistance R_{TH} (in K/W), defined as the ratio of the average active-region temperature increase $\Delta T_{A,av}$ to the total dissipated thermal power Q_T (Joyce and Dixon [1975], Manning [1981]):

$$R_{TH} = \frac{\Delta T_{A,av}}{Q_T}. \quad (49)$$

It should be noted that although the thermal resistance is a very useful parameter to compare the thermal properties of various devices, it may sometimes give

misleading information. Consider, for example, a device with a very poor electrical contact between the device chip and the heat sink. The resultant heat, generated at the laser/heat sink interface, would be very efficiently extracted by the heat sink (assuming it is made of a high thermal conductivity material), so its influence on the active-region heating would be relatively small. However, the heat generated near the heat sink would still contribute to the total heat power Q_T . Therefore, when eq. (49) is used to determine R_{TH} , such a device would have lower thermal resistance than a well mounted laser with low-electrical resistance contact.

Thermal-electrical behavior of VCSELS is described by a coupled system of partial differential equations with complicated boundary conditions. The approaches towards solving these equations can be classified into two major types: analytical and numerical models. In analytical models, the solution is written in the form of an analytical expression, usually at the expense of some approximations imposed by the postulated form of the solution. In numerical models, no functional form of the solution is sought, hence details of the device structure can be rendered more faithfully. However, in contrast to analytical models where the accuracy of the solution can be easily controlled, it is more difficult to verify that the purely numerical solution does not contain significant errors. Details of hitherto known analytical and numerical comprehensive thermal VCSEL models are compared in table 8a and table 8b, respectively.

5.1. COMPREHENSIVE ANALYTICAL MODELS

5.1.1. *Multilayer radially uniform structures*

The first comprehensive approach to the thermal properties of VCSELS was developed by Kinoshita, Koyama and Iga [1987], Iga, Koyama and Kinoshita [1988], and Iga and Koyama [1990], who assumed only a single flat-disk heat source located in the center of the active region, but considered the influence of multilayer device structure on the 2D heat-flux spreading. The heat exchange with the exterior is assumed to take place only through the heat sink, with adiabatic boundary conditions for all remaining surfaces defining the device. For each layer, assumed to be radially uniform, 2D azimuthally symmetric temperature profiles are expressed in terms of infinite series containing the Bessel and hyperbolic functions. The expansion coefficients are found by imposing the boundary conditions of continuity of the temperature and heat flux profiles across the interfaces between the layers. The method is analogous to that proposed originally by Joyce and Dixon [1975] for edge-emitting lasers. The main

Table 8a
Analytical comprehensive thermal VCSEL models

Ref.	Year	Structure	Method	Current spreading	Carrier diffusion	Structure modeling	Heat sources ^a					Self-consistency ^b				
							NR	SP	ST	VJ	BJ	CJ	$k(T)$	Th-El	Th-Op	El-Op
1	1987	DMEWL	Fourier	-	-	crude	+	-	-	-	-	-	-	-	-	-
2	1991	DMEWL	Green	+	-	good	+	+	-	+	+	+	+	+	-	-
3	1992	PITSEL	Fourier	+	-	exact	+	+	+	+	-	+	+	+	-	-
4	1995	DMEWL	Green	+	-	good	+	+	+	+	+	+	+	+	-	-
5	1995	PITSEL	Green	+	-	fair	+	+	-	-	-	-	-	-	-	-

^a Abbreviations: NR, nonradiative recombination; SP, absorption of spontaneous radiation; ST, absorption of stimulated radiation; VJ, volume Joule heating; BJ, barrier Joule heating at heterojunctions; CJ, barrier Joule heating at the p-side contact.

^b Abbreviations: $k(T)$, temperature-dependent thermal conductivity; Th-El, thermal-electrical; Th-Op, thermal-optical; El-Op, electrical-optical.

^c Partly.

References

- (1) Kinoshita, Koyama and Iga [1987]
- (2) Nakwaski and Osinski [1991a,b, 1993]
- (3) Nakwaski and Osinski [1992c, 1994]
- (4) Osinski and Nakwaski [1995b]
- (5) Zhao and McInerney [1995]

Table 8b
Numerical comprehensive thermal VCSEL models

Ref.	Year	Structure	Method ^a	Current spreading	Carrier diffusion	Structure modeling	Heat sources ^b							Self-consistency ^b		
							NR	SP	ST	VJ	BJ	CJ	k(T)	Th-El	Th-Op	El-Op
1	1993	UMEWL	FDM	-	-	fair	+	?	-	-	-	-	-	-	-	-
2	1993	TBEML	FEM	+	-	exact	+	+	+	+	+	-	+	-	-	-
3	1994	HMML	FEM	+	-	fair	+	+	-	-	-	-	-	-	-	-
4	1994	TEML	CVM	+	-	fair	+	+	+	+	+	-	-	-	-	-
5	1994	PITSEL	FEM	+	-	fair	+	+	+	+	+	-	-	-	-	-
6	1995	DMEWL	FEM	+	-	exact	+	+	-	+	+	+	+	+	+	-
7	1995	DMEWL	FEM	-	-	fair	+	+	-	-	-	-	-	-	-	-
8	1995	PITSEL	FEM	+	+	exact	+	+	+	+	+	+	+	+	+	-
9	1996	PITSEL	FEM	+	+	fair	+	+	+	+	+	-	-	-	-	+

^a Abbreviations: FDM, finite-difference method; FEM, finite-element method; CVM, control-volume method.
^b See table 8a.

References

- (1) Shimizu, Babić, Dudley, Jiang and Bowers [1993]
- (2) Michalzik and Ebeling [1993]
- (3) Piprek and Yoo [1994]
- (4) Norris, Chen and Tien [1994], Chen, Hadley and Smith [1994], and Chen [1995]
- (5) Piprek, Wenzel and Sztafka [1994], Piprek, Wenzel, Wünsche, Braun and Henneberger [1995]
- (6) Rahman, Lepkowski and Grattan [1995]
- (7) Baba, Kondoh, Koyama and Iga [1995a]
- (8) Sarzała, Nakwaski and Osiński [1995]
- (9) Hadley, Lear, Warren, Choquette, Scott and Corzine [1996]

limitation of this approach is that it neglects any structural nonuniformity in the radial direction. Consequently, in the case of buried-heterostructure DMEWLs (e.g., Koyama, Kinoshita and Iga [1989], see also fig. 3 and table 1), to which it was applied, neither the lateral confining layers nor the dielectric mirrors on the heat-sink side could be accounted for.

The model of Kinoshita, Koyama and Iga [1987], Iga, Koyama and Kinoshita [1988], and Iga and Koyama [1990] is not self-consistent; i.e., the effect of calculated temperature profiles on material parameters and heat source efficiencies was not considered. In VCSELs, where heating is much more intense than in EELs, non-self-consistent models can underestimate the severity of the thermal problems. The first self-consistent treatment of thermal problems in VCSELs (Nakwaski and Osiński [1991a,b]) was applied to buried-heterostructure DMEWL devices and is discussed in § 5.1.2. As a matter of fact, this was the very first self-consistent thermal-electrical model applied to any semiconductor laser, including the edge emitters and high-power laser arrays.

While the radially nonuniform DMEWL structure is too complex for the model of Kinoshita, Koyama and Iga [1987], Iga, Koyama and Kinoshita [1988], and Iga and Koyama [1990] to give accurate results, the same model can be applied to radially uniform structures, such as PITSELs. The thermal conductivity of highly electrically-resistive regions which funnel the injected current into the active region is practically unaffected by the implantation process (Vook [1964]), which combined with the planarity of the PITSEL structure, makes it particularly suitable to be modeled analytically.

We have incorporated an analytical approach similar to that of Kinoshita, Koyama and Iga [1987] in the analysis of PITSELs, as a portion of our comprehensive, thermal-electrical self-consistent model (Nakwaski and Osiński [1992a,c, 1994]), featuring the temperature-dependent distribution of multiple heat sources, and the temperature dependence of material and device parameters. In the analysis, all important heat-generation mechanisms are taken into account, including nonradiative recombination, reabsorption of spontaneous radiation in the active region, free-carrier absorption of laser radiation, volume Joule heating and absorption of stimulated radiation in all the layers, and barrier Joule heating at heterojunctions. These distributed heat-generation processes are lumped into three uniform flat-disk heat sources, each of the active-region diameter $D_A = 2r_A$, located in the centers of the active region and two Bragg mirrors. An analytical solution is obtained for the entire structure separately for each heat source. Using the superposition principle, a cumulative temperature distribution in the whole volume of the device is determined by adding together contributions from all heat sources. Subsequently, a self-consistent solution is found with the

aid of an iteration procedure, taking into account the temperature dependencies of material and device parameters, including thermal conductivities, threshold current, electrical resistivities, voltage drop at the p-n junction, free-carrier absorption as well as internal and external differential quantum efficiencies. The flow chart of numerical calculations of this type is shown in fig. 14, where, however, carrier diffusion is included additionally. Note that large temperature variations in VCSELS affects substantially their lasing characteristics, because of strongly nonlinear thermal-electrical interactions, eventually leading to thermal runaway.

For each flat heat source situated between the j th and the $(j+1)$ th layers and for each i th layer, we are looking for the transformed temperature distribution in the following form:

$$\begin{aligned} \Theta_{j,i}(r, z) = & T_{\text{amb}} + \Delta T_{\text{HS}} + \Delta T_{\text{C}} + \alpha_{j,i,0} + \beta_{j,i,0}(z - z_{i-1}) \\ & + \sum_{n=1}^{\infty} \{ \alpha_{j,i,n} \cosh[\kappa_n(z - z_{i-1})] \\ & + \beta_{j,i,n} \sinh[\kappa_n(z - z_{i-1})] \} \frac{J_0(\kappa_n r)}{J_0^2(\kappa_n r_S)}, \end{aligned} \quad (50)$$

where r_S is the structure radius, z_i is the coordinate of the top boundary of the i th layer, $z_{i-1} \leq z_i$ and κ_n are successive roots of the equation:

$$J_1(\kappa_n r_S) = 0. \quad (51)$$

J_0 and J_1 are the zeroth-order and the first-order Bessel functions of the first kind, while $\alpha_{j,i,n}$ and $\beta_{j,i,n}$ are the expansion coefficients to be determined below. Cumulative profiles of the transformed temperature $\Theta(r, z)$ should be recalculated using the reverse transformation (cf. § 4.4).

The $\alpha_{j,i,n}$ and $\beta_{j,i,n}$ coefficients are determined from the boundary conditions of temperature profiles and heat fluxes at all the boundaries between various layers. For temperature profiles, we obtain from eq. (50):

$$\alpha_{j,i,0} + \beta_{j,i,0} d_i = \alpha_{j,i+1,0}, \quad (52)$$

$$\alpha_{j,i,n} \cosh(\kappa_n d_i) + \beta_{j,i,n} \sinh(\kappa_n d_i) = \alpha_{j,i+1,n} \quad \text{for } n \geq 1, \quad (53)$$

where d_i is the thickness of the i th layer, whereas for heat fluxes we have:

$$k_i \beta_{j,i,0} = \begin{cases} k_{i+1} \beta_{j,i+1,0} & \text{for } i \neq j, \\ k_{i+1} \beta_{j,i+1,0} + q_j (r_A / r_S)^2 & \text{for } i = j, \end{cases} \quad (54)$$

$$k_i[\alpha_{j,i,n}\sinh(\kappa_n d_i) + \beta_{j,i,n}\cosh(\kappa_n d_i)] = \begin{cases} k_{i+1}\beta_{j,i+1,n} & \text{for } i \neq j \wedge n \geq 1, \\ k_{i+1}\beta_{j,i+1,n} + \frac{2q_j r_A J_1(\kappa_n r_A)}{(\kappa_n r_s)^2} & \text{for } i = j \wedge n \geq 1. \end{cases} \quad (55)$$

where k_i is the i th layer thermal conductivity and q_j stands for the density of a given heat flux generated at the boundary between the j th and the $(j+1)$ th layers.

From the boundary conditions (24) and (25), we have:

$$\alpha_{j,1,n} = 0 \quad \text{for } n \geq 0, \quad (56)$$

and

$$\beta_{j,N,0} = 0, \quad (57)$$

$$\alpha_{j,N,n}\sinh(\kappa_n d_N) + \beta_{j,N,n}\cosh(\kappa_n d_N) = 0 \quad \text{for } n \geq 1. \quad (58)$$

Using eq. (54), we can write

$$\beta_{j,i,0} = \begin{cases} \left(\frac{q_j}{k_i}\right) \left(\frac{r_A}{r_s}\right)^2 & \text{for } 1 \leq i \leq j, \\ 0 & \text{for } j < i \leq N, \end{cases} \quad (59)$$

where N is the total number of structure layers and hence, from eq. (52), we get

$$\alpha_{j,i,0} = q_j \left(\frac{r_A}{r_s}\right)^2 \sum_{i'=1}^{\min(i-1,j)} \left(\frac{d_{i'}}{k_{i'}}\right). \quad (60)$$

We now introduce the $r_{j,i,n}$ coefficients, defined as

$$r_{j,i,n} = \frac{\beta_{j,i,n}}{\alpha_{j,i,n}} \quad \text{for } i \neq 1. \quad (61)$$

Then, taking eqs. (53) and (55) for $i \neq j$, we obtain

$$r_{j,i+1,n} = \frac{k_i}{k_{i+1}} \frac{\tanh(\kappa_n d_i) + r_{j,i,n}}{1 + r_{j,i,n} \tanh(\kappa_n d_i)} \quad \text{for } i \neq j, \quad (62)$$

and from eq. (58) we have:

$$r_{j,N,n} = -\tanh(\kappa_n d_N) \quad \text{for } n \geq 1. \quad (63)$$

Again using eqs. (53) and (55) for $i \neq j$, but now for $i=1$, and taking advantage of eq. (56), we get:

$$\beta_{j,1,n} = \alpha_{j,2,n} \operatorname{cosech}(\kappa_n d_1) \quad \text{for } n \geq 1, \quad (64)$$

and

$$r_{j,2,n} = \left(\frac{k_1}{k_2} \right) \coth(\kappa_n d_1) \quad \text{for } n \geq 1. \quad (65)$$

Now we can determine for $2 \leq i \leq N$ all $r_{j,i,n}$ working inward from $r_{j,2,n}$ and $r_{j,N,n}$. To determine all $\alpha_{j,i,n}$, we once more return to eqs. (53) and (55), but this time for $i=j$. After some mathematical manipulation, we find:

$$\alpha_{j,j,n} = \frac{2q_j r_A J_1(\kappa_n r_A)}{\kappa_n^2 r_S^2 [A_{j,j,n} \sinh(\kappa_n d_j) + B_{j,j,n} \cosh(\kappa_n d_j)]} \quad \text{for } n \geq 1, \quad (66)$$

with

$$A_{j,j,n} = k_j - k_{j+1} r_{j,j,n} r_{j,j+1,n}, \quad (67)$$

$$B_{j,j,n} = k_j r_{j,j,n} - k_{j+1} r_{j,j+1,n}. \quad (68)$$

The remaining $\alpha_{j,i,n}$ coefficients can be determined from eq. (53), which after using the $r_{j,i,n}$ coefficients can be rewritten in the following form:

$$\alpha_{j,i+1,n} = \alpha_{j,i,n} [\cosh(\kappa_n d_i) + r_{j,i,n} \sinh(\kappa_n d_i)] \quad \text{for } n \geq 1. \quad (69)$$

All the $\beta_{j,i,n}$ coefficients can then be found from eq. (61).

Figure 16 shows the pumping current dependence of radial temperature profiles in the midplane of the active region calculated for a 35- μm PITSEL (Zhou, Cheng, Schaus, Sun, Zheng, Armour, Hains, Hsin, Myers and Vawter [1991]). The total number of layers in the simulation, from the highly doped cap layer on the p-type DBR side to the solder contact below the substrate, including the linearly graded interfaces, is 284. Note that the CW threshold current for this device is 10.2 mA, hence the lowest profile in fig. 16 shows the temperature profile just above threshold. Superlinear increase in the temperature at the center of the active region ($r=0$) in response to increased pumping

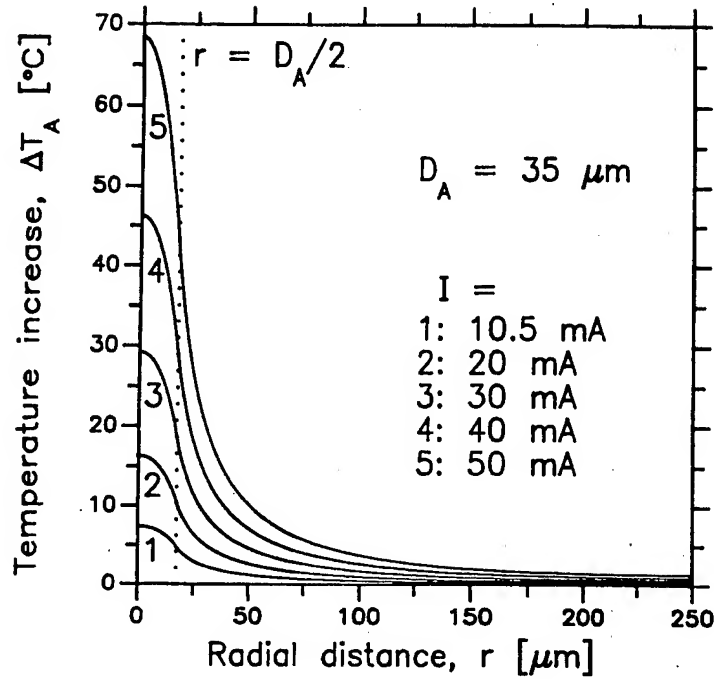


Fig. 16. Radial temperature profiles in the plane containing the active region of a 35 μm GaAs/AlGaAs/AlAs PITSEL for various CW pumping currents, calculated using self-consistent thermal-electrical model. Chip diameter D_S is 500 μm.

current can be seen clearly. Consequently, the temperature profile becomes increasingly inhomogeneous, with a large temperature step between the center and the edge ($r=r_A$) of the active region. This results in the creation of a strong thermal waveguide (cf. § 3.3), with the refractive index step as large as 1.4×10^{-2} at $I=50$ mA, which corresponds to an index step that would have been obtained if the active region were surrounded by $\text{Al}_{0.02}\text{Ga}_{0.98}\text{As}$ rather than GaAs. On the other hand, since the slope dT/dr is a measure of the lateral heat flow, it is evident that the importance of 2D heat flow increases with the pumping current.

Pumping-current evolution of the relative share of three major heat sources in the same PITSEL device is illustrated in fig. 17. The active-region heating is a dominant heat source near threshold, but gradually the p-type mirror heating takes over, due to its roughly quadratic dependence on the pumping current. The situation reverses again near the thermal runaway limit, where we observe an accelerated increase in relative importance of the active-region heating, caused primarily by nonlinear processes intensifying the nonradiative recombination.

Figure 18 illustrates the current dependence of the thermal resistance, R_{TH} , as defined in eq. (49), for PITSELS of the same vertical structure as in figs. 16 and

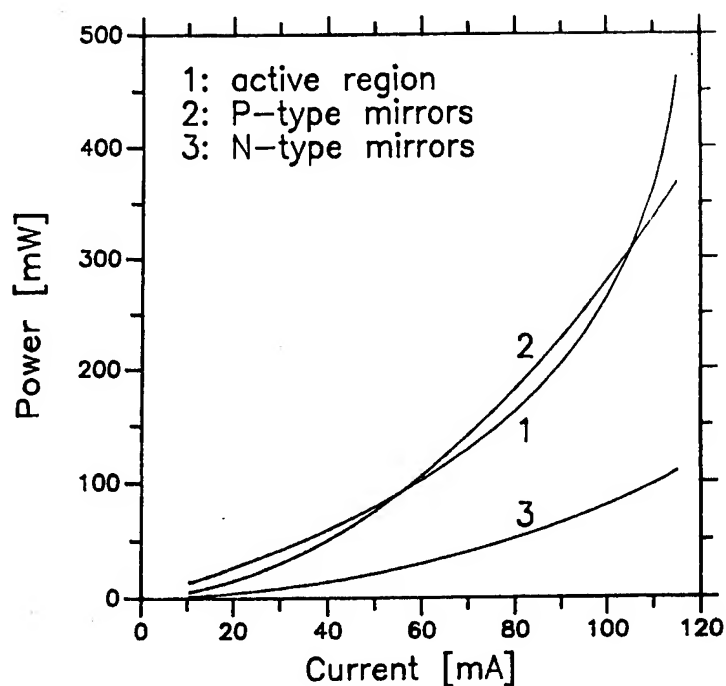


Fig. 17. Yields of three major heat sources in the 35 μm -diameter PITSEL of fig. 16 shown as a function of the pumping current.

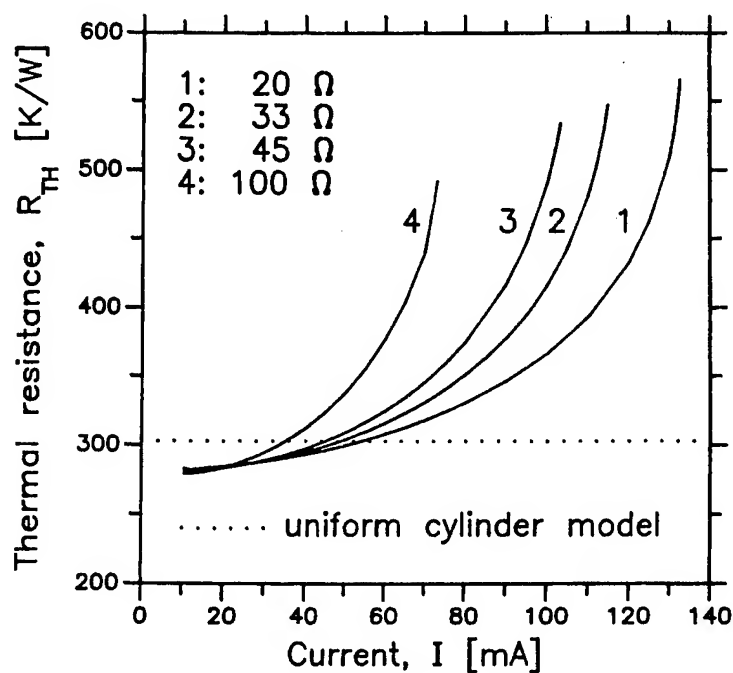


Fig. 18. Pumping-current dependence of thermal resistance R_{TH} for 35 μm -diameter PITSELs with various electrical series resistances. Curve 2 corresponds to the device simulated in figs. 16 and 17 and reported by Zhou, Cheng, Schaus, Sun, Zheng, Armour, Hains, Hsin, Myers and Vawter [1991].

17. In addition to the experimentally realized device with the series resistance $R_{s,0} = 33 \Omega$ (curve 2), we also consider hypothetical devices with lower (curve 1) or larger (curves 3 and 4) series resistances. Corresponding threshold voltages are readjusted using the following equation:

$$U_{th}(R_s) = U_{pn} + [U_{th}(R_{s,0}) - U_{pn}] \left(\frac{R_s}{R_{s,0}} \right), \quad (70)$$

where U_{pn} is the contribution of the p-n junction to the threshold voltage, assumed to be independent of the series resistance R_s , and determined from the I-V characteristic of the 33Ω device. No variation of pulsed threshold current with R_s is assumed to take place. The CW threshold, however, does depend on R_s due to changing temperature of the active region, although for the devices considered here these changes are very small, primarily due to the high value of $T_0 = 210 \text{ K}$ (Hasnain, Tai, Dutta, Wang, Wynn, Weir and Cho [1991]) (cf. table 6b, p. 193) assumed in the calculations.

Although R_{TH} is usually treated as a constant parameter with a value characteristic of any particular device, (cf. table 4, p. 187), it is clear that due to nonlinear processes it varies substantially with the pumping current (see Nakwaski and Osiński [1992b]). The relatively high values of R_{TH} displayed in fig. 18 are caused primarily by the "junction-up" configuration of PITSELS. The horizontal dotted line represents the thermal resistance calculated using the simplified uniform cylinder model (Nakwaski and Osiński [1992d]). It is clear that this model represents a reasonable approximation only in the linear regime, near the lasing threshold.

The effect of the series electrical resistance on the average temperature increase of the active region $\Delta T_{A,av}$, used in calculation of the thermal resistance R_{TH} , is illustrated in fig. 19. Due to nonlinear processes, the penalty for a too high series resistance of the device increases rapidly with the pumping current. The operating current range of the 100Ω device is nearly half that of the low-series-resistance (20Ω) device.

Zhao and McInerney [1995] have recently reported an analytical solution of the thermal conduction equation for a GaAs/AlGaAs PITSEL volume using the Green's function approach proposed for surface-emitting LEDs by Nakwaski and Kontkiewicz [1985]. In the model, the complex multilayer VCSEL structure seems to be replaced with an equivalent uniform structure, although the authors did not mention anything about it: in the solution, average (?) values of thermal conductivity and diffusivity are used for the entire VCSEL volume. The model would be exact if Green's function solutions (with unknown expansion coefficients) were assumed separately for each uniform structure layer. Then

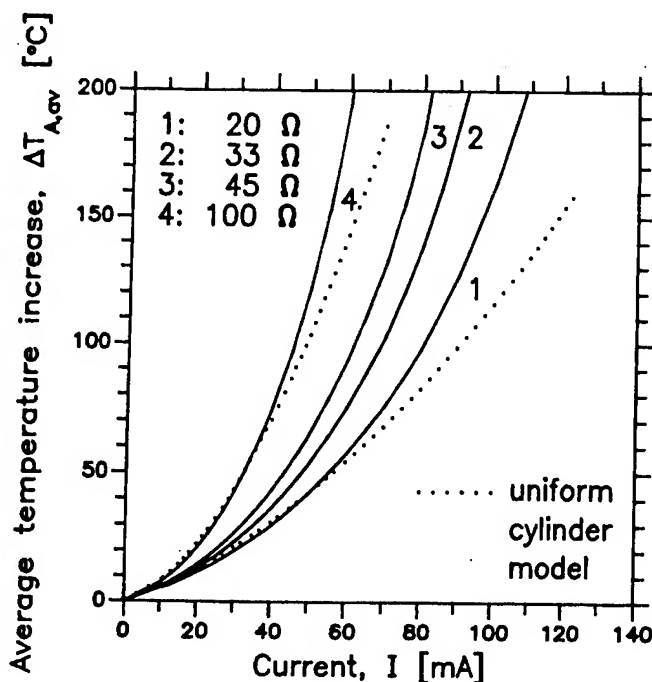


Fig. 19. Pumping-current dependence of the average active-region temperature increase $\Delta T_{A,av}$ in a $35\text{ }\mu\text{m}$ -diameter PITSEL. Curve 2 corresponds to the device reported by Zhou, Cheng, Schaus, Sun, Zheng, Armour, Hains, Hsin, Myers and Vawter [1991] and simulated in figs. 16 and 17.

the coefficients would be found from continuity conditions at all layer edges for profiles of both temperature and heat flux, similarly as in the approaches proposed for VCSELS by Nakwaski and Osiński [1992c] and earlier for EELs by Joyce and Dixon [1975]. As heat sources, Zhao and McInerney considered nonradiative recombination and absorption of spontaneous emission in the active region and volume Joule heating in layers of current spreading. Unfortunately, they did not solve exactly the current-flow process, using a simplified approach with two adjusting parameters of values difficult to estimate. The temperature dependence of all model parameters was neglected. Because of all the above facts, the exactness of the model seems to be very limited. Nevertheless, the model was used later in an interesting analysis of transverse modes in VCSELS (Zhao and McInerney [1996]).

5.1.2. Multilayer radially nonuniform structures

5.1.2.1. GaAs/AlGaAs lasers. Most VCSEL structures are either nonplanar, or contain laterally nonuniform layers confining the carriers, defining the waveguide/antiguide, or acting as reflectors. The analytical approach of § 5.1.1

may only be used for such structures for which the radially nonuniform layers can be replaced with thermally equivalent uniform layers.

An alternative analytical approach that takes into consideration lateral nonuniformity without requiring thermal equivalencies in the radial direction has been developed by Nakwaski and Osiński [1991a,b, 1993] and applied to buried-heterostructure DMEWLs (Koyama, Kinoshita and Iga [1989]) (see fig. 3 and table 1). First, current spreading between the etched-well substrate and the heat sink is found using approximate analytical formulae (Bugajski and Kontkiewicz [1982], Nakwaski and Osiński [1993]). Realistic, radially nonuniform, multiple heat sources associated with different layers of the device are considered, each with axially uniform distribution across the layer thickness. The following heat sources are included: the active region, the N-type and the P-type cladding layers and the p-side contact resistance. The device is then divided into two concentric cylinders (internal with $0 \leq r \leq D_A/2$ and external with $D_A/2 < r \leq D_S/2$) such that within each cylinder all layers are radially uniform. While the dividing wall at $r = D_A/2$ is considered to be thermally insulating, prior to finding the solution of the heat spreading problem the heat generated by each source is redistributed between the two cylinders using an electrical analog model (Nakwaski and Osiński [1991a]). Due to the smaller size of the inner cylinder, the redistribution of heat within that cylinder, containing the active region, is considered to be more accurate. For each cylinder, the multilayer structure is replaced with a thermally equivalent medium and an analytical solution for the temperature profiles is found for each i th heat source using the Green's function method in the following form:

Region I :

$$\Theta_{i,I}(r, z_{eq,I}) = T_R + \sum_{m=1}^{\infty} \sum_{n=1}^{\infty} A_{nm,i,I} J_0 \left(\frac{j_{1,n} r}{r_A} \right) \sin \left(\frac{c_m z_{eq,I}}{d_{eq,I}} \right), \quad (71)$$

Region II :

$$\Theta_{i,II}(r, z_{eq,II}) = T_R + \sum_{m=1}^{\infty} \sum_{n=1}^{\infty} A_{nm,i,II} J_0 \left(\frac{j_{1,n}(r - r_A)}{r_S - r_A} \right) \sin \left(\frac{c_m z_{eq,II}}{d_{eq,II}} \right). \quad (72)$$

In the above equations, T_R stands for the reference temperature equal to the temperature at the bottom edge of the laser crystal, r_A and r_S are the radii of the active region and of the laser structure, respectively, $j_{1,n}$ ($n = 1, 2, 3, \dots$) is the n th zero of the first-order Bessel function of the first kind, $c_m = \pi(m - \frac{1}{2})$ ($m = 1, 2, 3, \dots$) is the $(m + 1)$ -st zero of the cosine function, $z_{eq,\alpha}$ denotes the z coordinate after the space transformation, and $d_{eq,\alpha}$ is its value for the bottom of

the etched well (the n-GaAs/N-AlGaAs interface), both for Region α ($\alpha = \text{I, II}$). The coefficients $A_{nm,i,\text{I}}$ and $A_{nm,i,\text{II}}$ are calculated using the following formulae:

$$A_{nm,i,\text{I}} = \frac{4 \left[\cos \left(\frac{c_m z_{eq,i-1,\text{I}}}{d_{eq,\text{I}}} \right) - \cos \left(\frac{c_m z_{eq,i,\text{I}}}{d_{eq,\text{I}}} \right) \right]}{r_A^2 k_{eq,\text{I}} J_0^2(j_{1,n}) c_m \left[\left(\frac{j_{1,n}}{r_A} \right)^2 + \left(\frac{c_m}{d_{eq,\text{I}}} \right)^2 \right]} \quad (73)$$

$$\times \int_0^{r_A} g_{i,eq, \text{is}}(r) J_0 \left(\frac{j_{1,n} r}{r_A} \right) r dr,$$

$$A_{nm,i,\text{II}} = \frac{4 \left[\cos \left(\frac{c_m z_{eq,i-1,\text{II}}}{d_{eq,\text{II}}} \right) - \cos \left(\frac{c_m z_{eq,i,\text{II}}}{d_{eq,\text{II}}} \right) \right]}{(r_S^2 - r_A^2) k_{eq,\text{II}} J_0^2(j_{1,n}) c_m \left[\left(\frac{j_{1,n}}{r_S - r_A} \right)^2 + \left(\frac{c_m}{d_{eq,\text{II}}} \right)^2 \right]} \quad (74)$$

$$\times \int_{r_A}^{r_S} g_{i,eq, \text{is}}(r) J_0 \left(\frac{j_{1,n}(r - r_A)}{r_S - r_A} \right) r dr,$$

where $k_{eq,\alpha}$ stands for the equivalent thermal conductivity of Region α , $z_{eq,i,\alpha}$ is the transformed coordinate of the top of the i th layer in Region α , and $g_{i,eq, \text{is}}$ is the equivalent distribution of the i th heat source after its redistribution.

In each loop of the self-consistent calculations, the cumulative profiles of transformed temperature are found using the superposition principle by adding together contributions from all heat sources. Then, the actual temperature profiles are determined by performing the inverse Kirchhoff transformation (cf. § 4.4). At the boundary between the two cylinders, the temperature profiles are matched by adjusting the profile of the outer cylinder to the level of the inner cylinder. The adjustment only affects the near vicinity of the boundary, on the side of $r > D_A/2$.

A very important feature of the model is its self-consistency (cf. § 4.4), which accounts for mutual interactions between thermal and electrical phenomena. In an iterative loop, temperature dependencies of many material and device parameters are considered, including thermal conductivity, electrical resistivity, threshold current, quantum efficiencies, and voltage drop at the p-n junction. Also, the temperature dependence of all important heat generation mechanisms is taken into account, including nonradiative recombination, absorption of spontaneous emission, as well as the Joule heating in all layers. The model described here represents the first application of a self-consistent approach to thermal problems in any semiconductor laser, including the edge emitters. We

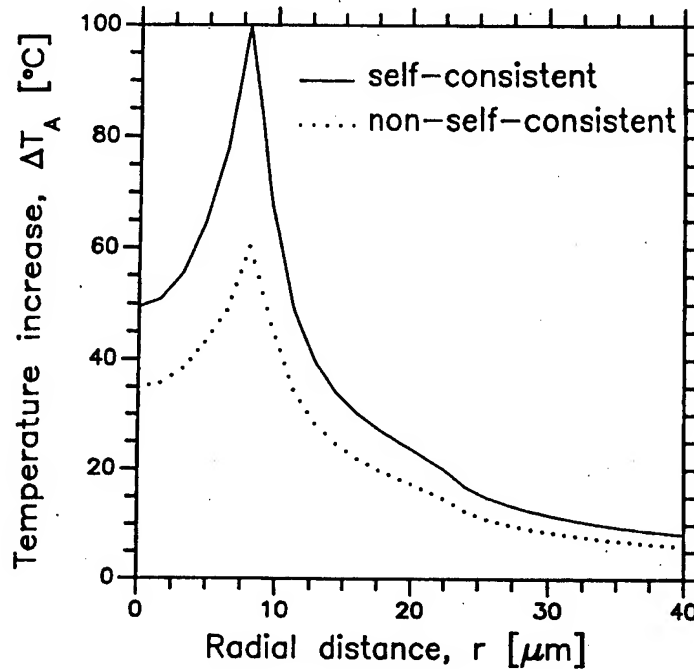


Fig. 20. Radial temperature profiles in the plane containing the active region of a $16\text{ }\mu\text{m}$ buried-heterostructure GaAs/AlGaAs DMEWL for the pumping current $I = 5I_{\text{th,P}}$ ($I_{\text{th,P}} = 38.4\text{ mA}$), where $I_{\text{th,P}}$ stands for the room-temperature pulsed threshold current, calculated using self-consistent thermal-electrical model (solid line) or taking the output of the first loop of the iterative process as a non-self-consistent solution (dotted line). Chip diameter D_S is $500\text{ }\mu\text{m}$. The kink near $r = 23\text{ }\mu\text{m}$ corresponds to the edge of the outer oxide layer.

have subsequently used the self-consistent approach in all of our comprehensive thermal modeling, including the model described in § 5.1.1.

The importance of self-consistency is illustrated in fig. 20, comparing radial temperature profiles in the active-region of a $16\text{ }\mu\text{m}$ GaAs/AlGaAs DMEWL, obtained using the self-consistent solution (solid line) and taking the output of the first loop of the iterative process as a non-self-consistent solution (dotted line). The device structure is similar to that of Koyama, Kinoshita and Iga [1989], except for an enhanced P-AlGaAs-cladding doping level of $2 \times 10^{18}\text{ cm}^{-3}$ which significantly improves device thermal properties (see Nakwaski and Osiński [1991a,c]). A pumping current of 192 mA was assumed, corresponding to 5 times the room-temperature pulsed threshold current. Clearly, at currents significantly above the threshold, the non-self-consistent solution grossly underestimates the active-region temperature increase.

Another interesting feature displayed in fig. 20 is the on-axis dip in the temperature profile, which is a direct consequence of nonuniform current injection. Associated with the dip is a thermally induced antiguide. Self-consistent analysis reported by Nakwaski and Osiński [1991a,c,d] and Osiński

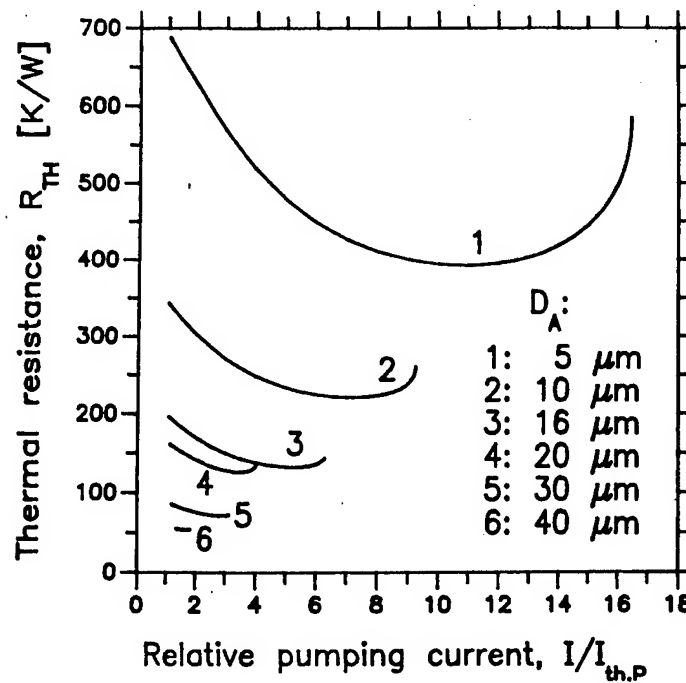


Fig. 21. Current-dependence of thermal resistance for buried-heterostructure GaAs/AlGaAs DMEWLs of various active-region diameters D_A .

and Nakwaski [1992] reveals that the sign of thermal waveguiding in the active region can be controlled by the N-AlGaAs doping level. Increasing the N-AlGaAs doping level beyond the value of $N = 7 \times 10^{17} \text{ cm}^{-3}$ used in fig. 20, results in improved uniformity of the injected current density. This is manifested initially by flattening of the active-region temperature profile, and eventually by occurrence of a maximum at $r = 0$ for $N = 7 \times 10^{18} \text{ cm}^{-3}$. Freedom to engineer thermal waveguide in the active region is a characteristic feature of all etched-well VCSELs. Depending on the application, it might be more beneficial to focus the output light into a narrower spot or to spread it over a wider area without changing the active-region diameter. A thermal antiguide can also enhance single-transverse-mode operation (cf. § 3.3).

Figure 21 displays the current dependence of thermal resistance R_{TH} for DMEWL devices with various active-region diameters. Except for their lateral dimensions, the devices have the same structure as the device of fig. 20. Comparison with fig. 18 reveals a device-type-dependent variation of R_{TH} with current. While the $R_{TH}(I)$ curves increase monotonically in PITSELs, they have distinct minima in DMEWL, particularly for small-size emitters that can operate in CW mode far above threshold (curves 1 and 2 in fig. 21). These seemingly contradictory results can be understood by considering various factors that can influence the evolution of R_{TH} with current.

Figures 18 and 21 indicate that the thermal resistance in VCSELS is governed by a number of mechanisms that may affect the $R_{TH}(I)$ dependence in opposite ways. Variation of VCSEL thermal resistances with a pumping current is caused by a temperature dependence of thermal conductivities of constituent materials and by a change of intensities of various heat generation processes located in different places of a laser. The former mechanism always increases the value of R_{TH} , whereas the latter one may increase or decrease R_{TH} depending on the laser structure. This is a reason for a different $R_{TH}(I)$ shown in figs. 18 and 21.

An increase in the pumping current invariably heats up the device, which in turn reduces the thermal conductivity and increases the thermal resistance $R_{TH}^{(\alpha)}$ associated with every heat source α . This effect is nearly negligible at low currents, but steadily becomes more and more significant at higher currents, as evidenced in fig. 21 by a sudden increase in R_{TH} near the thermal runaway conditions. A more subtle effect is that of the heat source distribution. The thermal resistance of the device is obtained by summing together fractional resistances $R_{TH}^{(\alpha)}$ with weights Q_α/Q_T determined by the relative shares of corresponding heat sources. If the relative share of heat sources with high fractional resistances $R_{TH}^{(\alpha)}$ increases, the total thermal resistance will have a tendency to increase. As shown in fig. 18, this is obviously the case of PITSELS. However, if the relative share of heat sources with high fractional resistances $R_{TH}^{(\alpha)}$ decreases, the variation of total R_{TH} will depend on which of the two opposite mechanisms prevails: the increase in thermal conductivity or the lower average fractional resistance. It follows from fig. 21 that this more complex behavior is the case for DMEWLs.

In a typical VCSEL configuration, where all heat flux is directed towards the heat sink located on the side opposite to the output mirror, the fractional resistances of all heat sources of the same diameter are determined primarily by their distance from the heat sink. Hence, in a junction-up configuration of PITSELS, the P-type Bragg mirror has the largest fractional resistance, while in DMEWLs mounted junction-down the P-AlGaAs cladding layer has the lowest fractional resistance. The Joule heating associated with DBRs or cladding layers is roughly proportional to I^2 (this dependence would have been exact if current spreading mechanisms and electrical resistivities were independent of temperature) and, at least well below the thermal runaway, tends to grow faster than the active-region heating. Due to relatively high electrical resistivity of p-type semiconductors, the p-type Joule heat sources are the most important ones to consider since they end up having higher weights Q_α/Q_T . From the above considerations it follows that the p-type Joule heat sources in PITSELS, being on the high end of fractional thermal resistances, cause a further increase in R_{TH}

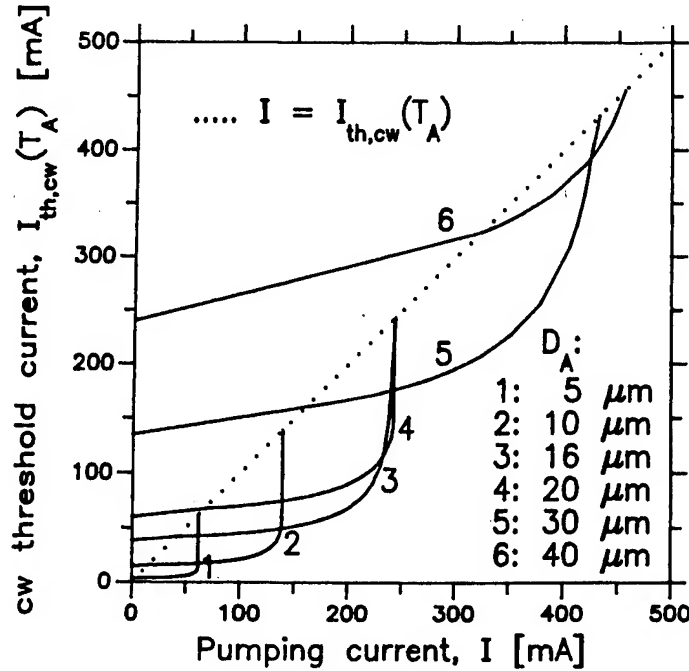


Fig. 22. Graph of effective CW threshold current $I_{th,cw}(T_A)$ variation with pumping current for buried-heterostructure GaAs/AlGaAs DMEWLs of various active-region diameters D_A . The ambient temperature is 300 K. Device parameters are the same as in fig. 21.

with current. In contrast, the increasing share of low-thermal-resistance P-type Joule heat sources in DMEWLs tends to reduce the total R_{TH} with current. That is why fig. 21 shows a reduction of R_{TH} , as long as the device is well below the thermal runaway regime where nonlinear effects cause a fast increase in the share of the active-region heating.

When no direct current flows through the laser (and, consequently, the active-region temperature is equal to ambient temperature), the CW threshold can be considered to coincide with the pulsed threshold. With increasing CW pumping current, the active-region temperature rises, hence the CW threshold, $I_{th,cw}(T_A)$, also increases. In order to avoid confusion with the CW threshold current, $I_{th,cw}$, corresponding to the onset of CW lasing action, the current-dependent CW threshold has been termed the *effective CW threshold*, after Scott, Geels, Corzine and Coldren [1993]. Figure 22 shows the evolution of the effective CW threshold current with pumping current for DMEWLs of various active-region diameters. If the thermally-induced increase in the effective CW threshold $I_{th,cw}(T_A)$ is slower than the increase in the pumping current I , at some pumping level the condition $I = I_{th,cw}(T_A) = I_{th,cw}$ will be met and the laser will start CW operation. The onset of CW lasing corresponds to the lower intersection of the $I_{th,cw}(T_A)$ curve (solid lines in fig. 22) with the $I = I_{th,cw}(T_A)$ line (dotted line).

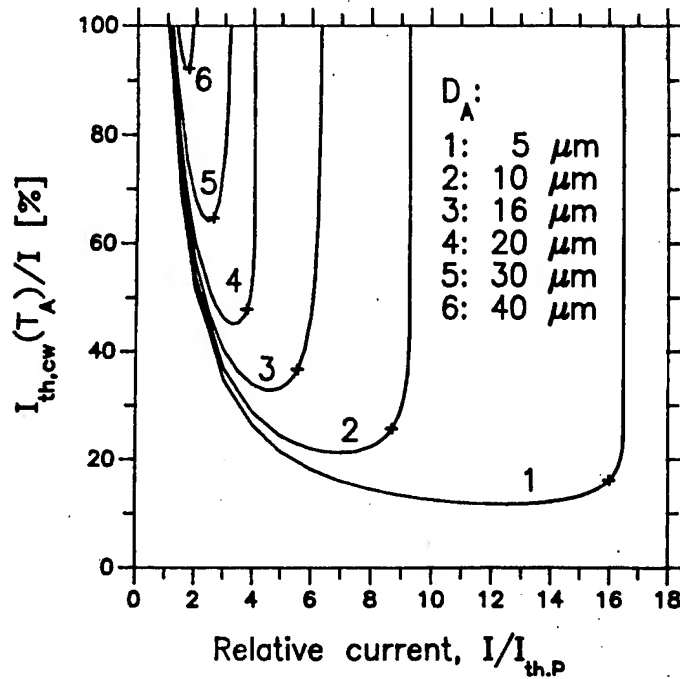


Fig. 23. Fraction of the total pumping current taken by the effective CW lasing threshold $I_{th,cw}(T_A)$ as a function of the total pumping current expressed in pulsed-threshold units, calculated for various values of the active-region diameter D_A . Crosses represent pumping conditions at which $[I - I_{th,cw}(T_A)]$ reaches a maximum. The ambient temperature is 300 K. Device parameters are the same as in fig. 21.

However, as the pumping current is increased further, $I_{th,cw}(T_A)$ starts increasing superlinearly, and eventually thermal runaway takes place. The CW lasing action is no longer possible when the second intersection of the $I_{th,cw}(T_A)$ curve with the $I = I_{th,cw}(T_A)$ line is reached. Thus, fig. 22 shows the entire CW operating range for each device. Within this range, the optical output power is roughly proportional to the excess pumping current $[I - I_{th,cw}(T_A)]$. For any particular device size, there exists an optimal pumping level such that $[I - I_{th,cw}(T_A)]$ reaches a maximum.

Another representation of the operating range (between the onset of CW lasing and the thermal runaway) for room-temperature CW excitation of etched-well VCSELs is illustrated in fig. 23. The value of $I_{th,cw}(T_A)/I$ can be interpreted as a measure of the efficiency of converting the supplied electrical energy into the energy dissipated into heat. It can be seen that from the point of view of their efficiency, the lowest-diameter devices display the best behavior. For 5 μm devices, only 10–20% of the pumping power is used to reach the threshold in the pumping current range of $4I_{th,P}$ through $16I_{th,P}$. Also, both the operating range, expressed in terms of the pulsed threshold current $I_{th,P}$, and the relative surplus

current available over and above the effective CW threshold, are the largest for small-diameter devices. With an increasing active-region diameter, the operating range shrinks systematically, while an ever increasing portion of the pumping current must be consumed to support the CW lasing action. When $D_A = 40 \mu\text{m}$, at least 90% of the pumping power is used up just to attain the threshold. As illustrated by fig. 23, the reduced operating range with increasing active-region diameter is directly associated with intense heating. However, even though the efficiency characteristics are superior for devices with the smallest D_A , their total output power remains small.

The points marked by crosses in fig. 23 indicate the pumping conditions such that $[I - I_{\text{th,cw}}(T_A)]$ (and, approximately, the optical power) reaches a maximum. It is worthwhile noting that optimal conditions for optical power and overall efficiency do not coincide, and the maximum output power is always reached at a pumping level higher than that yielding a maximum overall efficiency.

The self-consistent analytical model described in this section has also been used to optimize the DMEWL device design for high-power low-thermal-resistance operation (Osiński and Nakwaski [1992]). The tradeoff between an increasing pumping power, increasing $I_{\text{th,cw}}(T_A)$, and a shrinking operating range as the active region becomes wider, leads to an optimal value of $D_A = 16 \mu\text{m}$. The devices of this size offer the largest surplus current $[I - I_{\text{th,cw}}(T_A)]$ and, consequently, the largest total output power. Further optimization of the inner structure of $16 \mu\text{m}$ devices results in the thermal resistance R_{TH} of only 188 K/W at the pumping level of $I = 3I_{\text{th,P}}$. The average active-region temperature increase at that pumping level is less than 49°C . Note that this value of R_{TH} is significantly lower than the lowest limit in table 4 for TEML devices with $60 \mu\text{m}$ diameters (cf. Norris, Chen and Tien [1994], Chen, Hadley and Smith [1994]), especially if one recognizes that the rough scaling of R_{TH} with the active-region area indicates that the thermal resistance of $16 \mu\text{m}$ devices should be ~ 14 times higher than that of $60 \mu\text{m}$ devices.

5.1.2.2. InGaAsP/InP lasers. Compared with short-wavelength devices, thermal problems in all-semiconductor long-wavelength InGaAsP/InP VCSELS are exacerbated by a smaller refractive index step between InP and InGaAsP ($0.2\text{--}0.3$ vs. ~ 0.5 for AlGaAs/AlAs), which requires about a twice larger number of quarter-wave layers in distributed Bragg reflectors (DBRs) to achieve high reflectivities indispensable for low threshold current density. In addition, due to longer wavelength, all layers in the DBRs must be thicker. Thus, it can be expected that thermal behavior of long-wavelength VCSELS may be even more critical for device operation than is the case for GaAs-based VCSELS.

In view of these difficulties, dielectric mirrors are often used in long-wavelength VCSELs, in place of semiconducting Bragg reflectors (e.g., Wada, Babic, Crawford, Reynolds, Dudley, Bowers, Hu, Merz, Miller, Koren and Young [1991], Uchida, Miyamoto, Yokouchi, Inaba, Koyama and Iga [1992], Tadokoro, Okamoto, Kohama, Kawakami and Kurokawa [1992], Miyamoto, Uchida, Yokouchi, Inaba, Mori, Koyama and Iga [1993], Baba, Suzuki, Yogo, Iga and Koyama [1993a,b], Baba, Yogo, Suzuki, Koyama and Iga [1993, 1994]). This, however, imposes further limitations on the current path, and consequently on the electrical series resistance of the device. While room-temperature pulsed operation of electrically pumped VCSELs with dielectric mirrors was obtained both at $1.3\text{ }\mu\text{m}$ (Wada, Babic, Crawford, Reynolds, Dudley, Bowers, Hu, Merz, Miller, Koren and Young [1991]) and $1.5\text{ }\mu\text{m}$ (Uchida, Miyamoto, Yokouchi, Inaba, Koyama and Iga [1992]), so far room-temperature (up to 36°C) CW operation has been very recently achieved only at $1.3\text{ }\mu\text{m}$ (Uchiyama, Yokouchi and Ninomiya [1997]).

An alternative approach was proposed by Dudley, Ishikawa, Babic, Miller, Mirin, Jiang, Bowers and Hu [1993]. They used wafer fusion to integrate GaAs/AlAs mirrors with InP/InGaAsP double heterostructures. These lasers did not show any symptoms of device degradation despite a 3.7% lattice mismatch between the wafers. VCSELs fabricated using wafer fusion have demonstrated room-temperature pulse operation at $1.3\text{ }\mu\text{m}$ (Dudley, Babic, Mirin, Yang, Miller, Ram, Reynolds, Hu and Bowers [1994]) and at $1.5\text{ }\mu\text{m}$ (Babic, Dudley, Streubel, Mirin, Bowers and Hu [1995]), and recently also room-temperature CW operation at $1.5\text{ }\mu\text{m}$ (Babic, Streubel, Mirin, Margalit, Bowers, Hu, Mars, Yang and Carey [1995]).

The first comprehensive, self-consistent thermal-electrical analytical model of dielectric-mirror etched-well laser operation at long-wavelengths has been reported by Osiński and Nakwaski [1995b]. The model features a realistic, current-dependent distribution of heat sources and incorporates calculation of lasing threshold.

The circular planar buried heterostructure VCSELs modeled in this section (see the DMEWL structure in fig. 3a) are similar to those developed by Baba, Suzuki, Yogo, Iga and Koyama [1993a,b] and Baba, Yogo, Suzuki, Koyama and Iga [1993, 1994]. The reported external differential efficiency is very low ($\eta_d = 0.16\%$), and consequently the output power is very small. It is therefore worthwhile to examine the design of these lasers with the goal of identifying the main factors which determine their performance.

Nearly all semiconductor layers of the laser are made of InP (cf. fig. 24). Only the active region is manufactured from InGaAsP ($\lambda_g = 1.37\text{ }\mu\text{m}$, where λ_g

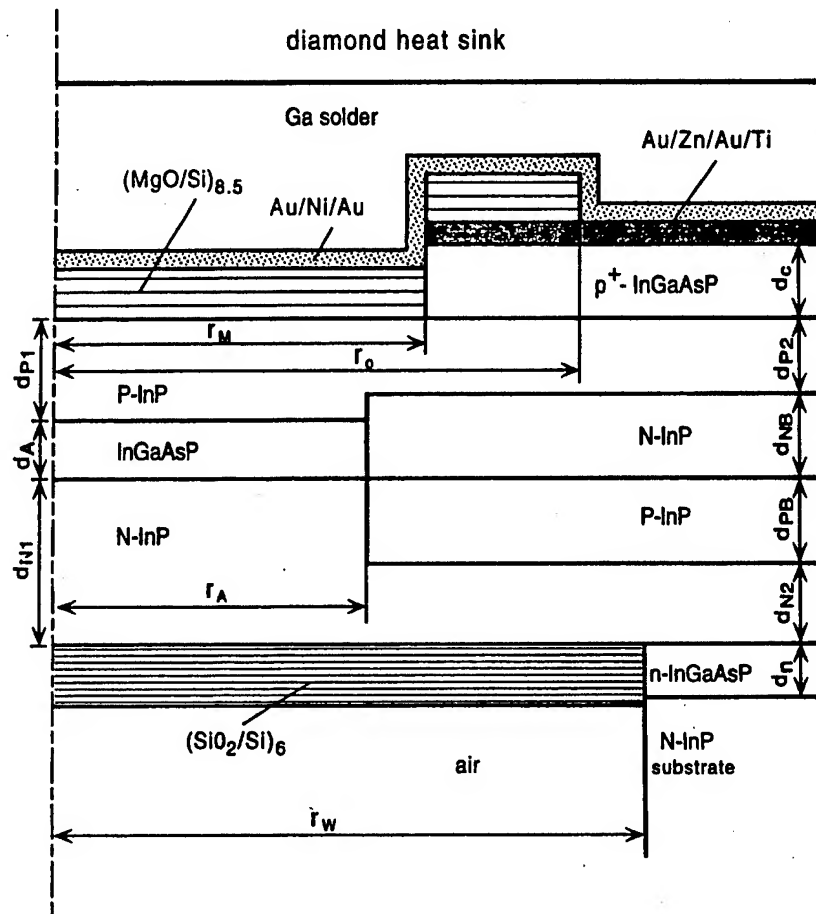


Fig. 24. Schematic structure of an InGaAsP/InP circular planar buried-heterostructure dielectric-mirrors etched-well laser (after Baba, Yogo, Suzuki, Koyama and Iga [1993, 1994]).

stands for the bandgap wavelength) and the cap layer is produced from InGaAs. (The thin n-type InGaAsP layer reduces heat flux penetration of the substrate layer, which is negligible and is neglected in the model). Both the above layers are relatively thin. Their thermal conductivities, however, are many times lower than that of InP, so they greatly influence the heat-spreading process.

Heat fluxes penetrate poorly low-thermal-conductivity areas, and when they do penetrate them, they go across these layers along the shortest possible path inside them. Therefore we may assume approximately a one-dimensional (1D) heat flow through both these layers, perpendicular to their long edges.

The space transformation was proposed by Nakwaski [1983] to solve similar problems. The transformation is fully justified for 1D heat flow. Therefore we may apply it to the InGaAsP active region, to the InGaAs cap layer, and also to the dielectric layers of the output mirror (of even lower thermal conductivity), replacing them by appropriate thermally equivalent layers of InP (see fig. 25).

Transformation of semiconducting layers

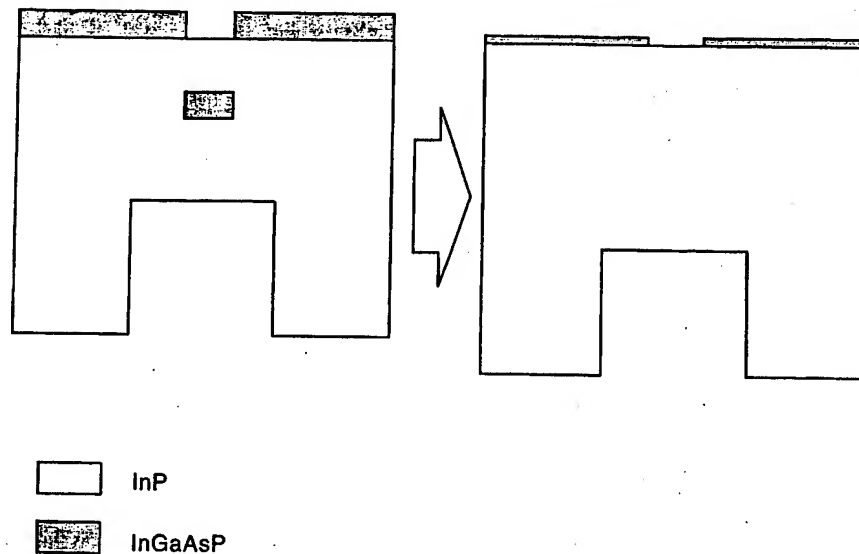


Fig. 25. Thermal equivalent of the central part of the circular buried heterostructure VCSEL under consideration.

After the transformation, the entire bulk of the device can be treated as a homogeneous InP cylinder.

The following heat generation mechanisms are included in the model:

- nonradiative recombination and absorption of the spontaneous radiation within the active region,
- absorption of the laser radiation in all layers of the resonator,
- volume Joule heating in all layers of the current path, and
- barrier Joule heating at the p-side contact.

For each of the heat generation areas, the transformed temperature profile (after the Kirchhoff transformation, cf. § 4.4) is calculated for the entire laser structure, and next the cumulative transformed temperature profile is found with the aid of the superposition principle, using the approach similar to that reported for GaAs/AlGaAs lasers by Nakwaski and Osiński [1991a, 1993].

The threshold carrier concentration is determined by considering the balance of gain and losses, with the gain coefficient changing linearly with the carrier density. The following loss mechanisms are included: free-carrier absorption in n-InP, intervalence band absorption in p-InP, active-region loss, diffraction loss, as well as absorption and scattering losses in dielectric mirrors. Threshold current is then found, taking account of Auger recombination, carrier loss due

to trap and interface recombination, and carrier leakage over the heterobarrier. Analytical approximations are used in the model to describe the current spreading in the device.

The main goal of the analysis was to determine which parameters have significant influence on device characteristics and to identify means of improving the device performance. In the following, we present a systematic discussion of the role of the most crucial device parameters.

Large differences between theoretical and experimental values of front and back mirror reflectivities indicate that the mirrors suffer from scattering loss, absorption, or poor control of layer thicknesses. While improvement of mirror quality may not be easy in practice, it is interesting to see what advantage could be expected from increased mirror reflectivity. From our calculations, we see that improvement in mirror quality leads to a dramatic reduction of the threshold current. This in turn reduces considerably the Joule heating and the Auger recombination, resulting in a reduction of the total generated heat power, the active region temperature increase, and the thermal resistance. At a fixed pumping current, the output power increases substantially.

Contrary to experimental results reported by Baba, Suzuki, Yogo, Iga and Koyama [1993b], our analysis indicates that the laser would operate in CW mode at an ambient temperature of 5°C, but not at 14°C. This may indicate that the particular device for which near-room-temperature CW operation was achieved may have had superior properties, such as very low scattering loss in the dielectric mirrors. In order for a 12 μm device to lase at 14°C, the mirror reflectivities must be increased to at least 99.8% and 99.9% for the front and the rear mirrors, respectively. The device with only a slightly lower front-mirror reflectivity of 99.7% would not lase in CW mode at that temperature. Mirror quality in the device reported by Baba, Suzuki, Yogo, Iga and Koyama [1993b] was therefore most probably higher than that measured typically for otherwise identical devices or Bragg mirrors.

In the above VCSELS, dielectric SiO_2/Si DBR structures were used as the front mirrors. It is worthwhile to consider how much improvement can be expected by replacing thermally insulating SiO_2 layers with highly conducting MgO layers, which are almost as good thermal conductors as InP . In order to account for a lower refractive index contrast between Si and MgO , compared to SiO_2/Si system, the number of periods in the front reflector is increased from 6 to 7. It is seen from our results that the above improvement is sufficient, for example, to make the difference between lasing and non-lasing at 14°C in 14 μm devices.

Let us now investigate the influence of the active-region diameter on device characteristics. Figure 26 shows that the original 12 μm diameter (Baba, Yogo,

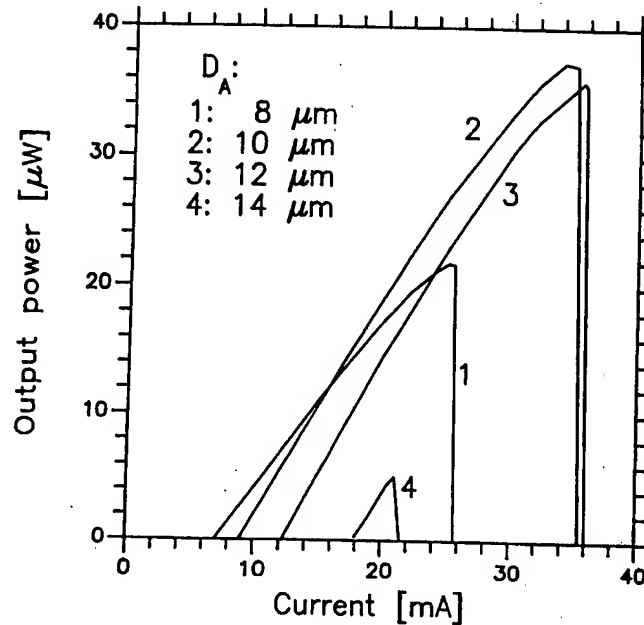


Fig. 26. Light-current characteristics calculated for etched-well 1.3 μm InGaAsP/InP lasers of various active-region diameters D_A of 7 periods of MgO/Si quarter-wave dielectric layers.

Suzuki, Koyama and Iga [1993]) is close to optimal. A slight improvement in maximum output power is expected for devices with 10 μm diameter. Altogether, however, the range of the active-region diameter for which the device would lase CW at 14°C is remarkably narrow. Figure 26 also illustrates the importance of nonlinear thermal effects in long-wavelength VCSELS. Thermally reduced roll-off of the light-current characteristics is much rapid than that calculated for GaAs/AlGaAs etched-well VCSELS by Osiński and Nakwaski [1995a].

In the range of the active-region diameters D_A between 8 μm and 14 μm , the thermal resistance, R_{TH} , reduces with decreasing D_A (e.g., at $I = 20$ mA, $R_{TH} \simeq 520$ K/W for $D_A = 14$ μm , and $R_{TH} \simeq 350$ K/W for $D_A = 8$ μm). This variation is, however, much smaller than the dynamic range of R_{TH} for each device, caused by an increasing share (with increasing current) of the P-InP Joule heat source with low fractional thermal resistance. For example, for $D_A = 10$ μm , $R_{TH} \simeq 1030$ K/W near threshold ($I = 9$ mA), and drops down to ~ 180 K/W near thermal runaway ($I = 35$ mA).

Known comprehensive analytical thermal VCSEL models are compared in table 8a (p. 220) taking into account the method used, accuracy of the structure modeling achieved, heat sources included and self-consistencies taken into consideration.

5.2. COMPREHENSIVE NUMERICAL MODELS

The comprehensive analytical approaches discussed in § 5.1 require extensive computations in order to determine the series expansion coefficients in temperature profiles. In addition, they can only be applied to those VCSELS whose structures are consistent with the formulation of the method. A purely numerical approach to heat conduction problems offers more flexibility in terms of defining the device structure, and is often easier to implement since existing general-purpose software packages can be utilized. In the following, we discuss the reported numerical models of VCSELS, focusing on essential features defining the model and addressing various assumptions and approximations made by their authors.

One potential problem with the application of multi-purpose finite-element packages is a difficulty in obtaining self-consistent solutions of nonlinear thermal problems. Accurate treatment would normally require an iterative approach. This can easily become a very complex task, since for each element, local values of device and material parameters would have to be determined using the average local temperatures. Besides, most authors choose to accept a linear solution of the problem, neglecting the temperature dependence of thermal conductivity, which can easily lead to significant errors. Therefore, it is usually recommended to prepare one's own numerical code for a strictly specified VCSEL structure, enabling an iterative self-consistent approach.

The finite difference method (FDM) was used to model thermal behavior of UMEWLs (cf. table 1 and fig. 3) by Shimizu, Babic, Dudley, Jiang and Bowers [1993]. The authors lumped all heat generation processes into the active region and neglected the temperature dependence of both heat generation mechanisms and thermal conductivities, which confines applicability of the model to relatively low operation currents. They also considered the heat sink contribution to the thermal resistance, assuming the heat flux at the laser/heat-sink interface to be uniform. A dramatic reduction in heat-sink thermal resistance was obtained for diamond heat sinks compared to the standard copper ones. A similar conclusion was reached by Osiński and Nakwaski [1993b], using the analytical model of PITSELS described in § 5.1.1.

Thode, Csanak, Hotchkiss, Snell and Campbell [1995] have reported on the FDM, time-dependent VCSEL model, which requires extensive mainframe computer resources to implement. To shorten the CPU time, the simulation region is limited to a cylinder of $12\text{ }\mu\text{m}$ radius and $6.75\text{ }\mu\text{m}$ height. A uniform mesh is used, therefore 80 uniform regions of average (?) material parameters are defined. The PISCES code was applied to approximate temperature

profiles. No details about heat sources and modeling thermal structure are given.

Piprek and Yoo [1994] used the finite-element method (FEM) to model operation characteristics of the $1.55\text{ }\mu\text{m}$ HMMLs. A single, uniform heat source located at the active region was assumed. For simplicity, each DBR mirror was replaced with an equivalent, uniform but thermally anisotropic medium, whose radial and axial thermal resistivities are calculated using formulae given by Osiński and Nakwaski [1993a]. This approximation, appropriate when simple analytical formulae are applied, is questionable when a fully numerical FEM solution is sought, as it inevitably deteriorates the accuracy of the numerical solution. This is especially important when layers of very different thermal conductivities are located close to small heat sources, as in the case of VCSELS. Since the FEM modeling can easily handle multilayer structures, it is better to avoid such approximations. More advanced was the model of Piprek, Wenzel and Sztefka [1994], prepared for the $0.98\text{ }\mu\text{m}$ InGaAs/AlGaAs PITSELS, where additionally the current spreading effect was considered and all important heat sources were taken into account, including active-region heating, laser light absorption as well as volume, contact and barrier Joule heating and some thermal-electrical-optical interactions. The model was generalized successfully by Piprek, Wenzel, Wünsche, Braun and Henneberger [1995] for long-wavelength VCSELS. Surprisingly, the very important temperature dependence of the thermal conductivity seems not to have been taken into consideration in these otherwise quite sophisticated models. Nevertheless, this simulation was used to model long-wavelength VCSEL performance characteristics (Piprek, Babic and Bowers [1996]).

FEM was also used by Michalzik and Ebeling [1993] in their comprehensive self-consistent thermal model of TBEMLS (cf. table 1 and fig. 3a), which includes the temperature dependence of thermal conductivity. The main emphasis is laid on realistic modeling of current spreading in a rather complicated TBEML structure, achieved with the aid of a 2D resistance network model. The electrical conductivity profile in the proton-implanted region is assumed to have Gaussian tails with different decay constants in the radial and axial directions. Multiple heat sources are considered, including distributed Joule heating (with an exception of the p-type contact Joule heating), heterobarrier heating, absorption of stimulated radiation within the laser cavity, and absorption of spontaneous radiation within the active region. The calculated temperature distribution is then used to define a thermally induced, axially nonuniform waveguide. VCSEL cavity modes are found by applying a one-dimensional transfer matrix method, similar to that developed for graded-index optical fibers

by Morishita [1991]. Carrier diffusion and spatial hole burning effects are neglected. Transverse profiles of cavity modes are found to be sensitive to driving current via the thermal lensing effect (cf. § 3.3). Calculated modal gains are then used to determine threshold gain, threshold carrier density, and threshold current density, including the effects of detuning between the mode and the gain peak wavelengths (cf. § 3.2.). The model does not include any feedback between the temperature distribution in the device and the electrical properties (including redistribution of the heat sources), nor between the calculated optical fields and the thermal-electrical phenomena. It was used later by Michalzik and Ebeling [1995] to determine CW performance characteristics of PITSELs.

Baba, Kondoh, Koyama and Iga [1995a] reported the FEM thermal model of InGaAsP/InP DMEWLs. The model is rather approximate, without any self-consistency. Its boundary conditions are artificial: without any justification, constant temperature is simply assumed to be maintained for all walls of the cylinder of 50 μm radius and 50 μm height. Only one heat source within the active region (nonradiative recombination and absorption of spontaneous emission) is considered. With the aid of the model, it was found that thermal resistances R_{TH} of 1.3 μm DMEWLs using MgO/Si mirrors are nearly half of those using SiO₂/Si ones. Similar simulation of BEMLS (Baba, Kondoh, Koyama and Iga [1995b]) revealed that R_{TH} of devices with GaAs/AlAs DBRs fused epitaxially to InGaAsP/InP emitting layers is 1/3 of that with InGaAsP/InP DBRs.

Another comprehensive thermal model of VCSELs was proposed by Norris, Chen and Tien [1994] and Chen, Hadley and Smith [1994] for p-substrate GaAs/AlGaAs TEMLs (cf. table 1 and fig. 3) with short-period-superlattice DBRs. It should be emphasized that these devices will in general have much poorer electrical and thermal properties than other AlGaAs-based VCSELs, since thermal and electrical conductivities in very thin layers are much higher than in their bulk counterparts, especially along the axial direction. In the model, a very careful evaluation of heat generation mechanisms is carried out including radiative transfer of spontaneous emission from the active region, nonradiative recombination, absorption of spontaneous and stimulated radiation, and all barrier and volume Joule heating processes except for the contact heating. Detailed analysis of the current flow is performed, including the thermionic and tunneling currents through heteroboundaries, the effect of band-gap discontinuity on the heterointerface resistance, and the anisotropy in the electrical conductivities caused by quantum effects in layered structures. However, carrier diffusion effects are neglected. Somewhat surprisingly, the temperature dependencies of material parameters and heat generation processes

are not included in this otherwise quite sophisticated model, which compromises its accuracy and limits its applicability to the linear regime well below thermal runaway. In addition, the entire VCSEL cavity, comprising the active region and the short-period-superlattice GaAs/AlGaAs DBR mirrors, is replaced with a uniform thermally equivalent medium, characterized by the anisotropic thermal conductivity ($k_r = 12$ W/mK and $k_z = 10$ W/mK), which is a rather crude approach for purely numerical modeling.

The same control volume method was used by Chen [1995] to compare thermal characteristics of various VCSEL structures. In the analysis, the microscale electrical and thermal conduction within VCSELs multi-layered volumes were taken into account, including anisotropy of both electrical resistivity and thermal conductivity. The study reveals the interesting fact that the p-type substrate VCSELs (e.g., Hadley, Wilson, Lau and Smith [1993]) are characterized by lower thermal resistances than the n-type substrate VCSELs (e.g., Young, Scott, F.H. Peters, M.G. Peters, Majewski, Thibeault, Corzine and Coldren [1993], Hasnain, Tai, Yang, Wang, Fischer, Wynn, Weir, Dutta and Cho [1991]). For all the VCSEL structures under consideration, the calculated maximum temperature rise occurs along the optical axis. This is in contrast to the results reported by Nakwaski and Osiński [1991a, 1993] for the etched-well VCSEL, where the temperature profiles peak usually (but not always, depending on the VCSEL structure) close to the edge of the active region. It is, however, very difficult to compare the results of the very sophisticated, self-consistent model given by Nakwaski and Osiński [1991a, 1993], which is very sensitive to modeling details (compare discussion of fig. 20), with those presented by Chen [1995]. The heat generation profiles assumed by Chen [1995] are, for example, essentially different from those determined by Nakwaski and Osiński (cf. Nakwaski and Osiński [1991e]).

Rahman, Lepkowski and Grattan [1995] have used FEM to model the thermal properties of GaAs/AlGaAs DMEWLs. With the exception of the numerical calculation procedure, the model is almost identical to the analytical one reported earlier by Nakwaski and Osiński [1991a]. All important heat sources are included in this simulation. Details of the complex multilayered buried-heterostructure are taken into account. Full thermal-electrical self-consistency is achieved. Surprisingly, the algorithm of this ambitious simulation is convergent very quickly. The solution is given in the form of temperature and heat-flux profiles as well as isotherm contour maps.

Sarzała, Nakwaski and Osiński [1995] developed a comprehensive, fully self-consistent thermal-electrical finite-element model to investigate the thermal properties of GaAs/AlGaAs PITSELs (cf. table 1 and fig. 3). In the model,

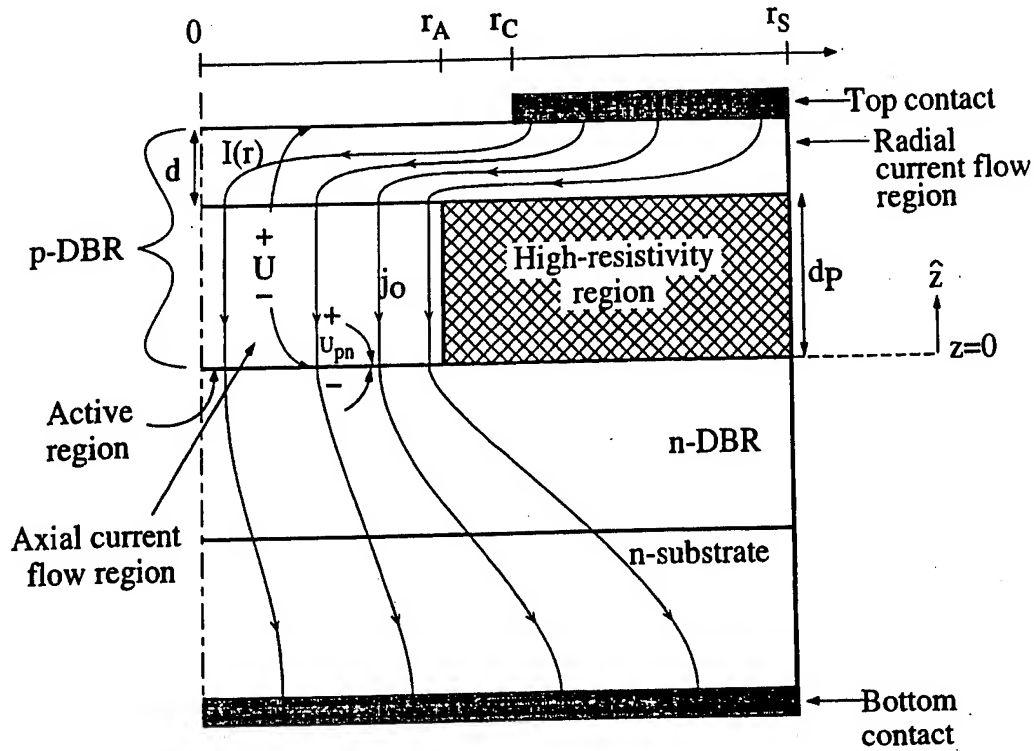


Fig. 27. Schematic illustration of current flow in a PITSEL. r_A , active region radius; r_C , inner radius of the annular contact; r_S , structure (chip) radius; d , thickness of the current spreading (radial current flow) region; d_p , thickness of the high-resistance proton-implanted region; U , voltage drop between the top contact and the active region; U_{pn} , voltage drop across the p-n junction; $I(r)$, radial current in the current spreading region; $j_0(r)$, axial current density in the current confinement region.

special attention is paid to radial carrier diffusion (Sarzała and Nakwaski [1997]) within the layer containing the active region and to its influence on temperature profiles. The radial diffusion is enhanced in structures of cylindrical geometry, so this effect is expected to play a significant role in the heat generation as well as in the heat spreading processes in PITSELS.

Knowledge of the local current density in the entire volume of the device is essential for proper treatment of the Joule heating source. The main factors affecting the current density distribution are: the cylindrical symmetry of the device, the annular shape of the top contact, and a very high electrical resistivity of the region exposed to the proton bombardment. Figure 27 shows schematically the current flow in a PITSEL structure. The top section, labeled as the radial-current-flow region, plays the dominant role in determining the radial distribution of the current injected into the active region. Inside the p-GaAs contact layer and an upper part of the P-type DBR mirror, not affected by the proton bombardment, an approximately two-dimensional (2D) radial flow of current $I(r)$ takes place. After that, in an inner part of the P-type DBR mirror, which was not exposed to

Layer #	Thickness	Conductivity
1	d_1	ρ_1
2	d_2	ρ_2
3	d_3	ρ_3
4	d_4	ρ_4
⋮	⋮	⋮
⋮	⋮	⋮
⋮	⋮	⋮
N	d_N	ρ_N

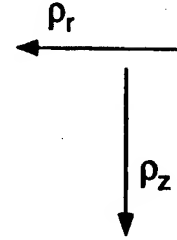


Fig. 28. Electrically equivalent anisotropic medium concept for a multilayer medium.

proton bombardment (axial current flow region), an approximately 1D current flow of a density $j_0(r)$ occurs, directed downwards along the main laser axis. Afterwards, a three-dimensional (3D) current spreading towards the bottom contact takes place below the p-n junction in the N-type DBR mirror and the n-type GaAs substrate. Note that due to the azimuthal symmetry, 2D and 3D current flows actually reduce to 1D (radius-dependent) and 2D problems, respectively.

In order to account for the multilayer composition of the DBR regions, we introduce an equivalent anisotropic medium illustrated in fig. 28, with radial and axial electrical resistivities ρ_r and ρ_z , calculated according to the following expressions (Osiński, Nakwaski and Cheng [1992]):

$$\rho_r = \frac{d_{\text{tot}}}{\sum_{i=1}^N (d_i / \rho_i)}, \quad (75)$$

$$\rho_z = \frac{\sum_{i=1}^N d_i \rho_i}{d_{\text{tot}}}, \quad (76)$$

where d_i and ρ_i stand for the thickness and the resistivity of the i th layer, N is the total number of layers contained in the region, and d_{tot} is their cumulative thickness.

The basic equations describing the current and voltage distributions in the top section of the device, comprising the radial and axial current flow regions, were given by Osiński, Nakwaski and Varangis [1994] (refer to fig. 27 for explanation of some of the symbols used):

$$\frac{dU(r)}{dr} = \left(\frac{\rho_r}{2\pi r d} \right) I(r), \quad (77)$$

$$\frac{dI(r)}{dr} = 2\pi r j_0(r), \quad (78)$$

$$U(r) = U_{pn}(r) + j_0(r) \rho_{zp} d_p, \quad (79)$$

$$j_0(r) = j_s \exp[\beta U_{pn}(r)], \quad (80)$$

where j_s is the reverse saturation current density at the p-n junction, β is the diode parameter, ρ_r is the effective resistivity in the lateral direction in the radial current flow region, and ρ_{zp} is the effective resistivity in the vertical direction in the axial current flow region. Approximate analytical solution to the above set of equations is given by Nakwaski [1995].

Before the carriers injected into the active region recombine radiatively or nonradiatively, they diffuse in the radial direction. Note that since the injected current density peaks near the edges of the active region, diffusion can occur in two directions: towards the center and away from the active region. In a cylindrically symmetric structure, the carrier diffusion is governed by the following equation:

$$D_a \left[\frac{\partial^2 n(r)}{\partial r^2} + \frac{1}{r} \frac{\partial n(r)}{\partial r} \right] - B n^2(r) - \frac{n(r)}{\tau_{nr}} + \frac{j_0(r)}{ed_A} = 0, \quad (81)$$

where $n(r)$ is the carrier concentration, d_A is the active region thickness, D_a is the ambipolar diffusion constant, B is the radiative bimolecular recombination constant, τ_{nr} is the carrier lifetime with respect to the nonradiative recombination, $j_0(r)$ is the pumping current density, and e is the electron charge. In our calculations, we adopt the following values of the above parameters, reported by Lengyel, Meissner, Patzak and Zschauer [1982]: $D_a = 40 \text{ cm}^2/\text{s}$, $B = 9.7 \times 10^{-11} \text{ cm}^3/\text{s}$, and $\tau_{nr} = 1.8 \times 10^{-8} \text{ s}$.

For an ideal laser structure, i.e., with perfect grading of all heterobarriers, its total series electrical resistance, R_{id} , is determined theoretically from known values of electrical resistivities and thicknesses of all the layers. For any particular device, the residual heterobarrier electrical resistance, R_{HB} , is then found from the measured value of resistance R and the calculated value of R_{id} :

$$R_{HB} = R - R_{id}. \quad (82)$$

In the model, the R_{HB} resistance is assumed to be distributed equally among all gradient layers in the p-type DBR mirror.

Operation-current dependence of the external quantum efficiency η_d was deduced from an experimental light-current characteristic reported by Zhou,

Cheng, Schaus, Sun, Zheng, Armour, Hains, Hsin, Myers and Vawter [1991]. A self-consistent solution is found numerically in the entire volume of the laser with the aid of an iteration procedure, taking into account the local-temperature dependencies of material and device parameters, including thermal conductivities, electrical resistivities, reverse saturation current density, free-carrier concentrations, absorption coefficients, threshold current, as well as internal and external differential quantum efficiencies. The flow chart of numerical calculations is illustrated in fig. 14, without, however, determination of a threshold current. Note that strongly nonlinear thermal-electrical interactions, enhanced by large temperature variations in VCSELs, affect substantially their lasing characteristics, eventually leading to thermal runaway.

Multiple nonhomogeneous heat sources are considered, including the carrier-concentration-dependent active-region heating (nonradiative recombination and absorption of spontaneous radiation), current-density-dependent volume and barrier (p-side contact and heterobarriers) Joule heat generations as well as internal-radiation-density-dependent absorption of laser radiation. More details may be found in the paper of Sarzała, Nakwaski and Osiński [1995].

In terms of thermal properties, the main effect of carrier diffusion is a reduction of the active-region temperature, compared with the temperature obtained at the same pumping current without diffusion. According to eq. (36), the local density of heat generated in the active-region plane is proportional to the local carrier density. Without diffusion, the active-region heat source would be contained within the circle $r \leq r_A$, and its spatial profile would be similar to that of current density. Consequently, intense heat generation would take place mostly around the edges of the active region. As a result of diffusion, the local carrier density decreases, especially at the edges of the active region, while the area occupied by the heat source becomes larger. The heat generated outside the circle $r \geq r_A$ is conducted away much more easily than the heat generated inside the active region. This leads to a significant reduction in the active-region temperature increase, as illustrated in fig. 29.

Figure 29 can be regarded as representing the key result of a paper presented by Sarzała, Nakwaski and Osiński [1995]. In addition to a remarkable lowering of the active-region temperature, dramatic changes take place in the radial temperature profiles. Without diffusion, the temperature profiles essentially reflect the nonuniform current injection, with large maxima at the edges of the active region. Inclusion of the diffusion results in nearly complete disappearance of these maxima. Only at very high pumping levels one can discern a slight positive slope of the $T_A(r)$ curve. The uniformity of temperature profiles within the active region is truly astonishing, bearing in mind that it was obtained with

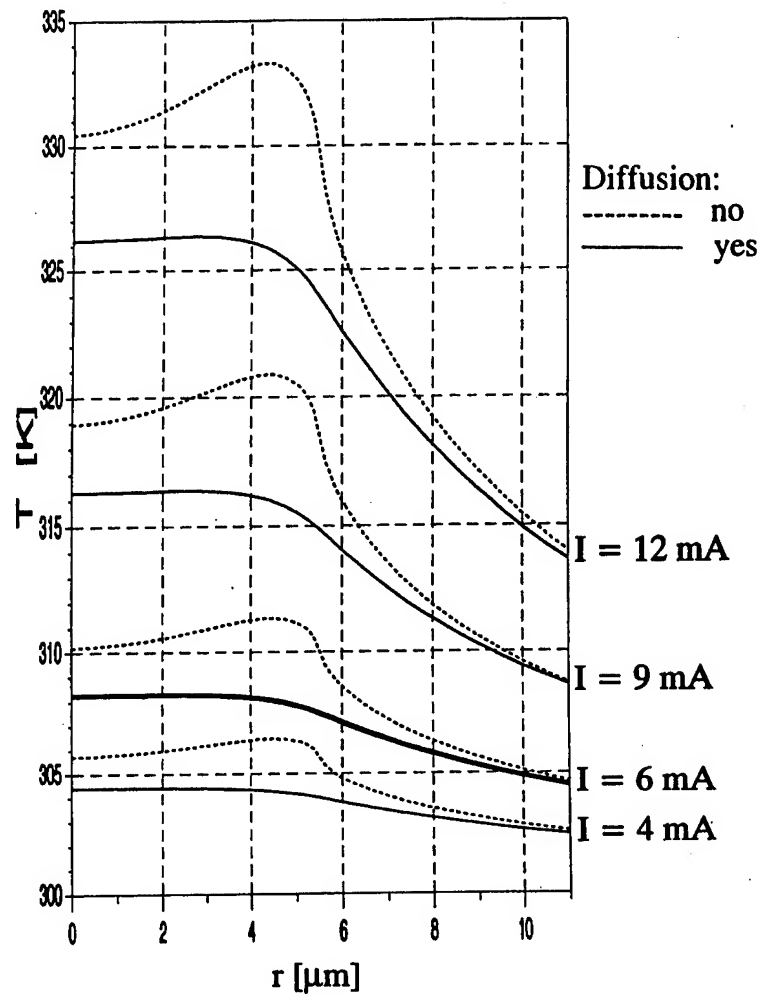


Fig. 29. Comparison of radial temperature profiles in the active-region plane, calculated with diffusion (solid lines) and without diffusion (broken lines) for indicated pumping currents.

highly inhomogeneous current injection. In fact, if a uniform active-region heat source is assumed in PITSELS, as by Nakwaski and Osiński [1994], the radial temperature profile has a bell shape. Hence, a slightly raised carrier density near the active-region edges turns out to be optimal for getting a uniform temperature distribution inside the entire active region. It should be emphasized, however, that the radial temperature profiles may well depend on the active-region diameter D_A . For devices with larger values of D_A , we expect a greater nonuniformity of injected current profiles, carrier density profiles, and active-region temperature profiles.

The analysis demonstrates that the carrier diffusion influences strongly the distribution of the main heat source located in the active region. As a result, both current- and heat-flux distributions are modified and a temperature spike,

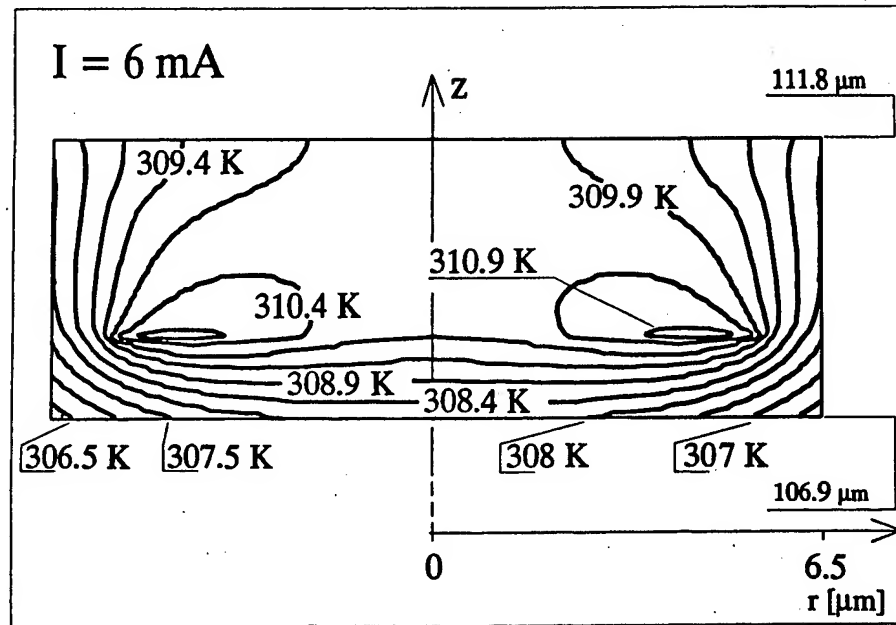


Fig. 30. Isotherm profiles in the vicinity of the active region in an 11 μm PITSEL driven at 6 mA, calculated by neglecting diffusion effects. The isotherms are drawn at intervals of $\sim 0.5^\circ\text{C}$. Note characteristic refraction effects at the interfaces between high- and low-thermal conductivity layers.

which appears at the edge of the active region when carrier diffusion is neglected, smooths out and practically disappears. This redistribution of carrier density results in a smaller number of carriers near the edges of the active region, which reduces considerably the modal gain for high-order modes and favors the excitation of the fundamental transverse mode.

Figures 30 and 31 display the isotherm profiles in a section of the device comprising the active region, obtained without and with diffusion, respectively. The two flat maxima in fig. 30, with the temperature of 310.9 K, are located in the active-region plane and correspond to the maximum of the 6 mA dashed line in fig. 29. They disappear entirely in fig. 31, and the active region has a remarkably flat temperature profile, again in accordance with the 6 mA solid line in fig. 29. Instead a lower-temperature maximum, just above 308.3 K, emerges in the central part of the P-type mirror.

Recently, Hadley, Lear, Warren, Choquette, Scott and Corzine [1996] have presented the results of their comprehensive (and very sophisticated in its optical part) full thermal-electrical-optical numerical modeling of PITSELS using a finite-difference technique. The model considers the following major physical processes (i) the ohmic transport of carriers through the cladding layers to an active region, (ii) the heat transport from multiple heat sources toward a heat

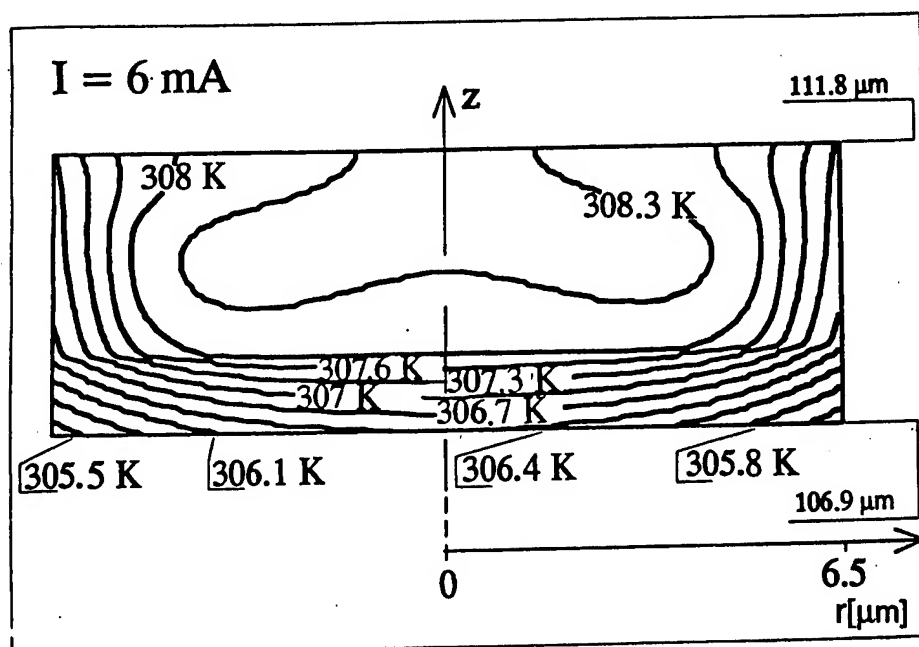


Fig. 31. Isotherm profiles in the vicinity of the active region in an 11 μm PITSEL driven at 6 mA, with diffusion effects taken into account. The isotherms are drawn at intervals of $\sim 0.3^\circ\text{C}$.

sink, (iii) the radial diffusion of carriers inside the active region, and (iv) the multimode optical field. In the model, many important features are taken into consideration, including carrier leakage effects, interaction of transverse modes with carriers, effects arising from the strained band structure usually present in the quantum wells, and so on. The model also contains some thermal-optical (*thermal lensing effect*) and electrical-optical (*spatial holeburning effect*) self-consistency procedures. Three main heat generation mechanisms are taken into account, namely nonradiative recombination, reabsorption of radiation, and ohmic dissipation. A temperature increase inside the contact layers and the heat sink does not seem to be taken into account. The authors claimed to successfully predict the threshold current, output powers, and transverse-mode behavior of gain-guided VCSELs, including thermal rollover effects at high injection currents. At least the last prediction is a real surprise: the validity of the above approach seems to be confined to only relatively low operation currents because both the heat and the carrier transports are assumed to be linear and the model does not contain the thermal-electrical self-consistent procedure. As in the model of Piprek and Yoo [1994], multi-layered DBR mirrors are replaced with an equivalent uniform and anisotropic medium whose composite thermal conductivities (and also some other model parameters) are additionally modified to reproduce the measured device temperature rise. Thus, the agreement between theory and experiment can hardly be regarded as a confirmation of the models

validity. Nevertheless, the above model seems to be now the most advanced thermal–electrical–optical simulation of a VCSEL operation.

An intricate thermal VCSEL analysis has been recently reported by Ning, Indik and Moloney [1995], Ning, Indik, Moloney and Koch [1995], and Ning and Moloney [1995]. They have introduced plasma and lattice temperatures as two independent variables described by kinetic equations coupled to the conventional laser equations for carrier density and field amplitude. According to this approach, lattice and plasma each absorb heat from their respective heat sources and dissipate heat to their heat sinks. In the CW region, lattice and plasma can each hold their individual temperatures and maintain a constant temperature difference because of the sustained pumping as well as the heat exchange and dissipation. New achievements of this approach seem, however, to be too subtle to have practical meaning now. Besides, there are also some essential drawbacks of this analysis. First of all, it considers important laser variables (e.g., temperature, carrier concentration and current density) as position independent, average quantities whereas their three-dimensional profiles are very important to model correctly VCSEL operation. Furthermore, most of decay rates in the kinetic equations are used as adjustable parameters. All construction and material details are hidden in these parameters. Their values, as used in example numerical calculations, are not justified or evaluated by any means. Finally, the above parameters depend, for example, on VCSEL thermal and electrical resistances, whose exact determination now seems to be more essential for modeling of VCSEL operation, than a subtle distinction between the temperatures of lattice and plasma. Thus, the approach based on this distinction seems to be premature at this moment, but it should not be neglected. It should serve as an important direction in which present VCSEL 3-D models can be extended and should be included into self-consistent comprehensive VCSEL analysis in future.

Numerical comprehensive thermal VCSEL models are compared in table 8b (p. 221). In the course of time, they become more and more involved, but also more and more exact.

§ 6. Conclusions

Although vertical-cavity surface-emitting lasers (VCSELs) are generally considered to be very promising, their relatively poor thermal properties still represent the main obstacle on the way towards their wide application, and are especially pressing when integration into densely-packed two-dimensional

arrays is contemplated. To overcome these difficulties, a good understanding of the thermal problems must be reached. In particular, detailed modeling of heat generation processes, heat-flux spreading, and mutual interactions between thermal, electrical, and optical phenomena is desirable to design thermally optimized devices. As long as the optical output power in VCSELs remains small, the coupling between optical and thermal effects can be ignored in determining the temperature distribution inside the device. On the other hand, thermal-electrical interactions are very important, and thermal-electrical self-consistency is essential for realistic modeling of thermal effects. It is also important to include a realistic distribution of heat sources in the model. The current-induced variation of thermal resistance is very sensitive to VCSEL structure, and in particular to the relative distribution of heat sources and their location with respect to the heat sink.

This chapter summarizes the present understanding of thermal effects in VCSELs. It is clear that these effects are preponderant and affect almost all device characteristics. As a rule, elevated temperature has a detrimental effect on these characteristics and should be minimized. There are, however, exceptions to this rule. Some aspects of thermal behavior of VCSELs may actually be beneficial. For example, thermally-induced optical waveguide in devices with no built-in lateral guiding helps to reduce losses and lower the threshold current. Unique opportunities for thermal-waveguide engineering exist in etched-well VCSELs. Elevated temperature may be also beneficial in VCSELs with transparent electrodes [Chua, Thornton, Treat, Yang and Dunnrowicz [1997]]. Finally, non-monotonous variation of threshold current with temperature has been exploited to design temperature-insensitive devices.

Acknowledgments

Much of our work reported here would not have been possible without the active contribution and support of many of our colleagues. In particular, we would like to acknowledge numerous fruitful discussions and advice from Julian Cheng of the University of New Mexico, Albuquerque, USA, and G. Ronald Hadley of the Sandia National Laboratories, Albuquerque, USA, as well as from Maciej Bugajski and Bohdan Mroziwicz of the Institute of Electron Technology, Warsaw, Poland. We are grateful to Bo Lu and Ping Zhou of the University of New Mexico, USA, for technical discussions and for providing their data on the temperature dependence of the threshold current. We acknowledge valuable contributions from our students, Robert P. Sarzała, Jacek Wilk, Georgi K.

Yanakiev, Petros M. Varangis, Antonio Leal, Jonathan Stohs, Gilles du Crest, and Joachim Kastner. We are also thankful to Mrs. Katarzyna A. Steele (Jezierska) and Mr. Bill Johnson for their apt technical assistance. This work was supported by the Polish State Committee for Scientific Research (KBN) (Grant # 8-T11B-018-12), the National Science Foundation (NSF), the Advanced Research Projects Agency (AREA), the Air Force Office for Scientific Research, and the New Energy and Industrial Technology Development Organization (NEDO) of Japan.

References

- Adachi, S., 1985, *J. Appl. Phys.* **58**, R1.
- Adachi, S., 1992, *Physical Properties of III-V Semiconductor Compounds: InP, InAs, GaAs, GaP, InGaAs, and InGaAsP* (Wiley, New York).
- Agrawal, G.P., and N.K. Dutta, 1993, *Semiconductor Lasers*, 2nd Ed. (Van Nostrand Reinhold, New York) p. 59.
- Aiki, K., M. Nakamura and J.-I. Umeda, 1976, *IEEE J. Quantum Electron.* **QE-12**, 597.
- Akulova, Y.A., B.J. Thibeault, J. Ko and L.A. Coldren, 1997, *IEEE Photon. Technol. Lett.* **9**, 277.
- Amith, A., I. Kudman and E.F. Steigmeier, 1965, *Phys. Rev.* **138**, A1270.
- Baba, T., T. Kondoh, F. Koyama and K. Iga, 1995a, *Opt. Rev.* **2**, 123.
- Baba, T., T. Kondoh, F. Koyama and K. Iga, 1995b, *Opt. Rev.* **2**, 323.
- Baba, T., K. Suzuki, Y. Yogo, K. Iga and F. Koyama, 1993a, *Electron. Lett.* **29**, 331.
- Baba, T., K. Suzuki, Y. Yogo, K. Iga and F. Koyama, 1993b, *IEEE Photon. Tech. Lett.* **5**, 744.
- Baba, T., Y. Yogo, K. Suzuki, F. Koyama and K. Iga, 1993, *Electron. Lett.* **29**, 913.
- Baba, T., Y. Yogo, K. Suzuki, F. Koyama and K. Iga, 1994, *Jpn. J. Appl. Phys. Pt. I* **33**, 1905.
- Babic, D.I., Y. Chung, N. Dagli and J.E. Bowers, 1993, *IEEE J. Quantum Electron.* **QE-29**, 1950.
- Babic, D.I., and S.W. Corzine, 1992, *IEEE J. Quantum Electron.* **QE-28**, 514.
- Babic, D.I., J.J. Dudley, K. Streubel, R.P. Mirin, J.E. Bowers and E.L. Hu, 1995, *Appl. Phys. Lett.* **66**, 1030.
- Babic, D.I., K. Streubel, R.P. Mirin, N.M. Margalit, J.E. Bowers and E.L. Hu, 1995, *Electron. Lett.* **31**, 653.
- Babic, D.I., K. Streubel, R.P. Mirin, N.M. Margalit, J.E. Bowers, E.L. Hu, D.E. Mars, L. Yang and K. Carey, 1995, *IEEE Photon. Technol. Lett.* **7**, 1225.
- Bissessur, H., R.D. Ettinger, F.A. Fernandez and J.B. Davies, 1993, *IEEE Photon. Technol. Lett.* **5**, 764.
- Buccafusca, O., J.L.A. Chilla, J.J. Rocca, S. Feld, C. Wilmsen, V. Morozov and R. Leibenguth, 1996, *Appl. Phys. Lett.* **68**, 590.
- Bugajski, M., and A.M. Kontkiewicz, 1982, *Electron Technol.* **13**(4), 63.
- Buus, J., 1983, *IEEE J. Quantum Electron.* **QE-19**, 953.
- Buus, J., and M.J. Adams, 1979, *IEEE J. Solid State Electron Dev.* **3**, 189.
- Carlsaw, H.S., and J.C. Jaeger, 1988, *Conduction of Heat in Solids* (Clarendon Press, Oxford).
- Casey Jr, H.C., and M.B. Panish, 1978, *Heterostructure Lasers, Part A: Fundamental Principles* (Academic Press, New York) p. 44.
- Catchmark, J.M., R.A. Morgan, K. Kojima, R.E. Leibenguth, M.T. Asom, G.D. Guth, M.W. Focht, L.C. Luther, G.P. Przybylek, T. Mullay and D.N. Christodoulides, 1993, *Appl. Phys. Lett.* **63**, 3122.

- Chang-Hasnain, C.J., 1994, Vertical cavity surface-emitting laser arrays, in: Diode Laser Arrays, eds D. Botez and D.R. Scifres (Cambridge University Press, Cambridge), ch. 9, p. 368.
- Chang-Hasnain, C.J., J.P. Harbison, L.T. Florez and N.G. Stoffel, 1991, *Electron. Lett.* **27**, 163.
- Chang-Hasnain, C.J., J.P. Harbison, G. Hasnain, A.C. Von Lehmen, L.T. Florez and N.G. Stoffel, 1991, *IEEE J. Quantum Electron.* **QE-27**, 1402.
- Chang-Hasnain, C.J., M. Orenstein, A. Von Lehmen, L.T. Florez, J.P. Harbison and N.G. Stoffel, 1990, *Appl. Phys. Lett.* **57**, 218.
- Chang-Hasnain, C.J., Y.A. Wu, G.S. Li, G. Hasnain, K.D. Choquette, C. Caneau and L.T. Florez, 1993, *Appl. Phys. Lett.* **63**, 1307.
- Chen, G., 1995, *J. Appl. Phys.* **77**, 4251.
- Chen, G., M.A. Hadley and J.S. Smith, 1994, *J. Appl. Phys.* **76**, 3261.
- Cherng, C.-P., and M. Osinski, 1991, *J. Appl. Phys.* **70**, 4617.
- Chong, C.H., and J. Sarma, 1993, *IEEE Photon. Technol. Lett.* **5**, 761.
- Choquette, K.D., W.W. Chow, M.H. Crawford, K.M. Geib and R.P. Schneider Jr, 1996, *Appl. Phys. Lett.* **68**, 3689.
- Choquette, K.D., R.P. Schneider Jr, M.H. Crawford, K.M. Geib and J.J. Figiel, 1995, Conference on Lasers and Electro-Optics, CLEO'95, Baltimore, MD, May 22-26, Paper CPD5-1.
- Choquette, K.D., R.P. Schneider Jr, K.L. Lear and K.M. Geib, 1994, *Electron. Lett.* **30**, 2043.
- Chow, W.W., S.W. Corzine, D.B. Young and L.A. Coldren, 1995, *Appl. Phys. Lett.* **66**, 2460.
- Chua, C.L., R.L. Thornton, D.W. Treat, V.K. Yang and C.C. Dunnrowicz, 1997, *IEEE Photon. Technol. Lett.* **9**, 551.
- Chua, C.L., Z.H. Zhu, Y.H. Lo, R. Bhat and M. Hong, 1995, *IEEE Photon. Techn. Lett.* **7**, 444.
- Coldren, L.A., R.S. Geels, S.W. Corzine and J.W. Scott, 1992, *Opt. Quantum Electron.* **24**, S105.
- Coldren, L.A.C., E.R.H. Hegblom, E.M.S. Strzelecka, J.K. Ko, Y.A.A. Akulova and B.J.T. Thibeault, 1997, *Proc. SPIE* **3003**, 2.
- Cook, D.D., and F.R. Nash, 1975, *J. Appl. Phys.* **46**, 1660.
- Crawford, M.H., and R.P. Schneider Jr, 1995, Conference on Lasers and Electro-Optics, CLEO'95, Baltimore, MD, May 22-26, Paper CWB1.
- Dudley, J.J., D.I. Babic, R.P. Mirin, L. Yang, B.I. Miller, R.J. Ram, T.E. Reynolds, E.L. Hu and J.E. Bowers, 1994, *Appl. Phys. Lett.* **64**, 1463.
- Dudley, J.J., D.L. Crawford and J.E. Bowers, 1992, *IEEE Photon. Technol. Lett.* **4**, 311.
- Dudley, J.J., M. Ishikawa, D.I. Babic, B.I. Miller, R.P. Mirin, W.B. Jiang, J.E. Bowers and E.L. Hu, 1993, *Appl. Phys. Lett.* **61**, 3095.
- Dutta, N.K., and R.J. Nelson, 1982, *J. Appl. Phys.* **53**, 74.
- Dutta, N.K., L.W. Tu, G. Hasnain, G.J. Zydzik, Y.H. Wang and A.Y. Cho, 1991, *Electron. Lett.* **27**, 208.
- Fisher, M.A., Y.-Z. Huang, A.J. Dann, D.J. Elton, M.J. Harlow, S.D. Perrin, J. Reed, I. Reid and M.J. Adams, 1995, *IEEE Photon. Technol. Lett.* **7**, 608.
- Floyd, F.D., B.J. Thibeault, L.A. Coldren and J.L. Merz, 1996, *Electron. Lett.* **32**, 114.
- Geels, R.S., and L.A. Coldren, 1990, *Appl. Phys. Lett.* **57**, 1605.
- Geels, R.S., and L.A. Coldren, 1991, *Electron. Lett.* **27**, 1984.
- Geels, R.S., S.W. Corzine, J.W. Scott, D.B. Young and L.A. Coldren, 1990, *IEEE Photon. Technol. Lett.* **2**, 234.
- Geels, R.S., B.J. Thibeault, S.W. Corzine, J.W. Scott and L.A. Coldren, 1993, *IEEE J. Quantum Electron.* **QE-29**, 2977.
- Goncher, G., B. Lu, W.-L. Luo, J. Cheng, S. Hersee, S.Z. Sun, R.P. Schneider and J.C. Zolper, 1996, *IEEE Photon. Technol. Lett.* **8**, 316.
- Grimmeiss, H.G., and B. Monemar, 1971, *Phys. Status Solidi A* **5**, 109.
- Hadley, G.R., J.P. Hohimer and A. Owyong, 1987, *IEEE J. Quantum Electron.* **QE-23**, 765.

- Hadley, G.R., K.L. Lear, M.E. Warren, K.D. Choquette, J.W. Scott and S.W. Corzine, 1996, IEEE J. Quantum Electron. **QE-32**, 607.
- Hadley, M.A., G.C. Wilson, K.Y. Lau and J.S. Smith, 1993, Appl. Phys. Lett. **63**, 1607.
- Hasnain, G., K. Tai, N.K. Dutta, Y.H. Wang, J.D. Wynn, B.E. Weir and A.Y. Cho, 1991, Electron. Lett. **27**, 915.
- Hasnain, G., K. Tai, L. Yang, Y.H. Wang, R.J. Fischer, J.D. Wynn, B. Weir, N.K. Dutta and A.Y. Cho, 1991, IEEE J. Quantum Electron. **QE-27**, 1377.
- Hayashi, Y., T. Mukaiharu, N. Hatori, N. Ohnoki, A. Matsutani, F. Koyama and K. Iga, 1995, Electron. Lett. **31**, 560.
- Huffaker, D.L., and D.G. Deppe, 1996, IEEE Photon. Technol. Lett. **8**, 858.
- Huffaker, D.L., D.G. Deppe, K. Kumar and T.J. Rogers, 1994, Appl. Phys. Lett. **64**, 97.
- Huffaker, D.L., D.G. Deppe and T.J. Rogers, 1994, Appl. Phys. Lett. **65**, 1611.
- Huffaker, D.L., L.A. Graham, H. Deng and D.G. Deppe, 1996, IEEE Photon. Technol. Lett. **8**, 974.
- Huffaker, D.L., J. Shin, H. Deng, C.C. Lin, D.G. Deppe and B.G. Streetman, 1994, Appl. Phys. Lett. **65**, 2642.
- Hughes, J.J., D.B. Gilbert and F.Z. Hawrylo, 1985, RCA Rev. **46**, 200.
- Iga, K., 1992a, Opt. Quantum Electron. **24**, S97.
- Iga, K., 1992b, Int. J. High Speed Electron. Systems **3**, 263.
- Iga, K., and F. Koyama, 1990, Surface Emitting Laser, Ohm-sha, Chapter 2.2, pp. 22-27.
- Iga, K., and F. Koyama, 1993, Vertical-Cavity Surface Emitting Lasers and Arrays, in: Surface Emitting Semiconductor Lasers and Arrays, eds G.A. Evans and J.M. Hammer (Academic Press, Boston), p. 71.
- Iga, K., F. Koyama and S. Kinoshita, 1988, IEEE J. Quantum Electron. **QE-24**, 1845.
- Jäger, R., M. Grabherr, C. Jung, R. Michalzik, G. Reiner, B. Weigl and K.J. Ebeling, 1997, Electron. Lett. **33**, 330.
- Jansen van Doorn, A.K., M.P. van Exter and J.P. Woerdman, 1995, Appl. Phys. Lett. **66**, 3561.
- Jewell, J.L., A.L. Scherer, S.L. McCall, Y.H. Lee, S. Walker, J.P. Harbison and L.T. Florez, 1989, Electron. Lett. **25**, 1123.
- Joyce, W.B., and R.W. Dixon, 1975, J. Appl. Phys. **46**, 855.
- Kajita, M., T. Kawakami, M. Nido, A. Kimura, T. Yoshikawa, K. Kurihara, Y. Sugimoto and K. Kasahara, 1995, IEEE J. Select. Topics Quantum Electron. **1**, 654.
- Kinoshita, S., F. Koyama and K. Iga, 1987, Proc. Tech. Group Meet., IECE Jpn., paper OQE86-188, p. 23.
- Kobayashi, T., and Y. Furukawa, 1975, Jpn. J. Appl. Phys. **14**, 1981.
- Koch, B.J., J.R. Leger, A. Gopinath, Z. Wang and R.A. Morgan, 1997, Appl. Phys. Lett. **70**, 2359.
- Koyama, F., S. Kinoshita and K. Iga, 1989, Appl. Phys. Lett. **55**, 221.
- Kudman, I., and E.F. Steigmeier, 1964, Phys. Rev. **133**, A1665.
- Lautenschlager, P., M. Garriga and M. Cardona, 1987, Phys. Rev. B **36**, 4813.
- Law, J.Y., and G.P. Agrawal, 1997, IEEE J. Quantum Electron. **QE-33**, 462.
- Lear, K.L., K.D. Choquette, R.P. Schneider Jr and S.P. Kilcoyne, 1995, Appl. Phys. Lett. **66**, 2616.
- Lear, K.L., A. Mar, K.D. Choquette, S.P. Kilcoyne, R.P. Schneider Jr and K.M. Geib, 1996, Electron. Lett. **32**, 457.
- Lear, K.L., R.P. Schneider Jr, K.D. Choquette, S.P. Kilcoyne, J.J. Figiel and J.C. Zolper, 1994, IEEE Photon. Techn. Lett. **6**, 1053.
- Lengyel, G., P. Meissner, E. Patzak and K.-H. Zschau, 1982, IEEE J. Quantum Electron. **QE-18**, 618.
- Lu, B., W.-L. Luo, C. Hains, J. Cheng, R.P. Schneider Jr, R.P. Choquette, K.L. Lear, S.P. Kilcoyne and J.C. Zolper, 1995, IEEE Photon. Technol. Lett. **7**, 447.
- Lu, B., P. Zhou, J. Cheng and K.J. Malloy, 1994, Proc. SPIE **2147**, 12.

- Lu, B., P. Zhou, J. Cheng, K.J. Malloy and J.C. Zolper, 1994, *Appl. Phys. Lett.* **65**, 1337.
- MacDougall, M.H., P.D. Dapkus, V. Pudikov, H. Zhao and G.M. Yang, 1995, *IEEE Photon. Technol. Lett.* **7**, 229.
- MacDougall, M.H., G.M. Yang, A.E. Bond, C.-K. Lin, D. Tishinin and P.D. Dapkus, 1996, *IEEE Photon. Technol. Lett.* **8**, 310.
- Manning, J.S., 1981, *J. Appl. Phys.* **52**, 3179.
- Marple, D.T.F., 1964, *J. Appl. Phys.* **35**, 1241.
- Michalzik, R., and K.J. Ebeling, 1993, *IEEE J. Quantum Electron.* **QE-29**, 1963.
- Michalzik, R., and K.J. Ebeling, 1995, *IEEE J. Quantum Electron.* **QE-31**, 1371.
- Miyamoto, T., T. Uchida, N. Yokouchi, Y. Inaba, K. Mori, F. Koyama and K. Iga, 1993, Conference on Lasers and Electro-Optics, CLEO'93, Baltimore, MD, May 2-7, 1993, p. 316.
- Morgan, R.A., 1994, *Proc. SPIE* **2147**, 97.
- Morgan, R.A., 1997, *Proc. SPIE* **3003**, 14.
- Morgan, R.A., G.D. Guth, M.W. Focht, M.T. Asom, K. Kojima, L.E. Rogers and S.E. Callis, 1993, *IEEE Photon. Technol. Lett.* **5**, 374.
- Morgan, R.A., M.K. Hibbs-Brenner, J.A. Lehman, E.L. Kalweit, R.A. Walterson, T.M. Marta and T. Akinwande, 1995, *Appl. Phys. Lett.* **66**, 1157.
- Morgan, R.A., M.K. Hibbs-Brenner, T.M. Marta, R.A. Walterson, S. Bounnak, E.L. Kalweit and J.A. Lehman, 1995, *IEEE Photon. Technol. Lett.* **7**, 441.
- Morgan, R.A., J.A. Lehman, Y. Liu, M.K. Hibbs-Brenner and J.P. Bristow, 1997, *Proc. SPIE* **3004**, Paper 3004-13.
- Morishita, K., 1991, *IEEE Trans. Microwave Theory Tech.* **MTT-29**, 348.
- Mroziewicz, B., M. Bugajski and W. Nakwaski, 1991, *Physics of Semiconductor Lasers* (North-Holland, Amsterdam).
- Mukaihara, T., Y. Hayashi, N. Hatori, N. Ohnoki, A. Matsutani, F. Koyama and K. Iga, 1995, *Electron. Lett.* **31**, 647.
- Nakwaski, W., 1979, *Sov. J. Quantum Electron.* **9**, 1544.
- Nakwaski, W., 1983, *Opt. Quantum Electron.* **15**, 513.
- Nakwaski, W., 1984, *IEEE Proc. Pt. I (Solid-State Electron Dev.)* **131**, 94.
- Nakwaski, W., 1988, *J. Appl. Phys.* **64**, 159.
- Nakwaski, W., 1995, *Appl. Phys. A* **61**, 123.
- Nakwaski, W., and A.M. Kontkiewicz, 1985, *IEEE Trans. Electron. Devices* **32**, 2282.
- Nakwaski, W., and M. Osiński, 1991a, *IEEE J. Quantum Electron.* **QE-27**, 1391.
- Nakwaski, W., and M. Osiński, 1991b, *Jpn. J. Appl. Phys. Pt. 2 (Lett.)* **30**, L596.
- Nakwaski, W., and M. Osiński, 1991c, *Proc. SPIE* **1582**, 277.
- Nakwaski, W., and M. Osiński, 1991d, Conference on Lasers and Electro-Optics, CLEO'91, Baltimore, MD, 12-17 May, 1991, Paper CWF26, pp. 262-263.
- Nakwaski, W., and M. Osiński, 1991e, *IEEE Photon. Technol. Lett.* **3**, 979.
- Nakwaski, W., and M. Osiński, 1992a, Conference on Lasers and Electro-Optics, CLEO'92, Anaheim, CA, 10-15 May, 1992, Paper JThA6, pp. 386-387.
- Nakwaski, W., and M. Osiński, 1992b, LEOS 1992 Summer Topical Meeting Digest on Smart Pixels, Santa Barbara, CA, 10-12 Aug., 1992, Paper TuA4, pp. 47-48.
- Nakwaski, W., and M. Osiński, 1992c, *Proc. SPIE* **1788**, 108.
- Nakwaski, W., and M. Osiński, 1992d, *Electron. Lett.* **28**, 1283.
- Nakwaski, W., and M. Osiński, 1993, *IEEE J. Quantum Electron.* **QE-29**, 1981.
- Nakwaski, W., and M. Osiński, 1994, *Proc. SPIE* **2146**, 365.
- Nakwaski, W., M. Osiński and J. Cheng, 1992, *Appl. Phys. Lett.* **61**, 3101.
- Nash, F.R., 1973, *J. Appl. Phys.* **44**, 4696.
- Ning, C.Z., R.A. Indik and J.V. Moloney, 1995, *J. Opt. Soc. Am. B* **12**, 1993.

- Ning, C.Z., R.A. Indik, J.V. Moloney and S.W. Koch, 1995, *Proc. SPIE* **2399**, 617.
- Ning, C.Z., and J.V. Moloney, 1995, *Opt. Lett.* **20**, 1151.
- Norris, P.M., G. Chen and C.-L. Tien, 1994, *Int. J. Heat Mass Transfer* **37** (Suppl. 1) 9.
- Oezisik, M.N., 1980, *Heat Conduction* (Wiley, New York), pp. 6, 8.
- Ohiso, Y., C. Amano, Y. Itoh, K. Tateno, T. Tadokoro, H. Takenouchi and T. Kurokawa, 1996, *Electron. Lett.* **32**, 1483.
- Ohiso, Y., Y. Kohama and T. Kurokawa, 1995, *Jpn. J. Appl. Phys. Pt. 1*, **34**, 6073.
- Ohiso, Y., K. Tateno, Y. Kohama, A. Wakatsuki, H. Tsunetsugu and T. Kurokawa, 1996, *IEEE Photon. Technol. Lett.* **8**, 1115.
- Onischenko, A., and J. Sarma, 1997, *IEE Proc. Optoelectron.* **144**, 39.
- Ortiz, G.G., C.P. Hains, B. Lu, S.Z. Sun, J. Cheng and J.C. Zolper, 1996, *IEEE Photon. Technol. Lett.* **8**, 1423.
- Osiński, M., and W. Nakwaski, 1992, *Proc. SPIE* **1634**, 61.
- Osiński, M., and W. Nakwaski, 1993a, *Electron Lett.* **29**, 1015.
- Osiński, M., and W. Nakwaski, 1993b, *Conference on Lasers and Electro-Optics, CLEO'93*, Baltimore, MD, 2-7 May, 1993, Paper CTuN5, pp. 150-152.
- Osiński, M., and W. Nakwaski, 1995a, *IEEE J. Selected Topics Quantum Electron.* **1**, 681.
- Osiński, M., and W. Nakwaski, 1995b, *Proc. SPIE* **2399**, 372.
- Osiński, M., W. Nakwaski and J. Cheng, 1992, *Proc. SPIE* **1788**, 121.
- Osiński, M., W. Nakwaski and A. Leal, 1994, *Proc. SPIE* **2147**, 85.
- Osiński, M., W. Nakwaski and P.M. Varangis, 1994, *Proc. SPIE* **2146**, 388.
- Paoli, T.L., 1973, *IEEE J. Quantum Electron.* **QE-9**, 267.
- Papannareddy, R., W. Ferguson and J.K. Butler, 1987, *J. Appl. Phys.* **62**, 3565.
- Petermann, K., 1991, *Laser Diode Modulation and Noise* (Kluwer Academic Publishers/KTK Scientific Publishers, Dordrecht/Tokyo), p. 34.
- Pettit, G.D., and W.J. Turner, 1965, *J. Appl. Phys.* **136**, 2081.
- Piprek, J., D.I. Babic and J.E. Bowers, 1996, *Appl. Phys. Lett.* **68**, 2630.
- Piprek, J., H. Wenzel and G. Sztefka, 1994, *IEEE Photon. Technol. Lett.* **6**, 139.
- Piprek, J., H. Wenzel, H.-J. Wünsche, D. Braun and F. Henneberger, 1995, *Proc. SPIE* **2399**, 605.
- Piprek, J., and S.J.B. Yoo, 1994, *Electron. Lett.* **30**, 866.
- Prince, F.C., N.B. Patel, D. Kasemset and C.S. Hong, 1983, *Electron. Lett.* **19**, 435.
- Rahman, B.M.A., S.P. Lepkowski and K.T.V. Grattan, 1995, *IEE Proc. Optoelectron.* **142**, 82.
- Rochus, S., M. Hauser, T. Röhr, H. Kratzer, G. Boehm, W. Klein, G. Traenke and G. Weimann, 1995, *IEEE Photon. Technol. Lett.* **7**, 968.
- Sarzała, R.P., and W. Nakwaski, 1997, *IEE Proc. Optoelectron.* **144**, in press.
- Sarzała, R.P., W. Nakwaski and M. Osiński, 1995, *Int. J. Optoelectron.* **10**, 357.
- Schneider Jr, R.P., K.D. Choquette, J.A. Lott, K.L. Lear, J.J. Figiel and K.J. Malloy, 1994, *IEEE Photon. Technol. Lett.* **62**, 313.
- Schnitzer, P., U. Fiedler, M. Grabherr, C. Jung, G. Reiner, W. Zick and K.J. Ebeling, 1996, *Electron. Lett.* **32**, 2145.
- Schröder, S., H. Grothe and W. Harth, 1996, *Electron. Lett.* **32**, 348.
- Scott, J.W., S.W. Corzine, D.B. Young and L.A. Coldren, 1993, *Appl. Phys. Lett.* **62**, 1050.
- Scott, J.W., R.S. Geels, S.W. Corzine and L.A. Coldren, 1993, *IEEE J. Quantum Electron.* **QE-29**, 1295.
- Scott, J.W., D.B. Young, B.J. Thibeault, M.G. Peters and L.A. Coldren, 1995, *IEEE J. Selected Topics Quantum Electron.* **1**, 638.
- Shimizu, M., D.I. Babic, J.J. Dudley, W.B. Jiang and J.E. Bowers, 1993, *Microw. Opt. Technol. Lett.* **6**, 455.

- Shin, H.-E., Y.-G. Ju, J.-H. Shin, J.-H. Ser, T. Kim, E.-K. Lee, I. Kim and Y.-H. Lee, 1996, *Electron. Lett.* **32**, 1287.
- Shoji, H., K. Otsubo, M. Matsuda and H. Ishikawa, 1994, *Electron. Lett.* **30**, 409.
- Sommers, H.S., 1971, *Appl. Phys. Lett.* **19**, 424.
- Stern, F., 1973, *IEEE J. Quantum Electron.* **QE-9**, 290.
- Streubel, K., S. Rapp, J. André and J. Wallin, 1996, *IEEE Photon. Technol. Lett.* **8**, 1121.
- Sugihwo, F., M.C. Larson and J.S. Harris Jr, 1997, *Appl. Phys. Lett.* **70**, 547.
- Swaminathan, V., and A.T. Macrander, 1991, *Material Aspects of GaAs and InP Based Structures* (Prentice Hall, Englewood Cliffs), p. 15.
- Tadokoro, T., H. Okamoto, Y. Kohama, T. Kawakami and T. Kurokawa, 1992, *IEEE Photon. Technol. Lett.* **4**, 409.
- Tai, K., R.J. Fischer, C.W. Seabury, N.A. Olsson, T.-C.D. Huo, Y. Ota and A.Y. Cho, 1989, *Appl. Phys. Lett.* **55**, 2473.
- Taylor, G.W., and P.A. Evaldson, 1994, *IEEE J. Quantum Electron.* **QE-30**, 2262.
- Tell, B., K.F. Brown-Goebeler, R.E. Leibenguth, F.M. Baez and Y.H. Lee, 1992, *Appl. Phys. Lett.* **60**, 683.
- Tell, B., R.E. Leibenguth, K.F. Brown-Goebeler and G. Livescu, 1992, *IEEE Photon. Technol. Lett.* **4**, 1195.
- Thibeault, B.J., K. Bertilsson, E.R. Hegblom, E. Strzelecka, P.D. Floyd, R. Naone and L.A. Coldren, 1997, *IEEE Photon. Technol. Lett.* **9**, 11.
- Thode, L., G. Csanak, R. Hotchkiss, C. Snell and M. Campbell, 1995, *Proc. SPIE* **2399**, 348.
- Thompson, G.H.B., 1980, *Physics of Semiconductor Laser Devices* (Wiley, Chichester).
- Thurmond, C.D., 1975, *J. Electrochem. Soc.* **122**, 1133.
- Tu, L.W., Y.H. Wang, E.F. Schubert, B.E. Weir, G.J. Zydzik and A.Y. Cho, 1991, *Electron. Lett.* **27**, 457.
- Uchida, T., T. Miyamoto, N. Yokouchi, Y. Inaba, F. Koyama and K. Iga, 1992, 12th International Semiconductor Laser Conference, Takamatsu, Japan, Sept. 21-25, 1992, p. 212.
- Uchiyama, S., and K. Iga, 1984, *IEEE J. Quantum Electron.* **QE-20**, 1117.
- Uchiyama, S., and S. Kashiwa, 1995, *Electron. Lett.* **31**, 1449.
- Uchiyama, S., Y. Ohmae, S. Shimizu and K. Iga, 1986, *J. Lightwave Technol.* **4**, 846.
- Uchiyama, S., N. Yokouchi and T. Ninomiya, 1997, *IEEE Photon. Technol. Lett.* **9**, 141.
- Vail, E.C., G.S. Li, W. Yuen and C.J. Chang-Hasnain, 1996, *Electron. Lett.* **32**, 1888.
- Vakhshoori, D., J.D. Wynn, G.J. Zydzik, R.E. Leibenguth, M.T. Asom, K. Kojima and R.A. Morgan, 1993, *Appl. Phys. Lett.* **62**, 1448.
- Valle, A., J. Sarma and K.A. Shore, 1995a, *Opt. Commun.* **115**, 297.
- Valle, A., J. Sarma and K.A. Shore, 1995b, *IEEE J. Quantum Electron.* **QE-31**, 1423.
- Van der Ziel, J.P., D.G. Deppe, N. Chand, G.J. Zydzik and S.N.G. Chu, 1990, *IEEE J. Quantum Electron.* **QE-26**, 1873.
- Von Lehmen, A., T. Banwell, L. Carrion, N. Stoffel, L. Florez and J. Harbison, 1992, *Electron. Lett.* **28**, 21.
- Vook, F.L., 1964, *Phys. Rev.* **135**, A1742.
- Wada, H., D.I. Babic, D.L. Crawford, T.E. Reynolds, J.J. Dudley, J.E. Bowers, E.L. Hu, J.L. Merz, B.I. Miller, U. Koren and M.G. Young, 1991, *IEEE Photon. Technol. Lett.* **3**, 977.
- Wada, H., D.I. Babic, M. Ishikawa and J.E. Bowers, 1992, *Appl. Phys. Lett.* **60**, 2974.
- Wilson, G.C., M.A. Hadley, J.S. Smith and K.Y. Lau, 1993, *Appl. Phys. Lett.* **63**, 3265.
- Wilson, G.C., D.M. Kuchta, J.D. Walker and J.S. Smith, 1994, *Appl. Phys. Lett.* **64**, 542.
- Wipiejewski, T., K. Panzlaff, E. Zeeb and K.J. Ebeling, 1993, *IEEE Photon. Technol. Lett.* **5**, 889.
- Wipiejewski, T., K. Panzlaff, E. Zeeb and K.J. Ebeling, 1994, *Proc. SPIE* **2147**, 48.

- Wipiejewski, T., M.G. Peters, B.J. Thibeault, D.B. Young and L.A. Coldren, 1996, IEEE Photon. Technol. Lett. **8**, 10.
- Wipiejewski, T., D.B. Young, M.G. Peters, B.J. Thibeault and L.A. Coldren, 1995, Electron. Lett. **31**, 279.
- Wu, C.C., K. Tai and K.F. Huang, 1993, Electron. Lett. **29**, 1953.
- Wu, Y.A., C.J. Chang-Hasnain and R. Nabiev, 1993, Electron. Lett. **29**, 1861.
- Wu, Y.A., C.J. Chang-Hasnain and R. Nabiev, 1994, IEEE Photon. Technol. Lett. **6**, 924.
- Wu, Y.A., G.S. Li, R.F. Nabiev, K.D. Choquette, C. Caneau and C.J. Chang-Hasnain, 1995, IEEE J. Selected Topics Quantum Electron. **1**, 629.
- Wüthrich, C., J.H. James, J.D. Ganière and F.K. Reinhart, 1990, Electron. Lett. **26**, 1600.
- Yan, R.H., and L.A. Coldren, 1990, Appl. Phys. Lett. **57**, 267.
- Yang, G.M., M.H. MacDougall and P.D. Dapkus, 1995, Conference on Lasers and Electro-Optics, CLEO'95, Baltimore, MD, May 22-26, Paper CPD4-1.
- Yoffe, G.W., W.C. van der Vleuten, M.R. Leys, F. Karouta and J.H. Wolter, 1994, Electron. Lett. **30**, 794.
- Yoo, B.-S., H.Y. Chu, M.S. Park, H.-H. Park and E.-H. Lee, 1996, Electron. Lett. **32**, 116.
- Yoo, B.-S., H.-H. Park and E.-H. Lee, 1994, Electron. Lett. **30**, 1060.
- Young, D.B., A. Kapila, J.W. Scott, V. Malhotra and L.A. Coldren, 1994, Electron. Lett. **30**, 233.
- Young, D.B., J.W. Scott, F.H. Peters, M.G. Peters, M.L. Majewski, B.J. Thibeault, S.W. Corzine and L.A. Coldren, 1993, IEEE J. Quantum Electron. **QE-29**, 2613.
- Young, D.B., J.W. Scott, F.H. Peters, B.J. Thibeault, S.W. Corzine, M.G. Peters, S.-L. Lee and L.A. Coldren, 1993, IEEE Photon. Technol. Lett. **5**, 129.
- Young, M., 1993, Optics and Lasers Including Fibers and Optical Waveguides (Springer, Berlin) p. 138.
- Yu, S.F., and C.W. Lo, 1996, IEE Proc. Optoelectron. **143**, 189.
- Zeeb, E., B. Möller, G. Reiner, M. Ries, T. Hackbarth and K.J. Ebeling, 1995, IEEE J. Select. Topics Quantum Electron. **1**, 616.
- Zeeb, E., G. Reiner, M. Ries, B. Möller and K.J. Ebeling, 1995, Conference on Lasers and Electro-Optics, CLEO'95, Baltimore, MD, May 22-26, Paper CWB4.
- Zhao, Y.-G., and J.G. McInerney, 1995, IEEE J. Quantum Electron. **QE-31**, 1668.
- Zhao, Y.-G., and J.G. McInerney, 1996, IEEE J. Quantum Electron. **QE-32**, 1950.
- Zhou, P., J. Cheng, C.F. Schaus, S.Z. Sun, K. Zheng, E. Armour, C. Hains, W. Hsin, D.R. Myers and G.A. Vawter, 1991, IEEE Photon. Technol. Lett. **3**, 591.

Lateral overgrowth mechanisms and microstructural characteristics of bulk-like GaN layers grown by sublimation method

Jie Wang,^{a)} R. S. Qhalid Fareed, M. Hao, and S. Mahanty

Satellite Venture Business Laboratory, University of Tokushima, 2-1 Minami josanjima, Tokushima, Japan

S. Tottori, Y. Ishikawa, T. Sugahara, Y. Morishima, and K. Nishino

Department of Electrical and Electronic Engineering, University of Tokushima, 2-1 Minami josanjima, Tokushima, Japan

M. Osinski

Centre for High Technology Materials, The University of New Mexico, Albuquerque, New Mexico 87106

S. Sakai

Department of Electrical and Electronic Engineering, University of Tokushima, 2-1 Minami josanjima, Tokushima, Japan

(Received 24 July 1998; accepted for publication 26 October 1998)

The selective overgrowth method has been used to grow bulk-like GaN layers by sublimation method. Si and SiO₂, which have a different evaporation rate, thermal conductivity, and thermal expansion coefficient, have been chosen as mask materials. The effect due to the reduction of dislocation density with different mask materials has been discussed. The lateral growth rates strongly depend on the direction of the mask stripe. For the stripe windows aligned in GaN(1 $\bar{1}$ 00) direction, the lateral growth rate is approximately four times higher than with stripe direction in GaN(11 $\bar{2}$ 0). The microstructure of selectively regrown GaN has been investigated by transmission electron microscopy, scanning electron microscopy, and cathodoluminescence to understand the lateral growth mechanisms in sublimation. The threading dislocations in the region of laterally regrown GaN are extended in two different ways. First, the threading dislocations are perpendicularly propagated into the top surface in the window region. In this case, the density of the threading dislocation is about 10⁹ cm⁻² within the window regions of the mask and is reduced to 10⁶ cm⁻² in the lateral overgrowth region of the mask due to termination of further propagation of dislocation by the mask. Second, the direction of propagation of dislocations is changed parallel to the *c* plane in laterally overgrown GaN, and finally, it changes in the direction perpendicular to the *c* plane in the middle region of the mask. © 1999 American Institute of Physics.

[S0021-8979(99)06603-7]

I. INTRODUCTION

Since no suitable substrate is presently available for GaN growth, most device structures have been fabricated on sapphire or 6H-SiC substrates.¹⁻³ Due to the large lattice mismatch, nitride epitaxial layers contain a high density of extended defects, which affect the device performance. One of the methods to reduce dislocation density in an active region of a device is to use the lateral overgrowth method.⁴⁻¹¹ In this method, the threading dislocations present in the GaN layers, originating at the GaN/sapphire interface, are blocked by the mask. The density of threading dislocation is dramatically reduced in the laterally regrown regions.

Most of the researchers have used SiO₂ as the mask material for the lateral growth. However, its low thermal conductivity and large mismatch of thermal expansion with GaN are serious problems when the lateral growth temperature of GaN is about 1050 °C. Compared to SiO₂, Si has a larger thermal conductivity and the thermal expansion coefficient

mismatch of Si/GaN is smaller than that of SiO₂/GaN, as listed in Table I. Thus, it is reasonable to choose Si as the mask material for the lateral overgrowth of GaN.

Compared to metalorganic chemical vapor deposition (MOCVD), the sublimation technique is the most suitable and simple method for lateral overgrowth.¹²⁻¹⁴ The sublimation method is a promising technique to grow bulk GaN crystals or thick GaN films on crystalline substrates. Since the system of this sublimation technique is very simple and is only an atmospheric process, scaling up is easier. It is also a cost effective process since only metallic gallium and NH₃ are used as sources. It should be emphasized that the growth rate in sublimation is very high. Over 50- μ m-thick GaN films can be deposited by sublimation in 1 h of growth at 1050 °C. These features of the sublimation method are important to grow thick GaN films on the large area substrates and make this technique very attractive for the lateral overgrowth of GaN on a partly covered GaN on sapphire substrate. In our previous research work, we have grown bulk crystals of GaN with a maximum size of about 3 mm in length and 0.8 mm in diameter.^{12,13}

^{a)}Electronic mail: jiewang@svbl.tokushima-u.ac.jp

TABLE I. Parameters of GaN and relevant mask materials.

Materials	Lattice parameters (Å)	Thermal conductivity (W/cm K)	Coefficients of thermal expansion (10^{-6} K $^{-1}$)
GaN	$A=3.189$, $C=5.185$	1.3	$A=5.59$, $C=3.17$
SiO ₂	Amorphous	0.014	0.5
Si	$A=5.4301$	1.5	3.59

II. EXPERIMENT

The lateral overgrowth of GaN has been carried out by the sublimation technique. During the growth, the source powder and substrate were placed in a graphite crucible and 50 sccm of NH₃ were introduced into the crucible. The growth temperature varied from 970 to 1100 °C. After 1 h of growth at 995 °C, the source powder becomes black from the original color of gray, indicating that the active species in the source powder were exhausted. Therefore, the grown layer thickness was not proportional to the growth time. Under these growth conditions, the growth rate is very high in the initial stages, but as the experiment progresses, growth rate decreases with time and finally stops due to the exhaustion of effective Ga source.

Each of the initial 1.5–3.0- μ m-thick GaN films was grown by MOCVD. These films were subsequently deposited with the 0.1–0.2 μ m Si and SiO₂ films by electron beam evaporation at room temperature. Stripe windows with different direction, width and, space were patterned by the conventional photolithography.¹⁴ Prior to the lateral overgrowth of sublimation, the patterned GaN substrates were first cleaned by acetone, methanol, and deionized water. Then they were dipped in KOH solution for 10 min using the photoassisted wet-etching method to remove the surface oxide of the underlying GaN layer.

The microstructure of selectively regrown GaN bulk-like layers and the lateral growth mechanisms have been investigated by transmission electron microscopy (TEM), scanning electron microscopy (SEM), and cathodoluminescence (CL).

III. RESULTS AND DISCUSSION

The strong dependence of growth conditions on the stripe orientation during the lateral overgrowth of GaN using MOCVD has been reported by many researchers. The optimized lateral overgrowth conditions of MOCVD have been presented by Kapolnek⁶ and Nam *et al.*¹⁵ However, the growth mechanisms of sublimation and MOCVD are very different. Hence, it is essential to know the best lateral overgrowth conditions in the sublimation method. In order to investigate orientational dependence of the lateral growth rate in sublimation, a star-like mask pattern was used. The mask pattern consists of a star feature with lines at 30° angular span, parallel to the $\langle 1\bar{1}00 \rangle$ and $\langle 11\bar{2}0 \rangle$ directions surrounded by the large masked regions. The star consists of 12 consecutive lines of 10 μ m opening width. Figure 1(a) is a top-view SEM image of a selectively regrown GaN sample with a star-like mask pattern grown at 995 °C for 1 h. The lateral growth rate varies between its maximum and mini-

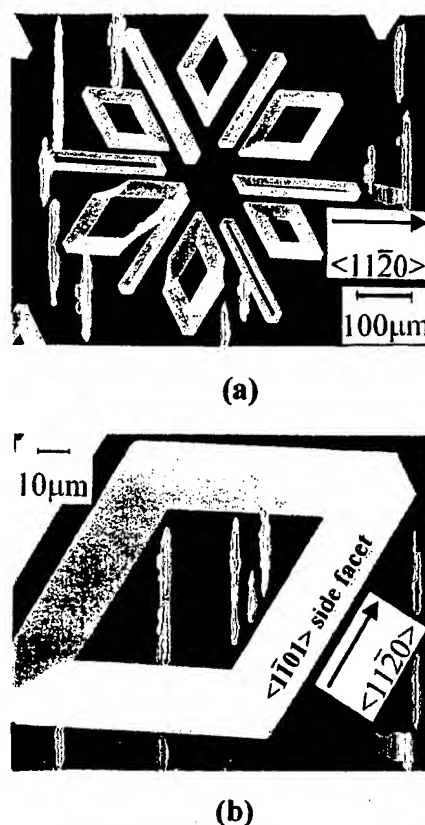


FIG. 1. (a) Top-view SEM image of a GaN sample with star-like mask pattern grown at 995 °C for 1 h. (b) Top-view SEM image of a lateral regrown GaN with an opening stripe window along the direction of GaN($1\bar{1}00$).

mum values at 60° intervals. The growth rate is the maximum when the stripe window is aligned along the $\langle 1\bar{1}00 \rangle$ direction of GaN, as in the case of MOCVD.¹⁵ After growth for 1 h with the stripe direction of GaN($1\bar{1}00$), the lateral and vertical growth lengths are about 60 and 20 μ m, respectively. It is important to note that the rate of lateral growth is about three times larger than the rate of vertical growth. However, the lateral growth length is only 15 μ m at the same growth condition when the stripe direction is parallel to the GaN($11\bar{2}0$). These results are almost the same with that of MOCVD overgrowth.¹⁵

Figure 1(b) is a top-view SEM image of laterally regrown GaN sample with one opening stripe at the same growth condition shown in Fig. 1(a), the stripe direction being oriented along GaN($1\bar{1}00$). As usual, the stripe subsequently developed into a rhombus with $\{1\bar{1}01\}$ side facets with the edge of the rhombus along $\langle 11\bar{2}0 \rangle$. In only a few cases, vertical $\{11\bar{2}0\}$ side facets were developed in the middle region of the rhombus. These results are different from that of MOCVD overgrowth. It usually forms rectangular stripes with vertical $\{11\bar{2}0\}$ side facets for MOCVD overgrowth.¹⁵ However, for the stripe direction along $\langle 1\bar{1}00 \rangle$, the result of sublimation overgrowth similar to that of MOCVD overgrowth, and a stripe with $\{1\bar{1}01\}$ side facets have always been developed as shown in Fig. 1(a). Due to the very high growth rate in sublimation, it was assumed that

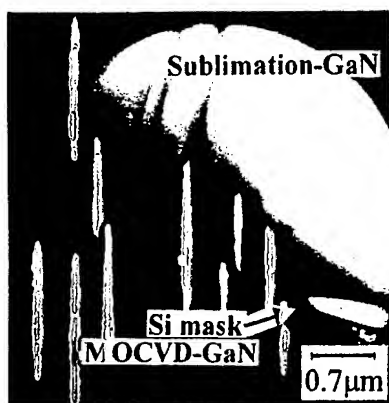


FIG. 4. Cross-section TEM micrograph from a selectively grown GaN on the Si mask with stripe direction in $\langle 1\bar{1}00 \rangle$ and having $\{11\bar{2}0\}$ side facets.

tions in initial MOCVD-GaN layer propagate into sublimation-GaN layers. Since there is no $\{1\bar{1}01\}$ side facet to intersect vertical threading dislocations, the dislocations subsequently propagate to the top surface of the regrown GaN. If the surface of initial MOCVD-GaN substrate was thoroughly clear prior to the select growth of GaN by sublimation, no threading dislocations were newly generated at the interface. In this case, the density of threading dislocations is about 10^9 cm^{-2} above the window areas, and is reduced to 10^6 cm^{-2} in the lateral overgrowth region on the Si mask. From Fig. 4, we did not find the voids in the central region of the sublimation-GaN on the masks. These voids were mostly observed in MOCVD grown layers under the lateral growth conditions, wherein rectangular stripe with vertical $\{11\bar{2}0\}$ side facets developed.

To investigate the distribution of radiative defects across the sublimation-GaN layer, room temperature CL experiments have been performed. The sample used for CL measurement contains the SiO_2 mask of $8\text{-}\mu\text{m}$ -wide windows spaced $8\text{ }\mu\text{m}$ apart with stripe direction in $\langle 1\bar{1}00 \rangle$ and having $\{1\bar{1}01\}$ side facets. Prior to the CL measurement, the top and cross-section surfaces of the sample were polished. Figure 5(a) shows the sample structure and the thin lines show $\{1\bar{1}01\}$ side facets. Figure 5(b) shows the room temperature cross-section CL images taken at 362 nm corresponding to the band-edge emission of GaN. It clearly shows a strong emission in region II. However, in regions I and III, it is difficult to observe the luminescence at 362 nm . Zheleva *et al.* have reported the inferior quality of regrown GaN in region I and the density of threading dislocations is about 10^9 cm^{-2} in region I.⁹ The change in the direction of the threading dislocations is focused in region III, as shown in Fig. 3. Thus, the weak band-edge emission of GaN is acceptable in these two regions. The edges between white and black regions are near $\{1\bar{1}01\}$ side facets.

According to TEM measurement, the density of the threading dislocation in region I is almost the same with the underlying MOCVD-GaN layer. However, the emission at 362 nm can be observed in the region of underlying MOCVD-GaN layer, and there is no emission from region I. Thus, the impurities and point defects originating from the

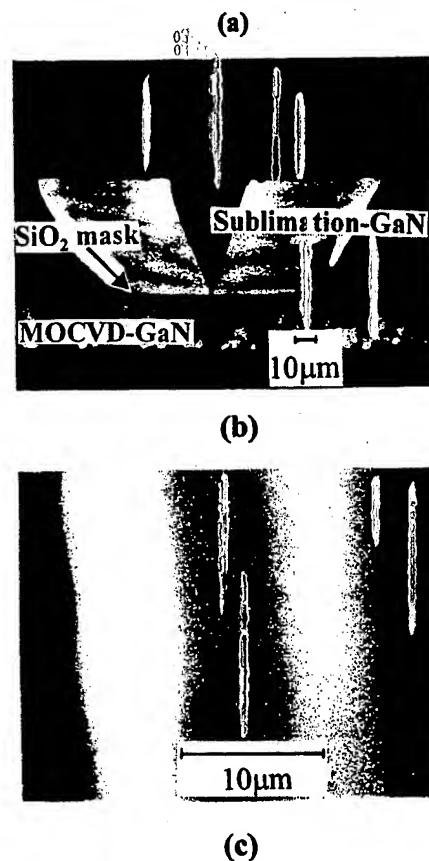
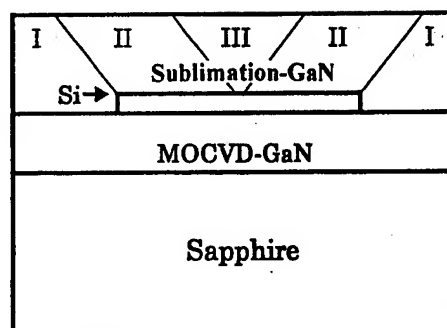


FIG. 5. (a) Structure of lateral overgrowth GaN sample used for CL measurement. (b) Room temperature cross-section CL images taken at 362 nm corresponding to the band-edge emission of GaN. (c) Top-view CL images of the sample taken at 362 nm at room temperature.

sublimation growth are other causes for the reduction of band-edge emission. Figure 5(c) is a top-view CL image of the sample taken at 362 nm at room temperature. The results correspond to that shown in Figs. 3 and 5(b). It is worth noting, the stronger emission is in region II than that in the underlying MOCVD-GaN layer.

For the sample with vertical $\{11\bar{2}0\}$ side facets, the threading dislocations are focussed on the window regions of the regrown GaN layer, and no new dislocations are generated on the mask regions in spite of Si and SiO_2 used as mask materials. For the sample with $\{1\bar{1}01\}$ side facets and in the window region, all threading dislocations turn the direction into the mask region, and no threading dislocations were observed in the top region of window. In this case, there is no difference in using Si and SiO_2 as mask materials.

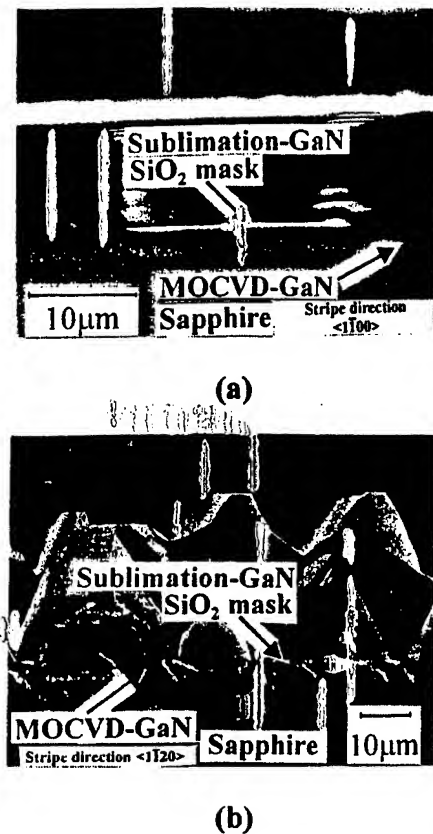


FIG. 2. (a) Cross-section SEM micrograph from selective grown GaN within 10 μm wide stripe windows spaced 20 μm apart and stripe direction in GaN($1\bar{1}00$). (b) Cross-section SEM micrograph of sample within 10- μm -wide stripe windows spaced only 8 μm apart and stripe direction in GaN($11\bar{2}0$).

it would be difficult to control the roughness of (0001) top surface. However, the top surface is found to be atomically flat, as shown in Fig. 1(b). Hence, it is possible to have a continuous thick layer and can be directly used as substrates for homoepitaxial growth of GaN.

Figure 2(a) is the cross-section SEM micrograph from a selectively regrown GaN sample within 10- μm -wide stripe windows spaced 20 μm apart with the stripe direction in GaN($1\bar{1}00$). Since the lateral growth rate is about three times larger than that of vertical growth, it is very easy for coalescence and to form a continuous film with a very flat surface. However, for the stripe direction of GaN($11\bar{2}0$), the situation of lateral overgrowth becomes very different. Due to low lateral growth rate, it is very difficult for the coalescence and to form a continuous film. Fig. 2(b) is the cross-section SEM micrograph of a sample within 10- μm -wide stripe windows spaced only 8 μm apart and stripe direction in GaN($11\bar{2}0$). After vertical growth length reaches 40 μm , coalescence takes place, but the surface is still very rough.

The distribution of threading dislocations in the region of laterally regrown GaN strongly depends on the formation of $\{1\bar{1}01\}$ and $\{11\bar{2}0\}$ side facets. Figure 3(a) is a cross-section TEM micrograph from a selectively regrown GaN on the SiO_2 mask with stripe direction in $\langle 1\bar{1}00 \rangle$ and having $\{1\bar{1}01\}$ side facets. In the region of regrown GaN, the per-

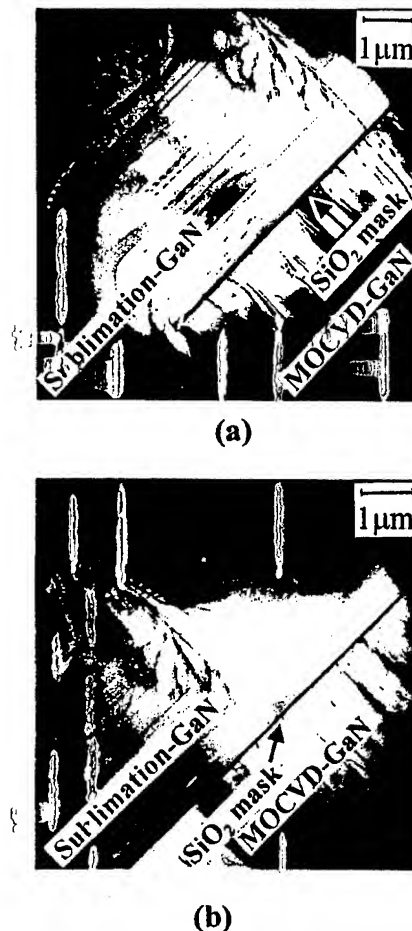


FIG. 3. (a) Cross-section TEM micrograph from a selectively grown GaN on the SiO_2 mask with stripe direction in $\langle 1\bar{1}00 \rangle$ and having $\{1\bar{1}01\}$ side facets. (b) Cross-section TEM micrograph from a selectively grown GaN in the middle region of the SiO_2 mask with stripe direction in $\langle 1\bar{1}00 \rangle$ and having $\{1\bar{1}01\}$ side facets.

pendicular propagation of threading dislocations in an underlying MOCVD-GaN layer was intersected by $\{1\bar{1}01\}$ side facets in the window region, and threading dislocations changes its direction parallel to the c plane. Then parallel propagation of threading dislocations extends into the mask region till the middle of the mask and they are intersected again by $\{1\bar{1}01\}$ side facets formed in the middle region of the mask. Thus, the extension of parallel threading dislocations changed direction again perpendicular to the c plane in the middle region of the mask, as shown in Fig. 3(a). Finally, all the dislocations were focused on the middle region of the mask to form a high-density threading dislocation band with a width of 2–3 μm , and they perpendicularly propagated to the top surface, as shown in Fig. 3(b). In this case, the $\{1\bar{1}01\}$ side facet acts as a mirror to refraction of dislocations.

Figure 4 shows a cross-section TEM micrograph from a selectively regrown GaN on the Si mask with stripe direction in $\langle 1\bar{1}00 \rangle$ and having vertical $\{11\bar{2}0\}$ side facets. In this case, the perpendicular extension of threading dislocations has been terminated by the Si mask in the mask region. However, in the stripe window region, almost all disloca-

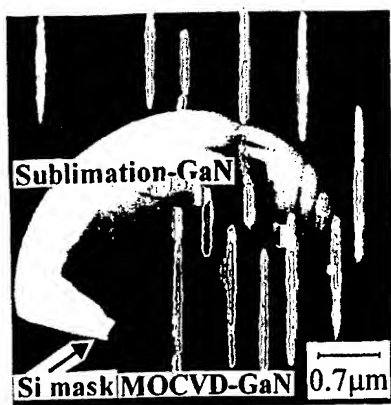


FIG. 6. Cross-section TEM micrograph of the lateral overgrowth GaN sample by sublimation with the Si mask and stripe direction in $\langle 11\bar{2}0 \rangle$.

In spite of the directional change of threading dislocations in the window region of the SiO_2 mask region for the sample with $\{1\bar{1}01\}$ side facets, many new stacking faults are found to be generated due to the very low thermal conductivity and large mismatch of thermal expansion with GaN, as observed in Fig. 3. In this case, the threading dislocations turning from the window region act as "seed" to cause the stacking faults in the region of the mask. Detailed studies of the phenomenon will be presented elsewhere. This different situation happens when the Si mask material is used. The threading dislocation density of perpendicular propagation is almost the same as that of parallel propagation, as shown in Fig. 6. It is difficult to observe the newly generated dislocation in the Si mask region.

IV. CONCLUSION

Lateral overgrowth of GaN has been carried out using the sublimation method. Compared to MOCVD, the sublimation technique is very suitable for lateral overgrowth due to a higher growth rate. The lateral growth rate of a stripe window along $\langle 1\bar{1}00 \rangle$ direction is about three times larger than that of vertical growth, and it is easy to form a continuous film with a mirror-like surface. However, in the stripe direction of $\langle 11\bar{2}0 \rangle$, the rate of lateral overgrowth is even less than that of vertical growth and is difficult to grow continu-

ously with a flat surface. For the sample with formation of vertical $\{11\bar{2}0\}$ side facets, the threading dislocations in the regrown GaN layers are mainly distributed in the window regions and only a small number of dislocations turn a 90° bend into the mask region. However, for the sample grown with $\{110\bar{1}\}$ side facets, almost all threading dislocations in the window region turn the direction from the nearly perpendicular to the c plane to parallel to the c plane. The formation of the 2–3 μm threading dislocation band in the middle region of the mask is very beneficial for growing device structure in top region. Si and SiO_2 materials have been chosen to make the mask on the MOCVD-GaN layers. Experimental results also show that Si is a better material for fabricating the mask due to the larger thermal conductivity and smaller thermal mismatch with GaN. For the sample with $\{110\bar{1}\}$ side facets, many stacking faults near the SiO_2 mask in selectively regrown GaN are observed. However, it is difficult to find newly generated stacking faults or threading dislocations in the regrown GaN layer with the Si mask.

¹S. Nakamura and G. Fasol, *The Blue Laser Diode* (Springer, Heidelberg, 1997).

²H. Morkoç, S. Strite, G. B. Gao, M. E. Lin, B. Sverdlov, and M. Burns, *J. Appl. Phys.* **76**, 1363 (1994).

³S. N. Mohammad, A. A. Salvador, and H. Morkoç, *Proc. IEEE* **83**, 1306 (1995).

⁴Y. Kato, S. Kitamura, K. Hiramatsu, and N. Sawaki, *J. Cryst. Growth* **144**, 133 (1994).

⁵S. Nakamura et al., *Jpn. J. Appl. Phys., Part 2* **36**, L1568 (1997).

⁶D. Kapolnek, S. Keller, R. Vetury, R. D. Underwood, P. Kozodoy, S. P. Den Baars, and U. K. Mishra, *Appl. Phys. Lett.* **71**, 1204 (1997).

⁷X. Li, A. M. Jones, S. D. Roh, D. A. Turnbull, S. G. Bishop, and J. J. Coleman, *J. Electron. Mater.* **26**, 306 (1997).

⁸S. Nakamura et al., *Jpn. J. Appl. Phys., Part 2* **37**, L309 (1998).

⁹T. S. Zheleva, O. H. Nam, M. D. Bremser, and R. F. Davis, *Appl. Phys. Lett.* **71**, 2472 (1997).

¹⁰A. Sakai, H. Sunakawa, and A. Usui, *Appl. Phys. Lett.* **71**, 2259 (1997).

¹¹A. Usui, H. Sunakawa, A. Sakai, and A. A. Yamaguchi, *Jpn. J. Appl. Phys., Part 2* **36**, L899 (1997).

¹²S. Kurai, K. Nishino, and S. Sakai, *Jpn. J. Appl. Phys., Part 2* **36**, L184 (1997).

¹³Y. Naoi, K. Kobatake, S. Kurai, K. Nishino, H. Sato, M. Nozaki, S. Sakai, and Y. Shintani, *J. Cryst. Growth* **190**, 163 (1997).

¹⁴J. Wang, S. Tottori, H. Sato, M. S. Hao, Y. Ishikawa, T. Sugahara, K. Yamashita, and S. Sakai, *Jpn. J. Appl. Phys., Part 1* **37**, 4475 (1998).

¹⁵O. H. Nam, M. D. Bremser, T. S. Zheleva, and R. F. Davis, *Appl. Phys. Lett.* **71**, 2638 (1997).

3. T.J. Schmidt, Y.H. Cho, G.H. Gainer, J.J. Song, S. Keller, U.K. Mishra, and S.P. DenBaars, *Appl. Phys. Lett.* 73, 560 (1998).
4. T.J. Schmidt, S. Bidnyk, Y.H. Cho, A.J. Fischer, J.J. Song, S. Keller, U.K. Mishra, and S.P. DenBaars, *MRS Internet J. Nitride Semicond. Res.* 4S1, G6.54 (1999).

CTuU5

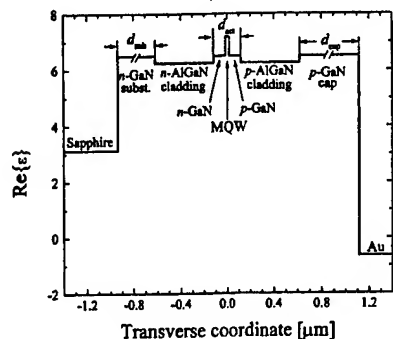
5:30 pm

Design limitations for InGaN/AlGaIn/GaN lasers imposed by resonant mode coupling

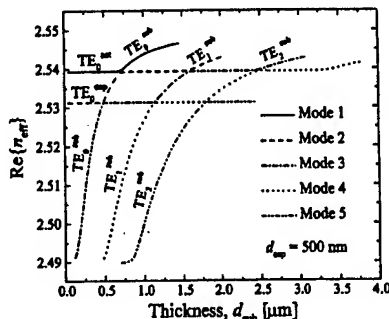
Gennady A. Smolyakov, Petr G. Eliseev,* Marek Osinski, *Center for High Technology Materials, University of New Mexico, 1313 Goddard SE, Albuquerque, New Mexico 87106 USA; E-mail: osinski@chtm.unm.edu*

Present-day InGaN/AlGaIn/GaN semiconductor lasers typically contain a multiple optical waveguide structure, with refractive indices of several layers (GaN buffer-substrate, active region, cap layer) higher than those of cladding layers. This leads to complex behavior of optical modes that has recently been subject of several investigations.¹⁻⁵ In particular, resonant effects have been obtained in simulations of modes localized in the active region, with modulation of modal gain when thicknesses of active waveguide core or cladding layers were changed.^{1,2} Those numerical solutions traced only the modes localized in the active layer, which is not sufficient to understand the nature of these resonances. Here, we show that resonant effects in nitride lasers result from coupling between nearly-degenerate normal modes of the entire laser structure, similarly to the case of InGaAs-based lasers analyzed previously.^{6,7} We also demonstrate the strong role of the parasitic waveguide thicknesses, in addition to previously investigated parameters.

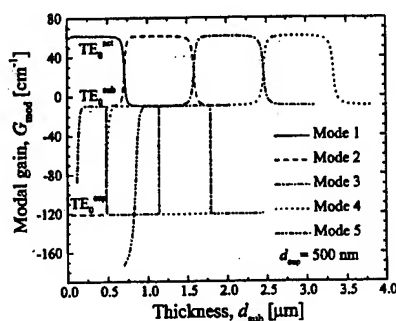
The analysis is performed in terms of TE normal modes of a multiple waveguide system, found as solutions of the scalar wave equation for a realistic profile of complex permittivity in a nitride laser structure (see Fig. 1). To demon-



CTuU5 Fig. 1. Permittivity profile of a typical InGaN/AlGaIn/GaN diode laser. The active region is assumed to consist of four $\text{In}_{0.15}\text{Ga}_{0.85}\text{N}$ quantum-well layers separated by three $\text{In}_{0.02}\text{Ga}_{0.98}\text{N}$ barriers. The material gain in the quantum wells is taken as 1000 cm^{-1} at the fixed wavelength of 400 nm. The absorption coefficient α is taken as 10 cm^{-1} in all remaining layers except for the Au contact layer, where the extinction coefficient $\kappa = 1.7$ corresponds to $\alpha = 5.34 \times 10^5 \text{ cm}^{-1}$.



CTuU5 Fig. 2. Calculated effective index n_{eff} for the first 5 lowest-order normal modes of TE polarization in the three-waveguide system of the p-GaN cap layer, active waveguide, and n-GaN substrate layer as a function of the GaN substrate layer thickness d_{sub} . Normal modes 1, 2, 3, ... are identified by careful tracing of the solution for n_{eff} near the resonance. The notation TE_N^{act} , TE_N^{cp} , and TE_N^{sub} ($N = 0, 1, 2, \dots$) identifies the TE_N modes of the corresponding individual uncoupled waveguides (active layer, cap layer, and substrate layer) to which the normal modes of the structure are very close for a particular range of values of d_{sub} .



CTuU5 Fig. 3. Modal gain G_{mod} calculated for the same first 5 lowest-order normal modes of TE polarization and the same InGaN/AlGaIn/GaN laser structure as in Fig. 2.

strate the resonant effects, we vary the thicknesses of various passive layers (GaN cap d_{cap} , GaN substrate layer d_{sub} , or claddings d_{clad}) and follow the solutions for several transverse modes. Calculated results are plotted in terms of the effective index and modal gain.

The effective index and modal gain for the first five normal modes in the three-waveguide system of GaN substrate layer—active waveguide—GaN cap layer are shown in Figs. 2–3 as a function of d_{sub} . The cap layer thickness is in this case fixed at $d_{\text{cap}} = 500 \text{ nm}$. Multiple resonances both in the active waveguide—GaN substrate system and in the GaN cap layer—GaN substrate system can be clearly seen. Dramatic drop in the modal gain occurs at every point of resonance, i.e. when the complex propagation constants of the modes localized in the active region and in the substrate become very close to each other. Note that the mode TE_0^{act} localized in the active layer actually corresponds to a sequence of normal modes emerging at subsequent resonances. We have found similar resonant effects and resonant values for d_{cap} in the active waveguide—GaN cap layer system. Obviously,

a device with an unfortunate design of d_{cap} or d_{sub} close to the resonant values would either have a much higher threshold, or would not lase at all.

We have found that the resonances become broader for thinner optical barriers, which means that AlGaIn claddings should be kept reasonably thick. This result agrees with observations of Nakamura *et al.*,⁸ who noticed that spectral modulation of superluminescence spectra, one of the signatures of resonant mode coupling,^{6,7} became much smaller when optical barriers were made thicker. However, we should emphasize that even with thin claddings it is still possible to avoid the resonances when laser design is combined with careful analysis of mode coupling.

In conclusion, we have analyzed numerically the optical modes of a system of coupled waveguides characteristic of InGaN/AlGaIn/GaN laser diodes and explained the nature of resonant effects in those devices. The results demonstrate that in order to obtain low-threshold operation, special care must be taken when deciding on what particular values should be chosen for d_{cap} , d_{sub} , d_{act} , and d_{clad} . Optimization of laser design should include conscious avoidance of resonant values for any combination of these parameters.

*Also with P.N. Lebedev Physics Institute, Russian Academy of Sciences, Moscow, Russia

1. V.E. Bougrov and A.S. Zubrilov, *J. Appl. Phys.* 81, 2952 (1997).
2. M.J. Bergmann and H.C. Casey, *J. Appl. Phys.* 84, 1196 (1998).
3. M. Onomura, S. Saito, K. Sasanuma, G. Hatakoshi, M. Nakasuji, J. Rennie, L. Sugiyama, S. Nunoue, M. Suzuki, J. Nishio, and K. Itaya, *Conf. Digest, 1998 IEEE 16th Int. Semicond. Laser Conf., Nara, Japan, 4–8 Oct. 1998*, p. 7.
4. M.P. Mack, D.K. Young, A.C. Abare, M. Hansen, L.A. Coldren, J.S. Speck, E.L. Hu, D.D. Awschalom, and S.P. DenBaars, *Conf. Digest, 1998 IEEE 16th Int. Semicond. Laser Conf., Nara, Japan, 4–8 Oct. 1998*, p. 9.
5. S. Heppel, J. Off, F. Scholz, and A. Hangleiter, *Conf. Digest, 1998 IEEE 16th Int. Semicond. Laser Conf., Nara, Japan, 4–8 Oct. 1998*, p. 11.
6. P.G. Eliseev and A.E. Drakin, *Laser Phys.* 4, 485 (1994).
7. I.A. Avrutsky, R. Gordon, R. Clayton, and J.M. Xu, *IEEE J. Quantum Electron.* 33, 1801 (1997).
8. S. Nakamura, M. Senoh, S. Nagahama, N. Iwasa, T. Yamada, T. Matsushita, H. Kiyoku, Y. Sugimoto, T. Kozaki, H. Umemoto, M. Sano, and K. Chocho, *Appl. Phys. Lett.* 72, 2014 (1998).

Articles in this publication may be cited in other publications. To facilitate access to the original publication source, the following form for the citation is suggested:

Name of Author(s), "Title of Paper," in *Conference on Lasers and Electro-Optics*,
OSA Technical Digest (Optical Society of America, Washington DC, 1999), pp. xx-xx.

Optical Society of America

ISBN

Conference Edition 1-55752-570-6

Postconference Edition 1-55752-595-1

(Note: Postconference Edition
includes postdeadline papers.)

1999 Technical Digest Series 1-55752-584-6

Institute of Electrical and Electronics Engineers

ISBN

Casebound 0-7803-5656-X

Microfiche 0-7803-5657-8

Catalog Number 99CH37013

Library of Congress Catalogue Card Number

Conference Edition 99-60510

Postconference Edition 98-89988

Copyright © 1999, Optical Society of America

Individual readers of this digest and libraries acting for them are permitted to make fair use of the material in it, such as to copy an article for use in teaching or research, without payment of fee, provided that such copies are not sold. Copying for sale is subject to payment of copying fees. The code 1-55752-584-6/99/\$15.00 gives the per-article copying fee for each copy of the article made beyond the free copying permitted under Sections 107 and 108 of the U.S. Copyright Law. The fee should be paid through the Copyright Clearance Center, Inc., 21 Congress Street, Salem, MA 01970.

Permission is granted to quote excerpts from articles in this digest in scientific works with the customary acknowledgment of the source, including the author's name and the name of the digest, page, year, and name of the Society. Reproduction of figures and tables is likewise permitted in other articles and books provided that the same information is printed with them and notification is given to the Optical Society of America. In addition, the Optical Society may require that permission also be obtained from one of the authors. Address inquiries and notices to Director of Publications, Optical Society of America, 2010 Massachusetts Avenue, NW, Washington, DC 20036-1023. In the case of articles whose authors are employees of the United States Government or its contractors or grantees, the Optical Society of America recognizes the right of the United States Government to retain a nonexclusive, royalty free license to use the author's copyrighted article for United States Government purposes.

Printed in the U.S.A.

CLEO®'99

Conference on Lasers and Electro-Optics

**1999 Technical
Digest Series**

**Marriott
Convention Center
Baltimore,
Maryland**

May 23-28, 1999

CLEO '99 Sponsored by
IEEE/Lasers and
Electro-Optics Society
Optical Society of America

In Cooperation with
Quantum Electronics
Division of the European
Physical Optical Society
Japanese Quantum
Electronics Joint Group



OSA
Optical Society of America

TECHNICAL DIGEST

**SUMMARY OF PAPERS PRESENTED
AT THE CONFERENCE ON LASERS
AND ELECTRO-OPTICS**



[Faint, illegible markings]

Ghost Modes and Resonant Effects in AlGaIn-InGaIn-GaN Lasers

Petr G. Eliseev, *Senior Member, IEEE*, Gennady A. Smolyakov, and Marek Osiński, *Senior Member, IEEE*

Abstract—Many diode laser structures, including those based on group-III nitride system, contain passive waveguide layers of higher refractive index than in the adjacent layers. Modes of such passive waveguides ("passive" modes) can interact with an active layer mode ("active" mode), giving rise to two kinds of normal modes or "supermodes" of a laser structure. Away from resonance, one of them is localized predominantly in the active region ("lasing" mode), while the other ones are located mostly in passive waveguides ("ghost" modes). The *lasing* mode is the mode at which laser generation occurs. The lossy *ghost* modes are parasitic modes of a laser structure that can consume energy from the active region. Resonant coupling occurs when the lasing mode and a ghost mode are in phase synchronism. In this paper, the concept of ghost modes is applied to InGaIn-based diode lasers. The values for critical thickness are calculated for p-GaN cap layer and for n-GaN buffer/substrate layer for a particular multilayer laser structure. The typical thickness of 0.5 μm of AlGaIn-cladding layer is found to be insufficient to prevent rather strong coupling between the modes. Under the resonant coupling conditions, the modal gain is shown to be strongly suppressed, allowing no lasing at all.

Index Terms—Coupled-mode analysis, ghost modes, group-III nitrides, optical waveguide theory, resonant coupling, semiconductor lasers, short-wavelength lasers.

I. INTRODUCTION

THE CONCEPT of *ghost* modes was originally introduced to explain some spectral features (periodic modulation in the envelopes of laser emission spectra) observed in InGaAs-GaAs-AlGaAs diode lasers on GaAs substrates [1]. Essentially, the issue was that passive waveguides existed within the diode chip, supporting their own systems of guided passive modes that could interact with an active layer mode (this effect was called *the internal mode coupling* [1]). The chip of those laser diodes was mostly transparent to the emission generated in the InGaAs active region. A very similar situation exists in InGaIn-GaN-AlGaIn laser diodes on sapphire [2]–[9] and GaN [10]–[12] substrates, where the laser emission easily penetrates into all the layers of the chip due to diffraction and scattering and can be accumulated within the layers with guiding properties. In an early study on spectral properties of InGaIn-GaN-AlGaIn diode lasers [13],

a "subband" modulation effect was found, closely resembling that observed in InGaAs lasers. All this indicates that the concept of ghost modes could be of practical importance for InGaIn-based lasers.

A typical design of a nitride-based laser incorporates a multiple optical waveguide structure (albeit unintentional), with refractive indices of several layers (GaN buffer/substrate, active region, etch-stop layers, GaN cap layer, and some auxiliary layers introduced to stabilize the epitaxial structure) being higher than those of adjacent layers. When any of the AlGaIn cladding layers is thin (500 nm or less), the laser light may penetrate into passive waveguides. This could lead to additional optical losses, higher threshold current, and lower efficiency of the device. A particularly strong effect is expected in the case of *phase synchronism*, when the phase velocities of eigenmodes of individual waveguides, treated as uncoupled, would be the same. Under those conditions, resonant mode coupling would occur, with significant reduction of the optical confinement factor and suppression of the modal gain. It is worthy to mention that low Al-content and thin cladding layers of AlGaIn are of technological advantage (lower misfit stresses, shorter and simpler growth process). Therefore, a thin-cladding structure should be carefully optimized when designing an InGaIn-based diode laser. In experimental studies of InGaIn-GaN-AlGaIn lasers, a complicated spectral and spatial effects have been reported [14]–[16]. In waveguide calculations, the resonant-like modal behavior has been observed [17]–[19]. Thus, the internal mode coupling described in [1] seems indeed to be very important in new InGaIn-based laser structures.

Complex behavior of modes in multilayer systems can be understood using the approach of normal modes of coupled waveguides (see, e.g., [20]). In this paper, we apply this approach to InGaIn-based laser structures. In Section II, the concept of ghost modes is discussed in more detail. The InGaIn-GaN-AlGaIn laser structure is described in Section III. The numerical technique adopted for solving the wave equation is briefly discussed in Section IV. The effective index and the modal gain of normal modes are calculated as a function of the thickness of either the passive waveguides (p-GaN cap layer and n-GaN buffer/substrate) or the optical barriers (AlGaIn cladding layers). The results of calculations are gathered in Section V. We consider separately the resonances in the active waveguide—cap layer system and in the active waveguide—GaN buffer/substrate system. We find that interaction between the lasing mode and the ghost modes can suppress the modal gain substantially, or even stop the

Manuscript received December 1, 1998; revised May 28, 1999. This work was supported by the Defense Advanced Research Projects Agency under the Optoelectronic Materials Center program and by the Air Force Office of Scientific Research.

P. G. Eliseev is with the Center for High Technology Materials, University of New Mexico, Albuquerque, NM 87106 USA. He is also with the Physics Institute, Russian Academy of Sciences, Moscow, 117924 Russia.

G. A. Smolyakov and M. Osiński are with the Center for High Technology Materials, University of New Mexico, Albuquerque, NM 87106 USA.

Publisher Item Identifier S 1077-260X(99)06947-6.

TABLE I
OPTICAL PARAMETERS OF THE MATERIALS COMPRISING THE InGaN-GaN-AlGaN MQW LASER STRUCTURE

Material	n	k	Thickness [nm]	Comments
Au	1.5	1.7	∞	Electrode material; data at 400 nm
Cr	2.75	3.0	∞	Electrode material; data at 488 nm
p-GaN	2.55	0.000032	100-2000	p-cap layer
p-Al _{0.14} Ga _{0.86} N	2.50	0.000032	300-800	p-cladding (optical barrier) layer
p-GaN	2.55	0.000032	100	p-waveguide layer
In _{0.13} Ga _{0.87} N(4) +	2.75	-0.0032	4×3.5	QWs (gain coefficient 1000 cm ⁻¹)
In _{0.02} Ga _{0.98} N(3)	2.63	0.000032	3×7	barriers (absorption ~10 cm ⁻¹)
n-GaN	2.55	0.000032	100	n-waveguide layer
n-Al _{0.14} Ga _{0.86} N	2.50	0.000032	300-800	n-cladding (optical barrier) layer
n-GaN	2.55	0.000032	100-4000	n-buffer/substrate
α -Al ₂ O ₃	1.77	0.000032	∞	sapphire substrate

lasing action entirely. Finally, Section VI contains discussion of the results presented in Section V and conclusions. The results shown in this paper should be useful in group-III nitride laser design as they provide guidelines for waveguide structure optimization and the rules how to avoid the undesirable resonances with ghost modes.

II. CONCEPT OF GHOST MODES

An accurate analysis of a coupled waveguide system gives field configurations (normal modes) that are often approximated by *supermodes* (see, e.g., [20]). These are in-phase or in-antiphase superpositions of the modes of individual uncoupled waveguides. This approximation is valid only *far away from resonance*, when the modes have different phase velocities.

Consider first the off-resonance situation. In this case, it is easy to identify the modes of individual uncoupled waveguides as the components of which a supermode is built up. For simplicity, consider a system of two waveguides and assume that one of the interacting modes is that of the active layer (*active mode*, for example, a mode of the active InGaN-GaN-AlGaN waveguide), while the other one is a mode of a passive waveguide (*passive mode*, for example, of p-GaN cap layer). The in-phase and out-of-phase superpositions of these modes give us the supermodes or normal modes that actually exist in this two-waveguide system. One of these modes is localized predominantly in the active region (*lasing supermode*, at which lasing action can occur), while the other one is located mostly in the passive waveguide (*ghost supermode*). In the case of the lasing supermode, the passive mode component can be observed as a local maximum of near-field intensity profile at the cap layer position. The highly doped cap-layer waveguide has a high internal loss, due to both free-carrier absorption and absorption in the contact metal. Therefore, coupling of the active mode to the cap-layer passive modes introduces some additional modal losses, thus reducing the modal gain of the lasing supermode [1]. The modal gain suppression is proportional to the coupling coefficient, with the latter decreasing exponentially as the thickness of the optical barrier (AlGaIn cladding layer) increases. The lossy ghost supermode is a parasitic mode of the laser structure that can consume

energy from the active region. In this case, the active mode can be viewed as a local maximum of the near-field intensity profile that the ghost supermode acquires at the active layer position.

Consider now the case when the phase velocities of the modes of individual uncoupled waveguides are very close to each other. In this case the language of supermodes may not be appropriate and we will instead consider only the exact solutions (normal modes) of the wave equation for a multilayer waveguide system. The two normal modes still resemble the in-phase and out-of-phase combinations of uncoupled modes of individual waveguides. However, contributions of the active mode and the passive mode into each of the two normal modes are now comparable. This implies a much weaker optical confinement for the lasing mode, which now experiences much greater optical losses in the passive waveguide. Consequently, the modal gain of the lasing mode decreases, and this may result in no lasing action at all. On the contrary, the ghost mode "benefits" under such close-to-resonance conditions, since it receives more optical power from the active region. Its modal gain increases, but not necessarily sufficiently to reach the lasing threshold. Obviously, it is possible to have an unlucky laser design (i.e., with resonant mode coupling) when the laser would not operate even though its active region is of perfect quality and properly supplied with high material gain. As shown in Section V, the accurate analysis demonstrates that normal modes change their character in passing through the resonance, that is the lasing mode turns into the ghost mode and vice versa. In other words, the lasing mode does not correspond to a single normal mode, but to a sequence of normal modes with the mode order increasing by one at each subsequent resonance. Generalizing this consideration for systems of more than two (active and passive) coupled waveguides in multilayer laser structures, we define ghost modes as the normal modes that have near-field distribution concentrated mostly in the passive waveguides.

III. DEVICE STRUCTURE UNDER CONSIDERATION

A typical InGaN-GaN-AlGaIn laser structure (see, e.g., [2], [21]) consists of multiple layers (19 or more, including metal electrodes) with different optical parameters. The layers with

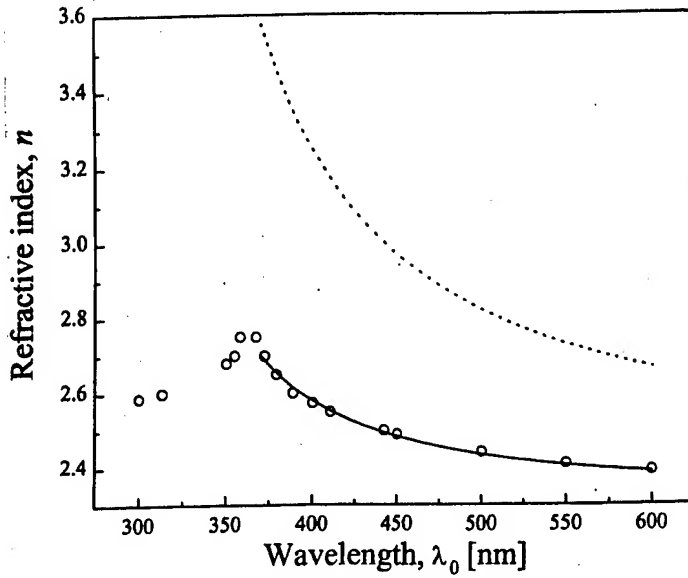


Fig. 1. Refractive index of GaN. Circles: Experimental data from [22]. Solid curve: Sellmeier fit to these data. Dotted curve: Group index calculated from the Sellmeier fit.

low values of the refractive index include sapphire substrate, AlGaIn claddings, and metallic contacts, whereas p-GaN cap layer, the system of active layers and n-GaN buffer/substrate layer all form separate waveguides. Note that all the layers are quite transparent to the laser emission, with the obvious exception of contact layers. Penetration of the optical field from the cap layer into metal is limited to a very short distance. For example, at the wavelength of 400 nm the penetration depth into the gold electrode is ~ 120 nm. The ghost mode, then, is sensitive to the optical parameters of a very thin intermediate layer formed at the nitride-metal interface. Since those parameters are not known, instead, we use the parameters of pure metals like Au, Cr, or Ti often employed as contact and adhesive materials. The values of optical parameters used in our calculations are listed in Table I for metal electrodes and for other layers in the laser structure. Note that the extinction coefficient of 3.2×10^{-5} corresponds at the wavelength of 400 nm to the absorption coefficient of 10 cm^{-1} .

The refractive index of GaN is calculated using the Sellmeier approximation of the experimental data given in [22]:

$$n^2(\lambda) = A + B/[1 - (C/\lambda)^2]$$

with fitting parameters $A = 4.37$; $B = 1.0$; $C = 0.3 \text{ } \mu\text{m}$ (the part of the dispersion curve corresponding to the normal dispersion below the absorption edge was fitted in the range from 370 to 600 nm). We also calculate the group index of GaN, important for interpretation of longitudinal mode emission spectra from GaN-based lasers:

$$n_g(\lambda) = n + B/nS^2$$

where $S = (\lambda/C) - (C/\lambda)$. The results are shown in Fig. 1. Correction for AlGaIn was made using the data for $\text{Al}_{0.1}\text{Ga}_{0.9}\text{N}$ from [22] by linear interpolation of Sellmeier parameters. Since no refractive index measurements have been reported for InGaIn, we assume that the InGaIn alloy, at

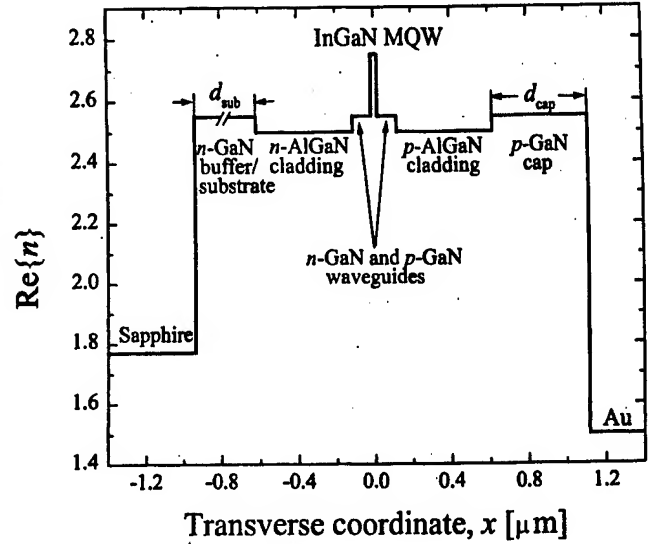


Fig. 2. Refractive index profile in a typical InGaIn-AlGaIn-GaN diode laser.

the lasing wavelength of 400 nm is characterized by the same index as GaN at its lasing wavelength of ~ 370 nm.

We consider an active region composed of four $\text{In}_{0.15}\text{Ga}_{0.85}\text{N}$ active quantum-well layers separated by three $\text{In}_{0.02}\text{Ga}_{0.98}\text{N}$ barrier layers. These seven layers are treated as one active layer with averaged optical parameters. The active layer as well as the n-GaN and p-GaN waveguide layers form together a 235-nm-thick active waveguide. The material gain inside the quantum wells is assumed to be 1000 cm^{-1} for a fixed wavelength of 400 nm. The refractive index profile of the laser structure assumed in our calculations is shown in Fig. 2.

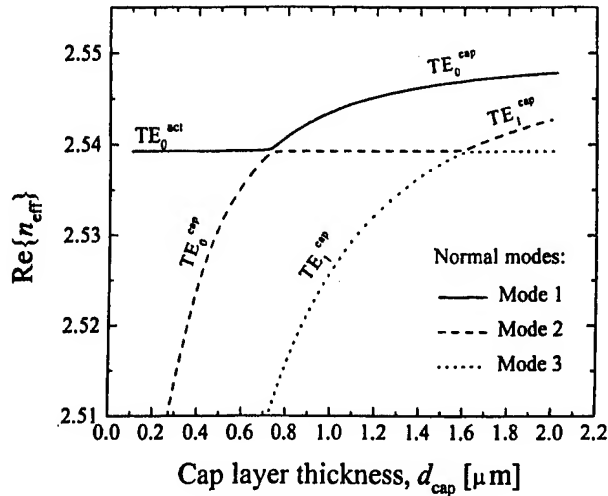
IV. CALCULATION TECHNIQUE

We consider a unidirectional propagation of modes in a planar multiwaveguide system, with one active waveguide having material gain in the core, and the remaining waveguides being passive. Taking into account that laser emission from InGaIn quantum wells is predominantly of linear TE polarization, we restrict our consideration to TE modes. Note, however, that in the case of metal-clad waveguide (the p-GaN cap layer), the lowest order TM ghost mode exists in the case of a very thin cap layer, whereas the TE ghost mode appears at rather large cap thickness (~ 200 nm for the structure described in Table I).

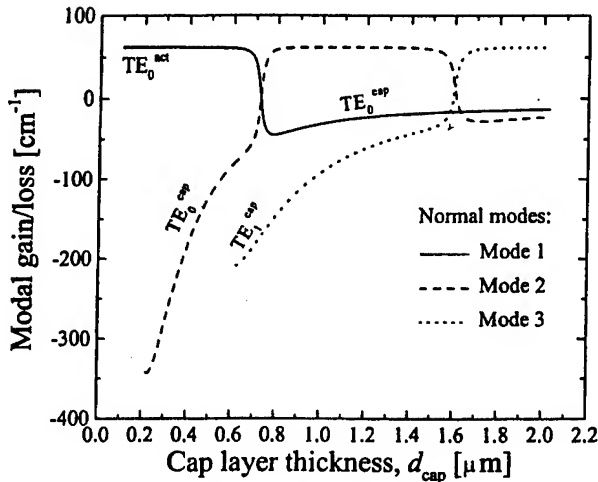
Assuming only transverse (vertical) spatial dependence of the electrical field amplitude $E_y(x)$, we solve the scalar wave equation for TE modes:

$$\partial^2 E_y / \partial x^2 + [k_0^2 \epsilon(x) - \beta^2] E_y = 0$$

where k_0 is the free-space wave vector, $\epsilon(x)$ is the complex dielectric constant profile of the multilayer structure of Fig. 2, and β is the longitudinal propagation constant. Using a combination of the complex Newton method and the Runge-Kutta method of integration of the fourth order, we find well-behaved guided wave solutions of the wave equation. The calculated results for normal modes are presented in terms of the modal effective index $n_{\text{eff}} = \text{Re}\beta/k_0$ and modal gain $G = -2\text{Im}\beta$. Note that although the concept of supermodes (understood



(a)



(b)

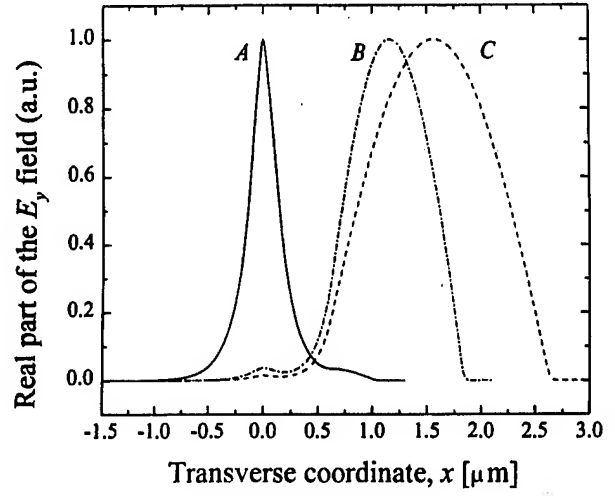
Fig. 3. Calculated effective index (a) and modal gain (b) for the first three lowest order normal modes in the two-waveguide system of the active waveguide and p-GaN cap layer. The notation TE_N^{act} , TE_N^{cap} ($N = 0, 1, 2, \dots$) identifies the TE_N modes of the corresponding individual uncoupled waveguides (active layer, cap layer) to which the normal modes of the structure are very close for a particular range of values of d_{cap} .

as superpositions of individual waveguide modes) is useful in understanding the nature of solutions, the normal modes of the laser structure are found here without invoking the coupled-mode theory.

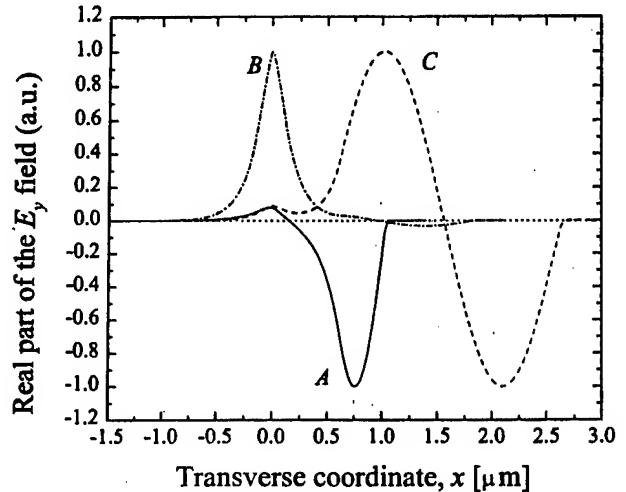
V. RESULTS OF CALCULATIONS

A. Resonance in the "Active Waveguide-Cap Layer" System

The effective index and modal gain for the first three normal modes versus the thickness d_{cap} of the p-GaN cap layer are shown in Fig. 3 for p-AlGaIn cladding layer thickness of 500 nm and Au taken as the p-side contact material. The calculated effective index of the lasing mode is ~ 2.539 , whereas that of the ghost modes varies from ~ 2.5 to ~ 2.549 . However, the effective index curves for normal modes of coupled waveguides do not cross. Rather, we can specify the points of *anti-crossing* (resonance) when two curves come very close to each other.



(a)



(b)

Fig. 4. Distribution of electrical field $E_y(x)$ for the two lowest order normal modes of the two-waveguide system of the active waveguide and p-GaN cap layer, corresponding to conditions below the first resonance ($d_{cap} = 400$ nm, curves A), between the first two resonances ($d_{cap} = 1.2$ μm , curves B), and between the second and third resonance ($d_{cap} = 2$ μm , curves C). (a) Normal mode 1. (b) Normal mode 2.

Evolution of the electrical field distribution $E_y(x)$ with increasing cap layer thickness d_{cap} is illustrated in Fig. 4 for the first two normal modes. The normal mode 1 resembles the TE_0 mode of the isolated active region waveguide (TE_0^{act}) up to the point when the first anti-crossing occurs. Up to that point, the normal mode 1 is the lasing mode of the structure or, in the language of coupled-mode theory, an in-phase supermode with the main maximum of intensity in the active region and a small intensity peak in the cap layer [cf. Fig. 4(a), curve A]. After the first anti-crossing point, the normal mode 1 changes its character to become a ghost mode that can be viewed as an in-phase supermode with the main maximum of intensity in the cap layer and a small intensity peak in the active region. Except for this insignificant side peak, it resembles closely the TE_0 mode of the isolated cap layer (TE_0^{cap}) [cf. Fig. 4(a), curves B and C].

The normal mode 2 appears first as a ghost mode and resembles the TE_0^{cap} mode up to the point when the first anti-

crossing occurs. It corresponds to an in-antiphase supermode with the main maximum of intensity in the cap layer and a small intensity peak in the active region [cf. Fig. 4(b), curve A]. After the first anti-crossing point, it changes its character to become the lasing mode of the structure. It can be thought of then as an in-anti-phase supermode with the main maximum of intensity in the active region and a small intensity peak in the cap layer [cf. Fig. 4(b), curve B]. It resembles closely the TE_0^{act} mode and has almost constant effective index all the way up to the point of the second anti-crossing, where the normal mode 2 changes its character once again to become a ghost mode. This time, however, it has two main intensity peaks in the cap layer and a small one in the active region. The latter being insignificant, the mode is close to the TE_1 mode of the isolated cap layer (TE_1^{cap}) [cf. Fig. 4(b), curve C].

The behavior of the normal mode 3 is very similar to that of the normal mode 2 with the only exception that the number of intensity peaks in the cap layer (whether primary or secondary) in each of the three regimes of behavior increases by one compared to mode 2. The same pattern of behavior applies also to all the subsequent normal modes. As the thickness d_{cap} gradually increases, all normal modes, except for the first one, experience resonance two times, first starting as a ghost mode of a certain order (i.e., with a certain number of nodes in the cap layer), then turning into the lasing mode, and ending up as a ghost mode once again but of a higher order (i.e., with the number of nodes in the cap layer increased by one). Note that the number of undesirable small intensity peaks acquired by the lasing mode in the cap layer increases by one after each successive resonance, which accounts for a slow reduction in its modal gain with increasing d_{cap} . Note also that the number of parasitic ghost modes in the structure increases with an increase in d_{cap} , which may have a negative effect on the overall efficiency of the device.

The calculated value of d_{cap} for the first resonance in the two-waveguide Au-clad structure is about 724 nm. In the case of the Cr-clad structure, the first resonance occurs at $d_{\text{cap}} = 733$ nm. The second resonant values of d_{cap} are 1605 nm and 1615 nm, respectively, with periodicity of resonances being the same in both cases (~ 880 nm).

Fig. 5 shows in more detail how the modal gain of the first two normal modes depends on d_{cap} for three different values of the optical barrier thickness d_{clad} . It is evident from this figure that a dip in the modal gain is characteristic of the lasing mode under resonant conditions. Increasing the optical barrier thickness makes the resonance narrower. It is still present even when the optical barrier is very thick, but cannot be fully resolved numerically because of limited computational accuracy. In Fig. 5, this is the case of $d_{\text{clad}} = 600$ nm, where the narrow resonance region is marked with a dotted line. The maximum value of $\sim 62 \text{ cm}^{-1}$ for the modal gain of the lasing mode is reached only when the corresponding normal modes have a dominant maximum of intensity within the active waveguide. This occurs only away from resonance, and the modal gain in this case is almost the same as it would be for the uncoupled TE_0^{act} mode. Close to resonance, the modal gain falls down dramatically, in spite of the same high

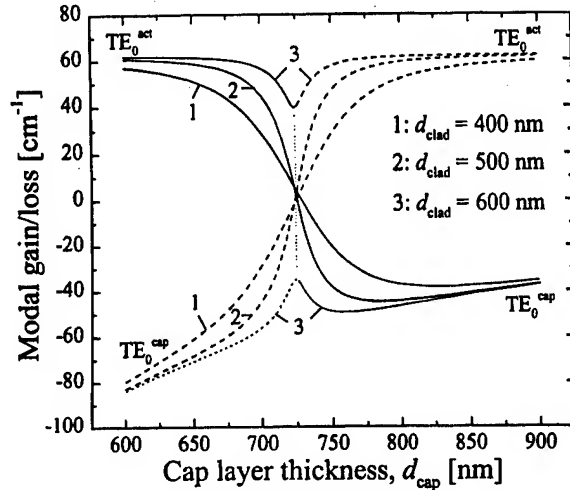


Fig. 5. Modal gain for the first two normal modes of TE polarization in the two-waveguide system of the active waveguide and Au-clad p-GaN cap layer as a function of the GaN cap layer thickness d_{cap} , calculated for three different values of the optical barrier thickness d_{clad} .

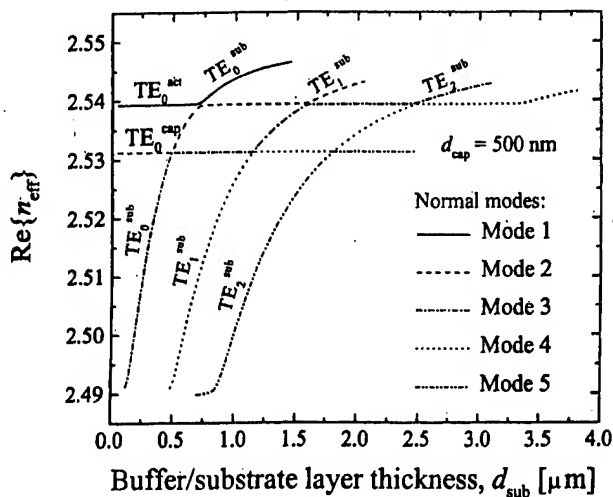
value of material gain (1000 cm^{-1}) in the quantum wells. The minimum of the modal gain (the point of intersection of modal gain curves at resonance) is almost independent of the thickness of the optical barrier. In the particular case of the 500-nm thick AlGaIn optical barrier, the calculated minimum modal gain is $\sim 2 \text{ cm}^{-1}$ for Au contact and $\sim 1.55 \text{ cm}^{-1}$ for Cr contact. Obviously, these levels of modal gain are not sufficient to reach lasing threshold. Therefore, a laser with a resonant value of d_{cap} would not be able to operate. The fact that the resonance becomes broader as the optical barrier gets thinner implies that in order to avoid an inadvertent resonance, it is important to keep the optical barriers reasonably thick.

B. Resonance in the "Active Waveguide-GaN Buffer/Substrate" System

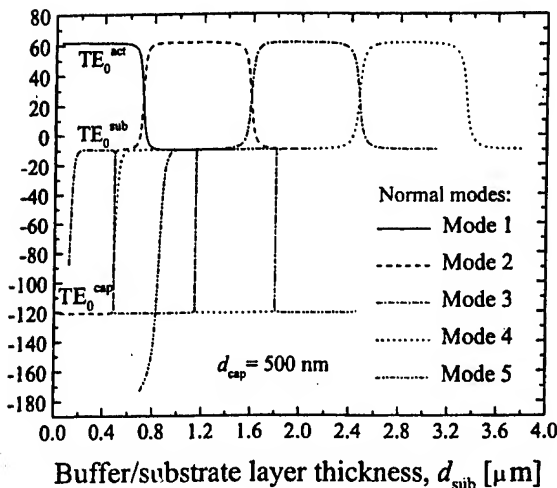
In this section, we consider possible effects that another passive waveguide in the InGaIn-based diode laser chip, namely n-GaN buffer/substrate, can have on laser performance. To be closer to the real situation in InGaIn-based diode lasers, we now treat the full system of three waveguides: p-GaN cap layer, active waveguide and n-GaN buffer/substrate. The thickness of the cap layer is fixed at $d_{\text{cap}} = 500$ nm (chosen to stay away from resonance with the active waveguide), while the n-GaN buffer/substrate thickness d_{sub} is varied from 0.05 μm to 4 μm .

In the system of three coupled waveguides, it is convenient to distinguish between the ghost modes of the cap layer (located primarily in the cap layer) and the ghost modes of the GaN buffer/substrate (located primarily in the GaN buffer/substrate layer).

The effective index and modal gain for the first five normal modes in this three-waveguide system are shown in Fig. 6 as a function of the GaN buffer/substrate thickness d_{sub} . Multiple resonances occur both in the "active waveguide-GaN buffer/substrate" system and in the "GaN cap layer-GaN buffer/substrate" system. Qualitatively, in the case of the



(a)



(b)

Fig. 6. Calculated effective index (a) and modal gain (b) for the first five lowest order normal modes of TE polarization in the three-waveguide system of the p-GaN cap layer, active waveguide, and n-GaN buffer/substrate layer as a function of the GaN buffer/substrate layer thickness d_{sub} . The notation TE_N^{act} , TE_N^{cap} , and TE_N^{sub} , ($N = 0, 1, 2, \dots$) identifies the TE_N modes of the corresponding individual uncoupled waveguides (active layer, cap layer, and buffer/substrate layer) to which the normal modes of the structure are very close for a particular range of values of d_{sub} .

“active waveguide–GaN buffer/substrate” interaction, the behavior of the normal modes is quite similar to that of the “active waveguide–cap layer” interaction described in the precedent section, and the periodicity of the resonances is also ~ 880 nm. The dips in the modal gain at the points of resonance are not, however, as deep as in the previous case, since the buffer/substrate waveguide is not nearly as lossy as the metal-clad cap layer (cf. Table I). The minimum modal gain is now about 25 cm^{-1} , while the maximum value reached away from resonance remains to be $\sim 62 \text{ cm}^{-1}$. Nevertheless, diode lasers with resonant values of d_{sub} will have much higher threshold than well-designed devices.

Evolution of normal modes in a system of three coupled waveguides can be much more complicated than in a system of two coupled waveguides. In the particular case illustrated in Fig. 6, this increased complexity is manifested by

a sequence of additional resonances in the “cap layer–GaN buffer/substrate” system, occurring with periodicity of ~ 650 nm in d_{sub} . It is interesting to note here that as the thickness d_{sub} gradually increases, all the normal modes of the order higher than 2 can experience resonance four times, starting first as the buffer/substrate ghost modes, then turning into cap-layer ghost modes, after that turning again into buffer/substrate ghost modes, then becoming the lasing mode, and eventually ending up once again as buffer/substrate ghost modes. Note also that for each value of d_{sub} this particular system of three coupled waveguides supports only one lasing mode, and only one ghost mode of the p-GaN cap layer, whereas the number of ghost modes of the n-GaN buffer/substrate increases with an increase in d_{sub} . The system of normal modes could easily be of even greater complexity should the individual cap layer waveguide or the active waveguide support more than one transverse mode.

C. Comments on Spectral Effects of Ghost Modes

We considered above how the modal gain of the normal modes depends on the thickness of the passive waveguides and optical barriers. Qualitatively, a similar behavior can be expected for the normal modes when the geometry of the device is fixed but the wavelength is varied. The only difference will be due to refractive index dispersion that should be properly included into consideration.

The main spectral effect of internal mode coupling is a periodic modulation of the superluminescent spectrum, similar to that reported in [2], [23]. The periodicity of spectral modulation observed in [2], [23] was 0.25 nm, and it could not be explained by an unintentional longitudinal Fabry–Perot cavity formed inside the laser structure. A similar effect is known in InGaAs-based lasers [1], where it can be understood within the framework of waveguide treatment by taking into account the ghost modes of a thick GaAs substrate. It should therefore be expected that a similar effect in InGaN-based lasers can arise from the presence of substrate ghost modes. However, the ghost modes of GaN buffer/substrate can produce only a much larger spectral periodicity, due to relatively small thickness of the n-GaN buffer/substrate and, correspondingly, to the relatively low order of the ghost modes. To account for the observed spectral periodicity of 0.25 nm, we then have to consider a composite sapphire/n-GaN substrate. Obviously, the resonant effects on the modal gain would be much weaker in that case, since the photon exchange with sapphire substrate is significantly reduced at GaN/sapphire interface. The periodicity of spectral modulation, though, can be reasonably well predicted.

When parasitic waveguides are thick, the number of transverse ghost modes is large, with a small spectral separation between two adjacent modes. In very thick waveguides (such as composite waveguide of n-GaN and sapphire substrate), this spectral distance is sufficiently small compared to the spectral bandwidth of the emission spectra. The distant mirror at the bottom of the sapphire substrate assists in forming ghost modes. Coupling to these modes can cause some periodic modulation in the superluminescent spectrum. In a typical

InGaIn-GaN-AlGaIn diode laser structure [23], the claddings are 500 nm thick, and the substrate is composite. It includes four layers of the total thickness $\sim 203 \mu\text{m}$. The spectral periodicity of ghost modes is

$$\Delta\lambda \sim \lambda/m$$

where m is the order of the ghost mode of the composite substrate. The value of m depends on the boundary conditions at the bottom of the substrate. They are not well known when the substrate is in contact with a heat-sinking material. If, however, there is no optical contact (the interface is sapphire-air), the dielectric constant step is $\Delta\epsilon = 2.133$, using 1.77 for the refractive index of sapphire. Estimation of the order of the mode that can be resonantly coupled to the active mode gives

$$m = (2d/\lambda)(\Delta\epsilon)^{1/2}$$

where d is the waveguide thickness. At $\lambda = 400 \text{ nm}$, we obtain $m = 1460$, and the periodicity of resonances will be $\Delta\lambda = 0.2697 \text{ nm}$. This is sufficiently close to the observed subband periodicity of 0.25 nm [2], [23] to consider internal mode coupling as a plausible explanation of the "subband modulation" effect.

We present no accurate calculation for the effect of coupling to ghost modes of the sapphire substrate as the waveguide theory predicts a very low penetration of the laser light into sapphire substrate for the structure shown in Fig. 2. However, the waveguide theory does not take into account the effect of light scattering that may also be responsible for the mode coupling. It is reasonable to expect an enhanced level of scattering at the interface of sapphire and the highly defective low-temperature GaN buffer layer.

VI. DISCUSSION AND CONCLUSIONS

Numerical analysis of a system of multiple coupled waveguides clearly shows a strong effect that ghost modes located primarily at passive waveguides can have on the modal gain of the lasing mode. The typical thickness for optical barrier (AlGaIn cladding layer) between the active waveguide and the p-GaN cap layer and between the active waveguide and the n-GaN buffer/substrate is about 500 nm, which is not sufficient for strong optical isolation. Consequently, internal mode coupling may occur, and at some specific values of the passive waveguide thickness it can become resonantly enhanced.

The modal gain suppression at resonance is the result of a strong decrease in the optical confinement factor Γ . Close to resonance, the volume of the lasing mode is increased due to substantial optical flux within the passive waveguide. Correspondingly, the lasing mode experiences additional optical losses in the passive waveguide. If the passive waveguide is the cap layer, the losses in the metal cladding are of importance.

In the case of resonant coupling with Au-clad cap layer, we found the critical thickness d^* of $\sim 724 \text{ nm}$ for the first resonance to occur. The resonance with the cap-layer ghost mode can be easily avoided if the cap layer thickness less than d^* is used. However, it is also important to note that

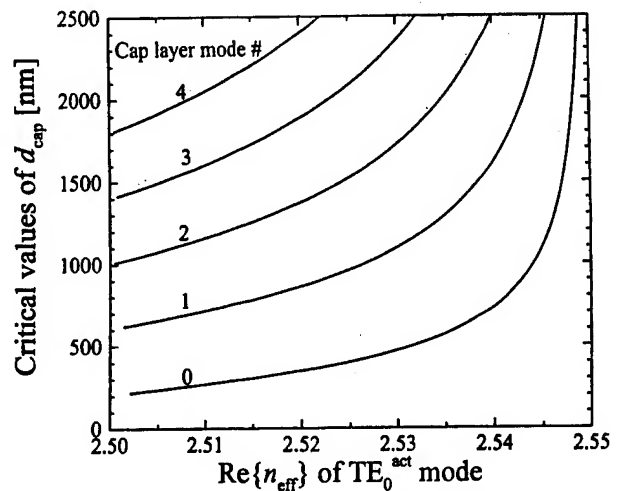


Fig. 7. Calculated dependence for the resonant thickness of the cap layer on the effective index of the uncoupled fundamental mode of the active waveguide. The numbers labeling the curves indicate the order of the corresponding uncoupled cap-layer mode.

the first resonant thickness d^* depends on the effective index of the lasing mode. The calculated dependence is shown in Fig. 7. Thus, proper design of the active waveguide is critical, as it determines the effective index of the lasing mode. For example, a greater number of QW's in the MQW structure will increase the effective index, making the resonant thickness of the cap layer larger. Also, an increase in the GaN-waveguide-layer thickness would produce an increase in the effective index.

In the case of internal mode coupling with GaN buffer/substrate, the resonance occurs with periodicity of 880 nm as the buffer/substrate thickness d_{sub} is increased. The critical values for the buffer/substrate thickness are 710, 1590, 2470, 3350, 4230 nm, and so on. Note that these values are also sensitive to the effective index of the lasing mode, with the dependence being quite identical to that of Fig. 7. At resonance with the buffer/substrate ghost modes, the calculated minimum modal gain is not as low as it is at resonance with cap-layer ghost modes. This is due to substantial contribution of the absorption in metal cladding in the latter case. Since the waveguide approach does not take into account the light scattering effects, our analysis neglects possible additional optical losses due to light scattering in the highly defective low-temperature GaN buffer layer adjacent to sapphire substrate. In a real laser structure, such scattering loss can lead to even lower modal gain at the points of resonance in the "active waveguide-GaN buffer/substrate" system.

The typical thickness of n-GaN buffer/substrate is 2–4 μm , therefore it can coincide occasionally with some of the critical values for resonant mode coupling. When such coincidence does occur, the modal gain of the lasing mode can be dramatically suppressed even though the active layers are supplied with high material gain. In diode laser manufacturing, the quality of a wafer with such critical thickness of the GaN buffer/substrate could be questioned, while the true origin of no-lasing (or high lasing threshold) would be the internal mode coupling. Therefore, considerations of resonant mode coupling

should be part of the laser design process to select the optimal thickness for the GaN buffer/substrate layer. In order to avoid the effect of resonant suppression of the modal gain by ghost modes, all parasitic waveguide thicknesses should be away from their expected resonant values. It is also possible to reduce the possibility of an unintentional resonance by making the optical barriers stronger, by increasing the thickness and/or Al content of cladding layers.

The important rules applied to the normal modes in a multiple-waveguide system when the thickness d of one of parasitic waveguides changes are as follows:

- 1) The calculated effective index of normal modes $n_{\text{eff}}(d)$ closely follows the corresponding curves for the modes of individual uncoupled waveguides everywhere except for the regions where *anti-crossing (resonance)* occurs. Since no crossing really occurs, there is no spatial mode degeneracy even if the modes of individual uncoupled waveguides might have the same phase velocity.
- 2) According to this anti-crossing behavior, the lasing mode (located primarily in the active waveguide) does not correspond to a single normal mode, but instead is represented by a series of different normal modes with gradually increasing mode order. The normal modes change their character (in terms of the location of the dominant peak in their intensity profile) at each anti-crossing point.
- 3) Away from anti-crossing points, the modal profile for each normal mode is close to that of the corresponding mode of an individual uncoupled waveguide, but contains additional contributions from the allowed modes of other waveguides.
- 4) When phase velocities of the modes of individual uncoupled waveguides coincide, the resonant coupling takes place. In such case, the interacting modes share optical flux almost equally, and the modal gain in both normal modes can be substantially suppressed.

In conclusion, we considered numerically the optical modes of a system of coupled waveguides characteristic of InGa_N-AlGa_N-GaN laser diodes. The diode chip contains parasitic waveguides (p-GaN cap layer, n-GaN buffer/substrate layer), and the normal modes located primarily in these waveguides (ghost modes) can interact resonantly with the lasing mode, causing a strong modal gain suppression. The means to prevent the undesirable suppression of modal gain include the use of stronger optical barriers and avoidance of the resonant values for the thickness of parasitic waveguides. The results of our analysis are important in laser design as well as in interpretation of some unusual patterns of behavior in InGa_N-based diode lasers.

REFERENCES

- [1] P. G. Eliseev and A. E. Drakin, "Analysis of the mode internal coupling in InGaAs/GaAs laser diodes," *Laser Phys.*, vol. 4, no. 3, pp. 485-492, 1994.
- [2] S. Nakamura and G. Fasol, *The Blue Laser Diode—GaN Based Light Emitters and Lasers*. Berlin, Germany: Springer-Verlag, 1997.
- [3] S. Nakamura, "GaN-based blue/green semiconductor laser," *IEEE J. Select. Topics Quantum Electron.*, vol. 3, pp. 435-442, Apr. 1997.
- [4] M. P. Mack, A. Abare, M. Aizcorbe, P. Kozodoy, S. Keller, U. K. Mishra, L. Coldren, and S. DenBaars, "Characteristics of indium-gallium-nitride multiple-quantum-well blue laser diodes grown by MOCVD," *MRS Internet J. Nitride Semiconduct. Res.*, vol. 2, Sept. 1997, Art. 41.
- [5] S. Nakamura, "InGa_N-based laser-diodes," *Annu. Rev. Mater. Sci.*, vol. 28, pp. 125-152, 1998.
- [6] S. Nunoue, M. Yamamoto, M. Suzuki, C. Nozaki, J. Nishio, L. Sugiura, M. Onomura, K. Itaya, and M. Ishikawa, "Reactive ion-beam etching and overgrowth process in the fabrication of InGa_N inner stripe laser diodes," *Jpn. J. Appl. Phys., Pt. 1*, vol. 37, no. 3B, pp. 1470-1473, Mar. 1998.
- [7] D. P. Bour, M. Kneissl, L. T. Romano, M. D. McCluskey, C. G. Van de Walle, B. S. Krusor, R. M. Donaldson, J. Walker, C. J. Dunrowicz, and N. M. Johnson, "Characteristics of InGa_N-AlGa_N multiple-quantum-well laser diodes," *IEEE J. Select. Topics Quantum Electron.*, vol. 4, pp. 498-504, June 1998.
- [8] S. Nakamura, "High-power InGa_N-based blue laser diodes with a long lifetime," *J. Cryst. Growth*, vol. 195, nos. 1-4, pp. 242-247, Dec. 1998.
- [9] Y. Park, B. J. Kim, J. W. Lee, O. H. Nam, C. Sone, H. Park, E. Oh, H. Shin, S. Chae, J. Cho, I. H. Kim, J. S. Khim, S. Cho, and T. I. Kim, "Characteristic of InGa_N/GaN laser diode grown by a multi-wafer MOCVD system," *MRS Internet J. Nitride Semiconduct. Res.*, vol. 4, no. 1, pp. 1-6, Jan. 19, 1999.
- [10] S. Nakamura, M. Senoh, S. Nagahama, N. Iwasa, T. Yamada, T. Matsushita, H. Kiyoku, Y. Sugimoto, T. Kozaki, H. Umemoto, M. Sano, and K. Chocho, "High-power, long-lifetime InGa_N/GaN/AlGa_N-based laser-diodes grown on pure Ga_N substrates," *Jpn. J. Appl. Phys., Pt. 2 (Lett.)*, vol. 37, no. 3B, pp. L309-L312, Mar. 15, 1998.
- [11] S. Nakamura, M. Senoh, S. Nagahama, N. Iwasa, T. Yamada, T. Matsushita, H. Kiyoku, Y. Sugimoto, T. Kozaki, H. Umemoto, and M. Sano, "InGa_N/GaN/AlGa_N-based laser-diodes grown on Ga_N substrates with a fundamental transverse mode," *Jpn. J. Appl. Phys., Pt. 2 (Lett.)*, vol. 37, no. 9AB, pp. L1020-L1022, Sept. 15, 1998.
- [12] M. Kuramoto, C. Sasaoka, Y. Hisanaga, A. Kimura, A. A. Yamaguchi, H. Sunakawa, N. Kuroda, M. Nido, A. Usui, and M. Mizuta, "Room-temperature continuous-wave operation of InGa_N multi-quantum-well laser diodes grown on an n-GaN substrate with a backside n-contact," *Jpn. J. Appl. Phys., Pt. 2 (Lett.)*, vol. 38, no. 2B, pp. L184-L186, Feb. 15, 1999.
- [13] S. Nakamura, M. Senoh, S. Nagahama, N. Iwasa, T. Yamada, T. Matsushita, Y. Sugimoto, and H. Kiyoku, "Subband emissions of InGa_N multi-quantum-well laser diodes under room-temperature continuous wave operation," *Appl. Phys. Lett.*, vol. 70, no. 20, pp. 2753-2755, May 19, 1997.
- [14] M. Onomura, S. Saito, K. Sasanuma, G. Hatakoshi, M. Nakasuji, J. Rennie, L. Sugiura, S. Nunoue, M. Suzuki, J. Nishio, and K. Itaya, "Analysis of transverse modes of nitride-based laser diodes," in *Conf. Dig., 16th IEEE Int. Semicond. Lasers*, Nara, Japan, Oct. 1998, pp. 7-8, paper MB1.
- [15] S. Heppel, J. Off, F. Scholz, and A. Hangleiter, "Complex spectral behavior of the waveguide modes in GaInN/GaN laser structures," in *Conf. Dig., 16th IEEE Int. Semiconduct. Lasers*, Nara, Japan, Oct. 1998, pp. 11-12, paper MB3.
- [16] D. K. Young, M. P. Mack, A. C. Abare, M. Hansen, L. A. Coldren, S. P. DenBaars, E. L. Hu, and D. D. Awschalom, "Near-field scanning optical microscopy of indium gallium nitride multiple-quantum-well laser diodes," *Appl. Phys. Lett.*, vol. 74, no. 16, pp. 2349-2351, Apr. 19, 1999.
- [17] V. E. Bougrov and A. S. Zubrilov, "Optical confinement and threshold currents in III-V nitride heterostructures: Simulation," *J. Appl. Phys.*, vol. 81, no. 7, pp. 2952-2956, Apr. 1, 1997.
- [18] M. J. Bergmann and H. C. Casey Jr., "Optical-field calculations for lossy multiple-layer Al_xGa_{1-x}N/In_xGa_{1-x}N laser diodes," *J. Appl. Phys.*, vol. 84, no. 3, pp. 1196-1203, Aug. 1, 1998.
- [19] P. G. Eliseev, G. A. Smolyakov, and M. Osinski, "Ghost modes and their signature in InGa_N diode laser spectra," in *Proc. 2nd Int. Symp. Blue Laser and Light Emitting Diodes, 2nd ISBLLED*, Kisarazu, Japan, Paper Th-10, Sept. 29-Oct. 2, 1998, pp. 413-416.
- [20] H. Haus, *Waves and Fields in Optoelectronics*. Englewood Cliffs, NJ: Prentice-Hall, 1984, section 7.6, pp. 217-220.
- [21] S. Nakamura, M. Senoh, S. Nagahama, N. Iwasa, T. Yamada, T. Matsushita, Y. Sugimoto, and H. Kiyoku, "First room-temperature continuous-wave operation of InGa_N multi-quantum-well-structure laser diodes," presented at the IEEE LEOS 9th Annu. Meeting, Boston, MA, Nov. 18-21, 1996, paper PD1.1.
- [22] H. Amano, N. Watanabe, N. Koide, and I. Akasaki, "Room-temperature low-threshold surface-stimulated emission by optical pumping from

Al_{0.1}Ga_{0.9}N/GaN double heterostructure," *Jpn. J. Appl. Phys., Pt. 2 (Lett.)*, vol. 32, no. 7B, pp. L1000-L1002, July 15, 1993.

- [23] S. Nakamura, M. Senoh, S. Nagahama, N. Iwasa, T. Yamada, T. Matsushita, Y. Sugimoto, and H. Kiyoku, "Subband emissions of InGaIn multi-quantum-well laser diodes under room-temperature continuous wave operation," *Appl. Phys. Lett.*, vol. 70, no. 20, pp. 2753-2755, May 19, 1997.



Petr G. Eliseev (SM'87) was born in St. Petersburg, Russia, on February 3, 1936. He graduated from Moscow State University in 1959 and received the Candidate Sci. degree in 1965, the Doctor Sci. degree in 1974 and the Professor Diploma in 1981, all from the P. N. Lebedev Physics Institute (FIAN), Russian Academy of Sciences, Moscow, Russia.

He worked at Physical Department of Moscow State University (1959-1963) and since 1963 at FIAN, Moscow, Russia, currently as a Head of the Injection Laser Laboratory. In 1991, he was with the Research Center for Advanced Science and Technology, University of Tokyo, Japan. In 1993-1994, he was at the F. Braun Institute Berlin, Germany, and in 1998-1999, at the University of Tokushima, Japan, as visiting researcher. Since 1995, he has been a Research Professor with the Center for High Technology Materials, University of New Mexico, Albuquerque, NM. The main field of his research activity is physics of semiconductor lasers. He is a correspondent member of Russian Academy of Natural Sciences since 1992.

Dr. Eliseev was awarded the State Prize of the U.S.S.R. in 1984, for pioneering development of quaternary heterostructure materials (InGaAsP, InGaSbAs, etc.).



Gennady A. Smolyakov graduated from Moscow Engineering Physics Institute, Moscow, Russia, in 1987. In 1987, he joined the Institute for Mechanics and Physics at Saratov University, Russia, where he was engaged in research in the field of semiconductor laser physics. He received the Candidate Sci. degree in physics and mathematics from Saratov University in 1997.

Since 1998, he has been a Post-Doctoral Fellow at the Center for High Technology Materials (CHTM), University of New Mexico, Albuquerque, NM. His current research interests include semiconductor lasers in group-III nitrides and vertical-cavity surface-emitting lasers. He has authored or co-authored over 20 technical papers and received one patent.



Marek Osiński (SM'86) was born in Wrocław, Poland, on May 28, 1948. He received the M.Sc. degree in theoretical physics from Warsaw University, Warsaw, Poland, in 1971, and the Ph.D. degree in physical sciences from the Institute of Physics of the Polish Academy of Sciences (PASC), Warsaw, Poland, in 1979.

In 1971, he joined the Institute of Physics of PASC, where he was engaged in investigations of waveguiding properties and modal characteristics of semiconductor lasers. From 1980 till 1984, he was a visiting research fellow at Southampton University, England, where he conducted research on long-wavelength injection laser properties, relevant to optical fiber communications. He also investigated optical properties of III-V compounds and heterostructures, including quantum-well devices. In 1984-1985, he was a British Telecom senior research associate in coherent optical communication, at Cambridge University, Cambridge, U.K., where he was involved in studying picosecond modulation, gain-switched spectra, external-cavity coupling, and injection locking of diode lasers. In 1985, he joined the Center for High Technology Materials (CHTM) at the University of New Mexico, Albuquerque, NM, where he became also a faculty member in the Department of Electrical and Computer Engineering and the Department of Physics and Astronomy, initially as Associate Professor, and since 1999 as Professor. His initial work at CHTM included high-power semiconductor laser arrays, spatially filtered external cavity coupling, side-mode injection locking, and material properties of AlGaAs and InGaAsP alloys. In 1988-1989, he held the NTT Endowed Chair in Telecommunications as visiting professor at the Research Center for Advanced Science and Technology, University of Tokyo, Japan. His main current research interests include short-wavelength optoelectronic devices in group-III nitrides, electrical, optical and thermal properties of GaN-AlIn-InN and their alloys, recombination and optical gain in wide-bandgap materials, failure analysis and degradation mechanisms, radiation effects on optoelectronic devices, surface-emitting lasers and two-dimensional arrays, thermal properties of semiconductor lasers, comprehensive simulation of optoelectronic devices, and new materials for mid-infrared lasers. In 1997, he was a visiting professor at the Satellite Venture Business Laboratory, University of Tokushima, Japan, where he was engaged in research on group-III nitride materials and devices. He is listed in *American Men and Women of Science*, *Who's Who in Science and Engineering*, *Dictionary of International Biography*, *Men of Achievement*, *Who's Who in the World*, and *Polish American Who's Who*. He has authored or co-authored over 310 technical papers, four book chapters, and four patents. He also co-edited six books of SPIE conference proceedings on Physics and Simulation of Optoelectronic Devices and three other SPIE volumes in the field of advanced high-power lasers and optoelectronics. Since January 1992, he has served as North American Editor of *Progress in Quantum Electronics*.

Dr. Osiński is a member of IEEE Lasers and Electro-Optics Society, the Optical Society of America, the International Society for Optical Engineering (SPIE), and the Materials Research Society.

Theory of angled grating semiconductor lasers: Comparison of an analytical model and BPM simulation

Marek Osinski^{*a}, William E. Thompson^{a,b}, Andrew Sarangan^a,
and Alexander P. Bogatov^{a,c}

^aCenter for High Technology Materials, University of New Mexico, 1313 Goddard SE
Albuquerque, New Mexico 87106

^bAlso at: Air Force Research Laboratory, Albuquerque, New Mexico

^cAlso at P. N. Lebedev Physics Institute, Russian Academy of Sciences, Moscow, Russia

ABSTRACT

An analysis of intensity filamentation in a broad area semiconductor laser having an optical cavity with an angled grating has been performed, using both an analytical six-wave mixing theory and beam propagation method (BPM) simulations. With the grating at the Bragg diffraction angle, the analytical theory shows that the use of the grating gives rise to lateral optical anisotropy, which suppresses filamentation of the laser radiation. For a given semiconductor laser design and operating condition, the predictions of the analytical theory are compared with those from a beam propagation method simulation.

Key words: Broad area semiconductor lasers, filamentation suppression, angled gratings, beam propagation method

1. INTRODUCTION

The output power of a semiconductor laser is limited primarily by optical damage to the semiconductor material, particularly at the laser facets. Output power can be increased by making the cross-section of the active region larger – the simplest method is to increase the lateral width of the active region, producing what are called broad area lasers (BALs). Scaling of the output power with the lateral size of the active region thus provides a very cost-effective approach towards reaching high power levels in semiconductor lasers. Unfortunately, it is very difficult to maintain the optical quality of the output beam in broad-area lasers.

In conventional, narrow-stripe waveguide lasers, designed to produce a single spatial mode, the electromagnetic field boundary conditions at the edge of the waveguide are principally responsible for mode selection in the lateral direction. However, as the lateral width of the active area increases above $\sim 5 \mu\text{m}$, the lateral boundary conditions no longer constrain the lateral field distribution to a single mode, and many lateral spatial modes become possible. Additionally, for lateral widths $> 50 \mu\text{m}$, the relative gain thresholds for different spatial modes are very close to one another, and increasing pumping tends to increase the number of lasing modes rather than increasing laser power in a single mode.

Even with a large number of lateral spatial modes lasing, it might be assumed that the homogeneous nature of the active region would produce a relatively homogeneous output laser beam. However, experimental data show that this is not the case; there is a universal trend to non-uniform lateral intensity with increased pumping – the formation of filaments.

2. FILAMENTATION IN SEMICONDUCTOR LASERS

The fundamental mechanism responsible for filamentation is a strong coupling between carrier-density dependence of the refractive index and gain [Thompson 1980]. As an illustration, assume that a slight increase in local field intensity occurs in

*Correspondence: Email: osinski@chtm.unm.edu; WWW: <http://www.chtm.unm.edu>; Telephone: 505 272 7812;
Fax: 505 272 7801

the active region, due for example to a minor material inhomogeneity. The higher field intensity reduces the local carrier density due to the higher rate of stimulated recombination. The decrease in carrier density causes an increase in the index of refraction, and tends to guide light rays from adjacent regions into the local area. This increases the local field intensity further, leading to self-focusing and creating regions of higher and lower intensity in the lateral field distribution.

The role of gain saturation and spatial hole burning in formation of filaments in semiconductor lasers and amplifiers has been analyzed extensively [Paxton 1991], [Marciante 1996], [Marciante 1997], [Dai 1997], [Egan 1998]. Additional contributions to filamentation may arise from current crowding associated with spatial hole burning and from accompanying thermal lensing [Eliseev 1997], and from the intensity-dependent changes of the refractive index in the claddings [Marciante 1996], but these are usually considered to be much less important.

An important feature of filamentation in broad-area semiconductor lasers is the periodicity of the filaments, with an observed spacing between nearest filaments typically in the range of 10-20 μm in the lateral direction. This observed periodicity can be described in terms of a series of spatial Fourier harmonics, and filamentation can be considered as the appearance of *perturbed waves*, where each wave represents a separate Fourier harmonic. The actual spatial period of the filamentation is determined by the *phase matching conditions* between the main laser mode, which propagates parallel to the optical cavity axis, and the perturbed waves, which propagate at some angle with respect to the axis. Thus, there are two main physical features that are responsible for the appearance and behavior of intensity filamentation in broad-area semiconductor lasers. The first is the optical nonlinearity of the semiconductor gain media due to the dependence of the refractive index on carrier density, and the second is the phase matching condition for waves which are affected by the nonlinear interaction.

Using this description, the spatial distribution of the filaments (the periodicity in the lateral direction) can be determined by the phase matching conditions between the fundamental laser mode and the perturbing waves:

$$\lambda/n_0 = d\sin(\varphi), \quad (1)$$

where λ is the mode wavelength, n_0 is the average effective refractive index, d is the lateral periodicity of the filamentation, and φ is the angle of perturbing wave propagation with respect to the optical axis.

The optical intensity in the center of a filament greatly exceeds the average optical intensity. Thus, optical damage to the semiconductor medium occurs much sooner than would be expected from average optical intensity considerations. Furthermore, presence of filamentation increases the output beam divergence: since filamentation can be considered as interaction of the fundamental mode with perturbing waves propagating at an angle with respect to the optical axis, increased pumping increases the fraction of the laser power appearing in the perturbing waves and thus increases the output beam divergence.

Techniques to suppress filamentation have received a lot of attention. Various methods have been applied, for example optical cavity designs to discriminate against perturbing waves, Bragg-resonance gratings that preferentially select a single propagation direction, master oscillator-power amplifier (MOPA) designs, epitaxial structure designs to increase losses for perturbing waves, etc.

The use of Bragg-resonance gratings has been investigated extensively, with good success in suppressing filamentation in so called α -DFB lasers. In this design, the grating period and orientation are chosen such that the wavelength and propagation direction of the light beam which satisfies the Bragg resonance condition will impinge at normal incidence to the optical cavity mirrors. The light beam completing a round trip through the laser cavity thus takes a serpentine path due to Bragg reflections from the grating. Other modes that do not satisfy the Bragg resonance condition either because of a difference in wavelength or in propagation direction, will incur additional optical losses. The grating in this laser thus operates as a spectral and spatial filter. Filamentation-suppression properties of this design have been demonstrated [DeMars 1996], but they have been attributed solely to the discriminating effect of Bragg reflections in the active region [Lang 1998]. The work reported here demonstrates that the optical anisotropy induced by the Bragg grating also contributes to the suppression of filamentation.

3. ANALYTICAL THEORY – SIX-WAVE MIXING APPROACH TO FILAMENTATION

The simplest implementation of the six-wave mixing (SWM) theory of filamentation ([Bogotov 1994], [Bogotov 1995]), illustrated schematically in Fig. 1, considers a strong plane wave laser mode and weak perturbing plane waves in a counter-propagating configuration. The plane wave approximation is equivalent to considering an infinitely broad laser and

neglecting the effects of the final width of the active region. In this respect, it is analogous to analytical treatment of [Marciante 1997], which nonetheless agreed reasonably well with subsequent experimental data [Marciante 1998].

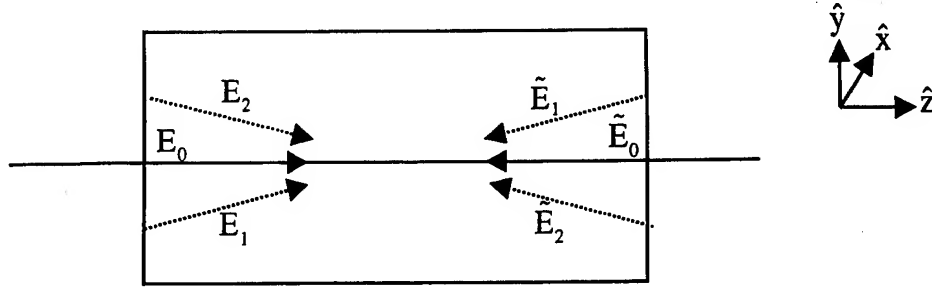


Fig. 1. Counter-propagating fundamental laser fields and weak perturbing waves in a broad area semiconductor laser.

Solving the wave equation for this system of counterpropagating six waves produces a system of coupled equations. The coupling between amplitudes for all waves occurs as a result of the optical nonlinearity in the semiconductor structure – the refractive index depends on the carrier density, which in turn depends of the local field intensity. These equations can be solved to determine the amplitudes of all six waves. The combined field $E(\vec{r}, t)$ inside the active region is a superposition of all six waves:

$$E(\vec{r}, t) = \frac{1}{2} \left\{ e^{-i\omega t} \left[E_0(z) + \tilde{E}_0(z) + E_1(\vec{r}) + \tilde{E}_1(\vec{r}) + E_2(\vec{r}) + \tilde{E}_2(\vec{r}) \right] + c.c. \right\} \quad (2)$$

where the individual waves are represented as:

$$\begin{aligned} E_0(z) &= E_0 \exp(ik_0 z) & \tilde{E}_0(z) &= \tilde{E}_0 \exp(-ik_0 z) \\ E_1(\vec{r}) &= E_1 \exp(ik_1^+ \vec{r}) & \tilde{E}_1(\vec{r}) &= \tilde{E}_1 \exp(-ik_1^- \vec{r}) \\ E_2(\vec{r}) &= E_2 \exp(ik_2^+ \vec{r}) & \tilde{E}_2(\vec{r}) &= \tilde{E}_2 \exp(-ik_2^- \vec{r}) \end{aligned} \quad (3)$$

The wave vectors k_1^+ , k_1^- , k_2^+ , and k_2^- are represented in the following form:

$$\begin{aligned} k_1^+ &= k_1^0 + h & k_1^- &= k_1^0 + h^* \\ k_2^+ &= k_2^0 - h^* & k_2^- &= k_2^0 - h \end{aligned} \quad (4)$$

The wave vectors k_1^0 and k_2^0 have only real values, with components along the y- and z-axes, while h has only a z-component. The unknown value of h represents the correction to the wave vectors that takes into account the gain and nonlinear interaction of the fields.

To investigate the tendency for filamentation in broad area semiconductor lasers, we must evaluate the stability (gain or loss) of the perturbing waves after a round trip through the active region. To this aim, it is sufficient to determine the amplitudes of “seed” waves after a round trip through the active region. We assume that at the first boundary of the active region ($z = 0$) the amplitudes of the fields that exit from the active region have some initial values \tilde{E}_1^0 and \tilde{E}_2^{0*} . By applying the appropriate boundary conditions at either end of the active region, we can finally obtain a set of equations in the form

$$\begin{pmatrix} \tilde{E}_2 \\ \tilde{E}_1^* \end{pmatrix}_{(z=0)} = \hat{M} \begin{pmatrix} \tilde{E}_2^0 \\ \tilde{E}_1^{0*} \end{pmatrix} \quad (5)$$

The eigenvalues of the matrix \hat{M} establish whether the perturbing waves will grow in intensity relative to the strong, on-axis waves. Each eigenvalue represents the gain (or loss) to the wave after one round trip through the active region. A complex eigenvalue implies an additional phase shift after one round trip – indicating an unstable mode (Fabry-Perot reflections).

Calculations of the eigenvalues as a function of the perturbing wave angle ϕ will establish which perturbing waves have the lowest threshold. An eigenvalue exceeding 1 indicates amplification of the wave after one round trip. The perturbing wave angle at which this occurs establishes the expected periodicity D_F of the filamentation through the relation given in Eq. (1).

Results of this type of analysis are illustrated in Fig. 2, which plots the largest eigenvalue for a range of periodicity values or, correspondingly perturbing wave angles. The different curves are for different values of pump current, normalized to the threshold current value I_{th} . As shown in the figure, a pump current value represented by $\eta = 0.4$, a perturbing wave at a filamentation periodicity of about $17 \mu m$ just reaches a relative intensity growth (eigenvalue) of 1, while the relative intensity growth at all other periodicity values is less than one. Thus we expect the onset of filamentation as pump current is increased to occur first at a periodicity of about $17 \mu m$. As the pump current is increased above $\eta = 0.4$, a broader range of periodicity values have relative intensity growths exceeding 1. For example, for $\eta = 0.6$, the relative intensity growth exceeds 1 over a range of periodicity values from about $12 \mu m$ to $22 \mu m$, with a maximum relative intensity growth at a periodicity of about $15.5 \mu m$. In this case, we would expect a much more complex filamentation pattern. With further increases in the pump current, the relative intensity growth exceeds 1 for an increasingly large range of periodicity values, and the maximum relative intensity growth occurs at smaller periodicity values.

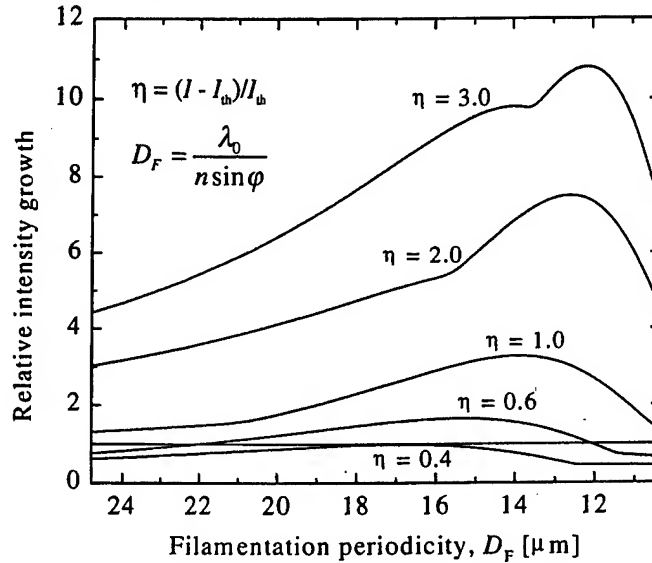


Fig. 2. Relative intensity growth as a function of filamentation periodicity.

4. BEAM PROPAGATION MODELING

To model a broad area semiconductor laser structure using the beam propagation method (BPM), the wave equation is discretized using forward and backward finite difference in a one-way tracing algorithm with no reflections. Given an input field profile at z , the 'propagator' will compute the field profile at $z+\Delta z$. In order to get a one-way tracing equation, the second derivative d^2E/dz^2 must be reduced to the first-order derivative dE/dz . This is done using the Pade recursion algorithm. Each recursion corresponds to a better approximation of dE/dz .

The resulting propagation equation can be written as $E^{z+\Delta z}(y) = A_n E^z(y)$, where A_n is the propagator. The subscript n is the order of the propagator: $n = 1$ (paraxial BPM) corresponds to no recursions to evaluate dE/dz ; $n = 2$ (wide-angle BPM) corresponds to one recursion (one correction term); etc. Filamentation in BPM is modeled using a nonlinear index $n(|E|)$, as follows:

$$n = n_0 - \frac{g_0 \alpha}{k_0 (1 + I/I_{sat})} \quad (6)$$

A 200 μm wide beam is launched into a 200 μm wide stripe with a 10% sinusoidal perturbation amplitude. The growth of the perturbation is observed over a distance of 400 μm . Figs. 3 through 5 illustrate this type of BPM calculation for different values of I/I_{sat} .

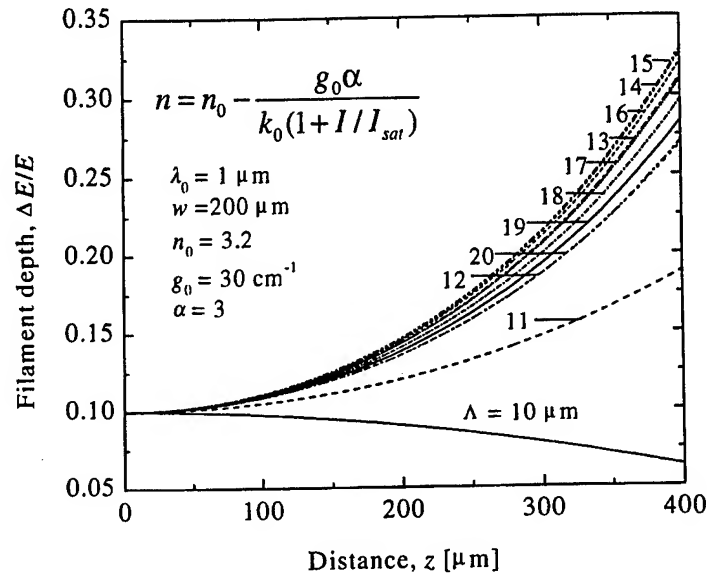


Fig. 3: Filamentation growth as a function of distance, for $I/I_{\text{sat}} = 1/15$.

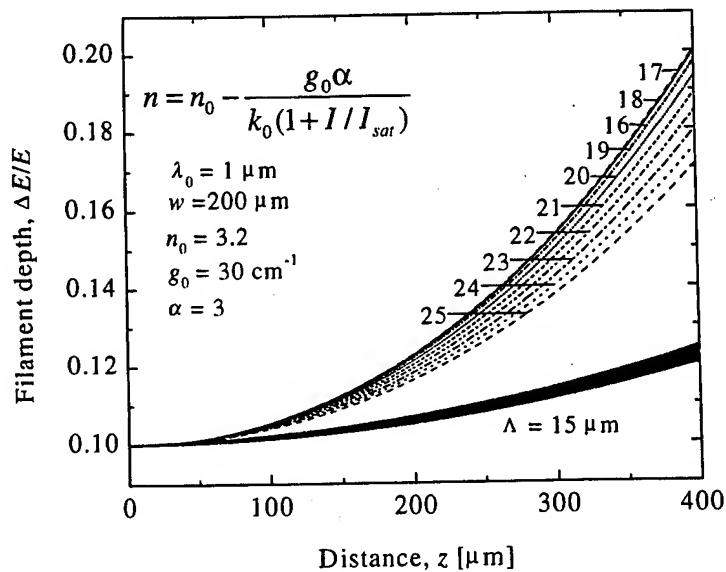


Fig. 4: Filamentation growth as a function of distance, for $I/I_{\text{sat}} = 0.1$.

In Fig. 3 ($I/I_{\text{sat}} = 1/15$), we see that the perturbation with the most rapid growth has a periodicity of about 17 μm . As the value of I/I_{sat} is increased in Figs. 4 and 5, the periodicity of the perturbation with most rapid growth decreases; for example, in Fig. 5, this periodicity is about 9 μm . Another interesting feature also shows up in Fig. 5, as the filament depth begins to decrease after a propagation distance of 300 μm or so. This effect is illustrated in another way in Fig. 6, in which the lateral intensity distribution for a perturbation periodicity of 10 μm is plotted at two different z distances: 340 μm (near the peak of filament depth) and 400 μm .

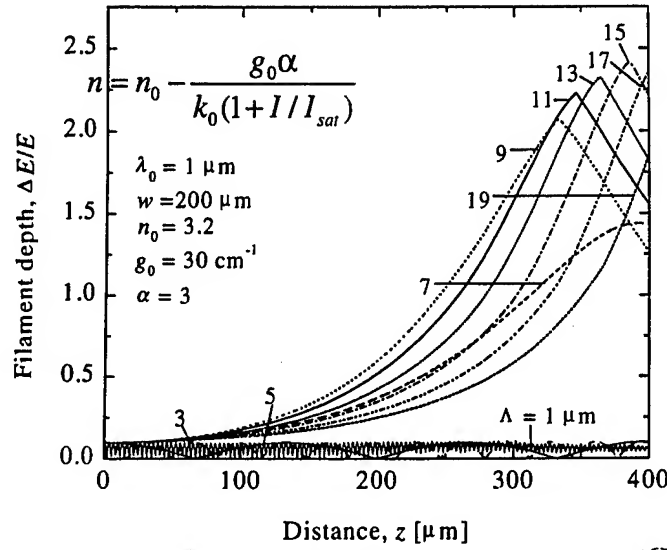


Fig. 5: Filamentation growth as a function of distance, for $I/I_{sat} = 0.5$

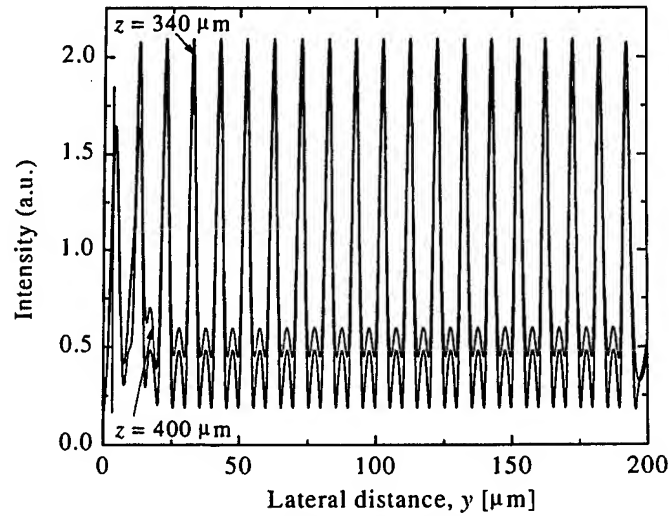


Fig. 6: Perturbation intensity distribution in the lateral dimension at $z = 340 \mu\text{m}$ and $z = 400 \mu\text{m}$.

Although the analytical theory and the BPM approaches are quite different, we note qualitative agreement in predictions of the periodicity of filamentation and in predictions of the trend of filamentation periodicity as pump current is increased. Next we use both approaches to evaluate the effect of Bragg-angle gratings on the formation of filamentation.

5. SUPPRESSION OF FILAMENTATION WITH BRAGG-ANGLE GRATINGS

The incorporation of a Bragg-angle grating into the structure of a broad area semiconductor laser is illustrated in Fig. 7. The cavity has length L , and its axis coincides with the z -axis. The grating, as shown in the figure, can be produced by a periodic spatial etching of one of the layers of the semiconductor wafer, with later regrowth in a manner typically used for DFB lasers.

The plan view of the semiconductor laser in Fig. 7 is illustrated in Fig. 8. The lines inside the cavity depict the grating teeth – lines with equal refractive index. The tilt angle between the grating teeth and the cavity axis (the z -axis) is equal to the Bragg angle α_B , defined by

$$2Dn_o \sin(\alpha_B) = m\lambda, \quad (7)$$

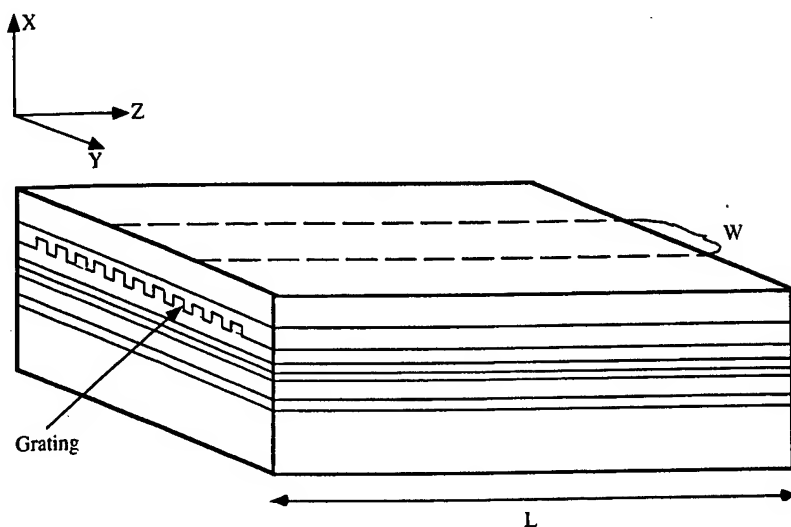


Fig. 7: Broad area semiconductor with Bragg-angle grating.

where D is the grating period; n_0 is the average effective waveguiding refractive index; m is an integer representing the diffraction order, and λ is the characteristic laser wavelength.

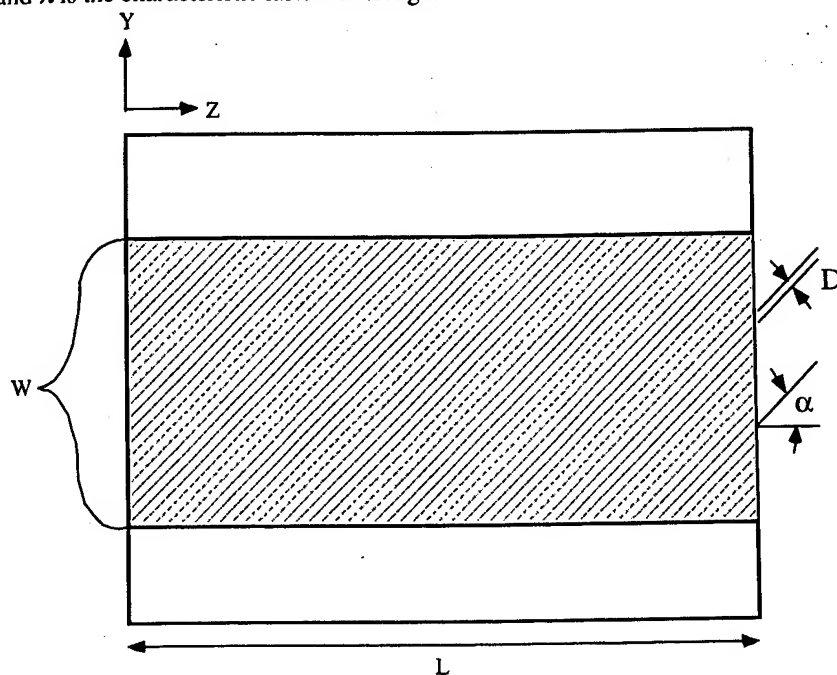


Fig. 8: Plan view of broad area semiconductor laser with Bragg-angle grating

If we assume that the index variations are sinusoidal in profile, the effective refractive index, n , for the fundamental transversal mode (in x -direction, Fig. 7) can be written as:

$$n = n_0 + \Delta n \cos(\mathbf{q} \cdot \mathbf{r}), \quad (8)$$

where n_0 is the average value of the effective refractive index, Δn is the modulation amplitude of the refractive index, and the vectors \mathbf{q} and \mathbf{r} have the following components:

$$\mathbf{q} = (q_y, q_z); \quad \mathbf{r} = (y, z)$$

$$q_y = (2\pi/D) \cos(\alpha_B); \quad q_z = (2\pi/D) \sin(\alpha_B)$$

By using the effective mode refractive index and the mode gain, instead of the material refractive index and the material gain, we can omit the x -coordinate dependence for the field.

We restrict our consideration to the case where the following relationship is observed:

$$\epsilon_0 \gg \Delta\epsilon \gg |\delta\epsilon|, \quad (9)$$

where $\epsilon_0 = n_0^2$; $\Delta\epsilon = 2n_0\Delta n$, and $\delta\epsilon$ is the complex additional to the dielectric permittivity due to the absorption, scattering, gain, and variation of the carrier concentration. The term $\delta\epsilon$ depends on pumping and optical intensity as a result of spatial hole burning. This circumstance leads to an optical nonlinearity and, in particular, to intensity filamentation.

In the general case of optical nonlinear processes, it is well known that the efficiency of the process depends primarily on the two parameters: the optical nonlinear coefficient and the phase matching for the waves participating in the nonlinear interaction. Consequently, two ways may be considered to reduce the nonlinear effect and hence suppress the formation of filamentation. The first one is to decrease the nonlinear coefficient. The second is the production of additional phase mismatching, due to optical anisotropy, for the wave participating in the formation of filamentation. In this paper, we specifically consider the effect of optical anisotropy induced by a Bragg-angle grating and its impact on phase matching conditions and the formation of filamentation.

5.1. Application in Six-Wave Mixing Analytical Theory

For purposes of this analysis, we ignore the diffraction of the fundamental mode that would actually occur in a broad-area semiconductor laser including a Bragg-angle grating. We are primarily interested in the effect of the grating on the perturbing waves (causing the onset of filamentation), and since these waves propagate at an angle with respect to the optical axis, they do not interact with the grating at the Bragg angle.

First we start with an general expression for E – the amplitude of a non-diffracted wave propagating in the medium that contains a general two-dimensional grating [Kogelnik 1969], [Gaylord 1982] (not necessarily at the Bragg angle), neglecting the presence of amplification (absorption) and the influence of carrier concentration on the refractive index:

$$E(\mathbf{r}, t) = u_0(z) \exp(ikz - i\omega t) = |u_0(z)| \cdot \exp(-i\omega t) \cdot \exp(ikz + i\psi(z)) \quad (10)$$

$$u_0(z) = \frac{1}{2} (1 + c/a) \exp(ik(a-c)z) \{1 + (a-c)/(a+c) \exp(-2ikaz)\}, \quad (11)$$

where $k = (\omega/c)n_0$ and $\psi(z)$ is the phase shift induced by grating. The coefficient a is expressed by using the dimensionless coupling coefficient b and the detuning coefficient c , as well as the grating parameters:

$$\begin{aligned} a &= (b^2 + c^2)^{1/2}; \quad b = \xi \Delta n / 2n_0; \quad \xi = [1 - \lambda \sin(\alpha) / (D n_0)]^{-1/2}; \\ c &= \{(\lambda/D)^2 \sin^2(\Delta\alpha/2) + n_0(\lambda/D) \cos(\alpha_B) \sin(\Delta\alpha)\} \xi / 2n_0^2; \\ \Delta\alpha &= \alpha_B - \alpha, \end{aligned} \quad (12)$$

α_B is the Bragg angle defined in accordance with Eq. (7), and $\Delta\alpha$ is the angle between the actual grating direction and the direction of a grating at the Bragg angle. In accordance with Eq. (11), the amplitude of the zero-order (undiffracted) wave periodically oscillates (is modulated) along the z axis. This suggests that, due to the diffraction, the intensity of the propagating wave is being transferred periodically to the first-order wave. The amplitude modulation and the phase shift, $\psi(z)$, depend strongly on the detuning, c , from the Bragg condition. Specifically for the Bragg resonance case at $c = 0$, the amplitude wave has the 100% modulation, varying from maximum (equal to unity, in our case) to minimum (zero), while $\psi(z) \equiv 0$. At other angles, the minimum amplitude, $|u_0(z)|$, will no longer be equal to zero. Additionally, $\psi(z)$ will vary with distance z , namely,

$$\psi(z) = k(a-c)z + \delta\psi(z) \quad (13)$$

The first term in the right-hand part of equation (13) represents the monotonously varying part, and the second term, $\delta\psi(z)$, represents the oscillating part. Here $|\delta\psi(z)| < \pi/2$ for any z .

With this foundation, we can investigate the effect of a Bragg-angle grating on the phase matching condition necessary to the formation of filamentation, within the framework of the six-wave mixing analytical theory. Phase mismatching is determined by a factor of p – the time difference between the wavevector z -components for the unperturbed wave propagating along cavity axis and for the perturbed wave, which is responsible for filamentation and is propagating at angle φ with respect to the cavity axis. For the case of isotropic active region (no grating) the factor p is equal to:

$$p = 4k \sin^2(\varphi/2) \quad (14)$$

The angle φ and spatial period of filamentation d are coupled by the relation as given in Eq. (1). For the case including a Bragg-angle grating, the expression for p will be more complicated, and will include parameters of the grating, which reflects the optical anisotropy:

$$p = 4k \sin^2(\varphi/2)(1-F) \equiv k(\lambda n_0 d)^2(1-F), \quad (15)$$

where F takes into account the anisotropy induced by grating and the period of filamentation d :

$$F \equiv 2(dn_0/\lambda)^2 \left\{ \frac{\Delta_1 - \Delta_0}{1 + \Delta_1} - \frac{(\Delta_1 - \Delta_{-1})(2 + \Delta_1 + \Delta_{-1})}{4(1 + \Delta_1)(1 + \Delta_0)} \right\}, \quad (16)$$

with

$$\begin{aligned} \Delta_j &= (b^2 + c_j^2)^{1/2} - c_j, \quad j = 0, \pm 1 \\ c_j &= \left(\frac{\xi}{2n_0} \right) \left[\left(\frac{\lambda}{D} \right) \sin^2 \left(\frac{\alpha_j}{2} \right) + \left(\frac{n_0 \lambda}{D} \right) \cos(\alpha_j) \sin(\alpha_j) \right]; \\ \alpha_j &= \alpha_B - \alpha - j \left(\frac{\lambda}{dn_0} \right) \end{aligned} \quad (17)$$

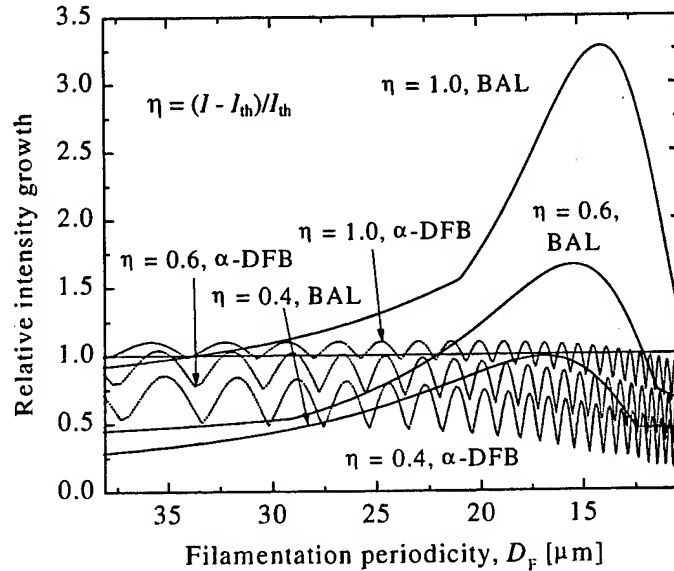


Fig. 9. Relative intensity growth as a function of filamentation periodicity - broad area lasers and α -DFB lasers

We assume that the filamentation period d is rather large, as compared to λ , so that from Eq. (1) one could obtain $\varphi \sim \lambda/(dn_0)$. Thus, by using the phase mismatching factor p in the form of Eq. (15) instead of the form of Eq. (14) in the theory of six-

wave mixing, we can use the same approach described in Section 3 to find the conditions for perturbation wave growth. The first of these results are shown in Fig. 9. This figure shows two sets of data for a broad area semiconductor laser with $L = 400 \mu\text{m}$, $\alpha_B = 20^\circ$, and $D = .45 \mu\text{m}$. The first set shows the theory prediction for a standard broad area laser (BAL), showing the relative intensity growth of perturbing waves as a function of filamentation periodicity (or, through Eq. (1), as a function of perturbing wave angle ϕ). The different curves within this set are for different values of η , where η is the fraction of pump current above threshold. The second set of curves is for the broad area laser including a Bragg-angle grating. The different curves in this set are for the same three values of η as used in the first set. A comparison of the curve from each set for the same value of η illustrates the effectiveness of the Bragg-angle grating in suppression of filamentation. For example, for $\eta = 0.6$, the broad area laser curve shows a relative intensity growth greater than 1.0 over a filamentation periodicities ranging from about 12 to 22 μm . With the presence of a Bragg-angle grating, we see that the relative intensity growth is significantly suppressed, with only a few locations at large filamentation periodicity where the relative intensity growth exceeds 1.0.

If we take the same laser and Bragg-angle grating conditions used for Fig. 9 and plot the results for larger values of η , we get the results shown in Fig. 10. The curves for $\eta = 1.0$ are the same as those in Fig. 9, plotted on a different vertical scale. These results show the continuing effectiveness of the Bragg-angle grating in the suppression of filamentation as the value of η is increased. These results indicate that the presence of the Bragg-angle grating in an α -DFB laser increases the lateral instability threshold, but does not completely suppress filamentation.

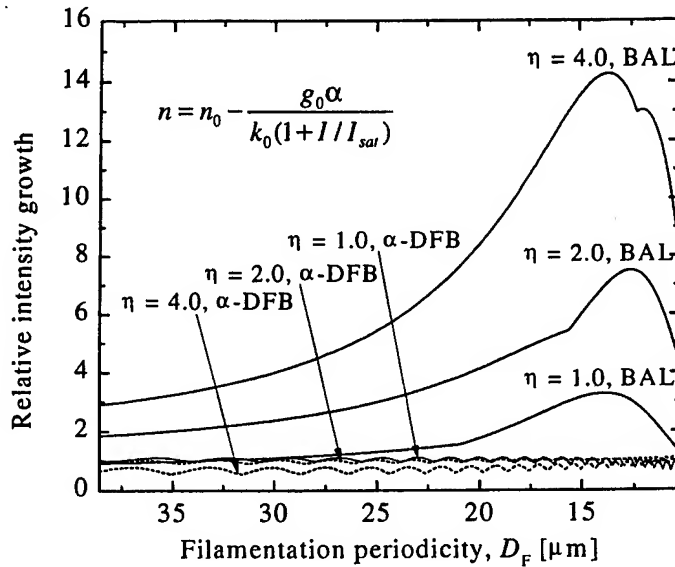


Fig. 10. Relative intensity gain as a function of filamentation periodicity - broad area lasers (BAL) and α -DFB lasers.

5.2. Application of the Beam Propagation Method

The application of BPM to a broad area semiconductor laser with a Bragg-angle grating is identical to that discussed in Section 4, except that the optical field nonuniformity in the device can strongly perturb the grating at large internal powers. In this case, the effective index of refraction for the grating is modified by the optical field nonuniformity, leading to a condition in which the grating is no longer perceived as a Bragg-angle grating by the propagating waves. This can require some trial-and-error adjustments to the grating periodicity in order to ensure that the Bragg-angle condition is met. Fig. 11 shows one case, with device parameters identical to those given in Fig. 4. In this case, we notice that the grating parameters are not exactly correct, because of the influence of the optical field, to produce a Bragg-angle condition. In comparing with the results shown in Fig. 4, we see essentially no effect of the grating in suppressing the growth of filamentation. With further tuning of the grating parameters, we obtain the results shown in Fig. 12. In this case, the effects of diffraction are more evident, and we can see the influence of the grating on the growth of filamentation. However, even in this case the Bragg-angle condition is not exactly matched; the requirement for trial-and-error adjustments is a limitation of the current BPM formulation.

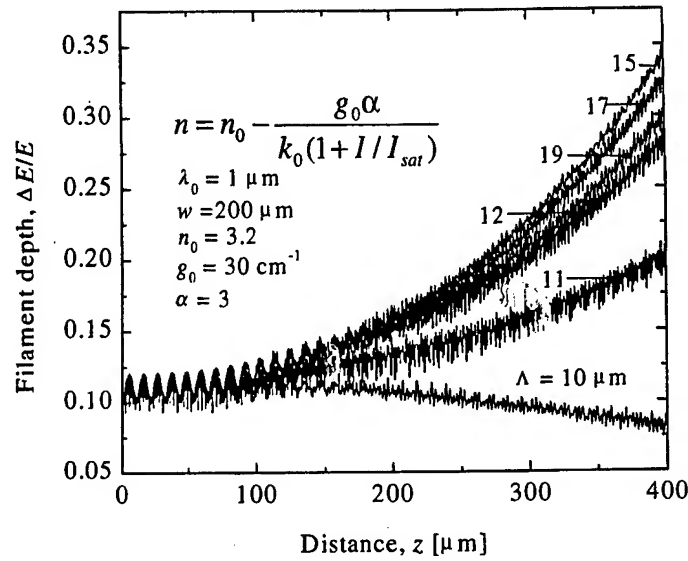


Fig. 11: Filamentation growth as a function of distance, for $I/I_{sat} = 0.1$ and $\alpha_B = 20^\circ$, $D = .4568 \mu\text{m}$.

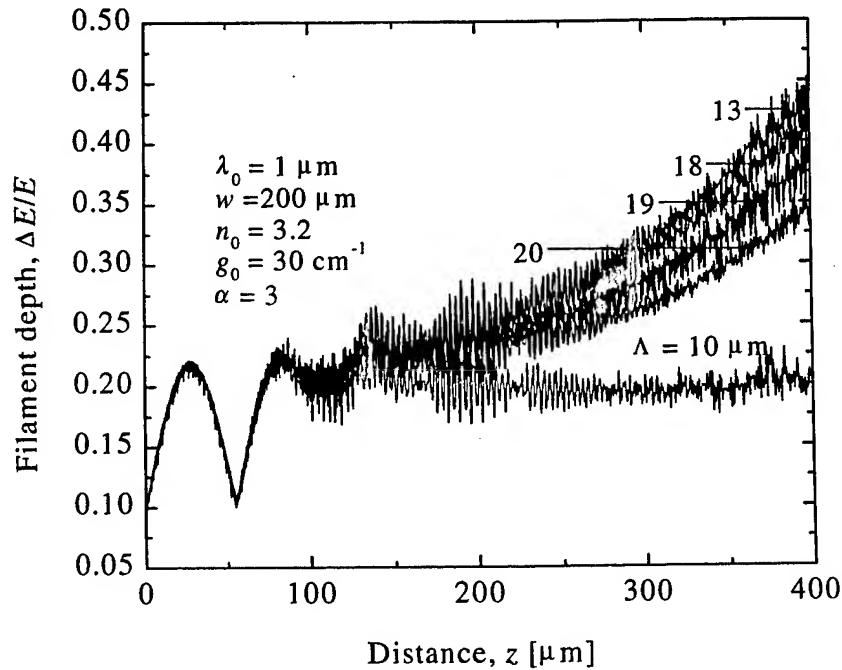


Fig. 12: Filamentation growth as a function of distance, for $I/I_{sat} = 0.1$ and $\alpha_B = 20^\circ$, $D = 0.4582 \mu\text{m}$.

6. CONCLUSIONS

In this paper, we have shown the ability of the six-wave mixing analytical theory to predict the onset and characteristics of filamentation in broad area semiconductor lasers, in reasonable agreement with similar predictions from a beam propagation model. Additionally, we have extended the six-wave mixing theory to account for the presence of a Bragg-angle grating; this revised theory predicts that the optical anisotropy introduced by the grating will, in itself, discriminate against the formation of filamentation. Attempts to replicate these results with the beam propagation model were less successful, however, hampered by the changes to the effective grating parameters due to the optical field nonuniformity in the device. Further work to compare the predictions of both models will require some modifications to the analysis methodology.

ACKNOWLEDGMENT

This work was supported by AFOSR under the Optoelectronics Research Center program.

REFERENCES

- [Bogatov 1994] A. P. Bogatov, "Lateral field instability and six-wave mixing in a diode laser with broad active area", *J. Russian Laser Res.*, vol. 15 (5), pp. 403-431 (1994).
- [DeMars 1996] S. D. DeMars, K. M. Dzurko, R. J. Lang, D. F. Welch, D. R. Scifres, and A. Hardy, "Angled-grating distributed feedback laser with 1 W cw single-mode, diffraction-limited output at 980 nm", *Techn. Digest, CLEO '96 Conf. on Lasers and Electro-Optics*, Anaheim, CA, 2-7 June, 1996, Paper CTuC2, pp. 77-78.
- [Egan 1998] A. Egan, C.-Z. Ning, J. V. Moloney, R. A. Indik, M. W. Wright, D. J. Bossert, and J. G. McInerney, "Dynamic instabilities in master oscillator - power amplifier semiconductor lasers", *IEEE J. Quantum Electron.*, vol. 34 (1), pp. 166-170 (1998).
- [Eliseev 1997] P. G. Eliseev, A. G. Glebov, and M. Osiński, "Modeling of current crowding accompanying optical filament formation in semiconductor lasers and amplifiers", *Physics and Simulation of Optoelectronic Devices V* (M. Osiński and W. W. Chow, Eds.), *Photonics West '97*, San Jose, CA, 10-14 Feb. 1997, *SPIE Proc.*, Vol. 2994, pp. 580-590.
- [Gaylord 1982] T. Gaylord and M. Monaram, "Planar dielectric grating diffraction theories", *Appl. Phys. B*, vol. 28, pp. 1-14 (1982).
- [Kogelnik 1969] H. Kogelnik, "Coupled wave theory for thick hologram gratings", *Bell System Techn. J.*, vol. 48 (9), pp. 2909-2947 (1969).
- [Lang 1998] R. J. Lang, K. Dzurko, A. A. Hardy, S. Demars, A. Schoenfelder, and D. F. Welch, "Theory of grating-confined broad-area lasers", *IEEE J. Quantum Electron.*, vol. 34 (11), pp. 2196-2210 (1998).
- [Marciante 1996] J. R. Marciante and G. P. Agrawal, "Nonlinear mechanisms of filamentation in broad-area semiconductor lasers", *IEEE J. Quantum Electron.*, vol. 32 (4), pp. 590-596 (1996).
- [Marciante 1997] J. R. Marciante and G. P. Agrawal, "Spatio-temporal characteristics of filamentation in broad-area semiconductor lasers", *IEEE J. Quantum Electron.*, vol. 33 (7), pp. 1174-1179 (1997).
- [Marciante 1998] J. R. Marciante and G. P. Agrawal, "Spatio-temporal characteristics of filamentation in broad-area semiconductor lasers: Experimental results", *IEEE Photon. Technol. Lett.*, vol. 10 (1), pp. 54-56 (1998).
- [Paxton 1991] A. H. Paxton and G. C. Dente, "Filament formation in semiconductor laser gain regions", *J. Appl. Phys.*, vol. 70 (6), pp. 2921-2925 (1991).
- [Thompson 1972] G. B. H. Thompson, "A theory for filamentation in semiconductor lasers including the dependence of dielectric constant on injected density", *Optoelectron.*, vol. 4, pp. 257-310 (1972).



PROCEEDINGS OF SPIE
SPIE - The International Society for Optical Engineering

Advanced High-Power Lasers

**Marek Osiński
Howard T. Powell
Koichi Toyoda**
Chairs/Editors

**1-5 November 1999
Osaka, Japan**

Sponsored by
LSJ-The Laser Society of Japan
SPIE- The International Society for Optical Engineering

Cooperating Organizations
Faculty of Engineering and ILE, Osaka University (Japan)
ICF Forum (Japan)
ILT-Institute for Laser Technology (Japan)
JAERI-Japan Atomic Energy Research Institute
OITDA-Optoelectronic Industry and Technology Development Association (Japan)
AMPI-The Advanced Material Processing Institute Kinki (Japan)
RIPE-R&D Institute for Photonics Engineering (Japan)

Published by
SPIE- The International Society for Optical Engineering



Volume 3889

SPIE is an international technical society dedicated to advancing engineering and scientific applications of optical, photonic, imaging, electronic, and optoelectronic technologies.

Design of InGaN/GaN/AlGaIn vertical-cavity surface-emitting lasers using electrical-thermal-optical simulation

Marek Osinski^{*a}, Vladimir A. Smagley^a, Chun-Sheng Fu^a, Gennady A. Smolyakov^a,
and Petr G. Eliseev^{*b}

^aCenter for High Technology Materials, University of New Mexico, 1313 Goddard SE,
Albuquerque, New Mexico 87106-4343

^bOn leave from P. N. Lebedev Physics Institute, Russian Academy of Sciences, Moscow, Russia

ABSTRACT

3D electric-thermal-optical numerical simulator is developed and applied to model group-III-nitride-based intracavity-contacted vertical-cavity surface-emitting lasers (VCSELs) with InGaIn multi-quantum-well active region. The optical model based on the effective frequency method is combined with electrical-thermal simulator using the control volume method. Isothermal (pulsed regime imitation) and CW modes of operation are calculated over a range of voltages, covering sub-threshold spontaneous emission and lasing emission. Effects of current crowding at the active-region periphery are examined, and in particular an impact on mode profiles of spatial hole burning superimposed on nonuniform gain distribution is studied. In order to reduce the current crowding and provide more uniform gain distribution within the active region, a semitransparent *p*-side contact design is proposed.

Keywords: VCSELs, intracavity contacts, group-III nitrides, semiconductor laser design, optoelectronic device simulation.

1. INTRODUCTION

Nitride-based semiconductor lasers continue to attract attention of optoelectronic research community. On the one hand, they promise revolutionary progress in many applications, *e.g.*, as light sources for high-density optical memory, high resolution printing, or full-color laser displays. On the other hand, they continue to pose serious challenge to both experimental and theoretical research. Strong coupling and interplay of multiple-level sub-systems make their analysis quite a formidable task for numerical modeling, too. In particular, it is important to take into account proper physical description of multiple-quantum-well active region, electrical and thermal properties, and optical resonator. It is preferable that the model includes spontaneous electrical polarization, residual stresses, piezoelectric fields, and thermoelectric field description.

In the case of nitride-based vertical-cavity surface-emitting semiconductor lasers (VCSELs) designed to operate in the UV/short-wavelength visible spectral range, complexity of numerical modeling increases considerably. First, compared to edge-emitting lasers, the situation becomes much more complicated due to the influence of specific VCSEL design features, such as ultrashort cavity length, complicated optical cavity structure, absence of a conventional waveguide, and strong thermal dependence of operational parameters.

Second, application of nitride-based materials further complicates physical description and design of VCSELs. Possible design problems include: (i) high operation current density necessary to maintain material gain sufficient for vertical mode to lase; (ii) non-conducting sapphire substrate; (iii) high resistance of bulk materials, especially, of *p*-side; (iv) very high electrical resistance of semiconductor distributed Bragg reflectors (DBRs); (v) high contact resistance at *p*-side; and (vi) high junction heating and high Joule heating of the laser chip resulting from poor elec-

^{*}Correspondence: Email: osinski@chtm.unm.edu; WWW: <http://www.chtm.unm.edu>; Telephone: (505) 272 7812;
Fax: (505) 272 7801

trical conductivity. Specific issues related to nitride-based VCSEL design are the problems of sufficient electrical conductivity in the device accounting for the poor conductivity (both in bulk and in contacts) of the *p* side of the diode, and inclusion of DBRs into the diode design. In principle, DBRs can comprise AlGaIn-GaN pairs, utilizing GaN as higher-index material and AlGaIn or AlN as lower-index material. However, the electrical conductivity of the material drops rapidly with increasing content of Al in AlGaIn. For this reason, implementation of nitride-based DBRs will require an intracavity contact configuration.

Third, numerical studies of electrically pumped nitride-based VCSELs can only have a heuristic character since there has been no practical demonstration of such devices so far. Although claims of optically pumped vertical cavity lasing have been made in a few reports [Redwing 1996], [Someya 1998], [Sakharov 1999], [Someya 1999a], [Krestnikov 1999b], [Someya 1999b], the designs and technology developed for optical pumping are of little use for the problem of electrically pumped VCSELs.

So far, most of the efforts on development of nitride-based VCSELs have been limited to studies of various semiconductor or dielectric distributed Bragg reflectors (DBRs) [Fritz 1995], [Sakaguchi 1995], [Ambacher 1997], [Ishikawa 1998], [Sakaguchi 1998], [Ng 1999], [Langer 1999], [Martin 1999]. Early estimations of threshold current density in GaN-based VCSELs have been made in [Honda 1995], and more recently in [Maćkowiak 1998a], [Maćkowiak 1998b].

There have been many reports concerning observation of stimulated emission in the vertical direction (surface emission) from AlGaIn/GaN and GaN/InGaIn/GaN structures under short-pulse optical pumping [Khan 1991], [Amano 1993], [Yung 1994], [Khan 1994], [Redwing 1996], [Jiang 1997], [Krestnikov 1999a]. A typical pumping rate required to achieve some spectral narrowing without using high-reflectivity mirrors was 1–4 MW/cm² [Khan 1991], [Amano 1993], [Yung 1994], which was equivalent to extremely high current densities (~0.3–1.4 MA/cm²). More recently, highly reflective DBR mirrors were used, and much lower threshold pump densities of ~2 kW/cm² were observed at 77 K in InGaIn/GaN vertical cavities emitting at 381 nm, pumped by a pulsed 367 nm dye laser [Someya 1998]. The laser structure contained a 3λ microcavity with a 184-nm thick bulk InGaIn active layer, top dielectric DBR and a bottom DBR composed of 35 pairs of Al_{0.34}Ga_{0.66}N/GaN quarter-wave layers.

Room-temperature optically pumped pulsed VCSEL operation at 399 nm has been reported recently in [Someya 1999a], [Someya 1999b]. The active region comprised 26 3-nm thick In_{0.1}Ga_{0.9}N quantum wells separated by 5-nm thick In_{0.01}Ga_{0.99}N barriers. The measured reflection coefficients of DBRs were 98% for the 43-pair Al_{0.34}Ga_{0.66}N/GaN bottom mirror and 99.5% for the 15-pair SiO₂/ZrO₂ top mirror. We estimate the threshold pumping power density as 250 kW/cm², assuming a reflectivity of nitride DBR at the pump wavelength of 367 nm to be 50%, and absorption in the quantum wells to be also 50%. The sheet threshold carrier density was estimated as (2–4)×10¹² cm⁻², and the material gain was ~890 cm⁻¹.

The aim of this paper is to investigate prospects for electrically pumped InGaIn/GaN/AlGaIn VCSELs, to identify the most critical device parameters essential for room-temperature CW operation, and to compare expected performance of devices with various contact geometries. For this purpose we have integrated our previously developed modules into a new 3D self-consistent electrical-thermal-optical (ETO) simulation tool. Previously, we had developed a self-consistent electrical-thermal (ET) simulator, based on the control-volume calculation method, and applied it to analysis of oxide-confined VCSELs [Smagley 1998], [Osiński 1998], [Osiński 1999a]. For optical analysis of VCSEL structures, the effective frequency method (EFM) was shown to offer an attractive approach [Smolyakov 1999]. As opposed to its original implementation in [Wenzel 1997], our EFM solver is capable of handling arbitrary geometries of VCSELs with non-uniform distributions of the refractive index and gain. Here, we couple both ET and EFM modules as well as a model for the material gain, thus enabling investigations of complex interplay between electrical, thermal, and optical phenomena in nonplanar and nonuniform VCSEL structures. We perform numerical experiments to investigate device behavior at the 400 nm emission wavelength. Two different intracavity-contacted VCSEL structures are compared, with ring-contact and semitransparent circular contact configurations.

2. ELECTRICALLY PUMPED INGAN/GAN/ALGAN VCSEL STRUCTURE

High electrical resistivity of AlGaIn and *p*-GaN makes it impractical to consider a VCSEL design in which current would have to flow across the DBR layers. Therefore, it is reasonable to assume that both *n*- and *p*-side contacts would have to be of intracavity type. This alone makes the analysis of electrical properties of the device difficult, and requires a sophisticated numerical tool. The simulated device structure is shown in Fig. 1. We use a basic diode

design with a closely confined current aperture provided by insulating GaN material. The insulating layer defines the window for vertical current flow. In high-performance GaAs-based VCSELs, the insulating material is normally created by steam oxidation of a thin high-Al-content layer. Based on recent reports of wet oxidation of AlN [Opila 1998] and GaN [Readinger 1999], a similar process can be envisaged for group-III nitrides. Alternatively, low-energy electron beam irradiation (LEEBI) treatment can be used to pattern a current confining window in *p*-type GaN [Inamori 1995]. The latter approach corresponds to the situation depicted in Fig. 1.

The biggest problem created by ring-type intracavity contacts is the inherent nonuniform distribution of current density injected into the active region, or, in other words, strong current crowding at the edges of the active region [Osiński 1999a]. Due to very short diffusion lengths of carriers in group-III nitrides grown on sapphire [Eliseev 1999], carriers injected into the active region cannot redistribute themselves in a more uniform fashion. This results in a highly undesirable effect of material gain nonuniformity that would normally favor higher-order-mode operation [Smolyakov 1999]. Therefore, we shall also consider an alternative design, in which a semitransparent circular contact (CC) is placed between the *p*-side spacer and the *p*-side DBR. We expect the CC layer to provide a substantial reduction in the current crowding and to result in an increased current density at the center of the active region. However, insertion of a metal layer into the resonant cavity can be expected to downgrade its optical characteristics, primarily by increasing the internal loss. To minimize this effect, the CC layer has to be very thin (up to 6 nm in our calculations), and the *p*- and *n*-spacer thicknesses have to be adjusted in such a way as to guarantee that the metal layer be placed in the node of standing wave for intensity. In the same instance, the active region has to be placed in the standing wave antinode, as is normally the case in microcavity VCSELs.

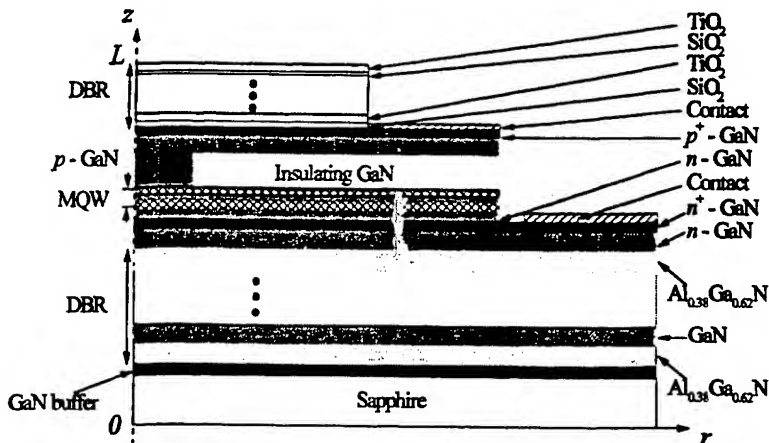


Fig. 1. Schematic structure of cylindrically symmetric intracavity-contacted (IC) InGaN/GaN/AlGaIn VCSEL considered in this paper.

The design of DBR mirrors illustrated in Fig. 1 and summarized in Table 1 is similar to optically pumped InGaIn/GaN/AlGaIn VCSELs reported recently in literature. The *n*-side DBR is composed of $\text{Al}_{0.38}\text{Ga}_{0.62}\text{N}/\text{GaN}$ pairs, with the refractive index data taken from [Ambacher 1997]. The design resonant wavelength is 400 nm. A stack of $\text{SiO}_2/\text{TiO}_2$ dielectric layers is taken for the *p*-side DBR. The number of $\text{SiO}_2/\text{TiO}_2$ pairs is fixed at 6, as in the device of [Someya 1998]. In our initial calculations, we set the number of AlGaIn/GaN pairs to be 35, also following [Someya 1998]. It turned out, however, that the reflectivity of *n*-side DBR was too small for the simulated device to reach CW lasing threshold at room temperature. Hence, we have increased the number of AlGaIn/GaN pairs to 45, with slightly higher reflectivity than that in the most recent design of [Someya 1999a], [Someya 1999b], where 43 pairs of $\text{Al}_{0.34}\text{Ga}_{0.66}\text{N}/\text{GaN}$ were used. It should be noted that in all of these cases the reflectivity of the top DBR is higher than that of the bottom DBR, thus the device emits most of its output through the sapphire substrate which is transparent at 400 nm. The on-axis distribution of optical field intensity in the top section of the device, calculated using the transfer matrix approach (*cf.* Section 3.3), is illustrated in Fig. 2.

The optical cavity between the DBRs is of 3λ thickness, as in [Someya 1998]. It is composed of a 132-nm thick *n*-GaN layer (contacted to the negative electrode by a ring contact, as shown in Fig. 1), the multiple-quantum-well (MQW) active region, and the 281-nm thick *p*-layer of GaN (contacted to the positive electrode by either a ring

contact outside the active window, or a semitransparent circular contact). The active window (electrical current aperture) radius is assumed to be 5 μm .

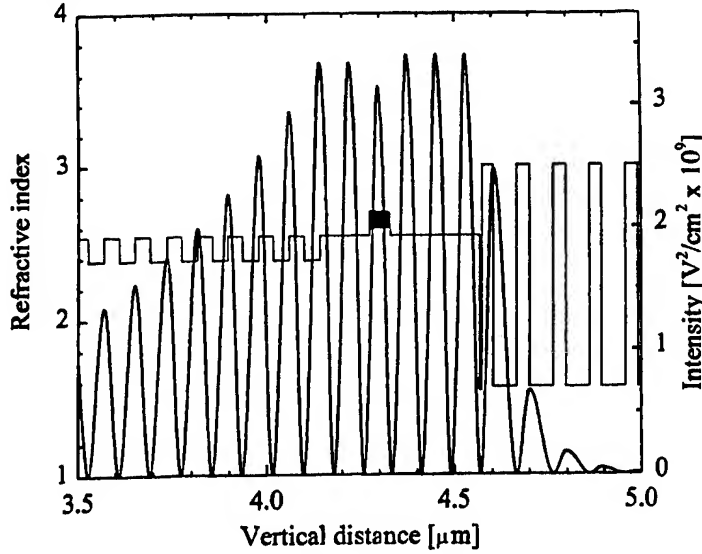


Fig. 2. Intensity of the standing wave and the refractive index profile along the cavity axis. Illustration of proper design of CC-VCSEL: The MQW active region is placed in the maximum intensity region, and the semitransparent metal contact is placed in the minimum intensity region.

Table 1. Device design parameters used in calculations

Parameter	Units	Value	Parameter	Units	Value
Sapphire substrate thickness	μm	100	p^+ -GaN layer thickness	nm	25
$\text{Al}_{0.38}\text{Ga}_{0.62}\text{N}$ DBR layer thickness	nm	42	p -GaN contact layer thickness	nm	10
GaN DBR layer thickness	nm	39.4	Geometrical cavity length	nm	470
Number of $\text{Al}_{0.38}\text{Ga}_{0.62}\text{N}$ DBR layers	-	46	SiO_2 DBR layer thickness	nm	64.1
Number of GaN DBR layers	-	45	TiO_2 DBR layer thickness	nm	33.3
n -GaN spacer thickness	nm	52.3	Number of SiO_2 DBR layers	-	6
n -GaN contact layer thickness	nm	27.4	Number of TiO_2 DBR layers	-	6
n^+ -GaN layer thickness	nm	52.3	Top mesa radius	μm	10
Active $\text{In}_{0.15}\text{Ga}_{0.85}\text{N}$ QW layer thickness	nm	3	Internal radius of p -contact	μm	10
$\text{In}_{0.02}\text{Ga}_{0.98}\text{N}$ barrier layer thickness	nm	3	External radius of p -contact	μm	50
Number of $\text{In}_{0.15}\text{Ga}_{0.85}\text{N}$ quantum wells	-	10	Second mesa radius	μm	50
Number of $\text{In}_{0.02}\text{Ga}_{0.98}\text{N}$ barrier layers	-	9	Internal radius of n -contact	μm	50
p -GaN spacer thickness	nm	186	External radius of n -contact	μm	200
Insulating GaN layer thickness	nm	60	Radius of electrical aperture	μm	5

The number of quantum wells (10) assumed in our calculations is limited by spatial extent of the optical intensity antinode. Although a significantly higher number of wells (26) was used in optical pumping experiments of [Someya 1999a], [Someya 1999b], we note that the efficiency of coupling to the gain medium drops significantly when the wells are near the node of the optical standing wave.

The material parameters used in numerical calculations are given in Table 2. The phase and group refractive indices of group-III nitrides are extracted from the data of [Ambacher 1997]. The refractive index data for the remaining materials are taken from [Palik 1985]. All calculations are performed for ambient temperature of 300 K. A linear variation with temperature is assumed for all material parameters, with tentatively estimated coefficients, except for the bulk resistivity of p -GaN taken in the form accounting for thermal ionization of acceptors [Maćkowiak 1999], which at 300 K are only partially ionized. Therefore, the bulk resistivity of the p -side of the device decreases with increasing temperature, thus causing the diode series resistance (mainly determined by the p -side) to decrease.

The ambipolar diffusion coefficient was calculated using published data on mobility in GaN (see [Maćkowiak 1999] and references therein). At 300 K, we estimate the ambipolar diffusion coefficient $D = 0.389 \text{ cm}^2/\text{s}$.

In our preliminary numerical simulations, a typical value of p -side contact specific resistance $\rho_c = 3.6 \times 10^{-3} \Omega\text{cm}^2$ was assumed. We have determined that VCSELs with such contact resistivity would suffer from strong heating problems, which combined with nonuniform injection current profile would prohibit CW room-temperature operation, irrespective of top contact configuration. Even at voltages as high as 100 V, the device would still operate in the amplified spontaneous emission mode, with the modal gain insufficient to reach threshold. Consequently, we have increased the value of ρ_c to $6 \times 10^{-5} \Omega\text{cm}^2$, which approaches some of the best results reported in literature [Suzuki 1999], [Ho 1999], [Jang 1999], [Lee 2000].

Temperature dependence of thermal conductivity in all layers is assumed in the same form as used previously for GaAs and related compounds [Nakwaski 1994], i.e. $k(T) = k(300) (300/T)^{5/4}$, where T is expressed in kelvins.

Table 2. Material parameters used in calculations

Parameter	Units	Value	Parameter	Units	Value
Refractive index of GaN at 400 nm	-	2.54	Heat conductivity of SiO ₂ at 300 K	W/cm-K	0.12
Group index at 400 nm, 300 K	-	3.8	Heat conductivity of TiO ₂ at 300 K	W/cm-K	0.13
Refractive index of In _{0.15} Ga _{0.85} N at 400 nm, 300 K	-	2.7	Electrical resistivity of Au contact at 300 K	Ωcm	6.8×10^{-6}
Group index at 400 nm, 300 K	-	4.5	Electrical resistivity of p -GaN at 300 K	Ωcm	0.264
Refractive index of Al _{0.38} Ga _{0.62} N at 400 nm, 300 K	-	2.38	Electrical resistivity of n -GaN at 300 K	Ωcm	0.0203
Group index at 400 nm, 300 K	-	2.88	Electrical resistivity of n -Al _{0.38} Ga _{0.62} N at 300 K	Ωcm	0.0203
Refractive index of SiO ₂ at 400 nm	-	1.56	Mg acceptor ionization energy	eV	0.153
Group index at 400 nm, 300 K	-	1.61	p -contact specific resistance	Ωcm^2	6×10^{-5}
Refractive index of TiO ₂ at 400 nm	-	3	n -contact specific resistance	Ωcm^2	3.65×10^{-6}
Group index at 400 nm, 300 K	-	5	Linear nonradiative recombination coefficient, A	s ⁻¹	10^8
Refractive index of sapphire at 400 nm, 300 K	-	1.79	Bimolecular radiative recombination coefficient, B	cm ³ /s	3.6×10^{-11}
Group index at 400 nm, 300 K	-	1.88	Spontaneous emission factor, β	-	10^{-4}
Refractive index of Au at 400 nm	-	1.54	Optical absorption coefficient (of all layers in the cavity)	cm ⁻¹	2
Imaginary part at 400 nm, 300 K	-	-1.81	Temperature coefficient of refractive index (of all layers in the cavity)	K ⁻¹	10^{-4}
Energy bandgap of GaN	eV	3.39	Temperature coefficient of InGaN/GaN energy bandgap	eV/K	-4.2×10^{-4}
Energy bandgap of In _{0.15} Ga _{0.85} N	eV	3.132	Temperature coefficient of electrical resistivity of n -type layers	K ⁻¹	5×10^{-3}
Electron effective mass in In _{0.15} Ga _{0.85} N	m_0	0.205			
Hole effective mass in In _{0.15} Ga _{0.85} N	m_0	0.755			
Conduction band offset at In _{0.15} Ga _{0.85} N/GaN interface	eV	0.22			
Valence band offset at In _{0.15} Ga _{0.85} N/GaN interface	eV	0.1031			
Energy parameter of spectral broadening in In _{0.15} Ga _{0.85} N	eV	0.068			
Heat conductivity of GaN at 300 K	W/cm-K	1.1			
Heat conductivity of Al _{0.38} Ga _{0.62} N at 300 K	W/cm-K	1.898			
Heat conductivity of sapphire at 300 K	W/cm-K	0.46			

3. VCSEL MODEL DESCRIPTION

In order to predict characteristics of electrically pumped group-III nitride VCSELs and evaluate prospects for room-temperature CW operation, we have integrated our previously developed electrical-thermal (ET), gain, and optical modules into a new 3D self-consistent electrical-thermal-optical (ETO) simulation tool. The following brief discussion summarizes the main features of these modules.

3.1. Electrical-Thermal Module

The ET part of our simulator is based on the control-volume calculation method and was described in our earlier publications [Smagley 1998], [Osiński 1998], [Osiński 1999]. The electrical problem involves solving the Laplace equation in the entire volume of the device and finding the electrical potential and vectorial current density distributions. The p - n junction is modeled as biased by direct voltage (Fermi voltage) corresponding to the quasi-Fermi-level separation in the active region. In this approach, a continuous function of the radial-distance-dependent Fermi voltage is assumed. Self-consistency of the electrical simulation requires that the local voltage and current at the p - n junction all correspond to the calculated current flow within the entire device (taking into account contact geometry, contact resistance, and bulk resistance outside the active region). Carrier diffusion in the active region plane is also taken into account. The effects of diffusion are especially important near the regions of high current crowding, and in those regions several control volumes per diffusion length are necessary in order to obtain adequate carrier distribution. Near the edges of the active region, where carrier density exceeds $2 \times 10^{19} \text{ cm}^{-3}$, the diffusion length is as short as 200-280 nm. Outside the current window, carrier diffusion determines the tail of the carrier density distribution, and the diffusion length there is about 600 nm (carrier density $\sim 10^{17} \text{ cm}^{-3}$).

The thermal problem involves solution of heat conduction equation with appropriate boundary conditions at the heat sink (located below the sapphire substrate) and outside walls of the chip. Local heat generation via Joule heating in passive regions and nonradiative recombination in the active region is included, and heat transport in laser chip is analyzed, producing thermal flux and temperature distributions in the entire volume of the device.

3.2. Gain Module

The carrier density profile produced by the ET module is used to calculate the local value of material gain/absorption coefficient. The material gain/absorption spectra are calculated using a modified version of the k - p model of [Fang 1995], originally developed for bulk GaN. Our modifications, explained briefly in [Smolyakov 1999], include choosing a transition matrix element appropriate for the quantum well active region and adding band tail states. Our model, described in more detail in [Osiński 1999a], assumes the recombination balance of carriers that includes linear nonradiative recombination, spontaneous bimolecular radiative recombination, and stimulated recombination, with position-dependent stimulated recombination lifetime as determined by the lasing mode profile. All recombination terms are balanced by the carrier generation term produced by the vertical component of the current density injected into the active region.

3.3. Optical Module

The 3D profile of temperature calculated in the ET module and the radial distribution of material gain/absorption in the active region plane calculated in the gain module are used in the optical module as input data. The optical model is based on the effective frequency method (EFM) [Wenzel 1997], [Smolyakov 1999] combined with the rate equations for photon and carrier densities. This approach allows us to calculate the lasing wavelength (that is always somewhat detuned from the Bragg resonance due to lateral nonuniformity of the device structure), modal intensity profile, emitted power, and electromagnetic energy flux density inside the cavity. For the first time in application of the EFM, we use dynamically readjusted spatial distributions of gain and refractive index, which allows us to treat arbitrary VCSEL structures of complex geometry. The model also includes temperature-induced variations of complex permittivity according to the calculated radial and vertical profiles of temperature. Combined with the ET module, the optical solver allows us to model effects associated with current crowding and self-distribution, spatial hole burning and thermal lensing. Thus, the fully integrated model takes into account the most important effects in both short-pulse (isothermal) and CW operation of the laser, and includes major physical processes self-consistently.

The effective frequency $\nu_{\text{eff}}(r)$ is found as a solution of the following "axial" equation, in which the radial distance r is treated as a parameter:

$$\left[\frac{d^2}{dz^2} + k_0^2 n^2(r, z) \right] f(z; r) = v_{\text{eff}}(r) k_0^2 n(r, z) n_g(r, z) f(z; r) , \quad (1)$$

where $f(z; r)$ is the axial field profile, $k_0 = \omega_0/c$ is the vacuum wave number, while $n = n' + in''$, and $n_g = n_g' + in_g''$ are the complex refractive phase and group indices evaluated at the nominal angular frequency ω_0 , corresponding to designed periodicity of DBR mirrors. We impose the following boundary conditions on $f(z; r)$, ensuring the outgoing plane waves at the bottom ($z = 0$) and top ($z = L$) surfaces of the laser cavity (for more details on the EFM, see [Wenzel 1997], [Smolyakov 1999]):

$$\frac{df}{dz} \pm ik_z f = 0 , \quad z = \begin{cases} L + \varepsilon \\ 0 - \varepsilon \end{cases} . \quad (2)$$

For any fixed radial position r in piecewise-constant geometries, we solve the "axial" equation (1) using the transfer matrix approach, similar to that described in [Bergmann 1998] and [Noble 1998]. The general solution of Eq. (1) in each axial region $[z_{j-1}, z_j]$ is given by:

$$f_j(z) = a_j \exp[-ih_j(z - z_j)] + b_j \exp[ih_j(z - z_j)] , \quad j = 1, \dots, M \quad (3)$$

where

$$h_j = k_0 \sqrt{n_j^2 - v_{\text{eff}} n_j n_g} . \quad (4)$$

Assuming TE polarization for the electric field vector, we join these solutions and their derivatives at each interface z_j , which corresponds to matching the tangential electric and magnetic fields. By applying these continuity conditions, we relate a_j, b_j to a_{j+1}, b_{j+1} at each axial boundary $z = z_j$ through the transfer matrix T_j :

$$\begin{bmatrix} a \\ b \end{bmatrix}_{j+1} = T_j \times \begin{bmatrix} a \\ b \end{bmatrix}_j \quad (5)$$

This recursive relationship connects the coefficients from the $j = 1$ region (substrate) to the coefficients in the $j = M$ region (air) via:

$$\begin{bmatrix} a \\ b \end{bmatrix}_M = T_{M-1} T_{M-2} \dots T_2 T_1 \begin{bmatrix} a \\ b \end{bmatrix}_1 = T_{\text{tot}} \begin{bmatrix} a \\ b \end{bmatrix}_1 . \quad (6)$$

The boundary conditions (2) for outgoing plane waves transform to:

$$a_1 = b_M = 0 . \quad (7)$$

The only variable in Eq. (6) is v_{eff} , with all other quantities being design and material parameters. For $a_1 = 0$ and arbitrarily chosen $b_1 = 1$, we seek the values of v_{eff} such that condition (7) for b_M is satisfied.

An important connection between the electrical-thermal, electronic and optical parts of the simulator is realized through the rate equations for carrier density N and a quantity S that replaces the usual photon density in position-independent rate equations:

$$\frac{dN}{dt} = D \nabla^2 N + \frac{J_z}{ed} - AN - BN^2 - \frac{N}{\tau_{st}} , \quad (8)$$

$$\frac{dS}{dt} = \beta BN^2 + \frac{N}{\tau_{st}} - \frac{S}{\tau_{ph}} , \quad (9)$$

where D is the diffusion coefficient, j_z is the vertical component of the current density, e is the electron charge, d is the total thickness of all quantum-well layers, β is the spontaneous emission factor, A is the linear nonradiative recombination coefficient, B is the bimolecular radiative recombination coefficient, τ_n is the stimulated lifetime for carriers, and τ_{ph} is the photon lifetime that accounts for the decrease in the photon density due to output losses and other losses, not directly associated with radiative transitions. S is defined here as twice the time-averaged density of electrical energy in the electromagnetic wave, divided by photon energy, and has the spatial dependence of $|E(r,z)|^2$.

Within the active region, the carrier density N is assumed to be uniform in the vertical z direction, i.e. all quantum wells are assumed to be pumped equally. This assumption allows us to find carrier density distribution $N(r)$ in all quantum wells by solving the diffusion equation (8) just once for an effective active region of total thickness d , instead of handling this problem separately for each quantum well.

Most importantly, S is not assumed to be uniform, but is defined as

$$S(r,z) = P n'^2(r,z) |E(r,z)|^2, \quad (10)$$

where P is the total number of photons in the mode, n' is the real part of the refractive index, and $E(r,z)$ is proportional to the electrical field profile calculated within the EFM [Wenzel 1997], [Smolyakov 1999] and normalized according to

$$2\pi \int_{V_M} n'^2(r,z) |E(r,z)|^2 r dr dz = 1, \quad (11)$$

with the integration performed over the entire mode volume V_M . Note that $E(r,z)$ does not have the dimension of the electrical field, but instead is expressed in units of $(1/\text{volume})^{1/2}$. With this normalization condition, integration of Eq. (10) over the mode volume V_M produces the total number of photons in the mode P .

The stimulated lifetime for carriers τ_n depends on the radial distance r and is determined as

$$\tau_n(r) = \frac{N(r)}{g(r)P \frac{1}{d} \int_{QW_s} v_g n'^2(r,z) |E(r,z)|^2 dz}, \quad (12)$$

where v_g is the group velocity, $g(r)$ is the local material gain and integration is performed over all quantum wells. This integration follows from our assumption of the carrier density N being uniform along the z direction and represents averaging the term $v_g gS$, originally present in the rate equations, over all quantum wells.

Integration of Eq. (9) over the mode volume V_M gives, under steady-state conditions, the following expression for the total number of photons in the mode P :

$$P = \tau_{ph} \int_{V_A} \left(\beta B N^2 + \frac{N}{\tau_n} \right) dV, \quad (13)$$

where V_A is the active region volume. Since the integrand itself (both the carrier density N and the stimulated carrier lifetime τ_n) depends on P according to Eqs. (8)-(10) and (12), Eq. (13) is used to find P by means of an iterative process of the type $P_{i+1} = F(P_i)$, where i is the iteration number.

After the total number of photons in the mode P is found, the value for the actual electrical field $E(r,z)$ is obtained by equating the calculated value for the electromagnetic energy in the mode with that calculated according to the well-known formula of electrodynamics:

$$\hbar\omega P = 2\pi \int_{V_M} \frac{1}{4} \epsilon_0 n^2(r,z) |E(r,z)|^2 r dr dz + 2\pi \int_{V_M} \frac{1}{4} \mu_0 |H(r,z)|^2 r dr dz = \pi \int_{V_M} \epsilon_0 n^2(r,z) |E(r,z)|^2 r dr dz, \quad (14)$$

where the left-hand side is the calculated electromagnetic energy, the right-hand side represents the time-averaged electromagnetic energy for the electromagnetic wave characterized by the electrical field $E(r,z)$ and magnetic field

$H(r,z)$, and $E(r,z)$ has the spatial dependence of $E(r,z)$ calculated within the EFM. For details on the procedure of calculating the output power from a known electrical field $E(r,z)$ inside the device, see [Osiński 1999b].

The electrical, thermal, electronic, and optical equations are coupled via the dependence of heat sources on the current and electrical potential distributions, and via temperature dependence of the barrier voltage at the junction and resistivity in the passive regions. Therefore, the model includes complex interaction phenomena such as spatial hole burning or current redistribution related to changes in material parameters due to local Joule heating.

4. INVESTIGATION OF RING-CONTACT AND CIRCULAR CONTACT DESIGNS

As described in Section 2, we consider two alternative designs of electrically pumped intracavity-contacted group-III nitride VCSELs. In view of relatively high p -side contact resistance, the common ring-contact (RC) design can be expected to suffer from strong current crowding effects at the edges of the active region. Therefore, we shall also explore the potential benefits that may arise from using a semitransparent circular contact (CC). Both RC and CC contact configurations are studied under low-duty-cycle short-pulse and CW operating conditions. The criterion for short-pulse operation would be a negligible temperature rise within the entire device over the time scale of a single current pulse. The non-stationary heat conduction equation predicts a monotonic temperature rise, reaching a maximum value in a steady state. The very first stage of the heating process is known as an adiabatic regime, with heat transport playing a negligible role. The heating rate in this case is

$$dT/dt \sim q/Cp, \quad (15)$$

where q is the density of heat generation, C is the heat capacity, and p is the density of the material. In the active region, $q \approx jV/d$, where j is the current density, V is the voltage applied to the junction, and d is the active region thickness. Typically, the initial heating rate in laser regime is $\sim 0.5\text{--}2$ K/ns, hence a 10-ns long pulse can produce a temperature rise of 5-20 K. Therefore, the "isothermal" case implies a pulse width of a few nanoseconds.

4.1. Current Crowding Effects and Improved Design of Ring-Contact VCSEL

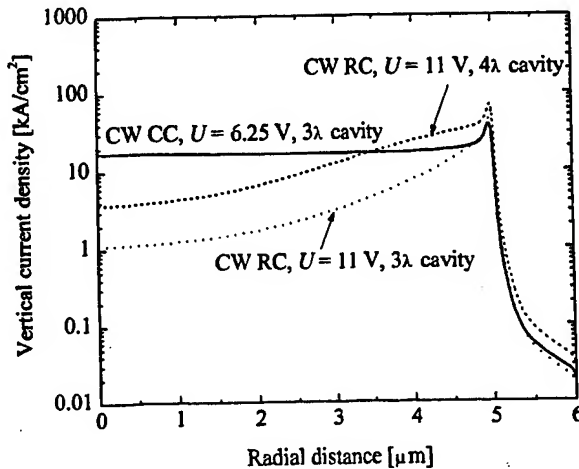


Fig. 3. Vertical current density profiles in the active region plane for CW operation of nitride-based IC-VCSELs at room temperature. The voltages of 11 V and 6.25 V are near the CW lasing threshold for RC device with 4λ cavity and CC device with 3λ cavity, respectively.

Our previous studies of current crowding effects in IC-VCSELs [Smagley 1998], [Osiński 1998], [Osiński 1999a] indicated that even in GaAs-based VCSELs nonuniformity of current injection in RC configuration can be very severe. We expected the situation to become much worse in GaN-based VCSELs, due to poor conductivity of p -GaN and high p -contact resistance. This expectation is confirmed in Fig. 3, showing vertical current density profiles for three CW cases: RC and CC configurations with 3λ cavity, and RC configuration with 4λ cavity. The CC geometry does improve current uniformity significantly, but even in this case there is a residual hump at the edge of the active region, indicating that a significant portion of current in the p -GaN spacer is still flowing in the radial direction. Most importantly, comparison of RC and CC results for 3λ cavity clearly indicates that the threshold for the 3λ RC

device would be much higher than that of the CC device. In spite of a higher voltage (11 V vs. 6.25 V for the CC device), the total current flowing through the 3λ -RC device is 2.2 times smaller (6.81 mA vs. 14.86 mA), and the series resistance is as high as $1615\ \Omega$. In the same instance, nonuniformity of the vertical current density is very strong already (the current crowding coefficient, defined as the ratio of vertical current density at its maximum near the edge of the active region to its value at the center of device, is as high as 55, compared to only 2.3 for the CC device), and is bound to become much worse with increasing bias. Hence, even if the 3λ -RC device could lase, it would definitely operate in a high-order mode. In order to reduce current nonuniformity and series resistance, and to increase the likelihood of fundamental mode operation, we have therefore replaced the 3λ cavity design for RC device with 4λ cavity, where the thickness of p -GaIn spacer was increased by one wavelength to 343 nm. The current crowding coefficient for the 4λ -RC device is 26, and the series resistance at 11 V is reduced to $671\ \Omega$ (current 16.4 mA). All of the results presented in subsequent sections for the RC case correspond to the 4λ design.

4.2. I - V and L - I Characteristics

Fig. 4 shows calculated current-voltage (I - V) characteristics of IC-VCSELs in both 4λ -RC and 3λ -CC configurations and under both CW and pulsed-current conditions. The range of voltages is in each case chosen such as to encompass below-threshold and above-threshold operation. Compared to the RC design, we expect the CC configuration to offer lower electrical resistance and smaller driving voltage at any given current. As shown in Fig. 4, this is indeed the case both under pulsed and CW conditions. For the case of pulsed RC device, the series resistance is practically unaffected by the driving voltage level. The calculated ohmic resistance is $985\ \Omega$. For the case of CW operation, the RC device resistance improves considerably, decreasing to $\sim 165\ \Omega$ at driving voltages exceeding 10 V. This effect can be easily explained by a strong temperature dependence of p -GaIn conductivity, with the concentration of ionized acceptors increasing exponentially with temperature. Interestingly enough, the situation is quite opposite in the case of semitransparent CC configuration. Here, the series resistance actually increases with temperature (from $200\ \Omega$ at 4 V to $260\ \Omega$ above 7 V). We ascribe this behavior to different current paths in RC and CC devices. In the case of CC geometry, current is not forced to flow through a long radial path on the p -side of the VCSEL device, hence the series resistance is mainly affected by variations in n -GaIn conductivity which deteriorates with temperature.

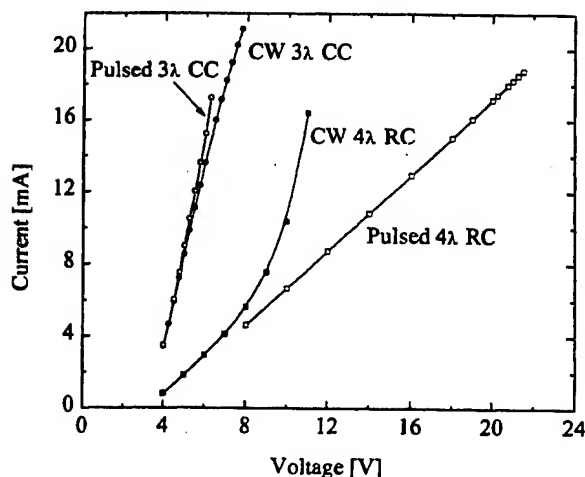


Fig. 4. Current-voltage characteristics of nitride-based IC-VCSELs.

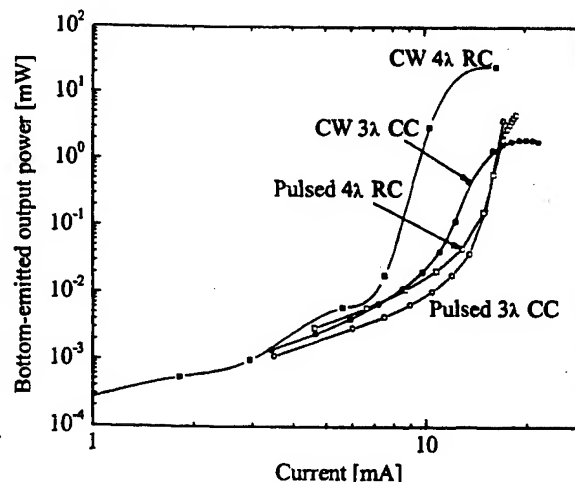


Fig. 5. Light-current characteristics of nitride-based IC-VCSELs.

Fig. 5 depicts light-current (L - I) characteristics of the 4λ -RC and 3λ -CC devices in the same range of voltages as in Fig. 4. At threshold, the output power increases by at least two orders of magnitude, although the transition may seem rather smooth on the logarithmic scale. We use the linear extrapolation of above-threshold L - I curves to de-

termine the threshold. Rather surprisingly, the lowest threshold current of 9.5 mA is obtained for the CW RC case, followed by 12.4 mA for the CW CC case, and almost equal (15.9 and 15.1 mA, respectively) threshold currents for RC and CC devices under pulsed conditions. We discuss these results in more detail in Section 5.

It should be noted that the L - I curves for CW operation saturate and eventually decline with increasing current. This kind of behavior is caused by the active region temperature increase with increasing pumping, and is quite typical of real devices.

4.3. Carrier Density and Material Gain Profiles

The radial distribution of carriers in the active region plane depends on the distribution of the injection current (z -component of the current density at the junction) as well as on the recombination and diffusion of carriers. Provided that temperature gradient within the active region is small, the material gain profile at the lasing wavelength closely resembles that of the carrier density. Consequently, gain distribution is strongly influenced by current crowding effects, especially since the diffusion length of carriers in GaN is relatively small. As shown in Fig. 6, carrier density distribution in 4λ -RC devices is very nonuniform, and its shape can be expected to favor high-order transverse modes. On the other hand, the 3λ -CC configuration offers a fairly uniform carrier profile, hence it can be expected to support fundamental LP_{01} mode operation.

Insertion of a semitransparent metal contact at the top side of the p -GaN mesa does, however, introduce an additional optical loss associated with strong absorption of lasing light in the metallic layer. This limits the thickness of semitransparent Au layer to less than 6 nm, and results in a residual peak of injected current density at the edges of the active region. Our calculations show that insertion of a 10-nm thick semitransparent Au contact reduces the photon lifetime τ_{ph} to 1.05 ps and produces an additional average internal loss of $\alpha_{met} \approx 76 \text{ cm}^{-1}$, compared to $\tau_{ph} = 2.27 \text{ ps}$ and $\alpha_{met} \approx 18 \text{ cm}^{-1}$ for a 6-nm thick CC layer. With the output loss of only ~ 31 - 33 cm^{-1} , the internal loss associated with the 10-nm thick semitransparent contact would therefore dominate the device behavior and would severely degrade its performance. These estimations have been made taking the average group index inside the cavity (weighted with longitudinal intensity distribution) as 3.47 for 6-nm thick metal and 3.49 for 10-nm-thick metal.

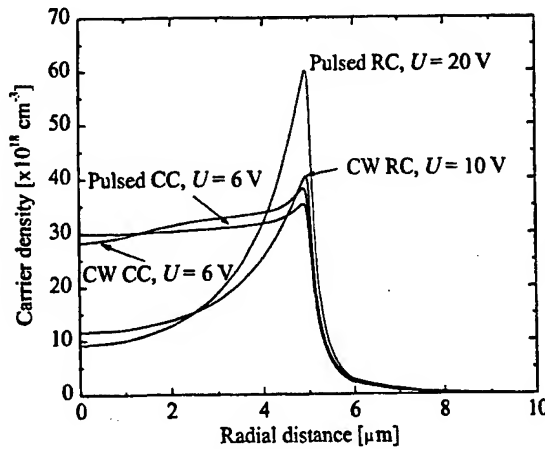


Fig. 6. Radial profiles of carrier density in the active region plane for pulsed and CW operation of nitride-based IC-VCSELs at room temperature, evaluated near threshold.

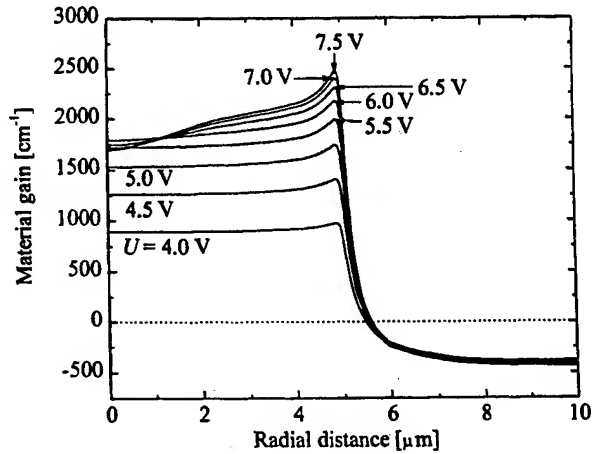


Fig. 7. Gain profile evolution for 3λ -CC device operating CW. Voltage is changing in upward direction from 4 to 7.5 V with step of 0.5 V. Threshold voltage is 5.8 V.

Above threshold, the lasing mode affects carrier distribution via the spatial hole-burning (SHB) effect. Self-consistency under lasing conditions implies a dynamic saturation of the modal gain near the threshold level. In the case of fundamental mode operation, this leads to enhanced depletion of carrier population in the center of the device and increases nonuniformity of carrier density and material gain distributions. This is illustrated in Fig. 7 for the case of a 3λ -CC device operating in the LP_{01} mode. It is clear that SHB can occur even at relatively low output power levels.

5. DISCUSSION

The improved design of nitride-based IC-VCSELs (low p -side contact resistance, higher number of DBR periods on the n -side, and thicker p -side spacer for RC configuration) has resulted in our prediction of relatively low threshold voltage and threshold current for both RC and CC geometries and under both short-pulse and CW operating conditions. Table 3 summarizes the threshold data in all four cases, including electrical, optical, and thermal properties.

Table 3. Threshold conditions

	Ring p -side contact (RC)		Semitransparent circular contact (CC)	
	Pulsed	CW	Pulsed	CW
U_{th} [V]	18.8	9.2	6.0	5.8
I_{th} [mA]	15.9	9.5	15.1	12.4
j_{th} [kA/cm ²]	20.4	12.1	19.1	15.9
Mode at threshold	LP ₀₁	LP ₁₁	LP ₀₁	LP ₂₁
T_A [°C]	-	38.6	-	49.2
$T_A(r_A)$ [°C]	-	43.1	-	35.6

Perhaps the most unexpected outcome of our simulations shown in Table 3 is the prediction of fundamental mode operation at threshold in pulsed RC-VCSELs and higher-order mode operation at threshold in CW CC-VCSELs. The latter results involves thermal effects and is discussed in the next subsection. The pulsed (isothermal) results, however, can be understood by considering only the EFM solutions of wave equation in VCSEL cavity. In view of a very strong nonuniformity of carrier density in RC lasers (see Fig. 6), it would be natural to expect a high-order mode operation. The most likely candidate might seem to be in the LP _{m 1} ($m = 1, 2, 3, \dots$) family of modes with a single maximum away from the waveguide axis. However, all of these modes extend far beyond the active region, where they experience significant loss from unpumped quantum wells. In contrast, the fundamental mode, while not overlapping well with the gain profile, is much better confined to the active region, and does not suffer from excessive loss in lateral unpumped layers.

5.1. Thermal Effects and Their Influence on Laser Performance

One of the most important aspects of ETO simulation is the study of thermal behavior of nitride-based IC-VCSELs. As indicated in Fig. 5, for both RC and CC configurations the lasing threshold under CW conditions is lower than under pulsed conditions, which is characteristic of thermal lensing effects in gain-guided or weakly index-guided VCSELs [Panajotov 1998], [Brunner 2000]. The situation in RC-VCSELs is, however, more complicated than in conventional thermal lensing case, since due to strong current crowding the temperature actually peaks at the edges of the active region, causing a thermal antiguiding effect. Fig. 8 shows normalized temperature profiles for RC and semitransparent CC configurations. For CC geometry, the temperature profile has the usual "bell-shape" form, consistent with the standard interpretation of thermal lensing. In contrast, the temperature profile for RC configuration creates a thermal waveguide at the periphery of the active region that pushes the optical field out of the center. Strong coupling between thermal and optical phenomena is reflected in large deformations of the fundamental mode profile, as illustrated in Fig. 9. This mode deformation produces a much better overlap between the mode profile and the gain distribution, and, consequently, the threshold and power performance under CW conditions is considerably improved compared to pulsed operation (*cf.* Table 3). In fact, the threshold for CW RC laser is the lowest of all four cases considered. Also, the CW slope efficiency of RC-VCSEL is rather high, providing an output power of ~3 mW at 400 nm under pumping current of ~10 mA (*cf.* Fig. 5).

As shown in Table 3, the lowest-threshold mode for the CW RC device is LP₁₁. Thermal lensing acts here in a rather unconventional fashion, trimming the tail of the LP₁₁ mode intensity in the unpumped part of the device ($r > 5 \mu\text{m}$), thus improving its overlap with the gain profile and cutting down the loss so that LP₁₁ has now a lower threshold than the fundamental LP₀₁ mode. On the other hand, the LP₀₁ mode itself undergoes a very significant transformation, illustrated in Fig. 9 (dotted profile "CW 4λ RC LP₀₁"). The extent of modal deformation in this particular case illustrates most forcefully how important it is to include thermal-optical interactions in consideration of optical modes in IC-VCSELs operating under CW conditions. Note that the gain profile nonuniformity plays here a

rather secondary role, as demonstrated by absence of such deformation in the RC LP₀₁ mode under pulsed conditions.

The improving overlap between the modal intensity and material gain profiles with increasing current may lead to a situation where the modal gain could increase in spite of a temperature-related decrease in material gain. Thus, the temperature behavior of RC-VCSELs can be quite complicated. An important design element is also a proper tuning of the gain spectrum to the cavity mode. Practically, this means that there is an optimal temperature of operation for any particular initial detuning. In some extreme cases, the temperature dependence of the threshold current can be a non-monotonic function, in contrast to edge-emitting semiconductor lasers.

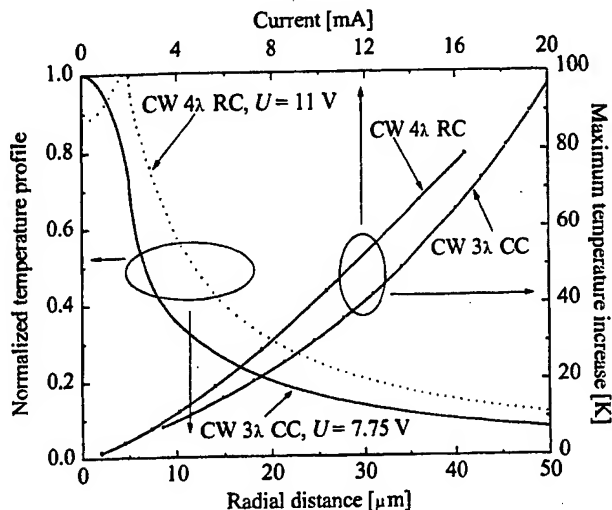


Fig. 8. Left/bottom axes: Normalized radial profiles of temperature in nitride-based IC-VCSELs operating CW above threshold; Right/top axes: Maximum temperature increase as a function of current in nitride-based IC-VCSELs operating CW.

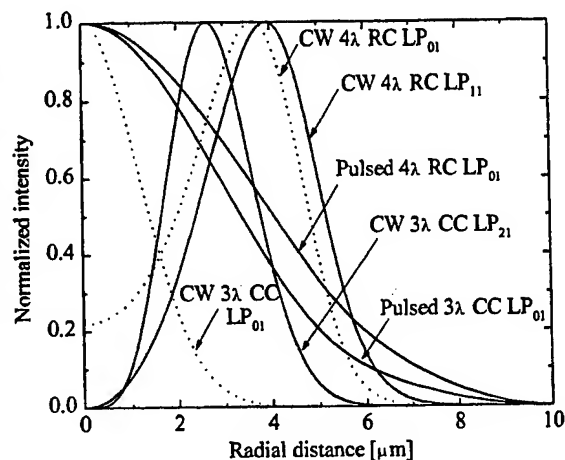


Fig. 9. Normalized radial profiles of intensity for the lowest-threshold modes listed in Table 3 (solid lines) and for the LP₀₁ modes under CW conditions in both RC and CC configurations. All profiles are calculated at close-to-threshold conditions.

Fig. 9 also explains why the CC device no longer favors the fundamental mode when operated under CW conditions. Comparison of “Pulsed 3λ CC LP₀₁” and “CW 3λ CC LP₀₁” profiles reveals that the thermal lensing effect in CC devices is quite strong, as it causes strong focusing of the fundamental mode. As a result, the LP₀₁ mode cannot utilize all of the gain available in the active region, but is limited only to ~2 μm radius. The higher-order LP₂₁ mode extends further towards the periphery of the active region, where the gain is slightly higher, and therefore ends up with a lower threshold.

The incomplete filling of the 5-μm-radius optical aperture by the LP₀₁ mode in CC-VCSEL indicates that a high-efficiency single-fundamental-mode device should have the active region radius of ~2 μm.

6. CONCLUSIONS

In our previous studies of current crowding in IC-VCSELs, the electrical-thermal simulator proved to be an essential tool. Present implementation of our electrical-thermal-optical simulator has an added dimension of interactions involving the optical field. The new tool can produce all main ETO characteristics, such as current density distribution, temperature distribution, mode profiles (in a single-mode approximation), profiles of the Poynting vector (in both radial and vertical directions), *etc.* It offers a very cost-effective approach to development of novel devices, and, as shown in this paper, is particularly useful in design of electrically-pumped nitride-based VCSELs.

The main conclusions of this paper can be summarized as follows:

1) Taking as an example the intracavity-contacted nitride-based VCSELs, we show that the effective frequency method is a useful numerical technique for optical analysis of complex VCSEL structures. It provides information about profiles of transverse mode profiles, spectra, and mode selectivity.

2) Combined with the electrical-thermal solver, the optical module can be used to treat temperature detuning, current crowding, nonuniform gain saturation, etc.

3) The rather high series resistance of the nitride-based IC-VCSELs is not an obstacle for CW operation, provided low-resistance *p*-side contact and high-reflectivity DBRs are used. Moderate heating of the active region is actually favorable, as it reduces the threshold current via the thermal lensing effect, and improves the efficiency.

4) Self-consistent simulation provides insight into complex interactions between thermal, electrical and optical phenomena in VCSELs. In particular, we demonstrate how the spatial hole burning occurs, and how the thermal perturbations of optical waveguide lead to strong mode profile deformations under conditions.

5) IC-VCSELs with a 5- μm radius of electrical window and with either a ring *p*-side contact or a semi-transparent circular contact are predicted to operate in the fundamental transverse mode under pulsed conditions. The semitransparent circular contact configuration offers the best prospects for CW operation in fundamental mode, provided the active region radius is reduced to 2 μm .

7. ACKNOWLEDGEMENT

Support from DARPA through the Optoelectronic Materials Center program and from AFOSR through the Optoelectronics Research Center is gratefully acknowledged.

8. REFERENCES

- [Amano 1993] H. Amano, N. Watanabe, N. Koide, and I. Akasaki, "Room-temperature low-threshold surface-stimulated emission by optical pumping from $\text{Al}_{0.1}\text{Ga}_{0.9}\text{N}/\text{GaN}$ double heterostructure", *Jpn. J. Appl. Phys., Pt. 2 (Lett.)*, vol. 32 (#7B), pp. L1000-L1002, 15 July 1993.
- [Ambacher 1997] O. Ambacher, M. Arzberger, D. Brunner, H. Angerer, F. Freudenberger, N. Esser, T. Wethkamp, K. Wilmers, W. Richter, and M. Stutzmann, "AlGaIn-Based Bragg Reflectors", *MRS Internet J. Nitride Semicond. Res.*, vol. 2, Art. 22, 28 Aug. 1997.
- [Anderson 1999] N. G. Anderson, D. A. S. Loeber, J. M. Redwing, M. A. Tischler, and J. S. Flynn, "Comment on "Lasing Emission from an $\text{In}_{0.1}\text{Ga}_{0.9}\text{N}$ Vertical Cavity Surface Emitting Laser"", *Jpn. J. Appl. Phys., Pt. 1 (Regul. Pap. & Short Notes)*, vol. 38 (#8), pp. 4794-4795, 15 Aug. 1999.
- [Bergmann 1998] M. J. Bergmann and H. C. Casey, Jr., "Optical-field calculations for lossy multiple-layer $\text{Al}_x\text{Ga}_{1-x}\text{N}/\text{In}_x\text{Ga}_{1-x}\text{N}$ laser diodes", *J. Appl. Phys.*, vol. 84 (#3), pp. 1196-1203, 1 Aug. 1998.
- [Brunner 2000] M. Brunner, K. Gulden, R. Hövel, M. Moser, and M. Illegems, "Thermal lensing effects in small oxide confined vertical-cavity surface-emitting lasers", *Appl. Phys. Lett.*, vol. 76 (#1), pp. 7-9, 3 Jan. 2000.
- [Eliseev 1999] P. G. Eliseev, M. Osiński, J. Lee, T. Sugahara, and S. Sakai, "Band-tail model and temperature-induced blue-shift in photoluminescence spectra of $\text{In}_x\text{Ga}_{1-x}\text{N}$ grown on sapphire", Special Issue on III-V Nitrides and SiC, *J. Electron. Mat.*, vol. 29 (#3), March 2000 (in print).
- [Fang 1995] W. Fang and S. L. Chuang, "Theoretical prediction of GaN lasing and temperature sensitivity", *Appl. Phys. Lett.*, vol. 67 (#6), pp. 751-753, 7 Aug. 1995.
- [Fritz 1995] I. J. Fritz and T. J. Drummond, "AlN-GaN quarter-wave reflector stack grown by gas-source MBE on (100) GaAs", *Electron. Lett.*, vol. 31 (#1), pp. 68-69, 5 Jan. 1995.
- [Ho 1999] J.-K. Ho, C.-S. Jong, C. C. Chiu, C.-N. Huang, K.-K. Shih, L.-C. Chen, F.-R. Chen, and J.-J. Kai, "Low-resistance ohmic contacts to *p*-type GaN achieved by the oxidation of Ni/Au films", *J. Appl. Phys.*, vol. 86 (#8), pp. 4491-4497, 15 Oct. 1999.
- [Honda 1995] T. Honda, A. Katsube, T. Sakaguchi, F. Koyama, and K. Iga, "Threshold estimation of GaN-based surface emitting lasers operating in ultraviolet spectral region", *Jpn. J. Appl. Phys., Pt. 1 (Regul. Pap., Short Notes, & Rev. Pap.)*, vol. 34 (#7A), pp. 3527-3532, 15 July 1995.
- [Inamori 1995] M. Inamori, H. Sakai, T. Tanaka, H. Amano, and I. Akasaki, "Direct patterning of the current confinement structure for *p*-type column-III nitrides by low-energy electron beam irradiation treatment", *Jpn. J. Appl. Phys. Pt. 1 (Regul. Pap., Short Notes, & Rev. Pap.)*, vol. 34 (#2B), pp. 1190-1193, Feb. 1995.

- [Ishikawa 1998] H. Ishikawa, N. Nakada, G. Y. Zhao, T. Egawa, T. Jimbo, and M. Umeno, "Al_{0.27}Ga_{0.73}N/GaN distributed Bragg reflector grown by atmospheric pressure MOCVD", *Proc. 2nd International Symp. Blue Laser & Light Emitting Diodes* (K. Onabe, K. Hiramatsu, K. Itaya, and Y. Nakano, Eds.), Kisarazu, Chiba, Japan, 29 Sept.-2 Oct. 1998, Paper Fr-15, pp. 727-730.
- [Jang 1999] J. S. Jang, S. J. Park, and T. Y. Seong, "Formation of low resistance Pt ohmic contacts to p-type GaN using two-step surface treatment", *J. Vacuum Science & Technology B: Microelectronics and Nanometer Structures*, vol. 17 (#6), pp. 2667-2670, Nov.-Dec. 1999.
- [Jiang 1997] H. X. Jiang, J. Y. Lin, M. A. Khan, Q. Chen, and J. W. Yang, "Surface emission of In_xGa_{1-x}N epilayers under strong optical excitation", *Appl. Phys. Lett.*, vol. 70 (#8), pp. 984-986, 24 Feb. 1997.
- [Khan 1991] M. A. Khan, D. T. Olson, J. M. Van Hove, and J. N. Kuznia, "Vertical-cavity, room-temperature stimulated emission from photopumped GaN films deposited over sapphire substrates using low-pressure metal-organic chemical vapor deposition", *Appl. Phys. Lett.*, vol. 58 (#14), pp. 1515-1517, 8 April 1991.
- [Khan 1994] M. A. Khan, S. Krishnakutty, R. A. Skogman, J. N. Kuznia, D. T. Olson, and T. George, "Vertical-cavity stimulated emission from photopumped InGaN/GaN heterojunctions at room temperature", *Appl. Phys. Lett.*, vol. 65 (#5), pp. 520-521, 1 Aug. 1994.
- [Krestnikov 1999a] I. L. Krestnikov, W. V. Lundin, A. V. Sakharov, V. A. Semenov, A. S. Usikov, A. F. Tsatsul'nikov, Zh. I. Alferov, N. N. Ledentsov, A. Hoffmann, and D. Bimberg, "Room-temperature photopumped InGaN/GaN/AlGaIn vertical-cavity surface-emitting laser", *Appl. Phys. Lett.*, vol. 75 (#9), pp. 1192-1194, 30 Aug. 1999.
- [Krestnikov 1999b] I. L. Krestnikov, W. V. Lundin, A. V. Sakharov, V. A. Semenov, A. S. Usikov, A. F. Tsatsul'nikov, Zh. I. Alferov, N. N. Ledentsov, A. Hoffmann, and D. Bimberg, "Photopumped InGaN/GaN/AlGaIn vertical cavity surface emitting laser operating at room temperature", *Proc. 3rd International Conf. Nitride Semiconductors*, Montpellier, France, 4-9 July 1999, *Phys. Status Solidi B*; vol. 216 (#1), pp. 511-515, 1 Nov. 1999.
- [Langer 1999] R. Langer, A. Barski, J. Simon, N. T. Pelekanos, O. Konovalov, R. André, and Le Si Dang, "High-reflectivity GaN/GaIn Bragg mirrors at blue/green wavelengths grown by molecular beam epitaxy", *Appl. Phys. Lett.*, vol. 74 (#24), pp. 3610-3612, 14 June 1999.
- [Lee 2000] J.-L. Lee; J. K. Kim; J. W. Lee; Y. J. Park; and T. Kim, "Transparent Pt ohmic contact on p-type GaN with low resistivity using (NH₄)₂S₂ treatment", *Electrochem. Solid-State Lett.*, vol. 3 (#1), pp. 53-55, Jan. 2000.
- [Mačkowiak 1998a] P. Mačkowiak and W. Nakwaski, "Threshold currents of nitride vertical-cavity surface-emitting lasers with various active regions", *MRS Internet J. Nitride Semicond. Res.*, vol. 3, Article 35, 7 Oct. 1998.
- [Mačkowiak 1998b] P. Mačkowiak, and W. Nakwaski, "Detailed threshold analysis of UV-emitting nitride vertical-cavity surface-emitting lasers", *J. Phys. D: Appl. Phys.*, vol. 31 (#19), pp. 2479-2484, 7 Oct. 1998.
- [Mačkowiak 1999] P. Mačkowiak and W. Nakwaski, "Thermal aspects of designing CW-operated nitride VCSELs", *Opt. Quantum Electron.*, vol. 31 (#11), pp. 1179-1188, Nov. 1999.
- [Martin 1999] R. W. Martin, T. Kim, D. Burns, I. M. Watson, M. D. Dawson, T. F. Krauss, J. H. Marsh, R. M. De La Rue, S. Romani, and H. Kheyrandish, "Dielectric Bragg mirrors for InGaIn surface-emitting lasers", *Proc. 3rd International Conf. on Nitride Semiconductors*, 4-9 July 1999, Montpellier, France, *Phys. Status Solidi A*, vol. 176 (#1), pp. 67-71, 16 Nov. 1999.
- [Nakwaski 1994] W. Nakwaski and M. Osiński, "Self-consistent thermal-electrical modeling of proton-implanted top-surface-emitting semiconductor lasers", in *Physics and Simulation of Optoelectronic Devices II* (W. W. Chow and M. Osiński, Eds.), Los Angeles, CA, 24-26 Jan., 1994, *SPIE Proc.*, Vol. 2146, pp. 365-387.
- [Ng 1999] H. M. Ng, D. Doppalapudi, E. Iliopoulos, and T. D. Moustakas, "Distributed Bragg reflectors based on AlN/GaN multilayers", *Appl. Phys. Lett.*, vol. 74 (#7), pp. 1036-1038, 15 Feb. 1999.
- [Noble 1998] M. J. Noble, J. P. Loehr, and J. A. Lott, "Analysis of microcavity VCSEL lasing modes using a full-vector weighted index method", *IEEE J. Quantum Electron.*, vol. 34 (#10), pp. 1890-1903, Oct. 1998.
- [Opila 1998] E. Opila, D. Humphrey, K. Oda, N. Jacobson, and T. Yoshio, "The oxidation of AlN in dry and wet oxygen", *Proc. Symp. on High Temperature Corrosion and Materials Chemistry* (P. Y. Hou, M. J. McNallan, R. Oltra, E. J. Opila, and D. A. Shores, Eds.), 3-8 May 1998, San Diego, CA, pp. 430-437, Electrochem. Soc., Pennington, NJ, 1998.
- [Osiński 1998] M. Osiński, V. A. Smagley, G. A. Smolyakov, T. Svimonishvili, P. G. Eliseev, and G. Simonis, "Three-dimensional simulation of oxide-confined vertical-cavity surface-emitting semiconductor lasers", in *Optoelectronic Materials and Devices* (M. Osiński and Y.-K. Su, Eds.), Taipei, Taiwan, 9-11 July, 1998, *SPIE Proc.*, Vol. 3419, pp. 196-207.

- [Osiński 1999a] M. Osiński, V. A. Smagley, T. Svimonishvili, G. A. Smolyakov, and P. G. Eliseev, "3D electro-thermal simulation of intracavity-contacted oxide-confined VCSELs operating at room-temperature and at 77 K", in *Physics and Simulation of Optoelectronic Devices VII* (P. Blood, A. Ishibashi, and M. Osiński, Eds.), San Jose, CA, 25-29 Jan. 1999, *SPIE Proc.*, Vol. 3625, pp. 371-382.
- [Osiński 1999b] M. Osiński and G. A. Smolyakov, "Integrated thermal-electrical-optical simulator of vertical-cavity surface-emitting lasers", in *Design, Fabrication, and Characterization of Photonic Devices* (M. Osiński, S. J. Chua, and S. F. Chichibu, Eds.), Singapore, 30 Nov. – 3 Dec. 1999, *SPIE Proc.*, Vol. 3896, pp. 143-154.
- [Palik 1985] E. D. Palik (Ed.), *Handbook of Optical Constants of Solids*, I, II, Academic Press, Orlando 1985.
- [Panajotov 1998] K. Panajotov, B. Ryvkin, J. Danckaert, M. Peeters, H. Thienpont, and I. Veretennicoff, "Polarization switching in VCSEL's due to thermal lensing", *IEEE Photon. Technol. Lett.*, vol. 10 (#1), pp. 6-8, Jan. 1998.
- [Readinger 1999] E. D. Readinger, S. D. Wolter, D. L. Waltemyer, J. M. Delucca, S. E. Mohny, B. I. Prenitzer, L. A. Giannuzzi, and R. J. Molnar, "Wet thermal oxidation of GaN", in *Proc. 40th Electronic Materials Conference (EMC)*, 24-26 June 1998, Charlottesville, VA, *J. Electron. Mater.*, vol. 28 (#3), pp. 257-260, March 1999.
- [Redwing 1996] J. M. Redwing, D. A. S. Loeber, N. G. Anderson, M. A. Tischler, and J. S. Flynn, "An optically pumped GaN-AlGaIn vertical cavity surface emitting laser", *Appl. Phys. Lett.*, vol. 69 (#1), pp. 1-3, 1 July 1996.
- [Sakaguchi 1995] T. Sakaguchi, T. Honda, A. Katsube, F. Koyama, and K. Iga, "MgO/SiO₂ dielectric multilayer reflectors formed by electron-beam evaporation for GaN surface emitting semiconductor lasers", *Proc. Top. Workshop III-V NitrideS (TWN'95)* (I. Akasaki and K. Onabe, Eds.), Nagoya, Japan, 21-23 Sept. 1995, pp. 255-258, Pergamon 1997.
- [Sakaguchi 1998] T. Sakaguchi, T. Shirasawa, N. Mochida, A. Inoue, M. Iwata, T. Honda, F. Koyama, and K. Iga, "Highly reflective AlN-GaN and ZrO₂-SiO₂ multilayer reflectors and their applications for InGaIn-GaN surface emitting laser structures", *Proc. LEOS '98 11th Annual Meeting*, Orlando, FL, 1-4 Dec. 1998, vol. 1, p. 34-35.
- [Sakharov 1999] A. V. Sakharov, W. V. Lundin, I. L. Krestnikov, V. A. Semenov, A. S. Usikov, A. F. Tsatsulnikov, Yu. G. Musikhin, M. V. Baidakova, and Zh. I. Alferov, N. N. Ledentsov, A. Hoffmann, and D. Bimberg, "Surface-mode lasing from stacked InGaIn insertions in a GaN matrix", *Appl. Phys. Lett.*, vol. 74 (#26), pp. 3921-3923, 28 June 1999.
- [Smagley 1998] V. A. Smagley, G. A. Smolyakov, P. G. Eliseev, M. Osiński, and A. J. Przekwas, "Current self-distribution effect in vertical-cavity surface-emitting semiconductor lasers", in *Physics and Simulation of Optoelectronic Devices VI* (M. Osiński, P. Blood, and A. Ishibashi, Eds.), San Jose, CA, 26-30 Jan. 1998, *SPIE Proc.*, Vol. 3283, pp. 171-182.
- [Smolyakov 1999] G. A. Smolyakov, V. A. Smagley, W. Nakwaski, P. G. Eliseev, and M. Osiński, "Design of InGaIn/GaN/AlGaIn VCSELs using the effective frequency method", in *Physics and Simulation of Optoelectronic Devices VII* (P. Blood, A. Ishibashi, and M. Osiński, Eds.), San Jose, CA, 25-29 Jan. 1999, *SPIE Proc.*, Vol. 3625, pp. 324-335.
- [Someya 1998] T. Someya, K. Tachibana, J.-K. Lee, T. Kamiya, and Y. Arakawa, "Lasing emission from an In_{0.1}Ga_{0.9}N vertical cavity surface emitting laser", *Jpn. J. Appl. Phys. Pt. 2 (Lett.)*, vol. 37 (#12A), pp. L1424-L1426, 1 Dec. 1998.
- [Someya 1999a] T. Someya, R. Werner, A. Forchel, M. Catalano, R. Cingolani, and Y. Arakawa, "Room temperature lasing at blue wavelengths in gallium nitride microcavities", *Science*, vol. 285 (5435), pp. 1905-1906, 17 Sep. 1999.
- [Someya 1999b] T. Someya, R. Werner, A. Forchel, and Y. Arakawa, "Growth and structural characterization of InGaIn vertical cavity surface emitting lasers operating at room temperature", *Proc. 3rd International Conf. on Nitride Semiconductors*, 4-9 July 1999, Montpellier, France, *Phys. Status Solidi A*, vol. 176 (#1), pp. 63-66, 16 Nov. 1999.
- [Suzuki 1999] M. Suzuki, T. Kawakami, T. Arai, S. Kobayashi, Y. Koide, T. Uemura, N. Shibata, and M. Murakami, "Low-resistance Ta/Ti Ohmic contacts for p-type GaN", *Appl. Phys. Lett.*, vol. 74 (#2), pp. 275-277, 11 Jan. 1999.
- [Wenzel 1997] H. Wenzel and H.-J. Wünsche, "The effective frequency method in the analysis of vertical-cavity surface-emitting lasers", *IEEE J. Quantum Electron.*, vol. 33 (#7), pp. 1156-1162, July 1997.
- [Yung 1994] K. Yung, J. Yee, J. Koo, M. Rubin, N. Newman, and J. Ross, "Observation of stimulated emission in the near ultraviolet from a molecular beam epitaxy grown GaN film on sapphire in a vertical-cavity, single pass configuration", *Appl. Phys. Lett.*, vol. 64 (#9), pp. 1135-1137, 28 Feb. 1994.

PROCEEDINGS OF SPIE



SPIE—The International Society for Optical Engineering

Physics and Simulation of Optoelectronic Devices VIII

Rolf H. Binder
Peter Blood
Marek Osiński
Chairs/Editors

24–28 January 2000
San Jose, USA



Volume 3944
Part One of Two Parts



The papers appearing in this book compose the proceedings of the technical conference cited on the cover and title page of this volume. They reflect the authors' opinions and are published as presented, in the interests of timely dissemination. Their inclusion in this publication does not necessarily constitute endorsement by the editors or by SPIE. Papers were selected by the conference program committee to be presented in oral or poster format, and were subject to review by volume editors or program committees.

Please use the following format to cite material from this book:

Author(s), "Title of paper," in *Physics and Simulation of Optoelectronic Devices VIII*, Rolf H. Binder, Peter Blood, Marek Osinski, Editors, Proceedings of SPIE Vol. 3944, page numbers (2000).

ISSN 0277-786X
ISBN 0-8194-3561-9

Published by
SPIE—The International Society for Optical Engineering
P.O. Box 10, Bellingham, Washington 98227-0010 USA
Telephone 1 360/676-3290 (Pacific Time) • Fax 1 360/647-1445
<http://www.spie.org/>

Copyright ©2000, The Society of Photo-Optical Instrumentation Engineers.

Copying of material in this book for internal or personal use, or for the internal or personal use of specific clients, beyond the fair use provisions granted by the U.S. Copyright Law is authorized by SPIE subject to payment of copying fees. The Transactional Reporting Service base fee for this volume is \$15.00 per article (or portion thereof), which should be paid directly to the Copyright Clearance Center (CCC), 222 Rosewood Drive, Danvers, MA 01923 USA. Payment may also be made electronically through CCC Online at <http://www.directory.net/copyright/>. Other copying for republication, resale, advertising or promotion, or any form of systematic or multiple reproduction of any material in this book is prohibited except with permission in writing from the publisher. The CCC fee code is 0277-786X/00/\$15.00.

Printed in the United States of America.

Band-Tail Model and Temperature-Induced Blue-Shift in Photoluminescence Spectra of $\text{In}_x\text{Ga}_{1-x}\text{N}$ Grown on Sapphire

PETR G. ELISEEV*, MAREK OSIŃSKI, and JINHYUN LEE

Center for High Technology Materials, University of New Mexico,

1313 Goddard SE, Albuquerque, NM 87106

TOMOYA SUGAHARA and SHIRO SAKAI

Department of Electrical and Electronic Engineering, University of Tokushima,

2-1 Minami-josanjima, Tokushima, Japan

Abstract: A band-tail model of inhomogeneously broadened radiative recombination is presented and applied to interpret experimental data on photoluminescence of various bulk and quantum-well epitaxial InGaN/GaN structures grown by MOCVD. The temperature dependence of the spectral peak position is analyzed according to the model, explaining the anomalous temperature-induced blue spectral shift. Significant differences are observed between epilayers grown on sapphire substrates and on GaN substrates prepared by the sublimation method. No apparent evidence of band tails in homoepitaxial structures indicates their higher crystalline quality.

Key words: Wide-bandgap semiconductors, InGaN, photoluminescence, band tails, homoepitaxy

* Also with P. N. Lebedev Physics Institute, Russian Academy of Sciences, Moscow, Russia

INTRODUCTION

The ternary alloy $\text{In}_x\text{Ga}_{1-x}\text{N}$ has become a very important material in semiconductor physics. It can be fabricated as a thin film in different multilayer group-III nitride structures, and in spite of its poor crystalline quality it serves as efficient luminescent material in UV and visible light-emitting diodes and diode lasers.¹⁻⁴ It also seems promising for high-temperature optoelectronics, since its radiative quantum yield does not drop significantly as the ambient temperature is increased from 300 to 450 K.⁵

Even though InGaN-based devices have reached commercial maturity, the radiative emission processes in this material are not yet well understood. According to Ref. 6, emission in InGaN can be assigned to recombination of excitons localized at potential energy minima in the quantum well. From a study of multiple quantum wells, it was concluded that the exciton localization occurs at deep traps, which could be originated from indium-rich regions acting as quantum dots.⁷ Some spectral features of InGaN-containing structures are rather unusual. As the ambient temperature increases, the emission peak undergoes an anomalous blue shift.⁸⁻¹¹ In addition, it was found that the emission peak spans continuously a wide spectral range (~ 0.2 eV) when the current ranges over ~ 6 decades.⁸ A strong contribution of non-thermal broadening is characteristic of the electroluminescence spectra of AlGaN/InGaN/GaN single quantum wells.⁹⁻¹⁰ A likely involvement of band-tail states was also pointed out.⁹⁻¹³

There are several issues with the InGaN alloy concerning its physical-chemical properties and fabrication methods. These are crystalline quality of hetero- and homoepitaxial material, residual stress/strain and piezoelectric fields, and alloy stability. All of these factors seem to influence the radiative recombination processes. In this paper, we present in detail a simple ana-

lytical model of recombination involving band-tail states that can be caused by a strong variation of the energy bandgap due to statistical fluctuations of alloy composition and, possibly, to correlated variations of composition that may be caused by technological factors or by instability associated with phase separation. The model is then applied to InGaN and compared with results of extensive spectral studies of photoluminescence from different InGaN-based epitaxial materials: bulk layers, single quantum wells, and multiple-quantum-well structures. We interpret the efficient radiative process in InGaN to be the result of fast capture of excess carriers into the band-tail states, with a subsequent radiative recombination. We focus on the temperature dependence of the spectral peak position, which allows us to describe different types of behavior in terms of the band-tail model and to derive the energy parameter of tails describing the inhomogeneous broadening of the band edges.

THE BAND-TAIL MODEL

General Remarks

Band tails can appear in the electron energy spectrum of solids as a result of disordering in the crystalline structure introduced by defects, impurities and non-uniformity of chemical composition. The best known examples of such tails are in amorphous and heavily doped semiconductors (see, *e.g.*, Ref. 14). Application of the band-tail concept to heavily-doped light-emitting diodes and diode lasers had been considered in Ref. 15, where occupation of the Gaussian density-of-states (DOS) tails was analyzed.

In a heavily doped semiconductor, disordering is associated with the random Coulomb fields of ionized impurities. In InGaN, the nature of band-tail states is different; they appear even in undoped material, due to strong compositional non-uniformity. We emphasize that composition-re-

lated tail states are suitable to provide efficient luminescence because, as opposed to ionized impurities, these states attract both types of carriers: potential wells for both electrons and holes are associated with the same site (indium-rich cluster). Due to this, the matrix element for optical transitions can be as large as in the case of free carriers. In heavily doped semiconductors, the random electric potential of the Coulomb centers produces distant extremes of band edges that separate carriers of opposite sign. This leads to an increase in the lifetime of carriers captured into deep tail states, due to a reduced matrix element.

Another particular feature of tail states in InGaN is that the composition variations are not only caused by statistical fluctuations, but may result from partial decay of the alloy, associated with its thermodynamic instability¹⁶. This can produce more significant broadening of band edges than in heavily doped semiconductors.

In light-emitting structures, the tail states are very important, because they provide the lowest-energy levels available for the carriers. Consequently, these states are occupied by excess minority carriers (or by both kinds of carriers) starting from very low pumping rates. Also, these states are the first ones to reach inverted population in lasers under higher pumping rate. The occupation of tails is more sensitive to the pumping rate than the occupation in regular energy bands, because the DOS in tails is much lower. This produces strong band-filling effects characteristic of band tails (blue shift of the emission peak with an increasing pumping rate). On the other hand, the tails are a result of excessive inhomogeneous broadening in the system, and its contribution to spectral bandwidth leads to broader spontaneous emission spectra and higher lasing threshold.

We consider the language of band tails to be adequate for quantitative analysis of broad emission from InGaN. This is not in contradiction with a concept of localized excitons, which is

more fruitful for very narrow linewidth emission in many semiconductors, including GaN. As an electron-hole pair is captured into tail states, the state occupation can be described as that of fermions, with Fermi-Dirac statistics. This is an important tool for analysis that distinguishes localized excitons from the usual Bose-Einstein excitonic statistics.

Here we deal with certain DOS distribution in the band tails, without regard to what is the predominant cause of the energy level spreading. In agreement with the traditional approach, we assume that multiple factors can lead to the Gaussian statistics of the spreading. These factors are: 1) a real shape of profiles for potential energy in cluster-related wells, 2) the Coulomb interaction of localized carriers, 3) free-carrier screening and other many-body effects, 4) exchange effects with neighboring clusters, 5) piezo-electric effects due to residual lattice strain, 6) pyroelectric effects due to spontaneous dielectric polarization. We believe that resulting DOS distribution is sufficiently stable in order to apply the regular distribution functions for occupation probability of tail states. If this approach were not producing satisfactory results, specific corrections would have to be introduced, for example, accounting for many-body effects.

DOS Distribution

The local band edge (1e, 1hh levels for quantum wells, conduction- and valence-band edges for bulk material) is assumed to fluctuate due to compositional variations. The average density of states (DOS) as a function of energy should be calculated as¹⁴

$$\rho(E) = \int \rho(E, V) P(V) dV , \quad (1)$$

where $\rho(E, V)$ is the local DOS function, $P(V)$ is the probability distribution, and V is the local band-edge energy. The averaging procedure leads to smoothening of the sharp edge of the DOS

distribution. Let us assume that the two-dimensional DOS in quantum wells has a step-like shape:

$$\rho(E, V) = (m^*/\pi\hbar^2) \sum_i \vartheta(E - V_i), \quad (2)$$

where m^* is the effective mass, ϑ is the Heaviside step function [$\vartheta(x) = 1$ for $x > 0$ and $\vartheta(x) = 0$ for $x < 0$], and i is the subband index. We consider the shape modification of the lowest subband edge, $i = 1$. The probability function is assumed to be Gaussian:

$$P(V) = (2^{1/2}\pi^{1/2}\sigma)^{-1} \exp [-(V - V_0)^2/(2\sigma^2)], \quad (3)$$

where σ is the energy parameter of the distribution, and V_0 is the central position of the local band edge (the nominal band edge). The averaging procedure as in Eq. (1) gives

$$\rho(E) = (m^*/2\pi\hbar^2) \{1 + \operatorname{erf} [(E - V_0)/(2^{1/2}\sigma)]\}. \quad (4)$$

This expression predicts the DOS to be twice lower at the nominal edge $E = V_0$ than before averaging, and to decrease in the tail below the nominal edge. The asymptotic behavior of $\rho(E)$ (at energies deep inside the nominal bandgap) corresponds to a Gaussian.

The parameter σ describes the broadening effect and the shape of the tail. In this simple approach, it is the only adjustable parameter. In general, this corresponds to the assumption of a distribution with non-vanishing moments only up to the second order. If higher-order moments are substantial, the distribution can be more complicated (asymmetric, *etc.*).

Under some circumstances, these assumptions can be modified. One case is correlation in the compositional clusters (due to phase separation or chemical reordering). For example, phase

separation caused by annealing can lead to formation of indium-rich clusters of ultimate phase composition. If this process is completed, there will be a predominance of clusters with a definite composition. The random factor would be the size of clusters, but not their composition. There would be no states deeper than some specific level, corresponding to the ultimate phase composition. Thus, the asymptotic part of the DOS distribution would deviate from the Gaussian shape.

Band-Tail Model: Carrier Occupation of Gaussian Band Tails

The model of quasi-equilibrium occupation with a Gaussian DOS was proposed earlier for heavily doped GaAs diode lasers.¹⁵ Under an increasing pumping rate, two types of behavior can in principle be observed in luminescence spectra: 1) a stable peak position, corresponding to non-degenerate occupation; and 2) a blue-shifting peak corresponding to degenerate occupation (band-filling). Both behaviors can be illustrated by a simple example of carrier distribution $N(E)$ in the energy scale of one of the tails, as shown in Fig. 1(a) for a range of Fermi-level positions in a quantum well. The DOS distribution corresponding to Eq. (4) is marked with a thick line. This distribution has a Gaussian asymptote deep inside the bandgap, but differs from the Gaussian function near the nominal (not-broadened) band edge E_0 . Thin lines in Fig. 1(a) represent the carrier distributions with their maxima marked by dots. At low pumping rates, when the normalized Fermi level $(F - E_0)/\sigma < -3$, the peak of the carrier distribution has a stable position with a constant bandwidth. At higher pumping rates, the peak is pulled by the Fermi level towards the high-energy side. The non-degenerate occupation is typical for lower pumping rates and higher temperatures, while the degenerate occupation is typical for higher pumping rates and lower temperatures. An interesting feature of the redistribution of carriers with

increasing temperature is shown in Fig. 1(b). As temperature rises, the peak of the curves moves towards higher energy. This effect is similar to ionization of local levels, but extended to the case of a continuous energy spectrum. This shift can lead to a blue temperature-induced shift of the emission peak, when the rate of the shift overcomes the rate of the temperature-induced bandgap shrinkage.

Using the fact that the asymptotic behavior of $\rho(E)$ as given in Eq. (4) corresponds to a Gaussian, we make the following approximation for the DOS function $\rho_{e,h}(E)$ in the conduction and valence bands, respectively:

$$\rho_{e,h}(E) = \rho_{0e,h} \exp[-(E - E_{0e,h})^2 / 2\sigma_{e,h}^2] , \quad (5)$$

where ρ_{0e} , ρ_{0h} , E_{0e} , E_{0h} , σ_e and σ_h are fixed parameters for band tails of electron and hole states. In particular, σ_e^2 and σ_h^2 are the dispersions of each Gaussian, E_{0e} is the center of the DOS Gaussian for the conduction band tail, and E_{0h} is the center of the DOS Gaussian for the valence band tail. Using Eq. (5), we can obtain analytical expressions for spontaneous emission spectra from non-degenerate band tails in a quantum well.

The optical transitions between the states of two tails are assumed to occur with no momentum conservation; hence the spectrum of spontaneous emission rate $r_{sp}(h\nu)$ can be represented by the integral convolution as follows:

$$r_{sp}(h\nu) = B(h\nu) \int \rho_e(E + h\nu) f_e(E + h\nu) \rho_h(E) f_h(E) dE , \quad (6)$$

where $f_e(E + h\nu)$ and $f_h(E)$ are the occupation functions for both involved tails, respectively, h is the Planck constant, ν is the photon frequency, and $B(h\nu)$ is the recombination coefficient. We

also assume that both occupation functions are Fermi-Dirac distributions with a separate quasi-Fermi level F_e , F_h for each tail (the quasi-equilibrium approximation). In this consideration, we shall neglect the spectral dependence of $B(h\nu)$.

We focus on the behavior of the spectral peak $h\nu_p$ of the emission band. In the low-current case, we can assume $h\nu_p - \Delta F > k_B T$, where $\Delta F = F_e - F_h$ is the quasi-Fermi-level separation and k_B is the Boltzmann constant. This condition corresponds to *non-degenerate occupation*. Therefore, the Boltzmann tails of the occupation function can be used:

$$f_e(E, T, F_e) \cong \exp[(F_e - E)/k_B T] , \quad (7a)$$

$$f_h(E, T, F_h) \cong \exp[(E - F_h)/k_B T] . \quad (7b)$$

The carrier distributions $N(E)$, $P(E)$ for electrons and holes, respectively, can be calculated as follows:

$$\begin{aligned} N(E) &= \rho_e(E) f_e(E, T, F_e) = \\ &= \rho_{0e} \exp[(F_e - E_{0e}^*)/k_B T] \exp(-\sigma_e^2/2k_B^2 T^2) \exp[-(E - E_{0e}^*)^2/2\sigma_e^2] , \end{aligned} \quad (8a)$$

$$\begin{aligned} P(E) &= \rho_h(E) f_h(E, T, F_h) = \\ &= \rho_{0h} \exp[(E_{0h}^* - F_h)/k_B T] \exp(-\sigma_h^2/2k_B^2 T^2) \exp[-(E - E_{0h}^*)^2/2\sigma_h^2] , \end{aligned} \quad (8b)$$

where

$$E_{0e}^* = E_{0e} - \sigma_e^2/k_B T , \quad (9a)$$

$$E_{0h}^* = E_{0h} + \sigma_h^2/k_B T . \quad (9b)$$

As shown in Eq. (8), both carrier distributions over the energy scale are Gaussian with the same

values of dispersion as in the corresponding DOS functions. The convolution of two Gaussians as specified in Eq. (6) gives again a Gaussian with the sum of partial dispersions:

$$\begin{aligned}
 r_{sp}(h\nu) &= B \int N(E + h\nu) P(E) dE \\
 &= B^* \rho_{0c} \rho_{0h} \int \exp[-(E + h\nu - E_{0c}^*)^2/2\sigma_c^2] \exp[-(E - E_{0h}^*)^2/2\sigma_h^2] dE \\
 &= B^* \rho_{0c} \rho_{0h} \exp[-(h\nu - h\nu_0)^2/2\sigma^2] ,
 \end{aligned} \tag{10}$$

where

$$B^* = B \exp[-(\sigma_c^2 + \sigma_h^2)/2k_B^2 T^2] \exp[(\Delta F - h\nu_0)/k_B T] , \tag{11a}$$

$$h\nu_0 = E_{0c}^* - E_{0h}^* , \tag{11b}$$

$$\sigma^2 = \sigma_c^2 + \sigma_h^2 . \tag{11c}$$

For a more general case, some non-Gaussian DOS distributions could be considered. Requirements for possible Gaussian-like distributions are: 1) reasonable asymptotic behavior deeply in the nominally forbidden band, 2) monotonic increase of the DOS from deep states to the nominal band edge, 3) smooth fitting to the undisturbed DOS somewhere near or above the nominal band edge.

A general rule for the position of the occupation maximum in a non-degenerate case for a monotonic DOS distribution is as follows:¹⁵

$$d \ln p / dE |_{\text{peak}} = (k_B T)^{-1} . \tag{12}$$

This position is rather stable with the increasing pumping range until degeneracy occurs [cf. Fig. 1(a)]. This means that the spontaneous emission peak is expected to be stable in the entire range

of non-degenerate occupation (no band-filling effect). Therefore, any changes of the spectral position of the emission peak should be tested carefully with respect to: 1) occurrence of degeneracy with a transition to the usual band-filling effect, where the peak position is pulled by the quasi-Fermi levels; 2) change of DOS distribution by many-body effects; 3) total change of the dominant emission mechanism.

Temperature-Induced Shift of the Peak

Using Eq. (10), we can find that the spontaneous emission spectrum has a *temperature-dependent peak* at the photon energy

$$h\nu_0 = E_{0e}^* - E_{0h}^* = E_{0e} - \sigma_e^2/k_B T - E_{0h} - \sigma_h^2/k_B T = E_0 - \sigma^2/k_B T, \quad (13)$$

where $E_0 = E_{e0} - E_{h0}$ is the energy separation between the centers of Gaussian DOS distributions for electrons and holes, and $\sigma^2/k_B T$ is the “red” shift of the emission peak relative to the energy distance between the Gaussian centers. The energy E_0 is close to the bandgap energy E_g , therefore, it can be assumed to depend on temperature in the same manner as E_g , namely,

$$E_0(T) = E_0(0) - \alpha T^2/(\beta + T), \quad (14)$$

where α and β are expected to be close to the usual Varshni parameters. We use Eqs. (13) and (14) to obtain curves of $(h\nu_0 - E_0)$ plotted in Fig. 2 as function of temperature. The upper thick curve illustrates the temperature dependence of E_0 , obtained with $\alpha = 1$ meV/K, $\beta = 1196$ K for the Varshni parameters. These values have been extracted from photorefectance measurements¹⁷ of $\text{In}_{0.14}\text{Ga}_{0.86}\text{N}$ samples rather than from photoluminescence (PL) spectra. It was noticed in Ref. 17 that the PL peak was significantly red-shifted compared to the actual bandgap energy. We

emphasize here that band-tailing effects influence PL spectra much more strongly than photoreflectance spectra. The calculated curves in Fig. 2 illustrate this effect. The peak position follows the thin lines corresponding to various values of the tail parameter σ . The curves for spectral peak position are valid for the case of non-degenerate occupation. At very low temperatures, the dramatic decrease of the peak energy shown in Fig. 2 would actually be compensated due to degenerate occupation. In practice, degenerate occupation can be easily identified by observation of the emission peak shift with increasing pumping (due to the band-filling process). This type of peak position behavior has been clearly observed in electroluminescence studies of InGaN/AlGaN/GaN quantum-well light-emitting diodes (LEDs).^{9-11,18-19}

Within the framework of the band-tail model, the temperature-induced shift of the low-current spectral peak position $h\nu_0$ is as follows:

$$d(h\nu_0)/dT = dE_g/dT - d[(\sigma_e^2 + \sigma_h^2)/k_B T]/dT = dE_g/dT + \sigma^2/k_B T^2. \quad (15)$$

The sign of the temperature-induced shift is determined by dominant term on the right hand side of Eq. (15), with the negative bandgap term, and the positive band-tail term.

EXPERIMENTAL

Epitaxial layers and multilayer structures used in this work have been grown at the University of Tokushima by horizontal atmospheric-pressure MOCVD epitaxy. TMG (trimethylgallium), TMI (trimethylindium) and NH_3 were used as source gases. A thin GaN buffer layer was grown at 500 °C, and then a GaN layer was grown at 1050 °C.

Two types of substrates have been used: 1) sapphire, *c*-plane (0001), 2) "bulk" (needle-shaped) GaN (10 $\bar{1}$ 0), *c*- and *m*-plane, grown by sublimation method.²⁰ Single-heterostructure

(SH) samples had an uncapped "bulk"-type InGaN layer grown at 800 °C on a 2- μ m-thick GaN buffer/substrate. The InGaN layer thickness ranged from 50 nm to 110 nm. Two other types of samples are single- and multiple-quantum-well (SQW and MQW) structures with InGaN wells and GaN barriers, sandwiched by GaN layers. Maximum cumulative InGaN thickness was in MQW samples was 20 nm, minimum (in SQW samples) was 0.8 nm. The average composition of alloys was in the range of 5-25% and had been controlled by the growth process. The average indium content was determined using x-ray diffraction measurements. All samples prepared for PL characterization were undoped. Data on structural analysis of such epitaxial structures were reported earlier.²¹⁻²⁴ For a single GaN layer, the transition of the film structure from grains with relatively independent orientation at about 300 nm to a uniform film with mosaic structure at 1.4 μ m was observed. The threading dislocation density in epilayers ranges from 10^8 to 10^9 cm⁻² in sapphire-substrate samples and is less than 10^6 cm⁻² in homoepitaxial samples.

In PL measurements, a 325-nm UV line from He-Cd laser was used for surface pumping and a blue line at 442 nm was used for selective pumping of InGaN layers covered by GaN. The illuminated spot was about 50 μ m in diameter. The incident optical power density was up to 180 W/cm². Measurements were performed using a closed-circuit refrigerator CTI-Cryogenics, model 22, to keep a sample at a fixed temperature. Spectra were recorded using a CVI double-grating spectrometer, model DK 242D, with a cooled GaAs-photocathode photomultiplier.

RESULTS OF MEASUREMENTS

In the course of PL measurements, we have observed several types of behavior of the InGaN spectral peak. The main differences have been found between structures grown on sapphire and on bulk GaN substrates. In addition, even though the same PL pumping rate was maintained in

all experiments, the actual excitation level could vary substantially from sample to sample, due to sample-dependent pumping efficiency (carrier collection into the InGaN layer) and variable nonradiative recombination rate. The *first type* of behavior is a non-monotonic temperature dependence as shown in Fig. 3 for the case of a SH InGaN structure with a 110-nm thick “bulk-type” InGaN layer. Experimental points show a continuous blue shift by ~ 20 meV when the temperature rises from 10 to 110 K. At higher temperatures, in the range from 70 to 300 K, the experimental points follow closely curve 2, calculated using Eqs. (13) and (14) with the tail parameter $\sigma = 14$ meV. This type of behavior includes a low-temperature part, where experimental points are above the “non-degenerate” curve 2, obviously because of some degeneracy, a middle-temperature part with an anomalous blue shift and a maximum photon energy (3.254 eV at 110 K in Fig. 3), and a high-temperature part with decreasing photon energy (110-300 K in Fig. 3).

Fig. 4 presents the first type of peak behavior at a low pumping rate of 0.7 W/cm^2 (full squares) and another, *second type* of behavior at a high pumping rate of 180 W/cm^2 . In the latter case (circles) the peak energy decreases in a monotonic manner from low temperature to room temperature by about 24 meV. However, this red shift is smaller than the corresponding band-gap temperature dependence, as shown by curve 1. The circles in Fig. 4 fall between curve 1 and curve 2, indicating that some contribution from tail-state filling is present even at high pump powers. An intermediate case, where the two effects almost cancel each other, leading to a largely temperature-independent peak position, is shown by open squares in Fig. 4 (pumping rate of 15 W/cm^2). As the temperature rises from 10 to 300 K, the spectral bandwidth of InGaN emission increases slowly from ~ 46 to ~ 70 meV.

We have inspected the low-temperature behavior (at 11 K) in more detail and found that the pumping rate influences the peak position in accordance with the concept of degenerate occupation. With increasing pumping rate, the peak position marked by dots in Fig. 5 shifts continuously to higher photon energies by 26 meV. This behavior is qualitatively the same as that illustrated in Fig. 1a. Therefore, at low temperatures the spectral peak is rather sensitive to the pumping rate. At low pumping rates, the first type (non-monotonic) of behavior is observed; it converts into the second type (monotonic) at high pumping rates. Such evolution had been also observed in InGaN/AlGaIn/GaN SQW LED electroluminescence spectra.^{9-11,18-19}

In Fig. 6, we show a comparison of spectral peak position curves for GaN and InGaIn emissions from a single sample (a SQW with an InGaIn well layer thickness of 0.8 nm). A *third type* of behavior is observed for GaN (full dots), following closely the Varshni-like temperature dependence of Eq. (14). The corresponding fit 1 was obtained using $E_0(0) = 3.488$ eV, $\alpha = 0.6$ meV/K, and $\beta = 700$ K, which are quite reasonable for GaN. At low temperatures, the peak position is not very sensitive to the pumping rate, suggesting there is no substantial tailing. The low-temperature emission in undoped GaN is associated with excitons localized at point centers rather than with band-tails. The red shift of the PL emission peak from low temperatures to 300 K is ~55 meV, much more than in samples with band tails.

In contrast to the GaN emission spectra, the InGaIn emission from the same sample is of the first type, namely, with some blue shift by a few meV in the middle-temperature range (100-150 K). The peaks at 30 K and at 250 K are at the same photon energy of ~3.16 eV, in sharp contrast to the Varshni-like behavior. Above 110 K, the experimental points are fitted by a "non-degenerate" curve 2 with tail parameter $\sigma = 24$ meV, $E_0(0) = 3.229$ eV, and $\alpha = 0.6$ meV/K. The

value of β was taken here as 700 K, the same as in GaN. Note that fitting accuracy in β is rather poor, as it influences the temperature dependence in a rather weak fashion.

Perhaps the most important result of this study is that *all homoepitaxial samples displayed Varshni-like behavior* (see Fig. 7), indicating that homogeneity of these samples may be much better than in samples grown on sapphire. However, luminescence efficiency of the homoepitaxial samples is not high, which may well in fact be related to their improved homogeneity. Consequently, it is difficult to follow the InGaN-related peak above ~ 200 K. Instead of a clear maximum, some broad emission is observed at room temperature with multiple weak peaks. Low luminescence efficiency suggests that the actual excitation level (*i.e.*, steady-state carrier concentration at any given level of pump power) is probably rather low even at low temperatures due to enhanced nonradiative recombination. The same conclusion can also be reached by integrating the spectra originating from the InGaN and GaN layers in the same samples. In addition, since the density of states in the bands is much higher than that in the tails, the temperature dependence of the spectral peak position is not influenced by the pumping rate as it was in the first two types of behavior. In summary, no evidence of band tailing was found in the homoepitaxial samples, in spite of their broad emission bandwidth (~ 62 meV at low temperatures).

Improved homogeneity of InGaN in homoepitaxial samples correlates with reduced threading dislocation density in those samples. This points out that threading dislocations are likely to act as preferred sites for In deposition during growth, leading to In-rich clusters around the dislocations. This interpretation is further supported by direct observation of cathodoluminescence (CL) in MOCVD-grown InGaN-GaN quantum wells on sapphire, correlated with AFM imaging.²²

DISCUSSION

Effect of Carrier Capture to Band-Tail States on Radiative Recombination Efficiency

Excess carriers are more likely to recombine radiatively when captured into indium-rich clusters. Otherwise, they can diffuse to dislocations and other nonradiative sinks, and this is the most plausible explanation of poor radiative recombination efficiency of GaN and homoepitaxial InGaN. Observation of cathodoluminescence dark spots correlated with the TEM pattern of dislocations in GaN strongly indicates that threading dislocations can act as nonradiative recombination centers.²⁵ The hole diffusion length was estimated from that observation as ~50 nm at room temperature. If the capture into band-tail states shortens the diffusion length (below the average distance between dislocations), the band-tail recombination can restrict the nonradiative process at dislocations and on other extended defects. In a simple approach, the radiative quantum yield η can be expressed as follows:

$$\begin{aligned}\eta &= 1 - (r_0/a)^2 - (2/a^2) \int_{r_0}^a \exp [-(r - r_0)/L_D] r dr \\ &= 1 - (r_0/a)^2 - (2L_D/a^2) \{r_0 + L_D - (a + L_D) \exp [-(a - r_0)/L_D]\} ,\end{aligned}\quad (16)$$

where r is the radial distance to the dislocation axis, r_0 is the radius of “dead zone” near the dislocation, $a = 1/2 N_d^{-1/2}$ is the average half-distance between dislocations, and L_D is the ambipolar diffusion length of carriers. Reported values of hole diffusion length L_p for GaN range from 50 nm²⁵ to an estimated upper limit of 250 nm,²⁶ while r_0 was estimated to be 50 nm by observation of CL dark spots associated with threading dislocations.²⁵ At $N_d = 10^8 \text{ cm}^{-2}$, Eq. (16) gives $\eta \approx$

95% at $L_D = 50$ nm and $\eta \approx 79\%$ at $L_D = 150$ nm. At $N_d = 10^9$ cm⁻², the radiative efficiency falls to $\eta \approx 60\%$ at $L_D = 50$ nm and $\eta \approx 30\%$ at $L_D = 150$ nm. Therefore, the quantum yield can be of device quality in spite of the high dislocation density and high nonradiative recombination efficiency of dislocations, but will drop rapidly when N_d exceeds 10^8 cm⁻².

It is not usual in optoelectronic semiconductors that a smaller diffusion length of excess carriers could lead to a higher radiative quantum yield. However, in the framework of this approach, Eq. (16) predicts higher η if the diffusive transport of excess carriers to dislocations is reduced by trapping of carriers into tail states. This can be an important factor influencing the excellent light-emission performance of InGaN with In content corresponding to blue and green light emission. Other defects and nonradiative centers can limit the positive effect of capture by the tail states in materials with high average In content, approaching the yellow light emission range.

Experimental Determination of σ Parameter

In the previous section, we fit the experimental curves for the PL peak position vs temperature using Eqs. (13) and (14). The same procedure can also be applied to other published data where a blue temperature-induced shift can be identified. The fitting results are summarized in Table I. It is clear that pronounced tailing is characteristic of InGaN alloys, but not of GaN (at least in undoped samples). The tail parameter σ correlates with an average indium content and increases from about zero in GaN to 30-35 meV in green-light-emitting structures. The tailing is found in both thick epilayers and in QWs on sapphire, but not in homoepitaxial samples on sublimation-grown GaN substrates.

Consider now the tail parameter σ from the point of view of microscopic material properties. Our first hypothesis is that the tail states are not quantum-confined states, due to slow variation of the band edges. The effect can therefore be treated in the framework of tilted-band-edge approximation, used in the above calculation of the DOS distribution. Deeper tail states are associated with clusters of larger indium molar fraction x . The magnitude of σ characterizes the energy scale for a substantial decrease in DOS. Using the average value of $dE_g/dx \approx -2$ eV in the range about $x = 0.20$, the composition variation corresponding to $\sigma = 30$ meV can be estimated to be ~ 0.015 , which is quite plausible.

In the case of QWs, the variation of quantum-confined levels could in principle also be associated with fluctuations of the well thickness L_z . Using the infinite well approximation, sensitivity of the photon energy to QW thickness variation can be expressed as

$$d(h\nu)/dL_z \approx -\pi^2 h^2 / (m_{\text{red}} L_z^3) , \quad (17)$$

where m_{red} is the reduced effective mass. When the average value of L_z is 3 nm, a change in the photon energy by 30 meV can result from a local increase in L_z to 5 nm. However, deep states inside the tail (3-5 times σ below nominal bandgap) would require an unreasonably high increase in the well thickness and may not even be attainable, since the bulk nominal bandgap represents the ultimate limit of well-thickness-related shift in energy level. In addition, the thickness variation interpretation could not be applied at all to a bulk material. We therefore conclude that *In content variations are a much more likely cause of the band tail states than the well thickness fluctuations.*

Another hypothesis is that the tail states are quantum-confined states. We restrict the consideration to a particular case when the random variation in the lateral well size determines the dispersion of the energy level position in QWs, whereas variations of the well depth are minimal (see Appendix). We use Eq. (A3) in order to estimate the average lateral size of random wells. We assume the following numerical parameters: well depths $U_{0c} = U_{0b} = U_0 = 0.5$ eV, $m_e = 0.18 m_0$, $m_b = 0.8 m_0$, $\sigma = 30$ meV, and a large relative variation of size, $\sigma_R/R_0 \approx 1$. With these assumptions, we have an expression

$$R_0 = (\hbar/\sigma)(\sigma_R/R_0)(2U_0/m_{red})^{1/2} = 24 \text{ nm} . \quad (18)$$

This estimate looks reasonable, and such clusters are rather large. Considering the total number of In atoms in such a cluster, statistical fluctuations of indium composition can produce deviations not higher than 0.5% from the average composition of $x = 0.20$. Therefore, composition variations are not of purely statistical nature, but result from some segregation process. For example, presence of threading dislocations during growth can result in local enhancement of In content.²²

CONCLUSIONS

Photoluminescence (PL) of InGaN/GaN bulk and quantum-well (QW) structures has been investigated and interpreted in terms of band-tail luminescence typical for structures grown on sapphire substrates. Different types of temperature dependence of the spectral peak position are identified. In the case of pronounced band-tailing, the dependence departs significantly from the usual Varshni-like bandgap shift. The PL peak is red-shifted with respect to the nominal bandgap energy, similarly to the Stokes shift. The tail-induced shift depends on temperature in a simple

manner, producing an anomalous blue shift of the spectral peak with increasing temperature. Such shifts were observed in electroluminescence spectra of InGaN QWs^{9-11,18-19} and later reported in other studies of both electroluminescence and photoluminescence in InGaN. The anomalous temperature-induced blue shift of the peak position can be used to estimate the tail parameter σ that describes the density-of-states distribution in the tails. The σ parameter correlates with the average indium content in the alloy. The tailing effect is associated with alloy composition variations observed in both QW and bulk epilayers. Threading dislocations are a likely factor enhancing compositional inhomogeneities in InGaN. On the other hand, in homoepitaxial material (QW structures on sublimation-grown bulk GaN substrates) and in undoped GaN epilayers, the temperature anomaly is not observed and σ is estimated to be near zero.

From the above discussion concerning the band-tail model and its comparison with experimental data, we can conclude the following:

- 1) There is a clear semi-quantitative agreement between the predicted effect of band tails on the spectral behavior of InGaN emission and the experimental PL data from InGaN-based epitaxial structures grown on sapphire substrates. The characteristic blue temperature-induced shift of the peak position was observed in all samples, including thick epilayers (50-110 nm) and different QW structures (with well thicknesses as small as 0.8 nm). This phenomenon is associated with band-tail formation due to compositional variations of the alloy, assisted by the presence of numerous dislocations.

- 2) The tail parameter σ is derived from the temperature dependence of the peak position and is found to correlate with the average indium content in the InGaN alloy. This parameter is prac-

tically zero in undoped GaN and grows to 30-40 meV in green-light-emitting InGaN structures. The σ parameter is suggested to describe the inhomogeneous broadening of the band edges due to bandgap variations in the alloy.

3) In sharp contrast to InGaN samples grown on sapphire, there is no evidence for band tailing in homoepitaxial structures grown on bulk GaN needles as substrates. The PL efficiency in these structures is found to be rather low, indicating much stronger nonradiative recombination. We interpret this as evidence that the capture of carriers into tail states is favorable to radiative processes, preventing the diffusion of excess carriers to extended defects (dislocations, etc.).

ACKNOWLEDGMENTS

This work was supported by DARPA under the Optoelectronic Materials Center program and by AFOSR. One of the authors (PGE) expresses his gratitude to the University of Tokushima for a possibility to stay there and to join the nitride studies at Satellite Venture Business Laboratory during December 1998 - February 1999. The authors are thankful to Vladimir A. Smagley of the University of New Mexico for his assistance in some of the calculations reported in this paper.

APPENDIX. TAIL PARAMETER σ IN THE CASE OF SIZE VARIATION

Consider the value of σ in the particular case of tail formation where the depth of wells is nearly constant, but their size can vary considerably. We use the model of the "quantum disk" for the indium-rich clusters with a parabolic shape of the potential energy profile. The bottom of all wells is assumed to be at the same energy, whereas the energy of the quantum-confined level E_{loc} (the kinetic energy of localization, calculated from the bottom of the well) varies depending

on the well size. For a parabolic well, the energy E_{loc} corresponds to the well known case of harmonic oscillator, and it depends on the oscillator mass and curvature of the potential energy profile. It is convenient to express it in terms of the well depth U_0 and the well radius R as follows

$$E_{\text{loc}} = (\hbar/R)(2U_0/m^*)^{1/2}, \quad (\text{A1})$$

where U_0 is the well depth and m^* is effective mass of the captured carrier. We consider the dispersion of E_{loc} to represent the parameter σ^2 for each carrier type. For example, for electrons

$$\sigma_e^2 = 2\hbar^2 U_{0e} \sigma_R^2 / (R_0^4 m_e), \quad (\text{A2})$$

where σ_R^2 is the dispersion of the well radius, R_0 is its average value, U_{0e} is the electron well depth, and m_e is the effective mass of electrons. Analogous expression can be written for holes with well depth U_{0h} and the mass m_h . By adding dispersions for both types of carriers, we obtain the total tail parameter

$$\sigma = (2^{1/2} \hbar / R_0) (\sigma_R / R_0) [(U_{0e}/m_e) + (U_{0h}/m_h)]^{1/2}. \quad (\text{A3})$$

REFERENCES

1. S. N. Mohammad and H. Morkoç, *Prog. Quantum Electron.* 20, 361 (1996).
2. S. Nakamura and G. Fasol, *The Blue Laser Diode: GaN Based Light Emitters and Lasers*, (Berlin: Springer-Verlag, 1997).
3. J. W. Orton and C. T. Foxon, *Rep. Prog. Phys.* 61, 1 (1998).
4. O. Ambacher, *J. Phys. D: Appl. Phys.* 31, 2653 (1998).
5. I. V. Akimova, P. G. Eliseev, and M. Osiński, *Quantum Electron.* 28, 987 (1998).
6. S. Chichibu, T. Azuhata, T. Sota, and S. Nakamura, *Appl. Phys. Lett.* 69, 4188 (1996).
7. Y. Narukawa, Y. Kawakami, M. Funato, S. Fujita, S. Fujita, and S. Nakamura, *Appl. Phys. Lett.* 70, 981 (1997).
8. I. V. Akimova, P. G. Eliseev, M. A. Osiński, and P. Perlin, *Quantum Electron.* 26, 1039 (1996).
9. M. Osiński, P. Perlin, P. G. Eliseev, and J. Furioli, in *Light-Emitting Diodes: Research, Manufacturing, and Applications*, ed. E. F. Schubert, (San Jose, CA, 13-14 Feb. 1997), *SPIE Proc.* 3002 (Bellingham, WA: SPIE, 1997), p. 15.
10. P. Perlin, M. Osiński, and P. G. Eliseev, in *III-V Nitrides*, eds. F. A. Ponce, T. D. Moustakas, I. Akasaki, and B. A. Monemar, (Boston, MA, 2-6 Dec., 1996), *Mater. Res. Soc. Symp. Proc.* 449 (Pittsburgh, PA: Mater. Res. Soc., 1997), p. 1173.
11. P. G. Eliseev, P. Perlin, J. Lee, and M. Osiński, *Appl. Phys. Lett.* 71, 569 (1997).
12. K. G. Zolina, V. E. Kudryashov, A. N. Turkin, and A. E. Yunovich, *MRS Internet J. Nitride Semicond. Res.* 1, Art. 11 (1996).

13. H. C. Casey, Jr., J. Muth, S. Krishnankutty, and J. M. Zavada, *Appl. Phys. Lett.* 68, 2867 (1996).
14. E. O. Kane, *Solid-State Electron.* 28, 3 (1985).
15. P. G. Eliseev, M. A. Manko, A. I. Krasilnikov, I. Z. Pinsker, *Phys. Stat. Sol.* 23, 587 (1968).
16. L. Robins, A. J. Paul, C. A. Parker, J. C. Roberts, S. M. Bedair, E. L. Piner, and N. A. El-Masry, *MRS Internet J. Nitride Semicond. Res.* 4S1, Article G3.22 (1999).
17. B. D. Little, W. Shan, J. J. Song, Z. C. Feng, M. Schurman, and R. A. Stall, *III-V Nitrides*, eds. F. A. Ponce, T. D. Moustakas, I. Akasaki, and B. A. Monemar, (Boston, MA, 2-6 Dec., 1996), *Mater. Res. Soc. Symp. Proc.* 449 (Pittsburgh, PA: Mater. Res. Soc., 1997), p. 823.
18. M. Osiński, P. G. Eliseev, P. Perlin, V. A. Smagley, J. Furioli, and J.-H. Lee, *Record of the 16th Electron. Mater. Symp.*, (Minoo, Osaka, Japan, 9-11 July, 1997), p. 273.
19. M. Osiński, P. Perlin, P. G. Eliseev, J. Lee, and V. A. Smagley, *Nitride Semiconductors 1997, Proc. of the 2nd International Conf. on Nitride Semiconductors*, eds. K. Hiramatsu, K. Kishino, S. Nakamura, and H. Amano, *Special Issue J. Cryst. Growth* 189/190 (Amsterdam: North-Holland, 1998), p. 803.
20. S. Sakai, H. Sato, T. Sugahara, Y. Naoi, S. Kurai, K. Yamashita, S. Tottori, M. Hao, and K. Nishino, *Mater. Science Forum* 264, 1107 (1998).
21. H. Sato, T. Sugahara, Y. Naoi, and S. Sakai, *Jpn. J. Appl. Phys., Pt. 1* 37, 2013 (1998).
22. T. Sugahara, M. Hao, T. Wang, D. Nakagawa, Y. Naoi, K. Nishino, and S. Sakai, *Jpn. J. Appl. Phys., Pt. 2 (Lett.)* 37, L1195 (1998).
23. T. Wang, D. Nakagawa, M. Lachab, T. Sugahara, and S. Sakai, *Appl. Phys. Lett.* 74, 3128 (1999).
24. S. Sakai, *J. Korean Phys. Soc.* 34, S220 (1999).

25. T. Sugahara, H. Sato, M. Hao, Y. Naoi, S. Kurai, S. Tottori, K. Yanashita, K. Nishino, L. Romano, and S. Sakai, *Jpn. J. Appl. Phys., Pt. 2 (Lett.)* 37, L398 (1998).
26. S. J. Rosner, E. C. Carr, M. J. Ludowise, G. Girolami, and H. I. Erikson, *Appl. Phys. Lett.* 70, 420 (1997).
27. Y. Narukawa, S. Saijou, Y. Kawakami, S. Fujita, T. Mukai, and S. Nakamura, *Appl. Phys. Lett.* 74, 558 (1999).
28. T. Taguchi, T. Maeda, Y. Yamada, S. Nakamura, and G. Shinomiya, *Proc. Int. Symp. "Blue Laser and Light Emitting Diodes"*, eds. A. Yoshikawa, K. Kishino, M. Kobayashi, and T. Yasuda, (Chiba, Japan, 5-7 March 1996), p. 372.
29. K. L. Teo, J. S. Colton, P. Y. Yu, E. R. Weber, M. F. Li, W. Liu, K. Uchida, H. Tokunaga, N. Akutsu, and K. Matsumoto, *Appl. Phys. Lett.* 73, 1697 (1998).
30. S. Chichibu, L. Sugiura, J. Nishio, A. Setoguchi, H. Nakanishi, and K. Itaya, *Proc. 2nd Int. Symp. "Blue Laser and Light Emitting Diodes"*, eds. K. Onabe, K. Hiramatsu, K. Itaya, and Y. Nakano, (Kisarazu, Japan, 29 Sept. - 2 Oct. 1998), p. 616.

FIGURE CAPTIONS

Fig. 1. Calculated normalized DOS distribution (thick lines) and carrier distributions (thin lines), both in units of $m^*/2\pi\hbar^2$, in function of the normalized energy $(E - E_0)/\sigma$, where E_0 is the nominal confined energy level in the quantum well. Dots mark the peak position. (a) Evolution of carrier distribution with increasing normalized Fermi energy $(F - E_0)/\sigma$ at constant temperature $T = \sigma/2k_B$. (b) Evolution of carrier distribution with temperature rise at approximately constant carrier density (normalized temperature is given in units of σ/k_B , where k_B is Boltzmann's constant).

Fig. 2. Calculated peak position shift in function of temperature for a non-degenerate occupation of tail states. Thick curve corresponds to $\sigma = 0$ (no tails) and is given in the Varshni approximation. Thin curves correspond to various values of σ .

Fig. 3. PL peak position (circles) in function of temperature in a 110-nm-thick InGaN epilayer (single-heterostructure) No. 5743 emitting in the UV range. Curve 1 represents the nominal bandgap, curve 2 is for a non-degenerate occupation of band-tail states. Fitting parameters are $E_0(0) = 3.284$ eV, $\sigma = 14$ meV, $\alpha = 1.1$ meV/K. The value of β was fixed at 1196 K after Ref. 17.

Fig. 4. PL peak position in function of temperature in GaN/InGaN/GaN SQW sample (thickness of InGaN layer is 1.4 nm) emitting in blue range (circles). Experimental points are for different pumping intensities at 325 nm, as indicated. Curve 1 is for a nominal band-gap variation with $E_0(0) = 2.862$ eV, $\alpha = 0.7$ meV/K, and $\beta = 1196$ K. Curve 2 is for a non-degenerate occupation of tail states with $\sigma = 18$ meV.

Fig. 5. PL spectra of the same GaN/InGaN/GaN SQW sample as in Fig. 4, taken at 11 K with varying pumping intensity controlled by calibrated neutral density filters. Peak position is marked by dots. The behavior of the main peak can be compared with curves in Fig. 1a.

Fig. 6. PL peak position in function of temperature in GaN/InGaN/GaN 0.8-nm-thick SQW emitting in UV range for both GaN barrier emission (dots, left scale) and InGaN well emission (circles, right scale). Different types of behavior are identified with partial fitting by calculated curves 1 and 2 (see text).

Fig. 7. PL peak position in function of temperature in homoepitaxial GaN/InGaN/GaN MQWs emitting in violet range (10 quantum wells, each 2-nm thick, separated by 5-nm-thick GaN barriers). C in brackets indicates a structure grown on the *c*-plane of GaN, M indicates a structure grown on *m*-plane of GaN. Experimental points are fitted using the Varshni expression (14).

Table I. Band-Tail Parameters in GaN and InGaN Epitaxial Structures

ΔE is the temperature-induced blue spectral shift; $E_0(0)$ and σ are fitting parameters

Structure	Method	x [%]	ΔE [meV]	$E_0(0)$ [eV]	σ [meV]
GaN, thick ($\sim 1 \mu\text{m}$) epilayer	PL	0	~ 0	~ 3.48	< 2
InGaN, DH, $d = 40 \text{ nm}^{\text{a)}$	PL	2	~ 3	3.432	8
InGaN:Si, SH ^{b)}	PL	6	6	3.387	13.7
InGaN, MQW ^{c)}	PL	~ 20	7.6	~ 3.4	6.5
InGaN, SH, $d = 110 \text{ nm}$	PL	8.5 ± 1.5	20	3.34	10
InGaN, DH, $d = 40 \text{ nm}$	PL	7.5 ± 1.5	30	3.284	14
InGaN, SH, $d = 200 \text{ nm}^{\text{d)}$	PL	20	24	3.05	16
InGaN, SQW, $d = 1.4 \text{ nm}$	PL	~ 20	17	2.862	18
InGaN, SQW, $d = 2.5 \text{ nm}^{\text{e)}$	EL	15-30	52	2.78	31.5
InGaN, SQW, $d = 2.5 \text{ nm}^{\text{e)}$	EL	30-45	30	2.394	28.6
InGaN, SQW, $d = 2.5 \text{ nm}^{\text{e)}$	EL	30-45	59	2.392	35
InGaN, MQW, $d = 10 \times 2 \text{ nm}$ (homoepitaxial)	PL	~ 20	0	3.036	~ 0

^{a)} Derived from PL spectral peak position plot²⁷

^{b)} Derived from PL measurements²⁸

^{c)} PL study reported in Ref. 29. Peak near 3.4 eV suggests lower x than 20% indicated in Ref. 29

^{d)} Derived from experimental plots³⁰

^{e)} Electroluminescence (EL) study reported in Ref. 11

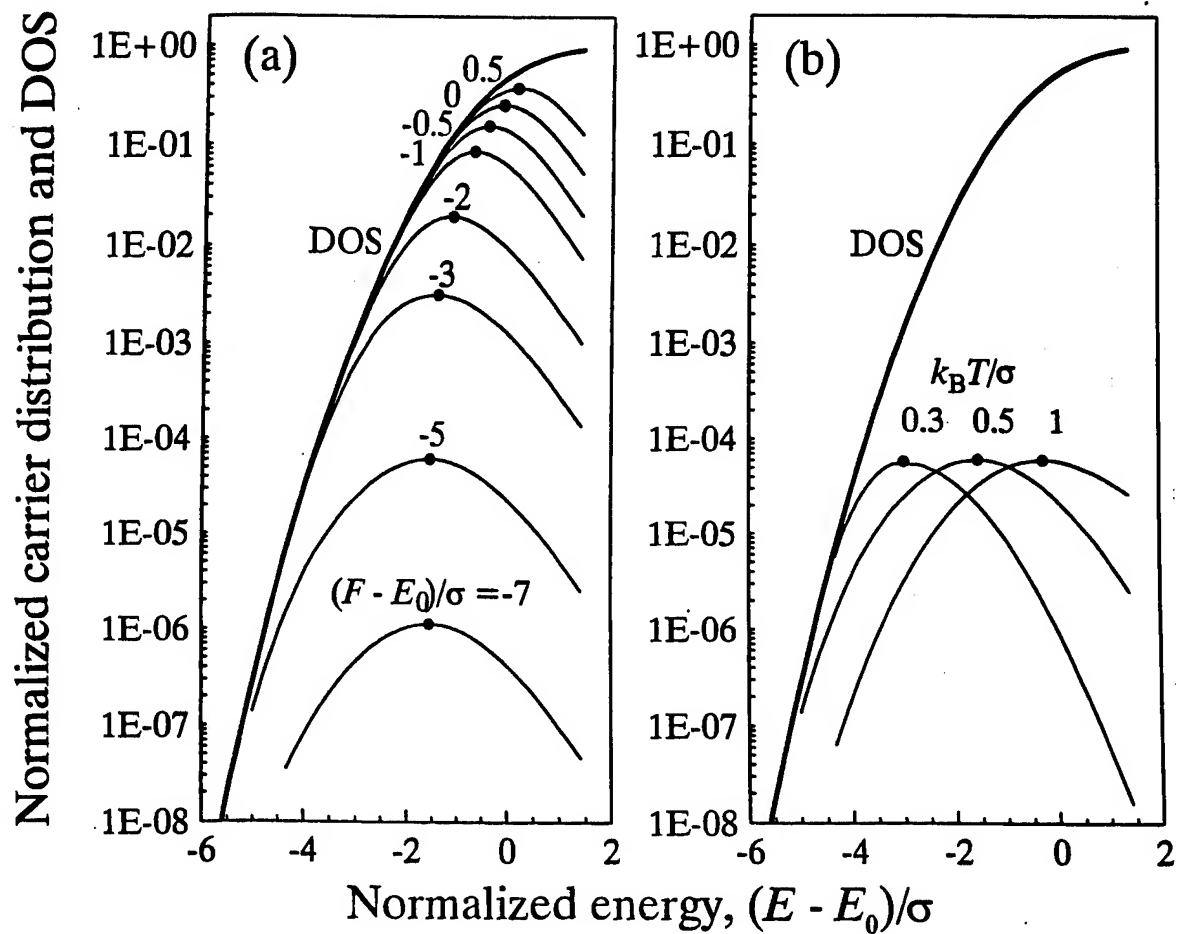


Fig. 1

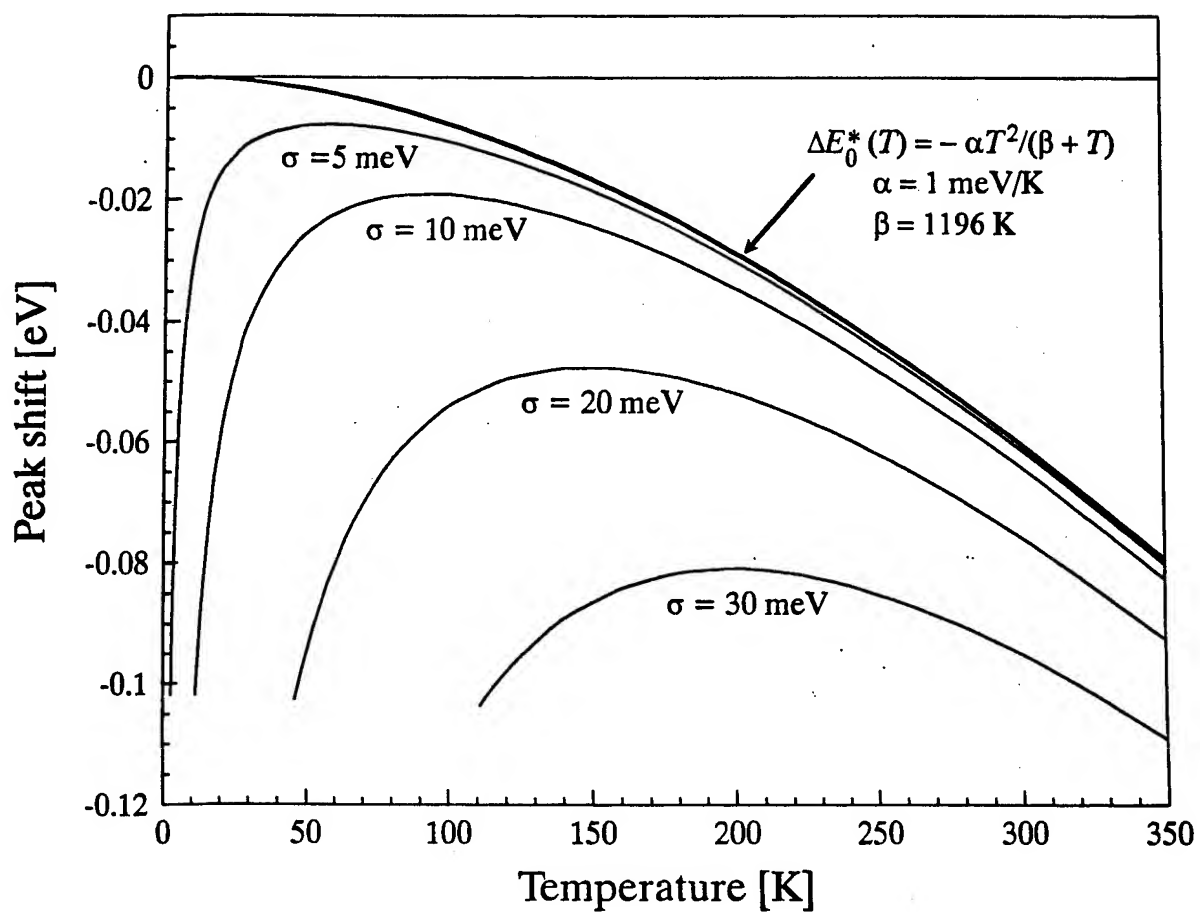


Fig. 2

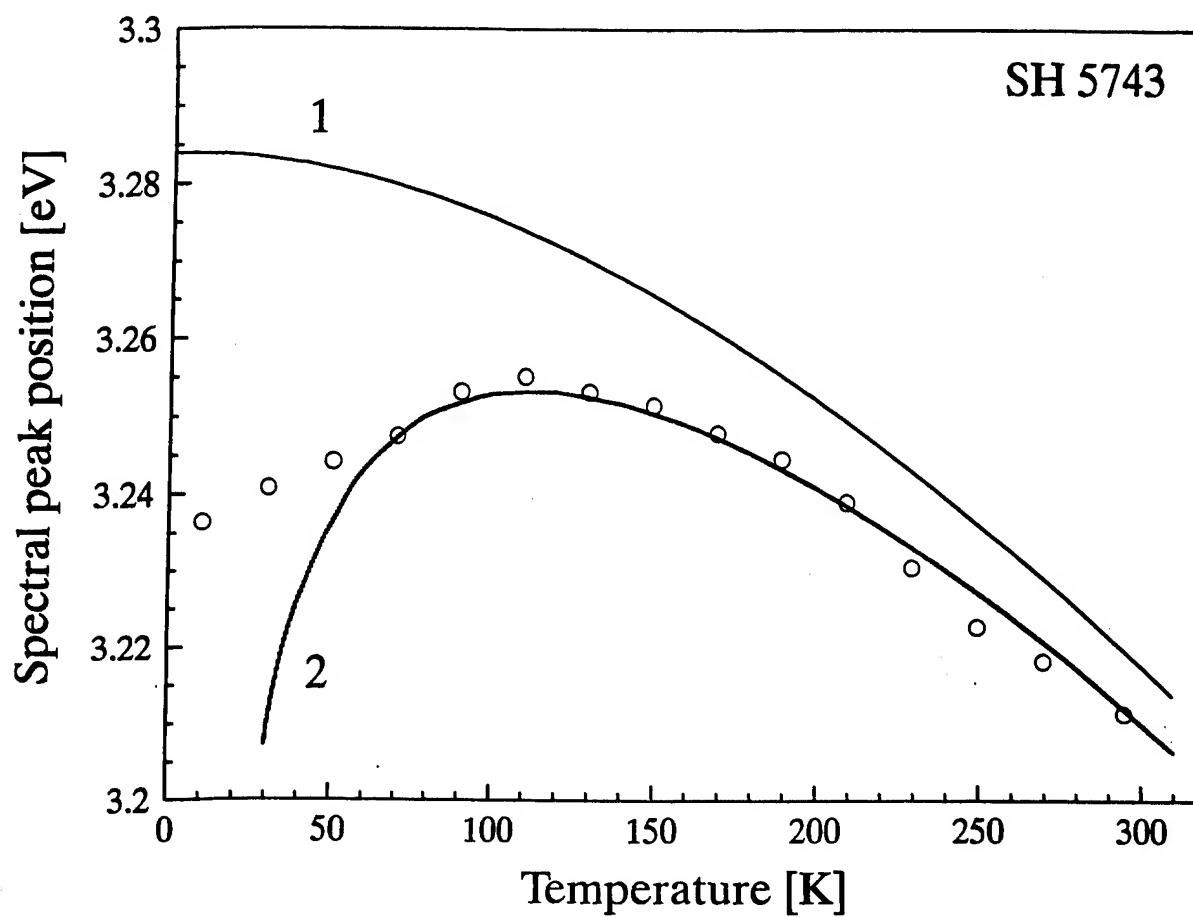


Fig. 3

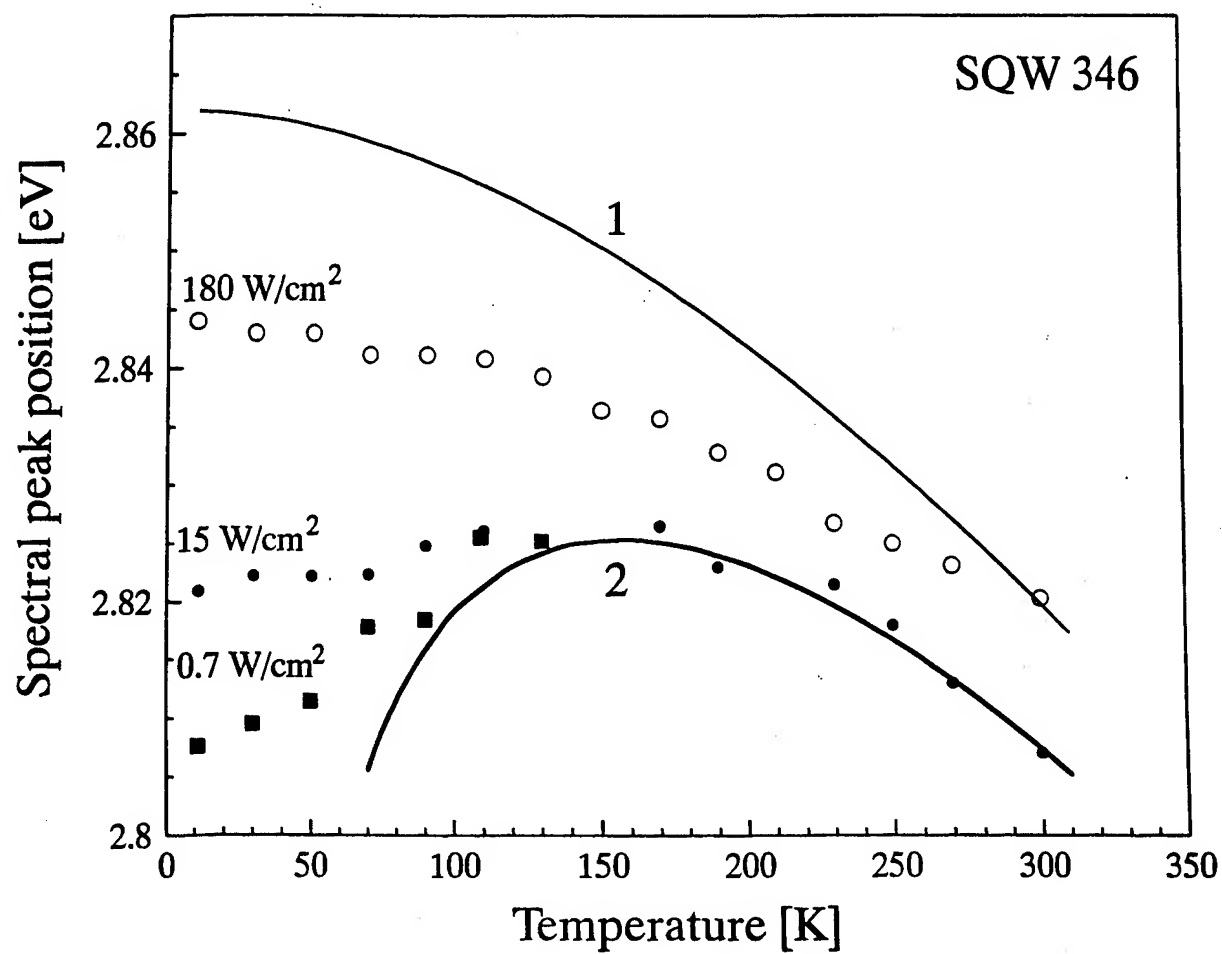


Fig. 4

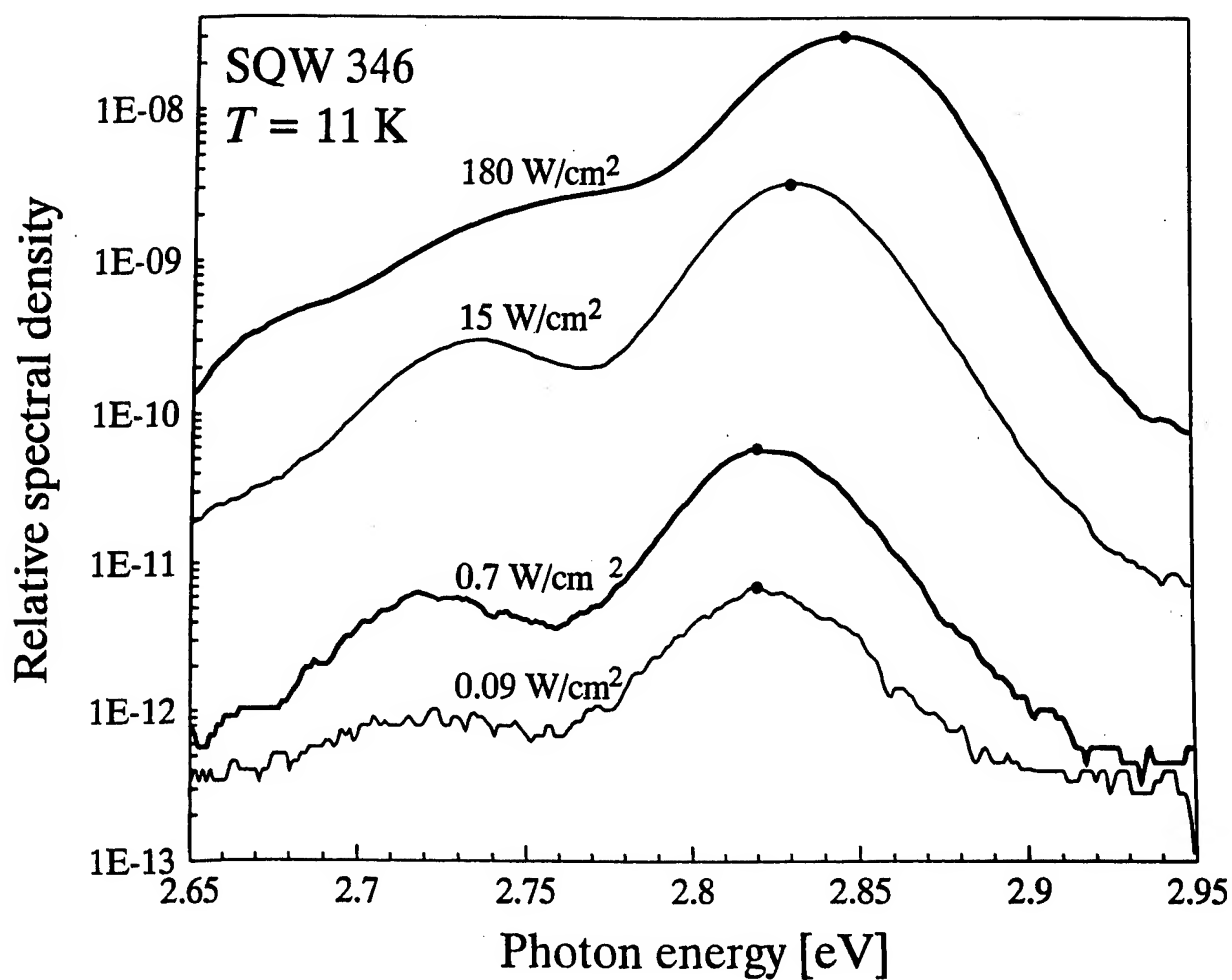


Fig. 5

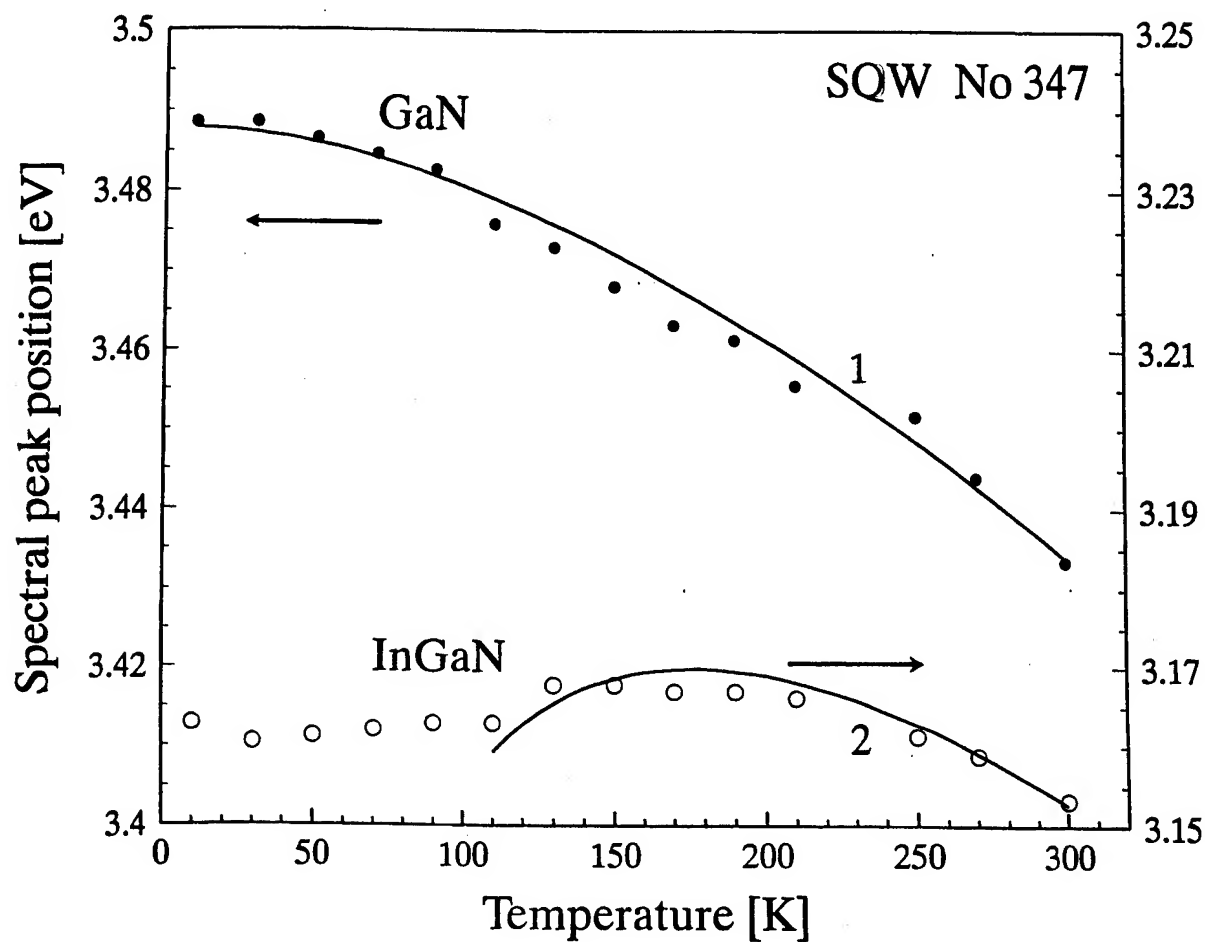


Fig. 6

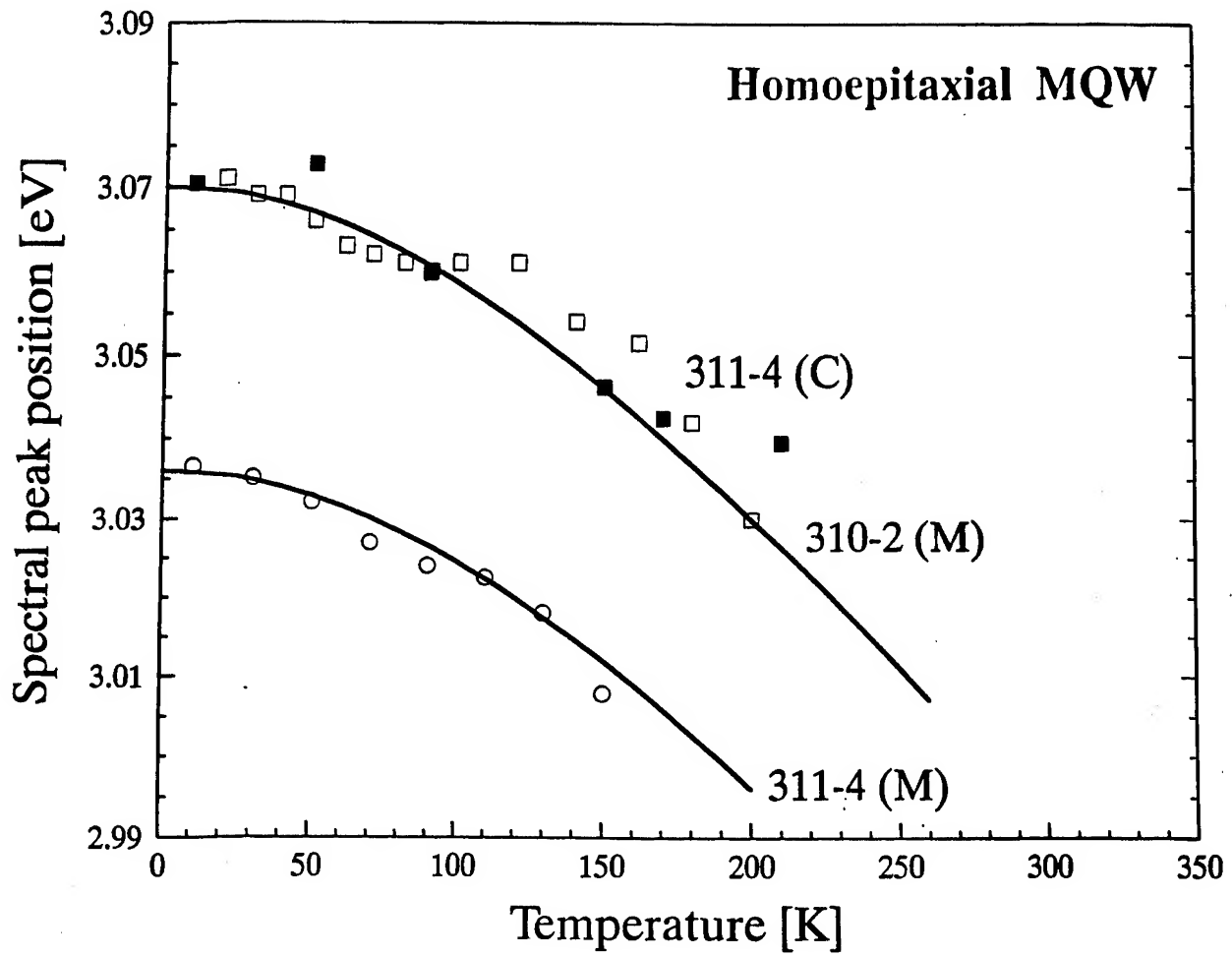


Fig. 7

Analysis of vector LP modes in VCSELs using the effective frequency method

Gennady A. Smolyakov^{a,*}, Petr G. Eliseev^{a,b}, and Marek Osinski^a

^aCenter for High Technology Materials, University of New Mexico, 1313 Goddard SE,
Albuquerque, New Mexico 87106-4343

^bAlso at P.N. Lebedev Physics Institute, Russian Academy of Sciences, Moscow, Russia

ABSTRACT

The effective frequency method (EFM) is generalized to the case of vector analysis of LP modes in VCSELs and applied to proton-implanted and oxide-confined VCSEL structures. Resonant wavelengths and mode profiles of a number of vector LP modes are calculated for different values of active region radius. The vector EFM is shown to provide important information about the vertical and radial components of the energy flux inside the laser structure. The maximum values for "weak" E_z and "strong" E_x components of the electrical field within the laser structure are calculated. Their intensity ratio in the "near-cutoff" situation is suggested as a quantitative verification of weak-guiding assumption in VCSELs, on which the derivation of the EFM was based.

Keywords: VCSELs, effective frequency method, semiconductor lasers, optoelectronic device simulation.

1. INTRODUCTION

A serious, still ongoing effort has been mounted in recent years to develop a comprehensive, all-encompassing optical model of VCSELs that would be universally recognized as a reliable versatile tool to be used in VCSEL design. Many approaches to that problem, different in terms of their generality, accuracy, efficiency and complexity, have been made, with none of them, as of now, having won general acceptance.

Since the permittivity profile and boundary conditions in modern VCSEL structures are not separable in any coordinate system, the optical fields cannot be found exactly and making the right approximation becomes a crucial point in optical modeling of VCSELs. Straightforward numerical methods such as finite-difference [Zhang 1995], [Hadley 1998] and finite-element [Vurgaftman 1998], [Mahmood 1998], [Noble 1998c] do not seem to be of much help when it comes to modeling semiconductor devices. Their use has been found [Noble 1998b] to be more difficult in dielectric structures than in metal-clad waveguides, since it is no longer possible to set selected field components equal to zero at the boundaries. Absorbing boundary conditions must be introduced, or the structure must be placed inside a very large perfectly conducting enclosure. Apart from that, structural unknowns (such as the threshold material gain profile or temperature distribution throughout the VCSEL and, hence, the dielectric profile of the structure itself) have been found [Noble 1998b] difficult to address using numerical techniques. Being computationally very involved and time-consuming, these methods can hardly be used as a part of self-consistent thermal-electrical-optical VCSEL solvers.

With straightforward numerical approaches being impractical for optical modeling of VCSELs, it is of interest to classify various models by examining the type of approximations made and the effect they may have on the generality, accuracy, efficiency, and complexity of the methods. From that point of view, we can divide the vector optical models of VCSELs into two categories. To the first category we assign the models that allow for only minimal approximations in mathematical treatment, and keep the exactness of their approach to the maximum possible extent. Such models may be remarkable for the accuracy they can provide, but usually there is a compromise in other aspects of their performance or applicability (increased complexity, reduced generality and efficiency, or oversimplified device structures) that might be of equal importance.

*Correspondence: Email: gen@chtm.unm.edu; WWW: <http://www.chtm.unm.edu>; Telephone: (505) 272-7804;
Fax: (505) 272-7801

Among the models belonging to the first category, Green's-function-based models [Deng 1997a], [Deng 1997b], [Klein 1998] have been successfully applied for a variety of dielectrically apertured planar VCSELs. The limitation of Green's-function-based models is the lack of generality, as their applicability seems to be restricted to planar VCSEL structures. Practical application of the methods depends on the ability to find the Green's function of the optical cavity, and it is unclear if that is possible, for example, in the very important case of intracavity-contacted VCSELs. Another group of models that we assign to the first category is the class of "mode expansion" models [Demeulenaere 1996], [Demeulenaere 1999], [Biestman 1999], [Bava 2001] which can be very exact, provided that the number of basis vector modes involved is high enough. This requirement, however, makes them rather complex in formulation and very intensive and time-consuming from the computational point of view.

To the second category we assign the models lacking in accuracy due to the level of approximations involved but, instead, gaining essentially in all the other above-mentioned aspects. Such models, usually based on fast, computationally efficient numerical techniques, are suitable for treating very sophisticated VCSEL structures. Approximate as they are, they often provide a very attractive combination of reasonable accuracy and very affordable computing time and may be most suitable for incorporation into self-consistent thermal-electrical-optical VCSEL solvers. A good example of the model belonging to the second category is the weighted index method (WIM) [van Exter 1997], [Noble 1998b]. It is to that category of models that we intend to contribute in this paper by extending the effective frequency method (EFM) from its scalar formulation [Wenzel 1997], [Smolyakov 1999] to the case of vector analysis of LP modes in VCSELs. Both WIM and EFM are based on (different) variational approximations to Maxwell's equations and on approximate variable separation in the wave equation, and both fit perfectly well into our classification scheme.

2. EFFECTIVE FREQUENCY METHOD IN THE ANALYSIS OF VECTOR LP MODES IN VCSELs

2.1. Basic Equations

We start our vector treatment of VCSELs from the system of Maxwell's equations written for a dielectric medium without sources:

$$\vec{\nabla} \times \vec{E} = -\mu_0 \frac{\partial \vec{H}}{\partial t} , \quad (1)$$

$$\vec{\nabla} \times \vec{H} = \epsilon_0 n^2(\vec{r}) \frac{\partial \vec{E}}{\partial t} , \quad (2)$$

$$\vec{\nabla} \cdot \vec{H} = 0 , \quad (3)$$

$$\vec{\nabla} \cdot [n^2(\vec{r}) \vec{E}] = 0 , \quad (4)$$

where $n(\vec{r})$ describes the complex refractive index profile of an arbitrary dielectric structure. We assume further that the VCSEL structure under consideration consists of a number of dielectric layers that are uniform in the z -direction. This allows us to exclude z -dependence of the refractive index, and from now on we assume $n^2(\vec{r}) = n^2(\rho)$, where ρ represents the radius in cylindrical coordinates. The discontinuity of the refractive index at the interfaces between the layers will be taken into account explicitly by applying the standard boundary conditions when matching the fields at those interfaces. The following vector wave equations for electric and magnetic fields can then be derived from Eqs. (1)-(4) [Adams 1981]:

$$\nabla^2 \vec{E} + \vec{\nabla}_t (\vec{E}_t \cdot \vec{\nabla}_t \ln n^2(\rho)) + k_0^2 n^2(\rho) \vec{E} = 0 , \quad (5)$$

$$\nabla^2 \vec{H} + \vec{\nabla}_t \ln n^2(\rho) \times (\vec{\nabla} \times \vec{H}) + k_0^2 n^2(\rho) \vec{H} = 0 , \quad (6)$$

where subscript "t" indicates the transverse component of a vector, and the fields are assumed to depend harmonically on time as $\exp(i\omega t)$, with $k_0 = \omega/c$.

We consider here the Cartesian components of the fields \vec{E} , \vec{H} , while their spatial dependence is described in cylindrical coordinate system, with $\vec{r} = (\rho, \varphi, z)$. Written for the components of the fields, Eqs. (5) and (6) become:

$$[\nabla^2 + k_0^2 n^2(\rho)]E_x + \frac{\partial}{\partial x} \left\{ [E_x \cos \varphi + E_y \sin \varphi] \frac{d \ln n^2(\rho)}{d\rho} \right\} = 0, \quad (7a)$$

$$[\nabla^2 + k_0^2 n^2(\rho)]E_y + \frac{\partial}{\partial y} \left\{ [E_x \cos \varphi + E_y \sin \varphi] \frac{d \ln n^2(\rho)}{d\rho} \right\} = 0, \quad (7b)$$

$$[\nabla^2 + k_0^2 n^2(\rho)]E_z + \frac{\partial}{\partial z} \left\{ [E_x \cos \varphi + E_y \sin \varphi] \frac{d \ln n^2(\rho)}{d\rho} \right\} = 0, \quad (7c)$$

$$[\nabla^2 + k_0^2 n^2(\rho)]H_x + \left\{ \frac{\partial H_y}{\partial x} - \frac{\partial H_x}{\partial y} \right\} \sin \varphi \frac{d \ln n^2(\rho)}{d\rho} = 0, \quad (8a)$$

$$[\nabla^2 + k_0^2 n^2(\rho)]H_y - \left\{ \frac{\partial H_y}{\partial x} - \frac{\partial H_x}{\partial y} \right\} \cos \varphi \frac{d \ln n^2(\rho)}{d\rho} = 0, \quad (8b)$$

$$[\nabla^2 + k_0^2 n^2(\rho)]H_z + \left\{ \left[\frac{\partial H_x}{\partial z} - \frac{\partial H_z}{\partial x} \right] \cos \varphi + \left[\frac{\partial H_y}{\partial z} - \frac{\partial H_z}{\partial y} \right] \sin \varphi \right\} \frac{d \ln n^2(\rho)}{d\rho} = 0. \quad (8c)$$

In order to relate the field components to each other, we use the *curl* equations (1) and (2) from the system of Maxwell's equations:

$$\vec{\nabla} \times \vec{E} = -i(\mu_0 / \epsilon_0)^{1/2} k_0 \vec{H}, \quad (9)$$

$$\vec{\nabla} \times \vec{H} = i(\epsilon_0 / \mu_0)^{1/2} k_0 n^2(\rho) \vec{E}. \quad (10)$$

Another assumption that will be used later is that the fields can be expressed as a superposition of two counter-propagating waves in each layer, that is the total field in j th layer is

$$\vec{E}_j(\rho, \varphi, z) = [\vec{E}_j^+(\rho, \varphi) \exp(-i\beta_j z) + \vec{E}_j^-(\rho, \varphi) \exp(i\beta_j z)] \exp(i\omega t). \quad (11)$$

Eqs. (9) and (10) give the following relations between the field components:

$$-i(\mu_0 / \epsilon_0)^{1/2} k_0 H_x = \frac{\partial E_z}{\partial y} - \frac{\partial E_y}{\partial z}, \quad (12a)$$

$$-i(\mu_0 / \epsilon_0)^{1/2} k_0 H_y = \frac{\partial E_x}{\partial z} - \frac{\partial E_z}{\partial x}, \quad (12b)$$

$$-i(\mu_0 / \epsilon_0)^{1/2} k_0 H_z = \frac{\partial E_y}{\partial x} - \frac{\partial E_x}{\partial y}, \quad (12c)$$

$$i(\epsilon_0/\mu_0)^{1/2}k_0n^2(\rho)E_x = \frac{\partial H_z}{\partial y} - \frac{\partial H_y}{\partial z}, \quad (13a)$$

$$i(\epsilon_0/\mu_0)^{1/2}k_0n^2(\rho)E_y = \frac{\partial H_x}{\partial z} - \frac{\partial H_z}{\partial x}, \quad (13b)$$

$$i(\epsilon_0/\mu_0)^{1/2}k_0n^2(\rho)E_z = \frac{\partial H_y}{\partial x} - \frac{\partial H_x}{\partial y}. \quad (13c)$$

We now invoke the "weak-guiding" approximation that enables us to look for solutions that would be analogous to LP modes of weak waveguides. By "weak-guiding" condition we imply not only small changes in the weighted refractive index along the radius but also, and most importantly, that the phase-resonance condition in the cavity does not change much along the radius. This assumption seems to be well justified, because the modes usually observed in VCSELs are linearly polarized [Chang-Hasnain 1993], [Martin-Regalado 1997], [Li 1998], [Ryvkin 1999].

As with LP modes of cylindrical waveguides [Adams 1981], two configurations of the fields may be considered that differ only in polarization. For the first polarization,

$$E_y = H_x = 0, \quad (14)$$

and all remaining components can be expressed in terms of E_x as

$$H_z = -\frac{i}{\mu_0\omega} \frac{\partial E_x}{\partial y}, \quad (15a)$$

$$H_y = \frac{i}{\beta^2} \left[\frac{1}{\mu_0\omega} \frac{\partial}{\partial z} \left(\frac{\partial^2 E_x}{\partial y^2} \right) + \omega\epsilon_0 n^2(\rho) \frac{\partial E_x}{\partial z} \right], \quad (15b)$$

$$E_z = \frac{1}{k_0^2 n^2(\rho) \beta^2} \frac{\partial}{\partial x} \frac{\partial}{\partial z} \left(\frac{\partial^2 E_x}{\partial y^2} \right) + \frac{1}{\beta^2} \frac{\partial^2 E_x}{\partial x \partial z}. \quad (15c)$$

For the other polarization,

$$E_x = H_y = 0, \quad (16)$$

and all remaining components can be expressed in terms of E_y as

$$H_z = \frac{i}{\mu_0\omega} \frac{\partial E_y}{\partial x}, \quad (17a)$$

$$H_x = -\frac{i}{\beta^2} \left[\frac{1}{\mu_0\omega} \frac{\partial}{\partial z} \left(\frac{\partial^2 E_y}{\partial x^2} \right) + \omega\epsilon_0 n^2(\rho) \frac{\partial E_y}{\partial z} \right], \quad (17b)$$

$$E_z = \frac{1}{k_0^2 n^2(\rho) \beta^2} \frac{\partial}{\partial y} \frac{\partial}{\partial z} \left(\frac{\partial^2 E_y}{\partial x^2} \right) + \frac{1}{\beta^2} \frac{\partial^2 E_y}{\partial y \partial z}. \quad (17c)$$

We can simplify these expressions further by assuming that the fields are slowly varying functions of ρ . Consider, for example, Eq. (15b) that can be written as follows

$$H_y = \frac{i\omega\epsilon_0 n^2(\rho)}{\beta^2} \frac{\partial}{\partial z} \left[\frac{1}{k_0^2 n^2(\rho)} \frac{\partial^2 E_x}{\partial y^2} + E_x \right] \approx \frac{i\omega\epsilon_0 n^2(\rho)}{\beta^2} \frac{\partial E_x}{\partial z} \quad (18)$$

Here, we neglected the first term in square brackets, consisting of the second derivative of the slowly-varying function E_x divided by a large number $k_0^2 n^2(\rho)$, as much smaller than the second term E_x . With this approximation, expressions (15) and (17) turn into:

(i) For $E_y = H_x = 0$ polarization:

$$H_z = -\frac{i}{\mu_0 \omega} \frac{\partial E_x}{\partial y} = -\frac{i}{\mu_0 \omega} \left[\sin \varphi \frac{\partial E_x}{\partial \rho} + \frac{\cos \varphi}{\rho} \frac{\partial E_x}{\partial \varphi} \right], \quad (19a)$$

$$H_y = \frac{i\omega\epsilon_0 n^2(\rho)}{\beta^2} \frac{\partial E_x}{\partial z}, \quad (19b)$$

$$E_z = \frac{1}{\beta^2} \frac{\partial^2 E_x}{\partial x \partial z} = \frac{1}{\beta^2} \frac{\partial}{\partial z} \left[\cos \varphi \frac{\partial E_x}{\partial \rho} - \frac{\sin \varphi}{\rho} \frac{\partial E_x}{\partial \varphi} \right], \quad (19c)$$

(ii) For $E_x = H_y = 0$ polarization:

$$H_z = \frac{i}{\mu_0 \omega} \frac{\partial E_y}{\partial x} = \frac{i}{\mu_0 \omega} \left[\cos \varphi \frac{\partial E_y}{\partial \rho} - \frac{\sin \varphi}{\rho} \frac{\partial E_y}{\partial \varphi} \right], \quad (20a)$$

$$H_x = -\frac{i\omega\epsilon_0 n^2(\rho)}{\beta^2} \frac{\partial E_y}{\partial z}, \quad (20b)$$

$$E_z = \frac{1}{\beta^2} \frac{\partial^2 E_y}{\partial y \partial z} = \frac{1}{\beta^2} \frac{\partial}{\partial z} \left[\sin \varphi \frac{\partial E_y}{\partial \rho} + \frac{\cos \varphi}{\rho} \frac{\partial E_y}{\partial \varphi} \right]. \quad (20c)$$

Let us consider now the case of $E_y = H_x = 0$. The other polarization can be treated in fully analogous way. Obviously, it is sufficient to find the component E_x , since all the other components can be then determined using Eqs. (19). To find the component E_x , we apply the standard EFM procedure. The method implies that E_x must be the strongest component of the electrical field, which should be verified *a posteriori* in each particular case when the vectorial EFM method is applied. It is indeed very important that the strongest component of the electrical field be used in determining the resonant wavelength of the laser structure. We then find $E_x(\vec{r}, t) = E_x(\vec{r}, \omega) \exp(i\omega t)$, with a complex mode frequency $\omega = \omega' + i\omega''$ accounting for facet losses as well as for possible losses or gain effects within the optical cavity, and serving as the eigenvalue of the equation:

$$\left[\nabla^2 + \left(\frac{\omega}{c} \right)^2 n^2(\rho, \omega) \right] E_x(\vec{r}, \omega) = 0, \quad (21)$$

which is Eq. (7a), with the neglected term containing $d \ln n^2(\rho)/d\rho$. Note that we neglect that term only in the regions of slow variation of the refractive index. Possible discontinuities of the refractive index in radial direction will be treated explicitly by applying the standard boundary conditions when matching the fields at the interfaces.

As in the scalar EFM [Wenzel 1997], [Smolyakov 1999], we search for eigenvalue solutions of Eq. (21) linearized around the real-valued nominal angular frequency ω_0 , corresponding to designed periodicity of DBR mirrors:

$$\left[\Delta + \frac{\omega_0^2}{c^2} n^2(\vec{r}, \omega_0) \right] E_x(\vec{r}, \omega) = v \frac{\omega_0^2}{c^2} n(\vec{r}, \omega_0) n_g(\vec{r}, \omega_0) E_x(\vec{r}, \omega) , \quad (22)$$

where $n(\vec{r}, \omega_0) = n'(\vec{r}, \omega_0) + i n''(\vec{r}, \omega_0)$ and $n_g(\vec{r}, \omega_0) = n'_g(\vec{r}, \omega_0) + i n''_g(\vec{r}, \omega_0)$ are the complex refractive phase and group indices evaluated at the nominal angular frequency ω_0 , and the dimensionless frequency parameter v , defined as

$$v = 2 \frac{\omega_0 - \omega}{\omega_0} = 2 \frac{\lambda - \lambda_0}{\lambda} - i \frac{2\omega''}{\omega_0} \quad (23)$$

now plays the role of the eigenvalue of Eq. (22). The real part of v gives the relative wavelength shift from the nominal wavelength λ_0 , whereas its imaginary part is the relative decay constant of the corresponding mode.

We assume the following end-point boundary conditions for E_x :

$$\frac{\partial E_x}{\partial z} \pm i k_z E_x = 0, \quad z = \begin{cases} L + \varepsilon \\ 0 - \varepsilon \end{cases} , \quad (24)$$

$$\frac{\partial E_x}{\partial \rho} + \frac{E_x}{2\rho} + i k_\rho E_x = 0, \quad \rho = \rho_\infty , \quad (25)$$

where ε is a small positive number. Eq. (24) ensures outgoing plane waves $\vec{E} = \vec{E}_0 \exp(\pm i k_z z)$ at the bottom ($z = 0$) and top ($z = L$) surfaces of the laser cavity, while Eq. (25) ensures a cylindrical outgoing wave $\vec{E} = \frac{\vec{E}_0}{\sqrt{\rho}} \exp(-i k_\rho \rho)$ at a sufficiently large value of $\rho = \rho_\infty$.

We then assume that for an axially symmetric structure, the spatially dependent field $E_x(\vec{r}, \omega)$ can be approximately factorized as follows:

$$E_x(\vec{r}) = f(z; \rho) \Phi(\rho, \varphi) , \quad (26)$$

where for simplicity of notation we have dropped the argument ω . The vertical part of the solution $f(z; \rho)$ is assumed to be a slow function of ρ and normalized according to

$$\int_0^L f^2(z; \rho) dz = 1 , \quad (27)$$

where L is the entire thickness of the multilayer epitaxial structure at a given radial position ρ .

The vertical part of the solution $f(z; \rho)$ satisfies Eq. (22) without in-plane derivatives:

$$\left[\frac{d^2}{dz^2} + \frac{\omega_0^2}{c^2} n^2(\rho) \right] f(z; \rho) = v_{eff}(\rho) \frac{\omega_0^2}{c^2} n(\rho) n_g(\rho) f(z; \rho) , \quad (28)$$

where again for simplicity we dropped the arguments ω and ω_0 . The end-point boundary conditions for $f(z; \rho)$ follow directly from Eq. (24):

$$\frac{df}{dz} \pm i k_z f = 0, \quad z = \begin{cases} L + \varepsilon \\ 0 - \varepsilon \end{cases} , \quad (29)$$

where $k_z = (\omega_0/c) (n^2 - v_{\text{eff}} n n_g)^{1/2}$.

For any fixed radial position ρ in piecewise-constant geometries, we solve the "axial" equation (28) using the transfer matrix approach, similar to that described in [Bergmann 1998] and [Noble 1998b]. The general solution of Eq. (28) in each axial region $[z_{j-1}, z_j]$ is given by:

$$f_j(z; \rho) = a_j \exp[-ih_j(z - z_j)] + b_j \exp[ih_j(z - z_j)] , \quad j = 1, \dots, M \quad (30)$$

where

$$h_j = \frac{\omega_0}{c} \sqrt{n_j^2 - v_{\text{eff}} n_j n_g} \quad (31)$$

The interface boundary conditions read as follows:

$$f_j = f_{j+1} , \quad z = z_j , \quad (32a)$$

$$\frac{df_j}{dz} = \frac{df_{j+1}}{dz} , \quad z = z_j , \quad (32b)$$

The first condition follows from the fact that E_x is a tangential component of the field that must be continuous across the interface. The other one follows from Eq. (19b) for the main component of magnetic field H_y which in the plane-wave approximation turns into the conventional relationship between the only nonzero field components E_x and H_y :

$$H_y = \frac{i}{\omega \mu_0} \frac{\partial E_x}{\partial z} \quad (33)$$

Thus, the continuity condition for the first derivative of the vertical function $f(z; \rho)$ implies continuity of the magnetic field in the plane-wave-like solutions of Eq. (28). It is consistent with the way Eq. (28) is derived and should not lead to any significant error in determining the resonant wavelength, since it is a well known fact that the LP modes are very close to the TEM modes.

By applying these continuity conditions, we relate a_j, b_j to a_{j+1}, b_{j+1} at each axial boundary $z = z_j$ through the transfer matrix $\|T_j\|$:

$$\begin{bmatrix} a \\ b \end{bmatrix}_{j+1} = \|T_j\| \begin{bmatrix} a \\ b \end{bmatrix}_j , \quad (34)$$

This recursive relationship connects the coefficients from the $j = 1$ region (substrate) to the coefficients in the $j = M$ region (air) via:

$$\begin{bmatrix} a \\ b \end{bmatrix}_M = \|T_{M-1}\| \|T_{M-2}\| \dots \|T_2\| \|T_1\| \begin{bmatrix} a \\ b \end{bmatrix}_1 = \|T_{\text{tot}}\| \begin{bmatrix} a \\ b \end{bmatrix}_1 \quad (35)$$

The boundary conditions (29) for the outgoing plane waves transform to:

$$a_1 = b_M = 0 . \quad (36)$$

The only variable in Eq. (35) is v_{eff} , with all other quantities being design and material parameters. For $a_1 = 0$ and arbitrarily chosen $b_1 = 1$, we seek the values of v_{eff} such that condition (36) for b_M is satisfied.

Thus, $f(z; \rho)$ and $v_{\text{eff}}(\rho)$ are the field distributions and frequency parameters of virtual stacks of planar layers, the vertical structures of which are those of the real device at the different positions ρ . The lateral profile of the effective frequency $v_{\text{eff}}(\rho)$ is then used in the equation for the in-plane part of the solution $\Phi(\rho, \varphi)$:

$$\left[\frac{c^2 \Delta_t}{\omega_0^2 \langle nn_g \rangle_\rho} + v_{\text{eff}}(\rho) \right] \Phi(\rho, \varphi) = v \Phi(\rho, \varphi) , \quad (37)$$

where

$$\langle nn_g \rangle_\rho = \int_0^L n(\rho) n_g(\rho) f^2(z; \rho) dz . \quad (38)$$

For axially symmetrical structures we can postulate the following azimuthal dependence for $\Phi(\rho, \varphi)$:

$$\Phi(\rho, \varphi) = R_\ell(\rho) \exp(i\ell\varphi) , \quad \ell = 0, 1, \dots \quad (39)$$

The equation for the radial part of the solution $R_\ell(\rho)$ is then:

$$\left[\frac{d^2}{d\rho^2} + \frac{1}{\rho} \frac{d}{d\rho} - \frac{\ell^2}{\rho^2} + v_{\text{eff}}(\rho) \frac{\omega_0^2}{c^2} \langle nn_g \rangle_\rho \right] R_\ell(\rho) = v \frac{\omega_0^2}{c^2} \langle nn_g \rangle_\rho R_\ell(\rho) , \quad \ell = 0, 1, \dots \quad (40)$$

The end-point boundary condition for $R_\ell(\rho)$ translates directly from (25):

$$\frac{dR_\ell}{d\rho} + \frac{R_\ell}{2\rho} + ik_\rho R_\ell = 0 , \quad \rho = \rho_\infty \quad (41)$$

where $k_\rho = (\omega_0/c_0) [(v_{\text{eff}} - v) \langle nn_g \rangle_\rho]^{1/2}$.

The interface boundary conditions for $R_\ell(\rho)$ and $dR_\ell(\rho)/d\rho$ at the possible radial discontinuities of the dielectric structure can be derived from the continuity condition for E_x , which is characteristic of LP modes approximation, and from the continuity condition for H_z , with the latter being defined by Eq. (19a). The approximate boundary conditions read:

$$\begin{aligned} R_\ell(\rho_i - \varepsilon) &= R_\ell(\rho_i + \varepsilon), & \varepsilon \rightarrow 0 \\ \left. \frac{dR_\ell}{d\rho} \right|_{\rho=\rho_i-\varepsilon} &= \left. \frac{dR_\ell}{d\rho} \right|_{\rho=\rho_i+\varepsilon}, & \varepsilon \rightarrow 0 \end{aligned} \quad (42)$$

In both cases we used the assumption $f(z; \rho - \varepsilon) \approx f(z; \rho + \varepsilon)$ ($\varepsilon \rightarrow 0$), which is consistent with the EFM approach.

Different solutions of Eq. (40) for a given value of ℓ are the radial parts $R_{\ell m}(\rho)$ of linearly polarized LP $_{\ell m}$ modes ($\ell = 0, 1, \dots$; $m = 1, 2, \dots$). Their full radial and azimuthal form is:

$$\Phi_{\ell m}(\rho, \varphi) = R_{\ell m}(\rho) \exp(i\ell\varphi) , \quad (39a)$$

The corresponding complex eigenvalues $v_{\ell m}$ give the resonant wavelengths and decay constants of the modes of the entire VCSEL resonator.

The remaining field components are then expressed through the factorized solution for the dominant field component. For example, for the $E_y = H_x = 0$ polarization, we have:

$$E_x = f(z; \rho) R_{tm}(\rho) \exp(i\ell\varphi) , \quad (43a)$$

$$E_z = \frac{1}{\beta^2} \frac{df(z; \rho)}{dz} \left[\cos \varphi \frac{dR_{tm}(\rho)}{d\rho} - i\ell \sin \varphi \frac{R_{tm}(\rho)}{\rho} \right] \exp(i\ell\varphi) , \quad (43b)$$

$$H_y = \frac{i\omega\epsilon_0 n^2(\rho)}{\beta^2} \frac{df(z; \rho)}{dz} R_{tm}(\rho) \exp(i\ell\varphi) , \quad (43c)$$

$$H_z = -\frac{i}{\mu_0\omega} f(z; \rho) \left[\sin \varphi \frac{dR_{tm}(\rho)}{d\rho} + i\ell \cos \varphi \frac{R_{tm}(\rho)}{\rho} \right] \exp(i\ell\varphi) . \quad (43d)$$

2.2. VCSEL Structures and Material Parameters

The method for optical analysis of vector LP modes in VCSELs described in the previous section was applied to two types of VCSEL structures – proton-implanted top-surface-emitting laser (PITSEL) shown schematically in Fig. 1, and oxide-confined surface-emitting laser (OCSEL) shown schematically in Fig. 2. As a prototype for our simulations of PITSELS, we used the structure of the device reported in [Zhou 1991]. The PITSEL structure (Table 1) consists of an undoped active region bounded by the *p*-doped and *n*-doped DBR mirror stacks, all of which were grown on an *n*-GaAs substrate. The upper *p*-DBR mirror contains 24 pairs of quarter-wave $\text{Al}_x\text{Ga}_{1-x}\text{As}$ and AlAs layers. The Al content *x* of $\text{Al}_x\text{Ga}_{1-x}\text{As}$ is 15%, except at the heterointerfaces, where it is linearly graded from 15% to 100% over a distance of 12 nm. The lower *n*-doped DBR mirror contains 43.5 pairs of quarter-wave $\text{Al}_x\text{Ga}_{1-x}\text{As}$ and AlAs layers, with Al composition graded similarly as in the *p*-mirror. The active layer contains a symmetrical graded-index separate-confinement heterostructure (GRINSCH) with four 8-nm quantum wells separated by 2-nm barriers. Two different profiles of grading are applied on either side of the active region: first, a thin layer adjacent to the DBR mirror, graded from 100% down to 55%, and second, a thick layer adjacent to quantum wells, graded from 55% to 15%. The total thickness of the GRINSCH-MQW structure corresponds to a single wavelength of the cavity mode, which is designed to lase at 846 nm.

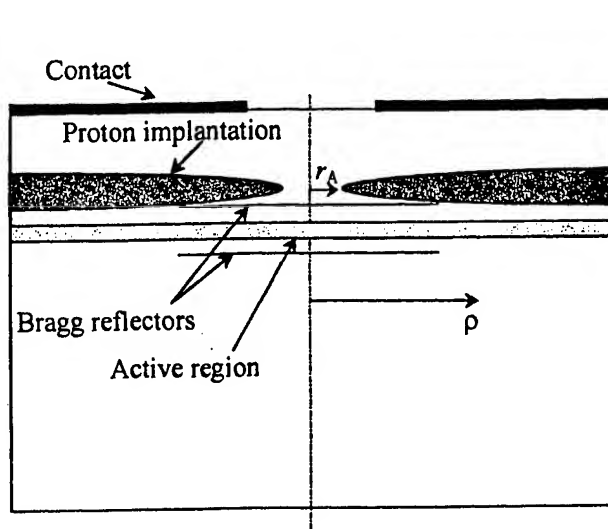


Fig. 1. Schematic structure of a proton-implanted top-surface-emitting laser (PITSEL). r_A - the radius of the window in proton implanted region and of the active region.

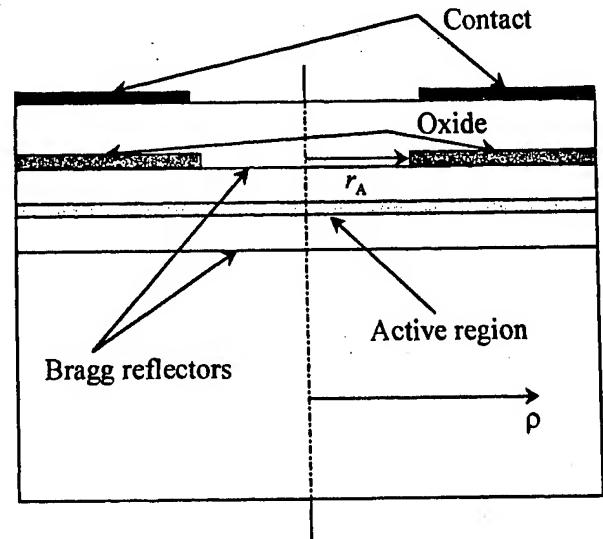


Fig. 2. Schematic structure of a planar oxide-confined surface-emitting laser (OCSEL). r_A - the radius of the window in the oxidized layer and of the active region.

The simulated OCSEL structure has the first quarter-wave *p*- AlAs layer above the GRINSCH-MQW structure oxidized in the outer radial section of the device, but otherwise it is identical to the PITSEL structure. Both PITSEL and OCSEL structures are treated as consisting of two sections in the radial direction, with the dimensions of the first radial section being determined by the active region radius. For simplicity, we assume that the active region radius is the same as either the radius

of the window in proton implanted region of the PITSEL structure or the radius of the window in the oxidized layer of the PITSEL structure. The material gain coefficient of 1000 cm^{-1} is assumed in the calculations within the first radial section in the active layer, while the resonant absorption coefficient of 2000 cm^{-1} is assigned to the outer radial section in the active layer. We also assume that the average temperature increase in the active region, as defined by the active region radius r_A and the thickness of the GRINSCH-MQW structure, is $\Delta T_A = 10 \text{ }^\circ\text{C}$, and the value of the parameter of refractive index temperature dependence used in the calculations is $dn/dT = 3 \times 10^{-4} \text{ }^\circ\text{C}^{-1}$.

Table 1. Layer parameters of PITSEL device structure

No.	Layer description	Thickness [nm]	n'	n_s'	n''
1	In	2000			
2	Au	100			
3	Sn	100			
4	<i>n</i> -GaAs substrate	10^5	3.67	4.58	-0.67×10^{-4}
5	<i>n</i> -AlAs	58.5	3	3.29	-0.67×10^{-4}
6	<i>n</i> -graded layer	12			-0.67×10^{-4}
7	<i>n</i> -Al _{0.15} Ga _{0.85} As	47.9	3.53	4.52	-0.67×10^{-4}
8	<i>n</i> -graded layer	12			-0.67×10^{-4}
•	•	•			
•	43 times	•			
•	•	•			
177	<i>n</i> -AlAs	58.5	3	3.29	-0.67×10^{-4}
178	graded layer 1	6			-0.67×10^{-4}
179	graded layer 2	100			-0.67×10^{-4}
180	GaAs – QW	8	3.67	4.58	
181	Al _{0.15} Ga _{0.85} As – barrier	2	3.53	4.52	-0.67×10^{-4}
182	GaAs – QW	8	3.67	4.58	
183	Al _{0.15} Ga _{0.85} As – barrier	2	3.53	4.52	-0.67×10^{-4}
184	GaAs – QW	8	3.67	4.58	
185	Al _{0.15} Ga _{0.85} As – barrier	2	3.53	4.52	-0.67×10^{-4}
186	GaAs – QW	8	3.67	4.58	
187	graded layer 2	100			-0.67×10^{-4}
188	graded layer 1	6			-0.67×10^{-4}
189	<i>p</i> -AlAs	58.5	3	3.29	-0.67×10^{-4}
190	<i>p</i> -graded layer	12			-0.67×10^{-4}
191	<i>p</i> -Al _{0.15} Ga _{0.85} As	47.9	3.53	4.52	-0.67×10^{-4}
192	<i>p</i> -graded layer	12			-0.67×10^{-4}
•	•	•			
•	23 times	•			
•	•	•			
281	<i>p</i> -AlAs	58.5	3	3.29	-0.67×10^{-4}
282	<i>p</i> -graded layer	12			-0.67×10^{-4}
283	<i>p</i> -Al _{0.15} Ga _{0.85} As	47.9	3.53	4.52	-0.67×10^{-4}
284	<i>p</i> -GaAs	6	3.67	4.58	-0.67×10^{-4}

2.3. Results of PITSEL Simulation

Figs. 3 – 6 show the results of calculations for the PITSEL structure taken as an example in order to illustrate the typical spatial distributions for various field components and their relative intensities. In Fig. 3, longitudinal intensity distributions of E_x and E_z components of the LP₀₁ mode are shown for the case of $E_y = H_x = 0$ polarization. The intensity of the main component of the electric field E_x along the z -axis was calculated at the radial position ρ where $R_{em}(\rho)$ reaches its maximum. The intensity of E_z along the z -axis was calculated for $\phi = 0$ and at the radial position ρ where $dR_{em}(\rho)/d\rho$ reaches its

maximum value. As shown in Fig. 3, $|E_x|^2$ is about four orders of magnitude stronger than $|E_z|^2$, which justifies the assumptions made in formulation of vectorial EFM.

In similar way, longitudinal distributions of intensities of the H_y and H_z components were calculated. Fig. 4 shows that the main component of the magnetic field H_y is about four orders of magnitude stronger than H_z in intensity. This means that the solution is indeed very close to the TEM mode.

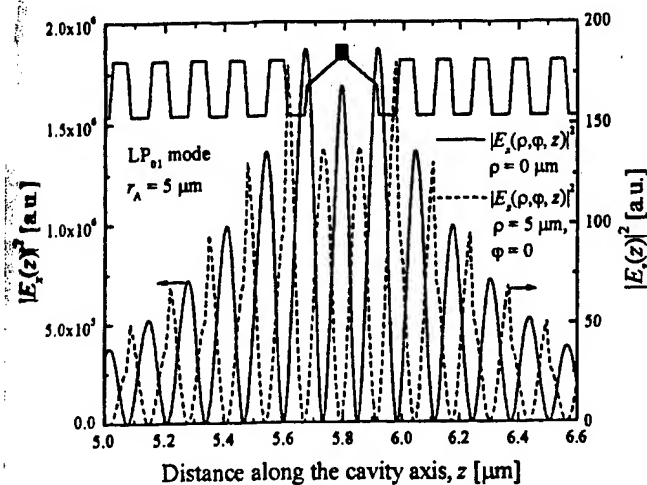


Fig. 3. Calculated intensity profiles of the E_x and E_z components along the cavity axis for the LP_{01} mode of the PITSEL structure. $z = 0$ corresponds to the top surface of the substrate. The refractive index profile is shown in the top part of the figure, with the corresponding values of n' given in Table 1.

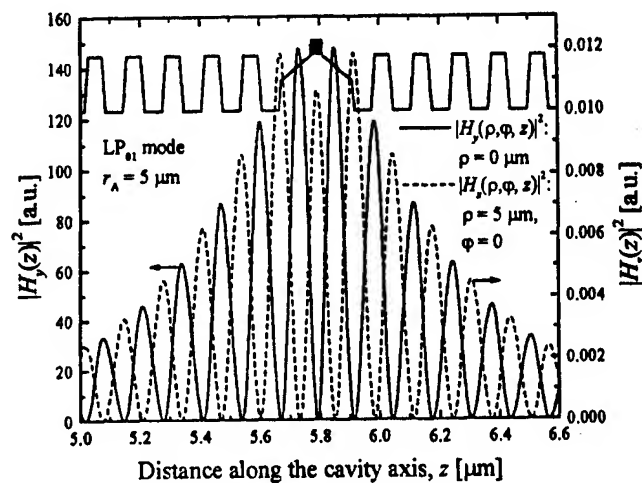


Fig. 4. Calculated intensity profiles of the H_y and H_z components along the cavity axis for the LP_{01} mode of the PITSEL structure. $z = 0$ corresponds to the top surface of the substrate. The refractive index profile is shown in the top part of the figure, with the corresponding values of n' given in Table 1.

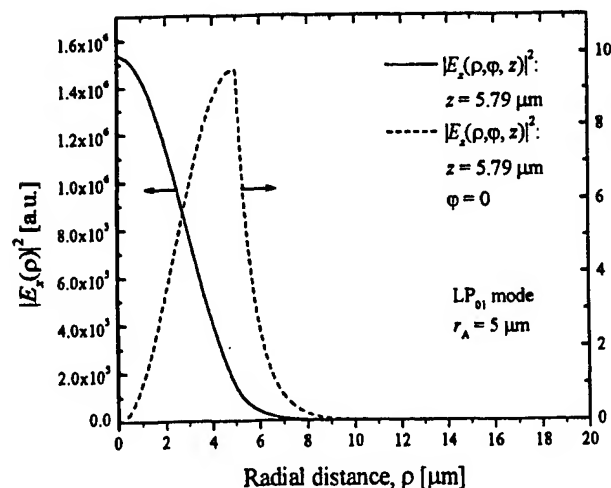


Fig. 5. Calculated intensities of the E_x and E_z components in the active region plane for the LP_{01} mode of the PITSEL structure. ϕ is set to 0 in the case of E_z .

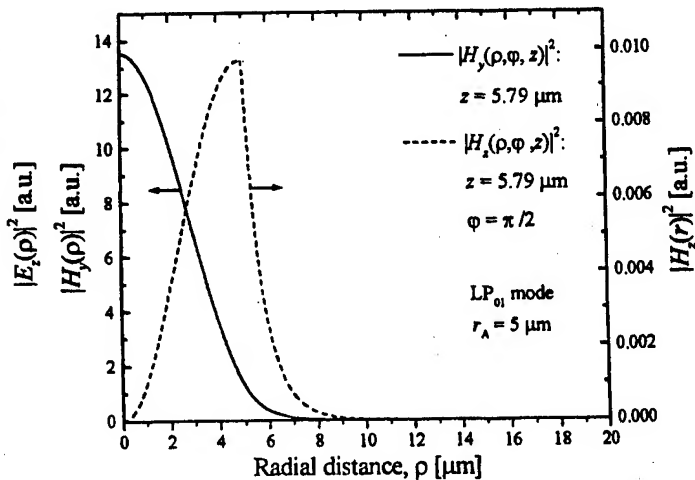


Fig. 6. Calculated intensities of the H_y and H_z components in the active region plane for the LP_{01} mode of the PITSEL structure. ϕ is set to $\pi/2$ in the case of H_z .

It is obvious from Eqs. (43a) and (43b) that E_x and E_z have different spatial dependence in general, and along the z direction in particular. Fig. 3 shows that the main component of the electric field E_x reaches its maximum in the active region, whereas the weak component E_z is at its minimum. The relative intensities of the E_x and E_z components in the active region plane are presented in Fig. 5. As follows from that figure, the E_z component of the electric field is negligible in the active region.

Fig. 6 shows a comparison of relative intensities of the magnetic field components H_y and H_z in the active region plane. Since

the strong component of the magnetic field H_y has a node of the standing wave in the active region plane (see Fig. 4), the magnetic field is of little importance in the active region.

Detailed information about the field components of vector LP modes obtained from the EFM analysis can be used to calculate the energy flux distribution throughout the laser structure. Figs. 7 and 8 illustrate the longitudinal and radial components of the energy flux calculated, respectively, along the cavity axis and in the active region plane for several LP modes. The negative values for the energy flux in Fig. 7 mean that the electromagnetic energy propagates downwards from the active region, towards the substrate. It should be noted that special care must be taken in interpreting the results of the energy flux calculations. It is not guaranteed in the purely optical, not self-consistent, analysis of a laser structure that a stationary solution with $\text{Im}\{v_m\} = 0$ would be found, unless the modal loss and modal gain are perfectly balanced. If they are not, the energy flux calculated for growing or decaying in time solutions might not lend itself to physical interpretation, and deviations from the energy conservation law might be expected. This means that the threshold condition $\text{Im}\{v_m\} = 0$ must be satisfied before any meaningful calculations of the energy flux are undertaken. This condition is certain to be met in any self-consistent thermal-electrical-optical VCSEL solver of which vector EFM could be a part.

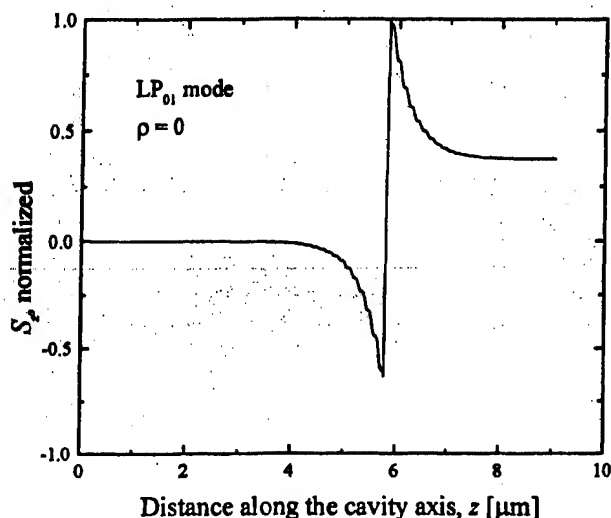


Fig. 7. Distribution of the longitudinal component of the Poynting vector calculated for the LP_{01} mode on the axis of the PITSEL structure ($\rho = 0$).

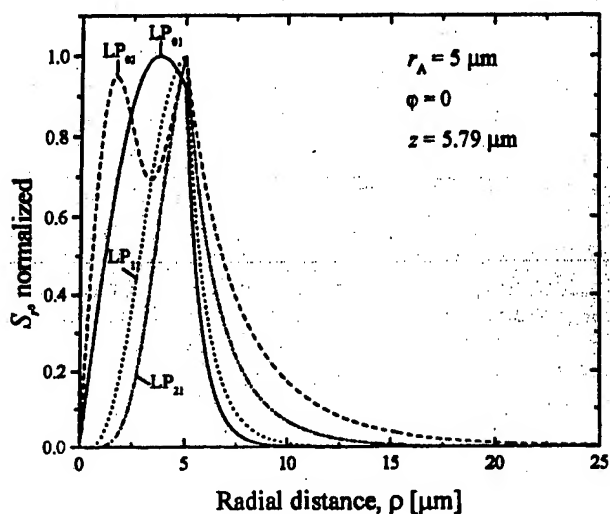


Fig. 8. Radial component of the Poynting vector calculated for the first four lowest-order LP_{lm} modes in the active region plane of the PITSEL structure

The situation with the energy flux, however, is even more complicated. Whereas the radial part $R_m(\rho)$ of general factorized solution (43a) can come out naturally as the stationary solution to the overall problem when the threshold condition for v_m is satisfied, its longitudinal part $f(z, \rho)$ is obtained in the process as a result of the local plane-wave analysis applied at each radial position ρ of the structure. The local value of $\text{Im}\{v_{\text{eff}}(\rho)\}$ then determines whether the corresponding function $f(z, \rho)$ describes a stationary local solution or not. Obviously, the result of the local plane-wave analysis is not bound to be a stationary solution even if the global condition $\text{Im}\{v_m\} = 0$ is satisfied for the mode as a whole, but, instead, depends on the local balance of gain and losses that the local plane wave experiences. Since the vertical part of the solution $f(z, \rho)$ is a weak function of ρ , we find it appropriate to take as the representative vertical distribution $f(z)$ the local plane-wave solution $f(z, \rho)$ taken at the radial position ρ such that $\text{Im}\{v_{\text{eff}}(\rho)\} = 0$. If such position cannot be found (as in the present case of an idealized highly nonuniform two-section device), then for the purpose of energy flux calculations the longitudinal part of solution (43a) can be found as the local plane-wave solution for the central part of the structure, with the material gain adjusted in such a way as to ensure $\text{Im}\{v_{\text{eff}}(0)\} = 0$.

2.4. Comparison of PITSEL and OCSEL Simulations

In this section, we discuss and compare the results of EFM analysis as applied to vector LP modes in PITSELS and OCSELS, with emphasis on different mechanisms of lateral mode confinement in these VCSEL structures. Optical modes in PITSELS near threshold are primarily gain-guided, since the lateral mode confinement is mostly due to the lateral material gain profile

in the active region. Above threshold, thermal waveguiding becomes more important. However, note that overheating of the central part of the structure may as well lead to significant detuning from the designed nominal DBR resonance (unless proper precautions are taken to design the structure accounting for the actual temperature profile at the operating current) and does not necessarily contribute to the resonator quality and, as a consequence, to the lateral mode confining mechanism. In contrast, rather than being related to gain or thermal effects, much better lateral mode confinement in the OCSEL structure is due to strong radial nonuniformity of the cavity that incorporates oxidized layers.

In order to facilitate the comparison, similarity of the PITSEL and OCSEL structures has been maintained to the maximum possible extent. Thus, the DBR structure was assumed to be identical in both cases, except that the OCSEL structure had the first quarter-wave p -AlAs layer above the GRINSCH-MQW structure oxidized in the outer radial section of the device. Other parameters, such as the active-region radius, thicknesses of all layers, etc., were kept identical from structure to structure.

The significant difference in strength of lateral mode confinement between OCSELS and PITSELS is illustrated in Figs. 9 and 10, showing the calculated radial intensity profiles for several LP modes. It is obvious from these figures that LP modes of the OCSEL structure are much better confined within the active region, as defined by the aperture in the oxidized layer. We have shown in our earlier work [Osiński 1999] that simple replacement of proton-implanted region with an oxidized layer leads to a remarkable improvement in the threshold current, efficiency, and the output power of a device, with all these improvements resulting from enhancing the resonator quality.

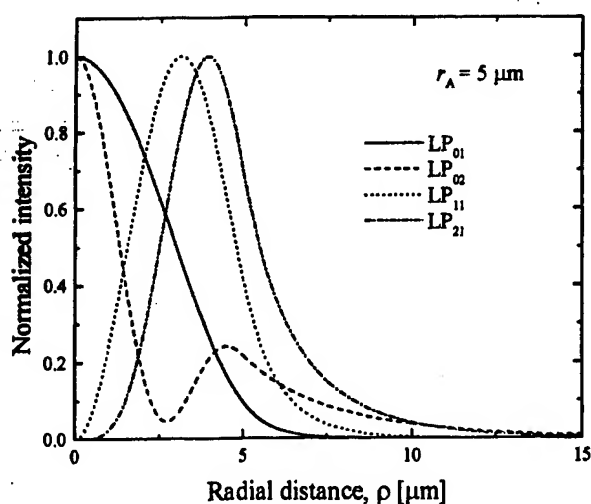


Fig. 9. Calculated radial intensity profiles for the first four lowest-order LP_m modes in the PITSEL structure.

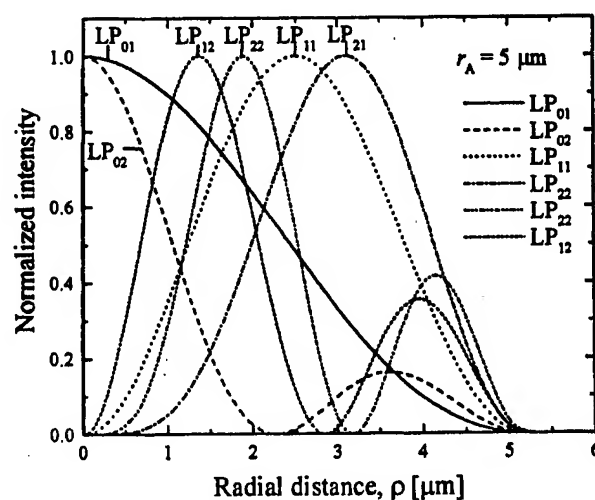


Fig. 10. Calculated radial intensity profiles for the first six lowest-order LP_m modes in the OCSEL structure.

Calculated resonant wavelengths are plotted in Figs. 11 and 12 for various LP modes of the PITSEL and OCSEL structures as functions of the active region radius. As the active region radius decreases, the resonant wavelengths demonstrate the characteristic blueshift [Noble 1998a], and that shift is evidently much larger for the OCSEL structure due to its strong radial nonuniformity. The range for the blueshift in a particular structure can be estimated already at the stage of the local plane wave analysis of that structure performed as a part of the EFM approach. For larger active regions, as long as the modes are well confined within the active region in the radial direction, the resonant wavelengths are close to their plane-wave values calculated for the *inner* radial section of the structure. For smaller active regions and for the poorly localized modes, the resonant wavelengths can be closer to their plane-wave values calculated for the *outer* radial section of the structure. While in the first case the modes are indeed very close to the plane wave propagating along the core region of the device, departures from the plane-wave solutions in the second situation can be quite significant if the conditions for mode guiding cannot be described as weak guiding. Since the EFM is based on the weak-guiding LP modes approximation, we consider it important to test the applicability of the method in each case by analyzing solutions obtained in the "near-cutoff" situation for possible deviations from the weak-guiding conditions. For that purpose, the maximum values for "weak" E_z and "strong" E_x components of the electrical field within the laser structure were calculated, and their intensity ratio in the "near-cutoff" situation was used as a quantitative measure of weak-guiding conditions in VCSELS. We consider the relation $|E_z^{\max 2}|/|E_x^{\max 2}| \ll 1$ in the "near-cutoff" situation as corresponding to the weak-guiding situation in VCSELS just like it is in waveguides.

Figs. 13 and 14 contain the calculated ratios $|E_z^{\max 2}|/|E_x^{\max 2}|$ for PITSELS and OCSELS with various active-region diameters. As evidenced by these results, application of the EFM is well justified for PITSELS and reasonably well justified for OCSELS. It should be mentioned here that very strong lateral mode confinement is not always an advantage as it may lead to poor mode selectivity with respect to modal gain and, as a result, to the onset of multimode generation. We did not optimize the OCSEL structure for the best mode selectivity with respect to the thickness and exact position of the oxidized layer inside the cavity. We expect that by putting a thin oxidized layer exactly in the standing wave node it is possible to minimize the effect of oxidized layers on the lateral mode confinement in VCSELS, in which situation the application of the EFM to OCSELS will be even better justified.

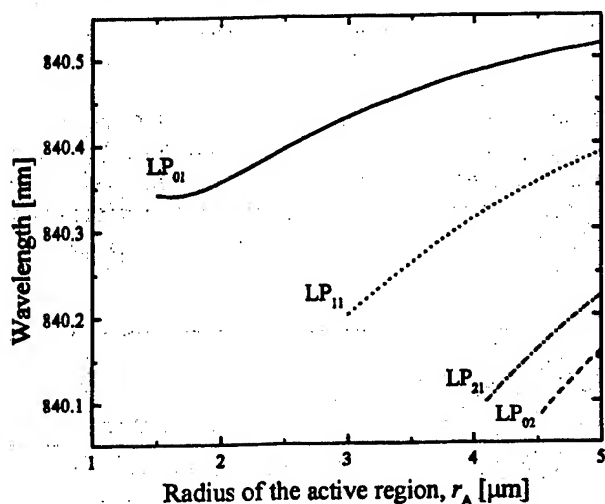


Fig. 11. Resonant wavelengths calculated for the first four lowest-order LP_{lm} modes in the PITSEL structure.

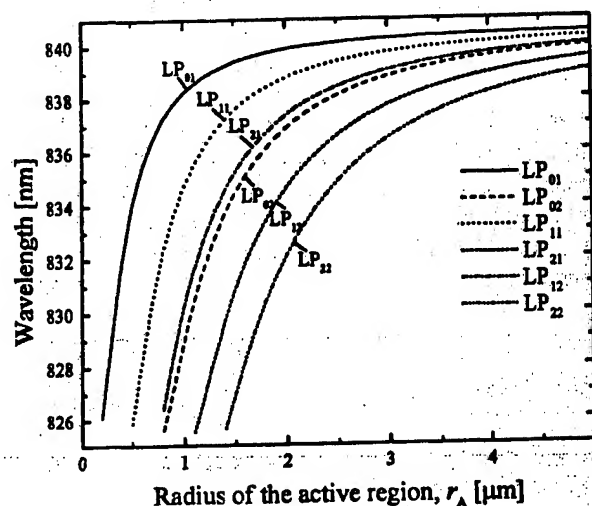


Fig. 12. Resonant wavelengths calculated for the first six lowest-order LP_{lm} modes in the OCSEL structure.

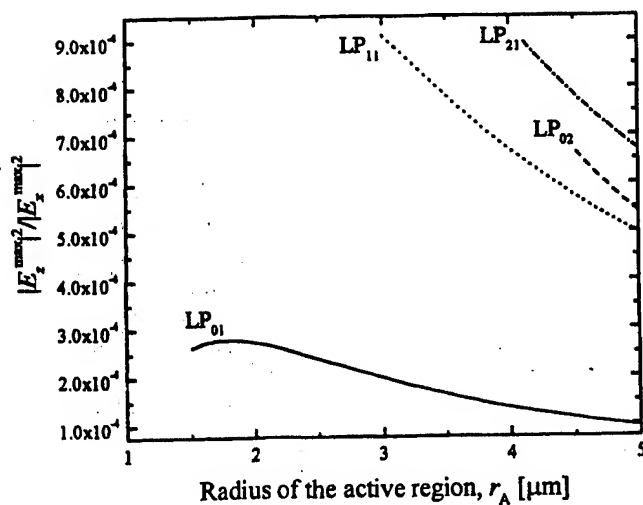


Fig. 13. $|E_z^{\max 2}|/|E_x^{\max 2}|$ ratio calculated for the first four lowest-order LP_{lm} modes in the PITSEL structure.

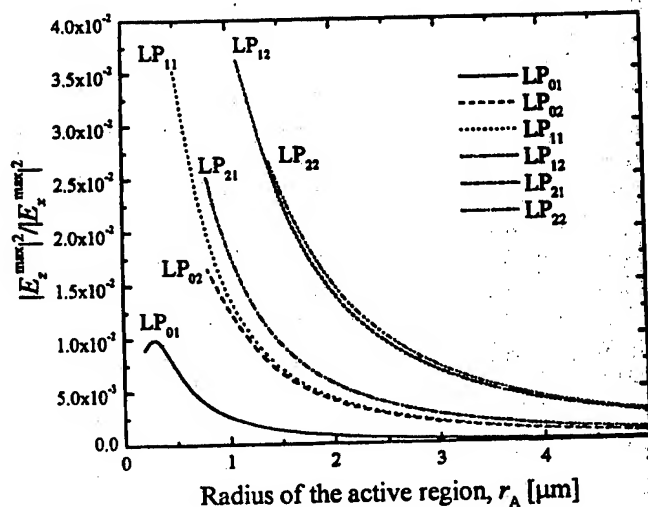


Fig. 14. $|E_z^{\max 2}|/|E_x^{\max 2}|$ ratio calculated for the first six lowest-order LP_{lm} modes in the OCSEL structure.

3. CONCLUSIONS

We have generalized the effective frequency method to the case of vector analysis of LP modes in VCSELs. Our results indicate that EFM is a convenient numerical technique that can provide information about 3D mode profiles, spectra and mode selectivity.

The generalized vectorial EFM has been applied to analyze optical modes in proton-implanted and oxide-confined VCSELs. Resonant wavelengths and mode profiles of a number of vector LP modes have been calculated for different values of the active region radius.

The vectorial EFM has been shown to give accurate information about the vertical and radial components of the energy flux inside the laser structure under steady-state conditions when modal losses are matched by modal gain.

The maximum values for "weak" E_z and "strong" E_x components of the electrical field within the laser structure have been calculated for a number of vector LP modes. Their intensity ratio in the "near-cutoff" situation has been suggested as a quantitative measure of weak-guiding conditions in VCSELs, under which the EFM is derived. The applicability of the EFM has been analyzed based on that criterion. The application of the EFM has been found to be well justified for PITSELs and reasonably well justified for OCSELs.

REFERENCES

- [Adams 1981] M. J. Adams, *An Introduction to Optical Waveguides*, Wiley, Chichester 1981, Ch. 3.
- [Bava 2001] G. P. Bava, P. Debernardi, and L. Fratta, "Three-dimensional model for vectorial fields in vertical-cavity surface-emitting lasers", *Phys. Rev. A (Atomic, Molecular, & Optical Phys.)*, vol. 63 (#2), pp. 023816-1 - 023816-13, 18 Jan. 2001.
- [Bergmann 1998] M. J. Bergmann and H. C. Casey, Jr., "Optical-field calculations for lossy multiple-layer $\text{Al}_x\text{Ga}_{1-x}\text{N}/\text{In}_x\text{Ga}_{1-x}\text{N}$ laser diodes", *J. Appl. Phys.*, vol. 84 (#3), pp. 1196-1203, 1 Aug. 1998.
- [Bienstman 1999] P. Bienstman, B. Demeulenaere, B. Dhoedt, and R. Baets, "Simulation results of transverse-optical confinement in airpost, regrown, and oxidized vertical-cavity surface-emitting laser structures", *J. Opt. Soc. Am. B - Optical Phys.*, vol. 16 (#11), pp. 2055-2059, Nov. 1999.
- [Chang-Hasnain 1993] C. J. Chang-Hasnain, Y. A. Wu, G. S. Li, G. Hasnain, K. D. Choquette, C. Caneau, and L. T. Florez, "Low threshold buried heterostructure vertical cavity surface emitting laser", *Appl. Phys. Lett.*, vol. 63 (#10), pp. 1307-1309, 6 Sept. 1993.
- [Demeulenaere 1996] B. Demeulenaere, D. DeZutter, and R. Baets, "Rigorous electromagnetic study of diffraction loss in VCSEL mirrors", *IEEE Proc.-Optoelectron.*, vol. 143 (#4) pp. 221-227, Aug. 1996.
- [Demeulenaere 1999] B. Demeulenaere, P. Bienstman, B. Dhoedt, and R. G. Baets, "Detailed study of AlAs-oxidized apertures in VCSEL cavities for optimized modal performance", *IEEE J. Quantum Electron.*, vol. 35 (#3), pp. 358-367, March 1999.
- [Deng 1997a] Q. Deng and D. G. Deppe, "Modeling the lasing mode in a 3-dimensionally confined Fabry-Perot microcavity", *Physics and Simulation of Optoelectronic Devices V* (M. Osifski and W. W. Chow, Eds.), San Jose, CA, 10-14 Feb. 1997, *Proc. SPIE*, Vol. 2994, pp. 267-274.
- [Deng 1997b] Q. Deng and D. G. Deppe, "Self-consistent calculation of the lasing eigenmode of the dielectrically apertured Fabry-Perot microcavity with idealized or distributed Bragg reflectors", *IEEE J. Quantum Electron.*, vol. 33 (#12), pp. 2319-2326, Dec. 1997.
- [Hadley 1998] G. R. Hadley, "Low-truncation-error finite difference equations for photonics simulation. II. Vertical-cavity surface-emitting lasers", *J. Lightwave Technol.*, vol. 16 (#1), pp. 141-151, Jan. 1998.
- [Klein 1998] B. Klein, L. F. Register, K. Hess, D. G. Deppe and Q. Deng, "Self-consistent Green's function approach to the analysis of dielectrically apertured vertical-cavity surface-emitting lasers", *Appl. Phys. Lett.*, vol. 73 (#23), pp. 3324-3326, 7 Dec. 1998.
- [Li 1998] H. Li, A. Hohl, A. Gavrielides, H. Hou and K. D. Choquette, "Stable polarization self-modulation in vertical-cavity surface-emitting lasers", *Appl. Phys. Lett.*, vol. 72 (#19), pp. 2355-2357, 11 May 1998.
- [Mahmood 1998] N. Mahmood, B. M. A. Rahman, and K. T. V. Grattan, "Accurate three-dimensional modal solutions for optical resonators with periodic layered structure by using the finite element method", *J. Lightwave Technol.*, vol. 16 (#1), pp. 156-161, Jan. 1998.

- [Martin-Regalado 1997] J. Martin-Regalado, F. Prati, M. San Miguel, and N. B. Abraham, "Polarization properties of vertical-cavity surface-emitting lasers", *IEEE J. Quantum Electron.*, vol. 33 (#5), pp. 765-783, May 1997.
- [Noble 1998a] M. J. Noble, J.-H. Shin, K. D. Choquette, J. P. Loehr, J. A. Lott, and Y.-H. Lee, "Calculation and measurement of resonant-mode blueshifts in oxide-apertured VCSEL's", *IEEE Photon. Technol. Lett.*, vol. 10 (#4), pp. 475-477, Apr. 1998.
- [Noble 1998b] M. J. Noble, J. P. Loehr, and J. A. Lott, "Analysis of microcavity VCSEL lasing modes using a full-vector weighted index method", *IEEE J. Quantum Electron.*, vol. 34 (#10), pp. 1890-1903, Oct. 1998.
- [Noble 1998c] M. J. Noble, J. A. Lott, and J. P. Loehr, "Quasi-exact optical analysis of oxide-apertured microcavity VCSELs using vector finite elements", *IEEE J. Quantum Electron.*, vol. 34 (#12), pp. 2327-2339, Dec. 1998.
- [Osiński 1999] M. Osiński and G. A. Smolyakov, "Integrated thermal-electrical-optical simulator of vertical-cavity surface-emitting lasers", *Design, Fabrication, and Characterization of Photonic Devices* (M. Osiński, S. J. Chua, and S. F. Chichibu, Eds.), *SPIE International Symposium on Photonics and Applications ISPA '99*, Singapore, 30 Nov. - 3 Dec. 1999, *Proc. SPIE*, vol. 3896, pp. 143-154, 1999.
- [Ryvkin 1999] B. Ryvkin, K. Panajotov, A. Georgievski, J. Danckaert, M. Peeters, G. Verschaffelt, H. Thienpont, and I. Veretennicoff, "Effect of photon-energy-dependent loss and gain mechanisms on polarization switching in vertical-cavity surface-emitting lasers", *J. Opt. Soc. Am. B - Optical Phys.*, vol. 16 (#11), pp. 2106-2113, Nov. 1999.
- [Smolyakov 1999] G. A. Smolyakov, V. A. Smagley, W. Nakwaski, P. G. Eliseev, and M. Osiński, "Design of InGaN/GaN/AlGaIn VCSELs using the effective frequency method", *Physics and Simulation of Optoelectronic Devices VII* (P. Blood, A. Ishibashi, and M. Osiński, Eds.), San Jose, CA, 25-29 Jan. 1999, *Proc. SPIE*, Vol. 3625, pp. 324-335.
- [van Exter 1997] M. P. van Exter, A. K. Jansen van Doorn, and J. P. Woerdman, "Electro-optic effect and birefringence in semiconductor vertical-cavity lasers", *Phys. Rev. A*, vol. 56 (#1), pp. 845-853, July 1997.
- [Vurgaftman 1998] I. Vurgaftman, J. R. Meyer, and L. R. Ram-Mohan, "Mid-IR vertical-cavity surface-emitting lasers", *IEEE J. Quantum Electron.*, vol. 34 (#1), pp. 147-156, Jan. 1998.
- [Wenzel 1997] H. Wenzel and H.-J. Wünsche, "The effective frequency method in the analysis of vertical-cavity surface-emitting lasers", *IEEE J. Quantum Electron.*, vol. 33 (#7), pp. 1156-1162, July 1997.
- [Zhang 1995] J.-P. Zhang and K. Petermann, "Numerical analysis of transverse mode in gain-guided vertical-cavity surface-emitting lasers", *IEE Proc.-Optoelectron.*, vol. 142 (#1), pp. 29-35, Feb. 1995.
- [Zhou 1991] P. Zhou, J. Cheng, C. F. Schaus, S. Z. Sun, K. Zheng, E. Armour, C. Hains, W. Hsin, D. R. Myers, and G. A. Vawter, "Low series resistance high-efficiency GaAs/AlGaAs vertical-cavity surface-emitting lasers with continuously graded mirrors grown by MOCVD", *IEEE Photon. Technol. Lett.* 3, pp. 591-593, 1991.

PROCEEDINGS OF SPIE



SPIE—The International Society for Optical Engineering

Physics and Simulation of Optoelectronic Devices IX

Yasuhiko Arakawa
Peter Blood
Marek Osinski
Chairs/Editors

22-26 January 2001
San Jose, USA



Volume 4283



The papers appearing in this book compose the proceedings of the technical conference cited on the cover and title page of this volume. They reflect the authors' opinions and are published as presented, in the interests of timely dissemination. Their inclusion in this publication does not necessarily constitute endorsement by the editors or by SPIE. Papers were selected by the conference program committee to be presented in oral or poster format, and were subject to review by volume editors or program committees.

Please use the following format to cite material from this book:

Author(s), "Title of paper," in *Physics and Simulation of Optoelectronic Devices IX*, Yasuhiko Arakawa, Peter Blood, Marek Osinski, Editors, Proceedings of SPIE Vol. 4283, page numbers (2001).

ISSN 0277-786X
ISBN 0-8194-3961-4

Published by
SPIE—The International Society for Optical Engineering
P.O. Box 10, Bellingham, Washington 98227-0010 USA
Telephone 1 360/676-3290 (Pacific Time) • Fax 1 360/647-1445
<http://www.spie.org/>

Copyright© 2001, The Society of Photo-Optical Instrumentation Engineers.

Copying of material in this book for internal or personal use, or for the internal or personal use of specific clients, beyond the fair use provisions granted by the U.S. Copyright Law is authorized by SPIE subject to payment of copying fees. The Transactional Reporting Service base fee for this volume is \$15.00 per article (or portion thereof), which should be paid directly to the Copyright Clearance Center (CCC), 222 Rosewood Drive, Danvers, MA 01923 USA. Payment may also be made electronically through CCC Online at <http://www.directory.net/copyright/>. Other copying for republication, resale, advertising or promotion, or any form of systematic or multiple reproduction of any material in this book is prohibited except with permission in writing from the publisher. The CCC fee code is 0277-786X/01/\$15.00.

Printed in the United States of America.

Design of InGaN–GaN–AlGaN Vertical-Cavity Surface-Emitting Lasers Using Electrical–Thermal–Optical Simulation

Marek Osinski, *Senior Member, IEEE*, Vladimir A. Smagley, Gennady A. Smolyakov, and Petr G. Eliseev, *Senior Member, IEEE*

Abstract—A three-dimensional electrical–thermal–optical numerical simulator is developed and applied to model group-III-nitride-based intracavity-contacted vertical-cavity surface-emitting lasers with InGaN multi-quantum-well active region. The optical model based on the effective frequency method is combined with an electrical–thermal simulator using the control volume method. Isothermal (pulsed regime imitation) and continuous-wave modes of operation are calculated over a range of voltages, covering sub-threshold spontaneous emission and lasing emission. Effects of current crowding at the active region periphery are examined, and in particular, an impact on mode profiles of spatial hole burning superimposed on nonuniform gain distribution is studied. In order to reduce the current crowding and provide more uniform gain distribution within the active region, a semitransparent p-side contact design is proposed.

Index Terms—Group-III nitrides, intracavity contacts, optoelectronic device simulation, semiconductor laser design, vertical-cavity surface-emitting lasers.

I. INTRODUCTION

NITRIDE-BASED semiconductor lasers continue to attract attention of optoelectronic research community. On the one hand, they promise revolutionary progress in many applications, e.g., as light sources for high-density optical memory, high resolution printing, or full-color laser displays. On the other hand, they continue to pose a significant challenge to both experimental and theoretical research. Strong coupling and interplay of multiple-level subsystems make their analysis quite a formidable task for numerical modeling as well. In particular, it is important to take into account proper physical description of multiple-quantum-well active region, electrical and thermal properties, and optical resonator. It is preferable that the model

includes spontaneous electrical polarization, residual stresses, piezoelectric fields, and thermoelectric field description.

In the case of nitride-based vertical-cavity surface-emitting semiconductor lasers designed to operate in the UV/short wavelength visible spectral range, complexity of numerical modeling increases considerably. First, compared to edge-emitting lasers, the situation becomes much more complicated due to the influence of specific vertical-cavity surface-emitting lasers (VCSELs) design features, such as ultrashort cavity length, complicated optical cavity structure, absence of a conventional waveguide, and strong thermal dependence of operational parameters.

Second, application of nitride-based materials further complicates physical description and design of VCSELs. Possible design problems include: 1) high operation current density necessary to maintain material gain sufficient for vertical mode to lase; 2) nonconducting sapphire substrate; (3) high resistance of bulk materials, especially of p-side; 4) very high electrical resistance of semiconductor distributed Bragg reflectors (DBRs); 5) high contact resistance at p-side; and 6) high junction heating and high joule heating of the laser chip resulting from poor electrical conductivity. Specific issues related to nitride-based VCSEL design are the problems of sufficient electrical conductivity in the device accounting for the poor conductivity (both in bulk and in contacts) of the p-side of the diode, and inclusion of DBRs into the diode design. In principle, DBRs can comprise AlGaIn–GaIn pairs, utilizing GaIn as higher index material and AlGaIn or AlIn as lower index material. However, the electrical conductivity of the material drops rapidly with increasing content of Al in AlGaIn. For this reason, implementation of nitride-based DBRs will require an intracavity contact configuration.

Third, numerical studies of electrically pumped nitride-based VCSELs can only have a heuristic character, since there has been no practical demonstration of such devices so far. Although claims of optically pumped vertical-cavity lasing have been made in a few reports [1]–[4], the designs and technology developed for optical pumping are of little use for the problem of electrically pumped VCSELs.

So far, most of the efforts on development of nitride-based VCSELs have been limited to studies of various semiconductor or dielectric distributed Bragg reflectors (DBRs) [5]–[9]. Early

Manuscript received September 16, 2000; revised July 03, 2001. This work was supported in part by the Defense Advanced Research Projects Agency under the Optoelectronic Materials Center Program and by the Air Force Office of Scientific Research under the Optoelectronics Research Center.

M. Osinski, V. A. Smagley, and G. A. Smolyakov are with the Center for High Technology Materials, University of New Mexico, Albuquerque, NM 87106-4343 USA (e-mail: osinski@chtm.unm.edu).

P. G. Eliseev is with the Center for High Technology Materials, University of New Mexico, Albuquerque, NM 87106-4343 USA and is also with the P. N. Lebedev Physics Institute, Russian Academy of Sciences, 117924 Moscow, Russia.

Publisher Item Identifier S 1077-260X(01)08021-2.

estimations of threshold current density in GaN-based VCSELS have been made in [10], and more recently in [11], [12].

There have been many reports concerning observation of stimulated emission in the vertical direction (surface emission) from AlGaIn–GaN and GaN–InGaIn–GaN structures under short-pulse optical pumping [1], [13]–[18]. A typical pumping rate required to achieve some spectral narrowing without using high-reflectivity mirrors was 1–4 MW/cm² [13]–[15], which was equivalent to extremely high current densities (~ 0.3 – 1.4 MA/cm²). More recently, highly reflective DBR mirrors were used, and much lower threshold pump densities of ~ 2 kW/cm² were observed at 77 K in InGaIn–GaN vertical cavities emitting at 381 nm, pumped by a pulsed 367-nm dye laser [2]. The laser structure contained a 3λ microcavity with a 184-nm-thick bulk InGaIn active layer, top dielectric DBR, and a bottom DBR composed of 35 pairs of Al_{0.34}Ga_{0.66}N–GaN quarter-wave layers.

Room-temperature optically pumped pulsed VCSEL operation at 399 nm has been reported recently in [4]. The active region comprised 263-nm-thick In_{0.1}Ga_{0.99}N quantum wells separated by 5-nm-thick In_{0.01}Ga_{0.99}N barriers. The measured reflection coefficients of DBRs were 98% for the 43-pair Al_{0.34}Ga_{0.66}N–GaN bottom mirror and 99.5% for the 15-pair SiO₂/ZrO₂ top mirror. We estimate the threshold pumping power density as 250 kW/cm², assuming a reflectivity of nitride DBR at the pump wavelength of 367 nm to be 50%, and absorption in the quantum wells to be also 50%. The sheet threshold carrier density was estimated as $(2\text{--}4 \times 10^{12} \text{ cm}^{-2})$, and the material gain was $\sim 890 \text{ cm}^{-1}$.

The aim of this paper is to investigate prospects for electrically pumped InGaIn–GaN–AlGaIn VCSELS, to identify the most critical device parameters essential for room-temperature continuous-wave (CW) operation, and to compare expected performance of devices with various contact geometries. For this purpose, we have integrated our previously developed modules into a new three-dimensional (3-D) self-consistent electrical–thermal–optical (ETO) simulation tool. Previously, we had developed a self-consistent electrical–thermal (ET) simulator, based on the control-volume calculation method, and applied it to analysis of oxide-confined VCSELS [19]–[21]. For optical analysis of VCSEL structures, the effective frequency method (EFM) was shown to offer an attractive approach [22]. As opposed to its original implementation in [23], our EFM solver is capable of handling arbitrary geometries of VCSELS with nonuniform distributions of the refractive index and gain. Here, we couple both ET and EFM modules, as well as a model for the material gain, thus enabling investigations of complex interplay between electrical, thermal, and optical phenomena in nonplanar and nonuniform VCSEL structures. We perform numerical experiments to investigate device behavior at the 400-nm emission wavelength. Two different intracavity-contacted VCSEL structures are compared with RC and semitransparent circular contact configurations.

II. ELECTRICALLY PUMPED InGaIn–GaN–AlGaIn VCSEL STRUCTURE

High electrical resistivity of AlGaIn and p-GaN makes it impractical to consider a VCSEL design in which current would have to flow across the DBR layers. Therefore, it is reasonable

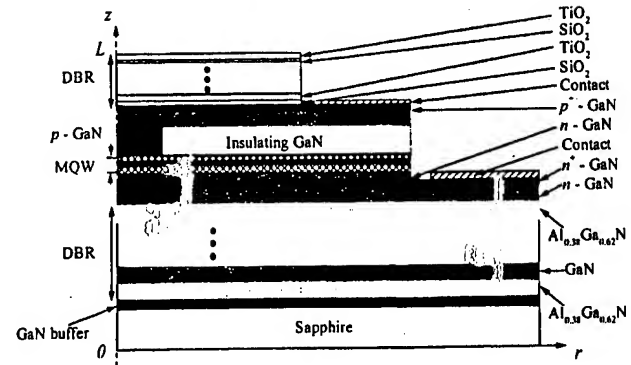


Fig. 1. Schematic structure of cylindrically symmetric intracavity-contacted (IC) InGaIn–GaN–AlGaIn VCSEL considered in this paper.

to assume that both n- and p-side contacts would have to be of intracavity type. This alone makes the analysis of electrical properties of the device difficult, and requires a sophisticated numerical tool.

The simulated device structure is shown in Fig. 1. We use a basic diode design with a closely confined current aperture provided by insulating GaN material. The insulating layer defines the window for vertical current flow. In high-performance GaAs-based VCSELS, the insulating material is normally created by steam oxidation of a thin high-Al-content layer. Based on recent reports of wet oxidation of AlN [24] and GaN [25], a similar process can be envisaged for group-III nitrides. Alternatively, low-energy electron beam irradiation (LEEBI) treatment can be used to pattern a current confining window in p-type GaN [26]. The latter approach corresponds to the situation depicted in Fig. 1.

The biggest problem created by ring-type intracavity contacts is the inherent nonuniform distribution of current density injected into the active region, or in other words, strong current crowding at the edges of the active region [21]. Due to very short diffusion lengths of carriers in group-III nitrides grown on sapphire [27], carriers injected into the active region cannot redistribute themselves in a more uniform fashion. This results in a highly undesirable effect of material gain nonuniformity that would normally favor higher order mode operation [22]. Therefore, we shall also consider an alternative design in which a semitransparent circular contact (CC) is placed between the p-side spacer and the p-side DBR. We expect the CC layer to provide a substantial reduction in the current crowding and to result in an increased current density at the center of the active region. However, insertion of a metal layer into the resonant cavity can be expected to downgrade its optical characteristics, primarily by increasing the internal loss. To minimize this effect, the CC layer has to be very thin (up to 6 nm in our calculations), and the p- and n-spacer thicknesses have to be adjusted in such a way as to guarantee that the metal layer be placed in the node of standing wave for intensity. In the same instance, the active region has to be placed in the standing wave antinode, as is normally the case in microcavity VCSELS.

The design of DBR mirrors illustrated in Fig. 1 and summarized in Table I is similar to optically pumped InGaIn–GaN–AlGaIn VCSELS reported recently in literature.

TABLE I
DEVICE DESIGN PARAMETERS USED IN CALCULATIONS

Parameter	Units	Value	Parameter	Units	Value
Sapphire substrate thickness	μm	100	p^+ -GaN layer thickness	nm	25
$\text{Al}_{0.38}\text{Ga}_{0.62}\text{N}$ DBR layer thickness	nm	42	p -GaN contact layer thickness	nm	10
GaN DBR layer thickness	nm	39.4	Geometrical cavity length	nm	470
Number of $\text{Al}_{0.38}\text{Ga}_{0.62}\text{N}$ DBR layers	-	46	SiO_2 DBR layer thickness	nm	64.1
Number of GaN DBR layers	-	45	TiO_2 DBR layer thickness	nm	33.3
n -GaN spacer thickness	nm	52.3	Number of SiO_2 DBR layers	-	6
n -GaN contact layer thickness	nm	27.4	Number of TiO_2 DBR layers	-	6
n^+ -GaN layer thickness	nm	52.3	Top mesa radius	μm	10
Active $\text{In}_{0.15}\text{Ga}_{0.85}\text{N}$ QW layer thickness	nm	3	Internal radius of p -contact	μm	10
$\text{In}_{0.02}\text{Ga}_{0.98}\text{N}$ barrier layer thickness	nm	3	External radius of p -contact	μm	50
Number of $\text{In}_{0.15}\text{Ga}_{0.85}\text{N}$ quantum wells	-	10	Second mesa radius	μm	50
Number of $\text{In}_{0.02}\text{Ga}_{0.98}\text{N}$ barrier layers	-	9	Internal radius of n -contact	μm	50
p -GaN spacer thickness	nm	186	External radius of n -contact	μm	200
Insulating GaN layer thickness	nm	60	Radius of electrical aperture	μm	5

The n -side DBR is composed of $\text{Al}_{0.38}\text{Ga}_{0.62}\text{N}$ -GaN pairs with the refractive index data taken from [7]. The design resonant wavelength is 400 nm. A stack of SiO_2 - TiO_2 dielectric layers is taken for the p -side DBR. The number of SiO_2 - TiO_2 pairs is fixed at six, as in the device of [2]. In our initial calculations, we set the number of AlGaIn -GaN pairs to be 35, also following [2]. It turned out, however, that the reflectivity of n -side DBR was too small for the simulated device to reach CW lasing threshold at room temperature. Hence, we have increased the number of AlGaIn -GaN pairs to 45, with slightly higher reflectivity than that in the most recent design of [4], where 43 pairs of $\text{Al}_{0.34}\text{Ga}_{0.66}\text{N}$ -GaN were used. It should be noted that in all of these cases, the reflectivity of the top DBR is higher than that of the bottom DBR, thus the device emits most of its output through the sapphire substrate which is transparent at 400 nm. The on-axis distribution of optical field intensity in the top section of the device, calculated using the transfer matrix approach, is illustrated in Fig. 2.

The optical cavity between the DBRs is of 3λ thickness, as in [2]. It is composed of a 132-nm-thick n -GaN layer (contacted to the negative electrode by a ring contact, as shown in Fig. 1), the multiple quantum-well (MQW) active region, and the 281-nm-thick p -layer of GaN (contacted to the positive electrode by either a ring contact outside the active window, or a semitransparent circular contact). The active window (electrical current aperture) radius is assumed to be $5\mu\text{m}$.

The number of quantum wells (ten) assumed in our calculations is limited by spatial extent of the optical intensity antinode. Although a significantly higher number of wells (26) was used in optical pumping experiments of [4], we note that the efficiency of coupling to the gain medium drops significantly when the wells are near the node of the optical standing wave.

The material parameters used in numerical calculations are given in Table II. The phase and group refractive indexes of group-III nitrides are extracted from the data of [7]. The re-

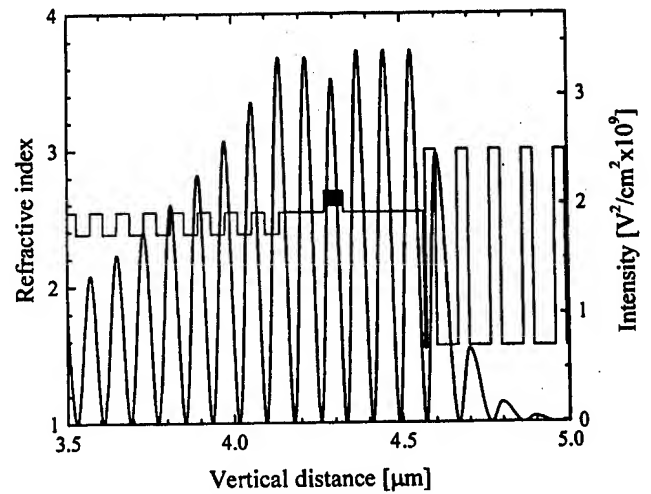


Fig. 2. Intensity of the standing wave and the refractive index profile along the cavity axis. Illustration of proper design of CC-VCSEL: The MQW active region is placed in the maximum intensity region, and the semitransparent metal contact is placed in the minimum intensity region.

fractive index data for the remaining materials are taken from [28]. All calculations are performed for ambient temperature of 300 K. A linear variation with temperature is assumed for all material parameters with tentatively estimated coefficients, except for the bulk resistivity of p -GaN taken in the form accounting for thermal ionization of acceptors [29], which at 300 K are only partially ionized. Therefore, the bulk resistivity of the p -side of the device decreases with increasing temperature, thus causing the diode series resistance (mainly determined by the p -side) to decrease.

The ambipolar diffusion coefficient was calculated using published data on mobility in GaN (see [29] and references therein). At 300 K, we estimate the ambipolar diffusion coefficient $D = 0.389\text{ cm}^2/\text{s}$.

TABLE II
MATERIAL PARAMETERS USED IN CALCULATIONS

Parameter	Units	Value	Parameter	Units	Value
Refractive index of GaN at 400 nm	-	2.54	Heat conductivity of SiO ₂ at 300 K	W/cm·K	0.12
Group index at 400 nm, 300 K	-	3.8	Heat conductivity of TiO ₂ at 300 K	W/cm·K	0.13
Refractive index of In _{0.15} Ga _{0.85} N at 400 nm, 300 K	-	2.7	Electrical resistivity of Au contact at 300 K	Ωcm	6.8×10 ⁻⁶
Group index at 400 nm, 300 K	-	4.5	Electrical resistivity of <i>p</i> -GaIn at 300 K	Ωcm	0.264
Refractive index of Al _{0.38} Ga _{0.62} N at 400 nm, 300 K	-	2.38	Electrical resistivity of <i>n</i> -GaIn at 300 K	Ωcm	0.0203
Group index at 400 nm, 300 K	-	2.88	Electrical resistivity of <i>n</i> -Al _{0.38} Ga _{0.62} N at 300 K	Ωcm	0.0203
Refractive index of SiO ₂ at 400 nm	-	1.56	Mg acceptor ionization energy	eV	0.153
Group index at 400 nm, 300 K	-	1.61	<i>p</i> -contact specific resistance	Ωcm ²	6×10 ⁻⁵
Refractive index of sapphire at 400 nm, 300 K	-	1.79	<i>n</i> -contact specific resistance	Ωcm ²	3.65×10 ⁻⁶
Group index at 400 nm, 300 K	-	1.88	Linear nonradiative recombination coefficient, <i>A</i>	s ⁻¹	10 ⁸
Refractive index of Au at 400 nm	-	1.54	Bimolecular radiative recombination coefficient, <i>B</i>	cm ³ /s	3.6×10 ⁻¹¹
Imaginary part at 400 nm, 300 K	-	-1.81	Spontaneous emission factor, <i>β</i>	-	10 ⁻⁴
Energy bandgap of GaN	eV	3.39	Optical absorption coefficient (of all layers in the cavity)	cm ⁻¹	2
Energy bandgap of In _{0.15} Ga _{0.85} N	eV	3.132	Temperature coefficient of refractive index (of all layers in the cavity)	K ⁻¹	10 ⁻⁴
Electron effective mass in In _{0.15} Ga _{0.85} N	<i>m</i> ₀	0.205	Temperature coefficient of InGaIn/GaN energy bandgap	eV/K	-4.2×10 ⁻⁴
Hole effective mass in In _{0.15} Ga _{0.85} N	<i>m</i> ₀	0.755	Temperature coefficient of electrical resistivity of <i>n</i> -type layers	K ⁻¹	5×10 ⁻³
Conduction band offset at In _{0.15} Ga _{0.85} N/GaN interface	eV	0.22			
Valence band offset at In _{0.15} Ga _{0.85} N/GaN interface	eV	0.1031			
Energy parameter of spectral broadening in In _{0.15} Ga _{0.85} N	eV	0.068			
Heat conductivity of GaN at 300 K	W/cm·K	1.1			
Heat conductivity of Al _{0.38} Ga _{0.62} N at 300 K	W/cm·K	1.898			
Heat conductivity of sapphire at 300 K	W/cm·K	0.46			

In our preliminary numerical simulations, a typical value of *p*-side contact specific resistance $\rho_c = 3.6 \times 10^{-3} \Omega \cdot \text{cm}^2$ was assumed. We have determined that VCSELs with such contact resistivity would suffer from strong heating problems, which combined with nonuniform injection current profile would prohibit CW room-temperature operation, irrespective of top contact configuration. Even at voltages as high as 100 V, the device would still operate in the amplified spontaneous emission mode, with the modal gain insufficient to reach threshold. Consequently, we have reduced the value of ρ_c to $6 \times 10^{-5} \Omega \cdot \text{cm}^2$, which approaches some of the best results reported in literature [30]–[32].

Temperature dependence of thermal conductivity in all layers is assumed in the same form as used previously for GaAs and related compounds [33], i.e., $k(T) = k(300)(300/T)^{5/4}$, where *T* is expressed in kelvins.

III. VCSEL MODEL DESCRIPTION

In order to predict characteristics of electrically pumped group-III nitride VCSELs and evaluate prospects for room-temperature CW operation, we have integrated our previously developed ET, gain, and optical modules into a new 3-D self-consistent ETO simulation tool. The following discussion summarizes the main features of these modules.

A. ET Module

The ET part of our simulator is based on the control-volume calculation method and was described in our earlier publications [19]–[21]. The electrical problem involves solving the Laplace equation in the entire volume of the device and finding the electrical potential and vectorial current density distributions. The *p*–*n* junction is modeled as biased by direct

voltage (Fermi voltage) corresponding to the quasi-Fermi-level separation in the active region. In this approach, a continuous function of the radial-distance-dependent Fermi voltage is assumed. Self-consistency of the electrical simulation requires that the local voltage and current at the p-n junction all correspond to the calculated current flow within the entire device (taking into account contact geometry, contact resistance, and bulk resistance outside the active region). Carrier diffusion in the active region plane is also taken into account. The effects of diffusion are especially important near the regions of high current crowding, and in those regions several control volumes per diffusion length are necessary in order to obtain adequate carrier distribution. Near the edges of the active region, where carrier density exceeds $2 \times 10^{19} \text{ cm}^{-3}$, the diffusion length is as short as 200–280 nm. Outside the current window, carrier diffusion determines the tail of the carrier density distribution, and the diffusion length there is about 600 nm (carrier density $\sim 10^{17} \text{ cm}^{-3}$).

The thermal problem involves solution of heat conduction equation with appropriate boundary conditions at the heat sink (located below the sapphire substrate) and outside walls of the chip. Local heat generation via Joule heating in passive regions and nonradiative recombination in the active region is included, and heat transport in laser chip is analyzed, producing thermal flux and temperature distributions in the entire volume of the device.

B. Gain Module

The carrier density profile produced by the ET module is used to calculate the local value of material gain/absorption coefficient. The material gain/absorption spectra are calculated using a modified version of the $k \cdot p$ model of [34], originally developed for bulk GaN. Our modifications, explained briefly in [22], include choosing a transition matrix element appropriate for the quantum-well active region and adding band tail states. Our model, described in more detail in [21], assumes the recombination balance of carriers that includes linear nonradiative recombination, spontaneous bimolecular radiative recombination, and stimulated recombination, with position-dependent stimulated recombination lifetime as determined by the lasing mode profile. All recombination terms are balanced by the carrier generation term produced by the vertical component of the current density injected into the active region.

C. Optical Module

The 3-D profile of temperature calculated in the ET module and the radial distribution of material gain/absorption in the active region plane calculated in the gain module are used in the optical module as input data. The optical model is based on the effective frequency method (EFM) [22], [23] combined with the rate equations for photon and carrier densities.

An important connection between the ET, electronic and optical parts of the simulator is realized through the rate equations for carrier density N and a quantity S that replaces the usual photon density in position-independent rate equations

$$\frac{dN}{dt} = D \nabla^2 N + \frac{j_z}{e d} - AN - BN^2 - \frac{N}{\tau_{st}} \quad (1)$$

$$\frac{dS}{dt} = \beta BN^2 + \frac{N}{\tau_{st}} - \frac{S}{\tau_{ph}} \quad (2)$$

where

- D diffusion coefficient;
- j_z vertical component of the current density;
- e electron charge;
- d total thickness of all quantum-well layers;
- β spontaneous emission factor;
- A linear nonradiative recombination coefficient;
- B bimolecular radiative recombination coefficient;
- τ_{st} stimulated lifetime for carriers;
- τ_{ph} photon lifetime that accounts for the decrease in the photon density due to output losses and other losses, not directly associated with radiative transitions;
- S defined here as twice the time-averaged density of electrical energy in the electromagnetic wave, divided by photon energy, and has the spatial dependence of $|E(r, z)|^2$, where $E(r, z)$ is proportional to the electrical field profile calculated within the EFM.

Within the active region, the carrier density N is assumed to be uniform in the vertical z direction, i.e., all quantum wells are assumed to be pumped equally. This assumption allows us to find carrier density distribution $N(r)$ in all quantum wells by solving the diffusion (1) just once for an effective active region of total thickness d , instead of handling this problem separately for each quantum well.

Most importantly, S is not assumed to be uniform, but is defined as

$$S(r, z) = S_{\text{tot}} n'^2(r, z) |E(r, z)|^2 \quad (3)$$

where S_{tot} is the total number of photons in the mode, n' is the real part of the refractive index, and $E(r, z)$ is normalized according to

$$2\pi \int_{V_M} n'^2(r, z) |E(r, z)|^2 r dr dz = 1 \quad (4)$$

with the integration performed over the entire mode volume V_M . Note that $E(r, z)$ does not have the dimension of the electrical field, but instead is expressed in units of $(1/\text{volume})^{1/2}$. With this normalization condition, integration of (3) over the mode volume V_M produces the total number of photons in the mode S_{tot} .

The stimulated lifetime for carriers τ_{st} depends on the radial distance r and is determined as

$$\tau_{st}(r) = \frac{N(r)}{g(r) S_{\text{tot}} \frac{1}{d} \int_{QW_s} v_g n'^2(r, z) |E(r, z)|^2 dz} \quad (5)$$

where v_g is the group velocity, $g(r)$ is the local material gain, and integration is performed over all quantum wells. This integration follows from our assumption of the carrier density N being uniform along the z direction and represents averaging the term $v_g g S$, originally present in the rate equations, over all quantum wells.

Integration of (2) over the mode volume V_M gives, under steady-state conditions, the following expression for the total number of photons in the mode S_{tot}

$$S_{\text{tot}} = \tau_{ph} \int_{V_A} \left(\beta B N^2 + \frac{N}{\tau_{st}} \right) dV \quad (6)$$

where V_A is the active region volume. Since the integrand itself (both the carrier density N and the stimulated carrier lifetime

τ_{st}) depends on S_{tot} according to (1)–(3) and (5), (6) is used to find S_{tot} by means of an iterative process of the type $S_{tot}^{i+1} = F(S_{tot}^i)$, where i is the iteration number.

After the total number of photons in the mode S_{tot} is found, the value for the actual electrical field $E(r, z)$ is obtained by equating the calculated value for the electromagnetic energy in the mode with that calculated according to the well-known formula of electrodynamics

$$\begin{aligned} \hbar\omega S_{tot} &= 2\pi \int_{V_M} \frac{1}{4} \epsilon_0 n'^2(r, z) |E(r, z)|^2 r dr dz \\ &\quad + 2\pi \int_{V_M} \frac{1}{4} \mu_0 \mu |H(r, z)|^2 r dr dz \\ &= \pi \int_{V_M} \epsilon_0 n'^2(r, z) |E(r, z)|^2 r dr dz \end{aligned} \quad (7)$$

where the left-hand side is the calculated electromagnetic energy, the right-hand side represents the time-averaged electromagnetic energy for the electromagnetic wave characterized by the electrical field $E(r, z)$ and magnetic field $H(r, z)$, and $E(r, z)$ has the spatial dependence of $E(r, z)$ calculated within the EFM.

To calculate the electromagnetic energy flux density, we use the standard formula for the time-averaged Poynting vector

$$\vec{S} = \frac{1}{2} \text{Re} [\vec{E} \times \vec{H}^*] \quad (8)$$

where the complex representation is assumed for the fields. Equation (8) involves vectorial quantities, hence, we need to identify at this stage a particular polarization chosen for the analysis. All LP modes in cylindrically symmetric waveguiding structures are two-fold degenerate with respect to polarization, with either $E_x = H_y = 0$, or $E_y = H_x = 0$. In what follows, we consider the modes with their electric field polarized along the x axis. Using the local-plane-wave approach, we can relate the longitudinal component of the Poynting vector to the only nonzero transverse components of the fields E_x and H_y , with the electric field $E_x(r, z)$ being found from (7).

The exact knowledge of the electromagnetic energy flux density inside the VCSEL resonator is very important for accurate calculation of the heat generation associated with the free-carrier absorption of laser radiation. In addition, it enables us to calculate the emitted power P_{out} as

$$P_{out} = 2\pi \int_0^{r_M} S_z(r, 0) r dr \quad (9)$$

where the upper integration limit r_M means that integration is performed over the mode area, and $z = 0$ indicates the bottom (emitting) surface of the cavity.

This approach allows us to calculate the lasing wavelength (that is always somewhat detuned from the Bragg resonance due to lateral nonuniformity of the device structure), modal intensity profile, emitted power, and electromagnetic energy flux density inside the cavity. For the first time in application of the EFM, we use dynamically readjusted spatial distributions of gain and refractive index, which allows us to treat arbitrary VCSEL structures of complex geometry. The model also includes temperature-induced variations of complex permittivity according to the calculated radial and vertical profiles of temperature. Combined with the ET module, the optical solver allows us to model effects associated with current crowding and self-distribution,

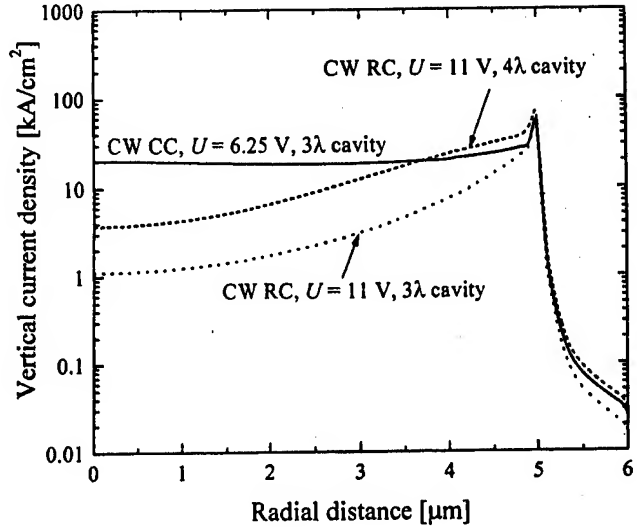


Fig. 3. Vertical current density profiles in the active region plane for CW operation of nitride-based IC-VCSELs at room temperature. The voltages of 11 and 6.25 V are near the CW lasing threshold for RC device with 4- λ cavity and CC device with 3- λ cavity, respectively.

spatial hole burning, and thermal lensing. Thus, the fully integrated model takes into account the most important effects in both short-pulse (isothermal) and CW operation of the laser, and includes major physical processes self-consistently.

The electrical, thermal, electronic, and optical equations are coupled via the dependence of heat sources on the current and electrical potential distributions, and via temperature dependence of the barrier voltage at the junction and resistivity in the passive regions. Therefore, the model includes complex interaction phenomena such as spatial hole burning or current redistribution related to changes in material parameters due to local Joule heating.

IV. INVESTIGATION OF RING-CONTACT AND CIRCULAR CONTACT DESIGNS

As described in Section II, we consider two alternative designs of electrically pumped intracavity-contacted group-III nitride VCSELs. In view of relatively high p-side contact resistance, the common ring-contact (RC) design can be expected to suffer from strong current crowding effects at the edges of the active region. Therefore, we shall also explore the potential benefits that may arise from using a semitransparent CC. Both RC and CC contact configurations are studied under low-duty-cycle short-pulse and CW operating conditions.

A. Current Crowding Effects and Improved Design of RC VCSEL

Our previous studies of current crowding effects in IC-VCSELs [19]–[21] indicated that even in GaAs-based VCSELs, nonuniformity of current injection in RC configuration can be very severe. We expected the situation to become much worse in GaN-based VCSELs, due to poor conductivity of p-GaN and high p-contact resistance. This expectation is confirmed in Fig. 3, showing vertical current density profiles for three CW cases: RC and CC configurations with 3 λ cavity, and RC

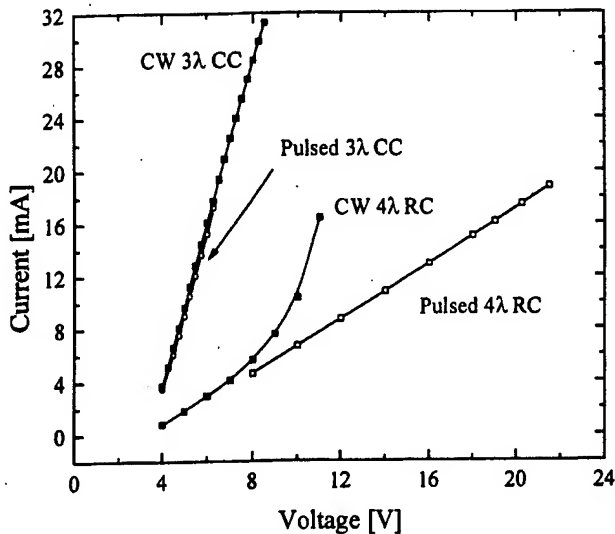


Fig. 4. Current-voltage characteristics of nitride-based IC-VCSELs.

configuration with 4λ cavity. The CC geometry does improve current uniformity significantly, but even in this case there is a residual hump at the edge of the active region, indicating that a significant portion of current in the p-GaN spacer is still flowing in the radial direction. Most importantly, comparison of RC and CC results for 3λ cavity clearly indicates that the threshold for the 3λ RC device would be much higher than that of the CC device. In spite of a higher voltage (11 V versus 6.25 V for the CC device), the total current flowing through the 3λ -RC device is 2.2 times smaller (6.81 mA versus 14.86 mA), and the series resistance is as high as 1615 Ω . In the same instance, nonuniformity of the vertical current density is very strong already (the current crowding coefficient, defined as the ratio of vertical current density at its maximum near the edge of the active region to its value at the center of device, is as high as 55, compared to only 2.3 for the CC device), and is bound to become much worse with increasing bias. Hence, even if the 3λ -RC device could lase, it would definitely operate in a high-order mode. In order to reduce current nonuniformity and series resistance, and to increase the likelihood of fundamental mode operation, we have therefore replaced the 3λ cavity design for RC device with 4λ cavity, where the thickness of p-GaN spacer was increased by one wavelength to 343 nm. The current crowding coefficient for the 4λ -RC device is 26, and the series resistance at 11 V is reduced to 671 Ω (current 16.4 mA). All of the results presented in subsequent sections for the RC case correspond to the 4λ design.

B. I - V and L - I Characteristics

Fig. 4 shows calculated current-voltage (I - V) characteristics of IC-VCSELs in both 4λ -RC and 3λ -CC configurations and under both CW and pulsed-current conditions. The range of voltages is in each case chosen such as to encompass below-threshold and above-threshold operation. Compared to the RC design, we expect the CC configuration to offer lower electrical resistance and smaller driving voltage at any given current. As shown in Fig. 4, this is indeed the case both under pulsed and

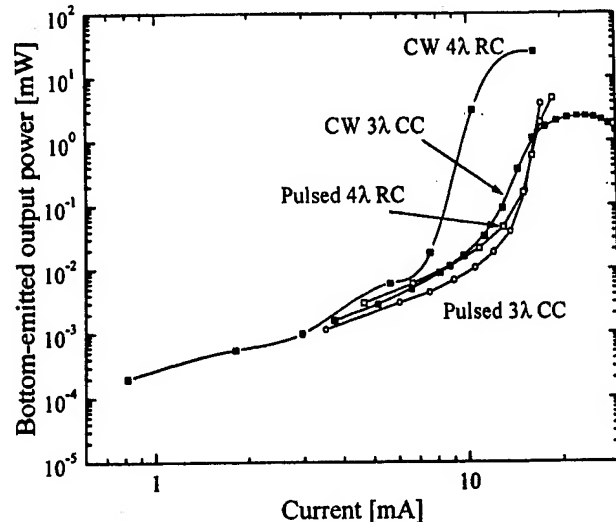


Fig. 5. Light-current characteristics of nitride-based IC-VCSELs.

CW conditions. For the case of pulsed RC device, the series resistance is practically unaffected by the driving voltage level. The calculated ohmic resistance is 985 Ω . For the case of CW operation, the RC device resistance improves considerably, decreasing to ~ 165 Ω at driving voltages exceeding 10 V. This effect can be easily explained by a strong temperature dependence of p-GaN conductivity, with the concentration of ionized acceptors increasing exponentially with temperature. Interestingly enough, this effect is not observed in the case of semitransparent CC configuration. We ascribe this behavior to different current paths in RC and CC devices. In the case of CC geometry, current is not forced to flow through a long radial path on the p-side of the VCSEL device, hence, the series resistance is not so strongly affected by variations in p-GaN conductivity with temperature.

Fig. 5 depicts light-current (L - I) characteristics of the 4λ -RC and 3λ -CC devices in the same range of voltages as in Fig. 4. At threshold, the output power increases by at least two orders of magnitude, although the transition may seem rather smooth on the logarithmic scale. We use the linear extrapolation of above-threshold L - I curves to determine the threshold. Rather surprisingly, the lowest threshold current of 9.5 mA is obtained for the CW RC case, followed by 13.5 mA for the CW CC case, and almost equal (15.9 and 15.1 mA, respectively) threshold currents for RC and CC devices under pulsed conditions. We discuss these results in more detail in Section V.

It should be noted that the L - I curves for CW operation saturate and eventually decline with increasing current. This kind of behavior is caused by the active region temperature increase with increasing pumping, and is quite typical of real devices.

C. Carrier Density and Material Gain Profiles

The radial distribution of carriers in the active region plane depends on the distribution of the injection current (z component of the current density at the junction), as well as on the recombination and diffusion of carriers. Provided that temperature gradient within the active region is small, the material gain

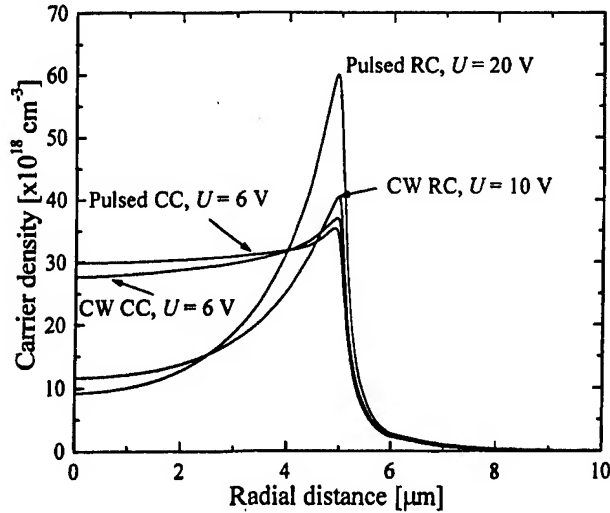


Fig. 6. Radial profiles of carrier density in the active region plane for pulsed and CW operation of nitride-based IC-VCSELs at room temperature evaluated near threshold.

profile at the lasing wavelength closely resembles that of the carrier density. Consequently, gain distribution is strongly influenced by current crowding effects, especially since the diffusion length of carriers in GaN is relatively small. As shown in Fig. 6, carrier density distribution in 4λ -RC devices is very nonuniform, and its shape can be expected to favor high-order transverse modes. On the other hand, the 3λ -CC configuration offers a fairly uniform carrier profile, hence, it can be expected to support fundamental LP_{01} mode operation.

Insertion of a semitransparent metal contact at the top side of the p-GaN mesa does, however, introduce an additional optical loss associated with strong absorption of lasing light in the metallic layer. This limits the thickness of semitransparent Au layer to less than 6 nm, and results in a residual peak of injected current density at the edges of the active region. Our calculations show that insertion of a 10-nm-thick semitransparent Au contact reduces the photon lifetime τ_{ph} to 1.05 ps and produces an additional average internal loss of $\alpha_{met} \approx 76 \text{ cm}^{-1}$, compared to $\tau_{ph} = 2.27 \text{ ps}$ and $\alpha_{met} \approx 18 \text{ cm}^{-1}$ for a 6-nm-thick CC layer. With the output loss of only $\sim 31\text{--}33 \text{ cm}^{-1}$, the internal loss associated with the 10-nm-thick semitransparent contact would, therefore, dominate the device behavior and would severely degrade its performance. These estimations have been made taking the average group index inside the cavity (weighted with longitudinal intensity distribution) as 3.47 for 6-nm-thick metal and 3.49 for 10-nm-thick metal.

Above threshold, the lasing mode affects carrier distribution via the spatial hole-burning (SHB) effect. Self-consistency under lasing conditions implies a dynamic saturation of the modal gain near the threshold level. In the case of fundamental mode operation, this leads to enhanced depletion of carrier population in the center of the device and increases nonuniformity of carrier density and material gain distributions. This is illustrated in Fig. 7, for the case of a 3λ -CC device operating in the LP_{01} mode. It is clear that SHB can occur even at relatively low output power levels.

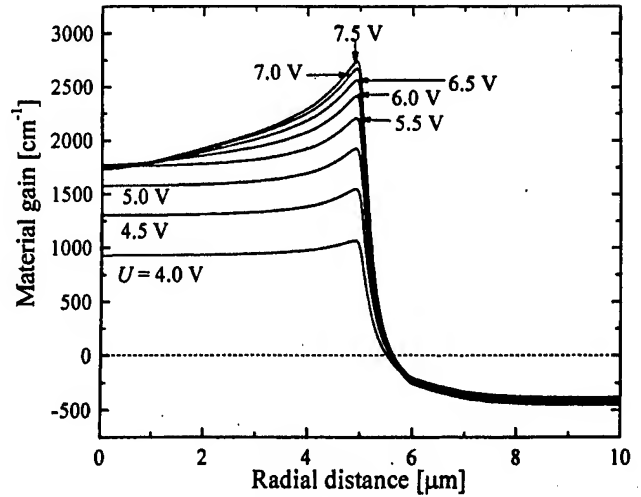


Fig. 7. Gain profile evolution for 3λ -CC device operating CW. Voltage is changing in upward direction from 4 to 7.5 V with step of 0.5 V. Threshold voltage is 5.8 V.

TABLE III
THRESHOLD CONDITIONS

	Ring p-side contact (RC)		Semitransparent circular contact (CC)	
	Pulsed	CW	Pulsed	CW
U_{th} [V]	18.8	9.2	6.0	5.6
I_{th} [mA]	15.9	9.5	15.1	13.5
J_{th} [kA/cm ²]	20.4	12.1	19.1	17.5
Mode at threshold	LP_{01}	LP_{11}	LP_{01}	LP_{21}
$T_A(0)$ [°C]	-	38.6	-	40.8
$T_A(r_A)$ [°C]	-	43.1	-	31.7

V. DISCUSSION

The improved design of nitride-based IC-VCSELs (low p-side contact resistance, higher number of DBR periods on the n-side, and thicker p-side spacer for RC configuration) has resulted in our prediction of relatively low threshold voltage and threshold current for both RC and CC geometries, and under both short-pulse and CW operating conditions. Table III summarizes the threshold data in all four cases, including electrical, optical, and thermal properties.

Perhaps the most unexpected outcome of our simulations shown in Table III is the prediction of fundamental mode operation at threshold in pulsed RC-VCSELs and higher order mode operation at threshold in CW CC-VCSELs. The latter results involve thermal lensing effects and can be accounted for by strong coupling between thermal and optical phenomena, which leads to large deformations of mode profiles. The pulsed (isothermal) results can be understood by considering only the EFM solutions of wave equation in VCSEL cavity. In view of a very strong nonuniformity of carrier density in RC lasers (see Fig. 6), it would be natural to expect a high-order mode operation. The most likely candidate might seem to be in the LP_{1l} ($l = 1, 2, 3, \dots$) family of modes with a single maximum away from the waveguide axis. However, all of these modes extend far beyond the active region, where they experience significant loss from unpumped quantum wells. In contrast, the fundamental mode, while not overlapping well with the gain

profile, is much better confined to the active region, and does not suffer from excessive loss in lateral unpumped layers.

VI. CONCLUSION

In our previous studies of current crowding in IC-VCSELs, the ET simulator proved to be an essential tool. Present implementation of our ET-optical simulator has an added dimension of interactions involving the optical field. The new tool can produce all main ETO characteristics, such as current density distribution, temperature distribution, mode profiles (in a single-mode approximation), profiles of the Poynting vector, etc. It offers a very cost-effective approach to the development of novel devices, and as shown in this paper, is particularly useful in design of electrically pumped nitride-based VCSELs.

The main conclusions of this paper can be summarized as follows.

- 1) Taking as an example the intracavity-contacted nitride-based VCSELs, we show that the effective frequency method is a useful numerical technique for optical analysis of complex VCSEL structures. It provides information about transverse mode profiles, spectra, and mode selectivity.
- 2) Combined with the ET solver, the optical module can be used to treat temperature detuning, current crowding, nonuniform gain saturation, etc.
- 3) The rather high series resistance of the nitride-based IC-VCSELs is not an obstacle for CW operation, provided low-resistance p-side contact and high-reflectivity DBRs are used.
- 4) Self-consistent simulation provides insight into complex interactions between thermal, electrical, and optical phenomena in VCSELs. In particular, we demonstrate how the spatial hole burning occurs.
- 5) IC-VCSELs with a 5- μm radius of electrical window and with either a ring p-side contact or a semitransparent circular contact are predicted to operate in the fundamental transverse mode under pulsed conditions. In order to reach CW operation on fundamental mode, the active region radius should be smaller than 5 μm .

REFERENCES

- [1] J. M. Redwing, D. A. S. Loeber, N. G. Anderson, M. A. Tischler, and J. S. Flynn, "An optically pumped GaN-AlGaIn vertical cavity surface emitting laser," *Appl. Phys. Lett.*, vol. 69, no. 1, pp. 1-3, 1996.
- [2] T. Someya, K. Tachibana, J.-K. Lee, T. Kamiya, and Y. Arakawa, "Lasing emission from an $\text{In}_{0.1}\text{Ga}_{0.9}\text{N}$ vertical cavity surface emitting laser," *Jpn. J. Appl. Phys. 2, Lett.*, vol. 37, no. 12A, pp. L1424-L1426, 1998.
- [3] A. V. Sakharov, W. V. Lunding, I. L. Krestnikov, V. A. Semenov, A. S. Usikov, A. F. Tsatsul'nikov, Y. G. Musikhin, M. V. Baidakova, Z. I. Alferov, N. N. Ledentsov, A. Hoffmann, and D. Bimberg, "Surface-mode lasing from stacked InGaIn insertions in a GaN matrix," *Appl. Phys. Lett.*, vol. 74, no. 26, pp. 3921-3923, 1999.
- [4] T. Someya, R. Werner, A. Forchel, M. Catalano, R. Cingolani, and Y. Arakawa, "Room temperature lasing at blue wavelengths in gallium nitride microcavities," *Science*, vol. 285, no. 5435, pp. 1905-1906, 1999.
- [5] I. J. Fritz and T. J. Drummond, "AlN-GaN quarter-wave reflector stack grown by gas-source MBE on (100) GaAs," *Electron. Lett.*, vol. 31, no. 1, pp. 68-69, 1995.
- [6] T. Sakaguchi, T. Honda, A. Katsube, F. Koyama, and K. Iga, "MgO/SiO₂ dielectric multilayer reflectors formed by electron-beam evaporation for GaN surface emitting semiconductor lasers," in *Proc. Top. Workshop III-V Nitrides (TWN'95)*, I. Akasaki and K. Onabe, Eds., Nagoya, Japan, Sept. 21-23, 1995, pp. 255-258.
- [7] O. Ambacher, M. Arzberger, D. Brunner, H. Angerer, F. Freudenberger, N. Esser, T. Wethkamp, K. Wilmers, W. Richter, and M. Stutzmann, "AlGaIn-Based Bragg reflectors," *MRS Internet J. Nitride Semicond. Res.*, vol. 2, Aug. 1997.
- [8] H. M. Ng, D. Doppalapudi, E. Iliopoulos, and T. D. Moustakas, "Distributed Bragg reflectors based on AlN/GaN multilayers," *Appl. Phys. Lett.*, vol. 74, no. 7, pp. 1036-1038, 1999.
- [9] R. Langer, A. Barski, J. Simon, N. T. Pelekanos, O. Kononov, R. André, and L. S. Dang, "High-reflectivity GaN/GaAlN Bragg mirrors at blue/green wavelengths grown by molecular beam epitaxy," *Appl. Phys. Lett.*, vol. 74, no. 24, pp. 3610-3612, 1999.
- [10] T. Honda, A. Katsube, T. Sakaguchi, F. Koyama, and K. Iga, "Threshold estimation of GaN-based surface emitting lasers operating in ultraviolet spectral region," *Jpn. J. Appl. Phys. 1 Regul. Rep. Short Notes and Rev. Pap.*, vol. 34, no. 7A, pp. 3527-3532, 1995.
- [11] P. Mackowiak and W. Nakwaski, "Threshold currents of nitride vertical-cavity surface-emitting lasers with various active regions," *MRS Internet J. Nitride Semicond. Res.*, vol. 3, Oct. 1998.
- [12] —, "Detailed threshold analysis of UV-emitting nitride vertical-cavity surface-emitting lasers," *J. Phys. D, Appl. Phys.*, vol. 31, no. 19, pp. 2479-2484, 1998.
- [13] M. A. Khan, D. T. Olson, J. M. Van Hove, and J. N. Kuznia, "Vertical-cavity, room-temperature stimulated emission from photopumped GaN films deposited over sapphire substrates using low-pressure metal-organic chemical vapor deposition," *Appl. Phys. Lett.*, vol. 58, no. 14, pp. 1515-1517, 1991.
- [14] H. Amano, N. Watanabe, N. Koide, and I. Akasaki, "Room-temperature low-threshold surface-stimulated emission by optical pumping from $\text{Al}_{0.1}\text{Ga}_{0.9}\text{N/GaN}$ double heterostructure," *Jpn. J. Appl. Phys. 2, Lett.*, vol. 32, no. 7B, pp. L1000-L1002, 1993.
- [15] K. Yung, J. Yee, J. Koo, M. Rubin, N. Newman, and J. Ross, "Observation of stimulated emission in the near ultraviolet from a molecular beam epitaxy grown GaN film on sapphire in a vertical-cavity, single pass configuration," *Appl. Phys. Lett.*, vol. 64, no. 9, pp. 1135-1137, 1994.
- [16] M. A. Khan, S. Krishnakutty, R. A. Skogman, J. N. Kuznia, D. T. Olson, and T. George, "Vertical-cavity stimulated emission from photopumped InGaIn heterojunctions at room temperature," *Appl. Phys. Lett.*, vol. 65, no. 5, pp. 520-521, 1994.
- [17] H. X. Jiang, J. Y. Lin, M. A. Khan, Q. Chen, and J. W. Yang, "Surface emission of $\text{In}_{0.2}\text{Ga}_{0.8}\text{N}$ epilayers under strong optical excitation," *Appl. Phys. Lett.*, vol. 70, no. 8, pp. 984-986, 1997.
- [18] I. L. Krestnikov, W. V. Lunding, A. V. Sakharov, V. A. Semenov, A. S. Usikov, A. F. Tsatsul'nikov, Z. I. Alferov, N. N. Ledentsov, A. Hoffmann, and D. Bimberg, "Room-temperature photo-pumped InGaIn/GaN/AlGaIn vertical-cavity surface-emitting laser," *Appl. Phys. Lett.*, vol. 75, no. 9, pp. 1192-1194, 1999.
- [19] V. A. Smagley, G. A. Smolyakov, P. G. Eliseev, M. Osinski, and A. J. Przekwas, "Current self-distribution effect in vertical-cavity surface-emitting semiconductor lasers," in *Physics and Simulation of Opto-Electronic Devices VI*, vol. 3283, SPIE Proc., M. Osinski, P. Blood, and A. Ishibashi, Eds., San Jose, CA, Jan. 26-30, 1998, pp. 171-182.
- [20] M. Osinski, V. A. Smagley, G. A. Smolyakov, T. Svimonishvili, P. G. Eliseev, and G. Simonis, "Three-dimensional simulation of oxide-confined vertical-cavity surface-emitting semiconductor lasers," in *Opto-electronic Materials Devices*, vol. 3419, SPIE Proc., M. Osinski and Y.-K. Su, Eds., Taipei, Taiwan, July 9-11, 1998, pp. 196-207.
- [21] M. Osinski, V. A. Smagley, T. Svimonishvili, G. A. Smolyakov, and P. G. Eliseev, "3D electro-thermal simulation of intracavity-contacted oxide-confined VCSEL's operating at room-temperature and at 77 K," in *Physics Simulation Optoelectronic Devices VII*, vol. 3625, SPIE Proc., P. Blood, A. Ishibashi, and M. Osinski, Eds., San Jose, CA, Jan. 25-29, 1999, pp. 371-382.
- [22] G. A. Smolyakov, V. A. Smagley, W. Nakwaski, P. G. Eliseev, and M. Osinski, "Design of InGaIn/GaN/AlGaIn VCSEL's using the effective frequency method," in *Physics Simulation Optoelectronic Devices VII*, vol. 3625, SPIE Proc., P. Blood, A. Ishibashi, and M. Osinski, Eds., San Jose, CA, Jan. 25-29, 1999, pp. 324-335.
- [23] H. Wenzel and H.-J. Wünsche, "The effective frequency method in the analysis of vertical-cavity surface-emitting lasers," *IEEE J. Quantum Electron.*, vol. 33, pp. 1156-1162, 1997.

- [24] E. Opila, D. Humphrey, K. Oda, N. Jacobson, and T. Yoshio, "The oxidation of AlN in dry and wet oxygen," in *Proc. Symp. High Temperature Corrosion Materials Chemistry*, P. Y. Hou, M. J. McNallan, R. Oltra, E. J. Opila, and D. A. Shores, Eds., San Diego, CA, May 3-8, 1998, pp. 430-437.
- [25] E. D. Readinger, S. D. Wolter, D. L. Waltemyer, J. M. Delucca, S. E. Mohny, B. I. Prenitzer, L. A. Giammizzi, and R. J. Molnar, "Wet thermal oxidation of GaN," in *Proc. 40th Electronic Materials Conference (EMC)*, Charlottesville, VA, June 24-26, 1998.
- [26] M. Inamori, H. Sakai, T. Tanaka, H. Amano, and I. Akasaki, "Direct patterning of the current confinement structure for p-type column-III nitrides by low-energy electron beam irradiation treatment," *Jpn. J. Appl. Phys. 1, Regul. Rep. Short Notes and Rev. Pap.*, vol. 34, no. 2B, pp. 1190-1193, 1995.
- [27] P. G. Eliseev, M. Osinski, J. Lee, T. Sugahara, and S. Sakai, "Band-tail model and temperature-induced blue-shift in photoluminescence spectra of $\text{In}_{1-x}\text{Ga}_x\text{N}$ grown on sapphire special issue on III-V nitrides and SiC," *J. Electron. Mater.*, vol. 29, no. 3, pp. 332-341, 2000.
- [28] *Handbook of Optical Constants of Solids, I, II*, E. D. Palik, Ed., Academic Press, Orlando, FL, 1985.
- [29] P. Mackowiak and W. Nakwaski, "Thermal aspects of designing CW-operated nitride VCSEL's," *Opt. Quantum Electron.*, vol. 31, no. 11, pp. 1179-1188, 1999.
- [30] M. Suzuki, T. Kawakami, T. Arai, S. Kobayashi, Y. Koide, T. Uemura, N. Shibata, and M. Murakami, "Low-resistance Ta/Ti ohmic contacts for p-type GaN," *Appl. Phys. Lett.*, vol. 74, no. 2, pp. 275-277, 1999.
- [31] J.-K. Ho, C.-S. Jong, C. C. Chiu, C.-N. Huang, K.-K. Shih, L.-C. Chen, F.-R. Chen, and J.-J. Kai, "Low-resistance ohmic contacts to p-type GaN achieved by the oxidation of Ni/Au films," *J. Appl. Phys.*, vol. 86, no. 8, pp. 4491-4497, 1999.
- [32] J.-L. Lee, J. K. Kim, J. W. Lee, Y. J. Park, and T. Kim, "Transparent Pt ohmic contact on p-type GaN with low resistivity using $(\text{NH}_4)_2\text{S}_x$ treatment," *Electrochem. Solid-State Lett.*, vol. 3, no. 1, pp. 53-55, 2000.
- [33] W. Nakwaski and M. Osinski, "Self-consistent thermal-electrical modeling of proton-implanted top-surface-emitting semiconductor lasers," in *Physics Simulation Optoelectronic Devices II*, vol. 2146, SPIE Proc., W. W. Chow and M. Osinski, Eds., Los Angeles, CA, Jan. 26, 1994, pp. 365-387.
- [34] W. Fang and S. L. Chuang, "Theoretical prediction of GaN lasing and temperature sensitivity," *Appl. Phys. Lett.*, vol. 67, no. 6, pp. 751-753, 1995.



Marek Osinski (SM'86) was born in Wrocław, Poland, on May 28, 1948. He received the M.Sc. degree in theoretical physics from Warsaw University, Warsaw, Poland, in 1971, and the Ph.D. degree in physical sciences from the Institute of Physics of the Polish Academy of Sciences (PASc), Warsaw, Poland, in 1979.

In 1971, he joined the Institute of Physics of PASc, where he was engaged in investigations of waveguiding properties and modal characteristics of semiconductor lasers. From 1980 to 1984, he was a Visiting Research Fellow at Southampton University, Southampton, U.K., where he conducted research on long-wavelength injection laser properties relevant to optical fiber communications. He also investigated optical properties of III-V compounds and heterostructures, including quantum-well devices. From 1984 to 1985, he was a British Telecom Senior Research Associate in coherent optical communication, at Cambridge University, England, where he was involved in studying picosecond modulation, gain-switched spectra, external-cavity coupling, and injection locking of diode lasers. In 1985, he joined the Center for High Technology Materials (CHTM), University of New Mexico, Albuquerque, NM, where he became a Faculty Member in the Department of Electrical and Computer Engineering and the Department of Physics and Astronomy, initially as Associate Professor, and since 1999 as Professor. In 1999, he also joined the Department of Computer Science, University of New Mexico. His initial work at CHTM included high-power semiconductor laser arrays, spatially filtered external cavity coupling, side-mode injection locking, and material properties of AlGaAs and InGaAsP alloys. From 1988 to 1989, he held the NTT Endowed Chair in Telecommunications as Visiting Professor at the Research Center for Advanced Science and Technology, University of Tokyo, Tokyo, Japan. In 1997, he was a Visiting Professor at the Satellite Venture Business Laboratory, University of Tokushima, Japan, where he was engaged in research on group-III nitride materials and devices. His main current research interests include short-wavelength optoelectronic devices in group-III nitrides, electrical, optical, and

thermal properties of GaN-AlN-InN and their alloys, recombination and optical gain in wide-bandgap materials, failure analysis and degradation mechanisms, radiation effects on optoelectronic devices, surface-emitting lasers and two-dimensional arrays, thermal properties of semiconductor lasers, comprehensive simulation of optoelectronic devices, new materials for mid-infrared lasers, and monolithically integrated optoelectronic circuits. He is listed in the *American Men and Women of Science*, *Who's Who in Science and Engineering*, *Dictionary of International Biography*, *Men of Achievement*, *Who's Who in the World*, and the *Polish American Who's Who*. He has authored or co-authored over 320 technical papers, four book chapters, and holds four patents. He also co-edited eight books of SPIE conference proceedings on *Physics and Simulation of Optoelectronic Devices* and three other SPIE volumes in the field of advanced high-power lasers and optoelectronics. Since January 1992, he has been serving as North American Editor of *Progress in Quantum Electronics*.

Dr. Osinski is a member of IEEE Lasers and Electro-Optics Society, the Optical Society of America, the International Society for Optical Engineering (SPIE), and the Materials Research Society.



Vladimir A. Smagley received the Diploma in theoretical physics from Kazakh State University, Almaty, Kazakhstan, in 1994. He is currently working toward the Ph.D. degree at the Department of Physics and Astronomy, University of New Mexico.

Since 1995, he has been a Research Assistant at the Center for High Technology Materials (CHTM), University of New Mexico, Albuquerque, NM. His research interests include III-V compound semiconductor lasers, and in particular, vertical-cavity surface-emitting lasers. He has authored and

co-authored more than 20 technical papers.



Gennady A. Smolyakov graduated from Moscow Engineering Physics Institute in 1987, and received the Candidate Sci. degree in physics and mathematics from Saratov University, Saratov, Russia, in 1997.

In 1987, he joined the Institute for Mechanics and Physics, Saratov University, Saratov, Russia, where he was engaged in research in the field of semiconductor laser physics. Since 1998, he has been a Post-Doctoral Fellow at the Center for High Technology Materials (CHTM), University of New Mexico, Albuquerque, NM, where he is currently a Research Scientist. His current research interests include semiconductor lasers in group-III nitrides and vertical-cavity surface-emitting lasers. He has authored or co-authored over 20 technical papers and holds one patent.



Petr G. Eliseev (SM'87) was born in St. Petersburg, Russia, on February 3, 1936. He graduated from Moscow State University, Moscow, Russia, in 1959, and received the Candidate Sci. degree, the Doctor Sci. degree, and the Professor Diploma, from the P. N. Lebedev Physics Institute (FIAN), Russian Academy of Sciences, Moscow, Russia, in 1965, 1974, and 1981, respectively.

He worked at the Physical Department of Moscow State University from 1959 to 1963, and since 1963 at FIAN, Moscow, Russia. In 1991, he was with the

Research Center for Advanced Science and Technology, University of Tokyo, Tokyo, Japan. From 1993 to 1994, he was at the Ferdinand Braun Institute Berlin, Berlin, Germany, from 1998 to 1999 at the University of Tokushima, Tokushima, Japan, and in 2000 at the University of Nagoya, Nagoya, Japan, as a Visiting Researcher. Since 1995, he has been a Research Professor with the Center for High Technology Materials, University of New Mexico, Albuquerque, NM. The main field of his research activity is physics of semiconductor lasers. He was awarded the State Prize of the USSR in 1984, for pioneering development of quaternary heterostructure materials (InGaAsP, InGaSbAs, etc.).

Dr. Eliseev is a correspondent member of Russian Academy of Natural Sciences since 1992.

Temperature and Thickness Dependence of Steam Oxidation of AlAs in Cylindrical Mesa Structures

Marek Osinski, *Senior Member, IEEE*, Tengiz Svimonishvili, Gennady A. Smolyakov, Vladimir A. Smagley, Pawel Mačkowiak, and Włodzimierz Nakwaski, *Member, IEEE*

Abstract—The Deal–Grove model of thermal oxidation kinetics is adapted to cylindrically symmetric mesa structures and applied to study steam oxidation of AlAs. Oxidation process parameters are extracted from available experimental data as functions of temperature and the AlAs layer thickness. The oxidation rate is found to be very sensitive not only to temperature, but also to the oxidation front position inside the mesa. The oxidation rate slows down as the oxidation front moves into the mesa, reaches a minimum, and then accelerates at the final stages of the oxidation process. Complex nonmonotonic dependence of the oxidation process on layer thickness is also revealed.

Index Terms—Oxidation, oxide aperture, semiconductor lasers, semiconductor process modeling, surface-emitting lasers.

I. INTRODUCTION

HYDROLYTIC oxidation of AlAs (or AlGaAs with high Al content) layers, transforming them into native oxide Al_2O_3 , has evolved into a key technology in fabrication of high-performance vertical-cavity surface-emitting lasers (VCSELs) [1], [2], and is a promising approach in development of GaAs-based metal–oxide–semiconductor electronic devices, photonic crystals, magnetic memories, etc. Reliable modeling can be very helpful in achieving good controllability and high yield of the oxidation process. Yet, modeling of steam oxidation in cylindrically symmetric structures relevant to VCSEL fabrication has received very little attention so far. To our best knowledge, there have been only two attempts to model AlAs oxidation kinetics in cylindrically symmetric mesa structures: an analytical model of Koley *et al.* [3], and a semianalytical model of Alonzo *et al.* [4]. In this letter, we develop a simple analytical model in order to quantify temperature and layer thickness dependence of AlAs oxidation process.

II. DEAL–GROVE MODEL IN CYLINDRICAL GEOMETRY

Similarly to one-dimensional (1-D) Cartesian models of steam oxidation of Al(Ga)As [1], [5]–[7], our approach is based

Manuscript received June 19 2000. This work was supported by Defense Advanced Research Projects Agency under the Optoelectronic Materials Center program, by CFD Research Corporation, and by the US–Poland Maria Skłodowska-Curie Joint Fund under Grant MEN/NSF-98-336.

M. Osinski, T. Svimonishvili, G. A. Smolyakov, and V. A. Smagley are with the Center for High Technology Materials, University of New Mexico, Albuquerque, NM 87106-4343 USA.

P. Mačkowiak is with the Institute of Physics, Technical University of Łódź, PL-93005 Łódź, Poland.

W. Nakwaski is with the Institute of Physics, Technical University of Łódź, PL-93005 Łódź, Poland and also with the Center for High Technology Materials, University of New Mexico, Albuquerque, NM 87106-4343 USA.

Publisher Item Identifier S 1041-1135(01)05591-4.

on a simple theory proposed by Deal and Grove in their seminal work on thermal oxidation of silicon [8]. The usual assumption made in 1-D Cartesian analysis is that the flux of the oxidant particles per unit cross-sectional area and per unit time should be constant, i.e., independent of the distance from the interface with the ambient. For a steady-state process in cylindrical structures, we require instead that the flux divergence vanishes. This leads to the following solution for time evolution of the oxidation length ρ :

$$Bt = (R_0 - \rho)^2 \ln \left(1 - \frac{\rho}{R_0} \right) + \rho(A + R_0) - \frac{\rho^2}{2} \left(1 + \beta \frac{A}{R_0} \right) \quad (1)$$

where t stands for the oxidation time, R_0 is the outer radius of the mesa, and $\rho = R_0 - r$, r is the radial distance from the symmetry axis, while the parameters β , A , and B are expressed as [3], [8]

$$\beta = \frac{k}{k + h} \quad (2)$$

$$A = 2D \left(\frac{1}{h} + \frac{1}{k} \right) = \frac{2D}{\beta h} \quad (3)$$

$$B = \frac{2DC^*}{N_0} \quad (4)$$

with k the oxidation reaction rate constant, h the gas-phase transport coefficient, D the diffusion constant, C^* the equilibrium oxidant concentration just outside the mesa, and N_0 the density of incorporated oxidant particles in the oxidized material.

Differentiation of (1) gives the oxidation rate $d\rho/dt$

$$\frac{d\rho}{dt} = \frac{B}{A \left(1 - \beta \frac{\rho}{R_0} \right) - 2(R_0 - \rho) \ln \left(1 - \frac{\rho}{R_0} \right)} \quad (5)$$

Note that the initial rate of oxidation (at $\rho = 0$) is equal to B/A , which is the same as in 1-D Cartesian model. The limit at $\rho \rightarrow R_0$ is $B/[A(1 - \beta)]$ and can be considerably greater than the initial rate if β is close to 1. Between these extremes, the oxidation process slows down (provided $R_0 > \beta A/2$), to reach the minimum rate of

$$\left(\frac{d\rho}{dt} \right)_{\min} = \frac{B}{[A(1 - \beta) + 2(R_0 - \rho_{cr})]} \quad (6)$$

at $\rho = \rho_{cr}$, where ρ_{cr} is given by

$$\rho_{cr} = R_0 \left\{ 1 - \exp \left[\left(\frac{\beta A}{2R_0} \right) - 1 \right] \right\}. \quad (7)$$

The time t_c necessary to reach complete oxidation of a cylindrical structure is obtained by setting $\rho = R_0$ in (1)

$$t_c = \frac{R_0(A + R_0)}{B} - \frac{R_0(\beta A + R_0)}{2B}. \quad (8)$$

The first term on the right-hand side of (8) is identical with the result of the 1-D Cartesian model for the oxidation front to reach the depth R_0 , whereas the second term represents the reduction of t_c due to cylindrical geometry.

III. TEMPERATURE AND THICKNESS DEPENDENCE OF PROCESS PARAMETERS

Oxidation process parameters for bulk AIAs can be determined from reported experimental data of [3]. Using these data, the following values of parameters A , B , and β are found for the oxidation process performed at 350 °C on relatively thick ($d = 2500 \text{ \AA}$) AIAs layers:

$$A = 3.92 \text{ } \mu\text{m}, \quad B = 1.48 \frac{\mu\text{m}^2}{\text{min}}, \quad \beta = 0.716. \quad (9)$$

Approximate values for the remaining process parameters are $h \approx 791 \text{ } \mu\text{m}/\text{min}$, $k \approx 1994 \text{ } \mu\text{m}/\text{min}$, and $D \approx 1110 \text{ } \mu\text{m}^2/\text{min}$.

The steam oxidation process is known to be very sensitive to temperature [5], [6]. In addition, it has been demonstrated that the oxidation process rate strongly depends on the AIAs layer thickness d if $d < 800 \text{ \AA}$ [1], [2], [6], [9]–[11]. We expect (1) to still apply at various temperatures and for thin layers, but with appropriately adjusted values of parameters A , B , and β . In general, all three of these parameters can be temperature and layer-thickness dependent. However, in the absence of any experimental data for cylindrical structures that could be used to determine possible variation of β with d and T , we assume β to be constant. We then use the published data for 1-D Cartesian geometry to determine $A(d, T)$ and $B(d, T)$, noting that they should coincide with the parameters used for cylindrical geometry as long as we consider them to be independent of the mesa radius R_0 . We postulate the following form of the process parameters $\Gamma(d, T)$, where Γ stands for A or B :

$$\Gamma(d, T) = \Gamma_\infty(d) \exp \left[-\frac{E_\Gamma(d)}{(k_B T)} \right], \quad \Gamma = A, B \quad (10)$$

with k_B the Boltzmann constant. Based on the experimental data of [3]–[6], the high-temperature limits $A_\infty(d)$ and $B_\infty(d)$ are postulated in the form

$$\Gamma_\infty(d) = \Gamma_0 \exp \left(-\frac{d}{d_{\Gamma 0}} \right), \quad \Gamma = A, B. \quad (11)$$

We find that the following form of layer thickness dependence well fits the activation energies $E_A(d)$, $E_B(d)$:

$$E_\Gamma(d) = E_{\Gamma b} + \frac{\epsilon_\Gamma \Gamma}{d}, \quad \Gamma = A, B \quad (12)$$

TABLE I
EXPERIMENTAL VALUES OF $A_\infty(d)$, $B_\infty(d)$ PARAMETERS
AND THEIR BEST-FIT COUNTERPARTS SATISFYING (11)

d [nm]	Parameters extracted from experimental data			Fitted parameters	
	$A_\infty(d)$ [$10^{-4} \mu\text{m}$]	$B_\infty(d)$ [10^3 $\mu\text{m}^2/\text{min}$]	Ref.	$A_\infty(d)$ [$10^{-4} \mu\text{m}$]	$B_\infty(d)$ [10^3 $\mu\text{m}^2/\text{min}$]
25	10.45	2.3	[6]	10.52	2.213
45	7.42	1.52	[5]	7.345	1.519
100	2.36	0.37	[4]	2.731	0.540
250	0.184	0.0320	[3]	0.184	0.0322

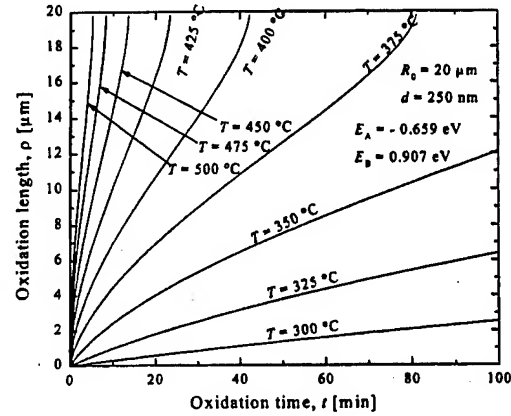


Fig. 1. Oxidation length ρ in a cylindrical mesa of radius $R_0 = 20 \text{ } \mu\text{m}$ with a thick AIAs layer ($d = 250 \text{ nm}$) versus time t of steam oxidation conducted at various temperatures.

where $E_{\Gamma b}$ represents the bulk limit of the activation energy E_Γ , $\Gamma = A, B$. The form of (12) is consistent with the layer thickness dependence of the activation energy $E_{B/A}$ for the linear rate coefficient B/A , as shown in [6, Fig. 3]

$$E_{B/A}(d) = E_{B/A,b} + \frac{\epsilon_{EB/A}}{d} \quad (13)$$

with $E_{B/A,b} = 1.55 \text{ eV}$ and $\epsilon_{EB/A} = 3.96 \text{ eV} \cdot \text{nm}$.

Using the data from [6] and assuming they should follow (12), we can obtain $E_{Bb} = 0.90 \text{ eV}$ and $\epsilon_{EB} = 1.75 \text{ eV} \cdot \text{nm}$.

The parameters E_{Ab} and ϵ_{EA} are determined using

$$E_A(d) = E_B(d) - E_{B/A}(d) \quad (14)$$

which gives $E_{Ab} = -0.65 \text{ eV}$ and $\epsilon_{AB} = -2.21 \text{ eV} \cdot \text{nm}$.

The first three columns in Table I contain a list of the $A_\infty(d)$, $B_\infty(d)$ parameters extracted from experimental data for samples of various thicknesses. We find the remaining parameters A_0 , B_0 , d_{A0} , and d_{B0} by fitting (11) to the data listed in columns 2 and 3 of Table I. The best fit is obtained by choosing $A_0 = 1.65 \times 10^{-3} \text{ } \mu\text{m}$, $B_0 = 3.54 \times 10^9 \text{ } \mu\text{m}^2/\text{min}$, $d_{A0} = 55.6 \text{ nm}$, and $d_{B0} = 53.2 \text{ nm}$. The last two columns in Table I show the values of $A_\infty(d)$ and $B_\infty(d)$ calculated using (11).

IV. RESULTS AND DISCUSSION

We now examine the temperature and layer thickness dependence of the oxidation process in cylindrically symmetric structures, using the parameters $A(d, T)$ and $B(d, T)$ described in Section III.

Fig. 1 illustrates temperature sensitivity of the oxidation process in a thick sample, calculated using (1). The initial slope

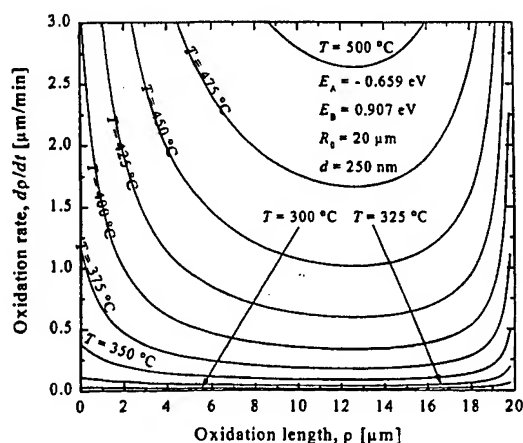


Fig. 2. Oxidation rate dp/dt versus oxidation length ρ for the same cylindrical structure as in Fig. 1.

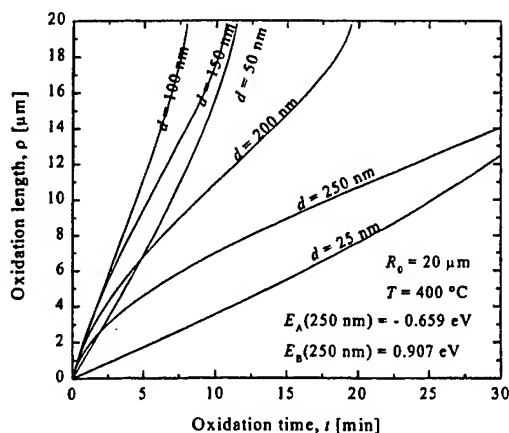


Fig. 3. Oxidation length ρ versus process time t for cylindrical mesas of radius $R_0 = 20 \mu\text{m}$ with various AlAs layer thicknesses, steam oxidized at $T = 400^\circ\text{C}$.

of $\rho(t)$ curves is shown to increase rapidly with temperature, as described by the activation energy $E_{B/A}$ (250 nm) $= 1.566 \text{ eV}$. Between 350°C and 467°C , the initial reaction rate increases by a factor of 100. Therefore, higher temperatures result in a substantial reduction of the oxidation time necessary to produce a required oxide aperture, while simultaneously rendering the process control more difficult.

Fig. 2 shows the temperature and position dependence of the oxidation rate dp/dt , calculated using (5). At temperatures lower than 350°C , the oxidation rate remains almost constant throughout the entire process. At higher temperatures ($\geq 400^\circ\text{C}$), the process is much more volatile, with significantly higher rates at the onset of the oxidation and at its very end (when the oxide aperture is less than $4 \mu\text{m}$ in diameter).

Fig. 3 reveals a fairly complex dependence of the oxidation process on the AlAs layer thickness d . It is possible to find the thickness d_c at which the complete oxidation time t_c , given by (8), reaches a minimum. The resultant equation is transcendental, and for the parameters listed in Section III we obtain $d_c = 93.4 \text{ nm}$, consistent with the picture presented in Fig. 3.

The initial oxidation rate B/A is nonmonotonic with d , reaching a maximum at a thickness d_{max} larger than those used in Fig. 3. Equations (10)–(12) give the following result for d_{max} :

$$d_{\text{max}} = \left\{ \frac{(\epsilon_{EB} - \epsilon_{EA})d_{A0}d_{B0}}{k_B T(d_{A0} - d_{B0})} \right\}^{1/2} \quad (15)$$

Using the parameter values given in Section III, we obtain $d_{\text{max}} = 290.1 \text{ nm}$ at $T = 400^\circ\text{C}$.

V. CONCLUSION

We have extended the classical Deal–Grove model of oxidation process to cylindrically symmetric structures. Compact analytical formulas describing the kinetics of the AlAs steam oxidation process have been obtained. Temperature and layer thickness dependence of the AlAs steam oxidation process parameters has been determined based on existing experimental data. The oxidation rate is independent of the mesa radius, but varies with time as the oxidation process progresses. In addition, it depends strongly on the layer thickness and ambient temperature. Such behavior hampers the control over the oxidation process in VCSELs with very small oxide-aperture diameters. Our results can therefore be very important for achieving a good control of the oxidation process in such structures.

REFERENCES

- [1] K. D. Choquette, K. M. Geib, C. I. H. Ashby, R. D. Twisten, O. Blum, H. Q. Hou, D. M. Follstaedt, B. E. Hammons, D. Mathes, and R. Hull, "Advances in selective wet oxidation of AlGaAs alloys," *IEEE J. Select Topics Quantum Electron.*, vol. 3, pp. 916–926, 1997.
- [2] D. G. Deppe and D. L. Huffaker, "Native oxide technology for III-V optoelectronic devices," in *Heterogeneous Integration: Systems on a Chip*, A. Husain and M. Fallahi, Eds. San Jose, CA: SPIE, Jan. 26–27, 1998, vol. CR70, pp. 141–183.
- [3] B. Koley, M. Dagenais, R. Jin, J. Pham, G. Simonis, G. McLane, and D. Stone, "Kinetics of growth of AlAs oxide in selectively oxidized vertical cavity surface emitting lasers," *J. Appl. Phys.*, vol. 82, pp. 4586–4589, 1997.
- [4] A. C. Alonzo, X.-C. Cheng, and T. C. McGill, "Effect of cylindrical geometry on the wet thermal oxidation of AlAs," *J. Appl. Phys.*, vol. 84, pp. 6901–6905, 1998.
- [5] M. Ochiai, G. E. Giudice, H. Temkin, J. W. Scott, and T. M. Cockerill, "Kinetics of thermal oxidation of AlAs in water vapor," *Appl. Phys. Lett.*, vol. 68, pp. 1898–1900, 1996.
- [6] R. L. Naone and L. A. Coldren, "Surface energy model for the thickness dependence of the lateral oxidation of AlAs," *J. Appl. Phys.*, vol. 82, pp. 2277–2280, 1997.
- [7] Z. Pan, Y. Zhang, Y. Du, and R. Wu, "Stability improvement of selective oxidation during the fabrication of InGaAs/GaAs vertical-cavity surface emitting laser," *Jpn. J. Appl. Phys.*, vol. 37, pp. 3673–3675, 1998.
- [8] B. E. Deal and A. S. Grove, "General relationship for the thermal oxidation of silicon," *J. Appl. Phys.*, vol. 36, pp. 3770–3778, 1965.
- [9] J.-H. Kim, D. H. Lim, K. S. Kim, G. M. Yang, K. Y. Lim, and H. J. Lee, "Lateral wet oxidation of $\text{Al}_x\text{Ga}_{1-x}\text{As}$ -GaAs depending on its structures," *Appl. Phys. Lett.*, vol. 69, pp. 3357–3359, 1996.
- [10] T. Langenfelder, S. Schröder, and H. Grothe, "Lateral oxidation of buried $\text{Al}_x\text{Ga}_{1-x}\text{As}$ layers in a wet ambient," *J. Appl. Phys.*, vol. 82, pp. 3548–3551, 1997.
- [11] T. Yoshikawa, H. Saito, H. Kosaka, Y. Sugimoto, and K. Kasahara, "Self-stopping selective-oxidation process of AlAs," *Appl. Phys. Lett.*, vol. 72, pp. 2310–2312, 1998.

phys. stat. sol. (b) 228, No. 1, 263–267 (2001)

MOCVD Growth of $\text{InN}_x\text{As}_{1-x}$ on GaAs Using Dimethylhydrazine

A. A. EL-EMAWY, H.-J. CAO, E. ZHMAEV, J.-H. LEE, D. ZUBIA, and M. OSIŃSKI¹⁾

*Center for High Technology Materials, University of New Mexico,
1313 Goddard SE, Albuquerque, New Mexico 87106-4343, USA*

(Received July 22, 2001; accepted August 4, 2001)

Subject classification: 68.37.Ps; 68.37.Vj; 68.65.Fg; 81.05.Ea; 81.15.Gh; S7.14; S7.15

InNAs/GaAs multiple-quantum-well samples were grown by MOCVD on (100) n^+ -GaAs substrates at 500 °C and 60 Torr using uncracked dimethylhydrazine (DMHy). Quantum well layers were grown using trimethylindium, tertiarybutylarsine, and 95–97.5% of DMHy in the vapor phase, while GaAs buffer, barrier, and cap layers were grown using trimethylgallium and arsine. The crystalline quality and solid phase composition were evaluated using high-resolution X-ray diffraction analysis. The nitrogen content in InNAs wells was determined to be 18%. Surface morphology was investigated by atomic force microscopy (AFM) and field emission microscopy (FEM). Photoluminescence measurements confirm that the bandgap energy of InNAs is significantly lower than that of InAs. The peak emission wavelength of $\sim 6.5 \mu\text{m}$ at 10 K is the longest reported so far for dilute nitride semiconductors.

Introduction The $\text{InN}_x\text{As}_{1-x}$ alloy is a very promising material for mid-infrared (2–5 μm) emitters and detectors. With a single exception of recently reported successful growth of InNAs by MOCVD with plasma cracked ammonia source [1], all studies of InNAs growth utilized plasma-source MBE [2–4] and related techniques, such as gas-source MBE [5, 6]. In this paper, we report a successful MOCVD growth of InNAs by using for the first time the uncracked dimethylhydrazine (DMHy) as nitrogen source.

As with other dilute nitrides, the bandgap of $\text{InN}_x\text{As}_{1-x}$ was predicted to shrink with increasing nitrogen content x [7, 8], although so far this has been confirmed experimentally only for compositions $x < 6\%$ [6]. The $\text{InN}_x\text{As}_{1-x}$ alloy can be lattice-matched to GaAs when $x = 38\%$ [2]. The large band offset between this material and GaAs barriers makes it particularly attractive for reducing temperature sensitivity of mid-IR lasers. Since the solubility limit of nitrogen in InAs is among the highest among binary III–V compounds (three orders of magnitude higher than in GaAs, for example) [9], we considered it feasible to attempt the low temperature growth using DMHy.

Growth Conditions and Procedures All samples were grown in a Thomas Swan vertical MOCVD reactor at 60 Torr. Arsine and trimethylgallium were used during the growth of GaAs buffer, barrier, and cap layers. InNAs films were grown using trimethylindium, tertiarybutylarsine and DMHy as source materials. Before the growth, epitaxially grown (100) n^+ -GaAs substrates were deoxidized at 760 °C for 5 min. 500 nm GaAs buffer layer was grown at 680 °C. Subsequently, the growth temperature T_g was lowered to 500 °C for the growth of InNAs/GaAs multiple quantum well (MQW) structures and the GaAs capping layer.

¹⁾ Corresponding author; Phone: +1 505 272 7812; Fax: +1 505 272 7801;
e-mail: osinski@chtm.unm.edu

The growth rate was kept constant at 7.5 and 1.25 Å/s for GaAs and InNAs films, respectively. The mole fraction of DMHy to total group-V sources in the vapor phase was maintained between 0.95 and 0.975, corresponding to DMHy flow rate of 600–900 sccm.

X-Ray Analysis of InNAs/GaAs MQW Structures Crystalline quality, composition, and thicknesses of grown layers were investigated by high-resolution X-ray diffraction (HRXRD) Philips triple axis X-ray apparatus. Figure 1 shows ω - 2θ scans of (004) reflections for two 15-period MQW structures grown under otherwise identical conditions, except for the presence of DMHy during the well layer growth. Sample DE217 contained InNAs/GaAs quantum wells, with the well layers grown under 600 sccm flow rate of DMHy. Sample DE218 was grown under the same conditions as sample DE217, but the well layers contained only InAs. Comparison of the two scans shown in Fig. 1 clearly reveals improvement in quality of the sample containing nitrogen, which we attribute to the reduced lattice constant mismatch between InNAs and GaAs. The full width at half maximum (FWHM) of the $m = 0$ InNAs peak (top scan in Fig. 1) is 65 arcsec, which together with a clearly resolved spectrum displaying up to six diffraction orders indicates high crystalline quality of the sample. The FWHM of the $m = -3$ satellite peak of sample DE217 is 115 arcsec, which compares favorably to 280 arcsec in $\text{InN}_{0.06}\text{As}_{0.94}/\text{InGaAsP}$ MQWs grown on InP [6]. The satellite peaks wash out in the case of InAs/GaAs MQWs (sample DE218), revealing poorer interface flatness and partial relaxation.

Measured HRXRD spectra of sample DE217 were analyzed using Bede Scientific Instruments RADS dynamic simulation software, assuming cubic InN and InAs lattice parameters. As shown in Fig. 2, nitrogen composition of 18% resulted in a very good fit between the measured and simulated spectra. Using the same simulation, the well and barrier layer thicknesses were determined as 2.5 nm and 375 nm, respectively.

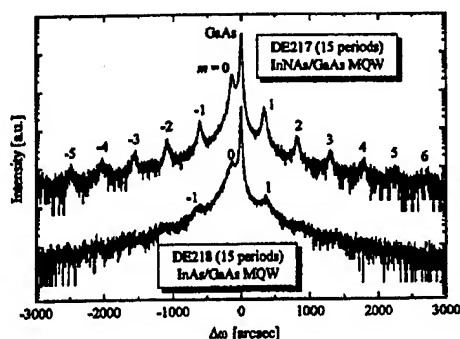


Fig. 1

Fig. 1. HRXRD spectra of 15-period MQW samples with InNAs wells (top scan) and InAs wells (bottom scan)

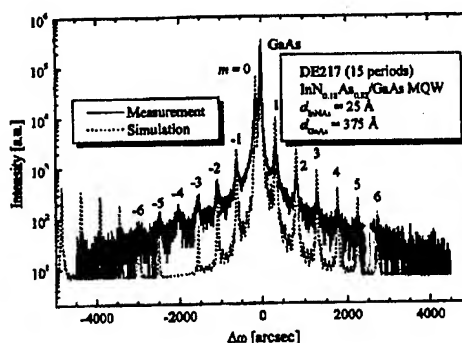


Fig. 2

Fig. 2. Measured (solid line) and simulated (dotted line) HRXRD spectra of 15-period InNAs/GaAs MQW sample

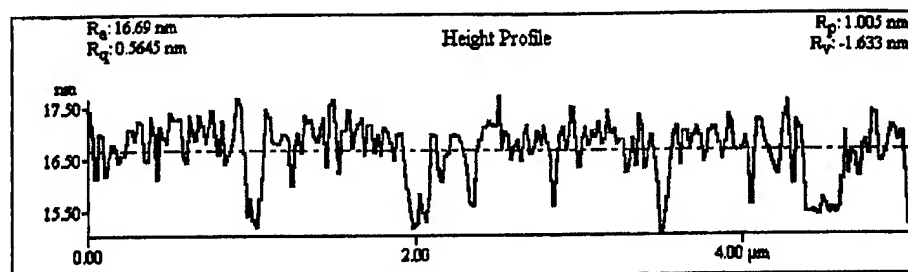


Fig. 3. AFM scan of a sample DE220 consisting of 2.5 nm InNAs/37.5 nm GaAs/2.5 nm InNAs structure grown on GaAs

Microscopic Analysis of InNAs/GaAs Samples The surface morphology of InNAs layers was investigated using Park Scientific Instruments Autoprobe CP atomic force microscope (AFM) and JEOL JSM-6400F high resolution field-emission scanning electron microscope (FEM). Figure 3 shows an AFM scan. The average surface roughness as determined by AFM was 0.5 nm, indicating complete coverage of GaAs buffer layer and high uniformity of the InNAs layer. Figure 4 shows a cross-sectional FEM micrograph revealing the quantum wells.

Photoluminescence (PL) Measurements In order to measure PL spectra, three sets of triple-quantum-well InNAsGaAs samples were grown at different nitrogen flow rates (600 sccm for samples DE208 and DE209, 900 sccm for sample DE210) and with different well thicknesses (2.5 nm for sample DE208, and 5 nm for samples DE209 and DE210). Each sample had a 0.25 μm GaAs cap layer at the top. HRXRD analysis showed that with increasing well thickness, the satellite peaks became broader, indicating partially relaxed films. With increasing nitrogen flow, almost no change in the HRXRD spectra was observed, which we attribute to saturation limit of DMHy decomposition at the low T_g of 500 $^{\circ}\text{C}$.

The PL setup included a Coherent Innova 300 Ar-ion laser source, with combined 514 and 488 nm lines pumping a Schwartz Electro-Optics Titan-ML tunable Ti:sapphire laser, a Nicolet Magna-IR 760 Fourier transform spectrometer, and a Nicolet MCT-B cooled detector. The samples were placed in a cryostat and cooled to 10 K. The output power from the argon-ion laser was 7.5 W, while the output power incident on the sample from the Ti:sapphire laser tuned to 890 nm was 170 mW, illuminating a spot with ~ 1 mm diameter.

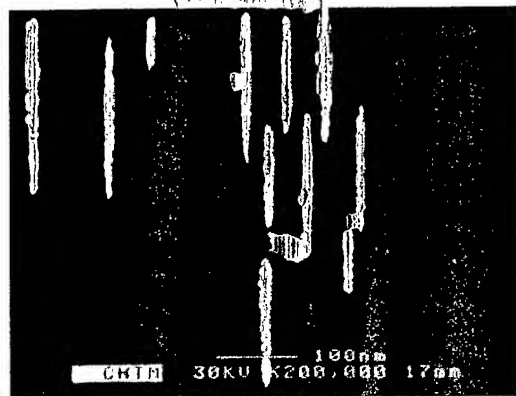


Fig. 4. Cross-sectional FEM micrograph of sample DE233 consisting of a three-period 5 nm InNAs/37.5 nm GaAs quantum well grown on GaAs. The bright part on the right-hand side corresponds to sample surface

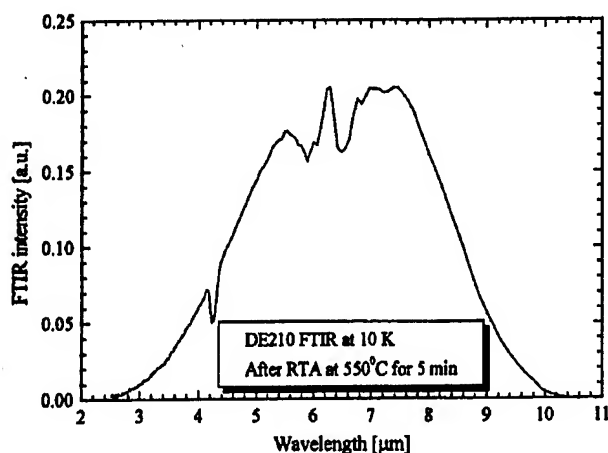


Fig. 5. PL spectrum of sample DE210 containing a triple quantum well 5 nm $\text{InNAs}/37.5$ nm GaAs structure

Initial experiments with as-grown samples resulted in no detected PL signal. The samples were then annealed at 550°C for 5 min using a rapid thermal annealer, and the PL measurements were repeated. Figure 5 shows the PL spectrum from sample DE210 that emitted intense PL signal after annealing. The peak emission wavelength was about $6.5\ \mu\text{m}$ (190 meV), and the FWHM of the PL spectrum was about $3.5\ \mu\text{m}$ (110 meV).

The dip at $4.26\ \mu\text{m}$ is due to CO_2 band absorption, while the broad minima near 5.9 and $6.5\ \mu\text{m}$ are caused by water vapor absorption in the ambient atmosphere. The maximum at $6.3\ \mu\text{m}$ coincides with water vapor transmission window.

Recently, Tit and Dharma-Wardana [8] reported tight-binding calculations of InNAs band structure, considering various possible arrangements of group-V atoms around a single In atom. For 17.6% nitrogen content, they predict a bandgap ranging from 8 meV for maximally nitrogen-rich clusters to 251 meV for maximally As-rich clusters. This wide range of bandgap energies is consistent with our observation of broad PL emission spectrum shown in Fig. 5. It is also very promising for widely tunable mid-IR lasers.

Conclusions We have successfully grown InNAs/GaAs multiple-quantum-well structures by MOCVD using uncracked dimethylhydrazine (DMHy). The crystalline quality and solid phase composition were evaluated by high-resolution X-ray diffraction. Nitrogen content in InNAs wells was determined to be 18%. Surface morphology was investigated by atomic force microscopy (AFM) and field emission microscopy (FEM). AFM and FEM micrographs indicate high quality of quantum-well structures. PL measurements confirm that the bandgap energy of InNAs is significantly lower than that of InAs . The peak emission wavelength of $\sim 6.5\ \mu\text{m}$ is the longest reported so far for dilute nitride semiconductors.

Acknowledgement Support from the U.S. Air Force Office of Scientific Research under the Optoelectronics Research Center program is gratefully acknowledged.

References

- [1] H. NAOI, D. M. SHAW, Y. NAOI, G. J. COLLINS, and S. SAKAI, *J. Cryst. Growth* **222**, 511 (2001).
- [2] Y. C. KAO, T. P. E. BROEKAERT, H. Y. LIU, S. TANG, I. H. HO, and G. B. STRINGFELLOW, *MRS Symp. Proc.* **423**, 335 (1996).
- [3] S. SAKAI, T. S. CHENG, T. C. FOXON, T. SUGAHARA, Y. NAOI, and H. NAOI, *J. Cryst. Growth* **189/190**, 471 (1998).
- [4] R. BERESFORD, K. S. STEVENS, and A. F. SCHWARTZMAN, *J. Vac. Sci. Technol. B* **16**, 1293 (1998).
- [5] J.-S. WANG and H.-H. LIN, *J. Vac. Sci. Technol. B* **17**, 1997 (1999).
- [6] J.-S. WANG, H.-H. LIN, L.-W. SONG, and G.-R. CHEN, *J. Vac. Sci. Technol. B* **19**, 202 (2001).
- [7] T. YANG, S. NAKAJIMA, and S. SAKAI, *Jpn. J. Appl. Phys.* **36**, L320 (1997).
- [8] N. TIT and M. W. C. DHARMA-WARDANA, *Appl. Phys. Lett.* **76**, 3576 (2000).
- [9] I.-H. HO and G. B. STRINGFELLOW, *J. Cryst. Growth* **178**, 1 (1997).

Operator ordering of a position-dependent effective-mass Hamiltonian in lattice-matched semiconductor superlattices and quantum wells

Vladimir A. Smagley, Mohammad Mojahedi, and Marek Osinski*

Center for High Technology Materials, University of New Mexico, 1313 Goddard SE
Albuquerque, New Mexico 87106-4343, USA

ABSTRACT

The position-dependent effective mass Hamiltonian $H = -(\hbar^2/2)[m(z)]^\alpha \nabla [m(z)]^\beta \nabla [m(z)]^\alpha + V(z)$ with $2\alpha + \beta = -1$ is applied to the problem of periodic heterostructure with abrupt interfaces and discontinuous mass distribution. In order to determine the most suitable operator ordering, numerical results for interband and intersubband transition energies are compared with experimental data for various GaAs/Al_xGa_{1-x}As superlattices and quantum wells. The ordering-related energy shift as a function of structural parameters (well thickness, barrier thickness and height) is investigated. We find that variation of kinetic energy operator ordering can cause transition energy shift exceeding 40 meV. The model with $\alpha = 0$ and $\beta = -1$ consistently produces the best fit to experimental results.

Keywords: Operator ordering, quantum wells, superlattices

1. INTRODUCTION

The effective-mass theory (EMT) is an important and widely used tool in semiconductor physics. Originally developed for analysis of homogenous crystals [Slater 1949], [James 1949], EMT when applied to heterostructures with position-dependent effective mass becomes asymptotically exact when perturbations to the electron and hole states are sufficiently smooth. The entire approach would have to be modified in order to accommodate the case of structures with abrupt heterointerfaces [Burt 1992], [Burt 1994]. In spite of that, EMT continues to be widely used as a major computational tool to determine dynamic and static electrical, electronic, and optical properties of many abrupt-interface heterostructures, including superlattices and quantum wells. It has been recognized for a long time [Morrow 1987a], [Einevoll 1990a], [Einevoll 1990b] that application of EMT to abrupt interfaces suffers from ambiguity in kinetic energy operator (KEO) ordering, caused by non-vanishing commutator of the momentum operator $-i\hbar\nabla$ and the position-dependent effective mass $m(z)$. This leads to non-uniqueness of KEO, which in its most general form can be written as [von Roos 1983]

$$K = -\frac{\hbar^2}{4} [m^\alpha \nabla m^\beta \nabla m^\gamma + m^\gamma \nabla m^\beta m^\alpha], \quad (1)$$

with $\alpha + \beta + \gamma = -1$. By construction, the KEO (1) is Hermitian. For abrupt interfaces with discontinuous step-like distribution of effective masses, α must be equal to γ , as otherwise the wave function would have to vanish at heterointerfaces, which would have been clearly unphysical [Morrow 1984]. Also, unless $\alpha = \gamma$, the ground-state energy diverges in the limit of abrupt interfaces [Thomsen 1989]. This reduces Eq. (1) to

$$K = -\frac{\hbar^2}{2} [m(z)]^\alpha \nabla [m(z)]^\beta \nabla [m(z)]^\alpha, \quad (2)$$

with $2\alpha + \beta = -1$. Possible values of the β parameter span the range from 0 to -1. Corresponding to this one-

*Correspondence: Email: osinski@chtm.unm.edu; WWW: <http://www.chtm.unm.edu>; Telephone: (505) 272-7812;
Fax: (505) 272-7801

transition energies do vary substantially with β . In addition, we show that within the framework of EMT for abrupt interfaces and discontinuous mass distribution, the intersubband transition energies can also vary substantially with β . Comparison with available data confirms that the choice of $\beta = -1$ provides the best fit to experimental results.

This paper is organized as follows. In Section 2 we formulate our theoretical model for superlattices and quantum wells based on the transfer matrix approach. The model is then used in Section 3 to calculate the miniband energies for GaAs/Al_xGa_{1-x}As superlattices. In Section 4, we study the ordering-related effects and determine conditions for maximum sensitivity of transition energies to the choice of β for various AlGaAs/GaAs superlattice parameters (well length, barrier height, and barrier thickness). Finally, Section 5 contains a comparison of theoretical results with available experimental data, which is then used to deduce the best value for the ordering parameter β . Concluding remarks are given in Section 6.

2. THEORETICAL MODEL

Consider a periodic superlattice that consists of lattice-matched semiconductors 1 and 2 (e.g., the GaAs/Al_xGa_{1-x}As system, illustrated in Fig. 1). The thicknesses of alternating well and barrier layers are d_1 and d_2 , respectively, with the superlattice period denoted as $d = d_1 + d_2$. When d_2 is large enough (≈ 15 -20 nm), the quantum wells are practically decoupled and the superlattice problem becomes equivalent to a single quantum well problem. The interfaces are assumed to be parallel to the x - y plane, while the superlattice axis is oriented along the z direction. The Schrödinger equation for an electron in the conduction band is given by

$$\{K + E_c(z) - E\}F_c(z) = 0, \quad (4)$$

with the KEO K given by Eq. (2), $E_c(z)$ standing for the bulk conduction band edge profile, $F_c(z)$ denoting the envelope wave function, and E representing the energy eigenvalue. Analogous equations can be written for the light- and heavy holes in the valence band. In the simplest case of rectangular wells and barriers (see Fig. 1), Eq. (4) takes the form

$$\left[-\frac{\hbar^2}{2m_{c_j}} \left(\frac{d^2}{dz^2} \right) + E_{c_j} - E \right] F_{c_j}(z) = 0 \quad \begin{cases} 0 < z < d_1 & j=1 \\ d_1 < z < d_1 + d_2 & j=2 \end{cases} \quad (5)$$

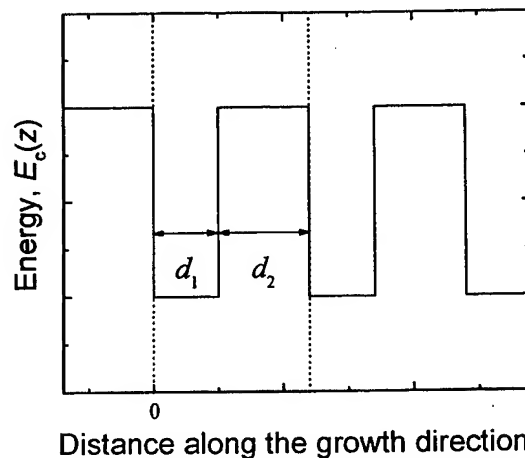


Fig. 1. Schematic representation of bulk conduction band edge for periodic superlattice structure. Alternating layers of two lattice-matched materials have thickness d_1 for the well and d_2 for the barrier, respectively.

Although β no longer appears explicitly in Eq. (5), it is still present in the boundary conditions connecting the solutions F_{c1} , F_{c2} at the interfaces. The miniband structure of superlattices with arbitrary well and barrier profiles can

$$\xi_{1,2} = \frac{1}{4} \left\{ \left[v_1 v_2 + \frac{1}{2} \mu_1 \mu_2 \left(MR + \frac{1}{MR} \right) \right] \pm \left[\left(v_1 v_2 + \frac{\mu_1 \mu_2}{2} \left(MR + \frac{1}{MR} \right) \right)^2 - (v_1^2 v_2^2 + \mu_1^2 \mu_2^2 - \mu_1^2 v_2^2 - \mu_2^2 v_1^2) \right]^{1/2} \right\} \quad (14)$$

where

$$\mu_j = \lambda_{j+}^{N_j} - \lambda_{j-}^{N_j}, \quad (15)$$

$$v_j = \lambda_{j+}^{N_j} + \lambda_{j-}^{N_j}, \quad (16)$$

$$M = \left(\frac{m_1}{m_2} \right)^\beta, \quad (17)$$

$$R = \left[\frac{m_1 (E_{c1} - E)}{m_2 (E_{c2} - E)} \right]^{1/2}. \quad (18)$$

Due to periodicity of the superlattice potential, the eigenvalues of $\tilde{T}(E)$ must satisfy the Bloch theorem with period d , i.e. they must have the form of $\exp(\pm i k d)$:

$$\xi_{1,2} = \exp(\pm i k d) = \cos(kd) \pm i \sin(kd). \quad (19)$$

Eq. (19) in conjunction with Eq. (14) provides us with a dispersion relation between E and k . We note that if the reference zero potential is chosen to coincide with the bottom of the well, i.e. $E_{c1} = 0$, then μ_1 is a purely imaginary number of the form

$$\mu_1 = 2i \left(1 + \frac{2\Delta_1^2 m_1 E}{\hbar^2} \right)^{N_1/2} \sin(N_1 \theta), \quad (20)$$

where

$$\theta = \tan^{-1} \left(\sqrt{\frac{2\Delta_1^2 m_1 E}{\hbar^2}} \right). \quad (21)$$

In addition, for E real and smaller than E_{c2} , (i.e. for confined states), R given in Eq. (18) is purely imaginary, while v_1 , v_2 , and μ_2 are all real. This implies that Eq. (19) can be further simplified (see [Burns 1985]) to

$$\frac{1}{4} \left[v_1 v_2 + \frac{1}{2} \mu_1 \mu_2 \left(MR + \frac{1}{MR} \right) \right] = \cos(kd) \quad (22)$$

and

$$\frac{1}{4} \left\{ \left[v_1 v_2 + \frac{\mu_1 \mu_2}{2} \left(MR + \frac{1}{MR} \right) \right]^2 - (v_1^2 v_2^2 + \mu_1^2 \mu_2^2 - \mu_1^2 v_2^2 - \mu_2^2 v_1^2) \right\}^{1/2} = \sin(kd). \quad (23)$$

3. MINIBAND ENERGY CALCULATION

In this section, we will examine sensitivity of GaAs/Al_xGa_{1-x}As superlattice band structure to the value of β parameter. The choice of GaAs/Al_xGa_{1-x}As is dictated by the fact that this material system is the most extensively studied among all III-V semiconductors. Material parameters are known to a very good precision [Vurtgafman 2001]. Furthermore, the lattice mismatch between GaAs and Al_xGa_{1-x}As is very small, hence the correction of the miniband energy due to strain effects is negligible. The Al_xGa_{1-x}As effective masses m_e , m_{hh} , m_{lh} , the bandgap energy E_g , and the band offset ratio $\Delta E_c:\Delta E_v$ used in our calculations are listed in the Table 1 (see [Adachi 1985], [Bosio 1988], [Vurtgafman 2001]). For comparison with the low-temperature experiments, we use the Varshni formula to estimate bandgap variation with temperature. The parameters appearing in the Varshni formula are taken from [Kangarlou 1988]. We use the approximation of a temperature-independent bowing parameter for Al_xGa_{1-x}As (see [Vurtgafman 2001]). In order to predict correctly the transition energy at low temperatures, it is imperative to take into account the exciton binding energies. Some of the experiments considered in our work provide this information alongside with their photoluminescence results. For the other cases, we consult [Gurioli 1993]. Generally, the exciton binding energy for the cases considered in this paper is in the range of 10-15 meV.

Table 1: Main Al_xGa_{1-x}As material parameters

m_e/m_0	m_{hh}/m_0	m_{lh}/m_0	E_g [eV]	$\Delta E_c:\Delta E_v$
$0.0667 + 0.083x$	$0.34 + 0.412x$	$0.094 + 0.0667x$	$1.427 + 1.247x$	65:35

Fig. 2 depicts the dispersion curves for the conduction-band electrons in a GaAs/Al_{0.25}Ga_{0.75}As superlattice. Dashed ($\beta = 0$) and solid ($\beta = -1$) curves indicate the ordering-related miniband energy shift. The thicknesses of GaAs wells and Al_{0.25}Ga_{0.75}As barriers are $d_1 = 15$ nm and $d_2 = 2.5$ nm, respectively. Each layer is divided into $N_1 = N_2 = 30,000$ segments.

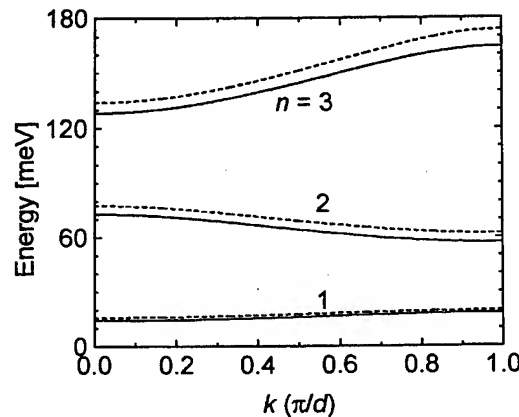


Fig. 2. Three lowest minibands CB₁, CB₂, and CB₃ for conduction-band electrons in a GaAs/Al_{0.25}Ga_{0.75}As superlattice with $d_1 = 15$ nm and $d_2 = 2.5$ nm. The dashed curves correspond to $\beta = 0$, and the solid curves to $\beta = -1$.

As indicated in Fig. 2, the shift in the miniband energies for the cases of $\beta = -1$ and $\beta = 0$ becomes larger as the miniband index increases. Thus, the higher minibands are more sensitive to the value of β than the lower minibands. For the case of Fig. 2, the calculated shift in energy at $k = 0$ is 1.66 meV for CB₁, 4.75 meV for CB₂, and 5.74 meV for CB₃.

As shown in Fig. 3, for intermediate values of β within the range of $-1 < \beta < 0$, the miniband energy levels fall between the two extreme cases of $\beta = -1$ and $\beta = 0$. The case illustrated in Fig. 3 corresponds to the miniband CB₁ of the same GaAs/Al_{0.25}Ga_{0.75}As superlattice as in Fig. 2. It is worthwhile to note that the shift of CB₁ to higher energies with increasing value of β is linear. This linear dependency simplifies the analysis of operator ordering effects, as it is sufficient to just consider the two extreme cases of $\beta = -1$ and $\beta = 0$.

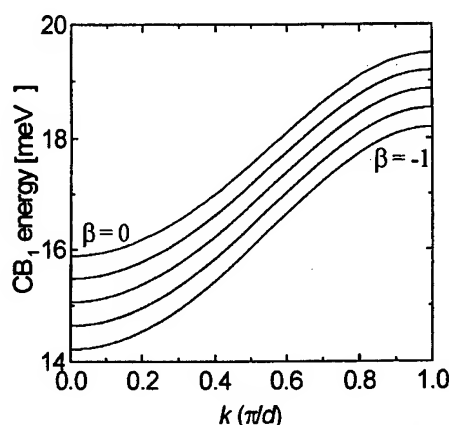


Fig. 3. Shift in the CB_1 dispersion curves associated with various choices of the KEO parameter β for a GaAs/ $Al_{0.25}Ga_{0.75}As$ superlattice with $d_1=15$ nm, $d_2=2.5$ nm. The intermediate results between the extreme cases of $\beta=0$ and $\beta=-1$ correspond to $\beta=-0.25$, $\beta=-0.50$, and $\beta=0.75$, respectively.

4. SENSITIVITY OF CONDUCTION BAND ENERGY LEVELS TO OPERATOR ORDERING

In this section, we investigate the effects of operator ordering on the lowest miniband energies at $k=0$ for GaAs/ $Al_xGa_{1-x}As$ superlattices, with the purpose of determining conditions under which the effect of the choice of β is maximal. We will then use these results in Section 5 to compare our theoretical results with experimental data for structures where the effect of operator ordering is expected to be significant.

4.1. Effects of Well Thickness Variation

Since the KEO ordering is a quantum-mechanical problem related mostly to the heterointerfaces and their adjacent areas, intuitively, we can expect that placing interfaces close enough should make the results more sensitive to the choice of β . We check this hypothesis by considering several quantum-well and superlattice cases with varied well thicknesses.

As a convenient measure of the sensitivity to KEO ordering, we define a parameter ζ_{CBi} which describes the ordering-related miniband energy difference for miniband i at $k=0$:

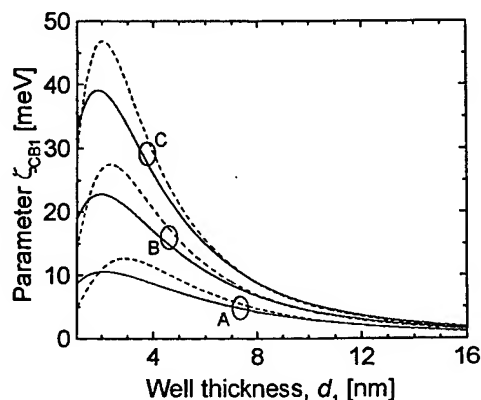


Fig. 4. Sensitivity of the fundamental transition energy shift due to KEO ordering, represented by the parameter ζ_{CB1} defined in Eq. (24), to the quantum well thickness variation in GaAs/ $Al_xGa_{1-x}As$ superlattices. The cases A, B, and C correspond to 20, 30, and 40 percent of aluminum in the barrier material. The dashed curves correspond to the barrier thickness $d_2=12.5$ nm, while solid curves represent the results for $d_2=2.5$ nm.

$$\zeta_{CB1} = CB_1|_{\beta=0} - CB_1|_{\beta=-1} \quad (24)$$

Here, the first term on the right-hand side stands for the CB_1 energy calculated assuming $\beta = 0$, while the second term is the CB_1 energy calculated with $\beta = -1$.

Fig. 4 shows dependence of the shift ζ_{CB1} in the lowest miniband energy CB_1 on the well thickness d_1 . Three different Al concentrations for GaAs/ Al_xGa_{1-x} As superlattices are considered, namely $x = 0.2$, $x = 0.3$, and $x = 0.4$. The barrier thicknesses are chosen to be $d_2 = 2.5$ nm (solid curves) and $d_2 = 12.5$ nm (dashed curves). The latter case corresponds to poor coupling between the wells, thus approaching a single-quantum-well situation. The energy shift parameter ζ_{CB1} has its peak value of more than 45 meV for a thin-well superlattice with $d_1 = 2$ nm (case C, dashed curve). It should be relatively easy to detect such a large energy difference experimentally. The smallest peak value of ζ_{CB1} is just above 10 meV (case A, solid curve). Given all possible experimental and numerical errors, such a small energy difference would be very difficult to verify. Most experimental results reported in literature are for $x = 0.3$ (case B). In this case, for thin decoupled quantum wells we can expect up to 20 meV energy shift due to different choices of the ordering parameter β .

4.2. Effects of Barrier Thickness Variation

The results of Section 4.1 indicate that the shift in the CB_1 energy at the Γ point for cases of $\beta = -1$ and $\beta = 0$ is expected to be higher for decoupled quantum wells. Fig. 5 shows the results of varying the barrier thickness for six different sets of GaAs/ Al_xGa_{1-x} As superlattices with well thicknesses of 2.5 and 12.5 nm and aluminum content of $x = 0.2$, $x = 0.3$, and $x = 0.4$. Our calculations show that the influence of barrier thickness on the parameter ζ_{CB1} is significant only for very thin barriers. All other calculations show negligible influence of the choice of β , which can be easily understood by recognizing that at sufficiently thick barriers the superlattice becomes equivalent to a collection of decoupled quantum wells.

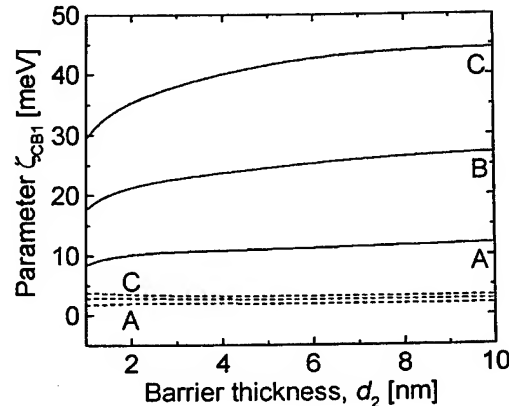


Fig. 5. Sensitivity of the lowest miniband energy shift due to KEO ordering, represented by the parameter ζ_{CB1} defined in Eq. (24), to the barrier thickness variation in GaAs/ Al_xGa_{1-x} As superlattices. The cases A, B, and C correspond to aluminum content of $x = 0.2$, $x = 0.3$, and $x = 0.4$ in the barriers. The dashed curves correspond to the well thickness $d_1 = 12.5$ nm, while solid curves represent the results for $d_1 = 2.5$ nm.

4.3. Effects of Barrier Height Variation

Next, we consider the effect of barrier height on the parameter ζ_{CB1} . The barrier height is increased by changing the aluminum concentration up to $x = 0.4$. As shown in Fig. 6, we find that as the barrier height increases, the shift in the CB_1 energy for cases of $\beta = 0$ and $\beta = -1$ also increases. Our calculations show a shift in the $k = 0$ energy of 15.04 meV and 33.54 meV for cases 1 and 2, respectively. Together with the variation of quantum well thickness, the variation of aluminum content leads to the strongest ordering-related miniband energy shift.

In principle, the aluminum content could be changed up to $x = 1$, with pure AlAs in the barriers. Although it would result in a significant increase of the parameter ζ_{CB1} , the accuracy of our model for a superlattice with an indirect-bandgap material in the barrier would be questionable. For this reason, the maximum concentration of aluminum we consider in this paper is $x = 0.5$.

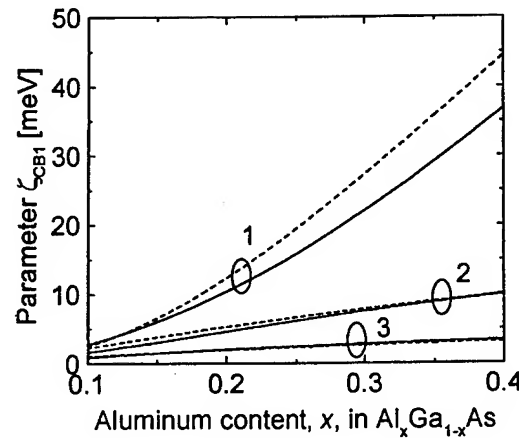


Fig. 6. Sensitivity of the lowest miniband energy shift due to KEO ordering, represented by the parameter ζ_{CB1} defined in Eq. (24), to aluminum content variation in GaAs/ $\text{Al}_x\text{Ga}_{1-x}\text{As}$ superlattices. The cases 1, 2, and 3 correspond to three different choices of well thickness d_1 , namely 2.5, 7.5, and 12.5 nm, respectively. The dashed curves correspond to barrier thickness $d_2 = 12.5$ nm, the solid curves represent the results for $d_2 = 2.5$ nm.

5. EFFECT OF OPERATOR ORDERING ON TRANSITION ENERGY SHIFT

To analyze the ordering-related interband or intersubband transition energy shift, we calculate subband energy levels at $k = 0$ in conduction and valence bands, and compare predicted transition energies with experimental data.

In analogy to the definition (24) of the parameter ζ_{CBi} , we define a parameter $\zeta_{\sigma i}$ which describes the ordering-related interband transition energy difference:

$$\zeta_{\sigma i} = (CB_i - \sigma H_i)_{\beta=0} - (CB_i - \sigma H_i)_{\beta=-1}, \quad (25)$$

where the symbol $\sigma = H, L$ specifies whether the transition involves heavy- or light-holes.

In order to minimize the uncertainty of numerical results and inaccuracy of experimental measurements, we used the results of Section 4 in which superlattice/quantum well structures with energy levels most sensitive to operator ordering were identified. To maximize the expected $\zeta_{\sigma i}$, we considered experiments where the aluminum content in the barriers was high (30-50%), the wells were thin (4-10 nm), and the barriers were thick (up to 50 nm). Using the two extreme cases of KEO ordering ($\beta = 0$ and $\beta = -1$), we compare deviation of the experimental results from the theoretical values and find relative and absolute errors (see Table 2). Twenty different experimental cases were considered. Most of them (10 cases) are CB_1 - HH_1 interband transitions. We also considered CB_1 - LH_1 (4 cases), CB_2 - HH_2 (2 cases), and one case for each CB_2 - LH_2 and CB_3 - HH_3 interband transition. In addition, we have also considered two cases of intersubband transition CB_2 - CB_1 . As indicated in Table 2, six transition energies were measured at room temperature, while the remaining data were measured at 2, 4, 8, and 77 K. In our calculations, the Varshni formula was used to account for bandgap variation with temperature [Vurtgafman 2001]. The exciton binding energy was neglected for room-temperature experiments.

Fig. 7 summarizes all results for the CB_1 - HH_1 and CB_1 - LH_1 transitions in the most concise form. Two extreme cases of operator ordering ($\beta = 0$ and $\beta = -1$) are compared. To clarify data analysis, we arrange all calculated results in order of increasing values of the parameter $\zeta_{\sigma i}$. For the purpose of generality, all theoretical results are normalized to zero-line (dashed curve). We plot experimental data with respect to this line. For every case, we vary

the well thickness within the range of plus-minus one monolayer. This is done to check implications of Li and Kuhn's argument that the exact position of an abrupt interface is not well defined [Li 1994]. The resulting triangular shaded areas are shown in Fig. 7. They indicate an increase in uncertainty of the calculated transition energy caused by the ill-defined interface position correlated with an increase in the value of ζ_{01} . The experimental results are expected to fall inside these shaded regions. The most important result of Fig. 7 is a definite preference for the $\beta = -1$ ordering.

Table 2. Effects of operator ordering on comparison between theoretical and experimental transition energies in $\text{Al}_x\text{Ga}_{1-x}\text{As}$ superlattices and quantum wells

Transition type	Temperature [K]	Al content	Thickness [nm]		Transition energy [eV]			Ref.*	Energy deviation** [meV]		Relative error [%]	
		(x)	Well	Barrier	$\beta = 0$	$\beta = -1$	Expt.		$\beta = 0$	$\beta = -1$	$\beta = 0$	$\beta = -1$
Interband transitions												
CB ₁ -HH ₁	4	0.465	10	20	1.549	1.542	1.538	1	-11	-4	0.72	0.26
CB ₁ -HH ₁	4	0.465	10	20	1.564	1.555	1.547	1	-17	-8	1.10	0.52
CB ₁ -HH ₁	4	0.3	8	50	1.571	1.563	1.564	2	-7	1	0.45	0.09
CB ₁ -HH ₁	300	0.5	8.5	8	1.488	1.477	1.480	3	-8	3	0.55	0.17
CB ₁ -LH ₁	300	0.5	8.5	8	1.513	1.499	1.490	3	-23	-9	1.53	0.60
CB ₁ -HH ₁	4	0.5	7	30	1.597	1.580	1.584	4	-12	4	0.78	0.25
CB ₁ -HH ₁	4	0.3	6	50	1.603	1.588	1.591	2	-12	2	0.76	0.14
CB ₁ -HH ₁	8	0.35	5.5	30	1.621	1.602	1.611	5	-10	9	0.62	0.57
CB ₁ -LH ₁	4	0.5	7	30	1.629	1.608	1.606	4	-23	2	1.42	0.11
CB ₁ -LH ₁	8	0.35	5.5	30	1.658	1.634	1.635	5	-23	1	1.38	0.06
CB ₁ -HH ₁	300	0.31	4.4	5.2	1.563	1.540	1.541	6	-22	1	1.41	0.08
CB ₁ -HH ₁	4	0.5	5	30	1.654	1.622	1.629	4	-25	6	1.56	0.39
CB ₂ -LH ₂	300	0.5	8.5	8	1.767	1.726	1.700	3	-67	-26	3.93	1.54
CB ₁ -HH ₁	4	0.3	4	50	1.665	1.640	1.647	2	-18	8	1.11	0.46
CB ₁ -LH ₁	4	0.5	5	30	1.703	1.663	1.660	4	-43	3	2.58	0.21
CB ₂ -HH ₂	300	0.5	8.5	8	1.728	1.691	1.630	3	-98	-61	6.01	3.75
CB ₂ -HH ₂	8	0.35	5.5	30	1.886	1.863	1.837	5	-49	-27	2.71	1.45
CB ₃ -LH ₃	300	0.5	8.5	8	2.002	1.970	1.820	3	-182	-150	10.0	8.24
Intersubband transitions												
CB ₂ -CB ₁	77	0.3	7.5	10	0.148	0.140	0.127	7	-20	-12	16.0	9.54
CB ₂ -CB ₁	2	0.3	26.4	19.8	0.020	0.019	0.019	8	1	0	6.88	0.88

*Reference numbers used in Table 2 are: 1 = [Ky 1992], 2 = [Martinez-Pastor 1993], 3 = [Kirchoefer 1982], 4 = [Gurioli 1993], 5 = [Galbraith 1988], 6 = [Racah 1987], 7 = [Jogai 1992], 8 = [Bajema 1987]

**Energy deviation is defined as the difference between experimental and theoretical transition energy values

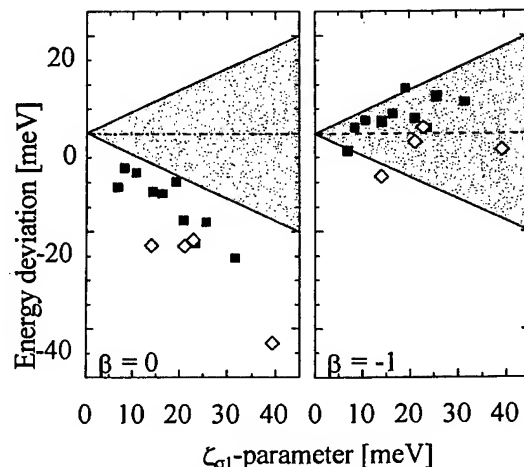


Fig. 7. Deviation of experimental results for the $\text{CB}_1\text{-HH}_1$ (full squares) and $\text{CB}_1\text{-LH}_1$ (open rhombs) transitions listed in Table 2 from their theoretical predictions (dashed line) corresponding to the two extreme choices of operator ordering. The triangular shaded areas indicate the range of uncertainty of theoretical transition energy caused by variation of quantum well thickness by plus-minus one GaAs monolayer.

6. DISCUSSION AND CONCLUSIONS

The main objective of this work was to find the correct KEO ordering for abrupt-interface heterostructures. The theoretical model was developed within the framework of the effective-mass theory. One-dimensional solutions of Schrödinger's equation for a periodic system with position-dependent mass have been considered. Using the Hamiltonian $H = -\frac{1}{2}[m(z)]^\alpha \nabla[m(z)]^\beta \nabla[m(z)]^\alpha + V(z)$ with $2\alpha + \beta = -1$, we have studied the effect of the parameter β on the transition energies for GaAs/Al_xGa_{1-x}As superlattices and quantum wells. We found that variation of this parameter resulted in a significant shift of subband energy levels. Our results clearly indicate that $\alpha = 0$ and $\beta = -1$ is the optimal choice of ordering parameters to provide the best fit of experimental data.

We have analyzed twenty different GaAs/Al_xGa_{1-x}As superlattice and quantum well systems using the transfer matrix technique. The results show that an increase in the miniband-edge energy within the conduction band is approximately linear within the entire range of $-1 \leq \beta \leq 0$. We investigated the effects of superlattice parameters, such as miniband index, thicknesses of both constituent materials, and barrier height (composition) effects on the ordering-related shifts of miniband-edge energy. The two extreme cases of $\beta = -1$ and $\beta = 0$ give larger energy shifts for higher miniband index, smaller well thickness, larger barrier thickness, and higher aluminum concentration in the barriers.

In order to maximize the accuracy of our test for the best choice of β , we have selected twenty sets of experimental data for structures with well thickness $4 \leq d_1 \leq 10$ nm, barrier thickness $5 \leq d_2 \leq 50$ nm, and aluminum concentration $0.3 \leq x \leq 0.5$. We define the parameter ζ_{oi} in Eq. (25) as a measure of ordering-related transition energy shift. For low temperature results, excitonic correction to transition energy was included in the calculations. Theoretical results indicate that the values of parameter ζ_{oi} for some experimental cases can be as high as 40 meV (Fig. 7). In principle, it is possible to increase the energy difference even further, for example, by considering ultrathin quantum wells with very high aluminum concentration ($x > 0.5$) in the barriers.

Uncertainty in the exact interface position was also taken into account. Deviations from the average well thickness by plus-minus one monolayer were considered. The effect of this variation is proportional to the ordering-related transition energy shift ζ_{oi} and can amount to more than 40 meV in magnitude (Fig. 7). Nevertheless, $\beta = -1$ gives much better results even when this uncertainty is considered. The results obtained with $\beta = 0$ all fall outside the range of one monolayer uncertainty.

For all twenty different experimental cases, the choice of $\beta = -1$ consistently gives a much better fit than $\beta = 0$. We therefore conclude that the correct choice for the kinetic energy operator ordering for abrupt heterointerfaces, consistent with experimental data, is $\beta = -1$.

ACKNOWLEDGEMENTS

This work was supported by the US Army Research Laboratory under the Advanced Sensors Collaborative Technology Alliance program and by AFOSR under the Optoelectronics Research Center program. The authors would like to acknowledge useful discussions with Prof. Petr G. Eliseev of the Center for High Technology Materials, University of New Mexico.

REFERENCES

- [Adachi 1985] S. Adachi, "GaAs, AlAs, and Al_xGa_{1-x}As: Material parameters for use in research and device applications", *J. Appl. Phys.*, vol. 58 (#3), pp. R1-R29, 1 Aug. 1985.
- [Bajema 1987] K. Bajema, R. Merlin, F.-Y. Juang, S.-C. Hong, J. Singh, and P. K. Bhattacharya, "Stark effect in GaAs-Al_xGa_{1-x}As quantum wells: Light scattering by intersubband transitions", *Phys. Rev. B*, vol. 36 (#2), pp. 1300-1302, 15 July 1987.
- [BenDaniel 1966] D. J. BenDaniel and C. B. Duke, "Space-charge effects on electron tunneling", *Phys. Rev.*, vol. 152 (#2), pp. 683-692, 9 Dec. 1966.
- [Bosio 1988] C. Bosio, J. L. Staehli, M. Guzzi, G. Burri and R. A. Logan, "Direct-energy-gap dependence on Al concentration in Al_xGa_{1-x}As", *Phys. Rev. B*, vol. 38 (#5), pp. 3263-3268, 15 Aug. 1988.
- [Burns 1985] G. Burns, *Solid State Physics*, Academic Press, New York 1985, pp. 252-253.

- [Burt 1992] M. G. Burt, "The justification for applying the effective-mass approximation to microstructures", *J. Phys.: Condens. Matter*, vol. 4 (#32), pp. 6651-6690, 10 Aug. 1992.
- [Burt 1994] M. G. Burt, "Direct derivation of effective-mass equations for microstructures with atomically abrupt boundaries", *Phys. Rev. B*, vol. 50 (#11), pp. 7518-7525, 15 Sept. 1994.
- [Cavalcante 1997] F. S. A. Cavalcante, R. N. Costa Filho, J. Ribeiro Filho, C. A. S. de Almeida, and V. N. Freire, "Form of the quantum kinetic-energy operator with spatially varying effective mass", *Phys. Rev. B*, vol. 55 (#3), pp. 1326-1328, 15 Jan. 1997.
- [Dekar 1999] L. Dekar, L. Chetouani, and T. F. Hammann, "Wave function for smooth potential and mass step", *Phys. Rev. A*, vol. 59 (#1), pp. 107-112, Jan. 1999.
- [Einevoll 1990a] G. T. Einevoll, P. C. Hemmer, and J. Thomsen, "Operator ordering in effective-mass theory for heterostructures. I. Comparison with exact results for superlattices, quantum wells, and localized potentials", *Phys. Rev. B*, vol. 42 (#6), pp. 3485-3496, 15 Aug. 1990.
- [Einevoll 1990b] G. T. Einevoll, "Operator ordering in effective-mass theory for heterostructures. II. Strained systems", *Phys. Rev. B*, vol. 42 (#6), pp. 3497-3502, 15 Aug. 1990.
- [Fu 1989] Y. Fu and K. A. Chao, "Subband structures of GaAs/Al_xGa_{1-x}As multiple quantum wells", *Phys. Rev. B*, vol. 40, pp. 8349-8356, 15 Oct. 1989.
- [Galbraith 1988] I. Galbraith and G. Duggan, "Envelope-function matching conditions for GaAs/(Al,Ga)As heterojunctions", *Phys. Rev. B*, vol. 38 (#14), pp. 10057-10059, 15 Nov. 1988.
- [Gurioli 1993] M. Gurioli, J. Martinez-Pastor, M. Colocci, A. Bosacchi, S. Franchi, and L. C. Andreani, "Well-width and aluminum-concentration dependence of the exciton binding energies in GaAs/Al_xGa_{1-x}As quantum wells", *Phys. Rev. B*, vol. 47 (#23), pp. 15755-15762, 15 June 1993.
- [James 1949] H. M. James, "Electronic states in perturbed periodic systems", *Phys. Rev.*, vol. 76 (#11), pp. 1611-1624, 1 Dec. 1949.
- [Jogai 1992] B. Jogai, M. O. Manasreh, C. E. Stutz, R. L. Whitney, and D. K. Kinell, "Intersubband optical absorption in heavily doped *n*-type GaAs/Al_{0.3}Ga_{0.7}As multiple quantum wells", *Phys. Rev. B*, vol. 46 (#11), pp. 7208-7211, 15 Sept. 1992.
- [Kangarlu 1988] A. Kangarlu, H. R. Chandrasekhar, M. Chandrasekhar, Y. M. Kapoor, F. A. Chambers, B. A. Vojak and J. M. Meese, "Temperature dependence of the quantized states in a GaAs-Ga_{1-x}Al_xAs superlattice", *Phys. Rev. B*, vol. 37 (#2), pp. 1035-1038, 15 Jan. 1988.
- [Kirchoefer 1982] S. W. Kirchoefer, N. Holonyak, Jr., K. Hess, D. A. Gulino, H. G. Drickamer, J. J. Coleman, and P. D. Dapkus, "Absorption measurements at high pressure on AlAs-Al_xGa_{1-x}As-GaAs superlattices", *Appl. Phys. Lett.*, vol. 40 (#9), pp. 821-824, 1 May 1982.
- [Ky 1992] N. H. Ky, J. D. Ganière, M. Gailhanou, F. Morier-Genoud, D. Martin, and F. K. Reinhart, "Influence of Al content in the barrier on the optical properties of GaAs/Al_xGa_{1-x}As ($x = 0.1 - 1$) multiple-quantum-well structures", *Phys. Rev. B*, vol. 46 (#11), pp. 6947-6954, 15 Sept. 1992.
- [Lévy-Leblond 1995] J.-M. Lévy-Leblond, "Position-dependent effective mass and Galilean invariance", *Phys. Rev. A*, vol. 52 (#3), pp. 1845-1849, Sept. 1995.
- [Li 1994] T. L. Li and K. J. Kuhn, "Validity of the connection-matrix approach to GaAs-Al_xGa_{1-x}As quantum wells", *Phys. Rev. B*, vol. 49 (#4), pp. 2608-2614, 15 Jan. 1994.
- [Martinez-Pastor 1993] J. Martinez-Pastor, A. Vinattieri, L. Carraresi, M. Colocci, Ph. Roussignol, and G. Weimann, "Temperature dependence of exciton lifetimes in GaAs/Al_xGa_{1-x}As single quantum wells", *Phys. Rev. B*, vol. 47 (#16), pp. 10456-10460, 15 April 1993.
- [Merzbacher 1997] E. Merzbacher, *Quantum Mechanics*, 3rd Ed., Wiley, New York 1997.
- [Morrow 1984] R. A. Morrow and K. R. Brownstein, "Model effective-mass Hamiltonians for abrupt heterojunctions and the associated wave-function-matching conditions", *Phys. Rev. B*, vol. 30 (#2), pp. 678-680, 15 July 1984.
- [Morrow 1987a] R. A. Morrow, "Establishment of an effective-mass Hamiltonian for abrupt heterojunctions", *Phys. Rev. B*, vol. 35 (#15), pp. 8074-8079, 15 May 1987.
- [Morrow 1987b] R. A. Morrow, "Effective-mass Hamiltonians for abrupt heterojunctions in three dimensions", *Phys. Rev. B*, vol. 36 (#9), pp. 4836-4840, 15 Sept. 1987.
- [Racah 1987] P. M. Racah, J. W. Garland, Z. Zhang, F. A. Chambers, and D. J. Vezetti, "Electrolyte electroreflectance study of the band offset in a GaAs/Ga_{0.69}Al_{0.31}As superlattice", *Phys. Rev. B*, vol. 36 (#8), pp. 4271-4278, 15 Sept. 1987.
- [Slater 1949] J. C. Slater, "Electrons in perturbed periodic lattices", *Phys. Rev.*, vol. 76 (#11), pp. 1592-1601, 1 Dec. 1949.

- [Strang 1988] G. Strang, *Linear Algebra and its Applications*, 3rd Ed., Harcourt Brace Jovanovich, San Diego 1988, p. 258.
- [Thomsen 1989] J. Thomsen, G. T. Einevoll, and P. C. Hemmer, "Operator ordering in effective-mass theory", *Phys. Rev. B*, vol. 39 (#17), pp. 12783-12788, 15 June 1989.
- [von Roos 1983] O. von Roos, "Position-dependent effective masses in semiconductor theory", *Phys. Rev. B*, vol. 27 (#12), pp. 7547-7552, 15 June 1983.
- [von Roos 1985] O. von Roos and H. Mavromatis, "Position-dependent effective masses in semiconductor theory. II", *Phys. Rev. B*, vol. 31 (#4), pp. 2294-2298, 15 Feb. 1985.
- [Vurtgafman 2001] I. Vurtgafman, J. R. Meyer, and L. R. Ram-Mohan, "Band parameters for III-V compound semiconductors and their alloys", *J. Appl. Phys.*, vol. 89 (#11), pp. 5815-5875, 1 June 2001.
- [Young 1989] K. Young, "Position-dependent effective mass for inhomogeneous semiconductors", *Phys. Rev. B*, vol. 39 (#18), pp. 13434-13441, 15 June 1989.
- [Zhu 1983] Q.-G. Zhu and H. Kroemer, "Interface connection rules for effective-mass wave functions at an abrupt heterojunction between two different semiconductors", *Phys. Rev. B*, vol. 27 (#6), pp. 3519-3527, 15 March 1983.

PROCEEDINGS OF SPIE



SPIE – The International Society for Optical Engineering

Physics and Simulation of Optoelectronic Devices X

**Peter Blood
Marek Osiński
Yasuhiko Arakawa**
Chairs/Editors

**21-25 January 2002
San Jose, USA**



Volume 4646



The papers appearing in this book compose the proceedings of the technical conference cited on the cover and title page of this volume. They reflect the authors' opinions and are published as presented, in the interests of timely dissemination. Their inclusion in this publication does not necessarily constitute endorsement by the editors or by SPIE. Papers were selected by the conference program committee to be presented in oral or poster format, and were subject to review by volume editors or program committees.

Please use the following format to cite material from this book:

Author(s), "Title of paper", in *Physics and Simulation of Optoelectronic Devices X*, Peter Blood, Marek Osiński, Yasuhiko Arakawa, Editors, Proceedings of SPIE Vol. 4646, page numbers (2002).

ISSN 0277-786X
ISBN 0-8194-4385-9

Published by
SPIE—The International Society for Optical Engineering
P.O. Box 10, Bellingham, Washington 98227-0010, USA
Telephone 1 360/676-3290 (Pacific Time) • Fax 1 360/647-1445
<http://www.spie.org/>

Copyright© 2002, The Society of Photo-Optical Instrumentation Engineers.

Copying of material in this book for internal or personal use, or for the internal or personal use of specific clients, beyond the fair use provisions granted by the U.S. Copyright Law is authorized by SPIE subject to payment of copying fees. The Transactional Reporting Service base fee for this volume is \$15.00 per article (or portion thereof), which should be paid directly to the Copyright Clearance Center (CCC), 222 Rosewood Drive, Danvers, MA 01923 USA. Payment may also be made electronically through CCC Online at <http://www.directory.net/copyright/>. Other copying for republication, resale, advertising or promotion, or any form of systematic or multiple reproduction of any material in this book is prohibited except with permission in writing from the publisher. The CCC fee code is 0277-786X/02/\$15.00.

Printed in the United States of America.

Effects of resonant mode coupling on near- and far-field characteristics of InGaN-based lasers

Gennady A. Smolyakov, Petr G. Eliseev^a, and Marek Osinski^{*}

Center for High Technology Materials, University of New Mexico, 1313 Goddard SE
Albuquerque, New Mexico 87106-4343, USA

^aAlso at P. N. Lebedev Physics Institute, Russian Academy of Sciences, Moscow, Russia

ABSTRACT

The phenomenon of resonant mode coupling is modeled and numerically investigated in InGaN-based multiple-quantum-well laser structures. It is shown that under resonant conditions the internal mode coupling can lead to severe distortions of both near- and far-field characteristics. Taking into account the carrier-induced change of the modal effective index for the lasing mode, we show that the resonant internal mode coupling can result in a strongly nonlinear dependence of the modal gain on injection current, with possible region of negative differential modal gain.

Keywords: InGaN lasers, near field, far field, coupled waveguides, normal modes, resonant mode coupling

1. INTRODUCTION

Group-III-nitride-based diode lasers [Nakamura 1996], [Nakamura 1997a] are of great importance as light sources for a variety of short-wavelength laser applications, such as high-capacity compact disks, UV irradiation, space communications, etc. The typical design of the lasers is a single- or multiple-quantum-well (MQW) separate-confinement heterostructure that incorporates a multiple optical waveguide structure in the direction perpendicular to the junction plane, with refractive indices of several layers (GaN buffer/substrate, active region, GaN cap layer) being higher than those of adjacent layers (AlGaIn cladding layers). The significant misfit stress associated with the lattice mismatch between AlGaIn and GaN makes it difficult to grow thick AlGaIn cladding layers due to the generation of cracks. The low Al-content and thin cladding layers of AlGaIn, on the other hand, do not provide perfect optical isolation between the active region and the passive waveguides of the diode chip, which could lead to higher-order-mode generation and, thus, to additional optical losses, higher threshold current, and lower efficiency of the device. If the phase velocities of eigenmodes of individual waveguides (of the active layer mode and of a passive waveguide mode), treated as uncoupled, happen to be the same or very close to each other, resonant mode coupling would occur with significant reduction of the optical confinement factor and suppression of the modal gain.

The problem of resonant internal mode coupling in a multiple-waveguide laser structure was previously considered for InGaAs/GaAs/AlGaAs separate-confinement heterostructure lasers [Eliseev 1994], where the concept of *ghost* modes was formulated. Away from resonance, the "parasitic" modes of passive waveguides reveal themselves as weak local maxima of near-field intensity that the lasing mode acquires in the passive waveguides. At resonance, the contribution of the passive mode into the lasing mode intensity becomes comparable with that of the active layer mode. This implies a much weaker optical confinement for the lasing mode, which can lead to a severe modal gain suppression and may result in no lasing at all. The concept was also shown to be useful in explaining some spectral variations of ASE in laser structures grown on a transparent substrate. The approach was further developed and adopted for analysis of nitride-based laser structures [Eliseev 1998], [Smolyakov 1999], [Eliseev 1999], [Eliseev 2000], where the values for critical thickness were calculated for p^+ -GaN cap layer and for n -GaN buffer/substrate layer for a particular multi-layer laser

^{*} Email: osinski@chtm.unm.edu; WWW: <http://www.chtm.unm.edu>; Telephone: (505) 272 7812; Fax: (505) 272 7801

structure. It was shown that the strength of the resonant coupling effect depends on the thickness and composition of cladding layers, and the technological advantage of thin-cladding structures comes at the risk of entering the regime of a resonant internal mode coupling in the laser structure and deteriorating the laser performance. A thin-cladding structure should be carefully optimized in designing an InGa_N-based diode laser by ensuring that all parasitic waveguide thicknesses are away from their expected resonant values. In waveguide calculations, the resonant-like modal behavior was observed also in [Bougrov 1997], [Bergmann 1998], [Hatakoshi 2001]. In experimental studies of InGa_N/AlGa_N/Ga_N lasers, complicated spectral and spatial effects were reported in [Onomura 1998], [Heppel 1998], [Young 1999], [Onomura 1999], [Summers 2001], with one typical feature being a substantial part of laser light emitted through the passive parts of the diode chip. Far field calculations were also reported in [Onomura 1998], [Onomura 1999], intended for comparison with the far-field patterns observed experimentally from some particular laser structures.

The spatial characteristics of the laser emission can change dramatically under the resonant conditions of the internal mode coupling. With the far-field pattern being rather sensitive to any modification of the modal profile inside the cavity, it would be of great advantage to be able to single out the devices impaired by the resonant mode coupling by mere looking at their far-field patterns. In this paper, we use the approach of normal modes of coupled waveguides to analyze the behavior of far-field patterns perpendicular to the junction plane both at and away from the resonance associated with the internal mode coupling in search of any features that would be characteristic of those resonant conditions. Taking into account the carrier-induced change of the modal effective index for the lasing mode, we show then that the resonant internal mode coupling can result in a strongly nonlinear dependence of the modal gain versus injection current, with possible region of negative differential modal gain.

2. INTERNAL MODE COUPLING AND THE CONCEPT OF "GHOST MODES"

The lasing mode in cladding layers exists as an evanescent wave, whose intensity decays exponentially into the cladding layers. Therefore, the optical losses associated with the penetration of the laser emission through the claddings into the passive waveguides are negligible when the cladding thickness is much larger than the penetration depth, with the latter being dependent on the refractive index step at the Ga_N waveguide layer/AlGa_N cladding layer interfaces. There are, however, certain reasons for using relatively thin cladding layers, which is often the case in the nitride-based diode lasers. Thin cladding layers are of technological advantage because they allow (i) to avoid an increase in the series resistance of the diode, and (ii) to avoid generation of cracks and other defects when there is a significant misfit stress associated with the lattice mismatch between AlGa_N and Ga_N layers, (iii) to reduce the growth time. In such laser structures, a significant part of laser emission can penetrate through the cladding layers and be accumulated within the passive waveguide layers. As a result, the lasing mode becomes a high-order mode with the corresponding modification in the modal spatial profile, optical confinement factor, propagation constant, and internal losses.

Complex behavior of modes in multilayer systems can be understood using the approach of normal modes of coupled waveguides, often approximated by supermodes which are either in-phase or in-anti-phase superpositions of the modes of individual uncoupled waveguides (see, for example, [Haus 1984], [Streifer 1987]). Modes of the passive waveguides (passive modes) can interact with an active-layer mode (active mode), giving rise to two kinds of normal modes or supermodes of a laser structure. Away from resonance, one of the normal modes is localized predominantly in the active region (lasing mode), while the other modes are located mostly in passive waveguides (ghost modes). The lasing mode is the mode at which laser generation occurs. The lossy ghost modes are parasitic modes of a laser structure that can consume energy from the active region. The approximation of supermodes is valid only far away from resonance, when the modes of individual uncoupled waveguides have different phase velocities. At resonance, only the exact solutions (normal modes) of the wave equation for a multilayer waveguide system should be considered. The normal modes, however, still resemble the in-phase and in-anti-phase combinations of uncoupled modes of individual waveguides. Resonant coupling occurs when the lasing normal mode and a ghost normal mode are in phase synchronism. The contributions of the active mode and the passive mode into each of the two normal modes become comparable in that case. This implies a much weaker optical confinement for the lasing mode, which now experiences much greater optical losses in the passive waveguide. Consequently, the modal gain of the lasing mode decreases, and this may result in no lasing action at all. On the contrary, the ghost mode "benefits" under such close-to-resonance conditions, since it receives more optical power from the active region. Its modal gain increases, but not necessarily sufficiently to reach the lasing threshold. Obviously, it is possible to have an unlucky laser design (*i.e.* with resonant mode coupling), where the

laser would not operate even though its active region is of perfect quality and properly supplied with high material gain. For more details on the complex behavior of normal modes in nitride-based laser diode see [Eliseev 1999].

3. DEVICE STRUCTURE AND MATERIAL PARAMETERS

The InGaN/AlGaN/GaN laser structure under consideration is based on typical design reported in [Nakamura 1997b] and used in our previous analysis [Eliseev 1999]. With the exception of the contact layers, all the layers outside the active region are quite transparent to the laser emission. We consider an active region composed of four $\text{In}_{0.15}\text{Ga}_{0.85}\text{N}$ quantum-well layers separated by three $\text{In}_{0.02}\text{Ga}_{0.98}\text{N}$ barrier layers. The MQW active region together with the n -GaN and p -GaN waveguide layers form a 235-nm thick active waveguide. The $\text{Al}_{0.14}\text{Ga}_{0.86}\text{N}$ cladding layers separate the active waveguide from p^+ -GaN cap layer and n -GaN buffer-substrate layer. Both GaN layers form "parasitic" passive waveguides where the photons of laser emission can be accumulated. The values of optical parameters used in our calculations are listed in Table 1 for all the layers in the laser structure. In Table 1, n stands for the refractive index, k is the extinction coefficient, and d is the layer thickness.

Table 1. Optical parameters of the materials comprising the InGaN/AlGaN/GaN MQW laser structure ($\lambda = 400$ nm)

Material	n	k	d [nm]	Comments
Au	1.5	1.7	200	Electrode material
p^+ -GaN	2.55	0.000032	100 – 2000	p^+ -cap layer
$p\text{-Al}_{0.14}\text{Ga}_{0.86}\text{N}$	2.50	0.000032	300 – 1000	p -cladding
p -GaN	2.55	0.000032	100	p -waveguide layer
$\text{In}_{0.15}\text{Ga}_{0.85}\text{N}(4) +$	2.75	0 – -0.0064	3.5	QWs (gain coefficient 0 – 2000 cm^{-1})
$\text{In}_{0.02}\text{Ga}_{0.98}\text{N}(3)$	2.63	0.000032	7.0	Barriers (absorption coefficient 10 cm^{-1})
n -GaN	2.55	0.000032	100	n -waveguide layer
$n\text{-Al}_{0.14}\text{Ga}_{0.86}\text{N}$	2.50	0.000032	300 – 1000	n -cladding layer
n -GaN	2.55	0.000032	200 – 4000	n -buffer-substrate
$\alpha\text{-Al}_2\text{O}_3$	1.77	0.000032	∞	Sapphire substrate

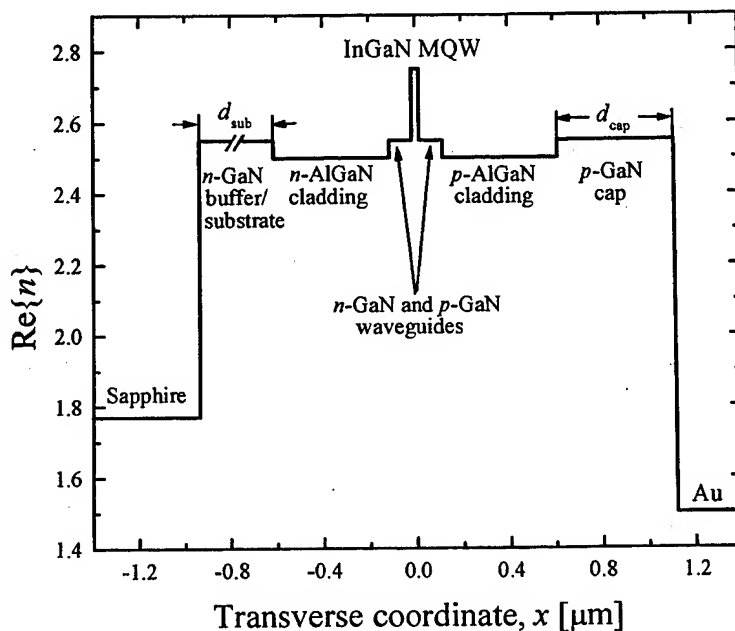


Fig. 1. Refractive index profile for a typical InGaN/AlGaN/GaN/sapphire diode laser.

The refractive indices for AlGaIn and InGaIn materials were obtained from interpolation of the known data [Lin 1993], [Amano 1993], [Morkoç 1999], [Laws 2001]. The material gain inside the quantum wells was assumed to be 1000 cm^{-1} for a fixed wavelength of 400 nm, unless otherwise indicated. Note that the extinction coefficient of 3.2×10^{-5} in the passive layers corresponds to the absorption coefficient of 10 cm^{-1} at the wavelength of 400 nm. The refractive index profile of the laser structure assumed in our calculations is shown in Fig. 1.

4. CALCULATION TECHNIQUE

Assuming only transverse (vertical) spatial dependence of the electrical field amplitude $E_y(x)$, we solve the scalar wave equation for TE modes, known to be predominant in nitride-based MQW lasers:

$$\frac{\partial^2 E_y}{\partial x^2} + [k_0^2 n^2(x) - \beta^2] E_y = 0, \quad (1)$$

where k_0 is the free-space wave vector, $n(x)$ is the complex refractive index of the laser dielectric structure, and β is the longitudinal propagation constant. Using a combination of the complex Newton method and the transfer matrix method, we find the guided wave solutions of the wave equation. The calculated results for normal modes are presented in terms of the modal effective index $n_{\text{eff}} = \text{Re}\beta/k_0$, net modal gain/loss $G_{\text{mod}} = -2\text{Im}\beta$, and normalized near-field and far-field intensity distributions. The far-field pattern perpendicular to the junction plane was calculated according to:

$$I(\theta) = \cos^2(\theta) \left| \int E_y(x) e^{ik_0 \sin \theta x} dx \right|^2. \quad (2)$$

Note that although the concept of supermodes (understood as superpositions of individual waveguide modes) is useful in understanding the nature of solutions, the normal modes of the laser structure are found here, without invoking the coupled-mode theory.

5. RESULTS OF CALCULATIONS

5.1. Resonant Conditions

Here, we summarize briefly the results on the resonant behavior of normal modes in the “active waveguide – cap layer” and “active waveguide – GaN buffer/substrate layer” two-waveguide systems previously reported in [Eliseev 1999]. For the laser structure with 4 quantum wells, the calculated effective index of the “lasing” mode is about 2.539, whereas that of the “ghost” modes varies from ~ 2.5 to ~ 2.55 , depending on the thickness of the corresponding passive waveguide to which those ghost modes belong. However, the effective index curves for normal modes of coupled waveguides do not cross. Rather, we can specify the points of *anti-crossing* (resonance) when two curves come very close to each other as can be seen, for example, in Fig. 2(a) where we show the calculated effective index for the first three lowest-order normal modes in the two-waveguide system of the active waveguide and the p^+ -GaN cap layer as a function of the p^+ -GaN cap layer thickness d_{cap} . As indicated in Fig. 2(a), the normal modes change their character in passing through the resonance, namely the lasing mode turns into a ghost mode and vice versa. In other words, the lasing mode is not represented by a single normal mode, but by a sequence of normal modes, with the mode order increasing by one at each subsequent resonance. At resonance, the modal gain of the lasing mode can be severely suppressed, as illustrated by Fig. 2(b). This is due to much poorer optical confinement of the lasing mode, which experiences much greater optical losses in the passive waveguide and in the metal contact layer. To see how the spatial characteristics of the laser evolve with increasing d_{cap} , we indicate four characteristic points around the first resonance in Fig. 2, at which we calculated the near-field and far-field intensity distributions (see Section 5.2). Although they belong to different normal modes, all four of them describe the lasing mode of the structure either far away from the resonance (points *a* and *d*) or close to the resonance (points *b* and *c*).

The multiple resonances in the two-waveguide system of the active waveguide and the n -GaN buffer/substrate are shown in Fig. 3 as a function of the GaN buffer/substrate thickness d_{sub} . In this case, the points *a-d* for calculating near and far-field patterns are taken around the third anti-crossing point. It should be noted that in both cases the exact positions of

the resonances depend on the effective index of the lasing mode which can be controlled, for example, by changing the number of quantum wells, the thickness and/or composition of quantum wells and barriers, or the thickness of the GaN waveguide layers.

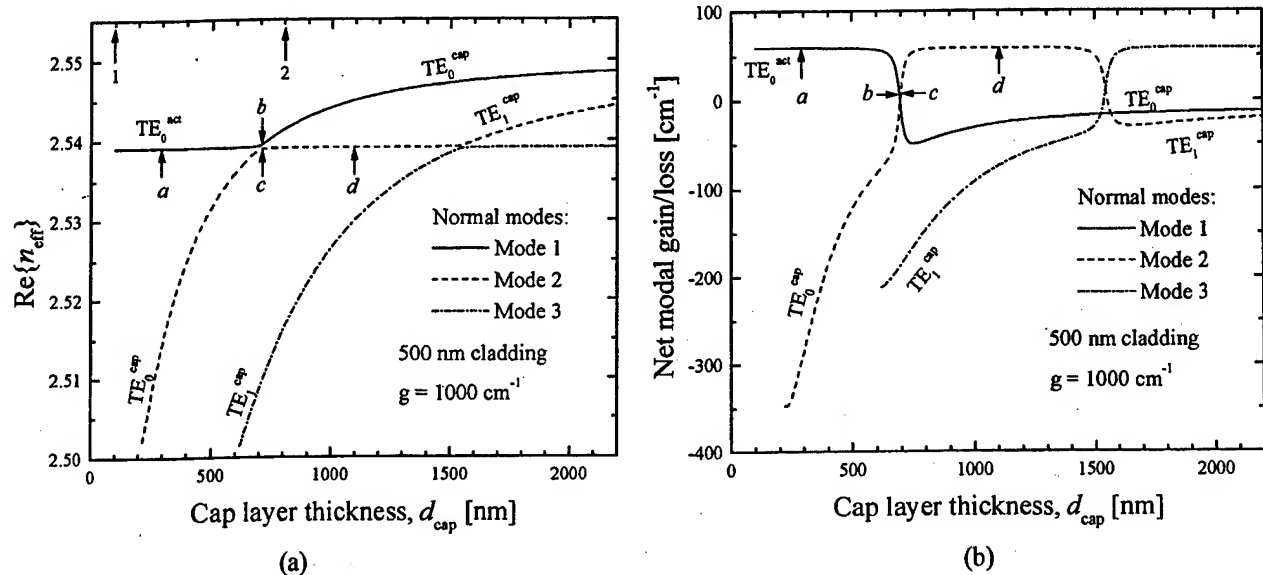


Fig. 2. Calculated effective index (a) and net modal gain/loss (b) for the first three lowest-order normal modes in the two-waveguide system of the active waveguide and the p^+ -GaN cap layer as a function of the GaN cap layer thickness d_{cap} . The notation TE_N^{act} , TE_N^{cap} ($N = 0, 1, 2, \dots$) identifies the TE_N modes of the corresponding individual uncoupled waveguides (active waveguide, cap layer) to which the normal modes of the structure are very close for a particular range of values of d_{cap} . The arrows labeled with numbers indicate the minimum and maximum values being used for the GaN cap layer thickness in nitride-based lasers as extracted from the literature data (1 – [Nakamura 2000], 2 – [Akasaki 1996]). The arrows labeled with letters indicate the points at which near- and far-field patterns are calculated (cf. Section 5.2)

5.2. Spatial Characteristics of Laser Emission under the Resonant Internal Mode Coupling

Normal modes in a system of two coupled waveguide layers are characterized by local field maxima in both waveguide layers. We restrict ourselves to considering a single-mode active waveguide, while the passive waveguides, treated as uncoupled from the active waveguide, can support higher-order modes. This means that the normal modes in our case can have only one field maximum localized within the active waveguide and a different number of field maxima in a passive layer, depending on its thickness. Recalling that normal modes of a coupled waveguide system can be effectively represented as in-phase or in-anti-phase superpositions of the modes of individual waveguides, we can expect the far-field pattern produced by a normal mode to be a rather complex result of interference from those local fields, strongly depending on their relative intensities and mutual phase relations. Far away from resonance, small intensity peaks acquired by the lasing mode in a passive waveguide layer can only slightly perturb the far-field intensity pattern dominated by the main intensity peak in the active waveguide. A particularly strong effect is expected in a close-to-resonance situation, when the lasing mode has peaks of comparable intensities both in the active waveguide and in a passive waveguide. Fig. 4 illustrates this point, showing the near-field and far-field intensity distributions for the lasing mode calculated at and away from the first resonance in a two-waveguide system of the active waveguide and the p^+ -GaN cap layer (cf. Fig. 2). Since only fundamental modes of the corresponding waveguides are involved in the internal mode coupling, we find this very simple case to be the most illustrative of the mechanism for far-field pattern formation in coupled waveguide systems.

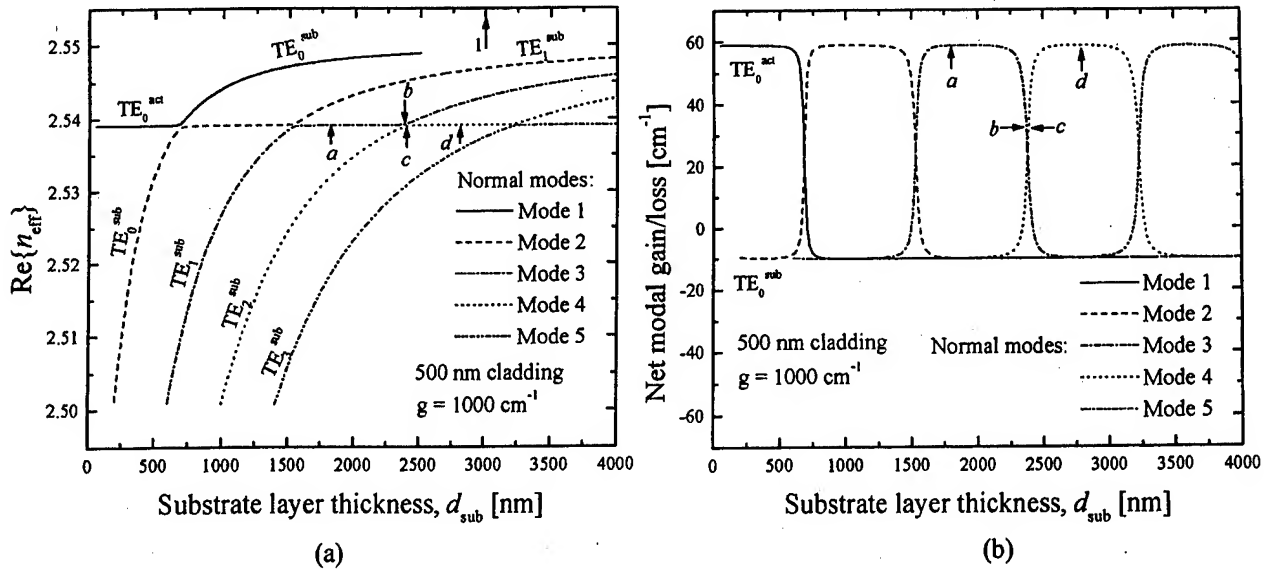


Fig. 3. Calculated effective index (a) and net modal gain/loss (b) for the first 5 lowest-order normal modes of TE polarization in the two-waveguide system of the active waveguide and the n -GaN buffer/substrate layer as a function of the GaN buffer/substrate layer thickness d_{sub} . The notation TE_N^{act} and TE_N^{sub} , ($N = 0, 1, 2, \dots$) identifies the TE_N modes of the corresponding individual uncoupled waveguides (active waveguide and buffer/substrate layer) to which the normal modes of the structure are very close for a particular range of values of d_{sub} . The arrow labeled "1" indicates the minimum value of d_{sub} used in nitride-based lasers, as extracted from the literature data [Nakamura 2000].

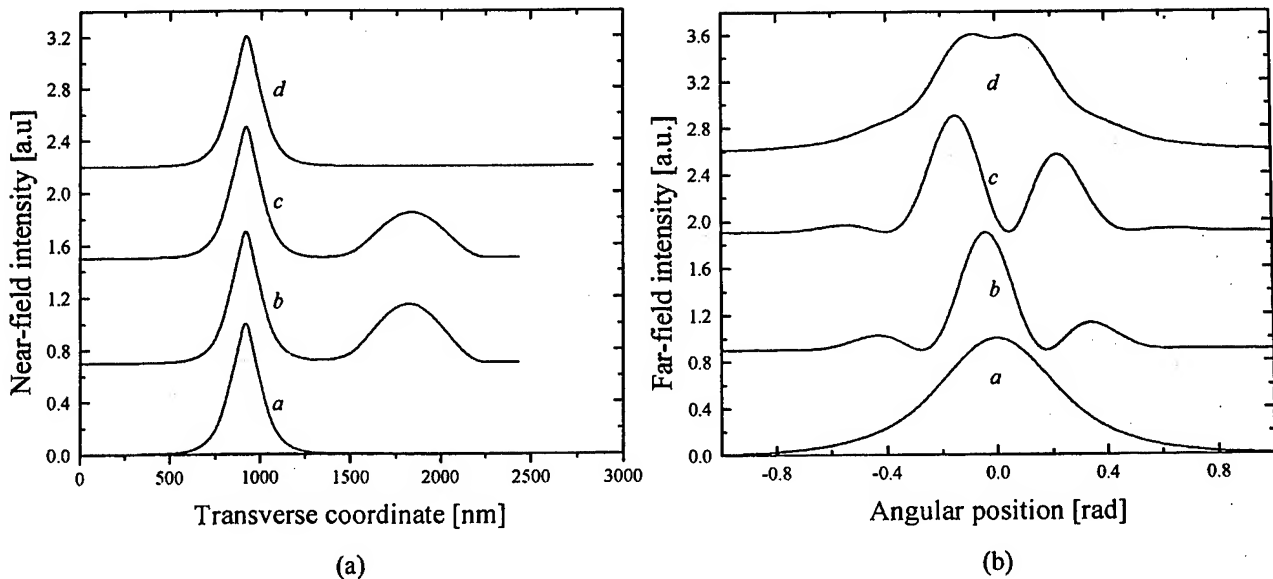


Fig. 4. Calculated near-field (a) and far-field (b) intensity distributions at (b, c) and away (a, d) from the first resonance in the "active layer-cap layer" system of Fig. 2.

The ideal situation of a laser emitting at the fundamental mode of the active waveguide is represented in Fig. 4 by curves *a*. Since the p^+ -GaN cap layer is very thin in this case (300 nm), the effective refractive index of its fundamental mode differs too much from that of the active waveguide mode to give any noticeable contribution to the lasing mode. Both curves *b* and *c* were calculated for close-to-resonance waveguide configurations. Although the near-field intensity

distributions look very much alike, the phase relations for the fields of individual waveguides are quite different, which changes the far-field pattern dramatically. While the in-phase superposition of the modes of individual waveguides (curves *b*) gives a strong central (very slightly off-axis) intensity peak and two smaller side peaks, the in-anti-phase superposition of the modes of individual waveguides (curves *c*) gives two characteristic, very pronounced off-axis peaks in the far-field intensity and much smaller side peaks. In both cases the peaks of intensity are much narrower than that obtained for the ideal case *a*, due to the near-field penetration into the passive waveguide. Curves *d* in Fig. 4 were calculated for $d_{\text{cap}} = 1.1 \mu\text{m}$, above the first resonance in the system and sufficiently far away from it. The intensity of the additional peak the lasing mode acquires in the passive waveguide becomes negligibly small, so that it cannot be seen in Fig. 4(a), which causes re-broadening of the far-field intensity distribution. The far-field pattern is, however, very sensitive to the additional tiny peak of intensity in the passive waveguide, as the slight local minimum of intensity appears at its axis according to the "in-anti-phase" character of the normal lasing mode after the first resonance.

Qualitatively, the same features can be observed in the far-field intensity distributions of Fig. 5 calculated at some points around the third resonance in the two-waveguide system of the active waveguide and *n*-GaN buffer/substrate layer (cf. Fig. 3). Apart from the obvious increased complexity of the far-field patterns in terms of the number of intensity maxima, the far-field pattern away from the resonance (curves *a*, *d*) is still a single, relatively wide, and slightly rippled maximum of intensity. Close to the resonance (curves *b*, *c*), it becomes a series of much narrower peaks of intensity. The "in-phase" normal lasing mode *b* produces peaks of comparable intensity, whereas the "in-anti-phase" normal lasing mode *c* produces again two distinct off-axis intensity peaks with several smaller peaks.

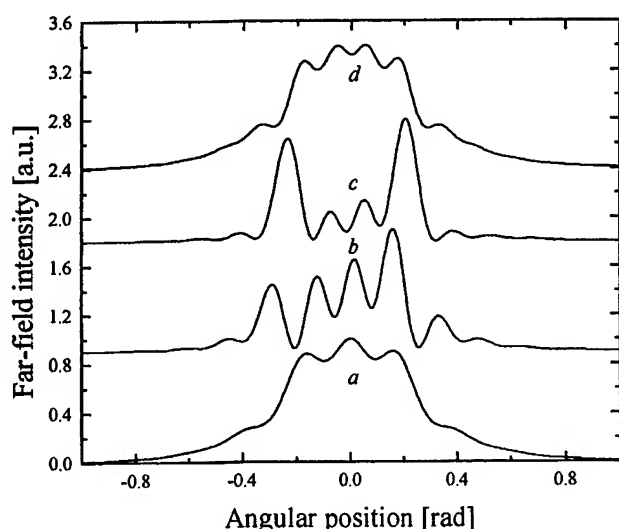


Fig. 5. Calculated far-field intensity distributions at (*b*, *c*) and away (*a*, *d*) from the third resonance in the "active waveguide – GaN buffer/substrate" system of Fig. 3.

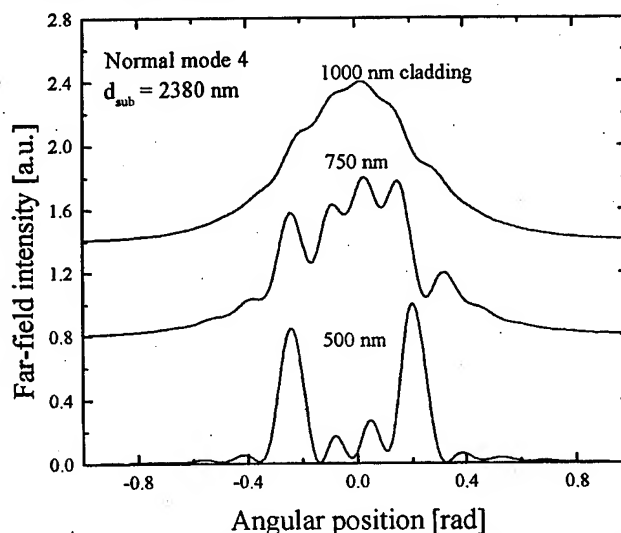


Fig. 6. Calculated far-field intensity distributions in the vicinity of the third resonance in the "Active waveguide – GaN buffer/substrate" system of Fig. 3. The labels indicate the AlGaIn cladding layer thickness d_{clad} .

The strength of the resonant internal mode coupling is known to depend on the cladding layer thickness. Increasing the cladding layer thickness makes the resonance narrower [Eliseev 1999]. Here we show again that it is important to keep the cladding layers reasonably thick in order to avoid an inadvertent resonance. In Fig. 6, we start with a laser structure impaired by the resonant internal mode coupling of the active waveguide mode with the second-order mode of the GaN buffer/substrate. As the thickness of the cladding layer is increased, the system comes out of resonance, demonstrating significant improvement in the far-field pattern. It should be noted that the results presented in this section are in good qualitative agreement with the experimental results reported in [Onomura 1998], [Onomura 1999].

5.3 Carrier-Induced Resonant Internal Mode Coupling

In Sections 5.1 and 5.2, we drove a system of coupled waveguides into resonance by varying the thickness of a passive waveguide. By doing this, we changed gradually the effective refractive index of a particular mode of the passive waveguide, making it closer to the effective refractive index of the active waveguide mode, while the latter was kept unchanged. Obviously, the thickness of a waveguide is not a parameter that can be easily controlled in a real experiment and, though very interesting, all the theoretical curves shown above (especially those of Figs. 2 and 3) have very little chance of being systematically reproduced experimentally. It is still possible, however, to induce the resonant internal mode coupling in a single device with fixed waveguide geometry if we employ the effect of carrier-induced variation of the refractive index in the active region, this time to gradually change the effective refractive index of the active waveguide mode. We consider here the same two-waveguide system of the active waveguide and the p^+ -GaN cap layer which, according to Fig. 2, would be at resonance for $d_{\text{cap}} = 696$ nm and material gain in the active region $g = 1000$ cm^{-1} . The system is then definitely not at resonance (although may be already relatively close to it) at the transparency point, i.e. when $g = 0$ cm^{-1} . We consider this situation to be possible below threshold in the laser structure under consideration, and take it as an initial condition for our numerical experiment. By increasing the material gain in the active region, we model the system behavior under increasing injection current. Due to the negative contribution of free carriers into the refractive index of the active region, the effective refractive index of the active waveguide mode would gradually decrease, thus driving the active waveguide mode into resonance with the fundamental mode of the cap layer. For the linewidth broadening parameter α , we used the value $\alpha = 2$ reported in [Renzoni 1999] for bulk GaN, assuming that the same value is valid for Ga-rich InGaN active medium.

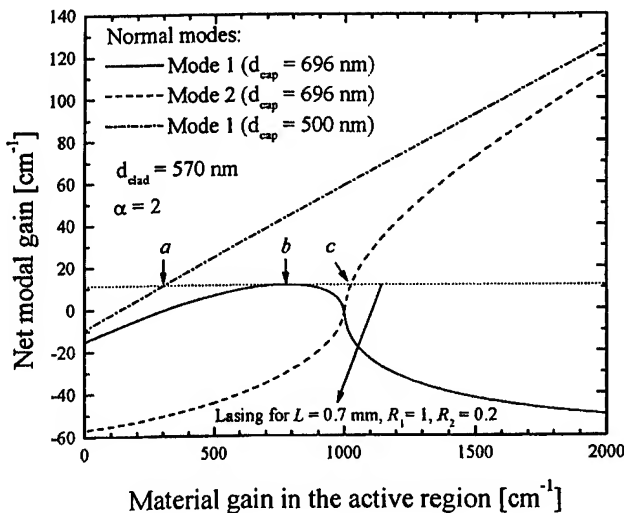


Fig. 7. Calculated net modal gain/loss for the first two lowest-order normal modes in the two-waveguide system of the active waveguide and the p^+ -GaN cap layer as a function of material gain in the active region.

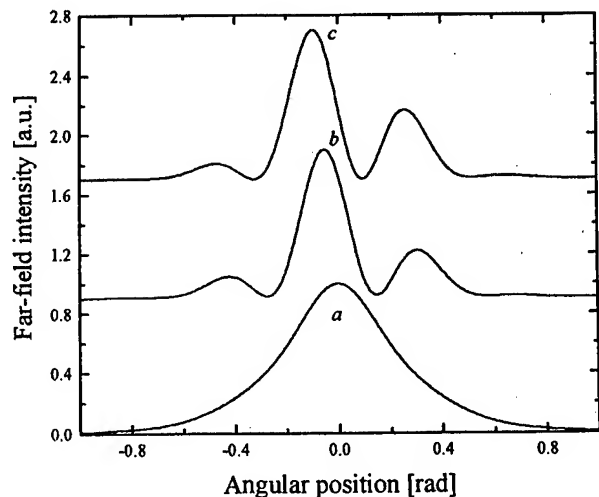


Fig. 8. Far-field intensity distributions calculated at points a , b , and c of Fig. 7.

The calculated net modal gain as function of the material gain is shown in Fig. 7 for the first two lowest-order normal modes of this coupled waveguide system. The lasing mode in Fig. 7 is sequentially represented by two normal modes that go through the resonance and change their roles at $g = 1000$ cm^{-1} . The result is a strongly nonlinear dependence of the modal gain on injection current, showing a region of *negative differential modal gain*. With the material gain monotonically increasing, this phenomenon is purely of waveguiding origin. On the one hand, as the system approaches the resonance, the optical confinement for the lasing mode starts weakening too rapidly for the increase in material gain to be able to compensate for that effect. On the other hand, as the system comes out of resonance, the optical confinement for the lasing mode starts improving equally rapidly, giving rise to the region of superlinear growth of the modal gain. The dotted-dashed line a is given for comparison, as it demonstrates the predictable linear growth of the

modal gain in a structure properly designed to be far away from the resonance with $d_{\text{cap}} = 500$ nm and all other parameters being the same.

We indicate three points in Fig. 7 corresponding to the same level of net modal gain. Though relatively low (~ 12 cm⁻¹), it is sufficient for lasing action in a long-cavity laser with the reflectance of one of the facets made very high. In the presence of the region of negative differential modal gain, the laser performance can be significantly modified by various kinds of oscillation instabilities (self-sustained pulsations, kinks and hysteresis in light-power characteristics [Eliseev 1995]). Fig. 8 shows what kind of the far-field pattern, impaired by resonant internal mode coupling, should be expected from such device.

6. DISCUSSION AND CONCLUSIONS

Resonant mode coupling is a general phenomenon that may occur in diode lasers whose internal structure incorporates multiple optical waveguides. Previously [Eliseev 1998], [Smolyakov 1999], [Eliseev 1999], we showed that this effect is particularly prominent in group-III nitride laser structures with thin cladding layers, where it can significantly suppress the modal gain and even stop the lasing action altogether. As possible measures to prevent the undesirable suppression of modal gain in such structures, we suggested to use thicker cladding layers, to avoid the resonant values for the thickness of parasitic waveguides and to increase the effective index of the lasing mode (for example by increasing the number of QWs in the active region). In this paper, we have again analyzed a typical group-III-nitride-based laser structure, this time paying special attention to spatial characteristics of laser emission under the resonant conditions of internal mode coupling. We have shown that under the resonant conditions the internal mode coupling can lead to severe distortions of both near- and far-field characteristics. We have identified typical features the far-field intensity pattern acquires under such conditions and suggested to use them to single out the devices impaired by the resonant mode coupling.

Furthermore, we have found that the carrier-induced variation of the propagation constant for the lasing mode can significantly modify the performance of laser structures vulnerable to resonant mode coupling. We have shown that the resonant mode coupling can be controlled by carrier-induced variation of the refractive index in the active region, and can result in a strongly nonlinear dependence of the modal gain on injection current with possible region of negative differential modal gain.

While undesirable in most situations, the resonant mode coupling, on the other hand, could be used in a controllable manner to modify the laser properties (mode tailoring, mode selection). Lasers with negative differential modal gain are expected to display strong nonlinear dynamic behavior, including self-pulsation, bistability, and multistability, which are potentially attractive for a number of applications.

In summary, we have analyzed numerically the optical modes of a system of coupled waveguides, characteristic of InGaN/AlGaIn/GaN diode lasers. The main conclusions are:

- 1) Modes of parasitic waveguides (p^+ -GaIn cap layer, n -GaIn buffer/substrate) in InGaN/AlGaIn/GaN diode laser chip can interact resonantly with modes of the active waveguide.
- 2) Under resonant conditions, the internal mode coupling can lead to severe modal gain suppression and distortions of both near- and far-field characteristics. Multiple narrow off-axis peaks of intensity in the far-field pattern indicate the resonant internal mode coupling, while a single relatively wide slightly rippled on-axis maximum of intensity in the laser far-field indicates a properly designed device not susceptible to resonant mode coupling.
- 3) Due to carrier-induced variation of the refractive index in the active region, the resonant internal mode coupling can result in a strongly nonlinear dependence of the modal gain on injection current, with possible region of negative differential modal gain.

ACKNOWLEDGMENTS

This work was supported by DARPA under the Optoelectronic Materials Center program and by AFOSR under the Optoelectronics Research Center program.

REFERENCES

- [Akasaki 1996] I. Akasaki, S. Sota, H. Sakai, T. Tanaka, M. Koike, and H. Amano, "Shortest wavelength semiconductor laser diode", *Electron. Lett.*, vol. 32 (#12), pp. 1105-1106, 6 June 1996.
- [Amano 1993] H. Amano, N. Watanabe, N. Koide, and I. Akasaki, "Room-temperature low-threshold surface-stimulated emission by optical pumping from $\text{Al}_{0.1}\text{Ga}_{0.9}\text{N}/\text{GaN}$ double heterostructure", *Jpn. J. Appl. Phys., Pt. 2 (Lett.)*, vol. 32 (#7B), pp. L1000-L1002, 15 July 1993.
- [Bergmann 1998] M. J. Bergmann and H. C. Casey, Jr., "Optical-field calculations for lossy multiple-layer $\text{Al}_x\text{Ga}_{1-x}\text{N}/\text{In}_x\text{Ga}_{1-x}\text{N}$ laser diodes", *J. Appl. Phys.*, vol. 84 (#3), pp. 1196-1203, 1 Aug. 1998.
- [Bougrov 1997] V. E. Bougrov and A. S. Zubrilov, "Optical confinement and threshold currents in III-V nitride heterostructures: Simulation", *J. Appl. Phys.*, vol. 81 (#7), pp. 2952-2956, 1 Apr. 1997.
- [Eliseev 1994] P. G. Eliseev and A. E. Drakin, "Analysis of the mode internal coupling in $\text{InGaAs}/\text{GaAs}$ laser diodes", *Laser Phys.*, vol. 4 (#3), pp. 485-492, May/June 1994.
- [Eliseev 1995] P. G. Eliseev and A. E. Drakin, "The negative differential gain in SL InGaAs QW laser diodes", *Physics and Simulation of Optoelectronic Devices III* (M. Osifski and W. W. Chow, Eds.), San Jose, CA, 6-9 Feb. 1995, *Proc. SPIE*, Vol. 2399, pp. 302-306.
- [Eliseev 1998] P. G. Eliseev, G. A. Smolyakov, and M. Osifski, "Ghost modes and their signature in InGaN diode laser spectra", *Proc. 2nd Int. Symp. Blue Laser and Light Emitting Diodes (2nd ISBLLED)*, Kisarazu, Japan, 29 Sept. - 2 Oct., 1998, Paper Th-10, pp. 413-416.
- [Eliseev 1999] P. G. Eliseev, G. A. Smolyakov, and M. Osifski, "Ghost modes and resonant effects in $\text{AlGaN}/\text{InGaN}/\text{GaN}$ lasers", *IEEE J. Select. Topics Quantum Electron.*, vol. 5 (#3), pp. 771-779, May/June 1999.
- [Eliseev 2000] P. G. Eliseev, "Waveguide optics of new short-wavelength laser diodes", *Laser Optics 2000: Semiconductor Lasers and Optical Communication* (S. A. Gurevich and N. N. Rosanov, Eds.), St. Petersburg, Russia, 26-30 June 2000, *Proc. SPIE*, Vol. 4354, pp. 12-23.
- [Hatakoshi 2001] G. Hatakoshi, M. Onomura, and M. Ishikawa, "Optical, electrical and thermal analysis for GaN semiconductor lasers", *Int. J. Numerical Modelling - Electronic Networks, Devices, & Fields*, vol. 14 (#4), pp. 303-323, July/Aug. 2001.
- [Haus 1984] H. Haus, *Waves and Fields in Optoelectronics*, Prentice-Hall, Englewood Cliffs, NJ, 1984, Section 7.6, pp. 217-220.
- [Heppel 1998] S. Heppel, J. Off, F. Scholz, and A. Hangleiter, "Complex spectral behaviour of the waveguide modes in GaInN/GaN laser structures", *Conf. Digest, 16th IEEE Int. Semicond. Laser Conf.*, Nara, Japan, 4-8 Oct. 1998, pp. 11-12.
- [Laws 2001] G. M. Laws, E. C. Larkins, I. Harrison, C. Molloy, and D. Somerford, "Improved refractive index formulas for the $\text{Al}_x\text{Ga}_{1-x}\text{N}$ and $\text{In}_y\text{Ga}_{1-y}\text{N}$ alloys", *J. Appl. Phys.*, vol. 89 (#2), pp. 1108-1115, 15 Jan. 2001.
- [Lin 1993] M. E. Lin, B. N. Sverdlov, S. Strite, H. Morkoç, and A. E. Drakin, "Refractive indices of wurtzite and zinc-blende GaN ", *Electron. Lett.*, vol. 29 (#20), pp. 1759-1761, 30 Sept. 1993.
- [Morkoç 1999] H. Morkoç, *Nitride Semiconductors and Devices*, Springer-Verlag, New York 1999.
- [Nakamura 1996] S. Nakamura, M. Senoh, S. Nagahama, N. Iwasa, T. Yamada, T. Matsushita, H. Kiyoku, and Y. Sugimoto, "InGaN-based multi-quantum-well-structure laser diodes", *Jpn. J. Appl. Phys., Pt. 2 (Lett.)*, vol. 35 (#1B), pp. L74-L76, 15 Jan. 1996.
- [Nakamura 1997a] S. Nakamura and G. Fasol, *The Blue Laser Diode*, Springer-Verlag, Berlin, 1997.
- [Nakamura 1997b] S. Nakamura, M. Senoh, S. Nagahama, N. Iwasa, T. Yamada, T. Matsushita, Y. Sugimoto, and H. Kiyoku, "Subband emissions of InGaN multi-quantum-well laser diodes under room-temperature continuous wave operation", *Appl. Phys. Lett.*, vol. 70 (#20), pp. 2753-2755, 19 May 1997.
- [Nakamura 2000] S. Nakamura, M. Senoh, S. Nagahama, N. Iwasa, T. Matsushita, and T. Mukai, "Blue InGaN -based laser diodes with an emission wavelength of 450 nm", *Appl. Phys. Lett.*, vol. 76 (#1), pp. 22-24, 3 Jan. 2000.

- [Onomura 1998] M. Onomura, S. Saito, K. Sasanuma, G. Hatakoshi, M. Nakasuji, J. Rennie, L. Sugiura, S. Nunoue, M. Suzuki, J. Nishio, and K. Itaya, "Analysis of transverse modes of nitride-based laser diodes", *Conf. Digest, 16th IEEE Int. Semicond. Laser Conf.*, Nara, Japan, 4-8 Oct. 1998, pp. 7-8.
- [Onomura 1999] M. Onomura, S. Saito, K. Sasanuma, G. Hatakoshi, M. Nakasuji, J. Rennie, L. Sugiura, S. Nunoue, J. Nishio, and K. Itaya, "Analysis of transverse modes of nitride-based laser diodes", *IEEE J. Select. Topics Quantum Electron.*, vol. 5 (#3), pp. 765-770, May/June 1999.
- [Renzoni 1999] F. Renzoni, J. F. Donegan, and C. H. Patterson, "Optical gain and linewidth enhancement factor in bulk GaN", *Semicond. Sci. Technol.*, vol. 14 (#6), pp. 517-520, June 1999.
- [Smolyakov 1999] G. A. Smolyakov, P. G. Eliseev, and M. Osirski, "Design limitations for InGaN/AlGaIn/GaN lasers imposed by resonant mode coupling", *Techn. Digest, 19th Annual Conf. Lasers & Electro-Optics CLEO '99*, Baltimore, MD, 23-28 May 1999, Paper CtuU5, p. 203.
- [Streifer 1987] W. Streifer, M. Osirski, and A. Hardy, "Reformulation of the coupled mode theory of multiwaveguide systems", *J. Lightwave Technol.*, vol. LT-5 (#1), pp. 1-4, Jan. 1987.
- [Summers 2001] H. D. Summers, P. M. Smowton, P. Blood, M. Dineen, R. M. Perks, D. P. Bour, and M. Kneissl, "Spatially and spectrally resolved measurement of optical loss in InGaIn laser structures", *J. Cryst. Growth*, vol. 230 (#3-4), pp. 517-521, Sept. 2001.
- [Young 1999] D. K. Young, M. P. Mack, A. C. Abare, M. Hansen, L. A. Coldren, S. P. DenBaars, E. L. Hu, and D. D. Awschalom, "Near-field scanning optical microscopy of indium gallium nitride multiple-quantum-well laser diodes", *Appl. Phys. Lett.*, vol. 74 (#16), pp. 2349-2351, 19 Apr. 1999.

PROCEEDINGS OF SPIE



SPIE – The International Society for Optical Engineering

Physics and Simulation of Optoelectronic Devices X

Peter Blood
Marek Osiński
Yasuhiko Arakawa
Chairs/Editors

21-25 January 2002
San Jose, USA



Volume 4646



The papers appearing in this book compose the proceedings of the technical conference cited on the cover and title page of this volume. They reflect the authors' opinions and are published as presented, in the interests of timely dissemination. Their inclusion in this publication does not necessarily constitute endorsement by the editors or by SPIE. Papers were selected by the conference program committee to be presented in oral or poster format, and were subject to review by volume editors or program committees.

Please use the following format to cite material from this book:

Author(s), "Title of paper", in *Physics and Simulation of Optoelectronic Devices X*, Peter Blood, Marek Osinski, Yasuhiko Arakawa, Editors, Proceedings of SPIE Vol. 4646, page numbers (2002).

ISSN 0277-786X
ISBN 0-8194-4385-9

Published by
SPIE—The International Society for Optical Engineering
P.O. Box 10, Bellingham, Washington 98227-0010, USA
Telephone 1 360/676-3290 (Pacific Time) • Fax 1 360/647-1445
<http://www.spie.org/>

Copyright© 2002, The Society of Photo-Optical Instrumentation Engineers.

Copying of material in this book for internal or personal use, or for the internal or personal use of specific clients, beyond the fair use provisions granted by the U.S. Copyright Law is authorized by SPIE subject to payment of copying fees. The Transactional Reporting Service base fee for this volume is \$15.00 per article (or portion thereof), which should be paid directly to the Copyright Clearance Center (CCC), 222 Rosewood Drive, Danvers, MA 01923 USA. Payment may also be made electronically through CCC Online at <http://www.directory.net/copyright/>. Other copying for republication, resale, advertising or promotion, or any form of systematic or multiple reproduction of any material in this book is prohibited except with permission in writing from the publisher. The CCC fee code is 0277-786X/02/\$15.00.

Printed in the United States of America.

Applications of High-Power Laser Technology to Wide-Bandgap Nitride Semiconductor Processing

Petr G. Eliseev^{a,b,*}, Andrei A. Ionin^b, Yuri M. Klimachev^b, Dimitri V. Sinitsyn^b,
Jinhyun Lee^a, and Marek Osiński^a

^aCenter for High Technology Materials, University of New Mexico, 1313 Goddard SE, Albuquerque, New Mexico 87106-4343, USA

^bP. N. Lebedev Physics Institute, 53 Leninski Prospect, Moscow, 117924 Russia

ABSTRACT

Laser annealing, laser surface processing and laser lift-off procedure are reviewed as applied to semiconductor nitride-based structures (GaN films and InGaN/GaN optoelectronic device structures grown on sapphire substrates). Data on laser ablation of composite GaN/sapphire material are reviewed with more detailed consideration of the ablation rate under subpicosecond laser pulses and under long-pulse irradiation in the IR range (wavelengths of 5.0-5.8 and 9.6 μm).

Keywords: Laser processing, ablation, surface processing, laser-induced damage, nitride semiconductors

1. INTRODUCTION

Group-III nitride semiconductors are novel important materials for solid-state electronics and, especially, for semiconductor optoelectronics applications. They already are used in commercial production of several types of optoelectronic devices, including visible and UV light-emitting diodes and visible laser diodes [Nakamura 1997]. Some data on these materials are shown in Table 1. Since no bulk GaN substrates are available, device structures are usually grown on heterogeneous substrates such as sapphire, silicon carbide, or silicon. Most devices are fabricated as multiplayer epitaxial structures on sapphire. For example, high-efficiency blue and green LEDs of the Nichia Chemical Industries are based on GaN-InGaN-AlGaIn quantum-well heterostructures, where the active medium is an InGaIn alloy (typically, 3.5-nm thick), while GaN and AlGaIn are used as wider-bandgap components. GaN also serves as a buffer-substrate. It should be noted that *p*-doping in device structures containing a *p-n* junction is not easy, due to probable hydrogenation of acceptors during MOCVD growth (primarily, Mg impurity is used as acceptor). The regular doping procedure includes after-growth thermal activation of acceptor impurity that results in conversion of the conductivity type of the *p*-region and reduction of its bulk resistivity.

Most of commercial nitride-based devices incorporate InGaIn quantum wells sandwiched between GaN or AlGaIn barrier layers. Also, some interesting results have been obtained for arsenide-nitride alloys, like GaAsN. The feature of this alloy is strong bowing of the bandgap dependence on the alloy composition. As a result, for small molar fractions of GaN (up to a few percent), the bandgap reduces rapidly if nitrogen replaces arsenic in GaAs. This is particularly important for fabrication of longer-wavelength emission sources using the GaAs-based technology.

There are several aspects of the application of high-power laser technology to the fabrication of device structures based on group-III nitride semiconductors. Laser processing is sometimes most suitable because of specific properties of nitride materials: hardness, chemical inertness, thin-film structure adjacent to non-conducting substrates. Due to chemical inertness, nitride-based devices are expected to be very stable for long-time operation and storage. On the other hand, the wet etching is very limited as applied to GaN and AlN. Therefore, simple traditional techniques utilizing wet etching are not effective in nitride technology.

*Correspondence: Email: eliseev@chtm.unm.edu; WWW: <http://www.chtm.unm.edu>; Telephone: (505) 272-7807; Fax: (505) 272-7801

Table 1. Properties of some group-III nitrides used in the optoelectronics

Material	Crystalline type	Lattice constant [nm]	Bandgap energy [eV]	Comments
BN	Zinc blende Wurtzite	0.3615 $a = 0.2536$ $c = 0.4199$	5.18 5.81	Very hard material; it can be prepared by similar methods as artificial diamond. Both crystalline types are indirect-gap materials
AlN	Zinc blende Wurtzite	0.435 $a = 0.3114$ $c = 0.4986$	6.2	Direct-gap semiconductor
AlGaIn	Wurtzite	$a = 0.3114$ - 0.3186 $c = 0.4986$ - 0.5125	6.2-3.4	Direct-gap semiconductor in all composition range High-resistivity material when mole fraction of AlN is more than 0.4
GaN	Zinc blende Wurtzite	0.450 $a = 0.3186$ $c = 0.5125$	3.20 3.49	Both crystalline types are direct-gap semiconductors. Wurtzite type is available in epilayers and in 0.5-1 cm wide platelets
InGaIn	Wurtzite	$a = 0.3186$ - 0.354 $c = 0.5125$ - 0.5705	3.4-1.95	Direct-gap semiconductor in all composition range. It is fabricated mainly as quantum-well epilayers: covers whole visible range

The most delicate laser-induced procedure is laser annealing. It is a non-destructive irradiation of nitride that has been reported to be useful for specific thermal treatment of acceptor-doped GaN in order to activate acceptor centers and to get *p*-type of conductivity [Cheng 2001], [Kim 2001]. Stronger irradiation produces the thermal decomposition of the nitride material that can be used as a tool for laser-induced thermal "etching" and surface processing. Precise surface processing has been reported with subpicosecond high-power irradiation [Eliseev 1999], [Eliseev 2000]. Also, thermal decomposition under UV irradiation through the transparent substrate has been used as a technique for accurate non-destructive separation of a thin nitride structure from the sapphire substrate [Wong 1998]. A deep ablation under high-power laser irradiation can be used for rough mechanical processing including "scribing" and cutting of wafers.

In this paper, we review results on various applications of laser technology in treatment of the GaN/sapphire structures, ranging from precise surface processing to severe damage under long-pulse IR irradiation. We also review results on laser-induced separation of nitride-based structure from the substrate.

2. EXPERIMENTAL SAMPLES

The composite target was GaN epilayer grown on the sapphire substrate at the Agilent Laboratories. Physical characteristics of the structure and both involved materials are shown in Table 2.

For better epitaxial interconnection between the substrate and the epilayer, a buffer layer of GaN was grown at first at relatively low growth temperature of ~500 °C. The thickness of the buffer layer was 30 nm. Subsequently, the growth of a 2-μm-thick GaN epilayer was performed with MOCVD epitaxy at 1050-1080 °C. The buffer layer is of low crystalline quality, due to significant differences between crystalline structures of sapphire and GaN. Actually, they both are of hexagonal symmetry, but of different crystalline type. Most importantly, there is a large lattice mismatch between the substrate and the epilayer. In spite of this, further growth of GaN (at higher growth temperature) is accompanied with improvement of the epilayer crystalline quality, allowing for device applications. However, the threading dislocation density remains very high (10^8 - 10^9 cm⁻²).

3. LASER ANNEALING EXPERIMENTS

In semiconductor technology, laser annealing was introduced in 1970-ies for treatment of semiconductors following ion implantation. It is known that implantation produces collateral damage in crystals, hence as-implanted material usually is not suitable for device applications. Annealing is necessary to provide annihilation of defects and also for appropriate displacement of implanted impurity into the desirable crystalline sites. An alternative technique of

thermal annealing is not always acceptable, because it can produce change of parameters outside the implanted region (which is usually limited to a very thin surface layer). Optical annealing under pulsed laser irradiation is a suitable technique to anneal selectively the thin near-surface region, without affecting the rest of the sample. In group-III nitride semiconductor technology, the *p*-doping during growth process does not result in good *p*-type conductivity in as-grown material. Annealing is necessary to activate the acceptor impurity of magnesium (the shallowest acceptor dopant available for GaN). Laser annealing is also suitable in this case. An important possibility that is specific to pulse laser irradiation is to produce arbitrary laterally-patterned structures (conducting regions in the shape of stripes, circles, rings, *etc.*) that cannot be fabricated with a static heat treatment.

Table 2. Characteristics of GaN/sapphire structures

Parameters	Units	Epilayer	Substrate
Chemical composition	-	GaN	α -Al ₂ O ₃
Mole mass	g	83.7	101.94
Crystalline type	-	Wurtzite	Corundum
Thickness	μ m	2	250
Density at 300 K	g/cm ³	6.100	3.974
Melting point	K	>2500	2310
Heat conductivity, at 300K 673 K 2323 K	W/cmK	1.3 (1.7*)	0.27 (0.46) 0.1256 0.0323
Bulk heat capacity at 300 K 1000 K 2000 K	J/cm ³ K	2.6 3.4	0.76 1.22 1.28
Latent heat of melting	kJ/mole	No melting under 1 atm	109
Optical absorption at 300 K wavelength 248 nm 400 nm 5650 nm 9600 nm	1/cm	10 ⁵ ~10 ~20 ~60	~5 <1 2-3 >50

* Data for ultra-high-quality material

Some thermal characteristics of nitride semiconductors can be found in [Mohammad 1996], [Newman 1998], [Krukowski 1999]. Laser-induced processes in group-III nitrides are reported in [Kelly 1996], [Wong 1996], [Kelly 1997], [Cohen 1998], [Herrera Zaldivar 1999]. For surface-related laser annealing of GaN, it is necessary to use UV lasers. In [Wong 1996], laser irradiation of thin AlN/GaN films on the sapphire substrate was investigated under 38-ns long pulses of excimer laser emission at 248 nm in a fluence range of up to 2 J/cm². Some roughening of surface was identified at 0.6 J/cm², indicating early stages of ablation. In GaN samples implanted with Mg, the threshold of surface modification appeared to be as low as 0.35 J/cm², probably, due to change of surface properties after ion implantation. In samples with AlN cap grown on top of GaN surface, the surface roughening was prevented up to 0.6 J/cm². At 2 J/cm² in a single shot, some microcracks appeared on the AlN/GaN epilayer. This was attributed to the tensile stress wave resulting from the difference in the thermal expansion coefficient between AlN, GaN and sapphire. For microcracks to appear, the stress must exceed the mechanical strength of the cap layer. Following thermal annealing, an improvement was detected in cathodoluminescence emission. Namely, the edge-emission peak at 3.47 eV became ~5 times stronger than in as-implanted GaN. After a second shot of the same fluence, the AlN cap was completely removed due to some ablation of GaN, ejecting fragments of the microcracked cap layer. At the same time, the cathodoluminescence peak at 3.47 eV disappeared.

At the sub-threshold fluence of 0.4 J/cm², multiple pulse irradiation was used to perform laser annealing of GaN after Mg-ion implantation. The Mg-related spectral peak was found to grow by several times with increasing number of shots (up to 150 pulses). Thus, pulsed laser annealing was demonstrated to be effective as a technique to activate implanted Mg acceptors in GaN, while an AlN cap layer was shown to protect GaN against surface thermal decomposition.

In another study [Herrera Zaldívar 1999], thermal annealing of GaN epilayer structures doped with Si and Mg was investigated. 12-ns pulses from a 193-nm ArF excimer laser were used in multiple-shot (50-250) experiments, at the fluence of 0.3 J/cm^2 per pulse. Inspection of the surface of irradiated samples revealed changes occurring even at the lowest irradiation doses. Some Ga-rich droplets were observed after 250 shots, indicating partial decomposition of the compound. Cathodoluminescence study revealed a complicated behavior of Mg-doped samples that was probably associated with a presence of Mg-related defects and complexes in GaN; the low-dose irradiation was found to induce an activation of Mg as acceptors while the annealing at high doses resulted in some degradation of luminescence efficiency in the blue spectral region.

Laser annealing of Si-doped *n*-GaN produced a marked decrease of the yellow band of luminescence that is attributed usually to point defects. This change is similar to that observed after thermal annealing in nitrogen atmosphere. Thus, it can be explained in terms of reduced nitrogen vacancy concentration at higher temperatures.

4. HIGH-POWER INFRARED IRRADIATION: PATTERN AND LIDT

In our experiments with high-power infrared lasers, pulsed electron-beam-controlled-discharge free-running CO_2 and CO lasers were used for sample irradiation. The lasers had ~ 1 liter active volume chamber (operating at room-temperature for the CO_2 laser and cryogenically cooled for the CO laser) and plane-mirror ~ 5 -meter-long resonator. The latter consisted of Au-coated Cu mirror and BaF_2 50%-reflectivity dielectric-coated output mirror (specified for each particular wavelength). The output aperture was 1 cm in diameter. Beam focusing was provided by a concave Cu-coated glass mirror of 15-cm focal length. The energy of the laser pulse was controlled by a thermopile calorimeter, on which a part of the laser radiation was directed by means of BaF_2 calibrated beam splitter. The intensity of the IR laser radiation on the target surface was varied by inserting calibrated IR filters into the laser beam. The pumping conditions during the experiments were constant (duration of electrical discharge pumping pulse is $40 \text{ } \mu\text{s}$) and the same laser pulse waveforms were supported for all energy fluences at the target surface.

The CO_2 laser emitted at $9.569 \text{ } \mu\text{m}$ and the spot size was $\sim 90 \text{ } \mu\text{m}$. The pulsewidth at half magnitude was $20 \pm 2 \text{ } \mu\text{s}$ with a short $0.3\text{-}\mu\text{s}$ pre-pulse of comparable magnitude (the effective pulsewidth for peak intensity estimate in the main part of the pulse is $20 \text{ } \mu\text{s}$).

The CO laser emitted several spectral lines in the wavelength range from 4.99 to $5.81 \text{ } \mu\text{m}$ with a weight center at $\sim 5.1 \text{ } \mu\text{m}$. The spot size at the target was $180 \text{ } \mu\text{m}$ in diameter. The pulse had a rise time of $\sim 10 \text{ } \mu\text{s}$ and decay time of $\sim 250 \text{ } \mu\text{s}$, with a tail reaching up to $500\text{-}550 \text{ } \mu\text{s}$ at the level of $\sim 10\%$ of the maximum intensity. Because of the complicated waveform, the effective pulsewidth (for calculation of the peak intensity) was taken as $255 \text{ } \mu\text{s}$, even though the actual FWHM pulsewidth was only $90 \pm 10 \text{ } \mu\text{s}$.

SEM pictures of the damage site are shown in Figs. 1-6. Irradiation by the CO_2 laser produced no damage below the fluence of $15\text{-}20 \text{ J/cm}^2$. Above this value, thermal dissociation of GaN was observed, with: Ga droplets appearing at the surface. The amount of metallic Ga seemed to be smaller than the thermally etched volume, therefore some Ga was ablated together with nitrogen. A visible light flash accompanied the damage process. Above $\sim 30 \text{ J/cm}^2$, a "window" in the epilayer appeared. At $\sim 190 \text{ J/cm}^2$, total removal of the epilayer in the irradiated spot occurred. Some Ga droplets with mean diameter of $\sim 5 \text{ } \mu\text{m}$ remained at the window rim. The sapphire substrate seemed to be not ablated and not melted, but microcracks were seen in the window. The substrate temperature did not achieve the melting point even at the fluence of 190 J/cm^2 (5.5 times above the window formation threshold). We estimate the laser-induced damage threshold (LIDT) for the window formation in a $2\text{-}\mu\text{m}$ -thick GaN epilayer to have the peak intensity of $\sim 1.5 \text{ MW/cm}^2$.

Irradiation by the CO laser pulses at fluences below 620 J/cm^2 did not produce any visible damage. Above this value, the irradiation produced conic craters as deep as $\sim 20\text{-}30 \text{ } \mu\text{m}$, with epilayer and sapphire ablated together (see Fig. 5). At the bottom of the crater, microcracks were observed in sapphire. The corona of the crater contained dispersed re-deposited material at the distance up to $500 \text{ } \mu\text{m}$ from the crater rim. Obviously, deep heating of sapphire took place under irradiation, therefore the debris surrounding the crater likely contained Al_2O_3 (melted and solidified) from the substrate mixed with some Ga from dissociated epilayer. In this run of irradiation experiments, a visible flash was observed at the rear side of the structure, with a damage of sapphire rear surface occurring at the pulse energy significantly lower than the damage threshold at the front surface. The LIDT peak intensity was

estimated as $\sim 2.4 \text{ MW/cm}^2$ for the crater formation on the GaN/sapphire side and $\sim 1 \text{ MW/cm}^2$ for the damage of sapphire at the rear side.

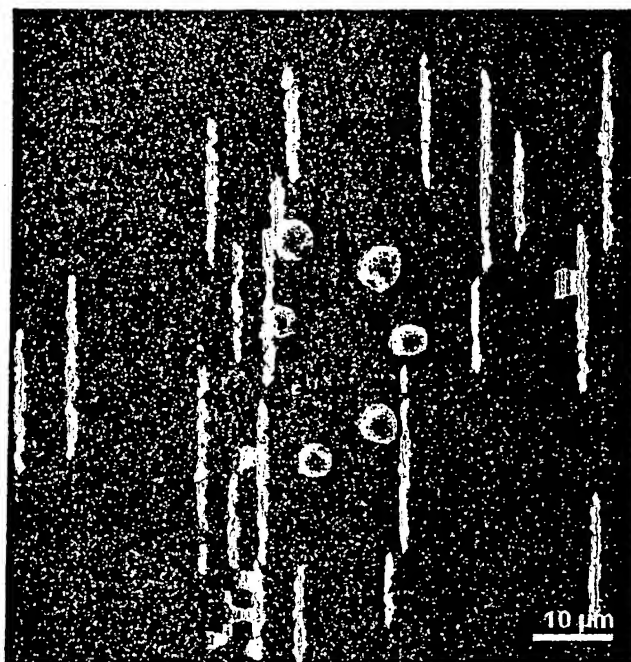


Fig. 1. Damaged site at the GaN epilayer surface under SEM inspection. Irradiation wavelength is $9.6 \mu\text{m}$. The laser irradiation fluence is $26 \pm 2 \text{ J/cm}^2$. Minor damage is caused by evaporation of nitrogen due to thermal decomposition of GaN and formation of excess Ga droplets on the surface.

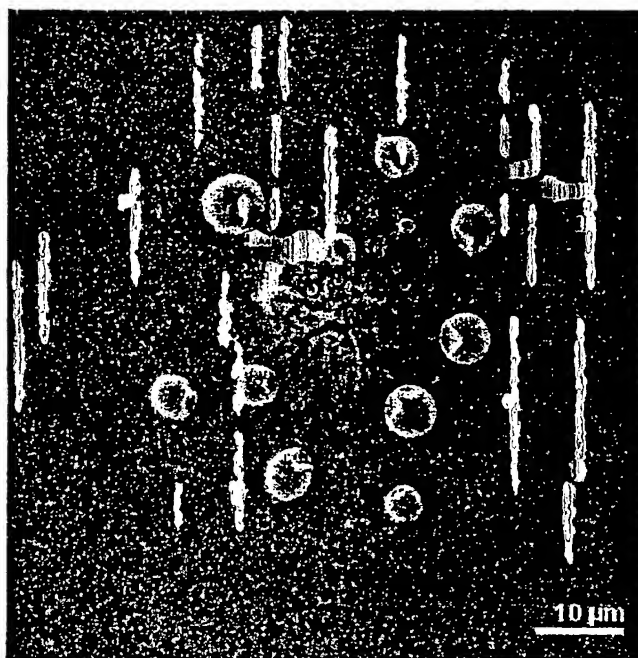


Fig. 2. Damaged site at a laser irradiation fluence slightly higher than in Fig. 1. Irradiation wavelength is $9.6 \mu\text{m}$. In addition to Ga droplets, microcracks appear at the center of the thinned epilayer, indicating significant thermal stress during the process.

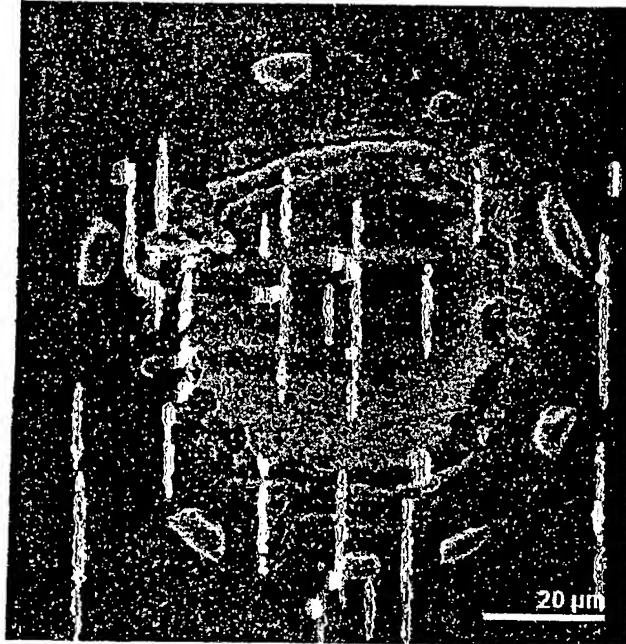


Fig. 3. Damaged site at a laser irradiation fluence of $48 \pm 2 \text{ J/cm}^2$. Irradiation wavelength is 9.6 μm . A "window" in the GaN epilayer is formed at the center, with some excess Ga droplets on peripheries.

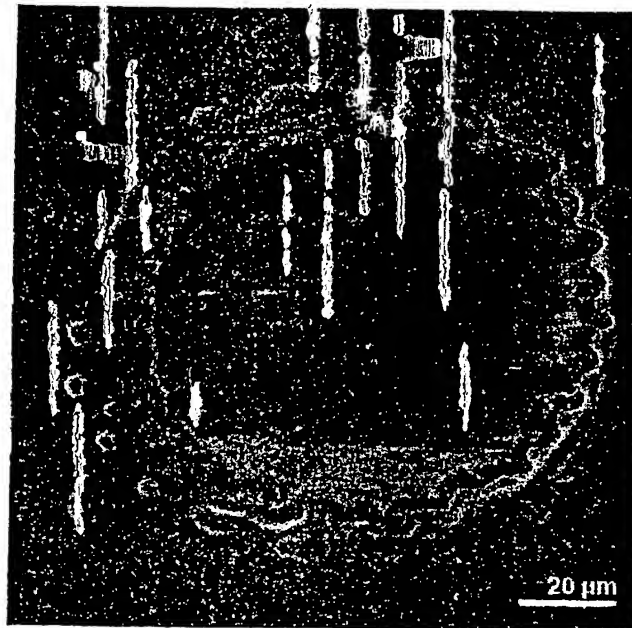


Fig. 4. Damaged site at a laser irradiation fluence of $83 \pm 3 \text{ J/cm}^2$. Irradiation wavelength is 9.6 μm . A full-diameter "window" in the GaN epilayer is formed. The SEM image in the non-conducting sapphire "window" is slightly distorted by bound charge.

Bandgap energies are 3.39 eV in GaN and 9.9 eV in sapphire. Both wavelengths under this investigation fall into the nominal transparency range of GaN and sapphire. However the material transparency is limited by free-carrier absorption (in GaN) and by lattice vibrations (in both). An extrapolation of free-carrier absorption data gives ~ 16

cm^{-1} at $5.1\text{ }\mu\text{m}$, 20 cm^{-1} at $5.65\text{ }\mu\text{m}$, and $\sim 60\text{ cm}^{-1}$ at $9.6\text{ }\mu\text{m}$. In sapphire, the IR absorption is estimated as $1\text{--}3\text{ cm}^{-1}$ at $5.0\text{--}5.8\text{ }\mu\text{m}$ and $>60\text{ cm}^{-1}$ at $9.6\text{ }\mu\text{m}$. In both materials, the absorption coefficient increases with increasing temperature. Therefore, after some initial heating both materials become poorly transparent. From rough heat balance, the energy density of $\sim 0.4\text{ J/cm}^2$ is sufficient to heat the $2\text{-}\mu\text{m}$ -thick epilayer adiabatically up to $\sim 850\text{ }^\circ\text{C}$, which leads to a rapid thermal dissociation of GaN. The GaN material does not melt under the atmospheric pressure (or even at high pressures up to some 10^3 atm). Therefore, a weak absorption in epilayer can supply sufficient heat generation for thermal etching. The energy density of $\sim 8\text{ J/cm}^2$ is needed to evaporate the epilayer totally, which suggests that a substantial part of incident light should be absorbed. An energy density of $\sim 10\text{ J/cm}^2$ is needed to heat and melt a $10\text{-}\mu\text{m}$ -thick layer of sapphire at its melting point of $\sim 2040\text{--}2045\text{ }^\circ\text{C}$, while $\sim 80\text{ J/cm}^2$ is needed to evaporate it (the boiling point is $3530\text{ }^\circ\text{C}$).

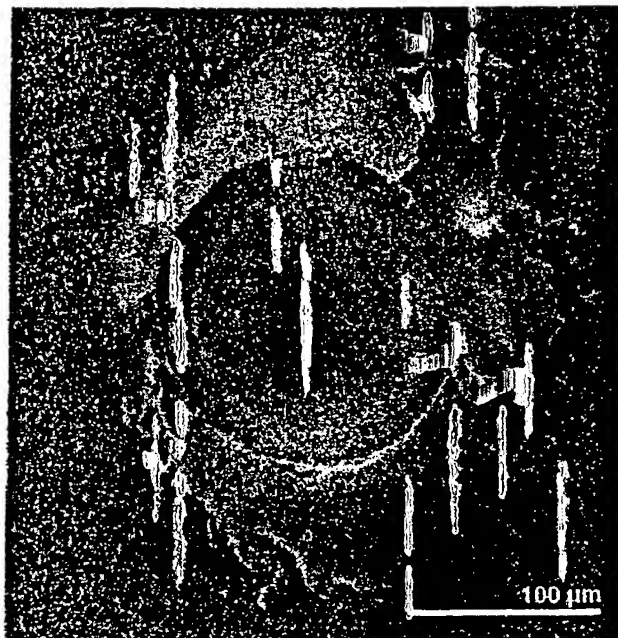


Fig. 5. Damaged site at the GaN epilayer surface under SEM inspection. Irradiation wavelength is $5.1\text{ }\mu\text{m}$. The laser irradiation fluence is 630 J/cm^2 . A crater is formed deeply in the sapphire substrate. Note that no damage was detected at 620 J/cm^2 .

The laser-induced damage under IR irradiation is of thermal nature. The case of CO_2 laser irradiation seems to be rather simple. The first step of the interaction is thermal decomposition of GaN into metallic Ga and gaseous N_2 . Gallium droplets are formed at the irradiated surface. There is no sharp threshold for this process. With increasing power density, the epilayer is thermally etched down to the substrate surface. Thus, the epilayer is selectively ablated at the second step with an opening of the sapphire surface. This surface is damaged by thermal elastic stress that produces some microcracks. Ablated material is partially re-deposited in a distance of up to $\sim 50\text{ }\mu\text{m}$ from the irradiated spot. It is quite probable that the heating is controlled by a linear absorption of GaN (rising up to $120\text{--}150\text{ cm}^{-1}$ at elevated temperatures), with no involvement of nonlinear mechanisms. The absorption in sapphire is also involved, but the substrate seems to be cooler than the epilayer, and some heat may be transported from the epilayer into the substrate. After the epilayer is removed, the substrate does not melt even at 5.5-times higher energy density, therefore the peak temperature does not exceed $2040\text{ }^\circ\text{C}$. Probably, screening of the substrate occurs due to the laser radiation absorption in the gaseous plasma appearing after the epilayer evaporation above the target surface. This can explain absence of severe damage of the sapphire substrate in the epilayer 'window'.

In contrast to CO_2 -laser experiments, the damage under CO-laser irradiation includes massive ablation of the sapphire substrate. Also, a more intense heating is expected in this case, as compared to CO_2 -laser irradiation, due to the larger pulsewidth. Conic craters are formed in this case and melted/resolidified sapphire is observed at the rim of the crater. There are no signs that the epilayer damage is selective, as the epilayer is ablated simultaneously with a larger amount of the substrate material. The linear absorption in the material is not sufficient to explain the extent of

the damage, and we suggest involvement of nonlinear absorption (probably, associated with a dielectric breakdown). It leads to the apparent threshold-like behavior with severe damage and ablation of the substrate. The distance of the heat diffusion during the laser pulse is 12-16 μm in the temperature range of 1500-2300 K. Therefore, a crater depth of this magnitude can be expected when the power is absorbed near the surface. The observed crater depth (20-30 μm) suggests the absorption length of ~ 10 μm . This value corresponds to the absorption coefficient of ~ 200 cm^{-1} . Thus, the absorption in sapphire should grow significantly during the irradiation. The maximum temperature in the irradiated site exceeds substantially the melting point of sapphire, whereas GaN is evaporated easily with no melting. The re-deposition of the ablation products is also substantial in this case, and this is associated with the ablation of sapphire and its partial deposition and solidification in the vicinity of the crater. Even under severe damage conditions, the fraction of pulse energy used for the heating of the structure remains to be small as compared with the incident energy (~ 12 -15%) and due to this fact, the damage and visible flash could be seen at the rear side of the sapphire substrate. The low fluence threshold of rear-side damage of sapphire ($\sim 40\%$ of the frontal surface damage) can be explained by effect of thermal lensing in the substrate, providing higher irradiation density at the beam exit. Also, the rear side surface can be of poorer quality than that on the front of the structure. No rear-surface damage has been observed under 9.6 μm irradiation, mainly due to higher bulk absorption in the structure at that wavelength.

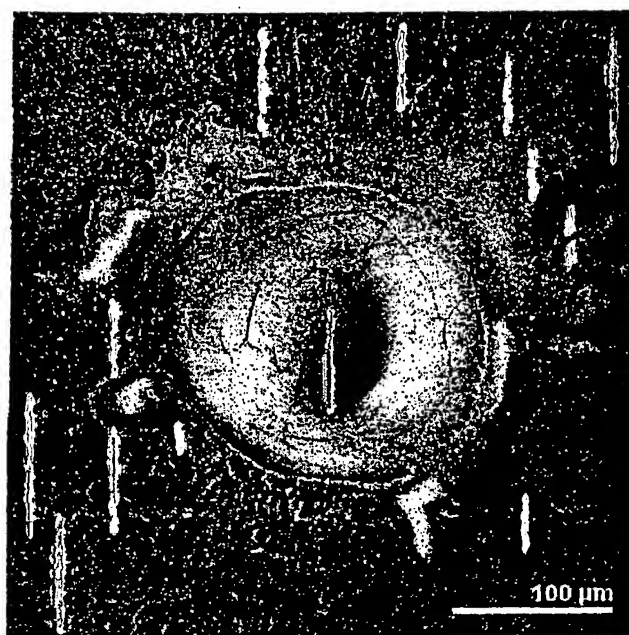


Fig. 6. Damaged site at the GaN epilayer surface under SEM inspection. Irradiation wavelength is 5.1 μm . The laser irradiation fluence is 890 J/cm^2 . Microcracks are seen on the ablation crater walls.

In conclusion to this section, the laser-induced damage of GaN epilayer on the sapphire substrate was investigated. The LIDT peak intensities were estimated as ~ 2.4 MW/cm^2 at 5.0-5.8 μm (crater formation) and ~ 1 MW/cm^2 at 9.6 μm (epilayer "window" formation). The damage had thermal nature. In case of irradiation at 9.6 μm wavelength, thermal decomposition of GaN occurred below the threshold and full ablation of GaN above it. Under irradiation at 5.0-5.8 μm wavelength, conic craters (indicating ablation of both the epilayer and the substrate materials) were formed. The laser ablation under 9.6- μm irradiation is suitable for thermal etching and for processing of nitride epilayers. In contrast, irradiation at 5.0-5.8 μm produces strongly nonlinear processes, hence it seems to be difficult to control and less attractive for material processing applications.

5. SURFACE PROCESSING OF GaN WITH SUB-PICOSECOND LASER IRRADIATION

With shortening of laser irradiation pulsewidth, the LIDT power goes up, and high-order nonlinear interactions become involved. Ultrafast ablation is more suitable for laser processing of the GaN surface due to a congruent

removal of both nitrogen and gallium products of thermal decomposition. A clean pattern of ablated pits on GaN was demonstrated in [Eliseev 1999]. The undoped GaN on sapphire samples used in these experiments were grown by atmospheric-pressure MOCVD at the University of Tokushima. The thickness of the GaN epilayer was about 3 μm . Laser irradiation at 400 nm was obtained by frequency doubling of pulses from a Tsunami mode-locked Ti:sapphire laser pumped by a Beamlok 2080 Ar-ion laser and operating at 800 nm. The system delivered sub-picosecond pulses (150 fs FWHM) at a repetition rate of 1 kHz. The laser pulse energy was changed by calibrated neutral filters, which allowed the irradiation energy to be adjusted with a constant light path. The emission was focused into a diffraction limited spot on the GaN layer surface, and the spot size for the round aperture was ~ 900 nm.

The critical value of pulse energy for ablation damage under 400-nm irradiation was found to be 34 ± 4 nJ from an optical transmission evaluation. It corresponds to a rather high fluence of ~ 5.4 J/cm², with a peak LIDT intensity of ~ 36 TW/cm². The depth of the pit ranged from 20 to 240 nm, depending on the incident pulse energy. Profiling by atomic force microscopy (AFM) indicated little material accumulation at the rim of the damaged spot [Eliseev 1999]. Therefore, the process of the material removal was mainly in the form of gaseous nitrogen and some nitride and oxide molecules, rather than by droplets.

When the wavelength of incident beam was changed from 400 nm to 795 nm (with the pulsewidth increased to ~ 150 fs), the LIDT pulse energy increased to 65 nJ [Sun 1999], [Eliseev 2000].

The critical pulse energy for GaN is compared in Table 3 with that in other optical materials with large bandgap energies. The optical damage in each material was induced under the same conditions (optical path, focusing, LIDT criterion). Compared to other high-transparency dielectrics, the LIDT for GaN was found to be the lowest. The increase of LIDT seems to correlate well with increasing bandgap energy.

Table 3. Experimental data on the laser-induced damage threshold (LIDT) as measured in terms of pulse energy under similar conditions of laser irradiation

Material	Formula	Bandgap energy [eV]	Pulse energy LIDT [nJ]
Gallium nitride (epilayer on sapphire substrate)	GaN	3.4	34
Germanium-doped silica	SiO ₂ :Ge	5.5*	177
Sapphire	Al ₂ O ₃	5.8	247
Vitreous silica	SiO ₂	9	710

* Absorption band of Ge-related defects

6. LASER LIFT-OFF TECHNIQUE

An important issue in the technology of nitride-based semiconductor devices is growth of epitaxial multilayer structures on heterogeneous substrates. The origin of this issue is the lack of bulk nitride single crystals, other than small and expensive platelets. Most of commercially produced device structures are grown on sapphire substrates. The lattice misfit is huge in this case, and this causes a rather poor crystalline quality of epilayers. This is a unique case in solid-state electronics that semiconductor material with extremely high dislocation density appears to be still useful for device fabrication. Meanwhile, there are other issues with sapphire substrates. First of all, sapphire is an electrically insulating material, therefore all devices should be designed with all electrical contacts at the top-side of the chip. Second issue is that sapphire and nitride have different crystallographic planes of easy cleavage. Therefore, a simple cleavage technique used commonly in the diode laser fabrication is not available for nitride structures grown on sapphire. Hence, a laser-based technique for post-growth separation of nitride structures from insulating heterogeneous substrates is very attractive. A technique of a non-destructive laser lift-off separation has been developed and demonstrated in [Kelly 1997], [Wong 1998], [Tavernier 1999], [Wong 1999a], [Wong 1999b], [Tavernier 2000], [Stach 2000], [Wong 2000], [Wong 2001], [Kneissl 2001]. It is based on selective absorption of UV laser emission on the nitride-side of the nitride-sapphire interface, in the highly defective buffer layer. The emission should be in the range where sapphire is quite transparent, whereas GaN is strongly absorbing (between ~ 350 and ~ 150 nm). Some excimer lasers are available in this spectral range.

Short-pulse heating produces a decomposition of a thin GaN layer into metallic Ga and gaseous nitrogen. Uniform decomposition by laser irradiation produces an intermediate Ga-rich layer. Ga melts above 30 °C, therefore moderate heating is sufficient to separate mechanically the GaN layer from sapphire substrate. As the GaN layer (with device heterostructure) is very thin, it is attached preliminarily to another holder that could be electrically conducting, for example, a copper slab. The slab can then be used as an electrode and a heat sink for the nitride-based device. Thus, the laser lift-off procedure can be used to transfer a thin-layer group-III nitride heterostructure from a non-conducting substrate onto a conducting substrate.

At the KrF excimer laser wavelength of 248 nm, the excitation is of surface nature, and the temperature at the surface of laser-irradiated GaN should depend on the fluence and time. As was mentioned above, to heat the surface up to ~800 °C (the temperature of thermal instability of GaN), the laser fluence should be ~0.2 J/cm² (30-ns long pulse). In experiments with excimer laser irradiation, the fluence of 0.3 J/cm² was sufficient to notice some change of the interface appearance, but for separation of the GaN layer a higher fluence of 0.4-0.6 J/cm² was necessary [Wong 2000]. The corresponding temperature rise at the irradiated surface was 1500-2000 °C, and the thickness of the heated region was estimated as ~800 nm.

In our laser lift-off experiments, we used KrF excimer laser. The single-shot fluence of 0.6-1.0 J/cm² was sufficient to achieve the epilayer separation, and near ~1 J/cm² the separation occurred just under irradiation (by pressure of excess nitrogen), with no need for additional heating procedure. Some degradation of the x-ray rocking curve was observed with the linewidth increasing from 264" in the initial state to 278", 293" and 340" after irradiation at 0.4, 0.52 and 0.76 J/cm², respectively. This can be explained by influence of the disordered material at the irradiated surface. The morphology of the surface is illustrated by Fig. 7 of sample after a heavy irradiation (~1 J/cm²). Round spots are traces of metallic gallium accumulated after nitride decomposition. The gallium droplets were removed by etching in HCl. The nitride epilayer was transferred onto a Si substrate.

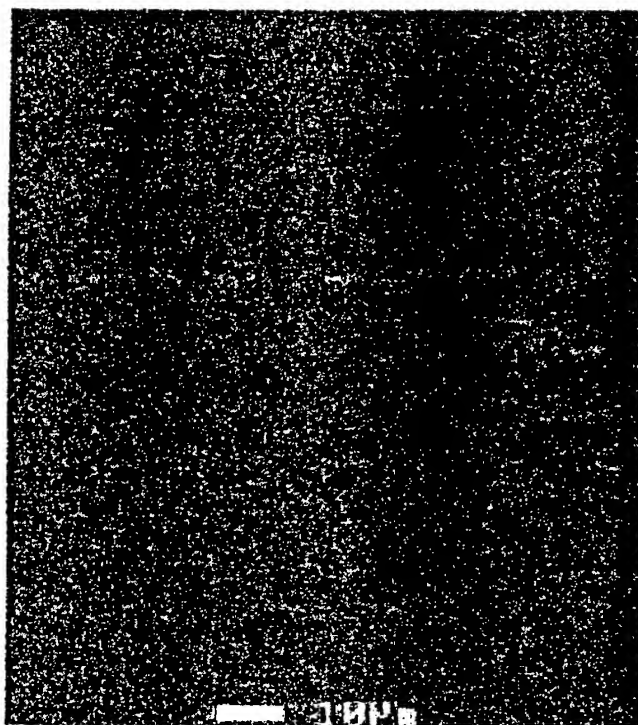


Fig. 7. SEM image of GaN epilayer after exposure to KrF excimer laser beam (wavelength 248 nm, pulsewidth 20 ns, fluence ~1 J/cm²). During the irradiation, the epilayer separated from sapphire substrate and then it was cleaned from residual gallium.

7. INTERACTION OF LASER LIGHT WITH GaN/SAPPHIRE STRUCTURES

The experimental results presented here focus on laser-induced thermal etching of GaN, surface-processing and damage patterns under high-power laser irradiation. Mechanisms of laser heating and laser-induced damage in these materials are sensitive to the wavelength. In the nominal transparency range (at the photon energy smaller than the energy bandgap), there is lattice-vibration mode absorption (in both GaN and sapphire) and also free-carrier absorption (in GaN, but not in sapphire). The absorption in sapphire increases strongly above the wavelength of $\sim 6 \mu\text{m}$ due to lattice vibration, whereas in GaN the absorption due to free carriers increases gradually with increasing wavelength. At very high-intensity irradiation, the nonlinear absorption appears, therefore absorption in the nominal transparency region can be much higher.

Surface absorption. The intrinsic absorption edge is about 125 nm for sapphire and ~ 355 nm for GaN. For irradiation through the transparent substrate, but with interband absorption in GaN, the wavelength range of 150-350 nm is therefore available. There is some temperature dependence of the semiconductor bandgap, and the sapphire background absorption is also temperature-sensitive. For example, at 600 K the intrinsic absorption edge of GaN shifts to ~ 380 nm. The surface of GaN becomes unstable at elevated temperatures due to thermal decomposition of the compound. From usual annealing experiments in gaseous ambient, the temperature of fast thermal decomposition is 1100-1200 °C [Hayes 1999]. In other experiments, signs of decomposition were observable at ~ 800 °C [Lin 1993]. In order to reach this temperature, the laser irradiation fluence of $\sim 0.2 \text{ J/cm}^2$ should be sufficient during 30 ns at a high-absorption wavelength. This is a 'threshold' fluence for irreversible modification of the surface. Hence, non-destructive laser annealing should be conducted below the 'threshold'. Note that melting of GaN does not occur under excessive heating, but it is preceded by thermal decomposition of the compound. High pressure is necessary to melt the GaN compound that does not exist in a liquid form at atmospheric pressure. Therefore, the irreversible process under higher laser fluence is associated mainly with thermal decomposition of GaN. Products of the decomposition are excess gallium as a metal and nitrogen gas that escapes into surrounding atmosphere. Hence, gallium droplets on the treated surface can be an indication of some decomposition occurrence. Excess gallium can be removed by etching that does not attack the GaN surface. Thus, laser-induced "thermal etching" can be used for surface processing of nitride semiconductors.

Irradiation in the transparency region. Irradiation in the nominal transparency region of GaN can be characterized by a long absorption distance for regular (linear) absorption. This leads to a lower surface temperature and more bulky heating under the same fluence, as compared with surface absorption. However, at sufficiently high laser intensity, nonlinear absorption mechanisms switch on. The absorption distance becomes intensity-dependent, and the heating process becomes governed by a complicated dynamics. In our experiments, various wavelengths were used, ranging from 398 nm (second harmonic of Ti-sapphire laser) to $9.6 \mu\text{m}$ (CO_2 laser), all in the nominal transparency region of GaN. The threshold for irreversible damage of the surface was determined. For example, the irradiation at $9.6 \mu\text{m}$ produced no damage below the fluence of $\sim 26 \text{ J/cm}^2$ (0.1-magnitude pulsewidth of 30 μs). The "thermal etching" is seen between 26 and $\sim 33 \text{ J/cm}^2$. Ga droplets indicate that decomposition occurs. At higher fluence, the entire depth of the epilayer is evaporated, with a "window" formation in the structure with virtually unaffected sapphire substrate. The power threshold for total removal of the epilayer was estimated to be 0.9 MW/cm^2 , corresponding to almost linear heating of the epilayer by the laser emission.

Interaction with subpicosecond laser pulses at ~ 400 nm was very different. These pulses produced surface heating, in spite of nominal transparency of the material. The power threshold for the pit formation was determined to be 36 TW/cm^2 for 150-fs pulsewidth (single-shot experiment). The above-threshold damage took form of clean pits with depth up to $0.5 \mu\text{m}$. The energy consumption for GaN ablation was estimated as $\sim 1 \text{ nJ/nm}$, with a diameter of the irradiated spot of ~ 200 nm. The minimal pit depth of ~ 20 nm suggests a very strong absorption of the ultrahigh-power laser light in the nominally transparent medium. Under terawatt power, multiphoton processes seem to be responsible for this.

8. CONCLUSIONS

In this paper, we have considered some applications of laser technology to novel semiconductor materials – group-III nitrides that are hard and inert, focusing in particular on optically induced annealing, surface processing, and laser lift-off technique. An important subject is laser-induced damage threshold (LIDT) that can be very different for various conditions of laser irradiation. Summarized results on the LIDT of GaN epilayers are given in Table 4. The

interaction processes specific for GaN are thermal decomposition ("thermal etching") and ablation. There is no melting of the target under laser emission. Thermal decomposition under long laser pulses is accompanied with accumulation of group-III element in a metal droplet form.

Table 4. Summary of laser irradiation effects on GaN.

Procedure	Wavelength, nm	Pulsewidth at 0.1 magnitude	Mechanism of interaction	LIDT, J/cm ²
Laser lift-off	248	30-50 ns	intrinsic absorption and thermal decomposition	0.3
Laser ablation	400 800	0.15 ps ~0.2-0.3 ps	Nonlinear absorption and ablation	5.4
Laser ablation	5600	255 μ s	Nonlinear absorption and ablation including ablation of the substrate	620
Laser "thermal etching"	9600	30 μ s	Both linear and nonlinear absorption and thermal decomposition	26

The cleanest pattern of ablation has been obtained with sub-picosecond pulse irradiation. Feasibility of different laser technologies has been demonstrated by a variety of research groups: laser-induced "thermal etching", precise surface processing, laser annealing of ion implanted material, laser-induced acceptor activation, laser lift-off (separation from an insulated substrate), laser-induced total removal of the epilayer (making windows in the epilayer), and laser-induced "scribing" (by crater formation involving substrate material).

ACKNOWLEDGMENTS

The authors are grateful to Richard P. Schneider of Agilent Laboratories, Palo Alto, CA, for providing GaN samples used in high power IR laser irradiation experiments. Part of this work was supported by Russian Federation state program "Integration". Part of this work conducted at the University of New Mexico was supported by DARPA under the Optoelectronic Materials Center program, and by AFOSR under the Optoelectronic Research Center program.

REFERENCES

- [Cheng 2001] Y.-C. Cheng, C.-C. Liao, S.-W. Feng, C.-C. Yang, Y.-S. Lin, K.-J. Ma, and J.-I. Chyi, "Activation of *p*-type GaN with irradiation of the second harmonics of a Q-switched Nd:YAG laser", *Phys. Stat. Sol.*, (b), vol. 228 (#2), pp. 357-360, 13 Nov. 2001.
- [Cohen 1998] D. A. Cohen, T. Margalith, A. C. Abare, M. P. Mack, L. A. Coldren, S. P. DenBaars, and D. R. Clarke, "Catastrophic optical damage in GaInN multiple quantum wells", *Appl. Phys. Lett.*, vol. 72 (#25), pp. 3267-3269, 22 June 1998.
- [Eliseev 1999] P. G. Eliseev, H. B. Sun, S. Juodkakis, T. Sugahara, S. Sakai, and H. Misawa, "Laser-induced damage threshold and surface processing of GaN at 400 nm wavelength", *Jpn. J. Appl. Phys.*, Pt. 2 (Lett.), vol. 38 (#7B), pp. L839-L841, 15 July 1999.
- [Eliseev 2000] P. G. Eliseev, S. Juodkakis, T. Sugahara, H.-B. Sun, S. Matsuo, S. Sakai, and H. Misawa, "GaN surface ablation by femtosecond pulses: Atomic force microscopy studies and accumulation effects", in "High-Power Laser Ablation III (C. R. Phipps, Ed.), 24-28 April 2000, Santa Fe, NM, *Proc. SPIE*, vol. 4065, pp. 546-556.
- [Hayes 1999] J. M. Hayes, M. Kuball, A. Bell, I. Harrison, D. Korakakis, and C. T. Foxon, "High temperature processing of GaN, "The influence of the annealing ambient on strain in GaN", *Appl. Phys. Lett.*, vol. 75 (#14), pp. 2097-2099 (1999).
- [Herrera Zaldivar 1999] M. Herrera Zaldivar, P. Fernandes, J. Piqueras, and J. Solis, "Effect of laser irradiation on the luminescence of Mg and Si-doped GaN films", *J. Appl. Phys.*, vol. 85 (#2), pp. 1120-1123, 15 Jan. 1999.
- [Kelly 1996] M. K. Kelly, O. Ambacher, B. Dahlheimer, G. Groos, R. Dimitrov, H. Angerer, and M. Stutzmann, "Optical patterning of GaN films", *Appl. Phys. Lett.*, vol. 69 (#12), pp. 1749-1751, 16 Sept. 1996.
- [Kelly 1997] M. K. Kelly, O. Ambacher, R. Dimitrov, R. Handschuh, and M. Stutzmann, "Optical process for liftoff of group III-nitride films", *Phys. Stat. Sol.*, (a) vol. 159 (#1), pp. R3-R4, 1997.

- [Kim 2001] D.-J. Kim, H.-M. Kim, M.-G. Han, Y.-T. Moon, S.-H. Lee, and S.-J. Park, "Activation of Mg acceptor in GaN:Mg with pulsed KrF (248 nm) excimer laser irradiation", *Phys. Stat. Sol. (b)*, vol. 228 (#2), pp. 375-378, 13 Nov. 2001.
- [Kneissl 2001] M. Kneissl, W. S. Wong, D. W. Treat, M. Teepe, N. Miyashita, and N. M. Johnson, "Continuous-wave operation of InGaN multiple-quantum-well laser diodes on copper substrates obtained by laser liftoff", *IEEE J. Select. Topics Quantum Electron.*, vol. 7 (#2), pp. 188-191, March-April 2001.
- [Krukowski 1999] S. Krukowski, M. Leszczyński, and S. Porowski, "Thermal properties of the group III nitrides", in *Properties, Processing and Applications of GaN and Related Semiconductors* (J. H. Edgar, S. Strite, I. Akasaki, H. Amano, and C. Wetzel, Eds.), Ch. A1.4, INSPEC, IEE, London, UK (1999).
- [Lin 1993] M. E. Lin, B. N. Sverdlov, and H. Morkoç, "Thermal stability of GaN investigated by low-temperature photoluminescence spectroscopy", *Appl. Phys. Lett.*, vol. 63 (#26), pp. 3625-3627, 27 Dec. 1993.
- [Mohammad 1996] S. N. Mohammad and H. Morkoç, "Progress and prospects of group-III nitride semiconductors", *Prog. Quantum Electron.*, vol. 20 (#5/6), pp. 361-525, Dec. 1996.
- [Nakamura 1997] S. Nakamura and G. Fasol, *The Blue Laser Diode: GaN Based Light Emitters and Lasers*, Springer-Verlag, Berlin 1997.
- [Newman 1998] N. Newman, "Thermochemistry of III-N Semiconductors", in *Gallium Nitride (GaN) I* (J. I. Pankove and T. D. Moustakas, Eds.), *Semiconductors and Semimetals*, vol. 50, Ch. 4, pp. 55-101, Academic Press, San Diego 1998.
- [Stach 2000] E. A. Stach, M. Kelsch, E. C. Nelson, W. S. Wong, T. Sands, and N. W. Cheung, "Structural and chemical characterization of free-standing GaN films separated from sapphire substrates by laser lift-off", *Appl. Phys. Lett.*, vol. 77 (#12), pp. 1819-1821, 18 Sept. 2000.
- [Sun 1999] H.B. Sun, S. Juodkazis, P.G. Eliseev, T. Sugahara, T. Wang, S. Matsuo, S. Sakai, and H. Misawa, "Laser-induced damage threshold and laser processing of GaN", in *High-Power Laser Ablation II* (C. R. Phipps, M. Niino, Eds.), 1-5 Nov. 1999, Osaka, Japan, *Proc. SPIE*, Vol. 3885, pp. 311-322.
- [Tavernier 1999] P. R. Tavernier, P. M. Verghese, and D. R. Clarke, "Photoluminescence from laser assisted debonded epitaxial GaN and ZnO films", *Appl. Phys. Lett.*, vol. 74 (#18), pp. 2678-2680, 3 May 1999.
- [Tavernier 2000] P. R. Tavernier and D. R. Clarke, "Mechanics of laser-assisted debonding of films", *J. Appl. Phys.*, vol. 89 (#3), pp. 1527-1536, 1 Feb. 2000.
- [Wong 1996] W. S. Wong, L. F. Schloss, G. S. Sudhir, B. P. Linder, K.-M. Yu, E. R. Weber, T. Sands, and N. W. Cheung, "Pulsed excimer laser processing of AlN/GaN thin films", in *III-V Nitrides* (F. A. Ponce, T. D. Moustakas, I. Akasaki, and B. A. Monemar, Eds.), 2-6 Dec. 1996, Boston, MA, *MRS Symp. Proc.*, vol. 449, pp. 1011-1016.
- [Wong 1998] W. S. Wong, T. Sands, and N. W. Cheung, "Damage-free separation of GaN thin films from sapphire substrates", *Appl. Phys. Lett.*, vol. 72 (#5), pp. 599-601, 2 Feb. 1998.
- [Wong 1999a] W. S. Wong, T. Sands, N. W. Cheung, M. Kneissl, D. P. Bour, P. Mei, L. T. Romano, and N. M. Johnson, "Fabrication of thin-film InGaN light-emitting diode membranes by laser lift-off", *Appl. Phys. Lett.*, vol. 75 (#10), pp. 1360-1362, 6 Sept. 1999.
- [Wong 1999b] W. S. Wong, A. B. Wengrow, Y. Cho, A. Salleo, N. J. Quitoriano, N. W. Cheung, and T. Sands, "Integration of GaN thin films with dissimilar substrate materials by Pd-In metal bonding and laser liftoff", *J. Electron. Mat.*, vol. 28 (#12), pp. 1409-1413, Dec. 1999.
- [Wong 2000] W. S. Wong, T. Sands, N. W. Cheung, M. Kneissl, D. P. Bour, P. Mei, L. T. Romano, and N. M. Johnson, "In_xGa_{1-x}N light emitting diodes on Si substrates fabricated by Pd-In metal bonding and laser lift-off", *Appl. Phys. Lett.*, vol. 77 (#18), pp. 2822-2824, 30 Oct. 2000.
- [Wong 2001] W. S. Wong, M. Kneissl, P. Mei, D. W. Treat, M. Teepe, and N. M. Johnson, "Continuous-wave InGaN multiple-quantum-well laser diodes on copper substrates", *Appl. Phys. Lett.*, vol. 78 (#9), pp. 1198-1200, 26 Feb. 2001.

PROCEEDINGS OF SPIE



SPIE—The International Society for Optical Engineering

High-Power Laser Ablation IV

Claude R. Phipps
Chair/Editor

22–26 April 2002
Taos, USA

Sponsored by
SPIE—The International Society for Optical Engineering

Cosponsored by
Los Alamos National Laboratory (USA)
U.S. Air Force Windows on Science Program



Volume 4760

Part One of Two Parts

search Association (FESTA), which is supported by the New Energy and Industrial Technology Development Organization (NEDO).

References

1. A. Neogi, H. Yoshida, T. Mozume, N. Georgiev, T. Akiyama and O. Wada, "Inter-subband transition in InGaAs/AlAsSb/InP coupled double quantum well structures optimized for communication wavelength operation," *Electron. Lett.* 36, 1972 (2000).
2. C. Gmachl, H.M. Ng, S.-N.G. Chu and A.Y. Cho, "Intersubband absorption at $\lambda \sim 1.55$ μm in well- and modulation-doped GaN/AlGaIn multiple quantum wells with superlattice barriers," *Appl. Phys. Lett.* 77, 3722 (2000).
3. N. Iizuka, K. Kaneko, N. Suzuki, T. Asano, S. Noda and O. Wada, "Ultrafast intersubband relaxation (<150 fs) in AlGaIn/GaN multiple quantum wells," *Appl. Phys. Lett.* 77, 648 (2000).
4. C. Gmachl, S.V. Frolov, H.M. Ng, S.-N.G. Chu and A.Y. Cho, "Sub-picosecond electron scattering time for $\lambda \sim 1.55$ μm intersubband transitions in GaN/AlGaIn multiple quantum wells," *Electron. Lett.* 37, 378 (2001).
5. C. Gmachl, H.M. Ng and A.Y. Cho, "Intersubband absorption in degenerately doped GaN/Al_xGa_{1-x}N coupled double quantum wells," *Appl. Phys. Lett.* 79, 1590 (2001).

CFG2

10:30 am

Characterization of MOCVD-grown InNAs/GaAs Quantum Wells

Hongjun Cao, Noppadon Nuntawong, Abdel-Rahman A. El-Emawy, and Marek Osiński, Center for High Technology Materials, University of New Mexico, 1313 Goddard SE, Albuquerque, New Mexico 87106-4343, Email: osinski@chtm.unm.edu

1. Introduction

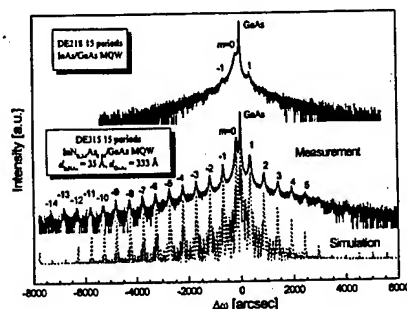
The In_xAs_{1-x} alloy is a very promising material for mid-infrared (3–8 μm) emitters and detectors. With a single exception of recently reported MOCVD growth of InNAs using plasma-cracked ammonia source,¹ all studies of InNAs utilized plasma-source MBE^{2,3} and related techniques, such as gas-source MBE.⁴ In this paper, we report a successful MOCVD growth of InNAs using dimethylhydrazine (DMHy) as nitrogen source.

As with other dilute nitrides, the In_xAs_{1-x} bandgap was predicted to shrink with increasing nitrogen content,^{5,6} although so far this has been confirmed experimentally only for $x < 6\%$.⁴ In_xAs_{1-x} can be lattice-matched to GaAs when $x = 38\%$.² The large band offsets between InNAs and GaAs barriers makes it particularly attractive for reducing temperature sensitivity of mid-IR lasers.

2. MOCVD growth and structural characterization

InNAs/GaAs multiple-quantum-well (MQW) samples were grown on (100) GaAs at 500 °C and 60 Torr using trimethylindium, trimethylgallium, arsine, and DMHy. The wells were grown using tertiarybutylarsine with 95–97.5% nitrogen in the vapor phase.

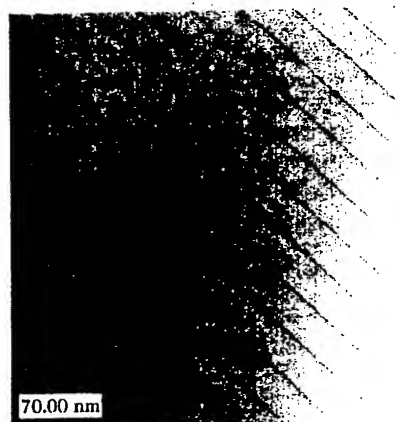
Crystalline quality, composition, and thicknesses of grown layers were investigated by high-



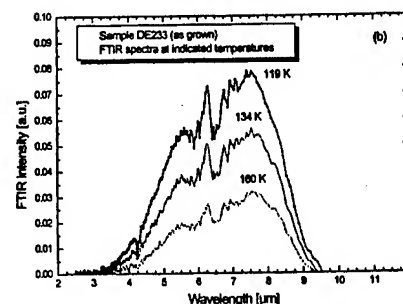
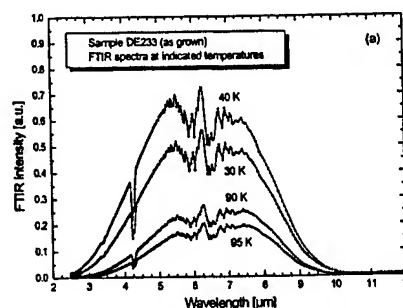
CFG2 Fig. 1. ω -2 θ scans of (004) reflections for 15-period MQW samples with InAs wells (top scan) and InNAs wells (middle scan). Dotted scan in represents simulated HRXRD spectrum. The FWHM of the $m = 0$ InNAs peak (middle scan) is 43 arcsec, which together with a clearly resolved spectrum displaying up to 14 diffraction orders indicates high crystalline quality of the sample. The FWHM of the $m = -3$ satellite peak of sample DE315 is 47 arcsec, comparing very favorably to 280 arcsec in In_{0.06}As_{0.94}/InGaAsP MQWs grown on InP.⁴ The satellite peaks wash out in the case of InAs/GaAs MQWs (top scan), revealing poorer interface flatness and partial relaxation.

resolution x-ray diffraction (HRXRD). Fig. 1 shows HRXRD spectra for two MQW structures grown under otherwise identical conditions, except for the presence of DMHy during the well layer growth. Sample DE218 (top scan) contained InAs/GaAs well layers, while sample DE315 (middle scan) contained InNAs/GaAs MQWs. Comparison of the two scans clearly reveals improvement in quality of the nitrogen-containing sample, which we attribute to a reduced lattice-constant mismatch between InNAs and GaAs. High quality of InNAs/GaAs MQWs is also confirmed by cross-sectional TEM measurements, illustrated in Fig. 2.

HRXRD spectra of sample DE315 were analyzed assuming cubic InN and InAs lattice parameters. As shown in Fig. 1, nitrogen composition of 34% resulted in a very good fit. Using the same simulation, the well and barrier layer thicknesses were determined as 3.5 nm and 33.3 nm, respectively.



CFG2 Fig. 2. Cross-sectional TEM image of 15-period InNAs/GaAs MQW sample DE315.



CFG2 Fig. 3. Photoluminescence spectra of sample DE233 containing a triple-quantum-well 5-nm In_{0.72}N_{0.18}As/37.5-nm GaAs structure. The temperatures indicated are actual sample temperatures determined by using the Varshni formula for PL emission peak from a bulk InSb sample placed in the cryostat, determining Varshni parameters for InNAs, and extrapolating beyond InSb emission temperatures. The dip at 4.26 μm is due to CO₂ absorption, while the broad minima near 5.9 and 6.5 μm are caused by water vapor absorption in the ambient atmosphere. The maximum at 6.3 μm coincides with water vapor transmission window.

3. Photoluminescence measurements

The PL setup included a 7.5-W Ar-ion laser pumping a tunable Ti:sapphire laser, and an FTIR spectrometer. The output power from the Ti:sapphire laser tuned to 890 nm was 320 mW, illuminating a spot with ~ 1 mm diameter.

Rather than relying on temperature-controller readings, we used a bulk InSb sample for in-situ temperature calibration of illuminated sample. Fig. 3 shows the measured PL spectra for sample temperatures ranging from 30 to 160 K. At 30 K, the peak emission wavelength was ~ 6.5 μm (190 meV), and the FWHM of the PL spectrum was ~ 3.5 μm (110 meV). Clear PL signals ~ 7 μm , with FWHM narrowing down to ~ 2 μm (~ 65 meV), were observed up to 160 K.

Recently, InNAs band structure calculations were reported,⁶ considering various possible arrangements of group-V atoms around an In atom. For 17.6% nitrogen content, bandgaps ranging from 8 meV for maximally nitrogen-rich clusters to 251 meV for maximally As-rich clusters were predicted. This wide bandgap range is consistent with our observation of broad PL emission spectra (Fig. 3). It is also very promising for widely tunable mid-IR lasers.

References

1. H. Naoi, D.M. Shaw, Y. Naoi, G.J. Collins, and S. Sakai, "Growth of InNAs by low-pressure metalorganic chemical vapor deposition employing microwave-cracked nitrogen and in

situ generated arsine radicals", J. Cryst. Growth 222, 511-517 (2001).

- Y.C. Kao, T.P.E. Broekaert, H.Y. Liu, S. Tang, I.H. Ho, and G.B. Stringfellow, "Lattice-matched InAsN ($x = 0.38$) on GaAs grown by molecular beam epitaxy", in *III-Nitride, SiC and Diamond Materials for Electronic Devices*, D.K. Gaskill, C.D. Brandt, and R.J. Nemanich, eds., 8-12 April 1996, San Francisco, CA, MRS Symp. Proc. 423, 335-340 (1996).
- R. Beresford, K.S. Stevens, and A.F. Schwartzman, "Microstructure and composition of InAsN alloys grown by plasma-source molecular beam epitaxy", J. Vac. Sci. & Technol. B 16, 1293-1296 (1998).
- J.-S. Wang, H.-H. Lin, L.-W. Song, and G.-R. Chen, "Growth of InAsN/InGaAs(P) quantum wells on InP by gas source molecular beam epitaxy", J. Vac. Sci. & Technol. B 19, 202-206 (2001).
- T. Yang, S. Nakajima, and S. Sakai, "Tight-binding calculation of electronic structures of InNAs ordered alloys", Jpn. J. Appl. Phys., Pt. 2 36, L320-L322 (1997).
- N. Tit and M.W.C. Dharma-wardana, "Electronic structure of $\text{InN}_{1-x}\text{As}_x$ alloys from tight-binding calculations", Appl. Phys. Lett. 76, 3576-3578 (2000).

CFG3

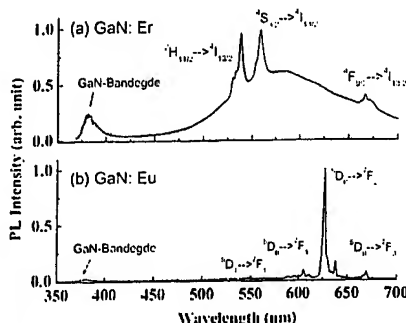
10:45 am

Spectroscopic Evaluation of Rare Earth Doped GaN for Full-color Display Applications

Ei Ei Nyein and U. H  mmerich, Department of Physics, Hampton University, Hampton, VA 23668, *Email: uwe.h  mmerich@hamptonu.edu
J. Heikenfeld, D.S. Lee, and A.J. Steckl, Nanoelectronics Laboratory, University of Cincinnati, Cincinnati, Ohio 45221

J.M. Zavada, U.S. Army Research Office, Research Triangle Park, NC 27709

Rare earth doped semiconductors have been studied for more than a decade because of the possibility to develop compact and efficient electroluminescence devices.^{1,2} Previous work has mainly focused on the infrared (1.54 μm) emission from Er^{3+} ions in III-V's and Si based materials for applications in optical communications. The recent observation of visible emission from RE doped GaN has spurred interest in this class of materials for applications in phosphor technology.^{3,4}



CFG3 Fig. 1. Room temperature photoluminescence spectra of GaN:Er and GaN:Eu excited with the 325 nm output of a HeCd laser.

We are currently engaged in a spectroscopic evaluation of Er doped GaN and Eu doped GaN as phosphor materials. The investigated samples were grown by solid-source molecular beam epitaxy on Si (111) substrates. An overview of the room-temperature emission spectra from both samples is shown in figure 1. Under above-gap pumping, GaN bandedge emission located near 365 nm, yellow-band emission centered around ~550 nm, and characteristic green (~537, 558 nm) and red emission lines (~622 nm) were observed from Er^{3+} and Eu^{3+} , respectively. Integrated PL intensity studies revealed that the green emission from GaN:Er was quenched by ~40% as the temperature increased from 15 to 300 K. The red emission from GaN:Eu decreased more rapidly for the same temperature range and was quenched by ~90% at room temperature. On the contrary, temperature dependent lifetime measurements suggest that non-radiative decay processes only weakly affect the intra-4f rare earth luminescence in both systems. The observed PL quenching is therefore attributed to a temperature dependence of the carrier-mediated energy transfer process from the semiconductor host to the rare earth center. A more detailed discussion of the luminescence properties of GaN:Er and GaN:Eu in terms of emission efficiency, rare-earth site occupation, and rare earth concentration will be presented at the conference.

References

- G.S. Pomrenke, P.B. Klein, and D.W. Langer, *Rare Earth Doped Semiconductors*, Material Research Society Symposium Proceedings, Vol. 301, Material Research Society, Pittsburgh, 1993.
- S. Coffa, A. Polman, and R.N. Schwartz, *Rare Earth doped Semiconductors II*, Materials Research Society Symposium Proceedings, Vol. 422, Material Research Society, Pittsburgh, PA, 1996.
- J.M. Zavada, T. Gregorkiewicz, and A.J. Steckl, (Eds.), *Rare Earth Doped Semiconductors III*, Materials Science & Engineering B, Vol. 81, 2001.
- A.J. Steckl and J.M. Zavada, MRS Bulletin, 24(9)(1999) 33.

CFG4

11:00 am

Optical Characterization and Device Fabrication of Laterally Patterned InGaN Blue Light Emitting Media on 50 nm Scale

L. Chen, A. Yin, J.S. Im, A.V. Nurmikko, J.M. Xu, Division of Engineering and Department of Physics, Brown University, Providence, RI 02912, Email: Lu-Chen@brown.edu

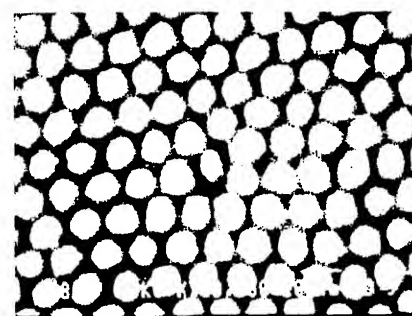
J. Han, Yale University, Department of Electrical Engineering, New Haven, CT

Laterally ordered, patterned subwavelength sized nitride structures are of interest for novel blue/ultraviolet light emitters as spontaneous and stimulated emission may be enhanced in these artificial structures. We describe a two-fold approach to produce such arrayed pattern of InGaN/GaN MQWs heterostructures by electron beam lithography (~100 nm feature size) and by pattern transfer from self-organized porous alumina (~50 nm). Spontaneous emission and light extraction of such subwavelength scale structure have been studied and a pn-junction structure

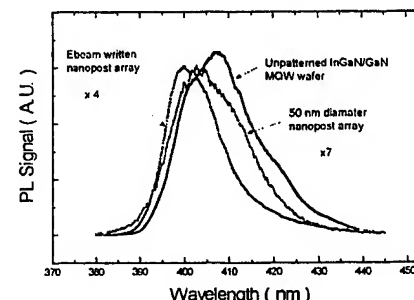
has been fabricated for current injection into the arrays of isolated nanoscale posts.

Epitaxially grown InGaN/GaN MQW material with room temperature photoluminescence spectrum centered at 400 nm was employed here to produce this structure. We use electron beam writing to define dense arrayed pattern on PMMA layer. Then the pattern was transferred to a nickel-based multilayer etch mask and then the GaN heterostructure by reactive ion etching (RIE). An etch depth on the order of 400 nm ensured that the etching reached well beyond the MQW regime. In the second approach to reach the sub-50 nm scale regime, self-assembled templates of porous alumina¹ with typical pore dimension ranging from 20-50 nm was first bonded onto the sample surface. By selective etching, a nanoprocesed InGaN/GaN QW sample (Fig.1) with individual post diameter of ~50 nm and hexagonal lattice constant of ~100 nm was produced up to 1 cm^2 area.

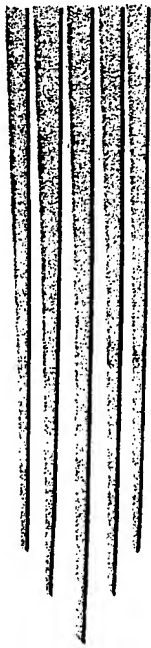
We used a high excitation pulsed photoluminescence technique to evaluate the patterned arrays (equivalent to producing an excess of 10^{18} e-h pairs per cm^{-3} in bulk equivalent terms) and to assure that the majority of carriers reside in extended states and that diffusion length exceeds the nanopost lateral size.² A comparison of the PL spectra for unpatterned and the two types of patterned arrays is shown in Fig. 2. It is evident that the PL efficiency from subwavelength structure is very robust, after additionally considering the actual area filling factors which influence both optical absorption and PL emission (14.5% and 22.7% for the ebeam written and porous alumina template etched samples, respectively). The enhancements in the spontaneous emission effi-



CFG4 Fig. 1. Top view of the arrayed pattern of InGaN/GaN QW nanopost structure with 50 nm diameter.



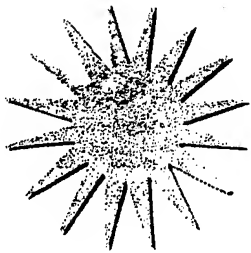
CFG4 Fig. 2. Comparison of PL emission between patterned and unpatterned InGaN QW heterostructures at room temperature.



TECHNICAL DIGEST

Summaries of papers presented at the
Conference on Lasers and Electro-Optics

Conference Edition



Long Beach Convention Center
Long Beach, California
May 19-24, 2002

CLEO® 2002 SPONSORED BY

IEEE/Lasers and Electro-Optics Society
OSA-Optical Society of America

In Cooperation with:

Quantum Electronics Division of the European Physical Society and
Optical Society Japanese Quantum Electronics Joint Group



Articles in this publication may be cited in other publications. To facilitate access to the original publication source, the following form for the citation is suggested:

Name of Author(s), "Title of Paper," in *OSA Trends in Optics and Photonics (TOPS)*
Vol. 73, Conference on Lasers and Electro-Optics, OSA Technical Digest,
Postconference Edition (Optical Society of America, Washington DC, 2002),
pp. xx-xx.

Technical Digest (meeting edition)

ISBN 1-55752-705-9
LCCN 2002101852

TOPS Vol 73: CLEO Technical Digest-Postconference Ed.

ISBN 1-55752-706-7
LCCN 2002101853

Institute of Electrical and Electronics Engineers

Catalog Number 02CH37337

Copyright © 2002, Optical Society of America

Individual readers of this digest and libraries acting for them are permitted to make fair use of the material in it, such as to copy an article for use in teaching or research, without payment of fee, provided that such copies are not sold. Copying for sale is subject to payment of copying fees. The code 1-55752-584-6/00/\$15.00 gives the per-article copying fee for each copy of the article made beyond the free copying permitted under Sections 107 and 108 of the U.S. Copyright Law. The fee should be paid through the Copyright Clearance Center, Inc., 21 Congress Street, Salem, MA 01970.

Permission is granted to quote excerpts from articles in this digest in scientific works with the customary acknowledgment of the source, including the author's name and the name of the digest, page, year, and name of the Society. Reproduction of figures and tables is likewise permitted in other articles and books provided that the same information is printed with them and notification is given to the Optical Society of America. In addition, the Optical Society may require that permission also be obtained from one of the authors. Address inquiries and notices to Director of Publications, Optical Society of America, 2010 Massachusetts Avenue, NW, Washington, DC 20036-1023. In the case of articles whose authors are employees of the United States Government or its contractors or grantees, the Optical Society of America recognizes the right of the United States Government to retain a non exclusive, royalty free license to use the author's copyrighted article for United States Government purposes.

Printed in the U.S.A.

Low-Threshold Current Density 1.3- μm InAs Quantum-Dot Lasers with the Dots-in-a-Well (DWELL) Structure

A. Stintz, G. T. Liu, *Student Member, IEEE*, H. Li, L. F. Lester, *Member, IEEE*, and K. J. Malloy, *Member, IEEE*

Abstract—The wavelength of InAs quantum dots in an $\text{In}_{0.15}\text{Ga}_{0.85}\text{As}$ quantum-well (DWELL) lasers grown on a GaAs substrate has been extended to 1.3- μm . The quantum dot lasing wavelength is sensitive to growth conditions and sample thermal history resulting in blue shifts as much as 73 nm. The room temperature threshold current density is 42.6 A cm^{-2} for 7.8-mm cavity length cleaved facet lasers under pulsed operation.

Index Terms—1.3 μm , low threshold current lasers, quantum dot lasers.

THE TECHNOLOGICAL importance of high-performance 1.3- μm semiconductor lasers compatible with existing GaAs technology has led to recent advances in GaAs-based material systems. GaAs-based laser diodes operating at this wavelength have potential applications in optical interconnects, and could be less expensive than InP-based alternatives. The utilization of self-assembled InGaAs quantum dots (QD's) grown on GaAs has extended the lasing wavelength beyond 1.3 μm [1]–[6]. One approach that has been used for QD lasers has been the dots-in-a-well (DWELL) design [2], [7]–[9], where InAs dots are placed in a strained InGaAs quantum well that both increases the emission wavelength and improves the threshold current density performance. A threshold current density as low as 26 A cm^{-2} has been demonstrated at 1.25 μm , the first time that the threshold current density performance of quantum dot lasers surpasses that of quantum well lasers [7].

The challenge in extending the lasing wavelength to 1.3- μm using the DWELL structure [7] can be illustrated by the results from an attempted 1.3- μm laser (sample A) shown in Fig. 1. A photoluminescence (PL) test structure that consists of the laser active region without cladding layers was first grown. The quantum dots originating from 2.4 monolayers of equivalent coverage were grown on 20 Å of $\text{In}_{0.15}\text{Ga}_{0.85}\text{As}$ at 510 °C at a growth rate of 0.05 ml s^{-1} and then capped with 70 Å of $\text{In}_{0.15}\text{Ga}_{0.85}\text{As}$ at 470 °C. The remainder of both the PL test structure and laser structure was grown at 610°C. PL was performed at room temperature using a CW He–Ne laser at an excitation density of $\sim 100 \text{ W cm}^{-2}$. The peak PL emission of the test structure is 1.314 μm . When the actual laser structure was grown, the PL peak wavelength is shifted to 1.273 μm . After the laser structure is fabricated into 100- μm -wide broad area lasers and cleaved into 7.8-mm laser bars, the actual lasing wavelength

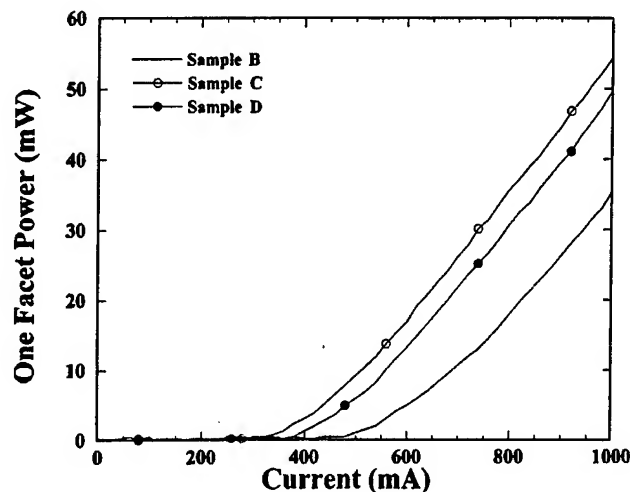


Fig. 1. Lasing spectrum of sample A at threshold current under pulsed excitation together with PL spectra of sample A and the corresponding test structure.

is further shifted to 1.241 μm , even shorter than the wavelength of the previously reported structure [7]. The threshold current density is 89.7 A cm^{-2} , high when compared with other lasers of similar design with thresholds well below 50 A cm^{-2} [7]. The quantum dot lasing wavelength is sensitive to growth conditions and thermal history. In particular, the emission wavelength of the DWELL lasers shifts to shorter wavelength with time and temperature annealing, probably because of In–Ga interdiffusion between the dot and the surrounding matrix and possibly because of reductions in the dot size.

Four laser structures (A, B, C, and D) are discussed here and all were grown by molecular beam epitaxy (MBE) on (100)-oriented n^+ doped GaAs substrates. These four structures possess only minor differences in the growth conditions of their active region, including the quantum well and quantum dots. The laser design is similar to [7], and the structure is schematically shown in Fig. 2. The epitaxial structure consists of an n -type (10^{18} cm^{-3}) 300-nm-thick GaAs buffer, a 2- μm n -type (10^{17} cm^{-3}) lower $\text{Al}_{0.7}\text{Ga}_{0.3}\text{As}$ cladding layer, a 230-nm-thick GaAs waveguide surrounding the laser active region, a 2- μm p -type (10^{17} cm^{-3}) upper cladding layer, and a p^+ -doped ($3 \times 10^{19} \text{ cm}^{-3}$) 60-nm-thick GaAs cap. In the center of the waveguide, one layer of InAs quantum dots was grown in the $\text{In}_{0.15}\text{Ga}_{0.85}\text{As}$ well.

To achieve lasing at 1.3- μm , modifications of the design and growth parameters were necessary: The total strained quantum

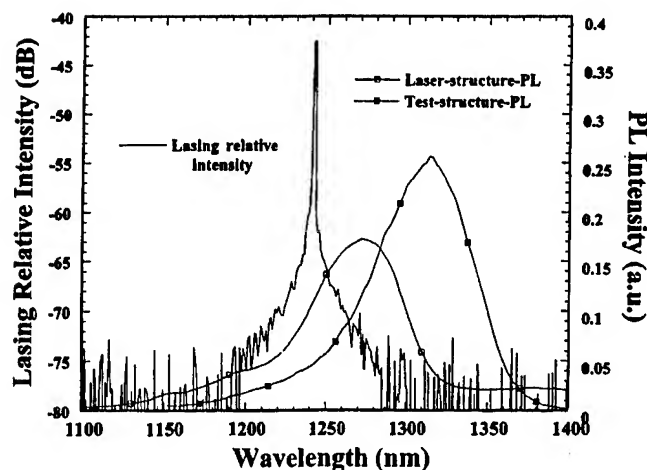
Manuscript received December 13, 1999; revised February 7, 2000.

The authors are with the Center for High Technology Materials, University of New Mexico, Albuquerque, NM 87106 USA.

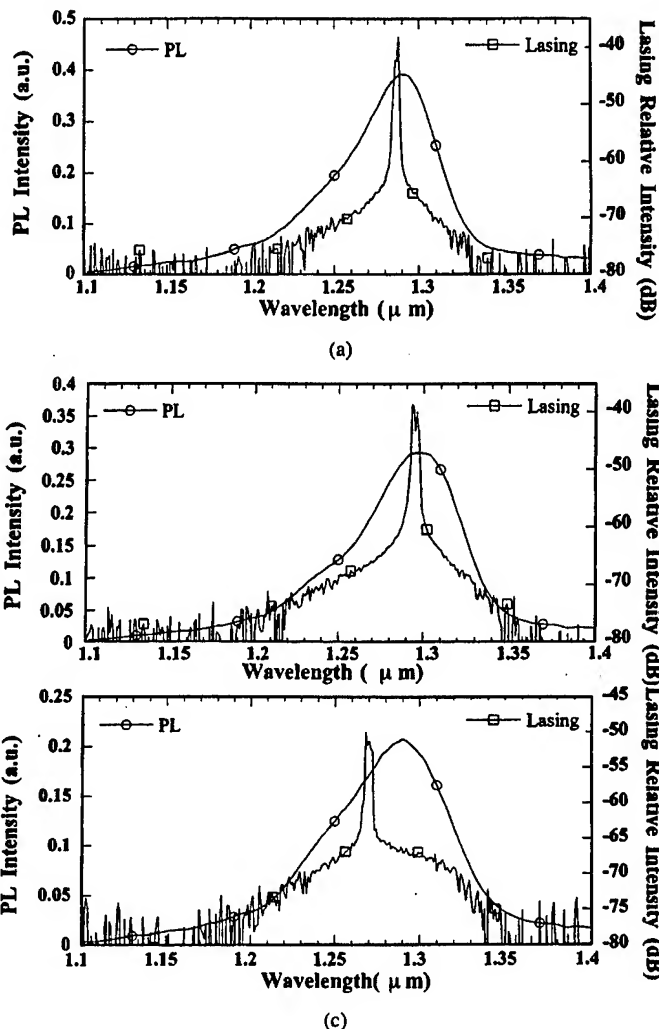
Publisher Item Identifier S 1041-1135(00)04615-2.

GaAs	Be: 3E19	60 nm
Al _{0.7} Ga _{0.3} As	Be: 1E17	2000 nm
GaAs		110 nm
In _{0.15} Ga _{0.85} As		8.6 nm
InAs quantum dots		
In _{0.15} Ga _{0.85} As		3 nm
GaAs		110 nm
Al _{0.7} Ga _{0.3} As	Si: 1E17	2000 nm
GaAs	Si: 1E18	300 nm
GaAs	N+	SUBSTRATE

Fig. 2. Schematic of the laser structure.

Fig. 3. Single facet output L - I curve of 7.8 mm cavity length lasers fabricated from samples B, C, and D.

well is increased to 126 Å to reduce possible In-Ga interdiffusion. In addition, the quantum dots were grown on 30 Å instead of 20 Å of In_{0.15}Ga_{0.85}As and were capped with 86 Å instead of 70 Å of In_{0.15}Ga_{0.85}As to prevent In segregation away from the islands during overgrowth. Next, the remaining laser structure above the active region was grown at a slightly lower growth temperature (600 °C) to minimize post-growth annealing and a possible diffusion resulting in a blue-shift of the emission wavelength. For the three different samples discussed here, the active regions including the well and dots were grown differently. The dots in sample B are formed after an equivalent coverage of 2.4 ml InAs and were grown at 510 °C at a growth rate of 0.05 ml s⁻¹. Sample C's dots were grown at 525 °C at 0.18 ml s⁻¹, with 2.7 ml InAs coverage, and sample D was the same as sample C except with a 3.0 ml InAs coverage. A high growth rate of the InAs dots also allows for a high growth rate of the In-GaAs capping the dots, thereby reducing In diffusion away from the dots during overgrowth, which favors longer wavelength emission. Room temperature photoluminescence experiments

Fig. 4. (a) PL spectrum and lasing spectrum of wafer B. (b) PL spectrum and lasing spectrum of wafer C. (c) PL spectrum and lasing spectrum of wafer D. PL excitation density is $\sim 100 \text{ W} \cdot \text{cm}^{-2}$. All lasing spectra are recorded under pulsed conditions at lasing threshold.

were performed on these three samples and the PL spectra have similar peak wavelengths of 1.290, 1.297, and 1.291 μm for samples B, C, and D, respectively. The corresponding FWHM linewidths are 62, 53, and 49 meV. Atomic force micrographs of the quantum dots grown under similar conditions as in sample B are between 6 and 8 nm high and have a base diameter of 40 nm or less. The dot density is $\sim 2.8 \cdot 10^{10} \text{ cm}^{-2}$.

Broad-area lasers with 100-μm stripe widths were fabricated from these samples. They were all cleaved into 7.8-mm-long laser bars. All devices were tested with the epi-side up on a thermoelectric cooler using pulsed excitation. The pulse width was 300 ns with a duty cycle of 0.5%, and the temperature of the thermoelectric cooler was set to be 20 °C. Fig. 3 shows the single facet output L - I curve of these three lasers. The threshold currents for sample B, C, and D are 481, 332, and 378 mA, corresponding to threshold current densities are 61.7, 42.6, and 48.5 A cm⁻², respectively. The lasers with quantum dots grown at a higher growth rate and higher growth temperature have lower threshold current densities. The lasing spectrum and PL spectrum of these three wafers are shown in three plots in Fig. 4. While the PL spectra of these three samples have

TABLE I
RESULTS FOR FOUR DIFFERENT LASER WAFERS

Sample	A	B	C	D
Growth Rate (ML s ⁻¹)	0.05	0.05	0.18	0.18
Equivalent Coverage (ML)	2.4	2.4	2.7	3.0
Growth Temperature (°C)	510	510	525	525
PL peak wavelength (μ m)	1.273	1.290	1.297	1.291
PL FWHM linewidth (meV)	52	62	53	49
Lasing peak wavelength (μ m)	1.241	1.269	1.293	1.288
PL and lasing peak wavelength difference (nm)	32	21	4	3
Threshold current (mA) for 7.8mm cavity length cleaved facets	700	481	332	378
Threshold current (A/cm ²) for 7.8mm cavity length cleaved facets	89.8	61.7	42.6	48.5

similar peak wavelengths, the lasing wavelengths vary considerably. The peak lasing wavelengths of sample B, C, and D are 1.269, 1.293, and 1.288 μ m. The respective shifts from the PL peak wavelength are 21, 4, and 3 nm. The data suggest that the quantum dots that were grown at a higher growth rate have a smaller blue shift and that the wider well leads to longer wavelength lasing. It is noteworthy that both the peak PL wavelength and lasing wavelength of sample D are shorter than sample C even though wafer D has a larger equivalent InAs coverage. The results for these four samples are summarized in Table I.

In summary, a low threshold current density of 42.6 A·cm⁻² for GaAs-based DWELL lasers at 1.3 μ m is reported. The quantum dot lasing wavelength is shown to be sensitive to growth conditions and thermal history. Careful adjustment of growth conditions is crucial for controlling the lasing wavelength near 1.3 μ m. A higher growth rate and QD growth temperature leads to a reduction in the threshold current density and an increase of the lasing wavelength.

REFERENCES

- [1] R. P. Mirin, J. P. Ibbetson, K. Nishi, A. C. Gossard, and J. E. Bowers, "1.3- μ m photoluminescence from InGaAs quantum dots on GaAs," *Appl. Phys. Lett.*, vol. 67, no. 25, pp. 3795-3797, 1995.
- [2] K. Nishi, H. Saito, S. Sugou, and J.-S. Lee, "A narrow photoluminescence linewidth of 21 meV at 1.35 μ m from strain-reduced InAs quantum dots covered by In_{0.2}Ga_{0.8}As grown on GaAs substrates," *Appl. Phys. Lett.*, vol. 74, no. 8, pp. 1111-1113, 1999.
- [3] V. M. Ustinov, N. A. Maleev, A. E. Zhukov, A. R. Kovsh, A. Y. Egorov, A. V. Lunev, B. V. Volovik, I. L. Krestnikov, Y. G. Musikhin, N. A. Bert, P. S. Kop'ev, Z. I. Alferov, N. N. Ledentsov, and D. Bimberg, "InAs/InGaAs quantum dot structures on GaAs emitting at 1.3- μ m," *Appl. Phys. Lett.*, vol. 74, no. 19, pp. 2815-2817, 1999.
- [4] D. L. Huffaker, G. Park, Z. Zou, O. B. Shchekin, and D. G. Deppe, "1.3- μ m room-temperature GaAs-based quantum-dot laser," *Appl. Phys. Lett.*, vol. 73, no. 18, pp. 2564-2566, 1998.
- [5] Y. M. Shernyakov, D. A. Bedarev, E. Y. Kondratyeva, P. S. Kopev, A. R. Kovsh, N. A. Maleev, M. V. Maximov, S. S. Mikhlin, A. F. Tsatsulnikov, V. M. Ustinov, B. V. Volovik, A. E. Zhukov, Z. I. Alferov, N. N. Ledentsov, and D. Bimberg, "1.3- μ m GaAs-based laser using quantum dots obtained by activated spinodal decomposition," *Electron. Lett.*, vol. 35, no. 11, pp. 898-900, 1999.
- [6] K. Mukai, Y. Nakata, K. Otsubo, M. Sugawara, N. Yokoyama, and H. Ishikawa, "1.3- μ m CW lasing of InGaAs/GaAs quantum dots at room temperature with a threshold current of 8 mA," *IEEE Photon. Technol. Lett.*, vol. 11, no. 10, pp. 1205-1207, 1999.
- [7] G. T. Liu, A. Stintz, H. Li, K. J. Malloy, and L. F. Lester, "Extremely low room-temperature threshold current density diode lasers using InAs dots in In_{0.15}Ga_{0.85}As quantum well," *Electron. Lett.*, vol. 35, no. 14, pp. 1163-1165, 1999.
- [8] L. F. Lester, A. Stintz, H. Li, T. C. Newell, E. A. Pease, B. A. Fuchs, and K. J. Malloy, "Optical characteristics of 1.24 μ m InAs quantum-dot laser diodes," *IEEE Photon. Technol. Lett.*, vol. 11, no. 8, pp. 931-933, 1999.
- [9] A. E. Zhukov, A. R. Kovsh, A. Y. Egorov, N. A. Maleev, V. M. Ustinov, B. V. Volovik, M. V. Maksimov, A. F. Tsatsulnikov, N. N. Ledentsov, Y. M. Shernyakov, A. V. Lunev, Y. G. Musikhin, N. A. Bert, P. S. Kopev, and Z. I. Alferov, "Photo- and electroluminescence in the 1.3- μ m wavelength range from quantum-dot structures grown on GaAs substrates," *Semiconductors*, vol. 33, no. 2, pp. 153-156, 1999.

Ground-State Emission and Gain in Ultralow-Threshold InAs-InGaAs Quantum-Dot Lasers

Petr G. Eliseev, *Senior Member, IEEE*, H. Li, G. T. Liu, Andreas Stintz, T. C. Newell, L. F. Lester, *Member, IEEE*, and K. J. Malloy, *Member, IEEE*

Abstract—Emission spectra and modal optical gain are investigated in ultralow-threshold MBE-grown InAs-InGaAs quantum dot (QD) structures. The record lowest room-temperature inversion current is found to be $\sim 13 \text{ A cm}^{-2}$. The rate-equation model is proposed describing the optical gain related to the ground-state (GS) transitions in QDs. The ground-state gain goes to the maximum value that corresponds to the total inversion of available levels. The gain cross section for the GS emission is estimated as $\sim 7 \times 10^{-15} \text{ cm}^2$.

Index Terms—Laser diodes, optical gain, quantum dots, semiconductor lasers, threshold current.

I. INTRODUCTION

LOW-DIMENSIONAL semiconductor structures are advantageous for laser applications [1]–[4]. Laser diodes with quantum dots (QDs) in the active region demonstrate the lowest oscillation thresholds among all other room-temperature semiconductor lasers [3]–[7]. A threshold current density as low as 26 A/cm^2 has been reported in MBE-grown laser structures of the dot-in-a-well (DWELL) type with an InGaAs quantum well (QW) in the active region containing a single layer of self-organized InAs QDs [5] and 16 A/cm^2 in subsequent papers [6], [7]. In [7], the effective cross section of the gain is evaluated for DWELL structures. Such ultralow threshold is achieved in the lowest energy spectral band emitted by QDs, the so-called *ground-state* (GS) spectral band. For example, in DWELL lasers [5]–[7], the GS lasing was observed in uncoated, long-cavity ($> 1.5 \text{ mm}$) laser diodes, with about 1 eV photon energies. Higher gain is needed for shorter cavity diodes, and there the laser action occurs in so-called *excited-state* (ES) bands at higher photon energies.

The evolution of the spectral distribution of emission intensity and of optical gain with current is of importance for designing QD-laser structures. In this paper, we present results of a spectral study of the GS spontaneous emission and of the modal gain in the GS emission band of ultralow QD laser structures. A rate equation model is developed describing the carrier densities in the quantum dot and surrounding quantum well. From a

steady-state analysis, the relation between the GS carrier density and injection current density is established. Subsequently, the modal gain for the low pump regime is calculated using the gain cross section along with the calculated optical confinement. The results of the model are compared favorably with experimental threshold gain versus threshold current density data taken from three different ultralow-threshold lots of DWELL lasers.

II. SAMPLES AND MEASUREMENTS

Samples used in this investigation are ultralow-threshold broad-area ($100 \mu\text{m}$ wide) laser diodes from three epitaxial wafers that feature a layer of InAs QDs grown within an InGaAs QW. Two of the laser wafers have a single layer of QDs, while the third, designated 638 and contains three active QW/QD layers that are separated by 10-nm -thick GaAs layers. Pertinent data is given in Table I. Molecular-beam-epitaxial (MBE) growth on GaAs substrates was used to provide a layer of self-organized InAs QDs in an InGaAs QW. The dot size was determined by AFM observation of a wafer grown under identical conditions, but whose growth was terminated after dot growth. The individual dots have a base diameter of $\sim 15 \text{ nm}$ and are $\sim 7 \text{ nm}$ in height. Waveguide and active layers were undoped, $\text{Al}_{0.7}\text{Ga}_{0.3}\text{As}$ cladding layers were doped with Be for the p-side and with Si for the n-side. All wafers have the same total waveguide thickness of 230 nm .

The processed material was cleaved into laser diodes with cavity lengths ranging from 285 to $7800 \mu\text{m}$. The threshold current density and optical power for diodes of different cavity lengths and uncoated facets were measured in order to determine the internal loss coefficient for each wafer and the dependence of modal gain on the current density. The lowest threshold current density of 21 A cm^{-2} is obtained with a long-cavity, as-cleaved diode from wafer 577 and about 13 A cm^{-2} is obtained with high-reflectivity coatings on the facets. Other optical characteristics of laser diodes fabricated from these wafers are reported in [5]–[7].

III. EXPERIMENTAL RESULTS

A. Spectral Study

The laser emission in the GS band is observed in the range $1.240\text{--}1.252 \text{ nm}$. The correlation of the lasing wavelength with current density at the threshold is rather weak. The variation of the lasing wavelength has been obtained by changing of the cavity length L . Within the GS band, a blue shift of the laser

Manuscript received October 16, 2000; revised April 10, 2001.

P. G. Eliseev is with the Center for High Technology Materials, University of New Mexico, Albuquerque, NM 87106 USA and also with the P. N. Lebedev Physics Institute, Russian Academy of Sciences, Moscow, 117924, Russia.

H. Li, G. T. Liu, A. Stintz, T. C. Newell, L. F. Lester, and K. J. Malloy are with the Center for High Technology Materials, University of New Mexico, Albuquerque, NM 87106 USA.

Publisher Item Identifier S 1077-260X(01)08115-1.

TABLE 1
PARAMETERS OF THE MBE-WAFERS STUDIED

Wafer #	M	d , nm	In-plane QD density, cm^{-2}	Equivalent bulk QD density, cm^{-3}	Indium content in InGaAs QW	λ , nm
SDWELL-577	1	10	2.5×10^{10}	2.5×10^{16}	0.15	1246
MDWELL-638	3	9.6	2.5×10^{10}	2.6×10^{16}	0.15	1250
SDWELL-432	1	10	7.5×10^{10}	7.5×10^{16}	0.20	1230

M is the number of the DWELL stacks in the structure (each containing one QD layer).
 d is the thickness of the individual DWELL layer.
 λ is the center wavelength of the laser emission.

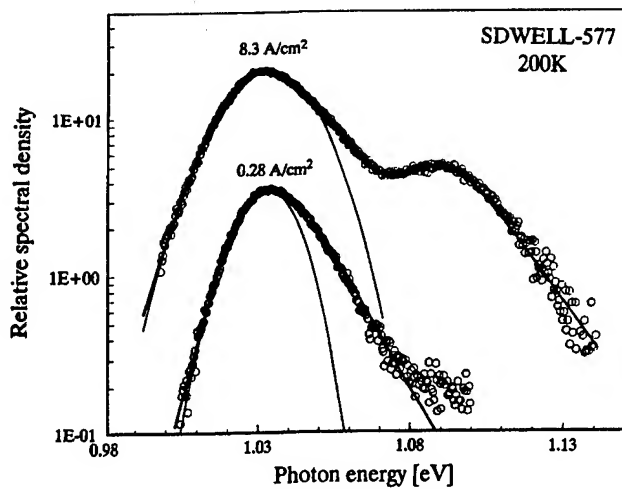


Fig. 1. Spontaneous emission spectra at 200 K of SDWELL-577 sample. Solid curves are obtained by analytical fit. The fitting parameters are given in Table II.

emission by about ~ 6 meV is seen along with an increase of the threshold current density as the threshold rises from 20 to $\sim 100 \text{ A cm}^{-2}$. At L shorter than ~ 1.5 mm the laser action is observed in the ES bands. The first ES provides the emission in the range of 1.05–1.07 eV, the second one in range of 1.09–1.12 eV.

Spontaneous emission has been studied from a 0.6 mm long sample. Laser action or spectral narrowing did not occur in pumping range up to 100 A cm^{-2} . Typical spectra are shown in Fig. 1 at 200 K at current densities below the lasing threshold. At 0.28 A cm^{-2} one GS peak is seen near 1.03 eV whereas at 8.3 A cm^{-2} the second peak is prominent at ~ 1.09 eV (first ES band). Photon energies of the peaks are shifted as compared to room temperature due to change of the bandgap. The curves in Fig. 1 are numerical fits as described later in this paper.

The GS emission saturates above $\sim 50 \text{ A cm}^{-2}$ whereas ES emission still growing. The saturation of the spectral density of spontaneous emission occurs about uniformly over whole band. Some red shift of the GS is seen, which is partially due to a temperature increase in the active region, but probably also due to many-body interactions. The first ES band is ~ 55 meV higher in the higher photon energy; it appears as a shoulder above 1 A cm^{-2} and becomes higher than the GS band above $\sim 55 \text{ A cm}^{-2}$. The second ES is seen as a high-energy shoulder.

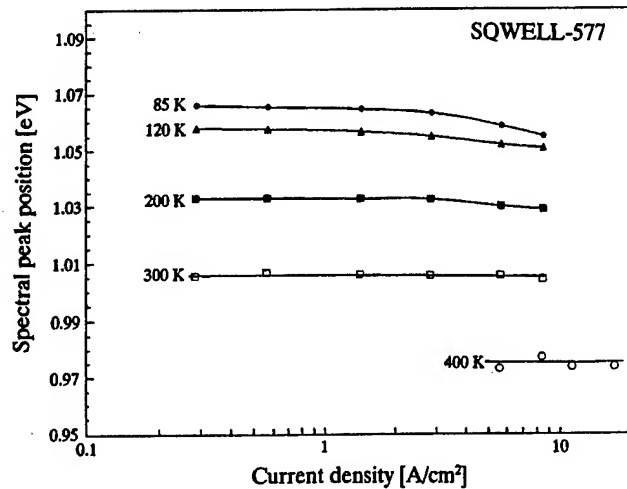


Fig. 2. Spectral peak position of ground-state emission band in function of current density at several temperatures. Sample SDWELL-577 (the same as in Fig. 1).

The spectral peak position as a function of current density is shown in Fig. 2 at several temperatures. A weak effect of current is observed in the low-current range. Some red shift is seen, which is more apparent at low temperatures. The magnitude of the shift is ~ 9.5 meV in a range from low current density to 8.3 A cm^{-2} at 85 K. The spectral peak position vs T is shown in Fig. 3. The well-known Varshni's expression is used to fit the GS peak in the range of 85 K–340 K ($J \sim 5.6 \text{ A cm}^{-2}$),

$$E(T) = E(0) + \frac{\alpha T^2}{T + \beta}, \quad (3.1)$$

where $E(0)$, α and β are Varshni fitting parameters. The results are shown in Table II. Varshni parameters are compared with energy bandgap parameters known for InAs and GaAs. One can see that the EL of the QDs closely follows the temperature dependence of InAs, as expected, in spite of strong difference in zero- T parameter $E(0)$.

The spectral peak position is also given for the first ES in Fig. 3, which is about 51–60 meV above the GS peak. The spectral bandwidth full-width at half-maximum (FWHM) is plotted vs temperature in Fig. 4 along with the low-energy partial width (LEPW). The latter is determined by the difference in energy between the half-magnitude level at the low-energy side of the

TABLE II
PARAMETERS OF THE VARSHNI APPROXIMATION TO THE TEMPERATURE DEPENDENCE OF THE SPECTRAL PEAK POSITION OF THE GS EMISSION (STRUCTURE #577) AND CORRESPONDING BANDGAP PARAMETERS FOR InAs, InGaAs AND GaAs

Parameter	$E(0)$	α	β
Units	eV	meV/K	K
InAs/InGaAs QDs, EL spectral peak position (this work)	1.008	-0.303	70
InAs, bulk energy bandgap [8]	0.418	-0.308	65
In _{0.21} Ga _{0.79} As QW, photoreflectance band edge [9]	1.312	-0.48	140
GaAs, bulk energy bandgap [8]	1.519	-0.5408	204

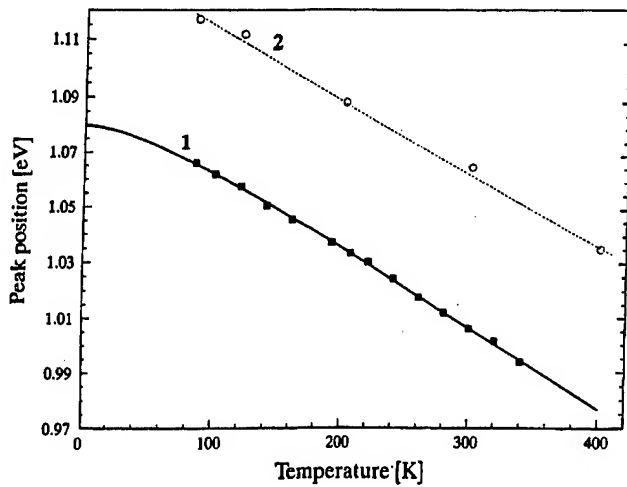


Fig. 3. Temperature dependence of the spectral peak position (the same sample as in Fig. 1) for ground-state band (1) and for first excited-state band (2). Curve 1 is Varshni-type approximation with fitting parameters given in Table II. Line 2 is a straight line.

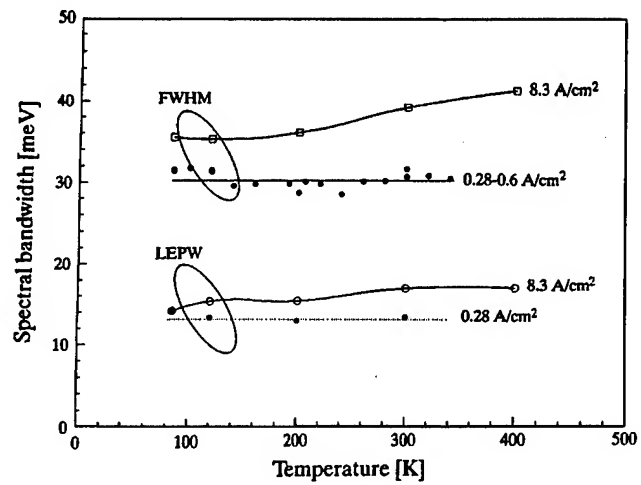


Fig. 4. Temperature dependence of the spectral bandwidth (FWHM) of the ground-state emission at two current densities. LEPW is the low-energy partial width as measured at half-magnitude from the peak to low-energy edge. Solid circles are for low current density and open ones are for 8.3 A/cm².

spectral profile and the peak position. At low current density there is a weak dependence on temperature, and the FWHM is about 30 meV (with deviations of 5% with some weak minimum in temperature range 200–250 K). At higher current the temperature dependence seems to be more prominent, and the FWHM grows by 6 meV from 35.6 meV at 85 K to 41.6 meV at 300 K (LEPW increases also in the range by ~ 2.6 meV). At high-energy side the temperature-induced broadening is mainly caused by overlapping with the first ES band, whereas low-energy broadening is probably associated only with a contribution of homogeneous broadening.

The band shape is analyzed as shown in Fig. 1 by examples at 200 K. The low-current spectrum is well fitted by the curve of $F^*(E)$, given in Appendix. The function includes two decay parameters, ϵ_{LE} and ϵ_{HE} , for a low-energy and high-energy sides, respectively, and the center energy E_0 , and magnitude factor as fitting parameters. Also the Gaussian approximation also shows satisfactory fitting on the low-energy side but not on the high-energy side at all. The exponential rather than Gaussian tail is seen at the high-energy side. The spectrum at higher current contains two peaks and it is fitted by summation of two functions of the

same functional shape of $F^*(E)$, but shifted in energy scale and with somewhat differing fitting parameters. These fitting parameters are given in Table III.

It is seen that the actual peak position (third column) and fitting center (4th column) are different because of the asymmetric form of function F^* . The tail fitting parameters are between 4.5 and 6.25 meV for the low-energy side and between 13 and 17.5 meV for the high-energy side. A non-Gaussian shape at the high-energy side is evident and the tail parameter ϵ_{HE} shows a weak effect of temperature being much higher than thermal energy kT at low T , but rather less than kT at high temperature. It is interesting that the first ES band is fitted with parameters rather close to that of the GS band (fitting at 200 K). There is also an exponential tail at the high-energy side.

B. Study of the Optical Gain

Measurements of the threshold current versus the cavity length L of the Fabry-Pérot type laser diodes are used to obtain the dependence of the modal optical gain on the injection current density J . The external losses are calculated with a simple expression $(1/L)\ln(1/R)$ assuming the Fresnel

TABLE III
RESULTS OF FITTING PROCEDURE FOR THE SPONTANEOUS EMISSION BANDS OF QD STRUCTURE SDWELL-577 AT SEVERAL TEMPERATURES. EXPRESSION (A.2) IS USED FOR FITTING WITH $n = 2$

T, K	$J, A/cm^2$	Peak position, eV	Parameter E_0 of F^*	ϵ_{LE}, meV	ϵ_{HE}, meV
85	0.28	1.0666	1.0565	4.5	17
200	0.28	1.032	1.026	5	13
	8.33	1.030 (GS)	1.021	6.25	17.5
		1.0875 (1-st ES)	1.081	4.75	16
300	0.28	1.0065	0.9975	4.75	15
	2.8	1.0055	0.9965	5.85	16.7
400	8.33	0.974	0.964	5.75	17

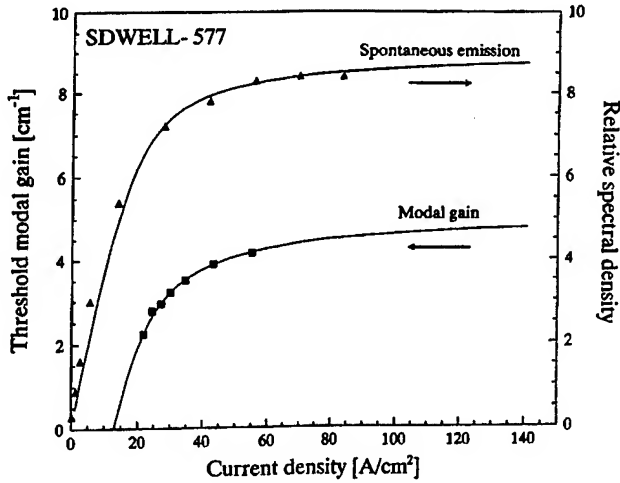


Fig. 5. The spontaneous emission peak magnitude (triangles) and the modal gain at threshold (squares) as a function of the current density. Samples of structure SDWELL-577. Curves are obtained by fitting based on the presented theoretical model with the same fitting parameters for both gain and spontaneous emission.

reflectivity coefficient R for semiconductor/air facet interfaces. The coefficient α_i of internal optical losses is determined from the dependence of the external differential efficiency on the cavity length that is close to linear one in the range $4 \text{ mm} < L < 1 \text{ mm}$. Very low values of α_i are found of 1.3 cm^{-1} in lasers from the wafer 432 and 1.5 cm^{-1} in lasers from wafers 577 and 638.

Plots in Fig. 5 show the relative spectral density of spontaneous emission (right axis) and the modal gain (left axis) versus current density. The spontaneous emission reaches a plateau and shows a trend toward saturation at a current above 30 A cm^{-2} . The modal gain curve also demonstrates a well-pronounced saturation. Solid curves are given for both quantities calculated according to the theoretical model with the same fitting parameters used both for spontaneous emission and gain. The modal gain versus the current density is given in Fig. 6 for various diodes from the different epitaxial wafers.

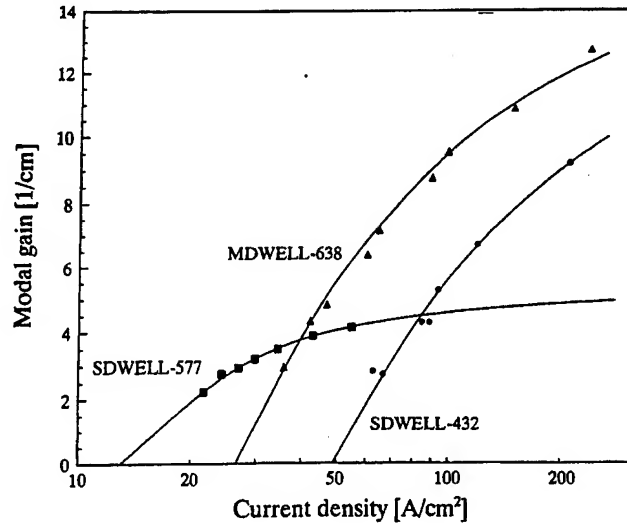


Fig. 6. Modal gain as a function of current density at room temperature for three lots of samples. Curves are calculated on the basis of the presented model.

IV. MODELING THE GAIN

A. Introductory Comments

A detailed kinetic model deals with a numerous variables: densities of several states of excess carriers in QDs (including ground and excited states, neutral and charged states), in the QW and in waveguide layers. In this paper we are interested in the steady-state population of the electron (upper level) and hole (lower level) that contribute to the lasing mode in the ground-state band. Furthermore we restrict the model to relatively low pump rates until these states are inverted. In this low-pumping case, we can neglect the detailed distribution of excess carriers in higher energy states. We consider that these excess carriers reside in a reservoir (for clarity, say an electronic state in the QW) and may accumulate substantially therein. Electrons from the reservoir can be captured to the upper state of the QD (a mainstream process) or recombine with any holes (parasitic process).

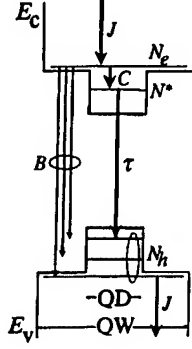


Fig. 7. Energy scheme of transitions in QD laser (DWELL type). Single upper and lower working levels are assumed in QD. Transitions labeled by: J is the electronic transition by injection pumping; C is the electron capture from the QW to QD, τ is the working ground-state transition of the dot-related recombination, B is "parasitic" recombination of QW electrons with both QW and QD holes.

Stimulated emission in the ground-state band is due only to the mainstream process. The effective capture coefficient C is used to describe the rate of the process (the reemission of electrons into the QW is assumed but not specified). All recombination processes that do not contribute to stimulated emission are lumped into an effective recombination coefficient B that governs the parasitic process. The transitions involved in this modeling are shown in Fig. 7. The model is identical to one that has been presented recently in [10] recently, so we omit some details here.

Electrons captured to the QD provide the population of the upper work state that is characterized by a simple radiative decay time τ . The density of upper work states N^* is the most important variable. We assume that holes will easily populate the lower work state so the density of inverted QD is equal to N^* . Thus, the positive gain occurs when more than half of the available upper states are populated by electrons. We do not consider the energy distribution over broadened GSs, nor the deviation from neutrality of QDs, and also neglect the excess carrier density in waveguide layers (the pumping is considered to occur immediately into the QW). These simplifications seem to be reasonable for a low-pumping regime.

Other approaches to the gain calculation in QD lasers have been reported [11]–[17]. In a recent analysis of gain characteristics of QD laser structures [16] the empirical approximation is used,

$$g(J) = g_0 \left\{ 1 - \exp \left[\frac{-\gamma(J - J_0)}{J_0} \right] \right\} \quad (4.1)$$

where g_0 is maximum ("saturated") value of the gain γ and J_0 are fitting parameters (γ is close to unity, J_0 is the inversion threshold). The rate equation model used here is applied only to the population of ground state levels. It is not in contradiction with the more general random-population (RP) model presented in [14]. More recently the saturable gain of InGaAs-GaAs QDs has been modeled in [17]. Our simplified model has an analytical solution whereas more detailed models are presented only by numerical solutions.

B. Equations and Solution

We consider rate equations for three density variables, namely, for N^* (density of QDs in the upper working state), N_e (density of electrons in the well/barrier) and N_h (total density of holes in the active region). Other involved parameters involved are as follows: N^o is the density of QDs in the lower working state; N_{QD} is the density (3-D) of QDs; τ is the lifetime of the upper state of a QD; B is the recombination coefficient of electron in the well/barrier and all holes; C is the capture coefficient of electrons from the well/barrier to the QDs; d is the QW thickness; J is the injection current density. In this model we assume that the quantity N^* relates to the active particles, and the decay of them contributes to the useful emission and gain. The quantities N_e and N_h describe the carriers of both signs that are not included into useful transitions. The rate equations are

$$\frac{dN^*}{dt} = -\frac{N^*}{\tau} + CN_e N^o \quad (4.2a)$$

$$\frac{dN_e}{dt} = \frac{J}{ed} - N_e(CN^o + BN_h) \quad (4.2b)$$

$$\frac{dN_h}{dt} = \frac{J}{ed} - BN_h N_e - \frac{N^*}{\tau} \quad (4.2c)$$

We consider stationary conditions ($d/dt = 0$) and assume that $N^* + N^o = N_{QD}$. To account for a trend to electrical neutrality in the active region we assume also that $N_e + N^* = N_h$. For a convenience, we introduce the following normalized variables and parameters: $z = N^*/N_{QD}$; $G = J\tau/(edN_{QD})$; $A = 1/(C\tau N_{QD})$; $T = \tau BN_{QD}$. Quantity z is the fraction of electrons in the upper state that can range from 0 to 1. Considering τ fixed, a large value of T implies a low efficiency laser. Also a small value of A is preferable since in this case the capture efficiency of the QDs is high. The system of (4.2) has a stationary solution

$$G = z \left[1 + \frac{ATz(1 + A - z)}{(1 - z)^2} \right] \quad (4.3)$$

The following special cases are distinguished: (1) when $G \ll 1$, we obtain $z \sim G$, which is the case of the linear regime; (2) when $G \gg 1$, we obtain $z \sim 1$. This is a saturation of the gain, namely, the gain goes asymptotically to the maximum value. The latter corresponds to a total inversion of GS emission levels, and all dots are in the upper state. Obviously, the model accounts for other recombination mechanisms consuming power under further increase of the current, whereas the GS recombination channel is saturated. A calculated curve for spontaneous emission is shown in Fig. 5 fitted to experimental data.

The quantity z increases linearly with G at small A and T up to $z \approx 1$ and then remains about constant at $G > 1$. At larger T , the smoothening of the curves is seen, and z approaches unity at larger G . Notice that this behavior is an intrinsic property of the QD occupation (with no stimulated emission included) and does not relate to dynamic saturation in the lasing regime. The ground-state optical absorption in the equilibrium is equal to σN_{QD} where σ is the effective gain/absorption cross section of the individual dot. Therefore, the optical gain changes from

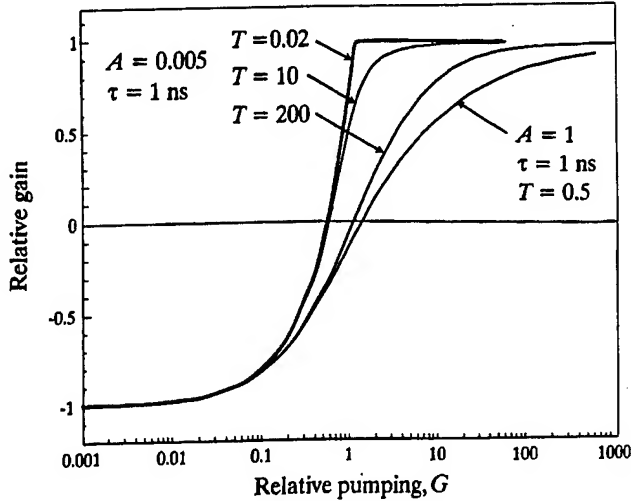


Fig. 8. Calculated gain normalized to the maximum value versus relative pumping rate at several values of dimensionless parameters.

$-\sigma N_{\text{QD}}$ at $z \approx 0$ to $\sim \sigma N_{\text{QD}}$ at $z \rightarrow 1$. The gain as a function of z can be written in the form of a linear law

$$g(z) = 2\sigma N_{\text{QD}}(z - 0.5) \quad (4.4)$$

and the inversion occurs at $z \geq 0.5$. In order to calculate the modal gain we use the waveguide modeling and obtain the optical confinement factor Γ for the QW layer assuming, the material gain $g(z)$ provided by QDs as one assigned to the QW layer. Therefore the modal gain is

$$g_{\text{mod}}(z) = \Gamma g(z). \quad (4.5)$$

The calculated optical confinement factor is 0.0302 for a single DWELL structure and 0.0906 for 3-QD layer structure of MDWELL. The dependence of the calculated modal gain on the pumping current is obtained then from (4.4) and (4.5) by substitution of z obtained from numerical solution of (4.3). The model is fitted to the experimental data using σ , A and T as fitting parameters. The curves shown in Fig. 8 relates to the calculated normalized gain $g(z)/(\sigma N_{\text{QD}})$ versus relative pumping rate. The shape of the curves and the inversion threshold are both dependent on the parameters A and T . The gain saturation is very sharp at small A and T and is quite slower at larger A and T . An increase of both of these parameters corresponds to an increase of the contribution of parasitic recombination. The calculated curves for the modal gain fitted to experimental data are also shown in Figs. 5 and 6.

V. DISCUSSION

The fitting of experimental data by calculated curves allows us to estimate the inversion threshold and the maximum gain provided by the GS of the QDs. The values are summarized in Table III. It is seen that the minimal inversion threshold $J_0 = 13 \text{ A cm}^{-2}$ is observed in laser diodes of wafer 577 which seems to be the lowest value for all room-temperature semiconductor lasers to the best of our knowledge. This structure provides rather low maximum modal gain (only $\sim 5.4 \text{ cm}^{-1}$) so the ground-state laser action could be obtained in high Q -factor

laser diodes (with long cavities or with high-reflectivity facet coatings). By optimizing the facet coating the lowest threshold has been obtained in this lot of laser diodes ($\sim 13 \text{ A cm}^{-2}$) that approaches actually the inversion current density. Higher gain has been achievable in MQW lasers (wafer 638) and SQW (wafer 432) with higher dot density. The inversion and oscillation thresholds increase along with an increase of the dot number in the active medium. Using the calculated optical confinement factor we determine the material gain in the QWs provided by the ground-state transitions in QDs. It allows us to derive the effective cross section σ of the gain by QDs from 6.9×10^{-15} to $7.2 \times 10^{-15} \text{ cm}^2$.

Parameters of the kinetic model A and T are also given in the Table IV. The value of A is close to the ratio of the effective capture time of carriers to the lifetime τ of the ground states. Estimation of τ is from 700 to 1000 ps [16], [18]–[20], so the effective capture time is estimated from 140 to 200 ps at $A = 0.2$. Actually, it includes diffusion and relaxation processes and it depends on the dot density and temperature. In the time-resolved measurements, the rise time of the GS emission can be associated with the effective capture time. Values of rise time from 400 to 200 ps have been reported [20] in study of InAs–GaAs QDs whereas an electron relaxation is found to occur rather fast (≤ 50 ps). Also fast capture and relaxation was reported in $\text{In}_{0.5}\text{Ga}_{0.5}\text{As}$ –GaAs self-assembled QDs [18] with a rise time of 93 ps when the GaAs barrier had been photoexcited. Thus our indirect estimate of the capture time is of a reasonable value.

Another estimation is made for the parasitic recombination coefficient B that is $(2.6 \pm 0.6) \times 10^{-8} \text{ cm}^3/\text{s}$. This is an effective value including not only the radiative processes but also nonradiative ones.

A satisfactory fitting obtained using the above rate-equation model as applied to the gain curves of ultralow-threshold laser QD laser structures indicates that the model is acceptable at least for the GS population. Also we think that the deviation from electrical neutrality of the dots is not an important factor in this case. The closest results on the modeling of the gain are reported in [17] for a multilevel QD system. It is based on a rate equation approach but does not include parallel channels of recombination. It also predicts a gain saturation for each transitions in the quantum dot including the ground-state transitions.

VI. CONCLUSION

We obtained the dependence of modal optical gain in MBE-grown InAs–InGaAs quantum dot structures on current density from an experimental study of the cavity length effect on the threshold current in ultralow-threshold laser diodes. The threshold current density at room temperature has been measured to be as low as 13 A/cm^2 . The ground-state gain in the spectral range 1230–1250 nm rises asymptotically to the maximum value corresponding to a total inversion of the work states. Also, we estimated the material gain dividing the modal gain by the optical confinement factor. From the maximum gain we determine the averaged gain cross section relating to the GS transitions of the InAs QDs in the InGaAs QW. It is about $7 \times 10^{-15} \text{ cm}^2$. In this approach we assigned the interaction

TABLE IV
PARAMETERS OF DWELL STRUCTURES FROM THE FITTING OF EXPERIMENTAL DATA

Wafer	J_0, Acm^{-2}	g_{\max}, cm^{-1}	σ, cm^2	A	T
SDWELL-577	13	5.43	7.17×10^{-15}	0.2	0.4
MDWELL-638	25.7	17	7.21×10^{-15}	0.5	0.4
SDWELL-432	50	15.6	6.89×10^{-15}	0.5	0.4

g_{\max} is the maximum modal gain.

cross section to the dot as an atomic object and did not specify the dot volume. Consequently, the QW active medium was considered as one containing a specific density of dots.

The theoretical model is proposed describing the GS gain as a function of the current. It allows us to fit the experimental gain versus the current density rather easily and to derive important characteristics of the InAs QDs. The characteristic capture coefficient C is estimated for carriers that relax to the GS by $\sim 2 \times 10^{-7} \text{ cm}^3/\text{s}$. The modeling is suitable at least for a low-pumping regime (below the total inversion of ground-state transitions). In conclusion, we summarize presented results.

- 1) Spectral and threshold characteristics are presented for laser structures with QDs of the DWELL type. The low-current spectral bandwidth of the GS emission is $\sim 30 \text{ meV}$ in ultralow-threshold samples. The bandwidth is weakly temperature dependent indicating a main contribution of inhomogeneous broadening. The temperature dependence of the peak position is described in terms of the Varshni approximation with temperature coefficients that are close to the ones in InAs.
- 2) The dependence of the modal gain on the current density is derived from experimental data on the dependence of the threshold current density on the cavity length with the experimental value of the internal optical losses (1.5 cm^{-1}). The gain in the GS band shows a saturation behavior associated with full inversion of available states. The upper limit of $5\text{--}15 \text{ cm}^{-1}$ is estimated, depending on the dot density.
- 3) A simple theoretical model of the occupation of ground states in QDs is proposed with an analytical solution. The solution is shown to be fruitful in the fitting of experimental data on the gain-versus-current curves. The lowest inversion current of $\sim 13 \text{ A cm}^{-2}$ is found by extrapolation of calculated and well-fitted curve. Satisfactory fit is demonstrated. Dimensionless parameters of the model are derived.

APPENDIX SPECTRAL-BAND SHAPE FITTING

The following function is considered in [21] in connection with proper line shape modeling in semiconductor lasers:

$$F(E) = \text{sech}^n \left[\frac{E - E_0}{n\epsilon} \right]. \quad (\text{A.1})$$

$F(E)$ has these properties: (1) it is symmetric and bell-shaped being centered at $E = E_0$; (2) it is normalized to the peak magnitude at $E = E_0$; (3) at both wings it has an exponential

decay with the same parameter ϵ ; (4) decay parameter ϵ is the same at any n ; (5) the ratio between ϵ and FWHM is dependent on n and it gives a flexibility in the fitting procedure; (6) by increasing n one can transform this function more and more close to a usual Gaussian form. In a central part the function (A.1) can be rather close to the well-known Lorentzian shape, but converging much better under integration because of sharper tails than those of the Lorentzian.

The non-Lorentzian line shape function is discussed to be more adequate to describe correlated collisional broadening in solids. It is typically of exponential wings to provide an explanation of the Urbach rule for the absorption edge in solids. A similar exponential wing is usually seen in spontaneous emission spectra of semiconductor materials (but never Lorentzian wings). This can be considered as an indication that the LSF has tails closer to an exponential form than to the Lorentzian. When the total emission spectrum is calculated, the integral convolution of some inhomogeneous core function with the LSF is performed. If the core function has an abrupt edge, the tails of the emission spectrum should be the same as that of the LSF.

There is a modified asymmetric function relative to the sech-function, namely

$$F^*(E) = \frac{A}{\left\{ \exp \left[\frac{E - E_0}{n\epsilon_{\text{HE}}} \right] + \exp \left[-\frac{E - E_0}{n\epsilon_{\text{LE}}} \right] \right\}^n} \quad (\text{A.2})$$

that is more flexible in purposes of analytical fitting. The function (A.2) has following properties: 1) it is of asymmetric bell-shape; 2) its peak does not generally coincide with E_0 ; 3) at its high-energy side, the function decays exponentially with parameter ϵ_{HE} and at its low-energy side, it decays exponentially with parameter ϵ_{LE} ; 4) these decay parameters are the same at any n ; 5) along with an increase of n the function approaches the Gaussian form. The function has also been used in the spectral fitting in [22] for InGaAs quantum wells. In this paper, we use this fitting function with $n = 2$.

ACKNOWLEDGMENT

The authors are thankful to G. A. Smolyakov of the Center for High Technology Materials, University of New Mexico, Albuquerque, for numerical waveguide calculations.

REFERENCES

- [1] Y. Arakawa and H. Sasaki, "Multidimensional quantum well lasers and temperature dependence of its threshold current," *Appl. Phys. Lett.*, vol. 40, no. 11, pp. 939-941, 1982.

- [2] A. E. Drakin and P. G. Eliseev, "Qualitative analysis of the threshold current in quantum-size semiconductor lasers," *Sov. J. Quantum Electron.*, vol. 14, p. 119, 1984.
- [3] H. Hirayama, K. Matsunaga, K. Asada, and Y. Suematsu, "Lasing action of $\text{Ga}_{0.67}\text{In}_{0.33}\text{As}/\text{InP}$ tensile-strained quantum box lasers," *Electron. Lett.*, vol. 30, pp. 142–143, 1994.
- [4] N. Kirstaedter, N. N. Ledentsov, M. Grundmann, D. Bimberg, V. M. Ustinov, S. S. Ruvimov, M. V. Maximov, P. S. Kop'ev, Z. I. Alferov, U. Richter, P. Werner, U. Goesele, and J. Heydenreich, "Low threshold, large T_0 injection laser emission from $(\text{InGa})\text{As}$ quantum dots," *Electron. Lett.*, vol. 30, no. 17, pp. 1416–1417, 1994.
- [5] G. T. Liu, A. Stintz, H. Li, K. J. Malloy, and L. F. Lester, "Extremely low room-temperature threshold current density diode lasers using InAs dots in $\text{In}_{0.15}\text{Ga}_{0.85}\text{As}$ quantum well," *Electron. Lett.*, vol. 35, no. 14, pp. 1163–1165, 1999.
- [6] L. F. Lester, A. Stintz, H. Li, T. C. Newell, E. A. Pease, B. A. Fuchs, and K. J. Malloy, "Optical characteristics of $1.24\text{-}\mu\text{m}$ InAs quantum-dot laser diode," *IEEE Photon. Technol. Lett.*, vol. 11, no. 8, pp. 931–933, 1999.
- [7] P. G. Eliseev, H. Li, A. Stintz, G. T. Liu, T. C. Newell, K. J. Malloy, L. Lester, and P. G. Eliseev, "Transition dipole moment of $\text{InAs}/\text{InGaAs}$ quantum dots from experiments on ultralow-threshold laser diodes," *Appl. Phys. Lett.*, vol. 77, no. 2, pp. 262–264, July 2000.
- [8] *Landolt-Boernstein Numerical Data and Functional Relationships in Science and Technology*, vol. 22, Semiconductors, Springer Verlag, Berlin, 1987, p. 118.
- [9] Y. S. Huang, H. Qiang, F. H. Pollack, G. D. Pettit, P. D. Kirchner, J. M. Woodall, H. Stagner, and L. B. Sorensen, "Temperature dependence of the photoreflectance of the strained layer $(001)\text{ In}_{0.21}\text{Ga}_{0.79}\text{As}/\text{GaAs}$ single quantum well," *J. Appl. Phys.*, vol. 70, no. 12, pp. 7537–7542, 1991.
- [10] P. G. Eliseev, H. Li, G. T. Liu, A. Stintz, T. C. Newell, L. F. Lester, and K. J. Malloy, "Optical gain in $\text{InAs}/\text{InGaAs}$ quantum-dot structures: experiments and theoretical model," *Quantum Electron.*, vol. 30, no. 8, pp. 664–668, 2000.
- [11] M. Asada, Y. Miyamoto, and Y. Suematsu, "Gain and the threshold of three-dimensional quantum-box lasers," *IEEE J. Quantum Electron.*, vol. 22, no. 9, pp. 1915–1921, 1986.
- [12] K. Mukai, N. Ohtsuka, H. Shoji, and M. Sugawara, "Emission from discrete levels in self-formed $\text{InGaAs}/\text{GaAs}$ quantum dots by electric carrier injection: influence of phonon bottleneck," *Appl. Phys. Lett.*, vol. 68, pp. 3013–3015, 1996.
- [13] N. Kirstaedter, O. G. Schmidt, N. N. Ledentsov, D. Bimberg, V. M. Ustinov, A. Y. Egorov, A. E. Zhukov, M. V. Maximov, P. S. Kop'ev, and Z. I. Alferov, "Gain and differential gain of a single layer InAs/GaAs quantum dot injection lasers," *Appl. Phys. Lett.*, vol. 69, no. 9, pp. 1226–1228, 1996.
- [14] M. Grundmann and D. Bimberg, "Theory of random population for quantum dots," *Phys. Rev., B*, vol. 55, no. 15, pp. 9740–9745, Apr. 1996.
- [15] L. V. Asryan and R. A. Suris, "Inhomogeneous line broadening and the threshold current density of a semiconductor quantum dot laser," *Semicond. Sci. Technol.*, vol. 11, pp. 554–567, 1996.
- [16] A. E. Zhukov, A. R. Kovsh, V. M. Ustinov, A. Y. Egorov, N. N. Ledentsov, A. F. Tsatsul'nikov, M. V. Maximov, Y. M. Shernyakov, V. I. Kopchatov, A. V. Lunev, P. S. Kop'ev, D. Bimberg, and Z. I. Alferov, "Gain characteristics of quantum dot injection lasers," *Semicond. Sci. Technol.*, vol. 14, no. 1, pp. 118–123, 1999.
- [17] G. Park, O. B. Shchekin, and D. G. Deppe, "Temperature dependence of gain saturation in multilevel quantum dot lasers," *IEEE J. Quantum Electron.*, vol. 36, no. 9, pp. 1065–1071, 2000.
- [18] B. Ohnesorge, M. Albrecht, J. Oshinowo, A. Forchel, and Y. Arakawa, "Rapid carrier relaxation in self-assembled $\text{In}_x\text{Ga}_{1-x}\text{As}/\text{GaAs}$ quantum dots," *Phys. Rev., B*, vol. 54, no. 16, pp. 11 532–11 538, 1996.
- [19] S. Raymond, S. Fafard, P. J. Poole, A. Wojs, P. Hawrylak, S. Charbonneau, D. Leonard, R. Leon, P. M. Petroff, and J. L. Merz, "State filling and time-resolved photoluminescence of excited states in $\text{In}_x\text{Ga}_{1-x}\text{As}/\text{GaAs}$ self-assembled quantum dots," *Phys. Rev., B*, vol. 54, no. 16, pp. 11 548–11 554, 1996.
- [20] F. Adler, M. Geiger, A. Bauknecht, D. Haase, P. Ernst, A. Doernen, F. Scholz, and H. Schweizer, "Self-assembled InAs/GaAs quantum dots under resonant excitation," *J. Appl. Phys.*, vol. 83, no. 3, pp. 1631–1636, 1998.
- [21] P. G. Eliseev, "Line shape function for semiconductor laser modeling," *Electron. Lett.*, vol. 33, no. 24, pp. 2046–2048, 1997.
- [22] P. G. Eliseev and I. V. Akimova, "Emission from quantum-well InGaAs structures," *Quantum Electron.*, vol. 28, no. 3, pp. 198–202, 1998.



Petr G. Eliseev (SM'87) was born in St. Petersburg, Russia, on February 3, 1936. He graduated from the Moscow State University in 1959. He received the Candidate Sci. degree in 1965, the Doctor Sci. degree in 1974, and the Professor Diploma in 1981, all from the P. N. Lebedev Physics Institute (FIAN), Russian Academy of Sciences, Moscow.

He was with the Physical Department of Moscow State University from 1959 to 1963, and since 1963 has been with FIAN, currently as a Head of the Injection Laser Laboratory. In 1991, he was with the

Research Center for Advanced Science and Technology, University of Tokyo, Japan. During 1993–1994, he was at the Ferdinand Braun Institute Berlin, Germany, and during 1998–1999 at the University of Tokushima, Japan, and in 2000 at the University of Nagoya, Japan, as visiting researcher. Since 1995, he has been a Research Professor with the Center for High Technology Materials, University of New Mexico, Albuquerque. The main field of his research activity in physics of semiconductor lasers.

Dr. Eliseev was awarded the State Prize of the USSR in 1984, for pioneering development of quaternary heterostructure materials (InGaAsP , InGaSbAs , etc.). He is a correspondent member of Russian Academy of Natural Sciences since 1992.

H. Li received the M.S. degree in physics from Peking University, Beijing, China and the Ph.D. degree in physics from the University of Hanover, Hanover, Germany, in 1981 and 1990, respectively.

In 1990, she joined the Center for High Technology Materials, University of New Mexico, Albuquerque. Her previous experience was in laser physics and technologies, laser stabilization techniques, dynamics of semiconductor lasers with optical feedback, applications of a variety of SL systems, such as vertical-cavity surface-emitting lasers, and broadband tunable quantum-dot lasers. Since 2000, she has been with New Focus, Inc., San Jose, CA. Her current interest is in tunable semiconductor lasers and other active components of telecommunications.

Dr. Li is a member of the Optical Society of America (OSA), and a member of IEEE Lasers and Electro-Optics Society (LEOS).

G. T. Liu photograph and biography was not available at the time of publication.

Andreas Stintz was born in Merseburg, Germany, in 1964. He received the Ph.D. degree in physics from the University of New Mexico, Albuquerque, in 1993. The subject of his dissertation was field desorption phenomena.

From 1994 to 1995, he was a Postdoctoral Fellow with the Department of Physics and Astronomy, University of New Mexico, where he investigated the singlet D resonance in the H^- ion. In 1996, he joined the Center for High Technology Materials and became involved in crystal growth for III–V semiconductors by molecular beam epitaxy. His research includes high-power quantum-well lasers, quantum dot lasers and detectors, saturable absorbers, and crystal growth on metamorphic buffer layers. He also cofounded Zia Laser, Inc., in 2000, a start-up company with the goal of marketing a new generation of telecom and datacom lasers.

T. C. Newell photograph and biography was not available at the time of publication.

L. F. Lester photograph and biography was not available at the time of publication.

K. J. Malloy photograph and biography was not available at the time of publication.

wavelength InAs quantum dot lasers

Xiaodong Huang, A. Stintz, C.P. Hains, G.T. Liu, J. Cheng and K.J. Malloy

Efficient, continuous-wave lasing operation of narrow-stripe, oxide-confined, long-wavelength InAs quantum dot lasers in the ground state ($\lambda \approx 1.28 \mu\text{m}$) has been achieved at temperatures up to 100°C . The lasers have a very low threshold current density ($J_{th} = 24 \text{ A/cm}^2$), high differential quantum efficiency (55), and very low internal loss ($\alpha_i = 0.77 \text{ cm}^{-1}$).

Introduction: Intensive research has been conducted towards improving the performance of long-wavelength quantum dot (QD) lasers which are of practical interest for telecommunication applications. QD layers have been used successfully as the active gain medium for edge-emitting lasers and vertical-cavity surface-emitting lasers (VCSELs) [1, 2]. More recently, room-temperature, continuous-wave (CW) lasing has been obtained at wavelengths around $1.3 \mu\text{m}$ with threshold current densities of $J_{th} = 65 \text{ A/cm}^2$ [3], 200 A/cm^2 [4] and 45 A/cm^2 [5]. The realisation of a QD laser that can operate at a much lower threshold current density while preserving a high slope efficiency, high output power, and ground-state lasing over a wide temperature range is necessary. In this Letter, we report the achievement of these objectives using narrow-stripe, laterally oxide-confined QD lasers containing two InAs quantum-dots-in-a-well (DWELL) layers [6]. Room-temperature, CW lasing in the ground state ($\lambda \approx 1.28 \mu\text{m}$) has been obtained for lasers with a cavity length (L) $> 2 \text{ mm}$, and stripe widths of 8.4 and $27.4 \mu\text{m}$. The laser cavity has a very low internal loss ($\alpha_i < 1 \text{ cm}^{-1}$), which allows a high external quantum efficiency of up to 55% to be achieved for a 3 mm long device. A low threshold current ($I_{th} = 10.9 \text{ mA}$) has also been achieved using a 3 mm long device with a width of $8.4 \mu\text{m}$, while a very low threshold current density ($J_{th} = 24 \text{ A/cm}^2$) was achieved using a longer device. The transparency current density is estimated to be $\approx 8.8 \text{ A/cm}^2$. Ground state CW lasing has been achieved at temperatures in excess of 100°C , with a characteristic temperature of $T_0 = 47 \text{ K}$.

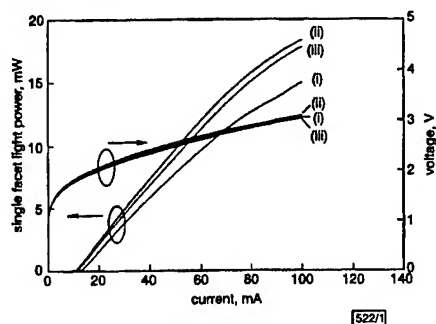


Fig. 1 Room temperature single-facet CW lasing and electrical characteristics of three lasers

$W = 8.4 \mu\text{m}$
(i) $L = 2 \text{ mm}$
(ii) $L = 3 \text{ mm}$
(iii) $L = 4 \text{ mm}$

Device structure and fabrication: The oxide-confined QD laser was grown by solid-source molecular beam epitaxy (MBE) on a (001) n^+ -GaAs substrate. The epitaxial structure is almost the same as that described in [6], except that there are two InAs DWELL layers, separated by a 30 nm GaAs barrier layer, that are situated in the middle of a 220 nm thick GaAs waveguide, and a 50 nm thick $\text{Al}_{0.98}\text{Ga}_{0.02}\text{As}$ oxidation layer has been added between the GaAs waveguide and the upper cladding layer. Each DWELL layer contains InAs QDs with an equivalent coverage of 2.4 monolayers, which are embedded within a 9.6 nm $\text{In}_{0.15}\text{Ga}_{0.85}\text{As}$ quantum well (QW). The QD lasers have an oxide-confined structure [2, 7], in which the $\text{Al}_{0.98}\text{Ga}_{0.02}\text{As}$ layer is selectively oxidised to provide current confinement as well as some degree of index guiding.

Device fabrication begins with the deposition of the p -contact metal (Ti/Pt/Au), which is patterned into stripes of different widths. After the deposition of a thin Si_3N_4 film over the p -contact metal by plasma enhanced chemical vapour deposition (PECVD), it is patterned into a

ring through the entire epitaxial structure. The $\text{Al}_{0.98}\text{Ga}_{0.02}\text{As}$ layer is then laterally and selectively oxidised from the periphery of each mesa in a saturated steam environment at 425°C , forming an AlO_x layer with apertures (W) of 8.4 and $27.4 \mu\text{m}$, respectively. The narrower width of the emission region ($W = 8.4 \mu\text{m}$) facilitates the coupling into a singlemode optical fibre. After removing the Si_3N_4 mask, the sample substrate is lapped down to a thickness of $\sim 125 \mu\text{m}$ and polished, followed by deposition of the n -contact metal (AuGe/Ni/Au) on the backside. The wafer is then cleaved into laser bars with different lengths, and no coating is applied to the laser facets. Finally, the lasers are mounted on a Cu heat-sink in a p -side-up configuration for testing.

Experimental results: CW lasing in the ground state has been achieved for lasers with $L \geq 2 \text{ mm}$ which, as a result of their lower mirror loss and threshold gain, are below gain saturation. Fig. 1 shows the single-facet CW lasing characteristics of lasers with $W = 8.4 \mu\text{m}$ and $L = 2, 3$ and 4 mm . The threshold current for lasing is $I_{th} = 12.6, 10.9$ and 11.2 mA , respectively, with corresponding threshold current densities of $J_{th} = 75, 43.3$, and 33.3 A/cm^2 . The CW light output from a single facet exceeds 18 mW for a laser with $L = 3 \text{ mm}$. The laser with $L = 2 \text{ mm}$ has a lower external quantum efficiency than that of the lasers with $L \geq 3 \text{ mm}$ as a result of its higher optical loss, which leads to a higher threshold gain that is closer to gain saturation, thus resulting in a higher threshold current density, increased thermal heating and lower efficiency. The lasing wavelength measured just above the threshold varies from $\sim 1274 \text{ nm}$ for lasers with $L \leq 4 \text{ mm}$ to $\sim 1285 \text{ nm}$ for lasers with $L \geq 5 \text{ mm}$. Owing to the smaller DC power dissipation and reduced self-heating of a narrower current aperture, thermal rollover is less pronounced and CW lasing can occur even at a drive current level of $I = 9 \times I_{th}$. The current-voltage characteristics for different devices are also shown in Fig. 1, which shows a threshold voltage of $< 2 \text{ V}$ for all the lasers.

To determine the transparency current density, J_0 , very long QD lasers have been measured. The threshold current density for a 19.2 mm device is $J_{th} = 24 \text{ A/cm}^2$, and the value of J_0 is estimated to be $\sim 8.8 \text{ A/cm}^2$ based on a linear extrapolation from the plot of modal gain against current density [8]. The threshold current density obtained by these uncoated QD lasers is among the lowest ever reported for CW operation at room temperature. A very low threshold current density can also be realised for shorter devices by applying a high-reflectivity coating to each laser facet, albeit at a reduction in optical output power.

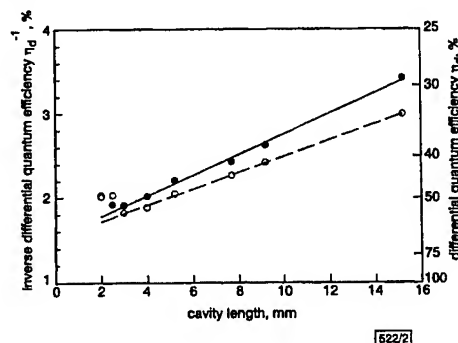


Fig. 2 Linear dependence of inverse differential quantum efficiency η_d^{-1} of both facets on cavity length L under CW operation for lasers with different W

● $W = 8.4 \mu\text{m}$, $\alpha_i = 0.97 \text{ cm}^{-1}$
○ $W = 27.4 \mu\text{m}$, $\alpha_i = 0.77 \text{ cm}^{-1}$

The peak external differential quantum efficiency for both facets is $\eta_d = 52.2\%$ for a laser with $L = 3 \text{ mm}$ and $W = 8.4 \mu\text{m}$, and the highest value obtained is $\eta_d = 55\%$ for a laser with $L = 3 \text{ mm}$ and $W = 27.4 \mu\text{m}$. The linear dependence of the inverse external differential quantum efficiency ($1/\eta_d$) on the cavity length (L) is shown in Fig. 2. The internal loss (α_i) derived from the slope of the linear fit is $\alpha_i = 0.97 \text{ cm}^{-1}$ for the lasers with $W = 8.4 \mu\text{m}$, and $\alpha_i = 0.77 \text{ cm}^{-1}$ for the lasers with $W = 27.4 \mu\text{m}$. The extremely low cavity loss is attributed to the very low optical scattering from a smooth oxidation front, to the extra lateral optical confinement provided by the low-index AlO_x layer, and to the fact that the emission level is well below the bandgaps of the InGaAs and GaAs of the active region. Both linear fits in Fig. 2 have the same y-intercept, which yielded an internal quantum efficiency of $\eta_i = 65.4\%$. Comparing the

$\alpha_i = 0.04$, which agrees with the calculated values of mirror loss (α_m) and internal loss (α_i), and illustrates that the higher efficiency can be attributed to the very low value of α_i . The internal quantum efficiency of the two-layer QD laser is improved compared with that of our single-layer QD lasers ($\eta_i = 60\%$). The use of a multiple stack of QD layers is thus an effective approach to improving the internal quantum efficiency and to avoiding gain saturation in the ground state.

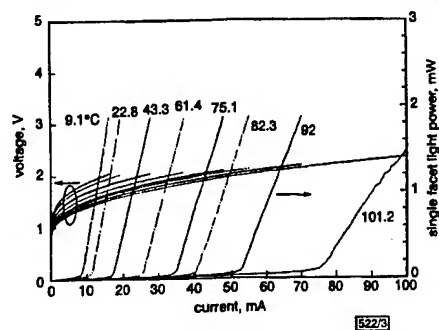


Fig. 3 Electrical and single-facet CW laser characteristics of laser at different temperatures

Ground state lasing has been achieved at ambient temperature of up to 100°C $L = 4\text{ mm}$, $W = 8.4\text{ }\mu\text{m}$

Fig. 3 shows the electrical and CW lasing characteristics of a QD laser ($L = 4\text{ mm}$, $W = 8.4\text{ }\mu\text{m}$) at temperatures ranging from 9.1 to 101.2°C . Ground state lasing is obtained throughout the entire temperature range, and the characteristic temperature of I_{th} is $T_0 = 47\text{ K}$. The differential quantum efficiency η_d changes only slightly with temperature until it is above 80°C , because of the reduced thermal self-heating in a narrow stripe laser with a low drive current. The lasing wavelength changes from 1268 to 1315 nm within this temperature range, with a temperature coefficient of $\Delta\lambda/\Delta T \approx 0.5\text{ nm/K}$, similar to that of an InGaAs quantum well laser. The threshold voltage remains at $< 2\text{ V}$ over the entire temperature range.

Conclusions: We have reported high-performance, oxide-confined, quantum-dots-in-a-well (DWELL) lasers operating in the ground state

lasing temperature (up to 100°C).

Acknowledgments: The research was supported in part by AFOSR and DARPA.

© IEE 2000

15 November 1999

Electronics Letters Online No: 20000124

DOI: 10.1049/el:20000124

Xiaodong Huang, A. Stintz, C.P. Hains, G.T. Liu, J. Cheng and K.J. Malloy (University of New Mexico, Center for High Technology Materials, 1313 Goddard SE, Albuquerque, NM 87106, USA)

References

- 1 HUFFAKER, D.L., PARK, G., ZOU, Z., SHCHEKIN, O.B., and DEPPE, D.G.: '1.3 μm room temperature GaAs-based quantum-dot laser', *Appl. Phys. Lett.*, 1998, **73**, (18), pp. 2564–2566
- 2 HUFFAKER, D.L., BAKLENOV, O., GRAHAM, L.A., STREETMAN, B.G., and DEPPE, D.G.: 'Quantum dot vertical cavity surface emitting laser with a dielectric aperture', *Appl. Phys. Lett.*, 1997, **70**, (18), pp. 2356–2358
- 3 SHERNYAKOV, YU.M., BEDAREV, D.A., KONDRAT'eva, E.YU., KOPEV, P.S., KOVSH, A.R., MALEEV, N.A., MAXIMOV, M.V., MIKHRAIN, S.S., TSATSUL'NIKOV, A.F., USTINOV, V.M., VOLOVNIK, B.V., ZHUKOV, A.E., ALFEROV, ZH.I., LEDENTSOV, N.N., and BIMBERG, D.: '1.3 μm GaAs-based laser using quantum dots obtained by activated spinodal decomposition', *Electron. Lett.*, 1999, **35**, (11), pp. 898–900
- 4 MUKAI, K., OHTSUKA, N., SHOJI, H., SUGAWARA, M., YOKOYAMA, N., and ISHIKAWA, H.: '1.3 μm CW lasing of InGaAs/GaAs quantum dots at room temperature with a threshold current of 8 mA', *IEEE Photonics Technol. Lett.*, 1999, **11**, (10), pp. 1205–1207
- 5 PARK, G., SHCHEKIN, O.B., CSUTAK, S., HUFFAKER, D.L., and DEPPE, D.G.: 'Room-temperature continuous-wave operation of a single-layered 1.3 μm quantum dot laser', *Appl. Phys. Lett.*, 1999, **75**, (21), pp. 3267–3269
- 6 LESTER, L.F., STINTZ, A., LI, H., NEWELL, T.C., PEASE, E.A., FUCHS, B.A., and MALLOY, K.J.: 'Optical characteristics of 1.24 μm InAs quantum dot laser diodes', *IEEE Photonics Technol. Lett.*, 1999, **11**, (8), pp. 931–933
- 7 DALLASSE, J.M., HOLONYAK, N., SUGG, A.R., and RICHARD, T.A.: 'Hydrolyzation oxidation of AlGaAs-AlAs-GaAs quantum well heterostructures and superlattices', *Appl. Phys. Lett.*, 1990, **57**, (26), pp. 2844–2846
- 8 GRUNDMANN, M., and BIMBERG, D.: 'Theory of random-population for quantum dots', *Phys. Rev. B*, 1997, **55**, (15), pp. 9740–9745

Bistable Operation of a Two-Section 1.3- μm InAs Quantum Dot Laser—Absorption Saturation and the Quantum Confined Stark Effect

Xiaodong Huang, *Member, IEEE*, A. Stintz, Hua Li, Audra Rice, G. T. Liu, *Student Member, IEEE*, L. F. Lester, *Member, IEEE*, Julian Cheng, *Senior Member, IEEE*, and K. J. Malloy, *Member, IEEE*

Abstract—Room temperature, continuous-wave bistability was observed in oxide-confined, two-section, 1.3- μm quantum-dot (QD) lasers with an integrated intracavity quantum-dot saturable absorber. The origin of the hysteresis and bistability were shown to be due to the nonlinear saturation of the QD absorption and the electroabsorption induced by the quantum confined Stark effect.

Index Terms—Absorption saturation, electroabsorption, hysteresis, optical bistability, quantum confined Stark effect, quantum-dot lasers, quantum dots, saturable absorber, semiconductor laser.

I. INTRODUCTION

SELF-ASSEMBLED InAs or InGaAs quantum dots (QDs) have been used as the gain medium to achieve laser diodes on GaAs substrates, with very low threshold current densities and emission wavelengths up to 1.3- μm [1]–[5]. The properties of the QD layers as an absorber in an active device have not been investigated in detail, however, and only weak (bias circuit dependent) bistability and self-pulsation have been reported in a shorter wavelength QD laser with an intracavity QD saturable absorber [6]. Optical bistability is usually associated with two-section laser structures where one section is actively pumped while the other acts as a saturable absorber. This bistable behavior has important applications in optical switching and modulation [7], [8]. More importantly, 1.3- μm QDs have been shown to exhibit ultrafast dynamic response [9], which suggests an ultrafast recovery time for a QD saturable absorber. An ultrafast QD saturable absorber may lead to high speed optical switching and modulation and to new techniques for semiconductor mode-locking. In this paper, we report the bistable operation of a long wavelength oxide-confined two-section QD laser with an integrated intracavity absorber formed with the same QD layers, in which both absorption saturation and electroabsorption induced by the quantum confined Stark effect (QCSE) play a role.

II. DEVICE STRUCTURE AND FABRICATION

The devices were fabricated from the same wafer as described in [5]. The wafer was grown by solid-source MBE on

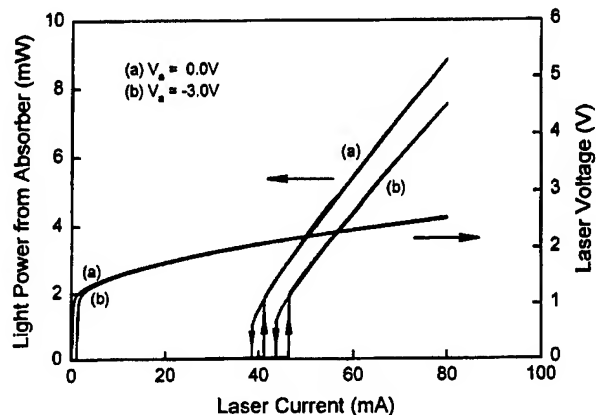


Fig. 1. Room-temperature CW lasing and electrical characteristics of a two-section QD laser with: (a) $V_a = -0.0$ V short circuit and (b) a reverse bias of $V_a = -3.0$ V, applied to the absorber section.

a (001) n^+ -GaAs substrate. The active region consists of two InAs quantum-dots-in-a-well (DWELL) layers [2] separated by a 30 nm GaAs barrier layer, situated in the middle of a 220-nm-thick GaAs waveguide bounded by $\text{Al}_{0.7}\text{Ga}_{0.3}\text{As}$ cladding layers. The devices have a typical two-section laser structure with a 50- μm gap in the top p -type contact metals. The lengths of the gain section and the absorber section are $L_g = 4.73$ and $L_a = 1.79$ mm, respectively, which ensure ground state lasing. An isolation resistance of 2.86 k Ω is achieved between these two sections by using shallow dry etching to remove the heavily doped cap layer in the gap region. Current confinement is provided by the wet lateral oxidation [10] of a 50-nm-thick $\text{Al}_{0.98}\text{Ga}_{0.02}\text{As}$ layer positioned between the waveguide and the upper cladding layers, resulting in a narrow current aperture of 10 μm . Detailed device processing has been reported in [5]. No coating is applied to the cleaved facets. The devices were mounted on a copper heat sink with the p -side up, and were tested under continuous-wave (CW) lasing operation at room temperature.

III. EXPERIMENTAL RESULTS

The devices were measured with current injection (I_g) into the gain section and a constant reverse bias voltage (V_a) applied to the absorber section. Room-temperature CW lasing occurred on the QD ground state. The peak external efficiency exceeded 25% for one facet and the lasing wavelength measured just above threshold is 1285 nm. Fig. 1 shows how the lasing

Manuscript received August 30, 2000.

The authors are with the Center for High Technology Materials, University of New Mexico, Albuquerque, NM 87106 USA (e-mail: xd-huang@chtm.unm.edu).

Publisher Item Identifier S 0018-9197(01)01631-1.

light power (L) emitted from the absorber facet and the voltage (V_g) across the laser section vary with the forward and backward sweep of the laser current under: 1) short-circuit conditions, with $V_a = 0.0$ V and 2) reverse bias, with $V_a = -3.0$ V across the absorber section. The L - I_g characteristics exhibit clear counterclockwise hysteresis loops and bistability. The loop position shifts to a higher laser current with increased reverse bias, while the loop width increases. The on-off ratio is about 27:1 at the center of the hysteresis loop. Unlike the devices described in [6], the appearance of bistability in this device does not require a resistive load in the absorber bias circuit to provide feedback via the photocurrent change. Only a constant reverse bias voltage was applied to the absorber section. When the gain section is biased in the middle of the hysteresis loop, on-off switching and modulation can be attained by applying a positive or a negative current pulse to the gain section. Note that the V_g - I_g characteristic for $V_a = -3.0$ V is displaced due to the leakage current between the gain section and the absorber section.

From the threshold conditions at the corners of the hysteresis loop, the modal loss of the absorber was estimated as a function of the light power out of the absorber under different reverse bias conditions, as shown in Fig. 2. The internal loss and the laser gain versus current density values obtained in [5] were used in the calculation with the leakage current subtracted from the threshold current. As expected, the modal loss of the absorber is comparable to the modal gain of the laser section. The absorption inside the absorber decreases nonlinearly as the light power output of the absorber is increased. Since the average light intensity within the absorber is proportional to the lasing light power output of the absorber, Fig. 2 also shows that the absorption of light by the absorber decreases nonlinearly as the light intensity inside the absorber is increased. This nonlinear saturation of absorption with increasing light intensity originates from the emptying of the QD ground state transition [11], [12], and is the origin of the hysteresis and bistability in the light power versus current characteristics. The saturation of absorption with increased light output introduces positive feedback and causes the sudden rise and fall of light power during the forward and backward current sweep. At higher injection current levels, gain saturation and the large difference between the unsaturated and saturated loss of the absorber under higher reverse bias result in a wider hysteresis loop. Finally, Fig. 2 also indicates the presence of electroabsorption, as absorption increases with increasing reverse bias on the absorber.

Hysteresis and bistability were also observed upon applying a constant laser injection current and varying the reverse bias voltage on the absorber. Fig. 3 shows how the light power out of the absorber and the photocurrent induced in the absorber vary with forward and backward sweep of the reverse bias voltage on the absorber. A clear and wide hysteresis loop exists in the light power versus reverse bias voltage characteristic, which is the combined result of both absorption saturation and the electroabsorption effect. This hysteresis and bistability appear not to have been reported in two-section quantum well (QW) lasers, although absorption saturation and electroabsorption can also simultaneously occur in a QW [13]. The total absorber current has two components—a leakage current between the gain sec-

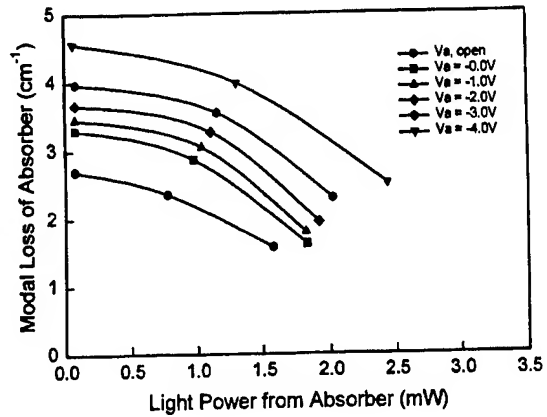


Fig. 2. Calculated modal loss inside the absorber as a function of light power out of the absorber under open circuit conditions ($V_a = 1.165$ V) and under a reverse bias of $V_a = 0.0, -1.0, -2.0, -3.0, -4.0$ V, respectively, across the absorber.

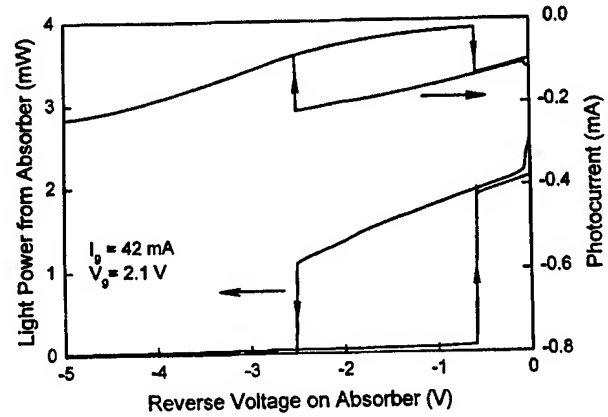


Fig. 3. Light power output of the absorber and its photocurrent under the forward and backward sweeps of the reverse bias voltage, showing hysteresis loops. The laser drive current is kept constant at $I_g = 42$ mA.

tion and the absorber section, and the photocurrent due to electron-hole pair creation via the absorption of light. The photocurrent in Fig. 3 was obtained by subtracting the leakage current from the total absorber current. Hysteresis loops also exist in the photocurrent characteristics corresponding to the loop in the light power, and there is a very large negative differential resistance corresponding to the sudden changes in light power. A device with the absorber biased in the middle of the hysteresis loop can be switched on and off by using a positive or negative voltage pulse, respectively. The reverse-biased absorber requires no current injection, the photocurrent change is quite small, and QD dynamics are intrinsically fast [9]. Therefore, using a shorter absorber section with better electrical isolation between the gain section and the absorber, high-speed switching and modulation controlled only by the absorber reverse bias are possible [14].

To explore the electroabsorption effect further, the absorption spectra were measured using the technique described in [15]. First, as shown in Fig. 4(a), the electroluminescence spectra out of the absorber was measured under different reverse bias conditions, while the laser is biased approximately at transparency

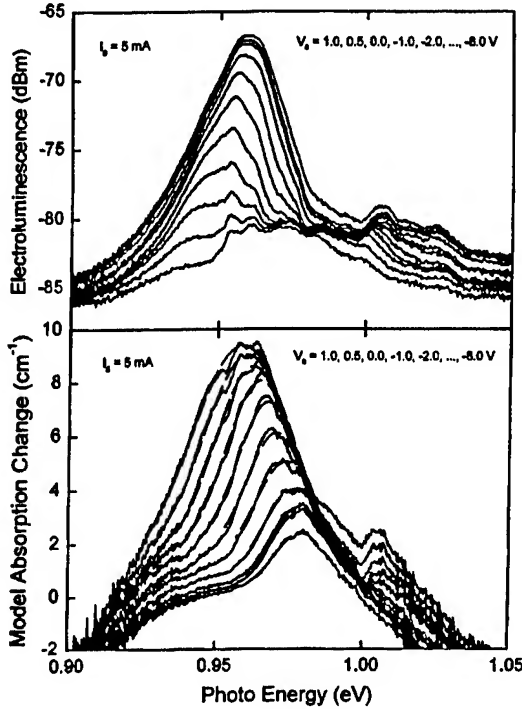


Fig. 4. (a) Electroluminescence from the absorber under constant laser injection current, $I_0 = 5$ mA and with different reverse bias voltages applied to the absorber, $V_a = 1.0, 0.5, 0.0, -1.0, -2.0, \dots, -8.0$ V. (b) Calculated modal absorption spectra, or change in modal absorption loss $\Delta\alpha$, of the absorber under different reverse bias conditions.

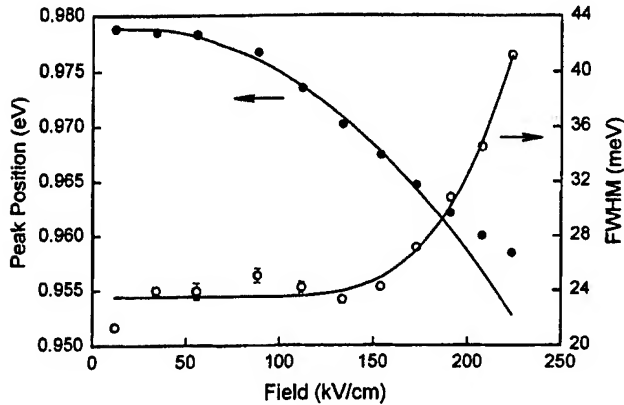


Fig. 5. Absorption spectrum peak position (in dark circles) and FWHM linewidth (in open circles) as a function of the internal electrical field. Error bars indicate the precision to which the data points could be determined from Gaussian envelope fitting. Solid lines are fit curves where a quadratic dependence and an exponential relation were assumed for the peak position and linewidth broadening, respectively.

($I_0 = 5$ mA). Fig. 4(a) shows the electroluminescence intensity from the absorber decreases as the bias voltage of the absorber changes from forward bias, $V_a = 1.0$ V, to reverse bias, $V_a = -8.0$ V. In the mean time, the electroluminescence peak position red-shifts to a smaller photon energy. The modal absorption spectra, or strictly, the changes in modal absorption

loss, $\Delta\alpha$, under different reverse bias conditions were calculated using the following equation:

$$\Delta\alpha = -\frac{1}{L_a} \ln\left(\frac{I}{I_{\text{ref}}}\right) \quad (1)$$

in which the cavity resonance was ignored, and the results are shown in Fig. 4(b). Here, I is the electroluminescence intensity at a certain bias voltage, and I_{ref} is the reference intensity level corresponding to the electroluminescence of the gain section under transparency, where any absorption or gain present is small. The peak position of $\Delta\alpha$ is actually the ground state transition peak of the absorption spectra. Fig. 4(b) shows both the redshift of the spectral absorption peak and the broadening of the absorption spectrum with increasing reverse bias. The absorption spectra peaks were fitted with Gaussian envelopes, shown as dashed lines in Fig. 4(b). For a higher reverse bias voltage, e.g., $|V_a| \geq 4.0$ V, a smaller peak arises at higher photon energy, corresponding to the absorption due to an excited state transition.

The redshift and broadening of the absorption spectrum under reverse bias conditions can be attributed to the QCSE, arising from the electric field in the QD layers. The internal electrical field across the QD was calculated for the laser structure under different reverse bias conditions. The ground state absorption peak position and the full-width at half-maximum (FWHM) of the absorption spectra were extracted from the Gaussian fitting parameters and plotted against the internal electrical field in Fig. 5. The peak positions at a reverse bias of $|V_a| \leq 5$ V can be approximately described by a quadratic dependence. The peak redshift deviates from the quadratic dependence at higher reverse biases, possibly because the field is large enough to begin dissociating the electron-hole pair and thus influences the transition energy [16]. The Stark shift has an amplitude of ~ 10 meV under an electric field of 150 kV/cm, which is comparable with the measurement of an InAs QD on GaAs in [17], and smaller than that in an ordinary QW under the same electric field [18]. This can be explained by the relatively high barrier height and the small size of the QD's along the electrical field [16]. The FWHM of the absorption spectra change only slightly at low electrical fields (less than 150 kV/cm), and rise sharply at higher fields.

This linewidth increase is attributed to a reduced lifetime of the exciton in the dot caused by the tunneling of carriers out of the dot [19]. The expression below, derived in [19] for linewidth broadening of a single QD under an electrical field, was used to fit the linewidth broadening of the absorption spectra peaks

$$\Gamma = \Gamma_0 + a \exp\left(-\frac{b}{F}\right) \quad (2)$$

Here, Γ is the linewidth as a function of electrical field, F , $\Gamma_0 = 23.52$ meV is the linewidth at zero field, and $a = 4517.2$ meV and $b = 1242.03$ kV/cm are fitting parameters. The fit indicates that the broadening of the absorption spectra follows the same dependence as linewidth broadening of a single QD.

IV. CONCLUSION

In summary, long wavelength, oxide-confined two-section QD lasers with an integrated intracavity QD saturable absorber have been fabricated. In addition to achieving efficient room temperature CW lasing operation in the ground state, hysteresis and bistability have also been observed in both the L - I_g characteristics of the laser voltage, and in the reverse-biased characteristics of the light-absorber. The origin of bistable operation in the laser's L - I_g characteristic was attributed to the nonlinear saturation of the QD absorption, presumably caused by state filling. The bistability of the light-absorber's reverse-biased characteristics is due to both nonlinear absorption saturation and the electroabsorption induced by the QCSE under the applied electrical field. The QD absorption spectra have been measured and the QCSE has been observed. The redshift and broadening of the absorption spectra have been obtained from the Gaussian envelope fitting of the absorption spectra as a function of internal electrical field. The Stark shift of the absorption spectra follows a quadratic dependence at small electric fields, while the linewidth broadening of the absorption spectra has the same electric field dependence as the linewidth broadening of a single QD.

REFERENCES

- [1] Yu. M. Shernyakov, D. A. Bedarev, E. Yu. Kondrat'eva, P. S. Kop'ev, A. R. Kovsh, N. A. Maleev, M. V. Maximov, S. S. Mikhrin, A. F. Tsatsul'nikov, V. M. Ustinov, B. V. Volovik, A. E. Zhukov, Zh. I. Alferov, N. N. Ledentsov, and D. Bimberg, "1.3 μm GaAs-based laser using quantum dots obtained by activated spinodal decomposition," *Electron. Lett.*, vol. 35, pp. 898–900, 1999.
- [2] L. F. Lester, A. Stintz, H. Li, T. C. Newell, E. A. Pease, B. A. Fuchs, and K. J. Malloy, "Optical characteristics of 1.24 μm quantum dot lasers," *IEEE Photon. Technol. Lett.*, vol. 11, pp. 931–933, 1999.
- [3] K. Mukai, Y. Nakata, K. Otsubo, M. Sugawara, N. Yokoyama, and H. Ishikawa, "1.3- μm CW lasing of InGaAs-GaAs quantum dots at room temperature with a threshold current of 8 mA," *IEEE Photon. Technol. Lett.*, vol. 11, pp. 1205–1207, Oct. 1999.
- [4] G. Park, O. B. Shchekin, D. L. Huffaker, and D. G. Deppe, "Low-threshold oxide-confined 1.3- μm quantum dot laser," *IEEE Photon. Technol. Lett.*, vol. 13, pp. 230–232, Mar. 2000.
- [5] X. Huang, A. Stintz, C. P. Hains, G. T. Liu, J. Cheng, and K. J. Malloy, "Efficient high temperature CW lasing operation of oxide-confined long-wavelength InAs quantum dot lasers," *Electron. Lett.*, vol. 36, no. 1, pp. 41–42, 2000.
- [6] O. Qasaimeh, W. D. Zhou, J. Philips, S. Krishna, P. Bhattacharya, and M. Dutta, "Bistability and self-pulsation in quantum-dot lasers with intracavity quantum-dot saturable absorbers," *Appl. Phys. Lett.*, vol. 74, no. 12, pp. 1654–1656, 1999.
- [7] H. Kawaguchi, "Bistable laser diodes and their application: State of the art," *IEEE J. Select. Topics Quantum Electron.*, vol. 3, pp. 1254–1270, 1997.
- [8] —, "Progress in optical functional devices using two-section laser diodes/amplifiers," in *IEE Proc. J*, vol. 140, 1993, pp. 3–15.
- [9] L. Zhang, T. F. Boggess, D. G. Deppe, D. L. Huffaker, O. B. Shchekin, and C. Cao, "Dynamic response of 1.3- μm -wavelength InGaAs/GaAs quantum dots," *Appl. Phys. Lett.*, vol. 76, no. 10, pp. 1222–1224, 2000.
- [10] J. M. Dallesasse, N. Holonyak, A. R. Sugg, and T. A. Richard, "Hydrolyzation oxidation of AlGaAs-AlAs-GaAs quantum well heterostructures and superlattices," *Appl. Phys. Lett.*, vol. 57, no. 26, pp. 2844–2846, 1990.
- [11] A. Schmitt-Rink, D. A. B. Miller, and D. S. Chemla, "Theory of the linear and nonlinear optical properties of semiconductor microcrystallites," *Phys. Rev. B*, vol. 35, no. 15, pp. 8113–8125, 1987.
- [12] T. Matsumoto, M. Ohtsu, K. Matsuda, T. Saiki, H. Saito, and K. Nishi, "Low-temperature near-field nonlinear absorption spectroscopy of InGaAs single quantum dots," *Appl. Phys. Lett.*, vol. 75, no. 21, pp. 3246–3248, 1999.
- [13] H. Uenohara, R. Takahashi, Y. Kawamura, and H. Iwamura, "Static and dynamic response of multiple-quantum-well voltage controlled bistable laser diodes," *IEEE J. Quantum Electron.*, vol. 32, pp. 873–883, May 1996.
- [14] E. Goutain, J. C. Renaud, M. Krakowski, D. Rondi, R. Blondeau, and D. Decoster, "30 GHz bandwidth, 1.55 μm MQW-DFB laser diode based on a new modulated scheme," *Electron. Lett.*, vol. 32, no. 10, pp. 896–897, 1996.
- [15] S. D. McDougall and C. N. Ironside, "Measurements of reverse and forward bias absorption and gain spectra in semiconductor laser material," *Electron. Lett.*, vol. 31, no. 25, pp. 2179–2181, 1995.
- [16] G. W. Wen, J. Y. Lin, H. X. Jiang, and Z. Zhen, "Quantum-confined Stark effects in semiconductor quantum dots," *Phys. Rev. B*, vol. 52, no. 8, pp. 5913–5922, 1995.
- [17] P. W. Fry, I. E. Itskevich, D. J. Mowbray, M. S. Skolnick, J. J. Finley, J. A. Barker, E. P. O'Reilly, L. R. Wilson, I. A. Larkin, P. A. Maksym, M. Hopkinson, M. Al-Khafaji, J. P. R. David, A. G. Cullis, G. Hill, and J. C. Clark, "Inverted electron-hole alignment in InAs-GaAs Self-assembled quantum dots," *Phys. Rev. Lett.*, vol. 84, no. 4, pp. 733–736, 2000.
- [18] R. Y.-F. Yip, P. Desjardins, L. Isnard, A. Ait-Ouali, H. Marchand, J. L. Brebner, J. F. Currie, and R. A. Masut, "Band alignment engineering for high speed, low drive field quantum confined Stark effect devices," *J. Appl. Phys.*, vol. 83, no. 3, pp. 1758–1769, 1998.
- [19] W. Heller, U. Bockelmann, and G. Abstreiter, "Electric-field effects on excitons in quantum dots," *Phys. Rev. B*, vol. 57, no. 11, pp. 6270–6273, 1998.

Xiaodong Huang, photograph and biography not available at the time of publication.

A. Stintz, photograph and biography not available at the time of publication.

Hua Li, photograph and biography not available at the time of publication.

Audra Rice, photograph and biography not available at the time of publication.

G. T. Liu, photograph and biography not available at the time of publication.

L. F. Lester, photograph and biography not available at the time of publication.

Julian Cheng, photograph and biography not available at the time of publication.

K. J. Malloy, photograph and biography not available at the time of publication.

Optical Characteristics of 1.24- μm InAs Quantum-Dot Laser Diodes

L. F. Lester, *Member, IEEE*, A. Stintz, H. Li, *Member, IEEE*, T. C. Newell, *Member, IEEE*,
E. A. Pease, *Student Member, IEEE*, B. A. Fuchs, *Member, IEEE*,
and K. J. Malloy, *Member, IEEE*

Abstract—The optical characteristics of the first laser diodes fabricated from a single-InAs quantum-dot layer placed inside a strained InGaAs QW are described. The saturated modal gain for this novel laser active region is found to be $9\text{--}10\text{ cm}^{-1}$ in the ground state. Room temperature threshold current densities as low as 83 A/cm^2 for uncoated $1.24\text{-}\mu\text{m}$ devices are measured, and operating wavelengths over a 190-nm span are demonstrated.

Index Terms—Epitaxial growth, quantum dots, semiconductor laser.

QUANTUM DOTS (QD's) hold tremendous promise for reducing the threshold current density in semiconductor lasers because of their large reduction in the density of states [1]. In particular, laser diodes based on self-assembled QD's as the active region have gained considerable interest in recent years due to their potentially superior performance characteristics compared to quantum-well (QW) lasers [2]. Threshold current densities have been predicted and shown to be low [3], [4] owing to the QD's delta-like density of states. In the GaAs-based material system, an extended wavelength range up to $1.3\text{ }\mu\text{m}$ has become feasible with QD's [5], previously limited to $\sim 1.1\text{ }\mu\text{m}$ by strained QW's. However, it is clear that decreasing the state density has the negative side effect of reducing the maximum optical gain. In addition, if the dots do not fill a plane, efficient carrier capture is hampered. If a single layer of QD material is not sufficient for lasing or high injection efficiency, then multiple layers can be designed and built, but this technique has been observed to increase dot size in successive layers if the barrier material is relatively thin [6]. Any broadening of the emission spectrum because of dot nonuniformity reduces the peak optical gain. This letter presents the first attempt at improving the injection efficiency of a single-layer InAs QD laser by inserting the dot material in a strained $\text{In}_{0.2}\text{Ga}_{0.8}\text{As}$ QW. This "dots in a well" (DWELL) design has been studied before, but typically with $\text{In}_x\text{Ga}_{1-x}\text{As}$ dots sandwiched in a GaAs QW [7], [8]. The method is analogous to the standard separate confinement heterostructure (SCH) except on a much smaller length scale. The optical characteristics of the DWELL laser including peak pulsed power, wavelength operating range, internal loss, and

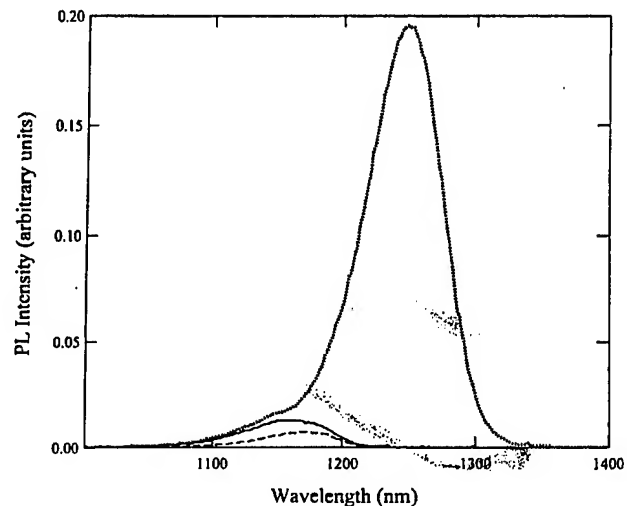


Fig. 1. Room-temperature PL intensity from InAs QD's grown on bulk GaAs (dashed line), InAs QD's grown in a $100\text{-}\text{\AA}$ $\text{Al}_{0.2}\text{Ga}_{0.8}\text{As}/\text{GaAs}$ QW (solid line), and InAs QD's grown in a $100\text{-}\text{\AA}$ strained $\text{In}_{0.2}\text{Ga}_{0.8}\text{As}-\text{GaAs}$ QW (dotted line). FWHM's are about 70 nm , indicative of the inhomogeneous energy broadening.

efficiency are analyzed with a focus toward determining the maximum modal gain [9] from a single-InAs dot layer and the anticipated wavelength tuning range. Improvement in the injection efficiency is inferred from photoluminescence (PL) experiments.

The DWELL laser structure was grown by elemental source molecular beam epitaxy (MBE) on an n^+ -doped, $\langle 100 \rangle$ oriented GaAs substrate. The epitaxial layers consist of an n -type (10^{18} cm^{-3}) 300-nm -thick GaAs buffer, an n -type lower $\text{Al}_{0.7}\text{Ga}_{0.3}\text{As}$ cladding layer, a 230-nm -thick GaAs waveguide surrounding the laser active region, a p -type upper cladding layer, and a p^+ -doped ($3 \times 10^{19}\text{ cm}^{-3}$) 60-nm -thick GaAs cap. The cladding layers are doped at 10^{17} cm^{-3} and are each $2\text{ }\mu\text{m}$ thick, following the design of [5]. In the center of the waveguide, an equivalent coverage of 2.4 monolayers InAs QD's are confined approximately in the middle of a $100\text{-}\text{\AA}$ $\text{In}_{0.2}\text{Ga}_{0.8}\text{As}$ QW. The QD's and QW were grown at 490°C , as measured by an optical pyrometer. The InAs growth rate is 0.075 monolayers/s, and the As_2/In beam equivalent pressure ratio is ~ 30 . The QD's formed under these conditions have an areal density of $7.5 \times 10^{10}\text{ cm}^{-2}$, a base diameter $< 400\text{ }\text{\AA}$, and are $\sim 70\text{ }\text{\AA}$ high, as determined by AFM measurements on a separate calibration sample.

Manuscript received March 1, 1999; revised April 20, 1999. This work was supported by the Defense Advanced Research Projects Agency under Grant MDA972-98-1-0002 and by the U.S. Air Force Office of Scientific Research under Grant F49620-96-1-0077.

The authors are with the Center for High Technology Materials, University of New Mexico, Albuquerque, NM 87106 USA.

Publisher Item Identifier S 1041-1135(99)05901-7.

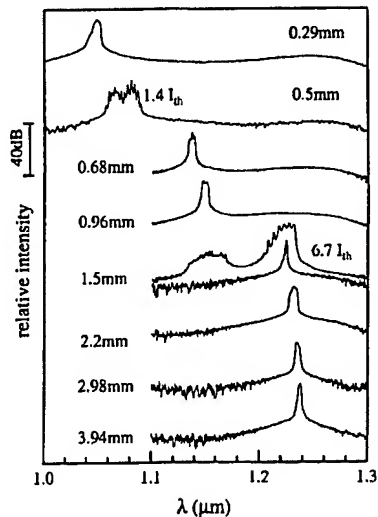


Fig. 2. The measured lasing spectra of InAs QD lasers with eight different cavity lengths. The pump current level is $1.1 \times$ threshold if not otherwise noted.

Fig. 1 shows that the PL intensity nearly doubles when InAs dots are placed within a 100-Å $\text{Al}_{0.2}\text{Ga}_{0.8}\text{As}$ -GaAs QW compared to when they are grown on bulk GaAs. This improvement is attributed to improved carrier capture by the DWELL design. In these two cases, the InAs dot densities are in the low 10^{10} cm^{-2} . A further fifteen-fold increase in luminescence is observed if the surrounding QW is strained $\text{In}_{0.2}\text{Ga}_{0.8}\text{As}$ -GaAs. In this instance, the improvement in light emission is ascribed to the increase in dot density that is observed when the InAs dots are grown on $\text{In}_{0.2}\text{Ga}_{0.8}\text{As}$ instead of GaAs.

The material was processed into 100- μm -wide broad-area lasers with cavity lengths L_{cav} ranging from 0.285 to 3.94 mm. All diodes had uncoated facets and were tested at room temperature under pulsed conditions with 0.3- μs pulses, 0.5% duty cycle. Fig. 2 shows a composite diagram of the wavelength spectra measured with an optical spectrum analyzer (OSA) of eight different cavity lengths. For lasers longer than 1.5 mm, the devices emit from the ground state of the InAs QD's at wavelengths varying from 1.22 to 1.24 μm . Although the 1.5-mm cavity begins lasing in the ground state, higher pump levels reveal competition between the ground state and the excited transitions due to gain saturation. At $L_{\text{cav}} \leq 1 \text{ mm}$, lasing occurs in the range of 1.05–1.15 μm with gain competition again happening at $L_{\text{cav}} = 0.5 \text{ mm}$. Very weak 980-nm emission from the strained $\text{In}_{0.2}\text{Ga}_{0.8}\text{As}$ well is observed at high current densities in only the 0.285-mm cavity laser. There are several characteristics in these spectra that manifest the unique nature of the QD active region: 1) the appreciable trough in the lasing spectrum between the ground and excited states of the 1.5-mm device; 2) the relatively narrow lasing mode spectrum in the 3.94-mm device (although this is certainly a function of pump level); and 3) the 190-nm range in lasing wavelengths. Although the continuity of the gain spectrum may be interrupted by dips as evidenced in the 1.5-mm cavity, these results show that a QD laser could be designed to have a very wide tuning range.

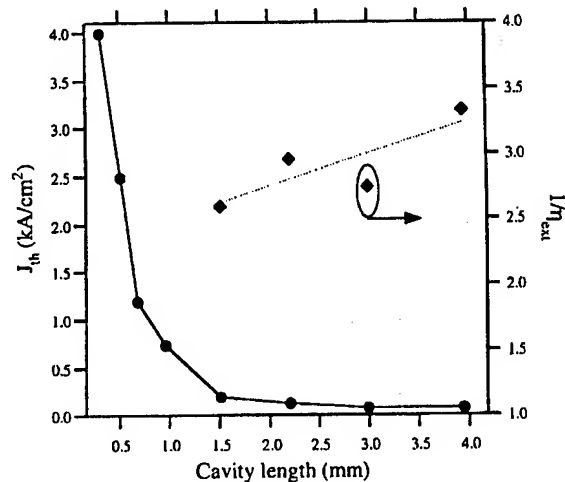


Fig. 3. The threshold current density and external efficiency as a function of cavity length. An internal loss of 1.3 cm^{-1} and internal injection efficiency of 45% are calculated from the efficiency data.

The threshold current density, J_{th} , at 295 K as a function of cavity length is plotted in Fig. 3. A minimum threshold current density of 83 A/cm^2 is obtained for the 3.94-mm cavity. This is the lowest reported room-temperature J_{th} for an as-cleaved QD laser with a wavelength longer than 1.1 μm . Two distinct trends are apparent in Fig. 3—one in which J_{th} is relatively small and slowly varying, and another in which the change in J_{th} is rapid. The first region, for which $L_{\text{cav}} \geq 1.5 \text{ mm}$, corresponds to lasing in the ground state of the QD, and the second correlates with saturation of the ground state and subsequent lasing in the excited states as seen in Fig. 2. The relatively long cavity length at which ground state lasing saturates is indicative of a small density of states, and to some degree a poorer overlap of the dots with the optical field. To estimate the maximum modal gain of the InAs QD layer, the threshold gain, $g_{\text{th}} = \alpha_i - (1/L_{\text{cav}}) \cdot \ln(R)$, of the 1.5 mm laser is calculated using a facet reflectivity, $R = 0.31$, and an internal loss value, $\alpha_i = 1.3 \text{ cm}^{-1}$, as determined from the external efficiency data plotted in Fig. 3. This internal loss value is reasonable considering that the laser cladding regions are designed to minimize free carrier absorption. The estimate for the maximum modal gain then is between 9–10 cm^{-1} . This number is considerably less than what can be achieved with a single QW [10] and highlights the tradeoff of high optical gain for low J_{th} .

The peak pulsed power at 295 K is plotted in Fig. 4 for a laser with $L_{\text{cav}} = 2.98 \text{ mm}$. With regard to efficiency, this device and others like it from the same laser bar have the best performance considering the cavity length. The external efficiency is 36% at $\lambda = 1.24 \mu\text{m}$, and the single-facet pulsed power of 220 mW is limited by the test equipment. From Fig. 3, an average internal injection efficiency η_i of 45% can be determined. Although this is not the highest reported η_i [11], [12] for a QD laser, the increase in PL efficiency suggests the DWELL structure does increase the efficiency. It remains to be seen if the exact position of the dot layer within the QW or the QW size influences the efficiency through modification of the nonradiative, defect recombination rate.

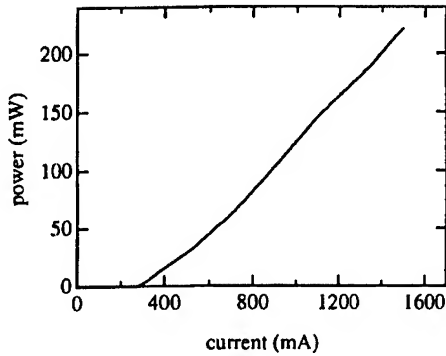


Fig. 4. The peak power as a function of pulsed bias current of a 100- μm -wide by 2.98-mm-long InAs QD laser. The current pulses are 300 ns and the duty cycle is 0.5%.

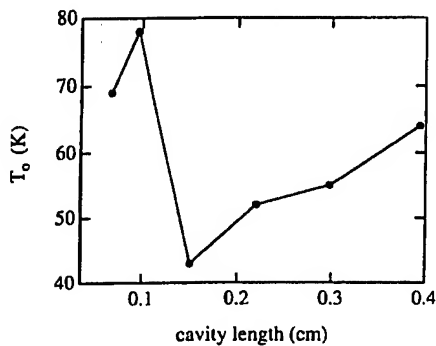


Fig. 5. The characteristic temperature versus cavity length for operation between 15 °C and 75 °C.

It is found that the characteristic temperature, T_0 , of the lasers is dependent upon cavity length and the state of the lasing transition. This data, which was calculated from measurement of J_{th} from 15 °C to 75 °C, is displayed in Fig. 5. For ground state lasing, the maximum T_0 is 63 K and decreases monotonically with decreasing cavity length. It is believed that this reduction in T_0 is explained by carrier heating and possible thermionic emission from the dots. For excited-lasing ($L_{\text{cav}} \leq 1 \text{ mm}$), T_0 jumps higher to values between 69 K and 78 K. This apparent improvement is deceptive because it is a consequence of the larger density of excited states. The latter is reflected in the significantly larger J_{th} 's of the shorter cavity length devices.

In conclusion, the optical characteristics of the first semiconductor lasers made from a single layer of InAs QD's sandwiched in a strained $\text{In}_{0.2}\text{Ga}_{0.8}\text{As}$ QW have been presented. It was found that the strained well was instrumental in improving carrier capture in the dots and increasing the InAs dot density. The minimum obtained J_{th} for uncoated lasers was 83 A/cm^2 , but the maximum modal gain of the ground state was only 9–10 cm^{-1} . The wide range of operating wavelengths (190 nm) makes the QD active region an attractive candidate for external cavity tuned lasers.

REFERENCES

- [1] H. Sakaki, "Quantum wires, quantum boxes, and related structures: Physics, device potentials and structural requirements," *Surface Sci.*, vol. 267, pp. 623–629, 1992.
- [2] K. Eberl, "Quantum dot lasers," *Phys. World*, vol. 10, pp. 47–50, 1997.
- [3] D. Bimberg, N. N. Ledentsov, M. Grundmann, F. Heinrichsdorff, V. M. Ustinov, P. S. Kop'ev, Zh. I. Alferov, and J. A. Lott, "Edge and vertical cavity surface emitting InAs quantum dot lasers," *Solid-State Electron.*, vol. 42, pp. 1433–1437, 1998.
- [4] K. Mukai, Y. Nakata, H. Shoji, S. Sugawara, K. Ohtsubo, N. Yokoyama, H. Ishikawa, "Lasing with low-threshold current and high-output power from columnar-shaped InAs/GaAs quantum dots," *Electron. Lett.*, vol. 34, pp. 1588–1590, 1998.
- [5] D. L. Huffaker, G. Park, Z. Zou, O. B. Shchekin, and D. G. Deppe, "1.3 μm room-temperature GaAs-based quantum-dot laser," *Appl. Phys. Lett.*, vol. 73, pp. 2564–2566, 1998.
- [6] F. Heinrichsdorff, M. H. Mao, N. Kirstaedter, A. Krost, D. Bimberg, A. O. Kosogov, and P. Werner, "Room-temperature continuous-wave lasing from stacked InAs/GaAs quantum dots grown by metalorganic chemical-vapor-deposition," *Appl. Phys. Lett.*, vol. 71, pp. 22–24, 1997.
- [7] A. Patane, A. Polimeni, M. Henini, L. Eaves, P. C. Main, and G. Hill, "Thermal effects in quantum dot lasers," *J. Appl. Phys.*, vol. 85, pp. 625–627, 1999.
- [8] D. Bimberg, N. Kirstaedter, N. N. Ledentsov, Zh. I. Alferov, P. S. Kop'ev, and V. M. Ustinov, "InGaAs-GaAs quantum dot lasers," *IEEE J. Select Topics Quantum Electron.*, vol. 3, pp. 196–205, 1997.
- [9] O. G. Schmidt, N. Kirstaedter, N. N. Ledentsov, M.-H. Mao, D. Bimberg, V. M. Ustinov, A. Y. Egorov, A. E. Zhukov, M. V. Maximov, P. S. Kop'ev, and Z. I. Alferov, "Prevention of gain saturation by multi-layer quantum dot lasers," *Electron. Lett.*, vol. 32, pp. 1302–1304, 1998.
- [10] K. Y. Lau in *Quantum Well Lasers*, P. S. Zory, Ed. New York: Academic, 1993, p. 195.
- [11] M. V. Maximov, Yu. M. Shernyakov, A. F. Tsatsul'nikov, A. V. Lunev, A. V. Sakharov, V. M. Ustinov, A. Yu. Egorov, A. E. Zhukov, A. R. Kovsh, P. S. Kop'ev, L. V. Asryan, Zh. I. Alferov, N. N. Ledentsov, D. Bimberg, A. O. Kosogov, and P. Werner, "High-power continuous-wave operation of a InGaAs/AlGaAs quantum dot laser," *J. Appl. Phys.*, vol. 83, pp. 5561–5563, 1998.
- [12] R. Mirin, A. Gossard, and J. Bowers, "Room temperature lasing from InGaAs quantum dots," *Electron. Lett.*, vol. 32, pp. 1732–1734, 1996.

Room-Temperature Operation of InAs Quantum-Dash Lasers on InP (001)

R. H. Wang, A. Stintz, P. M. Varangis, T. C. Newell, H. Li, K. J. Malloy, and L. F. Lester

Abstract—The first self-assembled InAs quantum dash lasers grown by molecular beam epitaxy on InP (001) substrates are reported. Pulsed room-temperature operation demonstrates wavelengths from 1.60 to 1.66 μm for one-, three-, and five-stack designs, a threshold current density as low as 410 A/cm² for single-stack uncoated lasers, and a distinctly quantum-wire-like dependence of the threshold current on the laser cavity orientation. The maximal modal gains for lasing in the ground-state with the cavity perpendicular to the dash direction are determined to be 15 cm⁻¹ for single-stack and 22 cm⁻¹ for five-stack lasers.

Index Terms—InAs, InP, quantum dash, quantum dot, self-assembled, semiconductor laser.

THERE IS increasing interest in employing semiconductor quantum dots (QDs) in optoelectronic devices, since QDs exhibit unique electrical and optical properties compared with conventional quantum-well (QW) structures [1]. Previous research has yielded impressive laser diode results on GaAs, including: 1) a very low room-temperature threshold current density [2]–[5]; 2) the observation of an ultra-small linewidth enhancement factor [6], [7]; and 3) the attainment of a 201-nm tuning range at bias currents ten times lower than those required in QW lasers [8]. However, these GaAs-based QDs lasers operate at wavelengths $\leq 1.33 \mu\text{m}$ [9]. It is very difficult to fabricate InAs–GaAs QDs with an emission wavelength as long as 1.55- μm range, which is desirable for long-distance optical communication systems. The problem arises from the large lattice mismatch (7%) between InAs and GaAs that significantly increases the bandgap due to the large compressive strain, and makes the growth of large QDs to minimize the quantum size effect difficult [10]. An InP substrate is preferable for the fabrication of long-wavelength InAs QD lasers due to the smaller lattice mismatch (3%) between InAs and InP. It has been reported that InAs–InGaAs–InP QDs lasers emit at 1.9 μm at 77 K [11]. Researchers have also reported ground-state lasing at room temperature in long-wavelength InAs QDs-lasers, but on InP (311) B substrates [12]. In this letter, we detail the first demonstration of room-temperature operation of one-, three-, and five-stack self-assembled InAs quantum-dash (QDASH) laser diodes with

wavelengths from 1.60 to 1.66 μm and low-threshold currents fabricated on InP (001) substrates.

The origin of the name “dash” comes from a physical description of the finite-length wire-like InAs structures that self-assemble when grown within an AlGaInAs QW on an InP substrate. The reason why self-assembled wire-like structures are formed instead of dots remains uncertain. Brault *et al.* [13] find that under identical growth conditions, wire formation is preferred on InGaAs buffer layers lattice matched to InP, while dots are observed on AlInAs lattice matched to InP. They attribute the wire-like shape of the nanostructures to a longer diffusion length on InGaAs compared to AlInAs, which is supported by surface roughness measurements. The preferred elongation of the dashes is along the $[1\bar{1}0]$ direction as observed by atomic force microscopy (AFM). This may be explained by the different nature of the step edges of InAs on a (001) oriented surface. Step edges along $[1\bar{1}0]$ are cation terminated and less reactive compared to step edges along $[110]$, which are anion terminated and more reactive with respect to indium [14]. As a result, the growth of InAs nanostructures proceeds faster in the $[1\bar{1}0]$ direction, and this leads to the formation of quantum dashes.

Previous research on one-dimensional (1-D) quantum-wire semiconductor lasers was most notably based on metal–organic chemical vapor deposition (MOCVD) regrowth into V-shaped grooves [15]. This technique is susceptible to etch damage, the wire array density is limited by the spacing between the etched grooves, and the laser cavity is undesirably oriented along the wire direction. Since self-assembled QDASHs do not suffer from these problems, they offer a new path for realizing quantum-wire lasers.

The three samples studied were grown on n-type InP (001) substrates using solid-source molecular beam epitaxy (MBE). A calibration wafer was grown in order to determine the dimensions of the InAs QDASHs. As shown in Fig. 1, typical dimensions for the dashes are 300, 25, and 5 nm for the length, width, and height, respectively, when measured uncapped by AFM. The length value is considerably longer than that reported from previous research [16]. From the image analysis, a density of $\sim 10^{10}$ QDASHs/cm² is deduced. The laser structure consists of a waveguide structure of lattice-matched AlInAs cladding layers around an AlGaInAs waveguide/barrier region with bandgap of 1.2 μm . The compressively strained AlGaInAs QW surrounding the InAs QDASHs has a bandgap of approximately 1.3 μm and a thickness of 7.5 nm. One, three, and five stacks of InAs QDASHs with 30-nm tensile-strained AlGaInAs barriers comprise the active regions.

Manuscript received March 2, 2001; revised May 4, 2001. This work was supported by the Air Force Office of Scientific Research under Grant F49620-99-1-0330 and by the Advanced Sensors Consortium of the Army Federated Laboratories. The views and conclusions contained in this document are those of the authors and should not be interpreted as representing the official policies, either expressed or implied, of the Army Research Laboratory or the U.S. Government.

The authors are with the Center for High Technology Materials, University of New Mexico, Albuquerque, NM 87106 USA (e-mail: rwang@chtm.unm.edu).

Publisher Item Identifier S 1041-1135(01)06417-5.

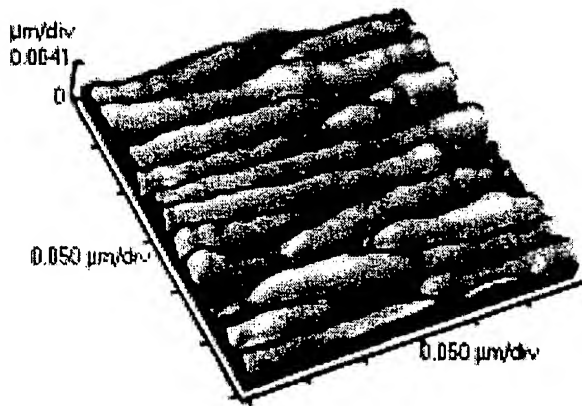


Fig. 1. An atomic force micrograph of the InAs quantum dashes.

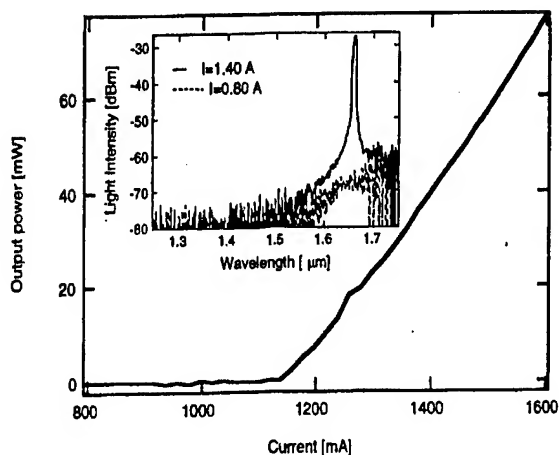


Fig. 2. A two-facet light output versus injection current measured on a five-stack laser diode with geometry of $100\text{ }\mu\text{m} \times 1500\text{ }\mu\text{m}$. The inset is the electroluminescence spectra under different pump levels for the device. The spectral peak is $1.66\text{ }\mu\text{m}$.

Broad area lasers with $100\text{-}\mu\text{m}$ stripe widths were processed from these wafers. For single and three-stack samples, lasers were only characterized with cavities along $[110]$, while five-stack lasers with cavity orientations of both $[110]$ and $[1\bar{1}0]$ were fabricated and measured. All devices were tested with the epitaxial side up on a thermoelectric cooler using pulsed excitation. The pulse width was $0.5\text{ }\mu\text{s}$ with a duty cycle of 0.5% , and the temperature of the thermoelectric cooler was set to $15\text{ }^\circ\text{C}$.

The room-temperature operation wavelengths are 1.60 , 1.62 , and $1.66\text{ }\mu\text{m}$ for the ground state of the one-, three-, and five-stack lasers, respectively. The trend of longer wavelength with increasing stack number may be explained by a size increase of the QDASHs, as more stacks are grown or band filling. The same trend has also been observed in QD lasers [17]. Fig. 2 shows the total light output as a function of injection current for a five-stack laser with the cavity perpendicular to the dash direction and a geometry of $100\text{ }\mu\text{m} \times 1500\text{ }\mu\text{m}$. The inset displays electroluminescence (EL) spectra under various current injection levels from the laser. The EL peaks are approximately $1.66\text{ }\mu\text{m}$ before and after the threshold condition is satisfied, which indicates that the diode operates in the ground-state. In contrast, when the cavity length is cleaved to be $300\text{ }\mu\text{m}$ the EL peak shifts to about $1.60\text{ }\mu\text{m}$. In fact, five-stack lasers with

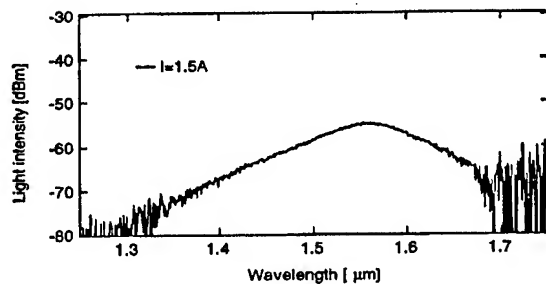


Fig. 3. Electroluminescence spectrum for a single-stack laser with cavity length of $1500\text{ }\mu\text{m}$ and under 1.5-A current injection (1 kA/cm^2).

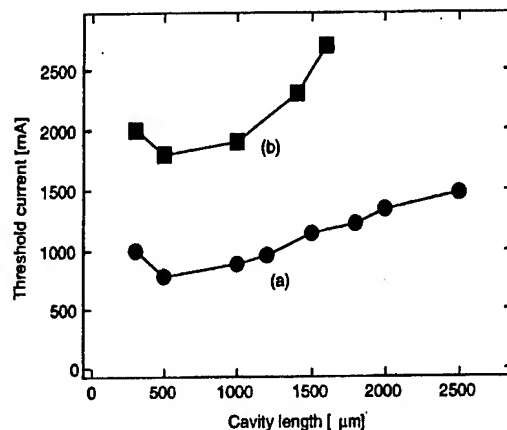


Fig. 4. Threshold current versus cavity length for five-stack lasers. (a) $[110]$ cavity orientation (perpendicular to the dash direction). (b) $[1\bar{1}0]$ cavity orientation (parallel to the dash direction).

cavity lengths shorter than $1000\text{ }\mu\text{m}$ emit at $1.60\text{ }\mu\text{m}$, which is believed to be the excited-state. The latter is the band of energies centered around the second quantized level determined by the shorter QDASH dimension in the growth plane. Therefore, the energy difference between the ground-state and the excited-state is approximately 32 meV , which is smaller than the value of 55 meV for the energy difference between the ground-state and the excited-state for InAs QD on InP (311) B substrates reported previously [12]. This result is reasonable since the QDASHs shorter dimension in the growth plane is larger than the QDs diameter. As shown in Fig. 3, the spontaneous emission spectrum for a one-stack laser under 1.5 A pump level (1 kA/cm^2) covers the range from 1.35 to $1.65\text{ }\mu\text{m}$, indicating that this one-stack QDASH structure has the potential for a very large tuning bandwidth in the wavelength range important for wavelength-division-multiplexing (WDM) optical communication systems.

Fig. 4 shows a significant dependence of the threshold current on the orientation of the laser cavity. Trace (a) portrays the five-stack lasers with cavities oriented along the $[110]$ direction (perpendicular to the QDASH direction), while curve (b) presents cavities that are aligned along the $[1\bar{1}0]$ direction (parallel to the dash direction). It is observed that the threshold currents for the laser diodes with cavities parallel to the QDASH direction are approximately two times higher than those with cavities perpendicular. This variation is related to the dependence of the optical gain on the electric field polarization. For the particular dimensions of these QDASHs, the transition matrix element is significantly larger when the electrical field is

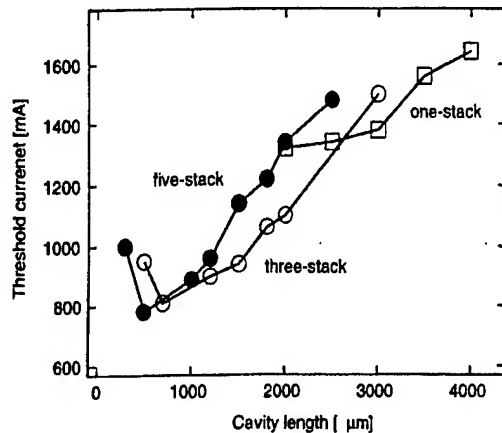


Fig. 5. Threshold current versus cavity length for one-, three-, and five-stack lasers, all with [110] cavity orientations. The modal gain for single-stack lasers is easier to saturate than multiple-stack ones.

parallel to the dash (i.e., the light propagates perpendicular to the QDASH direction) [18]. Indeed, the trend in the threshold current indicates that the light is highly TE polarized since the QDASH-TM polarization is not sensitive to changes in cavity orientation in the plane perpendicular to the growth direction. An independent measurement confirmed that the QDASH-laser emission is TE polarized. These results highlight the advantage that self-assembled QDASHs have in being able to adjust the laser cavity axis in the direction of maximum gain.

The inverse external quantum efficiency ($1/\eta_{ex}$) versus the cavity length (L) data for the single and multiple-stack lasers are used to calculate the internal loss (α_i) and the internal quantum efficiency (η_i). By fitting the data to the equation $1/\eta_{ex} = 1/\eta_i(1 - \alpha_i L/\ln(R))$, $\eta_i(\alpha_i)$ values of 62% (9.2 cm^{-1}), 66% (10.5 cm^{-1}), and 52% (10.1 cm^{-1}) are found for one, three-, and five-stack lasers, respectively. The reflectivity (R) is assumed to be 0.32 for the cleaved facets.

A threshold current density as low as 410 A/cm^2 was measured on a one-stack 4-mm-long cavity cleaved-facet laser diode. Fig. 5 shows the threshold current versus the cavity length for one-, three-, and five-stack lasers with the laser cavity oriented perpendicular to the dash direction. In spite of the relatively high internal losses ($\sim 10 \text{ cm}^{-1}$) observed in these particular structures, their threshold current densities are equal to that of low internal loss QW lasers operating at $1.52 \mu\text{m}$ [19]. The maximum modal gain (g_{max}) is inferred from the abrupt rise in threshold current at the shorter cavity lengths. This trend is obvious in the three- and five-stack lasers as seen in Fig. 5. For the single-stack devices, however, the saturation in the optical gain is sufficiently rapid that any laser with a cavity length shorter than 2 mm does not lase at current densities less than 1 kA/cm^2 . For the five- and single-stack lasers, g_{max} s of about 22 and 15 cm^{-1} are calculated, respectively. Compared with single-stack QD lasers on GaAs, the one-stack g_{max} for the QDASHs almost doubles [2], [4]. However, the g_{max} of the five-stack laser is less than 5/3 that of the three-stack version. Since there is a 30-nm barrier between the AlGaInAs QWs containing the QDASHs, uneven pumping of the stacks is probably occurring.

In conclusion, we have demonstrated the first self-assembled single- and multiple-stack quantum dash lasers on InP (001) substrates with a low threshold current density, room-temperature ground-state wavelengths from 1.60 to $1.66 \mu\text{m}$, and a clear quantum-wire-like dependence of the threshold current on laser cavity orientations.

REFERENCES

- [1] D. Bimberg, M. Grundmann, and N. Ledentsov, *Quantum Dot Heterostructures*. New York: Wiley, 1999.
- [2] G. T. Liu, A. Stintz, H. Li, T. C. Newell, A. L. Gray, P. M. Varangis, K. J. Malloy, and L. F. Lester, "The influence of quantum-well composition on the performance of quantum dot lasers using InAs-InGaAs dots-in-a-well (DWELL) structures," *IEEE J. Quantum Electron.*, vol. 36, pp. 1272–1279, Nov. 2000.
- [3] A. Stintz, G. T. Liu, H. Li, L. F. Lester, and K. J. Malloy, "Low-threshold current density $1.3 \mu\text{m}$ InAs quantum-dot lasers with the dots-in-a-well (DWELL) structure," *IEEE Photon. Technol. Lett.*, vol. 12, pp. 591–593, June 2000.
- [4] X. D. Huang, A. Stintz, C. P. Hains, G. T. Liu, J. Cheng, and K. J. Malloy, "Efficient high-temperature CW lasing operation of oxide-confined long-wavelength InAs quantum dot lasers," *Electron. Lett.*, vol. 36, pp. 41–42, Jan. 2000.
- [5] G. Park, O. B. Shchekin, D. L. Huffaker, and D. G. Deppe, "Low-threshold oxide-confined $1.3 \mu\text{m}$ quantum dot laser," *IEEE Photon. Technol. Lett.*, vol. 12, pp. 230–232, Mar. 2000.
- [6] T. C. Newell, D. J. Bossert, A. Stintz, B. Fuchs, K. J. Malloy, and L. F. Lester, "Gain and linewidth enhancement factor in InAs quantum dot laser diodes," *IEEE Photon. Technol. Lett.*, vol. 11, pp. 1527–1529, Dec. 1999.
- [7] H. Saito, K. Nishi, A. Kamei, and S. Sugou, "Low chirp observed in directly modulated quantum dot lasers," *IEEE Photon. Technol. Lett.*, vol. 12, pp. 1298–1300, Oct. 2000.
- [8] P. M. Varangis, H. Li, G. T. Liu, T. C. Newell, A. Stintz, B. Fuchs, K. J. Malloy, and L. F. Lester, "Low-threshold quantum dot lasers with 201 nm tuning range," *Electron. Lett.*, vol. 36, pp. 1544–1545, Aug. 2000.
- [9] G. Park, O. B. Shchekin, S. Csutak, D. L. Huffaker, and D. G. Deppe, "Room-temperature continuous-wave operation of a single-layered $1.3 \mu\text{m}$ quantum dot laser," *Appl. Phys. Lett.*, vol. 75, pp. 3267–3269, Nov. 1999.
- [10] P. Y. Yu and M. Cardona, *Fundamentals of Semiconductors*. New York: Springer, 1996.
- [11] V. M. Ustinov, A. E. Zhukov, A. Y. Egorov, A. R. Kovsh, S. V. Zaitsev, N. Y. Gordeev, V. I. Kopchatov, N. N. Ledentsov, A. F. Tsatsul'nikov, B. V. Volovik, P. S. Kop'ev, Z. I. Alferov, S. S. Ruvimov, Z. Liliental-Weber, and D. Bimberg, "Low threshold quantum dot injection laser emitting at $1.9 \mu\text{m}$," *Electron. Lett.*, vol. 34, pp. 670–671, Apr. 1998.
- [12] H. Saito, K. Nishi, and S. Sugou, "Ground-state lasing at room temperature in long-wavelength InAs quantum-dot lasers on InP (311)B substrates," *Appl. Phys. Lett.*, vol. 78, pp. 267–269, Jan. 2001.
- [13] J. Brault, M. Gendry, G. Grenet, G. Hollinger, Y. Desières, and T. Benyattou, "Role of buffer surface morphology and alloying effects on the properties of InAs nanostructures grown on InP(001)," *Appl. Phys. Lett.*, vol. 73, no. 20, pp. 2932–2934, Nov. 1998.
- [14] V. Bressler-Hill, A. Lorke, S. Varma, P. M. Petroff, K. Pond, and W. H. Weinberg, "Initial stages of InAs epitaxy on vicinal GaAs (001) – (2×4)," *Phys. Rev. B Condens. Matter*, vol. 50, no. 12, pp. 8479–8487, Sept. 1994.
- [15] H. Weman, E. Martinet, M. A. Dupertuis, A. Rudra, K. Leifer, and E. Kapon, "Two-dimensional quantum-confined Stark effect in V-groove quantum wires: Excited state spectroscopy and theory," *Appl. Phys. Lett.*, vol. 74, pp. 2334–2336, Apr. 1999.
- [16] K. Nishi, M. Yamada, T. Anan, A. Gomyo, and S. Sugou, "Long-wavelength lasing from InAs self-assembled quantum dots on (311)B InP," *Appl. Phys. Lett.*, vol. 73, pp. 526–528, July 1998.
- [17] L. F. Lester, A. Stintz, H. Li, T. C. Newell, E. A. Pease, B. A. Fuchs, and K. J. Malloy, "Optical characteristics of $1.24 \mu\text{m}$ quantum dot lasers," *IEEE Photon. Technol. Lett.*, vol. 11, pp. 931–933, Aug. 1999.
- [18] L. A. Coldren and S. W. Corzine, *Diode Lasers and Photonic Integrated Circuits*. New York: Wiley, 1995.
- [19] T. C. Newell, P. M. Varangis, E. Pease, A. Stintz, G. T. Liu, K. J. Malloy, and L. F. Lester, "High power AlGaInAs strained multiquantum well lasers operating at $1.52 \mu\text{m}$," *Electron. Lett.*, vol. 36, pp. 955–956, May 2000.

150-nm Tuning Range in a Grating-Coupled External Cavity Quantum-Dot Laser

H. Li, G. T. Liu, P. M. Varangis, T. C. Newell, A. Stintz, B. Fuchs, K. J. Malloy, and L. F. Lester

Abstract—An antireflection (AR) coated single-stack quantum-dot (QD) laser in a grating-coupled external cavity is shown to operate across a tuning range from 1.095 μm to 1.245 μm . This 150-nm range extends from the energy levels of the ground state to excited states. At any wavelength, the threshold current density is no greater than 1.1 kA/cm^2 . This large tunable range is the product of the rapid carrier filling of the higher energy states under a low pumping current and homogeneous broadening in the QD ensemble. The possibility of a larger tuning range is discussed with the further improvement of the AR-coating.

Index Terms—Quantum-dot lasers, semiconductor lasers, tunable lasers.

I. INTRODUCTION

TUNABLE lasers have many important applications in spectroscopy, optical communications such as wavelength-division multiplexing (WDM), and the fundamental study of the interaction between matter and photons. Semiconductor quantum-well (QW) lasers in a grating-coupled external cavity are widely used for their continuous tunability that is free of mode-hops and limited by the gain spectral width of the QW active medium [1]. When a very high pump level (normally greater than 10 kA/cm^2) is injected into a MQW laser, the $n = 2$ state can be populated, which makes the tuning range dramatically larger [2]–[6]. A tuning range of 240 nm around 1.5 μm (15.7% of the lasing wavelength) was reported with a pump level of 33 kA/cm^2 [5]. However, the necessarily high pump level restricts this broadband tunability for real applications. When an advanced QW engineering technique was used to grow uncoupled QW's with different well thicknesses, called the asymmetric multiple-quantum-well (AMQW), the tuning range was enlarged to ~ 90 nm at 950 nm [7] and at 1.5 μm [8]. The corresponding pump level was at a realistic level of ~ 2 kA/cm^2 and only the $n = 1$ state was populated. By increasing the pump level beyond 15 kA/cm^2 , the $n = 2$ state of AMQW started to be filled, and the tuning range was increased further to more than 100 nm [9], [10].

In contrast to QW lasers, the ground state of quantum dots (QD's) rapidly saturates for increasing pump levels. As a result, the excited states of QD lasers can be filled at a fairly low pump current density (~ 1 – 2 kA/cm^2), which produces a very wide spontaneous emission spectrum [11]. Thus an

Manuscript received January 19, 2000; revised March 20, 2000. This work was supported by the Defense Advanced Research Projects Agency under Grant MDA972-98-1-0002 and by the U.S. Air Force Office of Scientific Research under Grant F49620-96-1-0077.

The authors are with the Center for High Technology Materials, University of New Mexico, Albuquerque, NM 87106 USA.

Publisher Item Identifier S 1041-1135(00)05601-9.

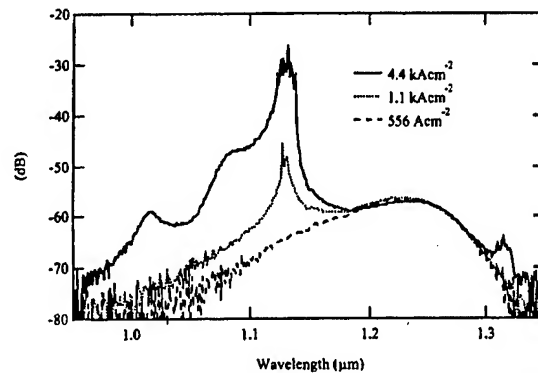


Fig. 1. Electroluminescence spectrum of the AR-coated DWELL laser for different pump levels.

excellent opportunity exists to obtain a very broad tuning range from QD lasers with low current densities. Furthermore, tuning throughout the energy gap between the ground state and the excited states is feasible due to the presence of homogeneous gain broadening [12], [13].

In this letter, a grating-coupled external cavity laser with a 150-nm tunable range is presented. For this arrangement, the threshold current density required for lasing is no greater than 1.1 kA/cm^2 . The quantum-dot active region employed has already demonstrated high performance [11], [14]. Among other characteristics, a room temperature J_{th} of 26 A/cm^2 [15] and a 0.1 linewidth enhancement factor [16] have been measured. These results suggest that numerous opportunities exist to use QD lasers as tunable coherent light sources.

The structure of the dots-in-a-well (DWELL) laser used in this experiment is described in detail in [11]. The structure contains one InAs QD layer incorporated into an $\text{In}_{0.2}\text{Ga}_{0.8}\text{As}$ 10-nm thick QW and is sandwiched by GaAs waveguide layers. The in-plane density of QD's is $7.5 \times 10^{10} \text{ cm}^{-2}$. The laser has a ridge waveguide structure with a width of 9 μm and a cavity length of 2.0 mm. It is mounted epitaxial-side up on a heatsink that is stabilized at a temperature of 20 $^{\circ}\text{C}$. The threshold current J_{th} for ground state lasing is $I = 35$ mA without any antireflection (AR)-coating. From this data, $J_{\text{th}} = 194 \text{ A}/\text{cm}^2$. A single $\lambda/4$ HfO_2 layer designed for minimum reflectivity at 1.24 μm was deposited on one facet. From the difference in slope efficiencies between the two mirrors, a residual reflectivity of approximately 1.6% is determined. This low reflectivity increases the total cavity loss. Thus, the ground state lasing of the solitary laser is completely extinguished.

The emission spectra of the solitary device under different pump levels is shown in Fig. 1. Light is coupled into an Anritsu MS9001A optical spectral analyzer using a multimode fiber. The resolution of the system was 0.5 nm. With a bias as low

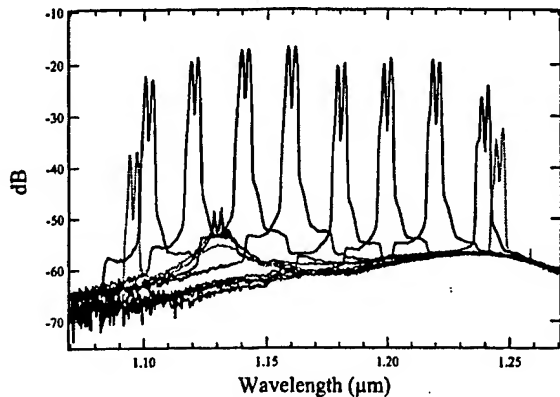


Fig. 2. Lasing spectra of the grating-coupled external cavity DWELL laser. When rotating the diffraction grating, the lasing wavelength is tuned across the wavelength range of 1.095–1.245 μm .

as 200 mA (1.1 kA/cm^2), the ground state at 1.24 μm is already well saturated and the first excited state is significantly populated. Since the AR-coating is not especially low, the device begins lasing under this pump level at the first excited state around 1.14 μm . The spectrum covered is from 1.1 to 1.25 μm . Upon increase of the pump level to 800 mA (4.4 kA/cm^2), the second excited state starts filling at 1.07 μm , accompanied by obvious carrier filling of the lowest energy QW state at 1.0 μm . This spectrum spans a wavelength range of more than 200 nm.

A Littrow external cavity configuration [17] that includes a collimator and a diffraction grating was subsequently constructed. Tuning was achieved by rotating the grating to select a certain wavelength emission to be reflected back to the laser. The laser was operated in pulsed mode with a pulse width of 500 ns and a duty cycle of 2%. The distance between the laser and the grating was about 25 cm, corresponding to a photon round trip time of $\sim 1.7 \text{ ns}$. The large ratio of pulsewidth time to photon lifetime means that the dynamics, which occur due to the interaction between the initial rise of the pulse and the incoming reflected field, can be neglected. Hence, pulsed operation is essentially identical to CW.

Fig. 2 shows the actual tuning range achieved in our experiment by rotating the grating. At each step the spectrum is measured by an optical spectrum analyzer. Across most of the 150-nm range, the lasing peak in the spectrum is higher than the amplified spontaneous emission level by at least 25–30 dB. The lasing linewidth is less than 3 nm. Its measurement is limited by the resolution of the detection system. A narrower linewidth could be obtained by using a Littman–Metcalf configuration [18] for the external cavity and by fabricating a narrower ridge waveguide laser. Significantly, no failure of lasing occurs across the energy gap between the ground and the first excited state. This is, as expected, due to homogenous gain broadening. It is possible that the double peaks appearing in the lasing spectrum are due to the spatial modes of the laser. However, it cannot yet be ruled out that the twin peaks are evidence of inhomogeneous broadening, similar to what has been observed in [13] for the free-running broadband emission in QD lasers at room temperature. The two traces (plotted as dotted lines) at the low and high ends of the spectrum shown in Fig. 2 portray the minimum and maximum tunable wavelengths. Also evident in the figure are small emission peaks from the excited

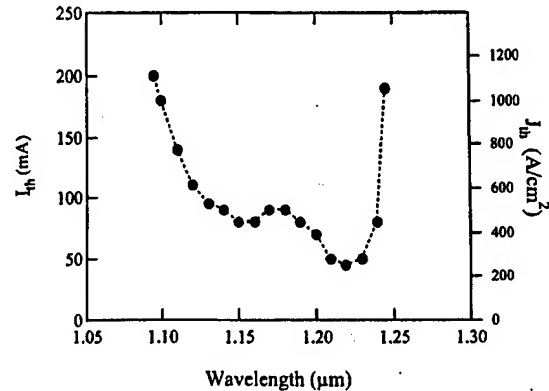


Fig. 3. Threshold current of the grating-coupled external cavity DWELL laser as a function of the lasing wavelength.

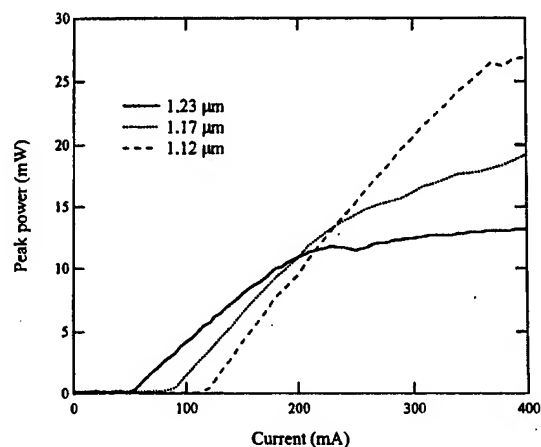


Fig. 4. Peak pulse power versus current for lasing at 1.23 μm (solid line), 1.17 μm (dotted line), and 1.12 μm (dashed line).

state energy level at 1.13 μm . These peaks arise when the laser is tuned at the extremes where the pumping is large. The combination of the residual reflectivity of the laser facet and excited state gain combine to produce a measurable amount of emission at this wavelength.

Fig. 3 shows the threshold current of the tunable external cavity DWELL laser as a function of the tuning wavelength. With no more than 200-mA bias (1.1 kA/cm^2) we are able to tune across 150 nm. At 1.18 μm , which is about halfway in the energy gap between the ground and first excited states, the threshold current increases only slightly. The lowest threshold current for the ground state is $\sim 45 \text{ mA}$, which is higher than the original uncoated laser threshold. This increase is due to the fact that only about 10% of the power is reflected back into the device. Consequently, the total loss is larger than that of the original uncoated laser. An increase of the external cavity feedback to a realistic 30% would decrease the threshold current and extend the tuning range further.

Fig. 4 shows light versus current ($L-I$) curves measured from the uncoated facet of the device at different wavelengths. The solid curve is for $\lambda = 1.23 \mu\text{m}$ in the ground state. The dotted curve is measured for $\lambda = 1.17 \mu\text{m}$ in the gap between the ground and the first excited states. The dashed curve is for $\lambda = 1.12 \mu\text{m}$ at the short-wavelength shoulder of the first excited state. The peak power at $\sim 200 \text{ mA}$ is about $\sim 10 \text{ mW}$ for all three wavelengths, and the slope efficiency is approximately 0.1 W/A.

Above 200 mA the slope efficiency decreases at $\lambda = 1.23 \mu\text{m}$ and $\lambda = 1.17 \mu\text{m}$ mainly because of the strong carrier filling at the first excited state under this pump level. A decrease in the reflectivity of the AR-coating will partially improve the slope efficiency and increase the linear range in the L - I curve. However, around the center wavelength of the first excited state, the slope efficiency remains constant for increasing pump level, as the dashed curve shows in Fig. 4. At the edge of the tuning range near $1.24 \mu\text{m}$ and $1.10 \mu\text{m}$, a slope efficiency of 0.041 W/A and 0.066 W/A is measured, respectively, and a useful output power in the milliwatt range is still obtained.

The tuning range and lasing behavior could be improved by decreasing the reflectivity of the AR-coating and modifying the external cavity design. From Fig. 1, the Fabry-Perot laser without external grating lases at a low pump current of ~ 200 mA. This device feature inhibits carrier filling of the higher energy states, therefore hindering the tuning range on the short wavelength side. If the residual reflectivity of the AR-coating at the first excited state were 5×10^{-4} , (which is a reasonable requirement for a laser diode used in commercial external-cavity lasers), the original laser cavity would not reach threshold until ~ 450 mA [11]. This situation would extend the tuning range to cover the second excited state and make a total tuning range of 200 nm possible. This figure represents a 17% tuning capability.

To extend the tuning range to longer wavelengths is not trivial since increasing the pump does not increase the gain very much at the wavelength longer than the center wavelength of the ground state. Only a reduction in the total cavity loss or a longer gain region can extend the tuning range on the long wavelength side. However, decreasing the cavity loss will put a more stringent requirement on the AR-coating to prohibit the internal Fabry-Perot modes from lasing. For the QD lasers presented here, we refer to suppression of the first excited states. From Fig. 1, we can estimate roughly that the extension to longer wavelengths is limited to several nanometers. Thus, efforts to enlarge the tuning range should be directed toward the short wavelength side.

The large tuning range of this type of laser does present new challenges. First, the threshold current across the tuning range is not constant and so the output power will fluctuate at constant current bias as the spectrum is scanned. It may be necessary to design a servo-loop to control the pump current to ensure good lasing behavior and a constant output power across the whole tuning range. Second, the ultrabroad-band spontaneous emission degrades the signal-to-noise (S/N) ratio of the laser output. Therefore, a tunable filter whose center wavelength is synchronized with the lasing wavelength would be important for certain applications. Another choice is to use a grating ring laser cavity, and to take the output power from the grating reflection beam [9]. In this way a low noise laser can be obtained.

One current effort in QD laser engineering is to reduce the fluctuation of the dot size by carefully controlling the wafer growth, thus narrowing the inhomogeneous gain broadening. This approach is crucial to achieve very low threshold currents. However, a reasonable distribution of the QD sizes may help smooth the tuning across the gaps between the discrete QD energy states. As a result, QD crystal growth should be optimized for different applications.

In conclusion, a continuous tuning range of 150 nm centered at $1.17 \mu\text{m}$ was achieved with an AR-coated DWELL laser inserted into a grating-coupled external cavity under a pump level of 1.1 kA/cm^2 . Further extension of the tuning range is possible by improving the AR-coating and careful design of the external cavity. Based on the realistic estimate of a 17% tuning capability and further progress in the development of long-wavelength QD lasers, it is anticipated that a single tunable QD external cavity laser could cover the entire wavelength range of the fiber-optic communication band from 1.3 to $1.55 \mu\text{m}$.

REFERENCES

- [1] P. S. Zory, Jr., *Quantum Well Lasers*, P. S. Zory, Jr., Ed. Boston, MA: Academic, 1993.
- [2] D. Mehuys, M. Mittelstein, A. Yariv, R. Sarfaty, and J. E. Ungar, "Optimized Fabry-Perot (AlGa) As quantum-well lasers tunable over 105 nm," *Electron. Lett.*, vol. 25, pp. 143-145, 1989.
- [3] D. C. Hall, J. S. Major, Jr., and N. Holonyak, Jr., "Broadband long-wavelength operation ($9700 \text{ \AA} \leq 8700 \text{ \AA}$) of $\text{Al}_y\text{Ga}_{1-y}\text{As-GaAs-In}_x\text{Ga}_{1-x}\text{As}$ quantum well heterostructure lasers in an external grating cavity," *Appl. Phys. Lett.*, vol. 55, pp. 752-754, 1989.
- [4] A. Lidgard, T. Tanbun-Ek, R. A. Logan, H. Temkin, K. W. Wecht, and N. A. Olsson, "External-cavity InGaAs/InP graded index multi-quantum well laser with a 200 nm tuning range," *Appl. Phys. Lett.*, vol. 56, pp. 816-817, 1990.
- [5] H. Tabucho and H. Ishikawa, "External grating tunable MQW laser with wide tuning range of 240 nm," *Electron. Lett.*, vol. 26, pp. 742-743, 1990.
- [6] C. P. Seltzer, M. Bagley, D. J. Elton, S. Perrin, and D. M. Cooper, "160 nm continuous tuning of an MQW laser in an external cavity across the entire 1.3 μm communication window," *Electron. Lett.*, vol. 27, pp. 95-96, 1991.
- [7] H. S. Gingrich, D. R. Chumney, S.-Z. Sun, S. D. Hersee, L. F. Lester, and S. R. J. Brueck, "Broadly tunable external cavity laser diodes with staggered thickness multiple quantum wells," *IEEE Photon. Technol. Lett.*, vol. 9, pp. 155-157, 1997.
- [8] M. J. Hamp, D. T. Cassidy, B. J. Robinson, Q. C. Zhao, D. A. Thompson, and M. Davies, "Effect of barrier height on the uneven carrier distribution in asymmetric multiple-quantum-well InGaAsP lasers," *IEEE Photon. Technol. Lett.*, vol. 10, pp. 1380-1382, 1998.
- [9] B.-L. Lee and C.-F. Lin, "Wide-range tunable semiconductor lasers using asymmetric dual quantum wells," *IEEE Photon. Technol. Lett.*, vol. 10, pp. 322-324, 1998.
- [10] X. Zhu, D. T. Cassidy, M. J. Hamp, D. A. Thompson, B. J. Robinson, Q. C. Zhao, and M. Davies, "1.4- μm InGaAsP-InP strained multiple-quantum-well laser for broad-wavelength tunability," *IEEE Photon. Technol. Lett.*, vol. 9, pp. 1202-1204, 1997.
- [11] L. F. Lester, A. Stintz, H. Li, T. C. Newell, E. A. Pease, B. A. Fuchs, and K. J. Malloy, "Optical properties of 1.24 μm quantum dot lasers," *IEEE Photon. Technol. Lett.*, vol. 11, pp. 931-933, 1999.
- [12] P. Borri, W. Langbein, J. Mork, J. M. Hvam, F. Heinrichsdorff, M.-H. Mao, and D. Bimberg, "Dephasing in InAs/GaAs quantum dots," *Phys. Rev. B*, vol. 60, pp. 7784-7787, 1999.
- [13] P. Eliseev, H. Li, A. Stintz, G. T. Liu, T. C. Newell, K. J. Malloy, and L. F. Lester, "Tunable grating-coupled laser oscillation and spectral hole burning in an InAs quantum-dot laser diode," *IEEE J. Quant. Electron.*, vol. 36, pp. 479-485, Apr. 2000.
- [14] X. Huang, A. Stintz, C. P. Hains, J. Cheng, and K. J. Malloy, "Efficient high-temperature CW lasing operation of oxide-confined long-wavelength InAs quantum dot lasers with low threshold current density," *Electron. Lett.*, vol. 36, 2000.
- [15] G. T. Liu, A. Stintz, H. Li, K. J. Malloy, and L. F. Lester, "Extremely low room temperature threshold current density diode lasers using InAs dots in an $\text{In}_{0.15}\text{Ga}_{0.85}\text{As}$ quantum well," *Electron. Lett.*, vol. 35, pp. 1163-1165, 1999.
- [16] T. C. Newell, D. Bossert, A. Stintz, B. Fuchs, K. J. Malloy, and L. F. Lester, "Gain and linewidth enhancement factor in InAs quantum dot laser diodes," *IEEE Photon. Technol. Lett.*, vol. 11, pp. 1527-1529, Dec. 1999.
- [17] P. W. Milonni and J. H. Eberly, *Lasers*. New York: Wiley, 1988.
- [18] M. G. Littman and H. J. Metcalf, "Spectrally narrow pulsed dye-laser without beam expander," *Appl. Opt.*, vol. 17, pp. 2224-2227, 1978.

Very Low Threshold Current Density Room Temperature Continuous-Wave Lasing from a Single-Layer InAs Quantum-Dot Laser

Xiaodong Huang, A. Stintz, C. P. Hains, *Member, IEEE*, G. T. Liu, Julian Cheng, *Senior Member, IEEE*, and K. J. Malloy

Abstract—Continuous-wave (CW) lasing operation with a very low threshold current density ($J_{th} = 32.5 \text{ A/cm}^2$) has been achieved at room temperature by a ridge waveguide quantum-dot (QD) laser containing a single InAs QD layer embedded within a strained InGaAs quantum well (dot-in-well, or DWELL structure). Lasing proceeds via the QD ground state with an emission wavelength of $1.25 \mu\text{m}$ when the cavity length is longer than 4.2 mm . For a 5-mm long QD laser, CW lasing has been achieved at temperatures as high as 40°C , with a characteristic temperature T_0 of 41 K near room temperature. Lasers with a $20 \mu\text{m}$ stripe width have a differential slope efficiency of 32% and peak output power of $>10 \text{ mW}$ per facet (uncoated).

Index Terms—Electroluminescence, epitaxial growth, quantum dots (QD's), semiconductor lasers.

SINCE it was first proposed [1], self-organized quantum-dot (QD) layers [2] have been used successfully as the active gain medium for edge-emitting lasers operating in the $1.3\text{-}\mu\text{m}$ wavelength range [3]–[7], and for vertical-cavity surface-emitting lasers (VCSEL's) emitting at shorter wavelengths [3], [8], [9]. For many future optic communication and interconnect applications, it is desirable to achieve lasers that can operate at a much lower threshold current density while preserving lasing efficiency and high output power, and providing a higher characteristic temperature T_0 . One of the advantages of QD lasers is their potential for achieving a long wavelength optical source on a GaAs substrate with an extremely low threshold current density, whose value has been theoretically predicted to be $\sim 10 \text{ A/cm}^2$ for QD layers with a 10% size dispersion [10]. Approaching this limit has posed a great challenge to both crystal growth and device design, especially for QD lasers operating near $1.3 \mu\text{m}$, where the modal gain of the QD layer in the ground state readily saturates at values that are often less than 10 cm^{-1} . Efficient lasing, especially continuous-wave (CW) lasing above room temperature, thus requires lasers with a higher modal gain and very low optical losses, as well as reduced self-heating. In this letter, we describe the achievement of efficient CW lasing operation of edge-emitting QD lasers in the ground state ($\lambda \sim 1.25 \mu\text{m}$) at temperatures up to 40°C , using a ridge waveguide geometry with a narrow stripe width. These

lasers are based on a single layer of InAs QD's embedded within an InGaAs quantum well (i.e., a dot-in-well, or DWELL structure [6]), which provides a higher injection efficiency and larger optical gain. A very low CW lasing threshold current density of $J_{th} = 32.5 \text{ A/cm}^2$ has been achieved at room temperature using a 9.2-mm long cavity with uncoated facets and a stripe width of $W = 20 \mu\text{m}$, which is the lowest value ever reported. CW lasing occurred in the ground state of the QD lasers whose cavity length L is greater than 4.2 mm . For $L = 5 \text{ mm}$, CW lasing occurred in the ground state at temperatures as high as 40°C , with a characteristic temperature of $T_0 = 41 \text{ K}$ near room temperature. These lasers achieved a differential slope efficiency of 32% and a peak output power of $>10 \text{ mW}$ per (uncoated) facet, and the estimated internal losses are 4.4 cm^{-1} .

The QD laser structure follows the design reported in Refs. [6] and [7], and was grown by solid-source molecular beam epitaxy (MBE) on a (001) n^+ -GaAs substrate. The epilayer structure consists of a 300-nm -thick n -GaAs (10^{18} cm^{-3}) buffer, a $2\text{-}\mu\text{m}$ -thick $n\text{-Al}_{0.7}\text{Ga}_{0.3}\text{As}$ (10^{17} cm^{-3}) lower cladding layer, a 220 nm thick unintentionally doped GaAs waveguide layer in which the active "dot in a well" (DWELL) layer is embedded, a 50-nm -thick $p\text{-Al}_{0.98}\text{Ga}_{0.02}\text{As}$ layer (10^{17} cm^{-3}), a 25-nm -thick graded $p\text{-Al}_x\text{Ga}_{1-x}\text{As}$ ($x = 0.98\text{--}0.7$) (10^{17} cm^{-3}) layer, a $1.9\text{-}\mu\text{m}$ -thick $p\text{-Al}_{0.7}\text{Ga}_{0.3}\text{As}$ (10^{17} cm^{-3}) upper cladding layer, and a 60-nm -thick n^+ -GaAs ($3 \times 10^{19} \text{ cm}^{-3}$) cap. The single DWELL layer, which is situated in the middle of the GaAs waveguide layer, contains InAs QD's with an equivalent coverage of 2.4 monolayers, which are embedded within a 9.6-nm $\text{In}_{0.15}\text{Ga}_{0.85}\text{As}$ quantum well (QW). The growth temperature is 510°C for the QD's and the QW, but is 610°C for the rest of the layers, as measured with an optical pyrometer. QD's formed under these condition usually have a density of $7 \times 10^{10} \text{ cm}^{-2}$. The insertion of an $\text{Al}_{0.98}\text{Ga}_{0.02}\text{As}$ layer makes it possible to fabricate a narrow Al-oxide confined inner stripe laser with a planar structure by selective wet oxidation. In this work, standard ridge waveguide structures with a ridge width of 20 or $16 \mu\text{m}$ were fabricated.

Device fabrication begins with formation of the ridges by wet chemical etching, followed by PECVD deposition of a thin Si_3N_4 film and plasma etching windows in the nitride above the ridges to define the stripe width and the contact area. After e -beam deposition of the Ti/Pt/Au p -contact, the sample substrate is lapped down to a thickness of $\sim 125 \mu\text{m}$, and AuGe-Ni-Au is e -beam deposited on the substrate to form the n -contact. The wafer is then cleaved into laser bars with a

Manuscript received September 28, 1999; revised November 23, 1999. This work was supported in part by the Defense Advanced Research Projects Agency and the Air Force Office of Scientific Research.

The authors are with the Center for High Technology Materials, University of New Mexico, Albuquerque, NM 87106 USA.

Publisher Item Identifier S 1041-1135(00)01991-1.

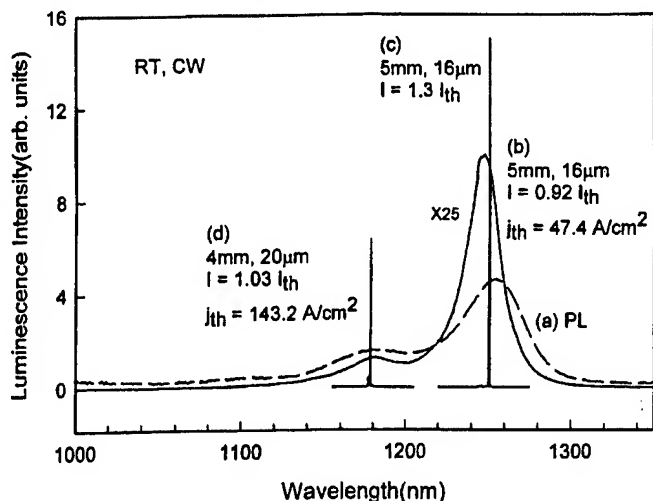


Fig. 1. (a) Photoluminescence spectrum of the as-grown wafer (dashed line) with a FWHM of 34 meV. (b) and (c) Electroluminescence and ground state lasing spectra of a 5-mm QD laser below and above threshold. (d) Excited state lasing spectrum of a 4-mm long QD laser above threshold.

cavity length (L) ranging from 3.0 to 9.2 mm, whose facets are uncoated. For CW measurements, the lasers were soldered to a Cu heat sink in the n-side down configuration.

Room temperature photoluminescence (PL) measurement of the as-grown wafer is shown in Fig. 1(a). The ground state PL peak has a narrower spectral full-width at half-maximum (FWHM $\approx 34 \text{ meV}$) than the PL results reported in [7], indicating the improved homogeneity of the QD's. No luminescence from the InGaAs QW is observed. Fig. 1 also shows the room temperature electroluminescence (EL) and lasing spectra of two lasers with different lengths under CW operation. Depending on cavity length, lasing proceeds via either the ground state ($\lambda \approx 1.25 \mu\text{m}$) or the first excited state ($\lambda \approx 1.18 \mu\text{m}$). For the laser with $L = 5 \text{ mm}$ and $W = 16 \mu\text{m}$, lasing occurs in the ground state with a threshold current density of $J_{th} = 47.4 \text{ A/cm}^2$. Fig. 1(b) and (c) show the EL spectra of this laser below threshold ($I = 0.92 I_{th}$) and above threshold ($I = 1.3 I_{th}$), respectively, both of which are centered at $1.25 \mu\text{m}$. Fig. 1(c) shows the excited state lasing spectrum ($\sim 1.18 \mu\text{m}$) of a shorter laser with $L = 4 \text{ mm}$ and $W = 20 \mu\text{m}$, with $J_{th} = 143.2 \text{ A/cm}^2$.

CW lasing with a threshold current density below 50 A/cm^2 has been achieved in the ground state when $L \geq 5 \text{ mm}$. Fig. 2 shows the single-facet CW lasing characteristics of three lasers with different cavity lengths. For the laser with $L = 5.6 \text{ mm}$ and $W = 20 \mu\text{m}$ [Fig. 2(a)], the threshold current density is $J_{th} = 43.5 \text{ A/cm}^2$ and the CW light output from a single facet exceeds 10 mW . Its lasing spectrum near threshold ($I = 1.06 I_{th}$) is shown in the inset of Fig. 2. Due to the smaller power dissipation of a narrow-stripe ridge waveguide structure, thermal rollover is reduced and CW lasing occurs even at a bias current of $I = 3 I_{th}$. For the device with $L = 5 \text{ mm}$ and $W = 16 \mu\text{m}$ [Fig. 2(b)], the threshold current density is $J_{th} = 47.4 \text{ A/cm}^2$, and the peak differential slope efficiency (η_d) for both facets is 32%. The lowest value of J_{th} obtained under CW lasing operation is 32.5 A/cm^2 [Fig. 2(c)], and 28.5 A/cm^2 for pulsed lasing operation, using a laser with $L = 9.2 \text{ mm}$ and $W = 20 \mu\text{m}$.

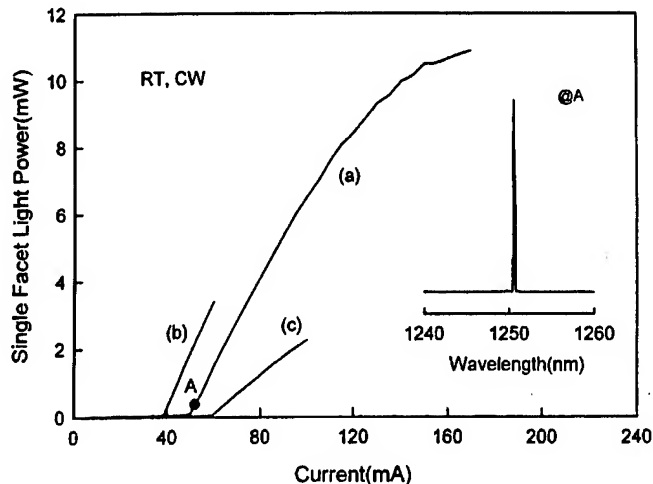


Fig. 2. Room temperature, single-facet, CW lasing characteristics of three QD lasers with different cavity lengths: (a) $L = 5 \text{ mm}$, $W = 16 \mu\text{m}$, (b) $L = 5.6 \text{ mm}$, $W = 20 \mu\text{m}$, (c) $L = 9.2 \text{ mm}$, $W = 20 \mu\text{m}$.

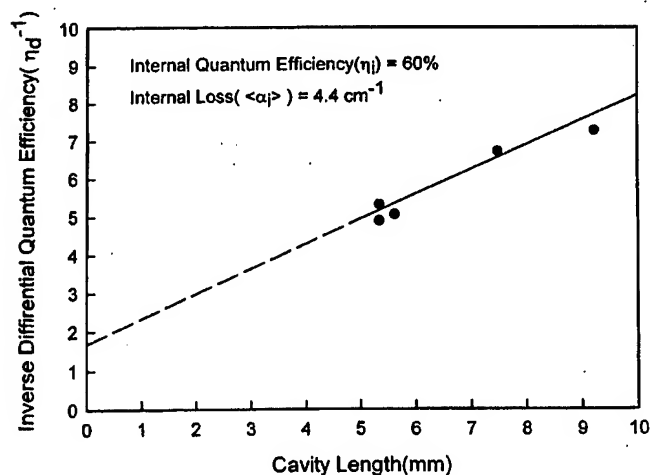


Fig. 3. Inverse differential slope efficiency $1/\eta_d$ (for both facets) plotted as a function of the cavity length L under CW lasing conditions. The y-intercept yields the internal quantum efficiency η_i (60%) while the slope yields the internal optical loss α_i (4.4 cm^{-1}).

The lowest threshold current densities reported previously for QD lasers at room temperature were $\sim 60 \text{ A/cm}^2$ for CW operation [3], [5] and 26 A/cm^2 for pulsed operation [7].

Fig. 3 shows the linear dependence of the inverse differential slope efficiency η_d^{-1} (for both facets) on the cavity length L , from which the internal quantum efficiency ($\eta_i = 60\%$) and the internal optical loss ($\langle \alpha_i \rangle = 4.4 \text{ cm}^{-1}$) were derived. For shorter cavity lengths ($L < 4.2 \text{ mm}$), CW lasing shifts to the first excited state ($\lambda = 1.18 \mu\text{m}$). The threshold gain of the shortest laser that is capable of lasing in the ground state is calculated to be 7 cm^{-1} , assuming a facet reflectivity of 0.32. Thus the modal gain of a single InAs QD layer in the ground state saturates at $\sim 7 \text{ cm}^{-1}$, which is very low compared to that of a single QW.

The temperature dependence of the threshold current of a QD laser with $L = 5 \text{ mm}$ and $W = 16 \mu\text{m}$ has been measured under both CW and pulsed operation (300-ns pulses with a duty cycle of 2.5%). Fig. 4 shows the single-facet CW lasing characteristics and electrical characteristics of this laser at temperatures

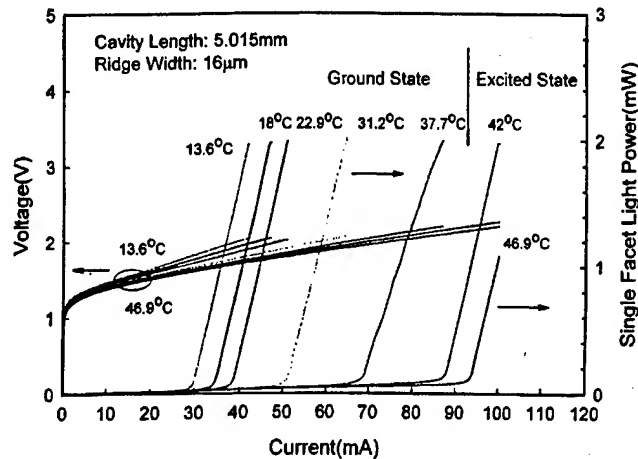


Fig. 4. Electrical characteristics and the single-facet, CW lasing characteristics of a DWELL laser at different temperatures.

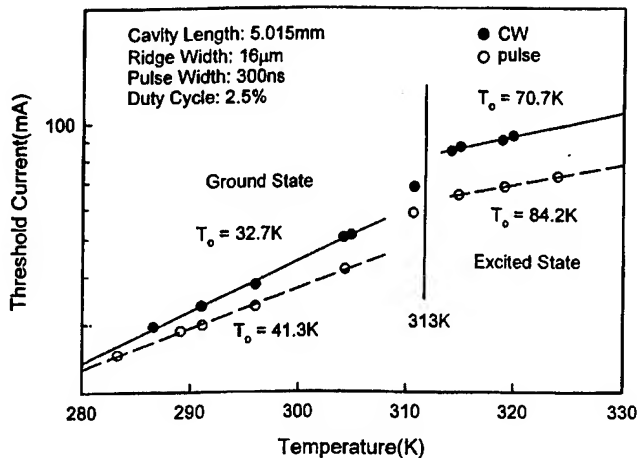


Fig. 5. Temperature dependence of the threshold current for both CW lasing (closed circles) and pulsed lasing (open circles). Lasing occurs in the ground state below 313 K, and in the excited state above 313 K.

ranging from 13.6 °C to 46.9 °C. The threshold voltage is <2 V throughout this temperature range. Lasing occurs in the ground state below 40 °C, but switches to the first excited state at higher temperatures. This is attributed to the reduction of the ground state gain of the QD's as a result thermally activated carrier loss at higher temperatures, and the increased band-filling in the first excited state as the ground state gain becomes saturated [4]. The measured slope efficiency decreases with increasing temperature, but rises again after lasing has shifted to the excited state.

Fig. 5 plots the temperature dependence of the CW and pulsed threshold currents, from which the characteristic temperature, T_0 , has been determined. At temperatures below 40 °C, T_0 is 32.7 K for CW operation and is 41.3 K for pulsed operation. Above 40 °C, these values of T_0 jump to 70.7 K and 84.2 K, respectively, as lasing switches into the excited state. The higher T_0 of the excited state is a consequence of its higher degeneracy and larger density of state. In the ground state, T_0 depends strongly on the cavity loss [6], which determines the proximity of the ground state modal gain to saturation. The higher the loss,

the higher is the modal gain that is required to achieve lasing and the closer it is to saturation. Gain saturation causes increased band filling in the excited state, which competes with the ground state for carriers and thus increases J_{th} for ground state lasing. A lower T_0 is thus expected for a laser whose modal gain in the ground state is near saturation. Since the cavity loss of the 5-mm laser is $\sim 6.7 \text{ cm}^{-1}$, its modal gain is operating very close to gain saturation in the ground state ($\sim 7 \text{ cm}^{-1}$), giving rise to a relatively small T_0 . The ratio of the modal gain to its saturation value is thus an important parameter that describes the degree of band filling. A higher gain saturation limit is thus desirable for improving the performance of QD lasers, especially for achieving a larger T_0 . Multiple QD layers can also be useful in alleviating the gain saturation problem [11].

In summary, we have demonstrated the efficient CW lasing of InAs QD lasers at temperatures ranging from 13.6 °C to 40.0 °C, and have achieved a very low threshold current density ($J_{th} = 32.5 \text{ A/cm}^2$) and a characteristic temperature of $T_0 = 41 \text{ K}$. Lasing has been realized via either the ground state or the excited state depending on cavity length. Lasers with a slope efficiency of 32%, and an output power of 11 mW/facet have been achieved using a 5-mm-long laser cavity.

REFERENCES

- [1] Y. Arakawa and H. Sakaki, "Multidimensional quantum well laser and temperature dependence of its threshold current," *Appl. Phys. Lett.*, vol. 40, pp. 939-941, 1982.
- [2] N. N. Ledentsov, V. M. Ustinov, A. Yu. Egorov, A. E. Maximov, I. G. Tabatadze, and P. S. Kop'ev, "Optical properties of heterostructures with InGaAs-GaAs quantum clusters," *Semicond.*, vol. 28, pp. 832-834, 1994.
- [3] D. Bimberg, N. N. Ledentsov, M. Grundmann, F. Heinrichsdorff, V. M. Ustinov, P. S. Kop'ev, M. V. Maximov, Zh. I. Alferov, and J. A. Lott, "Application of self-organized quantum dots to edge emitting and vertical cavity lasers," *Physica E*, vol. 3, pp. 129-136, 1998.
- [4] G. Park, D. L. Huffaker, Z. Zou, O. B. Shchekin, and D. G. Deppe, "Temperature dependence of lasing characteristics for long-wavelength (1.3 μm) GaAs-based quantum-dot lasers," *IEEE Photon. Technol. Lett.*, vol. 11, pp. 301-303, 1999.
- [5] Yu. M. Shernyakov, D. A. Bedarev, E. Yu. Kondrat'eva, P. S. Kop'ev, A. R. Kovsh, N. A. Maleev, M. V. Maximov, S. S. Mikhlin, A. F. Tsatsul'nikov, V. M. Ustinov, B. V. Volovik, A. E. Zhukov, Zh. I. Alferov, N. N. Ledentsov, and D. Bimberg, "1.3 μm GaAs-based laser using quantum dots obtained by activated spinodal decomposition," *Electron. Lett.*, vol. 35, pp. 898-900, 1999.
- [6] L. F. Lester, A. Stintz, H. Li, T. C. Newell, E. A. Pease, B. A. Fuchs, and K. J. Malloy, "Optical characteristics of 1.24 μm quantum dot lasers," *IEEE Photon. Technol. Lett.*, vol. 11, pp. 931-933, 1999.
- [7] G. T. Liu, A. Stintz, H. Li, K. J. Malloy, and L. F. Lester, "Extremely low room-temperature threshold current density diode lasers using InAs dots in an $\text{In}_{0.15}\text{Ga}_{0.85}\text{As}$ quantum well," *Electron. Lett.*, vol. 35, pp. 1163-1165, 1999.
- [8] J. A. Lott, N. N. Ledentsov, V. M. Ustinov, A. Yu. Egorov, A. E. Zhukov, P. S. Kop'ev, Zh. I. Alferov, and D. Bimberg, "Vertical cavity lasers based on vertically coupled quantum dots," *Electro. Lett.*, vol. 33, pp. 1150-1151, 1997.
- [9] D. L. Huffaker, H. Deng, and D. G. Deppe, "1.15 μm wavelength oxide-confined quantum-dot vertical cavity surface-emitting laser," *IEEE Photon. Technol. Lett.*, vol. 10, pp. 185-187, 1998.
- [10] M. Grundmann and D. Bimberg, "Theory of random-population for quantum dots," *Phys. Rev. B*, vol. 55, pp. 9740-9745, 1997.
- [11] O. G. Schmidt, N. Kirstaedter, N. N. Ledentsov, M.-H. Mao, D. Bimberg, V. M. Ustinov, A. Y. Egorov, A. E. Zhukov, M. V. Maximov, P. S. Kop'ev, and Z. I. Alferov, "Prevention of gain saturation by multi-layer quantum dot lasers," *Electron. Lett.*, vol. 32, pp. 1302-1304, 1998.

T.C. Newell, P.M. Varangis, E. Pease, A. Stintz,
G.T. Liu, K.J. Malloy and L.F. Lester

1.75 W CW power in AlGaInAs/InP strained QW lasers is demonstrated. Room temperature threshold current densities are 410 A/cm^2 , and the characteristic temperature is 69 K. The variation in the external differential efficiency with cavity length and temperature reveal the optimum length and show how nonradiative recombination mechanisms limit the performance.

Introduction: Eye-safe LADAR, free-space laser communication, and other near-IR illumination technologies are expanding the applications of $1.5 \mu\text{m}$ lasers, which in the case of AlGaInAs quantum well (QW) devices has traditionally focused on high speed devices for telecommunications. For these low power lasers, the best reported threshold current densities, J_{th} , are 190 to 530 A/cm^2 [1, 2], internal efficiencies, η_i , are up to 83% [3], and characteristic temperatures as high as 122 K have been measured [4]. Lacking in the AlGaInAs $1.5 \mu\text{m}$ laser literature is substantial research on high-power operation, which will expand the usefulness of these devices into applications for which eye-safety is of primary importance [5].

This Letter reports the growth and optical characteristics of compressively strained AlGaInAs 3-QW lasers operating near $1.52 \mu\text{m}$. A room temperature J_{th} of 410 A/cm^2 is observed along with a characteristic temperature, T_0 , of 69 K, and T_1 of 220 K. 1.75 W CW single sided emission at 5 A current has been obtained before thermal rollover occurs.

Growth: The material structure was grown by molecular beam epitaxy (MBE) using the digital alloy (DA) technique and is described in detail in [6]. Three 80 \AA $\text{Al}_{0.08}\text{Ga}_{0.25}\text{In}_{0.67}\text{As}$ QWs were centred in a $1 \mu\text{m}$ wide waveguide of $\text{Al}_{0.3}\text{Ga}_{0.18}\text{In}_{0.52}\text{As}$ with 50 \AA barriers. The QWs were compressively strained at 0.8%. The material was processed into broad area lasers with a $200 \mu\text{m}$ stripe width. The p -side metallisation consists of 500 \AA of Ti, 500 \AA of Pt, and 2000 \AA of Au. The n -side ohmic metal consists of 400 \AA of Au, 1500 \AA of Ni, and 1000 \AA of Au. A four-layer high reflectivity (HR) coating was applied by an e-beam dielectric evaporator to select devices. The HR stack consists of alternating $\lambda/4$ -layers of MgF_2 and poly-Si. The deposition was performed at 175°C to improve the adhesion of the coatings to the laser facets.

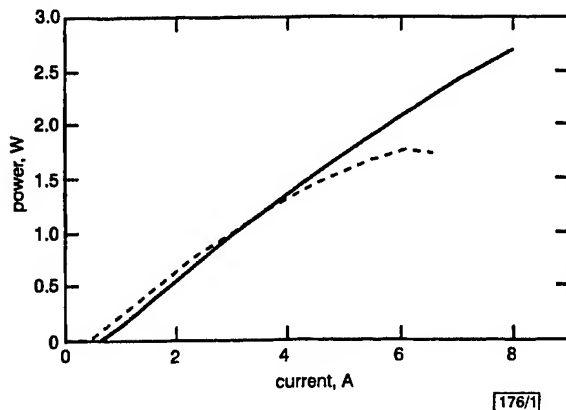


Fig. 1 Pulse and CW light current curves

— pulse
--- CW

Device performance: Individual emitters were mounted p -side down on copper mounts then attached to a thermo-electric cooler for testing. The advantage of the broadened waveguide [7] is that the internal loss, α_i , is only 2 cm^{-1} and the injection efficiency, η_i , is 62%. At room temperature, J_{th} is 410 A/cm^2 for the best uncoated 1 mm cavity length devices. Fig. 1 plots the light against current (LI) curve for a laser that had one facet HR coated with a four-layer stack. The other facet is uncoated and ~85% of the emission is emitted from this facet. CW and pulsed (100 μs pulses with 5% duty cycle) cases are shown. The heatsink temperature was maintained at -15°C for CW operation and -10°C for pulsed. This

arrangement. The relatively large series resistance is due in part to non-optimal doping in the cladding layers and an imperfect ohmic contact to the InP. At the low temperatures, the threshold currents are 457 and 607 mA for the CW and pulsed cases, respectively. In both modes of operation, the slope efficiency is 0.4 W/A although this decreases for CW powers $> 1 \text{ W}$. The maximum power in CW mode is 1.75 W , at which point thermal rollover occurs. In pulsed mode, the LI trace is linear to 8 A current where the power is 2.7 W . Partial damage of the uncoated facet occurred above this current, and catastrophic damage at this facet destroyed the device at 10 A current and 3 W power. Passivation of the uncoated facet in order to unpin the Fermi level would enlarge the available pumping range [8].

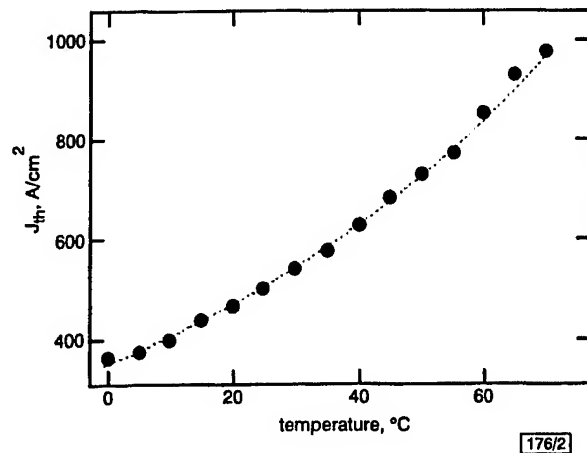


Fig. 2 J_{th} against temperature for pulsed mode operation (0.3 μs pulses, 1% duty cycle) yield T_0 of 69 K

The thermal issues raised by the high power limits lead to the investigation of the characteristic temperature of the laser, T_0 , and its variation in the slope efficiency with temperature, T_1 ($\eta_{ext}^{-1} \approx \exp(T/T_1)$). T_0 is obtained from a plot of J_{th} against temperature, which is shown in Fig. 2 for a 1 mm laser. The experimental data (solid circles) are well fit by an exponential curve with a T_0 of 69 K. The T_1 value is 220 K for temperatures up to 65°C but drops substantially at higher temperatures.

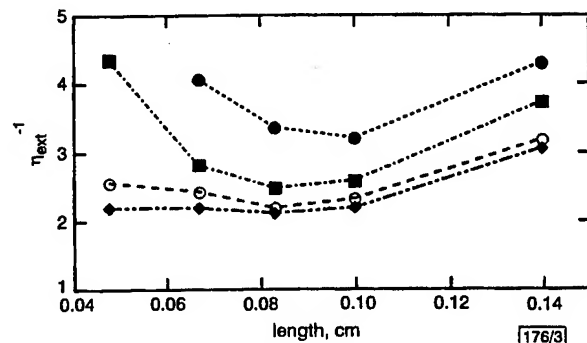


Fig. 3 η_{ext}^{-1} against cavity length of laser

◆ 10°C ,
○ 25°C ,
■ 40°C ,
● 55°C

The relationship between η_{ext}^{-1} and temperature can be examined in more detail by investigating it as a function of the cavity length of the laser. This provides an insight into the optimal cavity length as well as recombination processes occurring in the laser. In Fig. 3, η_{ext}^{-1} against cavity length is plotted for temperatures of 10, 25, 40, and 55°C under pulsed mode operation (0.3 μs pulses with a 1% duty cycle). As expected, the longer cavities have a large η_{ext}^{-1} due to the lower mirror losses. For the short cavities, η_{ext}^{-1} also increases. Here the injection current density is necessarily large so that the high mirror losses are overcome and lasing is established. As a result, both the Auger leakage current and a leakage due to thermionic emission of carriers into the

larger than the lattice temperature (T_0 , T_{th} , T_0 and T_1 are low ($T_{th} \sim 45K$) for short cavity lasers. This leakage current problem is particularly severe in $475\mu m$ cavity devices, which cannot generate sufficient gain at $55^\circ C$ to lase below 2 A bias current. The optimum cavity length is near 1 mm. At this length, not only is the efficiency highest, but its variation with temperature the smallest.

Conclusion: 1.75W CW power has been demonstrated in a 0.8% compressively strained AlGaInAs 3QW laser diode. For high power devices that simultaneously generate a large amount of heat, nonradiative processes play a significant role in J_{th} and η_{ext} . Based on the temperature, the optimum cavity length for highest efficiency operation is near 1 mm. Here, a T_0 of 69K and a T_1 of 220K have been obtained.

Acknowledgments: This work was supported by the US Army Federated Laboratories program and by the US Air Force Office of Scientific Research (AFOSR) under grant F49620-96-1-0079.

© IEE 2000

9 February 2000

Electronics Letters Online No: 20000731

DOI: 10.1049/el:20000731

T.C. Newell, P.M. Varangis, E. Pease, A. Stintz, G.T. Liu, K.J. Malloy and L.F. Lester (Center for High Technology Materials, University of New Mexico, 1313 Goddard SE, Albuquerque, NM 87106, USA)

- 1 'AlGaInAs/InP ridge-guide lasers operating at $1.55\mu m$ ', *Proc. SPIE*, 1998, Vol. 3284, pp. 205–210
- 2 MONDRY, M.J., CHUANG, Z.M., PETERS, M.G., and COLDREN, L.A.: 'Low threshold current density $1.5\mu m$ (In,Ga,Al)As quantum well lasers grown by MBE', *Electron. Lett.*, 1992, **28**, (15), pp. 1471–1472
- 3 STEGMULLER, B., BORCHERT, B., and GESSNER, R.: '1.57 μm strained-layer quantum-well GaInAlAs ridge-wave-guide laser-diodes with high-temperature ($130^\circ C$) and ultra high speed (17GHz) performance', *IEEE Photonics Technol. Lett.*, 1993, **5**, (6), pp. 597–599
- 4 OHNOKI, N., OKAZAKI, G., KOYAMA, F., and IGA, K.: 'Record high characteristic temperature ($T_0 = 122K$) of $1.55\mu m$ strain-compensated AlGaInAs/AlGaInAs MQW lasers with AlAs/AlInAs multiquantum barrier', *Electron. Lett.*, 1999, **35**, (1), pp. 51–52
- 5 STANN, B.L., RUFF, W.C., and SZTANKAY, Z.G.: 'Intensity-modulated diode laser radar using frequency-modulation/continuous-wave ranging techniques', *Opt. Eng.*, 1996, **35**, (11), pp. 3270–3278
- 6 LIU, G.T., STINTZ, A., PEASE, E.A., NEWELL, T.C., MALLOY, K.J., and LESTER, L.F.: '1.58- μm latticed-matched and strained digital alloy AlGaInAs-InP multiple-quantum-well lasers', *IEEE Photonics Technol. Lett.*, 2000, **12**, (1), pp. 4–6
- 7 GARBUZOV, D.Z., MARTINELLI, R.U., LEE, H., YORK, P.K., MENNA, R.J., CONNOLLY, J.C., and NARAYAN, S.Y.: 'Ultra-low loss broadened waveguide high-power $2\mu m$ AlGaAsSb/InGaAsSb/GaSb separate-confinement quantum-well lasers', *Appl. Phys. Lett.*, 1996, **69**, (14), pp. 2006–2008
- 8 VAUGHN, L.G., NEWELL, T.C., LESTER, L.F., and MACINNES, A.N.: 'Characterization of GaS-passivated quantum well lasers'. Mater. Res. Soc. Symp., 1999, Vol. 573, pp. 125–130
- 9 LESTER, L.F., and RIDLEY, B.K.: 'Hot carriers and the frequency-response of quantum-well lasers', *J. Appl. Phys.*, 1992, **72**, (7), pp. 2579–2588

Tunable Grating-Coupled Laser Oscillation and Spectral Hole Burning in an InAs Quantum-Dot Laser Diode

P. Eliseev, *Senior Member, IEEE*, H. Li, *Member, IEEE*, A. Stintz, G. T. Liu, *Student Member, IEEE*, T. C. Newell, K. J. Malloy, *Member, IEEE*, and L. F. Lester, *Member, IEEE*

Abstract—Emission spectra are investigated of a low-threshold InAs quantum-dot laser of the “dots-in-a-well” (DWELL) type operating near 1230 nm. An external dispersion cavity with a diffraction grating is coupled to the laser diode to suppress the subsidiary modes and to tune the central wavelength. A wavelength-dependent competition between the grating-coupled mode and the internal Fabry–Perot modes of the laser suggests that a hole burning in the spectral density of a DWELL laser occurs with a characteristic spectral half width of ~ 13 nm (10.5 meV). Simple models of spectral “flattening” and spectral hole burning are presented to explain the broad free-running and grating-coupled lasing spectra of the DWELL device.

Index Terms—Quantum-well devices, semiconductor lasers.

I. INTRODUCTION

RECENT success in reducing the threshold current density J_{th} in semiconductor lasers is associated with the application of self-organized quantum-dot (QD) active materials [1]–[10]. The lowest J_{th} at room temperature (26 A/cm²) has been achieved in a QD laser of the “dots-in-a-well” (DWELL) type [11]. A CW power as high as 3.3 W has been obtained in a QD laser based on a combination of InGaAs and InAlAs dots [12]. Optical characteristics of DWELL lasers were recently presented in [13]. Such lasers demonstrate a complicated spectral behavior. In long-cavity samples (where the cavity length L is longer than ~ 1.5 mm), ground-state oscillation occurs at 1.22–1.24 μ m, whereas in shorter cavities the oscillation moves to higher energy states at 1.1–1.2 μ m (0.6 mm $< L < 1.5$ mm) and at 1.04–1.06 μ m ($L < 0.6$ mm). Other important features are the rather broad oscillation spectrum and a competition between the ground state and higher energy oscillations. From these observations, it follows that the QD laser can be tuned over a very wide range. On the other hand, mode control is not an easy task. The inhomogeneous broadening of the gain band due to variation in the dot size is an important factor in QD lasers [14], [15] since it can cause oscillation in many spectral modes simultaneously. The problem of spatial hole burning (SHB) is considered

in [15] as one cause for multimode operation in QD lasers, attributing this effect to reduced lateral diffusion of charge carriers in the QD medium as compared to quantum well (QW) and bulk ones.

In this paper, the experimental results on the emission spectra of a QD laser with an external grating cavity are described. The use of an external cavity with a diffraction grating is well known as an efficient method for spectral narrowing and tuning in various types of lasers [16]. Here the grating coupled cavity is used to investigate how the emission spectrum of a QD laser is modified by spectrally selective feedback in comparison to the free-running laser spectrum. The obtained emission spectra suggest that mode competition depends on the spectral distance between the oscillation modes. We discuss this observation in terms of the spectral hole burning mechanism and develop a simple model for a quantitative analysis of the lasing spectra.

II. EXPERIMENTAL

Laser diodes are fabricated from the same epitaxial wafer as diodes investigated in [13]. The structure contains one InAs QD layer incorporated into an In_{0.2}Ga_{0.8}As 10-nm-thick QW and is sandwiched by GaAs waveguide layers. The in-plane density of the QD's is 7.5×10^{10} cm⁻². The base diameter of individual dots is about 20 nm and their average height is about 7 nm as determined by atomic force microscopy and transmission electron microscopy measurements on a separate calibration sample. The room-temperature J_{th} in broad-area samples is as low as 83 A/cm² for a 4-mm-long cavity. The internal loss is determined from the efficiency data to be as low as 1.3 cm⁻¹. The sample used in the following external cavity experiment is 2000 \times 30 μ m² and has no facet coatings. The current and wavelength at the oscillation threshold of the free-running laser are 88 mA and 1231 nm, respectively.

Spectra are recorded using an Anritsu optical spectrum analyzer with the light delivered by a multimode fiber coupler. The spectral resolution in this experiment is 0.5 nm. Therefore, the Fabry–Perot modes of the free-running and external-cavity lasers are not resolved.

The Littman–Metcalf external-cavity configuration is used and shown in Fig. 1. There are two configurations of the external cavity: 1) a return-mirror configuration with the first-order diffraction beam coupled to the diode and 2) a return-mirror configuration with the zeroth-order diffraction beam coupled to the diode (no spectral selection). The tuning of the ex-

Manuscript received October 21, 1999. This work was supported by DARPA under Grant MDA972-98-1-0002 and by AFOSR under Grant F49620-96-1-0077.

P. Eliseev is with the Center for High Technology Materials, University of New Mexico, Albuquerque, NM 87106 USA. He is also with the P.N. Lebedev Physics Institute, Russian Academy of Sciences, Moscow 117924, Russia.

H. Li, A. Stintz, G. T. Liu, T. C. Newell, K. J. Malloy, and L. F. Lester are with the Center for High Technology Materials, University of New Mexico, Albuquerque, NM 87106 USA.

Publisher Item Identifier S 0018-9197(00)02814-1.

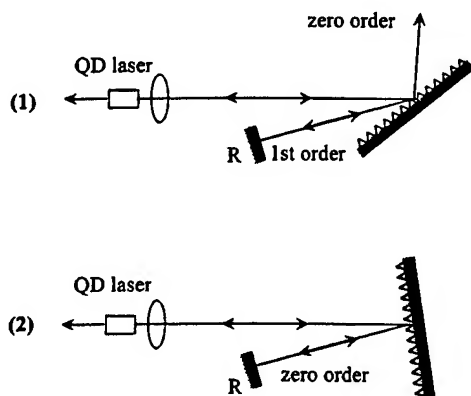


Fig. 1. Experimental setup for the grating coupled laser cavity.

ternal cavity in case 1) is performed by precise tilting of the return mirror. The emission spectra and optical power are also measured for the laser without the external cavity. The effect of the external cavity on the threshold current is to decrease it by $\sim 10\%$ compared to the free-running threshold with almost no difference between configurations 1) and 2).

III. RESULTS

The oscillation bandwidth $\Delta\lambda$ of the free-running laser increases with an increase in the pumping rate. Typical behavior of ground state lasing is shown in Fig. 2. The spectral density grows with the pumping current in a sublinear manner, and the width of the laser emission range increases approximately as P^m , where P is total laser emission power, and m is an exponent in the range of 0.35–0.4 typically. The width measured at the -10 -dB level is plotted as a function of current in Fig. 3. It is as large as ~ 38 nm at a current level ~ 20 times threshold. When the grating-coupled regime is switched on, the laser oscillation band can be significantly narrowed, and most of the free-running optical power can be collected in a narrow-band oscillation. Comparison of these emission spectra can be found in Fig. 4. The grating-coupled operation is observed in the tuning range from 1212 to 1240 nm, which is close to the observed maximum range of free-running oscillation $\Delta\lambda$. The relative change in the spectral density on a log scale is shown in Fig. 5. A central peak corresponds to a selected grating-coupled mode. The level outside this mode shows the spectral dependence of the subsidiary mode suppression (SMS spectrum) by opening the grating. The spectral density is almost unchanged in the spontaneous emission range, whereas the free-running laser oscillation is strongly influenced. As a result, there is a strong dip in the intensity surrounding the selected mode.

A maximum SMS of approximately -30 dB is obtained below 350 mA, whereas above this current the SMS does not exceed -20 dB. In Fig. 3, regions I and II are shown separated by a straight line at 350 mA. In region I, the free-running spectrum is narrower than 20 nm. When the wavelength-selective cavity is used, the SMS is strong over the whole spectrum. It suggests that in this region the free-running spectrum is narrower than the homogenous bandwidth.

In region II, the free-running spectrum broadens over the range of strong mode interaction, and the grating-coupled mode cannot suppress the distant free-running modes of laser

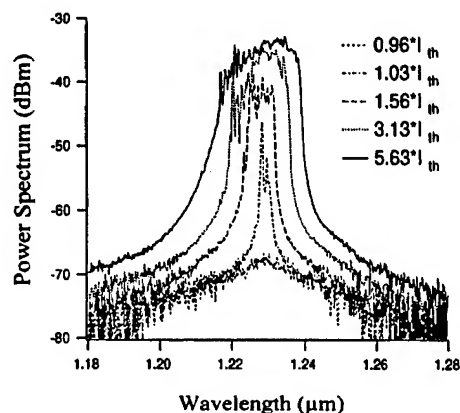


Fig. 2. Free-running spectra of the sample under investigation at several pumping currents as indicated.

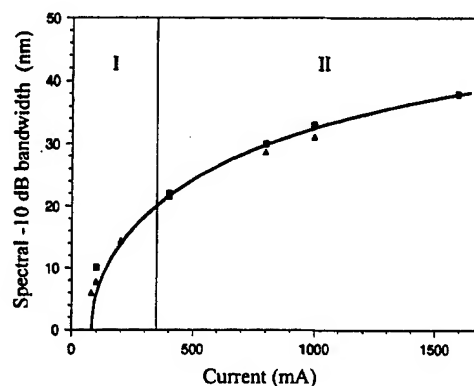


Fig. 3. The dependence of the laser emission range width (-10 -dB bandwidth) on the pumping current up to 20 times threshold. The solid curve is calculated (see text). Triangles are for the free-running laser with an external cavity (zeroth-order position), and squares are for the free-running lasing with no external cavity. The solid curve is calculated according to the spectral "flattening" model [see (6)]. In the current region I, the grating-coupled lasing can effectively suppress all subsidiary modes; in region II, the competition is seen between the grating-coupled mode and the subsidiary "free-running" lasing modes.

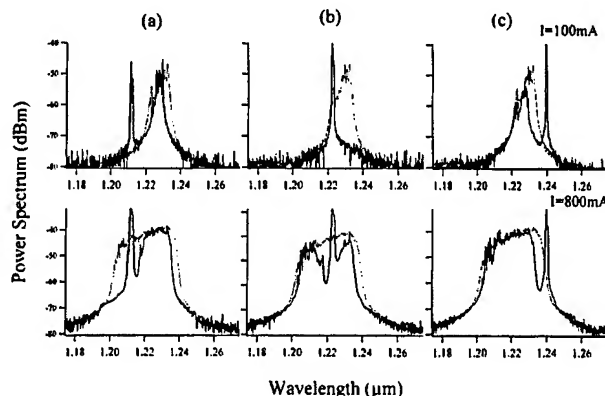


Fig. 4. Emission spectra with and without grating coupling: dotted curves are for the nonwavelength-selective external cavity (the grating in the zeroth-order position), and solid curves are for the wavelength-selective external cavity. The grating feedback has been tuned to 1212 nm (left column), 1231 nm (central column), and 1240 nm (right column).

emission. These competing modes are large, and the maximum SMS degrades.

When the grating-coupled mode is tuned from the center of the laser oscillation band to its edges, the SMS spectra changes:

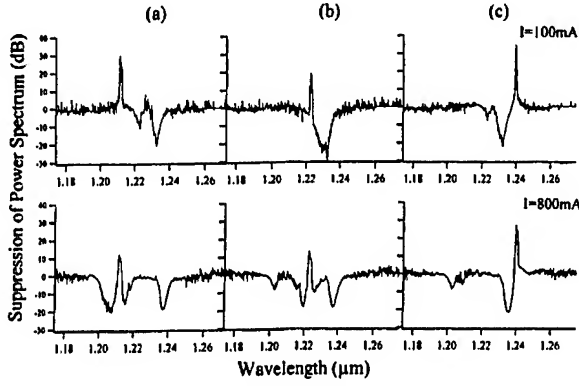


Fig. 5. The relative suppression curves derived from spectra shown in Fig. 4: the relative suppression factor is a ratio of the spectral density measured under grating-coupled spectral selective laser action to that with no spectral selection case (free-running case).

asymmetry in the intensity appears because there is spontaneous emission on one side of the selected mode and laser emission on the other. The visible suppression is much stronger on the lasing side than on the spontaneous emission side. The SMS spectra in Fig. 5(a) show the effect when the grating is tuned near the short-wavelength edge of the ground state laser range (1212 nm). In addition to a burning about the strong mode, another distant burning is seen at ~ 1237 nm, at the opposite (long-wavelength) side of the laser oscillation range. This situation occurs because the modes at the ends of the lasing range are more sensitive than the central modes to a small change in the gain. Thus, at a large distance of 25 nm from the grating-selected mode, the lasing action is easily quenched even though the competition with the selected mode is weak. On the other hand, the grating-selected mode at the short wavelength end cannot stop laser action in the strong central modes. In relative terms, this circumstance produces a larger suppression in the modes at the edge of the lasing spectrum.

The L - I characteristics are shown in Fig. 6 for different tuning configurations with the grating. The slope efficiency is improved by the external cavity, and the power far above the threshold is increased by about 12% in both the wavelength-selective and nonwavelength-selective regimes. Thus, the broad-band emission is narrowed by the wavelength-selective external cavity without degradation in the laser power output. However, the grating-coupled emission has a poor spectrum above ~ 350 mA as influenced by side-mode excitation.

IV. SPECTRAL "FLATTENING" MODEL

We first consider a spectral flattening model to characterize the distortion of the gain spectrum in the free-running case (see Fig. 5). The flattening is a result of spectral "holes" surrounding each lasing mode. The hole burning is distributed over the whole laser emission range and leads to a dense array of closely spaced modes. These measured effects are described in the proposed model by a combination of homogeneous and inhomogeneous factors. The homogeneous width is assumed to be less than the inhomogeneous one; therefore, the gain spectrum appears to be deformed under high-power laser oscillation. If many modes are excited across the range where the gain is sufficient for laser os-

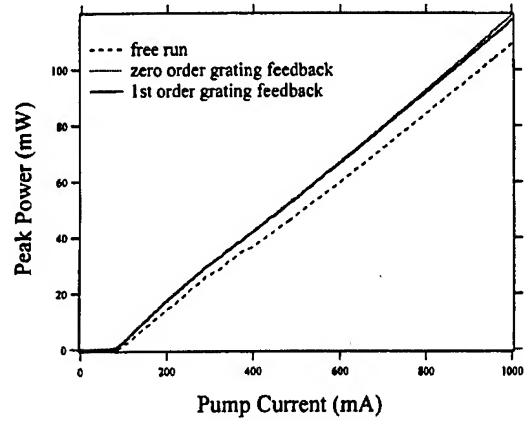


Fig. 6. Single-facet output power as a function of pumping current characteristics in three different modes of laser operation: 1) free-running with no external cavity; 2) external cavity with no spectral selection (grating is in the zeroth-order position); and 3) external cavity with the grating in the first-order position (grating-coupled operation) tuned to the center of the emission band (near 1230 nm).

cillation, the gain saturation will occur, and the "over-threshold" gain will be cut from the top of the spectral curve.

On the other hand, homogeneous gain saturation occurs that prevents the gain from increasing not only at the laser oscillation wavelength, but also at some spectral distance from this wavelength. Due to this saturation, mode competition takes place. In general, the suppression of weak modes by a strong one (the strength of the mode competition) increases with a decrease in the spectral distance.

In order to take into account the homogeneous effect, we assume that the gain across the spectral band increases with increasing injection current, but above threshold not as fast as below threshold. Thus, the features of the model are the following:

- 1) above laser threshold, a slow increase in the gain occurs outside the laser emission range;
- 2) a flattening of the gain takes place near the top of the gain spectrum in the lasing range;
- 3) the laser emission bandwidth is equivalent to the width of the flattened range.

For a quantitative description, we use a parabolic line-shape function that is a good approximation for the top of a quantum dot gain spectrum, which has either a Gaussian or other bell-shape contour

$$g(I, \lambda) = G(I)[1 - 2(\lambda - \lambda_0)^2 / \delta\lambda^2] \quad (1)$$

where λ_0 is the central emission wavelength, $G(I)$ is the gain magnitude at λ_0 , and $\delta\lambda$ is a parameter for characterizing the curvature of the undistorted gain contour at its top. It is assumed to be constant with different pump levels. Equation (1) does not include the blue shift of the center wavelength that occurs due to the band-filling process. This shift can lead to some spectral asymmetry in the evolution of the laser band, but this effect is not emphasized in this work.

At lasing threshold

$$G(I_{th}) = \alpha \quad (2)$$

where I_{th} is the threshold current and α is the threshold gain including internal and mirror losses of the cavity. When $I > I_{th}$, the stationary magnitude of the gain should be about the same as at threshold by (2). We assume that the gain curve rises with increasing I such that two wavelengths on the "red" and "blue" side of the threshold spectral point encompass the range where the gain is sufficient for laser action. The distance between them is

$$\Delta\lambda = 2^{1/2}\delta\lambda[1 - \alpha/G(I)]^{1/2}. \quad (3)$$

For $G(I)$, we use a simple linear expression [17]

$$G(I) = G_0\Gamma[(I/I_0) - 1] \quad (4)$$

where G_0 and I_0 are material constants (I_0 is the current at transparency), and Γ is the optical confinement factor. Equation (4) is valid in the current range below threshold. To account for the homogeneous saturation effect, we assume that the gain increases much more slowly above threshold [as defined by (2)] than below, namely,

$$G(I) = \alpha + \zeta\{G_0\Gamma[(I/I_0) - 1] - \alpha\}, \quad \text{at } I > I_{th} \quad (5)$$

where $\zeta < 1$ is the "slowing" coefficient. Equation (5) is valid for the gain calculation outside the laser emission range, inside which the gain is saturated at about the level of α . With these expressions, we obtain the dependence of $\Delta\lambda$ on current in the following form:

$$\Delta\lambda = 2^{1/2}\delta\lambda[1 + (1/\zeta)(I_{th} - I_0)/(I - I_{th})]^{-1/2}. \quad (6)$$

In Fig. 3, the emission bandwidth of the free-running laser as measured at the -10-dB level is compared with curve 1 which is drawn according to (6) for the flattening model. The agreement is good except near threshold where $\Delta\lambda$ is non-zero because limited narrowing occurs below threshold. In curve 1, the fitted values for the "slowing" coefficient ζ and the spectral width parameter $\delta\lambda$ are 0.033 and 40 nm, respectively. Other parameters are taken from experimental data: $I_{th} = 80$ mA and $I_0 = 18.5$ mA ($J_0 = 30.8$ A/cm², the diode area is 6.0×10^{-4} cm²). The good agreement of curve 1 with the experimental data supports the conclusion that our spectral flattening model successfully describes the free-running lasing spectrum.

V. SPECTRAL HOLE BURNING MODEL

Now we consider the effect of narrow-line oscillation within the inhomogeneously broadened band. Introducing spectral selection by feedback from the grating quenches the laser oscillation outside the selected narrow range. The "slowing" of the gain growth outside this narrow range is assumed to be dependent on the spectral detuning with respect to the narrow lasing mode at λ_L . Therefore, we introduce here the spectrally dependent "slowing" coefficient

$$\beta(\lambda, \lambda_L) = \zeta_0(\lambda - \lambda_L)^2 / [(\lambda - \lambda_L)^2 + b^2] \quad (7)$$

where b is the half-width of the homogeneous gain broadening and ζ_0 is the magnitude factor. $\beta(\lambda, \lambda_L)$ is based on the Lorentzian lineshape associated with a lifetime-type

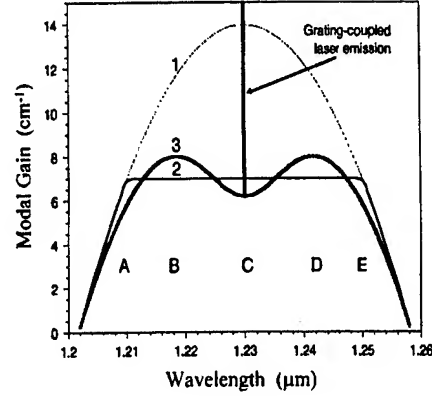


Fig. 7. Calculated spectral contours for nonsaturated gain (curve 1), for saturated gain according to the spectral "flattening" model for free-running laser emission (curve 2), and for spectral hole burning under narrow-line grating-coupled laser emission (curve 3). The transition from curve (2) to curve (3) leads to a reduction in gain in regions marked A, C, and E and an increase in regions B and D.

broadening. We use this simple shape in the vicinity of λ_L and do not deal much with the far wings of the lineshape function. According to (7), the gain increase above threshold is stopped totally at $\lambda = \lambda_L$, but occurs at other wavelengths. At $|\lambda - \lambda_L| \gg b$, the gain is not influenced by laser oscillation at all. For the case of laser oscillation in the center of the gain band, $\lambda_L = \lambda_0$, the distorted gain contour can be described as

$$g^*(I, \lambda) = (G_0\Gamma/I_0)[I_{th} - I_0 + \beta(\lambda, \lambda_0)(I - I_{th})] \times [1 - 2(\lambda - \lambda_0)^2/\delta\lambda^2]. \quad (8)$$

From (8), it follows that the presence of a strong oscillation at λ_0 leads to the spectral hole near λ_0 . Outside this range, if the gain is not sufficient for laser oscillation, the side mode will be suppressed across the whole spectrum. But, with an increase of the pumping current, the laser action can appear at distant wavelengths where the SMS factor degrades. The gain distortion is shown in Fig. 7 for three different regimes. The parameters used are as follows: $\zeta_0 = 0.11$, $b = 13$ nm, $G_0\Gamma = 1.65$ cm⁻¹, $\delta\lambda = 40$ nm, $I_0 = 18.5$ mA, and $I_{th} = 80$ mA. Contour 1 is for the unperturbed gain, contour 2 is the flattened gain corresponding to the free-running oscillations, and contour 3 is the gain spectrum subjected to spectral hole burning under the lasing in the center of the band. When the laser regime is switched from 2 to 3, the gain change occurs: the gain is depressed in the region marked C in Fig. 7 due to the effect of spectral hole burning. The gain in regions B and D is shown to increase, which causes some side modes distant from the center to be excited. In the peripheral regions A and E, the gain decreases. This leads to a decrease of the laser emission producing secondary spectral "holes" at the edges of the free-running lasing range. Thus, stronger SMS is expected in regions A, C, and E, whereas the suppression is weaker in regions B and D. Actually, the spectral hole in range C is divided into two sections by the strong lasing mode. In the experimental results shown in Fig. 5 for the case where the grating-coupled mode is tuned to the center of the band, four spectral holes of mode suppression are found in the spectrum, which fully supports the above explanations.

TABLE I
EXPERIMENTAL AND CALCULATED SPECTRAL DISTANCES BETWEEN THE LASER EMISSION OR GAIN PEAKS OUTSIDE
THE GRATING-COUPLED MODE EMISSION

Current, mA	Exp'l distance between free running laser peaks, nm	Calculated distance between subsidiary gain peaks*, nm	Calculated distance between subsidiary gain peaks**, nm
400	17.5	17.6	18.1
500	20	20	20
800	23	23.4	23

* Assuming $b = 13\text{ nm}$, $\zeta_0 = 0.11$.

** Assuming $b = 12\text{ nm}$, $\zeta_0 = 0.11$.

Using (8), we calculated the spectral distance between the gain peaks outside the "hole" and its dependence on the pump current (with the variable material parameters of the equation). The comparison with experimental data on the spectral distance is shown in Table I. The best fit is obtained when the following parameters are assumed: $b = 13\text{ nm}$ and $\zeta_0 = 0.11$. Other sets of these parameters give a larger rms error. Taking into account the interplay between the two parameters used in the fitting procedure and the experimental accuracy, we estimate the gain homogeneous broadening FWHM as $2b = 26\text{ nm}$ ($\sim 21\text{ meV}$).

We believe this simplified scheme gives an adequate qualitative explanation of the main experimental observations: competition between grating-coupled and free-running laser oscillations, multiple spectral holes, and the effects of detuning. The proposed scheme does not include the spectral asymmetric mode interaction [18] that probably also influences the picture of mode competition.

VI. DISCUSSION

The free-running laser spectrum has been described by a simple "flattening" model that is proposed for an inhomogeneously broadened gain band accounting for the contribution of the homogeneous broadening. The flattening model also suggests that there are no specific wavelength for preferential lasing. In the free-running regime, broad-band laser emission is observed with a relatively low spectral density. The mode competition is accounted for only by the "slowing" factor. The situation is rather different in the spectral selection case: the strong laser oscillation is maintained by the external cavity. A high spectral density in the selected mode produces SMS dependent on the spectral distance from the predominant mode. The half width at half maximum (HWHM) of the homogenous gain broadening b is determined to be 13 nm , and the corresponding energy half-width b^* is about 10.5 meV at room temperature. For the lifetime broadening approach, the dephasing time is $\hbar/b^* \approx 63\text{ fs}$. It can be compared with recent measurements of the dephasing time reported in [19] with QD's embedded in a GaAs matrix. A value of 290 fs has been derived from these experiments based on "self-induced" spectral hole burning in the QD

absorption band under external femtosecond pulses at $1.08\text{ }\mu\text{m}$ wavelength; 260 fs and 190 fs have been obtained from four-wave mixing experiments with the same QD structure. The values agree within experimental accuracy. This result has been attributed to the exciton relaxation in QD's. Our estimation of the dephasing time is $4.2\text{--}4.6$ times shorter, which can be attributed to the electron-hole transition under the laser level of excitation. The short dephasing time is associated with carrier-carrier and phonon-carrier scattering. This produces a fast hole relaxation between states closely spaced in energy. Usually such processes in QW lasers are described by dephasing time in the range $30\text{--}70\text{ fs}$. An elastic Coulombic collision of carriers in the matrix (wetting layer, quantum well) to that in the QD's can be responsible for the interlevel relaxation in QD's, and the dephasing time in the range $0.1\text{--}1\text{ ps}$ has been theoretically calculated when the carrier density in the wetting layer is $\sim 10^{11}\text{ cm}^{-2}$ [20]. In our case, we can estimate the carrier density in the QW assuming a carrier lifetime of 10 ps (as limited by capture to QD's). A density of 10^{11} cm^{-2} can be expected at a current density 1.5 kA/cm^2 , corresponding to 1 A current in the devices under investigation. Therefore, the rapid dephasing mechanisms described above can be involved in the homogeneous broadening in our laser diode.

Another report concerning the homogeneous broadening in QD lasers has been made in [21] concerning temperature-dependent multimode operation of a QD laser. Experimental data suggests a room-temperature homogeneous broadening of $\sim 13\text{ meV}$ in agreement with a dephasing time of 0.1 ps that has been theoretically derived accounting for carrier-carrier scattering with a carrier density of $7 \times 10^{17}\text{ cm}^{-3}$ in the wetting layer. It was also stated in [21] that at 80 K the homogeneous width seems to be negligible as compared with the inhomogeneous one (45 meV). This is not the case at 300 K , and we can conclude that the homogeneous broadening seems to be quite significant in QD and DWELL laser structures.

An issue for a short discussion is the asymmetry that is noticeable in the spectral holes: the suppression factor in the short-wave side is systematically stronger than that at the long-wave side when the grating-coupled oscillation is not at the ends of the laser emission range. This can be explained in terms of the asymmetric nonlinear mode interaction [18]

by the same mechanism as that for four-wave mixing. The interaction produces some nonlinear addition to the gain at the long-wave side of the strong laser line. Therefore, mode competition is stronger at the short-wave side than at the long-wave side.

VII. CONCLUSION

- 1) The broad laser oscillation bandwidth in the QD laser has been quantitatively described in terms of a spectral "flattening" model for free-running operation. The fitting parameter in this model is the "slowing" coefficient ζ , which is the ratio of the gain increment outside the laser emission range under laser oscillation to that with no laser oscillation. A value of $\zeta = 0.033$ is found that indicates that the discussed gain change is ~ 30 times slower in the laser regime than below the oscillation threshold.
- 2) Under grating-coupled operation, the spectrum can be significantly narrowed, and the operating wavelength can be tuned over a range of wavelengths that is also understood in terms of flattening model. It is important to note that most of optical power emitted in the free-running regime can be collected into a selected mode when the laser operates in the grating-coupled regime under a certain pump level.
- 3) Mode competition is found to be dependent on the distance between modes. Because of this, the SMS is quite strong (up to -30 dB) when the free-running bandwidth $\Delta\lambda$ is less than the homogeneous spectral width (region I in Fig. 3). The SMS reduces from -20 dB to approximately -10 dB along with an increase of the free-running bandwidth above 20 nm (region II in Fig. 3). Here, competing modes that are spectrally distant from the selected mode become prominent. From the position of distant modes that appear simultaneously with the selected mode, we estimate that the HWHM of the homogenous broadening is approximately 10.5 meV.
- 4) The dephasing time is estimated as 63 fs, which is of the same order as values in QW lasers in a comparable wavelength range. It is quite shorter than those derived from measurements of externally induced spectral hole burning and four-wave mixing experiments [19]. The shorter dephasing time is reasonable under the higher level of the pumping typical for laser operation.
- 5) The observed spectral features of mode suppression (four "holes" within the laser emission range) are explained qualitatively in terms of a spectral hole burning model. A primary "hole" (split into two by the laser line) is produced by the direct mode suppression within a short spectral distance from the strong laser line. Two secondary "holes" are associated with shrinkage of the laser emission range from the free-running regime when the strong laser line appears.

ACKNOWLEDGMENT

The authors would like to acknowledge valuable discussions with S. R. J. Brueck.

REFERENCES

- [1] H. Hirayama, K. Matsunaga, K. Asada, and Y. Suematsu, "Lasing action of $\text{Ga}_{0.67}\text{In}_{0.33}\text{As}/\text{GaInAsP}/\text{InP}$ tensile-strained quantum box lasers," *Electron. Lett.*, vol. 30, no. 2, pp. 142–143, 1994.
- [2] N. Kirstaedter, N. N. Ledentsov, M. Grundmann, D. Bimberg, V. M. Ustinov, S. S. Ruvimov, M. V. Maximov, P. S. Kop'ev, Zh. I. Alferov, U. Richter, P. Werner, U. Goesele, and J. Heydenreich, "Low threshold, large T_0 injection laser emission from $(\text{InGa})\text{As}$ quantum dots," *Electron. Lett.*, vol. 30, no. 17, pp. 1416–1417, 1994.
- [3] D. Bimberg, N. Kirstaedter, N. N. Ledentsov, Zh. I. Alferov, P. S. Kop'ev, and V. M. Ustinov, "InGaAs-GaAs quantum dot lasers," *IEEE J. Select. Topics Quantum Electron.*, vol. 3, no. 2, pp. 196–205, 1997.
- [4] Z. Zou, D. L. Huffaker, S. Csutak, and D. G. Deppe, "Ground state lasing from a quantum-dot oxide-confined vertical-cavity surface-emitting laser," *Appl. Phys. Lett.*, vol. 75, no. 1, pp. 22–24, 1999.
- [5] D. Bhattacharyya, E. A. Avrutin, A. C. Bryce, J. H. Marsh, D. Bimberg, F. Heinrichsdorff, V. M. Ustinov, S. V. Zaitsev, N. N. Ledentsov, P. S. Kop'ev, Zh. I. Alferov, A. I. Onischenko, and E. P. O'Reilly, "Spectral and dynamic properties of InAs-GaAs self-organized quantum dot lasers," *IEEE J. Select. Topics Quantum Electron.*, vol. 5, pp. 648–657, 1999.
- [6] D. G. Deppe, D. L. Huffaker, S. Csutak, Z. Zou, G. Park, and O. B. Shchekin, "Spontaneous emission and threshold characteristics of $1.3\text{ }\mu\text{m}$ InGaAs-GaAs quantum-dot GaAs-based lasers," *IEEE J. Quantum Electron.*, vol. 35, pp. 1238–1246, Aug. 1999.
- [7] H. Shoji, K. Mukai, N. Ohtsuka, M. Sugawara, T. Uchida, and H. Ishikawa, "Lasing at three-dimensionally quantum-confined sublevel of self-organized $\text{In}_{0.5}\text{Ga}_{0.5}\text{As}$ quantum dots by current injection," *IEEE Photon. Technol. Lett.*, vol. 7, pp. 1385–1387, Dec. 1995.
- [8] P. Bhattacharyya, K. K. Kamath, J. Singh, D. Klotzkin, J. Phillips, H. T. Jiang, N. Chervela, T. B. Norris, T. Sosnowski, J. Laskar, and M. R. Murty, "In(Ga)As/GaAs self-organized quantum dot lasers: DC and small-signal modulation properties," *IEEE Trans. Electron Devices*, vol. 46, pp. 871–883, May 1999.
- [9] M. Grundmann, O. Stier, S. Bogner, C. Ribbat, F. Heinrichsdorff, and D. Bimberg, "Optical properties of self-organized quantum dots: Modeling and experiments," *Physica Status Solidi*, to be published.
- [10] M. Grundmann, "The present status of quantum dot lasers," *Physica E*, vol. 5, pp. 167–184, 1999.
- [11] G. T. Liu, A. Stintz, H. Li, K. J. Malloy, and L. F. Lester, "Extremely low room-temperature threshold current density diode lasers using InAs dots in $\text{In}_{0.15}\text{Ga}_{0.85}\text{As}$ quantum well," *Electron. Lett.*, vol. 35, no. 14, pp. 1163–1165, 1999.
- [12] A. R. Kovsh, D. A. Livshits, A. E. Zhukov, A. Y. Egorov, V. M. Ustinov, M. V. Maximov, N. N. Ledentsov, P. S. Kop'ev, Zh. I. Alferov, and D. Bimberg, "3.3 W injection heterolaser based on self-organized quantum dots," in *Proc. Nanostructures: Physics and Technology, 7th Int. Symp.*, St. Petersburg, Russia, June 14–18, 1999, pp. 128–130.
- [13] L. F. Lester, A. Stintz, H. Li, T. C. Newell, E. A. Pease, B. A. Fuchs, and K. Malloy, "Optical characteristics of $1.24\text{-}\mu\text{m}$ InAs quantum-dot laser diode," *IEEE Photon. Technol. Lett.*, vol. 11, pp. 931–933, Aug. 1999.
- [14] L. V. Asryan and R. A. Suris, "Inhomogeneous line broadening and the threshold current density of a semiconductor quantum dot laser," *Semicond. Sci. Technol.*, vol. 11, no. 4, pp. 554–567, 1996.
- [15] L. V. Asryan and R. A. Suris, "Spatial hole burning and multimode generation threshold in quantum-dot lasers," *Appl. Phys. Lett.*, vol. 75, no. 9, pp. 1215–1217, 1999.
- [16] H.-J. Bachert, A. P. Bogatov, P. G. Eliseev, A. Keiper, and K. Khairidinov, "Spectral band homogeneous broadening and narrow-band emission of AlGaAs/GaAs injection lasers," *IEEE J. Quantum Electron.*, vol. 15, pp. 786–790, Aug. 1979.
- [17] K. J. Vahala, "Quantum box fabrication tolerance and size limits in semiconductors and their effect on optical gain," *IEEE J. Quantum Electron.*, vol. 24, pp. 523–530, Mar. 1988.
- [18] A. P. Bogatov, P. G. Eliseev, and B. N. Sverdlov, "Anomalous interaction of spectral modes in a semiconductor lasers," *IEEE J. Quantum Electron.*, vol. QE-11, pp. 510–509, July 1975.
- [19] P. Borri, W. Langbein, J. Mork, J. M. Hvam, F. Heinrichsdorff, M.-H. Mao, and D. Bimberg, "Dephasing in InAs/GaAs quantum dots," *Phys. Rev. B*, vol. 60, pp. 7784–7787, 1999.
- [20] A. V. Uskov, K. Nishi, and R. Lang, "Collisional broadening and shift of spectral lines in quantum dot lasers," *Appl. Phys. Lett.*, vol. 74, no. 21, pp. 3081–3083, 1999.

- [21] M. Sugawara, K. Mukai, and Y. Nakata, "Light emission spectra of columnar-shaped self-assembled InGaAs/GaAs quantum-dot lasers: Effect of homogeneous broadening of the optical gain on lasing characteristics," *Appl. Phys. Lett.*, vol. 74, no. 11, pp. 1561–1563, 1999.
- P. Eliseev (S'M'99), photograph and biography not available at the time of publication.
- H. Li (M'93), photograph and biography not available at the time of publication.
- A. Stintz, photograph and biography not available at the time of publication.
- G. T. Liu (S'99), photograph and biography not available at the time of publication.
- T. C. Newell, photograph and biography not available at the time of publication.
- K. J. Malloy (S'76–M'79), photograph and biography not available at the time of publication.
- L. F. Lester (S'89–M'91), photograph and biography not available at the time of publication.

A grating-coupled external-cavity quantum dot laser is tuned across a 201 nm range at a maximum bias of 2.87 kA/cm², one order of magnitude less than the bias required for comparable tuning of quantum well lasers. The tuning range increases for higher cavity losses of the quantum dot laser.

Widely tunable semiconductor lasers will be essential components of high-capacity wavelength-division-multiplexed transmission and photonic switching systems. External-cavity configurations employing a grating as a dispersive feedback element have enabled tuning of quantum well (QW) lasers across 105 nm at $\lambda = 0.8 \mu\text{m}$ [1], and 240 nm at $\lambda = 1.5 \mu\text{m}$ [2], for injection current densities of 21 and 33 kA/cm², respectively. This high bias is necessary to achieve lasing from the second quantised state of the QW and causes device heating that restricts commercial applications of these sources.

In contrast to QW lasers, quantum dot (QD) emitters are well-suited for use as low-threshold, broadband tunable sources owing to two unique features of QD structures [3]. First, the low QD density of states causes the QD ground state optical gain to saturate easily. This means that the higher-order energy levels are populated by carriers at fairly low current densities of $\sim 1 \text{ kA/cm}^2$. Secondly, due to homogeneous and inhomogeneous broadening, continuous coverage of the wavelength spectrum is possible. The dot size variation, which is normally undesirable for low-threshold operation, can be exploited to extend the tuning range towards the shorter wavelength side.

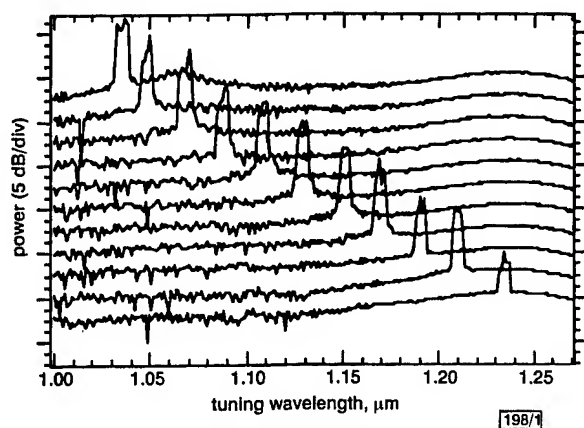


Fig 1 Lasing spectra of external-cavity QD laser, tuned across the 1033–1234 nm wavelength range

In this Letter a 201 nm tuning range in a grating-coupled external-cavity quantum dot laser is demonstrated and its variation as a function of the cavity losses of the internal Fabry-Perot (FP) laser is investigated. The maximum bias is 400 mA (2.87 kA/cm²), which is approximately 10 times lower than the bias required for tuning QW lasers across similar ranges. Fig. 1 shows the 201 nm-wide lasing spectrum (1033–1234 nm) obtained with a QD device arranged in a Littrow external-cavity configuration. Across the 201 nm range, the lasing peak is $\sim 20 \text{ dB}$ higher than the spontaneous emission spectrum. The laser active region is composed of a single InAs quantum dot layer confined in the middle of a 10 nm-thick In_{0.2}Ga_{0.8}As QW and sandwiched by GaAs waveguide layers [4]. Details of the crystal growth are described in [5]. The laser has a 9 μm -wide ridge waveguide and the cavity is 1.7 mm long. A single $\lambda/4$ antireflection layer of HfO₂ is deposited on one of the laser facets by electron-beam evaporation, and the other facet remains as-cleaved. A residual reflectivity of the AR-coated mirror is $\sim 1\%$ at the free-running lasing wavelength of $\lambda = 1.05 \mu\text{m}$ (second excited state). The AR coating increases the total cavity loss and completely extinguishes lasing at the ground state ($\lambda = 1.24 \mu\text{m}$) and the first excited state ($\lambda = 1.15 \mu\text{m}$).

Curves (i) and (ii) in Fig. 2 compare the threshold current density across the tuning range as a function of the wavelength for two grating-coupled AR-coated emitters with cavity lengths of 1.7 and 2 mm, respectively. The device structure and external-cavity-configuration are the same for both lasers. Since both devices have the same AR coating, the

level increases, the ground gain will increase and the gain peak will shift to the higher energy transitions. As a consequence, the free-running lasing wavelength and threshold current are $\lambda = 1.05 \mu\text{m}$, $J_{th} = 3.46 \text{ kA/cm}^2$ for the 1.7 mm-long device, and $\lambda = 1.09 \mu\text{m}$, $J_{th} = 2.83 \text{ kA/cm}^2$ for the 2 mm-long device.

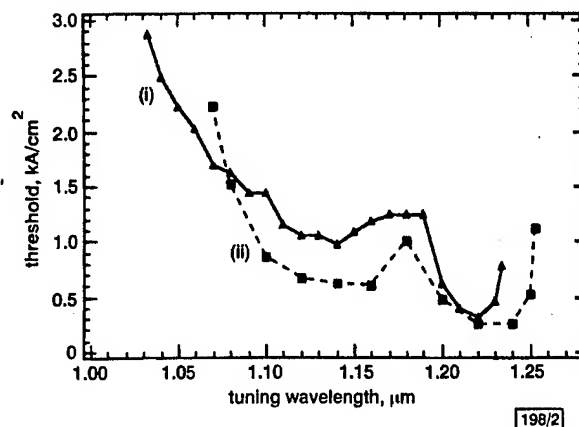


Fig 2 Threshold current density against lasing wavelength across the tuning range for different cavity lengths L

- (i) 1.7 mm
- (ii) 2.0 mm

Fig. 2 shows that a judicious increase in the internal FP cavity loss yields a broader tuning range. The 1.7 mm-long laser can be tuned across 201 nm ($\lambda = 1033\text{--}1234 \text{ nm}$) compared to 183 nm ($\lambda = 1070\text{--}1253 \text{ nm}$) for the 2.0 mm-long emitter, at the expense, however, of the maximum threshold current density. For constant mirror reflectivities, the technique of increasing the internal FP loss to expand the tuning range can be motivated as follows: as long as the external cavity loss does not exceed the ground-state saturated gain, then shortening the internal FP cavity length does not sacrifice tuning on the long-wavelength side. This condition puts a lower limit on the laser diode cavity length. To extend the tuning to shorter wavelengths, higher pump is required which means the internal FP losses must be increased to prevent free-running lasing. On the short wavelength end, the grating-forced operation can only suppress the internal FP within $\sim 20 \text{ nm}$ of the free-running wavelength by means of homogeneous broadening [6]. Further tuning to shorter wavelengths and an increase in the pump cause simultaneous free-running and grating-selected lasing. This situation defines the limit to the tuning range at the short wavelength end.

A tuning range of 201 nm in a grating-coupled external-cavity QD laser for maximum bias of 2.87 kA/cm² has been demonstrated. Similar tuning ranges in QW lasers require current densities higher by an order of magnitude. Further extension of the tuning range could be achieved by designing a QD with a deeper potential well, a smaller size, and a broader size distribution. This approach would enlarge the energy separation between the various states in the QD and minimise the local increases in threshold current.

Acknowledgments: This work was supported by the Defense Advanced Research Projects Agency under Grant MDA972-98-1-0002 and by the US Air Force Office of Scientific Research under Grant F49620-96-1-0077.

© IEE 2000

Electronics Letters Online No: 20001080

DOI: 10.1049/el:20001080

P.M. Varangis, H. Li, G.T. Liu, T.C. Newell, A. Stintz, B. Fuchs, K.J. Malloy and L.F. Lester (Center for High Technology Materials, University of New Mexico, 1313 Goddard SE, Albuquerque, NM 87106, USA)

E-mail: petrosva@chtm.unm.edu

References

- 1 MEHUY, D., MITTELSTEIN, M., YARIV, A., SARFATY, R., and UNGAR, J.E.: 'Optimized Fabry-Perot (AlGa)As quantum-well lasers tunable over 105 nm', *Electron. Lett.*, 1989, 25, (2), pp. 143–145

- 3 LI, H., LIU, G.T., VARANGIS, P.M., NEWELL, T.C., STINTZ, A., FUCHS, B., MALLOY, K.J., and LESTER, L.F.: '150nm tuning range in a grating-coupled external-cavity quantum dot laser', to appear in *IEEE Photonics Technol. Lett.*, 2000
- 4 LESTER, L.F., STINTZ, A., LI, H., NEWELL, T.C., PEASE, E.A., FUCHS, B., and MALLOY, K.J.: 'Optical characteristics of 1.24 μm InAs quantum dot laser diodes', *IEEE Photonics Technol. Lett.*, 1999, **11**, (8), pp. 931-933
- 6 ELISSEV, P., LI, H., STINTZ, A., LIU, G.T., NEWELL, T.C., MALLOY, K.J., and LESTER, L.F.: 'Tunable grating-coupled laser oscillation and spectral hole burning in an InAs quantum-dot laser diode', *IEEE J. Quantum Electron.*, 2000, **36**, (4), pp. 479-485

2 μm GaInAsSb/AlGaAsSb midinfrared laser grown digitally on GaSb by modulated-molecular beam epitaxy

C. Mourad^{a)}

Center for High Technology Materials, University of New Mexico, Albuquerque, New Mexico 87106

D. Gianardi

Boeing Defense and Space Group, Albuquerque, New Mexico 87106

K. J. Malloy

Center for High Technology Materials, University of New Mexico, Albuquerque, New Mexico 87106

R. Kaspi

Air Force Research Laboratory, Directed Energy Directorate, AFRL/DELS, Kirtland Air Force Base, Albuquerque, New Mexico 87106

(Received 26 June 2000; accepted for publication 30 August 2000)

Stimulated emission at 1.994 μm was demonstrated from an optically pumped, double quantum well, semiconductor laser that was digitally grown by modulated-molecular beam epitaxy. This "digital growth" consists of short period superlattices of the ternary GaInAs/GaInSb and GaAsSb/GaSb/AlGaSb/GaSb alloys grown by molecular beam epitaxy with the intent of approximating the band gaps of quaternary GaInAsSb and AlGaAsSb alloys in the active region and barriers of the laser, respectively. For a 50 μs pulse and a 200 Hz repetition rate, the threshold current density was 104 W/cm² at 82 K. The characteristic temperature (T_0) was 104 K, the maximum operating temperature was 320 K and the peak output power was 1.895 W/facet at 82 K with pumping power of 7.83 W. © 2000 American Institute of Physics. [S0021-8979(00)04023-8]

I. INTRODUCTION

Antimonide-based semiconductor materials¹ are important due to their potential application as semiconductor mid-infrared lasers with emission wavelength in the range of 2–4 μm .^{2–9} These GaSb devices are promising for a variety of military and civil applications such as infrared imaging sensors, fire detection and monitoring environmental pollution. The GaInAsSb/AlGaAsSb system has many growth problems including compositional control as well as reproducibility of the structures that are designed. Growth and compositional control of mixed anion III/V compound semiconductor alloys by solid-source molecular beam epitaxy (MBE) is extremely difficult due to the lack of unity incorporation of group V fluxes. The arsenic mole fraction that is incorporated is determined by competition which depends on the growth temperature, the III/V ratio, the As/Sb ratio and the growth rate. Abrupt compositional changes are difficult, and reproducibility within heterostructures and from run to run are poor. However, when short-period superlattices (or digital alloys) composed of binary or ternary layers of a single group V composition are used as an alternative to mixed anion random alloys, we find that the structural, optical and electronic properties are suitable substitutes for the random alloy.¹⁰ The above-mentioned disadvantages encountered in conventional MBE growth of mixed group V alloys are minimized as well. For digital growth of $\text{Ga}_x\text{In}_{1-x}\text{As}_y\text{Sb}_{1-y}$, for example, compositional control of group V, i.e., of the As

mole fraction, is achieved through control of the As shutter duty cycle where the As_2 and Sb_2 shutters are alternately modulated.^{11,12}

$$\text{As mole fraction} = \text{As}_{\text{shutter time}} / (\text{As}_{\text{shutter time}} + \text{Sb}_{\text{shutter time}}).$$

Consequently the ratio of thicknesses of the deposited layers (if the growth rates of the individual layers are assumed to be identical) can be used to deduce the composition of the alloy. Alloys grown by conventional MBE are referred to as random alloys, and those grown by modulated-MBE (MMBE) by creating short-period superlattices are referred to as digital alloys. Growing digitally by MMBE shifts the emphasis placed on control of incident fluxes (which are hard to reset in conventional MBE) to shutter timing and layer thicknesses (which are easy to control). Hence both reproducibility and compositional control difficulties are reduced.

In this article, we report results on an optically pumped quaternary GaInAsSb/AlGaAsSb^{2,7,13} digital alloy laser, in which both the quantum wells and the barriers are grown digitally via MMBE.^{12,11,14,15}

II. GROWTH OF THE LASER STRUCTURE

The laser structure studied was grown using a conventional solid-source MBE system and was designed for optical pumping. A schematic band diagram of the GaInAsSb/AlGaAsSb double quantum well laser is shown in Fig. 1 and it has the following nominal structure.

A 0.16 μm thick GaSb buffer layer was grown on top of an *n*-type GaSb (Te doped) substrate followed by a 1.5 μm thick randomly grown cladding layer with composition

^{a)}Electronic mail: mourad@unm.edu

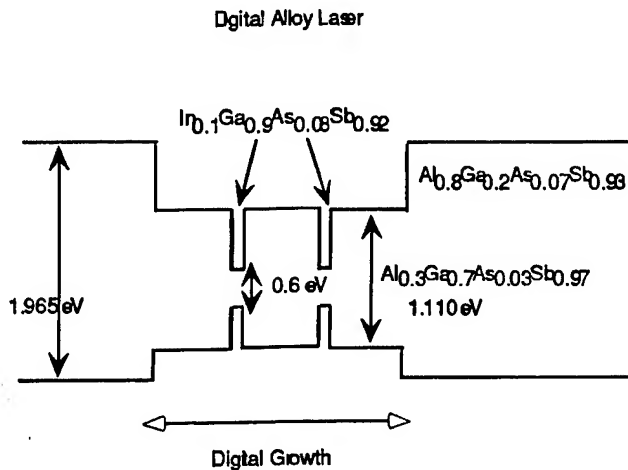


FIG. 1. Schematic energy band diagram of the double quantum well digital alloy laser structure studied.

$\text{Al}_{0.8}\text{Ga}_{0.2}\text{As}_x\text{Sb}_{1-x}$. This was followed by two 150 Å quantum well regions separated by a 0.1 μm thick barrier region, all of which were digitally grown. The shutter time sequence for digital growth of the barrier region by MMBE is shown in Fig. 2, where the Al and As₂ shutters are modulated while keeping the Ga and Sb₂ shutters open. For the quantum well region only the As₂ and Sb₂ shutters are alternately modulated while the In and Ga shutters are kept open. This was followed by a 1 μm thick randomly grown cladding layer topped by a 50 Å thick GaSb cap. The barriers and quantum wells have the following compositions: $\text{Al}_{0.3}\text{Ga}_{0.7}\text{As}_y\text{Sb}_{1-y}$ and $\text{Ga}_{0.9}\text{In}_{0.1}\text{As}_z\text{Sb}_{1-z}$, respectively.

Prior to growth of the laser structure, the cladding layer, the quantum wells and the barriers are calibrated for the desired compositions. For the random alloy region in the cladding, the appropriate incident As₂ and Sb₂ fluxes at a given growth rate and temperature are used. For digital growth in the barriers and active regions, the incident fluxes are calibrated for the group III elements at a specific growth rate and temperature, while the group V compositions are determined by the duty cycles at the lattice-match condition. These are determined by growing several test samples with various duty cycles, and are characterized by x-ray diffraction. The

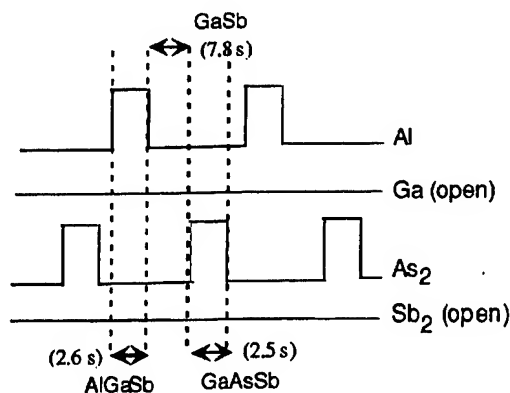


FIG. 2. Schematic time shutter sequence utilized during MMBE growth of the AlGaAsSb digital alloy barrier region of the laser structure lattice matched to GaSb.

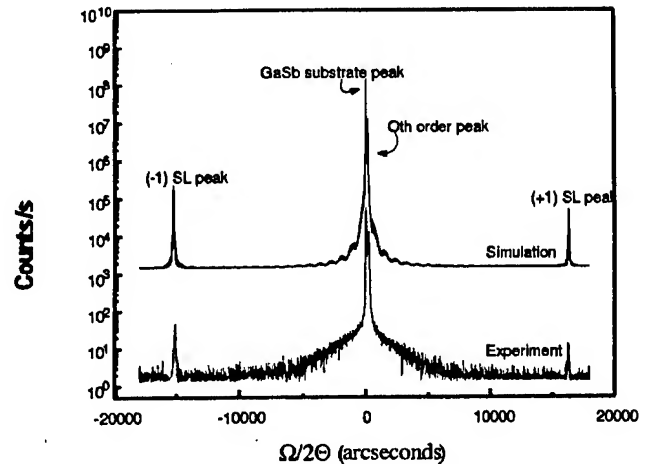


FIG. 3. 004 reflection high-resolution x-ray diffraction curve from a 3000 Å $\text{Ga}_{0.9}\text{In}_{0.1}\text{As}_y\text{Sb}_{1-y}$ bulk digital alloy test structure consisting of 248 layers with composition of $\text{Ga}_{0.9}\text{In}_{0.1}\text{As}/\text{Ga}_{0.9}\text{In}_{0.1}\text{Sb}$ including a rocking curve dynamical simulation of the nominal structure.

duty cycles that correspond to the lattice-match condition are selected for growth of the entire structure. The attractiveness of the digital alloy growth technique by MMBE lies in the fact that only the shutter time sequences will determine the compositions of the barrier and quantum well regions and the entire structure is grown without variation of the incident fluxes.

The procedure for digital growth is as follows: the barriers are grown at 550 °C at a 6 monolayer (18.3 Å) periodicity with the alloy consisting of layers of GaAsSb (2.5 s)/GaSb (7.8 s)/GaAlSb (2.6 s)/GaSb (3.8 s) to produce an average composition of $\text{Al}_{0.3}\text{Ga}_{0.7}\text{As}_{0.03}\text{Sb}_{0.97}$ shown in Fig. 2. This shutter sequence was repeated 55 times to grow a 0.1 μm thick barrier and is one possible sequence among numerous ones making the digital alloy technique flexible. The quantum wells are digitally grown at 440 °C with a periodicity of 4 monolayers (ML) (12.2 Å) consisting of 2 ternary layers $\text{Ga}_{0.9}\text{In}_{0.1}\text{As}$ (2.5 s) and $\text{Ga}_{0.9}\text{In}_{0.1}\text{Sb}$ (4.3 s), grown at 0.59 ML/s, and 12 repetitions to grow a 150 Å thick layer. The laser structure is composed of a total of 710 layers.

III. STRUCTURAL AND OPTICAL PROPERTIES

The structural properties of the laser are studied noninvasively via high-resolution x-ray diffraction (HRXRD) with a Philips double-crystal x-ray diffractometer that utilizes the $\text{Cu } K_{\alpha_1}$ line after four symmetric 022 reflections on the surfaces of four Ge crystals (four crystal Bartel's monochromator) and no receiving slits (open face detector mode). Figure 3 shows a symmetric experimental and theoretical dynamical simulation¹⁶ of the 004 reflection $\Omega/2\theta$ x-ray diffraction scan of a 3000 Å thick bulk $\text{Ga}_{0.9}\text{In}_{0.1}\text{As}_y\text{Sb}_{1-y}$ digital alloy test structure, lattice matched to GaSb (001) which has the same periodicity and composition as the quantum wells of the laser structure. Distinct satellite peaks corresponding to a short-period superlattice with a period of 11.7 Å are observed, which is consistent with the nominal periodicity of 12.2 Å, indicating the high structural quality obtained from this digital alloy growth. The lattice mismatch of the

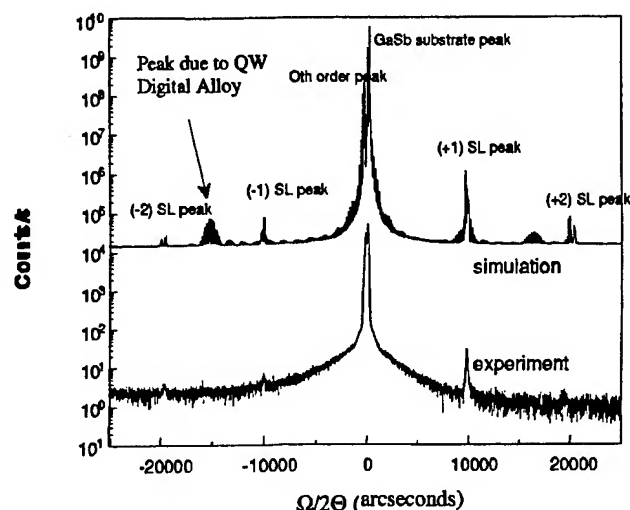


FIG. 4. 004 reflection high-resolution x-ray diffraction curve from the 710 layer double quantum well digital alloy laser structure with a simulation of the nominal structure.

$\text{Ga}_{0.9}\text{In}_{0.1}\text{As}_y\text{Sb}_{1-y}$ digital alloy to the GaSb substrate is less than 9.2×10^{-4} . The zeroth-order peak has a full width at half maximum (FWHM) of 108 arcsec and the GaSb substrate a FWHM of 82.8 arcsec.

In Fig. 4, a symmetric 004 reflection $\Omega/2\theta$ x-ray diffraction spectrum of the more complex digital alloy laser structure is shown. We can clearly observe two orders of the superlattice digital alloy Bragg peaks corresponding to a periodicity of 19.1 Å. This agrees well with the nominal barrier periodicity of 18.3 Å. The lattice mismatch of the spacer layer $\text{Al}_{0.8}\text{Ga}_{0.2}\text{As}_y\text{Sb}_{1-y}$ to the substrate is 0.296×10^{-2} . The FWHM of the zeroth-order is 176.4 arcsec and that of the substrate is 158.4 arcsec. Also plotted in Fig. 4 is a rocking curve simulation of the nominal structure, where two orders of the superlattice peaks are observed at the expected positions. However, two extra peaks due to quantum well digital alloy periodicity are also observed in the simulation but not experimentally since these peaks have weak intensities and fall below the noise level of the diffractometer.

The optical properties of the material are characterized using a continuous wave (cw) Ti:sapphire laser with pump wavelength of 700 nm, and an InSb detector to record the photoluminescence (PL) intensity and wavelength. A single PL peak at 1941 nm with two shoulders at 1798 and 1710 nm are observed. The main peak corresponds to the recombination between the first electron subband and the first heavy-hole subband (C-HH₁) and has a FWHM of 35.5 meV. Comparison with theoretical calculations indicates that the shoulder at 1798 nm is likely to be due to transitions involving light holes (C-LH₁), and the shoulder at 1710 nm corresponds to the GaSb substrate band gap. These results are indicative of the good optical quality of the laser material, as well as of the material producing the expected optical wavelength.

IV. LASER RESULTS AND DISCUSSION

A 2.55 mm digital alloy laser cavity was pumped using an 808 nm pump array pulsed at a 1% duty cycle, 200 Hz

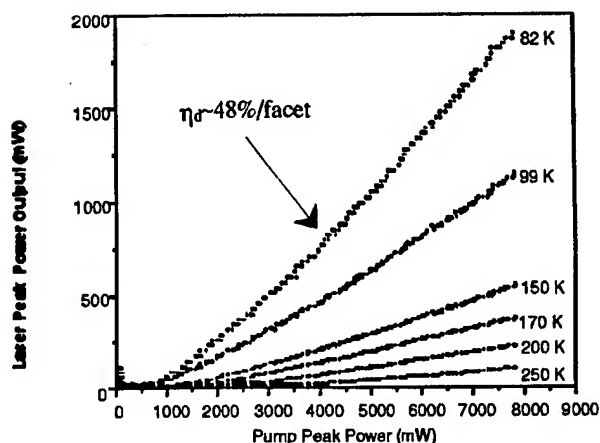


FIG. 5. L - L curves of the laser at increasing operating temperatures.

repetition rate and a duration of 50 μs . The excitation stripe of the focused pump light was estimated to be 250 μm . Figure 5 shows L - L curves obtained from optically pumping the laser cavity at operating temperatures varying from 82 to 320 K. The differential quantum efficiency η_d for optically pumped lasers is

$$\eta_d(T) = \frac{\Delta P_{\text{out}}(T)}{\Delta P_{\text{in}}} \frac{\lambda_{\text{out}}(T)}{\lambda_{\text{pump}}},$$

where $\lambda_{\text{pump}} = 808$ nm is the pump wavelength, λ_{out} is the emitting wavelength in nm and $\Delta P_{\text{out}}/\Delta P_{\text{in}}$ is the differential slope efficiency of the L - L curve at a particular operating temperature. The differential quantum efficiency is 48%/facet at 82 K. A characteristic temperature T_1 using $\eta_d = \eta_{d0} e^{(-T/T_1)}$ is obtained. The T_1 value of 77 K (shown in Fig. 6) indicates that the differential quantum efficiency η_d falls off rapidly at higher temperatures due to the onset of internal losses, which are influenced by defects and nonradiative regions where Auger recombination processes dominate.¹⁷ The peak output power measured is 1.895 W/facet at 82 K and the pumping peak power is 7.83 W. At maximum pumping power no catastrophic degradation of the device is observed. Therefore, it is reasonable to believe that

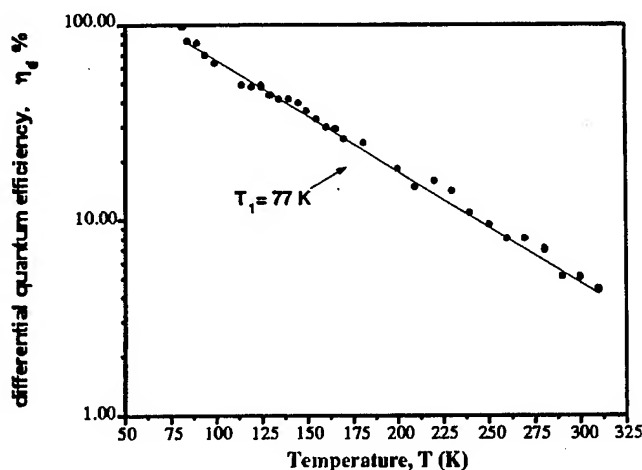


FIG. 6. Differential quantum efficiency η_d vs operating temperature of the laser.

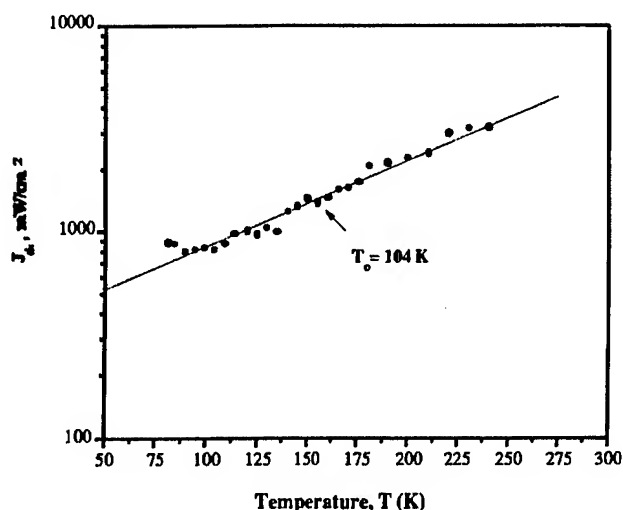


FIG. 7. Threshold current densities J_{th} vs operating temperature of the laser.

a higher maximum peak power could be achieved using even higher pumping power. It is also observed that the threshold current density is low at ~ 104 W/cm², which is approximately equivalent to 148 A/cm² for an electrically injected laser at 82 K. Figure 7 shows the characteristic temperature T_0 calculated for the laser using the equation $J_{th} = J_0 e^{(T/T_0)}$. The T_0 is 104 K (Fig. 7), which is comparable to 113 K obtained for 2.1 μ m diode lasers² and 140 K for a four quantum well electrically pumped laser.¹⁸ However this is larger than the 65 K obtained for 2 μ m optically pumped double heterostructure (DH) lasers grown by liquid phase epitaxy (LPE)¹³ and 49 K for 2.2 μ m diode lasers grown by MBE.⁴ The laser operates up to 320 K, with the laser mode shifting at a rate ~ 0.88 nm/K below 200 K, and at ~ 1.15 nm/K above 200 K.

V. CONCLUSIONS

In this article, we have reported on a GaInAsSb/AlGaAsSb double quantum well digital alloy laser, in which the digital alloy approach by modulated-MBE has been used to build strain compensated very short-period superlattices to replace conventionally MBE-grown mixed group V random alloys. The intent was to create digital alloys that have band gaps equivalent to conventional randomly grown quaternary GaInAsSb and AlGaAsSb alloys. This technique is beneficial from the growth point of view, where the incident fluxes remain unaltered, and compositions are controlled well sim-

ply by varying the shutter sequence of the effusion cells, hence minimizing many growth problems encountered in the growth of mixed As/Sb mixed alloys. From HRXRD and PL data, there is evidence that the laser is of high structural and optical quality. Well defined digital alloy superlattice Bragg peaks corresponding to periodicity as small as 4 ML and a PL peak at the expected wavelength of 1941 nm at room temperature are observed. When the laser was tested, we discovered that the optically pumped laser has a T_0 comparable to that found in the literature for other mid-IR lasers. The laser operates up to 320 K, the threshold current density is small at 104 W/cm² and has a high power output of 1.895 W/facet at 82 K. These results demonstrate the applicability of the digital alloying technique to complex heterostructure optoelectronic devices in which a large number of layers (~ 710) have been grown.

ACKNOWLEDGMENTS

The authors would like to thank the Phillips Labs/LIDA group at Kirtland Air Force Base for their support, in particular Dr. A. Ongstad and C. Moeller for useful discussions and for help in the laser measurements. Dr. G. T. Liu is also to be thanked for his assistance in the PL measurements.

- ¹H. L. Bhat, P. S. Dutta, and V. Kumar, J. Appl. Phys. **81**, 5821 (1997).
- ²S. J. Eglash and H. K. Choi, Appl. Phys. Lett. **61**, 1154 (1992).
- ³R. U. Martinelli, D. Z. Garbuzov, H. Lee, P. K. York, R. J. Menna, J. C. Connolly, and S. Y. Narayan, Appl. Phys. Lett. **69**, 2006 (1996).
- ⁴H. K. Choi and S. J. Eglash, Appl. Phys. Lett. **59**, 1165 (1991).
- ⁵H. K. Choi, G. W. Turner, and M. J. Manfra, Appl. Phys. Lett. **72**, 876 (1997).
- ⁶H. Temkin, B. V. Dutt, E. D. Kolb, and W. A. Sunder, Appl. Phys. Lett. **47**, 111 (1985).
- ⁷H. K. Choi and S. J. Eglash, IEEE J. Quantum Electron. **27**, 1555 (1991).
- ⁸C. H. Lin, S. S. Pei, and H. Q. Le, Appl. Phys. Lett. **72**, 3434 (1998).
- ⁹S. J. Eglash and H. K. Choi, Appl. Phys. Lett. **64**, 833 (1994).
- ¹⁰C. Mourad, Ph.D. thesis, University of New Mexico, Albuquerque, NM, 2000.
- ¹¹Y.-H. Zhang and D. H. Chow, Appl. Phys. Lett. **65**, 3239 (1994).
- ¹²Y.-H. Zhang, J. Cryst. Growth **150**, 838 (1995).
- ¹³Y. Zhao, A. Z. Li, Y. L. Zheng, G. T. Chen, G. P. Ru, W. Z. Shen, and J. Q. Zhong, J. Cryst. Growth **175/176**, 873 (1997).
- ¹⁴J. Y. Marzin, B. Jusserand, and J. M. Gerard, J. Cryst. Growth **111**, 205 (1991).
- ¹⁵H. Q. Le, Y. H. Zhang, D. H. Chow, and R. H. Miles, Inst. Phys. Conf. Ser. (unpublished).
- ¹⁶Bede Scientific Instruments Ltd., Rocking Curve Analysis by Dynamical Simulation. Windows Ver. 3.00, UK, 1998.
- ¹⁷J. R. Meyer *et al.*, Appl. Phys. Lett. **68**, 2976 (1996).
- ¹⁸X. Wu, T. Newell, A. L. Gray, S. Dorato, H. Lee, and L. F. Lester, IEEE Photonics Technol. Lett. **11**, 30 (1999).

Characterization of InAs quantum dots in strained $\text{In}_x\text{Ga}_{1-x}\text{As}$ quantum wells

A. Stintz,^{a)} G. T. Liu, A. L. Gray, R. Spillers, S. M. Delgado, and K. J. Malloy
Center for High Technology Materials, University of New Mexico, Albuquerque, New Mexico 87106

(Received 10 October 1999; accepted 27 January 2000)

The properties of InAs quantum dots placed in a strained InGaAs quantum well are investigated. The structures are grown by solid-source molecular beam epitaxy on GaAs substrates and are characterized using photoluminescence and atomic force microscopy. Emission wavelength and the optical quality of the quantum dots vary with growth temperature and also depend on the position of the dots in the well. A strong dependence of the dot properties on the capping conditions is established. A postgrowth anneal similar to a typical laser cladding growth results in a large photoluminescence (PL) blueshift and reduces the PL intensity by more than two orders of magnitude. It is shown that these dots-in-a-well structures have superior optical properties as compared to conventional InAs dots in a GaAs matrix, and their emission wavelength can be tuned past the technologically important wavelength of 1.3 μm . © 2000 American Vacuum Society. [S0734-211X(00)02103-X]

I. INTRODUCTION

For almost a decade researchers have been studying the properties of self-assembled In(Ga)As quantum dots formed on single-crystal GaAs substrates by Stranski–Krastanov¹ epitaxial growth.^{2,3} Besides the interesting properties of these zero-dimensional, coherently strained objects,⁴ numerous device applications have emerged from this growth technique.^{5–15}

For device applications, it can be advantageous to place the quantum dots in a quantum well. For example, laser diodes exhibit much better performance characteristics when the quantum dots are inserted into a narrow GaAs well surrounded by an AlGaAs matrix.¹⁶ The well aids in capturing charge carriers and suppresses their thermionic emission at high temperatures,¹⁷ thereby leading to higher gain and lower threshold current densities. The increased carrier capture efficiency of wells over dots is in part due to the typically relatively low areal coverage¹⁸ of quantum dots fabricated by the Stranski–Krastanov growth method. A low areal dot coverage translates into relatively small cross sections for trapping electrons in a planar device. Although the wetting layer preceding the formation of self-organized quantum dots could be considered a quantum well, its narrow extent (1.6 monolayers for InAs¹⁹) limits its effectiveness in carrier capture.

In the literature, the vast majority of InGaAs quantum dots formed by Stranski–Krastanov growth are covered with GaAs or even AlGaAs at the same temperature the dots are grown. This temperature is typically at least 60 to 100 °C lower than the optimum growth temperature for this material. From a crystal growth point of view, capping Stranski–Krastanov quantum dots with an InGaAs layer has the advantage that the cap layer can be grown near its optimum growth temperature, thus improving the optical quality of the structure.²⁰ Recently, experimental efforts have been dedicated to the study of planar, pseudomorphically strained

$\text{In}_x\text{Ga}_{1-x}\text{As}$ layers ($x < 0.3$) bordering quantum dots on one or both sides, thereby forming a strained well. Atomic force microscope studies of quantum dots formed on a strained $\text{In}_{0.1}\text{Ga}_{0.9}\text{As}$ buffer suggest that the dot density increases compared to direct deposition on GaAs,²¹ which is a desirable feature for device applications. Other reports indicate that a naturally occurring $\text{In}_{0.1}\text{Ga}_{0.9}\text{As}$ quantum well is formed around quantum dots when they are grown by atomic layer epitaxy.^{22,23} Some authors report that the deposition of an $\text{In}_x\text{Ga}_{1-x}\text{As}$ layer ($x \leq 0.1$) before and after dot growth can shift the photoluminescence wavelength to longer values up to 1.5 μm , which could have important technological implications.^{22,24} Recently, a research group has employed InAs quantum dots in an InGaAs quantum well to obtain a technologically important wavelength of 1.3 μm .²⁵

In this publication, the properties of InAs quantum dots in narrow, pseudomorphically strained $\text{In}_x\text{Ga}_{1-x}\text{As}$ ($x \leq 0.2$)

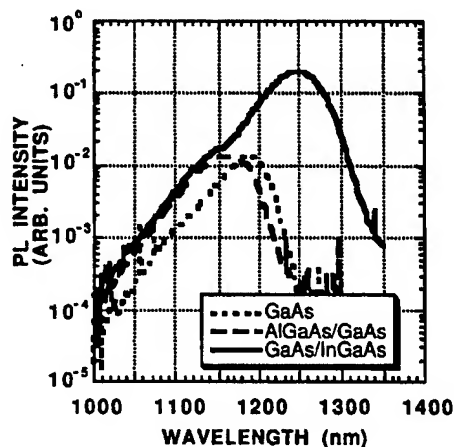


FIG. 1. PL spectra of 2.4 monolayer InAs quantum dots embedded in a GaAs matrix (dotted curve), a GaAs well in an $\text{Al}_{0.2}\text{Ga}_{0.8}\text{As}$ matrix (dashed curve), and an $\text{In}_{0.2}\text{Ga}_{0.8}\text{As}$ well in a GaAs matrix (solid curve). The PL amplitude is an order of magnitude larger for the strained InGaAs well. The FWHM are 49, 78, and 69 nm, respectively.

^{a)}Electronic mail: andreas@chtm.unm.edu

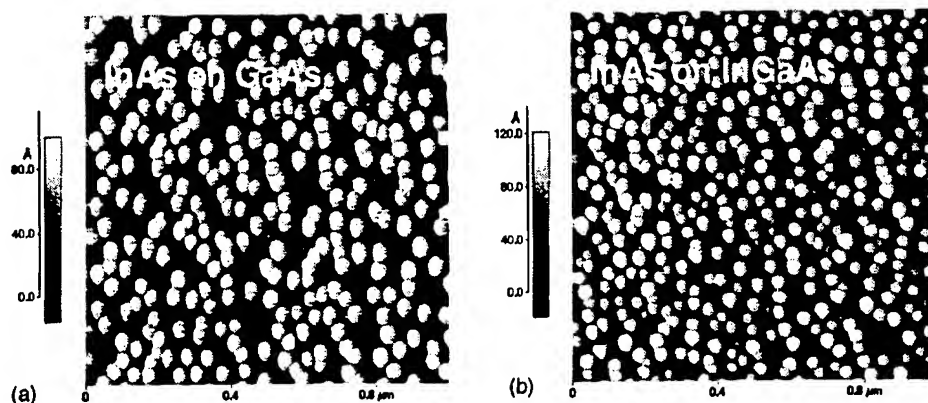


FIG. 2. AFM pictures of InAs dots on (a) GaAs, and (b) 10 Å strained $\text{In}_{0.15}\text{Ga}_{0.85}\text{As}$, grown under identical conditions. The dot densities are (a) $2.8 \times 10^{10} \text{ cm}^{-2}$ and (b) $4.2 \times 10^{10} \text{ cm}^{-2}$.

quantum wells are reported. The characterization will focus on crystal growth issues and comparison of photoluminescence (PL) results and atomic force microscopy (AFM). The usefulness of such a dots-in-a-well structure has been demonstrated by incorporation into a diode laser with the lowest threshold current density to date.²⁶

II. EXPERIMENT

The structures were grown by elemental source molecular beam epitaxy (MBE) in a VG Semicon V80H reactor on (100) oriented GaAs substrates. After growing a 2000 Å thick GaAs buffer at 610 °C, the substrate temperature was lowered during a 3 min growth interruption to grow a ~100 Å wide InGaAs well containing the quantum dots. Afterwards, during another 3 min growth interruption, the substrate temperature was raised back to 600–610 °C to grow a 1000 Å GaAs cap. The interfaces between the InGaAs quantum well and the surrounding GaAs matrix were made compositionally abrupt (unless noted otherwise) by predeposition of an InAs layer prior to opening Ga and In shutters simultaneously at the beginning of the well growth.²⁷ The thickness of this preadsorbed layer varied depending on the composition of the well and the well growth temperature.²⁷ At the end of the well growth, 3–17 monolayers of GaAs were deposited at the well growth temperature before raising the substrate temperature. When this GaAs layer is thin enough, the remaining InAs segregated to the growth surface is hereby evaporated.²⁸ This procedure also helps to narrow down the quantum dot vertical size distribution by eliminating very tall quantum dots that may not be completely covered.^{29,30} InAs quantum dots were grown after 0–30 Å of the strained well was completed. The equivalent InAs coverage was varied between 2.4 and 3.6 monolayers (which includes the segregated InAs layer of the strained InGaAs well). Then, after another 3 min growth interruption, the remaining strained quantum well was grown. Growth temperatures were measured with an optical pyrometer. The As_2/In beam equivalent pressure ratio was ~30, and the InAs growth rate was varied between 0.05 and 0.08 monolayers s^{-1} .

PL spectra were taken at room temperature with a 2.5 mW He–Ne laser, a grating spectrometer, and a cooled Ge detector with standard lock-in techniques. For AFM measurements, growth was stopped after formation of the quantum dots. AFM measurements were performed in air using the noncontact mode.

III. RESULTS AND DISCUSSION

To demonstrate the advantages of quantum dots in a strained well, Fig. 1 displays a PL comparison of quantum dots placed in bulk GaAs, in a 100 Å GaAs/ $\text{Al}_{0.2}\text{Ga}_{0.8}\text{As}$ quantum well, and in a 100 Å $\text{In}_{0.2}\text{Ga}_{0.8}\text{As}/\text{GaAs}$ quantum well. The intensity of the latter is over an order of magnitude larger, and the PL maximum is significantly redshifted. The redshift is likely due to a reduction in the In outdiffusion from the dots because of the InGaAs well, while the higher intensity may arise from a combination of better crystalline quality of the material surrounding the dots (high quality InGaAs can be grown around 500 °C, too low for high quality GaAs or AlGaAs) and the more effective carrier capture by the well. Another contributing factor is the increased dot density observed on strained InGaAs layers in comparison with GaAs, as shown in Fig. 2. The two samples were grown under identical conditions, except that the second sample has a 10 Å $\text{In}_{0.15}\text{Ga}_{0.85}\text{As}$ layer under the InAs quantum dots.

The PL emission varies with the position of the dots in the quantum well. Figure 3 represents photoluminescence data

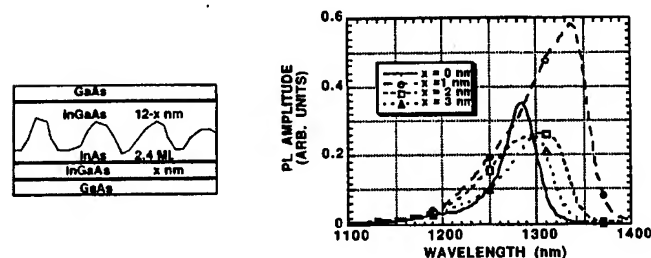


FIG. 3. Room temperature PL spectra of quantum dots placed at different positions inside a 130 Å wide $\text{In}_{0.15}\text{Ga}_{0.85}\text{As}$ quantum well. With increasing x , the FWHM are 16, 79, 92, and 59 nm.

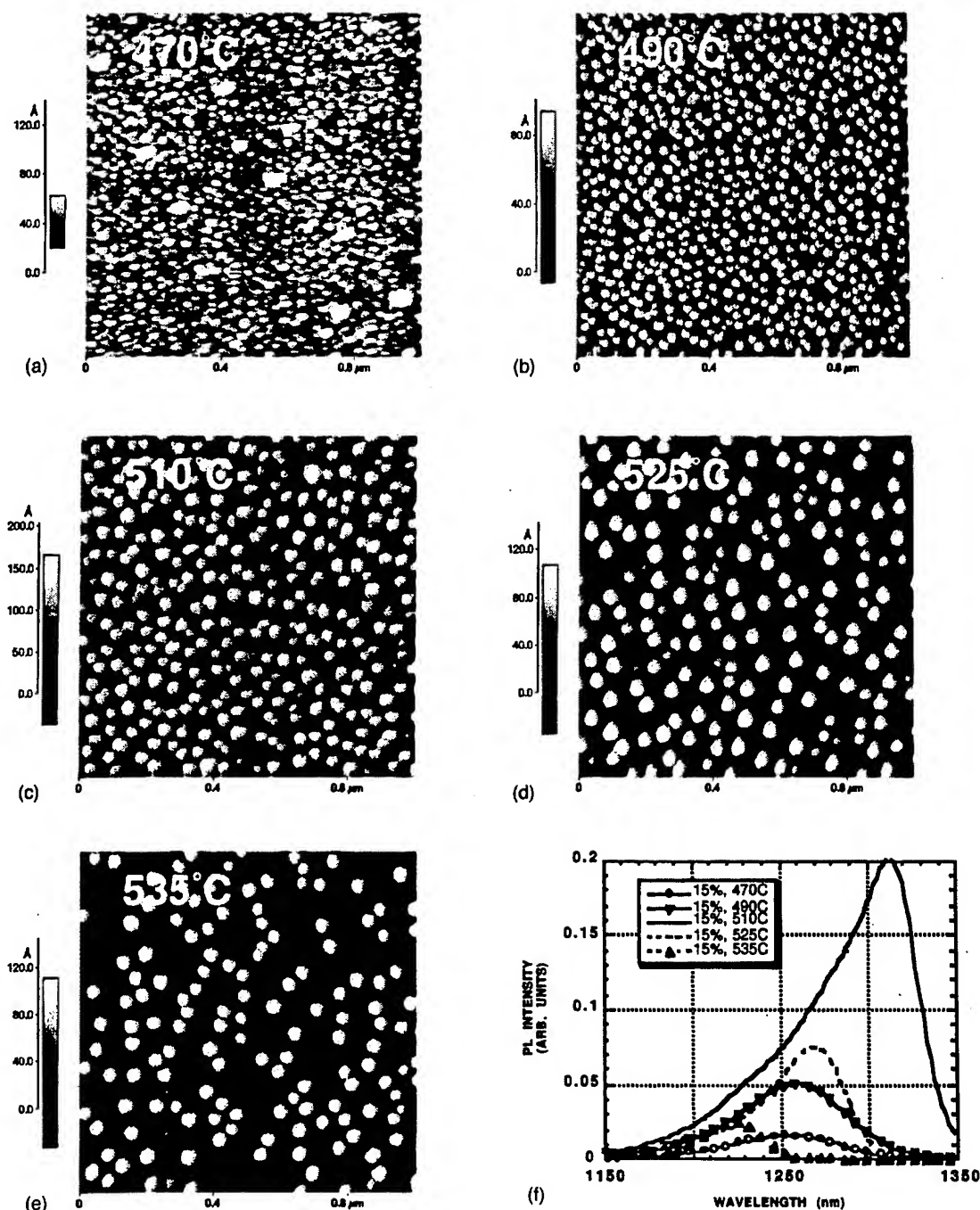


FIG. 4. Growth temperature dependence of 2.4 ML InAs on 20 Å $\text{In}_{0.15}\text{Ga}_{0.85}\text{As}$: AFM (a)–(e) and PL (f). Underlying InGaAs layer and dots were grown at the temperature indicated. Dot densities are (a) 1.1×10^{11} , (b) 7.0×10^{10} , (c) 3.3×10^{10} , (d) 1.8×10^{10} , and (e) $1.4 \times 10^{10} \text{ cm}^{-2}$. With increasing growth temperature, PL FWHM are 76, 72, 86, 52, and 39 nm.

of dots in a 130 Å wide well with the InAs dots grown in four different positions: directly on GaAs at the beginning of the well, and on 10, 20, and 30 Å $\text{In}_{0.15}\text{Ga}_{0.85}\text{As}$, respectively. A relatively narrow size distribution is inferred from the small full width at half maximum (FWHM) of the dots grown directly on GaAs; however, the integrated PL intensity improves upon growing the dots on a strained layer, owing to the higher dot density. In addition, the PL maximum shifts to a longer wavelength initially. An analysis of

the AFM scan in Fig. 2 reveals that the average height of the dots on a strained layer is greater (~ 100 vs 80 Å), which could explain that result. The reduction in wavelength and intensity with placing the dots closer to the top of the well could be due to the dots not being completely covered by the upper part of the well.

Figures 4 and 5 show the growth temperature dependence of dot density and size for 2.4 ML InAs on 20 Å $\text{In}_x\text{Ga}_{1-x}\text{As}$, where $x=0.15$ in Fig. 4, and $x=0.2$ in Fig. 5.

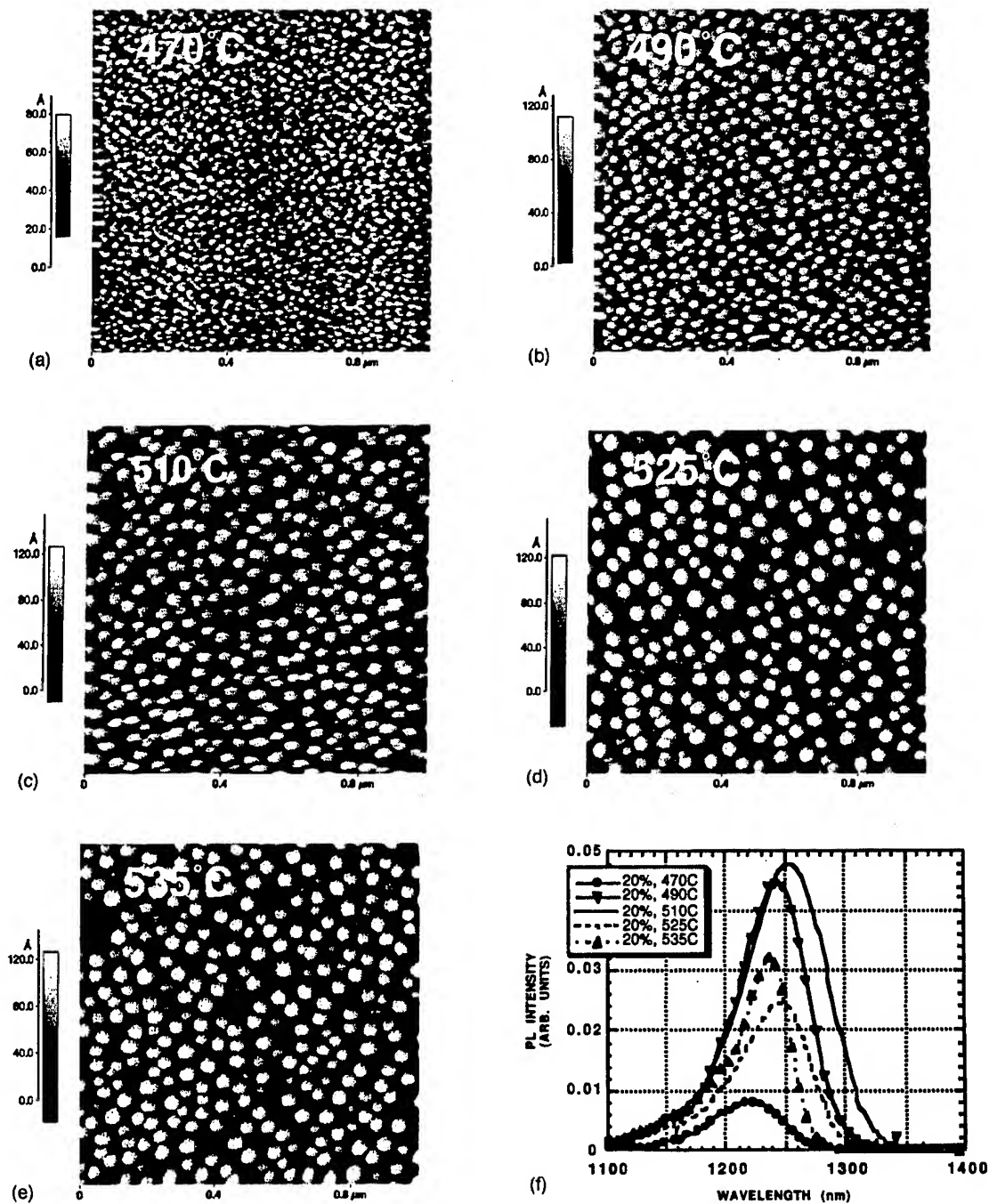


FIG. 5. Growth temperature dependence of 2.4 ML InAs on 20 Å $\text{In}_{0.2}\text{Ga}_{0.8}\text{As}$: AFM (a)–(e) and PL (f). Underlying InGaAs layer and dots were grown at the temperature indicated. Dot densities are (a) 1.5×10^{11} , (b) 6.8×10^{10} , (c) 3.7×10^{10} , (d) 2.8×10^{10} , and (e) $2.9 \times 10^{10} \text{ cm}^{-2}$. With increasing growth temperature, PL FWHM are 70, 70, 82, 70, and 51 nm.

For the PL studies in Figs. 4(f) and 5(f), the dots were capped with 100 Å $\text{In}_{0.15}\text{Ga}_{0.85}\text{As}$ at 470 °C before growing 50 Å of GaAs at 525 °C and 1000 Å of GaAs at 600 °C. It is obvious that the dot size increases and the dot density decreases with increased growth temperature. When the growth temperature is low [Fig. 4(a)], some large clusters can be observed. The clusters are absent in Fig. 5(a), where there is more strain in the underlying InGaAs layer, suggesting that compressive strain may inhibit dot coalescence under certain

conditions. Closer examination reveals the dots in Fig. 4(e), and to some extent Fig. 5(e), have a lower surface in their immediate vicinity as compared to the rest of the flat surface. Since these were grown at the highest temperature investigated, the surface mobility during dot formation was high, and the dots may have consumed part of the surrounding wetting layer.

The photoluminescence data in Figs. 4(f) and 5(f) show an interesting trend. While integrated intensity and wave-

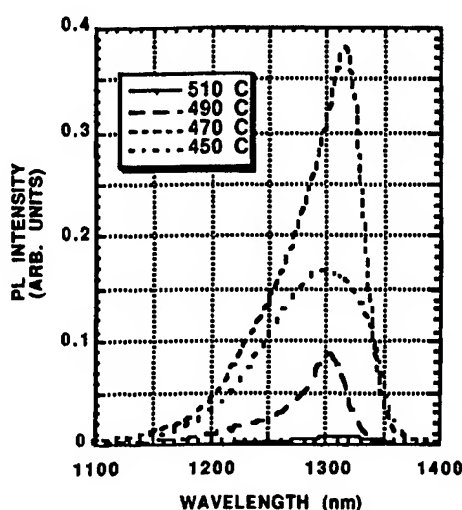


FIG. 6. PL spectra as a function of the growth temperature of the upper part of the quantum well covering the dots. All other growth parameters are identical. With increasing temperature, the corresponding FWHM are 48, 66, 65, and 108 nm.

length both increase with temperature up to 510 °C, the trend reverses above 510 °C. From AFM it is clear that the dot size increases up to 525 °C, and dot density decreases. So the intensity behavior up to 510 °C must be due to changes in optical quality of the dots. The wavelength decrease above 510 °C could be caused by Ga diffusion into the dots.

An important change in the PL properties of the quantum dots is also caused by varying the growth temperature of the InGaAs layer capping the dots, i.e., the upper part of the well. Figure 6 demonstrates this behavior. In a range of growth temperatures from 450 to 510 °C, the intensity peaks at 470 °C. It is important to note that all other growth conditions were kept fixed, in particular the growth temperature of the quantum dots. No obvious trend is established with respect to the changing wavelength maximum. Apparently, the capping process of the (at this point) partially relaxed dots with a ternary strained alloy is a nontrivial process. At higher temperatures, lattice mismatch driven partial decomposition of the cap layer is feasible,²⁵ while at lower temperatures a more uniform alloy distribution occurs, but perhaps at the expense of good crystalline quality.

It is also observed that annealing time strongly influences the PL peak position and amplitude (Fig. 7). A 2.5 h anneal at 600 °C (a typical time and temperature to grow a cladding layer of a laser) can introduce a blueshift of the quantum dot PL by up to 100 nm. An additional 2 h anneal at 640 °C (at temperature where Ga desorption starts to become significant in MBE) shortens the wavelength maximum by another 80 nm. An anneal at 710 °C, a temperature where clad layers of high-quality quantum well lasers are frequently grown, introduces a further significant blueshift. During the entire process of annealing, the PL intensity becomes weaker by up to three orders of magnitude. One reason for the observed behavior may be that the zero-dimensional character of the quantum dots is lost in the process due to bulk diffusion. It is also possible that dislocations are created (whose formation

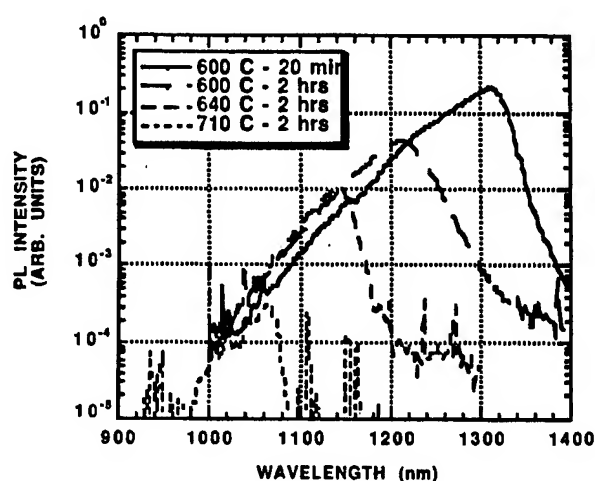


FIG. 7. PL spectra of the same sample annealed for different times and temperatures. With increasing time/temperature, the corresponding FWHM are 64, 66, 44, and 29 nm.

was suppressed during growth at low temperature) that act as nonradiative recombination centers.

IV. CONCLUSION

It has been shown that high quality, three-dimensionally confined InAs structures can be grown in pseudomorphically strained InGaAs quantum wells on GaAs substrates. By changing the growth conditions, shape, size, and density of the InAs dots can be controlled, as well as their carrier capture and light emitting properties. Emission wavelengths at 1.3 μm can be obtained without sacrificing the dot density. Because the InGaAs surrounding the InAs quantum dots is grown near the optimum growth conditions, an increased photonic yield is observed compared to quantum dots not grown in a strained well.

ACKNOWLEDGMENT

This work was supported by AFOSR Grant No. F49620-C-1-0530.

¹I. N. Stranski and L. von Krastanov, *Akad. Wiss. Lit. Mainz Abh. Math. Naturwiss. Kl.* **146**, 797 (1939).

²S. Guha, A. Madukar, and K. C. Rajkumar, *Appl. Phys. Lett.* **57**, 2110 (1990).

³C. W. Snyder, B. G. Orr, D. Kessler, and L. M. Sander, *Phys. Rev. Lett.* **66**, 3032 (1991).

⁴H. Sakaki, *Surf. Sci.* **267**, 623 (1992).

⁵N. Kirstaedter et al., *Electron. Lett.* **30**, 1416 (1994).

⁶R. Mirin, A. Gossard, and J. Bowers, *Electron. Lett.* **32**, 1732 (1996).

⁷K. Hinzer, S. Fafard, A. J. SpringThorpe, J. Arlett, E. M. Griswold, Y. Feng, and S. Charbonneau, *Physica E (Amsterdam)* **2**, 729 (1998).

⁸K. Mukai, Y. Nakata, H. Shoji, M. Sugawara, K. Ohtsubo, N. Yokoyama, and H. Ishikawa, *Electron. Lett.* **34**, 1588 (1998).

⁹H. Saito, K. Nishi, I. Ogura, S. Sugou, and Y. Sugimoto, *Appl. Phys. Lett.* **69**, 3140 (1996).

¹⁰D. L. Huffaker, H. Deng, and D. G. Deppe, *IEEE Photonics Technol. Lett.* **10**, 185 (1998).

¹¹S. J. Xu et al., *Appl. Phys. Lett.* **73**, 3153 (1998).

¹²G. Yusa and H. Sakaki, *J. Cryst. Growth* **175/176**, 730 (1997).

¹³J. Phillips, K. Kamath, T. Brock, and P. Bhattacharya, *Appl. Phys. Lett.* **72**, 3509 (1998).

- ¹⁴J. J. Finley, M. Skaltz, M. Arzberger, A. Zrenner, G. Böhm, and G. Abstreiter, *Appl. Phys. Lett.* **73**, 2618 (1998).
- ¹⁵J. L. Jimenez, L. R. C. Fonseca, D. J. Brady, J. P. Leburton, D. E. Wohlert, and K. Y. Cheng, *Appl. Phys. Lett.* **71**, 3558 (1997).
- ¹⁶D. Bimberg, N. Kirstaedter, N. N. Ledentsov, Zh. I. Alferov, P. S. Kop'ev, and V. M. Ustinov, *IEEE J. Sel. Top. Quantum Electron.* **3**, 196 (1997).
- ¹⁷M. V. Maximov *et al.*, *Jpn. J. Appl. Phys., Part 1* **36**, 4221 (1997).
- ¹⁸M. Sugawara, K. Mukai, and Y. Nakata, *Appl. Phys. Lett.* **74**, 1561 (1999).
- ¹⁹T. R. Ramachandran, A. Madhukar, I. Mukhametzhanov, R. Heitz, A. Kalburge, Q. Xie, and P. Chen, *J. Vac. Sci. Technol. B* **16**, 1330 (1998).
- ²⁰F. Heinrichsdorff, M.-H. Mao, N. Kirstaedter, A. Krost, and D. Bimberg, *Appl. Phys. Lett.* **71**, 22 (1997).
- ²¹J.-I. Chyi, T.-E. Nee, C.-T. Lee, J.-L. Shieh, and J.-W. Pan, *J. Cryst. Growth* **175/176**, 777 (1997).
- ²²K. Mukai, N. Ohtsuka, M. Sugawara, and S. Yamazaki, *Jpn. J. Appl. Phys., Part 2* **33**, L1710 (1994).
- ²³H. Shoji, K. Mukai, N. Ohtsuka, M. Sugawara, T. Uchida, and H. Ishikawa, *IEEE Photonics Technol. Lett.* **7**, 1385 (1995).
- ²⁴K. Mukai, N. Ohtsuka, H. Shoji, and M. Sugawara, *Appl. Surf. Sci.* **112**, 102 (1997).
- ²⁵V. M. Ustinov *et al.*, *Appl. Phys. Lett.* **74**, 2815 (1999).
- ²⁶G. T. Liu, A. Stintz, H. Li, K. J. Malloy, and L. F. Lester, *Electron. Lett.* **35**, 1163 (1999).
- ²⁷R. Kaspi and K. R. Evans, *Appl. Phys. Lett.* **67**, 819 (1995).
- ²⁸O. Brandt, K. Ploog, L. Tapfer, M. Hohenstein, R. Bierwolf, and F. Philipp, *Phys. Rev. B* **45**, 8443 (1992).
- ²⁹Z. R. Wasilewski, S. Fafard, and J. P. McCaffrey, *J. Cryst. Growth* **201/202**, 1131 (1999).
- ³⁰G. D. Lian, J. Yuan, L. M. Brown, G. H. Kim, and D. A. Ritchie, *Appl. Phys. Lett.* **73**, 49 (1998).

Gain and Linewidth Enhancement Factor in InAs Quantum-Dot Laser Diodes

T. C. Newell, *Member, IEEE*, D. J. Bossert, *Member, IEEE*, A. Stintz, B. Fuchs, *Member, IEEE*, K. J. Malloy, *Member, IEEE*, and L. F. Lester, *Member, IEEE*

Abstract—Amplified spontaneous emission measurements are investigated below threshold in InAs quantum-dot lasers emitting at 1.22 μm . The dot layer of the laser was grown in a strained quantum well (QW) on a GaAs substrate. Ground state gain is determined from cavity mode Fabry–Perot modulation. As the injection current increases, the gain rises super-linearly while changes in the index of refraction decrease. Below the onset of gain saturation, the linewidth enhancement factor is as small as 0.1, which is significantly lower than that reported for QW lasers.

Index Terms—Linewidth enhancement factor, quantum dots, semiconductor laser.

A N IMPORTANT, but often undesirable, property of semiconductor lasers is the degree to which variations in the carrier density N alter the index of refraction n of the active layer. This phenomena is often characterized by the linewidth enhancement parameter, $\alpha = -4\pi/\lambda(dn/dN)(dg/dN)^{-1}$ where g is the optical gain. Large values of α can result in antiguiding in narrow stripe lasers, self-focusing and filamentation in broad-area emitters, and chirp under modulation. For strained InGaAs single-quantum-well (QW) lasers operating near 980 nm, the value of α is typically 2 or higher at carrier densities corresponding to threshold [1], although 0.5, a record low, has been measured [2]. At the communications wavelengths of 1.3 and 1.55 μm , α is usually much higher unless modulation doping [3] or a large number of QW's are employed [4]. From the Kramers–Kronig relation, a symmetric gain spectrum will yield an α of zero at the peak gain because here the index of refraction will not change with carrier density. Since the density of states of a quantum dot (QD) is theoretically a series of delta-function spikes at the quantized energy levels, its gain spectrum ideally satisfies this criteria. Thus a substantial reduction in α should be realized by using QD lasers [5], [6].

In this letter, spectral and gain measurements are investigated using QD lasers that emit at 1.22 μm . Amplified spontaneous emission (ASE) profiles portray the physics of a structure with characteristics distinct from those of QW lasers. As a function of wavelength, the gain is relatively flat over a

3-nm range centered on the lasing line. The differential gain with respect to current, $\Delta g/\Delta I$, is initially small, but increases with current. Near threshold, however, the gain saturates and correspondingly, $\Delta g/\Delta I$ decreases. We find that before gain saturation begins to occur, α is 0.1. To our knowledge, this is the lowest α value experimentally measured to date.

The QD lasers feature a single layer of InAs QD's centered in a 100-Å $\text{In}_{0.2}\text{Ga}_{0.8}\text{As}$ QW structure and have been described elsewhere [7], [8]. The "dots-in-well" (DWELL) design is analogous to the common separate confinement heterostructure of typical QW lasers but on a smaller scale. Material was processed into 30- μm ridge waveguide lasers, which is in an intermediate width between narrow stripe devices and broad area lasers. These devices are predominantly single lateral mode while simultaneously being wide enough for a large signal and reasonably uniform current injection, which improves the accuracy in determining α [1].

1.5-mm cavity length lasers are biased in pulsed mode (0.3- μs pulse and 1.5% duty cycle) with a Hewlett-Packard 8114A pulse generator. The lasers did not show any detectable evidence of wavelength shifts due to heating under these conditions. The collimated light is modulated with a Stanford Research Systems SR540 optical chopper, then focussed onto the entrance slit of a 1.3-m Acton Research Corp. monochromator. The entrance and exit slits are set at 40 μm and a 1200 lines/mm grating is used. The effective resolution is approximately 0.1 Å. Exiting light is collected with a cooled InGaAs photodetector, and a Stanford Research Systems SRS830 lock-in amplifier measures the generated photocurrent.

Gain and refractive index were determined from below-threshold ASE spectra [9], [10]. The net modal gain, g , is extracted from the peak to valley ratio of subthreshold Fabry–Perot oscillations using $g = (1/L) \ln[r^{-1}(\sqrt{x}-1)(\sqrt{x}+1)^{-1}]$ where L is the cavity length, x is the ratio of peak to valley heights, and r is the facet reflectivity. Using $\Delta g/\Delta I$ for the differential gain and $\Delta n/\Delta I = -(n/\lambda)\Delta\lambda/\Delta I$ for differential index, where ΔI is the current increment, the experimental value for α is $-(4\pi n/\lambda^2)\Delta\lambda/\Delta g$.

In order to reduce the error in measuring wavelength shifts, the current was stepped incrementally at each wavelength before scanning the monochromator to its subsequent position. By proceeding in this manner, as opposed to sweeping the monochromator for each current bias, no drift can be attributed to the monochromator, and the observed wavelength shifts with respect to current $\Delta\lambda/\Delta I$, are revealed more accurately.

Manuscript received August 13, 1999; revised September 10, 1999. This work was supported by the Defense Advanced Research Projects Agency under Grant MDA972-98-1-0002 and by the Air Force Office of Scientific Research under Grant F49620-96-1-0077.

T. C. Newell, A. Stintz, B. Fuchs, K. J. Malloy, and L. F. Lester are with the Center for High Technology Materials University of New Mexico, Albuquerque, NM 87106 USA.

D. J. Bossert is with the Air Force Research Laboratory, Kirtland AFB, NM 87117 USA.

Publisher Item Identifier S 1041-1135(99)09533-6.

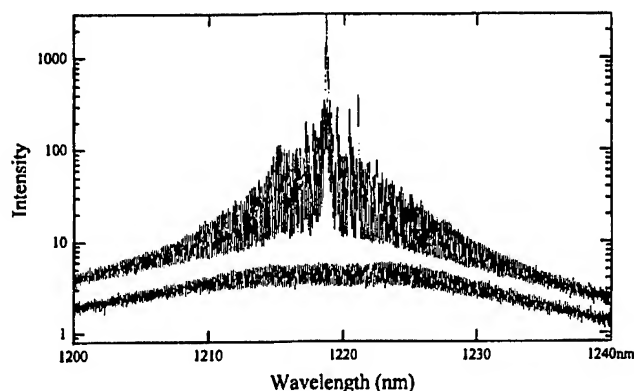


Fig. 1. QD amplified spontaneous emission spectra at 45 and 50 mA (just below threshold) of a 1.5-mm cavity length laser show a nearly symmetric shape in the depth of the Fabry-Perot fringes. The average intensity at shorter wavelengths increases more than longer ones due to the influence of excited states.

Due to the relatively long length of the QD lasers, accuracy in determining wavelength shifts and peaks/valleys in the ASE spectrum was limited largely by the resolving power of the monochromator.

Fig. 1 shows a typical spontaneous emission (SE) profile from 1.2 to 1.24 μm for currents below and near lasing threshold. The spectrum is centered on ground state transitions. Excited state energy levels correspond to 1.05- μm transitions, as observed from short cavity ($L < 1$ mm) lasers. 1.4-Å Fabry-Perot fringes are clearly revealed in the figure. Overall the profiles possess a strikingly symmetric aspect with respect to the 1218.6-nm central line (The same symmetry exists when plotted as a function of energy.). A determination of the net modal gain from this data, not shown, also shows a high degree of near-Gaussian symmetry. The profile is a legacy of the random size distribution of the QD's. On closer observation, with respect to the central peak, the average intensity is greater at shorter wavelengths than at longer ones. Initially, carriers are more likely to fill the ground state energy levels of all dots and in particular that of the larger dots (corresponding to the lowest energy states available). Subsequent carrier distribution results in population of the smaller dots and excited energy states. In addition, we have observed evidence of homogenous broadening in efficiency measurements of QD lasers subjected to external feedback from a grating. These results will be presented elsewhere. The combination results in a blue shifting of the spectral center and the greater intensity levels at shorter wavelengths. This also breaks the symmetry of the overall gain profile and prevents the α -parameter from being identically zero.

A plot of the measured gain versus wavelength is shown in Fig. 2 for currents of 52 to 64 mA with 2-mA steps between data sets ($I_{th} = 73$ mA). This laser is different from the one used to produce the spectrum in Fig. 1, and the sweep is centered on this particular laser's center line. The dot markers in Fig. 2 are placed to indicate the location of the Fabry-Perot peaks. From 1221.0 to 1224.2 nm, the gain is relatively flat for each current set. This result is again due to the size distribution of the QD's. This is quite different from QW lasers, which would show a definite gain rolloff across this range. The peak gain at 88% threshold is 6 cm^{-1} . A net gain of 7 cm^{-1} was

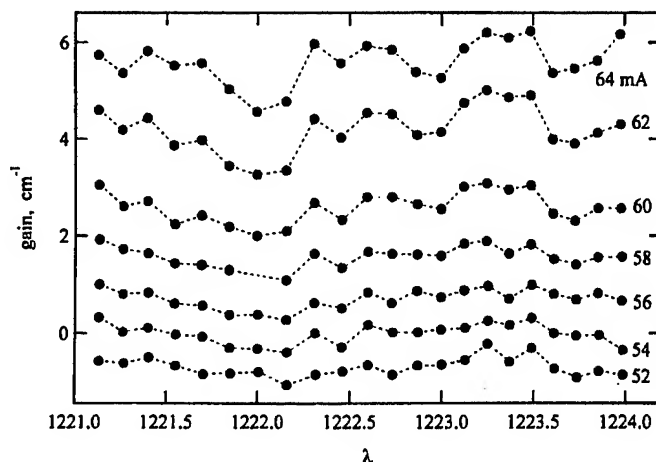


Fig. 2. Gain versus λ derived from the ratio of peak to valley heights for 52 to 64 mA currents. This particular 1.5 mm laser has $I_{th} = 73$ mA. The graph markers denote the position of the fringe peaks. In contrast to QW lasers, the gain across this 3-nm sweep is nearly constant.

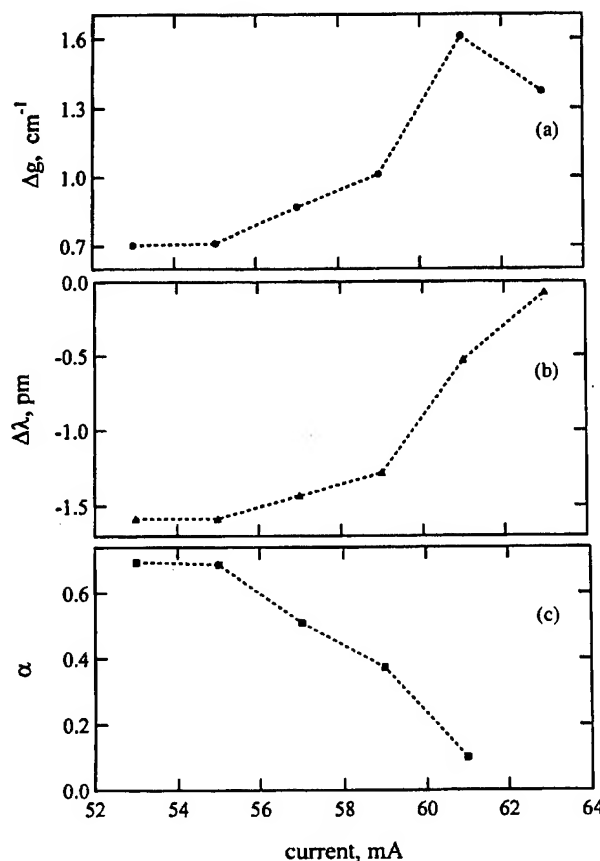


Fig. 3. (a) Average Δg as a function of current. The differential gain begins to rise rapidly at $\sim 79\%$ I_{th} and gain saturation begins to occur above 64 mA. (b) $\Delta \lambda$ is relatively large for low bias, but approaches zero at larger currents. (c) α , as a result, becomes 0.1 at 61 mA.

measured at the lasing threshold. Considering the experimental error noted above, this value is consistent with our maximum modal gain estimate of $7.5\text{--}8.5\text{ cm}^{-1}$ (taking into account the internal loss) determined in [7].

Fig. 3(a) shows the evolution of the differential gain, $\Delta g/\Delta I$, Fig. 3(b) shows the wavelength shift, $\Delta \lambda/\Delta I$, and

Fig. 3(c) the resulting α parameter for the same laser as in Fig. 2. $\Delta g/\Delta I$ is obtained by averaging the gain over the 3-nm wavelength range shown in Fig. 2. A curve fit to the correlation function determined $\Delta\lambda/\Delta I$ between successive data sets. In these plots, the abscissa of the graph markers are placed at the average of the two current levels used. Due to the low threshold current density of the QD laser, useful data can only be taken over a relatively small range of current levels. Antireflection coatings could be applied to increase the threshold current density, although in the QD laser this would be of limited benefit since excited state levels become populated at higher current densities, altering the entire spectrum.

At the lowest current densities measured not only is the gain low, but the differential gain is low as well. At a current of roughly $0.79I_{th}$, however, the differential gain increases dramatically as seen in Fig. 3(a). This is followed by gain saturation and the corresponding decrease in differential gain as the current nears threshold as seen by the last point in Fig. 3(a). Thus, with respect to current density, the gain shows an inflexion point. These QD trends are in contrast to that of QW structures. In the latter case, the differential gain is highest at low current density, gradually decreasing with increasing density as states associated with the $n = 1$ transition fill.

A qualitative model can be used to explain the trends in the gain and differential gain and underscore the difference between QD and QW active regions [11], [12]. Assuming that electrons and holes populate only the ground state of the dots, that the filling is random, and that charge neutrality in the dot is not required, the probability of dot occupation by either an electron or hole is n_c/n_t , where n_c is the 2-D density of electrons or holes, and n_t is the dot density. Since dot filling is biased toward the larger dots, the assumptions are not strictly accurate. However, this will not affect the general result. Here the gain is a function of the ground state occupation probability. Since electrons and holes do not necessarily fill the dots in pairs, the gain is small until a significant number of dots are filled, at which point it increases super-linearly as shown in Figs. 2 and 3(a). In this scenario, our results are consistent with electroluminescence efficiency measurements described by Huffaker in [13]. In contrast, QW laser theory, using quasi-Fermi levels and a staircase-like density of states function, yields a sublinear increase in gain with current.

In Fig. 3(b), $\Delta\lambda$ slowly decreases in magnitude up to the point where a large increase in the gain occurs. It then rapidly approaches zero as the current is incremented. We have also observed that for wavelengths both longer and shorter than the central region, $\Delta\lambda$ was always negative for currents below threshold. Wavelength shifts in QW structures are generally much larger in magnitude and reduce with increasing current in a much more gradual fashion.

The linewidth enhancement factor decreases to 0.1 at a current near 61 mA, as seen in Fig. 3(c). This value is obtained at a point sufficiently below threshold so that the gain is not saturating and, correspondingly, $\Delta\lambda$ is not negligible. To our knowledge, this is the lowest measured α value experimentally measured to date. Other QD lasers from the same wafer exhibit

similar characteristics as the one shown in Figs. 2 and 3 and yield similar though slightly larger values for α across this current range.

In conclusion, edge-emitted amplified spontaneous emission from QD lasers whose dot layer is grown in a strained QW has been studied spectrally. Gain, differential gain, and wavelength shifts were measured for subthreshold current levels. In contrast to QW lasers whose differential gain decreases on increase of carrier density, QD devices show an increase in differential gain up to the point of gain saturation. This unique characteristic can be explained by considering that the dots are filled randomly. As a result, a linewidth enhancement factor of 0.1 has been observed in a 1.5-mm laser with a 30- μm stripe width. This feature is a benefit of the nearly symmetric gain spectrum created by the combination of the delta function density of states and the random size distribution of the dots. Theoretical investigations of filamentation in broad area semiconductor lasers predict that the α values measured in this study will not provoke filamentation regardless of the pumping level [14]. Thus QD lasers are promising devices for high power semiconductor lasers and amplifiers.

REFERENCES

- [1] D. J. Bossert and D. Gallant, "Gain, refractive index, and α -parameter in InGaAs-GaAs SQW broad-area lasers," *IEEE Photon. Technol. Lett.*, vol. 8, pp. 322-324, 1996.
- [2] N. K. Dutta, W. S. Hobson, D. Vakhshoori, H. Han, P. N. Freeman, J. F. Dejong, and J. Lopata, "Strain compensated InGaAs-GaAsP-InGaP laser," *IEEE Photon. Technol. Lett.*, vol. 8, pp. 852-854, 1996.
- [3] P. A. Morton, D. A. Ackerman, G. E. Shtengel, R. F. Kazarinov, M. S. Hybertsen, T. Tanbunek, R. A. Logan, and A. M. Sergent, "Gain characteristics of 1.55- μm high-speed multiple-quantum-well lasers," *IEEE Photon. Technol. Lett.*, vol. 7, pp. 833-835, 1995.
- [4] H. R. Choo, B. H. O. C. D. Park, H. M. Kim, J. S. Kim, D. K. Oh, H. M. Kim, and K. E. Pyun, "Improvement of linewidth enhancement factor in 1.55- μm multiple-quantum-well laser-diodes," *IEEE Photon. Technol. Lett.*, vol. 10, pp. 645-647, 1998.
- [5] M. Willatzen, T. Tanaka, Y. Arakawa, and J. Singh, "Polarization dependence of optoelectronic properties in quantum dots and quantum wires: Consequences of valence-band mixing," *IEEE J. Quantum Electron.*, vol. 30, pp. 640-653, 1994.
- [6] D. Bimberg, N. Kirstaedter, N. N. Ledentsov, Zh. I. Alferov, P. S. Kop'ev, and V. M. Ustinov, "InGaAs-GaAs quantum-dot lasers," *IEEE J. Select. Topics Quantum Electron.*, vol. 3, pp. 196-205, 1997.
- [7] L. F. Lester, A. Stintz, H. Li, T. C. Newell, E. A. Pease, B. A. Fuchs, and K. J. Malloy, "Optical characteristics of 1.24-mm InAs quantum-dot laser diodes," *IEEE Photon. Technol. Lett.*, vol. 11, pp. 931-933, 1999.
- [8] G. T. Liu, A. Stintz, H. Li, K. J. Malloy, and L. F. Lester, "Extremely low room-temperature threshold current density diode lasers using InAs dots in $\text{In}_{0.15}\text{Ga}_{0.85}\text{As}$ quantum well," *Electron. Lett.*, vol. 35, pp. 1163-1165, 1999.
- [9] B. W. Hakki and T. L. Paoli, "Gain spectra in GaAs double-heterostructure injection lasers," *J. Appl. Phys.*, vol. 46, pp. 1299-1306, 1975.
- [10] D. J. Bossert and D. Gallant, "Improved method for gain/index measurements of semiconductor-lasers," *Electron. Lett.*, vol. 32, pp. 338-339, 1996.
- [11] M. Grundmann and D. Bimberg, "Theory of random population for quantum dots," *Phys. Rev. B*, vol. 55, pp. 9740-9745, 1997.
- [12] L. V. Asryan and R. A. Suris, "Charge neutrality violation in quantum-dot lasers," *IEEE J. Select. Topics Quantum Electron.*, vol. 3, pp. 148-157, 1997.
- [13] D. L. Huffaker and D. G. Deppe, "Electroluminescence efficiency of 1.3 μm wavelength InGaAs/GaAs quantum dots," *Appl. Phys. Lett.*, vol. 73, pp. 520-522, 1998.
- [14] J. R. Marcianite and G. P. Agrawal, "Spatio-temporal characteristics of filamentation in broad-area semiconductor lasers," *IEEE J. Quantum Electron.*, vol. 33, pp. 1174-1179, 1997.

The lowest room-temperature threshold current density, 26A/cm², of any semiconductor diode lasers is reported for a quantum dot device with a single InAs dot layer contained within a strained In_{0.15}Ga_{0.85}As quantum well. The lasers are epitaxially grown on a GaAs substrate, and the emission wavelength is 1.25µm.

Introduction: It has been predicted that the threshold current density of quantum dot lasers should be lower than that of quantum well lasers due to the reduction of density of states [1]. In particular, efforts have been made in the past few years to reduce the threshold current density of quantum dot lasers on GaAs substrates [2, 3]. A recently developed approach is to put the InAs dots in a strained In_{0.2}Ga_{0.8}As quantum well [3, 4]. This 'dot in a well' (DWELL) design not only improves carrier capture by the dots, but also increases the density of quantum dots (to 7×10^{10} cm⁻²) over growth on GaAs directly. Consequently, lasing from a single layer of dots is possible at reasonable cavity lengths. While competition with radiative quantum well transitions was suggested as a concern [5], quantum well transitions were not observed in previous work [3] or in this study. In this Letter, we present further improvements that have been made by putting a single layer of InAs quantum dots into a strained In_{0.15}Ga_{0.85}As quantum well. An extremely low threshold current density of 26A cm⁻² has been achieved for a 7.8mm cavity length, cleaved facet laser. Other operating characteristics of these DWELL lasers are described.

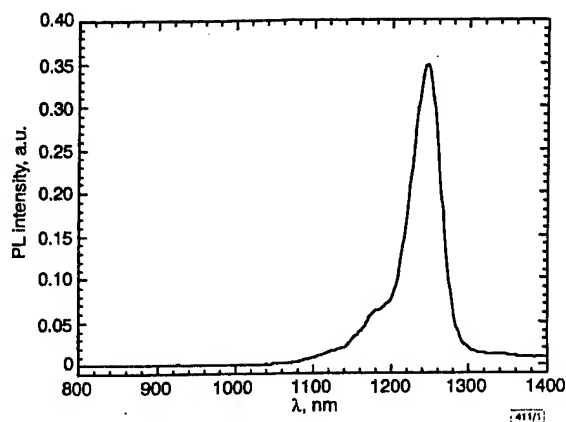


Fig. 1 Photoluminescence spectrum of laser wafer
No emission from quantum well is observed; FWHM is 37meV

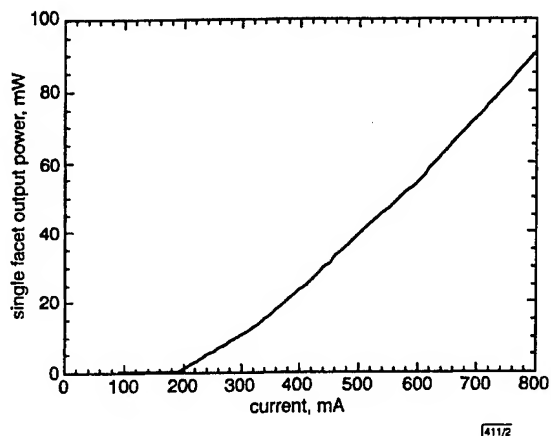


Fig. 2 Single facet output L-I curve of 7.8mm cavity length laser
Threshold current density is 26A/cm²; external efficiency is 31%

GaAs waveguide surrounding the laser active region, a 2µm *p*-type (10^{17} cm⁻³) upper cladding layer, and a *p*⁺-doped (3×10^{19} cm⁻³) 60nm thick GaAs cap. This cavity was a low-loss design following [6]. In the centre of the waveguide, an equivalent coverage of 2.4 monolayers of InAs results in quantum dots grown approximately in the middle of the 100Å In_{0.15}Ga_{0.85}As quantum well. The quantum dots and quantum well were grown at 510°C, and all other layers were grown at 610°C, as measured by an optical pyrometer.

Room temperature photoluminescence (PL) results are shown in Fig. 1. The PL linewidth is 37meV and has been reduced compared with that in [3]. No emission from the quantum well is observed, providing clear proof of minimal competition from quantum well radiative transitions. This implies that the relaxation time from the quantum well to the quantum dots is much faster than the spontaneous lifetime of the quantum well.

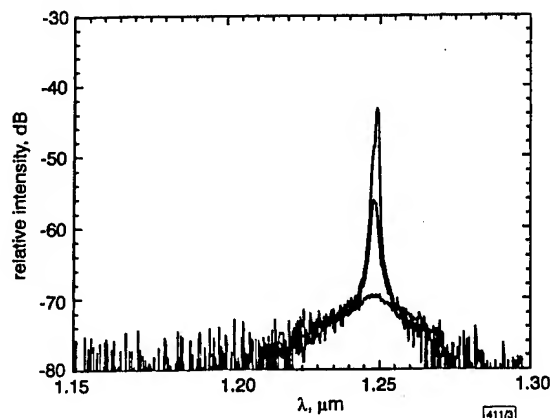


Fig. 3 Lasing spectrum at 0.90I_{th} (180mA), 0.95I_{th} (190mA), and I_{th} (200mA)

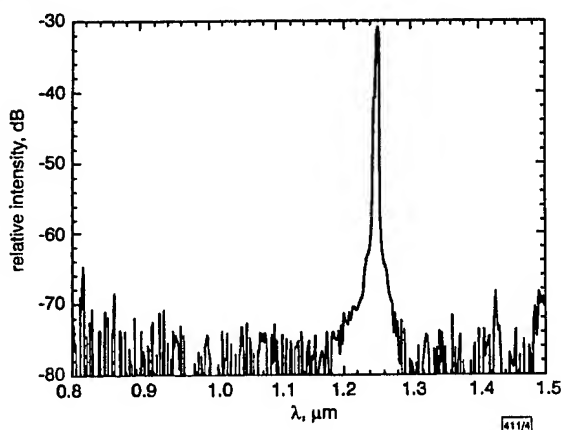


Fig. 4 Lasing spectrum at five times threshold current density
No emission from well is observed

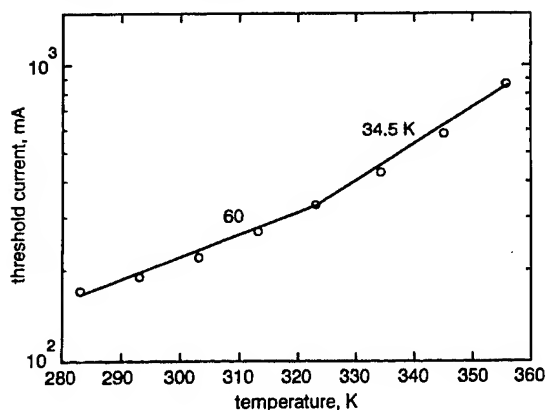


Fig. 5 Threshold current against temperature for 7.8mm cavity length device

Device structures and growth: The laser structure was grown by solid-source molecular beam epitaxy (MBE) on a (100) *n*⁺-GaAs substrate. The laser structure was the same as reported in [3] except that

laser bars. All devices were tested with the *n*-side down on a thermoelectric cooler using pulsed excitation. The pulsewidth was 300ns with a duty cycle of 0.5%. The temperature of the thermoelectric cooler was set to be 20°C. The single facet output *L-I* curve from a typical bar is shown in Fig. 2. The lasing threshold current is 200mA, which corresponds to a threshold current density of 26 A cm⁻². The external quantum efficiency is 31%. The lowest previously reported threshold current densities for quantum wells lasers were ~50 A cm⁻² [7, 8]. The near-threshold lasing spectra at three different injection current levels, 0.90 I_{th} (180mA), 0.95 I_{th} (190mA) and I_{th} (200mA) were measured by an optical spectrum analyser (OSA) and are shown in Fig. 3. The lasing wavelength is 1.25µm. Clear spectral narrowing can be observed at 0.95 I_{th} (190mA). A much broader spectrum was also taken at five times the threshold current and is shown in Fig. 4. No emission from the quantum well layer is observed, again suggesting the lack of radiative competition from the quantum well and the rapid capture of carriers by the dots from the well. The dependence of the threshold current on temperature was also measured and is shown in Fig. 5. The characteristic temperature T_0 is 60K between 10 and 50°C, and decreases significantly to 34.5K between 50 and 80°C. Carrier heating out of the quantum well may be one reason why the T_0 value of this laser is smaller than predicted T_0 values for quantum dot lasers [1].

Conclusion: We have demonstrated an extremely low threshold current density DWELL laser with a single layer of InAs quantum dots in an In_{0.15}Ga_{0.85}As quantum well. This is the first time that the threshold current density performance of quantum dot lasers has surpassed that of quantum well lasers. Experimental evidence suggests that the relaxation time from the quantum well to the quantum dots is much shorter than the spontaneous lifetime of the quantum well. The T_0 value for these DWELL lasers is 60K between 10 and 50°C.

© IEE 1999

Electronics Letters Online No: 19990811
DOI: 10.1049/el:19990811

1 June 1999

G.T. Liu, A. Stintz, H. Li, K.J. Malloy and L.F. Lester (University of New Mexico, Center for High Technology Materials, 1313 Goddard SE, Albuquerque, NM 87106, USA)

References

- 1 ARAKAWA, Y., and SAKAI, H.: 'Multidimensional quantum well laser and temperature dependence of its threshold current', *Appl. Phys. Lett.*, 1982, **40**, (11), pp. 939-941
- 2 SCHÄFER, F., REITHMAIER, J.P., and FORCHEL, A.: 'High-performance GaInAs/GaAs quantum-dot lasers based on a single active layer', *Appl. Phys. Lett.*, 1999, **74**, (20), pp. 2915-2917
- 3 LESTER, L.F., STINTZ, A., LI, H., NEWELL, T.C., PEASE, E.A., FUCHS, B.A., and MALLOY, K.J.: 'Optical characteristics of 1.24µm quantum dot lasers', to be published in *IEEE Photonics Technol. Lett.*, 1999
- 4 USTINOV, V.M., MALEEV, N.A., ZHUKOV, A.E., KOVSH, A.R., EGOROV, A.YU., LUNEV, A.V., VOLOV, B.V., KRESTNIKOV, I.L., MUSIKHIN, YU.G., BERT, N.A., KOPEV, P.S., ALFEROV, ZH.I., LEDENTSOV, N.N., and BIMBERG, D.: 'InAs/InGaAs quantum dot structures on GaAs substrates emitting at 1.3µm', *Appl. Phys. Lett.*, 1999, **74**, (19), pp. 2815-2817
- 5 SUGAWARA, M., MUKAI, K., and SHOJI, H.: 'Effect of phonon bottleneck on quantum-dot laser performance', *Appl. Phys. Lett.*, 1997, **71**, (19), pp. 2791-2793
- 6 HUFFAKER, D.L., PARK, G., ZOU, Z., SHCHEKIN, O.B., and DEPPE, D.G.: '1.3µm room-temperature GaAs-based quantum-dot laser', *Appl. Phys. Lett.*, 1998, **73**, (18), pp. 2564-2566
- 7 CHAND, N., BECKER, E.E., VAN DER ZEIL, J.P., CHU, S.N.G., and DUTTA, N.K.: 'Excellent uniformity and very low (less-than-50 Acm²) threshold current density strained InGaAs quantum-well diode-lasers on GaAs substrate', *Appl. Phys. Lett.*, 1991, **58**, (20), pp. 1704-1706
- 8 TURNER, G.W., CHOI, H.K., and MANFRA, M.J.: 'Ultralow-threshold (50A/cm²) strained single-quantum-well GaInAsSb/AlGaAsSb lasers emitting at 2.05µm', *Appl. Phys. Lett.*, 1998, **72**, (8), pp. 876-878

The Influence of Quantum-Well Composition on the Performance of Quantum Dot Lasers Using InAs/InGaAs Dots-in-a-Well (DWELL) Structures

G. T. Liu, A. Stintz, H. Li, T. C. Newell, A. L. Gray, P. M. Varangis, K. J. Malloy, and L. F. Lester

Abstract—The optical performance of quantum dot lasers with different dots-in-a-well (DWELL) structures is studied as a function of the well number and the indium composition in the InGaAs quantum well (QW) surrounding the dots. While keeping the InAs quantum dot density nearly constant, the internal quantum efficiency η_i , modal gain, and characteristic temperature of 1-DWELL and 3-DWELL lasers with QW indium compositions from 10 to 20% are analyzed. Comparisons between the DWELL lasers and a conventional $\text{In}_{0.15}\text{Ga}_{0.85}\text{As}$ strained QW laser are also made. A threshold current density as low as 16 A/cm^2 is achieved in a 1-DWELL laser, whereas the QW device has a threshold 7.5 times larger. It is found that η_i and the modal gain of the DWELL structure are significantly influenced by the quantum-well depth and the number of DWELL layers. The characteristic temperature T_0 and the maximum modal gain of the ground-state of the DWELL structure are found to improve with increasing indium in the QW. It is inferred from the results that the QW around the dots is necessary to improve the DWELL laser's η_i for the dot densities studied.

Index Terms—Quantum dot lasers, semiconductor lasers.

I. INTRODUCTION

RECENT progress in long-wavelength quantum dot laser research has been associated with either embedding or covering $\text{In}_x\text{Ga}_{1-x}\text{As}$ quantum dots (QDs) with two-dimensional (2-D) InGaAs layers [1]–[6]. Park *et al.* have also improved their QD lasers by growing InGaAs QDs on an InGaAs buffer layer [7]. It is known that the InGaAs layers help to achieve higher dot density [2], [4], [5], [7] and to extend the luminescence wavelength up to $1.35 \mu\text{m}$ without intensity degradation [2], [6]. Very impressive laser performance has been achieved with QDs surrounded by InGaAs layers compared to those embedded in a GaAs matrix [8], including a threshold current density of 26 A/cm^2 at $1.25 \mu\text{m}$ [1]. This result is the first time that a threshold current density of a QD laser has been reported that is lower than that of any quantum-well (QW) laser. A continuous-wave output power of 2.7 W has also been achieved near $1.3 \mu\text{m}$ [4]. Many reports only attribute these successes to a higher dot density [4], [5], [7]. However, it has been contended that an InGaAs QW around the dots is also very important in helping the quantum dots to capture carriers [1], [2]. Thus, a new semiconductor laser

design name has been proposed—the dots-in-a-well (DWELL) laser.

Previous InGaAs QD laser research has described the use of InGaAs layers with various indium compositions around the dots [1]–[3], [5]–[7]. In this paper, a systematic study of the DWELL approach is performed. InAs QDs are sandwiched between InGaAs layers (hereafter, the InGaAs QW) containing 10%, 15%, or 20% In. These structures are employed to study the influence of the QW depth on the device performance of three separate InAs/InGaAs one-DWELL (1-DWELL) lasers. A schematic diagram of the electron energy levels in the laser active gain region material design is shown in Fig. 1. An $\text{InAs/In}_{0.15}\text{Ga}_{0.85}\text{As}$ 3-DWELL laser and an $\text{In}_{0.15}\text{Ga}_{0.85}\text{As}$ single-quantum-well (1-QW) laser are grown for comparison. The efficiency, threshold current density, modal gain, and temperature performance of the five different lasers are analyzed and compared with the goal of determining the role of the InGaAs QW in the DWELL structure. A simple analytical gain model is also presented to fit the modal gain and threshold current density results.

II. DEVICE STRUCTURES AND GROWTH

Five laser structures were grown by solid-source molecular beam epitaxy (MBE) on an n^+ GaAs substrate with identical waveguide cavities but different active gain regions. Issues pertaining to growth conditions and photoluminescence properties of DWELL structures are detailed in [9]. The three $\text{InAs/In}_x\text{Ga}_{1-x}\text{As}$ 1-DWELL laser structures are the same as reported in [1] except that three different QWs, $\text{In}_{0.10}\text{Ga}_{0.90}\text{As}$, $\text{In}_{0.15}\text{Ga}_{0.85}\text{As}$, and $\text{In}_{0.20}\text{Ga}_{0.80}\text{As}$, are used. An $\text{InAs/In}_{0.15}\text{Ga}_{0.85}\text{As}$ 3-DWELL laser differs from the $\text{InAs/In}_{0.15}\text{Ga}_{0.85}\text{As}$ 1-DWELL only in DWELL number and in the inclusion of 10-nm GaAs barriers between the DWELL layers. The $\text{In}_{0.15}\text{Ga}_{0.85}\text{As}$ 1-QW laser is realized by growing the $\text{InAs/In}_{0.15}\text{Ga}_{0.85}\text{As}$ 1-DWELL structure without including the InAs dot layer. The epitaxial structure of the 1-DWELL designs consists of an n -type (10^{18} cm^{-3}) 300-nm-thick GaAs buffer, a $2\text{-}\mu\text{m}$ n -type (10^{17} cm^{-3}) lower $\text{Al}_{0.7}\text{Ga}_{0.3}\text{As}$ cladding layer, a 230-nm-thick GaAs waveguide surrounding the laser active region, a $2\text{-}\mu\text{m}$ p -type (10^{17} cm^{-3}) upper cladding layer, and a p^+ -doped ($3 \times 10^{19} \text{ cm}^{-3}$) 60-nm-thick GaAs cap. In the center of the waveguide, an equivalent coverage of 2.4 monolayers of InAs results in quantum dots grown approximately in the middle of the 10-nm $\text{In}_x\text{Ga}_{1-x}\text{As}$ quantum well. The QDs and QW are grown at 510°C , and all

Manuscript received May 25, 2000; revised July 10, 2000. This work was supported by DARPA under Grant MDA972-98-1-0002 and by AFOSR under Grant F49620-96-1-0077.

The authors are with the Center for High Technology Materials, University of New Mexico, Albuquerque, NM 87106 USA.

Publisher Item Identifier S 0018-9197(00)09755-4.

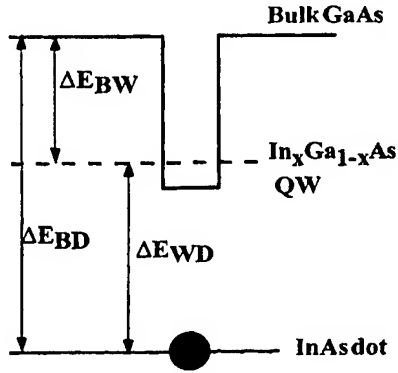


Fig. 1. Conduction band plots of the 1-DWELL structure. For the different DWELL structures considered, ΔE_{BD} is the same while ΔE_{BW} and ΔE_{WD} vary.

other layers are grown at 610 °C, as measured by an optical pyrometer. The photoluminescence linewidths are 57, 37, and 54 meV for the InAs/In_{0.10}Ga_{0.90}As, InAs/In_{0.15}Ga_{0.85}As, and InAs/In_{0.20}Ga_{0.80}As 1-DWELL laser structures, respectively. The corresponding dot densities are $4 \times 10^{10} \text{ cm}^{-2}$, $3.2 \times 10^{10} \text{ cm}^{-2}$, and $3.7 \times 10^{10} \text{ cm}^{-2}$ measured with atomic force microscopy (AFM) on calibration wafers with uncapped QDs. As measured by an optical spectrum analyzer, the peak lasing wavelengths are 1.227, 1.250, and 1.231 μm for the InAs/In_{0.10}Ga_{0.90}As 1-DWELL, InAs/In_{0.15}Ga_{0.85}As 1-DWELL, and InAs/In_{0.20}Ga_{0.80}As 1-DWELL lasers, respectively. It is noted that the lasing wavelengths are nearly identical in spite of the different surrounding alloys and the corresponding strain. This result is different from what is generally reported in the literature [6], [10]–[12]. However, the lasing wavelength is very dependent on growth conditions [9]. In preliminary investigations, we have observed an emission peak red-shift with increasing quantum-well growth rate after the formation of the QDs. This was counteracted by varying the growth of the quantum well through the GaAs flux rate. AFM data show a typical QD diameter of 20 nm and a height of 7 nm for these same layers. A cross-sectional transmission electron microscope (TEM) image of the InAs/In_{0.15}Ga_{0.85}As 1-DWELL laser is shown in Fig. 2. The quantum dot size in the image appears bigger than its actual dimensions due to the strain contrast. Also, strain most likely causes the white line across the dots and the QW in the image.

III. RESULTS AND DISCUSSION

A. Internal Quantum Efficiency

The prime motivation for the DWELL structure originates from the small fill factor of the QDs in the junction plane. For the in-plane QD diameters and densities reported here, which average about 20 nm and $3.6 \times 10^{10} \text{ cm}^{-2}$, respectively, the areal fill factor is approximately 11%. This small QD coverage creates the possibility that, in the absence of a surrounding QW, injected electrons and holes may not be trapped in the dot as efficiently, causing significant, unwanted recombination outside of the dot. This situation can arise since an empty, or, more generally, a neutral QD cannot capture a carrier through the long-range Coulombic attraction as a charged dot can, i.e., the

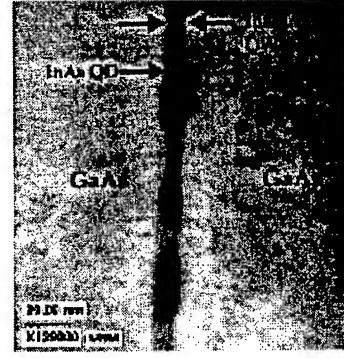


Fig. 2. Cross-sectional transmission electron microscope (TEM) image of the InAs/In_{0.15}Ga_{0.85}As 1-DWELL.

carrier must physically enter the space occupied by the neutral QD to be captured. For the neutral dot, one can estimate the effective increase in the QD cross section for electrons using the Heisenberg uncertainty principle and the fact that the average momentum transverse to the current injection direction is zero

$$\Delta x \approx \frac{\hbar}{2 \sqrt{2m^* \Delta E}} \quad (1)$$

where m^* is taken to be the electron effective mass in the GaAs barrier ($0.067 m_0$) and $\Delta E \approx k_B T$ due to the random thermal motion of the carriers in the plane of the quantum dots. For room temperature, Δx is 2.3 nm, which is much less than the average edge to edge spacing of 34 nm between adjacent QDs studied in this work. Consequently, injected carriers do not see a very large capture cross-section from neutral dots. On the other hand, if the layer of quantum dots is placed inside a quantum well, the QW could first capture the carriers and then turn them into the 2-D plane to enhance capture into the QDs. Thus, the fill factor is effectively 100%, and the internal quantum efficiency η_i of the DWELL laser should be superior to a conventional QD laser. This is supported by the photoluminescence (PL) experiment reported by Lester [2], in which the PL intensity was observed to increase by at least an order of magnitude when the dots were grown in an InGaAs quantum well as compared to grown directly on a GaAs waveguide. The same sort of carrier “funneling” could conceivably be achieved in QDs embedded in a graded-index separate confinement heterostructure (GRINSCH) [13]. However, larger optical confinement factors are possible in SCH designs than GRINSCH structures using the same composition waveguides. The efficiency data below for different DWELL lasers further elucidate the role of the QW in improving injection efficiency in the devices.

Broad area lasers with 100- μm stripe widths were fabricated from the five laser structures with cavity lengths as long as 7.8 mm. All devices were tested epitaxial-side up on a thermoelectric cooler at 20 °C in pulsed mode. The pulse width was 300 ns with a duty cycle of 0.5%. Since the devices have similar lasing wavelengths and AFM measurements indicate that the QDs are physically similar, the ground-state electron and hole QD energy levels with respect to the bulk GaAs, ΔE_{BD} , are essentially the same. Only the QW energy levels change for the different InGaAs wells (see Fig. 1). For reference, the results are consolidated in Table I.

TABLE I
A SUMMARY OF THE MEASURED RESULTS FROM ALL FIVE LASERS

	InAs/In _{0.10} Ga _{0.90} As 1-DWELL	InAs/In _{0.15} Ga _{0.85} As 1-DWELL	InAs/In _{0.20} Ga _{0.80} As 1-DWELL	In _{0.15} Ga _{0.85} As 1-QW	InAs/In _{0.15} Ga _{0.85} As 3-DWELL
PL linewidth (meV)	69	37	54		37
Dot Density (10 ¹⁰ cm ⁻²)	4.0	3.2	3.7		3.2
T ₀ value	37 K	45 K	51 K	119K	84K
Internal efficiency	30%	38%	55%	77%	53%
Internal Loss (cm ⁻¹)	0.57	0.63	1.44	5.9	1.17
Peak lasing wavelength at 7.8mm cavity length (μm)	1.227	1.250	1.231	0.990	1.241
Lowest Threshold Current density (A cm ⁻²)	17	16	22	188	31
Ground state Saturated modal gain (cm ⁻¹)	~2.4	~3.6	~5.7		12.5
Transparency Current Density (A cm ⁻²)	11.0	10.1	12.2		20.1

The significance of the QW on the QD lasing properties is first examined by studying the efficiency results of the three 1-DWELL lasers along with the 3-DWELL and 1-QW laser. The inverse external slope efficiency $1/\eta_{\text{ex}}$ versus cavity length L results for the three 1-DWELL lasers in Fig. 3 are used to calculate the internal loss α_i and the internal quantum efficiency η_i . By fitting the data to $1/\eta_{\text{ex}} = 1/\eta_i[1 - \alpha_i L / \ln(R)]$ with $R = 0.32$, $\eta_i(\alpha_i)$ values of 30% (0.57 cm⁻¹), 38% (0.63 cm⁻¹), and 55% (1.44 cm⁻¹) are found for the InAs/In_{0.10}Ga_{0.90}As, InAs/In_{0.15}Ga_{0.85}As, and InAs/In_{0.20}Ga_{0.80}As 1-DWELL lasers, respectively. The internal losses are very small, which is consistent with previous results [2], and presumably arises from the fact that the emission wavelength is well below the bandgap of the GaAs waveguide. The inverse slope efficiency data in Fig. 3 show that as the depth of the QW increases, η_i is improved. In Fig. 4, η_i is plotted as a function of QW indium composition. In an informative extrapolation, a linear fit of the η_i data shows that in the 0% In (no-QW) limit, a very small internal quantum efficiency would exist. Unfortunately, we are not able to test this hypothesis since such a device would possess a substantially different dot density and emission wavelength [2]. Nevertheless, the current and past work supports the hypothesis that the quantum well and its depth strongly influence η_i in a DWELL laser.

We can be more specific about the role of the QW in the DWELL structure by analyzing the $1/\eta_{\text{ex}}$ versus L results for the InAs/In_{0.15}Ga_{0.85}As 1-DWELL, InAs/In_{0.15}Ga_{0.85}As 3-DWELL and In_{0.15}Ga_{0.85}As 1-QW lasers shown in Fig. 5. $\eta_i(\alpha_i)$ values of 38% (0.63 cm⁻¹), 53% (1.17 cm⁻¹) and 77% (5.9 cm⁻¹) are found for the InAs/In_{0.15}Ga_{0.85}As 1-DWELL, InAs/In_{0.15}Ga_{0.85}As 3-DWELL, and In_{0.15}Ga_{0.85}As 1-QW lasers, respectively. The 1-QW lasers have a better internal efficiency than the 1-DWELL lasers, which implies that not all the carriers captured by the quantum well recombine radiatively in the QDs. The 3-DWELL lasers, having more quantum wells, have an improved internal quantum efficiency compared to the 1-DWELL lasers. It is noted that the 1-QW lasers have much higher α_i , which is attributed to a seven times higher threshold current density (see the next section) and, thus, larger free carrier absorption.

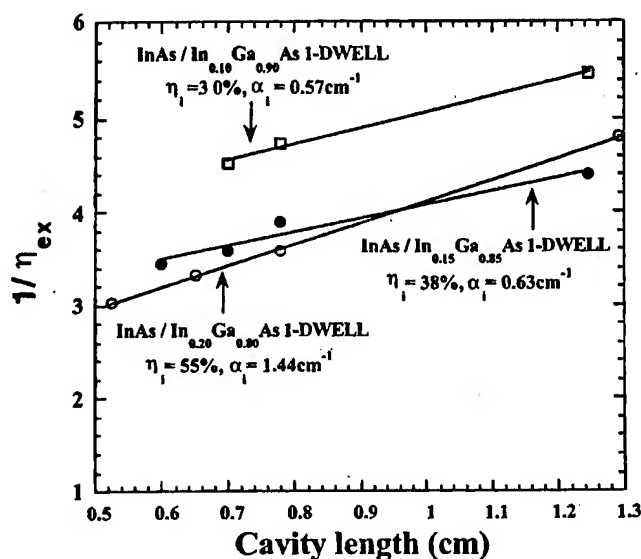


Fig. 3. Inverse external quantum efficiency versus cavity length plot for the three 1-DWELL lasers. The internal quantum efficiency increases with the increase of indium composition in the well.

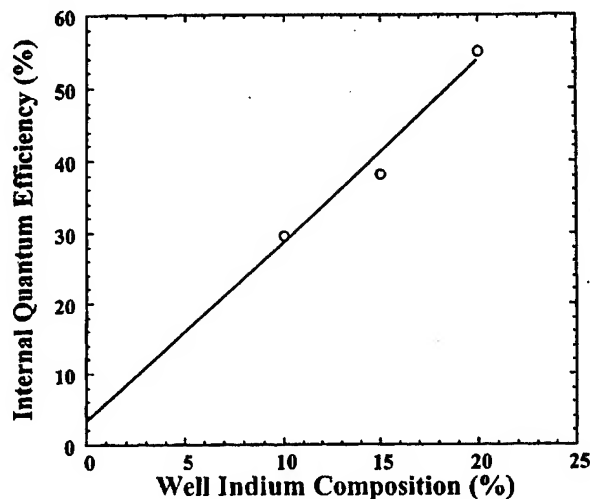


Fig. 4. Plot of internal quantum efficiency as a function of quantum-well indium composition. A linear fit of the η_i data shows that in the 0% indium (no-QW) limit, a very small internal quantum efficiency would exist.

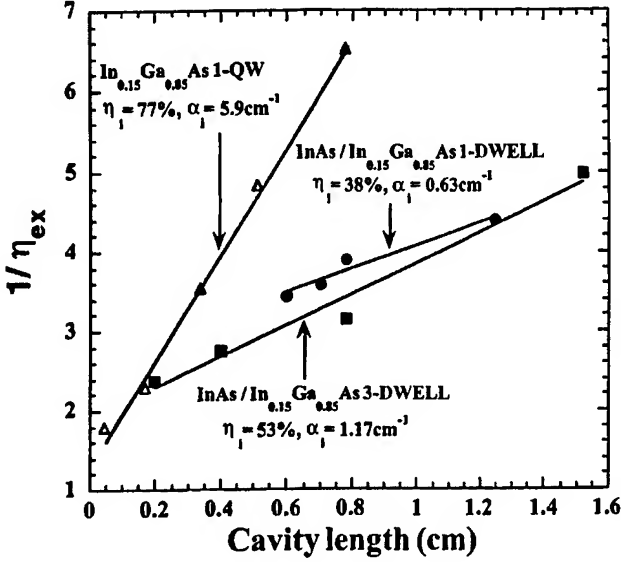


Fig. 5. Inverse external quantum efficiency versus cavity length plot for the InAs/In_{0.15}Ga_{0.85}As 1-DWELL, InAs/In_{0.15}Ga_{0.85}As 3-DWELL, and In_{0.15}Ga_{0.85}As 1-QW lasers.

The internal quantum efficiency data above may be explained physically using the following assumptions

- 1) The internal quantum efficiency of the 1-QW laser η_i^{QW} is dominated by the capture of carriers into the active region. This is equivalent to stating that the quasi-Fermi level in the QW clamps at threshold, but the quasi-Fermi level in the SCH does not. Consequently, it is assumed that any carriers that get into the QW radiate, but some percentage of carriers miss the active region at all biases above threshold. The latter constitutes the 1-QW laser η_i measured in our experiments of 77%.
- 2) For the DWELL structure, the percentage of carriers that get into the active region is determined by the QW. Direct capture into the QDs is considered insignificant. This is consistent with the fitting results of Fig. 4. We assume that all the carriers that are captured by the quantum well are further captured by the quantum dots since very little QW emission is observed in our electroluminescence and PL experiments [2].
- 3) The internal quantum efficiency of a DWELL laser is $\eta_i^{DWELL} = \eta_i^{QW} \cdot \eta_i^{QD}$. Knowing η_i^{QW} from assumption 1), this equation allows us to calculate the percentage of carriers in the QDs that result in stimulated emission. Leakage current out of the dots is accounted for by η_i^{QW} .

Given these assumptions, it is appropriate to call η_i^{QW} and η_i^{QD} the injection and stimulated emission efficiencies, respectively, of the DWELL laser. When comparing the η_i s of the InAs/In_{0.15}Ga_{0.85}As 1-DWELL and In_{0.15}Ga_{0.85}As 1-QW lasers, the injection efficiency of the quantum wells is assumed to be the same. From the data in Fig. 5, this hypothesis puts η_i^{QD} of the QDs at about 50%. The 3-DWELL data are also consistent with this picture. The increase in η_i^{DWELL} for the InAs/In_{0.15}Ga_{0.85}As 3-DWELL laser is presumably because of the improvement in the injection efficiency from having

multiple wells. In this instance, the injection efficiency of a multiple DWELL system can be estimated as

$$\eta_i^{MQW} = 1 - (1 - \eta_i^{QW})^M \quad (2)$$

where M equals the number of wells. If $\eta_i^{QW} = 77\%$, then the injection efficiency of the 3-DWELL device is estimated to be 99%. Consequently, η_i^{QD} in the 3-DWELL is similar to that in the InAs/In_{0.15}Ga_{0.85}As 1-DWELL—close to 50%.

For the three 1-DWELL lasers, the QDs are assumed to have the same η_i^{QD} while only the injection efficiency of the QW is changing. As the QW gets deeper, it becomes more effective in capturing carriers, suppressing their thermionic emission from the well and transferring them to the QDs. This same sort of trend in laser performance has been observed in strained QW lasers [14]. Typically, strained In_{0.2}Ga_{0.8}As QW lasers have η_i close to 100%. If this value is assumed for the injection efficiency of the InAs/In_{0.2}Ga_{0.8}As 1-DWELL device, an η_i^{QD} close to 50% is again calculated for the InAs QDs. In summary, these results have shown that the QW in a DWELL structure plays an important role in capturing carriers and controls the injection into the active region. It also has been demonstrated that nonradiative paths clearly exist in the QDs. Although the exact nature of the nonradiative recombination is not known currently, it significantly limits the internal quantum efficiency of DWELL lasers with wavelength around 1.24 μ m.

B. Lasing Threshold and Modal Gain

1) *Threshold Current Density:* An impressive difference in light-current (L - I) curves between the InAs/In_{0.15}Ga_{0.85}As 1-DWELL and In_{0.15}Ga_{0.85}As 1-QW lasers can be seen in Fig. 6. With a threshold current density J_{th} , of only 26 A/cm², the 7.8-mm as-cleaved facet 1-DWELL laser is over seven times less than the identical length 1-QW laser whose $J_{th} = 188$ A/cm². This low QD J_{th} is a benefit of the inherently small QD density of states that allows for carrier inversion to be rapidly reached. In addition, as noted above, the low carrier densities imply that free carrier absorption is restricted and so the threshold gain can be small. For the 7.8-mm as-cleaved InAs/In_{0.10}Ga_{0.90}As and InAs/In_{0.20}Ga_{0.80}As 1-DWELL lasers, J_{th} is 40 and 31 A/cm², respectively. J_{th} can be further reduced by decreasing the cavity loss. HR coatings of 75% and 98% were applied to both facets of the 7.8-mm-long cavities. As a result, the threshold current densities dropped to 17, 16, and 22 A/cm² for the InAs/In_{0.10}Ga_{0.90}As, InAs/In_{0.15}Ga_{0.85}As, and InAs/In_{0.20}Ga_{0.80}As 1-DWELL devices. These are the lowest threshold current densities of any semiconductor lasers and are well below the 40–50 A/cm² of the lowest threshold current density quantum-well lasers [1], [15]. No clear trend exists in DWELL J_{th} as a function of the In composition in the QW, dot density, or PL linewidth. The threshold current density achieved by the InAs/In_{0.15}Ga_{0.85}As 3-DWELL laser is 36 A/cm² at a cleaved cavity length of 7.8 mm as compared to 26 A/cm² of InAs/In_{0.15}Ga_{0.85}As 1-DWELL laser of the same cavity length. With a 98% HR coating on one side, the threshold current density of the 3-DWELL laser is further reduced to 31 A/cm². This is only two times the lowest threshold current of the 1-DWELL laser. At a cavity length of 4 mm, the

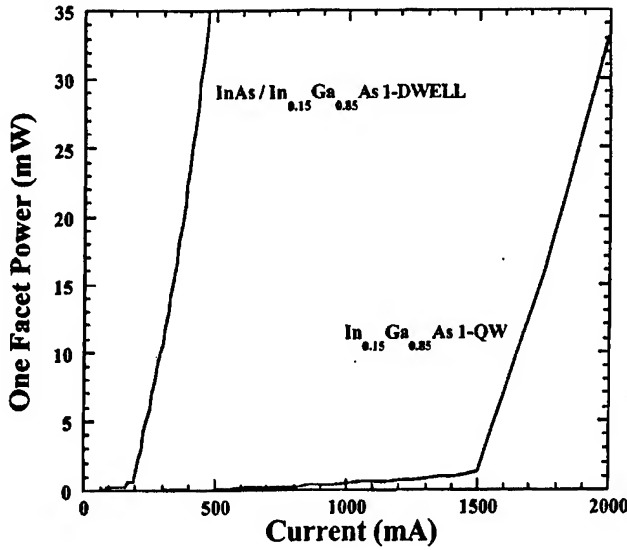


Fig. 6. L - I curve of the InAs/In_{0.15}Ga_{0.85}As 1-DWELL and In_{0.15}Ga_{0.85}As 1-QW lasers of 7.8-mm as-cleaved cavity length. The threshold current density of the 1-DWELL laser is only 13% of the 1-QW laser. The slope efficiency of the 1-DWELL laser is also better than the 1-QW laser due to lower internal loss.

3-DWELL laser has a threshold current density of 42 A/cm², which is even lower than the 50 A/cm² of the corresponding 1-DWELL laser.

As a note on the beam quality, no clear evidence of filamentation is observed. The high-quality beam profile is a benefit of the QD laser's 0.1 linewidth enhancement factor [16] that theoretically could result in the complete absence of filament formation [17].

2) *Modal Gain*: Using the results of threshold current density and internal loss and the condition that gain is equal to loss at threshold, the ground-state modal gains of the three 1-DWELL lasers versus their respective threshold current densities are plotted in Fig. 7. The open circles in the figure denote the experimental values for the InAs/In_{0.10}Ga_{0.90}As structure. The filled circles and open squares plot the InAs/In_{0.15}Ga_{0.85}As and InAs/In_{0.20}Ga_{0.80}As structures, respectively. The solid lines are the results of curve fitting using the model to be described below. As the QW deepens with larger indium concentration, the differential modal gain dg/dJ and the saturated ground-state modal gain g_{sat} increase. Since the three 1-DWELL lasers have similar dot densities and the PL linewidth dependence is not strong, the change in dg/dJ can only be accounted for by the higher η_i in the DWELL designs with deeper QWs. This information corroborates the data in Fig. 3 regarding η_i . The reason for the differing g_{sat} values is less obvious. It is hypothesized that the smaller g_{sat} in designs with shallower QWs (and deeper dots) arises from a phonon bottleneck that permits the excited QD levels, which have a higher density of states, to become populated and lase before the ground-state gain can be fully maximized. The g_{sat} s of 2.4, 3.6, and 5.7 cm⁻¹ for the InAs/In_{0.10}Ga_{0.90}As, InAs/In_{0.15}Ga_{0.85}As, and InAs/In_{0.20}Ga_{0.80}As lasers, respectively, differ roughly in proportion with their η_i s.

The g_{sat} for the 3-DWELL lasers improves to 12.5 cm⁻¹, more than three times the g_{sat} of the corresponding 1-DWELL lasers. The improvement is due to both the increases in quantum

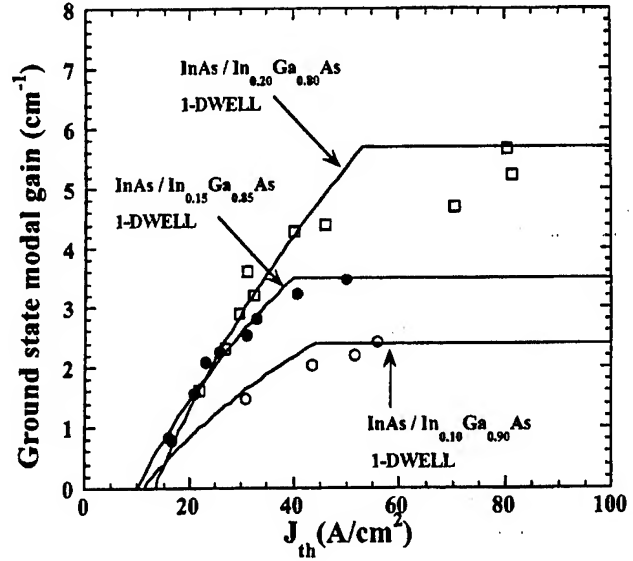


Fig. 7. Ground-state modal gains versus J_{th} for the three 1-DWELL lasers. The open circles, filled circles, and open squares refer to the InAs/In_{0.10}Ga_{0.90}As, InAs/In_{0.15}Ga_{0.85}As, and InAs/In_{0.20}Ga_{0.80}As structures, respectively. The solid lines are from the low-pump limit model. At gain saturation where the model is invalid, these arcs are replaced by straight lines, $g = g_{sat}$.

dot density and the improved η_i , as noted above. This result is particularly significant for QD vertical-cavity surface-emitting lasers (VCSELs), which require large gains to overcome the high cavity losses. For a small increase in current density, the gain can be appreciably augmented. The ground-state modal gain of the 3-DWELL laser is still relatively small compared to quantum-well lasers. This is mostly a result of the small confinement factor of a quantum dot layer as compared to a quantum-well layer, even though the material gain of the quantum dot may be very high [19].

3) *Theoretical Ground-State Gain Model for the Low Pump Limit*: Various studies have modeled the gain of quantum dot lasers for a broad range of carrier densities and multiple QD and QW energy levels [13], [18]–[23]. By restricting the range to the low-pump limit, a simple analytical equation can be derived that describes the relationship between gain and current density. In this circumstance, only the ground-state of the QD is sufficiently populated to produce a meaningful contribution to the spontaneous emission. Since the threshold current densities in the 7.8-mm HR-coated lasers are extremely low, their carrier/current densities and gain relations are suitably described by this model.

Consider that the normally Gaussian-broadened QD density of states can be adequately represented by a theoretical delta-function like spike, $\rho(E) = 2N_o\delta(E - E_o)$, where the "2" accounts for spin, N_o is the physical quantum dot density, and E_o is the ground QD energy. The ground-state electron density is obtained from the Fermi integral

$$n = \int f_c(E) \cdot \rho(E) \cdot dE = 2N_o f_c(E_o). \quad (3)$$

Note that if $f_c(E)$ is slowly changing with respect to $\rho(E)$, which is reasonably true when $E_f \neq E_o$, then (3) is essentially correct even when $\rho(E)$ is not approximated. Equation

(3) shows that a simple linear relationship exists between $f_c(E)$ and n , $n/2N_o = f_c(E)$. If the quantum dots are initially empty and charge neutrality is maintained as carriers are injected into them, i.e., electrons and holes in the ground-state are equal, then

$$f_v = 1 - f_c = 1 - \frac{n}{2N_o}. \quad (4)$$

The spontaneous emission current likewise becomes a straightforward calculation

$$\begin{aligned} J &= e \int R_{sp}(E) \rho(E) f_c(E) [1 - f_v(E)] dE \\ &= \frac{2eN_o}{\tau} f_c^2(E_o) = \frac{2eN_o}{\tau} \left(\frac{n}{2N_o} \right)^2. \end{aligned} \quad (5)$$

Thus a parabolic relationship exists between the current and carrier density. The maximum current that contributes to ground-state spontaneous emission is $J_{sat} = 2eN_o/\tau$, and this occurs when the ground level of the QDs is saturated. The gain at energy E_o is given by

$$\begin{aligned} g &= g_{sat} [f_c(E_o) - f_v(E_o)] \\ &= g_{sat} [2f_c(E_o) - 1] \\ &= g_{sat} \left[2\sqrt{\frac{J}{J_{sat}}} - 1 \right]. \end{aligned} \quad (6)$$

The transparency condition occurs when $J = J_{sat}/4$, and the maximum ground-state modal gain g_{sat} occurs at J_{sat} . Since other carrier recombination terms are ignored, (6) sets the theoretical limit of QD performance. The g_{sat} is determined from the measurement and, subsequently, J_{sat} is found from the curve fit to (6). In Fig. 7, the fitted transparency current densities are 11.0, 10.1, 12.2 A/cm² for the InAs/In_{0.10}Ga_{0.90}As, InAs/In_{0.15}Ga_{0.85}As, and InAs/In_{0.20}Ga_{0.80}As 1-DWELL lasers, respectively. They are all very low. Even though the 1-DWELL lasers have similar dot densities, we found no strong correlation between the photoluminescence linewidth and g_{sat} as summarized in Table I. However, the slope of the gain versus J is dependent upon η_i , and thus the data in Fig. 7 follows the trend of increasing η_i with indium in the quantum well. The transparency current density for the InAs/In_{0.15}Ga_{0.85}As 3-DWELL laser is found to be 20.1 A/cm², which is only two times higher than that of the InAs/In_{0.15}Ga_{0.85}As 1-DWELL laser.

When applying the model to the experimental data, it is important to acknowledge the excited state contributions. For lasers that possess low thresholds, i.e., long cavities or HR-coated short cavities, only ground-state lasing is observed even at high injection currents. Here, the model is most appropriate since the excited states are not highly populated. In contrast, the shorter cavity as-cleaved lasers, which require higher threshold current densities, emit significantly from excited state transitions even though ground-state lasing can occur. Consequently, the model overestimates the gain as a function of J . While it is straightforward to generalize the model to account for excited states, the resulting equations do not show the fundamental relationship among n , g , and J . As a result, when curve-fitting the data, the model is used until $g = g_{sat}$, at which point g is clamped. We also note that

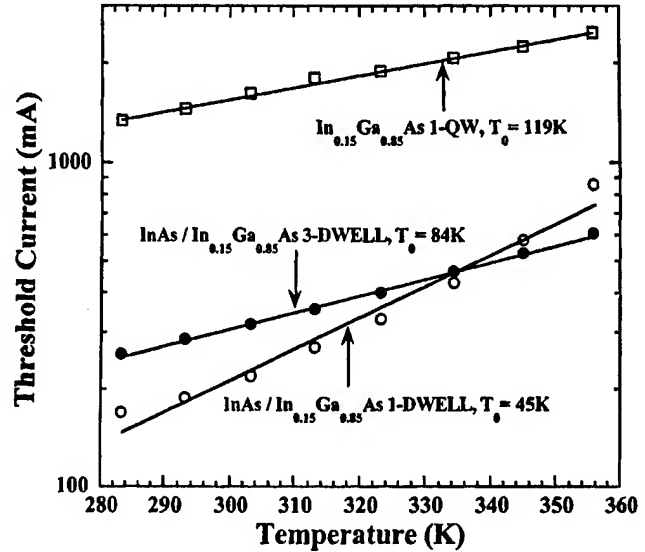


Fig. 8. Threshold current versus temperature plot for the InAs/In_{0.15}Ga_{0.85}As 1-DWELL, InAs/In_{0.15}Ga_{0.85}As 3-DWELL, and In_{0.15}Ga_{0.85}As 1-QW lasers.

homogeneous broadening, which could cause a contribution to the ground-state gain from higher energy levels [24], [25], is not explicitly included here.

C. Temperature Performance

The pulsed threshold current versus temperature of the InAs/In_{0.15}Ga_{0.85}As 1-DWELL, InAs/In_{0.15}Ga_{0.85}As 3-DWELL, and In_{0.15}Ga_{0.85}As 1-QW lasers with cavity length equal to 7.8 mm and cleaved facets is shown in Fig. 8. The temperature is varied from 10 to 80 °C, and the results are curve-fit to the empirical formula $I_{th} = I_0 \exp(T/T_0)$. From this fitting, T_0 values of 45, 84, and 119K are obtained for the 1-DWELL, 3-DWELL and 1-QW lasers. For the 1-DWELL device, the T_0 fitting does not show a linear behavior; rather, a super-linear curve best fits the data. Higher energy QD states are becoming progressively more populated at higher pumping due to thermal excitation and gain saturation. These levels contribute only minutely to the maximum gain mode via homogeneous broadening, and so their radiative recombination current is undesirable. Thus J_{th} increases more rapidly than the simple exponential fit predicts, and this explains the decrease in T_0 . On the other hand, a good linear fit is obtained for the 3-DWELL laser, which demonstrates its superior temperature dependent threshold current performance to the 1-DWELL. As noted above, the 3-DWELL J_{th} is only about twice that of the 1-DWELL. Hence, the carrier density on a per-well basis is less in the 3-DWELL, and the quasi-Fermi levels will be lowered. Correspondingly, thermal excitation from the QD ground-state into the QD excited states and QW ground-state is beneficially reduced.

At 119K, the T_0 of the QW laser is substantially greater than the QD devices. However, a direct comparison between the two structures cannot be readily made. Due to its much higher transparency current density, and thus J_{th} , the QW laser is less sensitive to temperature fluctuations than the QD devices. As a result, the T_0 of the QD devices will be affected more than the

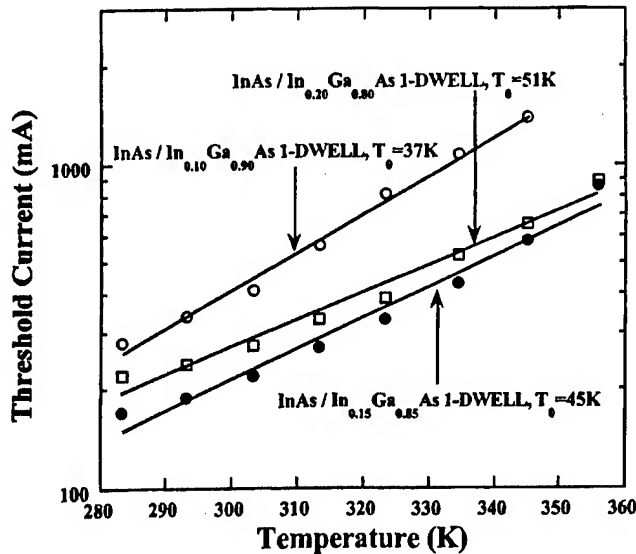


Fig. 9. Threshold current versus temperature plot for the three 1-DWELL lasers. The fitted T_0 value increases with the increase of indium composition in the well.

QW laser. Assuming that differences in the T_0 between the devices originate from changes in thermionic emission, increasing the QW depth, ΔE_{bW} in Fig. 1, should decrease the thermionic emission out of it and improve the T_0 of the QD laser. This is, in fact, observed for the three 1-DWELL lasers.

The threshold current versus temperature of the InAs/In_{0.10}Ga_{0.90}As, InAs/In_{0.15}Ga_{0.85}As, and InAs/In_{0.20}Ga_{0.80}As 1-DWELL lasers with $L = 7.8$ mm cavity length is plotted in Fig. 9. T_0 increases from 37 to 51 K as the QW gets deeper, and the QD simultaneously becomes shallower. Although the energy separation between the QW ground-state and QD state, ΔE_{WD} in Fig. 1, is decreasing with larger In content in the well, any thermally induced excitation current from QD to QW appears to be less significant than the thermal emission current from the QW. In any event, the QD T_0 cannot be entirely attributed to simply QW escape currents. Certainly, there are yet unknown QD processes that also contribute to the T_0 value. These are difficult to distinguish from other recombination mechanisms and are not the focus of this investigation. Rather, we have considered how the design parameters (In composition and well number) affect the temperature performance of the QD laser. Again, the results for the five lasers are summarized in Table I.

IV. CONCLUSION

The efficiency, threshold current density, modal gain, and temperature performance of quantum dot lasers with different dots-in-a-well structures are studied as a function of the well number and the indium composition in the InGaAs quantum well surrounding the dots. It is found that the internal quantum efficiency and the modal gain of the DWELL structure are significantly influenced by the quantum-well depth and the number of DWELL layers. The QW is essentially improving the injection efficiency of the quantum dots. We infer from the results that the QW around the dots is necessary to improve the laser

internal quantum efficiency and ground-state saturated gain performance for the dot densities studied. The lowest threshold current density achieved by the DWELL laser is 16 A/cm². The characteristic temperature T_0 of the DWELL structure can be improved by reducing thermionic emission from the well, which was accomplished here by increasing the well depth. The modal gain of the DWELL lasers may be improved by adding more DWELL layers without much tradeoff with the threshold current density. The highest modal gain achieved by the 3-DWELL laser is 12.5 cm⁻¹. This improvement in modal gain can lead to the possibility of electrically pumped 1.3- μ m QD VCSELs on GaAs.

ACKNOWLEDGMENT

The authors would like to thank X. Huang for helping with the HR coatings and R. Spillers for helping with the TEM sample preparation.

REFERENCES

- [1] G. T. Liu, A. Stintz, H. Li, K. J. Malloy, and L. F. Lester, "Extremely low room-temperature threshold current density diode lasers using InAs dots in an In_{0.15}Ga_{0.85}As quantum well," *Electron. Lett.*, vol. 35, pp. 1163–1165, 1999.
- [2] L. F. Lester, A. Stintz, H. Li, T. C. Newell, E. A. Pease, B. A. Fuchs, and K. J. Malloy, "Optical characteristics of 1.24 μ m quantum dot lasers," *IEEE Photon. Technol. Lett.*, vol. 11, pp. 931–933, 1999.
- [3] Y. M. Shernyakov, D. A. Bedarev, E. Y. Kondrat'eva, P. S. Kopev, A. R. Kovsh, N. A. Maleev, M. V. Maximov, S. S. Mikhlin, A. F. Tsatsulnikov, V. M. Ustinov, B. V. Volovik, A. E. Zhukov, Z. I. Alferov, N. N. Ledentsov, and D. Bimberg, "1.3 μ m GaAs-based laser using quantum dots obtained by activated spinodal decomposition," *Electron. Lett.*, vol. 35, pp. 898–900, 1999.
- [4] A. E. Zhukov, A. R. Kovsh, V. M. Ustinov, Y. M. Shernyakov, S. S. Mikhlin, N. A. Maleev, E. Y. Kondrat'eva, D. A. Livshits, M. V. Maximov, B. V. Volovik, D. A. Bedarev, Yu. G. Musikhin, N. N. Ledentsov, P. S. Kopev, Z. I. Alferov, and D. Bimberg, "Continuous-wave operation of long-wavelength quantum-dot diode laser on a GaAs substrate," *IEEE Photon. Technol. Lett.*, vol. 11, pp. 1345–1347, 1999.
- [5] K. Mukai, Y. Nakata, K. Otsubo, M. Sugawara, N. Yokoyama, and H. Ishikawa, "1.3- μ m CW lasing of InGaAs-GaAs quantum dots at room temperature with a threshold current of 8 mA," *IEEE Photon. Technol. Lett.*, vol. 11, pp. 1205–1207, 1999.
- [6] K. Nishi, H. Saito, S. Sugou, and J. S. Lee, "A narrow photoluminescence linewidth of 21 meV at 1.35 μ m from strained-reduced InAs quantum dots covered by In_{0.2}Ga_{0.8}As grown on GaAs," *Appl. Phys. Lett.*, vol. 74, pp. 1111–1113, 1999.
- [7] G. Park, O. B. Shchekin, D. L. Huffaker, and D. G. Deppe, "Low-threshold oxide-confined 1.3 μ m quantum-dot laser," *IEEE Photon. Technol. Lett.*, vol. 13, pp. 230–232, 2000.
- [8] D. L. Huffaker, G. Park, Z. Zou, O. B. Shchekin, and D. G. Deppe, "1.3 μ m room-temperature GaAs-based quantum-dot laser," *Appl. Phys. Lett.*, vol. 73, pp. 2564–2566, 1998.
- [9] A. Stintz, G. T. Liu, A. L. Gray, R. Spillers, S. M. Delgado, and K. J. Malloy, "Characterization of InAs quantum dots in strained In_{0.2}Ga_{0.8}As quantum wells," *J. Vac. Sci. Technol.*, vol. 18, pp. 1496–1501, 2000.
- [10] K. Mukai and M. Sugawara, "Suppression of temperature sensitivity of interband emission energy in 1.3- μ m region by an InGaAs overgrowth on self-assembled InGaAs GaAs quantum dots," *Appl. Phys. Lett.*, vol. 74, pp. 3963–3965, 1999.
- [11] N. T. Yeh, T. E. Nee, J. I. Chyi, T. M. Hsu, and C. C. Huang, "Matrix dependence of strain-induced wavelength shift in self-assembled InAs quantum-dot heterostructures," *Appl. Phys. Lett.*, vol. 76, pp. 1567–1569, 2000.
- [12] A. E. Zhukov, A. R. Kovsh, A. Y. Egorov, N. A. Maleev, V. M. Ustinov, B. V. Volovik, M. V. Maksimov, A. F. Tsatsulnikov, and N. N. Ledentsov, "Photo- and electroluminescence in the 1.3- μ m wavelength range from quantum-dot structures grown on GaAs substrates," *Semiconductors*, vol. 33, pp. 153–156, 1999.

- [13] A. E. Zhukov, A. R. Kovsh, V. M. Üstinov, A. Yu. Egorov, N. N. Ledentsov, A. F. Tsatsul'nikov, M. V. Maximov, Yu. M. Shernyakov, V. I. Kopchatov, A. V. Lunev, P. S. Kop'ev, D. Bimberg, and Zh. I. Alferov, "Gain characteristics of quantum dot injection lasers," *Semiconduct. Sci. Technol.*, vol. 14, pp. 118–123, 1999.
 - [14] J. J. Coleman, *Quantum Well Lasers*, P. S. Zory Jr., Ed. New York: Academic, 1993, ch. 8.
 - [15] G. W. Turner, H. K. Choi, and M. J. Manfra, "Ultralow-threshold (50 A/cm²) strained single-quantum-well GaInAsSb/AlGaAsSb lasers emitting at 2.05 μm ," *Appl. Phys. Lett.*, vol. 72, pp. 876–878, 1998.
 - [16] T. C. Newell, D. J. Bossert, A. Stintz, B. Fuchs, K. J. Malloy, and L. F. Lester, "Gain and linewidth enhancement factor in InAs quantum-dot laser diodes," *IEEE Photon. Technol. Lett.*, vol. 11, pp. 1527–1529, 1999.
 - [17] J. R. Marciano and G. P. Agrawal, "Spatio-temporal characteristics of filamentation in broad-area semiconductor lasers," *IEEE J. Quantum Electron.*, vol. 33, pp. 1174–1179, 1997.
 - [18] K. J. Vahala, "Quantum box fabrication tolerance and size limits in semiconductors and their effect on optical gain," *IEEE J. Quantum Electron.*, vol. 24, pp. 523–530, 1988.
 - [19] M. Asada, Y. Mityamoto, and Y. Suematsu, "Gain and the threshold of 3-dimensional quantum-box lasers," *IEEE J. Quantum Electron.*, vol. QE-22, pp. 1915–1921, 1986.
 - [20] N. Kirstaedter, O. G. Schmidt, N. N. Ledentsov, D. Bimberg, V. M. Ustinov, A. Y. Egorov, A. E. Zhukov, M. V. Maximov, P. S. Kopev, and Z. I. Alferov, "Gain and differential gain of single layer InAs/GaAs quantum dot injection lasers," *Appl. Phys. Lett.*, vol. 69, pp. 1226–1228, 1996.
 - [21] M. Grundmann and D. Bimberg, "Gain and threshold of quantum dot lasers: Theory and comparison to experiments," *Jpn. J. Appl. Phys.*, vol. 36, pp. 4181–4187, 1997.
 - [22] —, "Theory of quantum dot laser gain and threshold: Electron and hole capture," *Phys. Status Solidi A*, vol. 164, pp. 297–300, 1997.
 - [23] H. Jiang and J. Singh, "Nonequilibrium distribution in quantum dot lasers and influence on laser spectral output," *J. Appl. Phys.*, vol. 85, pp. 7438–7442, 1999.
 - [24] P. Eliseev, H. Li, A. Stintz, G. T. Liu, T. C. Newell, K. J. Malloy, and L. F. Lester, "Tunable grating-coupled laser oscillation and spectral hole burning in an InAs quantum-dot laser diode," *IEEE J. Quantum Electron.*, vol. 36, pp. 479–485, 2000.
 - [25] H. Li, G. T. Liu, P. M. Varangis, T. C. Newell, A. Stintz, B. A. Fuchs, K. J. Malloy, and L. F. Lester, "150 nm tuning range in a grating-coupled external cavity quantum dot laser," *IEEE Photon. Technol. Lett.*, vol. 12, pp. 759–761, 2000.
- G. T. Liu, photograph and biography not available at the time of publication.
- A. Stintz, photograph and biography not available at the time of publication.
- H. Li, photograph and biography not available at the time of publication.
- T. C. Newell, photograph and biography not available at the time of publication.
- A. L. Gray, photograph and biography not available at the time of publication.
- P. M. Varangis, photograph and biography not available at the time of publication.
- K. J. Malloy, photograph and biography not available at the time of publication.
- L. F. Lester, photograph and biography not available at the time of publication.

Gain without inversion in interband transitions of semiconductor quantum wells from a single-particle perspective

Dong S. Lee and Kevin J. Malloy

Center for High Technology Materials, University of New Mexico, Albuquerque, New Mexico 87131

(Received 12 December 1995)

The quantum interferences arising in three-level atomic systems are investigated in analogous asymmetric semiconductor quantum well structures. These investigations lead to the conditions necessary for induced zero absorption and gain without population inversion in interband transitions. Asymmetric quantum well configurations are proposed and analyzed for induced zero absorption and gain without inversion using a single-particle density-matrix approach. This density-matrix approach is described and shown to give the steady-state solutions for absorption and gain without the approximations required for perturbative or iterative methods. Both excitonic and continuum transitions are examined using typical semiconductor parameters with excitonic transitions contributing the largest fraction of gain without inversion. While interband transitions differ from intraband and atomic transitions, results for the proposed quantum well configurations validate the basic concept of inversionless gain in semiconductors and point the way to ultralow threshold semiconductor microlasers. [S0163-1829(96)00424-9]

I. INTRODUCTION

Lasing without population inversion and induced zero absorption have been predicted as resulting from either Fano interference or coherent quantum-mechanical superposition in atomic systems.^{1,2} Electromagnetically induced transparency (EIT),³ gain without population inversion (GWI),⁴ and observation of inversionless lasing have been reported for atomic systems.⁵ Since lasing without inversion in a solid-state system would have further technological importance, we have studied semiconductor quantum configurations analogous to atomic systems for the potential of exhibiting similar phenomena.⁶⁻¹¹ Several related investigations have been ongoing. Thus far, a type-II quantum well configuration exhibiting Fano interference has been proposed,⁶ reduced absorption in symmetric quantum wells based on the optical Stark effect analyzed and observed,⁷⁻⁹ intersubband lasing demonstrated,¹² and intersubband lasing without inversion proposed.⁹⁻¹¹ However, investigations of gain without population inversion for interband transitions in semiconductor quantum structures have not been reported. Here, we examine interband transitions in three-level semiconductor quantum wells, and discuss possible configurations exhibiting electromagnetically induced transparency and gain without inversion. Results are obtained for coupling induced by either an extrinsic electromagnetic field or by intrinsic effects such as a tunneling barrier.

Normally two-level atomic systems exhibit Lorentzian resonant absorption profiles. However, three-level atomic systems show strongly modified absorption and gain profiles upon coupling two of the levels. In order to observe EIT or GWI arising from the optical Stark effect, it is desirable that one of the coupled states have a fast, nonreciprocal decay path. In semiconductor quantum wells, the atomic levels are replaced by the subband energy levels, and in principle should also exhibit similar destructive quantum interference effects. In order to study these phenomena for interband tran-

sitions of semiconductor quantum wells, this work uses a single-particle density-matrix approach. The approach describes the steady-state absorption and gain factors not possible with perturbative or iterative approaches, and reveals a Fano-interference-like configuration as a proper choice for observing GWI in semiconductor quantum structures.

Previous work has shown that because of the near rigorous application of the interband selection rules, symmetric quantum wells show only reduced interband absorption,⁸ and not the true transparency in EIT. Therefore asymmetric quantum well configurations are examined. Using experimentally reported semiconductor scattering rates and dephasing times,⁹ numerical solution of the density-matrix equation integrated over momentum space is shown to give zero absorption and GWI. Achieving GWI in interband transitions requires combining control of energy levels and scattering mechanisms in asymmetric quantum wells to achieve Fano-like quantum interference.^{9,10}

The single-particle density-matrix solutions for the proposed three-level configurations ignore many-body effects. In addition, quasi-Fermi energy levels are used to describe the populations of both electrons and holes and equivalent exciton populations. For both excitonic and continuum transitions, "inversionless" requires that the respective quasi-Fermi levels be below the conduction-subband edge or above the valence-subband edge.⁹ The simplicity of the equivalent atomic effects is retained in this single-particle viewpoint without the phenomenology of many-body approaches. However, approaches including many-body effects or perhaps ultimately an elementary excitation description have been offered by others.¹³ In semiconductors, excited electrons and holes are accompanied by excitons and if concentrations are high enough, corrections due to many-body effects are necessary to describe properties such as gain.¹³

These quantum interference effects can also be applied to semiconductor devices such as group velocity compensators, nonlinear generation, optical amplifiers, inversionless and thresholdless laser diodes, unipolar far-infrared (IR) laser di-

odes, and even excitonic microlasers. Several device implications follow from the existence of GWI. Since a single atom microlaser has been recently demonstrated,¹⁴ a single carrier semiconductor microcavity laser is conceivable. The many-body effects dominating semiconductor laser diodes would be eliminated, permitting the operation of excitonic lasers. The necessity of population inversion in a semiconductor implies a threshold for lasing as well as the inevitable presence of noise. GWI provides possible routes to thresholdless lasing or optical amplification with the added benefit of noise reduction from suppressed spontaneous emission.¹⁰

In this paper single-particle density matrix results are briefly described, and semiconductor configurations analogous to atomic systems illustrated. Two principle semiconductor quantum well configurations, the optically coupled asymmetric single quantum well and the intrinsically coupled asymmetric double quantum well, are illustrated. Numerical results follow, showing the conditions for induced zero absorption and GWI.

II. FORMULATION AND CONFIGURATIONS

A new general density-matrix approach has been developed to analyze multilevel configurations under the assumption of known population distributions.⁸ For a three-level system, this results in analytic steady-state expression for the optical properties. Solutions cover all cases of induced zero absorption and GWI from either intrinsic or dc coupling, to optical coupling including coherent superposition, for both atoms to semiconductors, without further approximation.¹⁵

In real systems, optical fields and relaxation mechanisms provide the following single-particle density-matrix equation:

$$\frac{\partial \rho}{\partial t} = \frac{1}{i\hbar} [(\mathbf{H}_0 + \mathbf{H}_I), \rho] - \frac{1}{2} (\Gamma \rho + \rho \Gamma), \quad (1)$$

where ρ is a density operator with ρ_{ij} density-matrix elements, and Γ is the diagonal matrix given as the inverse of

the relaxation time τ_i for each state $|i\rangle$. H_0 is the unperturbed Hamiltonian, a diagonal matrix in $|a\rangle$, $|b\rangle$, $|c\rangle$, and $|d\rangle$ with energies E_a , E_b , E_c , and E_d . H_I is the interaction Hamiltonian, an off-diagonal matrix given by $H_I = u_p F_p + u_c F_c = M_p + M_c$, where F_p and F_c represent probing and coupling fields, and u_p and u_c are dipole matrix operators for interband and intersubband transitions in semiconductor quantum wells, respectively.

The electronic polarization P arising from probing and coupling fields is expressed in the following in terms of susceptibility, optical fields, dipole moment, and density matrix:

$$P(t) = \epsilon_0 \chi(t) [F_p(t) + F_c(t)] = \frac{2}{V} \sum [\mathbf{u} \rho(t) + \rho(t) \mathbf{u}], \quad (2)$$

where χ is the complex susceptibility, the factor of 2 arises from spin, and the summation could cover transverse momenta within volume V . If ρ can be solved in the frequency domain, then $\chi(\omega)$ is found from $\rho(\omega)$ as the solution of Eq. (1). The absorption coefficient and refractive index follow directly from $\text{Im}(\chi)$ and $\text{Re}(\chi)$, respectively. The goal of the density-matrix approach is, therefore, to solve only for $\rho(\omega)$ in terms of the level distributions. However, the solution of $\rho(\omega)$ does not include the effects of a continuous density of states and the Fermi distribution function, so the generalization to semiconductor quantum structures is necessary for numerical results by using the following relation of Eq. (3):

$$\chi(\omega) = \frac{1}{\epsilon_0 F(\omega)} \int f(E) D(E) [\mathbf{u} \rho(\omega) + \rho(\omega) \mathbf{u}] dE, \quad (3)$$

where $f(E)$ and $D(E)$ are the Fermi function and the density of states, respectively, and have fixed functional values. In Eq. (3) only $\rho(\omega)$ is undetermined.

The density-matrix element $\rho_{cb}(\omega_p)$ in the frequency domain embodies the result sought. The solution of ρ_{cb} from Eq. (1) follows as

$$\rho_{cb}(\omega_p) = \frac{(D_{db} D_{dc} - |\Omega_{cb}|^2) \Omega_{cb} (\rho_{bb} - \rho_{cc}) - \Omega_{cb} |\Omega_{cd}|^2 (\rho_{cc} - \rho_{dd})}{D_{cb} (D_{db} D_{dc} - |\Omega_{cb}|^2) - D_{dc} |\Omega_{cd}|^2}, \quad (4)$$

where $D_{ij} = [\omega - (E_i - E_j)/\hbar] + i\gamma_{ij}$ with $\gamma_{ij} = (\Gamma_{ii} + \Gamma_{jj})/2$, and $\Omega_{ij} = u_{ij} F/\hbar$. Since Ω_{cb} is the Rabi frequency of the probing field, it is usually small compared with Ω_{cd} , the Rabi frequency of the coupling field. When the population of the ground state, ρ_{bb} , dominates and is taken to have value unity, ρ_{cc} and ρ_{dd} have values close to zero, and $\Omega_{cd} \gg \Omega_{cb}$, Eq. (4) reduces to the equation

$$\rho_{cb}(\omega_p) = \frac{D_{db} \Omega_{cb}}{D_{cb} D_{db} - |\Omega_{cd}|^2}. \quad (5)$$

The same result is obtained from iterative perturbation, first-order perturbation, or renormalization diagram solutions.^{7,16,17} Furthermore, if there is no coupling or $\Omega_{cd} \ll \Omega_{cb}$, the solution, Eq. (4), is equivalent to a simple

two-level resonant transition. Comparing Eqs. (4) and (5), the importance of nonperturbative solutions is revealed. Perturbation solutions corresponding to Eq. (5) do not give the second and third terms of Eq. (4), which embody the nonlinear and emission processes, respectively.

The solution of Eq. (4) is represented in the terms of constant population diagonal density-matrix elements. This solution results in the steady-state populations, and is valid for arbitrary electromagnetic coupling field strength only in the presence of a weak probing field. Strong coupling and weak probing results in diagonal matrix elements that exhibit population trapping (through their representation as dressed states).¹⁸ However, dc or intrinsic coupling usually results in population oscillations damped to zero.¹⁹ Therefore this pa-

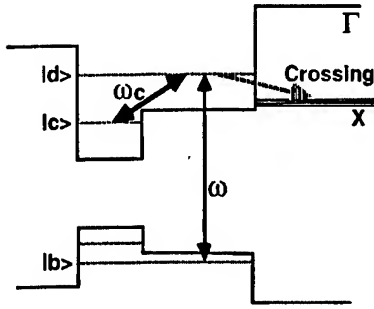


FIG. 1. Electromagnetically coupled asymmetric quantum well configuration with a band-crossing-induced scattering decay path for interband transitions.

per assumes that a quasi-steady-state situation is established upon carrier injection for the case of intrinsic coupling. In the following numerical calculations, optical injection is assumed to result in equal numbers of excited electrons and holes. Equal pumping is also a reasonable choice for configurations using electrical injection. Using quasi-Fermi-energy levels, the initial population distribution diagonal matrix elements are calculated and kept below population inversion.

In order to show induced zero absorption and GWI using the above density-matrix result, two asymmetric quantum well configurations are proposed. Figure 1 shows an asymmetric quantum well with a fast decay path introduced by band crossing between Γ and X conduction bands. The band crossing is the energy proximity of the direct band (Γ) of quantum wells with the indirect band (X) of a barrier. This permits fast scattering rates between the two energetically resonant states. In $\text{Al}_x\text{Ga}_{1-x}\text{As}$, the energy gap crossover from Γ to X bands occurs at an Al composition ratio of $x=0.4$. The Γ to X band scattering occurs only for the $n=2$ conduction subband, resulting in an unbalanced lifetime combination. In Fig. 1, an optical field (CO_2 laser) couples the $n=1$ and 2 conduction subbands, creating dressed states with the unbalanced lifetime combination and leading to induced zero absorption and GWI. The asymmetric quantum well configuration given in Fig. 1 consists of an $\text{Al}_{0.5}\text{Ga}_{0.5}\text{As}$ barrier, a narrow, 5-nm, $\text{Al}_{0.25}\text{Ga}_{0.75}\text{As}$ quantum well, a wide, 10-nm, $\text{Al}_{0.4}\text{Ga}_{0.6}\text{As}$ quantum well, and an AlAs barrier serving as the final state for band-crossing-induced scattering. While the $n=1$ states are localized in the narrow quantum well region, giving the $n=1$ transition a very limited envelope function overlap in the dipole matrix transition approximation, the $n=2$ states have increased spatial envelope function overlap. This increases the transition probability for the $n=2$ states and reduces the $n=1$ transition rates.

To utilize induced zero absorption or GWI in practical devices, external optical coupling schemes should be replaced by some form of internal coupling such as a dc electric field or intrinsic coupling via tunneling barriers. The asymmetric optical coupling configuration can be easily modified for dc or intrinsically coupled asymmetric double quantum well structures. Upon insertion of a thin barrier for intrinsic coupling, the system now has a pair of coupled states analogous to the dressed states of optical coupling. In order to utilize dc electric field coupling, degenerate states are necessary, requiring widely separated, identical wells,

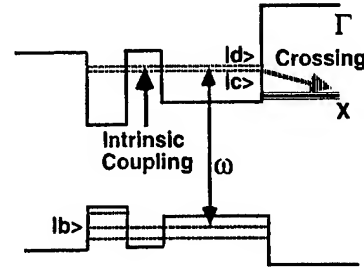


FIG. 2. Intrinsically coupled asymmetric quantum well configuration with a band-crossing-induced scattering decay path for interband transitions.

which then eliminates the coherence between the states. Therefore this paper considers only the intrinsic coupling configuration.

Figure 2 shows the intrinsic coupling configuration using a band-crossing decay path. The band-crossing-induced scattering is preferred here because it does not perturb valence-subband scattering as does the usual tunneling mechanism. The configuration in Fig. 2 consists of the $\text{Al}_{0.5}\text{Ga}_{0.5}\text{As}$ barrier, the narrow 2.5-nm $\text{Al}_{0.25}\text{Ga}_{0.75}\text{As}$ quantum well, the wide 7.0-nm $\text{Al}_{0.35}\text{Ga}_{0.65}\text{As}$ quantum well, the 2.5-nm $\text{Al}_{0.5}\text{Ga}_{0.5}\text{As}$ coupling barrier, and the higher AlAs barrier introducing the band-crossing-induced scattering.

III. NUMERICAL RESULTS

Both excitonic and continuum transitions are modeled numerically in these asymmetric configurations. Interband continuum transitions require numerical integration over all unconfined momentum space within the first Brillouin zone. The final result is assumed to be a superposition of both excitonic and continuum transitions (in the presence of strong electrical or optical injection, excitonic transitions will be screened out, leaving only modified continuum transitions). The numerical results for the configurations of Figs. 1 and 2 use an energy scale (in eV) for subband lifetimes and coupling field and probing field strength. The following semiconductor dephasing lifetimes are used: valence-subband lifetimes about $6 \mu\text{eV}$ corresponding to the ground state of elementary excitation (on the order of nanoseconds based on radiative recombination limitations²⁰), an $n=1$ conduction-subband lifetime of 0.3 meV (on the order of subnanoseconds deduced from elementary excitation²⁰ and excitonic lifetime²¹ measurements), and an $n=2$ conduction-subband lifetime of 6 meV (on the order of 100 fs due to Γ to X band scattering^{20,6}). As pointed out in the Introduction, coupled subband lifetimes unbalanced by more than one order of magnitude are crucial to induced zero absorption and GWI.

For excitonic transitions, the following results are calculated directly from the three-level atomic system as given by Eq. (4). Since excitons are elementary excitations consisting of pairs of electrons and holes, their energy levels and coupling mechanisms differ from the one-electron picture. However, excitonic systems can in many ways be treated as atomic systems. Therefore, without considering exact wave functions, a δ -function-like density of states is assumed for excitonic transitions, and as mentioned, excitonic and con-

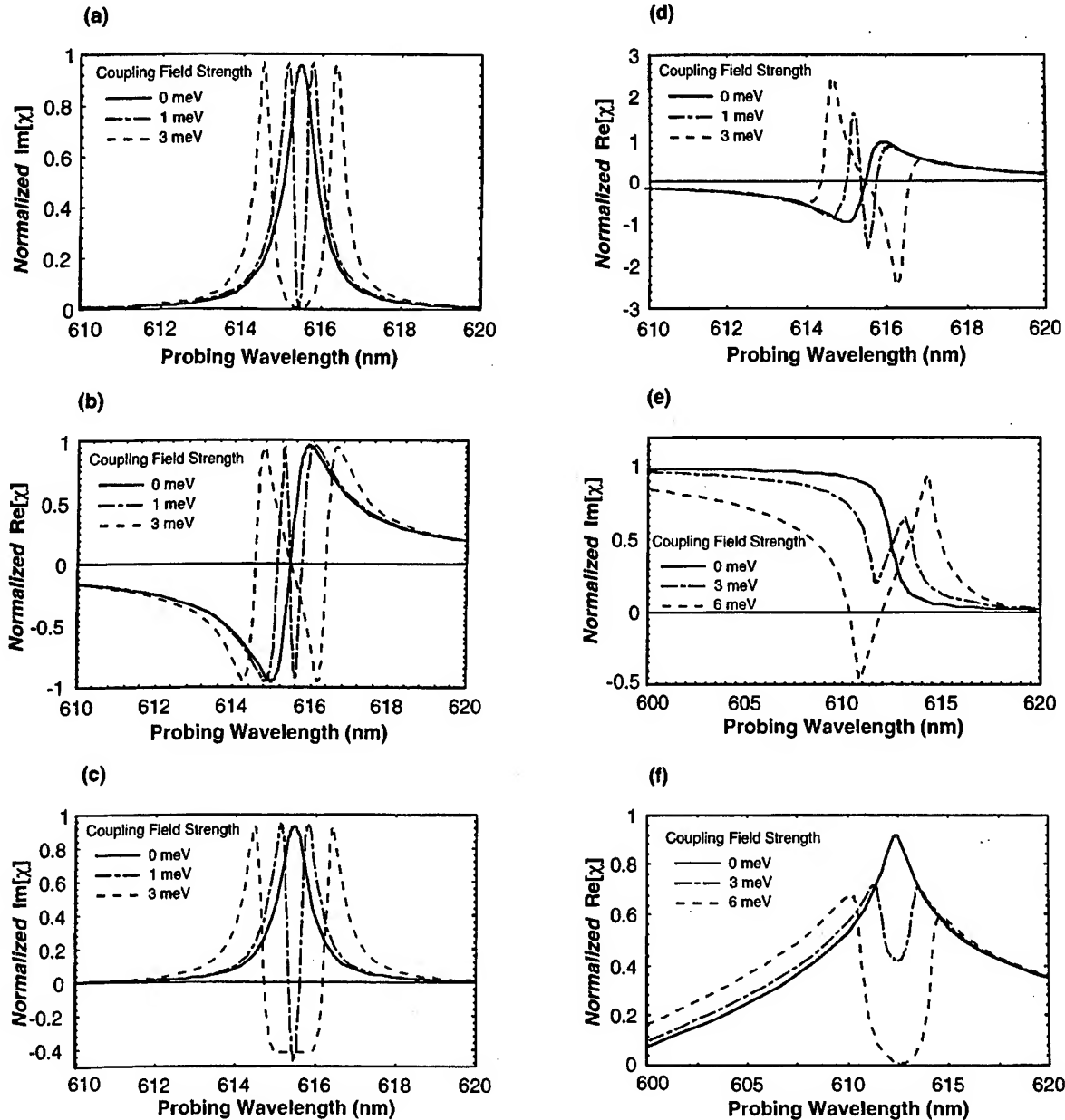


FIG. 3. Induced zero absorption and gain without inversion with corresponding index change in an electromagnetically coupled asymmetric quantum well configuration. All profiles are normalized to the two-level interband transitions (the solid lines). (a) Normalized susceptibility profiles for heavy-hole excitonic absorption. (b) Normalized susceptibility profiles for refractive index change in heavy-hole excitonic transitions. (c) Normalized susceptibility profiles for heavy-hole excitonic gain. (d) Normalized susceptibility profiles for refractive index change in heavy-hole excitonic gain. (e) Normalized susceptibility profiles for heavy-hole continuum absorption and gain. (f) Normalized susceptibility profiles for refractive index change in heavy-hole continuum transitions.

tinuum transitions are superimposed. In contrast to the continuum transitions, excitonic transitions are based on the empirical parametrization of excitonic oscillator strengths (dipole matrix elements) and lifetimes using the experimental data of Chemla *et al.* and Weisbuch and Vinter. Usually, excitonic oscillator strengths are larger than the continuum oscillator strength as reported by most experimentalists.^{20,21} In typical experiments using undoped multiple quantum well structures, the $n=1$ heavy-hole excitonic absorption coefficient is about $11\,000\text{ cm}^{-1}$, and the $n=1$ heavy-hole continuum absorption coefficient is about 5000 cm^{-1} . In the low injection limit, excitonic transitions dominate quantum well optical properties.

Figure 3 shows the absorption and index changes for the asymmetric quantum well structure for various electromagnetic coupling field strengths. Figure 3(a) depicts induced zero absorption for the $n=2$ excitonic transitions without excited carriers. The absorption modulation is as large as $11\,000\text{ cm}^{-1}$ (the full zero-field excitonic absorption), and the corresponding index change around the resonant wavelength is about 0.06 (without including the optical field confinement factor). These effects are large enough to be useful in optical modulators or group velocity compensators within the limited bandwidth.

Using the joint optical effective density of states as the reference population (about 10^{18} cm^{-3} in GaAs), an injected

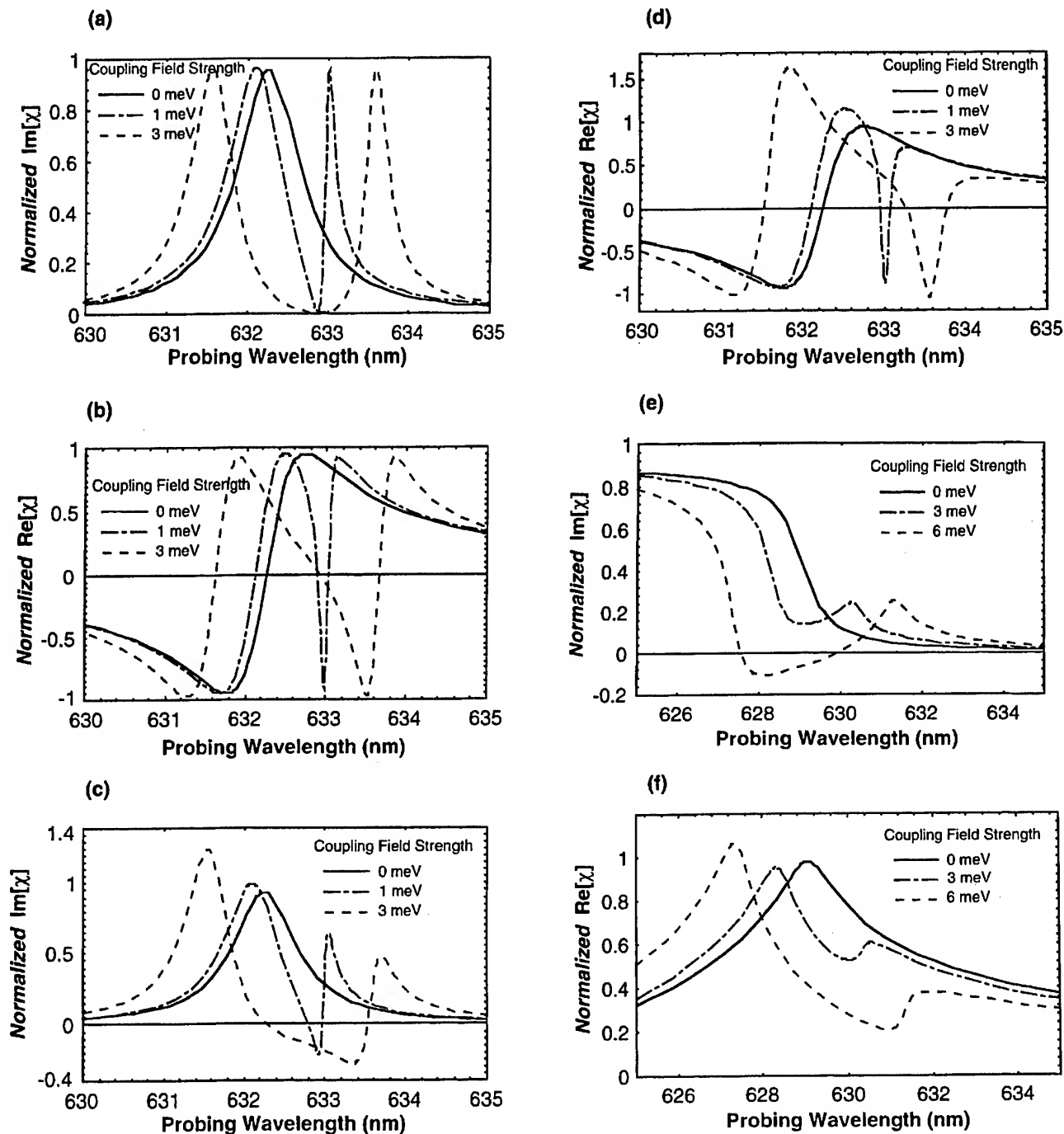


FIG. 4. Induced interband zero absorption and gain without inversion with corresponding index change in an intrinsically coupled asymmetric double quantum well configuration. All profiles are normalized by the two-level interband transitions (the solid lines). (a) Normalized susceptibility profiles for heavy-hole excitonic absorption. (b) Normalized susceptibility profiles for refractive index change in heavy-hole excitonic transitions. (c) Normalized susceptibility profiles for heavy-hole excitonic gain. (d) Normalized susceptibility profiles for refractive index change in heavy-hole excitonic gain. (e) Normalized susceptibility profiles for heavy-hole continuum absorption and gain. (f) Normalized susceptibility profiles for refractive index change in heavy-hole continuum transitions.

carrier concentration is introduced. With a slightly excited population of $\rho_{bb}=0.98$ and $\rho_{dd}=0.02$, this configuration exhibits GWI as shown in Fig. 3(b). The material gain (again, without considering the confinement factor) is as high as 5000 cm^{-1} , and the related index change is about 0.09 around the center frequency. The symmetric absorption pro-

file results in zero index change at the resonant transition frequency. Furthermore, the gain profile has a very narrow peak, resulting in extremely low spontaneous emission noise. This is very attractive for devices such as optical amplifiers and microlasers. Thus far atomic systems have been shown to lase with one atom in an ultrahigh- Q cavity. Such a laser

is called a microlaser,¹⁴ and is different from semiconductor microcavity lasers (a microcavity alters the spectral mode density). The asymmetric quantum well configuration is a good candidate for the active region of a single carrier semiconductor microlaser using an ultrahigh- Q cavity.

For continuum transitions, integration over transverse momentum space requires more excited carriers or stronger coupling to exhibit GWI. Stronger coupling and excited carriers both result in wider and deeper gain and the index modulation, as shown in Fig. 3(c). Momentum integration causes the gain profile to shift and become asymmetric. However, the maximum index changes still occur at the same point. Unlike the zero index change in excitonic transitions, the corresponding index change at the center wavelength is no longer zero because of density of state effects. The material gain is close to 2500 cm^{-1} with 6-meV coupling strength, the index change at the gain peak is negligible, and the maximum index change at the resonant point is about 0.05.

The intrinsically coupled asymmetric double quantum well differs from the electromagnetically coupled asymmetric quantum structure primarily due to off-resonant effects. In principle, it is possible to make two different sized quantum wells with the same energy levels that would result in exactly the same resonant intrinsic coupling as the *electromagnetic coupling field with zero frequency*. However, the more likely situation is to have slightly different energy levels resulting in off-resonant coupling effects. If the off-resonant difference is large, transitions will not have the destructive quantum interferences necessary for induced zero absorption or GWI. Figure 4 depicts the off-resonant results for induced zero absorption and GWI in both excitonic and continuum transitions.

Figure 4(a) shows induced zero absorption based on excitonic transitions. While zero absorption is possible, off-resonant effects reduce the absorption modulation to 5000 cm^{-1} . The corresponding index change is no longer zero at the center frequency, and the peak point of refractive index change also moves. The peak index change is about 0.07. Assuming proper electrically injected occupation of excited states ($\rho_{bb}=0.9$ and $\rho_{dd}=0.1$), Fig. 4(b) shows excitonic GWI. The material gain reaches about 2000 cm^{-1} , and the corresponding index change is approximately 0.05. Since only a small number of upper level excitons need be electrically injected, the intrinsic configuration can serve as the active region of an excitonic microlaser. For continuum transitions, Fig. 4(c) shows GWI under moderate coupling field strength and electrical injection. This continuum gain profile can have a very narrow linewidth with stronger coupling strength (10 meV, not in Fig. 4), and may be applicable to a thresholdless laser diode (ideal lasing without inversion). Figure 4(c) also shows the coupling field strength dependence of gain [same coupling field strength as Fig. 3(c)]. However, intrinsic coupling can be equivalent to very large electromagnetic coupling. The intrinsic coupling between 25- and 75-Å quantum wells separated by a 25-Å barrier is equivalent to a 10-meV electromagnetic coupling assuming the wells to be within the coherence length of the system. The resulting material gain in Fig. 4(c) is close to 600 cm^{-1} with 6-meV intrinsic coupling and moderate electrical pumping (same quasi-Fermi levels as excitonic transitions). The index change at the gain peak is again negligible, and the

maximum index change is about 0.02. This material gain is large enough for a microlaser, but more gain is also possible by using the normal coupling strength (10 meV) or increasing injection.

IV. SUMMARY AND DISCUSSION

This paper theoretically examined induced zero absorption and GWI in asymmetric quantum wells using a single-particle density-matrix approach and experimentally measured semiconductor parameters. In order to examine the optical properties of these semiconductor quantum well configurations, quasi-Fermi-energy levels are kept well below the conduction subband (or above an active valence subband) involved in the optical transitions. GWI based on excitonic transitions in semiconductor quantum wells possesses many properties similar to atomic transitions and hence may give comparable performance. However, continuum transitions in semiconductors are considerably different than those in atomic systems and can impede the observation of GWI in quantum wells. However, the gain present in semiconductor quantum wells is still considerably larger than the gain of any atomic system, giving promise to practical devices based on semiconductor laser diodes. This paper concludes that asymmetric semiconductor quantum well structures can be designed so that the basic requirements of lasing without inversion are met.

Using these phenomena, the results based on intrinsic coupling were shown to be consistent with the requirements of semiconductor laser diodes. Since GWI requires only low carrier concentrations, it is also possible that excitonic lasing may occur in such a microlaser diode. GWI reduces the required number of injected carriers in an active region, and should result in a considerable reduction in the lasing threshold. Since the gain profiles are narrower than normal Lorentzian line shapes, spontaneous emission noise is reduced, offering a new mechanism for low noise optical amplifiers.

Several issues remain, principally the exact dephasing mechanisms occurring for each subband energy level in a semiconductor, the role of many-body effects on those lifetimes and the use of intrinsic coupling to establish quantum-mechanical coherence. Intrinsic coupling is certainly a requirement for any practical implementation. However, as intrinsic coupling is generally absent in atomic systems, there are few investigations of the utility of such coupling mechanisms in multiphoton quantum electronic phenomena. When compared with optical coupling, understanding of such coherent effects as population trapping is lacking. However, the broad array of coherent phenomena already demonstrated in semiconductor structures (described in Refs. 6–12) suggests the ability to tailor both the excitation spectra and their respective lifetimes and promises still further innovation.

ACKNOWLEDGMENT

This work was supported by The Air Force Office of Scientific Research (AFOSR).

- ¹S. E. Harris, Phys. Rev. Lett. **62**, 1033 (1989); S. E. Harris, J. E. Field, and A. Imamoglu, *ibid.* **64**, 1107 (1990).
- ²M. O. Scully, S. Zhu, and A. Gavrielides, Phys. Rev. Lett. **62**, 2813 (1989); M. O. Scully, *ibid.* **67**, 1855 (1991).
- ³K.-J. Boller, A. Imamoglu, and S. E. Harris, Phys. Rev. Lett. **66**, 2593 (1991).
- ⁴A. Nottelmann, C. Peters, and W. Lange, Phys. Rev. Lett. **70**, 1783 (1993); E. S. Fry *et al.*, *ibid.* **70**, 3235 (1993); W. E. van der Veer *et al.*, *ibid.* **70**, 3243 (1993).
- ⁵A. S. Zibrov, M. D. Lukin, D. E. Nikonov, L. Hollberg, M. O. Scully, and V. L. Velichansky, Phys. Rev. Lett. **75**, 1499 (1995).
- ⁶K. Maschke, P. Thomas, and E. O. Göbel, Phys. Rev. Lett. **67**, 2646 (1991).
- ⁷D. Fröhlich *et al.*, Phys. Rev. Lett. **59**, 1748 (1987).
- ⁸D. S. Lee and K. J. Malloy, in *Optical Society of America Annual Meeting, Albuquerque, 1992*, Technical Digest Vol. 23 (Optical Society of America, Washington, DC, 1992), p. 99; IEEE J. Quantum Electron. **QE-30**, 85 (1994).
- ⁹D. S. Lee *et al.*, in *International Quantum Electronics Conference, Anaheim, 1994*, Technical Digest Vol. 9 (Optical Society of America, Washington, DC, 1994), p. QPD24/61; in *Quantum Electronics Conference, Baltimore, 1995*, Technical Digest Vol. 16 (Optical Society of America, Washington, DC, 1995), p. 79.
- ¹⁰D. S. Lee, Ph.D. dissertation, University of New Mexico, 1995.
- ¹¹A. Imamoglu and R. J. Ram, Opt. Lett. **19**, 1744 (1994).
- ¹²J. Faist *et al.*, Science **264**, 553 (1994).
- ¹³Z. Yang and D. Huang, Phys. Rev. A **51**, 1617 (1995).
- ¹⁴K. An *et al.*, Phys. Rev. Lett. **73**, 3375 (1994).
- ¹⁵K. Hakuta, L. Marnet, and B. P. Stoicheff, Phys. Rev. A **45**, 5152 (1992).
- ¹⁶K. H. Hahn, D. A. King, and S. E. Harris, Phys. Rev. Lett. **65**, 2777 (1990).
- ¹⁷P. J. Harshman *et al.*, Opt. Lett. **18**, 1706 (1993).
- ¹⁸R. W. Boyd, *Nonlinear Optics* (Academic, Boston, 1992), p. 214.
- ¹⁹C. Cohen-Tannoudji, B. Diu, and F. Laloë, *Quantum Mechanics* (Hermann, Paris, 1977).
- ²⁰G. Weisbuch and B. Vinter, *Quantum Semiconductor Structures* (Academic, San Diego, 1991).
- ²¹D. S. Chemla *et al.*, IEEE J. Quantum Electron. **QE-20**, 265 (1984).

Blocking of resonant tunneling by electron Bragg reflectors in GaAs/Al_xGa_{1-x}As quantum well structures

Seung-Chang Lee and Kevin J. Malloy

Center for High Technology Materials, University of New Mexico, 1313 Goddard, SE, Albuquerque, New Mexico 87106

(Received 6 July 2000; accepted for publication 18 October 2000)

We examine the blocking of electrons selectively incident on a GaAs/Al_{0.22}Ga_{0.78}As electron Bragg reflector (EBR) from a GaAs/Al_{0.3}Ga_{0.7}As double barrier resonant tunneling structure (DBRTS). An EBR has a minimum transmittance at a specified blocking energy level, E_B . This energy level is varied with respect to a resonant tunneling energy, E_{INJ} , of the DBRTS. We find that the blocking efficiency is decreased as E_B moves away from E_{INJ} . To satisfy the Bragg condition, any potential barrier in the EBR must be lower than E_{INJ} . We present experimental evidence of blocking by EBRs and compare it with blocking by potential barriers higher than E_{INJ} . © 2001 American Institute of Physics. [DOI: 10.1063/1.1332094]

I. INTRODUCTION

Electron Bragg reflectors (EBRs) consist of one-quarter de-Broglie-wave stacks of semiconductor layers and are analogous to optical Bragg reflectors. Recently, EBRs have been used in quantum cascade (QC) laser diodes.¹ The lasing mechanism in QC lasers consists of the injection of electrons into a upper emission state of an active region, followed by an intersubband transition to a lower state emitting an infrared (IR) photon and concluding with the transit of the electrons through a relaxation-injection (RI) region. In the RI region, the electrons lose their kinetic energy and are guided into the next upper emission state.

In a QC laser, however, electrons injected from the previous RI region into an emission state can tunnel through an active region without undergoing an intersubband IR emission transition. To enhance the IR emission, the RI region must prevent this direct tunneling out of the emission state. It has been known that an EBR can be designed to have a minimum transmittance at a selected energy level. Therefore, if the selected EBR blocking energy level coincides with the emission state, it can suppress this tunneling from the emission state, increasing the nonradiative lifetime of the emission state and improving the radiative efficiency. This EBR blocking effect is crucial to efficient QC emission.

Generally, there are two ways of blocking electron tunneling: one is an EBR and the other is a potential barrier with energy greater than the injected energy of the electron. These two cases are illustrated in Fig. 1. Blocking by the EBR depends on constructive interference between injected and reflected electrons which limits electron transport while blocking by the high potential barrier is limited by quantum mechanical tunneling. In this work, we quantitatively examine blocking of resonant tunneling by EBRs. We also compare it with blocking by potential barriers higher than injected energy level.^{2,3}

II. DEVICE DESIGN

As shown in Fig. 2(a), our device structure is an EBR combined with a double barrier resonant tunneling structure (DBRTS), which together we call a double barrier-Bragg reflector diode (DBBRD).

In our device structure, the DBRTS serves as an energy filter, selecting the energy of the electrons incident on the EBR. The DBRTS is undoped and composed of 16 monolayers (MLs) of Al_{0.3}Ga_{0.7}As, 24 MLs of GaAs, and 16 MLs of Al_{0.3}Ga_{0.7}As. At zero bias, it provides two quantized states at $E_1 = 51$ meV and $E_2 = 178$ meV with respect to the bottom of conduction band of GaAs. Thus the DBRTS can mimic the role of an active region of a QC emission structure if we inject electrons into the E_2 state. This is accomplished by employing an Al_{0.12}Ga_{0.88}As layer, with a conduction band offset of $\Delta E_C = 95$ meV, as an emitter. Since $E_1 < \Delta E_C < E_2$, the raised emitter precludes resonant injection into the E_1 state. It also lowers the peak resonance voltage. The EBR is therefore designed to block the tunneling from the E_2 state.

We designed the EBRs using the following condition:⁴

$$\int_{L_{w,j}} k_{w,j}(z) dz = \frac{\pi}{2}, \quad \int_{L_{b,j}} k_{b,j}(z) dz = \frac{\pi}{2}, \quad (1)$$

where

$$k_{w,j}(z) = \sqrt{\frac{2m_w^*}{\hbar^2} [E - V_{w,j}(z)]},$$

$$k_{b,j}(z) = \sqrt{\frac{2m_b^*}{\hbar^2} [E - V_{b,j}(z)]}.$$

Here, $k_{w,j}(k_{b,j})$ and $L_{w,j}(L_{b,j})$ are the electron wavevector and thickness of the j th well (barrier), $m_w^*(m_b^*)$ and $V_{w,j}(V_{b,j})$ the effective mass and potential energy of an electron in the j th well (barrier) of the EBR, respectively, z the axis along the growth direction, E the total energy of the electron, and $\hbar = h/2\pi$ where h is Planck's constant. It is important to note that the Bragg condition is not defined if

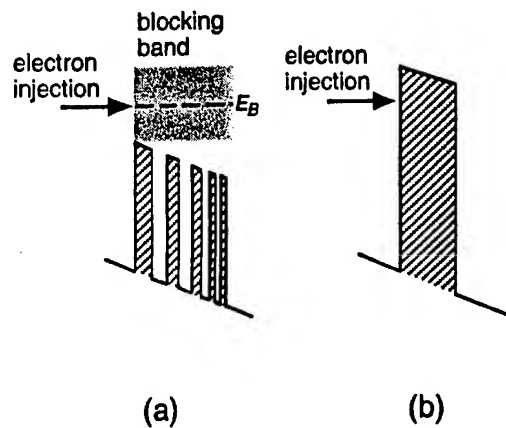


FIG. 1. Schematic conduction band diagram of blocking of electron injection by (a) an EBR and (b) a high potential barrier born under bias.

$k_{w,j}$ or $k_{b,j}$ is imaginary. This is the case in potential barrier blocking of Fig. 1(b) where the injected energy of the electron is less than the barrier and transmission occurs through tunneling. Design begins by choosing an applied field, F_a , at which the E_2 state and the energy level localized in the emitter accumulation region, E_{acc} , are in resonance. This then determines the energy of the electrons injected into the EBR, E_{INJ} . Self-consistent calculations give $F_a = 2.75 \times 10^4$ V cm^{-1} for the resonant tunneling of the E_2 state in our DBRTS. From this condition, $E_{INJ} = 195$ meV with respect to the zero-energy reference shown in Fig. 2(a). For the given F_a , we can design an EBR which has a specified blocking energy level, E_B , indicated in Fig. 2(a). This can be achieved through replacing E by the desired E_B in Eq. (1). Since the blocking efficiency defined later in this work directly depends on the separation between E_{INJ} and E_B , the shift of E_B from E_{INJ} reduces the blocking efficiency of EBR. Several EBRs, each with a different E_B were designed using Eq. (1). We expect maximum blocking when $E_B = E_{INJ}$.

Letting L denote the total thickness $[\sum_j (L_{w,j} + L_{b,j})]$ of the EBR, we constrain L to 99 ± 1 MLs, shorter than the reported electron mean-free path in undoped GaAs. Replacing the EBR by undoped GaAs of the same thickness should result in the ballistic transport through this 99 ML thick region of most electrons tunneling from the DBRTS.⁵

As mentioned previously, Eq. (1) holds only if E_B is higher than any barrier in the EBR for a given F_a . Otherwise, the wave vectors of incident electrons become imaginary. To avoid this condition, the barrier height of the EBR

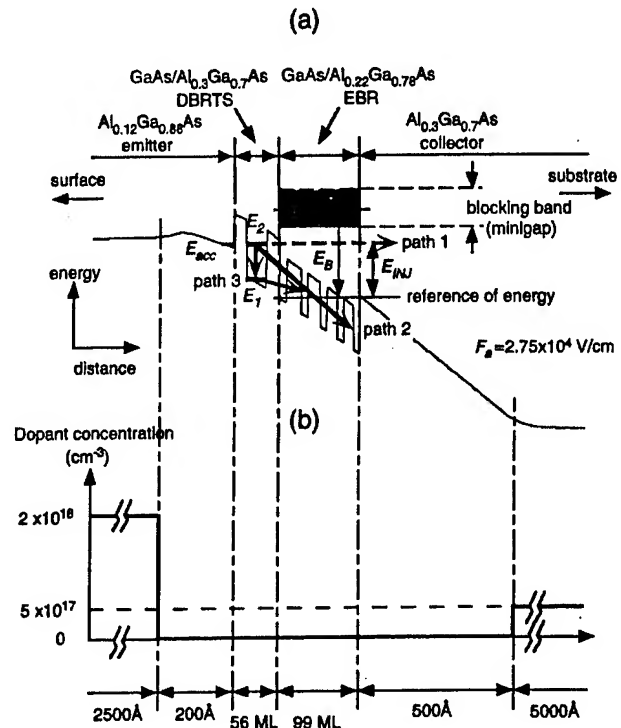


FIG. 2. (a) Schematic diagram of the conduction band of a GaAs/Al_xGa_{1-x}As DBBRD. Bold arrows indicate the possible current paths. In this figure, $E_{INJ} = 195$ meV $< E_B$. (b) Si dopant distribution in the device structure. A 200 Å undoped Al_{0.12}Ga_{0.88}As spacer was inserted before the first barrier and a 500 Å Al_{0.3}Ga_{0.7}As spacer inserted before the collector to avoid charge transfer into a DBRTS and an EBR at zero bias.

layers should be chosen so that all tunneled electrons are more energetic. For our F_a , the highest barrier allowed is Al_{0.24}Ga_{0.76}As. Furthermore, as can be seen from Eq. (1), lower Al compositions increase the thickness of each barrier, leading to a reduction in the total number of layers in the EBR, N , for a fixed L . Smaller N results in less constructive interference and hence higher transmittance. Al_{0.22}Ga_{0.78}As, which maximizes N for a given L without blocking E_{INJ} , was chosen as the barrier material.

Because of the small number of periods shown in Table I, a distance miniband and a blocking band may not form.^{1,6,7} Instead, a minimum transmittance as a function of energy occurs. At the given F_a and L , E_B was varied from 195 meV to 347 meV as detailed in Table I. For E_B of 195, 238, 287, and 347 meV, the calculated transmittance at E_{INJ} has the

TABLE I. Structure of EBRs determined by Eq. (1). Odd and even layer numbers correspond to wells and barriers, respectively. Considering interface roughness in MBE growth, we used ML as a unit of thickness.

E_B (meV)	Layer number															Total thickness (ML)
	1	2	3	4	5	6	7	8	9	10	11	12	13	14	15	
195	9	18	8	15	8	13	8	12	7							98
238	8	13	7	12	7	11	7	10	7	10	7					99
287	7	10	7	9	7	9	6	9	6	8	6	8	6			98
347	6	8	6	8	6	8	6	7	6	7	6	7	6	7	6	100

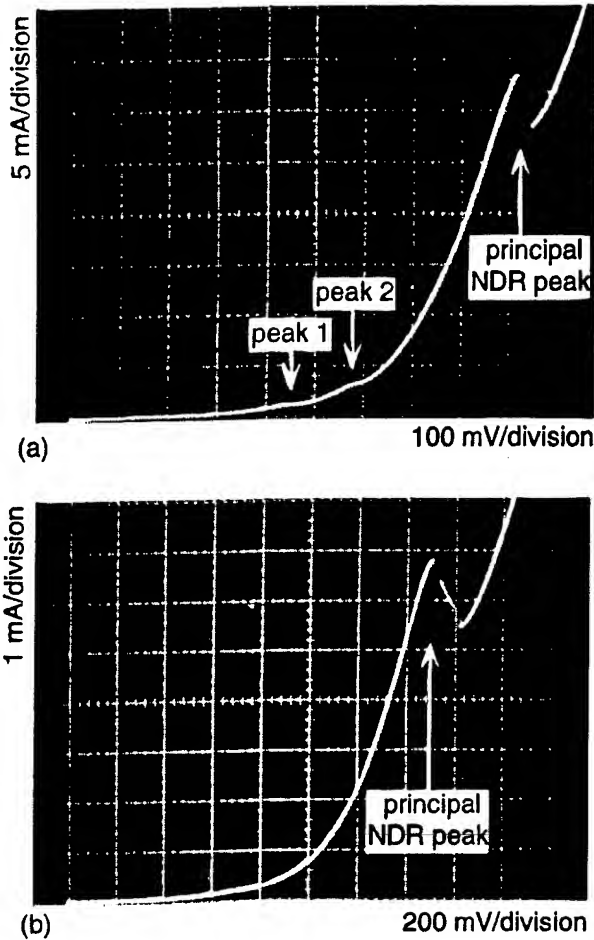


FIG. 3. I - V characteristics of (a) the $E_B = 195$ meV EBR and (b) the high potential barrier at 77 K.

value of 2.81×10^{-3} , 0.201, 0.487, 0.901, respectively. This means that the transmittance is increased and approaches unity as E_B moves away from E_{INJ} . We refer to $E_B = E_{\text{INJ}}$ as the optimal level alignment for a maximum blocking (or a minimum transmittance). In Table I, E_B was selected from the constraint of fixed L . As previously discussed, for a given L , the N for the EBR increases with E_B and is also reflected in the designs summarized in Table I.

In Fig. 2(a), as indicated by bold arrows, the EBR has several current paths through which the injected electrons can contribute to the collector current. To examine the blocking efficiency, all the current paths except ballistic transport through the EBR [path 1 in Fig. 1(a)] should be eliminated.⁸ For this purpose, $\text{Al}_{0.3}\text{Ga}_{0.7}\text{As}$ having a potential barrier higher than the EBR under bias was used as the collector. This high-barrier collector blocks path 2 which includes all current contribution through the EBR except paths 1 and 3 and blocks path 3 which results in IR emission from the intersubband transition in Fig. 2(a). However, this collector will not eliminate thermionic emission from electron accumulation regions in the DBRTSs or EBRs. This results in a residual background current not considered in our experiment.

In principle, the EBR can be precisely designed for alignment of E_{acc} , E_2 , and E_B indicated in Fig. 1(a), at a

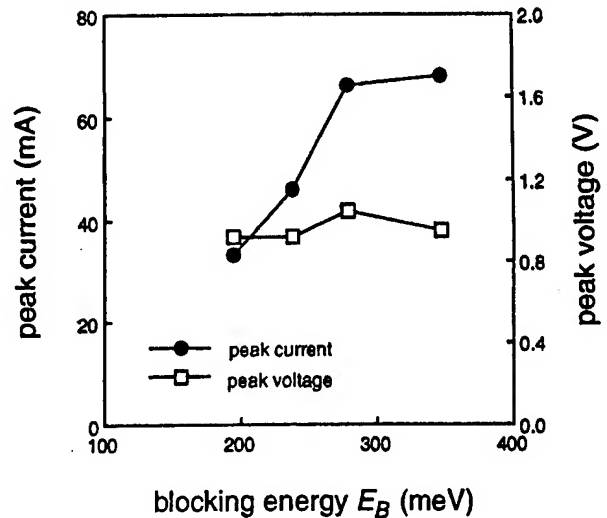


FIG. 4. 77 K E_B -dependencies of the peak current and voltage of the principal NDR observed in DBBRDs.

given F_a . However, thickness fluctuations of ± 1 ML in the layers of the EBR result in a change of $\sim \pm 30\%$ in F_a . Fortunately, an EBR has a narrow but finite energy width of significant blocking efficiency with respect to E_B .¹ In this experiment, as seen in Table I, E_B is varied around the value for optimal level alignment.

III. FABRICATION

The samples were grown on n^+ ($2 \times 10^{18} \text{ cm}^{-3}$) GaAs(001) substrates by molecular beam epitaxy. Two Al effusion cells and one Ga cell were used for three Al compositions. Figure 2(b) shows the dopant distribution in the basic structure. Devices were processed with conventional photolithography using Ge/Au/Ni/Au metallization for the top and substrate contacts. Devices were defined by $50 \mu\text{m} \times 50 \mu\text{m}$ Ohmic contacts which served as masks for chemical mesa etching. The current-voltage (I - V) characteristics of the DBBRDs were measured at 77 K with a curve tracer.

IV. RESULTS AND DISCUSSION

Figure 3(a) shows the 77 K I - V characteristic of the DBBRD with $E_B = 195$ meV. In Fig. 3(a), a negative differential resistance (NDR) was observed at 0.92 V. Two additional peaks appear in the I - V at 0.41 V (peak 1) and 0.55 V (peak 2). A similar I - V curve has been previously reported and was attributed to NDRs from quantized levels localized at the accumulation layer between an emitter and a double barrier.⁹ In both these situations, the principal NDR occurs for tunneling from the ground state of these localized accumulation region levels into the E_2 state.⁹⁻¹¹

Figure 4 presents the dependence of the peak current and voltage of the principal NDR on E_B . As E_B varies from 195 meV to 347 meV, the peak current increases from 33.5 mA to 67.0 mA. The two additional NDRs (not shown in this figure) also show similar dependencies. As previously described for the device design, minimum transmittance through the structure occurs for E_B around $E_{\text{INJ}} = 195$ meV.

The NDR peak current should also have a minimum around this value and should increase with E_B , as Fig. 4 shows it does. However, Fig. 4 shows that the peak *voltage* of the principal NDR depends only weakly on E_B with a value near 0.95 V for all samples. This implies that the overall electric field distribution and conduction band profiles of the DBBRDs are not strongly affected by the EBR design of Table I. This makes it possible to compare peak currents of Fig. 4 with each other directly without detailed consideration of field variation over the device structure. Therefore, Fig. 4 provides important experimental evidence that an EBR can selectively block transport through the E_2 state of a DBRTS. Also in Fig. 4, the peak current saturates for E_B around 347 meV. This is reasonable since the tunneling peak current should remain finite as E_B increases and transmittance approaches unity.

Let I_{P0} denote the peak current for the EBR for $E_B = 347$ meV which occurs for the highly-nonoptimal alignment. If I_P is the peak current observed for the optimal alignment of E_B , we can define the blocking efficiency, γ , as

$$\gamma = \frac{I_{P0} - I_P}{I_{P0}}. \quad (2)$$

Experimentally, we find an optimally designed EBR, where $E_B = E_{\text{INJ}}$, blocks resonantly injected current as compared with the highly-nonoptimal EBR with an efficiency γ of about 50% (33.5 out of 67.0 mA). It should be emphasized that γ defined in Eq. (2) is an approximation to the blocking efficiency which underestimates the actual value. This is because other current contributions than those in Fig. 1 occur in the device. In particular, thermionic emission from electron accumulation regions in a device will not be identical in all cases and constitute an uncontrolled residual current contribution to I_P and I_{P0} .¹²

To compare γ of the EBR with that of a high potential barrier like Fig. 1(b), we increase the barrier height by adding more Al to the $\text{Al}_{0.22}\text{Ga}_{0.78}\text{As}$ layers. For the $E_B = 195$ meV EBR design in Table I, we grew another sample with Al composition increased from $x = 0.22$ to 0.35 in the EBR region only. This change in Al composition violates the condition given by Eq. (1) and resonant tunneling is now blocked by the high potential barriers as suggested in Fig. 1(b). Figure 3(b) shows the I - V curve obtained from this high barrier DBBRD which is otherwise identical to the device in Fig. 3(a).¹³ Its peak current has decreased to 6.8 mA and the peak voltage has moved to 1.52 V.

We draw one conclusion and make one comment from our experiments. The blocking efficiency of the optimally designed EBR is much lower than the value based on the calculated transmittance. While more careful design and growth of the EBR might improve the experimental blocking efficiency, current leakage due to the finite blocking energy width and inelastic or incoherent scattering at the many interfaces in the EBR must allow excess current flow. The peak-to-valley ratios of 1.20 and 1.26 in Figs. 3(a) and 3(b) respectively, are low compared with those of typical DBRTSs. This degradation can also be attributed to interface and alloy scattering in the EBRs.¹² As seen in Fig. 4, however, it is evident that the peak current is increased from 33.5

mA to 67.0 mA as E_B increased from E_{INJ} to 347 meV. Thus, we conclude that the EBRs studied in this work can block the tunneling of electrons out of the E_2 state with a maximum blocking efficiency of 50%.

According to our results, the EBR does block some tunneling electrons, but its efficiency is lower than expected from reported QC laser performance.^{4,6,7,14} It should be noted that the design of our active region differs from the actual active regions of QC lasers. As previously mentioned, any RI region may block electron transport in two ways. In an EBR, the transmittance is minimized *only* through the constructive interference between injected and reflected electrons described by the phase relation of Eq. (1). In high potential barriers, the wave vectors of injected electrons are imaginary in the barrier, the transmittance is proportional to $\exp(-2\int |k_b| dz)$, and is rapidly reduced by increasing the barrier height or thickness. The calculated transmittance of the high barrier DBBRD is on the order of 10^{-6} . Although the high barrier DBBRD has a higher peak voltage than the EBR with $E_B = 347$ meV, implying a different energy band alignment, its experimental transmittance is about 10% of the assumed 100% current flow giving γ of about 90%. Therefore, we comment that a high potential barrier is better than an EBR in blocking electron tunneling.

In QC lasers reported thus far, multilayer structures having barrier heights greater than E_{INJ} have been used for RI regions (and active regions) to block electron tunneling. Strictly speaking, they do not satisfy Eq. (1) for electron energies at E_{INJ} and achieve blocking through high potential barrier. As shown in this work, the high potential barrier is more effective than the EBR in suppressing tunneling out of an emission state, ultimately leading to high QC laser efficiency. Adjusting well widths to eliminate nearby states reduces the possibility of sequential tunneling out of the emission state and also improves the blocking efficiency. Simultaneously, the ground states of these wells can be used to form a miniband guiding electrons after undergoing intersubband transitions into the next emission state. Again, transport through such a miniband is not a Bragg phenomenon.

While Eq. (1) leads to extremely low calculated transmittances at E_{INJ} , in our devices, current leakage could occur owing to the finite EBR blocking energy width and to inelastic scattering processes. Attempts to apply EBR design rules based on Eq. (1) when the barrier heights exceed E_{INJ} may create an unfavorable distribution of quantized states. The formation of a proper miniband consisting of ground states in such a RI region is probably more critical to QC laser operation.

V. CONCLUSION

We have investigated electron transport through $\text{GaAs}/\text{Al}_x\text{Ga}_{1-x}\text{As}$ DBBRDs which mimic a single stage of a basic QC structure. A properly designed EBR was shown to selectively block about 50% of the injected resonant tunneling current. However, a high potential barrier blocks resonant tunneling with a blocking efficiency of about 90%. This

suggests that a high potential barrier can be a better choice for blocking of direct tunneling out of the emission state in QC structures.

ACKNOWLEDGMENTS

This work was supported by AFOSR under grant F49620-95-I-0325.

- ¹For review, see J. Faist, F. Capasso, D. L. Sivco, C. Sirtori, A. L. Hutchinson, and A. Y. Cho, *Science* **264**, 553 (1994), and references therein.
- ²T. Nakagawa, H. Imamoto, T. Sakamoto, T. Kojima, K. Ohta, and N. Kawai, *Electron. Lett.* **21**, 883 (1985).
- ³T. Takeshi, F. Koyama, and K. Iga, *Appl. Phys. Lett.* **59**, 2877 (1991).
- ⁴C. Sirtori, J. Faist, F. Capasso, D. L. Sivco, and A. Y. Cho, *Appl. Phys. Lett.* **62**, 1931 (1993).
- ⁵A. G. J. Levi, J. R. Hayes, P. M. Platzman, and W. Wiegmann, *Phys. Rev. Lett.* **55**, 2071 (1985).

⁶C. Sirtori, F. Capasso, J. Faist, D. L. Sivco, A. L. Hutchinson, and A. Y. Cho, *Appl. Phys. Lett.* **66**, 4 (1995).

⁷J. Faist, F. Capasso, C. Sirtori, D. L. Sivco, A. L. Hutchinson, and A. Y. Cho, *Appl. Phys. Lett.* **66**, 538 (1996).

⁸We assume no charge accumulation in the EBR that significantly alters the electrostatic band diagram. This assumption is supported by experimental results discussed later.

⁹J. S. Wu, C. Y. Chang, C. P. Lee, K. H. Chang, D. G. Liu, and D. C. Liou, *Appl. Phys. Lett.* **57**, 2311 (1991).

¹⁰P. Mouniz, O. Vanbesien, and D. Lippens, *Appl. Phys. Lett.* **57**, 1517 (1990).

¹¹T. Fiig and A. P. Jauho, *Appl. Phys. Lett.* **59**, 2245 (1991).

¹²C. Weisbuch and B. Vinter, *Quantum Semiconductor Structures* (Academic, New York, 1991).

¹³In the real sense, the device of Fig. 3(b) does not include an EBR but for convenience we call it a high barrier DBBRD.

¹⁴C. Sirtori, P. Kruck, S. Barbieri, P. Collot, J. Nagle, M. Beck, J. Faist, and U. Oesterle, *Appl. Phys. Lett.* **73**, 3486 (1998).

Passive mode-locking in 1.3 μm two-section InAs quantum dot lasers

Xiaodong Huang,^{a)} A. Stintz, Hua Li, L. F. Lester, Julian Cheng, and K. J. Malloy
*University of New Mexico, Center for High Technology Materials, 1313 Goddard SE, Albuquerque,
 New Mexico 87106*

(Received 24 January 2001; accepted for publication 14 March 2001)

Passive mode locking was achieved at 1.3 μm in oxide-confined, two-section, bistable quantum dot (QD) lasers with an integrated intracavity QD saturable absorber. Fully mode-locked pulses at a repetition rate of 7.4 GHz with a duration of 17 ps were observed under appropriate bias conditions. No self-pulsation accompanied the mode locking. These results suggest that a carefully designed QD laser is a candidate for ultrashort pulse generation. © 2001 American Institute of Physics.
 [DOI: 10.1063/1.1371244]

Quantum dot (QD) laser characteristics have significantly improved, and now show advantages over quantum well (QW) lasers. Room temperature cw operation with very low threshold density at 1.3 μm ,¹⁻⁵ high characteristic temperatures,⁶ high power,⁷ high temperature cw operation,⁸ high efficiency,⁹ and high speed¹⁰ have all been recently demonstrated in QD lasers. A 1.3 μm vertical cavity surface emitting laser has also been reported.¹¹ Thus far, however, mode locking of QD lasers to generate ultrashort pulses has not been reported. Mode-locked semiconductor lasers are attractive for many applications,¹² particularly for high-speed, optical time division multiplexed telecommunication systems, because of their capability of producing pulses at repetition rates well beyond the modulation bandwidths of semiconductor lasers.^{13,14} In this letter, we report the passive mode locking of an 1.3 μm , oxide-confined, two-section lasers with an integrated intracavity QD saturable absorber.

The devices were fabricated from the same wafer as described in Ref. 3. The wafer was grown by solid-source *molecular beam epitaxy* on a (001) n^+ -GaAs substrate. The active region consists of two InAs quantum-dots-in-a-well layers¹⁵ separated by a 30 nm GaAs barrier layer, situated in the middle of a 220-nm-thick GaAs waveguide bounded by $\text{Al}_{0.7}\text{Ga}_{0.3}\text{As}$ cladding layers. The devices have a typical two-section laser structure with a 50 μm gap in the top p -type contact metals. The lengths of the gain section and the absorber section are $L_g = 4.73$ mm and $L_a = 0.85$ mm, respectively. An isolation resistance of 2.86 k Ω is achieved between these two sections by using shallow dry etching to remove the heavily doped cap layer in the gap region. Current confinement is provided by the wet lateral oxidation of a 50-nm-thick $\text{Al}_{0.98}\text{Ga}_{0.02}\text{As}$ layer positioned between the waveguide and the upper cladding layers, resulting in a narrow current aperture of 10 μm .³ No coating is applied to the cleaved facets. The devices were mounted on a copper heat sink with the p -side up, and were tested at room temperature.

The dc characteristics of the device were measured with current injection into the gain section (I_g) and a constant reverse bias voltage (V_a) applied to the absorber section. Room temperature lasing occurred on the QD ground state ($\lambda = 1278$ nm). Figure 1 shows the output power (L) emitted from the absorber facet and the voltage (V_g) across the gain

section versus the forward and backward sweep of the laser current under two different absorber bias conditions: (a) short-circuited, $V_a = 0.0$ V and (b) a reverse bias of $V_a = -5.0$ V. The L - I_g characteristics exhibit clear counterclockwise hysteresis loops and bistability. The loop position shifts to higher laser current with increasing absorber reverse bias, while the loop width increases. Note that the V_g - I_g characteristic for $V_a = -5.0$ V is slightly displaced due to the leakage current between the gain section and the absorber section. Unlike the device described in Ref. 16, bistability in this device occurs even under a constant reverse bias voltage on the absorber section. Hysteresis and bistability were also observed upon applying a constant laser injection current and varying the reverse bias voltage on the absorber.¹⁷ The origin of bistable operation was related to the nonlinear saturation of the QD absorption occurring due to state filling and the electroabsorption originating from the quantum confined Stark effect under the applied electrical field.¹⁷

Passive mode locking at a repetition rate of 7.4 GHz was achieved when both the gain and absorber sections of the lasers were dc biased. The mode-locking pulsewidth was characterized by collinear second harmonic generation intensity measured by using an autocorrelator. The narrowest mode-locked pulse was observed for absorber reverse biases between -4.0 and -5.5 V. Figure 2 shows the normalized autocorrelation traces for different gain section currents at an absorber bias of $V_a = -4.0$ V. A fully mode-locked pulse

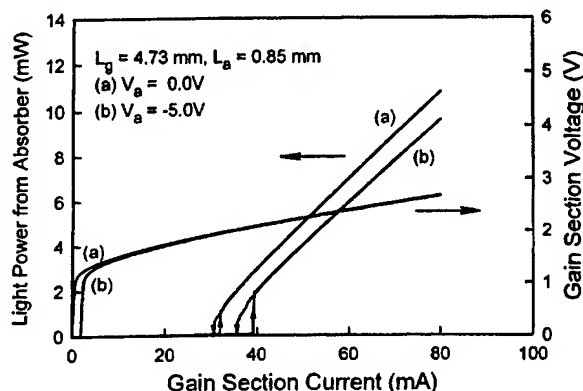


FIG. 1. Room temperature lasing and electrical characteristics of a two-section QD laser under (a) an absorber short circuit with $V_a = 0.0$ V, and (b) a reverse bias of $V_a = -5.0$ V, applied to the absorber section.

^{a)}Electronic mail: xdhuang@chtm.unm.edu

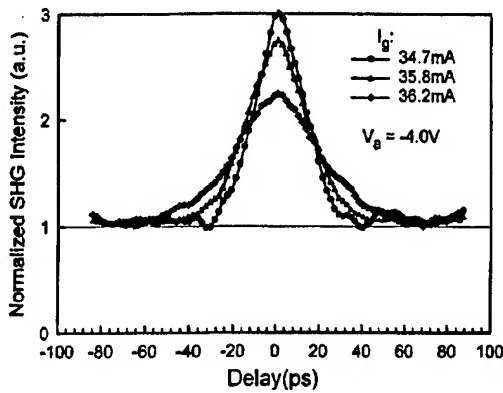


FIG. 2. The normalized intensity autocorrelation traces for different gain section currents at an absorber bias of $V_a = -4.0$ V.

(giving an autocorrelation signal with a peak-to-background ratio of 3:1) was obtained for gain section current very close to the lower hysteresis threshold, $I_g = 34.7$ mA. The corresponding pulsewidth is about 17 ps, assuming a hyperbolic secant-squared pulse. As the gain section current increases, the modulation depth of the mode-locked pulse decreases and the pulsewidth quickly broadens. We observe that the closer the bias current in gain section to the lower hysteresis threshold, the narrower the mode-locked pulse. Similar phenomenon has been observed in a mode-locked quantum well distributed Bragg reflector (DBR) laser,¹⁸ though in DBR lasers the hysteresis may be caused by a dispersive bistability.

The region of mode locking and the region of bistability are shown on the $I_g - V_a$ plot in Fig. 3. Bistability occurs between the lower lasing threshold and the upper lasing threshold. The mode-locking region is bounded by the lower lasing threshold and the upper limit of measurable mode locking and overlaps with the whole bistability region. Mode locking occurs for absorber reverse biases from $V_a = -6.0$ V to $V_a = 0.0$ V, but occurs only for a relatively narrow region of gain section currents.

To measure the time-averaged optical spectrum, the output of the mode-locked QD laser was coupled into a single mode fiber and measured by an optical spectrum analyzer. Figure 4 shows that the optical spectral bandwidth of the mode-locked QD laser, under optimum bias conditions of $I_g = 34.7$ mA and $V_a = -4.0$ V, is about 1 nm corresponding

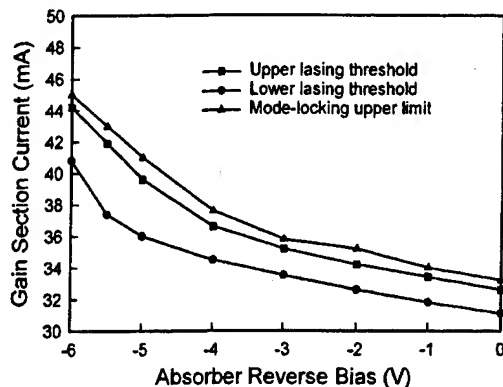


FIG. 3. The mode-locking region and bistability region. The region between the lower lasing threshold and the upper lasing threshold is the region of bistability. The mode-locking region extends from the lower lasing threshold to the upper limit of measurable mode locking.

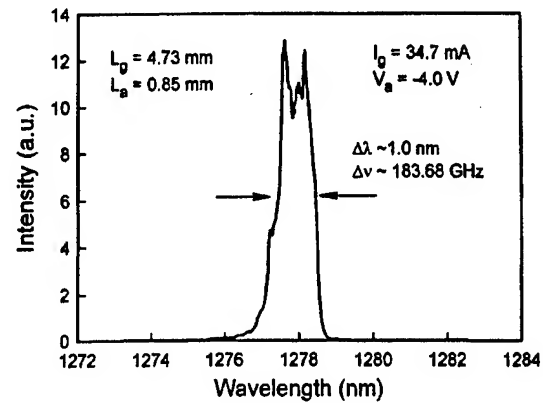


FIG. 4. The optical spectrum of the mode-locked QD laser under the optimum bias condition of $I_g = 34.7$ mA and $V_a = -4.0$ V. The optical bandwidth is about 1 nm.

to a time-bandwidth product of ~ 3.1 , more than six times of the Fourier transform limit. This suggests the presence of phase modulation or pulse chirp. However, it should also be noted that at least two transverse modes exist in this laser under cw operation.

The power spectrum of the mode-locked QD laser under the optimum bias condition of $I_g = 34.7$ mA and $V_a = -4.0$ V was also measured with a high-speed photodetector followed by microwave amplifiers and a rf spectrum analyzer. Two harmonics appeared in the range of 0–20 GHz, as shown in Fig. 5. No self-pulsation was observed. The inset reveals the detail of the fundamental signal with a peak position at 7.4035 GHz and a 3 dB width of about 370 KHz. The 3 dB width is comparable to passively mode-locked QW lasers,¹² and implies comparable phase noise and timing jitter.

Further comparison with reports of passively mode-locked QW lasers^{12,14} show this mode-locked QD laser has a larger pulse width. Taken with the larger-than-bandwidth-limited response mentioned earlier, this implies the presence of larger phase modulation. Several pulse broadening mechanisms^{12,14} may be considered. Unlike QW lasers, gain dispersion and bandwidth limitations should not be important in QD lasers.¹⁹ Group-velocity dispersion, on the other hand, will be more severe given the longer QD cavity lengths. Furthermore, the population of QD excited states will slow

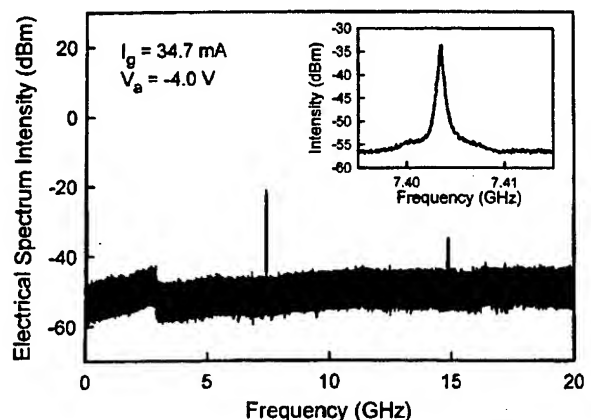


FIG. 5. The power spectrum of the mode-locked QD laser under the optimum bias condition of $I_g = 34.7$ mA and $V_a = -4.0$ V. No self-pulsation was observed.

the gain saturation owing to interlevel carrier relaxation, and result in a wider net gain window and pulse width. Finally, the population of dot excited states will increase the asymmetry of the gain spectrum,²⁰ increasing the linewidth enhancement factor and the self-phase modulation. Higher ground state gain from multiple QD layers should reduce the excited state population. A colliding pulse mode-locking scheme may further shorten the pulse width, because a transient absorption grating is likely to form due to reduced lateral diffusion of carriers in the QD active medium.²¹

In conclusion, we have fabricated long wavelength, oxide-confined, two-section QD lasers with an integrated intracavity QD saturable absorber. In addition to bistability, we have observed passive mode locking. Fully mode-locked pulses at a repetition rate of 7.4 GHz with duration of about 17 ps have been achieved under appropriate bias conditions. No self-pulsation has been observed accompanying the mode locking. Further improvement of the mode-locking performance may be achieved by using multiple QD layers and improved cavity design. Mode-locked QD lasers are candidates for ultrashort pulse generation.

The research was supported in part by AFOSR and DARPA.

- ¹G. T. Liu, A. Stintz, H. Li, K. J. Malloy, and L. F. Lester, *Electron. Lett.* **35**, 1163 (1999).
- ²G. Park, O. B. Shchekin, D. L. Huffaker, and D. G. Deppe, *IEEE Photonics Technol. Lett.* **13**, 230 (2000).
- ³X. Huang, A. Stintz, C. P. Hains, G. T. Liu, J. Cheng, and K. J. Malloy, *Electron. Lett.* **36**, 41 (2000).
- ⁴Yu M. Shernyakov, D. A. Bedarev, E. Yu. Kondrat'eva, P. S. Kop'ev, A. R. Kovsh, N. A. Maleev, M. V. Maximov, S. S. Mikhlin, A. F. Tsatsul'nikov, V. M. Ustinov, B. V. Volovik, A. E. Zhukov, Zh. I. Alf-
erov, N. N. Ledentsov, and D. Bimberg, *Electron. Lett.* **35**, 898 (1999).
- ⁵K. Mukai, Y. Nakata, K. Otsubo, M. Sugawara, N. Yokoyama, and Y. Ishikawa, *IEEE Photonics Technol. Lett.* **11**, 1205 (1999).
- ⁶H. Chen, Z. Zou, O. B. Shchekin, and D. G. Deppe, *Electron. Lett.* **36**, 1703 (2000).
- ⁷A. R. Kovsh, A. E. Zhukov, D. A. Livshits, A. Y. Egorov, V. M. Ustinov, M. V. Maximov, Y. G. Musikhin, N. N. Ledentsov, P. S. Kopev, A. I. Alferov, and D. Bimberg, *Electron. Lett.* **35**, 1161 (1999).
- ⁸F. Schafer, J. P. Reithmaier, and A. Forchel, *Appl. Phys. Lett.* **74**, 2915 (1999).
- ⁹F. Klopff, J. P. Reithmaier, and A. Forchel, *Appl. Phys. Lett.* **77**, 1419 (2000).
- ¹⁰P. Bhattacharya, D. Klotzkin, O. Qasaimeh, W. D. Zhou, S. Krishna, and D. H. Zhu, *IEEE J. Sel. Top. Quantum Electron.* **6**, 426 (2000).
- ¹¹J. A. Lott, N. N. Ledentsov, V. M. Ustinov, N. A. Maleev, A. E. Zhukov, A. R. Kovsh, M. V. Maximov, B. V. Volovik, V. I. Alferov, and D. Bimberg, *Electron. Lett.* **36**, 1384 (2000).
- ¹²E. A. Avrutin, J. H. Marsh, and E. L. Portnoi, *IEE Proc.: Optoelectron.* **147**, 251 (2000).
- ¹³K. Y. Lau, *IEEE J. Quantum Electron.* **26**, 250 (1990).
- ¹⁴D. J. Derickson, R. J. Helkey, A. Mar, J. R. Karin, J. G. Wasserbauer, and J. E. Bowers, *IEEE J. Quantum Electron.* **28**, 2186 (1992).
- ¹⁵L. F. Lester, A. Stintz, H. Li, T. C. Newell, E. A. Pease, B. A. Fuchs, and K. J. Malloy, *IEEE Photonics Technol. Lett.* **11**, 931 (1999).
- ¹⁶O. Qasaimeh, W. D. Zhou, J. Philips, S. Krishna, P. Bhattacharya, and M. Dutta, *Appl. Phys. Lett.* **74**, 1654 (1999).
- ¹⁷X. Huang, A. Stintz, H. Li, A. Rice, G. T. Liu, L. F. Lester, J. Cheng, and K. J. Malloy, *IEEE J. Quantum Electron.* **37**, 414 (2001).
- ¹⁸S. Arahira, Y. Matsui, T. Kunii, S. Oshiba, and Y. Ogawa, *IEEE Photonics Technol. Lett.* **5**, 1362 (1993).
- ¹⁹T. C. Newell, D. J. Bossert, A. Stintz, B. Fuchs, K. J. Malloy, and L. F. Lester, *IEEE Photonics Technol. Lett.* **11**, 1527 (1999).
- ²⁰M. H. Mao, F. Heinrichsdorff, and D. Bimberg, *Proceedings of the Eleventh International Conference on Indium Phosphide and Related Materials*, Davos, Switzerland, 16–20 May, 1999 (IEEE Lasers and Electro-optics Society), pp. 569–572.
- ²¹R. A. Salvatore and A. Yariv, *IEEE Photonics Technol. Lett.* **7**, 1151 (1995).

Orientation dependence of the optical properties in InAs quantum-dash lasers on InP

A. A. Ukhanov,^{a)} R. H. Wang, T. J. Rotter, A. Stintz, L. F. Lester, P. G. Eliseev,
and K. J. Malloy

Center for High Technology Materials, University of New Mexico, 1313 Goddard SE, Albuquerque,
New Mexico 87106

(Received 22 April 2002; accepted for publication 11 June 2002)

The anisotropy of the modal gain and the linewidth enhancement factor was experimentally measured in InAs/AlGaInAs/InP semiconductor lasers with an active region composed of quantum confined structures in the form of short wires called quantum dashes. This anisotropy is due to the polarization dependence of the transition matrix element in these quantum nanostructures. The spectral dependence of the gain and linewidth enhancement factor was investigated in a wavelength range from 1540 to 1640 nm at subthreshold current densities. The largest gain and the smallest linewidth enhancement factor were obtained when the quantum dashes were oriented perpendicular to the axis of the laser cavity. © 2002 American Institute of Physics. [DOI: 10.1063/1.1498875]

Semiconductor lasers based on quantum confined structures such as quantum wires, quantum dashes (QDashes), and quantum dots are of great interest because of their attractive optoelectronic properties.¹⁻³ For instance, a small linewidth enhancement factor,⁴ a low threshold current density,⁵⁻⁹ and a wide tuning range¹⁰ have been demonstrated for quantum dot lasers. However, the spectral and polarization dependence of the modal gain and the linewidth enhancement factor (α) have not yet been reported. The wavelength dependence of α and modal gain is relevant to the operation of tunable lasers and laser amplifiers. Knowledge of their polarization properties establishes the optimal orientation of quantum-confined structures in a laser cavity. In this letter, we report the spectral dependence of modal gain and the linewidth enhancement factor for two different orientations of the quantum-confined structures called QDashes with respect to a diode laser cavity.

The active media of the laser was composed of low-dimensional nanostructures in the form of short wires called QDashes. These wirelike nanostructures typically have length-to-width ratios of between 6:1 and 20:1. It was reported previously¹ that such lasers showed a dependence of the threshold current density on the laser cavity orientation. Here, we extend the study of these lasers by investigating the wavelength dependence of the modal gain and the linewidth enhancement factor at subthreshold current densities for dashes orientated parallel and perpendicular to the axis of the laser cavity.

The InAs QDashes were grown by molecular-beam epitaxy on an InP (001) substrate in a compressively strained AlGaInAs quantum well which had a thickness of 7.5 nm as described in Ref. 1. The QDash lasers had five layers of QDashes and the dashes had lengths up to 500 nm, widths up to 25 nm, and heights up to 5 nm. These dimensions were measured by atomic force microscope for uncapped dashes. It was determined that QDashes were elongated along the $[1\bar{1}0]$ direction.

Laser diodes (LDs) with dashes aligned along the axis of the laser cavity and with dashes oriented perpendicular to the cavity were investigated. The laser cavities had a 5 μm oxide-confined ridge waveguide with a cavity length of 1.68 mm. Most of the optical power of these lasers was emitted in a single-transverse mode with transverse electric polarization. Lasers with dashes oriented along the cavity axis lased at $\lambda = 1578$ nm and had a threshold current density of $I_{\text{th}} = 607 \text{ A cm}^{-2}$. LDs with dashes perpendicular to the cavity lased at $\lambda = 1600$ nm and had a threshold current density of $I_{\text{th}} = 473 \text{ A cm}^{-2}$.

The modal gain and the linewidth enhancement factor were determined from the below-threshold amplified spontaneous emission spectra using the Hakki-Paoli technique.^{11,4} The lasers were excited by current pulses with a duty cycle of 1% (pulse width = 200 ns) to avoid effects due to heating of the structure. A Fourier transform infrared spectrometer (FTIR) was used to measure the amplified spontaneous emission spectra. In contrast to previous work,^{12,13} information about not only the gain but also the carrier induced refractive index change was extracted from the FTIR spectra.

The modal gain for both dash orientations is shown in Fig. 1 for a descriptive subset of the data. Two general observations may be made. The peak value of modal gain was 2.3 ± 0.3 times larger for lasers with QDashes oriented perpendicular to the cavity axis than that for lasers with dashes along the cavity axis at all experimental current densities from 250 to 392 A cm^{-2} . The position of the peak modal gain for dashes perpendicular to the cavity axis was shifted by ~ 10 nm to a longer wavelength with respect to the peak position of modal gain for dashes parallel to the cavity axis. These results are described by the orientation dependence of the transition matrix element for the QDash active media. Modeling the QDash as a finite quantum wire, the polarization dependence of the transition matrix element is different for heavy hole (HH) and light hole (LH) states in quantum wire structures.^{2,14} Because of the compressive strain in the QDashes, the lowest-energy interband transitions are primarily conduction band-to-HH band, which have the largest

^{a)}Electronic mail: ukhanov@chtm.unm.edu

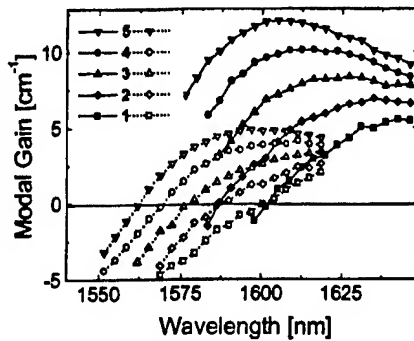


FIG. 1. Wavelength dependence of the modal gain of QDash lasers with dashes oriented parallel and perpendicular to the cavity axis. Solid lines and solid symbols correspond to the modal gain of the laser with dashes oriented perpendicular to the cavity axis. Dotted lines and open symbols represent the modal gain for the laser with dashes oriented parallel to the cavity axis. Lines 1, 2, 3, 4, and 5 correspond to the current densities 250, 285, 321, 356, and 392 A cm⁻², respectively. All curves used in this and in following figures are an aid to the eye.

transition strength when the electric field is parallel to the quantum wire axis. The shift in the peak modal gain suggests an increase in the relative contribution to the gain from the conduction band-LH band transitions when the orientation of the dashes is changed from perpendicular to parallel to the cavity axis, since conduction band-to-LH band transitions have the largest transition strength when the electric field is perpendicular to the quantum wire axis.

A blueshift of the gain spectra was observed with increasing current density due to band filling. The relatively small numbers of the largest, lowest-energy dashes are occupied first with the smaller, more numerous dashes occupied as the current density increases. Gain saturation occurs primarily at longer wavelengths for both orientations. Note also that the gain spectra for both dash orientations cross at zero-modal gain for the same current densities as quasiequilibrium ensures that transitions at the same energy have the same occupation probabilities.

Taking the difference in gain for consecutive current values as an approximation to the differential gain, the ratio of the differential gain for dashes perpendicular and parallel to the cavity axis is presented in Fig. 2. This ratio is approximately equal to the ratio of dipole transition matrix elements if the product of the density of states, difference in occupation probabilities, and transition matrix element varies more slowly with wavelength than the line shape function. It can

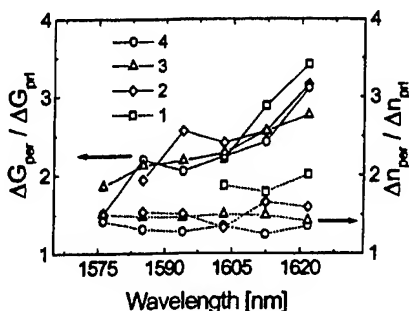


FIG. 2. Wavelength dependence of the gain difference ratio (solid lines) and carrier induced refractive index change ratio (dash lines) for QDash lasers with dashes oriented perpendicular and parallel to the cavity axis. Lines 1, 2, 3, and 4 correspond to the differences between current densities at 285–250, 321–285, 356–321, and 392–356 A cm⁻², respectively.

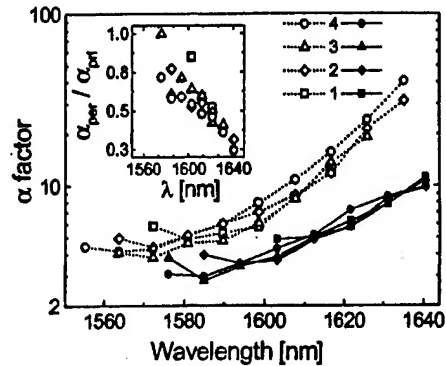


FIG. 3. Wavelength dependence of the linewidth enhancement factor (α) for QDash lasers with dashes oriented parallel and perpendicular to the cavity axis. Solid lines and solid symbols correspond to α of the laser with dashes oriented perpendicular to the cavity axis. Dotted lines and open symbols represent α for the laser with dashes oriented parallel to the cavity axis. Lines 1, 2, 3, and 4 correspond to the differences between current densities at 285–250, 321–285, 356–321, and 392–356 A cm⁻², respectively. The ratio of the linewidth enhancement factor for perpendicular and parallel dash orientations is shown in the inset.

be observed from Fig. 2 that the ratio of transition matrix elements continuously increases with wavelength from a value of ~ 1.5 at 1580 nm to 3.3 at 1620 nm. The ratio of the carrier induced refractive index change for dashes perpendicular and parallel to the cavity axis is shown in Fig. 2. This ratio is almost constant with wavelength mainly because of the experimental fact that the carrier induced refractive index change is almost constant with wavelength for both dash orientations. This suggests that contributions from optical transitions outside the region studied here minimize index dispersion.

The variation in the orientation dependence of the differential gain with wavelength is consistent with a mixing of light hole states into the HH-conduction electron transitions with decreasing emission wavelength.¹⁵ The data also show that this anisotropy decreases as the emission energy increases, again, which is consistent with the suggestion that LH transitions, which have the opposite polarization properties, are making increasing contributions to transitions at shorter wavelengths.

The wavelength dependence of the linewidth enhancement factor, α , for lasers with both dash orientations is presented in Fig. 3. The spectrum of the linewidth enhancement factor has the quantum wirelike dependence first described in Ref. 3, indicated by the presence of a minimum in α , the rapid increase for long wavelengths and an increase for short wavelengths (note the logarithmic scale). The linewidth enhancement factor is larger in lasers with dashes along the cavity axis than in lasers with dashes orthogonal to the cavity axis for the whole wavelength range from 1555 to 1640 nm. The smallest values of α factor at lasing wavelength were found to be 3.6 and 4.5 for dashes perpendicular and parallel to the laser cavity, respectively. This anisotropy of linewidth enhancement factor is attributed to differences in energy dependence of transition matrix element with orientation in quantum dash medium.

The variation in the anisotropy of α with wavelength follows directly from wavelength and orientation dependence of the differential index and differential gain (and, hence, the transition matrix element). From the inset of Fig.

3, it is noted that the ratio of α for dashes perpendicular and parallel to the cavity axis decreases with wavelength from a value of 0.75 at 1580 nm to 0.25 at 1545 nm. This is the result of the increase of the differential gain ratio with wavelength and the relatively constant ratio of carrier induced refractive index change described herein.

In conclusion, the spectral dependence of the linewidth enhancement factor and the modal gain was investigated in a QDash laser for two different dash orientations. These QDashes show the same polarization properties anticipated for quantum wire lasers. It was experimentally determined that gain peak position depends on the orientation of the QDashes in the laser cavity and was about 10 nm shorter for QDashes parallel to the cavity than for QDashes perpendicular to the cavity. The polarization dependence of the linewidth enhancement factor was experimentally measured in such quantum wirelike lasers. The observed variation of optical anisotropy with wavelength was attributed to the addition of LH contributions into the primarily HH transitions in these quantum-confined nanostructures.

¹R. H. Wang, A. Stintz, P. M. Varangis, T. C. Newell, H. Li, K. J. Malloy, and L. F. Lester, *IEEE Photonics Technol. Lett.* **13**, 767 (2001).

- ²M. Asada, Y. Miyamoto, and Y. Suematsu, *IEEE J. Quantum Electron.* **9**, 1915 (1986).
- ³Y. Miyake and M. Asada, *Jpn. J. Appl. Phys., Part 1* **28**, 1280 (1989).
- ⁴T. C. Newell, D. J. Bossert, A. Stintz, B. Fuchs, K. J. Malloy, and L. F. Lester, *IEEE Photonics Technol. Lett.* **11**, 1527 (1999).
- ⁵G. T. Liu, A. Stintz, H. Li, K. J. Malloy, and L. F. Lester, *Electron. Lett.* **35**, 1163 (1999).
- ⁶G. Park, O. B. Shchekin, D. L. Huffaker, and D. G. Deppe, *IEEE Photonics Technol. Lett.* **13**, 230 (2000).
- ⁷X. Huang, A. Stintz, C. P. Hains, G. T. Liu, Julian Cheng, and K. J. Malloy, *Electron. Lett.* **36**, 41 (2000).
- ⁸Y. M. Shernyakov, D. A. Bedarev, E. Yu. Kondrat'eva, P. S. Kop'ev, A. R. Kovsh, N. A. Maleev, M. V. Maximov, S. S. Mikhlin, A. F. Tsatsul'nikov, V. M. Ustinov, B. V. Volovik, A. E. Zhukov, Z. I. Alferov, N. N. Ledentsov, and D. Bimberg, *Electron. Lett.* **35**, 898 (1999).
- ⁹K. Mukai, Y. Nakata, K. Otsubo, M. Sugawara, N. Yokoyama, and H. Ishikawa, *IEEE Photonics Technol. Lett.* **11**, 1205 (1999).
- ¹⁰P. Varangis, H. Li, G. T. Liu, T. C. Newell, A. Stintz, B. Fuchs, K. J. Malloy, and L. F. Lester, *Electron. Lett.* **36**, 1544 (2000).
- ¹¹B. W. Hakki and T. L. Paoli, *J. Appl. Phys.* **44**, 4113 (1973).
- ¹²D. Hofstler and R. L. Thornton, *IEEE J. Quantum Electron.* **34**, 1914 (1998).
- ¹³D. Hofstler and J. Faist, *IEEE Photonics Technol. Lett.* **11**, 1372 (1999).
- ¹⁴L. A. Coldren and S. W. Corzine, *Diode Lasers and Photonics Integrated Circuits* (Wiley, New York, 1995).
- ¹⁵M. Willatzen, T. Tanaka, Y. Arakawa, and J. Singh, *IEEE J. Quantum Electron.* **30**, 640 (1994).

Transition dipole moment of InAs/InGaAs quantum dots from experiments on ultralow-threshold laser diodes

P. G. Eliseev,^{a)} H. Li, A. Stintz, G. T. Liu, T. C. Newell, K. J. Malloy, and L. F. Lester
Center for High Technology Materials, University of New Mexico, 1313 Goddard, SE Albuquerque,
New Mexico 87106

(Received 15 March 2000; accepted for publication 20 May 2000)

Semiconductor ultralow-threshold InAs quantum-dot lasers are investigated operating at 1230–1250 nm at room temperature (laser threshold range is of 16–83 A/cm² for ground-state emission). The dependence of gain on current is derived from measurements of the threshold current as a function of the cavity length. The ground-state gain appears at very low current: the inversion threshold of ~ 13 A/cm² is a record low value. Analysis of these data for diodes of different molecular beam epitaxial-grown wafers leads to a squared dipole moment of the transition of $\sim 9.2 \times 10^{-57}$ C² m² that corresponds to the length of elementary dipole of ~ 0.6 nm. © 2000 American Institute of Physics. [S0003-6951(00)03228-9]

Semiconductor quantum dots (QDs) are the artificial atom-like formation of one solid inserted into the matrix of another solid.^{1–6} These dots have a discrete energy spectrum that can be excited by a simple carrier injection in a p – n junction. This is used effectively in laser diodes that are shown to operate at the lowest threshold current among any semiconductor lasers: 26 A/cm² at room temperature.⁵ Important parameters of QDs are the transition energy and transition probability, which determine the absorption and gain spectra of the medium containing dots. While the general nature of optical transitions in QDs is known, no detailed description yet exists. Upon optical or electrical excitation, there are several spectral bands of emission from QDs usually referred to as the ground state, first excited state, second excited state, and so on. The ground-state emission is the basis of the very low threshold laser action^{3,5} and is of the most interest. However the optical gain that can be achieved with these transitions is limited, and when this maximum gain is not sufficient for laser oscillation, the laser device operates on a higher-energy excitation.

In this letter we report a study of ultralow threshold laser diodes with InAs QDs imbedded in an InGaAs quantum well (QW) layer (with threshold currents as low as 16 A/cm² at room temperature) aimed at understanding the emission characteristics of QDs in terms of the effective optical cross section and transition probability. We analyze the laser threshold current as a function of total optical losses to estimate the dipole matrix element of the ground-state transitions.

Molecular beam epitaxial growth on GaAs substrates was used to provide a layer of self-organized InAs QDs in an InGaAs quantum well “dots-in-a-well” (DWELL) type. The structural details of the wafers are given in Table I. Typically, the dots were of ~ 15 nm in base diameter and ~ 7 nm in height. In device 638, three QD/QW layers were separated by 10-nm-thick GaAs layers. Waveguide and QD/QW layers were undoped, and Al_{0.7}Ga_{0.3}As cladding layers were doped

by Be for p side and by Si for n side. All wafers have the same total waveguide thickness of 230 nm. Broad-area (100- μ m-wide) laser diodes were fabricated by cleaving, giving cavity lengths ranging from 285 to 7800 μ m. The threshold current density and optical power for diodes of different cavity lengths with uncoated facets were measured. This allowed derivation of the internal loss coefficient for each wafer and the dependence of modal gain on the current density. The lowest threshold current density of 16 A/cm² was obtained from wafer 577 with high-reflectivity coatings on the facets. Other optical characteristics of laser diodes fabricated from these samples are reported in Refs. 5 and 6.

An important feature of these QD lasers is that ground state emission is only achieved in diodes with low modal gain (long cavity lengths). For example, in diodes from wafer 432, the ground-state emission at ~ 1230 nm was obtained in long (>1.5 mm) uncoated units. When the cavity length L was 1.5 mm, a competitive oscillation at ~ 1140 nm was also observed. This higher energy state dominates in shorter-cavity diodes. When $L < 0.5$ mm, laser action appears in a third excited state at 1040–1060 nm. This is an indication that the gain supplied by the optical transitions saturates at higher current. In Fig. 1 the interrelationship between the threshold current density and the laser photon energy at threshold is plotted. In bulk-type lasers this dependence is continuous, reflecting the continuous density of states. In QD lasers the laser photon energy curve is fragmented into branches according to the discrete energy spectrum of the QDs, and the lowest energy branch corresponds to the

TABLE I. Parameters of molecular beam epitaxial wafers: M is a number of QD/QW layers, N_{2D} is in-plane QD density, t to QW thickness, x is indium content in QW.

Wafer	M	N_{2D} (cm ⁻²)	t (nm)	N_{QD} (cm ⁻³)	x (%)
432	1	7.5×10^{10}	10	7.5×10^{16}	20
638	3	2.5×10^{10}	9.6	2.6×10^{16}	15
577	1	2.5×10^{10}	10	2.5×10^{16}	15
650	1	2.5×10^{10}	10	2.5×10^{16}	15

^{a)}Also with: P. N. Lebedev Physics Institute, Moscow, Russia; electronic mail: eliseev@chtm.unm.edu

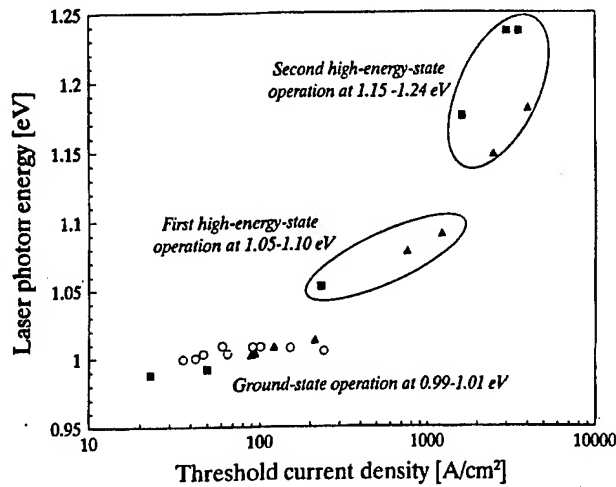


FIG. 1. Interrelationship between the current density and photon energy of laser emission at the threshold in several groups of InAs QD laser diodes (DWELL type). Different experimental points relate to different wafers.

ground-state emission. In our specimens this photon energy is in the range of 0.99–1.01 eV. A jump from ground state to first excited state occurs at ~ 200 A/cm² and from first to second excited state at 1.5 kA/cm².

The dependence of the modal gain on the current density is shown in Fig. 2. Curves are fitted on the basis of a kinetic model assuming the gain is supplied by transitions between the inverted states of QDs. Details of the model will be given elsewhere. Our purpose here is to determine the maximum gain g_{\max} in the emission bands for each wafer. The values for g_{\max} can be found from the experimental points of Fig. 2 and the kinetic model merely allows specifying these values more precisely. Results of this fitting are given in Table II.

In order to obtain the effective optical cross section of the gain in QDs, we determine the material gain of the QW/QD medium using an optical confinement factor Γ calculated on the basis of a waveguide model. Optical parameters assumed in these calculations are listed in Table III for a photon energy of 1 eV. $\Gamma = 0.0302$ is found in a single-well structure and $\Gamma = 0.0906$ in a three-well one. We treat the

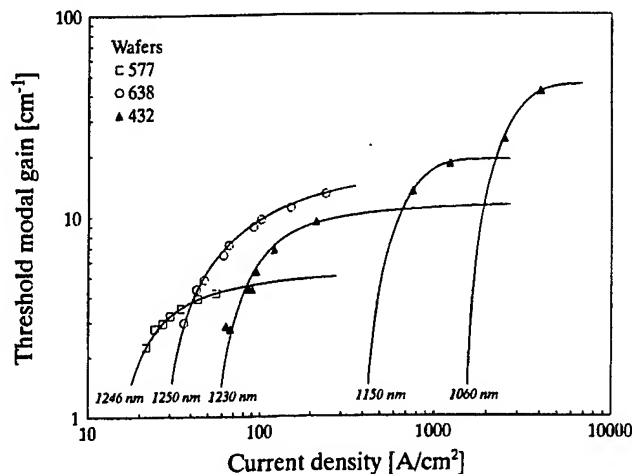


FIG. 2. Dependence of the modal gain on the current density from laser threshold measurements with QD lasers. Curves are given for a modeled gain as fit to experimental data with fitting parameters indicated in Table II. The central wavelength of each band is indicated.

TABLE II. Fitting parameters of gain curves for low-threshold QD lasers; α_i is internal optical loss coefficient, J_{th} is minimum threshold current density, g_{\max} is maximum modal gain in the specific emission band, J_0 is the inversion threshold current density, GS is for ground states, 1S and 2S are for first and second excited states, respectively.

Wafer	α_i (cm ⁻¹)	J_{th} (A/cm ²)	g_{\max} (cm ⁻¹)	J_0 (A/cm ²)	States and wavelength (nm)
432	1.3	83	11.8	51.5	GS, 1224–1237
			19	400	1S, 1137–1150
			45	1500	2S, 1050–1080
577	1.5	16	5.4	13	GS, 1243–1248
638	1.5	26	18.5	26.4	GS, 1229–1241
650	1.5	23	5.5	11.7	GS, 1250–1255
			9	100	1S, 1178
			55	1000	2S, 1003–1050

active QD/QW layers as optically uniform with the same refractive index as the InGaAs matrix, taking into account a small relative volume of InAs dots. Results of the analysis are given in Table IV. The effective gain cross section is found by dividing the material gain by the bulk density of dots. We assume that the saturation of the ground-state gain occurs when all available ground states of QD are totally inverted. For further analysis, we use the expression for the material gain/absorption $G(E)$ in a medium containing active centers⁷

$$G(E) = -\alpha(E) = (N_2 - N_1)|d|^2 E \gamma(E) / (2\hbar^2 c n \epsilon_0), \quad (1)$$

where E is the photon energy of the transition, N_2 and N_1 are densities of QDs occupied and empty of electron-hole pairs, respectively, $\gamma(E)$ is the spectral line shape function, $|d|^2$ is the squared dipole matrix element of the transition, n is the refractive index, and ϵ_0 is the permittivity of vacuum. We assume the dipole interaction of QDs with linearly polarized radiation (transverse electric mode). The line shape is assumed to be Gaussian, and for this case the normalized gain in the spectral peak is determined by the expression

$$\gamma_0 = 4\hbar(\pi \ln 2)^{1/2} / \Delta E, \quad (2)$$

where ΔE is the full width half maximum of the spontaneous ground-state emission. We consider that limiting value of the material gain G_{\max} is reached when $N_2 = N_{QD}$, $N_1 = 0$, and we define $G_{\max} = \sigma N_{QD}$, where σ is the effective optical gain cross section of the QD. In order to find the quantity $|d|^2$ we use the following expression:

$$|d|^2 = 0.339 \sigma \hbar c n \epsilon_0 \Delta E / E. \quad (3)$$

Calculation results for σ and for the dipole moment are given in Table IV. The length of the dipole with an elementary charge corresponding to the transition dipole momentum

TABLE III. Assumed parameters of dielectric structures.

Layer	Material	Refractive index	Absorption coefficient (cm ⁻¹)
Cladding	Al _{0.7} Ga _{0.3} As	3.0978	1
Waveguide	GaAs	3.4254	1
Active	In _{0.15} Ga _{0.85} As	3.4600	0
Active	In _{0.2} Ga _{0.8} As	3.4780	0

TABLE IV. Parameters and results of calculations (ground-state emission). G_{\max} is the maximum material gain, σ is for effective gain cross section, and a is the length of elementary dipole.

Wafer	G_{\max} (cm^{-1})	σ (cm^2)	ΔE (meV)	$ d ^2$ ($\text{C}^2 \text{m}^2$)	a (nm)
432	389	5.19×10^{-15}	65	1.11×10^{-56}	0.658
577	180	7.20×10^{-15}	35	8.40×10^{-57}	0.572
638	204	7.85×10^{-15}	37	9.73×10^{-57}	0.616
650	182	7.28×10^{-15}	30.9	7.56×10^{-57}	0.543

(last column of Table IV) is found in the range 0.543–0.658 nm with an average value of 0.6 nm and with an average deviation of $\sim 7\%$. This indicates a good reproducibility for QD lasers from different wafers. The optical cross sections have a wider distribution in these samples but the difference seems correlated with differences in spectral broadening. A mean value of $|d|^2$ is $\sim 9.2 \times 10^{-57} \text{ C}^2 \text{m}^2$, which seems to be averaged over both emitting ground states of QD (with one and two pairs captured).

For a comparison, the transition dipole moment of the electron–hole pair in a bulk semiconductor can be modeled in the $k \cdot P$ approximation as^{8,9}

$$|d|^2 = (e^2 \hbar^2 / 6 E^2 m^*) E_g (E_g + \Delta) / (E_g + 2\Delta/3), \quad (4)$$

where m^* is the electron effective mass, and Δ is the spin-orbit splitting energy. We assume that this value can be applied to large dots.⁸ In the case of InAs QDs we have some uncertainty in the energy gap as the InAs islands in the InGaAs matrix are highly stressed. The bulk value of E_g is ~ 0.4 eV, whereas the transition energy E is ~ 1 eV. When other bulk InAs parameters are used, $m^* = 0.22 m_0$, $\Delta = 0.371$ eV,¹⁰ and E_g is varied from 0.4 to 0.8 eV, the calculated dipole length varies from 0.52 to 0.71 nm. This range agrees quite well with our experimentally determined values.

In conclusion, the optical gain versus current curves of

the InAs QD lasers are analyzed to derive the gain cross section and dipole matrix element of ground-state transitions in the QD. Very low-threshold laser samples are used in this study. The lowest inversion threshold is found to be $\sim 13 \text{ A/cm}^2$. The gain cross section $\sim 7 \times 10^{-15} \text{ cm}^2$ is derived for a single QW/QD structure with a dot density of $2.5 \times 10^{10} \text{ cm}^{-2}$. The dipole transition matrix element is derived and it is found to be almost the same in different QD wafers. The length of the elementary dipole is ~ 0.6 nm, and this assessment of the InAs QD matrix element agrees with the bulk InAs matrix element.¹¹

This work was supported by DARPA under Grant No. MDA972-98-1-0002 and by AFOSR under Grant No. F49620-96-1-0077. The authors are grateful to Dr. G. A. Smolyakov of CHTM, UNM, for waveguide calculations.

¹Y. Arakawa and H. Sasaki, Appl. Phys. Lett. **40**, 939 (1982).

²A. E. Drakin and P. G. Eliseev, Sov. J. Quantum Electron. **14**, 119 (1984).

³H. Hirayama, K. Matsunaga, K. Asada, and Y. Suematsu, Electron. Lett. **30**, 142 (1994).

⁴N. Kirstaedter, N. N. Ledentsov, M. Grundmann, D. Bimberg, V. M. Ustinov, S. S. Ruvimov, M. V. Maximov, P. S. Kop'ev, Zh. I. Alferov, U. Richter, P. Werner, U. Goesele, and J. Heydenreich, Electron. Lett. **30**, 1416 (1994).

⁵G. T. Liu, A. Stintz, H. Li, K. J. Malloy, and L. F. Lester, Electron. Lett. **35**, 1163 (1999).

⁶L. F. Lester, A. Stintz, H. Li, T. C. Newell, E. A. Pease, B. A. Fuchs, and K. Malloy, IEEE Photonics Technol. Lett. **11**, 931 (1999).

⁷A. Yariv, Optical Electronics, 4th ed. Harcourt Brace Jovanovich College Press, Fort Worth (1991).

⁸M. Asada, Y. Miyamoto, and Y. Suematsu, IEEE J. Quantum Electron. **22**, 1915 (1986).

⁹L. V. Asryan and R. A. Suris, Semicond. Sci. Technol. **11**, 554 (1996).

¹⁰Landolt-Boernstein Numerical Data and Functional Relationships in Science and Technology, Vol. 22, Semiconductors (Springer, Berlin, 1987), p. 118.

¹¹R. Heitz, M. Veit, N. N. Ledentsov, A. Hoffmann, D. Bimberg, V. M. Ustinov, P. S. Kop'ev, and Zh. I. Alferov, Phys. Rev. B **56**, 10435 (1997).

Moisture stability and structure relaxation processes in plasma-deposited SiOF films

V. Pankov,^{a)} J. C. Alonso, and A. Ortiz

Instituto de Investigaciones en Materiales, Universidad Nacional Autonoma de Mexico, AP 70-360, 04510 Mexico D.F., Mexico

(Received 9 November 1998; accepted 23 July 1999)

Fluorinated silicon dioxide (SiOF) films have been prepared by remote plasma enhanced chemical vapor deposition using SiF₄, O₂, H₂, and He gases. Fourier transform infrared spectroscopy has been used to study structural changes in SiOF films caused by interaction with atmospheric moisture. It is shown that the increased incorporation of fluorine into the SiOF network during film deposition gradually increases the value of the average Si–O–Si angle in the SiOF network, $\langle\theta\rangle$, from 138° to 153°. It is concluded that the value of about 144° corresponds to nearly relaxed SiOF network and therefore can be considered as an equilibrium angle for SiOF films. Subsequent increase in the fluorine concentration in the film results in $\langle\theta\rangle$ larger than the equilibrium $\langle\theta\rangle$ ("overequilibrium") and causes structural relaxation of the SiOF network towards the equilibrium $\langle\theta\rangle$ during the post-deposition period. Both "under-" and "overequilibrium" values of $\langle\theta\rangle$ seem to be the sources of SiOF film structural instability and increased reactivity with moisture. However, film hydrolysis and structural relaxation processes in the SiOF films characterized by "underequilibrium" values of $\langle\theta\rangle$ are effectively suppressed by F presence in moderate concentrations. On the contrary, SiOF films characterized by "overequilibrium" $\langle\theta\rangle$ have low density network and heavily absorb atmospheric water, which strongly promotes both structural relaxation and hydrolysis during the post-deposition period. © 1999 American Vacuum Society. [S0734-2101(99)02406-9]

I. INTRODUCTION

Advances in ultralarge scale integrated (ULSI) technology have led to the necessity for an intermetal dielectric with dielectric constant as low as possible to reduce the interlayer capacitance and overcome the signal delay limitations. One of the insulator films which has received much attention recently is fluorinated silicon dioxide (SiOF). SiOF films have been shown the ability to substantially reduce the dielectric constant^{1–4} while providing enhanced gap fill over undoped oxide films.⁵ However, the main problem, low moisture stability of highly fluorinated SiOF films deposited by various plasma enhanced chemical vapor deposition (PECVD) techniques remains a practical problem to be solved and attracts a great deal of interest from the scientific community.^{1,6–10}

The main factors that affect the moisture instability of SiOF films are (i) weakening of the Si–O bonding due to the electron shift toward the highly electronegative F atom,¹¹ (ii) the presence of highly hygroscopic Si–F bonding paralleling the behavior of P=O in P₂O₅ glasses,¹² and (iii) the presence of Si–O–Si groups characterized by small Si–O–Si angles.^{6,13} While the F content in the SiOF film certainly controls the first two factors, its effect on the Si–O–Si angle is less clear. Han and Aydil have shown that F incorporation causes the Si–O–Si bond angle to relax.¹⁴ Yoshimaru *et al.*⁶ have surmised that the network structure in the heavily fluorine-doped SiOF film is totally relaxed by fluorine doping. Tamura *et al.*⁷ have assumed that the more fluorinated the SiOF the more relaxed network structure it has. Their

assumption was based on the finding that the incorporation of fluorine atoms into SiO₂ suppresses the formation of threefold and fourfold rings resulting in the chain-like SiOF network.^{2,7} In our previous study, we demonstrated that the average value of Si–O–Si angle in the SiOF films with maximal F content attains about 148°,¹⁵ similar to the results reported by Han and Aydil.¹⁴ However, relaxed thermal SiO₂ films are characterized by the average value of Si–O–Si angle as low as 144°. ^{13,16,17} Here, it is quite natural to expect that the SiOF network in high-fluorinated SiOF films is far from the equilibrium state and should attempt to relax during post-deposition period towards the average value of Si–O–Si angle corresponding to the relaxed thermal oxide.

In the present work, based on the analysis of the structural changes in SiOF films with different F content after their exposure to the ambient atmosphere, we consider the main sources of the films structural instability and discuss the probable mechanisms contributing to the post-deposition structural relaxation of SiOF films.

II. EXPERIMENT

SiOF films were deposited on 200 Ω cm *n*-type (100) silicon substrates in a remote plasma enhanced chemical vapor deposition system using SiF₄+O₂+H₂+He mixture. The reaction chamber was equipped by an inductively coupled plasma source and operated in the high-density plasma regime. The detailed geometry of the reaction chamber is described elsewhere.¹⁵ Flow rates of SiF₄, O₂, and H₂ were varied in a wide range from 0.1 to 100 sccm to obtain SiOF films with different fluorine content. The total pressure was

^{a)}Electronic mail: pankov@servidor.unam.mx

500 mTorr. The plasma discharge was maintained using 13.56 MHz rf power at 200 W for all depositions. The substrate temperature was held constant at 175 °C. Film thickness was targeted for 1000 Å to assure the accuracy of the Fourier transform infrared (FTIR) spectroscopy studies. To study the stability of the obtained SiOF films, all the samples were exposed to the ambient atmosphere at room temperature for one month.

FTIR absorption spectra from 400 to 4000 cm^{-1} were measured by Nicolet 210 double-beam spectrometer. The Si-F_x absorption band within the range of 900–1000 cm^{-1} was used to estimate the total atomic concentration of Si-F_x units in SiOF films through the procedure used by Han and Aydil.¹⁴ Average value of the Si-O-Si bonding angle, $\langle \theta \rangle$, was derived from the position of the Si-O stretching (s) vibration peak, as it was described *ibid.* The error in $\langle \theta \rangle$ estimation was about 2°, which is due to the resolution limit of the FTIR spectrometer of about 4 cm^{-1} . The value of $\Delta \theta$, characteristics of film structural homogeneity, was estimated through the analysis of full width at half maximum (FWHM) of Si-O (s) peak intensity using the technique also described by Han and Aydil.¹⁴

III. RESULTS

A. As-deposited SiOF films

FTIR spectra of all our as-deposited SiOF films in the entire range of F concentration show three major peaks located at about 1090, 800, and 450 cm^{-1} corresponding to the stretching, bending, and rocking vibrational modes of the Si-O-Si bonding, respectively¹⁸ (see Fig. 1). The presence of other hydrogen-related peaks, e.g., Si-OH groups,^{13,19,20} H-OH,^{1,5,14,20} and Si-H²¹ in our as-deposited samples is below the FTIR detection limit, ~1%¹³ in the entire range of F content, as seen in the Fig. 1.

The main effect of fluorine incorporation is the appearance of the absorption band ranging from about 900 to 1000 cm^{-1} . This band is reportedly attributed to the contribution of Si-F stretching vibration at about 940 cm^{-1} , Si-F₂ asymmetric stretching mode vibration at about 980 cm^{-1} , and Si-F₂ symmetric stretching mode at about 920 cm^{-1} (see Fig. 2).^{1,6,14,22} Several researches have controversially attributed the latter feature to the bending vibration of Si-OH, which must be accompanied by a stronger absorption band ranging from about 2800 to 3800 cm^{-1} .^{13,18,23} The fact that none of our as-deposited SiOF films show any FTIR absorption in the above range (see Fig. 1) suggests that in our case the feature at about 920 cm^{-1} is most probably due to the Si-F₂ symmetric stretching vibration. Figure 3 shows that the area of the deconvoluted Si-F stretching peak at about 945 cm^{-1} monotonically increases with F content, accompanied by slight increase in the area of the symmetric and asymmetric Si-F₂ assigned features located at about 920 and 985 cm^{-1} , respectively.

Another effect of fluorine incorporation considered in detail in previous studies^{14,15} was an incremental shift of Si-O (s) vibration peak position from 1065 cm^{-1} toward higher wave numbers until the value of 1097 cm^{-1} , which corre-

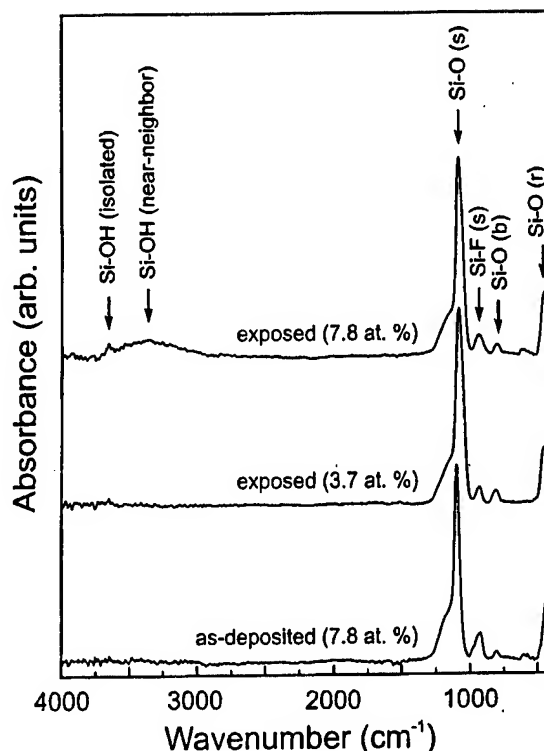


FIG. 1. FTIR spectra of SiOF film prepared with different Si-F_x bond concentrations as-deposited and after one month of exposure to the ambient atmosphere. Si-O-Si stretching, bending, and rocking vibrational modes are labeled as (s), (b), and (r), respectively.

sponds to the increase of $\langle \theta \rangle$ from 138° to 153° (see Fig. 4). The above shift was accompanied by a decrease in the peak FWHM from 81.1 to 45.8 cm^{-1} corresponding to the gradual reduction in $\Delta \theta$ from 33.5° to 28°, which indicates the improvement of films structural homogeneity with increasing the F content (see Fig. 5).

B. SiOF films after exposure to the ambient atmosphere

FTIR spectra of SiOF films with Si-F_x bond content below 3.7 at. % show no peaks associated with H-OH, Si-OH,

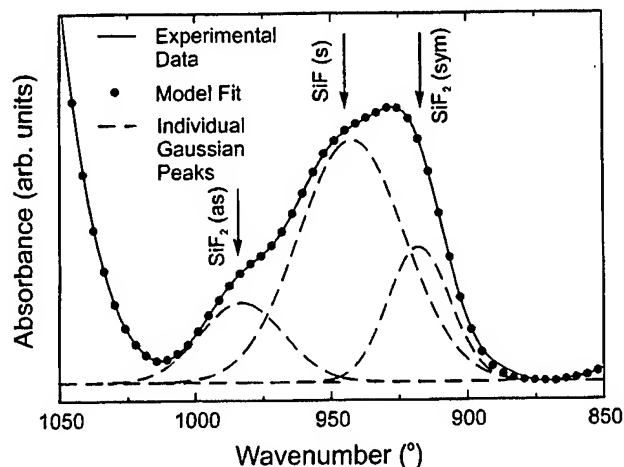


FIG. 2. FTIR spectrum of SiOF film with Si-F_x bond concentration of 7.8 at. % in 850–1050 cm^{-1} region with deconvolution to Gaussian peaks.

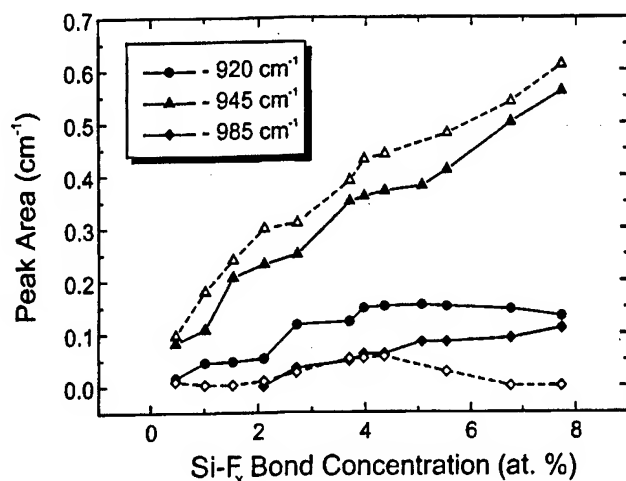


FIG. 3. Areas of 920 and 980 cm^{-1} Gaussian peaks derived from the Si-F_x absorption band deconvolution vs Si-F_x bond concentration in SiOF films as-deposited (filled symbols) and after their exposure to the ambient atmosphere for one month (open symbols). The peak at 920 cm^{-1} in the exposed samples is almost disappeared.

or Si-H bonds (see Fig. 1) after their exposure to the ambient atmosphere for one month. The moisture stability of SiOF films drops sharply when Si-F_x bond content in the films exceeds 3.7 at. %. Two additional absorption bands appear in the FTIR spectra of the SiOF films with Si-F_x bond content exceeding 3.7 at. % after their exposure to the ambient atmosphere (see Fig. 1). The absence of any detectable FTIR response at about 1640 cm^{-1} attributable to the bending vibration of H₂O^{14,20} allows us to assign a broad symmetric band observed at 2800–3750 cm^{-1} to the stretching vibrations of hydrogen-bonded near-neighbor silanol groups.^{13,19} The smaller absorption peak at about 3650 cm^{-1} is usually attributed to the stretching vibrations of isolated silanol groups within closed pores.^{13,19,20} The area of the

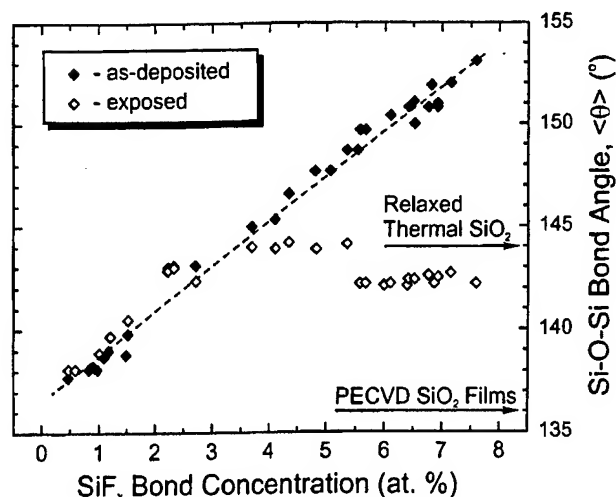


FIG. 4. Average Si-O-Si bond angle vs Si-F_x bond concentration in SiOF films as-deposited (filled symbols) and after exposure to the atmosphere for one month (open symbols). The values of Si-O-Si bond angle for relaxed thermal SiO₂ (144°) (see Refs. 13, 16, 17) and PECVD SiO₂ films (136°) (see Ref. 14) are demonstrated as a reference.

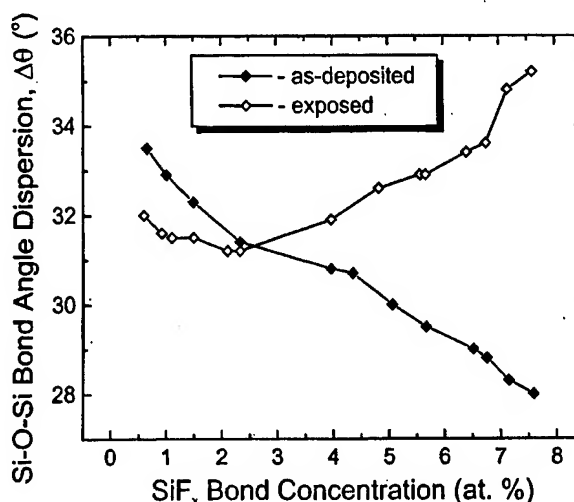


FIG. 5. Si-O-Si bond angle dispersion vs Si-F_x bond concentration in SiOF films as-deposited (filled symbols) and after exposure to the atmosphere for one month (open symbols).

band corresponding to the near-neighbor silanols increases drastically when Si-F_x bond content in films exceeds 3.7 at. % and then saturates with further increase in the F content, as seen in Fig. 6, whereas the area of the band corresponding to the isolated silanols does not change with F content.

Significant changes in the shape of the absorption band ranging from about 900 to 1000 cm^{-1} related to the contribution of various Si-F_x units are also observed in FTIR spectra of SiOF films exposed to the ambient atmosphere (see Fig. 7). However, individual changes of the peaks contributing to the above absorption band are quite different. Thus, the area of Si-F stretching peak located at about 945 cm^{-1} increases in the entire range of F content after exposure of the films to the atmosphere (see Fig. 3). On the contrary, the area of the peak at 920 cm^{-1} , assigned to the symmetric

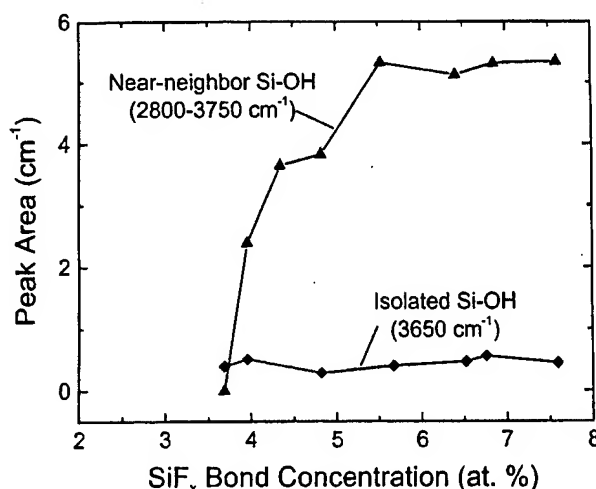


FIG. 6. Areas of the absorption band in the range 2800–3750 cm^{-1} and of the absorption peak at 3650 cm^{-1} corresponding to the near-neighbor and isolated silanol groups, respectively, vs Si-F_x bond concentration after exposure of SiOF films to the atmosphere for one month.

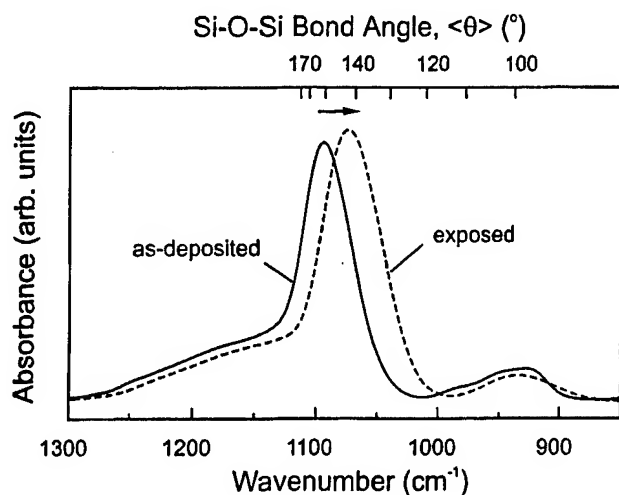


FIG. 7. FTIR spectra in the 850–1300 cm^{-1} region of a SiOF film with Si-F_x bond concentration of 7.8 at. % as-deposited and after exposure to the atmosphere for one month.

Si-F_2 stretching vibrations, drastically reduces after exposure of the films to the atmosphere similar to the observations reported by Nakasaki *et al.*²² The feature at 985 cm^{-1} , corresponding to the symmetric Si-F_2 stretching vibrational mode, completely disappears after exposure of SiOF films to the atmospheric moisture.

The shape and position of the Si-O (s) vibration peak remain almost unchanged for the samples with less than 3.7 at. % of Si-F_x bonds after their exposure to the atmosphere. However, for the films with higher F content, the Si-O (s) peak shifts towards lower wave numbers and slightly broadens, as seen in Fig. 7. Based on the procedures described by Han and Aydil,¹⁴ the above redshift corresponds to the reduction in $\langle \theta \rangle$ and increase of $\Delta \theta$ (see Figs. 4 and 5). Moreover, it was found that the final value of the Si-O (s) peak position differs for the films with Si-F_x bond content ranging from 3.7 to 5.6 at. % and those with higher F content. For the former group of samples, the final peak location after exposure to the ambient atmosphere for one month is about 1080 cm^{-1} corresponding to $\langle \theta \rangle$ of 144° , whereas in the latter case the Si-O (s) peak shifts to about 1076 cm^{-1} , which corresponds to about 142.2° . Increase of $\Delta \theta$ in the samples with Si-F_x bond content above 3.7 at. % after their exposure to the atmosphere, as seen in Fig. 5, indicates worsening of the film structural homogeneity.

IV. DISCUSSION

A. Microstructure and energetics of as-deposited SiOF films

Low-temperature deposition results in low surface mobility of the precursors making them occupy energetically unfavorable sites on the film surface. The presence of charged and high-energetic particles in the incoming flux, typical for PECVD processes, generates the additional nucleation centers. As a result, pure or low-fluorinated PECVD SiO_2 films are mainly built from heavily strained low-order threefold

and fourfold ring units^{2,6,7} and are characterized by low $\langle \theta \rangle$ ranging from 136° to 144° , as it was observed elsewhere^{14,20} and seen in Fig. 4.

In our previous study based on the results of molecular orbital modeling it was shown that the increased content of highly reactive F species in the incoming flux should cause a continuous shift of the ring distribution function towards the high-order rings resulting in corresponding changes in $\langle \theta \rangle$ within the SiOF network, film density and moisture reactivity.²⁴ It was concluded *ibid* that the network of high-fluorinated SiOF films should consist of high-order ring units. Due to the large size of the high-order rings and multiple F termination, which reduces the total interconnectedness of the SiOF network, high-fluorinated SiOF films should have reduced density, increased water absorptivity and should be more susceptible to attack by water. Moreover, high-order rings can be considered as individual microvoids capable of trapping water. It is assumed that both moisture reactivity and structure relaxation processes in SiOF films during post-deposition period are strongly controlled by the inner energetics of as-deposited film whereas water absorption enables to reduce the activation barriers of the above processes.

The energetics of as-deposited SiOF films can be explained based on the results of *ab initio* MO calculations by Newton and Gibbs.²⁵ They have estimated the energy of a $\equiv\text{Si-O-Si}\equiv$ bridging unit as a function of θ and have found that the minimum energy occurs at $\theta \sim 140^\circ$, which is very close to 144° , the experimental value for relaxed thermal SiO_2 films.^{13,16,17} It was reported elsewhere that pure PECVD SiO_2 films, usually characterized by the values of $\langle \theta \rangle$ ranging from 136° to 144° as-deposited,^{14,20} attempt to increase their $\langle \theta \rangle$ towards the 144° value, when exposed to the atmospheric moisture, producing Si-O (s) peak blueshift.²¹ Our results demonstrate that SiOF samples with Si-F_x bond content ranging from 3.7 to 5.6 at. % attempt to reduce their $\langle \theta \rangle$ towards the same value equal to 144° after exposure to the ambient atmosphere (see Fig. 4). It can be concluded that the value of 144° corresponds to the energetically lowest state of the SiOF network and can be considered as an equilibrium value. It is assumed that both "under-" and "overequilibrium" angles are the sources of instability and increased reactivity of SiO_2 -based films during post-deposition period. The above conclusions are in good agreement with the numerous studies of SiOF films moisture stability versus F content. As it was reported elsewhere^{1,8,14,26} the amount of silanols in SiOF films initially reduces with increasing the F content, but then starts to increase again demonstrating the existence of minimum at certain F content. The position of this minimum can be assigned to the nearly equilibrium value of $\langle \theta \rangle$ in these films. In the present studies only the films with Si-F_x bond concentration of about 3.7 at. % are characterized by almost equilibrium value of $\langle \theta \rangle$ as-deposited and therefore can be considered as nearly relaxed films. The subsequent increase in the F content of the SiOF films results in "overequilibrium" $\langle \theta \rangle$ and causes structural instability and increased reactivity of the films,

which results in their structural relaxation towards the equilibrium $\langle \theta \rangle$ during post-deposition period, as seen in Fig. 4.

Figure 4 shows that SiOF films with Si-F_x bond concentration of 3.7–5.6 at. % reduce their $\langle \theta \rangle$ to the value of about 144° after exposure to the ambient atmosphere for one month. However, for the films with Si-F_x bond content above 5.6 at. % the final value of $\langle \theta \rangle$ is a little smaller. The origin of this difference is not clear at this time. However, it is possible that the increased concentration of hydroxyls in high-fluorinated SiOF films (see Fig. 6) causes this slight reduction in the value of the equilibrium angle for SiOF compound with respect to the value of 144° appropriated to hydroxyl-free relaxed thermal SiO₂.

B. Different paths of film structural relaxation

It is assumed that the relaxation of the strained bonds in SiOF films during post-deposition period can undergo through several mechanisms, namely: (i) change of the ring geometry by means of bond rotation, relaxation of both bonding angles and lengths; (ii) bond rearrangement without chemical interaction with environmental reagents; and (iii) chemical reactions with environmental reagents, water molecules, for instance, accompanied by structural reconstruction of the network.

SiOF films with Si-F_x bond content below 3.7 at. % are characterized by "underequilibrium" $\langle \theta \rangle$ however, demonstrate excellent moisture stability and "frozen" structure relaxation, opposite to PECVD films with the same values of $\langle \theta \rangle$. It is assumed that at room temperatures the change in ring geometry, the first mechanism, is heavily constrained in both groups by "steric hindrance" effect. The presence of F in moderate concentration completely suppresses the third, water-induced relaxation mechanism in low-fluorinated SiOF films. Indeed, F effectively passivates oxygen vacancies,⁹ and suppresses Si-H and Si-OH terminations (see Fig. 1) during film deposition process, well known channels of the nucleophilic attack of water to the network of PECVD SiO₂ films.²⁷ However, the second, bond-rearrangement mechanism, successfully undergoes without any water assistance in the entire range of F content. It can be supposed that the increase in the Si-F absorption peak area accompanied by the reduction of the areas of features assigned to the Si-F₂ units (Fig. 3) is due to the conversion of unstable Si-F₂ units into the Si-F groups probably yielding F atoms as a by-product of this reaction. This is consistent with the fluorine desorption from SiOF films observed at moderate temperatures in numerous thermal desorption studies.^{4,10} However, even in this case, the total structural relaxation effect of the first and second mechanisms is only a minute increase in θ toward the equilibrium value of 144° (see Fig. 4).

C. Water-induced relaxation in high-fluorinated SiOF films

The structure relaxation process in SiOF films with Si-F_x bond content above 3.7 at. % is assumed to be strongly promoted both by high water absorption and hydrolysis, due to highly open network built mainly from high-order ring units.

Data of Haque *et al.*²⁸ demonstrate no changes in the FTIR spectra of PECVD SiO₂ films that are postannealed in the deposition chamber without breaking vacuum. The presence of water seems to have three effects. First, absorption of water molecules reduces the activation barrier for both film structural relaxation and hydrolysis.²⁷ Second, near-neighbor silanols produced by the hydrolysis promote additional water absorption, as it was confirmed *ibid.* And third, breaking of the Si-O bonds due to the hydrolysis seems to strongly enhanced the flexibility of the SiOF network promoting effective network relaxation.

Figure 6 exhibits the abrupt loss of moisture stability when Si-F_x bond content in SiOF films exceeds 3.7 at. %. Drastic increase of the silanol concentration when F content in the films reaches a critical concentration was reported in many studies.^{1,3,26,29} Low-fluorinated SiOF films are characterized by relatively dense H- and OH-free network (see Fig. 1) built from low-order ring structural units.^{2,7} With increased F content in the incoming flux during the deposition process, the SiOF network is also H- and OH-free as-deposited, as seen in Fig. 1, but is more open and less dense due to the presence of large high-order rings and multiple F termination. As a consequence, high-fluorinated films quickly absorb atmospheric water in large quantities during post-deposition, which effectively reduces activation barriers for both the hydrolysis and structural relaxation processes. As a result, even a minute excess of $\langle \theta \rangle$ in as-deposited SiOF films above its equilibrium value equal to 144° is enough to activate both structural relaxation and hydrolysis processes in these films during post-deposition period.

Galeener suggested that high-order rings of the SiO₂ glass network, which are characterized by a high value of $\langle \theta \rangle$, should exhibit strong "puckering" during post-deposition period in order to reduce $\langle \theta \rangle$ toward the minimum energetic state.³⁰ Si-O bond breaking by the hydrolysis reactions seems to strongly enhance the network flexibility reducing rotation barriers. However, the presence of F in the SiOF network can induce additional mechanisms that may or may not involve water molecules. Recently, Yang and Lucovsky¹⁰ have shown, on the basis of *ab initio* calculations, that near-neighbor F atoms within common ring unit can exothermically react with water molecule through the following reaction:



It is assumed that reconstruction of Si-O-Si bridging units, as a result of this reaction, increases the amount of low-order component in ring statistics of the SiOF network. Even the hydrolysis of mono- and difluoride sites can cause strong structural deformations promoting Si-O bond rearrangement toward small-angular low-order ring units.

It is also likely that as F content in SiOF films exceeds a certain value, the amount of weakly bonded Si-F_x units in the SiOF network drastically increases with F content giving rise to the intense F desorption, as it was found by Bhan *et al.*³ HF presence in the film,⁴ as a result of F reacting with

water, can cause deterioration of the film network and make it more open.

The range of possible reactions involving F, H₂O, and Si–O bonds is very large and is not a subject of the present study. However, considering the attack of moisture on the SiOF network, it is likely that water molecules should initially attack pore-faced Si–O units developing their attack in the bulk of film. Taking into account the difference in the surrounding of pore-faced and bulk rings, it is assumed that the resulting structural homogeneity of the film can worsen after its hydrolysis, as it was found in our studies (see Fig. 5). Moreover, additional Si–O–Si units produced through the reaction (1) should also have a large $\Delta\theta$ about the equilibrium value of $\langle\theta\rangle$ additionally worsening the film homogeneity.

V. CONCLUSIONS

The increased incorporation of fluorine into the SiOF network during film deposition gradually increases the value of the average Si–O–Si angle, $\langle\theta\rangle$, in the Si–O–Si groups from 138° to 153°. It is concluded that only the value of about 144° corresponds to nearly relaxed SiOF network and therefore can be considered as an equilibrium angle for SiOF films. This value of $\langle\theta\rangle$ is appropriate to the films that contain about 3.7 at. % of Si–F_x bonds. Subsequent increase of fluorine content in the films results in “overequilibrium” values of $\langle\theta\rangle$ and causes structural relaxation of the SiOF network towards the equilibrium $\langle\theta\rangle$ during exposure of the films to the atmospheric moisture. Both “under-” and “overequilibrium” values of $\langle\theta\rangle$ seem to be the sources of SiOF film structural instability and increased reactivity with atmospheric moisture. However, film hydrolysis and structural relaxation processes in the SiOF films characterized by “underequilibrium” values of $\langle\theta\rangle$ are effectively suppressed by F presence in moderate concentrations. On the contrary, SiOF films characterized by “overequilibrium” $\langle\theta\rangle$ have low-dense network and heavily absorb atmospheric water, which strongly promotes both structural relaxation and hydrolysis during the post-deposition period.

ACKNOWLEDGMENTS

This work was partially supported by DGAPA-UNAM under Project No. IN100997 and CONACyT under the Project No. 26423-A.

- ¹M. Yoshimura, S. Koizumi, and K. Shimokawa, *J. Vac. Sci. Technol. A* **15**, 2915 (1997).
- ²T. Tamura, J. Sakai, M. Satoh, Y. Inoue, and H. Yoshitaka, *Jpn. J. Appl. Phys., Part 1* **36**, 1627 (1997).
- ³M. K. Bhan, J. Huang, and D. Cheung, *Thin Solid Films* **308–309**, 507 (1997).
- ⁴T. Usami, K. Shimokawa, and M. Yoshimaru, *Jpn. J. Appl. Phys., Part 1* **33**, 408 (1994).
- ⁵W. S. Yoo, R. Swope, and D. Mordo, *Jpn. J. Appl. Phys., Part 1* **36**, 267 (1997).
- ⁶M. Yoshimaru, S. Koizumi, and K. Shimokawa, *J. Vac. Sci. Technol. A* **15**, 2908 (1997).
- ⁷T. Tamura, J. Sakai, Y. Inoue, M. Satoh, and H. Yoshitaka, *Jpn. J. Appl. Phys., Part 1* **37**, 2411 (1998).
- ⁸M. T. Weise, S. C. Selbrede, L. J. Arias, and D. Carl, *J. Vac. Sci. Technol. A* **15**, 1399 (1997).
- ⁹H. Kudo, R. Shinohara, S. Takeishi, N. Awaji, and M. Yamada, *Jpn. J. Appl. Phys., Part 1* **35**, 1583 (1996).
- ¹⁰H. Yang and G. Lucovsky, *J. Vac. Sci. Technol. A* **16**, 1525 (1998).
- ¹¹W. T. Tseng, Y. T. Hsieh, C. F. Lin, M. S. Tsai, and M. S. Feng, *J. Electrochem. Soc.* **144**, 1100 (1997).
- ¹²G. Lucovsky and H. Yang, *Jpn. J. Appl. Phys., Part 1* **36**, 1368 (1997).
- ¹³J. A. Theil, D. V. Tsu, M. W. Watkins, S. S. Kim, and G. Lucovsky, *J. Vac. Sci. Technol. A* **8**, 1374 (1990).
- ¹⁴S. M. Han and E. S. Aydil, *J. Vac. Sci. Technol. A* **15**, 2893 (1997).
- ¹⁵V. Pankov, J. C. Alonso, and A. Ortiz, *Jpn. J. Appl. Phys., Part 1* **37**, 6135 (1998).
- ¹⁶R. A. B. Devine, R. Dupree, I. Farman, and J. J. Capponi, *Phys. Rev. B* **35**, 2560 (1987).
- ¹⁷F. L. Galeener, R. A. Barrio, E. Martinez, and R. J. Elliott, *Phys. Rev. Lett.* **53**, 2429 (1984).
- ¹⁸W. A. Pliskin, *J. Vac. Sci. Technol.* **14**, 1064 (1977).
- ¹⁹N. Hirashita, S. Tokitoh, and H. Uchida, *Jpn. J. Appl. Phys., Part 1* **32**, 1787 (1993).
- ²⁰A. Brunet-Bruneau, J. Rivory, B. Rafin, J. Y. Robic, and P. Chaton, *J. Appl. Phys.* **82**, 1330 (1997).
- ²¹D. V. Tsu, B. N. Davidson, and G. Lucovsky, *Phys. Rev. B* **40**, 1795 (1989).
- ²²Y. Nakasaki, H. Miyajima, R. Katsumata, and N. Hayasaka, *Jpn. J. Appl. Phys., Part 1* **36**, 2545 (1997).
- ²³J. C. Alonso, R. Vazquez, A. Ortiz, V. Pankov, and E. Andrade, *J. Vac. Sci. Technol. A* **16**, 3211 (1998).
- ²⁴V. Pankov, J. C. Alonso, and A. Ortiz, *J. Appl. Phys.* **86**, 275 (1999).
- ²⁵M. D. Newton and G. V. Gibbs, *Phys. Chem. Miner.* **6**, 221 (1980).
- ²⁶M. J. Shapiro, S. V. Nguyen, T. Matsuda, and D. Dobuzinsky, *Thin Solid Films* **270**, 503 (1995).
- ²⁷Y. Nakasaki, H. Miyajima, R. Katsumata, and N. Hayasaka, *Jpn. J. Appl. Phys., Part 1* **36**, 2533 (1997).
- ²⁸M. S. Haque, H. A. Naseem, and W. D. Brown, *J. Electrochem. Soc.* **144**, 3265 (1997).
- ²⁹Y. Nakasaki, H. Miyajima, R. Katsumata, and N. Hayasaka, *Jpn. J. Appl. Phys., Part 1* **36**, 5259 (1997).
- ³⁰F. L. Galeener, *J. Non-Cryst. Solids* **49**, 53 (1982).

1.59 μm Lattice-Matched AlGaInAs/InGaAs/InP Lasers With Digital Alloy Barrier and Waveguide Layers

LEOs '98

G.T. Liu, A. Stintz, E.A. Pease, T.C. Newell, K.J. Malloy, L.F. Lester
Center For High Technology Materials, University of New Mexico,
1313 Goddard SE, Albuquerque, NM 87106
(gliu@chtm.unm.edu)

Introduction

The AlGaInAs on InP material system with a 70/30 $\Delta E_c/\Delta E_v$ ratio has a more favorable energy band offset than the InGaAsP on InP system and, consequently, lasers with improved temperature and power performance are anticipated from the former. Several 1.5 μm lasers have been demonstrated using AlGaInAs grown by both molecular beam epitaxy (MBE) [1-2] and metal-organic chemical vapor deposition (MOCVD) [3]. The previous MBE work on 1.5 μm lasers has focused on the conventional growth of strained InGaAs or AlGaInAs quantum wells. In this paper, we present the first lattice-matched InGaAs quantum well lasers with barriers and waveguide grown using a digital alloy MBE technique. By rapidly switching the ternaries of AlInAs and InGaAs, the digital alloy process permits the growth of any quaternary AlGaInAs composition. Therefore, this technique allows greater flexibility in the design of device structures and reduces the growth complexity associated with quaternary materials, i.e., problems with abrupt changes in composition and compositional grading, or the need for multiple, identical Group III effusion cells. The potential drawback of digital alloying, however, is the introduction of many heterojunction interfaces that can getter impurities that enhance non-radiative recombination. The objective of this work is to compare the threshold current density of AlGaInAs/InGaAs multiple quantum well (MQW) lasers with digital alloy barrier and waveguide layers to those previously grown by conventional MBE.

Results

The laser structure is grown on an n-type, sulfur doped, epi-ready InP wafer with a (100) orientation. The surface oxide is desorbed under an arsenic flux at $\sim 520^\circ\text{C}$. The substrate is heated radiatively, and a constant substrate growth temperature is maintained throughout the growth. Silicon and beryllium are used for n- and p-type doping, respectively. The structure is grown without interruption and all epitaxial layers are lattice-matched. The optimum growth temperature is determined to be 510°C from a photoluminescence study (Fig.1.) of a test structure with four 95 \AA InGaAs wells and three 50 \AA AlGaInAs barriers sandwiched between two 1000 \AA $(\text{Al}_{0.4}\text{Ga}_{0.6})_{0.47}\text{In}_{0.53}\text{As}$ layers grown at three different temperatures. The barriers and thick layers are both digital alloys of the same composition.

In order to minimize the free carrier absorption loss in the cladding layers, a broadened waveguide laser design [4] is employed with a total waveguide thickness near 1 μm (Fig.2.). A numerical simulation indicates that less than 10% of the optical mode propagates in the doped cladding layer. To achieve barrier and waveguide layers with a composition of $(\text{Al}_{0.48}\text{In}_{0.52}\text{As})_{0.4}(\text{Ga}_{0.47}\text{In}_{0.53}\text{As})_{0.6}$, a digital alloy approach is employed to grow alternating layers of 3.3 \AA $\text{Al}_{0.48}\text{In}_{0.52}\text{As}$ and 4.9 \AA $\text{Ga}_{0.47}\text{In}_{0.53}\text{As}$ to the desired total thickness. Based on a previous study of the minimum necessary cladding layer thickness in separate confinement heterostructure lasers [5], a relatively thin thickness of 1 μm is used to ease the growth of the AlInAs clad.

100 μm wide broad-area lasers with a wavelength peaked at 1.59 μm have been fabricated using the material shown in Fig. 2. A pulsed threshold current density, J_{th} , of $981\text{A}/\text{cm}^2$, which is comparable to that of previously published lasers grown by conventional MBE [1-2], is achieved for 1 mm long cavity, 4-QW lasers (Fig.3.). These devices are the first lattice-matched AlGaInAs/InGaAs quantum well lasers with an emission wavelength close to 1.55 μm that use digital alloy MBE growth. The threshold current results demonstrate that non-radiative recombination is not a problem in MQW AlGaInAs/InGaAs lasers with digital alloy barrier and waveguide layers.

References

- [1] M. Quillec, M. Allovon, F. Brillouet, A. Gloukhian, J.P. Praseuth, B. Sermage, "Very low threshold current density GaInAs/AlGaInAs MQW lasers made by phosphorus-free MBE and operating in 1.5-1.6 μ m range," Electronics letters, Vol.25, No.25, p.1731, December 1989.
- [2] M.J. Mondry, E.J. Tarsa, L.A. Coldren, "Molecular-beam epitaxial-growth of strained AlGaInAs multi-quantum-well lasers on InP," Journal of Electronic Materials, Vol.25, No.6, p. 948, June 1996.
- [3] G.A. Evans, J.P. Sih, T.M. Chou, J.B. Kirk, J.K. Butler, L.Pang, "AlGaInAs/InP ridge-guide lasers operating at 1.55 μ m," SPIE Proceedings Vol. 3284, p.205, January 1998.
- [4] D.Z. Garbuzov, R.U. Martinelli, H. Lee, P.K. York, R.J. Menna, J.C. Connolly and S.Y. Narayan, "Ultralow-loss broadened-waveguide high-power 2 μ m AlGaAsSb/InGaAsSb/GaSb separate-confinement Quantum-well Lasers," Apply Physics Letters, Vol.69, No.14, p.2006, September 1996.
- [5] A. Behfar-Rad, J.R. Shealy, S. R. Chinn, S.S. Wong, "Effect of cladding layer thickness on the performance of GaAs-AlGaAs graded index separate confinement heterostructure single quantum-well lasers," IEEE Journal of Quantum Electronics, Vol.26, No.9, p.1476, September 1990.

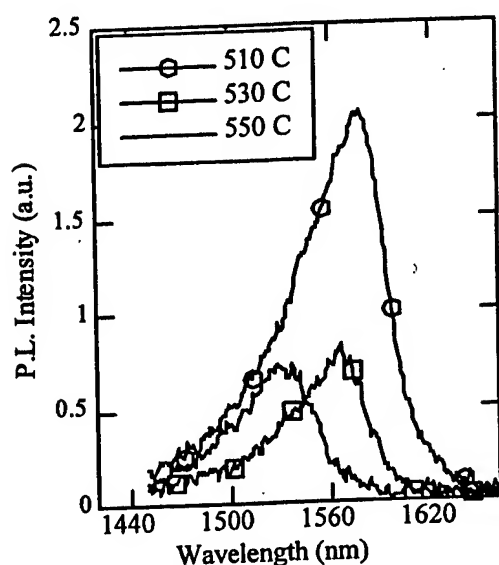


Fig.1. Photoluminescence spectra from a test structure grown at three different temperatures.

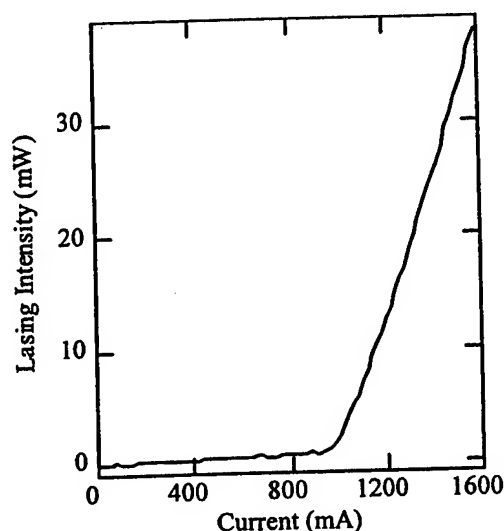


Fig.3. Lasing intensity versus drive current for quasi-CW operation.

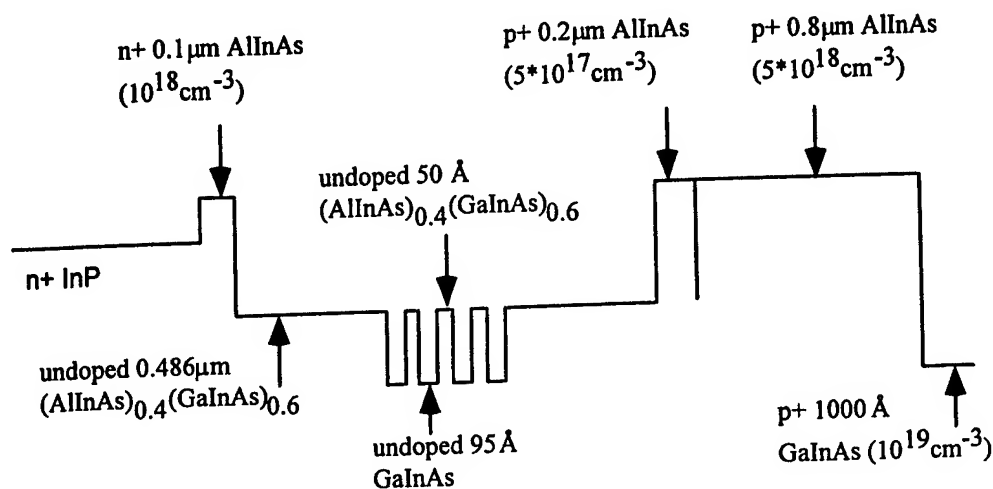


Fig.2. The broadened waveguide 1.59 μ m laser structure.

Improved Efficiency in 2 μm Broadened Waveguide GaInAsSb/AlGaAsSb Multiple Quantum Well Lasers

LEOS'98

T. Newell, A. L. Gray*, H. Lee*, S. Dorato†, and L. F. Lester
Center for High Technology Materials, University of New Mexico
1313 Goddard SE, Albuquerque, NM 87106
Tel: (505) 272-7852, Fax: (505) 272-7801, newell@chtm.unm.edu

*Also at: U.S. Army Research Laboratory, 2800 Powder Mill Rd. Adelphi MD 20783

†Sarnoff Corporation, CN5300, Princeton, NJ 08543-5300

‡Also at: Air Force Research Laboratory, 3550 Aberdeen Ave SE, Kirtland AFB, 87106

Broadened waveguide 2 μm GaInAsSb/AlGaAsSb QW lasers have low internal loss ($\alpha_i \sim 2\text{cm}^{-1}$ [1]) since the overlap between the lossy cladding regions and the optical field is small. However, a broadened waveguide increases the likelihood of recombination in the barrier region, especially if QW carrier confinement is poor, and could cause injection efficiency to decrease. In latticed-matched GaInAsSb/AlGaAsSb QWs, the valence band barrier is very small for a wide range of compositions. While it is known that compressive strain can deepen the hole QW [2], an analysis of the effect of strain and barrier offsets on the device performance has yet to be performed. We investigate the influence of Al barrier percentage and QW arsenic content on the energy offsets. We compare the performance of 2 μm multiple QW (MQW) GaInAsSb/AlGaAsSb lasers with deeper hole QW's to previously published devices [1] and show that a higher internal efficiency, η_i , is the benefit of the improved hole confinement.

In Ref. [1], the saturated gain/well of 20 cm^{-1} suggests that the 25% Al barrier composition produces a valence band well that is too shallow. Consequently, we chose to increase the Al composition to 40%. Computations show that the valence band potential well is thus increased by 69 meV. We also found that the small arsenic percentage in the QW that is typical for these 2 μm lasers needs to be precisely controlled or else the valence band offset can change significantly. In Fig. 1, the potential well energy, ΔE_v , is plotted versus the As percentage for the 25% Al and 40% Al cases. Materials parameters for GaInAsSb and AlGaAsSb are based upon published values of binaries [3] and bandgap models of Adachi [4] and DeWinter [5]. Notice that for some As percentages, ΔE_v is more than a factor of 2 different. Thus, accurate knowledge of the barrier and well thickness' and compositions is vital. Our 4-QW structure is shown in Fig. 2. By combining X-ray diffraction and TEM scans, all material properties may be pinpointed [6]. A TEM image of the 4-QW wafer is shown in Fig. 3. The materials analysis yields that the wafer contains 105 Å $\text{Ga}_{0.85}\text{In}_{0.15}\text{As}_{0.06}\text{Sb}_{0.94}$ wells with 180 Å $\text{Al}_{0.4}\text{Ga}_{0.6}\text{As}_{0.04}\text{Sb}_{0.96}$ barriers.

Figure 4 shows the peak power of a pulsed 900 μm 2-QW laser with nearly identical composition wells to the 4-QW version. J_{th} is 208 A/cm², and the differential efficiency, η_d , is 74% [7], which is the highest value presently reported for 2 μm lasers of comparable length. The internal efficiency, η_i , and internal loss, α_i , are 80% and 2.5 cm^{-1} , respectively. In comparison to the broadest waveguide laser of Ref. [1], our measured η_i is greater (80% compared to 60%). Additionally, the Ref. [1] lasers have a saturated g_{mod}/QW of roughly 20 cm^{-1} while these devices produce 31 cm^{-1} . Superiority stems from the greater barrier potential imposed by the $\text{Al}_{0.4}\text{Ga}_{0.6}\text{As}_{0.03}\text{Sb}_{0.97}$ barrier. For the $\text{Ga}_{0.85}\text{In}_{0.15}\text{As}_{0.06}\text{Sb}_{0.9}$ wells studied here, the increase from 25% to 40% Al in the barrier nearly doubles the well depth. The thermionic emission time of carriers from the well, τ_e , which critically influences the internal efficiency [8], increases exponentially with the barrier height. A longer τ_e increases η_i since the probability of recombination in the QW is enhanced at the expense of barrier recombination processes.

We have investigated the influence of arsenic and barrier aluminum compositions on the QW strain and valence band barrier heights. Our investigations show that the barrier height is critically influenced by the As well percentage and that an increase of barrier Al from 25% to 40% leads to an increase in well depth by 69 meV. We also have fabricated 105 Å $\text{Ga}_{0.85}\text{In}_{0.15}\text{As}_{0.06}\text{Sb}_{0.94}/\text{Al}_{0.4}\text{Ga}_{0.6}\text{As}_{0.04}\text{Sb}_{0.96}$ QW lasers and have established uniquely the structure and elemental compositions. These devices yield internal

efficiencies of up to 80% and g_{mod}/QW of 31 cm^{-1} , which represents a 33% and 50% improvement, respectively, over 25% Al barrier devices.

References

- [1] D. Z. Garbuzov, R. U. Martinelli, H. Lee, P. K. York, R. J. Menna, J. C. Connolly, and S. Y. Narayan, Appl. Phys. Lett. **69**, 2006, 1996.
- [2] H. K. Choi and S. J. Eglash, IEEE Photon. Technol. Lett. **6**, 7, 1994.
- [3] Y. Tsou and A. Ichii and E. M. Garmire, J. Quantum Elect **28**, 1261, 1992; Landolt and Bornstein, "Numerical Data and Functional Relationships in Science and Technology, vols 17a and 17b", Edited by O. Madelung. M. Shultz and H. Weiss, ("Springer, New York", 1982).
- [4] S. Adachi, J. Appl. Phys. **61**, 4869, 1987.
- [5] J. C. DeWinter and M. A. Pollack and A. K. Srivastava and J. L. Zyskind, J. Electron. Mater. **14**, 729, 1985.
- [6] A.L. Gray, T.C. Newell, S. Dorato, L. F. Lester, to be presented at the Electronic Materials Conference, 1998.
- [7] T.C. Newell, L. F. Lester, X. Wu, Y. Zhang, and A.L. Gray, Proc. of the SPIE **3284**, pp. 258, 1998.
- [8] R. Nagarajan, R. P. Mirin, T. E. Reynolds, and J. E. Bowers, IEEE Photon. Technol. Lett. **4**, pp. 832, 1992.

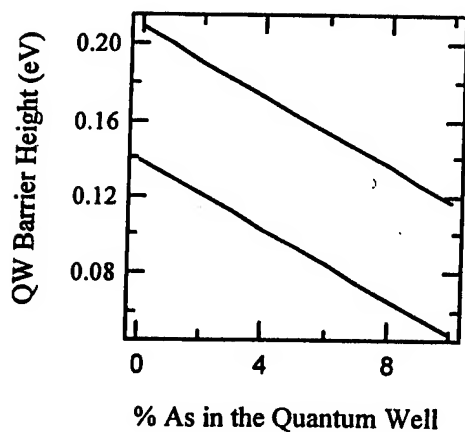


Fig. 1. ΔE_v as a function of As percentage for a for a $\text{Ga}_{0.85}\text{In}_{0.15}\text{As}_{1-x}\text{Sb}_x/\text{AlGaAsSb}$ QW (solid line 40% Al barrier, dashed line 25% Al barrier).

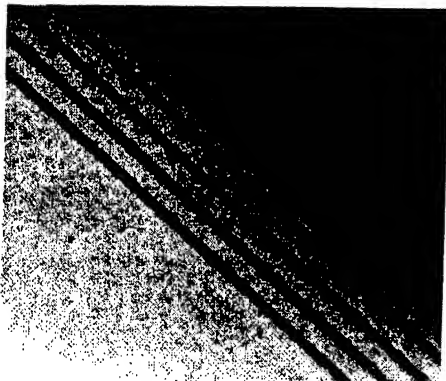


Fig. 3. TEM image of the 4-QW structure.

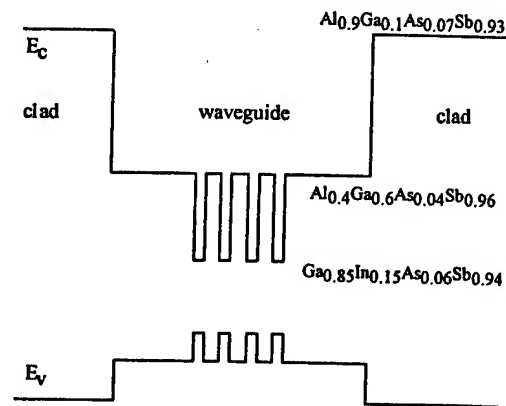


Fig. 2. 4-QW layer schematic.

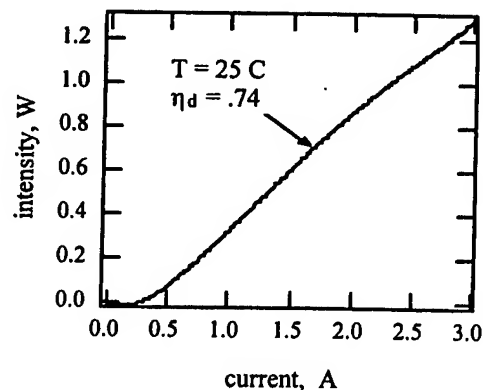


Fig. 4. L-I curve of the 900 μm 2-QW laser.

Materials Growth and Device Characterization of InAs Quantum Dot Lasers

LEOS 2000

Luke F. Lester

Center for High Technology Materials, University of New Mexico
1313 Goddard SE, Albuquerque, NM 87106
Tel: (505)272-7851; Fax: (505)272-7801; e-mail: luke@chtm.unm.edu

Recent progress in long-wavelength quantum dot lasers on GaAs substrates has been associated with either initiating, embedding, or covering growth of $\text{In}_x\text{Ga}_{1-x}\text{As}$ quantum dots (QD) with 2D InGaAs layers [1-7]. It has been established that strained InGaAs layers help to achieve higher dot density [2, 4, 5, 7] and to extend the luminescence wavelength up to $1.35\text{-}\mu\text{m}$ without intensity degradation [2, 6]. Very impressive laser performance has been achieved with QDs surrounded by InGaAs layers compared to those embedded in a GaAs matrix [8], including a threshold current density as low as 16 A/cm^2 at $1.25\text{-}\mu\text{m}$ [9]. A CW output power of 2.7 W near $1.3\text{ }\mu\text{m}$ [4], a linewidth enhancement factor, $\alpha = 0.1$, and a tuning range of 201 nm [10] have also been demonstrated. Many reports attribute these successes only to a higher dot density [4, 5, 7]. However, it has been argued that an InGaAs quantum well (QW) around the dots is also very important in helping the QDs to capture carriers or, alternatively, to funnel carriers to the dots much like a separate confinement heterostructure [1, 2]. Thus, a new semiconductor laser design name has been proposed—the dots-in-a-well (DWELL) laser.

Previous InGaAs QD laser research has described the use of InGaAs layers with various indium compositions around the dots [1-3, 5-7]. In this presentation, a systematic study of the DWELL approach is described. In the first part, the properties of InAs QD's grown by molecular beam epitaxy (MBE) in narrow, pseudomorphically strained $\text{In}_x\text{Ga}_{1-x}\text{As}$ ($x \leq 0.2$) QW's are reported. The materials characterization focuses on crystal growth issues that effect dot size, dot density, emission wavelength, and photoluminescence (PL) linewidth. PL and atomic force microscopy data elucidate the role played by growth temperature, QW composition, and position of the QD within the QW in determining the important QD parameters. In general, dot density, which is a crucial in deciding the maximum optical gain, increases with larger In composition in the QW and lower growth temperature. There is a tradeoff, however, because the PL linewidth tends to narrow and the emission wavelength to get longer with higher growth temperature. In the second part, the optical performance of quantum dot lasers with different DWELL structures is studied as a function of the well number and the indium composition in the InGaAs QW surrounding the dots. While keeping the InAs quantum dot density nearly constant, the internal quantum efficiency, η_i , modal gain, and characteristic temperature of 1-DWELL and 3-DWELL lasers with QW indium compositions from 10% to 20% are analyzed. Comparisons between the DWELL lasers and a conventional $\text{In}_{0.15}\text{Ga}_{0.85}\text{As}$ strained QW laser are also made. As the indium content rises in the InGaAs QW, η_i and the maximum ground-state gain of the InAs QD active region improve significantly. The characteristic temperature, T_0 , of the DWELL structure also gets better with increasing In% in the well, but a more substantial rise is observed with an increasing number of DWELL stacks. From these results, it is inferred that the QW around the dots is necessary to improve the DWELL laser's performance for the dot densities studied.

- [1] G. T. Liu, A. Stintz, H. Li, K. J. Malloy, and L. F. Lester, "Extremely Low Room-Temperature Threshold Current Density Diode Lasers Using InAs Dots in an In_{0.15}Ga_{0.85}As Quantum Well," *Electron. Lett.*, vol. 35, pp. 1163-1165, 1999.
- [2] L.F. Lester, A. Stintz, H. Li, T.C. Newell, E.A. Pease, B.A. Fuchs and K.J. Malloy, "Optical characteristics of 1.24 μ m quantum dot lasers," *IEEE Photon. Technol. Lett.*, vol. 11, pp. 931-933, 1999.
- [3] Y.M. Shernyakov, D.A. Bedarev, E.Y. Kondrat'eva, P.S. Kopev, A.R. Kovsh, N.A. Maleev, M.V. Maximov, S.S. Mikhlin, A.F. Tsatsulnikov, V.M. Ustinov, B.V. Volovik, A.E. Zhukov, Z.I. Alferov, N.N. Ledentsov, D. Bimberg, "1.3 μ m GaAs-based laser using quantum dots obtained by activated spinodal decomposition," *Electron. Lett.*, vol. 35, pp. 898-900, 1999.
- [4] A.E. Zhukov, A.R. Kovsh, V.M. Ustinov, Y.M. Shernyakov, S.S. Mikhlin, N.A. Maleev, E.Y. Kondrat'eva, D.A. Livshits, M.V. Maximov, B.V. Volovik, D.A. Bedarev, Yu. G. Musikhin, N.N. Ledentsov, P.S. Kopev, Z.I. Alferov, D. Bimberg, "Continuous-Wave Operation of Long-Wavelength Quantum-Dot Diode Laser on a GaAs substrate," *IEEE Photon. Technol. Lett.* vol. 11, pp. 1345-1347, 1999.
- [5] K. Mukai, Y. Nakata, K. Otsubo, M. Sugawara, N. Yokoyama, H. Ishikawa, "1.3- μ m CW Lasing of InGaAs-GaAs Quantum Dots at Room Temperature with a Threshold current of 8mA," *IEEE Photon. Technol. Lett.*, vol. 11, pp. 1205-1207, 1999.
- [6] K. Nishi, H. Saito, S. Sugou, J.S. Lee, "A narrow photoluminescence linewidth of 21meV at 1.35 μ m from strained-reduced InAs quantum dots covered by In_{0.2}Ga_{0.8}As grown on GaAs," *Appl. Phys. Lett.*, vol. 74, pp. 1111-1113, 1999.
- [7] G. Park, O.B. Shchekin, D.L. Huffaker, D.G. Deppe, "Low-Threshold Oxide-confined 1.3 μ m Quantum-Dot Laser," *IEEE Photon. Technol. Lett.*, vol. 13, pp. 230-232, 2000.
- [8] D.L. Huffaker, G. Park, Z. Zou, O.B. Shchekin, and D. G. Deppe, "1.3 μ m room-temperature GaAs-based quantum-dot laser," *Appl. Phys. Lett.*, vol. 73, pp. 2564-2566, 1998.
- [9] G.T. Liu, et. al., "The Influence of Quantum Well Composition on the Performance of Quantum Dot Lasers Using InAs/InGaAs Dots-in-a-Well (DWELL) Structures," to be published in *IEEE J. Quantum Electron.*
- [10] P. M. Varangis, H. Li, G. T. Liu, T. C. Newell, A. Stintz, B. Fuchs, K. J. Malloy, and L. F. Lester, "Low-Threshold Quantum Dot Laser with a 201 nm Tuning Range," submitted to *Electronics Letters*.

Carrier Lifetime and Radiative Recombination in Quantum Dot LEDs

H. Li, T. C. Newell, G. T. Liu, A. Stintz, K. Malloy, and L. F. Lester

Center for High Technology Materials, University of New Mexico

1313 Goddard SE, Albuquerque, NM 87106

Tel: (505)272-7850; Fax: (505)272-7801; e-mail: huali@chtm.unm.edu

LEOS 2000

Spontaneous emission and even lasing from excited state transitions can be readily observed in quantum dot (QD) devices at low current densities. This is a consequence of the low QD density and small density of states that forces the ground state gain to saturate rapidly. Such properties open new avenues for investigation. In this presentation, the carrier lifetime and radiation recombination rates are determined from experimental measurements. Distinctly different properties characterize the ground and excited state emission.

The differential carrier lifetime τ_d as function of pump current density J for quantum dot LED samples [1] were measured (Fig. 1) by using the technique reported in [2,3]. The total carrier density, n , and carrier lifetime τ_r were obtained from the measured τ_d using $n(I) = \frac{1}{qS} \int_0^I \tau_d(I') dI'$ and $\tau_r(I) = qn(I)/J$ [4].

Analysis shows that the carrier lifetime is a strong function of the pump level. Once J increases beyond 20 A/cm², i.e. typical lasing levels, τ_r decreases from 0.8 to 0.4 ns.

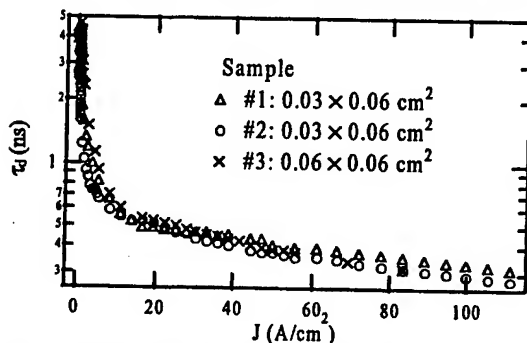


Fig. 1. Measured differential lifetime versus pump current for three QD LED samples.

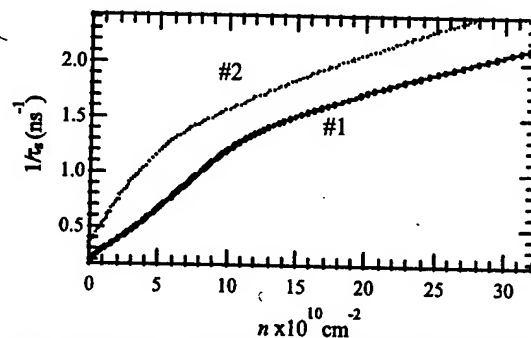


Fig. 2. Inverse carrier lifetime $1/\tau_r$ versus carrier density for two QD LED samples.

The recombination rate R is traditionally expressed in terms of the carrier density by $R = An + Bn^2$, where the coefficients A , and B characterize defect and radiative recombination respectively, and Auger recombination is insignificant. The recombination A and B coefficients can be obtained from $\tau_r^{-1} = R/n = A + Bn$. Thus a plot of $1/\tau_r$ versus n should yield a straight line with an intercept of A and a slope of B , and this has been observed for some QW lasers [4]. However, the curve of $1/\tau_r$ versus n for the QD LED samples presents a clearly different behavior (Fig. 2) showing intersecting lines of different slopes in two pump regimes. Since these two pump regimes correspond to carrier filling mainly on the ground state and the 1st excited state, the different slopes in the plot of $1/\tau_r \sim J$ indicate that these two levels have different radiative recombination rates. This circumstance could be caused by lower wavefunction overlap between electrons and holes involved in the 1st excited state transition. To account for these results, the total recombination rate R is generalized to reflect the carrier densities in the QD ground and excited states along with the QW ground state

$$R = \sum_{i=0}^2 (A_{di} \cdot n_{di} + B_{di} \cdot n_{di}^2) + (A_w \cdot n_w + B_w \cdot n_w^2).$$

Here A_d and B_{di} are A , B coefficients for QD states, and n_{di} is the 2D carrier density of the i th ($i=0$ is for the ground state, $i=1,2$ are for the 1st and 2nd excited states). The terms in the last brackets are the recombination rates associated with carrier filling in the lowest energy QW state. The total carrier density n is the sum of the component densities, $n=n_{d0}+n_{d1}+n_{d2}+n_w$. The carrier concentrations n_{d0} , n_{d1} , and n_{d2} are found using discrete energy levels, and Fermi-Dirac statistics within the QDs and between the QDs and the QW is assumed [5]. The values of n_{d0} , n_{d1} , n_{d2} and n_w for a given n are obtained from this assumption, and then R is calculated to fit the experimental $J(=qR)$ versus n . The A , B coefficients as fitting parameters obtained in the calculation are $A_d=(2.9\pm0.7)\times10^8\text{ s}^{-1}$, $B_{d0}=(3.2\pm0.3)\times10^{-2}\text{ cm}^2\text{ s}^{-1}$, $B_{d1}=(2.4\pm0.3)\times10^{-2}\text{ cm}^2\text{ s}^{-1}$ and $B_{d2}=(3.0\pm0.5)\times10^{-2}\text{ cm}^2\text{ s}^{-1}$ for QDs. In Fig. 3 the fitted $n\sim J$ curve (solid line) for sample #2 shows very good agreement with the experimental data (dashed line). The corresponding carrier densities in each of the QD energy levels are also plotted in Fig. 3. The curves show several regimes of carrier filling on different energy states for an increase in current density. For most pump levels in this measurement n_w in the QW state is a small number compared to the carrier density in the dots.

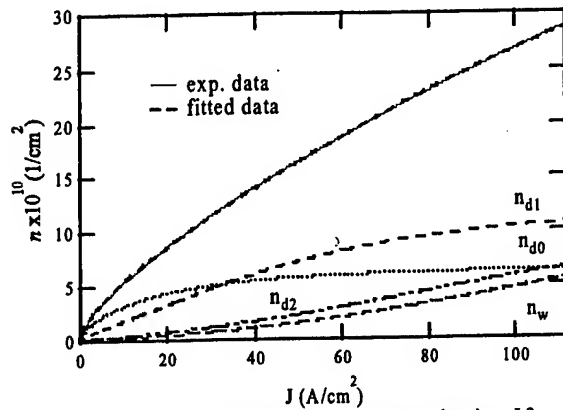


Fig. 3. The total carrier density n versus current density, J for experimental and theoretical data. Also shown are the carrier densities in the QD and QW states.

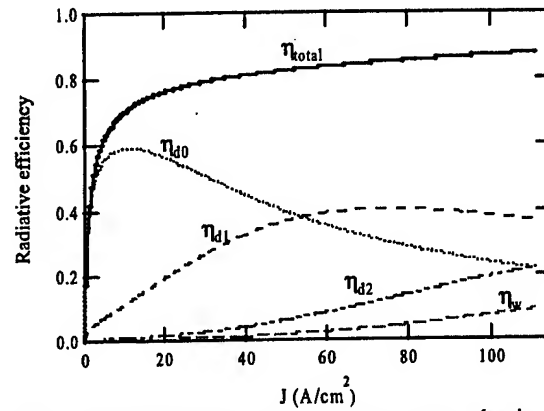


Fig. 4. Radiative efficiencies η versus pump current density J for emission from each state.

Figure 4 shows the radiative efficiency: $\eta_{d0}=B_{d0}n_{d0}^2/R$ for the QD ground state, $\eta_{d1}=B_{d1}n_{d1}^2/R$ for the QD 1st excited state, $\eta_{d2}=B_{d2}n_{d2}^2/R$ for QD 2nd state, and $\eta_w=B_w n_w^2/R$ for QW state. $\eta_{total}=\eta_{d0}+\eta_{d1}+\eta_{d2}+\eta_w$. Here R is the recombination rate defined above. The interesting result is that the radiative efficiency, η , for a particular QD state is strongly influenced by carrier filling in the upper energy states. Therefore, the η will rise initially with increasing pump, reach a maximum, and then decrease with further increase in the pump as carrier filling saturates and occupation of higher energy states becomes significant.

In conclusion we have measured τ_d as a function of current density for QD LED samples and used this data to calculate the functional relationship between the carrier lifetime, carrier density, and radiative efficiency. The results indicate that carrier filling on the different dot energy levels has a strong influence on the radiative behavior of the devices and that the radiative rate coefficient, B , for different QD levels can vary considerably.

- [1] G. T. Liu, A. Stinz, H. Li, K. J. Malloy, and L. F. Lester, *Electron Lett.*, vol. 35, pp.1163-1165, 1999.
- [2] G. E. Shtengel, D. A. Ackerman, P. A. Morton, E. J. Flynn, and M. S. Hybertsen, *Appl. Phys. Lett.*, vol. 67, pp.1505-1508, 1995.
- [3] G. E. Giudice, D. V. Kuksenkov, H. Temkin, and K. L. Lear, *Appl. Phys. Lett.*, vol. 74, pp. 899-901, 1999.
- [4] R. Olshansky, C.B. Su, J. Manning, and W. Powazinik, *IEEE J. Quant. Electron.*, vol. QE-20, pp. 838-854, 1984.
- [5] H. Jiang and J. Singh, *J. Appl. Phys.*, vol. 85, pp.7438-7442, 1999.

Low Threshold Oxide-Confined InAs Quantum Dash Ridge Waveguide Lasers on InP Substrates

LEOS 2001
R. H. Wang, A. Stintz, T. J. Rotter, K. J. Malloy, and L. F. Lester
Center for High Technology and Materials, University of New Mexico
Goddard SE, Albuquerque, NM 87106
Tel: (505)272-7849, Fax: (505)272-7801, Email: rwang@chtm.unm.edu
A. L. Gray, T. C. Newell, and P. M. Varangis
Zia Laser Inc.
7817 Pinewood NW, Albuquerque, NM 87120
Tel: (505)272-7586, Fax: (505)272-7801, Email: agray@chtm.unm.edu

Introduction: There is strong interest in using low-dimensional semiconductor systems, such as quantum dots (QDs) and quantum wires, in optoelectronic devices due to the unique optical properties of these nanostructures [1]. In addition, wet oxidation of Al-containing semiconductor layers is an increasingly popular process for laser diodes since Al-oxide provides excellent current confinement and optical mode control with a simple fabrication technique. In previous research, wet oxidation of $\text{Al}_x\text{Ga}_{1-x}\text{As}$ has been extensively used for making current apertures in vertical cavity surface emitting lasers (VCSEL) and in-plane lasers on GaAs substrates [2,3]. More relevant to this work, an InP-based quantum well (QW) laser diode with selective oxidation of $\text{Al}_{0.48}\text{In}_{0.52}\text{As}$ as a current blocking layer has also been reported [4]. In this letter, oxide-confined ridge waveguide semiconductor lasers with a new type of low-dimensional active region - the self-assembled InAs "quantum dash" - are demonstrated [5]. The name "dash" comes from a physical description of what is essentially an InAs QD that is elongated in one crystalline direction.

Device design and growth: The typical quantum dash (QDASH) dimensions are 300 nm, 25 nm, and 5 nm for the length, width, and height respectively when measured uncapped by atomic force microscope (AFM). The AFM image also shows that the InAs QDASH's are elongated along the $[0\bar{1}1]$ direction. These QDASH's are the active regions in a laser diode design that consists of lattice-matched $\text{Al}_{0.48}\text{In}_{0.52}\text{As}$ cladding layers grown by molecular beam epitaxy (MBE) on an InP substrate around an AlGaInAs waveguide region that has a bandgap of 1.03 eV ($\lambda=1.2\text{ }\mu\text{m}$). The InAs QDASH's are grown within a strained AlGaInAs QW, which has a bandgap of approximately 0.95 eV ($\lambda=1.3\text{ }\mu\text{m}$) and a thickness of 7.5 nm. Five stacks of QW/QDASH's with 30 nm tensile strained AlGaInAs barriers are employed. Heavily p-type lattice-matched InGaAs is deposited last to facilitate a low-resistance ohmic contact.

Results: The laser cavity is align along $[011]$ direction (perpendicular to the dash) to maximize the transverse electric (TE) gain. To prepare the wafers for wet oxidation, 5- μm wide ridges are first formed by BCl_3 inductively coupled plasma (ICP) etching to expose the $\text{Al}_{0.48}\text{In}_{0.52}\text{As}$ cladding layers. The oxidation is then carried out in a horizontal quartz tube in a furnace fed by nitrogen gas passed through a deionized water bubbler maintained at 95 °C. The oxidation temperature was set to 520 °C. After a one-hour oxidation using SiN_x to mask the ridges, the oxidation surface appeared smooth as indicated by a Nomarski image. This process converts $\text{Al}_{0.48}\text{In}_{0.52}\text{As}$ into $\text{Al}(\text{In})\text{O}_x$, which serves as the electrical isolation layer. After removing the SiN_x and depositing the upper p-contact metallization, a self-aligned ridge waveguide is achieved.

The devices were tested with the epitaxial-side up under pulsed conditions with a 0.5 μs pulse width and a 0.5% duty cycle at 15 °C. The L - I and V - I curves for a cleaved laser diode with 1.4 mm-cavity are shown in Fig. 1. There is no significant current leakage through the oxide layer as indicated by the V - I curve. The inset of Fig. 1. illustrates the operation wavelength is 1.57 μm . The lowest threshold current density of 450 A/cm² was measured from an uncoated oxide-confined ridge waveguide laser with 1.8 mm cavity length. The devices were also tested under continuous wave (cw) operation. Fig. 2 shows the cw V - I curve for a 5- μm ridge width and 1-mm cavity length laser diode. The device was mounted epitaxial-side down and uncooled. The total output power is about 25 mW with $4\times I_{th}$ biased.

The inverse external quantum efficiency, $1/\eta_{ex}$, vs. the cavity length, L , data are used to determine the internal loss, α_i , and the injection efficiency, η_i . By fitting the data to the equation $1/\eta_{ex} = 1/\eta_i(1 - \alpha_i L/\ln(R))$, η_i (α_i) values of 87% (10 cm⁻¹) are found. The reflectivity, R , is assumed to be 0.32 for the cleaved facets.

In summary, we have demonstrated oxide-confined self-assembled InAs quantum dash ridge waveguide lasers on InP substrates with room-temperature operation wavelength of 1.57 μm , a high injection efficiency of 87%, and a low threshold current density of 450 A/cm².

Reference:

- [1] Liu, G. T., Sintz, A., Li, H., Newell, T. C., Gray, A. L., Varangis, P. M., Malloy, K. J., and Lester, L. F., *IEEE J. Quantum Electron.*, 2000, **36**, pp. 1272-1279.
- [2] Maranowski, S. A., Sugg, A. R., Chen, E. I., and Holonyak, N., *Appl. Phys. Lett.*, 1993, **63**, pp. 1660-1662.
- [3] Maranowski, S. A., Sugg, A. R., Chen, E. I., and Holonyak, N., *Appl. Phys. Lett.*, 1993, **63**, pp. 1660-1662.
- [4] Iwai, N., Mukaiharu, T., Itoh, M., Yamanaka, N., Arakawa, S., Shimizu, H., and Kasukawa, A., *Electron. Lett.*, 1998, **34**, pp. 1427-1428.
- [5] Utzmeier, T., Postigo, P. A., Tamayo, J., Garcia, R., and Briones, F., *Appl. Phys. Lett.*, 1996, **69**, pp. 2674-2676.

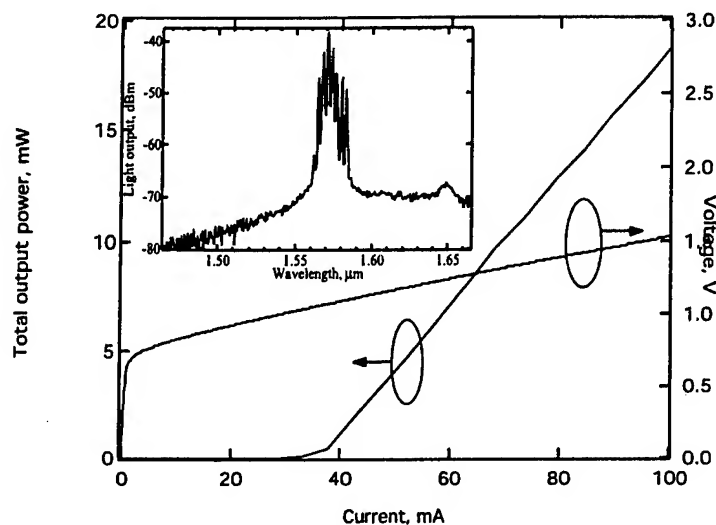


Fig. 1. The L - I and V - I curves for a 5- μm width oxide-confined ridge waveguide laser diode with 1.4-mm cavity length. The inset shows the operation wavelength is 1.57 μm .

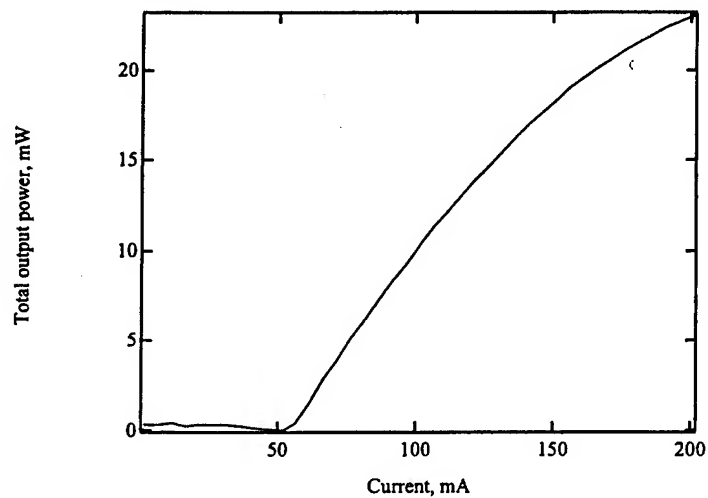


Fig. 2. The L - I curve for a 5- μm width oxide-confined ridge waveguide laser with 1-mm cavity length under cw operation. The sample was mounted p-side down and uncooled.

AlGaInSb/GaInSb Multiple Quantum Well Mid-Infrared Lasers

LEOS 2001

E. A. Pease, L. R. Dawson, A. L. Gray and L. F. Lester

The University of New Mexico, Center for High Technology Materials, 1313 Goddard SE, Albuquerque, New Mexico 87106
edwinp@unm.edu

D. M. Gianardi

Air Force Research Laboratory, AFRL/DELS, Kirtland AFB, Albuquerque, New Mexico 87106

There is a need for antimonide-based, room-temperature, mid-infrared semiconductor lasers in the 2-5 μm band with applications in chemical sensing, countermeasures, and laser radar. Typically arsenic is added to GaInSb to extend the emission wavelength of Type I quantum well active regions for mid-IR lasers fabricated on GaSb. Most notably, highly strained, electrically injected, InGaAsSb Type-I quantum well (QW) lasers with large arsenic content have been reported with wavelengths to 2.78 μm [2]. With increased wavelength in this materials system, however, comes a loss in efficiency and degradation in the characteristic temperature, T_0 . As a remedy, Type-II heterojunctions can provide longer wavelength lasers, but these structures suffer from small spatial overlap of the electron and hole wave-function[3]. The wave-function spatial overlap and the heavy-hole splitting can be increased by growing more complex Type-II wells such as the 'W' laser. These devices have shown strong optically-pumped performance [4] but still suffer from poor electrical characteristics [5]. Improved performance is expected by growing quaternary AlInGaAsSb alloys in the miscibility gap [6] and complex Type-II quantum wells where arsenic and antimony competition [7] makes repeatability an issue.

Arsenic-free GaInSb QW lasers for 2-5 μm applications are realized by growing a graded AlInSb metamorphic buffer layer on GaSb to tailor the lattice constant. This approach maintains larger valence band offsets than adding arsenic to the active region making high performance Type I long wavelength lasers possible. The relaxation of the AlInSb buffer layer generates dislocations that are turned along the slip plane at strained heterojunctions. By increasing the number of heterojunctions, filtering of dislocations is possible. We have found that the filtering is optimally accomplished by fabricating the AlInSb buffer layer from a digital alloy that is step-graded to the desired lattice constant. Using this growth method, strong room-temperature photoluminescence has been observed at 2.5, 2.7, and 3.3 μm indicating high quality active regions.

Figure 1 shows the optically pumped results for two samples with room-temperature target wavelengths of 2.5 and 2.7. The wafers are composed of 4 compressively-strained QWs sandwiched in a 1- μm AlGaInSb waveguide region. The samples were cleaved into 1-mm cavity lengths and pumped with 222- μm stripe widths. The pump is a 980 nm array using 50 μs pulses and 5% duty cycle. The 2.5 μm wavelength sample is composed of 100 Å $\text{Ga}_{0.60}\text{In}_{0.40}\text{Sb}$ wells with $\text{Al}_{0.20}\text{Ga}_{0.48}\text{In}_{0.32}\text{Sb}$ barriers grown on a metamorphic buffer step-graded to $\text{Al}_{0.73}\text{In}_{0.27}\text{Sb}$. Room temperature operation was achieved with 15% differential quantum efficiency and 426 W/cm^2 threshold. The second sample is composed of 100 Å $\text{Ga}_{0.50}\text{In}_{0.50}\text{Sb}$ wells with $\text{Al}_{0.20}\text{Ga}_{0.41}\text{In}_{0.39}\text{Sb}$ barriers grown on a metamorphic buffer step-graded to $\text{Al}_{0.64}\text{In}_{0.36}\text{Sb}$. 2.8 μm room-temperature lasing was achieved with 28% differential quantum efficiency and 360 W/cm^2 threshold. Figure 2 shows the threshold power density versus

temperature measurements between 100K and 320K for the second sample. Below 200K the threshold was virtually constant, and a T_0 of 107K was found above 200K. This is the highest reported T_0 for a semiconductor laser at this wavelength.

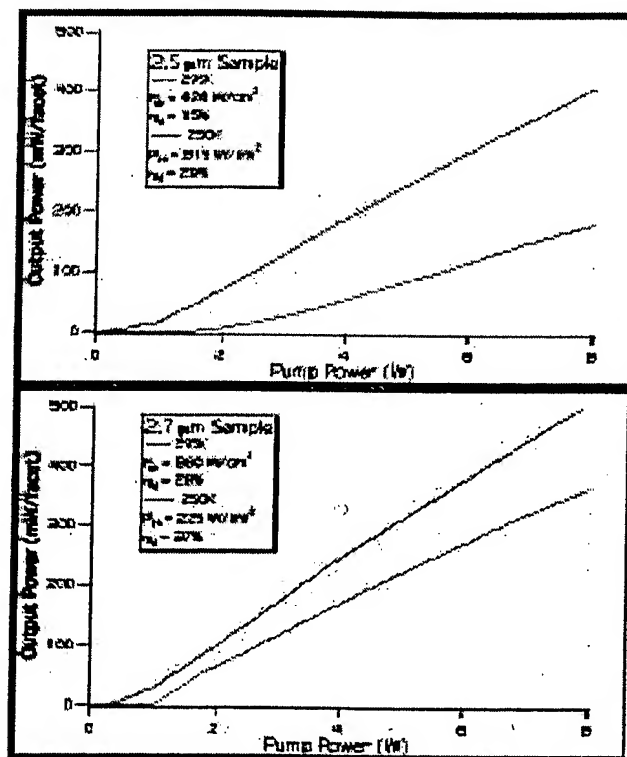


Fig. 1. Optically pumped results.

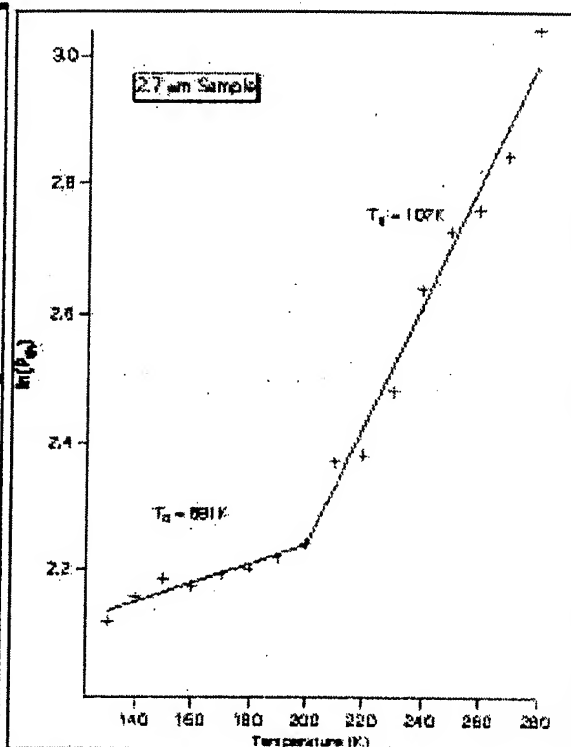


Fig. 2. Power Threshold measurements.

- [1] D. Z. Garbuzov, R. U. Martinelli, H. Lee, P. K. York, R. J. Menna, J. C. Connolly, and S. Y. Narayan, *Applied Physics Letters* **69**, 13 (1996).
- [2] H. Lee, P. K. York, R. J. Menna, and R. U. Martinelli, *Applied Physics Letters* **66**, 15 (1995).
- [3] A. N. Baranov, N. Bertru, Y. Cuminal, G. Boissier, C. Alibert, and A. Joullie, *Applied Physics Letters* **71**, 6 (1997).
- [4] W. W. Bewley, C. L. Felix, E. H. Aifer, I. Vurgaftman, L. J. Olafsen, and J. R. Myers, *Applied Physics Letters* **73**, 26 (1998).
- [5] W. W. Bewley, E. H. Aifer, C. L. Felix, I. Vurgaftman, and J. R. Myers, *Applied Physics Letters* **71**, 25 (1997).
- [6] H. K. Choi, G. W. Turner, M. J. Manfra, and M. K. Connors, *Applied Physics Letters* **68**, 21 (1996).
- [7] Qianghua Xie, J. E. Van Nostrand, J. L. Brown, and C. E. Stutz, *Journal of Applied Physics* **86**, 1 (1999).

2003

tel. (505) 414-1852, fax (505) 272-7801, email: newell@unm.edu

spontaneous emission spectrum [2]

near 10 mW for 200 mA current across the lasing range



1.245 μm (b) J_A as a function of the lasing wavelength

This work was supported by the Defense Advanced Research Projects Agency of the United States Army.

U.S. DEPARTMENT OF SCIENCE & TECHNOLOGY
OFFICE OF SCIENTIFIC RESEARCH (F49620-96-1-00)

Photon. Technol. Lett., vol. 9, pp. 155-157, 1997.

Technol. Lett., vol. 11, pp. 931-933, 1999

Monda

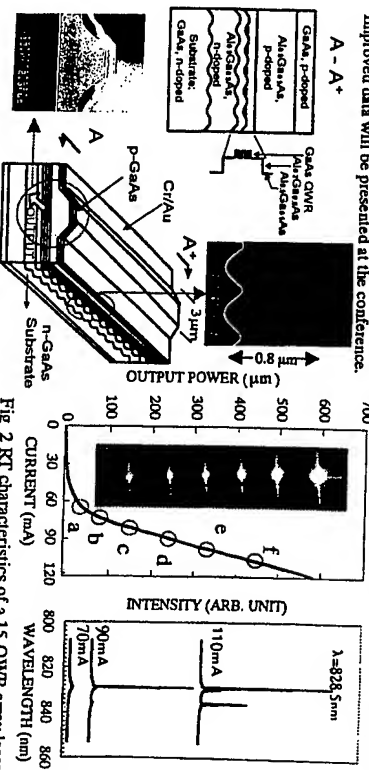
in both distributed feedback- and wire-directions

Jae Geun Kim, Chang-Sik Son, and Mutsuo Ogura

CREST-Japan Science and Technology Corporation (JST)

Phone: +81-298-61-5500; Fax: +81-298-61-3357. Email: info@nissai.co.jp

... of QWK array lasers in directions parallel to the wire. Fig. 1



CHARACTERISTICS OF A 1.5-QW ARRAY LASER

OC-DFB lasers. The emission wavelength is 827 nm at RT

Pulsed-Laser-Induced Quantum Well Interfacing in GaInAs/GaInAsP Laser Structures

T. K. Ong, B. S. Ooi, Y. L. Lam, Y. C. Chan, and Y. Zhou

Photonics Research Group, School of Electrical and Electronics Engineering,
Block S1, Nanyang Technological University, Singapore 639798.
Tel: (65)-7904517, Fax: (65)-7912687 and Email: obooi@ntu.edu.sg

The application of postgrowth tuning of III-V quantum well (QW) structures using pulsed-laser-induced disordering (P-LID) in photonic integrated circuits is an attractive alternative to selective growth and regrowth processes. P-LID is impurity free and offers direct writing capability. This technique also requires lower processing cost compared to quantum well intermixing (QWI) realized using ion implantation.

Here, we report a significant modification of the bandgap energy of GaInAs/GaInAsP laser structure using the P-LID technique. A Q-switched Nd:YAG laser with wavelength of 1.064 μm , generating pulses of 8 ns and pulse repetition rate of 10 Hz was used in the experiment. Samples were irradiated at room temperature with normal incidence to the surface and then annealed at 625°C for 120 s using a rapid thermal processor. We demonstrate that the degree of intermixing is dependent on the pulse energy density and the irradiation time of the Nd:YAG laser. A maximum bandgap shift of up to 112 meV has been observed. The spatial resolution of this technique was shown to be better than 2.5 μm [1].

The effect of laser processing on the material structure was investigated using photoluminescence (PL) measurements and transmission electron microscopy (TEM). Before annealing, no PL signal could be detected from the front surface of the irradiated samples. However, PL spectrum could still be retrieved from the substrate. The PL peak obtained was identical to that of the as-grown samples although the intensity decreased. The TEM images from the intermixed samples are shown in Fig. 1. No damages can be seen from the wells and barriers. However, a small amount of dislocation loops can be observed from the Ga_{0.45}In_{0.55}P_{0.4} graded-index (GRIN) layers. These observations suggest that most of the lattice disruption and bond breaking caused by the laser irradiation were limited to the GRIN layers. A closer observation of the material structure found that the bandgap energy of GaInAs and Ga_{0.45}In_{0.55}P_{0.4} with $\lambda_g = 1.26 \mu\text{m}$ and $1.18 \mu\text{m}$ are 0.72 eV, 0.984 eV and 1.051 eV respectively, which are smaller than that of the 1.064 μm laser source (1.165 eV). Thus, the contact layers and also the GRIN layers of the laser structure are very absorbing and the number of photon from the Nd:YAG laser that reaches the active region might be small. Subsequent annealing recrystallised the materials, caused the interdiffusion of III-V materials in this region, and enhanced the rate of QWI.

Oxide stripe bandgap-tuned lasers have been fabricated from intermixed samples with bandgap tuned by 38 nm and 82 nm by exposing to laser energy densities of 2.4 mJ/mm² and 3.4 mJ/mm², respectively. Figure 2 shows the normalized laser spectra from 500 μm long as-grown, control and bandgap-tuned lasers. The corresponding threshold current densities (J_{th}) are plotted along with the laser spectra. The J_{th} of the lasers increases from 1.08 kA/cm² for the as-grown sample, to about 1.88 kA/cm² for lasers with bandgap tuned to 1.468 μm . Besides dislocation loops formed during the intermixing process, the increase in the J_{th} could also be attributed to the alteration of the shape of the QW that will lead to the loss of carrier confinement.

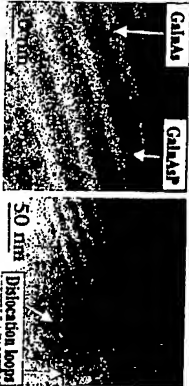


Fig.1. (a) Bright field image from intermixed GaInAs/GaInAsP wells and barriers. (b) The dislocation loops, which appeared in the GRIN layers.

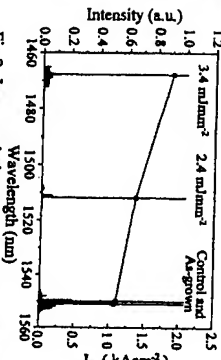


Fig.2. Laser emission spectra of 500 μm long GaInAs/GaInAsP as-grown, control and bandgap-tuned lasers plotted along with the J_{th} .

[1] T. K. Ong, O. Gunawan, B. S. Ooi, Y. L. Lam, Y. C. Chan, Y. Zhou, A. Saker Helmy, and J. H. Marsh, *J. Appl. Phys.* (March 2000 issue).

High-power 1.52- μm AlGaInAs strained multi-quantum well lasers

T. C. Newell, P. M. Varangis, E. Pease, A. Stintz, G. T. Liu, K. J. Malloy, and L. F. Lester

Center for High Technology Materials, University of New Mexico, Albuquerque, NM 87106
Tel (505) 272-7852, Fax (505) 272-7801, email: newell@unm.edu

Eye-safe laser radar, free-space laser communication, and other near-IR illumination technologies are expanding the applications of 1.5 μm lasers, which in the case of AlGaInAs quantum well (QW) devices has traditionally focused on low-power high-speed telecommunications devices.

Here the high-power characteristics and recombination mechanisms of compressively strained AlGaInAs QW lasers operating near 1.52 μm are investigated. The material structure is grown by molecular beam epitaxy (MBE) using the digital alloy technique [1]. Three 80 Å Al_{0.6}Ga_{0.4}In_{0.6}As QWs are centered in a 1- μm wide waveguide of Al_{0.5}Ga_{0.5}In_{0.5}As with 50 Å barriers. The QWs are compressively strained at 0.8%. The material was processed into 200- μm stripe width broad area lasers that demonstrate an internal loss, α_i , of 2 cm⁻¹ and an injection efficiency, η_i , of 62%. At room temperature, the threshold current density, J_{th} , is 410 A/cm² for the best as-cleaved 1-mm cavity length devices. Figure 1(a) plots CW and pulsed light versus current curves for a laser that had one facet HR coated with a 4-layer MgF₂ and poly-Si 3A-layer stack. The large non-radiative recombination currents that exist at high temperatures limit the CW power to 1.75 W before thermal rollover.

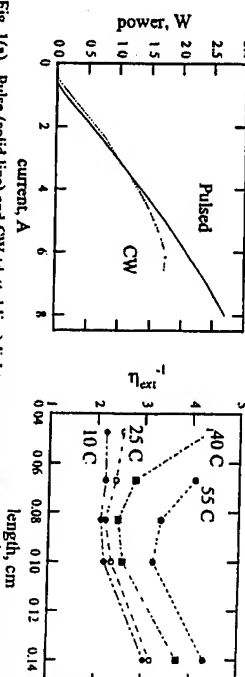


Fig. 1(a). Pulse (solid line) and CW (dotted line) light current curves. (b) η_{ext} is plotted versus the cavity length of the laser for 10 °C, 25 °C, 40 °C, and 55 °C.

The limiting effect of the nonradiative recombination current can be observed in Fig. 1(b), which plots η_{ext} versus the cavity length for temperatures of 10, 25, 40, and 55 °C under pulsed mode operation. While long cavities have a large η_{ext} due to the lower mirror losses, η_{ext} is also large for the short cavities. Here the threshold current density is necessarily large so that the high mirror losses are overcome. As a result, both the Auger leakage current and leakage due to thermionic emission of carriers into the QW barriers are increased. The latter process is particularly significant since it is extremely dependent on the carrier temperature, which can be larger than the lattice temperature [2]. Thus, the barrier height is crucial for high temperature operation, and because of the larger conduction band offset, Al containing lasers should have an advantage over InGaAsP devices. The optimum cavity length is near 1 mm. At this length, not only is the efficiency highest, but its variation with temperature the smallest. This work was supported by the U. S. Army Federated Laboratories program and by the U. S. Air Force Office of Scientific Research (AFOSR) under grant F49620-96-1-0079.

[1] G. T. Liu, A. Stintz, E. A. Pease, T. C. Newell, K. J. Malloy, and L. F. Lester, *IEEE Photon. Technol. Lett.*, vol. 12, pp. 4-6, 2000.
[2] L. F. Lester and B. K. Ridley, *J. Appl. Phys.*, vol. 72, pp. 2579-2588, 1992.

We find that the total efficiency for the 150-fs pulses in a finesse = 9 microcavity is not enhanced. However, spectral content at the resonance is enhanced, resulting in markedly different spectral character (Fig. 1), with a 2-nm FWHM for the microcavity and a 9-nm FWHM for the non-resonant structure. In contrast, a 1-ps pulse, which requires less than 1 nm of bandwidth, showed a total enhancement of a factor of 10 for a cavity finesse of 21. Thus, significant enhancement is available for pulses shorter than 1 ps, with some enhancement possible for pulses as short as a few hundred fs. The data is consistent with our numerical assessment, and has allowed the demonstration of efficient optical demultiplexing.

*Nortel Networks Advanced Tech Lab, Canada

1. K.A. Shore, X. Chen, P. Blood, "Frequency doubling and sum frequency generation in semiconductor optical waveguide devices," *Prog. Quant. Electr.* **20**, 181-218 (1996).
2. R.K. Tan, C.M. Verber, A.J. SpringThorpe, "Self-timed integrated-optical serial-to-parallel converter for 100 Gbit/s time demultiplexing," *IEEE Photon. Technol. Lett.* **6**, 1228-1231 (1994).
3. R. Lodenkamper, M.L. Bortz, M.M. Fejer, K. Bacher, J.S. Harris, Jr., "Surface-emitting second-harmonic generation in a semiconductor vertical resonator," *Opt. Lett.* **18**, 1798-1800 (1993).
4. S. Janz, Y. Beaulieu, A. Fiore, P. Bravetti, V. Berger, E. Rosencher, J. Nagle, "Surface emitted second-harmonic generation from a quasi-phase matched waveguide in an $\text{Al}_x\text{Ga}_{1-x}\text{As}/\text{Al}_2\text{O}_3$ microcavity," *Opt. Express* **2**, 462-470 (1998).
5. T.G. Ulmer, R.K. Tan, Z. Zhou, S.E. Ralph, R.P. Kenan, C.M. Verber, A.J. SpringThorpe, "Two-photon absorption-induced self-phase modulation in GaAs-AlGaAs waveguides for surface-emitted second-harmonic generation," *Opt. Lett.* **24**, 756-758 (1999).
6. P.A. Ramos, R. Towe, "Second-order nonlinear polarization and harmonic generation in [111]-oriented III-V heterostructures," *Opt. Commun.* **132**, 121-127 (1996).

CWQ

4:45 pm-6:30 pm

CLEO 2000

Room 100

Quantum-Dot Lasers 2

Rajeev J. Ram, MIT, USA, *Presider*

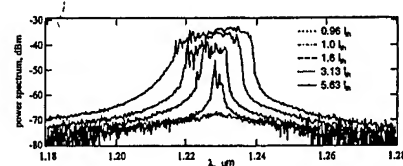
CWQ1

4:45 pm

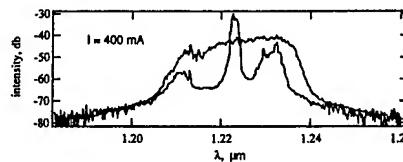
Broadening mechanisms, gain, and low linewidth enhancement factor in InAs quantum-dot lasers

T.C. Newell, H. Li, P. Eliseev, G.T. Liu, A. Stintz, K.J. Malloy, L.F. Lester, *Ctr. for High Tech. Materials, Univ. of New Mexico, Albuquerque, New Mexico 87131, USA; E-mail: newell@chtm.unm.edu*

A detailed understanding of many optical characteristics of quantum dot lasers remains



CWQ1 Fig. 1. Emission spectra at increasing injection currents.



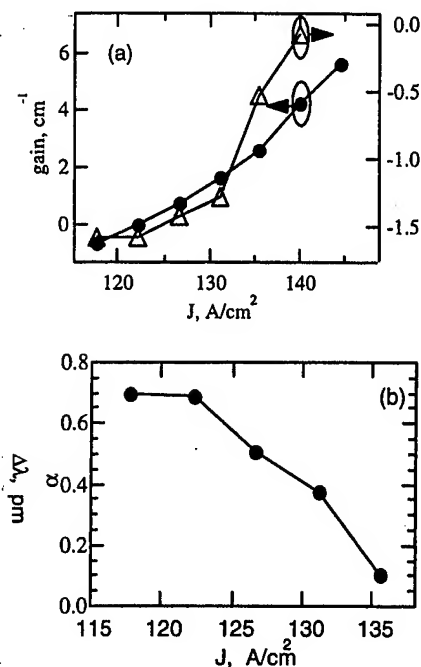
CWQ1 Fig. 2. Quantum dot emission spectra from an external cavity configuration. The dotted (solid) line is for the 0th (1st) order case.

in a nascent stage. However, its density of states function suggests many intriguing features. Here we present experimental investigations of homogeneous broadening, gain, and linewidth enhancement factor measurements in quantum dot laser diodes. A gain model that describes the evolution of the emission spectra along with subsidiary mode suppression is also presented.

The oscillation bandwidth $\Delta\lambda$ of the free-running laser increases with the pumping rate in a sub-linear manner, which is shown in Fig. 1. Homogeneous broadening is investigated by studying the emission spectra from an external-cavity laser arrangement using a diffraction grating. In the case of 0th order feedback (i.e. all spectral components are reflected), the dotted line in Fig. 2 again shows this wide bandwidth. However, the spectrum can be significantly narrowed with frequency selective feedback. The solid line in Fig. 2 shows that most of optical power emitted lies in the selected mode with suppressed modes on both sides of the central peak. This subsidiary mode suppression (SMS) can be quite strong when the free-running bandwidth $\Delta\lambda$ is less than the homogeneous spectral width. In contrast, as the injection current is increased, the SMS decreases along with an increase of the free-running bandwidth. From the position of distant modes that appear simultaneously with the selected mode, we estimate that the HWHM of the homogeneous broadening is approximately 10.5 meV ($\tau \sim 63$ fs). This behavior can be qualitatively described in terms of a gain model that describes the evolution of a symmetric peak region subject to gain suppression by a homogeneous broadening mechanism.

Gain, differential gain, and linewidth enhancement factor measurements are investigated in a free-running QD laser. The gain is determined by resolving the Fabry-Perot fringes in below-threshold amplified spontaneous emission spectra (ASE).^{1,2} A high degree of Gaussian-like symmetry observed in these profiles indicates that the gain peak and the zero dispersion point lie in close proximity. As a result, the index of refraction is nearly independent from variations in the carrier density.

The evolution of the gain and index of re-



CWQ1 Fig. 3. (a) The gain and the change in wavelength with J . (b) The linewidth enhancement factor versus J .

fraction is shown in Fig. 3(a) as a function of the injected current density, J . The gain increases super-linearly with J over a relatively small region until saturation occurs. Concurrently, the change in index of refraction, which is small even for low J , gradually decreases. As a result, α , shown in Fig. 3(b), decreases to 0.1 at $0.8 J_{th}$.

Quantum dot lasers optical characteristics were investigated. A FWHM of 21 meV is determined from mode suppression measurements. A symmetric gain profile is also observed. This gain symmetry leads to a record low linewidth enhancement factor of 0.1.

1. B.W. Hakki, T.L. Paoli, "Gain Spectra in GaAs double-heterostructure injection lasers," *J. Appl. Phys.* **46**, 1299-1306 (1975).
2. D.J. Bossert, D. Gallant, "Improved Method for Gain/Index Measurements of Semiconductor-Lasers," *Electron. Lett.* **32**, 338-339 (1996).

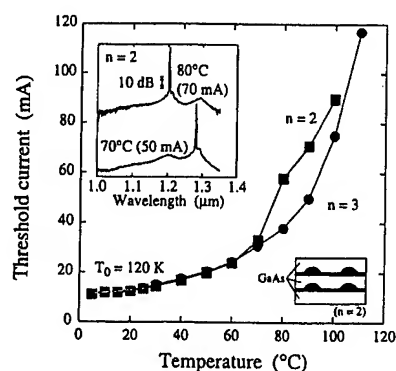
CWQ2

5:00 pm

High characteristic temperature of near-1.3-μm InGaAs/GaAs quantum-dot lasers

Kohki Mukai, Yoshiaki Nakata, Koji Otsubo, Mitsuru Sugawara, Naoki Yokoyama, Hiroshi Ishikawa, *Fujitsu Labs Ltd., 10-1 Morinosato-Wakamiya, Atsugi 243-0197, Japan; E-mail: kmukai@flab.fujitsu.co.jp*

Quantum-dot lasers are expected to attain remarkable reduction in threshold current and temperature-insensitive operation, however, high characteristic temperature of threshold current (T_0) has not yet been achieved except lasers which required huge current injection. For example, the dot lasers with low threshold current density or currents close to 10 mA have



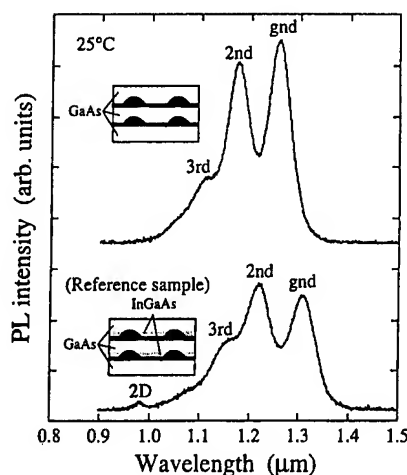
CWL1 Fig. 1. Temperature dependence of threshold current of lasers with 1.26- μm emission dots. Inset lasing spectra indicate the lasing level jump. Cross-sectional dot structures for $n = 2$ are also schematically shown.

current density or currents close to 10 mA have T_0 of 40–80 K.^{1–3} In this paper, we report T_0 of 120 K in near-1.3- μm InGaAs/GaAs quantum-dot lasers having a threshold current of 13 mA at room temperature. The ground-level lasing occurred up to 100°C. We compared the optical properties of the lasers with those of other dot lasers to indicate what were the key points for the achievements.

We fabricated ridge-type lasers using molecular beam epitaxy. The active layer was composed of 2 or 3 sheets ($=n$) of InGaAs/GaAs Stranski-Krastanov-dot layers, which were grown with the low growth rate of 0.007 monolayers per second and covered by GaAs. We also prepared reference dot lasers where the low-rate-grown dots were covered by 4-nm-thick $\text{In}_{0.17}\text{Ga}_{0.83}\text{As}$ before GaAs embedding.³ Transmission electron microscopy images indicated for the reference samples that dot density decreased in the upper sheets. The cavity size was $5 \times 1800 \mu\text{m}$ and a high-reflective coating was applied to the facets.

Figure 1 shows the threshold current as a function of temperature. T_0 between 5 and 25°C was 120 K, which is quite larger than previously reported values. The threshold current increased remarkably between 70 and 80°C for $n = 2$. Inset spectra shows that the increase owed to the lasing level shift from the ground level (1.28 μm) to the second level (1.20 μm). For $n = 3$, the ground-level lasing was observed up to 100°C. In the reference lasers, T_0 was 65 K and the ground-level lasing occurred up to 40°C for $n = 2$ and 50°C for $n = 3$.

Figure 2 reveals that GaAs-covered dots have four superior characteristics to InGaAs-covered dots; (1) ground-level intensity was higher, (2) integrated intensity was higher, (3) relative second-level intensity was weaker, and (4) potential depth of the ground level from the continuum was deeper. High peak intensity suggests high gain originated from high dot volume density, which causes small carrier overflow. High integrated intensity suggests small thermally activated nonradiative channels in the structures. Relatively weak peak intensity of upper level suggests the small influence of the state filling and the phonon bottleneck enhancing carrier overflow. Deep



CWL1 Fig. 2. Photoluminescence spectra of two types of dots for $n = 2$. In the reference sample spectrum, emission from the two-dimensional layer appears at 0.98 μm . Insets show the cross-sectional dot structures.

potential reduces the amount of carrier leakage.

Advantages in volume density, quantum efficiency, and potential depth enabled our quantum-dot lasers to exhibit high temperature characteristics. The results in this work will help future designs of quantum-dot lasers aiming for high temperature characteristics.

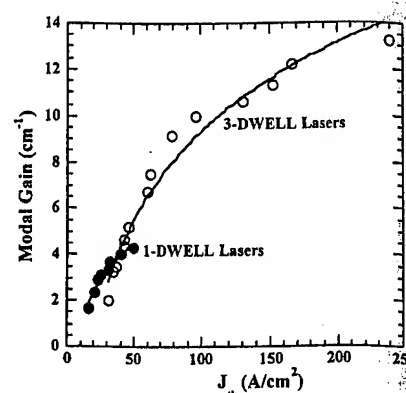
1. K. Mukai et al., *Electro. Lett.*, **34**, 1588 (1998).
2. G. Park et al., *IEEE Photon. Tech. Lett.*, **11**, 301 (1999).
3. K. Mukai et al., *IEEE Photon. Tech. Lett.*, **11**, 1205 (1999).

CWL2 CLEO 2000 3:00 pm

One and three-stack quantum dot lasers with very low threshold current density

G.T. Liu, A. Stintz, H. Li, T.C. Newell, P. Varangis, K.J. Malloy, L.F. Lester, *Ctr for High Tech. Materials, Univ. of New Mexico, 1313 Goddard SE, Albuquerque, NM 87106, USA; E-mail: gliu@chtm.unm.edu*

Quantum dot lasers with the dots-in-a-well (DWELL) structure have demonstrated very low threshold current densities.^{1,2} In particular, DWELL lasers with a single layer of InAs dots in an $\text{In}_{0.15}\text{Ga}_{0.85}\text{As}$ well have demonstrated threshold current densities as low as 16 A/cm^2 , which is the lowest threshold current density of any semiconductor laser.³ However, there are potential limitations to these lasers. Even though the ground state lasing threshold current density is very low, the ground state also has low saturated modal gain ($\sim 4.5 \text{ cm}^{-1}$). At a cavity length of 4 mm, the first excited state emission can be observed at high current levels. When the cavity length is further decreased increasing the cavity loss, lasing will be purely from excited states. Also, the average T_0 value of these 1-DWELL lasers is only 45 K between 10°C and 80°C, lower than that reported by other groups for QD lasers.³ In this work, three DWELL layers are used to increase the ground state gain and T_0 value. A



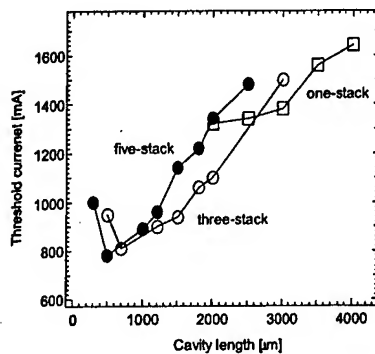
CWL2 Fig. 1. Ground state modal gain as a function of threshold current density.

quantum well laser is also grown to study limitations on the T_0 value of the DWELL structure.

The 3-DWELL laser is the same as a 1-DWELL laser¹ except that there are 3 DWELL stacks separated by 10 nm thick barriers with one dot layer in each well. A single quantum well laser of exactly the same structure as the 1-DWELL laser except without the dot layer was also grown for comparison.

Broad area lasers with 100 μm stripe width were fabricated from these structures and tested under pulsed conditions.¹ The lowest threshold current densities observed for the 1-DWELL and 3-DWELL lasers are 16 A/cm^2 and 31 A/cm^2 at a cavity length of 7.8 mm with 75% and 98.5% HR coatings on two facets. At a cavity length of 4 mm, the 3-DWELL laser has a threshold current density of 42 A/cm^2 , lower than the 50 A/cm^2 value of the 1-DWELL laser. The inverse external quantum efficiency, $1/\eta_{\text{ex}}$, versus cavity length, L , results for the 1-DWELL and 3-DWELL lasers are used to calculate the internal loss, α_i , and the internal quantum efficiency, η_i . By fitting the data to the equation $1/\eta_{\text{ex}} = 1/\eta_i(1 - \alpha_i L / \ln(R))$, $\eta_i(\alpha_i)$ values of 51.8% (1.46 cm^{-1}) and 62.0% (1.82 cm^{-1}) are found for 1-DWELL and 3-DWELL lasers, respectively. The reflectivity, R , is assumed to be 0.32. The ground state gain of the 1-DWELL and 3-DWELL lasers is plotted as a function of threshold current density in Fig. 1 using the condition that gain equals cavity loss at threshold. The threshold currents versus temperature of both the 1-DWELL and 3-DWELL lasers with $L = 7.8 \text{ mm}$ cavity length cleaved facets have also been measured and are shown in Fig. 2. The results for the single quantum well laser are also shown in Fig. 2. The testing temperatures are varied from 10°C to 80°C. The results are fitted to $I_{\text{th}} = I_0 \exp(T/T_0)$, giving T_0 values of 45 K, 84 K and 119 K for the 1-DWELL lasers, 3-DWELL lasers and 1-QW lasers, respectively. The T_0 value of the 1-QW laser is much higher than the 1-DWELL laser, indicating that the quantum well itself is not limiting the T_0 value of the DWELL structure. Carrier heating out of the quantum dots is suggested as the limiting factor. This argument is further supported by the increased T_0 value in the 3-DWELL structure.

In summary, the 3-DWELL lasers have demonstrated much improved ground state



CTuO7 Fig. 3. Threshold current vs. cavity length for one, three, and five-stack lasers, all with [110] cavity orientations.

optical gain on the polarization of the light. The transition matrix element is larger when the electrical field is parallel to the dash.

A threshold current density as low as 410 A/cm^2 was measured on a one-stack 4-mm long cavity cleaved facet laser diode. Fig. 3 shows the threshold current versus cavity length for one, three and five-stack lasers with cavity along [110]. We can see the gain is easier to saturate for single-stack lasers than multiple-stack ones. The maximum modal gain for the five-stack and single-stack lasers are about 22 and 10 cm^{-1} , respectively, for lasing in the ground-state with the cavity perpendicular to the dash direction.

The ground-state wavelengths of operation are near $1.62 \mu\text{m}$. Excited state lasing occurs at $\lambda = 1.55 \mu\text{m}$.

In conclusion, we have demonstrated the first self-assembled quantum dash lasers on InP (001) with a low threshold current density, ground-state wavelength of operation near $1.62 \mu\text{m}$, and a clear quantum wire-like dependence of the threshold current on laser cavity orientation.

References

1. G.T. Liu, A. Stintz, H. Li, A.L. Gray, P.M. Varangis, T.C. Newell, K.J. Malloy, and L.F. Lester, "Optical properties of quantum dot lasers using dots-in-a-well (DWELL) structures," submitted to *IEEE J. Quant. Electron.*
2. T.C. Newell, D.J. Bossert, A. Stintz, B. Fuchs, K.J. Malloy, and L.F. Lester, "Gain and linewidth enhancement factor in InAs quantum-dot laser diodes," *IEEE Photon. Tech. Lett.*, vol. 11, pp. 1527-1529, 1999.
3. P.M. Varangis, H. Li, G.T. Liu, T.C. Newell, A. Stintz, B. Fuchs, K.J. Malloy, and L.F. Lester, "Low-Threshold Quantum Dot Lasers with a 201 nm Tuning Range," *Electron. Lett.*, August 31, 2000 issue.
4. E. Kapon, et. al., *Surf. Sci.*, vol. 267, 593 (1992).

CTuP

2:30 pm-4:15 pm
Room 321-323

Nanoscale and Low-Dimensional Optical Materials

Thomas F. Krauss, *Univ. of St. Andrews, UK*
President

CTuP1

2:30 pm

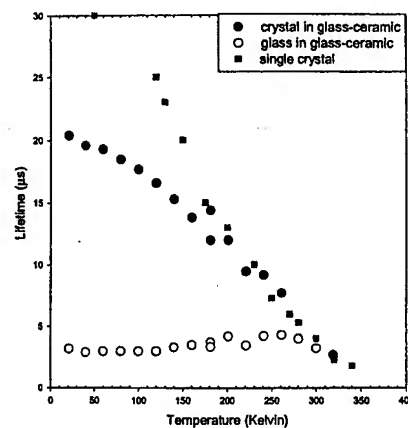
Cr⁴⁺:forsterite nanocrystalline glass-ceramic fiber

KE Downey, BN Samson, GH Beall, EJ Mozdy, LR Pinckney, NF Borrelli, A Mayolet, * A Kerdoncuff, * C Pierron, * *Corning Incorporated, Sullivan Park, Corning, NY 14831, USA*
*downeyke@corning.com; *Corning Incorporated, Fontainebleau Research Center, 7bis, Avenue de Valvins, 77210 Avon, France*

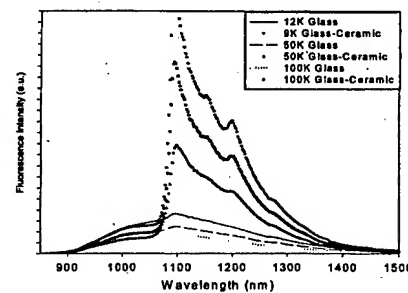
Glass-ceramics are two-phase systems consisting of a base glass within which crystals are grown by heat treatment, a process known as ceramming. Recent progress on fiberization of these materials led to the demonstration of a rare earth doped fiber laser and amplifier with an efficiency uncompromised by the presence of the crystals embedded within the core of the single mode fiber.¹ Transition metal ions are notoriously inefficient when incorporated into a glass host, due to the difficulty of controlling the local environment, to which they are very sensitive. However to date, the properties of Cr⁴⁺-doped glass-ceramic systems have received little attention, despite the apparent advantages of crystal site control. This paper investigates the fluorescence properties of Cr⁴⁺-doped forsterite glass-ceramics and shows that many of the important characteristics of the single crystal are reproduced in the glass-ceramic system. Furthermore, many of the spectroscopic parameters are also observed in glass-ceramic fiber, highlighting the potential for a new class of fiber laser and amplifier made from transition metal-doped glass-ceramics.

The lifetimes and their temperature dependence ($\lambda_{\text{pump}} = 1064 \text{ nm}$) of bulk Cr:forsterite glass-ceramic samples, as shown in Figure 1, are substantially similar to those reported for single crystal Cr:forsterite.² As Figure 1 reflects, the glass-ceramic fluorescence is best described with a biexponential decay; the single crystal excitation decays monoexponentially. As Figure 2 illustrates, the sharp portion of the fluorescence in the glass-ceramic mimics the spectrum of single crystal Cr:forsterite, though without polarization sensitivity. The underlying broad feature echoes the short-lived fluorescence observed in the uncerammed base silicate glass samples of identical composition. Thus, the short lifetime component plotted in Figure 1 can be attributed to residual chromium in the glass.

For any application as a laser or amplifier, loss is a prime concern. In particular, glass-ceramic systems with large crystal size have high scattering losses. However, as Figure 3a makes evident, in this system, losses actually decrease upon ceramming. This increase in transparency may be a result of loss of Cr³⁺ in the glass, either upon oxidation or upon incorporation into octahedral forsterite sites; the associated decrease in absorp-



CTuP1 Fig. 1. Temperature dependence of lifetimes of a Cr-doped forsterite glass-ceramic, which may be described with a biexponential decay, and single crystal forsterite data are taken from reference 2.



CTuP1 Fig. 2. Fluorescence of both glass and glass-ceramic samples of identical composition, at varying temperatures.

tion leads to decreased loss. For comparison the absorption and fluorescence of cerammed core/clad fiber are displayed in Figure 3b, again showing the characteristic Cr⁴⁺ spectroscopic features.

Although the current fibers are highly multimoded ($\sim 50 \mu\text{m}$ core diameter), single mode fibers may readily be drawn by the current fabrication method. Fiber losses, although higher than in the unclad canes, are approaching acceptable levels for future device studies. Further details will be presented at the conference.

In conclusion, we have shown for the first time that many of the spectroscopic parameters displayed by Cr:forsterite single crystals can be attained in glass-ceramic fibers. We believe this work opens the door to a new range of fiber devices based on transition metal-doped glass-ceramics, such as broadly tunable fiber lasers, amplifiers and short pulse fiber lasers.

References

1. B.N. Samson, P.A. Tick, N.F. Borrelli, "Efficient Nd-doped glass-ceramic fiber laser," in *CLEO Proceedings*, 2000, p545.
2. T.J. Carrig, C.R. Pollock, "Performance of a Continuous-Wave Forsterite Laser with Krypton Ion, Ti:sapphire, and Nd:YAG Pump Lasers," *IEEE J. of Quantum Electronics*, Vol. 29, No. 11, 1993, pp2835-2844.

trafast Gain Dynamics in InAs-InGaAs Quantum-Dot Amplifiers," IEEE Photon. Technol. Lett. 12, 594-596 (2000).

2. M. Grundmann, R. Heitz, D. Bimberg, J.H.H. Sandmann and J. Feldmann, "Carrier Dynamics in Quantum Dots: Modeling with Master Equations for the Transitions between Micro-States," Phys. Stat. Sol. (b) 203, 121-132 (1997).
3. P. Bhattacharya, D. Klotzkin, O. Qasaimeh, W. Zhou, S. Krishna, and D. Zhu, "High-Speed Modulation and Switching Characteristics of In(Ga)As-Al(Ga)As Self-Organized Quantum-Dot Lasers," IEEE J. Quantum Electron. 6(3), 426-438 (2000).
4. F. Heinrichsdorff, M.-H. Mao, N. Kirstaedter, A. Krost, D. Bimberg, A.O. Kosogov, and P. Werner, "Room-temperature continuous-wave lasing from stacked InAs/GaAs quantum dots grown by metalorganic chemical vapor deposition," Appl. Phys. Lett. 71(1), 22-24 (1997).

CWK7

6:15 pm

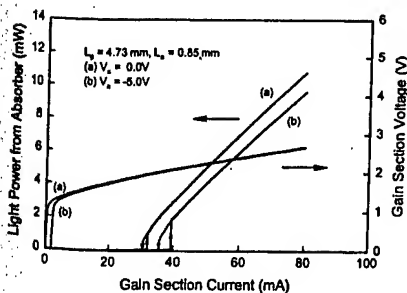
Demonstration of passive Q-switching and passive mode-locking in 1.3 μm , two-section InAs quantum dot lasers

Xiaodong Huang, A. Stintz, Hua Li, L.F. Lester, Julian Cheng, K.J. Malloy, *Center for High Technology materials, University of New Mexico, 1313 Goddard SE, Albuquerque, NM 87106; Email: xahuang@chtm.chtm.unm.edu*

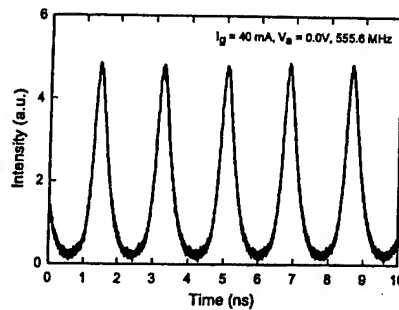
The properties of quantum dot (QD) layers as absorbers in an active device have not been investigated in detail. In this paper, we describe the bistable operation of a long-wavelength, oxide-confined, two-section quantum dot laser with an integrated QD saturable absorber. Our structure exhibits passive Q-switching and passive mode-locking.

The devices were fabricated from the same wafer as described in Refs. [1] and [2] with a 50 μm gap in the top p-type contact metals. The laser section and the absorber section are $L_g = 4.73$ mm and $L_a = 0.85$ mm long, respectively. Current confinement is provided by the lateral wet oxidation of a 50 nm thick $\text{Al}_{0.98}\text{Ga}_{0.02}\text{As}$ layer, giving a current aperture of 10 μm . The cleaved facets were uncoated and the devices were mounted p-side up on a copper heat sink and tested at room temperature.

DC characteristics were measured with cur-



CWK7 Fig. 1. Room temperature lasing and electrical characteristics of a two-section QD laser with (a) $V_a = 0.0\text{V}$, and (b) a reverse bias of $V_a = -5.0\text{V}$, applied to the absorber section.

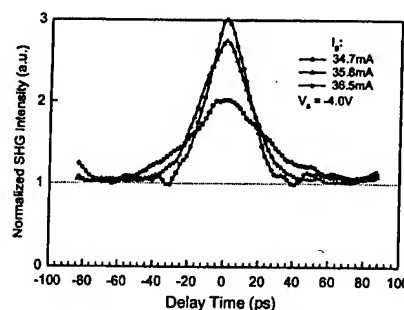


CWK7 Fig. 2. Q-switching pulse train under bias condition of $I_g = 40$ mA, $V_a = 0.0\text{V}$ for a modulation frequency of 555.6 MHz. The pulsewidth is about 450 ps.

rent injection (I_g) into the gain section and a constant reverse bias voltage (V_a) applied to the absorber section. Lasing occurred on the ground state ($\lambda = 1278$ nm). Figure 1 shows the variation in lasing light power (L) emitted from the absorber facet and the voltage (V_g) across the laser section with the forward and backward sweep of the laser current under (a) $V_a = 0.0$ V, and (b) with $V_a = -5.0$ V across the absorber section. The L - I_g characteristics exhibit clear counterclockwise hysteresis loops and bistability. The physical origin of the bistability will be discussed.

To observe Q-switching operation, a constant current superimposed with a square wave modulation signal was applied to the gain section via a bias tee, while a constant reverse bias was applied to the absorber. Q-switching up to 1 GHz was achieved. The narrowest pulsewidth was 330 ps for modulation at 294 MHz. Q-switching pulse parameters, pulsewidth, peak power, and turn-on delay vary with the gain section current. Figure 2 shows the pulse train obtained under optimum bias condition for a modulation signal of 555.6 MHz. The modulation depth decreases with increasing modulation frequency. Spectral broadening was observed associating with the Q-switching. Possible reasons for the wide Q-switching pulsewidth will be presented.

Mode-locking at 7.4 GHz was achieved when both the gain and absorber sections of the lasers were dc biased. The mode-locking pulsewidth was measured using collinear autocorrelation. Figure 3 shows how the autocorrelation varies with the gain section current at an absorber bias of -4.0 V. Full mode-locking was achieved for



CWK7 Fig. 3. Autocorrelation trace for different gain section current at absorber reverse bias of -4.0 V. The best mode-locking occurs inside the bistable region.

gain section currents close to the lower hysteresis threshold. The corresponding pulsewidth is about 17 ps assuming a hyperbolic secant squared pulse, and the optical spectral bandwidth was measured to be about 1 nm. The time-bandwidth product is about 3.1, more than 6 times of the transform limit, and suggests the presence of phase modulation. The modulation depth of the mode-locked pulse decreases as the gain current increases. No self-pulsation was observed as verified by the electrical spectrum of the mode-locked laser output.

In conclusion, we report the demonstration of passive Q-switching and passive mode-locking in bistable, oxide-confined, two-section, 1.3 μm quantum dot lasers.

References

1. Xiaodong Huang, A. Stintz, C.P. Hains, G.T. Liu, J. Cheng and K.J. Malloy, "Efficient high temperature CW lasing operation of oxide-confined long-wavelength InAs quantum dot lasers," *Electron. Lett.*, 36, 41-42 (2000).
2. L.F. Lester, A. Stintz, H. Li, T.C. Newell, E.A. Pease, B.A. Fuchs, K.J. Malloy, "Optical characteristics of 1.24 μm InAs quantum dot laser diodes," *IEEE Phot. Tech. Lett.*, 11, 931-933 (1999).

CWL

4:45 pm-6:30 pm

Room: 321-323

Spectroscopic Approaches for Biomedical Diagnostic

Amir H. Gandjbakche, *National Inst. of Health, USA, Presider*

CWL1

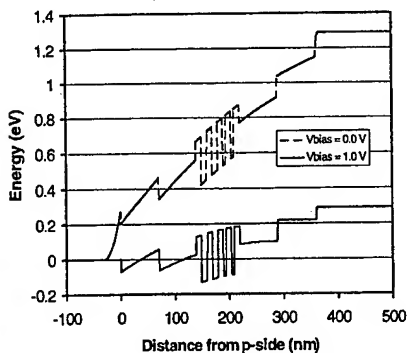
4:45 pm

5-D fluorescence imaging using an all-solid-state diode-pumped laser system

D.S. Elson, S.E.D. Webb, J. Siegel, S. Leveque-Fort, D. Parsons-Karavassilis, M.J. Cole, P.M.W. French, M. Hopkins, * M.J. Lever, ** L.O. Sucharov, † M.A.A. Neil, † R. Juškaitis, † T. Wilson, † *Femtosecond Optics Group, Physics Dept., Imperial College, London SW7 2BW, U.K.; email: paul.french@ic.ac.uk; *Optical Insights, 1807 2nd St., Suite #60, Santa Fe, NM 87505; email: mhopkins@optical-insights.com; **Department of Biological and Medical Systems, Imperial College, London SW7 2BY, U.K. Tel: 44-20-7594 5172, m.j.lever@ic.ac.uk; †Department of Engineering Science, University of Oxford, Parks Road, Oxford OX1 3PJ, U.K.; email: tony.wilson@eng.ox.ac.uk*

Fluorescence is widely used in biomedicine and other applications both to track specific fluorophores and study anatomical features. Fluorescence lifetime measurements add functional information because they are dependent on the local environment of the fluorophores (e.g. oxygen, $[\text{Ca}^{2+}]$, pH etc.) e.g., ¹ Fluorescence Lifetime Imaging (FLIM) is particularly exciting since it can exploit this feature to provide non-invasive functional/diagnostic imaging. Complementary functional information may be obtained using spectrally-resolved fluorescence imaging.² In or-

Wednesday, May 9



CTuA50 Fig. 2. Electric potential across the active region due to the p-i-n junction.

1. H. Yamazaki, A. Tomita, M. Yamaguchi, Appl. Phys. Lett. 71, 767 (1997).
2. M.J. Hamp, D.T. Cassidy, B.J. Robinson, Q.C. Zhao, D.A. Thompson, Appl. Phys. Lett. 74, 744 (1999).
3. S.L. Chuang, "Physics of Optoelectronic Devices," (John Wiley and Sons, New York, 1995).

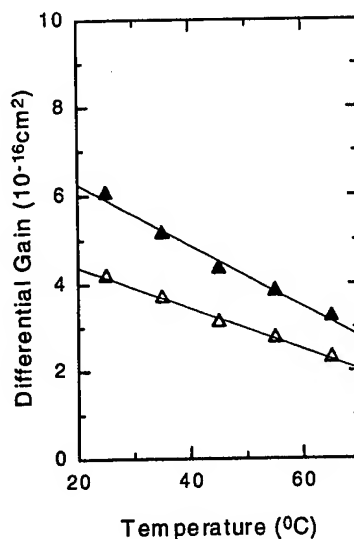
CTuA51

Differential gain in 1.3- μm InGaAsP/InP MQW lasers with p-doped active region

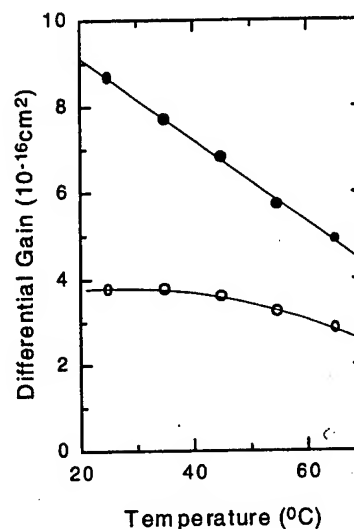
L. Shterengas, C.L. Reynolds, Jr.,* G. Belenky,** M. Hybertsen,* D. Donetsky, G. Shtengel,* State Univ. of New York at Stony Brook, Stony Brook, New York 11794, USA; E-mail: garik@ece.sunysb.edu

We measured the temperature dependence of differential gain of 1.3- μm InGaAsP/InP MQW FP and DFB lasers with the same design¹ and two different doping profiles: moderately ($2 \cdot 10^{17} \text{ cm}^{-3}$) and heavily ($2 \cdot 10^{18} \text{ cm}^{-3}$) Zn doped active region. SIMS was applied to control doping levels. Differential gain values was obtained from corresponding RIN measurements. Experiments showed that the change of the active region doping level from $2 \cdot 10^{17} \text{ cm}^{-3}$ to $2 \cdot 10^{18} \text{ cm}^{-3}$ leads to a 50% increase of the differential gain for FP lasers at 25°C (see Table 1). Heavily doped devices also exhibit more rapid reduction of the differential gain with increasing temperature. The effect of active region doping on the energy separation between the electron Fermi level and electronic states coupled into the laser mode explains the observations.

The temperature dependence of the differential gain for DFB devices is further influenced by the position of the lasing wavelength relative to the wavelength of the gain peak. Spectral measurements showed that at 25°C the DFB spectral line was placed at the short-wavelength slope of the gain spectra for heavily doped devices (negative detuning) and at the



a



b

CTuA51 Fig. 1. Temperature dependence of the differential gain for moderately (open symbols) and heavily (solid symbols) doped, FP (a) and DFB (b) lasers.

longwavelength slope for moderately doped ones (positive detuning). For moderately doped devices the detuning changed the sign from positive to negative at about 40°C. For devices with negative detuning the rise of temperature leads to additional suppression of the differential gain due to an increase of the detuning value. In case of moderately doped devices increase of the temperature decreases the positive detuning, thus suppressing the temperature dependence of the differential gain up to about 40°C. After this temperature the effect

of negative detuning becomes apparent again [Fig. 1(b)]

To summarize, we carried out measurements of the differential gain values of 1.3- μm InGaAsP/InP MQW DFB and FP lasers with two different doping profiles. It is shown that an increase of Zn concentration in the middle of the active region from $2 \cdot 10^{17} \text{ cm}^{-3}$ to $2 \cdot 10^{18} \text{ cm}^{-3}$ leads to a 50% differential gain increase for FP lasers at 25°C. However, the differential gain drops with temperature more quickly for heavily doped devices. We have shown that these two effects are directly linked. The position of the laser wavelength relative to the gain peak is another critical factor influencing the temperature dependence of the differential gain for the devices.

*Lucent Technologies, Bell Labs., USA

**also with Lucent Technologies, Bell Labs., USA

1. S. Swaminathan, C.L. Reynolds, M. Giannopoulos, "1.3 μm InGaAsP/InP capped mesa based heterostructure laser with an undoped cladding layer in base epitaxial growth," J. Appl. Phys. 83, 4540-4541 (1998).
2. P.A. Morton, T. Tanbun-Ek, R.A. Lofgren, N. Chang, K.W. Wecht, A.M. Sergent, J. Sciortino, Jr., "Packaged 155 μm DFB laser with 25 GHz modulation bandwidth," Electron. Lett. 30, 2044-2046 (1994).
3. I.F. Lealman, M.J. Harlow, S.D. Perlow, "Effect of Zn doping on modulation bandwidth of 1.55 μm InGaAs/InGaAsP multiple quantum well lasers," Electron. Lett. 29, 1197-1198 (1993).

CTuA52

1.5- μm AlGaInAs quantum well lasers grown by the digital alloy technique

T.C. Newell, P. Varangis, E. Pease, G.T. Li, A. Stintz, K. Malloy, L.F. Lester, Center for High Tech. Materials, Univ. of New Mexico Albuquerque, New Mexico 87131, USA; E-mail: newell@chtm.unm.edu

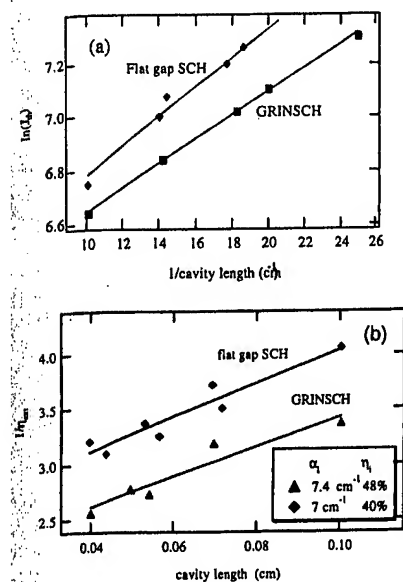
1.5- μm lasers are of particular interest since this wavelength enjoys the dual role of being optimum for fiber optics and the lowest threshold considered eye-safe. Our investigations are focused on digital alloy (DA) MBE grown lattice matched and strained AlGaInAs multiple quantum well lasers. The DA method reduces many growth complexities associated with quaternary materials. The AlGaInAs alloy produces a better conduction band offset between InGaAsP on InP.

The digital alloy growth process consists of precisely controlling the flux of AlGaAs, InGaAs to produce a narrow superlattice whose layers are between 3 and 5 Å. Laser grown on an InP substrate and incorporating a 1- μm -wide waveguide design to reduce carrier absorption losses.

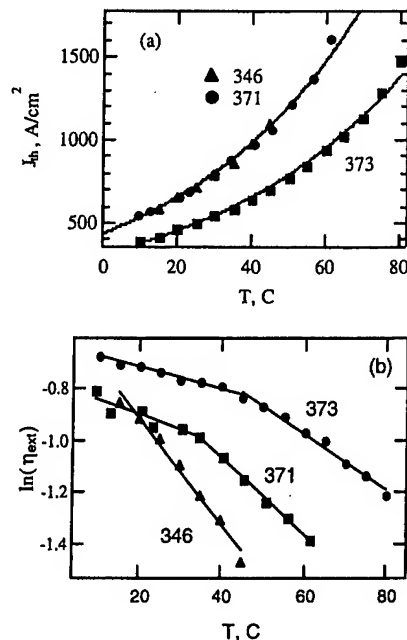
Two 4-QW lattice matched devices were grown. The QWs are identical while the substrate confinement heterostructure (SCH) one is flat bandgap and the other graded (GRINSCH). Figure 1(a) shows the internal quantum efficiency versus the inverse of the cavity length, L. Figure 1(b) plots the inverse of the external quantum efficiency (η_{ext}^{-1}) versus

CTuA51 Table 1. Typical Parameters for the Devices Studied at 25°C. Zn Concentration N_{Zn} is Shown for the Middle of the Active Region According to the Data in Figs. 1(a) and Fig. 1(b)

		$N_{\text{Zn}}, 10^{18} \text{ cm}^{-3}$	I_{th}, mA	$(dg/dN)/\gamma, 10^{-16} \text{ cm}^2$	K, ns	Total Loss, cm^{-1}
Moderately doped	DFB	≈ 0.2	7.5	3.78	≈ 0.37	65
	FP		6	4.18		
Heavily doped	DFB	≈ 2	9.5	8.66	≈ 0.30	83
	FP		9	6.04		



CTuA52 Fig. 1. Lattice matched flat bandgap SCH and GRINSCH laser traits. (a) $\ln(J_{th})$ versus inverse cavity length. (b) inverse of the differential efficiency vs. the cavity length.



CTuA52 Fig. 2. (a) J_{th} and (b) $\ln(\eta_{ext})$ vs. T .

CTuA52 Table 1. Strained Laser Characteristics

Wafer	QW	Strain	Al	J_{th}	J_{th}/QW	η_{ext}	η_i	T_o	T_1
346	4x100Å	1%	.2%	510	128	54%	65%	50	49
371	3x100Å	.72%	.3%	555	185	43%	60%	49	164
373	3x80Å	.8%	.3%	510	170	70%	-	54	238
376	1x80Å	.8%	.3%	545	545	37%	-	-	-

L. The GRINSCH structure outperforms the flat gap SCH, which is due to the built in electric field that forces carriers towards the wells. A J_{th} of 770 A/cm² at room temperature was measured in the GRINSCH structure.

Strained 1, 3, and 4-QW devices were also fabricated. The principle results are summarized in Table 1. Note that the 4th column refers to the barrier Al percentage and the last column, T_1 , refers to the change in η_{ext} with temperature, $\eta = \eta_o e^{T/T_1}$. The highest optical performance is observed in a 3-QW device, #373 which produces 1 W per uncoated facet CW power before thermal roll-over. For strained devices a 510 A/cm² threshold current density was measured. This is the lowest MBE result for this material system at 1.5- μ m to date.

In Fig. 2, J_{th} and $\ln(\eta_{ext})$ are plotted versus the temperature. The superiority of #373 over #371 can be traced to the amount the barrier Al percentage. Also, although #371 is similar to #373, the larger QW width may suggest that partial relaxation has occurred. Unfortunately this is difficult to detect due to the complicated x-ray diffraction profile of digital alloy lasers.

Lattice-matched and strained QW laser observations show that the barrier Al percentage, strain, and QW width are critical parameters for 1.5- μ m laser design. The barrier height is particularly important in high power applications where a substantial amount of heat is generated.

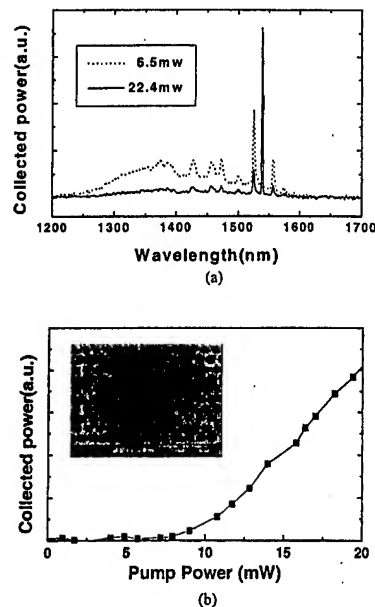
CTuA53

Room-temperature optical characterization of two-dimensional photonic bandgap lasers at 1.55 μ m

Han Youl Ryu, Jeong-Ki Hwang, Dae-Sung Soong, Il-Young Han, Yong Hee Lee, Dong-Hoon Jang,*
Department of Physics, Korea Advanced Inst. of Science and Tech., Taejeon 305-701, Korea;
E-mail: rhy@cais.kaist.ac.kr

During the last decade, there has been considerable interest in the photonic bandgap materials or photonic crystals. Now, at least for two-dimensional structures, the potential ability of photon control is being successfully demonstrated in the optical regime. Lasing actions from two-dimensional photonic crystal structures are realized by a few groups. The first reported laser structure is a freestanding slab in the air.^{1,2} Very recently, our group has introduced a photonic crystal slab structure on the low-index material to improve the thermal property.³ In this work, we report the lasing characteristics of the photonic crystal cavity of various geometries and the enhanced extraction of spontaneous emission from the photonic crystal pattern.

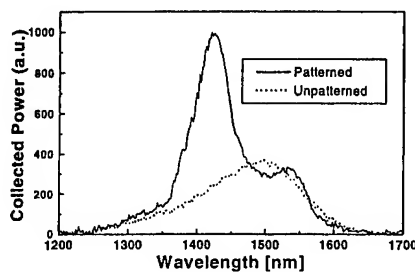
The InGaAsP material system is employed as an active medium to reduce non-radiative surface recombination. The emission wavelength of six pairs of strain-compensated quantum wells is placed at 1.55 μ m. One side



CTuA53 Fig. 1. (a) Spectra below and above threshold and (b) L-L curve of the two-dimensional photonic bandgap laser. The scanning electron micrograph of the measured cavity structure is shown in the inset.

of the InGaAsP/InP guiding layer was fused with the AlAs layer on top of a GaAs substrate. This wafer fusion step is required to realize a thermally stable and mechanically robust device. After electron-beam lithography and chemically assisted ion-beam etching, the AlAs layer was converted to Al-oxide by wet-oxidation for the optical confinement in the vertical direction. The resulting structure is a triangular array of air holes with etch depth of about 1 μ m. The thickness of the InGaAsP/InP guiding layer is about 300 nm, which corresponds to approximately $\lambda/2$ thickness of the slab at 1.55 μ m.

The optical characteristics of fabricated photonic crystals are investigated by optical pumping with a 980-nm diode laser at room temperature. The pump laser is modulated with 50-ns pulses at duty cycle of 5-10%. The photoluminescence was collected from the top of the sample using a microscope objective. Pump spot is adjusted to cover the entire cavity region. Lasing action was observed for the cavities of various sizes. The lattice constant of each laser ranges from 400 nm to 500 nm. The ratio of the radius of each



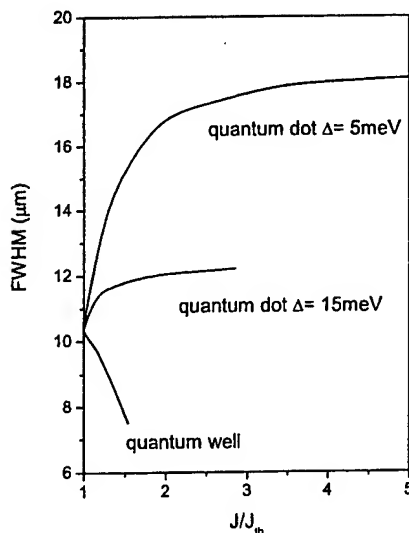
CTuA53 Fig. 2. Photoluminescence spectra from patterned and unpatterned regions from the two-dimensional photonic crystal.

edge-emitting lasers is the behavior of the intracavity laser field (i.e., the beam quality) above threshold. Especially important are self-focusing effects which narrow the laser beam and eventually lead to beam break-up or filamentation.^{2,3} This paper presents theoretical and experimental results on the beam quality of edge-emitting lasers with InGaAs quantum dot active media.

In a self-organized quantum dot structure, the quantum dots are either embedded in a quantum well or connected to a quantum-well wetting layer,¹ and the Coulomb interaction provides a coupling between carriers in the localized dot states and extended continuum states in the quantum-well. Therefore, the optical and transport properties of quantum dots are decisively influenced by carrier populations in the quantum well. For instance, the quantum-dot gain undergoes density-dependent shifts and Coulomb enhancement.⁴

Here, we use a screened Hartree-Fock theory⁴ to compute the complex susceptibility for a shallow quantum dot for different excitations. The inclusion of Coulomb effects not only influences the gain (imaginary part of the susceptibility), but also changes the dispersive behavior, i.e., the carrier induced refractive index (real part of the susceptibility) of a quantum dot active medium. We use the susceptibility as input in a wave optical laser model to obtain the full width at half maximum (FWHM) of the output beam under cw current injection.³ Figure 1 shows that, if the inhomogeneous broadening in the quantum dot material is not too large, we actually obtain an expanding beam waist with increasing pump current. This is drastically different from quantum wells where the beam waist always decreases.

We compare this to experimental data for edge-emitting lasers that contain 7 layers of In_{0.5}Ga_{0.5}As quantum dots between GaAs barriers.⁵



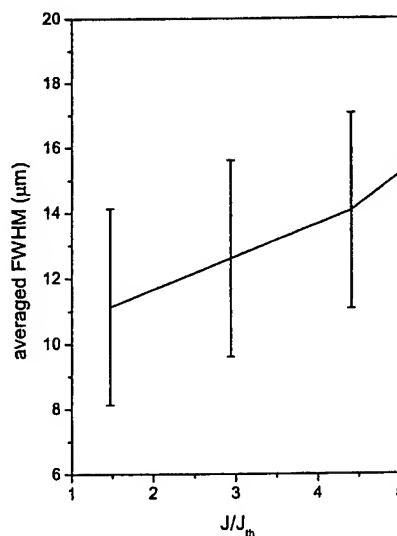
CThP3 Fig. 1. Computed full width at half maximum (FWHM) of the output beam waist of a quantum-dot and a quantum-well laser vs. injection current. The resonator length is 500 μm and the stripe width is 20 μm . The quantum dot results are computed for different inhomogeneous broadening $\Delta = 5$ meV and 15 meV. The current is measured in units of the threshold current J_{th} .

The stripe width of the laser is 50 μm and the device length 560 μm . The near field of the laser was recorded as a function of current up to five times threshold. The device output shows filaments across its entire facet.⁶ The experimental results shown in Fig. 2 indicate that the filament width broadens with increasing drive current in contrast to the behavior obtained for quantum-well devices. However, the magnitude of filament broadening is relatively small. A reduced increase in the filament broadening is obtained with the calculation when the dot gain spectrum is inhomogeneously broadened as shown in Fig. 1. The degree of inhomogeneous broadening required to produce the experimentally observed filament broadening is consistent with that observed in low temperature photoluminescence measurements of these dot samples.⁵

In summary, our theoretical results show that the filamentation tendency in quantum-dot lasers can be substantially weakened for sufficiently small inhomogeneous broadening, contrary to what is observed in quantum-well lasers. An indication of this is observed in our experimental results which show indeed a weaker filamentation tendency than quantum-well lasers. However, the calculations predict a still better beam quality for lasers fabricated from dot material with reduced inhomogeneous broadening.

References

1. D. Bimberg, M. Grundmann, and N.N. Ledentsov, *Quantum Dot Heterostructures* (Wiley, New York, 1999).
2. P. Kirkby, A. Goodwin, G. Thompson, and P. Selway, *IEEE J. Quantum Electron.* 13, 705 (1977).
3. W.W. Chow and D. Depatie, *IEEE J. Quantum Electron.* 24, 1297 (1988).
4. H.C. Schneider, W.W. Chow, and S.W. Koch, *Phys. Rev. B* 64, 115315 (2001).
5. P.M. Smowton, E. Herrmann, Y. Ning, H.D. Summers, P. Blood, and M. Hopkinson, *Appl. Phys. Lett.* 78, 2629 (2001).



CThP3 Fig. 2. Average measured full width at half maximum (FWHM) of the filaments in the output beam of a quantum-dot laser vs. injection current. The resonator length is 560 μm and the stripe width 50 μm .

6. P.M. Smowton, E.J. Pearce, Y. Ning, E. Herrmann and M. Hopkinson, talk CWK2, *Conference on Lasers and Electro-Optics* 2001.

CThP4

4:00 pm

Anisotropy of Optoelectronic Properties in InAs Quantum-dash Lasers on InP

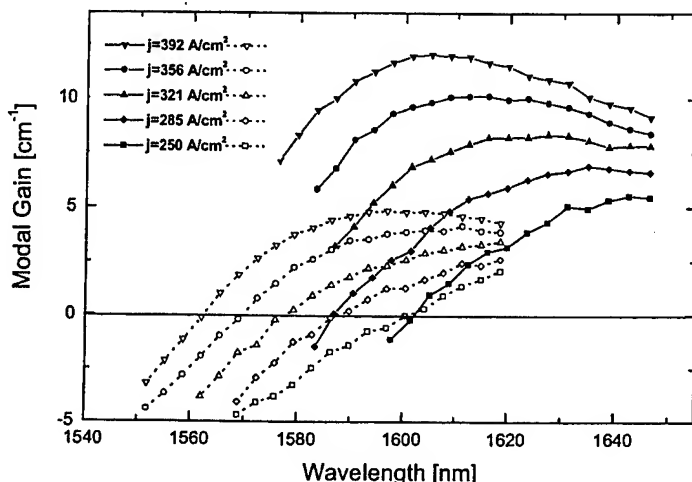
A.A. Ukhonov, P.G. Eliseev, R.H. Wang, A. Stintz, L.F. Lester, K.J. Malloy, *Center for High Technology Materials, University of New Mexico, Albuquerque, NM87106, Email: ukhanov@chtm.unm.edu*

The spectral dependence of modal gain and the linewidth enhancement factor was investigated for a new type of diode laser. The active media of the laser was composed of low-dimensional nanostructures in the form of short wires. These wire-like nanostructures typically have length-to-width ratios of between 6:1 and 15:1 and are called "quantum dashes" (QDashes). It was shown previously¹ that such lasers showed dependence of the threshold current density on the laser cavity orientation. Here we extend the study of these lasers by investigating wavelength dependence of modal gain and the linewidth enhancement factor at subthreshold current densities for two different orientations of the dashes with respect to the axis of the laser cavity.

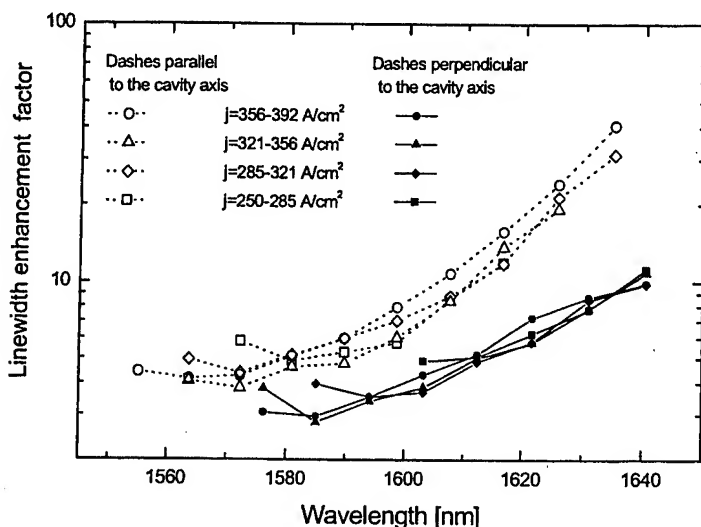
The InAs QDashes were grown by molecular beam epitaxy on an InP (001) substrate in a compressively strained AlGaInAs quantum well which had a thickness of 7.5 nm as described in Ref. [1]. The QDash lasers had 5 layers of quantum dashes and the dashes had lengths up to 500 nm, widths up to 25 nm, and heights up to 5 nm. Laser diodes with dashes aligned along the axis of the laser cavity and laser diodes with dashes oriented perpendicular to the cavity were investigated. The modal gain and the linewidth enhancement factor were determined from the below-threshold amplified spontaneous emission spectra using the Hakki-Paoli technique.^{2,3}

The modal gain for both dash orientations is shown in Fig. 1. The peak value of modal gain was 2.3 ± 0.3 times larger for lasers with QDashes oriented perpendicular to the cavity axis than that for lasers with dashes along the cavity axis at all experimental current densities. We believe such an effect is the result of the polarization dependence of the transition matrix element for the QDash active media. Modeling the QDash as a finite quantum structure, its transition matrix element should have the largest value when the electric field is oriented along the longest dash side.⁴ The peak modal gain for dashes oriented perpendicular to the cavity axis was shifted by ~ 8 nm to a longer wavelength with respect to the peak position of modal gain for dashes oriented along the cavity axis.

The wavelength dependence of linewidth enhancement factor (α) for lasers with both dash orientations is presented in Fig. 2. The spectrum of the linewidth enhancement factor has the quantum wire-like dependence first described in Ref. [5], indicated by the presence of a minimum in α , the rapid increase for long wavelengths and an increase in α for short wavelengths (note the logarithmic scale). The linewidth enhancement factor is larger in lasers with dashes orthogonal to



CThP4 Fig. 1. Wavelength dependence of the modal gain of quantum-dash lasers with dashes oriented parallel and perpendicular to the cavity axis. Solid lines and solid symbols correspond to the modal gain of the laser with dashes oriented perpendicular to the cavity axis. Dotted lines and open symbols represent the modal gain for the laser with dashes oriented parallel to the cavity axis.



CThP4 Fig. 2. Wavelength dependence of the linewidth enhancement factor for quantum-dash lasers with dashes oriented parallel and perpendicular to the cavity axis.

the cavity axis for the whole wavelength range from 1555 nm to 1640 nm.

While the modal gain results clearly illustrate the polarization dependence expected for this quantum wire-like active media, the difference in the linewidth enhancement factor with orientation also suggests a strong wavelength dependence of the transition matrix element.

1. R.H. Wang et al., "Room-temperature operation of InAs quantum-dash lasers on InP (011)", *IEEE Photon. Tech. Lett.*, 13, 767-769 (2001).
2. B.W. Hakki and T.L. Paoli, "CW degradation at 300 K of GaAs double-heterostructures junction lasers. II. Electronic gain", *J. Appl. Phys.*, 44, 4113-4119 (1973).
3. T.C. Newell, D.J. Bossert, A. Stinta, B. Fuchs, K.J. Malloy, and L.F. Lester, "Gain and linewidth enhancement factor in InAs quantum-dot laser diodes", *IEEE Photon Technol. Lett.*, 11, 1527-1529 (1999).
4. M. Asada, Y. Miyamoto, Y. Suematsu, "Gain and the threshold of three-dimensional quantum-box lasers", *IEEE J. Quantum Electron.*, 9, 1915-1921 (1986).
5. Y. Miyake, M. Asada, "Spectral characteristics of linewidth enhancement factor α of multi-dimensional quantum wells", *Jpn. J. Appl. Phys.*, 28, 1280-1281 (1989).

CThQ

2:30 pm-4:15 pm

Room: 101B

Fluorescence Methods for Tissue Characterization

TBA, President

CThQ1

2:30 pm

Imaging of Fluorescence, Absorption, and Scattering Properties in Diffuse Media Using Pump and Emission Wavelength Measurements

A.B. Milstein, S. Oh, K.J. Webb, and C.A. Bouman, School of Electrical and Computer Engineering, Purdue University, West Lafayette, IN 47907-1285

R.P. Millane, Department of Electrical and Electronic Engineering, University of Canterbury, Private Bag 4800, Christchurch, New Zealand, Email: webb@ecn.purdue.edu

Optical diffusion imaging, where the scattering and absorption properties of tissue are reconstructed from noninvasive measurements, offers potential advantages of safety and diagnostic specificity over other imaging modalities.¹ In addition, fluorescent contrast agents may provide enhanced chemical specificity, with greater potential to distinguish between diseased and healthy tissue.² Imaging simulations of fluorescence lifetime and yield^{2,3,4} have assumed known scattering and partially known absorption properties. In this work we demonstrate a Bayesian reconstruction in which absorption and scattering parameters at the excitation and emission wavelengths are imaged, in addition to the fluorescent yield and lifetime.

The transport of modulated light (at ω , with $e^{j\omega t}$ variation) in a fluorescent, highly scattering medium can be modeled using coupled diffusion equations:³

$$\nabla \cdot [D_x(r) \nabla \phi_x(r, \omega)] - [\mu_a x(r) + j\omega/c] \phi_x(r, \omega) = -S_x(r, \omega) \quad (1)$$

$$\nabla \cdot [D_m(r) \nabla \phi_m(r, \omega)] - [\mu_a m(r) + j\omega/c] \phi_m(r, \omega) = -\phi_x(r, \omega) [\gamma(r, \omega) + j\beta(r, \omega)] \quad (2)$$

$$\gamma(r, \omega) + j\beta(r, \omega) = \eta \mu_{ax \rightarrow m}(r) \frac{1 - j\omega\tau(r)}{1 + [\omega\tau(r)]^2} \quad (3)$$

where x and m denote excitation and emission wavelengths, $\phi(r, \omega)$ is the photon fluence, and $S(r, \omega)$ is the source. The optical parameters are the diffusion coefficient $D(r)$ and the absorption coefficient $\mu_a(r)$. The fluorescence parameters are the lifetime $\tau(r)$ and the fluorescent yield $\eta \mu_{ax \rightarrow m}(r)$.²

To image the excitation and emission optical parameters, measurements may be made with a set of sources and detectors at each wavelength. Our proposed reconstruction algorithm⁵ iteratively minimizes a Bayesian cost function to determine the maximum *a posteriori* estimate of the optical parameter image, given a measurement vector. Once reconstructions for $\mu_{ax, m}$ and $D_{x, m}$ are obtained, additional measurements with

183 nm Tuning Range in a Grating-Coupled External-Cavity Quantum Dot Laser

P. M. Varangis, H. Li, G. T. Liu, T. C. Newell, A. Stintz, B. Fuchs, K. J. Malloy, and, L. F. Lester

*Center for High Technology Materials, University of New Mexico, Albuquerque, NM 87106
Tel. (505) 272-7800, Fax. (505) 272-7801, petrosva@chtm.unm.edu*

The development of tunable semiconductor lasers has been the subject of intense investigation because of their applications in wavelength division multiplexing and absorption spectroscopy. Multiple-quantum well (MQW) semiconductor lasers have been successfully used as broadband tunable, single-frequency, narrow-linewidth sources of radiation when coupled to an external cavity with a frequency-selective tuning element, such as a diffraction grating. Experiments have demonstrated tuning ranges up to 105 nm at $\lambda = 0.8 \mu\text{m}$ [1], and 240 nm at $\lambda = 1.5 \mu\text{m}$ [2], for injection current densities of 21 kA/cm² and 33 kA/cm², respectively. Such high current densities are necessary in order to achieve lasing from the second quantized state of the quantum well, and therefore restrict commercial applications of these tunable sources.

In contrast to QW lasers, semiconductor lasers based on self-assembled quantum dots (QDs) are capable of broadband continuous tunability at significantly lower injection current density levels [3]. This advantage arises from two features of the QD laser. First, because of inhomogeneous and homogeneous broadening, continuous coverage of the wavelength spectrum is possible. The inhomogeneous size distribution of QDs, which is normally undesirable for achieving enhanced differential gain and ultra-low threshold current, is deliberately exploited in tuning applications. Second, the QD ground state saturates relatively easily, and the higher-order energy subbands are populated by carriers at current densities on the order of 1 kA/cm².

In this paper we report on the 183 nm tuning range of an anti-reflection coated QD laser using a diffraction grating in an external-cavity configuration. Over this range the laser threshold current density varied between 0.25 kA/cm² and 2.22 kA/cm² with an average value of 0.84 kA/cm². The laser active region is composed of a single InAs quantum dot layer confined in the middle of a 10-nm thick In_{0.2}Ga_{0.8}As quantum well and sandwiched by GaAs waveguide layers [4]. The in-plane dot density is $7.5 \times 10^{10} \text{ cm}^{-2}$. The photoluminescence FWHM is about 70 nm. The laser has a 9- μm wide ridge waveguide and the cavity is 2 mm long. A single $\lambda/4$ antireflection layer of HfO₂ was deposited on the laser facet by electron-beam evaporation. A residual reflectivity of 1.1 % was measured at the free-running lasing wavelength of $\lambda = 1.09 \mu\text{m}$. The AR coating increases the total cavity loss and thus completely extinguishes lasing at the ground state ($\lambda = 1.24 \mu\text{m}$) and the first excited state ($\lambda = 1.15 \mu\text{m}$). The lasing wavelength lies between the first and second ($\lambda = 1.05 \mu\text{m}$) excited states.

Figure 1 shows the attained tuning range (1.07 μm – 1.253 μm) using a Littrow external cavity configuration. Tuning was achieved by rotating the grating to select a certain emission wavelength to be reflected back to the laser. Across the 183-nm range, the lasing peak is at least 20 dB higher than the spontaneous emission spectrum. Figure 2 shows the threshold current density of the external-cavity quantum dot laser as a function of the tuning wavelength. We are able to tune over a 173-nm range (1.253 μm – 1.08 μm) with no more than 275 mA bias (1.52 kA/cm²), and over the entire 183-nm range (1.253 μm – 1.07 μm) with no more than 400 mA bias (2.22 kA/cm²). Similar tuning ranges in QW lasers require approximately 10 times higher current density. The lowest threshold current for the ground state is 45 mA, which is higher than the original uncoated laser threshold (35 mA) due to increased cavity losses.

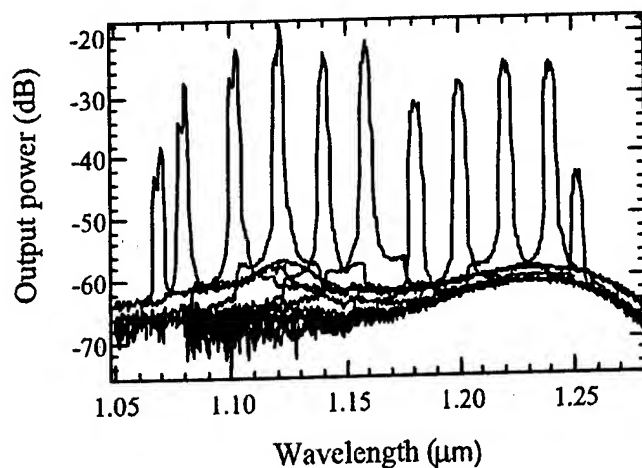


Figure 1. The lasing spectrum of the external-cavity quantum dot laser. The lasing wavelength is tuned over the 1.07 μm - 1.253 μm range.

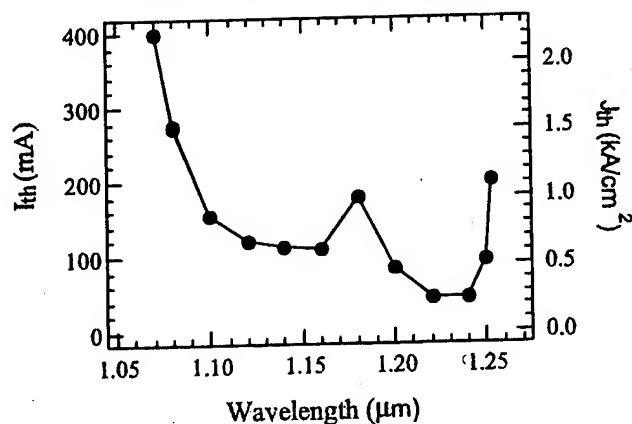


Figure 2. The threshold current of the external-cavity laser as a function of the lasing wavelength.

Further increase of the tuning range may be achieved by increasing the cavity losses of the internal QD Fabry-Perot laser either with an improved AR coating or a shorter cavity length. Finally, optimizing the QDs by increasing the deviation in dot sizes could help reduce the rise in threshold observed at 1.18 μm although at the expense of the threshold current of the free-running laser.

- [1] D. Mehuys, M. Mittelstein, A. Yariv, R. Sarfaty, and J. E. Ungar, *Electron. Lett.* 25(2), 143-145 (1989).
- [2] H. Tabuchi, and H. Ishikawa, *Electron. Lett.* 26(11), 742-743 (1990).
- [3] H. Li, G. T. Liu, P. M. Varangis, T. C. Newell, A. Stintz, B. Fuchs, K. J. Malloy, and L. F. Lester, to appear in *IEEE Phot. Technol. Lett.* (2000).
- [4] L. F. Lester, A. Stintz, H. Li, T. C. Newell, E. A. Pease, B. A. Fuchs, and K. J. Malloy, *IEEE Phot. Technol. Lett.* 11(8), 931-933 (1999).

Modal Gain and T_0 Value Improvements in Quantum Dot Lasers Using Dots-in-a-Well (DWELL) Structure

G. T. Liu, H. Li, A. Stintz, T. C. Newell, L. F. Lester and K. J. Malloy
Center for High Technology Materials, University of New Mexico
1313 Goddard SE, Albuquerque, NM 87106

Introduction

Quantum dot (QD) lasers have demonstrated impressive lasing properties, such as low threshold current density of 26 A cm^{-2} [1], low linewidth enhancement factor of 0.1 [2], a 150 nm tunable range with an external cavity [3], and 2Ws of CW operation near $1.3 \mu\text{m}$ [4]. While QD lasers have demonstrated higher T_0 values than InGaAsP quantum well (QW) lasers at $1.3 \mu\text{m}$, a major disadvantage of QD lasers is the low modal gain. This is mostly due to low dot densities, inhomogeneous broadening and the small optical confinement factor of the QD layer. These factors potentially limit the application of QDs for $1.3 \mu\text{m}$ VCSELs and elsewhere.

In this work, the issues necessary to achieve high ground state modal gain and high T_0 value will be addressed. It is found that modal gain and T_0 value can be increased simultaneously. Three different ways to improve the modal gain and T_0 value will be discussed. Additionally, it will be pointed out that the low threshold current density of QD lasers, is due primarily to "physical scaling" rather than any quantum effect. The performance tradeoffs occur between the threshold current density and the ground state modal gain and T_0 value.

Results

QD lasers with InAs/In_xGa_{1-x}As dots-in-a-well (DWELL) structure are used. The laser structures are the same as Ref. [1] except that several different active regions are considered. The lasing wavelengths are between $1.23 \mu\text{m}$ and $1.26 \mu\text{m}$. There are three different ways to improve the modal gain and T_0 values simultaneously:

- 1) Higher dot density. The ground state modal gain as a function of threshold current density for InAs/In_{0.2}Ga_{0.8}As DWELL lasers with dot densities of $3.7 \times 10^{10} \text{ cm}^{-2}$ and $7.5 \times 10^{10} \text{ cm}^{-2}$ are plotted in Fig.1. The corresponding ground state saturated modal gains are 5.7 and 9.0, respectively. The corresponding transparency current densities are approximately 20 A/cm^2 and 50 A/cm^2 , respectively. The threshold current as a function of temperature for 4-mm InAs/In_{0.2}Ga_{0.8}As DWELL lasers are plotted in Fig.2. The corresponding T_0 values are 52 K and 64 K. It is shown clearly from the above experimental results that the ground state modal gain and T_0 value may be increased simultaneously by increasing the dot density. The tradeoff is the increase of threshold current density because more carriers are needed to populate a larger number of QDs. Since the two laser structures studied here all have PL linewidths above 40 meV and are far from the ideal δ function, the low threshold current densities observed in these two lasers as compared to a QW laser are mostly due to a physical scaling of the active volume rather than quantum effects. The low laser internal loss is also necessary to achieve these low threshold current densities. The tradeoff of this low threshold current density is the low confinement factor and low modal gain as compared to a QW laser.

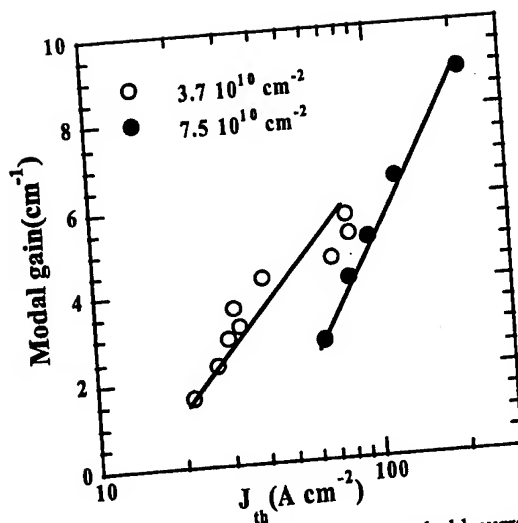


Fig.1 Modal gain as a function of threshold current density for InAs/In_{0.2}Ga_{0.8}As DWELL lasers with dot densities of $3.7 \times 10^{10} \text{ cm}^{-2}$ and $7.5 \times 10^{10} \text{ cm}^{-2}$, respectively.

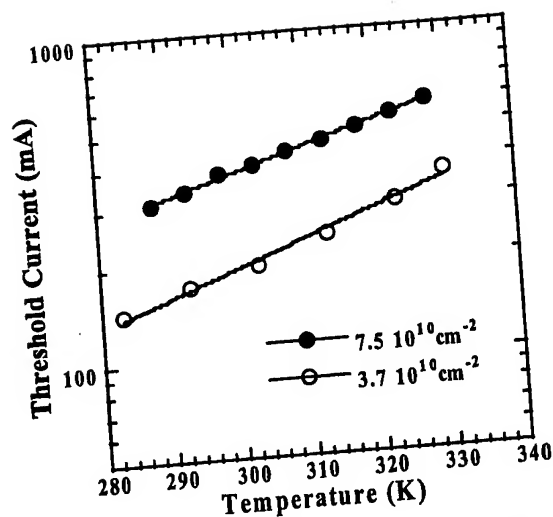


Fig.2 Threshold current as a function of temperature for 4-mm InAs/In_{0.2}Ga_{0.8}As DWELL lasers with dot densities of $3.7 \times 10^{10} \text{ cm}^{-2}$ and $7.5 \times 10^{10} \text{ cm}^{-2}$, respectively.

2) Deeper quantum well. Different indium composition QWs may be used for the InAs/In_xGa_{1-x}As DWELL lasers. The ground state saturated modal gain for the InAs/In_{0.10}Ga_{0.90}As, InAs/In_{0.15}Ga_{0.85}As, and InAs/In_{0.20}Ga_{0.80}As 1-DWELL lasers are 2.4 cm⁻¹, 3.6 cm⁻¹ and 5.7 cm⁻¹, respectively. As the In_xGaAs_{1-x} QW deepens, the injection efficiency is improved, and thus the ground state modal gain is improved. The corresponding T₀ values of 7.8-mm as-cleaved lasers are 37 K, 45 K and 51 K, which follows the same trend of increasing with the modal gain.

3) More DWELL layers. The ground state saturated modal gain for InAs/In_{0.15}Ga_{0.85}As 1-DWELL and 3-DWELL lasers are 3.6 cm⁻¹ and 12.5 cm⁻¹, respectively. This improvement in modal gain is due to the factor of 3 increase in the number of dots and to the resulting increase in injection efficiency. The corresponding T₀ values of 7.8-mm as-cleaved lasers are 45 K and 84 K, again following the same increasing trend with the modal gain.

In conclusion, three different ways to improve the modal gain and T₀ value of DWELL lasers are demonstrated. By using InAs/In_{0.20}Ga_{0.80}As 3-DWELL with a dot density per layer of $7.5 \times 10^{10} \text{ cm}^{-2}$ or above, a modal gain of 30 cm⁻¹ and above may be achieved with a possible T₀ value of above 100 K.

References

- [1] G. T. Liu, A. Stintz, H. Li, K. J. Malloy, and L. F. Lester, *Electron. Lett.* **35**, 1163-1165 (1999)
- [2] T. C. Newell, D. J. Bossert, A. Stintz, B. Fuchs, K. J. Malloy, L. F. Lester, *IEEE Photon. Technol. Lett.* **11**, 1527-1529 (1999)
- [3] H. Li, G. T. Liu, P. M. Varangis, T. C. Newell, A. Stintz, B. A. Fuchs, K. J. Malloy and L. F. Lester, accepted for publication in *IEEE Photonics Technology Letters*, July, 2000
- [4] A.E. Zhukov, A.R. Kovsh, V.M. Ustinov, Y.M. Shernyakov, S.S. Mikhlin, N.A. Maleev, E.Y. Kondrat'eva, D.A. Livshits, M.V. Maximov, B.V. Volovik, D.A. Bedarev, Yu. G. Musikhin, N.N. Ledentsov, P.S. Kopev, Z.I. Alferov, D. Bimberg, *IEEE Photon. Technol. Lett.* **11**, 1345-1347 (1999)

route to fabrication of 1.3 micron lasers based on GaAs substrates and may well offer advantages for high power lasers and for short pulse generation. Commercial ventures are being formed to exploit quantum dot technologies so interest is spread from fundamental research to commercial exploitation.

This tutorial is intended for those with a background in the area of diode lasers but with no specialist knowledge of quantum dot structures and lasers. The aim is to summarise the basic principles of quantum dot lasers and the current status of their development, and to assess their future potential.

Peter Blood has worked for many years on the gain and recombination characteristics of quantum confined laser diode structures. He was involved in early work on GaAs quantum wells, moving on to detailed studies of gain and carrier leakage processes in red-emitting GaInP quantum well structures. Having developed improved techniques for measurements of spontaneous emission and gain he has been involved in detailed comparisons between experimental data and many-body gain theories, particularly in collaboration with Koch and Chow. These techniques are being used to obtain a closer understanding of fundamental processes in quantum dot structures and the ways in which the distribution of electrons between localised dots is established.

CTHP2

3:30 pm

Modeling of Long Wavelength Quantum-dot Lasers with Dots-in-a-well Structure

Xiaodong Huang, A. Stintz, Hua Li, Julian Cheng, K.J. Malloy, Center for High Technology materials, University of New Mexico, 1313 Goddard SE, Albuquerque, NM87106, Email: xdh Huang@ieee.org

The physical properties of self-assembled quantum-dot (QD) lasers are attracting attention because of their potential application in telecommunication systems. The zero-dimensional nature and three-dimensional confinement of QDs give rise to widely-spaced discrete states, resulting in carrier dynamics and lasing characteristics that differ significantly from double heterostructure or quantum well lasers. In this paper, we propose a rate equation model for the dots-in-a-well (DWELL) structure,¹ and analyze the

steady-state and transient behavior of the DWELL lasers in detail using the model.

The size of the InAs QDs and their presence in an InGaAs quantum well (QW) suggest the presence of only one bound electron state but three hole states exist in an InAs QD. A degeneracy was assigned to each electron and hole state. In the QW region of the DWELL structure, we assume in our model that there exist only one electron sublevel and one hole sublevel, provided the electron and hole densities in the QW are small and the carriers in the QW principally reside in the first QW sublevel. The QW will serve as the carrier reservoir for the QDs. All the important processes involved in the DWELL structure, including carrier capture and emission, interlevel relaxation and interband recombination, were incorporated into the model and illustrated in Fig. 1. Charge neutrality is imposed to the whole DWELL structure and to ensure that the total number of electrons in the QW and the QD ensemble equals to the total number of holes in the QW and the QD ensemble. Within the framework of the model, an approximation was derived to account for the microscopic states of the QD ensemble.²

The DC characteristics were first compared by solving the steady state equations assuming a variety of carrier capture times and interlevel relaxation times. As shown in Fig. 2, the calculated L-I characteristics are dramatically different for different carrier capture and interlevel relaxation time constants. Only upon assuming very fast carrier capture and interlevel relaxation rates does the model show similar threshold current density and external quantum efficiency with the measured results from actual DWELL lasers described in Ref 3. The effects of carrier emission,

recombination in the quantum well, and interband recombination will also be presented.

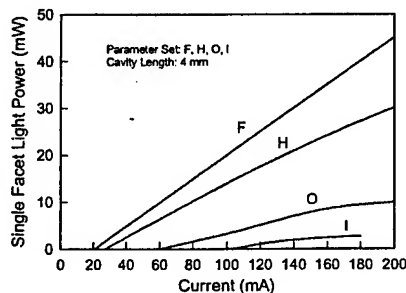
Gain and absorption saturation behavior of the DWELL structure was studied by directly accounting for light-induced stimulated processes. The gain and absorption saturation with increased light intensity was shown to be due to the carrier depletion and carrier filling caused by the photon-induced interband stimulated processes in the QDs. The absorption of the QD ensemble saturates very quickly with increasing light intensity due to the finite number of QDs. The proposed model was also simplified to facilitate the fitting of the measured linear ground state modal gain and absorption. As shown in Fig. 3, a close fit was obtained simultaneously for both the modal gain and the modal absorption data. The fitting parameters again required fast carrier capture rates.

In addition, turn-on behavior of the DWELL lasers was studied using the rate equation model. The saturated modal gain was shown to be a key parameter in to increase the frequency response of the photons. Furthermore, simulation of the steady-state bistable operation and Q-switched operation of the two-section DWELL laser can qualitatively explain the experimental results from the actual two-section lasers described in Ref 4.

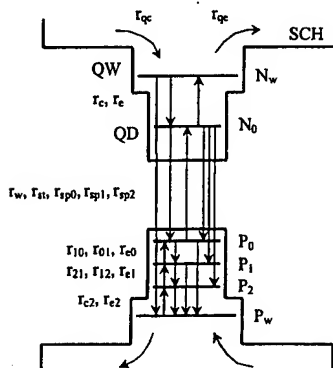
In summary, a comprehensive rate equation model has been proposed to describe the steady state and transient behavior of the DWELL lasers. Comparisons between the modeling results and the experimental results improve our understanding of the dynamic properties of the DWELL lasers.

References

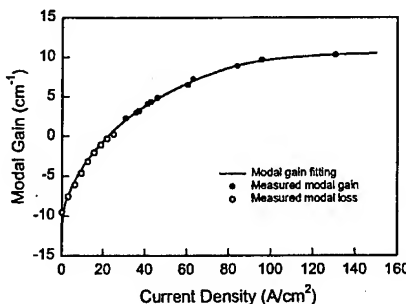
1. L.F. Lester, A. Stintz, H. Li, T.C. Newell, E.A. Pease, B.A. Fuchs, K.J. Malloy, "Optical characteristics of 1.24 μm InAs quantum dot laser diodes," IEEE Phot. Tech. Lett., 11, 931-933 (1999).
2. M. Grundmann and D. Bimberg, "Theory of random population for quantum dots," Phys. Rev. B, 55, 9740-9745 (1997).
3. Xiaodong Huang, A. Stintz, C.P. Hains, G.T. Liu, J. Cheng and K.J. Malloy, "Efficient high temperature CW lasing operation of oxide-confined long-wavelength InAs quantum dot lasers," Electron. Lett., 36, 41-42 (2000).
4. Xiaodong Huang, A. Stintz, Hua Li, L.F. Lester, Julian Cheng, and K.J. Malloy, "Passive mode-locking in 1.3 μm two-section InAs quantum dot lasers," Appl. Phys. Lett., 78, 2825-2827 (2001).



CTHP2 Fig. 2. The L-I characteristics calculated for DWELL lasers with cavity length $L = 4$ nm using different time constants.



CTHP2 Fig. 1. The model diagram of electron and hole levels in the DWELL structure.



CTHP2 Fig. 3. The measured and fitted modal gain as a function of the injected current density.

CTHP3

3:45 pm

Filamentation in InGaAs Quantum-dot Lasers: Theory and Experiment

H.C. Schneider and W.W. Chow, Sandia National Laboratories, Albuquerque, NM 87185-0601
Email: hcschne@sandia.gov

E.J. Pearce and P.M. Smowton, Department of Physics and Astronomy, Cardiff University, Cardiff CF24 3YB, United Kingdom

Self-organized quantum-dot structures are presently investigated both for their unusual electronic and optical properties, as well as for their applications in semiconductor lasers.¹ One question concerning active media for semiconductor

High temperature continuous wave operation of InAs quantum dot lasers near 1.3 μm

LEOS 2001

Y. Qiu, P. Gogna, S. Forouhar

Center for Space Microelectronics Technology, Jet Propulsion Laboratory, California Institute of Technology, 4800 Oak Grove Drive, Pasadena, CA 91109, Tel: (818)354-2234, Fax: (818)393-4540.

A. Stintz, and L. Lester

Center for High Technology Materials, University of New Mexico, 1313 Goddard SE, Albuquerque, NM 87106, Tel: 505 272-7095, Fax: 505 272 7801.

Despite significant improvements in recent years, quantum dot (QD) lasers still have difficulties operating at the ground state without high reflectivity coating¹, either show a characteristic temperature T_0 abruptly decreasing at or above room temperature² or switch to higher energy lasing states³. For reducing the temperature sensitivity, one approach is using deep potential wells to thermally decouple the QD ground state from the wetting layer and by designing QDs to have a wide energy separation between the ground and first excited. But a more fundamental approach is to increase the gain of QD ground state¹, by packing more dots in the active region and reducing the inhomogeneous broadening. We report here high performance narrow ridge waveguide InAs QD edge-emitting lasers lasing CW at ground state near 1.3 μm up to the temperature of 100°C.

These lasers are based on four stack InAs QDs embedded within strained InGaAs quantum well, with dot density of 10^{11} cm^{-2} , and fabricated using narrow ridge waveguide design with ridge width of 5 μm . Ground state CW lasing has been achieved at room temperature, showing lasing wavelength between 1.25~1.26 μm . Then depend on cavity length, with increasing injection current CW lasing continues at ground state (for 1 mm, 1.5 mm cavity length) or switches to the first excited state at wavelength of 1.20~1.22 μm (for 500 μm , 750 μm cavity length). Fig.1 plots ground state CW lasing spectra of a 1 mm cavity laser, showing the lasing wavelength of 1.3 μm at 90°C with 90 mA injection current. For 1 mm and 1.5 mm cavity length lasers, ground state CW lasing

was even obtained up to 100°C, which is the temperature limit of the thermoelectric cooler. To our knowledge, this is so far the highest temperature ever reported for QD lasers lasing CW at ground state near 1.3 μm . With increasing temperature, a wavelength shift of 3.7 $\text{\AA}/\text{K}$ is found for these QD lasers, comparable to that of quantum well lasers, which is bigger than 2 $\text{\AA}/\text{K}$ reported for QD lasers at wavelength near $\sim 1 \mu\text{m}$ ⁴. The temperature dependence of gain peak for both QD and quantum well depend on the bandgap of the active material and the barriers, if state filling happens in QD due to limited dot density, the blue shift of state filling will partially compensate for the temperature dependence of the bandgap. Therefore in our case, multi stack and high dot density of $\sim 10^{11} \text{ cm}^{-2}$ QDs obviously provided

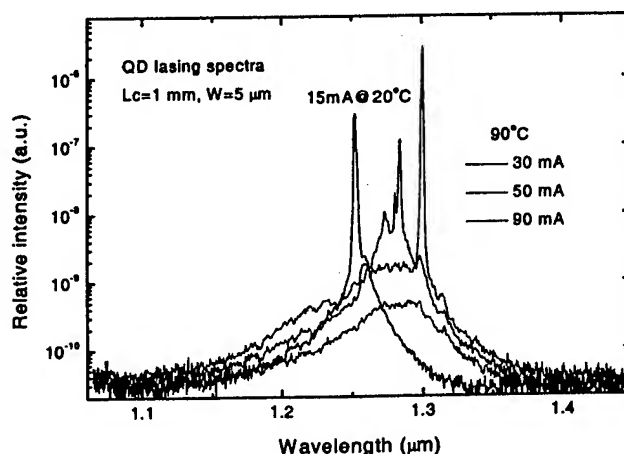


Fig.1 Ground state CW lasing spectra at 90°C of a 1 mm cavity length laser measured at various currents, indicating a ground state lasing wavelength of 1.3 μm . For comparison a spectrum at 20°C shown.

enough gain for lasing CW at ground state, and the state filling is negligible for 1 mm and 1.5 mm cavity lasers.

As mentioned above, for both 1 mm and 1.5 mm long lasers, CW ground state lasing were obtained at any injection current until thermal roll over up to the temperature of 100°C, which is the limit of our thermoelectric cooler. Fig. 2 shows the single facet light output characteristics versus current of a 1.5 mm cavity length laser operating CW measured at different temperature. At room temperature, the threshold current and threshold current density is about 10 mA, 133 A/cm² respectively, the single facet output power exceeds 50 mW and the differential slope efficiency is 55%. Due to the smaller power dissipation of a very narrow stripe ridge waveguide structure, thermal rollover is reduced and CW lasing occurs even at an injection current of $I > 20I_{th}$. While at the temperature of 100°C, the threshold current and threshold current density are about 33 mA, 440 A/cm² respectively, the single facet output power exceeds 15 mW and the differential slope efficiency is 35%.

The temperature dependence of the threshold current of a 1.5 mm cavity length QD laser has been measured for ground state lasing under both CW and pulsed operation (5 μ s pulses with a duty cycle of 0.5%). For temperature ranging from 283 K to 373 K, the characteristic temperatures T_0 are 78 K for CW operation, and 86 K for pulsed operation. To our knowledge, the 78 K characteristic temperature is the largest reported value in this temperature range for ground state CW operation of a QD laser. Comparing with either low T_0 or shifting to excited state lasing reported previously^{3,5}, multi stack and high QD density of $\sim 10^{11}$ cm⁻² thus larger gain are the key reasons for achieving ground state lasing with temperature insensitive threshold current for temperatures up to 100°C.

In summary, we have demonstrated high performance temperature insensitive narrow ridge waveguide QD lasers near 1.3 μ m using four stacks of InAs QD layer embedded within strained InGaAs quantum wells as an active region. For a 1.5 mm long cavity QD laser, ground state CW lasing has been achieved with single facet output power of 15 mW and a differential slope efficiency of 35% at temperature as high as 100°C, while at room temperature having a differential quantum efficiency about 55% and single facet output power of 50 mW. The characteristic temperature T_0 for ground state CW lasing is 78 K at temperatures ranging from 20°C to 100°C.

Reference

1. N. Hatori, M. Sugawara, K. Mukai, Y. Nakata, and H. Ishikawa, Appl. Phys. Lett. 77, 773(2000).
2. G. Park, D. L. Huffaker, Z. Zou, O. B. Shchekin, and D. G. Deppe, IEEE Photo. Technol. Lett. 11, 301(1999).
3. X. Huang, A. Stintz, C. P. Hains, G. T. liu, J. Cheng, and K. J. Malloy, IEEE Photo. Technol. Lett. 12, 227(2000).
4. F. Schafer, J. P. Reithmaier, and A. Forchel, Appl. Phys. Lett. 74, 2915(1999).
5. O. B. Shchekin, G. Park, D. L. Huffaker, Q. Mo, and D. G. Deppe, IEEE Photo. Technol. Lett. 12, 1120(2000).

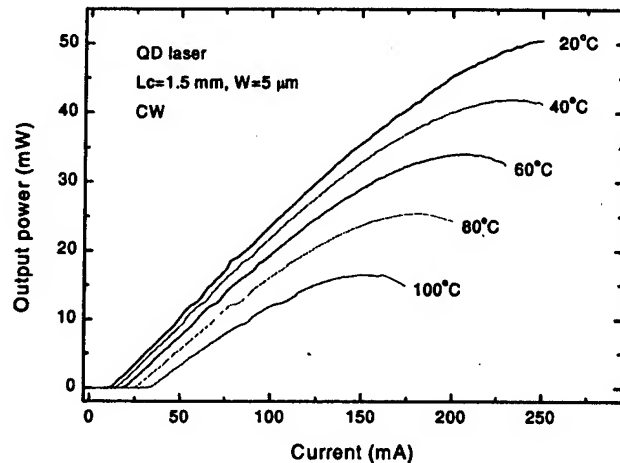


Fig.2 Light versus current for a 1.5 mm cavity length laser without facet coating measured at different temperature.

Gain in Ultra-Low-Threshold InAs/InGaAs Quantum Dot Lasers

P. G. Eliseev*, H. Li, G. T. Liu, A. Stintz, T. C. Newell, L. F. Lester,
and K. J. Malloy

Center for High Technology Materials, University of New Mexico, Albuquerque, NM 87106

Tel. (505) 272-7800, Fax. (505) 272-7801, e-mail: eliseev@chtm.unm.edu

*also at the P. N. Lebedev Physics Institute, Russian Academy of Sciences, Moscow, 117924, Russia

Semiconductor lasers are grown on a GaAs substrate by MBE containing self-assembled InAs quantum dots (QDs) in an InGaAs quantum well, the so-called dot-in-a-well (DWELL) structure [1,2]. The QDs are ~ 15 nm in diameter in the basal plane and ~7 nm in height. Several wafers are investigated in detail (see Table 1). The in-plane dot density is either 2.5×10^{10} or $7.5 \times 10^{10} \text{ cm}^{-2}$. The ground-state emission wavelength is 1230-1250 nm at room temperature, and the spectral FWHM is from 40 to 75 nm.

Table 1. Parameters of the MBE-wafers studied. M is a number of DWELL stacks in the structure, d is thickness of individual DWELL layer, λ is the central wavelength of the laser emission.

Wafer #	M	d , nm	In-plane QD density, cm^{-2}	Equivalent bulk density, cm^{-3}	InGaAs QW Indium content	λ , nm
SDWELL-577	1	10	2.5×10^{10}	2.5×10^{16}	0.15	1246
MDWELL-638	3	9.6	2.5×10^{10}	2.6×10^{16}	0.15	1250
SDWELL-432	1	10	7.5×10^{10}	7.5×10^{16}	0.20	1230

A threshold current density as low as 16 A/cm^2 is measured. The dependence of the modal optical gain on current density is obtained from an experimental study of the cavity length effect on the threshold current in ultra-low-threshold laser diodes. The ground-state rises asymptotically to the maximum value corresponding to a total inversion of the work states. Also, we estimated the material gain by dividing the modal gain by the optical confinement factor. From the maximum gain we determine the average gain cross-section relating to the ground state transitions of the InAs QDs in the InGaAs QW (see Table 2). In this approach we assign the interaction cross-section to the dot as an atomic object and do not specify the dot volume. The theoretical model is proposed describing the gain as a function of the current. It allows us to fit the experimental gain versus the current density rather easily and to derive important characteristics of the InAs QDs. A saturation of the optical gain is caused by total inversion of the ground-state levels. The competition from the lossy channel is described to be dependent on the capture coefficient C of carriers to the dots, and the effective coefficient B of lossy recombination. There are several fitting parameters in this model. The important parameters are $A = 1/(C\tau N_{\text{QD}})$ and $T = \tau B N_{\text{QD}}$, where τ is the electron lifetime at the ground-state upper level, and N_{QD} is the volume density of quantum dots in the well. An increase in both coefficients A and T corresponds to a decrease of the yield of ground-state recombination. Data on these fitting parameters are given in Table 2. The characteristic capture coefficient C is estimated for carriers that relax to the ground state by $\sim 2 \times 10^{-7} \text{ cm}^3/\text{s}$.

Table 2. Parameters of DWELL structures from the fitting of experimental data.
 g_{max} is the maximum modal gain.

Wafer	J_0 , A/cm^2	g_{max} , cm^{-1}	σ , cm^2	A	T
SDWELL-577	13	5.43	7.17×10^{-15}	0.2	0.4
MDWELL-638	25.7	17	7.21×10^{-15}	0.5	0.4
SDWELL-432	50	15.6	6.89×10^{-15}	0.5	0.4

The model includes the non-radiative losses due to nonradiative recombination in the well and due to some tunneling component through the junction that does not contribute to the carrier injection. The component is described in terms of excess current with a factor n of the nonideality. In ultra-low-threshold lasers, this component produces reduction of the quantum yield in the current range of lasing, above 16 A/cm^2 . This growing-injection-

efficiency (GIE) correction allows us also to explain an anomalous behavior of the differential gain in QD lasers reported in Ref. [2]. It passes a maximum when current increases, and this behavior has not been predicted in commonly-accepted models of the optical gain. We calculate the differential gain taking the GIE-correction into account and find such a non-monotonic behavior.

In conclusion, we obtained and analyzed the dependence of the gain on current density in ultra-low-threshold laser diodes with DWELL quantum-dot structures. The inversion threshold as low as 13 A/cm^2 and lasing threshold as low as 16 A/cm^2 are obtained. From the saturation behavior of the ground-state gain associated with total inversion of the population of work levels, The effective cross-section of the gain is estimated to be $\sim 7 \times 10^{-15} \text{ cm}^2$. Specific equations and details of the model will be given at the time of presentation.

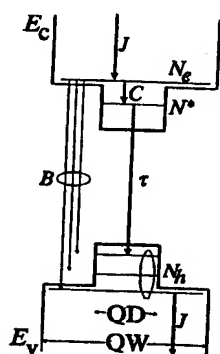


Fig. 1. Energy diagram of the levels and transitions taken into account. One electron level is assumed and several hole levels in the dots. The ground-state recombination in the dot is characterized by a single lifetime τ . Quantity N^* is the density of quantum dots with an electron at the upper level and a hole at the lower level.

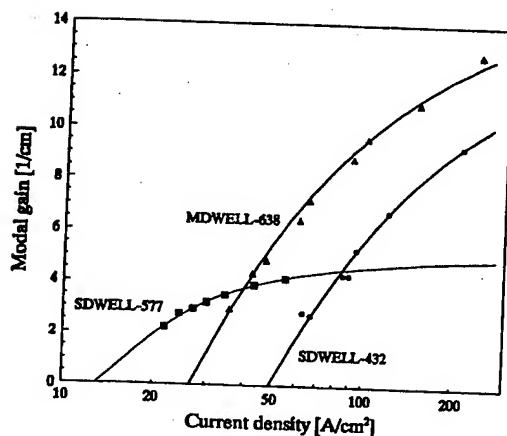


Fig. 2. Ground-state gain as a function of current density for three DWELL-type groups of laser diodes (see Table 1 for their parameters).

1. G. T. Liu, A. Stintz, H. Li, K. J. Malloy, and L. F. Lester, *Electron. Lett.*, 35 (14) 1163-1165 (1999).
2. L. F. Lester, A. Stintz, H. Li, T. C. Newell, E. A. Pease, B. A. Fuchs, and K. Malloy, *IEEE Photon. Technol. Lett.*, 11 (8), 931-933 (1999).

High-performance InAs quantum-dot lasers near 1.3 μm

Y. Qiu,^{a)} P. Gogna, and S. Forouhar

Jet Propulsion Laboratory, California Institute of Technology, Pasadena, California 91109

A. Stintz and L. F. Lester

Center for High Technology Materials, University of New Mexico, Albuquerque, New Mexico 87106

(Received 23 July 2001; accepted for publication 5 October 2001)

High-performance quantum dot (QD) lasers near 1.3 μm were fabricated using four stacks of InAs QDs embedded within strained InGaAs quantum wells as an active region and a reactive-ion-etched 5- μm -ridge waveguide design. For a 1.5-mm-long cavity QD laser, ground-state continuous-wave (cw) lasing has been achieved with a single facet output power of 15 mW at temperatures as high as 100 °C, while at room temperature having a differential quantum efficiency of 55% and a single facet output power of 50 mW. The characteristic temperature T_0 for ground-state cw lasing is 78 K up to our temperature measurement limit of 100 °C. © 2001 American Institute of Physics. [DOI: 10.1063/1.1421428]

Quantum dot (QD) lasers are expected to have superior lasing properties, such as a lower threshold current density and an improved temperature stability of the threshold current density, and to have many other advantages because of their delta function-like density of states. Significant improvements in the characteristics of QD lasers have been achieved by using self-assembled QD layers as the active gain medium.¹ The best GaAs-based InAs QD lasers have been achieved at the longest-wavelength range between 1.2 and 1.3 μm .^{2–7} So far, QD lasers near 1.3 μm have been demonstrated to have a minimum continuous-wave room-temperature operation threshold current density³ of 19 A/cm², which is much lower than any reported for planar quantum-well lasers, and a single lateral-mode maximum output power of 210 mW.⁴ However, QD lasers still have difficulty operating at the ground state without high-reflectivity coating,⁵ either show a characteristic temperature T_0 abruptly decreasing at or above room temperature,⁶ or switch to higher-energy lasing states.⁷ One approach to reduce the temperature sensitivity is to use deep potential wells to thermally decouple the QD ground state from the wetting layer and to design the QDs to have a wide energy separation between the ground and first-excited states through carefully controlled growth conditions.² Another approach is to increase the gain of the QD ground state⁵ by increasing the number density of dots in the active region and to reduce the inhomogeneous broadening. Vertically stacking multilayer QDs while simultaneously increasing QD density have been proved an effective way for preventing gain saturation.⁸ To date, InAs QD ground-state lasing has been observed up to 100 °C,⁹ and the highest reported cw characteristic temperature above room temperature is ~126 K from 300 to 325 K.²

In this letter, we report high-performance, narrow-ridge-waveguide InAs QD edge-emitting lasers operating at cw in the ground state near 1.3 μm up to a temperature of 100 °C. These lasers are based on four stacks of InAs QDs embedded within strained InGaAs quantum wells [i.e., dot-in-a-well (DWELL) structure,¹⁰] which provides a high injection effi-

ciency and larger optical gain.¹¹ For a 1.5-mm-long cavity QD laser without facet coating, single lateral-mode ground-state cw lasing has been achieved with single facet output power of 15 mW at temperatures as high as 100 °C and a characteristic temperature T_0 of 78 K up to 100 °C, which is a high T_0 for QD ground-state cw lasing near 1.3 μm reported for this temperature range. At room temperature, the lasers have a differential quantum efficiency of about 55% and a single facet output power of 50 mW.

The QD laser structure was grown by solid-source molecular-beam epitaxy on a (001) GaAs substrate and similar growth conditions to those published previously were used.¹⁰ The primary difference is that the four-stack DWELL region is formed by deposition of 2.3 ML of bulk InAs within 70 Å strained In_{0.15}Ga_{0.85}As quantum wells separated by 29 nm GaAs barriers. Room-temperature photoluminescence (PL) measurements showed a ground-state peak at 1.26 μm with a spectral full width at half maximum of 34 meV, indicating a good homogeneity of the QDs.

Device fabrication begins with the formation of 5 μm ridges by reactive ion etching followed by plasma-enhanced chemical-vapor deposition of a thin oxide layer. Windows are plasma etched in the oxide above the ridges to enable electrical contact. The Ti/Pt/Au *p*-type contacts are e-beam deposited. Finally, AuGe/Ni/Au *n*-type contacts are thermally deposited after the substrate has been lapped down to a thickness of ~125 μm . Figure 1 is a cross-section scanning electron microscope (SEM) image of a QD laser and a schematic drawing of the four-stack QD active region, indicating a well-controlled etch profile and a narrow-ridge width of 5 μm . In order to minimize current spreading, the AlGaAs upper cladding layer is etched away almost completely outside the ridge, as shown in Fig. 1. The wafer is then cleaved into laser bars with a cavity length ranging from 500 μm to 1.5 mm, with no facet coating. The lasers are tested in bar form using a temperature-controlled probe station with an epitaxial-side-up configuration. The thermal impedance is negligible between laser bar and the copper block, providing a large contact area of the laser bar.

Ground-state cw lasing has been achieved for all four

^{a)}Electronic mail: yueming.qiu@jpl.nasa.gov

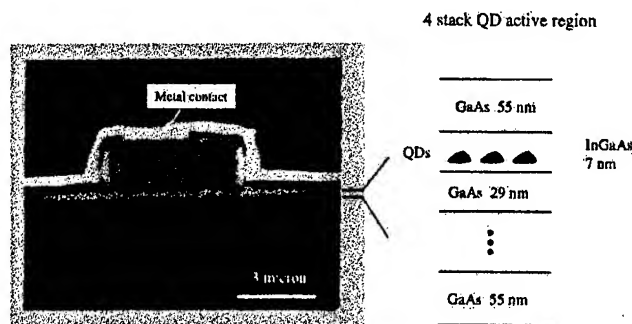


FIG. 1. Cross-sectional SEM image of the ridge waveguide QD laser. Ridge width $W=5\text{ }\mu\text{m}$.

lengths at room temperature, with the lasing wavelength between 1.25 and 1.26 μm . Depending on the cavity length and with increasing injection current, cw lasing either continues at the ground state (for 1 and 1.5 mm cavity lengths) or switches to the first-excited state at a wavelength of 1.20–1.22 μm (for 500 and 750 μm cavity lengths). Shown in Fig. 2(a), the room-temperature ground-state cw lasing spectra of a 1-mm-cavity QD laser, display some spectral features unique to QD lasers. Just above threshold, there is only one broadened longitudinal mode that dominates the spectrum. With increasing current, sets of longitudinal modes appear, each of which reach a similar maximum intensity, implying power saturation. In fact, each of these broadened modes consists of a series of individual longitudinal modes¹² that are not visible due to the resolution of the optical spectrum

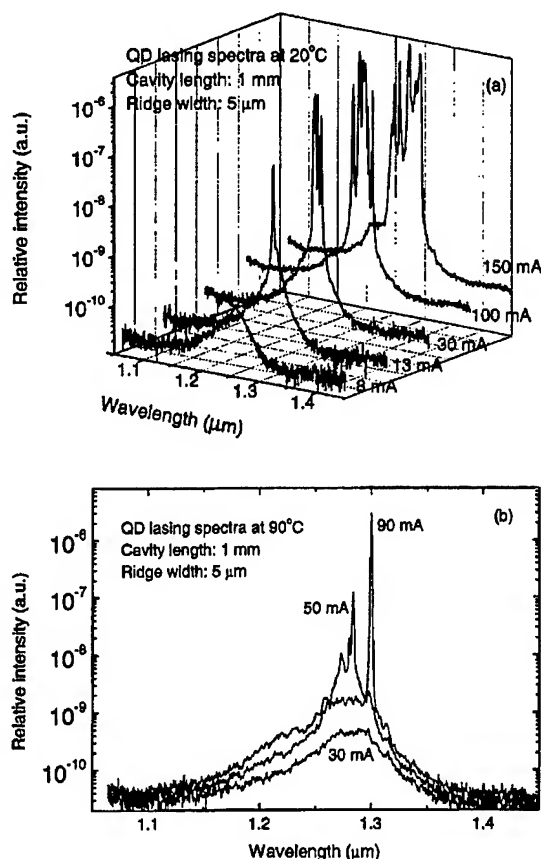


FIG. 2. Ground-state cw lasing spectra of a 1-mm-cavity-length laser measured at various currents at (a) room temperature and (b) 90 °C, indicating a ground-state lasing wavelength of 1.3 μm .

analyzer. Over the entire range of injection current and temperature, however, these lasers have shown single lateral modes, despite the fact that the cladding layer was etched almost all the way through, as shown in Fig. 1. The unique behavior of QD lasing spectra can be understood in terms of an inhomogeneously broadened gain spectrum resulting from the presence of noninteracting dots. Each of these broadened modes represents a subset of dots having sufficient gain to overcome the cavity losses. When the gain of these dots saturates, the gain of another subset of dots corresponding to neighboring modes continues to increase until they, in turn, reach threshold. Therefore, the number of lasing modes increases with current, reflecting an increase in the number of subsets of dots reaching threshold gain. But with increasing temperature, homogeneous broadening becomes comparable or exceeds inhomogeneous broadening, lasing-mode photons are emitted not only from energetically resonant dots, but also from other nonresonant dots within the scope of homogeneous broadening, eventually leading to collective lasing of the dot ensemble.¹³ Thus, the number of broadened longitudinal modes significantly decreases, resulting in a single broadened mode lasing at high temperature with high injection current. Figure 2(b) plots ground-state cw lasing spectra of a 1-mm-cavity laser, showing a single broadened longitudinal mode at a wavelength of 1.3 μm at 90 °C with 90 mA injection current. For 1 and 1.5 mm cavity length lasers, ground-state cw lasing was even obtained up to 100 °C, which is the temperature limit of the thermoelectric cooler.

With increasing temperature, a wavelength shift of 3.7 Å/K is found for these QD lasers, comparable to that of quantum-well lasers, which is greater than the 2 Å/K reported for QD lasers at a wavelength near $\sim 1\text{ }\mu\text{m}$.¹⁴ The temperature dependence of the gain peak for both QD and quantum-well lasers depends on the band gap of the active material and the barriers. If state filling happens in the QD due to limited dot density, the blueshift of state filling will partially compensate for the temperature dependence of the band gap. Therefore, in our case a multistack and a high total dot density of $\sim 3\text{--}4 \times 10^{11}\text{ cm}^{-2}$ obviously provides enough gain for lasing cw at ground state, and the state filling is negligible for 1- and 1.5-mm-cavity lasers.

As mentioned above, for both 1- and 1.5-mm-long lasers, cw ground-state lasing is obtained at any injection current until thermal roll over up to the temperature of 100 °C, which is the limit of our thermoelectric cooler. Figure 3 shows the single facet light output characteristics versus current of a 1.5-mm-cavity-length laser operating cw measured at different temperatures. At room temperature, the threshold current and threshold current density are about 10 mA and 133 A/cm², respectively. The single facet output power exceeds 50 mW and the differential slope efficiency is 55%. Due to the smaller power dissipation of a very narrow stripe ridge waveguide structure, thermal rollover is reduced and cw lasing occurs even at an injection current of $I > 20I_{th}$. While at a temperature of 100 °C, the threshold current and threshold current density are about 33 mA and 440 A/cm², respectively. The single facet output power exceeds 15 mW and the differential slope efficiency is 35%. The inverse differential quantum efficiency shows a linear dependence on the cavity length, except for 500 μm , from which an internal

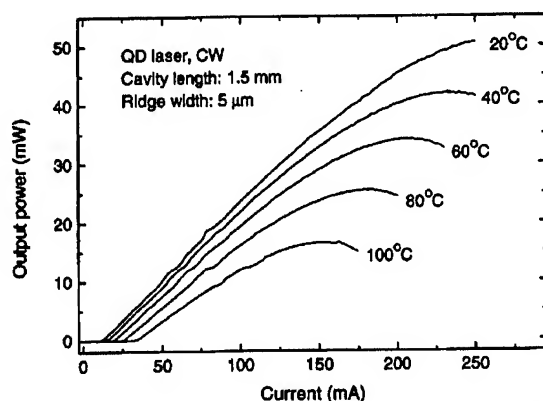


FIG. 3. Light vs current for a 1.5-mm-cavity-length laser without facet coating measured at different temperatures.

quantum efficiency of 68% and an internal optical loss of 2 cm^{-1} could be obtained, respectively.

The temperature dependence of the threshold current of a 1.5-mm-cavity-length QD laser has been measured for ground-state lasing under both cw and pulsed operation ($5 \mu\text{s}$ pulses with a duty cycle of 0.5%), as shown in Fig. 4. For temperatures ranging from 283 to 373 K, the characteristic temperatures T_0 are 78 K for CW operation, and 86 K for pulsed operation. The 78 K characteristic temperature is a large reported value in this temperature range for ground-state CW operation near $1.3 \mu\text{m}$ of a QD laser. Further improvement is possible considering the high series resistance, 50Ω , of the device.

In summary, we have demonstrated high-performance temperature-insensitive narrow-ridge waveguide QD lasers

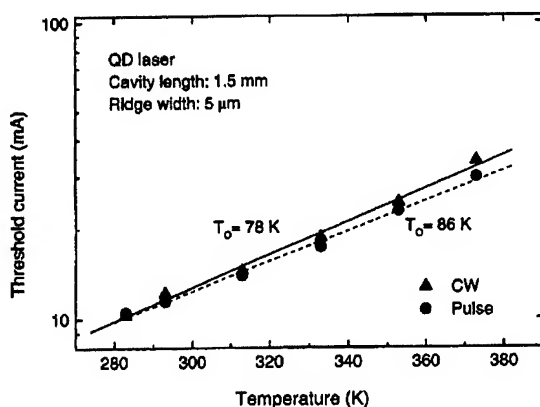


FIG. 4. Temperature dependence of the threshold current for both cw and pulse lasing at ground state for a 1.5-mm-cavity-length laser.

near $1.3 \mu\text{m}$ using four stacks of a InAs QD layer embedded within strained InGaAs quantum wells as an active region. For a 1.5-mm-long cavity QD laser, ground-state cw lasing has been achieved with a single facet output power of 15 mW and a differential slope efficiency of 35% at temperature as high as 100°C , while at room temperature having a differential quantum efficiency about 55% and single facet output power of 50 mW. The characteristic temperature T_0 for ground-state cw lasing is 78 K at temperatures ranging from 20 to 100°C . The high total QD density of $3\text{--}4 \times 10^{11} \text{ cm}^{-2}$ for the multistack active region is the key reason for achieving ground-state lasing with temperature-insensitive threshold current for conditions up to 100°C .

This work has been supported by the Revolutionary Computing Technology Program Element and the Cross-Enterprise Technology Development Program at the Jet Propulsion Laboratory (under a contract with the National Aeronautics and Space Administration). The authors thank Dr. Yongkun Sin of TRW, Inc., for interesting discussions, Dr. Daniel Wilson, Dr. Kamjou Mansour, Dr. Peter Deelman, and Rebecca Chacon of JPL for technical assistance.

- ¹N. Kirstaedter, N. N. Ledentsov, M. Grundmann, D. Bimberg, V. M. Ustinov, S. S. Ruvimov, M. V. Maximov, P. S. Kop'ev, Zh. I. Alferov, U. Richter, P. Werner, U. Gosele, and J. Heydenreich, *Electron. Lett.* **30**, 1416 (1994).
- ²H. Chen, Z. Zou, O. B. Shchekin, and D. G. Deppe, *Electron. Lett.* **36**, 1703 (2000).
- ³D. L. Huffaker, G. Park, Z. Zou, O. B. Shchekin, and D. G. Deppe, *IEEE J. Sel. Top. Quantum Electron.* **6**, 452 (2000).
- ⁴M. V. Maximov, L. V. Asryan, Yu. M. Shernyakov, A. F. Tsatsul'nikov, I. N. Kaiander, V. V. Nikolaev, A. R. Kovsh, S. S. Mikhlin, V. M. Ustinov, A. E. Zhukov, Zh. I. Alferov, N. N. Ledentsov, and D. Bimberg, *IEEE J. Quantum Electron.* **37**, 676 (2001).
- ⁵N. Hatori, M. Sugawara, K. Mukai, Y. Nakata, and H. Ishikawa, *Appl. Phys. Lett.* **77**, 773 (2000).
- ⁶G. Park, D. L. Huffaker, Z. Zou, O. B. Shchekin, and D. G. Deppe, *IEEE Photonics Technol. Lett.* **11**, 301 (1999).
- ⁷X. Huang, A. Stintz, C. P. Hains, G. T. Liu, J. Cheng, and K. J. Malloy, *IEEE Photonics Technol. Lett.* **12**, 227 (2000).
- ⁸O. G. Schmidt, N. Kirstaedter, N. N. Ledentsov, M.-H. Mao, D. Bimberg, V. M. Ustinov, S. S. Ruvimov, A. Y. Egorov, A. E. Zhukov, M. V. Maximov, P. S. Kop'ev, and Zh. I. Alferov, *Electron. Lett.* **32**, 1302 (1996).
- ⁹K. Mukai, Y. Nakata, K. Otsubo, M. Sugawara, N. Yokoyama, and H. Ishikawa, *Appl. Phys. Lett.* **76**, 3349 (2000).
- ¹⁰L. F. Lester, A. Stintz, H. Li, T. C. Newell, E. A. Pease, B. A. Fuchs, and K. J. Malloy, *IEEE Photonics Technol. Lett.* **11**, 931 (1999).
- ¹¹G. T. Liu, A. Stintz, H. Li, T. C. Newell, A. L. Gray, P. M. Varangis, K. J. Malloy, and L. F. Lester, *IEEE J. Quantum Electron.* **36**, 1272 (2000).
- ¹²L. Harris, D. J. Mowbray, M. S. Skolnick, M. Hopkinson, and G. Hill, *Appl. Phys. Lett.* **73**, 969 (1998).
- ¹³M. Sugawara, K. Mukai, Y. Nakata, K. Otsubo, and H. Ishikawa, *IEEE J. Sel. Top. Quantum Electron.* **6**, 462 (2000).
- ¹⁴F. Schafer, J. P. Reithmaier, and A. Forchel, *Appl. Phys. Lett.* **74**, 2915 (1999).

All-optical double-sideband suppressed-carrier modulation of semiconductor lasers

P. M. Varangis, A. Gavrielides, and V. Kovanis

Nonlinear Optics Center, Air Force Research Laboratory/DELO, Kirtland Air Force Base, New Mexico 87117

T. Erneux

Université Libre de Bruxelles, Optique Nonlinéaire Théorique, Campus Plaine, C.P. 231, 1050 Bruxelles, Belgium

L. F. Lester

Center for High Technology Materials, University of New Mexico, Albuquerque, New Mexico 87106

(Received 4 December 1997; accepted for publication 14 March 1998)

We demonstrate theoretically and verify experimentally that injection locking may be used to achieve double-sideband suppressed-carrier modulation of semiconductor lasers. Our theoretical investigation explains the suppression of the optical carrier and illustrates the dominant role of the phase in prescribing the response of the injected laser. © 1998 American Institute of Physics. [S0021-8979(98)02112-4]

Injection locking of semiconductor lasers has been extensively investigated due to its significance in improving the laser response, by suppressing mode-hopping and spurious-feedback effects, and reducing the emission linewidth.¹ Applications in optical communications include, among others, frequency to phase modulation conversion and locking of a laser diode array to a unique master.²

In this article, we propose a scheme for double-sideband suppressed-carrier (DSB-SC) modulation of an optically injected semiconductor laser. Our experimental measurements demonstrate that in the dynamically unstable locking region the optical carrier may be significantly suppressed and the relaxation oscillation sidebands dominate the frequency response of the locked laser. Such a configuration, coupled with narrow-linewidth laser sources (such as distributed feedback (DFB) lasers), is potentially useful for optical coherent communication systems. Since the carrier component is suppressed, the signal, i.e., the information-carrying sidebands, may be correspondingly amplified before suffering any processing losses.³ Motivated by the experimental results, we perform a theoretical investigation in order to determine the dominant mechanism underlying the induced response of the laser. We subsequently obtain an analytical description of the laser dynamics, in terms of the evolution of the phase, that captures the essential dynamical behavior of the system.

The single-mode rate equations that describe the operation of an optically injected semiconductor laser may be written in dimensionless form as follows:⁴

$$\dot{E} = (1/2)[G - 1]E + \eta \cos(\psi), \quad (1)$$

$$\dot{\psi} = \Omega - \alpha N - \eta E^{-1} \sin(\psi), \quad (2)$$

$$T\dot{N} = P - N - PGE^2, \quad (3)$$

where, $G = (1 + 2N)/[1 + Y(E^2 - 1)]$. In Eqs. (1)–(3), $E(t)$ is the amplitude of the slave laser electric field, $\psi(t)$ is the phase difference between the master and slave laser electric

fields, $N(t)$ is the excess carrier density, α is the linewidth enhancement factor, η is proportional to the amplitude of the externally injected field, $\Omega = \omega_m - \omega_s$ is the angular frequency detuning between the master and slave lasers, $T = \tau_s/\tau_p$ is equal to the ratio of the carrier (τ_s) to the photon lifetime (τ_p), $P \sim (J/J_{th}) - 1$ is proportional to the pumping above threshold, Y denotes the nonlinear gain saturation, and the time t is normalized to τ_p . E and N are normalized with respect to their steady-state values.

Figure 1 shows numerical bifurcation diagrams for the maxima of the electric field amplitude E as a function of the injection level η , for different values of the linewidth enhancement factor α . Initially, the slave laser is stably injection locked to the external signal ($E = 1$). When the injection strength increases beyond a critical value (η_{Hopf}) the system undergoes a Hopf bifurcation into a periodic regime where the damping of the relaxation oscillations vanishes. In this regime of unstable locking⁵ the slave laser exhibits self-sustained oscillations at a bifurcation frequency which is close to its free-running relaxation oscillation frequency.

For the experimental measurement of the optical spectrum we used two temperature and current stabilized AlGaAs channel substrate planar (CSP) index-guided semiconductor lasers (Hitachi HLP-1400) emitting at 830 nm. The experimental setup is described in Ref. 6. The free-running relaxation oscillation frequency is $f_r = \omega_r/2\pi \approx 4.3$ GHz, corresponding to a pumping level of 60% above threshold. Figure 2 illustrates experimentally measured and numerically calculated optical spectra of the slave laser in the injection-locking region, for zero frequency detuning and increasing levels of injection. Figure 2(a) shows the transition from stable, in (i), to unstable injection locking, in (ii), and the subsequent suppression of the optical carrier (center line), in (iii). At this stage, most of the power is concentrated near the first-order sidebands that appear at the laser relaxation oscillation frequency. Further increase of the injection strength leads to the coherence collapse of the laser emission,

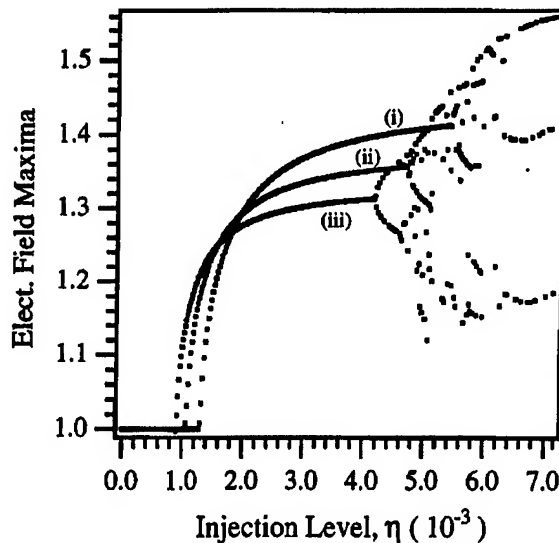


FIG. 1. Numerical bifurcation diagrams of the maxima of the electric field amplitude E vs the injection strength η . The values of the laser parameters appearing in Eqs. (1)–(3) are $\Delta=0$, $P=2.276$, $T=1740$ and $Y=3 \times 10^{-3}$. The value of the linewidth enhancement factor is varied from (i) $\alpha=5$, to (ii) $\alpha=6$, to (iii) $\alpha=7$. The deviation from the steady state, $E-1$, saturates at approximately j_0/α , where $j_0 \approx 2.405$ is the first zero of the Bessel function $J_0(x)$.

through a sequence of period-doubling bifurcations,⁷ as shown in Fig. 1.

The theoretical study that follows aims to explain the experimentally observed laser response and determine the dominant factor that induces it. The solution of the linearized problem⁸ motivates us to rescale the electric field amplitude as $b=(E-1)\alpha$, the carrier density as $n=N\alpha\omega_r^{-1}$, and time as $s=\omega_r t$, where $\omega_r=\sqrt{2P/T}$ represents the free-running relaxation oscillation frequency of the slave laser. The rescaling for the electric field amplitude is also motivated by our numerical results, shown in Fig. 1, which suggest that the deviation from the steady-state, $E-1$, saturates at a constant $O(1/\alpha)$ amplitude. Similarly, we have observed numerically that $N \sim O(T^{-1/2})$. After introducing these new variables in the rate equations (1)–(3), we keep the leading-order contributions in α , eliminate b and n from the resulting expressions, and we obtain a third-order nonlinear differential equation for the phase ψ :

$$\psi''' + \xi\psi'' + \psi' = \Delta + \Lambda \cos \psi, \quad (4)$$

where, $\Delta = \Omega/\omega_r$ is the normalized frequency detuning, $\Lambda = \eta\alpha/\omega_r$ is proportional to the level of injection, $\xi = \omega_r[(1+2P)/2P] + Y/\omega_r$, represents the damping rate of the laser relaxation oscillations, and prime denotes differentiation with respect to time s .

The phase equation (4) represents a major simplification over the rate equations (1)–(3). It retains the original order of the system and corrects the first-order Adler equation, which is frequently used to describe injection-locked lasers.⁹ The laser parameters are grouped into three new coefficients Δ , Λ , and ξ , with Δ and Λ directly controlled experimentally. An important feature of the phase equation is that, by employing multiple time-scale perturbation methods,¹⁰ we may determine approximate analytical solutions which are useful

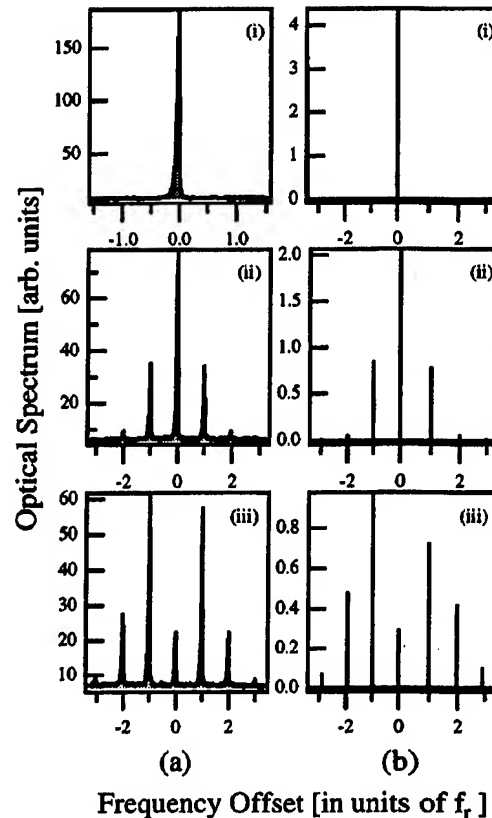


FIG. 2. (a) Experimental measurements of the optical spectrum of the slave laser for zero frequency detuning and increasing levels of injection. (i) Stable injection locking ($A=0$). (ii) Unstable injection locking after the onset of the Hopf bifurcation ($A \leq 1$). (iii) Carrier suppression ($A \approx 2.405$). A is defined in Eq. (5). The frequency axis is given in units of the RO frequency $f_r = \omega_r/2\pi$. (b) Corresponding numerical calculations of the slave laser spectrum, for $\Delta=0$, $P=2.276$, $T=1740$, $Y=3 \times 10^{-3}$, and $\alpha=5$. (i) $\eta=1.0 \times 10^{-3}$, (ii) $\eta=1.67 \times 10^{-3}$, (iii) $\eta=5.37 \times 10^{-3}$.

for comparison with the experimental measurements. Such techniques use power-series expansions of the solution ψ and the system variables in terms of a small expansion parameter which, for the current analysis, is chosen equal to Λ . The authors have recently demonstrated in Ref. 6 that, under conditions of weak injection ($\Lambda < 1$), the phase equation indeed accurately describes the response of the slave laser in the phase-drift (nonlocking) region, ($|\Delta| > \Lambda$).

In the injection-locking region, ($|\Delta| < \Lambda$), the leading order approximation to the optical phase is given by

$$\psi = A \sin(s) + B + O(\Lambda), \quad (5)$$

where the variables A and B are functions of a *slow* time variable $\tau = \Lambda s$, and may be determined by applying the appropriate solvability conditions to the higher order, $O(\Lambda)$, problem obtained from Eq. (4). Physically, $A(\tau)$ represents the magnitude of the undamped laser relaxation oscillations: $A=0$ and $A \neq 0$ correspond to stable and dynamically unstable injection locking, respectively. At steady-state ($\dot{A} = \dot{B} = 0$), for nonzero A , $\xi \sim O(\Lambda)$, and for small values of the frequency detuning, [$\Delta \sim O(\Lambda^2)$], we find two solutions given by the implicit expressions

$$B = \pm \pi/2 \quad \text{and} \quad \Lambda = \pm \xi A/2J_1(A) > 0, \quad (6)$$

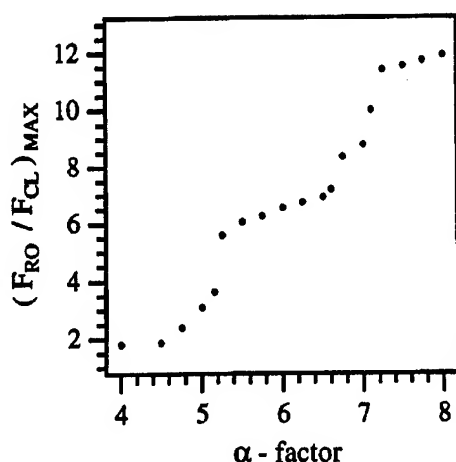


FIG. 3. Variation of the maximum carrier suppression, $(F_{RO}/F_{CL})_{MAX}$, as a function of the linewidth enhancement factor α , for $\Delta=0$, $P=2.276$, $T=1740$, and $Y=3 \times 10^{-3}$.

$$J_0(A)=0 \quad \text{and} \quad \Lambda=\xi A/2J_1(A)\sin B>0. \quad (7)$$

The relevance of solutions (5), (6), and (7) to the experimental measurements and numerical results becomes apparent if we compute analytically the optical spectrum of the injected laser, which is given by $|\int_{-\infty}^{\infty} e^{-i\Delta s + iA \sin(s)} e^{-i\omega s} ds|^2$. The zeroth-order approximations to the magnitudes of the center line frequency component (carrier) and the undamped relaxation oscillation sidebands are given by

$$\text{carrier: } F_{CL}(\omega)=J_0^2(A), \quad (8)$$

$$\text{RO sideband: } F_{RO}(\omega)=J_1^2(A). \quad (9)$$

Condition (6) describes the phase evolution close to the Hopf bifurcation point, near the onset of the instability ($A \ll 1$). In the limit of $A \rightarrow 0$ we obtain $\eta_{\text{Hopf}} = \xi\omega_r/\alpha$ which agrees with the large- α expression of the exact Hopf bifurcation point.⁸ Most of the power of the laser is concentrated near the centerline, as is illustrated in Figs. 2(a) (ii) and 2(b) (ii).

Condition (7) applies to the experimental situation depicted in Fig. 2(a) (iii), for increased levels of injection. Solution (7) emerges from solution (6) through a pitchfork bifurcation, as described in detail in Ref. 10. The value of the phase modulation index ($A \approx 2.405$) results in the suppression of the optical carrier component, $J_0(A)=0$, and most of the laser power is concentrated near the relaxation oscillation sidebands [$\sim J_1^2(A)$]. If we include higher-order, $O(1/\alpha)$, correction terms in both the phase and amplitude of the electric field, we find that the ratio $F_{RO}/F_{CL} \sim O(\alpha^2)$, and therefore increases for larger values of the linewidth enhancement factor. Figure 3 plots the ratio F_{RO}/F_{CL} , which is a measure of the carrier suppression, as a function of α . There is clear evidence of enhanced suppression as the α -factor increases. The rate equations (1)–(3) were numerically integrated and the optical spectra were calculated just before the onset of the period-doubling bifurcation, thus corresponding to the point of maximum suppression of the optical carrier. The response of the injected laser in Figs. 2(a) (iii) and 2(b) (iii) bears remarkable resemblance to the behavior of directly

modulated semiconductor lasers, under driving conditions that lead to corresponding values for the phase modulation index.¹¹

Our theoretical analysis leads to some interesting observations regarding the response of the injection-locked semiconductor laser. Due to the strong phase-amplitude coupling, i.e., large value of α , the optical phase contains all the information necessary for the description of the essential behavior of the system. The theoretical analysis also captures the effect of the nonlinear gain saturation, Y , on the system response. Specifically, it affects the modulation response of semiconductor lasers by increasing the damping rate of the relaxation oscillations.¹² Our investigation indeed reveals that it tends to suppress the occurrence of the instabilities by delaying the onset of the Hopf bifurcation, $\eta_{\text{Hopf}} = \xi\omega_r/\alpha = Y/\alpha + (1+2P)/\alpha T$, where the damping rate ξ is proportional to Y as $\xi = \omega_r[(1+2P)/2P] + Y/\omega_r$.

In summary, we proposed an all-optical configuration for double-sideband suppressed-carrier modulation of an injection-locked semiconductor laser. DSB-SC modulation of optical fields, which traditionally has been performed by coupling the laser output to an external modulator (such as a Mach-Zehnder electro-optic phase modulator³), is of primary importance in signal distribution systems. The absence of a strong carrier component allows us to amplify the information-carrying sidebands immediately following the modulation and hence preserve the high signal-to-noise ratio throughout the system. In addition, our theoretical analysis complements the experimental investigation. Over the past several years, various studies have demonstrated the effect of phase-amplitude coupling on the locking properties of semiconductor lasers.² The current investigation adds to the previous work by illustrating explicitly that the injection-induced modulation of the optical phase essentially prescribes the dynamical response of the locked laser.

The work of L.F.L. was supported by the Optoelectronics Research Grant No. AFOSR-F49620-96-1-0079.

¹R. Lang, IEEE J. Quantum Electron. **18**, 976 (1982).

²*Coherence, Amplification and Quantum Effects in Semiconductor Lasers*, edited by Y. Yamamoto (Wiley-Interscience, New York, 1991), and references therein.

³R. Montgomery and R. DeSalvo, IEEE Photonics Technol. Lett. **7**, 434 (1995).

⁴P. M. Alsing, V. Kovanis, A. Gavrielides, and T. Erneux, Phys. Rev. A **53**, 4429 (1996).

⁵I. Petitbon, P. Gallion, G. Debarge, and C. Chabran, IEEE J. Quantum Electron. **24**, 148 (1988).

⁶P. M. Varangis, A. Gavrielides, T. Erneux, V. Kovanis, and L. F. Lester, Phys. Rev. Lett. **78**, 2353 (1997).

⁷T. B. Simpson, J. M. Liu, A. Gavrielides, V. Kovanis, and P. M. Alsing, Appl. Phys. Lett. **64**, 3539 (1994); J. Sacher, D. Baums, P. Panknin, W. Elsässer, and E. O. Göbel, Phys. Rev. A **45**, 1893 (1992).

⁸T. Erneux, V. Kovanis, A. Gavrielides, and P. M. Alsing, Phys. Rev. A **53**, 4372 (1996).

⁹W. A. van der Graaf, A. M. Levine, and D. Lenstra, IEEE J. Quantum Electron. **33**, 434 (1997).

¹⁰A. Gavrielides, V. Kovanis, P. M. Varangis, T. Erneux, and G. Lythe, Quantum Semiclass. Opt. **9**, 785 (1997).

¹¹S. Kobayashi and T. Kimura, IEEE J. Quantum Electron. **18**, 582 (1982).

¹²G. P. Agrawal, J. Appl. Phys. **63**, 1232 (1988).

150-nm Tuning Range in a Grating-Coupled External Cavity Quantum-Dot Laser

H. Li, G. T. Liu, P. M. Varangis, T. C. Newell, A. Stintz, B. Fuchs, K. J. Malloy, and L. F. Lester

Abstract—An antireflection (AR) coated single-stack quantum-dot (QD) laser in a grating-coupled external cavity is shown to operate across a tuning range from 1.095 μm to 1.245 μm . This 150-nm range extends from the energy levels of the ground state to excited states. At any wavelength, the threshold current density is no greater than 1.1 kA/cm^2 . This large tunable range is the product of the rapid carrier filling of the higher energy states under a low pumping current and homogeneous broadening in the QD ensemble. The possibility of a larger tuning range is discussed with the further improvement of the AR-coating.

Index Terms—Quantum-dot lasers, semiconductor lasers, tunable lasers.

I. INTRODUCTION

TUNABLE lasers have many important applications in spectroscopy, optical communications such as wavelength-division multiplexing (WDM), and the fundamental study of the interaction between matter and photons. Semiconductor quantum-well (QW) lasers in a grating-coupled external cavity are widely used for their continuous tunability that is free of mode-hops and limited by the gain spectral width of the QW active medium [1]. When a very high pump level (normally greater than 10 kA/cm^2) is injected into a MQW laser, the $n = 2$ state can be populated, which makes the tuning range dramatically larger [2]–[6]. A tuning range of 240 nm around 1.5 μm (15.7% of the lasing wavelength) was reported with a pump level of 33 kA/cm^2 [5]. However, the necessarily high pump level restricts this broadband tunability for real applications. When an advanced QW engineering technique was used to grow uncoupled QW's with different well thicknesses, called the asymmetric multiple-quantum-well (AMQW), the tuning range was enlarged to ~ 90 nm at 950 nm [7] and at 1.5 μm [8]. The corresponding pump level was at a realistic level of ~ 2 kA/cm^2 and only the $n = 1$ state was populated. By increasing the pump level beyond 15 kA/cm^2 , the $n = 2$ state of AMQW started to be filled, and the tuning range was increased further to more than 100 nm [9], [10].

In contrast to QW lasers, the ground state of quantum dots (QD's) rapidly saturates for increasing pump levels. As a result, the excited states of QD lasers can be filled at a fairly low pump current density (~ 1 – 2 kA/cm^2), which produces a very wide spontaneous emission spectrum [11]. Thus an

Manuscript received January 19, 2000; revised March 20, 2000. This work was supported by the Defense Advanced Research Projects Agency under Grant MDA972-98-1-0002 and by the U.S. Air Force Office of Scientific Research under Grant F49620-96-1-0077.

The authors are with the Center for High Technology Materials, University of New Mexico, Albuquerque, NM 87106 USA.

Publisher Item Identifier S 1041-1135(00)05601-9.

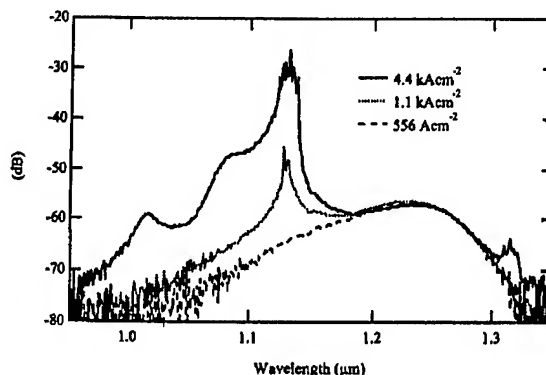


Fig. 1. Electroluminescence spectrum of the AR-coated DWELL laser for different pump levels.

excellent opportunity exists to obtain a very broad tuning range from QD lasers with low current densities. Furthermore, tuning throughout the energy gap between the ground state and the excited states is feasible due to the presence of homogeneous gain broadening [12], [13].

In this letter, a grating-coupled external cavity laser with a 150-nm tunable range is presented. For this arrangement, the threshold current density required for lasing is no greater than 1.1 kA/cm^2 . The quantum-dot active region employed has already demonstrated high performance [11], [14]. Among other characteristics, a room temperature J_{th} of 26 A/cm^2 [15] and a 0.1 linewidth enhancement factor [16] have been measured. These results suggest that numerous opportunities exist to use QD lasers as tunable coherent light sources.

The structure of the dots-in-a-well (DWELL) laser used in this experiment is described in detail in [11]. The structure contains one InAs QD layer incorporated into an $\text{In}_{0.2}\text{Ga}_{0.8}\text{As}$ 10-nm thick QW and is sandwiched by GaAs waveguide layers. The in-plane density of QD's is $7.5 \times 10^{10} \text{ cm}^{-2}$. The laser has a ridge waveguide structure with a width of 9 μm and a cavity length of 2.0 mm. It is mounted epitaxial-side up on a heatsink that is stabilized at a temperature of 20 $^{\circ}\text{C}$. The threshold current J_{th} for ground state lasing is $I = 35$ mA without any antireflection (AR)-coating. From this data, $J_{\text{th}} = 194 \text{ A}/\text{cm}^2$. A single $\lambda/4$ HfO_2 layer designed for minimum reflectivity at 1.24 μm was deposited on one facet. From the difference in slope efficiencies between the two mirrors, a residual reflectivity of approximately 1.6% is determined. This low reflectivity increases the total cavity loss. Thus, the ground state lasing of the solitary laser is completely extinguished.

The emission spectra of the solitary device under different pump levels is shown in Fig. 1. Light is coupled into an Anritsu MS9001A optical spectral analyzer using a multimode fiber. The resolution of the system was 0.5 nm. With a bias as low

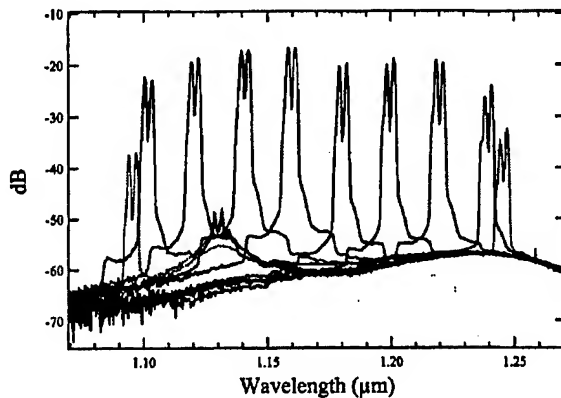


Fig. 2. Lasing spectra of the grating-coupled external cavity DWELL laser. When rotating the diffraction grating, the lasing wavelength is tuned across the wavelength range of 1.095–1.245 μm .

as 200 mA (1.1 kA/cm^2), the ground state at $1.24 \mu\text{m}$ is already well saturated and the first excited state is significantly populated. Since the AR-coating is not especially low, the device begins lasing under this pump level at the first excited state around $1.14 \mu\text{m}$. The spectrum covered is from 1.1 to $1.25 \mu\text{m}$. Upon increase of the pump level to 800 mA (4.4 kA/cm^2), the second excited state starts filling at $1.07 \mu\text{m}$, accompanied by obvious carrier filling of the lowest energy QW state at $1.0 \mu\text{m}$. This spectrum spans a wavelength range of more than 200 nm.

A Littrow external cavity configuration [17] that includes a collimator and a diffraction grating was subsequently constructed. Tuning was achieved by rotating the grating to select a certain wavelength emission to be reflected back to the laser. The laser was operated in pulsed mode with a pulse width of 500 ns and a duty cycle of 2%. The distance between the laser and the grating was about 25 cm, corresponding to a photon round trip time of $\sim 1.7 \text{ ns}$. The large ratio of pulsewidth time to photon lifetime means that the dynamics, which occur due to the interaction between the initial rise of the pulse and the incoming reflected field, can be neglected. Hence, pulsed operation is essentially identical to CW.

Fig. 2 shows the actual tuning range achieved in our experiment by rotating the grating. At each step the spectrum is measured by an optical spectrum analyzer. Across most of the 150-nm range, the lasing peak in the spectrum is higher than the amplified spontaneous emission level by at least 25–30 dB. The lasing linewidth is less than 3 nm. Its measurement is limited by the resolution of the detection system. A narrower linewidth could be obtained by using a Littman–Metcalf configuration [18] for the external cavity and by fabricating a narrower ridge waveguide laser. Significantly, no failure of lasing occurs across the energy gap between the ground and the first excited state. This is, as expected, due to homogenous gain broadening. It is possible that the double peaks appearing in the lasing spectrum are due to the spatial modes of the laser. However, it cannot yet be ruled out that the twin peaks are evidence of inhomogeneous broadening, similar to what has been observed in [13] for the free-running broadband emission in QD lasers at room temperature. The two traces (plotted as dotted lines) at the low and high ends of the spectrum shown in Fig. 2 portray the minimum and maximum tunable wavelengths. Also evident in the figure are small emission peaks from the excited

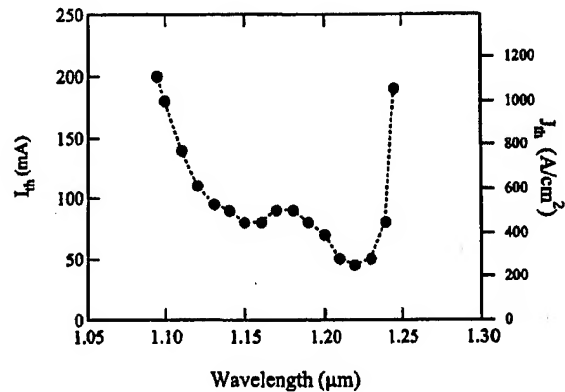


Fig. 3. Threshold current of the grating-coupled external cavity DWELL laser as a function of the lasing wavelength.

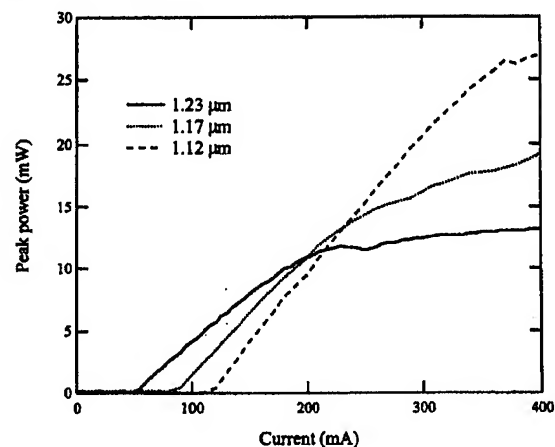


Fig. 4. Peak pulse power versus current for lasing at $1.23 \mu\text{m}$ (solid line), $1.17 \mu\text{m}$ (dotted line), and $1.12 \mu\text{m}$ (dashed line).

state energy level at $1.13 \mu\text{m}$. These peaks arise when the laser is tuned at the extremes where the pumping is large. The combination of the residual reflectivity of the laser facet and excited state gain combine to produce a measurable amount of emission at this wavelength.

Fig. 3 shows the threshold current of the tunable external cavity DWELL laser as a function of the tuning wavelength. With no more than 200-mA bias (1.1 kA/cm^2) we are able to tune across 150 nm. At $1.18 \mu\text{m}$, which is about halfway in the energy gap between the ground and first excited states, the threshold current increases only slightly. The lowest threshold current for the ground state is $\sim 45 \text{ mA}$, which is higher than the original uncoated laser threshold. This increase is due to the fact that only about 10% of the power is reflected back into the device. Consequently, the total loss is larger than that of the original uncoated laser. An increase of the external cavity feedback to a realistic 30% would decrease the threshold current and extend the tuning range further.

Fig. 4 shows light versus current ($L-I$) curves measured from the uncoated facet of the device at different wavelengths. The solid curve is for $\lambda = 1.23 \mu\text{m}$ in the ground state. The dotted curve is measured for $\lambda = 1.17 \mu\text{m}$ in the gap between the ground and the first excited states. The dashed curve is for $\lambda = 1.12 \mu\text{m}$ at the short-wavelength shoulder of the first excited state. The peak power at $\sim 200 \text{ mA}$ is about $\sim 10 \text{ mW}$ for all three wavelengths, and the slope efficiency is approximately 0.1 W/A .

Above 200 mA the slope efficiency decreases at $\lambda = 1.23 \mu\text{m}$ and $\lambda = 1.17 \mu\text{m}$ mainly because of the strong carrier filling at the first excited state under this pump level. A decrease in the reflectivity of the AR-coating will partially improve the slope efficiency and increase the linear range in the L - I curve. However, around the center wavelength of the first excited state, the slope efficiency remains constant for increasing pump level, as the dashed curve shows in Fig. 4. At the edge of the tuning range near $1.24 \mu\text{m}$ and $1.10 \mu\text{m}$, a slope efficiency of 0.041 W/A and 0.066 W/A is measured, respectively, and a useful output power in the milliwatt range is still obtained.

The tuning range and lasing behavior could be improved by decreasing the reflectivity of the AR-coating and modifying the external cavity design. From Fig. 1, the Fabry-Perot laser without external grating lases at a low pump current of $\sim 200 \text{ mA}$. This device feature inhibits carrier filling of the higher energy states, therefore hindering the tuning range on the short wavelength side. If the residual reflectivity of the AR-coating at the first excited state were 5×10^{-4} , (which is a reasonable requirement for a laser diode used in commercial external-cavity lasers), the original laser cavity would not reach threshold until $\sim 450 \text{ mA}$ [11]. This situation would extend the tuning range to cover the second excited state and make a total tuning range of 200 nm possible. This figure represents a 17% tuning capability.

To extend the tuning range to longer wavelengths is not trivial since increasing the pump does not increase the gain very much at the wavelength longer than the center wavelength of the ground state. Only a reduction in the total cavity loss or a longer gain region can extend the tuning range on the long wavelength side. However, decreasing the cavity loss will put a more stringent requirement on the AR-coating to prohibit the internal Fabry-Perot modes from lasing. For the QD lasers presented here, we refer to suppression of the first excited states. From Fig. 1, we can estimate roughly that the extension to longer wavelengths is limited to several nanometers. Thus, efforts to enlarge the tuning range should be directed toward the short wavelength side.

The large tuning range of this type of laser does present new challenges. First, the threshold current across the tuning range is not constant and so the output power will fluctuate at constant current bias as the spectrum is scanned. It may be necessary to design a servo-loop to control the pump current to ensure good lasing behavior and a constant output power across the whole tuning range. Second, the ultrabroad-band spontaneous emission degrades the signal-to-noise (S/N) ratio of the laser output. Therefore, a tunable filter whose center wavelength is synchronized with the lasing wavelength would be important for certain applications. Another choice is to use a grating ring laser cavity, and to take the output power from the grating reflection beam [9]. In this way a low noise laser can be obtained.

One current effort in QD laser engineering is to reduce the fluctuation of the dot size by carefully controlling the wafer growth, thus narrowing the inhomogeneous gain broadening. This approach is crucial to achieve very low threshold currents. However, a reasonable distribution of the QD sizes may help smooth the tuning across the gaps between the discrete QD energy states. As a result, QD crystal growth should be optimized for different applications.

In conclusion, a continuous tuning range of 150 nm centered at $1.17 \mu\text{m}$ was achieved with an AR-coated DWELL laser inserted into a grating-coupled external cavity under a pump level of 1.1 kA/cm^2 . Further extension of the tuning range is possible by improving the AR-coating and careful design of the external cavity. Based on the realistic estimate of a 17% tuning capability and further progress in the development of long-wavelength QD lasers, it is anticipated that a single tunable QD external cavity laser could cover the entire wavelength range of the fiber-optic communication band from 1.3 to $1.55 \mu\text{m}$.

REFERENCES

- [1] P. S. Zory, Jr., *Quantum Well Lasers*, P. S. Zory, Jr., Ed. Boston, MA: Academic, 1993.
- [2] D. Mehuys, M. Mittelstein, A. Yariv, R. Sarfaty, and J. E. Ungar, "Optimized Fabry-Perot (AlGa) As quantum-well lasers tunable over 105 nm ," *Electron. Lett.*, vol. 25, pp. 143-145, 1989.
- [3] D. C. Hall, J. S. Major, Jr., and N. Holonyak, Jr., "Broadband long-wavelength operation ($9700 \text{ \AA} \leq 8700 \text{ \AA}$) of $\text{Al}_{1-y}\text{Ga}_y\text{As-GaAs-In}_x\text{Ga}_{1-x}\text{As}$ quantum well heterostructure lasers in an external grating cavity," *Appl. Phys. Lett.*, vol. 55, pp. 752-754, 1989.
- [4] A. Lidgard, T. Tanbun-Ek, R. A. Logan, H. Temkin, K. W. Wecht, and N. A. Olsson, "External-cavity InGaAs/InP graded index multiquantum well laser with a 200 nm tuning range," *Appl. Phys. Lett.*, vol. 56, pp. 816-817, 1990.
- [5] H. Tabucho and H. Ishikawa, "External grating tunable MQW laser with wide tuning range of 240 nm ," *Electron. Lett.*, vol. 26, pp. 742-743, 1990.
- [6] C. P. Seltzer, M. Bagley, D. J. Elton, S. Perrin, and D. M. Cooper, "160 nm continuous tuning of an MQW laser in an external cavity across the entire $1.3 \mu\text{m}$ communication window," *Electron. Lett.*, vol. 27, pp. 95-96, 1991.
- [7] H. S. Gingrich, D. R. Chumney, S.-Z. Sun, S. D. Hersee, L. F. Lester, and S. R. J. Brueck, "Broadly tunable external cavity laser diodes with staggered thickness multiple quantum wells," *IEEE Photon. Technol. Lett.*, vol. 9, pp. 155-157, 1997.
- [8] M. J. Hamp, D. T. Cassidy, B. J. Robinson, Q. C. Zhao, D. A. Thompson, and M. Davies, "Effect of barrier height on the uneven carrier distribution in asymmetric multiple-quantum-well InGaAsP lasers," *IEEE Photon. Technol. Lett.*, vol. 10, pp. 1380-1382, 1998.
- [9] B.-L. Lee and C.-F. Lin, "Wide-range tunable semiconductor lasers using asymmetric dual quantum wells," *IEEE Photon. Technol. Lett.*, vol. 10, pp. 322-324, 1998.
- [10] X. Zhu, D. T. Cassidy, M. J. Hamp, D. A. Thompson, B. J. Robinson, Q. C. Zhao, and M. Davies, "1.4- μm InGaAsP-InP strained multiple-quantum-well laser for broad-wavelength tunability," *IEEE Photon. Technol. Lett.*, vol. 9, pp. 1202-1204, 1997.
- [11] L. F. Lester, A. Stintz, H. Li, T. C. Newell, E. A. Pease, B. A. Fuchs, and K. J. Malloy, "Optical properties of $1.24 \mu\text{m}$ quantum dot lasers," *IEEE Photon. Technol. Lett.*, vol. 11, pp. 931-933, 1999.
- [12] P. Borri, W. Langbein, J. Mork, J. M. Hvam, F. Heinrichsdorff, M.-H. Mao, and D. Bimberg, "Dephasing in InAs/GaAs quantum dots," *Phys. Rev. B*, vol. 60, pp. 7784-7787, 1999.
- [13] P. Eliseev, H. Li, A. Stintz, G. T. Liu, T. C. Newell, K. J. Malloy, and L. F. Lester, "Tunable grating-coupled laser oscillation and spectral hole burning in an InAs quantum-dot laser diode," *IEEE J. Quant. Electron.*, vol. 36, pp. 479-485, Apr. 2000.
- [14] X. Huang, A. Stintz, C. P. Hains, J. Cheng, and K. J. Malloy, "Efficient high-temperature CW lasing operation of oxide-confined long-wavelength InAs quantum dot lasers with low threshold current density," *Electron. Lett.*, vol. 36, 2000.
- [15] G. T. Liu, A. Stintz, H. Li, K. J. Malloy, and L. F. Lester, "Extremely low room temperature threshold current density diode lasers using InAs dots in an $\text{In}_{0.18}\text{Ga}_{0.82}\text{As}$ quantum well," *Electron. Lett.*, vol. 35, pp. 1163-1165, 1999.
- [16] T. C. Newell, D. Bossert, A. Stintz, B. Fuchs, K. J. Malloy, and L. F. Lester, "Gain and linewidth enhancement factor in InAs quantum dot laser diodes," *IEEE Photon. Technol. Lett.*, vol. 11, pp. 1527-1529, Dec. 1999.
- [17] P. W. Milonni and J. H. Eberly, *Lasers*. New York: Wiley, 1988.
- [18] M. G. Littman and H. J. Metcalf, "Spectrally narrow pulsed dye-laser without beam expander," *Appl. Opt.*, vol. 17, pp. 2224-2227, 1978.

1.58- μm Lattice-Matched and Strained Digital Alloy AlGaInAs-InP Multiple-Quantum-Well Lasers

G. T. Liu, A. Stintz, E. A. Pease, T. C. Newell, K. J. Malloy, and L. F. Lester

Abstract—A versatile, digital-alloy molecular beam epitaxy (MBE) technique is employed to grow lattice-matched and strained AlGaInAs multiple-quantum well (MQW) 1.58- μm laser diodes on InP. A threshold current density as low as 510 A/cm² has been demonstrated for broad area lasers with 1% strained AlGaInAs MQW's, which is the best MBE result in this material system. A single facet pulsed power as high as 0.56 W is obtained. It is also found that the efficiency and internal loss of digital alloy AlGaInAs QW devices are comparable to lasers grown by conventional MBE.

Index Terms—AlGaInAs lasers, digital alloys, semiconductor quantum wells.

I. INTRODUCTION

THE DIGITAL alloy, a superlattice with a period width on the order of 10 Å, has been employed in molecular beam epitaxy (MBE) for growing light emitters [1], [2], graded structures [3], and distributed Bragg reflector (DBR) mirrors [4]–[6]. By toggling between two compositions and changing their relative thicknesses, the digital alloy technique circumvents the problem with growing graded structures in conventional MBE, i.e., the inability to change the effusion cell flux rapidly and reproducibly. Digital alloying also reduces the complexity associated with growing quaternary materials [7], including problems with abrupt changes in composition, compositional grading, and the need for multiple identical group-III effusion cells. A potential drawback of digital alloying, however, is the introduction of many heterojunction interfaces that can getter impurities and enhance nonradiative recombination.

Previously, the digital alloy technique has been used to grow GaInAs asymmetric triangular QW laser structures [1] and AlGaInAs broad-band light-emitting diodes [2]. In this letter, the digital alloy process is used in MBE-grown 1.58- μm AlGaInAs lattice matched and strained 4-QW laser diodes. By rapidly switching between the ternaries of AlInAs and GaInAs, the digital alloy process enables the growth of all the quaternary AlGaInAs compositions. Previous 1.5- μm AlGaInAs–GaInAs–InP lasers with strained quantum wells have been grown by both conventional MBE techniques [8], [9] and metal–organic chemical vapor deposition (MOCVD) techniques [10]–[12]. It will be shown that digital alloy MBE lasers have similar threshold current density, efficiency, and internal losses to conventional MBE devices. It is inferred from

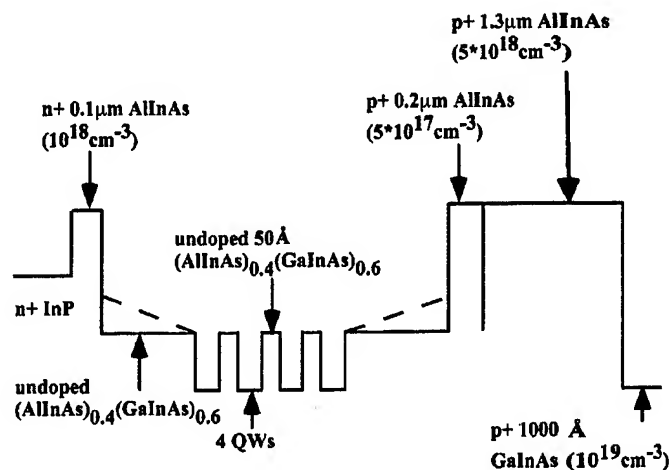


Fig. 1. The epitaxial layer design for the SCH and GRINSCH lasers.

these results that the multiple interfaces in the digital alloy AlGaInAs QW's, barriers, and waveguide do not degrade laser performance. A threshold current density, J_{th} , of 510 A/cm² is achieved which is the lowest MBE result for this material system at 1.5 μm to the best of our knowledge. Single-facet pulsed output power as high as 0.56 W is obtained under 3 A of injection current.

II. MATERIALS AND FABRICATION

Three different laser structures were grown on n-type, sulfur doped, epi-ready InP wafers with a (100) orientation. During growth, the surface oxide was desorbed under an arsenic flux at $\sim 520^\circ\text{C}$. The substrate was heated radiatively, and a constant substrate growth temperature was maintained throughout the growth. Silicon and beryllium were used for n- and p-type doping, respectively. The structures were grown without interruption. An optimum growth temperature of 510°C was determined from a photoluminescence (PL) study of a test structure with four 95-Å lattice-matched GaInAs wells and three 50-Å AlGaInAs barriers sandwiched between two 1000 Å $(\text{Al}_{0.48}\text{In}_{0.52}\text{As})_{0.4}(\text{Ga}_{0.47}\text{In}_{0.53}\text{As})_{0.6}$ layers. Temperatures from 470°C to 550°C were examined and 510°C resulted in samples with the strongest PL.

A conduction band diagram of the shared layers between each laser is shown in Fig. 1. The first laser has four 95-Å lattice-matched GaInAs wells contained within an AlGaInAs–AlInAs separate confinement heterostructure (SCH). The second laser also has four 95-Å lattice-matched GaInAs wells but with a graded index SCH (GRINSCH). The grading is from $(\text{Al}_{0.48}\text{In}_{0.52}\text{As})_{0.4}(\text{Ga}_{0.47}\text{In}_{0.53}\text{As})_{0.6}$ adjacent to the wells to $(\text{Al}_{0.48}\text{In}_{0.52}\text{As})_{0.6}(\text{Ga}_{0.47}\text{In}_{0.53}\text{As})_{0.4}$ next to the

Manuscript received July 8, 1999; revised September 29, 1999. This work was supported by the Air Force Office of Scientific Research under Grant F49620-96-1-0079 and by the Army Federated Laboratories.

The authors are with the University of New Mexico, Center for High Technology Materials, Albuquerque, NM 87106 USA.

Publisher Item Identifier S 1041-1135(00)00328-1.

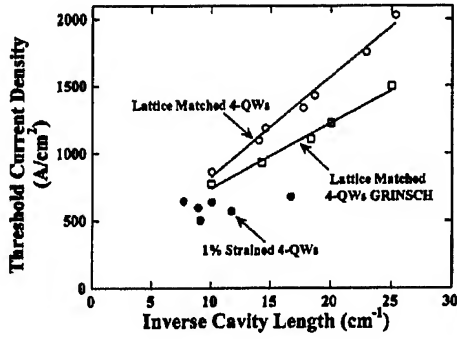


Fig. 2. The threshold current density as a function of the inverse cavity length for the lattice-matched and strained QW lasers.

cladding. The third laser is the same as the first one except the wells are 100-Å 1% strained quaternary $\text{Al}_{0.08}\text{Ga}_{0.25}\text{In}_{0.67}\text{As}$ wells. A broadened waveguide design [13], which minimizes the free carrier absorption loss in the doped cladding layers, is employed for all the lasers. The total waveguide thickness is 1 μm resulting in less than 10% of the optical mode propagating in the cladding layers.

All epitaxial layers except the strained QW's are lattice-matched and the AlGaInAs quaternaries are grown by the digital alloy technique. To achieve barrier and waveguide layers with a composition of $(\text{Al}_{0.48}\text{In}_{0.52}\text{As})_{0.4}(\text{Ga}_{0.47}\text{In}_{0.53}\text{As})_{0.6}$, alternating digital alloy layers of 3.3 Å $\text{Al}_{0.48}\text{In}_{0.52}\text{As}$ and 4.9-Å $\text{Ga}_{0.47}\text{In}_{0.53}\text{As}$ are grown to the desired total thickness. To fabricate the 1% strained quaternary wells, alternating digital alloy layers of 6.1-Å $\text{Al}_{0.17}\text{In}_{0.83}\text{As}$ and 6.2 Å $\text{Ga}_{0.47}\text{In}_{0.53}\text{As}$ are grown to yield equivalent quaternary composition of $\text{Al}_{0.08}\text{Ga}_{0.25}\text{In}_{0.67}\text{As}$. The QW strain is also confirmed by X-ray analysis of the laser wafer. Only the $\text{Al}_{0.17}\text{In}_{0.83}\text{As}$ layers are strained. Based on a previous study of the minimum necessary cladding layer thickness in separate confinement heterostructure lasers [14], a relatively thin thickness of 1.5 μm is used to ease the growth of the AlInAs clad.

III. RESULTS AND DISCUSSION

Ti-Pt-Au and Au-Ni-Au have been used for the p- and n-contacts, respectively. The broad area laser stripe width is 100 μm . After processing, the laser wafers were cleaved into laser bars of various cavity lengths. All devices were tested with n-side down on a thermo-electric cooler at 22 °C under pulsed conditions. The pulsewidth was 300 ns with a duty cycle of 1%. The two lattice-matched MQW lasers displayed consistent power and threshold current results on all lasers bars. The strained MQW lasers, however, had large variations in their data. The AlGaInAs barriers between the highly strained wells may have been too thin causing relaxation. Despite the scatter in the strained MQW results, individual strained lasers demonstrated significantly improved performance compared to the lattice-matched devices. Therefore, only the best results for each cavity length from each wafer are reported below.

J_{th} , as a function of the inverse cavity length of the three lasers, is shown in Fig. 2. For 1-mm cavity length lasers, a J_{th} as low as 860 A/cm^2 has been achieved for the lattice-matched GaInAs MQW SCH lasers. By changing the waveguide to a

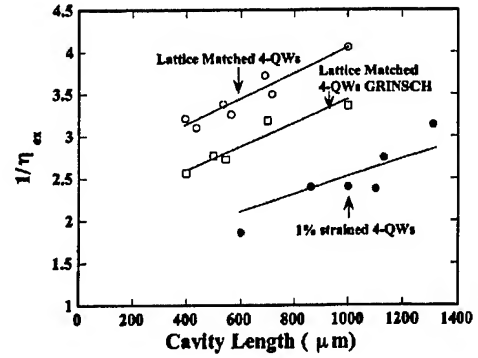


Fig. 3. The inverse external quantum efficiency versus the cavity length.

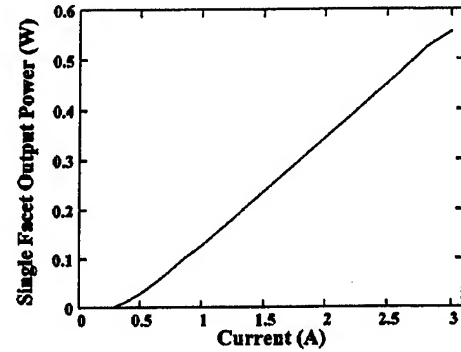


Fig. 4. Pulsed power output of a strained AlGaInAs MQW laser with a 600 μm cavity length.

GRINSCH, the J_{th} is further reduced to 770 A/cm^2 . A threshold current density as low as 510 A/cm^2 has been achieved for the 1% strained AlGaInAs MQW lasers with 1.1-mm cavity length. This J_{th} is the lowest reported for a 1.5- μm MBE-grown AlGaInAs QW semiconductor laser to the best of our knowledge.

The inverse external quantum efficiency, $1/\eta_{\text{ex}}$, versus cavity length, L , results in Fig. 3 are used to calculate the internal loss, α_i , and the internal quantum efficiency, η_i . By fitting the data to the equation $1/\eta_{\text{ex}} = 1/\eta_i(1 - \alpha_i L / \ln(R))$, $\eta_i(\alpha_i)$ values of 40% (7.4 cm^{-1}) and 48.5% (8 cm^{-1}) are found for the GaInAs SCH and GRINSCH lasers, respectively. The reflectivity, R , is assumed to be 0.31. The higher efficiency in the GRINSCH lasers is presumably due to the built-in electric field that funnels carriers toward the wells. The change in $1/\eta_{\text{ex}}$ with L for the strained AlGaInAs MQW lasers is also shown in Fig. 3. Due to the scatter in the data, an internal loss similar to that of the GaInAs SCH lasers must be assumed to get a realistic η_i ($<100\%$). Since the waveguide regions in the first and third laser structures are identical, this is a reasonable supposition. Using a fixed internal loss of 7.4 cm^{-1} to fit the data, we estimate the internal quantum efficiency to be 64.5%. The pulsed power output of a strained QW laser with 600 μm cavity length is shown in Fig. 4. A power as high as 0.56 W is obtained from a single facet at a current of 3 A.

The threshold current densities versus temperature of devices with $L = 1$ mm have also been measured. The testing temperatures are varied from 15 °C to 50 °C. T_0 values of 45, 50, and 55 K are measured for the lasers with lattice-matched MQW's and SCH, lattice-matched MQW's and GRINSCH, and the 1% strained quantum wells, respectively. The results are shown in

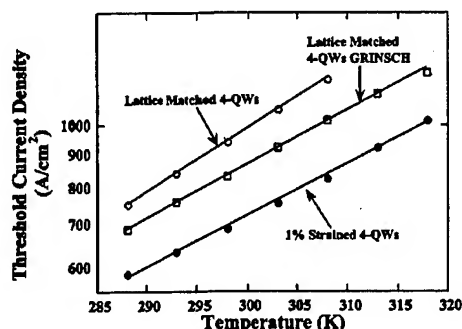


Fig. 5. The variation of the threshold current density with temperature. The data yield characteristic temperatures, T_0 , of 45, 50, and 55 K for the lattice-matched SCH, lattice-matched GRINSCH, and strained lasers, respectively.

Fig. 5. The trend is consistent with the threshold current density results—a lower J_{th} reduces carrier heating, which should increase T_0 [15]. In general, however, much higher T_0 's are desirable for CW operation. One likely reason for the low T_0 's is the relatively shallow QW's that are used. Whereas 300 meV is typical for previously reported conduction band well depths [8], [10], the lasers in this letter has only 200-meV-deep conduction band wells. This design might accentuate carrier heating and may also affect η_i and, thus, J_{th} and the power output. By using a higher barrier, a better T_0 value is anticipated. The GRINSCH and deeper strained quantum wells may also be combined to improve the overall performance of the lasers.

IV. CONCLUSION

Lattice-matched and strained AlGaInAs/InP lasers grown by the digital alloy MBE technique have been reported. The lowest J_{th} and highest power output of MBE-grown AlGaInAs-InP lasers at 1.5 μm have been achieved. It is also found that the efficiency and internal loss of digital alloy AlGaInAs MQW devices are comparable to lasers grown by conventional MBE. The introduction of many heterojunction interfaces by the digital alloy technique does not have an adverse effect on the laser performance. A GRINSCH waveguide has been shown to improve the laser performance. Thicker quantum well barriers or strain-balanced barriers may be needed to eliminate the problems associated with relaxation. By combining the GRINSCH and higher QW barriers, better laser performance is anticipated.

ACKNOWLEDGMENT

The authors would like to thank R. Kaspi and R. Dawson for the enlightening discussions. The views and conclusions con-

tained in this document are those of the authors and should not be interpreted as representing the official policies, either expressed or implied, of the Army Research Laboratory or the U.S. Government.

REFERENCES

- [1] J. G. Cody, D. L. Mathine, R. Droopad, G. N. Maracas, R. Rajesh, and R. W. Carpenter, "Application of the digital alloy composition grading technique to strained InGaAs/GaAs/AlGaAs diode-laser active regions," *J. Vac. Sci. Technol. B*, vol. 12, pp. 1075–1077, 1994.
- [2] I. J. Fritz, M. J. Hafich, J. F. Klem, and S. A. Casalnuovo, "Barrier-width dependence of emission in triple-quantum-well broadband light-emitting diodes," *Electron. Lett.*, vol. 35, pp. 171–172, 1999.
- [3] M. Sundaram, A. Wixforth, R. S. Geels, A. C. Gossard, and J. H. English, "A direct method to produce and measure compositional grading in $\text{InAl}_x\text{Ga}_{1-x}\text{As}$ alloys," *J. Vac. Sci. Technol. B*, vol. 9, pp. 1524–1529, 1991.
- [4] J. D. Walker, K. Malloy, S. Wang, and J. S. Smith, "Precision AlGaAs Bragg reflectors fabricated by phase-locked epitaxy," *Appl. Phys. Lett.*, vol. 56, pp. 2493–2495.
- [5] O. Blum, I. J. Fritz, L. R. Dawson, and T. J. Drummond, "Digital alloy AlAsSb/AlGaAsSb distributed Bragg reflectors lattice-matched to InP for 1.3–1.55- μm wavelength range," *Electron. Lett.*, vol. 31, pp. 1247–1248, 1995.
- [6] M. G. Peters, B. J. Thibeault, D. B. Young, J. W. Scott, F. H. Peters, A. C. Gossard, and L. A. Coldren, "Band-gap engineered digital alloy interfaces for lower resistance vertical-cavity surface-emitting lasers," *Appl. Phys. Lett.*, vol. 63, pp. 3411–3413, 1993.
- [7] I. J. Fritz, L. R. Dawson, J. A. Olsen, and A. J. Howard, "Graded-composition buffer layers using digital AlGaAsSb alloys," *Appl. Phys. Lett.*, vol. 67, pp. 2320–2322, 1995.
- [8] M. J. Mondry, E. J. Tarsa, and L. A. Coldren, "Molecular-beam epitaxial-growth of strained AlGaInAs multi-quantum-well lasers on InP," *J. Electron. Mater.*, vol. 25, pp. 948–954, 1996.
- [9] M. Quillec, M. Allovon, F. Brillouet, A. Gloukhian, J. P. Praseuth, and B. Sermage, "Very low threshold current density GaInAs/AlGaInAs MQW lasers made by phosphorus-free MBE and operating in 1.5–1.6 μm range," *Electron. Lett.*, vol. 25, pp. 1731–1732, 1989.
- [10] A. Kasukawa, R. Bhat, C. E. Zah, M. A. Koza, and T. P. Lee, "Very low threshold current-density 1.5 μm GaInAs/AlGaInAs graded-index separate-confinement-heterostructure strained quantum-well laser-diodes grown by organometallic chemical vapor-deposition," *Appl. Phys. Lett.*, vol. 59, pp. 2486–2488, 1991.
- [11] G. A. Evans, J. P. Sih, T. M. Chou, J. B. Kirk, J. K. Butler, and L. Pang, "AlGaInAs/InP ridge-guide lasers operating at 1.55 μm ," *Proc. SPIE*, vol. 3284, pp. 205–210, 1998.
- [12] C. C. Lin, K. S. Liu, M. C. Wu, and H. P. Shiao, "Highly uniform characteristics 12-element 1.5- μm strain-compensated AlGaInAs/InP laser arrays with low-threshold current and high characteristic temperature," *Electron. Lett.*, vol. 34, pp. 186–187, 1998.
- [13] D. Z. Garbuzov, R. U. Martinelli, H. Lee, P. K. York, R. J. Menna, J. C. Connolly, and S. Y. Narayan, "Ultralow-loss broadened-waveguide high-power 2 μm AlGaAsSb/InGaAsSb/GaSb separate-confinement quantum-well lasers," *Appl. Phys. Lett.*, vol. 69, pp. 2006–2008, 1996.
- [14] A. Behfar-Rad, J. R. Shealy, S. R. Chinn, and S. S. Wong, "Effect of cladding layer thickness on the performance of GaAs-AlGaAs graded index separate confinement heterostructure single quantum-well lasers," *IEEE J. Quantum Electron.*, vol. 26, pp. 1476–1480, 1990.
- [15] L. F. Lester and B. K. Ridley, "Hot carriers and the frequency-response of quantum-well lasers," *J. Appl. Phys.*, vol. 72, pp. 2579–2588, 1992.

Room-Temperature Operation of InAs Quantum-Dash Lasers on InP (001)

R. H. Wang, A. Stintz, P. M. Varangis, T. C. Newell, H. Li, K. J. Malloy, and L. F. Lester

Abstract—The first self-assembled InAs quantum dash lasers grown by molecular beam epitaxy on InP (001) substrates are reported. Pulsed room-temperature operation demonstrates wavelengths from 1.60 to 1.66 μm for one-, three-, and five-stack designs, a threshold current density as low as 410 A/cm² for single-stack uncoated lasers, and a distinctly quantum-wire-like dependence of the threshold current on the laser cavity orientation. The maximal modal gains for lasing in the ground-state with the cavity perpendicular to the dash direction are determined to be 15 cm⁻¹ for single-stack and 22 cm⁻¹ for five-stack lasers.

Index Terms—InAs, InP, quantum dash, quantum dot, self-assembled, semiconductor laser.

THERE IS increasing interest in employing semiconductor quantum dots (QDs) in optoelectronic devices, since QDs exhibit unique electrical and optical properties compared with conventional quantum-well (QW) structures [1]. Previous research has yielded impressive laser diode results on GaAs, including: 1) a very low room-temperature threshold current density [2]–[5]; 2) the observation of an ultra-small linewidth enhancement factor [6], [7]; and 3) the attainment of a 201-nm tuning range at bias currents ten times lower than those required in QW lasers [8]. However, these GaAs-based QDs lasers operate at wavelengths $\leq 1.33 \mu\text{m}$ [9]. It is very difficult to fabricate InAs–GaAs QDs with an emission wavelength as long as 1.55- μm range, which is desirable for long-distance optical communication systems. The problem arises from the large lattice mismatch (7%) between InAs and GaAs that significantly increases the bandgap due to the large compressive strain, and makes the growth of large QDs to minimize the quantum size effect difficult [10]. An InP substrate is preferable for the fabrication of long-wavelength InAs QD lasers due to the smaller lattice mismatch (3%) between InAs and InP. It has been reported that InAs–InGaAs–InP QDs lasers emit at 1.9 μm at 77 K [11]. Researchers have also reported ground-state lasing at room temperature in long-wavelength InAs QDs-lasers, but on InP (311) B substrates [12]. In this letter, we detail the first demonstration of room-temperature operation of one-, three-, and five-stack self-assembled InAs quantum-dash (QDASH) laser diodes with

wavelengths from 1.60 to 1.66 μm and low-threshold currents fabricated on InP (001) substrates.

The origin of the name “dash” comes from a physical description of the finite-length wire-like InAs structures that self-assemble when grown within an AlGaInAs QW on an InP substrate. The reason why self-assembled wire-like structures are formed instead of dots remains uncertain. Brault *et al.* [13] find that under identical growth conditions, wire formation is preferred on InGaAs buffer layers lattice matched to InP, while dots are observed on AlInAs lattice matched to InP. They attribute the wire-like shape of the nanostructures to a longer diffusion length on InGaAs compared to AlInAs, which is supported by surface roughness measurements. The preferred elongation of the dashes is along the $[1\bar{1}0]$ direction as observed by atomic force microscopy (AFM). This may be explained by the different nature of the step edges of InAs on a (001) oriented surface. Step edges along $[1\bar{1}0]$ are cation terminated and less reactive compared to step edges along $[110]$, which are anion terminated and more reactive with respect to indium [14]. As a result, the growth of InAs nanostructures proceeds faster in the $[1\bar{1}0]$ direction, and this leads to the formation of quantum dashes.

Previous research on one-dimensional (1-D) quantum-wire semiconductor lasers was most notably based on metal–organic chemical vapor deposition (MOCVD) regrowth into V-shaped grooves [15]. This technique is susceptible to etch damage, the wire array density is limited by the spacing between the etched grooves, and the laser cavity is undesirably oriented along the wire direction. Since self-assembled QDASHs do not suffer from these problems, they offer a new path for realizing quantum-wire lasers.

The three samples studied were grown on n-type InP (001) substrates using solid-source molecular beam epitaxy (MBE). A calibration wafer was grown in order to determine the dimensions of the InAs QDASHs. As shown in Fig. 1, typical dimensions for the dashes are 300, 25, and 5 nm for the length, width, and height, respectively, when measured uncapped by AFM. The length value is considerably longer than that reported from previous research [16]. From the image analysis, a density of $\sim 10^{10}$ QDASHs/cm² is deduced. The laser structure consists of a waveguide structure of lattice-matched AlInAs cladding layers around an AlGaInAs waveguide/barrier region with bandgap of 1.2 μm . The compressively strained AlGaInAs QW surrounding the InAs QDASHs has a bandgap of approximately 1.3 μm and a thickness of 7.5 nm. One, three, and five stacks of InAs QDASHs with 30-nm tensile-strained AlGaInAs barriers comprise the active regions.

Manuscript received March 2, 2001; revised May 4, 2001. This work was supported by the Air Force Office of Scientific Research under Grant F49620-99-1-0330 and by the Advanced Sensors Consortium of the Army Federated Laboratories. The views and conclusions contained in this document are those of the authors and should not be interpreted as representing the official policies, either expressed or implied, of the Army Research Laboratory or the U.S. Government.

The authors are with the Center for High Technology Materials, University of New Mexico, Albuquerque, NM 87106 USA (e-mail: rwang@chtm.unm.edu).
Publisher Item Identifier S 1041-1135(01)06417-5.

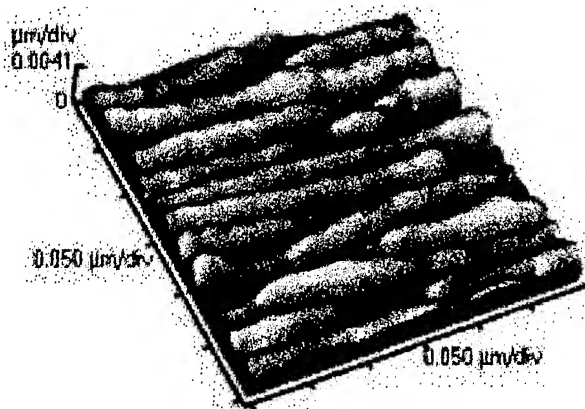


Fig. 1. An atomic force micrograph of the InAs quantum dashes.

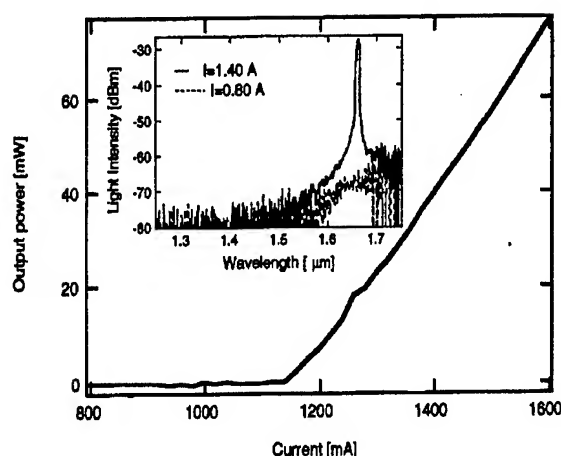


Fig. 2. A two-facet light output versus injection current measured on a five-stack laser diode with geometry of $100\ \mu\text{m} \times 1500\ \mu\text{m}$. The inset is the electroluminescence spectra under different pump levels for the device. The spectral peak is $1.66\ \mu\text{m}$.

Broad area lasers with $100\text{-}\mu\text{m}$ stripe widths were processed from these wafers. For single and three-stack samples, lasers were only characterized with cavities along $[110]$, while five-stack lasers with cavity orientations of both $[110]$ and $[1\bar{1}0]$ were fabricated and measured. All devices were tested with the epitaxial side up on a thermoelectric cooler using pulsed excitation. The pulse width was $0.5\ \mu\text{s}$ with a duty cycle of 0.5% , and the temperature of the thermoelectric cooler was set to $15\ ^\circ\text{C}$.

The room-temperature operation wavelengths are 1.60 , 1.62 , and $1.66\ \mu\text{m}$ for the ground state of the one-, three-, and five-stack lasers, respectively. The trend of longer wavelength with increasing stack number may be explained by a size increase of the QDASHs, as more stacks are grown or band filling. The same trend has also been observed in QD lasers [17]. Fig. 2 shows the total light output as a function of injection current for a five-stack laser with the cavity perpendicular to the dash direction and a geometry of $100\ \mu\text{m} \times 1500\ \mu\text{m}$. The inset displays electroluminescence (EL) spectra under various current injection levels from the laser. The EL peaks are approximately $1.66\ \mu\text{m}$ before and after the threshold condition is satisfied, which indicates that the diode operates in the ground-state. In contrast, when the cavity length is cleaved to be $300\ \mu\text{m}$ the EL peak shifts to about $1.60\ \mu\text{m}$. In fact, five-stack lasers with

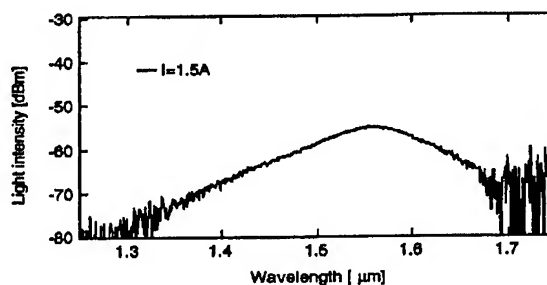


Fig. 3. Electroluminescence spectrum for a single-stack laser with cavity length of $1500\ \mu\text{m}$ and under 1.5-A current injection ($1\ \text{kA}/\text{cm}^2$).

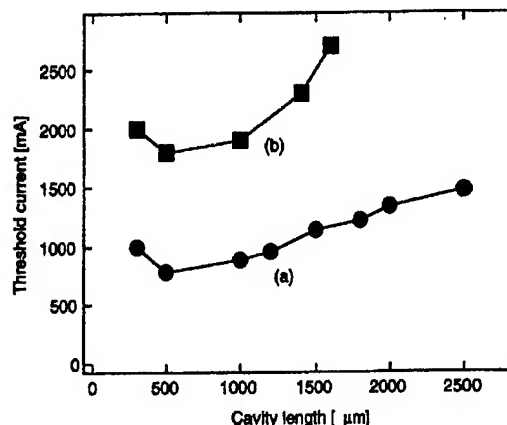


Fig. 4. Threshold current versus cavity length for five-stack lasers. (a) $[110]$ cavity orientation (perpendicular to the dash direction). (b) $[1\bar{1}0]$ cavity orientation (parallel to the dash direction).

cavity lengths shorter than $1000\ \mu\text{m}$ emit at $1.60\ \mu\text{m}$, which is believed to be the excited-state. The latter is the band of energies centered around the second quantized level determined by the shorter QDASH dimension in the growth plane. Therefore, the energy difference between the ground-state and the excited-state is approximately $32\ \text{meV}$, which is smaller than the value of $55\ \text{meV}$ for the energy difference between the ground-state and the excited-state for InAs QD on InP (311) B substrates reported previously [12]. This result is reasonable since the QDASHs shorter dimension in the growth plane is larger than the QDs diameter. As shown in Fig. 3, the spontaneous emission spectrum for a one-stack laser under $1.5\ \text{A}$ pump level ($1\ \text{kA}/\text{cm}^2$) covers the range from 1.35 to $1.65\ \mu\text{m}$, indicating that this one-stack QDASH structure has the potential for a very large tuning bandwidth in the wavelength range important for wavelength-division-multiplexing (WDM) optical communication systems.

Fig. 4 shows a significant dependence of the threshold current on the orientation of the laser cavity. Trace (a) portrays the five-stack lasers with cavities oriented along the $[110]$ direction (perpendicular to the QDASH direction), while curve (b) presents cavities that are aligned along the $[1\bar{1}0]$ direction (parallel to the dash direction). It is observed that the threshold currents for the laser diodes with cavities parallel to the QDASH direction are approximately two times higher than those with cavities perpendicular. This variation is related to the dependence of the optical gain on the electric field polarization. For the particular dimensions of these QDASHs, the transition matrix element is significantly larger when the electrical field is

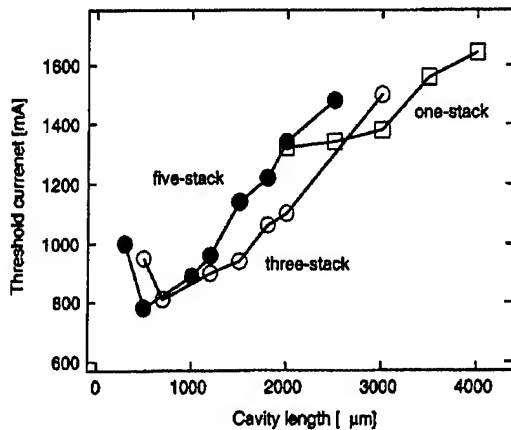


Fig. 5. Threshold current versus cavity length for one-, three-, and five-stack lasers, all with [110] cavity orientations. The modal gain for single-stack lasers is easier to saturate than multiple-stack ones.

parallel to the dash (i.e., the light propagates perpendicular to the QDASH direction) [18]. Indeed, the trend in the threshold current indicates that the light is highly TE polarized since the QDASH-TM polarization is not sensitive to changes in cavity orientation in the plane perpendicular to the growth direction. An independent measurement confirmed that the QDASH-laser emission is TE polarized. These results highlight the advantage that self-assembled QDASHs have in being able to adjust the laser cavity axis in the direction of maximum gain.

The inverse external quantum efficiency ($1/\eta_{ex}$) versus the cavity length (L) data for the single and multiple-stack lasers are used to calculate the internal loss (α_i) and the internal quantum efficiency (η_i). By fitting the data to the equation $1/\eta_{ex} = 1/\eta_i(1 - \alpha_i L/\ln(R))$, $\eta_i(\alpha_i)$ values of 62% (9.2 cm^{-1}), 66% (10.5 cm^{-1}), and 52% (10.1 cm^{-1}) are found for one, three, and five-stack lasers, respectively. The reflectivity (R) is assumed to be 0.32 for the cleaved facets.

A threshold current density as low as 410 A/cm^2 was measured on a one-stack 4-mm-long cavity cleaved-facet laser diode. Fig. 5 shows the threshold current versus the cavity length for one-, three-, and five-stack lasers with the laser cavity oriented perpendicular to the dash direction. In spite of the relatively high internal losses ($\sim 10 \text{ cm}^{-1}$) observed in these particular structures, their threshold current densities are equal to that of low internal loss QW lasers operating at $1.52 \mu\text{m}$ [19]. The maximum modal gain (g_{max}) is inferred from the abrupt rise in threshold current at the shorter cavity lengths. This trend is obvious in the three- and five-stack lasers as seen in Fig. 5. For the single-stack devices, however, the saturation in the optical gain is sufficiently rapid that any laser with a cavity length shorter than 2 mm does not lase at current densities less than 1 kA/cm^2 . For the five- and single-stack lasers, g_{max} s of about 22 and 15 cm^{-1} are calculated, respectively. Compared with single-stack QD lasers on GaAs, the one-stack g_{max} for the QDASHs almost doubles [2], [4]. However, the g_{max} of the five-stack laser is less than 5/3 that of the three-stack version. Since there is a 30-nm barrier between the AlGaInAs QWs containing the QDASHs, uneven pumping of the stacks is probably occurring.

In conclusion, we have demonstrated the first self-assembled single- and multiple-stack quantum dash lasers on InP (001) substrates with a low threshold current density, room-temperature ground-state wavelengths from 1.60 to $1.66 \mu\text{m}$, and a clear quantum-wire-like dependence of the threshold current on laser cavity orientations.

REFERENCES

- [1] D. Bimberg, M. Grundmann, and N. Ledentsov, *Quantum Dot Heterostructures*. New York: Wiley, 1999.
- [2] G. T. Liu, A. Stintz, H. Li, T. C. Newell, A. L. Gray, P. M. Varangis, K. J. Malloy, and L. F. Lester, "The influence of quantum-well composition on the performance of quantum dot lasers using InAs-InGaAs dots-in-a-well (DWELL) structures," *IEEE J. Quantum Electron.*, vol. 36, pp. 1272–1279, Nov. 2000.
- [3] A. Stintz, G. T. Liu, H. Li, L. F. Lester, and K. J. Malloy, "Low-threshold current density $1.3 \mu\text{m}$ InAs quantum-dot lasers with the dots-in-a-well (DWELL) structure," *IEEE Photon. Technol. Lett.*, vol. 12, pp. 591–593, June 2000.
- [4] X. D. Huang, A. Stintz, C. P. Hains, G. T. Liu, J. Cheng, and K. J. Malloy, "Efficient high-temperature CW lasing operation of oxide-confined long-wavelength InAs quantum dot lasers," *Electron. Lett.*, vol. 36, pp. 41–42, Jan. 2000.
- [5] G. Park, O. B. Shchekin, D. L. Huffaker, and D. G. Deppe, "Low-threshold oxide-confined $1.3 \mu\text{m}$ quantum dot laser," *IEEE Photon. Technol. Lett.*, vol. 12, pp. 230–232, Mar. 2000.
- [6] T. C. Newell, D. J. Bossert, A. Stintz, B. Fuchs, K. J. Malloy, and L. F. Lester, "Gain and linewidth enhancement factor in InAs quantum dot laser diodes," *IEEE Photon. Technol. Lett.*, vol. 11, pp. 1527–1529, Dec. 1999.
- [7] H. Saito, K. Nishi, A. Kamei, and S. Sugou, "Low chirp observed in directly modulated quantum dot lasers," *IEEE Photon. Technol. Lett.*, vol. 12, pp. 1298–1300, Oct. 2000.
- [8] P. M. Varangis, H. Li, G. T. Liu, T. C. Newell, A. Stintz, B. Fuchs, K. J. Malloy, and L. F. Lester, "Low-threshold quantum dot lasers with 201 nm tuning range," *Electron. Lett.*, vol. 36, pp. 1544–1545, Aug. 2000.
- [9] G. Park, O. B. Shchekin, S. Csutak, D. L. Huffaker, and D. G. Deppe, "Room-temperature continuous-wave operation of a single-layered $1.3 \mu\text{m}$ quantum dot laser," *Appl. Phys. Lett.*, vol. 75, pp. 3267–3269, Nov. 1999.
- [10] P. Y. Yu and M. Cardona, *Fundamentals of Semiconductors*. New York: Springer, 1996.
- [11] V. M. Ustinov, A. E. Zhukov, A. Y. Egorov, A. R. Kovsh, S. V. Zaitsev, N. Y. Gordeev, V. I. Kopchatov, N. N. Ledentsov, A. F. Tsatsul'nikov, B. V. Volovik, P. S. Kop'ev, Z. I. Alferov, S. S. Ruvimov, Z. Liliental-Weber, and D. Bimberg, "Low threshold quantum dot injection laser emitting at $1.9 \mu\text{m}$," *Electron. Lett.*, vol. 34, pp. 670–671, Apr. 1998.
- [12] H. Saito, K. Nishi, and S. Sugou, "Ground-state lasing at room temperature in long-wavelength InAs quantum-dot lasers on InP (311)B substrates," *Appl. Phys. Lett.*, vol. 78, pp. 267–269, Jan. 2001.
- [13] J. Brault, M. Gendry, G. Grenet, G. Hollinger, Y. Desières, and T. Benyattou, "Role of buffer surface morphology and alloying effects on the properties of InAs nanostructures grown on InP(001)," *Appl. Phys. Lett.*, vol. 73, no. 20, pp. 2932–2934, Nov. 1998.
- [14] V. Bressler-Hill, A. Lorke, S. Varma, P. M. Petroff, K. Pond, and W. H. Weinberg, "Initial stages of InAs epitaxy on vicinal GaAs (001) – (2×4)," *Phys. Rev. B Condens. Matter*, vol. 50, no. 12, pp. 8479–8487, Sept. 1994.
- [15] H. Weman, E. Martinet, M. A. Dupertuis, A. Rudra, K. Leifer, and E. Kapon, "Two-dimensional quantum-confined Stark effect in V-groove quantum wires: Excited state spectroscopy and theory," *Appl. Phys. Lett.*, vol. 74, pp. 2334–2336, Apr. 1999.
- [16] K. Nishi, M. Yamada, T. Anan, A. Gomyo, and S. Sugou, "Long-wavelength lasing from InAs self-assembled quantum dots on (311)B InP," *Appl. Phys. Lett.*, vol. 73, pp. 526–528, July 1998.
- [17] L. F. Lester, A. Stintz, H. Li, T. C. Newell, E. A. Pease, B. A. Fuchs, and K. J. Malloy, "Optical characteristics of $1.24 \mu\text{m}$ quantum dot lasers," *IEEE Photon. Technol. Lett.*, vol. 11, pp. 931–933, Aug. 1999.
- [18] L. A. Coldren and S. W. Corzine, *Diode Lasers and Photonic Integrated Circuits*. New York: Wiley, 1995.
- [19] T. C. Newell, P. M. Varangis, E. Pease, A. Stintz, G. T. Liu, K. J. Malloy, and L. F. Lester, "High power AlGaInAs strained multiquantum well lasers operating at $1.52 \mu\text{m}$," *Electron. Lett.*, vol. 36, pp. 955–956, May 2000.



ELSEVIER

21 December 1998

PHYSICS LETTERS A

Physics Letters A 250 (1998) 117–122

Linewidth broadening across a dynamical instability

P.M. Varangis^{a,b}, A. Gavrielides^a, V. Kovanis^a, L.F. Lester^b

^a Air Force Research Laboratory/DELO, Kirtland AFB, NM 87117-5776, USA

^b Center for High Technology Materials, University of New Mexico, Albuquerque, NM 87106, USA

Received 5 August 1998; revised manuscript received 22 October 1998; accepted for publication 22 October 1998

Communicated by C.R. Doering

Abstract

We investigate experimentally and theoretically the variation of the emission linewidth of an optically-injected semiconductor laser across a resonant period-doubling bifurcation. Close to the dynamical instability, the intrinsic and external phase fluctuations are amplified, resulting in a spectral linewidth in excess of that accounted for by the spontaneous-emission process alone. © 1998 Elsevier Science B.V.

Keywords: Semiconductor laser; Noise; Linewidth; Bifurcation

Noise characterization of laser sources is of primary importance for applications requiring a high degree of coherence, such as high-resolution spectroscopy, interferometric sensors and coherent optical communications [1]. Issues related to the efficient transmission and detection of optical signals are directly dependent on the noise properties of the device. The dominant contribution to laser noise arises from the fluctuations of the optical phase which produce the spectral broadening of each longitudinal mode [2]. The dependence of the observed linewidth on the enhancement factor α [2] explained the considerably broader emission of semiconductor lasers as opposed to gas or solid-state lasers, which are described by the Schawlow–Townes theory [3].

Due to the high level of intrinsic noise, semiconductor lasers constitute from a dynamical point of view an excellent case study of the response of driven nonlinear oscillators subject to a strong random excitation [4]. Numerous investigations have focused on the spectral properties of the solitary source [5], and

how these are modified under conditions of injection-locking [6], current modulation [7], or external feedback [8]. Nevertheless, a study of how the laser linewidth characteristics are modified near the onset and across a dynamical instability is still lacking. Semiconductor lasers subject to external optical perturbations exhibit an interesting dynamical behavior, which includes Hopf and period-doubling bifurcations [9], and nonlinear subharmonic and ultraharmonic resonances [10]. The potential application of these responses in coherent optical communications requires a detailed study of the linewidth variation as a function of the deterministic response of the system.

In this Letter, we investigate the effect of a resonant period-doubling bifurcation on the coherence properties of a single-mode semiconductor laser subject to monochromatic optical injection. The region of the dynamical instability is approached when the value of the frequency detuning Ω , between the master and slave lasers, is in the neighborhood of $2\omega_r$, with ω_r denoting the intrinsic relaxation-oscillation frequency

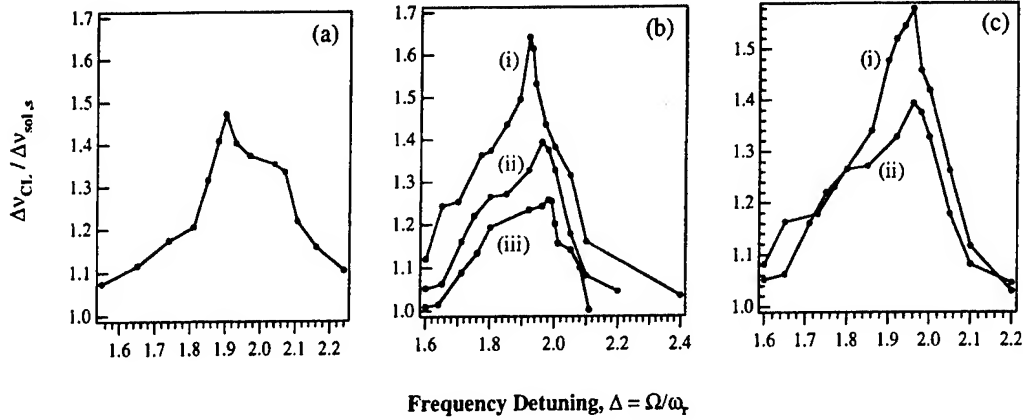


Fig. 2. Variation of the linewidth of the injected laser across the bifurcation. The vertical axis displays the spectral width of the center line $\Delta\nu_{CL}$, normalized with respect to that of the solitary laser ($\Delta\nu_{0,s} \approx 230$ MHz). The horizontal axis displays the frequency detuning $\Delta = \Omega/\omega_r$. (a) Experimental measurements. Results from the numerical integration of the single-mode rate equations (1)–(6) are shown in (b) and (c). We have assumed that two lasers are identical which is essentially in agreement with the experimental situation ($\Delta\nu_{0,m} \approx 260$ MHz). (b) For $\alpha = 5$, $T = 1740$, $P = 2.276$ ($J/J_{th} = 1.6$) and $Y = 3 \times 10^{-3}$, we vary the value of injection strength η . (i) $\eta = 2.55 \times 10^{-3}$, (ii) $\eta = 2.04 \times 10^{-3}$, (iii) same as previously but neglected the noise of the master source. (c) For $\alpha = 5$, $T = 1740$, $P = 2.276$ ($J/J_{th} = 1.6$) and $\eta = 2.04 \times 10^{-3}$, we vary the value of the damping rate ξ of the laser relaxation oscillations. In dimensionless form, ξ is given by $\xi = \omega_r(1 + 2P)/2P + Y/\omega_r$. (i) $Y = 0$ ($\xi = 0.06238$), and (ii) $Y = 3 \times 10^{-3}$ ($\xi = 0.121$).

$$\dot{\psi}_m = -\alpha_m N_m + F_{p,m}/E_m, \quad (5)$$

$$T_m \dot{N}_m = P_m - N_m - P_m G_m E_m^2, \quad (6)$$

where $G_i = (1 + 2N_i)[1 + Y_i(E_i^2 - 1)]^{-1}$ ($i = s, m$), and $\Delta\Phi = \psi_s(t) - \psi_m(t)$. Eqs. (1)–(6) are given in dimensionless form with the electric field amplitude $E(t)$ and the carrier density $N(t)$ normalized with respect to their steady-state values, and time t with respect to the photon lifetime [12]. $\psi_m(t)$ denotes the optical phase of the master laser, $\psi_s(t)$ is the optical phase of the slave laser shifted by the frequency detuning Ω between the two sources, α is the linewidth enhancement factor, $P \sim J/J_{th} - 1$ is proportional to the pumping above threshold, $T = \tau_s/\tau_p$ is equal to the ratio of the carrier (τ_s) to the photon (τ_p) lifetime, η is the coupling factor, and Y is the nonlinear gain suppression coefficient. The amplitude and phase fluctuations are represented by the Langevin noise sources $F_a(t)$ and $F_p(t)$, which are zero-mean, $\langle F_i(t) \rangle = 0$, and delta-correlated, $\langle F_i(t) F_j(t') \rangle = D \delta_{ij} \delta(t - t')$ ($i, j = a, p$) [15]. The diffusion coefficient D is given by $D = R_{sp} \tau_p / I_0$, with R_{sp} denoting the spontaneous-emission rate, and I_0 the steady-state output intensity.

The rate equations (1)–(6) were solved numerically using a second-order, stochastic Runge–Kutta integrator [13]. We have assumed that the two lasers

are identical, which is essentially in agreement with the experimental situation, whereas the value of noise used in the calculations is determined by the linewidth of the solitary laser. The results are shown in Figs. 2b and 2c for two different values of injection strength and damping rate of the laser relaxation oscillations. In Fig. 2b we vary the value of injection strength from $\eta = 2.55 \times 10^{-3}$, in (i), to $\eta = 2.04 \times 10^{-3}$, in (ii). In curve (iii), $\eta = 2.04 \times 10^{-3}$, but we have neglected the noise of the master source. We observe that the spectral broadening of the laser emission is proportional to the level of injection. In addition, for the case of an ideally coherent master source the magnitude of the effect is considerably reduced. The values of the laser parameters $\alpha = 5$, $T = 1740$, $P = 2.276$ ($J/J_{th} = 1.6$) and $Y = 3 \times 10^{-3}$, are appropriate for the type of semiconductor lasers (Hitachi HLP-1400) used in the experiment [14]. In Fig. 2c for $\alpha = 5$, $T = 1740$, $P = 2.276$ ($J/J_{th} = 1.6$), and constant level of injection, $\eta = 2.04 \times 10^{-3}$, we vary the value of the damping rate ξ of the laser relaxation oscillations. In dimensionless form it is given by $\xi = \omega_r(1 + 2P)/2P + Y/\omega_r$. The spectral broadening is inversely proportional to the value of ξ , as can be seen from comparison of curves (i), $Y = 0$ ($\xi = 0.06238$), and (ii), $Y = 3 \times 10^{-3}$ ($\xi = 0.121$). In the FWM region (arbitrary Ω), the

spectral linewidth of the laser emission (center line) is essentially determined solely by that of the solitary source. However, in the subharmonic resonance regime ($\Omega \approx 2\omega_r$) the intrinsic and external random phase fluctuations are amplified, resulting in a spectral linewidth in excess of that accounted for by the spontaneous-emission process alone.

In what follows, we present a systematic method to investigate analytically the linewidth characteristics of an optically-injected semiconductor laser. The motivation behind this approach has been the need for a more thorough understanding of the laser stochastic dynamics. The method focuses on the quantity that essentially prescribes not only the deterministic but also the stochastic response of the injected laser, i.e., the optical phase.

Results from the linear stability analysis of the problem [9] motivate the introduction of a new set of rescaled variables for the electric field amplitude, $b = (E_s - 1)\alpha$, the carrier density, $n = N_s\alpha/\omega_r$, and time, $\tau = \omega_r t$, into the rate equations (1)–(3) which describe the operation of the injected laser. In the above expressions, $\omega_r = \sqrt{2P/T}$ denotes the free-running relaxation oscillation frequency of the slave laser. If we disregard the amplitude fluctuations of the master laser, represented by E_m , keep the leading-order contributions in α and eliminate b and n , we obtain a third-order nonlinear stochastic differential equation for the optical phase ψ_s ,

$$\psi_s''' + \xi\psi_s'' + \psi_s' = \Delta + \Lambda \cos(\psi_s - \psi_m) + f_s(\tau), \quad (7)$$

where $\Delta = \Omega/\omega_r$ is the normalized frequency detuning, $\Lambda = \eta\alpha/\omega_r$ is proportional to the level of injection, $\xi = \omega_r[(1 + 2P)/2P] + Y/\omega_r$ represents the damping rate of the laser relaxation oscillations, and prime denotes differentiation with respect to $\tau = \omega_r t$. The noise source $f_s(\tau) = \alpha F_d(t)/\omega_r$ signifies the coupling between intensity and phase fluctuations through the linewidth enhancement factor α , and satisfies $\langle f_s(\tau)f_s(\tau') \rangle = \epsilon^2\delta(\tau - \tau')$, where $\epsilon^2 = \alpha^2 D/\omega_r$. The stochastic phase equation (7) incorporates also the phase fluctuations of the externally-injected signal. These are accounted for by the phase ψ_m of the master, whose autocorrelation is given by $\langle \tilde{\psi}_m(\omega)\tilde{\psi}_m(\omega') \rangle = \epsilon^2[1/\omega(\omega^2 - 1)]^2\delta(\omega - \omega')$.

If we assume that noise acts as a weak perturbation on the periodic response of the system, the following

expansions are justified,

$$\begin{aligned} \psi_s &= \Psi_s + \epsilon\delta\psi_s, & \psi_m &= \epsilon\delta\psi_m, \\ f_s &= \epsilon\delta f_s, \end{aligned} \quad (8)$$

where Ψ_s and $\epsilon\delta\psi_s$ denote the deterministic solution and the random fluctuations, respectively, of the phase ψ_s of the slave laser. These expansions allow us to linearize Eq. (7) about Ψ_s and obtain

$$\Psi_s''' + \xi\Psi_s'' + \Psi_s' = \Delta + \Lambda \cos \Psi_s, \quad (9)$$

$$\delta\psi_s''' + \xi\delta\psi_s'' + \delta\psi_s' = -\Lambda(\delta\psi_s - \delta\psi_m) \sin \Psi_s + \delta f_s. \quad (10)$$

Eqs. (9) and (10) constitute a major simplification over the original rate equations (1)–(6). Eq. (10) allows for the analytical investigation of the linewidth characteristics of the slave laser as a function of its deterministic response Ψ_s . The latter is obtained from Eq. (9) using multiple-scales singular-perturbation techniques. It has been shown that Eq. (9) describes accurately the dynamical behavior of the slave laser in both the injection-locking ($|\Delta| < \Lambda$) [9] and phase-drift ($|\Delta| > \Lambda$) [10] regions. In the phase-drift region, it yields approximate analytical expressions for the evolution of the optical phase when the injected laser exhibits FWM (arbitrary Δ) or subharmonic resonant ($\Delta \approx 2$) response.

For arbitrary detuning, the FWM response of the slave laser is described by [10]

$$\Psi_s = C\tau + \Lambda Q \sin(C\tau), \quad (11)$$

where $C = \Delta + \delta$ incorporates the effect of the injection-induced shift δ of the slave laser operating frequency, $\delta = \Lambda^2/2\Delta(\Delta^2 - 1)$, and $Q = 1/C(1 - C^2)$. The relevance of solution (11) to the experimental picture is readily identified. The $O(\Lambda)$ term $\Lambda Q \sin(C\tau)$ describes the laser response at the location of injection (regenerative signal), denoted by the solid arrow in Fig. 1. Since the deterministic response of the system is only slightly perturbed by the presence of noise, the expression for the stochastic component $\delta\psi_s$ of the optical phase is dictated by Eq. (11). We thus assume a form

$$\delta\psi_s = \tilde{\alpha} + \tilde{\beta} \sin(C\tau) + \tilde{\gamma} \cos(C\tau), \quad (12)$$

where $\tilde{\alpha}$, $\tilde{\beta}$ and $\tilde{\gamma}$ are slowly-varying functions of time, and therefore their higher-order derivatives may be

neglected. If we substitute (12) and (11) into (10), group together and set to zero the summation of the slowly-varying terms and the coefficients of the periodic terms $\sin(C\tau)$ and $\cos(C\tau)$, we obtain the following expression for the complex electric field of the injected laser,

$$E \propto e^{i\epsilon\delta\psi_0(\tau)} - (\Lambda Q/2)e^{-i[C\tau - \psi_m(\tau)]} + (\Lambda Q/2)e^{i[C\tau + 2\epsilon\delta\psi_0(\tau) - \psi_m(\tau)]}, \quad (13)$$

where $\delta\psi_0(\tau) = \text{FT}^{-1}\{i\delta f_s(\omega)/\omega(\omega^2 - 1)\}$, and FT^{-1} denotes the inverse Fourier transform operator. The three terms on the r.h.s. of Eq. (13) correspond to the center line of the laser emission, the regenerative signal at the location of injection, and the conjugate signal at the symmetric location about the center line. Accordingly, the stochastic terms $\epsilon\delta\psi_0(\tau)$, $\psi_m(\tau)$ and $[2\epsilon\delta\psi_0(\tau) - \psi_m(\tau)]$ denote the random phase fluctuations of the respective frequency components. In order to calculate the linewidth characteristics of the injected laser we make use of the Wiener-Khinchin theorem, which defines the optical spectrum $G(\omega)$ by the Fourier transform of the normalized autocorrelation function $G(\tau)$ of the complex electric field, $G(\tau) = \langle \hat{E}(t+\tau)\hat{E}^*(t) \rangle / \langle |\hat{E}(t)|^2 \rangle$ [15]. In addition, the assumption of Gaussian-distributed phase noise allows us to express $G(\tau)$ solely in terms of the variance $\sigma(\tau)$ of the fluctuations, $G(\tau) = \exp[-\sigma^2(\tau)/2]$, where $\sigma^2(\tau) = (1/\pi) \int_{-\infty}^{+\infty} |\tilde{\Phi}(\omega)|^2 (1 - \cos \omega\tau) d\omega$, and $|\tilde{\Phi}(\omega)|^2$ denotes the correlation strength of the phase fluctuations at the respective location of the optical spectrum [15].

The linewidth of the center line, $\Delta\nu_{cl}$, the regenerative signal, $\Delta\nu_{reg}$, and the conjugate signal, $\Delta\nu_{con}$, satisfy

$$\Delta\nu_{cl} = \Delta\nu_{0,s}, \quad (14)$$

$$\Delta\nu_{reg} = \Delta\nu_{0,m}, \quad \Delta\nu_{con} = 4\Delta\nu_{0,s} + \Delta\nu_{0,m}. \quad (15)$$

$\Delta\nu_{0,s}$ and $\Delta\nu_{0,m}$ denote the spectral linewidth of the solitary slave and master laser, respectively, which is generally given by $\Delta\nu_0 = \epsilon^2/2\pi$, where $\epsilon^2 = \alpha^2 D/\omega_r$. Expressions (14) and (15) agree with our own and reported measurements of the linewidth of the injected laser, when the latter exhibits FWM behavior [16]. It is the first time however that these relations are obtained in a systematic fashion from basic principles. The derivation of corresponding analytical expressions

for the linewidth variation of the injected laser in the subharmonic-resonance regime ($\Omega \approx 2\omega_r$) is still in progress, and results will be presented in a future communication.

The interaction of noise with the intrinsic nonlinearity of a system and external driving forces has been extensively studied in disciplines ranging from pure mathematics to physics and engineering. These investigations have demonstrated that often noise induces responses not possible in the noise-free limit (stochastic resonance [17], noise-induced transitions [18]), and introduces new features (noisy precursors) in the spectrum of the deterministic system when the latter is about to become unstable [19]. The current study adds to the previous work by addressing the critical issue of how the coherence properties of an optical system are modified by the onset of a resonant period-doubling bifurcation. It is the first time that the linewidth characteristics of an optically-injected semiconductor laser are systematically investigated away from a regime of a stable, steady-state response. The spectral linewidth of the laser emission is a characteristic worth investigating not only to understand the physical processes that modify it in the neighborhood of an instability, but also in view of the potential application of the various coupling schemes in modern communication systems.

P.M.V. acknowledges support from the National Research Council.

References

- [1] Y. Yamamoto, *Coherence, Amplification, and Quantum Effects in Semiconductor Lasers* (Wiley Interscience, New York, 1991), and references therein.
- [2] C.H. Henry, *IEEE J. Quant. Elect.* 18 (1982) 259; *J. Light. Tech.* 4 (1986) 298.
- [3] M. Lax, *Phys. Rev.* 157 (1967) 231; *Phys. Rev.* 160 (1967) 290.
- [4] K. Lindenberg, B.J. West, *The Nonequilibrium Statistical Mechanics of Open and Closed Systems* (VCH Publishers, 1990).
- [5] G. Gray, R. Roy, *Phys. Rev. A* 40 (1989) 2452.
- [6] T.B. Simpson, J.M. Liu, K.F. Huang, K. Tai, *Quant. Semiclass. Opt.* 9 (1997) 765; P. Spano, S. Piazzolla, M. Tamburrini, *IEEE J. Quant. Elect.* 22 (1986) 427; W.W. Chow, *IEEE J. Quant. Elect.* 19 (1983) 243.
- [7] T.M. Shen, G.P. Agrawal, *J. Light. Tech.* 5 (1987) 653.
- [8] D. Lenstra, B.H. Verbeek, A.J. den Boef, *IEEE J. Quant. Elect.* 21 (1985) 674;

- M.W. Fleming, A. Mooradian, IEEE J. Quant. Elect. 17 (1981) 44;
W.A. Hamel, M.P. van Exter, J.P. Woerdman, IEEE J. Quant. Elect. 28 (1992) 1459.
- [9] T. Erneux, V. Kovanis, A. Gavrielides, P.M. Alsing, Phys. Rev. A 53 (1996) 4372.
- [10] P.M. Varangis, A. Gavrielides, T. Erneux, V. Kovanis, L.F. Lester, Phys. Rev. Lett. 78 (1997) 2353;
A. Gavrielides, T. Erneux, V. Kovanis, P.M. Alsing, T.B. Simpson, Quant. Semiclass. Opt. 9 (1997) 575.
- [11] J.M. Liu, T.B. Simpson, IEEE J. Quant. Elect. 30 (1994) 957.
- [12] P.M. Alsing, V. Kovanis, A. Gavrielides, T. Erneux, Phys. Rev. A 53 (1996) 4429.
- [13] K. Jansons, G.D. Lythe, J. Stat. Phys. 90 (1998) 227.
- [14] H. Li, J. Ye, J.G. McInerney, IEEE J. Quant. Electron. 29 (1993) 2421.
- [15] G.P. Agrawal, R. Roy, Phys. Rev. A37 (1988) 2495.
- [16] R. Hui, A. Mecozzi, Appl. Phys. Lett. 60 (1992) 2454.
- [17] B. McNamara, K. Wiesenfeld, R. Roy, Phys. Rev. Lett. 60 (1988) 2626.
- [18] W. Horsthemke, R. Lefever, Noise-Induced Transitions (Springer, Berlin, 1984).
- [19] K. Wiesenfeld, B. McNamara, Phys. Rev. Lett. 55 (1985) 13;
C. Jeffries, K. Wiesenfeld, Phys. Rev. A 31 (1985) 1077.

Ultrafast carrier-relaxation dynamics in self-assembled InAs/GaAs quantum dots

Dzmitry A. Yarotski, Richard D. Averitt, Nicolas Negre, Scott A. Crooker, and Antoinette J. Taylor*

Materials Science and Technology Division, Los Alamos National Laboratory, Los Alamos, New Mexico

Giovanni P. Donati, Andreas Stintz, Luke F. Lester, and Kevin J. Malloy

Center for High Technology Materials, University of New Mexico, Albuquerque, New Mexico

Received July 5, 2001; revised manuscript received November 26, 2001

We apply the recently developed technique of ultrafast scanning tunneling microscopy to study carrier dynamics in InAs/GaAs self-assembled quantum-dot samples. The results obtained with this new technique are compared with standard ensemble-averaging ultrafast optoelectronic techniques such as femtosecond optical pump/probe reflectivity measurements and time-resolved terahertz spectroscopy. These measurements reveal a unified picture of the relaxation dynamics in InAs/GaAs self-assembled quantum-dot samples at $T = 300$ K. The initial carrier relaxation proceeds by Auger carrier capture from the InAs wetting layer on a time scale of 1–2 ps, followed by recombination of carriers in the wetting layer, GaAs substrate, and quantum dots on time scales of 350 ps, 2.3 ns, and 900 ps, respectively. The consistency of these three experimental techniques demonstrates ultrafast scanning tunneling microscopy as a reliable tool for probing the local dynamics of nanostructures. © 2002 Optical Society of America

OCIS codes: 320.7100, 320.7130, 320.7150.

1. INTRODUCTION

Enhanced performance in next-generation optoelectronic devices will rely on the development of novel materials and devices such as zero-dimensional semiconductor heterostructures or quantum dots (QDs). In such materials the strong localization of the electronic wave function leads to an atomlike electronic density of states that enables novel photonic devices with tunable optical properties.¹ One type of QD structure is produced by the self-assembly of defect-free QDs during the epitaxial deposition of strained semiconductor layers. Indeed, QD injection lasers made from such self-assembled InAs/GaAs material have exhibited nearly an order of magnitude improvement in performance (for characteristics such as threshold current, linewidth enhancement factor, and tuning range) over structurally similar quantum-well lasers.^{2–4} Further development of these novel materials, particularly for ultrafast-device applications, requires an understanding of their structure-dependent carrier-relaxation mechanisms. To enable such an understanding, special techniques are required that allow the investigation of dynamical properties of individual species on nanometer scales. In recent years, a new scanning probe microscopy technique, ultrafast scanning tunneling microscopy (STM), has been developed, which potentially can satisfy the requirements for high spatial and temporal resolution.^{5,6}

To establish ultrafast STM as a reliable and powerful probe for local dynamics, here we present comparative studies of relatively well understood ultrafast carrier

dynamics in InAs/GaAs self-assembled quantum-dot (SAQD) samples following nonresonant excitation by ~100-fs, 1.5-eV optical pulses. Three complementary ultrafast optoelectronic techniques are used for this study: standard femtosecond optical pump/probe reflectivity measurements, ultrafast microscopy STM, and time-resolved terahertz spectroscopy. These measurements reveal a unified picture of the relaxation dynamics following nonresonant optical excitation in InAs/GaAs SAQDs.

2. SAMPLE PREPARATION

The InAs/GaAs SAQDs are prepared by molecular-beam epitaxy on a 10×10 mm GaAs substrate. Figure 1 shows a section of the structure. After removal of the GaAs oxide by heating at 790 °C, a 200-nm-thick GaAs buffer layer is grown at 590 °C. The sample is then cooled to 510 °C, and an InGaAs layer 2 nm thick is grown. This layer allows the formation of a QD layer with higher density and tends to confine the photogenerated carriers to the QD layer. The QDs are then formed by deposition of 2.4 monolayers (MLs) of InAs at 510 °C. An STM image of the SAQD reveals a QD density of $2.7 \times 10^{10} \text{ cm}^{-2}$ and an average diameter for the dots of ~40 nm, consistent with previous observations.^{7,8} A thin (1.5 MLs) InAs wetting layer (WL) forms underneath the QD's (see Fig. 1). The height of a QD is estimated to be 3 nm.

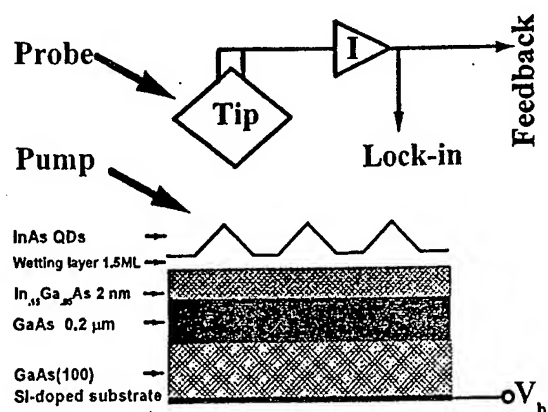


Fig. 1. Experimental setup for photoconductively-gated scanning tunneling microscopy of the InAs/GaAs self-assembled quantum dots.

3. FEMTOSECOND OPTICAL PUMP/PROBE REFLECTIVITY MEASUREMENTS

Standard femtosecond optical pump/probe reflectivity measurements are performed on the sample, where differential detection of the probe is implemented to enhance sensitivity. A comparison of the results of these measurements at 1.5 eV and a photoexcitation fluence of 40 $\mu\text{J}/\text{cm}^2$ is shown in Fig. 2(a) for both the SAQD sample (dotted curve) and a bare GaAs substrate (solid curve), where the differential reflectivity $\Delta R(t)$ is plotted versus pump-probe delay. For the GaAs sample, two decay processes are present in the dynamics. $\Delta R(t)$ first peaks to a positive value near zero delay and then exponentially decays to about half this initial value with $\tau_1 = 1.5$ ps. This rapid process is followed by a much slower relaxation with $\tau_2 \sim 2$ ns. The fast process corresponds to the creation of a nonthermal carrier distribution following optical excitation that rapidly thermalizes, while the slow process results from the recombination of carriers.⁹

The carrier-relaxation dynamics for the SAQD sample is qualitatively different from the trace for the GaAs dynamics. A decrease in $\Delta R(t)$ upon photoexcitation is followed by a rapid increase to a positive peak in $\Delta R(t)$ at a pump-probe delay of 7 ps. The width of the negative peak is 0.6 ps (much greater than the 0.1-ps optical pulse width); therefore this feature is not a coherent artifact. A slow-relaxation process, similar to that seen in the GaAs data, then ensues. Although the slow-relaxation process corresponds to carrier recombination, the non-monotonic signature of the fast process cannot result from carrier thermalization. Further, Fig. 2(b) reveals the dynamics in the 0–20-ps range (ΔR versus pump-probe delay) for excitation over a range of pump/probe wavelengths (at the same excitation fluence as used for the 1.5-eV data), demonstrating that qualitatively similar features are observed with different amplitudes as the photon energy is varied. Note that the negative peak disappears above 875 nm (1.416 eV). The bandgap of the InAs wetting layer is reported to be near 1.443 eV;¹⁰ however, in our case the WL is thicker than the WL used in Ref. 10, so the gap energy should be smaller and can have a value of ~ 1.42 eV. These two facts, along with the fact that this signal does not resemble the thermalization dynamics in GaAs, allow us to attribute the initial decrease

of the reflectivity to a bleaching process in the InAs wetting layer.¹¹ Therefore we attribute the absence of the negative peak in the reflectivity signal to the transition from nonresonant excitation to resonant excitation of the quantum dots, where the carrier-capture process is no longer relevant. The rising edge in the differential reflectance spectra can be attributed to carrier trapping by the InAs QDs from the substrate.^{12,13} Since electrons and holes have different capture dynamics, it is necessary to fit this rise to a two-exponential process.^{10,14} The longer component corresponds to hole capture, and the shorter component reveals the electron capture time. Results of this two-component fit for different pump-probe wavelengths are presented in Fig. 3. Note that the capture time for holes increases monotonically with wavelength, unlike the capture time for electrons, which, taking into account our temporal resolution of ~ 0.2 ps, remains almost unchanged from 800 to 890 nm. In order to further interpret the reflectivity dynamics in the SAQD sample, we employ two other ultrafast optoelectronic techniques, ultrafast STM and ultrafast optical-pump/THz-probe spectroscopy. These techniques are less standard than conventional optical pump/probe reflectivity;

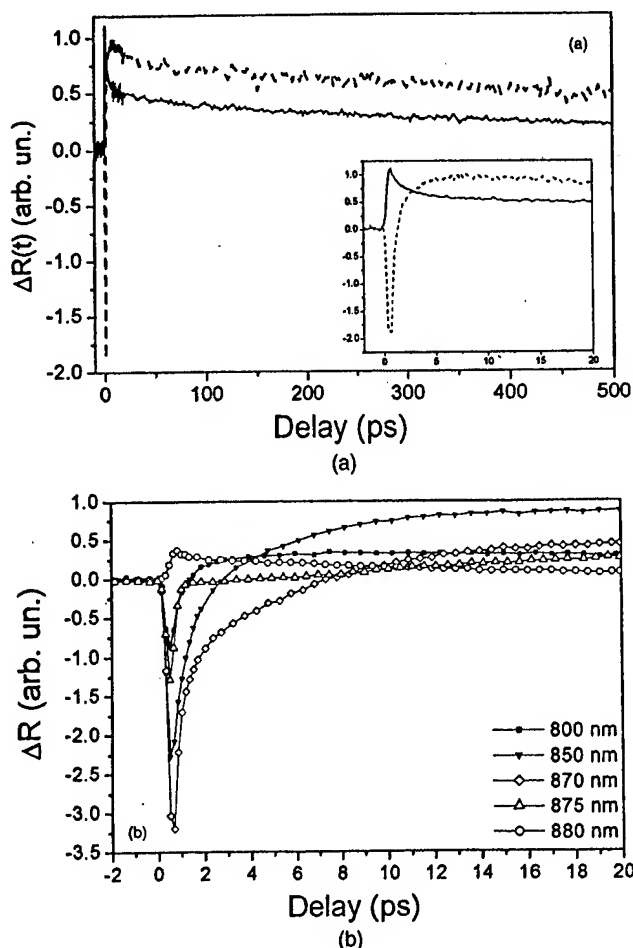


Fig. 2. (a) Differential reflectance signals for the InAs SAQD (dashed curve) and for the bare GaAs substrate (solid curve) at 300 K. The inset emphasizes the initial dynamics of these materials at the energy fluence of 40 mJ/cm^2 . (b) Differential reflectance spectra for the InAs SAQD taken at different laser wavelengths.

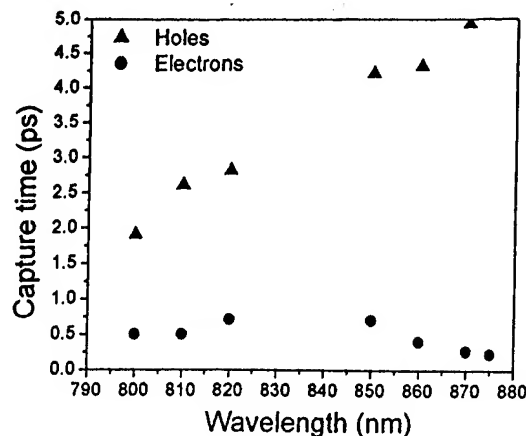


Fig. 3. Dependence of the capture time on the pump-probe wavelength, obtained by fitting the curves presented in Fig. 2(b).

however, they allow more direct access to low-energy carrier dynamics.

4. ULTRAFAST SCANNING TUNNELING MICROSCOPY MEASUREMENTS

The experimental setup for the ultrafast STM, also shown in Fig. 1, is based on a semiconductor STM tip that photoconductively gates the tunneling signal with picosecond temporal resolution. Using low-temperature-grown GaAs with an ~ 1 -ps carrier lifetime as the tip material, we have demonstrated simultaneous 2-ps/20-nm resolution with this technique, described in detail in Ref. 15. Briefly, ~ 120 -fs, 800-nm pulses from a Ti:sapphire oscillator (82-MHz repetition rate) are split into an excitation (pump) pulse and a temporally delayed gating (probe) pulse. The pump pulse excites the surface area of the SAQD sample beneath the STM tip. The probe pulse excites the STM tip. The pump and probe beams have average powers of 60 mW and 20 mW, respectively. These beams are focused to 20- μm -diameter spots, resulting in a pump fluence of 40 $\mu\text{J}/\text{cm}^2$. The pump beam is modulated at 45 kHz to prevent the STM feedback loop from following the modulation. The STM used in this experiment is a model UHV-300 from RHK Technology, Troy, Michigan. All of the STM measurements are performed in a vacuum of $\sim 10^{-8}$ Torr at room temperature.

The STM tip is positioned above an InAs QD or above the InAs WL between dots. Measurement of the tunneling current at different time delays between pump and probe beams yields a transient signal, $\Delta I(t)$. These data are taken at a bias voltage, $V_b = 3$ V and a tunneling current, $I_t = 1$ nA. In Fig. 4(a), $\Delta I(t)$ from the ultrafast STM on top of the SAQD and WL are plotted as a function of pump-probe delay (triangles) for 1.5 eV excitation. The signal from the WL simply represents excitation and recombination dynamics of the carriers inside the layer following the optical pulse, as expected for a photoexcited semiconductor. However, as can be seen from the picture, there is a negative peak in the signal from the SAQD (this peak corresponds to a value for ΔI of -40 pA). In order to determine whether the negative peak in the tunneling current describes a real process, not the capacitively coupled derivative of this process, we use the modified model of Groeneveld and van Kempen¹⁶ to calculate the transient tunneling current from a GaAs substrate with a 100-ps carrier lifetime. The results of this calculation reveal no sign of the negative peak observed in the tunneling signal.

Superimposed on $\Delta I(t)$ in Fig. 4(b) is a scaled version of $\Delta R(t)$ (squares, also for 1.5-eV excitation). The two curves lie on top of one another, except near zero delay, where $\Delta I(t)$ is broadened relative to $\Delta R(t)$ due to the lower (~ 1 -ps) resolution of the ultrafast STM.¹⁵ [The width of the negative peak in $\Delta R(t)$ is 0.6 ps, but it is 1.6 ps in $\Delta I(t)$.] Given the nearly identical shapes of $\Delta I(t)$ and $\Delta R(t)$, it is reasonable to assume that the two techniques probe the same processes.

The initial carrier relaxation in InAs/GaAs SAQDs is believed to proceed by carrier capture from the wetting layer to the QD.^{10,14,17} The strain distribution around the QDs leads to a lateral potential for electrons and holes in the vicinity of a QD, as depicted in Fig. 5. The potential for holes has a barrier that impairs the transfer of a hole from the wetting layer into the QD.¹⁸ However, a hole can be captured by the QD through the Auger effect.^{14,17} At the same time, the strain only weakly influences the electrons, and the potential for electrons drops monotonically. It follows from $\Delta I(t)$ and $\Delta R(t)$

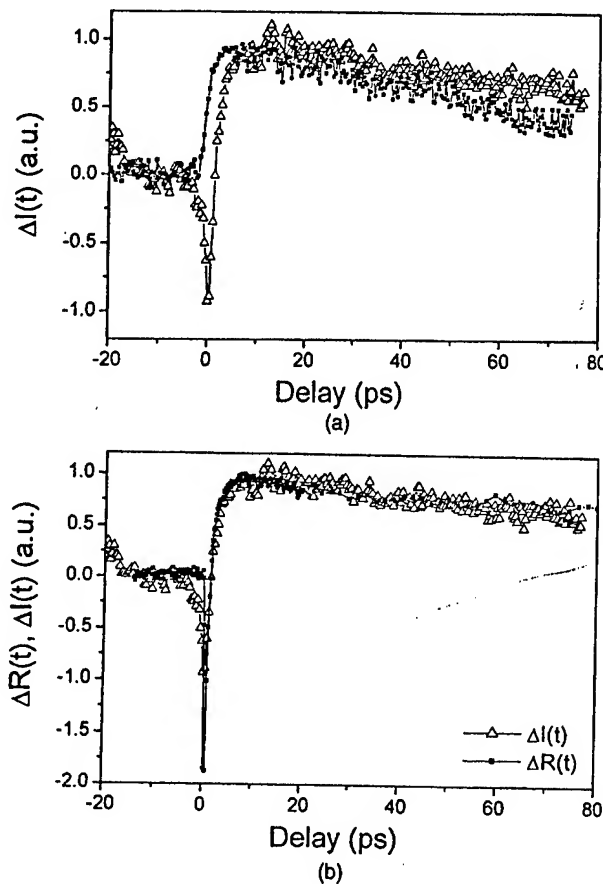


Fig. 4. (a) Transient tunneling signals from the InAs SAQD (open triangles) and InAs WL (solid squares) taken at $U_b = 3$ V and $I_t = 1$ nA. (b) Transient tunneling signal from the InAs SAQD taken at $V_b = 3$ V and $I_t = 1$ nA (open triangles) is plotted together with the differential reflectance signal at 800 nm (solid squares).

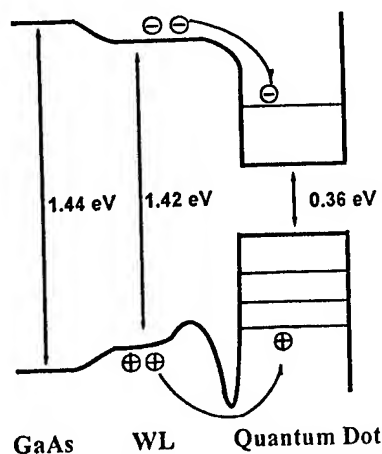


Fig. 5. Lateral potential of the InAs SAQD structure at $T = 300$ K. Close to the edges of the QD, a barrier is present for holes due to the strong influence of the strain on the hole system.¹⁸

that several hundred femtoseconds after excitation, electrons from the wetting layer are captured by the QD. This process negatively charges the QD, effectively reducing the positive bias applied to the sample and resulting in a negative peak in $\Delta I(t)$. Subsequently (~ 1.9 ps later), holes are captured from the wetting layer via an Auger mechanism,^{10,14} making the QD neutral again and increasing $\Delta I(t)$. However, now there are excess carriers in the QD, so its conductivity is higher than it was before excitation, and therefore $\Delta I(t)$ becomes positive. At this stage electron-hole recombination becomes the dominant relaxation process, and both $\Delta I(t)$ and $\Delta R(t)$ decay with a recombination time of $\tau_2 = 890$ ps.

The presence of the interface potential barrier for the hole subsystem and its absence for the electron subsystem may explain the different behavior of the dependence of the carrier-capture time on pump wavelength, revealed in Fig. 3. When the excitation energy decreases, holes in the wetting layer require a larger energy to jump over the barrier. The necessary amount of energy can be transferred to the holes in the wetting layer from the holes in the QD through Auger relaxation. Thus at lower pump photon energy, participation of the higher, less populated, quantum-dot states is necessary for carrier capture to occur. Since the probability of the Auger energy transfer decreases with decreasing number of available carriers, the capture time for holes will increase with pump wavelength. Electrons do not require an energy-transfer mechanism because there is no barrier for the electron subsystem in this structure, so they are captured with a rate that is almost independent of excitation wavelength.

5. TIME-RESOLVED TERAHERTZ SPECTROSCOPY

A final technique for the investigation of the ultrafast carrier dynamics in the SAQD structure is time-resolved terahertz spectroscopy (TRTS). Terahertz (THz) time-domain spectroscopy is an ultrafast optical technique in which nearly single-cycle, free-space electric field tran-

sients are used to measure the complex conductivity σ of a material.¹⁹ The electrical pulses contain Fourier components from ~ 100 GHz to several THz (0.4–15 meV) making them an ideal source for probing carrier transport in semiconductors.²⁰ The THz pulses are derived from 100-fs optical pulses, and therefore the optical and THz pulses are synchronized temporally. Thus using TRTS, a sample is optically excited and then probed with the THz pulse as a function of time delay between the optical (pump) and THz (probe) pulses to measure the induced conductivity change on an ultrafast time scale.^{21,22}

TRTS distinguishes the dynamics of carriers in the conductive n -doped GaAs substrate from the dynamics in the nonconductive QDs. Curve (1) in Fig. 6 presents the results from a TRTS experiment on the SAQD sample, at a 1.5-eV excitation of $10 \mu\text{J}/\text{cm}^2$ (lower than the $40\text{-}\mu\text{J}/\text{cm}^2$ fluence used for the other measurements). We plot in Fig. 6 the induced terahertz transmission change $\Delta T(t)$ (for frequencies in the range 0.4–2.0 THz) versus pump-probe delay. These changes in transmission are due to changes in conductivity of the sample because $T(t) \approx 1/\sigma(t)$. There are several processes contributing to $\Delta\sigma(t)$. Immediately following excitation, $\Delta\sigma(t)$ rises due to the conductivity of photoexcited carriers in GaAs substrate, the $\text{In}_{0.15}\text{Ga}_{0.85}\text{As}$ layer, and the wetting layer. The recombination time for carriers in the GaAs substrate is ~ 2 ns, and therefore its contribution to the signal on the time scale of Fig. 6 is essentially constant. (Since the $\text{In}_{0.15}\text{Ga}_{0.85}\text{As}$ layer has a composition close to GaAs, we assume that its recombination time is also >1 ns, and therefore its conductivity does not relax significantly over the time scale of this scan.)

Two distinct relaxation processes are evident over this 30-ps scan: a fast component relaxing within several picoseconds after excitation and a much slower process occurring on an ~ 100 -ps time scale. The fast process is due to carrier capture by QDs, removing carriers from the conductive layers and reducing $\Delta\sigma(t)$. The QDs act as traps in conventional bulk semiconductors, reducing the conductivity of depleted layers (the GaAs substrate, the InGaAs layer, and the InAs wetting layer). The measured decay time (~ 2 ps) is comparable to the capture

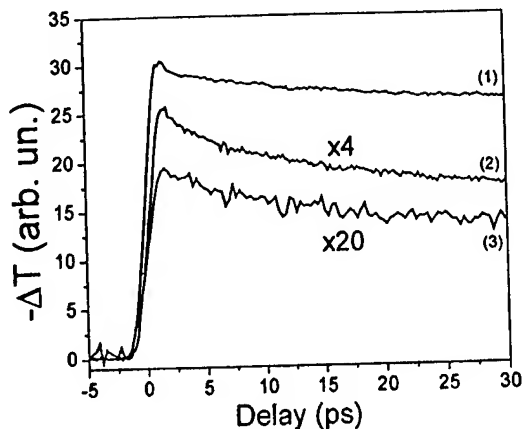


Fig. 6. Differential terahertz transmission through the InAs/GaAs SAQD excited with pump fluences of (1) $10 \mu\text{J}/\text{cm}^2$, (2) $1 \mu\text{J}/\text{cm}^2$, and (3) $0.1 \mu\text{J}/\text{cm}^2$. Curve (2) is multiplied by 4 and curve (3) is multiplied by 20.

times we measure with ultrafast STM and induced reflectivity measurements, although slightly longer, both because the temporal resolution of this technique is lower (~ 1 ps) and because of the lower fluence used here ($10 \mu\text{J}/\text{cm}^2$ versus $40 \mu\text{J}/\text{cm}^2$), since the Auger carrier-capture time decreases rapidly with increasing fluence. Indeed, Fig. 6 reveals $\Delta\sigma(t)$ at lower fluences [(2) $1 \mu\text{J}/\text{cm}^2$, (3) $0.1 \mu\text{J}/\text{cm}^2$], where the fast-relaxation process becomes slower with decreasing pump power. Finally, the slow component in $\Delta\sigma(t)$ has a $1/e$ recovery time of ~ 350 ps. We attribute this process to recombination of carriers in the wetting layer (1.5 MLs in our case, ~ 0.9 nm). This value is very close to the carrier lifetime of 270 ps measured in Ref. 14 for a 1.2-MLs InAs wetting layer.

6. SUMMARY AND CONCLUSIONS

In summary, we have investigated the ultrafast carrier dynamics in InAs/GaAs self-assembled quantum-dot samples using three ultrafast techniques: standard femtosecond optical pump/probe reflectivity measurements, ultrafast scanning tunneling microscopy, and time-resolved terahertz spectroscopy. These measurements reveal a unified picture of the relaxation dynamics, which demonstrates that, although most of the experiments with ultrafast STM have investigated carrier dynamics on metallic transmission lines and surfaces of bulk semiconductors, the application of ultrafast STM to investigate dynamics of the mesoscopic structures is both feasible and promising.

ACKNOWLEDGMENTS

This research is supported by the Los Alamos Directed Research and Development Program by the U.S. Department of Energy.

*Corresponding author's e-mail address: ttaylor@lanl.gov.

REFERENCES

1. S. Schmitt-Rink, D. Miller, and D. Chemla, "Theory of the linear and nonlinear optical properties of semiconductor microcrystallites," *Phys. Rev. B* **35**, 8113-8125 (1987).
2. L. F. Lester, A. Stintz, H. Li, T. C. Newell, E. A. Pease, B. A. Fuchs, and K. J. Malloy, "Optical characteristics of $1.24\text{-}\mu\text{m}$ InAs quantum-dot laser diodes," *IEEE Photon. Technol. Lett.* **11**, 931-933 (1999).
3. G. T. Liu, A. Stintz, H. Li, K. J. Malloy, and L. F. Lester, "Extremely low room-temperature threshold current density diode lasers using InAs dots in $\text{In}_{0.15}\text{Ga}_{0.85}\text{As}$ quantum well," *Electron. Lett.* **35**, 1163-1165 (1999).
4. T. C. Newell, D. J. Bossert, A. Stintz, B. A. Fuchs, K. J. Malloy, and L. F. Lester, "Gain and linewidth enhancement factor in InAs quantum-dot laser diodes," *IEEE Photon. Technol. Lett.* **11**, 1527-1529 (1999).
5. S. Weiss, D. F. Ogletree, D. Botkin, M. Salmeron, and D. S. Chemla, "Ultrafast scanning probe microscopy," *Appl. Phys. Lett.* **63**, 2567-2569 (1993).
6. G. Nunes and M. R. Freeman, "Picosecond resolution in scanning tunneling microscopy," *Science* **262**, 1029-1032 (1993).
7. D. Morris and N. Perret, "Carrier energy relaxation by means of Auger processes in InAs/GaAs self-assembled quantum dots," *Appl. Phys. Lett.* **75**, 3593-3595 (1999).
8. K. Yamanaka, K. Suzuki, S. Ishida, and Y. Arakawa, "Light emission from individual self-assembled InAs/GaAs quantum dots excited by tunneling current injection," *Appl. Phys. Lett.* **73**, 1460-1462 (1998).
9. J. Shah, "Ultrafast spectroscopy of semiconductors and semiconductor nanostructures," (Springer, Berlin, 1995), p. 133.
10. F. Adler, M. Geiger, A. Bauknecht, F. Scholz, H. Schweizer, M. H. Pilkuhn, B. Ohnesorge, and A. Forchel, "Optical transitions and carrier relaxation in self-assembled InAs/GaAs quantum dots," *J. Appl. Phys.* **80**, 4019-4026 (1996).
11. D. S. McCallum, X. R. Huang, M. D. Dawson, T. F. Boggess, A. L. Smirl, T. C. Hasenberg, and A. Kost, "Optical nonlinearities and ultrafast charge transport in all-binary InAs/GaAs strained hetero n-i-p-i's," *J. Appl. Phys.* **70**, 6891-6897 (1991).
12. Q. Li, Z. Y. Xu, and W. K. Ge, "Carrier capture into InAs/GaAs quantum dots detected by a simple degenerate pump-probe technique," *Solid State Commun.* **115**, 105-108 (2000).
13. T. S. Sosnowski, T. B. Norris, H. Jiang, J. Singh, K. Kamath, and P. Bhattacharya, "Rapid carrier relaxation in $\text{In}_{0.4}\text{Ga}_{0.6}\text{As}$ /GaAs quantum dots characterized by differential transmission spectroscopy," *Phys. Rev. B* **57**, R9423-R9426 (1998).
14. A. V. Uskov, J. McInerney, F. Adler, H. Schweizer, and M. H. Pilkuhn, "Auger carrier capture kinetics in self-assembled quantum dot structures," *Appl. Phys. Lett.* **72**, 58-60 (1998).
15. G. P. Donati, G. Rodriguez, and A. J. Taylor, "Ultrafast, dynamical imaging of surfaces by use of a scanning tunneling microscope with a photoexcited, low-temperature-grown GaAs tip," *J. Opt. Soc. Am. B* **17**, 1077-1083 (2000).
16. R. H. M. Groeneveld and H. van Kempen, "The capacitive origin of the picosecond electrical transients detected by a photoconductively gated scanning tunneling microscope," *Appl. Phys. Lett.* **69**, 2294-2296 (1996).
17. R. Ferreira and G. Bastard, "Intra-dot Auger relaxation in quantum dots," *C.R. Acad. Sci., Ser. IIB: Mec. Phys. Chim. Astron.* **327**, 901-906 (1999).
18. M. Grundmann, O. Stier, and D. Bimberg, "InAs/GaAs pyramidal quantum dots: strain distribution, optical phonons, and electronic structure," *Phys. Rev. B* **52**, 11969-11981 (1995).
19. M. C. Nuss and J. Orenstein, "Terahertz time-domain spectroscopy," in *Millimeter and Submillimeter Wave Spectroscopy of Solids*, G. Gruner, ed. (Springer-Verlag, Berlin, 1998), pp. 7-50.
20. T. I. Jeon and D. Grischkowsky, "Nature of conduction in doped silicon," *Phys. Rev. Lett.* **78**, 1106-1109 (1997).
21. R. D. Averitt, G. Rodriguez, J. L. W. Siders, S. A. Trugman, and A. J. Taylor, "Conductivity artifacts in optical-pump THz-probe measurements of $\text{YBa}_2\text{Cu}_3\text{O}_{7-x}$," *J. Opt. Soc. Am. B* **17**, 327-331 (2000).
22. R. D. Averitt, G. Rodriguez, A. I. Lobad, J. L. W. Siders, S. A. Trugman, and A. J. Taylor, "Nonequilibrium superconductivity and quasiparticle dynamics in $\text{YBa}_2\text{Cu}_3\text{O}_{7-\Delta}$," *Phys. Rev. B* **63**, 140502/1-4 (2001).

confinement layer. The precisely defined laser diameter, the small index difference between the mesa and the burying material, the SI properties and the efficient heat removal provided by the regrown material, make this technique very promising for high-speed singlemode VCSEL fabrication.

Acknowledgment: The authors would like to thank F. Salomonsen and R. Stevens for their support in the characterisation tasks, and the Swedish National Board for Industrial and Technical Development (NUTEK) for their financial support, within the framework of KOFUMA project.

© IEE 2000
Electronics Letters Online No: 20001082
 DOI: 10.1049/el:20001082

C. Angulo Barrios, E. Rodríguez Messmer and S. Lourduoss
 (Department of Electronics, Laboratory of Semiconductor Materials,
 Royal Institute of Technology, KTH-Electrum 229, S-16440 Kista,
 Sweden)

E-mail: carlos@ele.kth.se

C. Carlsson, J. Halonen and A. Larsson (Department of
 Microelectronics ED, Photonics Laboratory, Chalmers University of
 Technology, S-41296 Göteborg, Sweden)

A. Risberg and M. Ghisoni (Mitel Semiconductor AB, Optoelectronic
 BU, Box 520, 175 26 Järfälla, Sweden)

References

- IGA, K., KOYAMA, F., and KINOSHITA, S.: 'Surface emitting semiconductor lasers', *IEEE J. Quantum Electron.*, 1988, 24, pp. 1845-1855
- CHANG-HASNAIN, C.J., WU, Y.-A., LI, G.S., HASNAIN, G., CHOQUETTE, K.D., CANEAU, C., and FLOREZ, L.T.: 'Low threshold buried heterostructure vertical cavity surface-emitting laser'. Conf. Lasers and Electro-Optics, Tech. Dig. Ser., 1993, Vol. 11, pp. 136-138
- YOO, B.-S., CHU, H.-Y., PARK, H.-H., LEE, H.-G., and LEE, J.: 'Transverse mode characteristics of vertical-cavity surface-emitting lasers buried in amorphous GaAs antiguide layer', *IEEE J. Quantum Electron.*, 1997, 33, pp. 1794-1800
- LOURDUOSS, S., HOLZ, R., KJEBON, O., and LANDGREN, G.: 'Iron doped GaInP for selective regrowth around GaAs mesas', *J. Crystal Growth*, 1995, 154, pp. 410-414
- ANGULO BARRIOS, C., RODRIGUEZ MESSMER, E., HOLMGREN, M., and LOURDUOSS, S.: 'Semi-insulating GaInP:Fe and GaAs:Fe regrowth around GaAs/AlGaAs laser mesas', 3rd Int. Conf. Materials for Microelectronics, Dublin, Ireland, 2000
- GAARDER, A., ANGULO BARRIOS, C., RODRIGUEZ MESSMER, E., LOURDUOSS, S., and MARCINKEVICIUS, S.: 'Dopant distribution in selectively regrown InP:Fe and InGaP:Fe studied by time-resolved photoluminescence', 12th Int. Conf. InP and Related Materials, Williamsburg, USA, 2000

Low-threshold quantum dot lasers with 201nm tuning range

P.M. Varangis, H. Li, G.T. Liu, T.C. Newell, A. Stintz, B. Fuchs, K.J. Malloy and L.F. Lester

A grating-coupled external-cavity quantum dot laser is tuned across a 201nm range at a maximum bias of 2.87kA/cm², one order of magnitude less than the bias required for comparable tuning of quantum well lasers. The tuning range increases for higher cavity losses of the quantum dot laser.

Widely tunable semiconductor lasers will be essential components of high-capacity wavelength-division-multiplexed transmission and photonic switching systems. External-cavity configurations employing a grating as a dispersive feedback element have enabled tuning of quantum well (QW) lasers across 105nm at $\lambda = 0.8\mu\text{m}$ [1], and 240nm at $\lambda = 1.5\mu\text{m}$ [2], for injection current densities of 21 and 33kA/cm², respectively. This high bias is necessary to achieve lasing from the second quantised state of the QW and

In contrast to QW lasers, quantum dot (QD) emitters are well-suited for use as low-threshold, broadband tunable sources owing to two unique features of QD structures [3]. First, the low QD density of states causes the QD ground state optical gain to saturate easily. This means that the higher-order energy levels are populated by carriers at fairly low current densities of $\sim 1\text{kA/cm}^2$. Secondly, due to homogeneous and inhomogeneous broadening, continuous coverage of the wavelength spectrum is possible. The dot size variation, which is normally undesirable for low-threshold operation, can be exploited to extend the tuning range towards the shorter wavelength side.

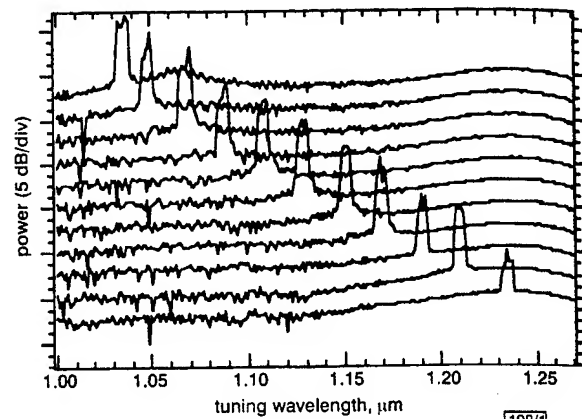


Fig 1 Lasing spectra of external-cavity QD laser, tuned across the 1033-1234nm wavelength range

In this Letter a 201nm tuning range in a grating-coupled external-cavity quantum dot laser is demonstrated and its variation as a function of the cavity losses of the internal Fabry-Perot (FP) laser is investigated. The maximum bias is 400mA (2.87kA/cm²), which is approximately 10 times lower than the bias required for tuning QW lasers across similar ranges. Fig. 1 shows the 201nm-lasing spectrum (1033-1234nm) obtained with a QD device arranged in a Littrow external-cavity configuration. Across the 201nm range, the lasing peak is $\sim 20\text{dB}$ higher than the spontaneous emission spectrum. The laser active region is composed of a single InAs quantum dot layer confined in the middle of a 10nm-thick In_{0.2}Ga_{0.8}As QW and sandwiched by GaAs waveguide layers [4]. Details of the crystal growth are described in [5]. The laser has a 9 μm -wide ridge waveguide and the cavity is 1.7mm long. A single $\lambda/4$ antireflection layer of HfO₂ is deposited on one of the laser facets by electron-beam evaporation, and the other facet remains as-cleaved. A residual reflectivity of the AR-coated mirror is $\sim 1\%$ at the free-running lasing wavelength of $\lambda = 1.05\mu\text{m}$ (second excited state). The AR coating increases the total cavity loss and completely extinguishes lasing at the ground state ($\lambda = 1.24\mu\text{m}$) and the first excited state ($\lambda = 1.15\mu\text{m}$).

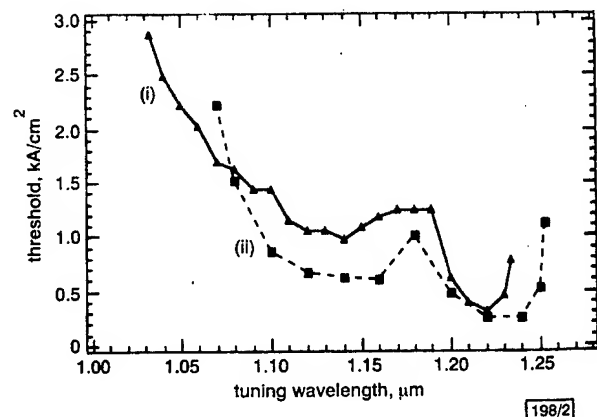


Fig 2 Threshold current density against lasing wavelength across the tuning range for different cavity lengths L

- (i) 1.7mm
- (ii) 2.0mm

Comparison of (i) and (ii) in Fig. 2 compares the threshold current den-

and 2mm, respectively. The device structure and external-cavity configuration are the same for both lasers. Since both devices have the same AR coating, the free-running loss of the 1.7mm-long device is larger than the 2mm device owing to the shorter cavity length. It is known that as the pump level increases, the modal gain will increase and the gain peak will shift to the higher energy transitions. As a consequence, the free-running lasing wavelength and threshold current are $\lambda = 1.05\mu\text{m}$, $J_{th} = 3.46\text{kA/cm}^2$ for the 1.7mm-long device, and $\lambda = 1.09\mu\text{m}$, $J_{th} = 2.83\text{kA/cm}^2$ for the 2mm-long device.

Fig. 2 shows that a judicious increase in the internal FP cavity loss yields a broader tuning range. The 1.7mm-long laser can be tuned across 201nm ($\lambda = 1033\text{--}1234\text{nm}$) compared to 183nm ($\lambda = 1070\text{--}1253\text{nm}$) for the 2.0mm-long emitter, at the expense, however, of the maximum threshold current density. For constant mirror reflectivities, the technique of increasing the internal FP loss to expand the tuning range can be motivated as follows: as long as the external cavity loss does not exceed the ground-state saturated gain, then shortening the internal FP cavity length does not sacrifice tuning on the long-wavelength side. This condition puts a lower limit on the laser diode cavity length. To extend the tuning to shorter wavelengths, higher pump is required which means the internal FP losses must be increased to prevent free-running lasing. On the short wavelength end, the grating-forced operation can only suppress the internal FP within $\sim 20\text{nm}$ of the free-running wavelength by means of homogeneous broadening [6]. Further tuning to shorter wavelengths and an increase in the pump cause simultaneous free-running and grating-selected lasing. This situation defines the limit to the tuning range at the short wavelength end.

A tuning range of 201nm in a grating-coupled external-cavity QD laser for maximum bias of 2.87kA/cm^2 has been demonstrated. Similar tuning ranges in QW lasers require current densities higher by an order of magnitude. Further extension of the tuning range could be achieved by designing a QD with a deeper potential well, a smaller size, and a broader size distribution. This approach would enlarge the energy separation between the various states in the QD and minimise the local increases in threshold current.

Acknowledgments: This work was supported by the Defense Advanced Research Projects Agency under Grant MDA972-98-1-0002 and by the US Air Force Office of Scientific Research under Grant F49620-96-1-0077.

© IEE 2000

Electronics Letters Online No: 20001080

DOI: 10.1049/el:20001080

P.M. Varangis, H. Li, G.T. Liu, T.C. Newell, A. Stintz, B. Fuchs, K.J. Malloy and L.F. Lester (Center for High Technology Materials, University of New Mexico, 1313 Goddard SE, Albuquerque, NM 87106, USA)

E-mail: petrosva@chtm.unm.edu

References

- MEHUY, D., MITTELSTEIN, M., YARIV, A., SARFATY, R. and UNGAR, J.E.: 'Optimized Fabry-Perot (AlGa)As quantum-well lasers tunable over 105nm'. *Electron. Lett.*, 1989, 25, (2), pp. 143-145
- TABUCHI, H. and ISHIKAWA, H.: 'External grating tunable MQW laser with wide tuning range of 240nm'. *Electron. Lett.*, 1990, 26, (11), pp. 742-743
- LI, H., LIU, G.T., VARANGIS, P.M., NEWELL, T.C., STINTZ, A., FUCHS, B., MALLOY, K.J. and LESTER, L.F.: '150nm tuning range in a grating-coupled external-cavity quantum dot laser', to appear in *IEEE Photonics Technol. Lett.*, 2000
- LESTER, L.F., STINTZ, A., LI, H., NEWELL, T.C., PEASE, E.A., FUCHS, B. and MALLOY, K.J.: 'Optical characteristics of 1.24μm InAs quantum dot laser diodes'. *IEEE Photonics Technol. Lett.*, 1999, 11, (8), pp. 931-933
- STINTZ, A., LIU, G.T., GRAY, A.L., SPILLERS, R., DELGADO, S.M. and MALLOY, K.J.: 'Characterization of InAs quantum dots in strained In_{0.53}Ga_{0.47}As quantum wells'. *J. Vac. Sci. Technol.*, 2000, B18, (3), pp. 1496-1501
- ELISSEV, P., LI, H., STINTZ, A., LIU, G.T., NEWELL, T.C., MALLOY, K.J. and LESTER, L.F.: 'Tunable grating-coupled laser oscillation and spectral hole burning in an InAs quantum-dot laser diode'. *IEEE J. Quantum Electron.*, 2000, 36, (4), pp. 479-485

cryogenic vertical cavity lasers

H.X. Shi, D.A. Cohen, D. Lofgreen and L.A. Coldren

The noise and linearity properties of oxide-apertured vertical cavity lasers optimised for low-power cryogenic operation is reported. The relative intensity noise is lower than -140dB/Hz , and the spur-free dynamic range is between $90\text{--}100\text{dB}\cdot\text{Hz}^{2/3}$.

Introduction: Infrared focal plane arrays operating at cryogenic temperatures must transmit wide bandwidth data outside of their cryostat with minimal power dissipation. The high speed, high efficiency, and low power consumption of oxide-apertured vertical cavity lasers (VCLs) make them promising candidates for this application [1, 2]. An analogue data format avoids the power consumption of an analogue-to-digital converter, and is often used. In this case, a signal-to-noise ratio $> 60\text{dB}$ must be maintained for transmission of high-fidelity images [3]. While the noise and distortion in VCLs operating at room temperature have been reported previously [4], these properties may be different when the lasers are optimised for low-power operation. In particular, does the laser relative intensity noise (RIN) remain low enough so that the system remains shot-noise limited, and does the dynamic range at low bias current remain high? The results reported here indicate that they do.

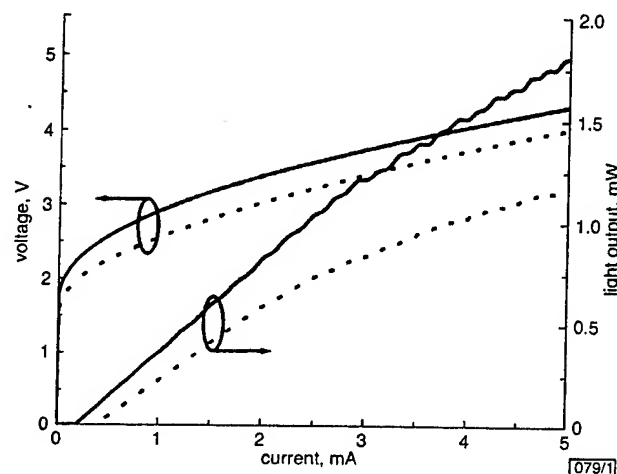


Fig. 1 L-I-V characteristics for 5.4μm diameter 940nm VCL at 120 and 297K

— 120K
..... 297K

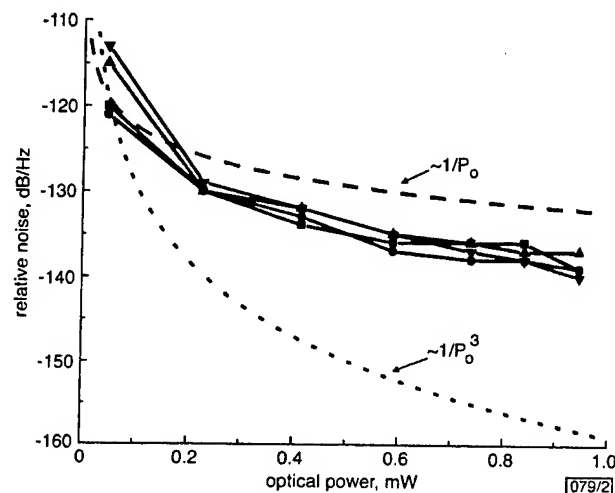


Fig. 2 Link noise against DC optical power

● 0.5GHz
■ 1.0GHz
▲ 1.5GHz
▼ 2.0GHz

The approximate $1/P_0$ dependence indicates the system is shot-noise limited

external quantum efficiency $\eta_i \approx 100\%$ [2], the η_d for the 2mm DFB laser was calculated to be $\sim 51\%$, which is in good agreement with the measured η_d value of 52%.

The wavelength of the DFB laser changes at a rate of $0.7\text{\AA}/^\circ\text{C}$. due to the mode index variation with temperature. The 2mm-long DFB laser maintains a narrow spectrum (0.5\AA) to 0.5W . This narrow spectral width is predominantly due to simultaneous oscillation of many lateral spatial modes sharing the same longitudinal mode number [1]. Beyond $\sim 0.5\text{W}$ CW, oscillation at a second longitudinal resonance occurs, which causes spectral broadening such that at 1W the spectral width is 1.3\AA FWHM.

As the coupling coefficient κ is low ($\sim 2\text{cm}^{-1}$), a more uniform longitudinal field profile is obtained from 2mm-long devices than from 1mm-long devices. Better uniformity of the longitudinal field suppresses the onset of multi-longitudinal-mode operation at high power levels. Thus, while 2mm-long devices have FWHM spectra of only 0.5\AA to 0.5W (i.e. single-longitudinal-mode operation), 1mm-long devices can be operated in a single longitudinal mode to only 0.2W CW. Narrow-spectrum operation to higher CW powers can be obtained by either making longer cavity devices or by increasing the grating coupling coefficient in order to obtain a κL product value close to 1, which in turn enables single-longitudinal-mode operation to Watt-range powers [1] to be obtained.

In conclusion, high CW power (1W), narrow-spectral-width, efficient operation of diode lasers has been achieved at 980nm by using long, $100\text{-}\mu\text{m}$ -stripe devices with regrowth over gratings in Al-free material.

© IEE 2000

Electronics Letters Online No: 20000692

DOI: 10.1049/el:20000692

C.H. Chang, T. Earles and D. Botez (Reed Center for Photonics, University of Wisconsin-Madison, 1415 Engineering Dr., Madison, WI 53706, USA)

20 March 2000

References

1. EARLES, T., MAWST, L.J., and BOTEZ, D.: '1.1W continuous-wave, narrow spectral width ($<1\text{\AA}$) emission from broad-stripe, distributed-feedback diode lasers ($\lambda = 0.897\text{\mu m}$)'. *Appl. Phys. Lett.*, 1998, 73, (15), pp. 2072-2074
2. AL-MUHANNA, A., MAWST, L.J., BOTEZ, D., GARBUSOV, D.Z., MARTINELLI, R.U., and CONNOLLY, J.C.: 'High-power ($>10\text{W}$) continuous-wave operation from $100\text{-}\mu\text{m}$ -aperture $0.97\text{-}\mu\text{m}$ -emitting Al-free diode lasers'. *Appl. Phys. Lett.*, 1998, 73, (9), pp. 1182-1184
3. MAWST, L.J., BHATTACHARYA, A., LOPEZ, J., BOTEZ, D., GARBUSOV, D.Z., DEMARCO, L., CONNOLLY, J.C., JANSEN, M., FANG, F., and NABIEV, R.F.: '8W continuous wave front-facet power from broad-waveguide Al-free 980nm diode lasers'. *Appl. Phys. Lett.*, 1996, 69, (11), pp. 1532-1534
4. STREIFER, W., SCIFRES, D.R., and BURNHAM, R.D.: 'Coupling coefficients for distributed feedback single- and double-heterostructure diode laser'. *IEEE J. Quantum Electron.*, 1975, QE-11, pp. 876-873
5. SCHATZ, R., BERGLIND, E., and GILLNER, L.: 'Parameter extraction from DFB lasers by means of a simple expression for the spontaneous emission spectrum'. *IEEE Photonics Technol. Lett.*, 1994, 10, pp. 1182-1184

High-power AlGaInAs strained multiquantum well lasers operating at 1.52\mu m

T.C. Newell, P.M. Varangis, E. Pease, A. Stintz, G.T. Liu, K.J. Malloy and L.F. Lester

1.75W CW power in AlGaInAs/InP strained QW lasers is demonstrated. Room temperature threshold current densities are $410\text{A}/\text{cm}^2$, and the characteristic temperature is 69K . The variation in the external differential efficiency with cavity length and temperature reveal the optimum length and show how nonradiative recombination mechanisms limit the performance.

applications of 1.5\mu m lasers, which in the case of AlGaInAs quantum well (QW) devices has traditionally focused on high speed devices for telecommunications. For these low power lasers, the best reported threshold current densities, J_{th} , are 190 to $530\text{A}/\text{cm}^2$ [1, 2], internal efficiencies, η_i , are up to 83% [3], and characteristic temperatures as high as 122K have been measured [4]. Lacking in the AlGaInAs 1.5\mu m laser literature is substantial research on high-power operation, which will expand the usefulness of these devices into applications for which eye-safety is of primary importance [5].

This Letter reports the growth and optical characteristics of compressively strained AlGaInAs 3-QW lasers operating near 1.52\mu m . A room temperature J_{th} of $410\text{A}/\text{cm}^2$ is observed along with a characteristic temperature, T_0 , of 69K , and T_1 of 220K . 1.75W CW single sided emission at 5A current has been obtained before thermal rollover occurs.

Growth: The material structure was grown by molecular beam epitaxy (MBE) using the digital alloy (DA) technique and is described in detail in [6]. Three 80\AA $\text{Al}_{0.08}\text{Ga}_{0.25}\text{In}_{0.6}\text{As}$ QWs were centred in a 1\mu m wide waveguide of $\text{Al}_{0.3}\text{Ga}_{0.18}\text{In}_{0.5}\text{As}$ with 50\AA barriers. The QWs were compressively strained at 0.8% . The material was processed into broad area lasers with a 200\mu m stripe width. The p -side metallisation consists of 500\AA of Ti, 500\AA of Pt, and 2000\AA of Au. The n -side ohmic metal consists of 400\AA of Au, 1500\AA of Ni, and 1000\AA Au. A four-layer high reflectivity (HR) coating was applied by an e-beam dielectric evaporator to select devices. The HR stack consists of alternating $\lambda/4$ -layers of MgF_2 and poly-Si. The deposition was performed at 175°C to improve the adhesion of the coatings to the laser facets.

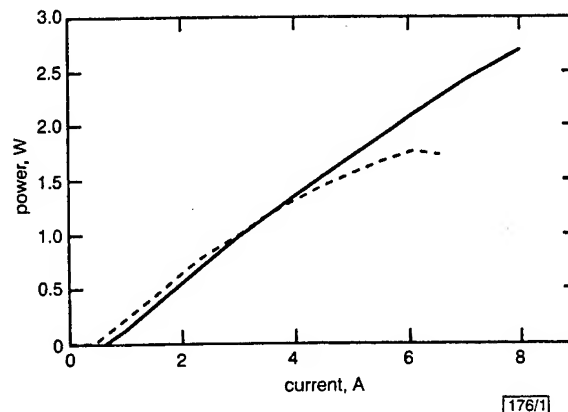


Fig. 1 Pulse and CW light current curves

— pulse
--- CW

Device performance: Individual emitters were mounted p -side down on copper mounts then attached to a thermo-electric cooler for testing. The advantage of the broadened waveguide [7] is that the internal loss, α_i , is only 2cm^{-1} and the injection efficiency, η_i , is 62% . At room temperature, J_{th} is $410\text{A}/\text{cm}^2$ for the best uncoated 1mm cavity length devices. Fig. 1 plots the light against current (LI) curve for a laser that had one facet HR coated with a four-layer stack. The other facet is uncoated and $\sim 85\%$ of the emission is emitted from this facet. CW and pulsed (100\mu s pulses with 5% duty cycle) cases are shown. The heatsink temperature was maintained at -15°C for CW operation and -10°C for pulsed. This cooling was intended to overcome the large thermal generation due to a series resistance of almost 0.1Ω and thermal resistances in the mounting arrangement. The relatively large series resistance is due in part to non-optimal doping in the cladding layers and an imperfect ohmic contact to the InP. At the low temperatures, the threshold currents are 457 and 607mA for the CW and pulsed cases, respectively. In both modes of operation, the slope efficiency is $0.4\text{W}/\text{A}$ although this decreases for CW powers $>1\text{W}$. The maximum power in CW mode is 1.75W , at which point thermal rollover occurs. In pulsed mode, the LI trace is linear to 8A current where the power is 2.7W . Partial damage of the uncoated facet occurred above this current, and catastrophic damage at this

facet destroyed the device at 10A current and 3W power. Passivation of the uncoated facet in order to unpin the Fermi level would enlarge the available pumping range [8].

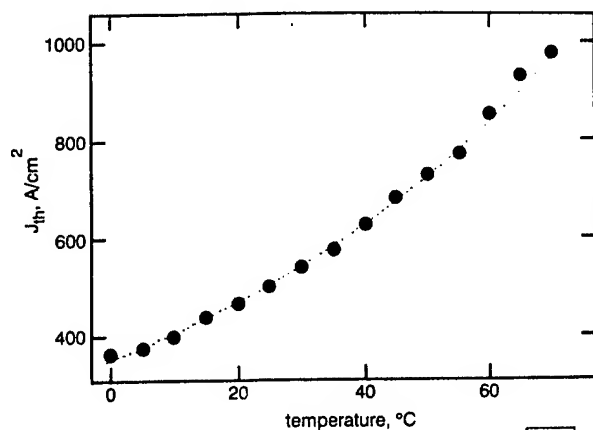


Fig. 2 J_{th} against temperature for pulsed mode operation (0.3μs pulses, 1% duty cycle) yield T_0 of 69K

The thermal issues raised by the high power limits lead to the investigation of the characteristic temperature of the laser, T_0 , and its variation in the slope efficiency with temperature. T_1 ($\eta_{ext}^{-1} = \exp(T/T_1)$). T_0 is obtained from a plot of J_{th} against temperature, which is shown in Fig. 2 for a 1mm laser. The experimental data (solid circles) are well fit by an exponential curve with a T_0 of 69K. The T_1 value is 220K for temperatures up to 65°C but drops substantially at higher temperatures.

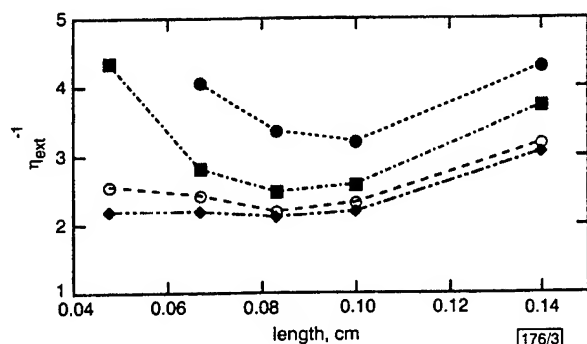


Fig. 3 η_{ext}^{-1} against cavity length of laser

◆ 10°C.
○ 25°C.
■ 40°C.
● 55°C

The relationship between η_{ext}^{-1} and temperature can be examined in more detail by investigating it as a function of the cavity length of the laser. This provides an insight into the optimal cavity length as well as recombination processes occurring in the laser. In Fig. 3, η_{ext}^{-1} against cavity length is plotted for temperatures of 10, 25, 40, and 55°C under pulsed mode operation (0.3μs pulses with a 1% duty cycle). As expected, the longer cavities have a large η_{ext}^{-1} due to the lower mirror losses. For the short cavities, η_{ext}^{-1} also increases. Here the injection current density is necessarily large so that the high mirror losses are overcome and lasing is established. As a result, both the Auger leakage current and a leakage due to thermionic emission of carriers into the QW barriers is increased. The latter process is particularly significant since it is extremely dependent on the carrier temperature, which can be larger than the lattice temperature [9]. Thus, T_0 and T_1 are low (both ~45K) for short cavity lasers. This leakage current problem is particularly severe in 475μm cavity devices, which cannot generate sufficient gain at 55°C to lase below 2A bias current. The optimum cavity length is near 1mm. At this length, not only is the efficiency highest, but its variation with temperature the smallest.

Conclusion: 1.75W CW power has been demonstrated in a 0.8%

power devices that simultaneously generate a large amount of heat, nonradiative processes play a significant role in J_{th} and η_{ext} . Based on the temperature, the optimum cavity length for highest efficiency operation is near 1mm. Here, a T_0 of 69K and a T_1 of 220K have been obtained.

Acknowledgments: This work was supported by the US Army Federated Laboratories program and by the US Air Force Office of Scientific Research (AFOSR) under grant F49620-96-1-0079.

© IEE 2000

Electronics Letters Online No: 20000731

DOI: 10.1049/el:20000731

9 February 2000

T.C. Newell, P.M. Varangis, E. Pease, A. Stintz, G.T. Liu, K.J. Malloy and L.F. Lester (Center for High Technology Materials, University of New Mexico, 1313 Goddard SE, Albuquerque, NM 87106, USA)

References

- EVANS, G.A., SIH, J.P., CHOU, T.M., KIRK, J.B., BUTLER, J.K., and PANG, L.: 'AlGaInAs/InP ridge-guide lasers operating at 1.55μm', *Proc. SPIE*, 1998, Vol. 3284, pp. 205-210
- MONDRY, M.J., CHUANG, Z.M., PETERS, M.G., and COLDREN, L.A.: 'Low threshold current density 1.5μm (In, Ga, Al)As quantum well lasers grown by MBE', *Electron. Lett.*, 1992, 28, (15), pp. 1471-1472
- STEGMULLER, B., BORCHERT, B., and GESSNER, R.: '1.57μm strained-layer quantum-well GaInAlAs ridge-waveguide laser-diodes with high-temperature (130°C) and ultra high speed (17GHz) performance', *IEEE Photonics Technol. Lett.*, 1993, 5, (6), pp. 597-599
- OHNOKI, N., OKAZAKI, G., KOYAMA, F., and IGA, K.: 'Record high characteristic temperature ($T_0 = 122K$) of 1.55μm strain-compensated AlGaInAs/AlGaInAs MQW lasers with AlAs/AlInAs multiquantum barrier', *Electron. Lett.*, 1999, 35, (1), pp. 51-52
- STANN, B.L., RUFF, W.C., and SZTANKAY, Z.G.: 'Intensity-modulated diode laser radar using frequency-modulation/continuous-wave ranging techniques', *Opt. Eng.*, 1996, 35, (11), pp. 3270-3278
- LIU, G.T., STINTZ, A., PEASE, E.A., NEWELL, T.C., MALLOY, K.J., and LESTER, L.F.: '1.58-μm latticed-matched and strained digital alloy AlGaInAs-InP multiple-quantum-well lasers', *IEEE Photonics Technol. Lett.*, 2000, 12, (1), pp. 4-6
- GARBUZOV, D.Z., MARTINELLI, R.U., LEE, H., YORK, P.K., MENNA, R.J., CONNOLLY, J.C., and NARAYAN, S.Y.: 'Ultra-low loss broadened waveguide high-power 2μm AlGaAsSb/InGaAsSb/GaSb separate-confinement quantum-well lasers', *Appl. Phys. Lett.*, 1996, 69, (14), pp. 2006-2008
- VAUGHN, L.G., NEWELL, T.C., LESTER, L.F., and MACINNES, A.N.: 'Characterization of GaS-passivated quantum well lasers', *Mater. Res. Soc. Symp.*, 1999, Vol. 573, pp. 125-130
- LESTER, L.F., and RIDLEY, B.K.: 'Hot carriers and the frequency-response of quantum-well lasers', *J. Appl. Phys.*, 1992, 72, (7), pp. 2579-2588

High frequency permittivity determination by spectra simulation and measurement of microstrip ring resonators

E. Semouchkina, W. Cao and M. Lanagan

The S_{21} spectra of microstrip ring resonators have been measured experimentally and also computed using the finite-difference time-domain (FDTD) method. The dielectric constant of the substrate was determined by fitting the simulation results to the experimental data. The results are more self-consistent than those obtained using the Wheeler-Hammerstad method.

Introduction: The performance of microwave circuits is strongly dependent on the fundamental properties of the substrate and conducting strip materials. Therefore, the development of more accurate material characterisation methods in the microwave range is of great importance. Amey and Horowitz [1] proposed the use of a 'T-pattern' microstrip resonator for determining the permittivity and losses in dielectrics as well as the conductivity of metal layers. They used a relationship between the resonance frequencies and dielectric constant, which was introduced to

loss for diodes with such L was estimated to be as low as $1.2 \pm 0.3 \text{ cm}^{-1}$. The internal quantum efficiency was estimated to be $\sim 75\%$.

The light output power per both facets (P_{out}) as a function of the drive current (I) for the 920 μm -long diode in pulsed and CW regimes are presented in Fig. 3. The heatsink temperature was 10°C . The CW lasing spectra for several values of I are shown inset. The 0.4 A spectrum was taken just above the threshold. The threshold current (I_{th}) was 380 mA, which corresponds to a J_{th} of $\sim 400 \text{ A/cm}^2$. Under pulsed operation the slope efficiency is nearly constant and equals 1.05 W/A ($\eta_d = 73\%$) up to the sudden failure due to catastrophic optical mirror damage (COMD). The CW power-current dependence becomes slightly sublinear beyond 2.5 A due to the heating of the active region, which is accompanied by a slight red-shift of the lasing line. The maximum output power recorded in CW and pulsed regimes is 3.5 and 4.8 W at $I = 4$ and 5 A, respectively. The effective (transverse) mode size [7] was calculated to be $0.41 \mu\text{m}$. The internal density of the optical power at COMD per facet is $\sim 8 \text{ MW/cm}^2$, which is in agreement with the COMD level for InGaAs-based lasers with uncoated facets [7]. The device reaches COMD under pulsed operation at an internal optical power density of 11 MW/cm^2 , which is 40% higher than the COMD level under CW operation.

Fig. 3 shows the current-voltage (I - U_d) characteristic and the calculated conversion efficiency (η_c) for the device under investigation. The specific series resistance (ρ_s) is as low as $1.2 \times 10^{-4} \Omega \text{ cm}^2$ which is one of the best values for AlGaAs-cladded devices [8]. The maximum η_c value of 45% occurs at 2 W.

Conclusion: QD diode lasers with active region based on composite vertically coupled self-organised InAlAs-InAs QDs in an AlGaAs matrix have been fabricated. Room temperature CW operation with a maximum output power of 3.5 W and peak conversion efficiency of 45% has been demonstrated. To the best of our knowledge these are the highest values ever reported for QD lasers of any kind. Thus QD lasers can be used for high-power applications. We believe that further progress can be achieved by optimising both the laser design and the fabrication process.

Acknowledgments: This work is supported by INTAS 96-0467 and BMBF 13 N 7231.

© IEE 1999

Electronics Letters Online No. 19990813

DOI: 10.1049/el:19990813

5 May 1999

A.R. Kovsh, A.E. Zhukov, D.A. Livshits, A.Yu. Egorov, V.M. Ustinov, M.V. Maximov, Yu.G. Musikhin, N.N. Ledentsov, P.S. Kop'ev and Zh.I. Alferov (A.F. Ioffe Physico-Technical Institute, Politekhnicheskaya 26, 194021 St. Petersburg, Russia)

D. Bimberg (Institut für Festkörperphysik, Technische Universität Berlin, D-10623 Berlin, Germany)

References

- 1 KOVSH, A.R., ZHUKOV, A.E., MAKSIMOV, M.V., TSATSUL'NIKOV, A.F., GORDEEV, N.YU., ZAITSEV, S.V., SHERNYAKOV, YU.M., BERT, N.A., KOPEV, P.S., ALFEROV, ZH.I., LEDENTSOV, N.N., BOHRER, J., BIMBERG, D., KOSOGOV, A.O., WERNER, P., and GOSELE, U.: 'Low-threshold injection lasers based on vertically coupled quantum dots', *J. Cryst. Growth*, 1997, **175/176**, pp. 689-695
- 2 HUFFAKER, D.L., PARK, G., ZOU, Z., SHCHEKIN, O.B., and DEPPE, D.G.: '1.3 μm room-temperature GaAs-based quantum-dot laser', *Appl. Phys. Lett.*, 1998, **73**, pp. 2564-2566
- 3 MAXIMOV, M.V., SHERNYAKOV, YU.M., TSATSUL'NIKOV, A.F., LUNEV, A.V., SAKHAROV, A.V., USTINOV, V.M., EGOROV, A.YU., ZHUKOV, A.E., KOVSH, A.R., KOPEV, P.S., ASRYAN, L.V., ALFEROV, ZH.I., LEDENTSOV, N.N., BIMBERG, D., KOSOGOV, A.O., and WERNER, P.: 'High-power continuous-wave operation of a InGaAs/AlGaAs quantum dot laser', *J. Appl. Phys.*, 1998, **83**, pp. 5561-5563
- 4 KOVSH, A.R., ZHUKOV, A.E., EGOROV, A.YU., USTINOV, V.M., SHERNYAKOV, YU.M., MAXIMOV, M.V., VOLOV, B.V., TSATSUL'NIKOV, A.F., MUSIKHIN, YU.V., LEDENTSOV, N.N., KOPEV, P.S., BIMBERG, D., and ALFEROV, ZH.I.: 'MBE growth of composite (In,Al)As/(In,Ga)As vertically coupled quantum dots and their application in injection lasers', *Proc. 10th Int. Conf. MBE, Cannes, France*, 1998

- 6 BIMBERG, D., KRISTAEDER, N., LEDENTSOV, N.N., ALFEROV, ZH.I., KOPEV, P.S., and USTINOV, V.M.: 'InGaAs-GaAs quantum-dot lasers', *IEEE J. Sel. Topics Quantum Electron.*, 1997, **3**, pp. 196-205
- 7 MAWST, L.J., BHATTACHARYA, A., LOPEZ, J., BOTEZ, D., GARBUZOV, D.Z., DEMARCO, L., CONNOLLY, J.C., JANSEN, M., FANG, F., and NABIEV, R.F.: '8 W continuous wave front-facet power from broad-waveguide Al-free 980 nm diode lasers', *Appl. Phys. Lett.*, 1996, **69**, pp. 1532-1534
- 8 O'BRIEN, S., ZHAO, H., SCHOENFELDER, A., and LANG, R.J.: '9.3 W CW (In)AlGaAs 100 μm wide lasers at 970 nm', *Electron. Lett.*, 1997, **33**, pp. 1869-1870

Extremely low room-temperature threshold current density diode lasers using InAs dots in $\text{In}_{0.15}\text{Ga}_{0.85}\text{As}$ quantum well

G.T. Liu, A. Stintz, H. Li, K.J. Malloy and L.F. Lester

The lowest room-temperature threshold current density, 26 A/cm^2 , of any semiconductor diode lasers is reported for a quantum dot device with a single InAs dot layer contained within a strained $\text{In}_{0.15}\text{Ga}_{0.85}\text{As}$ quantum well. The lasers are epitaxially grown on a GaAs substrate, and the emission wavelength is $1.25 \mu\text{m}$.

Introduction: It has been predicted that the threshold current density of quantum dot lasers should be lower than that of quantum well lasers due to the reduction of density of states [1]. In particular, efforts have been made in the past few years to reduce the threshold current density of quantum dot lasers on GaAs substrates [2, 3]. A recently developed approach is to put the InAs dots in a strained $\text{In}_{0.15}\text{Ga}_{0.85}\text{As}$ quantum well [3, 4]. This 'dot in a well' (DWELL) design not only improves carrier capture by the dots, but also increases the density of quantum dots (to $7 \times 10^{10} \text{ cm}^{-2}$) over growth on GaAs directly. Consequently, lasing from a single layer of dots is possible at reasonable cavity lengths. While competition with radiative quantum well transitions was suggested as a concern [5], quantum well transitions were not observed in previous work [3] or in this study. In this Letter, we present further improvements that have been made by putting a single layer of InAs quantum dots into a strained $\text{In}_{0.15}\text{Ga}_{0.85}\text{As}$ quantum well. An extremely low threshold current density of 26 A/cm^2 has been achieved for a 7.8 mm cavity length, cleaved facet laser. Other operating characteristics of these DWELL lasers are described.

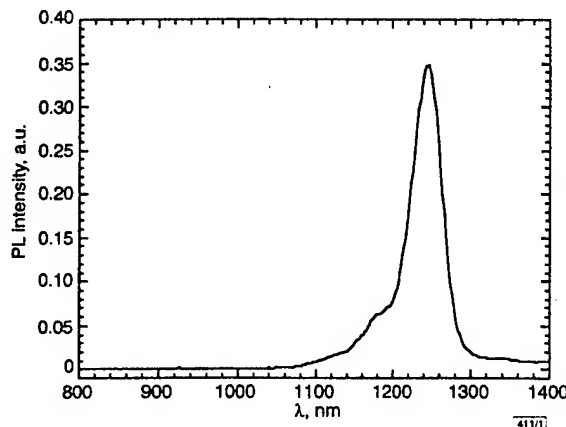


Fig. 1 Photoluminescence spectrum of laser wafer

No emission from quantum well is observed; FWHM is 37 meV

Device structures and growth: The laser structure was grown by solid-source molecular beam epitaxy (MBE) on a (100) n -GaAs substrate. The laser structure was the same as reported in [3] except that $\text{In}_{0.15}\text{Ga}_{0.85}\text{As}$ was used as the quantum well. The epitaxial structure consists of an n -type (10^{18} cm^{-3}) 300 nm thick GaAs

buffer, a $2\mu\text{m}$ n -type (10^{17}cm^{-3}) lower $\text{Al}_{0.15}\text{Ga}_{0.85}\text{As}$ cladding layer, a 230nm thick GaAs waveguide surrounding the laser active region, a $2\mu\text{m}$ p -type (10^{17}cm^{-3}) upper cladding layer, and a p -doped ($3 \times 10^{19}\text{cm}^{-3}$) 60nm thick GaAs cap. This cavity was a low-loss design following [6]. In the centre of the waveguide, an equivalent coverage of 2.4 monolayers of InAs results in quantum dots grown approximately in the middle of the 100\AA $\text{In}_{0.15}\text{Ga}_{0.85}\text{As}$ quantum well. The quantum dots and quantum well were grown at 510°C , and all other layers were grown at 610°C , as measured by an optical pyrometer.

Room temperature photoluminescence (PL) results are shown in Fig. 1. The PL linewidth is 37meV and has been reduced compared with that in [3]. No emission from the quantum well is observed, providing clear proof of minimal competition from quantum well radiative transitions. This implies that the relaxation time from the quantum well to the quantum dots is much faster than the spontaneous lifetime of the quantum well.

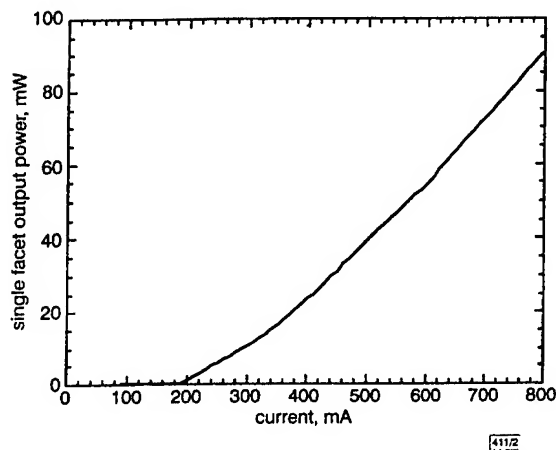


Fig. 2 Single facet output L - I curve of 7.8mm cavity length laser. Threshold current density is $26\text{A}/\text{cm}^2$; external efficiency is 31%

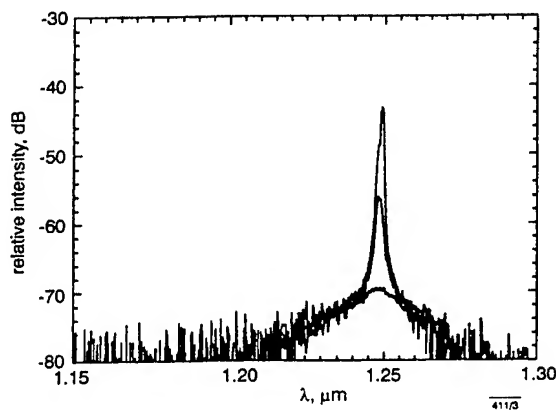


Fig. 3 Lasing spectrum at $0.90I_{th}$ (180mA), $0.95I_{th}$ (190mA), and I_{th} (200mA)

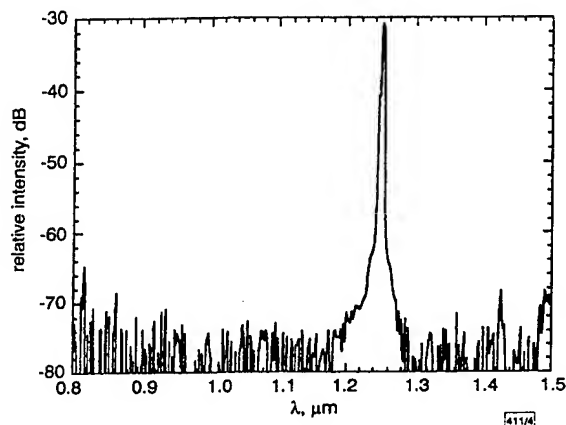


Fig. 4 Lasing spectrum at five times threshold current density. No emission from well is observed

Results: Broad area lasers with $100\mu\text{m}$ stripe widths were fabricated from this structure. The wafer was then cleaved into 7.8mm long laser bars. All devices were tested with the n -side down on a thermoelectric cooler using pulsed excitation. The pulsewidth was 300ns with a duty cycle of 0.5% . The temperature of the thermoelectric cooler was set to be 20°C . The single facet output L - I curve from a typical bar is shown in Fig. 2. The lasing threshold current is 200mA , which corresponds to a threshold current density of $26\text{A}/\text{cm}^2$. The external quantum efficiency is 31% . The lowest previously reported threshold current densities for quantum wells lasers were $\sim 50\text{A}/\text{cm}^2$ [7, 8]. The near-threshold lasing spectra at three different injection current levels, $0.90I_{th}$ (180mA), $0.95I_{th}$ (190mA) and I_{th} (200mA) were measured by an optical spectrum analyser (OSA) and are shown in Fig. 3. The lasing wavelength is $1.25\mu\text{m}$. Clear spectral narrowing can be observed at $0.95I_{th}$ (190mA). A much broader spectrum was also taken at five times the threshold current and is shown in Fig. 4. No emission from the quantum well layer is observed, again suggesting the lack of radiative competition from the quantum well and the rapid capture of carriers by the dots from the well. The dependence of the threshold current on temperature was also measured and is shown in Fig. 5. The characteristic temperature T_0 is 60K between 10 and 50°C , and decreases significantly to 34.5K between 50 and 80°C . Carrier heating out of the quantum well may be one reason why the T_0 value of this laser is smaller than predicted T_0 values for quantum dot lasers [1].

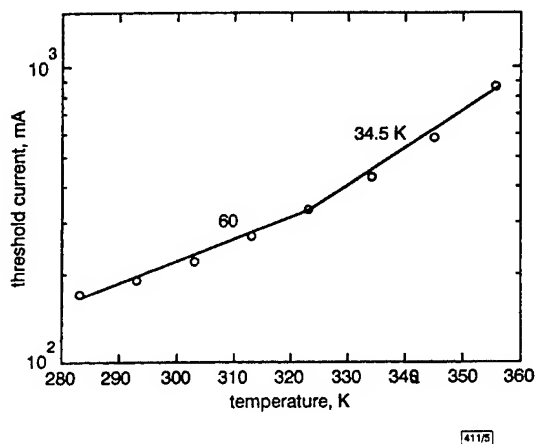


Fig. 5 Threshold current against temperature for 7.8mm cavity length device

Conclusion: We have demonstrated an extremely low threshold current density DWELL laser with a single layer of InAs quantum dots in an $\text{In}_{0.15}\text{Ga}_{0.85}\text{As}$ quantum well. This is the first time that the threshold current density performance of quantum dot lasers has surpassed that of quantum well lasers. Experimental evidence suggests that the relaxation time from the quantum well to the quantum dots is much shorter than the spontaneous lifetime of the quantum well. The T_0 value for these DWELL lasers is 60K between 10 and 50°C .

Acknowledgments: This work was supported by DARPA under grant #MDA972-98-1-0002 and by AFOSR under grant #F49620-96-1-0077.

© IEE 1999

1 June 1999

Electronics Letters Online No: 19990811

DOI: 10.1049/el:19990811

G.T. Liu, A. Stintz, H. Li, K.J. Malloy and L.F. Lester (University of New Mexico, Center for High Technology Materials, 1313 Goddard SE, Albuquerque, NM 87106, USA)

References

1. ARAKAWA, Y., and SAKAI, H.: 'Multidimensional quantum well laser and temperature dependence of its threshold current', *Appl. Phys. Lett.*, 1982, **40**, (11), pp. 939-941
2. SCHÄFER, F., REITHMAIER, J.P., and FORCHEL, A.: 'High-performance GaInAs/GaAs quantum-dot lasers based on a single active layer', *Appl. Phys. Lett.*, 1999, **74**, (20), pp. 2015-2017

4. USTINOV, V.M., MILEEV, S.V., EGOV, A.YU., LUNEV, A.V., VOLOV, B.V., KRESTNIKOV, I.L., MUSIKHIN, YU.G., BERT, N.A., KOPEV, P.S., ALFEROV, ZH.I., LEDENTSOV, N.N., and BIMBERG, D.: 'InAs/InGaAs quantum dot structures on GaAs substrates emitting at $1.3\mu\text{m}$ ', *Appl. Phys. Lett.*, 1999, 74, (19), pp. 2815-2817
5. SUGAWARA, M., MUKAI, K., and SHOJI, H.: 'Effect of phonon bottleneck on quantum-dot laser performance', *Appl. Phys. Lett.*, 1997, 71, (19), pp. 2791-2793
6. HUFFAKER, D.L., PARK, G., ZOU, Z., SHCHEKIN, O.B., and DEPPE, D.G.: ' $1.3\mu\text{m}$ room-temperature GaAs-based quantum-dot laser', *Appl. Phys. Lett.*, 1998, 73, (18), pp. 2564-2566
7. CHAND, N., BECKER, E.E., VAN DER ZEIL, J.P., CHU, S.N.G., and DUTTA, N.K.: 'Excellent uniformity and very low (less-than-50 Acm^{-2}) threshold current density strained InGaAs quantum-well diode-lasers on GaAs substrate', *Appl. Phys. Lett.*, 1991, 58, (20), pp. 1704-1706
8. TURNER, G.W., CHOI, H.K., and MANFRA, M.J.: 'Ultralow-threshold ($50\text{A}/\text{cm}^2$) strained single-quantum-well GaInAsSb/AlGaAsSb lasers emitting at $2.05\mu\text{m}$ ', *Appl. Phys. Lett.*, 1998, 72, (8), pp. 876-878

High-power grating coupled surface emitting flared laser

H. Luo, R. Bedford, S. Penner and M. Fallahi

A high-power surface emitting flared laser with curved feedback grating is reported. Low threshold, low divergence out-coupling is achieved. Single longitudinal mode operation with surface emitting power in excess of 110mW and sidemode suppression of > 40dB is demonstrated.

Introduction: Semiconductor lasers with flared section are attractive due to their single lateral mode operation and high power capability [1]. While high-power flared edge-emitting devices have been widely reported [2], the output power from surface emission is relatively low. In comparison to edge emitting lasers, surface-emitting devices have several advantages: low divergence, compatibility with beamforming elements, suitability for on-wafer testing and 2D array integration [3]. In this Letter, we report the design and fabrication of a grating coupled surface emitting flared laser with high power potential and very high sidemode suppression.

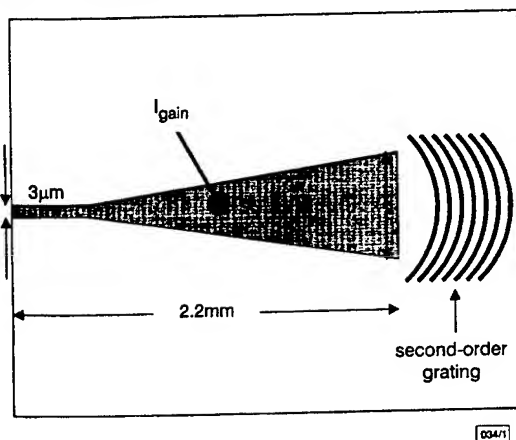


Fig. 1 Schematic diagram of top view of grating coupled surface emitting laser

Design and fabrication: A schematic diagram of the top view of the surface emitting laser is shown in Fig. 1. The laser consists of a ridge waveguide and a tapered section. The ridge is used to ensure single lateral mode operation and thus functions like a spatial mode filter. The tapered section is used to increase the output power while maintaining a relatively small power density at the output side. The full angle of the taper is $\sim 7^\circ$, large enough to accommodate free beam diffraction. The resonator consists of a

also provides more efficient feedback. This configuration is different from that of the conventional unstable resonator design. The result of a preliminary numerical calculation indicates that the effect of the grating curvature on the lateral mode stability is not significant, and filamentation can be prevented as long as the feedback reflectivity of the grating is not high. Experimentally a grating duty cycle of 50% is chosen to achieve low reflectivity and to enhance surface out-coupling [4].

The lasers are fabricated from an InGaAs/GaAs strained single quantum well, graded-index separate confinement heterostructure. First, the top contact (Ti/Pt/Au) for the gain section is formed by lift-off. The ridge section is defined by ECR-RIE dry etching. The grating area is opened and etched down to the desired depth prior to grating fabrication. Curved second-order Bragg gratings are then defined by electron beam lithography and dry etching. Spoiling grooves are defined to prevent multilateral operation. The back contact is formed using Ni/Ge/Au.

Results and discussion: The lasers are probe-tested *p*-side up under pulsed operation at temperatures from 15 to 25°C . The lasers are first tested with the ridge side as cleaved (power reflectivity $\sim 30\%$). The measured light-current characteristic of the laser is shown in Fig. 2. The device has a threshold current of 480mA, corresponding to a threshold current density of $189\text{A}/\text{cm}^2$. A surface emitting power of 45mW is obtained at 1A driving current, which is the limit of the current source. This corresponds to an external quantum efficiency for surface emission of 6.6%. The low efficiency is caused by the substrate radiation and the partial reflectivity from the cleaved end. To increase the efficiency, an HR coating is applied to the cleaved end to achieve a reflectivity of 95%. The threshold current, threshold current density and external quantum efficiency of the HR-coated device are 390mA, $154\text{A}/\text{cm}^2$, and 14.1%, respectively. A surface emitting power of 110mW is obtained at 1A driving current. No decrease in laser power is observed throughout the current range, which indicates that higher power is achievable at higher current.

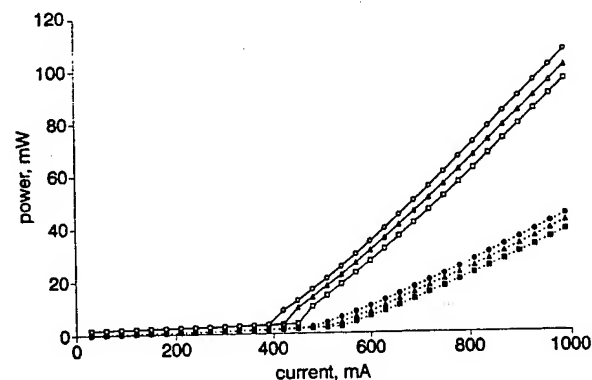


Fig. 2 Light-current characteristics of surface emitting laser

- HR, $T = 25$
- △ HR, $T = 20$
- HR, $T = 15$
- no HR, $T = 25$
- ▲ no HR, $T = 20$
- no HR, $T = 15$

The near field of the laser is determined at different currents, to investigate the beam quality. Fig. 3 shows the near field emission of the laser at 570mA. A uniform near field is obtained over a wide range of currents. However, as the current increases above 700mA, filamentation starts to build up. Despite this effect, the far field divergence remains below 1° in the lateral direction and below 0.4° in the longitudinal direction over the whole current range. We believe that the reason for the filamentation at high current is a large thermal lens effect and stress under the probe tip. Better packaging should improve the beam quality of the laser.

Identification of Type I offset behavior in AlInAsSb/InAsSb MQW Structures

Leslie G. Vaughn, L. Ralph Dawson, Edwin Pease, Luke F. Lester
University of New Mexico, Center for High Technology Materials, 1313 Goddard SE,
Albuquerque, NM 87106 USA

Until recently, the dominant materials systems used for mid-infrared semiconductor lasers have been limited to Type II bandgap structures. The demonstration of stable MBE growth of AlInAsSb quaternary alloys using a digital alloy method allows exploration of AlInAsSb/InAsSb MQW structures for aluminum compositions well into the predicted miscibility gap. Photoluminescence (PL) measurements for structures in this materials system suggest that it has a nested bandgap structure and varying the composition of the well material, while introducing more compressive strain, has led to longer wavelengths. Al(0.3)In(0.7)As(x)Sb(1-x) alloys, known to be well within the miscibility gap for essentially all values of x, were grown by MBE using the digital alloy technique, and used as the barrier material in a multiple quantum well (MQW) structure. This structure, grown on GaSb substrates, has lattice-matched barriers and compressively strained InAsSb wells as determined by XRD. Using an experimentally confirmed quaternary bandgap model and Type I band offsets taking into account strain, the wavelengths for InAsSb wells with 0.3 to 1.1% strain are predicted to be 3.58 to 4.12 microns at room temperature. We have observed consistent PL peak wavelengths of 3.25 microns at 90K in 0.3% strained wells, which translates to a room temperature wavelength of about 3.46 microns. Structures with 1.1% strain result in 3.97 microns at 99K, or 4.17 microns equivalent for room temperature. The good agreement of these experimental results with the theoretical model indicates that the AlInAsSb/InAsSb material system is one of the few Type I quantum wells having demonstrated light emission in the technologically important mid-IR band from 3.3 to 4.2 microns. The results are very promising for the use of these heterojunctions in mid-IR semiconductor lasers.

EMC 2002



Identification of Type I offset behavior in AlInAsSb/InAsSb MQW Structures

L. G. Vaughn, L. R. Dawson, E. Pease, L. F. Lester

The Center for High Technology Materials

University of New Mexico

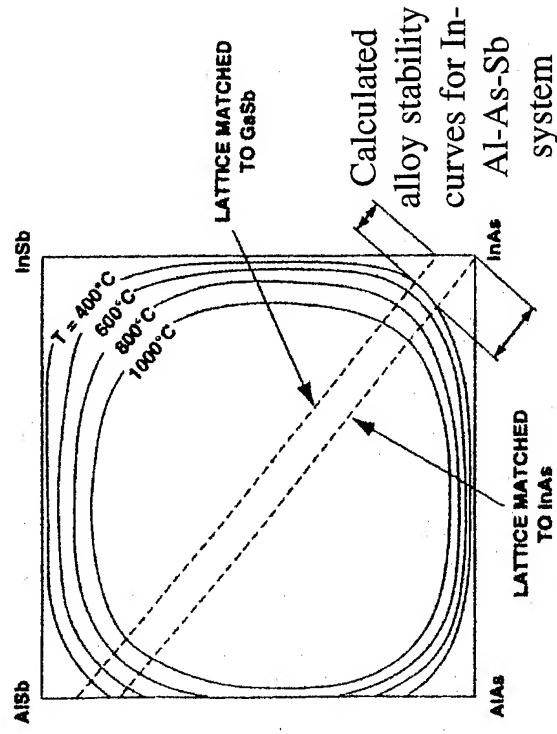
This research was supported by the Ballistic Missile Defense Organization



Motivation

- Mid IR interest - atmospheric transmission window between 3.3 and 4.2 microns
- Dominant materials systems in this range are Type II bandgap structures
- MQW structures of InAsSb wells and AlInAsSb barriers have been shown to produce wavelengths within this range--but, are predicted to be barely Type I with respect to the valence band offset

Better valence band offset is predicted if more aluminum can be incorporated in the barriers--unfortunately, there is a large predicted miscibility gap between 6 and 96% Al



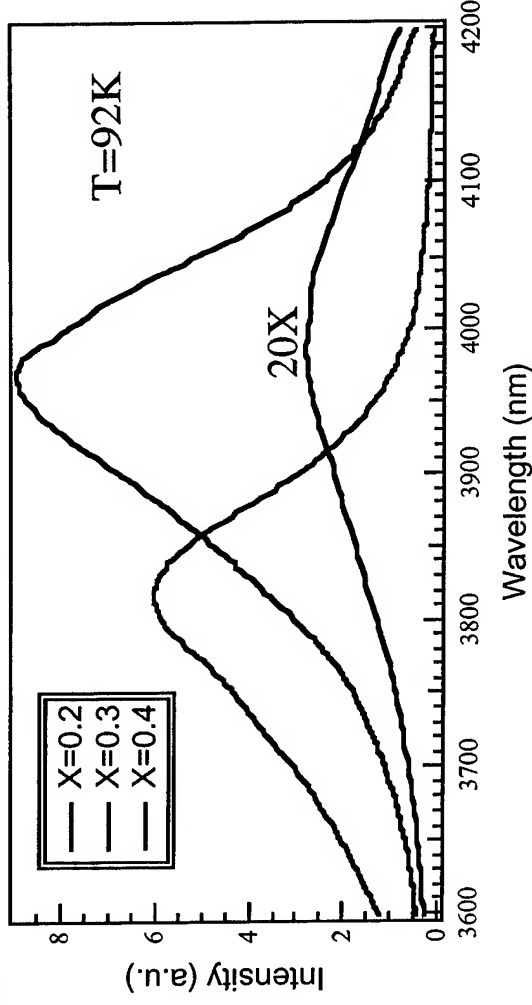


Stable quaternary growth

- A digital alloy technique has been used to grow stable AlInAsSb for Al compositions well into the miscibility gap (5 - 50%Al)
- DCXRD results show films to be highly crystalline
- The overall composition of the quaternary is lattice matched to GaSb, so the strain is confined to the wells



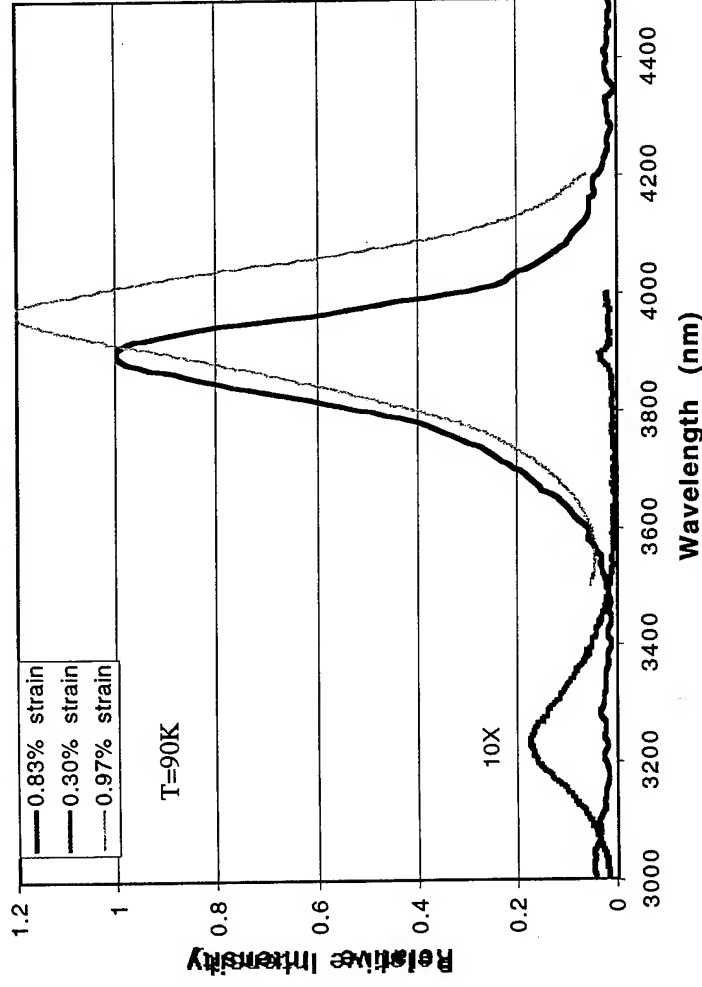
Effects of Varying Aluminum Composition on Photoluminescence



- With increasing aluminum concentration,
 - Slightly shorter wavelength
 - Increased PL intensity (almost two orders of magnitude!)
- Changes are due to increasing confinement energies (larger barrier bandgap)
- Could suggest transition from Type II to Type I



Effects of Varying Compressive Well Strain on Photoluminescence



- All samples have 30% Al quaternary barriers
- Amount of strain in the wells is varied by changing the well composition, resulting in increased wavelength
- Expected wavelength decrease from the strain only slightly counteracts this

- The PL intensity increase with added well strain demonstrates the expected decrease in Auger recombination and suggests the transition from barely Type I/slightly Type II to definitely Type I



Predicted Wavelength vs. Measured Wavelength

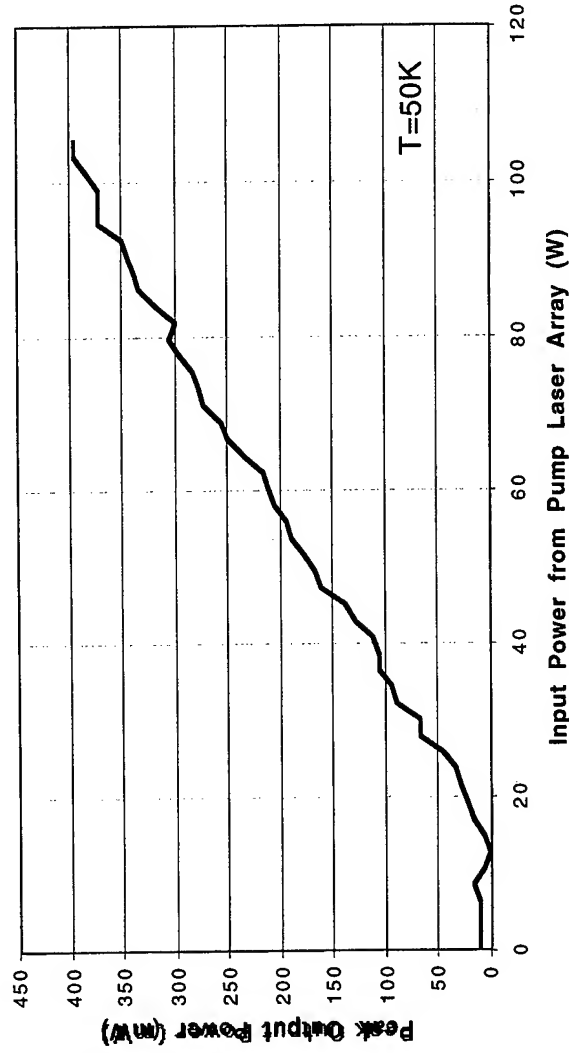




Optically-Pumped Laser Results

- Low strain in the well (0.3%) results in superluminescence, but no lasing
- Higher strain ($\sim 0.83\%$) results in lasing
- Even higher strain should be better yet

L2-037 10QW Laser with 30% Al quaternary barriers





Auger Effects

- This wavelength range is susceptible to Auger
- To decrease amount of Auger recombination, must operate devices well below room temperature
- Reported studies have shown that adding Ga to the quaternary may alter the subband structure enough to allow higher temperature operation





Quinternary

- Quinternaries have been successfully grown with very small amounts of the fifth element
 - What happens in the middle of the variable space?
 - What will happen with this alphabet soup?
Phase segregation even more of an issue?
- The current digital alloy approach makes this a viable next step



Conclusions

- Stable quaternary alloys with Al compositions of 5 to 50% lattice-matched to GaSb have been successfully grown and used in laser structures
- Characterization of these quaternaries thus far have shown them to produce predictable wavelengths in strained quantum well structures
- Lasing has been observed for 0.83% compressively strained wells with 30% aluminum quaternary barriers
- Addition of a fifth element (Ga) to the barrier may further decrease Auger effects and allow for higher operating temperatures of this materials system within the 3.3-4.2 micron wavelength range



Stable Growth of AlInAsSb Quaternaries Using a Digital Alloy Technique

Leslie G. Vaughn¹; L. Ralph Dawson¹; A. L. Gray¹; Edwin Pease¹; Luke F. Lester¹

¹University of New Mexico, Center for High Technology Materials, 1313 Goddard SE, Albuquerque, NM 87106 USA

Alloys of the $\text{Al}(x)\text{In}(1-x)\text{As}(y)\text{Sb}(1-y)$ quaternary are very useful in mid-IR laser structures such as barrier materials for InAs or InAsSb quantum wells on GaSb substrates. The region of stable growth of these alloys on GaSb is limited to $x < 0.06$ [1]. The trend in reported results indicates that increasing the aluminum content may improve the efficiency and To of laser structures by improving the hole confinement

in the quantum well. Unfortunately, for larger aluminum mole fractions a miscibility gap is predicted, and very rough surfaces and multiple XRD peaks are observed for bulk-grown samples. Stable growth of these alloys at higher aluminum concentrations will open up a new material system for mid-IR applications. Using a digital alloy technique, smooth, bulk-like 1 micron-thick films of $\text{Al}(x)\text{In}(1-x)\text{As}(y)\text{Sb}(1-y)$ quaternary alloys have been grown lattice-matched to GaSb with aluminum concentrations well into the predicted miscibility gap. Films with an overall x of 0.20 to 0.40 were grown incorporating very thin layers of AlSb, InAs and InSb binaries, with each binary period on the order of a few monolayers and a total digital alloy period of 20-25 angstroms. These binaries allowed for independent adjustment of the Al to In ratio and the As to Sb ratio without the nuances of ternaries and competing Group V species. For each composition, the Al to In ratio was fixed and the As to Sb ratio was varied to achieve lattice-match to GaSb. Optical inspection of these 1 micron-thick samples using Nomarski shows very smooth film surfaces with no crosshatching or microcracks, which occur due to dislocations. Preliminary x-ray diffraction data also show that the average composition of the digital alloy is lattice matched to within 50-200 arcseconds of the GaSb substrate for each of these films, and that the films are of high single-crystal quality. Additionally, photoluminescence measurements taken at 90-100 K indicate a peak for the film with an overall $x=0.2$ at around 2.15 microns. The PL peak confirms that the material has a direct bandgap, as expected for bulk material of this composition and that the film is of optical device quality. These results are very promising for the use of $\text{Al}(x)\text{In}(1-x)\text{As}(y)\text{Sb}(1-y)$ to increase performance in mid-IR laser structures. [1] H. K. Choi, G. W. Turner, M. J. Manfra, and M. K. Connors, Applied Physics Letters 68, 21 (1996).



Stable MBE Growth of AlInAsSb Quaternaries Using a Digital Alloy Technique

L. G. Vaughn, L. R. Dawson, A. L. Gray, E. Pease, L. F. Lester

The Center for High Technology Materials

University of New Mexico

This research was supported by the Ballistic Missile Defense Organization



Outline

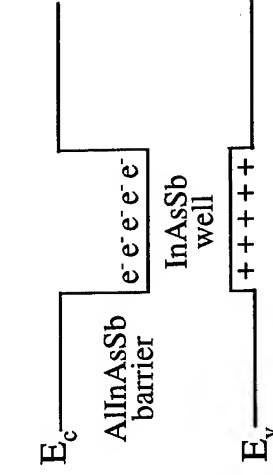
- Motivation
- Materials Characterization
- Optical Characterization
 - Bandgap model for AlInAsSb quaternary
 - PL results for InAsSb well/AlInAsSb barrier quantum well structure
- Conclusions



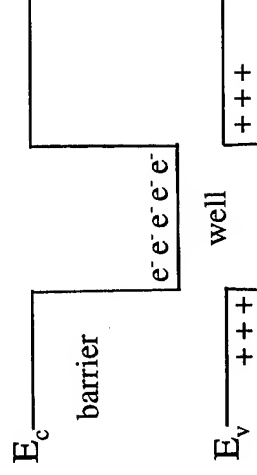


Motivation

- $\text{Al}_x\text{In}_{1-x}\text{AsSb}$ alloys have been explored for use in mid-IR laser structures, specifically in the range of 2-5 μm
 - MIT/Lincoln Lab reported strained QW lasers of $\text{InAsSb}/\text{Al}_{0.06}\text{In}_{0.94}\text{AsSb}$ with emission at 3.9 μm
 - Trends suggest that increased Al content may improve efficiency and T_0 by improving hole confinement in the quantum well
 - Models of binary band alignments predict this system to be Type I
 - But, unknown over what range of quaternary composition this is Type I, because can't grow high quality films across entire range



Type I Band Offset

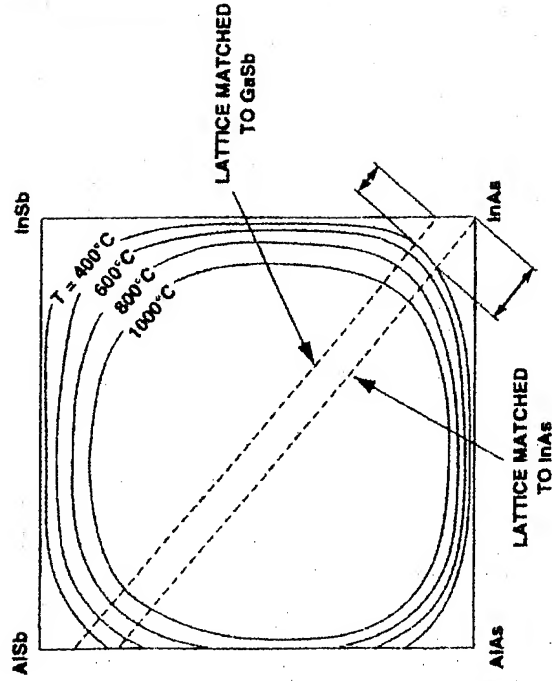


Type II Band Offset

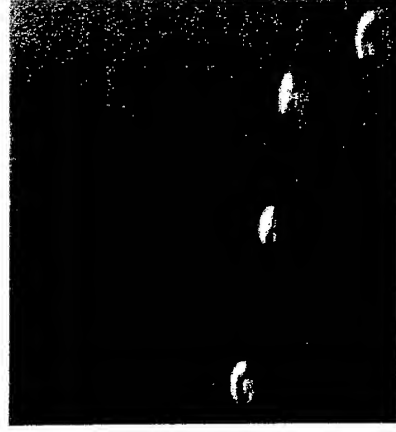


Challenge of Increased Aluminum

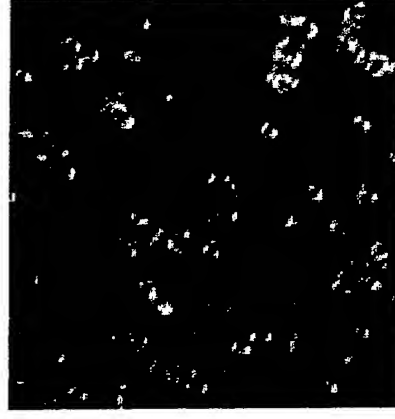
- In the $\text{Al}_x\text{In}_{1-x}\text{AsSb}$ system, a miscibility gap for Al compositions greater than $x = 0.06$ (on GaSb) has delayed further studies



Calculated alloy stability curves for In-Al-As-Sb system



Best Bulk Growth
For $x = 0.2$ at 500X



Typical Bulk Growth
For $x = 0.2$ at 500X



Digital Alloy Approach

- Digital alloy is made up of very thin alternating layers of quaternaries, ternaries, and/or binaries that yield a desired average overall film composition
- From all possible permutations, chose binaries (AlSb, InSb, InAs) for the following inherent advantages
 - No competition between the Group V elements in any single layer
 - Easier to adjust for lattice match conditions compared to a ternary or quaternary approach
- Total period thickness is on the order of 15-20 Å with each binary anywhere from 0.5-5.0 monolayers thick



Digital Alloy Calculations

Example: $\text{Al}_{.20} \text{In}_{.80} \text{As}_{.73} \text{Sb}_{.27}$

Let $d_1 + d_2 + d_3 = 20 \text{ \AA}$ (DA period)

Thicknesses:

$\text{InAs}, d_1 = 14.6 \text{ \AA}$

$\text{InSb}, d_2 = 1.4 \text{ \AA}$

$\text{AlSb}, d_3 = 4.0 \text{ \AA}$

$$x_{\text{Al}} = 0.20 = d_3 / (d_1 + d_2 + d_3)$$

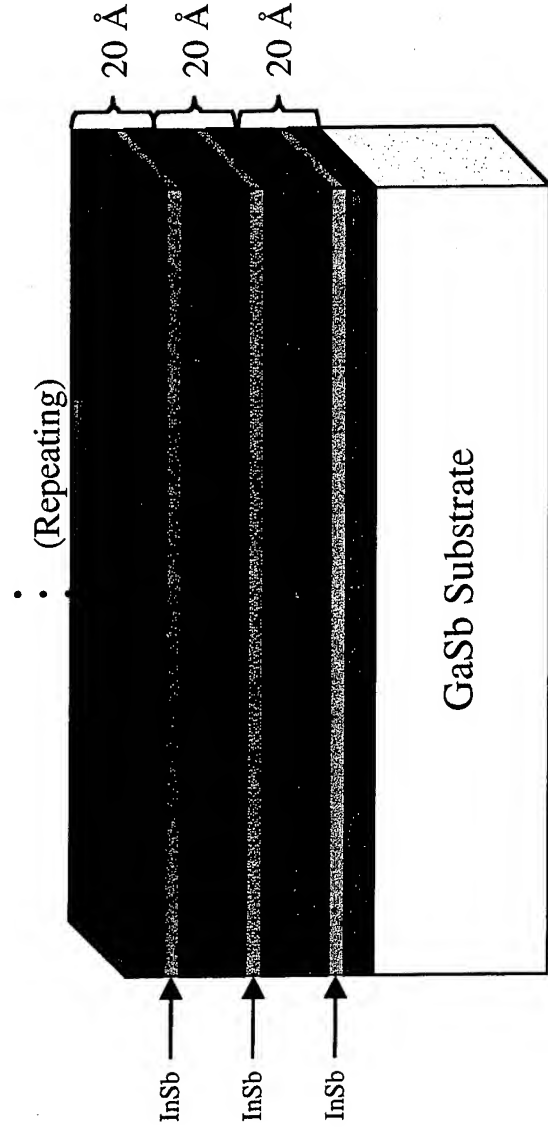
$$x_{\text{In}} = 0.80 = (d_1 + d_2) / (d_1 + d_2 + d_3)$$

$$x_{\text{As}} = 0.73 = d_1 / (d_1 + d_2 + d_3)$$

Given the source fluxes, each binary thickness translates into a shutter time.

$$d_3 = 0.20 (d_1 + d_2 + d_3) = 4.0 \text{ \AA}$$

$$d_1 = 0.73 (d_1 + d_2 + d_3) = 14.6 \text{ \AA}$$



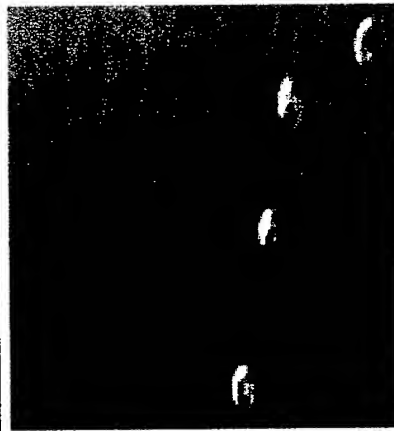


Materials Characterization

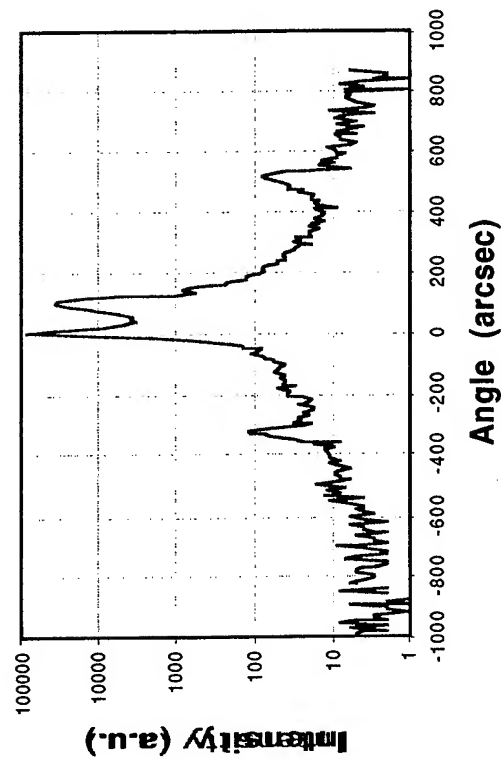
Typical
Digital Alloy
Growth, 500X



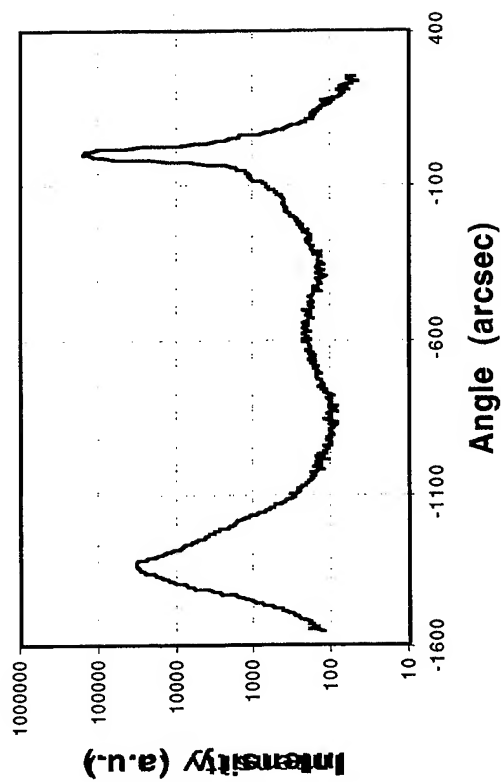
Best Bulk
Growth,
500X



L0-221 004 Reflection X=0.3



L9-98 004 Reflection X=0.2





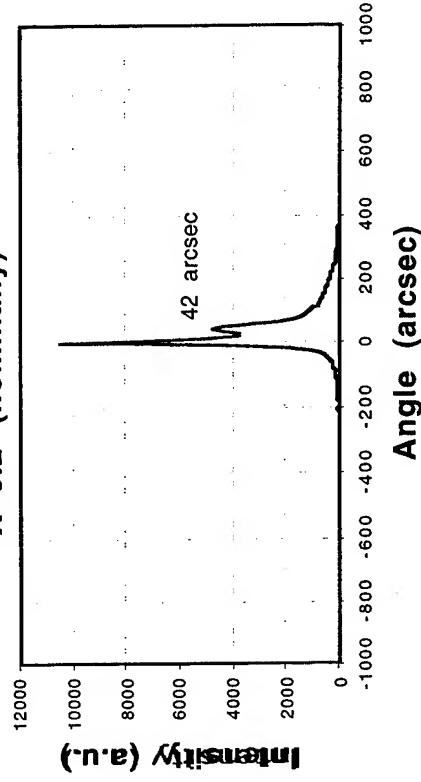
X-Ray Diffraction Results

Lattice-match to GaSb was achieved for compositions with X from 0.2 to 0.4.

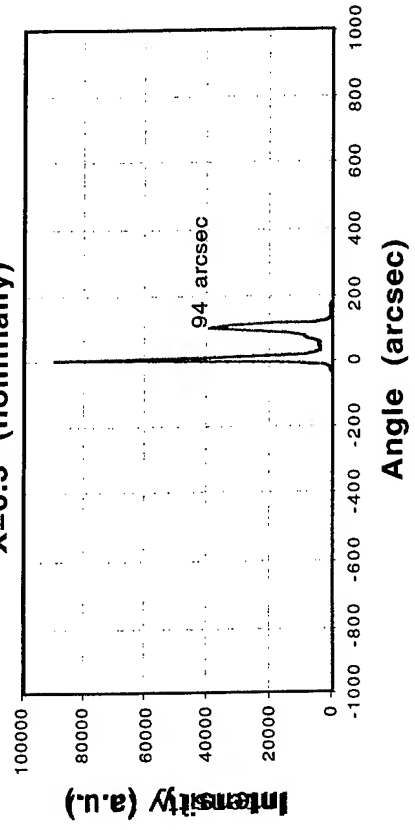
Thickness fringes were observed for all three samples, indicating a high degree of crystallinity.

Microscope inspection under Nomarski conditions showed a very smooth surface with no crosshatching or microcracks.

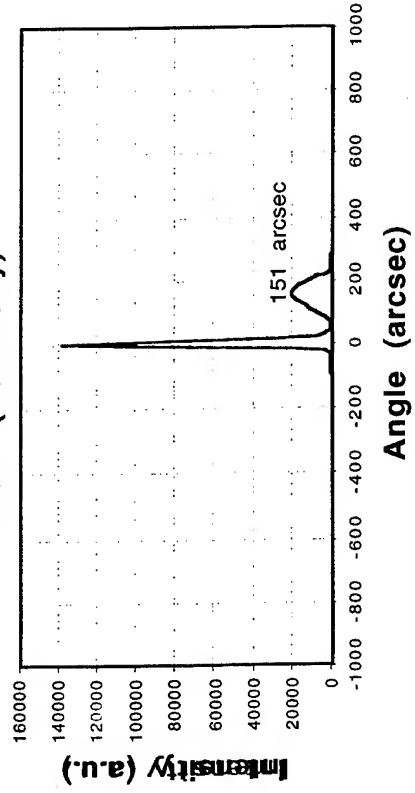
L0-217 004 Reflection
X=0.2 (nominally)

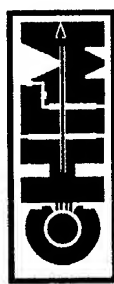


L0-221 004 Reflection
X=0.3 (nominally)



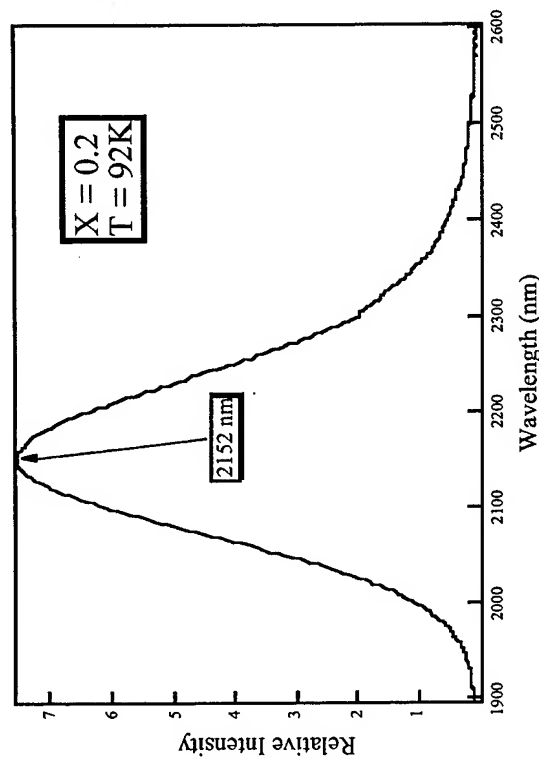
L0-222 004 Reflection
X=0.4 (nominally)





Optical Characterization

Typical Photoluminescence of the Quaternary

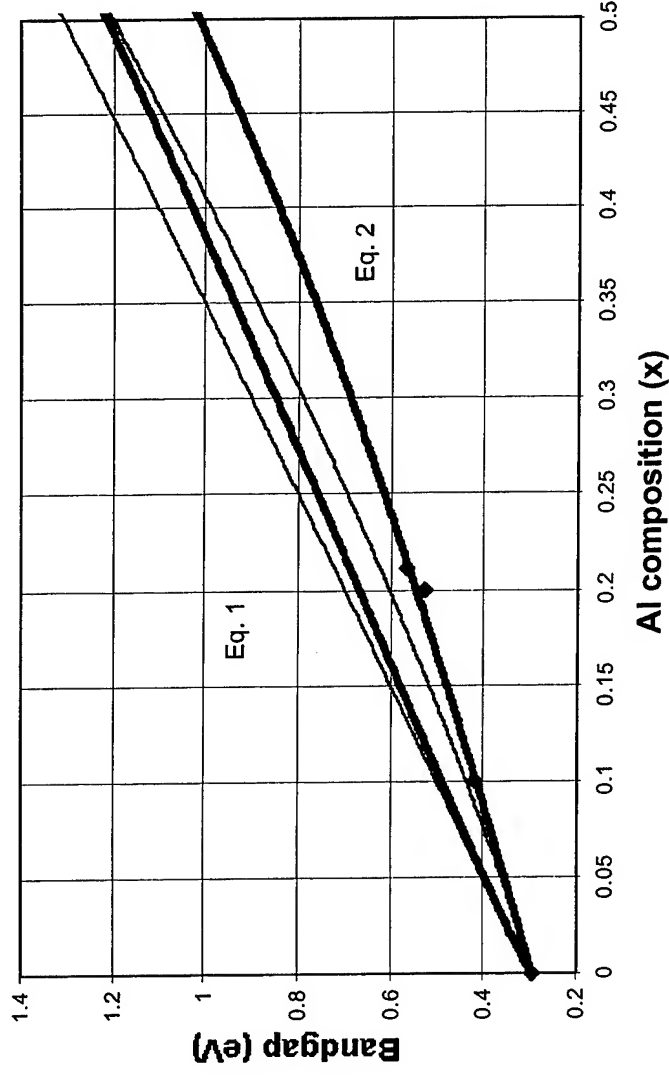


- Photoluminescence was measured for $\text{AlIn}_{1-x}\text{AsSb}$ samples with $X=0.1$ and 0.2 at $\sim 90\text{K}$ and room temperature
- Preliminary results indicate no PL from the $X=0.3$ and 0.4 samples. Further studies are being conducted to determine if the quaternary is indirect at these compositions.



Bandgap Prediction

Al_xIn_{1-x}As_ySb_{1-y} Lattice Matched to GaSb



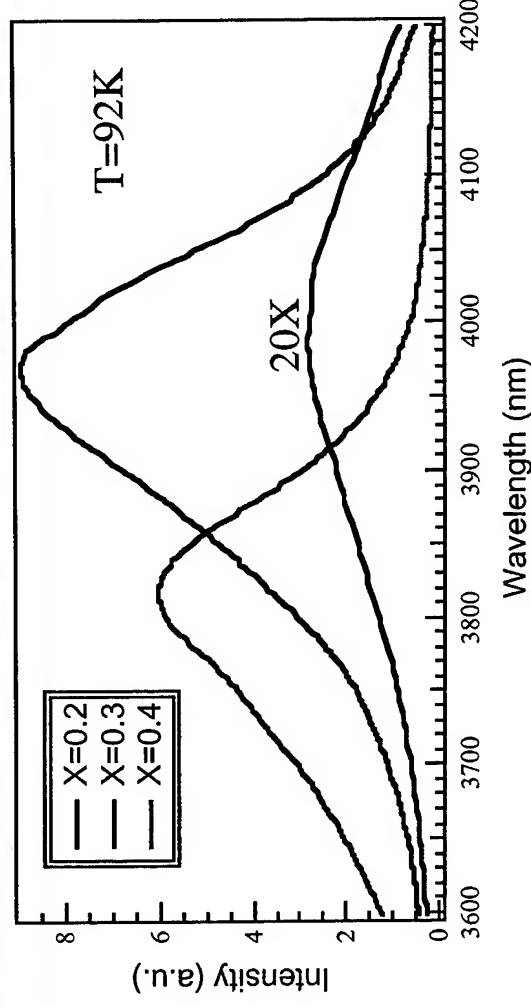
- Γ point bandgap energy, 300K
- Eq. 1 is interpolation equation of compositionally weighted ternary bandgaps (Glisson, Hauser, Littlejohn, Williams, 1978)
- Eq. 2 is compositionally weighted combo of binary bandgaps with separate quaternary bowing parameter term (Moon, Antypas, James, 1974)
- Assuming a bowing parameter for AlAsSb of 1.5 eV, the data is best fit with Equation 2

$$(1) \quad E_g = \frac{x(1-x)[y \cdot E_{g(\text{AlInAs})} + (1-y) \cdot E_{g(\text{InSb})}] + y(1-y)[x \cdot E_{g(\text{AlAsSb})} + (1-x) \cdot E_{g(\text{InAsSb})}]}{[x(1-x) + y(1-y)]}$$

$$(2) \quad E_g = (1-x)y \cdot E_{g(\text{InAs})} + (1-x)(1-y) \cdot E_{g(\text{InSb})} + xy \cdot E_{g(\text{AlAs})} + x(1-y) \cdot E_{g(\text{AlSb})} + x(1-x)[(1-y) \cdot C_{(\text{AlInSb})} + y \cdot C_{(\text{AlInAs})}] + y(1-y)[(1-x) \cdot C_{(\text{InAsSb})} + x \cdot C_{(\text{AlAsSb})}]$$



Photoluminescence of 4-QW Structure



- With increasing aluminum concentration,
 - Slightly shorter wavelength
 - Increased PL intensity (almost two orders of magnitude!)
- Changes are due to increasing confinement energies (larger barrier bandgap)
- Could suggest transition from Type II to Type I



Conclusions

- Digital alloy technique allowed stable growth of AlInAsSb within the miscibility gap
- Films demonstrated good structural properties (no indication of phase separation)
- Established bandgap model for AlInAsSb that fits experimental data well
- Films demonstrated good optical properties
 - Nearly two orders of magnitude increase in PL intensity with increased Al in the barrier material of the PL structure
 - Possible transition from Type II to Type I band offset



Characterization of AlInAsSb and AlGaInAsSb MBE-grown Digital Alloys

L. G. Vaughn¹, L. R. Dawson¹, H. Xu²Center for High Technology Materials, University of New Mexico, 1313 Goddard SE,
Albuquerque, NM 87106 USA

Department of Earth and Planetary Sciences, University of New Mexico,

AlInAsSb alloy barriers with InAsSb wells have been used in multiple quantum well laser structures to produce mid-infrared light in the region 3.3 to 4.2 microns. One of the few Type I bandgap offset material systems available in the antimony-based systems, Al(x)In(1-x)AsSb quaternary alloys have been grown by Molecular Beam Epitaxy (MBE) as random alloys up to an aluminum fraction, $x=0.06$ on GaSb substrates. Above this aluminum fraction, a miscibility gap is predicted. Stable, single phase, GaSb lattice-matched quaternary alloys have been successfully grown by MBE using a digital alloy technique for aluminum fractions of 0.05 to 0.5, well into the miscibility gap. DCXRD results show the full width half-maximum (FWHM) of 0th order alloy peaks are within 1.5 to 2 times the FWHM of highly crystalline GaSb substrate peaks with well defined thickness fringes for the total film and the digital alloy period. TEM micrographs show very well ordered alloys with characteristic ultrathin superlattice structure.

Photoluminescence alloy bandgap measurements correspond to predicted values for bulk material using the Moon, et. al. [1] quaternary bandgap equation with a compositionally weighted combination of binary bandgaps and separate weighting of the bowing parameters.

Furthermore, using the digital alloy technique, gallium has been added to the quaternary alloy to produce a quinary alloy lattice-matched to GaSb. This material is of specific interest for mid-infrared lasers because the fifth element, gallium, appears to affect the subband structure in such a way as to suppress Auger recombination. This is a dominant non-radiative carrier sink, keeping these materials from operating at or near room temperature. DCXRD of these quinary alloys give results similar to the quaternary alloys. The stable, single-phase growth of these quinary alloys is promising for improving mid-IR laser structures.

[1] Moon, et. al., Journal of Electronic Materials, Vol. 3, No. 3, 1974

High-responsivity, normal-incidence long-wave infrared ($\lambda \sim 7.2 \mu\text{m}$) InAs/In_{0.15}Ga_{0.85}As dots-in-a-well detector

S. Raghavan, P. Rotella, A. Stintz, B. Fuchs, and S. Krishna^{a)}

Center for High Technology Materials, University of New Mexico, Albuquerque, New Mexico 87106

C. Morath and D. A. Cardimona

Air Force Research Lab (AFRL/VSSS), 3550 Aberdeen Avenue S. E., Building 426, Kirtland Air Force Base, New Mexico 87117

S. W. Kennerly

Army Research Laboratory, Sensors and Electron Devices Directorate, Adelphi, Maryland 20783

(Received 6 May 2002; accepted for publication 12 June 2002)

Normal incidence InAs/In_{0.15}Ga_{0.85}As dots-in-a-well detectors operating at $T=78 \text{ K}$ with $\lambda_p \sim 7.2 \mu\text{m}$ and a spectral width ($\Delta\lambda/\lambda$) of 35% are reported. The peak at $7.2 \mu\text{m}$ is attributed to the bound-to-bound transitions between the ground state of the dot and the states within the InGaAs well. A broad shoulder around $5 \mu\text{m}$, which is attributed to the bound-to-continuum transition, is also observed. Calibrated blackbody measurements at a device temperature of 78 K yield a peak responsivity of 3.58 A/W ($V_b = -1 \text{ V}$), peak detectivity $= 2.7 \times 10^9 \text{ cm Hz}^{1/2}/\text{W}$ ($V_b = -0.3 \text{ V}$), conversion efficiency of 57% and a gain ~ 25 . © 2002 American Institute of Physics.
[DOI: 10.1063/1.1498009]

In the past few years, there has been active research studying the performance characteristics of quantum dot (QD) infrared detectors (QDIPs) for midwave infrared (MWIR, $3\text{--}5 \mu\text{m}$) and long-wave infrared (LWIR, $8\text{--}12 \mu\text{m}$) applications.^{1–10} MWIR and LWIR detectors are in great need for a variety of applications ranging from night vision cameras and battle recognition systems to chemical spectroscopy and remote sensing. Present day photon detectors in this wavelength range need to be cooled to liquid nitrogen temperature or below to reduce the deleterious effects arising due to the large thermionic emission. QDIPs are expected to display low dark current,¹¹ large detectivity,¹² and better response at elevated temperature from the longer lifetime of excited electrons due to greatly suppressed electron-phonon scattering.^{13,14} QD detectors have already demonstrated normal incidence MWIR operation at temperatures as high as 150 K (Ref. 15) and the reported results in literature from several groups show significant promise for this technology.^{1–10} Nevertheless, the responsivity and specific detectivity of QDIPs is significantly lower than those observed in mercury cadmium telluride (MCT) detectors. However, due to difficulties with the epitaxial growth of mercury based compounds, material defects cause problems with uniformity and operability across an array that continue to plague MCT focal plane arrays (FPA). QDIPs, on the other hand, are based on a comparatively mature GaAs technology and the uniformity of their response suggests that they can be incorporated into large-area FPA.

Most of the QD detectors fabricated so far use either InAs or InGaAs dots placed in a GaAs matrix. Recently, some researchers have fabricated QD detectors in which the InAs dots are capped with an InGaAs layer.¹⁶ In this letter, we report a dots-in-a-well (DWELL) detector in which InAs

dots are placed in a thin In_{0.15}Ga_{0.85}As well, which, in turn, is placed in a GaAs matrix. The DWELL structure provides better confinement for the carriers trapped in the QDs by lowering the ground state of the QD relative to the GaAs bandedge. This leads to lower thermionic emission. Owing to the higher density of dots ($1 \times 10^{11} \text{ cm}^{-2}$) and better collection mechanism, the effective “area” seen by the incident photons is larger in the DWELL structure as compared to a conventional InAs/GaAs structure. This is expected to improve the responsivity and conversion efficiency of the detector. State-of-the-art lasers with extremely low threshold current and high characteristic temperature have already been demonstrated using this DWELL structure.¹⁷ In this letter, we report a DWELL detector operating at $\lambda = 7.2 \mu\text{m}$ (spectral width $\sim 35\%$) with a large responsivity ($R_{\text{peak}} = 3.58 \text{ A/W}$ at $T = 78 \text{ K}$) and a large detectivity ($D_{\text{peak}}^* = 2.7 \times 10^9 \text{ cm Hz}^{1/2}/\text{W}$, $T = 78 \text{ K}$). To the best of our knowledge, this is the highest responsivity and detectivity reported in a LWIR QDIP at 78 K .

The DWELL samples were grown in a VG-80 solid-source molecular-beam epitaxy system with a cracked As₂ source. The GaAs layers were grown at $T_{\text{sub}} = 580^\circ\text{C}$ whereas the In_{0.15}Ga_{0.85}As well and the InAs dots were grown at $T_{\text{sub}} = 480^\circ\text{C}$. Several calibration samples with different doping levels in the dots were grown, and absorption measurements were performed to optimize the number of dopant atoms per dot. From this study, it was found that the optimal sheet density for our InAs/In_{0.15}Ga_{0.85}As DWELL dots was about $1 \times 10^{11} \text{ cm}^{-2}$, which corresponds to about 1 electron/dot. The detector structures with ten layers of n -doped InAs/In_{0.15}Ga_{0.85}As were then grown. The heterostructure schematic is shown in Fig. 1(a).

Cross-sectional transmission electron microscopy images of the detectors, as shown in Fig. 1(b), reveal that there are no dislocations in the sample. Figure 1(b) also shows the

^{a)}Electronic mail: skrishna@chtm.unm.edu

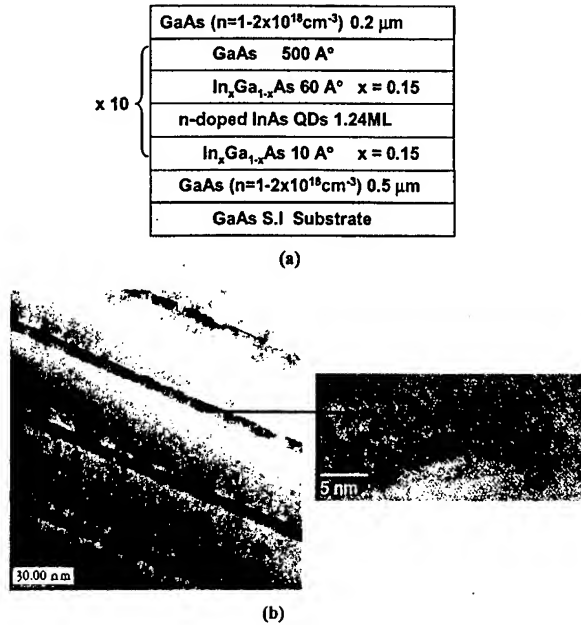


FIG. 1. (a) Heterostructure schematic and (b) cross-sectional transmission electron microscopy image of the ten-layer InAs/In_{0.15}Ga_{0.85}As DWELL detector. A high-resolution image of a single QD is also shown in (b).

high-resolution TEM image of a single dot in the detector. Using standard lithography, metal evaporation, and a combination of wet and dry etching, *n-i-n* detectors were fabricated for top side illumination with the diameter of the illuminated area ranging from 25–300 μm. Dark current characteristics for a 25 μm diameter device, in the temperature range of 10–300 K, is shown in Fig. 2(a). The dark current is much lower in the InAs/In_{0.15}Ga_{0.85}As DWELL detector ($I_{\text{dark}} = 3.2$ pA, $V_b = 0.1$ V, 60 K) than that measured in a similar quantum well infrared photodetector (QWIP) containing three periods of 80 Å In_{0.15}Ga_{0.85}As/500 Å GaAs quantum wells ($I_{\text{dark}} = 10$ μA, $V_b = 0.1$ V, 60 K). This clearly shows that the QDs provide better confinement for the carriers and reduce thermionic emission in the DWELL heterostructures. The activation energy extracted from an Arrhenius plot in the temperature range of 50–150 K is shown in Fig. 2(b) for different values of the applied bias. The activation energy at lower biases is about 150 meV and drops significantly at higher biases due to band bending effects.

The detectors were wire bonded to a leadless chip carrier and spectral measurements were performed using a global source and a Nicolet 670 spectrometer. Figure 3 shows the normalized normal incidence spectral response obtained from a 200 μm device at 78 K for different bias voltages. The peak of the response is close to 7.2 μm (170 meV) with a spectral width ($\Delta\lambda/\lambda$) of 35%. Such a broad response is a desirable feature for LWIR detectors. The spectra appear noisy due to the strong atmospheric absorption at these wavelengths. It is interesting to note that the cutoff energy obtained from spectral response measurement (~ 151 meV, $V_b = -0.1$ V) agrees very well with the activation energy extracted from the dark current measurements (~ 152 meV, $V_b = -0.1$ V), as shown in Fig. 2(b). Moreover both of them display a redshift at increased values of the applied bias due to band bending effects.

Downloaded 09 Aug 2002 to 64.106.37.79. Redistribution subject to AIP license or copyright, see <http://ojps.aip.org/aplo/aplcr.jsp>

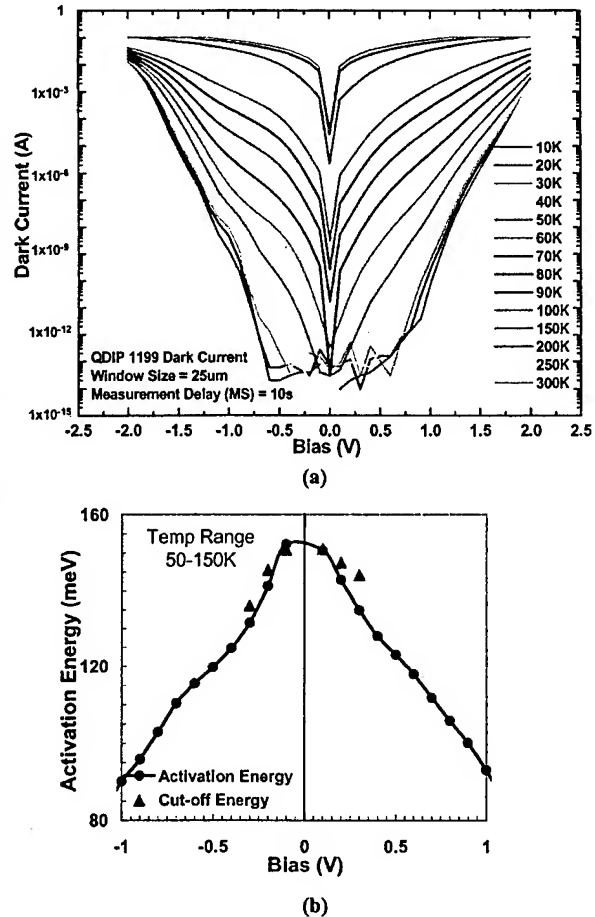


FIG. 2. (a) Dark current characteristics of a 25 μm DWELL detector in the range of 10–300 K, (b) the activation energy extracted from the Arrhenius plot in the temperature range of 50–100 K. The cutoff energy obtained from the spectral response measurements are also shown (▲).

In order to examine the origin of the observed peaks in the spectral response, data obtained from photoluminescence (PL) measurements were analyzed. The energy difference between the position of the ground state of the dot and the

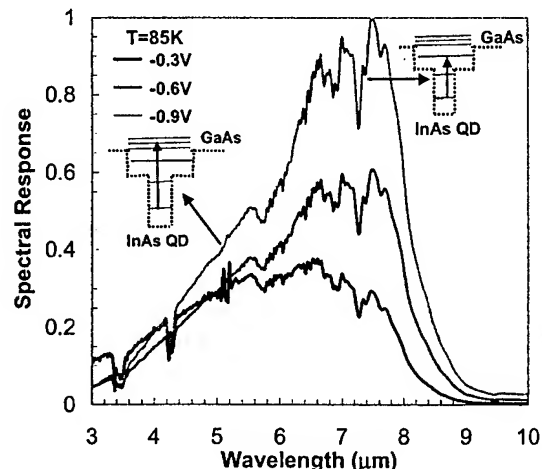


FIG. 3. Spectral response obtained from a 200 μm DWELL detector at $T = 85$ K for different values of applied bias. The bound-to-bound and bound-to-continuum schematic is shown in the inset.

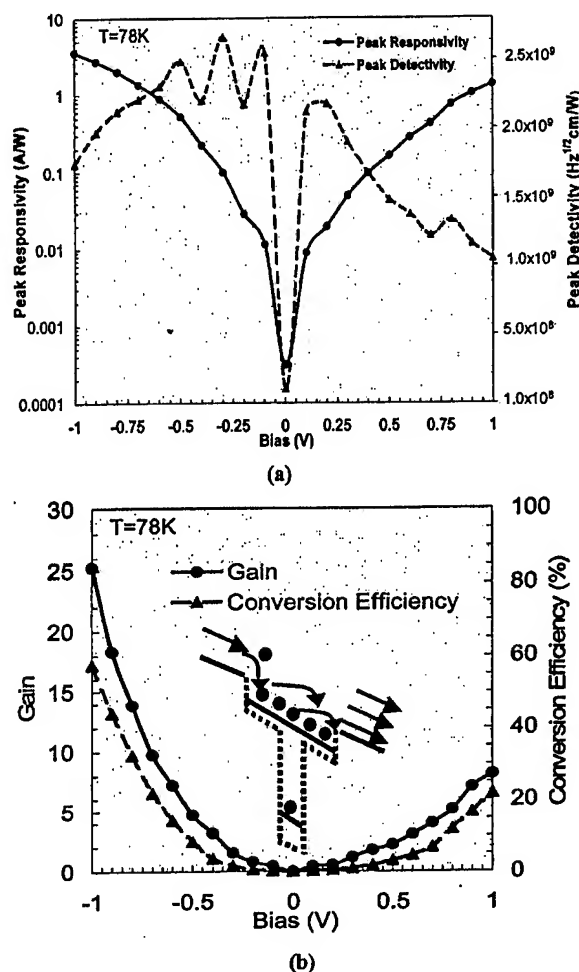


FIG. 4. (a) Peak responsivity, detectivity (b), conversion efficiency, and photoconductive gain as a function of applied bias for a 100 μm diameter DWELL detector operating at 78 K. The avalanche gain mechanism is shown in the inset to (b).

position of the GaAs bandedge from the PL spectrum is found to be 424 meV. In accordance with the analysis by Kim *et al.*,¹⁶ the sum of binding energies for the electrons and holes can be estimated to be 424 meV. Realizing that the electron binding energy is much larger than the hole binding energy, the difference between the conduction-band bandedge of GaAs and ground state of the dot is expected to be greater than 212 meV. Hence, we believe that the peak at 7.2 μm (172 meV, which is less than 212 meV) is due to a bound-to-bound transition between the ground state of the dot and states within the $\text{In}_{0.15}\text{Ga}_{0.85}\text{As}$ quantum well whereas the broad shoulder observed around 5 μm (248 meV, which is greater than 212 meV) is due to the bound-to-continuum transition as depicted in the inset to Fig. 3.

Noise spectra and responsivity measurements were performed at the Army Research Laboratory using a calibrated blackbody at 800 K and an Ono-Sokki fast-Fourier transform analyzer. A germanium block was used to block the interband response of the detector. Figure 4(a) shows the peak responsivity and detectivity of a 100 μm device. To the best of our knowledge, the responsivity and detectivity are higher than that reported for any QDIP at 78 K. However,

they are at least two orders of magnitude lower than that observed in state-of-the-art MCT detectors. Figure 4 shows the conversion efficiency and gain of the detector. The quantum efficiency ($\sim 3\%$) obtained for these devices is comparable to that obtained in QWIPs but the gain is larger than that measured in QWIPs. Such large values of gain have been reported in QDIPs.^{2,15} It is believed that the main contribution to the gain in QDIPs arises due an avalanche mechanism [shown in inset to Fig. 4(b)]. Since the carriers are believed to live longer in the excited state of the dot due to suppressed electron-phonon scattering, there are many carriers in the upper energy level of the dot. Hence, a single carrier trapped from the continuum into the dot can eject many secondary carriers from the upper energy level in the dot into the continuum thereby contributing to the photocurrent. Thus, a single-photoexcited carrier can eject many more electrons as it travels through the subsequent dot layers, leading to a large avalanche gain.¹⁵

In conclusion, we report a broad-band, normal-incidence LWIR detector using a DWELL heterostructure with a peak responsivity = 3.58 A/W and peak detectivity = $2.5 \times 10^9 \text{ cm}^2/\text{Hz}^{1/2}/\text{W}$ at $T=78\text{K}$. The peak around 7.2 μm (172 meV) is attributed to a bound-to-bound transition within the DWELL structure whereas the shoulder at $\sim 5 \mu\text{m}$ (248 meV) is attributed to the bound-to-continuum transition. These values agree with the data obtained from PL and activation energy measurements. The small bias voltages used make these QDIPs compatible with the readily available Si-readout circuits making them an attractive technology for the fabrication of FPAs.

This work is supported by Air-Force Research Laboratory (AFRL) Grant No. F29601-01-C-0156 and by the Army Research Laboratory, Contract No. DAAD19-01-2-0008.

¹K. W. Berryman, S. A. Lyon, and M. Segev, Appl. Phys. Lett. **70**, 1861 (1997).

²J. Phillips, P. Bhattacharya, S. W. Kennerly, D. W. Beekman, and M. Dutta, IEEE J. Quantum Electron. **35**, 936 (1999).

³S. Maimon, E. Finkman, G. Bahir, S. E. Schacham, J. M. Garcia, and P. M. Petroff, Appl. Phys. Lett. **73**, 2003 (1998).

⁴D. Pan, E. Towe, and S. Kennerly, Appl. Phys. Lett. **73**, 1937 (1998).

⁵H. C. Liu, M. Gao, J. McCaffrey, Z. R. Wasilewski, and S. Fafard, Appl. Phys. Lett. **78**, 79 (2001).

⁶S. Kim, H. Mohseni, M. Erdtmann, M. Michel, J. Jelen, and M. Razeghi, Appl. Phys. Lett. **73**, 963 (1998).

⁷L. Chu, A. Zrenner, G. Bohm, and G. Abstreiter, Appl. Phys. Lett. **75**, 3599 (1999).

⁸S.-W. Lee, K. Hirakawa, and Y. Shimada, Appl. Phys. Lett. **75**, 1428 (1999).

⁹N. Rappaport, E. Finkman, T. Brunhes, P. Boucaud, S. Sauvage, N. Yam, V. Le Thanh, and D. Boucher, Appl. Phys. Lett. **77**, 3224 (2000).

¹⁰Z. Chen, O. Baklenov, E. T. Kim, I. Mukhametzhanov, J. Tie, and A. Madhukar, J. Appl. Phys. **89**, 4558 (2001).

¹¹V. Ryzhii, I. Khmyrova, V. Mitin, M. Strosio, and M. Willander, Appl. Phys. Lett. **78**, 3523 (2001).

¹²J. D. Phillips, J. Appl. Phys. **91**, 4590 (2002).

¹³U. Bockelman and G. Bastard, Phys. Rev. B **42**, 8947 (1990).

¹⁴H. Benisty, C. M. Sotomayer-Torres, and C. Weisbuch, Phys. Rev. B **44**, 10945 (1991).

¹⁵A. D. Stiff, S. Krishna, P. Bhattacharya, and S. Kennerly, Appl. Phys. Lett. **79**, 421 (2001).

¹⁶E.-T. Kim, Z. Chen, and A. Madhukar, Appl. Phys. Lett. **79**, 3341 (2001).

¹⁷L. T. Lester, A. Stintz, H. Li, T. C. Newell, E. A. Pease, B. A. Fuchs, and K. J. Malloy, IEEE Photonics Technol. Lett. **11**, 931 (2000).

Theoretical Model for a Cloudy-Channel Laser Communications Experiment

T. M. Shay

*University of New Mexico
Center for High Technology Materials
1313 Goddard SE
Albuquerque, NM 87106
(505)-272-7818
tshay@chtm.unm.edu*

M. Enoch

*Lockheed-Martin Space Systems Company
Advanced Technology Center
1155 University Blvd., SE, Room W227
Albuquerque, NM 87106
(505)-843-4079
michael.enoch@lmco.com*

Lt. Col. R. Ewart

*USAF
Space and Missiles Systems Center
180 Skynet Way
El Segundo, CA 90245
(310)-363-5423
roberta.ewart@losangeles.af.mil*

Abstract

The authors will present a simplified system model for an experiment to collect the optical channel characterization data for high data rate ground to low-earth-orbit optical communications system through clouds. The experiment consists of a 1550-nm ground-to-space shuttle uplink and a round-trip link where the signal photons are transmitted up to the space shuttle and back down to the ground. The system will be designed to operate with thin to intermediate thickness clouds in the communications channel. The results of calculated link margins and system requirements will be presented.

Introduction

We present the model for an earth-to-space shuttle optical communications system. The system is designed to transmit at data rates of up to 2.5 Gbps through thin and intermediate density optical clouds.

Free space laser communications, both for space-ground (vertical path) and terrestrial or ground-ground (horizontal path), offer great promise for providing high data rate wireless communications. These optical wireless communications systems offer mass, power and volume

advantages for the transmitter and receiver when compared with RF systems [1], while avoiding the problems of frequency management and regulatory issues, interference, and signal security encountered with RF communication systems. There is great interest in using laser communications to support satellite uplink and downlink requirements to take advantage of these benefits.[1,2]

Optical wavelengths have been shown to be generally more affected by particular environmental conditions that reduce the reliability of the link. (RF systems, particularly at higher frequencies, such as Ku and Ka band, can also suffer significant degradation from other types of weather.)[3] In addition, the characteristics of the atmospheric channel, especially adverse weather conditions, can result in a number of conditions that can degrade or disrupt communications.[4] The optical effects include scintillation resulting from atmospheric turbulence, scattering in clouds, fog, and precipitation and attenuation from atmospheric absorption.

Scattering in clouds, fog, precipitation, and aerosols results from interaction of the optical signal with the suspended particles in the atmosphere. The sizes of these particles are typically between 0.01 and 10.0 microns, and result in a Mie scattering behavior.[5] (The interaction between the air molecules and the optical signal are for the most part in the Rayleigh scattering range and are not considered a

significant effect.) The Mie scattering effectively diffuses the optical signal over a much wider area, while also stretching out the temporal characteristics of the signal. Since most optical communication systems use diffraction-limited optics, with narrow beamwidths, the majority of the signal energy ends up outside of the view of the receiving telescope, and may not be sufficient to allow detection and demodulation. The temporal spreading of the signal can lead to serious degradation of high speed communications, because there is no way to determine if the received signal energy traveled directly or traveled a longer path via multiple scatters and if the received signal energy belongs to the current symbol or a previously received symbol. This phenomenon is called intersymbol interference and it also occurs in RF and guided wave communications.

The optical communications channel has not been characterized in the presence of clouds. It is not possible to determine when the cloudy communications channel is limited by signal attenuation and when the cloudy channel is limited by pulse stretching (intersymbol interference). Until the channel characterization data is available we will not be able to develop channel compensation techniques. In order for optical communications to be used as a viable alternative to RF communications, it is necessary to develop techniques to allow for effective communications under all these circumstances. In this paper, we present a simple link model for an optical communications system that can communicate through thin to intermediate clouds and characterize the cloudy channel link was designed to allow for the characterization of the medium.

Communications Link Analysis

We model a 1.5 μm free-space optical channel operating at a data rate of 2.5-Gbps for both the uplink from the ground to the space shuttle and for an up-and-back or round trip link where the uplink signal beam is retro-reflected from space shuttle back to the transmitting telescope. Thus, we can diagnose the characteristics at both ends of the link. On board the space shuttle, the received average power and the bit-error-rate of the 1.5 μm uplink data stream will be measured in order to provide a simple measurement of the channel losses. The link quality is characterized by the measured bit-error-rate of the uplink. For the uplink bit-error-rate measurements we will transmit predetermined blocks of pseudorandom data that can be compared with identical blocks of data that are stored on the spacecraft. We will perform the same experiments with the 1.5 μm round-trip link and this will give us additional information. On the ground we have the luxury of many more diagnostics than we do in space. Hence, on the ground, the temporal response of the roundtrip signal can be directly measured. Thus providing a direct measurement of any

pulse shape distortion that might occur as the data pulses propagate through the channel.

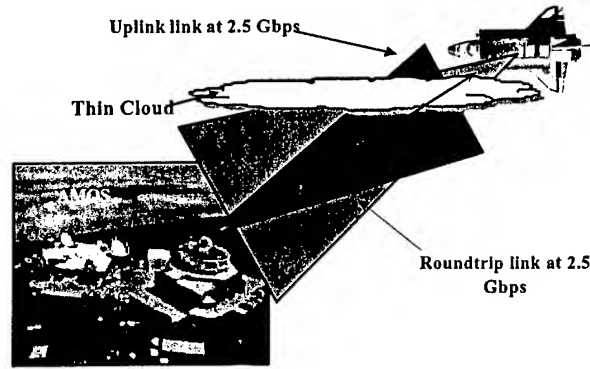


Fig. 1 Cloudy Channel Optical Communications System

Figure 1 illustrates the communications link at 1.5 μm . The telescope on the ground transmits an OC-48 data stream, which is, transmitted to the space shuttle where a receiver on board measures the average power received as well as the bit-error-rate. The OC-48 (2.5 Gbps) data stream is also directed back to the ground receiver by the flight system's retro-reflector. The range from the ground to the spacecraft is,

$$R = \frac{h_{\text{orbit}}}{\cos(\phi)} \quad (1)$$

where h_{orbit} represents the orbital altitude of the orbit and ϕ represents the Zenith angle of the spacecraft. The altitude of a typical space shuttle orbit is 320-km.[6]

Uplink Signal to Noise Ratio

The optical power incident upon the spacecraft's photoreceiver's is,

$$P_{\text{flight}} = P_{\text{laser}} \cdot \eta_T \cdot \eta_{\text{Atm}} \cdot \eta_{\text{flight}} \cdot T_{\text{flight}} \cdot \frac{A_{\text{flight}} \cdot \cos^2(\phi) \cdot \cos(\phi - \alpha)}{h_{\text{orbit}}^2 \cdot \Delta\Omega_{\text{up}}} \quad (2)$$

where P_{flight} represents the signal power received at the spacecraft. P_{laser} represents the ground transmitter power. η_T , η_{Atm} , and η_{flight} represent the telescope, atmospheric and flight receiver efficiencies, respectively. T_{flight} represents the signal transmission of the optical filter. $A_{\text{flight_eff}}$ represents the effective area of the flight receiver. $\Delta\Omega_{\text{up}}$ represents the uplink beam divergence. α represents the spacecraft roll angle. The last term in Eq. 2 represents the uplink propagation loss, which is simply the effective area of the flight receiver, as seen from the ground station, divided by the area of the uplink beam at the spacecraft.

The uplink signal-to-noise ratio is,

$$\text{SNR} = \frac{(P_{\text{flight}} \cdot R_{\text{PD}})^2}{2qB(P_{\text{flight}} \cdot R_{\text{PD}}) + 2qB \cdot P_{\text{noise}} \cdot R_{\text{PD}} + i_{\text{noise}}^2} \quad (3),$$

where q represents the electron charge,
 B represents the electronic bandwidth,
 R_{PD} represents the photodetector responsivity,
 P_{noise} represents the received background noise power,
 i_{noise} represents the photoreceiver's noise current.

The lowest received signal occurs when the spacecraft is at a Zenith angle of $\pi/3$. The uplink solid angle, $\Delta\Omega_{\text{up}} = \pi \cdot 10^{-10}$ sr. For a 6-inch diameter collecting optic, a 10-watt transmitter, and the spacecraft roll angle, $\alpha = 34^\circ$, the received power at spacecraft is 32- μW when the Zenith angle is $\pi/3$. Using the specifications for a Discovery Semiconductor model DSC50 high-speed optical receiver, the responsivity, $R_{\text{PD}} = 0.6$ amps/watt, and the receiver noise current for OC-48 (2.5 Gbps) is 3/4 μA . Using Eqs. 1 and 2, we calculate an uplink signal-to-noise ratio of 64-dB. This is 44-dB above the SNR required for a bit error rate of 10^{-6} . If we allow for a 10-dB loss due to scintillation we can still provide a margin of 34-dB at the worse case Zenith angle of $\pi/3$.

Round Trip Link Signal to Noise Ratio

The received signal power for the round trip link P_s , is

$$P_s = P_{\text{laser}} \cdot (\eta_{\text{r}} \cdot \eta_{\text{atm}})^2 \cdot \eta_{\text{retro}} \cdot \eta_{\text{rbt}} \cdot T_{\text{F}} \cdot \frac{A_{\text{retro_eff}}}{R^2 \cdot \Delta\Omega_{\text{up}}} \cdot \frac{A_{\text{r}}}{R^2 \cdot \Delta\Omega_{\text{return}}} \quad (4),$$

where η_{retro} and η_{rbt} represent the retro-reflector, and receiver beam train losses, respectively. T_{F} represents the signal transmission of the optical filter. $A_{\text{retro_eff}}$ represents the retro-reflectors effective areas, as seen from the ground terminal. A_{r} represents the ground receiver's area. $\Delta\Omega_{\text{up}}$ and $\Delta\Omega_{\text{return}}$ represent the uplink beam and the return beam solid angles, respectively. In this case the light must propagate up to the spacecraft and return. Thus the telescope and atmospheric loss terms are squared in Eq. 4. The first fraction on the right hand side of Eq. 4 represents the propagation loss for the beam directed to the spacecraft. This is merely the effective area of the retro-reflector divided by the area of the transmitted beam at the spacecraft. This is equivalent to the signal intercept loss given in the previous section. The final term is the propagation loss of the return beam. It is the area of the ground receiver divided by the return beam area on the ground.

The round trip link return signal is,

$$P_s = P_{\text{laser}} \cdot (\eta_{\text{r}} \cdot \eta_{\text{atm}})^2 \cdot \eta_{\text{retro}} \cdot \eta_{\text{rbt}} \cdot \left(T_{\text{F}} \cdot \frac{A_{\text{r}} \cdot D_{\text{retro}}^4 \cdot \cos^4(\phi) \cos^2(\phi - \alpha)}{h_{\text{orbit}}^4 \cdot (1.22 \cdot \lambda)^2 \cdot \Delta\Omega_{\text{up}}} \right) \quad (5),$$

where D_{retro} represents the diameter of the retro-reflector and λ represents the wavelength of the signal. Note that rolling the spacecraft through an angle, α equal to the latitude of the ground station increases the effective area of the retro-reflector and hence increases the signal as can be seen from Eq. 5. The return signal depends on the orbit altitude, h_{orbit} , to the fourth power as expected, and also on the retro-modulator diameter to the fourth power. But the signal depends upon the Zenith angle to the sixth power. Thus, a small increase in spacecraft acquisition intercept angle yields a large decrease in the required laser transmitter power. The maximum signal power, $P_s(\phi)$ occurs when the spacecraft is near Zenith. To be conservative we performed all of our signal calculations for the worse case that is a Zenith angle = $\pi/3$.

The signal-to-noise ratio for an optical pre-amplified receiver in free space when inter-symbol interference can be neglected the is

$$\text{SNR} = \frac{(P_s \cdot G)^2}{4 \cdot G \cdot P_s \cdot P_{\text{ASE}} + P_{\text{ASE}}^2 \cdot \left(2 - \frac{B}{B_{\text{opt}}} \right) + \frac{2 \cdot q \cdot B}{R_{\text{res}}} \cdot (G \cdot P_s + P_{\text{ASE}}) + i_{\text{noise}}^2} \quad (6),$$

where

G represents the gain of the EDFA preamplifier.

R_{res} represents the responsivity of the photodetector,

P_{ASE} represents the amplified spontaneous emission noise of the EDFA

B_{opt} represents the bandwidth of the receiver's optical filter,

q represents the electron charge,

B represents the electronic bandwidth,

P_{sky} represents the total solar optical noise power that is incident upon the photodetector,

i_{noise} represents equivalent input noise current of the receiver electronics.

The first term in the denominator is the amplifier signal-amplified spontaneous emission noise term. The next term is the amplified spontaneous emission self-beating noise term. The third term is the shot noise term that includes contribution from the signal and the amplifier ASE and the final term quantifies the electronic of the photo-receiver noise.

For a well designed optically pre-amplified receiver, the noise is dominated by the signal-spontaneous beat noise

term in Eq. 6. Thus, to a good approximation the signal-to-noise ratio is,

$$SNR = \frac{P_s}{(4 \cdot h \cdot \nu \cdot n_{sp} \cdot B_{opt})} \quad (7)$$

where $h\nu$ represents the photon energy and n_{sp} represents the spontaneous emission factor.

Equation 7 shows that the receiver signal-to-noise ratio is directly proportional to the received signal power and inversely proportional to the optical amplifier spontaneous emission factor and optical bandwidth. Note that a low noise optically preamplified receiver provides 8-dB higher sensitivity compared to a simple pin receiver.

The system characteristics for the 1.5-micron round trip link are listed in Table I.

Table I. 1.5- μ m SYSTEM CHARACTERISTICS

Transmitter power	10 dBW (10 W)
Receiver diameter	3.67-m
Data rate	OC-48 (2.5 Gbps)
Scintillation Margin	10-dB
Atmospheric loss	3-dB
Interference filter loss	1-dB
Retro-reflector loss	0.25-dB
Transmit beam divergence (Communications mode)	5- μ radians
Spacecraft intercept angle	$\pi/3$
Orbital altitude	320-km
Spontaneous emission factor of Optical Amplifier	1.1

Using the link equation formulation, the received signal power for this link is given by,

$$P_{sdB} = P_{laserdB} - L_{roundtrip} \quad (8)$$

where P_{sdB} and $P_{laserdB}$ represent the received signal and transmitter powers, respectively in units of dBW. $L_{roundtrip}$ represents the total link round trip loss in dB. The total optical link loss is,

$$L = L_{upprop} + L_{downprop} + L_{retro} + 2 \cdot L_{atm} + 2 \cdot L_T + L_{rbi} + L_F \quad (9)$$

where $L_{downprop}$ and L_{upprop} represent the propagation losses for the upward and downward traveling beams, respectively. L_{retro} , L_T , and L_F represent the losses of the retro-reflector, the telescope, and the optical filter, respectively. L_{rbi} represents the loss in the portion of the receiver beam train that is not part of the transmitter beam train. L_{atm} represents the single pass atmospheric loss. Table II summarizes the round trip link losses.

The final entry in Table II is the total link loss for the round trip link, 52-dB. Using the system characteristics in

Table I and the total link loss from Table II the received signal power at a spacecraft intercept angle of $\pi/3$ from Zenith is 32- μ W. In atmospheric communications the power must be increased to account for atmospheric scintillation. Therefore, we need to be certain that these received signal powers produce a signal-to-noise ratio that is at least 10-dB higher than the minimum signal-to-noise ratio required for the link.

Table II. Round trip link losses

Uplink beam propagation loss	L_{upprop}	30-dB
Downlink beam propagation loss	$L_{downprop}$	7-dB
Retro-reflector loss	L_{retro}	1.4-dB
Atmospheric loss	$2 L_{Atm}$	6-dB
Receiver beam train loss	L_{rbi}	0.1-dB
Telescope loss	$2 L_T$	1-dB
Optical filter loss	L_F	1-dB
Total link loss	$L_{roundtrip}$	52-dB

Link Margin Summary

The bit-error-rate is the performance metric for digital communications systems. Therefore, we will in this section calculate the minimum received signal powers for the four earth-space communications links in our experiments.

The bit-error-rate, BER, of an on-off keyed, unbiased data, binary digital communications link with equal noise for zeros and ones is given by,

$$BER = \frac{1}{2} \operatorname{erfc} \left(\frac{\sqrt{SNR}}{2 \cdot \sqrt{2}} \right) \quad (10)$$

where erfc represents the well known complementary error function.

For space communications a bit error rate of 10^{-6} is considered acceptable for most data. Using Eq. 10, we find that a bit error rate of 10^{-6} requires the electrical SNR = 91. Thus 91 is the minimum SNR that will provide a bit error rate of 10^{-6} . The 10-dB optical scintillation margin provided a BER of $\sim 10^{-3}$ to 10^{-4} in the GOLD experiment.[7,8] Thus, the link margin needs to be 10-dB to compensate for the effects of scintillation.

Using the system characteristics illustrated in Table I and a good quality optical pre-amplifier, then from Eq. 7 it can be shown that a bit-error-rate of 10^{-6} is achieved for a received signal power of 0.13- μ W for the round trip link. Since the received power at spacecraft intercept will be 37- μ W, the worse case link margin is 34-dB for an optically pre-amplified receiver. An optically pre-amplified receiver increased the sensitivity by 8-dB compared to a pin photoreceiver.

The uplink and roundtrip link margins are summarized in Table III.

Table III. AMOS Link Margin Summary

	1.5-μm uplink	1.5-μm roundtrip
Data rate	2.5 Gbps	2.5 Gbps
Transmitter	10-W	10-W
Clear sky margin	34-dB	44-dB

The signal to noise ratios for the 1.5- μ m links are calculated using the equations in the previous section. These results illustrate that, even allowing a 10-dB margin for scintillation; there is sufficient margin to compensate for the uplink and roundtrip links to sustain a 34-dB and 24-dB attenuation, respectively, before the link BER drops below 10^{-6} . Thus sufficient margin is available to explore the attenuation due to thin clouds and intermediate density clouds. We have calculated the signal-to-noise ratio at the longest distance to be conservative.

Summary

The use of a large aperture telescope such as the 3.6-m AEOS telescope provides a significant margin making it possible to test the cloudy channel in an uplink as well as in the round trip link. We plan to transmit data at a rate of OC-48 in clear sky conditions. That OC-48 data stream can be sent to the space shuttle and then retro-reflected directly back to the ground station. Preliminary calculations indicate that the uplink margin is 44-dB and the round trip link margin is 34-dB at the longest ranges of this experiment. Hence, there is sufficient margin to explore the attenuation due not only due to thin clouds but also due to intermediate and dense clouds.

Such an experiment would be the first step in mitigating adverse weather effects in the optical communications channel. Once the channel has been characterized, the selection and evaluation of promising channel mitigation techniques can begin. The mitigation of the optical channel will result in a significant increase in optical channel availability. These are key steps in realizing optical communications high bandwidth links for future communications architectures and directly linking free space and terrestrial grids for the warfighter.

References

- [1] "System-level comparison of optical and RF technologies for space-to-space and space-to-ground communications links circa 2000," by R. G. Marshalek, G. S. Mercherle, and P. Jordan, Proceedings of the Society of Photo-optical Engineers, vol. 2699, pp. 134-145, 1996.
- [2] "Comparative Study of optical and rf communication systems for a Mars mission," H. Hemmati, K. E. Wilson, M. Sue, D. L. Roscoe, F. Lansing, M. D. Wilhelm, L. Harcke, and C. Chen, Proceedings of the Society of Photo-optical Engineers, vol. 2699, pp. 146-165, 1996.
- [3] "The Communications Handbook," Jerry D. Gibson, Editor, Chapter 69, "Satellite Transmission Impairments," by Louis J. Ippolito Jr., CRC Press, 1997.
- [4] "A preliminary Weather Model for Optical communications through the Atmosphere," by K. Shaik, TDA Progress Report, 42-115, pp. 212-218, 1988.
- [5] "Optical Channels," Sherman Karp, Robert M. Gagliardi, Steven E. Moran, and Larry B. Stotts, page 223, 1988, Plenum Press, New York and London.
- [6] Tracy, William, Shuttle Flight Information Officer, private communication. The typical uncertainties in the downtrack position when the position vector is updated within 20 minutes of pass.
- [7] Wilson, K. E., Lesh, J. R., Araki, K., Arimoto, Y., "Overview of the Ground to Orbit Lasercom Demonstration," SPIE Proceedings, 2990, pp. 23-30, 1997, in Free-Space Laser Communications Technologies IX, G. Stephen Mercherle, Ed.
- [8] M. Jeganathan et. al., Proceedings of the SPIE, vol. 2990, 70-81, (1997).

Full-Duplex Communication on Single Laser Beam

T. M. Shay and J. A. MacCannell
University of New Mexico
Center for High Technology Materials
1313 Goddard SE
Albuquerque, NM 87106
Email: tshay@chtm.unm.edu

and

D. A. Hazzard, G. Lee, C. D. Garrett*, J. A. Payne**, N. Dahlstrom, and S. Horan
New Mexico State University
Klipsch School of Electrical and Computer Engineering
Las Cruces, NM 88003

ASBTRACT

We present the first experimental demonstration of full-duplex communication on a single laser beam. The forward link beam simultaneously transmits the forward link data and serves as the carrier wave for the return link. A fraction of incident forward link beam is modulated and retro-reflected back to the receiver location. The forward link data format must be designed so that it is invisible to the return link's data detection system. We have named this architecture the "Lightwire. In addition there was no system trade-off required by the system. Thus we have demonstrated full-duplex on a single optical beam without any performance penalty. We will present the experimental system and discuss the experimental results.

* Now with Sandia National Laboratories.

** Now with University of Arizona.

2.5-3.5 μm optically pumped GaInSb/AlGaInSb multiple quantum well lasers grown on AlInSb metamorphic buffer layers

E. A. Pease, L. R. Dawson, L. G. Vaughn, P. Rotella, and L. F. Lester
The Center for High Technology Materials, University of New Mexico, 1313 Goddard
SE, Albuquerque, New Mexico 87106

(Received OCT – 4 2002 REF# JR02-2743

Room-temperature emission is observed as long as 3.26 μm in optically pumped type-I quantum well lasers on relaxed epitaxial layers grown by molecular beam epitaxy. A superlattice is used to filter dislocations in the metamorphic buffer to reduce Shockley-Read-Hall losses. The longest wavelength emission of 3.45 μm from these structures is observed at 170K, and the brightest room-temperature laser emits 0.5 W/facet peak power at 2.81 μm . It has a low threshold power density of 169 W/cm² and a differential quantum efficiency of 28%. The characteristic temperatures, T_0 and T_1 , are 119K and 171K, respectively. Stimulated emission is observed in this sample at a maximum operating temperature of 370K.

I. INTRODUCTION

Lasers operating in the 2-4 μm mid-infrared wavelength range find application in trace-gas detection¹, ultralow-loss fiber communication², and atmospheric transmission for ladar³, communication, and countermeasures. The temperature performance of mid-infrared semiconductor lasers grown on GaSb is always a central issue. They require thermoelectric or even cryogenic cooling to operate. This limit on operating temperature depends on the exponential change in threshold and slope efficiency with temperature. Unfortunately, there is a general lack of reported results of T_1 for mid-IR semiconductor lasers.

Near 2 μm Type-I GaInAsSb/AlGaAsSb lasers have been previously reported with large characteristic threshold temperatures, T_0 : 140K⁴, 104K⁵ and 110K⁶. By increasing the arsenic content in the quantum wells, longer wavelengths have been reported with smaller characteristic temperatures. A T_0 of 58K⁷ was reported at 2.8 μm . Longer wavelength emission has been reported at 4.5 μm from InAsSb/AlInAsSb, which had a T_0 of 26K⁸ and only operate at cryogenic temperatures. Increased indium and arsenic content cause a deleterious loss in valence band offset in these structures.

AlSb and GaSb have a nested type-I alignment with a positive valence band offset of 400 meV whereas AlSb and InAs have a staggered type-II alignment with a small negative offset of 100 meV. The performance of these mid-infrared structures can be improved by keeping the larger valence band offsets achievable with GaInSb quantum

wells. On GaSb substrates, this limits the emission wavelength to about 2 μm . However, the emission wavelength can be significantly increased by growing on a substrate with a lattice constant larger than GaSb. This paper reports the design and characterization of GaInSb/AlGaInSb quantum well lasers grown on AlInSb metamorphic buffers. A theoretical study of this material system has recently been reported.⁹

II. DEVICE STRUCTURES

Samples were grown by solid-source molecular beam epitaxy on a Vacuum Generators V80H machine. All structures were grown on (100) undoped GaSb. Figure 1 shows a schematic for the metamorphic buffer. It is composed of a 0.5 μm thick AlSb layer followed by equal sized steps of $\text{Al}_{1-s}\text{In}_s\text{Sb}$ layers where the indium content, s , is increased in 9% steps. Buffers with steps larger than 9% produce significantly rougher surfaces. The fraction s is the average indium composition of the stepped layer, which is composed of a 100 \AA period superlattice of $\text{Al}_{1-x}\text{In}_x\text{Sb}/\text{Al}_{1-y}\text{In}_y\text{Sb}$. x and y were 0.0, 0.3, and 0.5 for most structures. Samples were grown at 500 $^\circ\text{C}$ with growth rates between 0.75 and 1 monolayer per second. The GaInSb ternary wells were grown as bulk but the AlGaInSb quaternary barriers are grown by the digital alloy technique using a 12.5 \AA period.

The $\text{Al}_{1-x}\text{In}_x\text{Sb}/\text{Al}_{1-y}\text{In}_y\text{Sb}$ superlattice is used to filter threading dislocations. It was observed early on in epitaxial growth of III-V semiconductors that threading dislocations propagate perpendicular to the growth direction at heterojunctions.¹⁰ By

using a superlattice, many heterojunctions are formed creating a “filter” for dislocation. This may occur by the dislocation propagating to a free edge or for multiple threading dislocations to annihilate each other. Photoluminescence integrated intensities indicate some defects accumulate together possibly along the free edge of slip planes. Dislocation filtering with superlattices has been demonstrated with mobility studies in other material systems.¹¹ The ability of AlSb/GaSb superlattice to filter dislocations to produce an optically active region has been demonstrated by growing AlGaSb/GaSb double heterostructure lasers on silicon.¹²

Figure 2 shows the flat band schematic for the laser structures grown on the metamorphic buffers. It is composed of a 1 μm waveguide surrounded by a 2 μm clad made of the terminating metamorphic buffer layer. The top metamorphic layers serve as part of the lower clad. The active area is composed of 4 100-Å compressively strained GaInSb wells separated by 100 Å lattice matched AlGaInSb barriers having a 20% Al content. The valence band offset was calculated to be more than 75 meV for all structures. The active area in Figure 2 has the largest offset near 100 meV.

The valence band offsets were calculated using a linear interpolation. The ternary gamma point band positions were calculated using a quadratic fit¹³. The quaternary band positions are calculated using a linear interpolation of its constituent ternaries at the midpoint of the compositional plane¹⁴, and the bow in the band gap was given to the conduction band making a linear interpolation of valence band offsets¹⁵. The effects of

strain on the quantum well gamma points were incorporated from solutions of the Luttinger-Kohn Hamiltonian¹⁶.

III. MORPHOLOGY AND PHOTOLUMINESCENCE

All samples show crosshatching using a Nomarski phase-contrast microscope. This crosshatching becomes visible with a standard microscope on the 45% and 54% buffers. Table I shows the surface roughness for these step-graded buffers. The root-mean-squared surface roughness across 1 cm² areas was measured with an atomic force microscope. The surface roughness of the metamorphic buffers increase at a slow constant rate with respect to indium content until an indium content of 45% is reached where a dramatic increase is observed in the surface roughness. It was also observed that continuously graded buffers and slower growth rates will slightly decrease surface roughness, but buffers with lattice constants larger than 6.29 Å still had significantly larger surface roughness.

Locally, the buffers are very smooth to Al_{0.64}In_{0.36}Sb. Figure 3 shows transmission electron micrograph of the first step of the superlattice from an Al_{0.64}In_{0.36}Sb buffer taken near the AlSb layer, which is in the direction of the dark area. Disorder is shown trapped by the superlattice in the lower epilayers preventing the dislocations from threading up through the buffer. During the relaxation of each step, similar regions of defects are observed, but the layers in the end step are well ordered. The micrograph in Figure 3

shows the most disorder, which is near the AlSb interface. The brighter layers in this micrograph are AlSb.

A double crystal x-ray diffraction rocking curve of the $\text{Al}_{0.64}\text{In}_{0.36}\text{Sb}$ buffer using a symmetric 004-scan is shown in Figure 4. This buffer was continuously graded to highlight the thickness fringes. This x-ray diffraction indicates a completely relaxed top layer with an average composition of $\text{Al}_{0.64}\text{In}_{0.36}\text{Sb}$. Its full-width-at-half-maximum (FWHM) is twice the GaSb substrate peak. The thickness fringes are labeled A, B, C, and D. The FWHM and thickness fringes indicate a well-ordered buffer.

A simple measurement will demonstrate the dominant recombination channel for semiconductors from integrated photoluminescence intensity. The total recombination is the radiative rate plus the total loss rate, $R_{21} + R_0 = R_2$. The radiative rate is $R_{21} = BN^2$, where N is the number of carriers. The total loss can include Shockley-Read-Hall (SRH) and Auger losses, $R_0 = AN + CN^3$. The total rate is

$$\frac{P_{in}}{h\nu_{in}}\eta_{in} = R_2,$$

where P_{in} is the pump power, ν_{in} is the pump wavelength, and η_{in} is the pump efficiency.

Combining these equations, the carrier concentration can be seen to have a different dependence on the pump power depending on which recombination process is the dominant.

$$\text{If } A \gg B \text{ and } C \text{ then } N = \frac{P_{in}}{Ah\nu_{in}}\eta_{in}.$$

If $B \gg A$ and C then $N^2 = \frac{P_{in}}{Bh\nu_{in}} \eta_{in}$.

If $C \gg A$ and C then $N^3 = \frac{P_{in}}{Ch\nu_{in}} \eta_{in}$.

Finally, the collected photoluminescence intensity, P_{out} , with collection efficiency, η_{out} , and emission wavelength, ν_{out} is $P_{out} = \eta_{out} h\nu_{out} R_{21}$. Combining this equation with the limiting cases, the integrated photoluminescence intensity can be fit with $P_{out} \propto P_{in}^\beta$, where $P_{out} \propto P_{in}^2$ when SRH recombination is dominant, $P_{out} \propto P_{in}^1$ when radiative recombination is dominant, and $P_{out} \propto P_{in}^{2/3}$ when Auger recombination is dominant.

β is 1.06, 1.12, and 1.23 at room temperature for active areas grown on metamorphic buffers terminating with 27%, 36%, and 45% indium content, respectively. This parameter was generally larger at lower temperatures, but all three samples were larger than 1 at 350K. This indicates that radiative recombination is the dominant recombination channel. It also shows that SRH rates are larger than Auger rates, and SRH losses increases for active regions on larger lattice constant buffers. This is attributed to the decrease of AlSb content in the filter for larger lattice constant buffers.

IV. LASER RESULTS

Lasers were fabricated by lapping and polishing the substrate to $\sim 100 \mu\text{m}$. The thinned samples were cleaved into 1 mm cavities and mounted epi-side up to copper

heatsinks with indium. The maximum operating temperatures and emission wavelengths are included in Table II for the six samples. The maximum operating temperatures were obtained using pump intensities of approximately 5 kW/cm^2 . Even with a surface roughness 1.5 times the quantum well thickness, lasers grown on metamorphic buffers terminating with $\text{Al}_{0.46}\text{In}_{0.54}\text{Sb}$ still lased. However, these samples showed reduced photoluminescence and poor laser performance. Only small regions of the mounted bars lase at 100K. Lasers on the 27% and 36% buffer have only small regions that do not lase at 300K.

Samples were pumped with a 980 nm stacked laser diode array using $50 \mu\text{s}$ pulses, and the pump stripe was $250 \mu\text{m}$ wide. The multimode above threshold spectra for a 0.5% compressively strained MQW laser on the 27% buffer, a 1% compressively strained MQW laser on the 36% buffer and a 1% compressively strained MQW laser on the 45% buffer at 300K are shown in Figure 5. The respective emission wavelengths are $2.53 \mu\text{m}$, $2.81 \mu\text{m}$, and $3.26 \mu\text{m}$. The insert shows the 170K emission from a 1% compressively strained MQW laser on a 54% buffer. Samples on the 27% and 36% buffer lase above room temperature, but only with 1% compressively strained MQW laser on the 45% buffer operated at room temperature. The beneficial effect of compressive strain is also evident in the threshold and efficiencies. Compressive strain in quantum wells has been shown to increase the maximum gain¹⁷ and reduce Auger rates¹⁸.

The 1% compressively strained MQW laser on the 54% buffer has the longest emission at $3.45 \mu\text{m}$ but only to 170K. The 300K power curves using a 5% duty cycle are

shown in Figure 6 for the three samples in Figure 5. The pump power is the power transmitted into the sample where a 31% loss due to reflectance from the uncoated surface was calculated. Other losses in the experimental setup were measured and are accounted for in the power measurements. All samples showed significant thermal rollover. However, larger duty cycles did not affect the threshold or efficiency near threshold but limited the maximum emitted power. The 1% compressively strained MQW laser on 36% buffer emits the most power of 0.5 W/facet peak power at 2.81 μm . It also has the lowest threshold power density of 169 W/cm^2 . Assuming all of pump power transmitted into the sample is absorbed, the differential quantum efficiency was 28%.

Lasers with equal strain on the 27% and 36% buffers have identical performance. The 0.5% compressively strained MQW laser on the 45% buffer only operated to 230K but the 1% compressively strained MQW laser on the 45% buffer operated as high as 310K. This shows a reduced performance on the 45% buffer to lasers grown on the 36% buffer but still indicates a large strain effect.

Figure 7 shows the rate of increase of the thresholds between 200K and 300K for the three samples in Figure 6. Figure 8 shows the rate of decrease of quantum efficiencies with increasing temperatures between 200K and 300K for these same samples. The 0.5% compressively strained MQW laser on the 27% buffer has a T_0 of 98K and a T_1 of 114K. The larger 1% compressively strained MQW laser on the 36% buffer has a T_0 of 120K and a T_1 of 171K showing the best performance. Larger compressive strains result in significantly larger characteristic temperatures, but the performance decreases on buffer

larger than $\text{Al}_{0.64}\text{In}_{0.36}\text{Sb}$. The 1% compressively strained MQW laser on the 45% buffer has a T_0 of 76K and a T_1 of 71K.

V. CONCLUSION

Arsenic-free optically pumped mid-infrared lasers were fabricated on AlInSb metamorphic buffers. The emission wavelengths of GaInSb type-I quantum well lasers are extended past 3 μm . The longest room temperature emission is 3.26 μm . The performance of AlGaInSb/GaInSb MQW wells lasers grown on metamorphic buffers quickly degrades beyond 3 μm . The degradation in performance for larger lattice constant buffers is attributed to SRH recombination. The strain has a dramatic effect on the performance of the tested samples. The 1% compressively strained MQW laser on the $\text{Al}_{0.64}\text{In}_{0.36}\text{Sb}$ buffer lase well above room temperature at 370K with an emission wavelength of 2.93 μm , and it has a large T_0 of 119K when operated between 200K and 300K. The extremely large T_1 of 171K results in a large differential quantum efficiency at room temperature. The dramatic loss of performance of GaInAsSb/AlGaAsSb with wavelength larger than 2 μm has been staid to wavelengths larger than 3 μm . This indicates that the valence band offset plays an important role in the performance of mid-infrared quantum well lasers, and the advent of low defect GaInSb substrates should substantially improve the performance of quantum wells lasers in the 2-5 μm range.

ACKNOWLEDGMENTS

This material is based on research sponsored by the Air Force Office of Scientific Research under agreement number F49620-99-0330, Office of Naval Research under agreement number N00014-99-1-1023, and Defense Advanced Research Projects Agency under agreement number MDA972-00-1-0024. The U.S. Government is authorized to reproduce and distribute reprints for Governmental purposes notwithstanding any copyright notation thereon.

The views and conclusions contained herein are those of the authors and should not be interpreted as necessarily representing the official policies or endorsements, either expressed or implied, of the Air Force Office of Scientific Research, Office of Naval Research, or Defense Advanced Research Projects Agency.

Figure 1 Schematic for the step graded $\text{Al}_{0.73}\text{In}_{0.27}\text{Sb}$ metamorphic buffer with dislocation filtering using a superlattice with a 100 Å period. The steps are 0.5 μm thick. x and y for the given layer are 0% and 30% indium content, respectively.

Figure 2 Flat band of schematic of the 1% compressively strained GaInSb 100-Å MQW laser on a 36% buffer. The valence band offset for all samples is between 75 meV and 100 meV.

Table I Root-mean-squared surface roughness of the metamorphic buffers across of 1 cm² areas measured with an atomic force microscope.

Figure 3 Transmission electron micrograph of the bottom filter layers of an $\text{Al}_{0.64}\text{In}_{0.36}\text{Sb}$ metamorphic buffer near the AlSb interface. Disorder is trapped in the lower epi-layers of each step.

Figure 4 Symmetric 004-reflection double-crystal x-ray diffraction pattern of the 36% metamorphic buffer showing the terminating upper superlattice and its thickness fringes. This buffer was continuously graded rather than step graded to clearly indicate the thickness fringes.

Table II Active area compositions on several metamorphic buffers are tabulated showing the percent strain of the quantum wells, emission wavelengths, and maximum temperatures.

Figure 5 Above threshold 300K spectra for 0.5% compressively strained MQW lasers on the 27% buffer and 1% compressively strained MQW lasers on the 36% and 45% buffers. The insert shows the longest

emission occurred at 170K from 1% compressively strained MQW laser on the 54% metamorphic buffer. These broad area lasers were multimode.

Figure 6 300K power curves for 0.5% compressively strained MQW lasers on the 27% buffer and 1% compressively strained MQW lasers on the 36% and 45% buffers using a 980 nm stacked diode array with 50 μ s pulses at 5% duty cycle for 1mm cleaved samples. The 2.8 μ m sample emitted 0.5 W/facet peak power.

Figure 7 Plots to determine the characteristic threshold temperatures between 200K and 300K for 0.5% compressively strained MQW lasers on the 27% buffer and 1% compressively strained MQW lasers on the 36% and 45% buffers. The 2.8 μ m sample showed substantially lower threshold than other tested sample.

Figure 8 Plots to determine the characteristic efficiency temperatures between 200K and 300K for 0.5% compressively strained MQW lasers on the 27% buffer and 1% compressively strained MQW lasers on the 36% and 45% buffers. The 2.8 μ m sample has the largest efficiency of all grown samples.

-
- ¹ R. U. Martinelli, *Laser Focus World* **32**, 77 (1996).
- ² S. A. Miller, *Photonics Spectra* **20**, 87 (1986).
- ³ F. Hanson, *Optical Engineering* **39**, 3044 (2000).
- ⁴ T. Newell, X. Wu, A. L. Gray, S. Dorato, H. Lee, and L. F. Lester, *IEEE Photonics Technology Letters* **11**, 30 (1999).
- ⁵ C. Mourad, D. Gianardi, K. J. Malloy, and R. Kaspi, *Journal of Applied Physics* **88**, 5534 (2000).
- ⁶ C. Mermelstein, S. Simanowski, M. Mayer, R. Kiefer, J. Schmitz, M. Walther and J. Wagner, *Applied Physics Letters* **77**, 1581 (2000).
- ⁷ H. Lee, P. K. York, R. J. Menna, R. U. Martinelli, D. Z. Garbuzov, S. Y. Narayan, and J. C. Conolly, *Applied Physics Letters* **66**, 1942 (1995).
- ⁸ H. K. Choi, G. W. Turner, and H. Q. Le, *Applied Physics Letters* **66**, 3543 (1995).
- ⁹ A. D. Andreev, E. P. O'Reilly, A. R. Adams, and T. Ashley, *Applied Physics Letters* **78**, 2640 (2001).
- ¹⁰ M. S. Abrahams and C. J. Buiocchi, *J. Appl. Phys.* **45**, 3315 (1974).
- ¹¹ I. J. Fritz, L. R. Dawson, J. A. Olsen, and A. J. Howard, *Applied Physics Letters* **67**, 2320 (1995).
- ¹² J.P. Van Der Ziel, R. J. Malik, J. F. Walker, and R. M. Mikulyak, *Journal of Quantum Electronics* **QE-22**, 1587 (1986).
- ¹³ A. G. Thompson and J. C. Wolley, *Canadian Journal of Physics* **45**, 255 (1967).
- ¹⁴ R. L. Moon, G. A. Antypas, and L. W. James, *Journal of Electronic Materials* **3**, 635 (1974).
- ¹⁵ A. Ichii, Y. Tsou and E. Garmire, *Journal of Applied Physics* **74**, 2112, (1993).
- ¹⁶ S. L. Chuang, *Physical Review B* **43**, 9649 (1991).
- ¹⁷ M. Sugawara, *Applied Physics Letters* **60**, 1842 (1992).
- ¹⁸ A. D. Andreev and G. G. Zegrya, *Applied Physics Letters* **70**, 601 (1997).

Figure 1 Schematic for the step graded $\text{Al}_{0.73}\text{In}_{0.27}\text{Sb}$ metamorphic buffer with dislocation filtering using a superlattice with a 100 Å period. The steps are 0.5 μm thick. x and y for the given layer are 0% and 30% indium content, respectively.

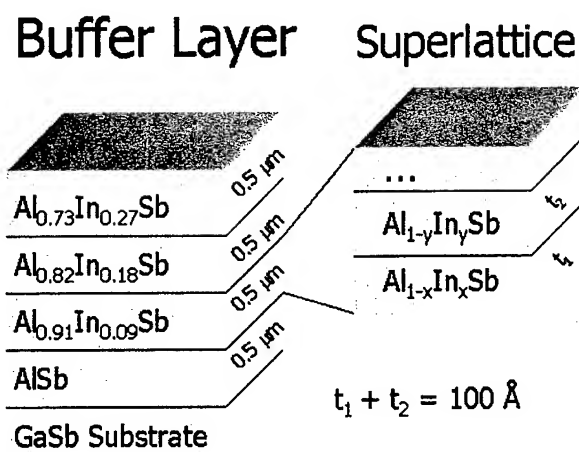


Figure 2 Flat band of schematic of the 1% compressively strained GaInSb 100-Å MQW laser on a 36% buffer. The valence band offset for all samples is between 75 meV and 100 meV.

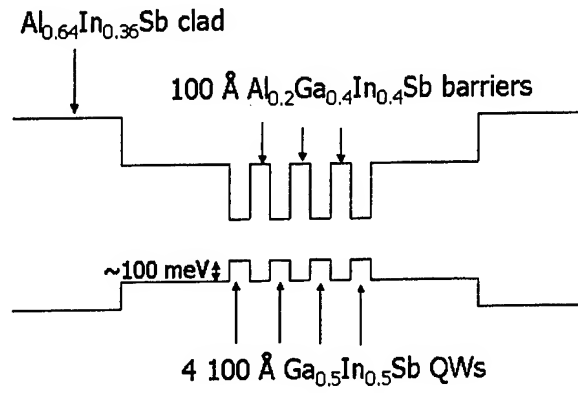


Figure 3 Transmission electron micrograph of the bottom filter layers of an $\text{Al}_{0.64}\text{In}_{0.36}\text{Sb}$ metamorphic buffer near the AlSb interface. Disorder is trapped in the lower epi-layers of each step.

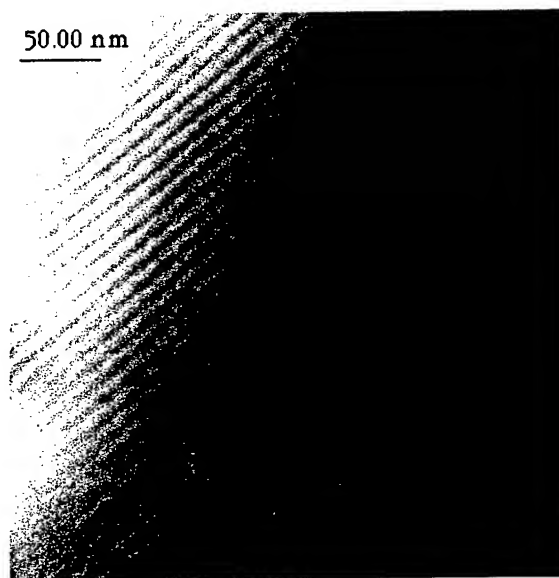


Figure 4 Symmetric 004-reflection double-crystal x-ray diffraction pattern of the 36% metamorphic buffer showing the terminating upper superlattice and its thickness fringes. This buffer was continuously graded rather than step graded to clearly indicate the thickness fringes.

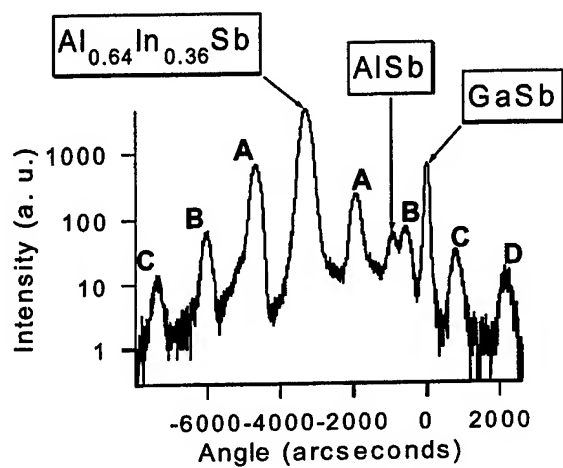


Table I Root-mean-squared surface roughness of the metamorphic buffers across of 1 cm² areas measured with an atomic force microscope.

Metamorphic sample	GaSb substrate	AlSb	Al _{0.73} In _{0.27} Sb	Al _{0.55} In _{0.45} Sb	Al _{0.50} In _{0.50} Sb	Al _{0.46} In _{0.54} Sb
RMS surface roughness (nm)	0.7	1.0	2.4	4.1	7.2	15.2

Table II Active area compositions on several metamorphic buffers are tabulated showing the percent strain of the quantum wells, emission wavelengths, and maximum temperatures.

Clad $\text{Al}_{1-x}\text{In}_x\text{Sb}$	Barrier	QW $\text{Ga}_{1-x}\text{In}_x\text{Sb}$	QW Strain	Maximum operating temperature	Emission wavelength @ max. temp.
27%	$\text{Al}_{0.20}\text{Ga}_{0.48}\text{In}_{0.32}\text{Sb}$	42%	0.5%	330K	2.58 μm
36%	$\text{Al}_{0.20}\text{Ga}_{0.40}\text{In}_{0.40}\text{Sb}$	50%	0.5%	330K	2.85 μm
36%	$\text{Al}_{0.20}\text{Ga}_{0.40}\text{In}_{0.40}\text{Sb}$	60%	1.1%	370K	2.93 μm
45%	$\text{Al}_{0.20}\text{Ga}_{0.31}\text{In}_{0.49}\text{Sb}$	60%	0.6%	230K	3.12 μm
45%	$\text{Al}_{0.19}\text{Ga}_{0.41}\text{In}_{0.40}\text{Sb}$	68%	1.1%	310K	3.28 μm
54%	$\text{Al}_{0.20}\text{Ga}_{0.23}\text{In}_{0.57}\text{Sb}$	76%	1.1%	170K	3.45 μm

Figure 5 Above threshold 300K spectra for 0.5% compressively strained MQW lasers on the 27% buffer and 1% compressively strained MQW lasers on the 36% and 45% buffers. The insert shows the longest emission occurred at 170K from 1% compressively strained MQW laser on the 54% metamorphic buffer. These broad area lasers were multimode.

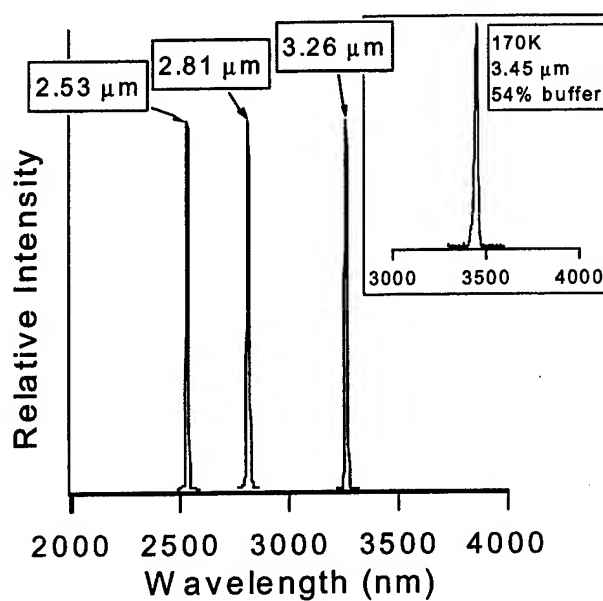


Figure 6 300K power curves for 0.5% compressively strained MQW lasers on the 27% buffer and 1% compressively strained MQW lasers on the 36% and 45% buffers using a 980 nm stacked diode array with 50 μ s pulses at 5% duty cycle for 1mm cleaved samples. The 2.8 μ m sample emitted 0.5 W/facet peak power.

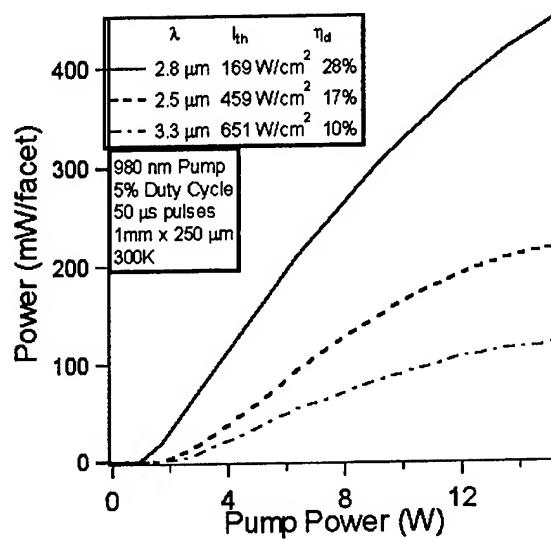


Figure 7 Plots to determine the characteristic threshold temperatures between 200K and 300K for 0.5% compressively strained MQW lasers on the 27% buffer and 1% compressively strained MQW lasers on the 36% and 45% buffers. The 2.8 μm sample showed substantially lower threshold than other tested sample.

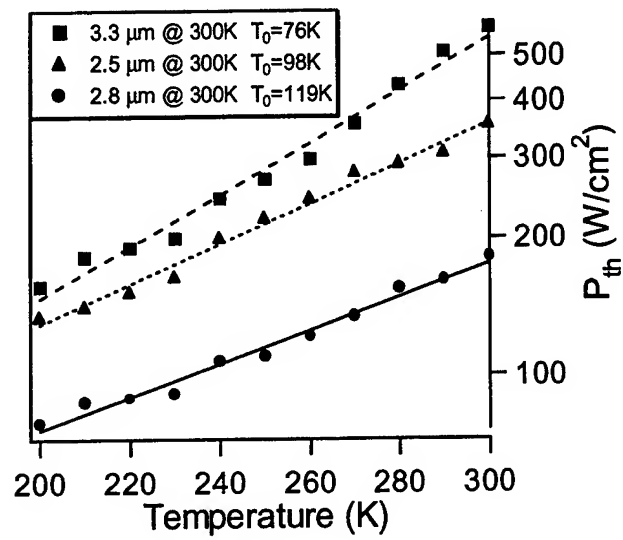
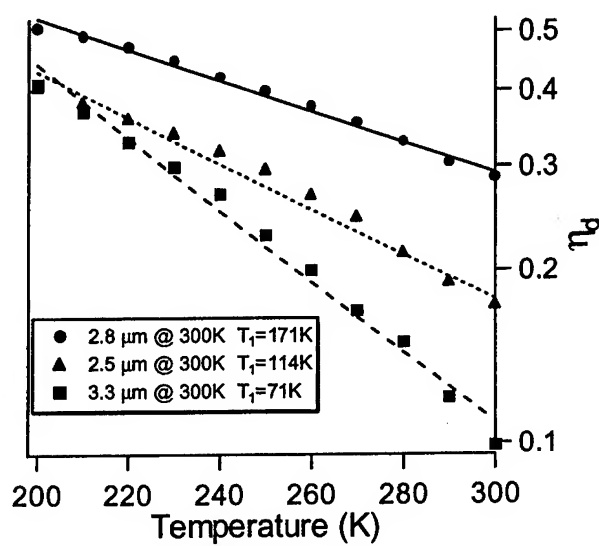


Figure 8 Plots to determine the characteristic efficiency temperatures between 200K and 300K for 0.5% compressively strained MQW lasers on the 27% buffer and 1% compressively strained MQW lasers on the 36% and 45% buffers. The 2.8 μm sample has the largest efficiency of all grown samples.





Materials
Research
Society

☐ Spring
Meeting
☒ Fall Meeting

Year
2002

Document ID
57319

Symposium Letter/Paper Number
M7.2

Copyright Form

This form must be properly completed and signed by an authorized person and accompany any paper submitted for publication by the Materials Research Society. **Note: Company or other forms may not be substituted for this form.**

Title of Paper Characterization of AlInAsSb and AlGaInAsSb MBE-grown Digital Alloys

Authors L.G. Vaughn, L.R. Dawson, Huifang Xu, Yingbing Jiang, ~~Robert F. Schaefer~~
Luke F. Lester

Part A: Copyright Transfer

I hereby transfer copyright of the paper named above to the Materials Research Society, under the terms outlined and hereby certify that I am legally empowered to transfer copyright and that the paper has not been offered for publication to any other publisher.

Leslie G. Vaughn
▲ Authorized Signature

Leslie G. Vaughn
Name (please print)

11/25/02
Date

work was Made For Hire, name of the employer (company/institution) for whom work was performed (please print)

Note: If co-authors are from different companies/institutions, one authorized signature is needed from each company/institution. Please use additional space on the right.

☒ Check here if this work was performed under government contract.

Part B: Government Employee Certification

I certify that, as author of this paper, I am an employee of the U.S. or foreign government and performed this work as part of my employment, and that the government retains royalty-free right to reproduce all or portions of the paper and to authorize others to do so for government purposes.

▲ Authorized Signature

Name (please print)

Date

Name of Government Organization

▲ Authorized Signature

Name (please print)

Date

Name of Government Organization

Additional Signatures

▲ Authorized Signature

Name (please print)

Date

Name of Organization

▲ Authorized Signature

Name (please print)

Date

Name of Organization

▲ Authorized Signature

Name (please print)

Date

Name of Organization

▲ Authorized Signature

Name (please print)

Date

Name of Organization

▲ Authorized Signature

Name (please print)

Date

Name of Organization

Characterization of AlInAsSb and AlGaInAsSb MBE-grown Digital Alloys

Leslie G. Vaughn¹, L. Ralph Dawson¹, Huifang Xu, Yingbing Jiang and Luke F. Lester¹
Earth and Planetary Science Department, University of New Mexico, Albuquerque, NM 87131
¹Center for High Technology Materials, University of New Mexico, 1313 Goddard SE,
Albuquerque, NM 87106, U.S.A.

ABSTRACT

As one of the few Type I band offset, antimony-based material systems available for 3.3 to 4.2 micron mid-infrared multiple quantum well lasers, AlInAsSb alloys have been used as barriers with InAsSb wells. Previously, $\text{Al}_x\text{In}_{(1-x)}\text{As}_y\text{Sb}_{(1-y)}$ quaternary alloys have been grown by MBE as random alloys up to an aluminum fraction, $x = 0.10$ on GaSb substrates and $x = 0.15$ on InAs substrates. Random alloy growth of quaternary films with increased aluminum content, although beneficial to the devices, is limited by a miscibility gap. We have used a digital alloy technique to grow stable, single phase, GaSb lattice-matched, optically smooth quaternary alloys for aluminum fractions of 0.05 to 0.5, well into the miscibility gap. DCXRD results show FWHM of 0th order alloy peaks are within 1.5 to 2 times that of the highly crystalline GaSb substrates and have well defined thickness fringes corresponding to the total film thickness and the digital alloy period. TEM images show very well ordered alloys with characteristic ultrathin superlattice structure having smooth interfaces, very little strain and atomic ordering limited to that imposed by the digital alloy technique. Photoluminescence measurements are used to fit a model for bandgap prediction from known alloy compositions. Theoretical studies have predicted that the addition of a fifth element, gallium, may help suppress Auger recombination through its effects on the subband structure. So, gallium is added to the quaternary to produce a quinary alloy lattice-matched to GaSb. These AlGaInAsSb alloys have DCXRD and TEM results similar to the quaternary. The stable, single-phase growth of these quinary alloys across the composition range is promising for improving the operating characteristics of mid-IR lasers.

INTRODUCTION

The search for materials systems that will produce high power, room temperature mid-infrared (IR) semiconductor diode lasers operating between 2 and 5 microns has been of particular interest over the last 15 years. Potential applications include field communications and laser radar, pollution monitoring, remote toxic gas sensing and molecular spectroscopy. There are some inherent challenges to achieving this goal. Longer wavelength materials have smaller bandgaps and are more susceptible to Auger recombination, so must be operated well below room temperature to decrease the probability of this multi-step process. Further, most of the materials systems capable of this wavelength range have a Type II or broken band offset, leading to lower efficiencies than Type I or nested band offset systems. AlInAsSb/InAsSb is one of the few materials systems with a predicted Type I band offset. Results of some of our related research

(to be published) confirm Type I band offset behavior for multiple quantum well (MQW) photoluminescence (PL) structures.

To decrease Auger recombination and increase operating temperature, two strategies can be used. One is to add compressive strain to the well. This will cause the heavy hole and light hole energy levels to separate. This separation causes a decrease in the density of states of the holes, resulting in a decrease in the number of intermediate and final energy states available for Auger. Another strategy that has been suggested to decrease Auger recombination is the addition of a fifth element, gallium, to the alloy to make a quaternary¹. The presence of the fifth element may help by altering the subband structure of the valence band so the hole density of states is decreased.

Although the quaternary barrier/InAsSb well conduction and valence band offsets are predicted to be Type I, the valence band offset is small, so hole confinement is a concern. The higher the aluminum content, the larger the valence band offset. This becomes even more important when the well is compressively strained and the well valence subbands separate because both move down to lower energies, causing the valence band offset between the barriers and the well to decrease².

Below room temperature MQW lasers with $\text{Al}_{0.15}\text{In}_{0.85}\text{As}_{0.9}\text{Sb}_{0.1}$ barriers and InAsSb wells on InAs and $\text{Al}_{0.1}\text{In}_{0.9}\text{As}_{0.9}\text{Sb}_{0.1}$ barriers and InAsSb wells on GaSb have been demonstrated at 3.5 and 3.9 microns, respectively^{3,4}. Higher aluminum content may help increase the operating temperature of this laser structure by increasing the conduction and valence band offsets to improve carrier confinement. Increased aluminum content will also decrease the index of refraction, improving the optical confinement within the laser. Unfortunately, a miscibility gap is predicted for the quaternary alloy at aluminum fractions of 0.06 and greater for material lattice-matched to GaSb substrates and 0.12 and greater for material lattice-matched to InAs substrates⁵. Growth of material beyond these limits is predicted to phase separate under equilibrium or near-equilibrium growth conditions and has been observed for non-equilibrium MBE growth.

It should also be noted that the phase stability diagram for the quaternary is bounded by quaternary phase stability diagrams with large miscibility gaps—at least for the alloys with both As and Sb—so it is expected that the quaternary will have large regions of immiscibility also.

In related HEMT and kinetic heterojunction research, single phase thin film AlInAsSb alloys have been grown well into the miscibility gap at temperatures around 350°C using molecular beam epitaxy (MBE)^{6,7} and metal organic vapor phase epitaxy (MOVPE)⁸ systems. However, that temperature is not suitable for the AlInAsSb/InAsSb laser structure because InAsSb must be grown above 400 - 430°C to avoid atomic ordering⁹⁻¹². The phenomena of atoms naturally ordering into lamella of alternating composition is undesirable because the degree to which it occurs is unpredictable, usually occurring in patches throughout the alloy, and the resulting film has a reported smaller bandgap than expected for the random alloy.

Since MBE has the capability of growing under near-equilibrium to far from equilibrium conditions, this flexibility can be exploited to promote single-phase growth of alloys within the miscibility gap. This paper describes the digital alloy approach used to grow stable $\text{Al}_x\text{In}_{(1-x)}\text{As}_y\text{Sb}_{(1-y)}$ one-micron thick films lattice-matched to the GaSb substrates for quaternary alloy aluminum fractions, $x = 0.05$ to 0.5 , well into the miscibility gap. Further, this digital alloy

technique used for the quaternary can easily accommodate the addition of GaSb itself into the binary film sequence to make a quinary that is also lattice-matched to GaSb. Quinary films have been grown and tested with the results also presented in this paper.

EXPERIMENT

All quaternary and quinary films were grown using a VG V80H solid source MBE system. Random alloys were grown with all source shutters open, while digital alloy films were grown using a sequence of binaries. A digital alloy, sometimes called an ultrathin superlattice, is a sequence of thin films of binaries, ternaries and/or quaternaries. In this case, AlSb, InSb and InAs films were used to grow the quaternary digital alloy. The thickness of each determined the overall composition. For example, a superlattice period with 2 monolayers (ML) of AlSb, 0.5 ML of InSb and 7.5 ML of InAs results in an overall composition of $\text{Al}_{0.2}\text{In}_{0.8}\text{As}_y\text{Sb}_{(1-y)}$. Since the sticking coefficients of the Group V elements are less than unity and As tends to leak around the shutter and displace some of the bonded Sb during growth, the mole fractions y and $(1-y)$ are not only influenced by layer thicknesses but also by the ratio of the beam equivalent pressures (BEPs). The ratio of these pressures and the ratio of the InSb to InAs thicknesses were used to adjust the Group V composition until GaSb lattice match conditions were achieved. The quinary was grown in the same fashion with the addition of a thin layer of GaSb in the digital alloy sequence. The overall thickness of the films was one micron and the digital alloy period was 1.5 - 2.5nm.

Quaternary random alloys and digital alloys were grown in the temperature range of 460-520°C, with most being grown at an optimal temperature of 480°C. All quinary alloys were grown at 480°C. The substrate temperature was monitored using an optical pyrometer. The temperature range was chosen to be low enough to ensure that all Group III elements would have a sticking coefficient of approximately one, and high enough to ensure that InAsSb would be single phase with no atomic ordering.

For most samples, composition was determined using calibrated Group III growth rates and double crystal X-ray diffraction (DCXRD). These growth rates were calibrated using refractive high-energy electron diffraction (RHEED) oscillations and binary film thickness fringes from DCXRD. Periodically, sample compositions were verified using Rutherford Backscattering Spectroscopy (RBS) or Secondary Ion Mass Spectroscopy (SIMS).

Both Group V elements were supplied by EPI valved cracker sources run at sufficiently high temperatures to produce predominantly As_2 and Sb_1 . The ratio of BEPs for As to Sb was maintained at 4:3, and the Group V to Group III BEP ratios were 5:1 for As to In, 13:1 for Sb to Al, and 4:1 for Sb to In. Both aluminum and indium growth rates were 0.75ML/sec and the gallium growth rate was maintained at 0.5ML/sec.

Photoluminescence was measured using a 980nm-laser diode pump array and a scanning monochromator. The sample was mounted in a liquid nitrogen-cooled cryostat chamber.

DISCUSSION

Before beginning experimentation with the digital alloy growth technique, much effort was made to grow the "best" random alloy film of $\text{Al}_{0.2}\text{In}_{0.8}\text{As}_{0.73}\text{Sb}_{0.27}$, within the miscibility gap. One-micron thick films of $\text{Al}_x\text{In}_{(1-x)}\text{As}_y\text{Sb}_{(1-y)}$ bulk random alloys were grown with an aluminum fraction, x , of 0.2. In an attempt to grow under conditions that would yield a crystalline, single-phase film, the temperature was varied from 460°C to 520°C and the growth rate was varied from 0.75 $\mu\text{m/hr}$ to 1.0 $\mu\text{m/hr}$. Also, keeping the As:Sb BEP ratio constant, the total Group V BEP was varied such that the Group V:Group III BEP ratio went from 5:1 to 20:1. The best random alloy film grown was at 480°C, with combined Al and In growth rate of 0.75 ML/sec and an As:Sb BEP ratio of 2:1. The sample appeared very smooth using Nomarski microscopy, but DCXRD revealed two broad 0th order peaks. This observation is consistent with phase segregation.

Digital Alloys

To overcome the tendency for phase segregation while maintaining a highly crystalline film that behaves as predicted for a bulk random alloy, a digital alloy (DA) technique has been employed. The growth parameters that affect the overall behavior of digital alloys are the usual for any growth, that is growth temperature, III-V BEP ratios and growth rate. Along with those, digital alloys have the added variables of digital alloy period, constituents (binaries, ternaries, quaternaries, etc.), and sequence of growth. For the digital alloys described in this work, growth temperatures, III-V BEP ratios and binary growth rates on the order of those used in the bulk random alloy growth were employed to maintain a far from equilibrium growth environment. Digital alloy binary constituents were covered with the next layers before much layer intermixing or surface segregation could occur, as seen in the indium map of a quaternary DA sample, Figure 1, taken using Energy-filtering TEM (3-window method). Lower growth rates of 0.5 ML/sec or less resulted in rougher surfaces and multiple 0th order peaks within the DCXRD scans, much like those observed for the bulk random alloy growths.

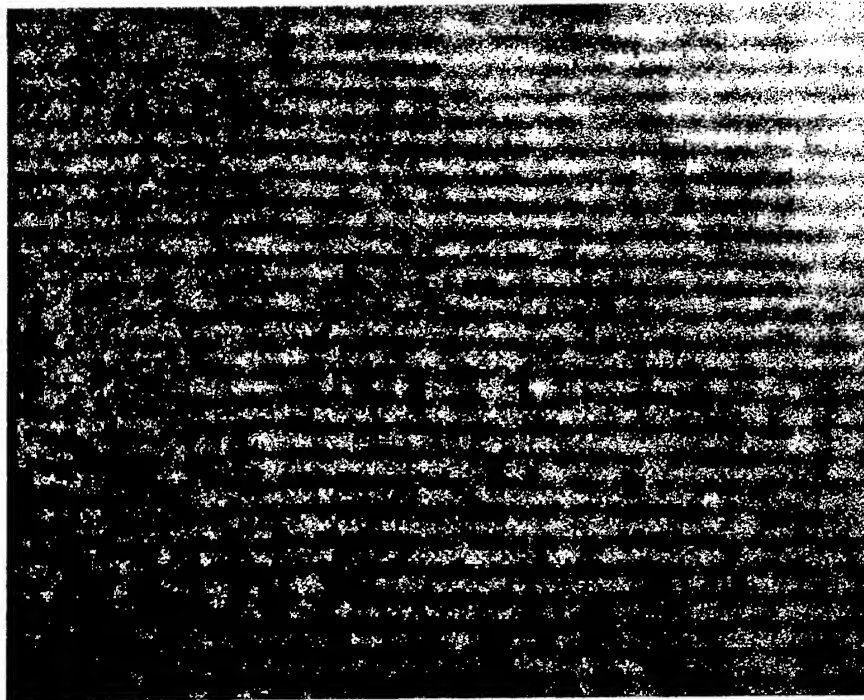


Figure 1. Map of Indium in a 30% aluminum quaternary DA sample using Energy-filtering transmission electron microscopy (TEM). The bright regions indicate indium layers.

The optimal digital alloy period was designed to accommodate the intended use of the quaternary film. In mid-IR lasers, the quaternary serves as the barrier between wells in a MQW structure, with barrier thickness in the range of 15 - 30nm. Further, the smaller the DA period the more bulk-like the behavior, and to enhance compositional uniformity, each barrier needs to contain several periods. Growths at less than 1.5nm DA period showed signs of phase segregation and were not consistent and reproducible from run to run. However, a DA period of 1.5 - 2.5nm produced films that were very reproducible, with smooth surfaces and with DCXRD, Figure 2(a), and TEM, Figure 2(b) confirmation of very regular atomic spacing consistent with single phase, high quality films.

The AlSb, InSb and InAs binaries were chosen as superlattice/digital alloy constituents to avoid the unpredictable nature of competing Group V elements at any one layer, to capitalize on the very stable single phase growth of binaries, and to use the almost equal and opposite strain of AlSb and InAs with respect to GaSb for strain compensation within the quaternary film. Moreover, the quaternary composition can easily be changed by adjusting the layer thickness ratio of AlSb to InSb/InAs for the Group III elements and the layer thickness ratio of InSb to InAs for the Group V elements.

The sequence of binaries is also important. Several studies¹³⁻¹⁵ have shown that InSb bonds at the layer interfaces reduce Sb-As mixing and promote a more distinct transition from one layer to the next. Attention to this detail avoids diffuse interfaces by keeping the layers as binaries and not ternaries or worse, phase segregated quaternaries. These distinct interfaces are abrupt and reproducible which may lead to better electronic properties by reduction of defects.

In the digital alloy quaternaries, the layer sequence used was AlSb, InSb, InAs then an antimony soak before the next AlSb layer. The TEM image and Z-contrast image in Figure 3, typical of the DA quaternaries and quinternaries, show very smooth, abrupt interfaces and very regular atomic spacing with no visible defects.

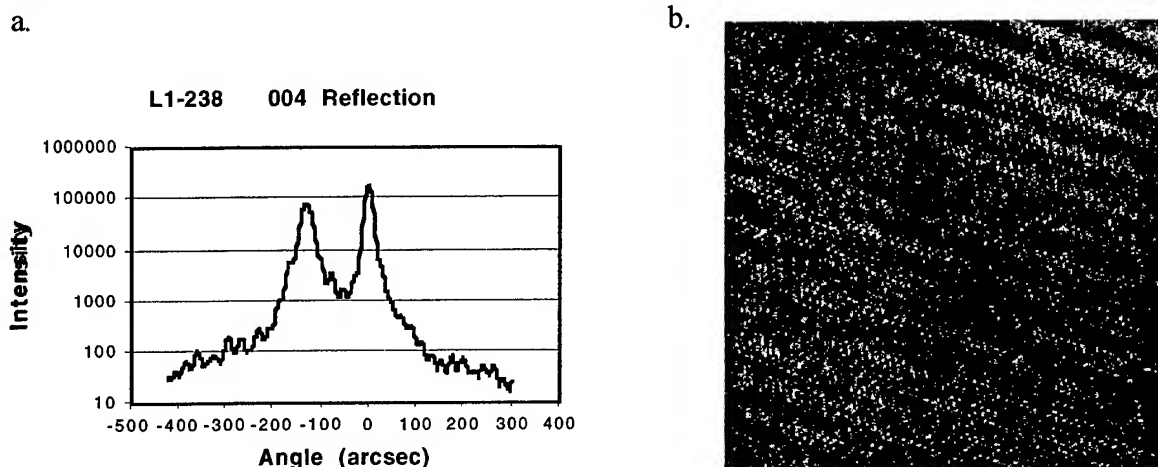


Figure 2. Results from an $\text{Al}_{0.2}\text{In}_{0.8}\text{As}_{0.73}\text{Sb}_{0.27}$ DA sample: (a) DCXRD (004) scan and (b) High-resolution TEM image.

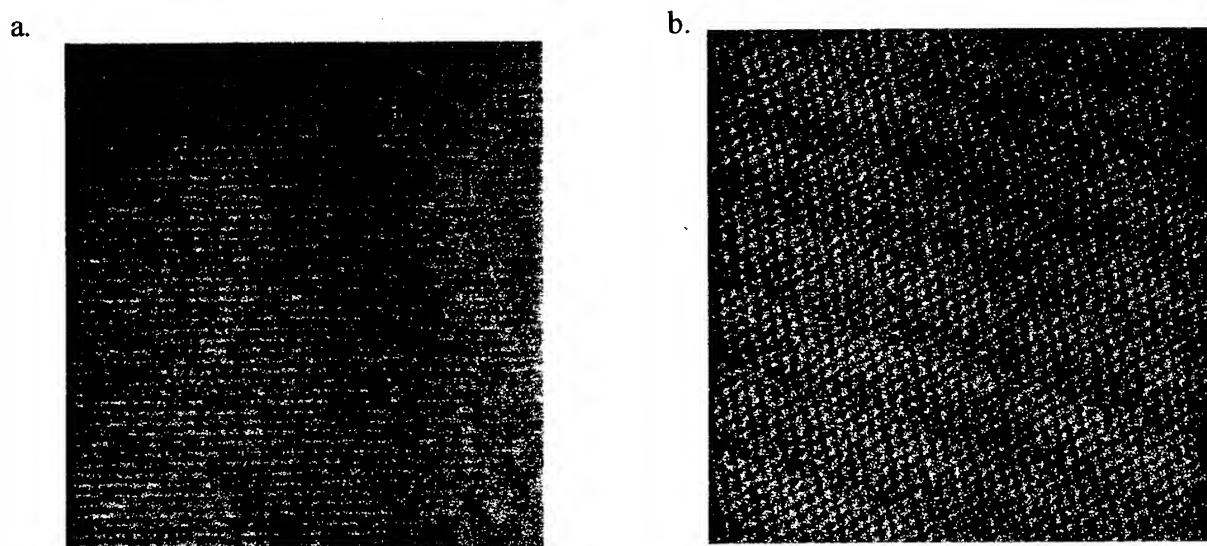


Figure 3. (a) Low magnification bright-field TEM image of 30% aluminum quaternary DA sample and, (b) Z-contrast image of 20% aluminum quaternary DA sample, showing the straight, abrupt interfaces between the AlSb and InAs layers of the DA.

Thermal stability

For the quaternary and quinary DA films, the growth temperature was maintained at 480°C for the hour and fifteen minutes necessary to grow approximately one micron of material. At the end of each growth run, there was a 5-10 minute period while the sample was kept at this temperature to check the RHEED pattern. The initial periods of digital alloy certainly experienced this growth temperature for close to the entire growth time and all periods saw this temperature for at least 5-10 minutes, most for longer time. Therefore, any phase segregation that is going to occur at that time and temperature would be observed in the DCXRD results since DCXRD samples the entire thickness. However, very distinct thickness fringes for the digital alloy period and the narrow 0th order digital alloy film peak, 1.5 to 2 times full width half maximum (FWHM) of the substrate, Figure 4, confirm the overall high degree of crystallinity of the samples. TEM images, like the one in Figure 2(b), of these digital alloys also confirm very regular, highly crystalline material.

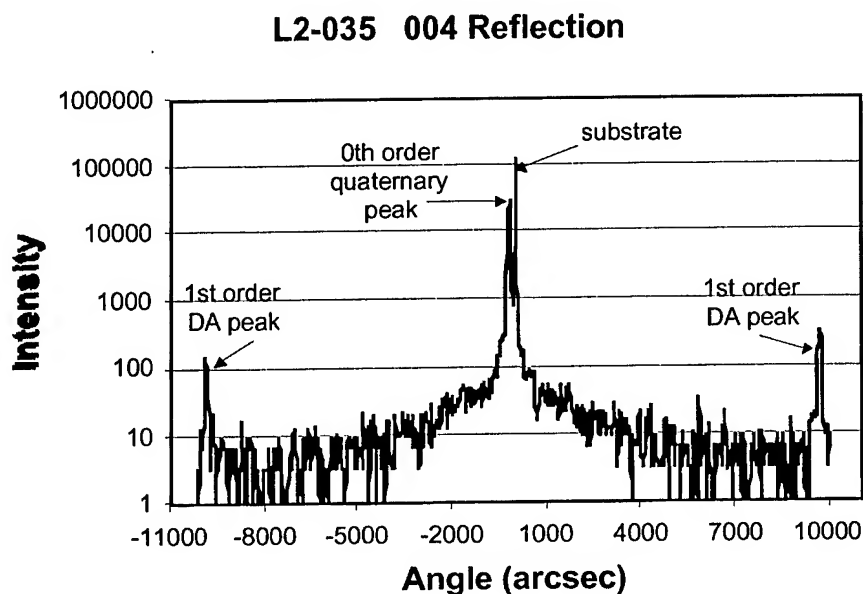


Figure 4. (004) DCXRD scan of an $\text{Al}_{0.32}\text{In}_{0.68}\text{As}_{0.62}\text{Sb}_{0.38}$ DA sample showing the thickness fringes corresponding to the digital alloy period.

The thermodynamically stable configuration for these alloys is multiple microscopic phases with multiple compositions as expected for a miscibility gap. At a high enough temperature for a long enough period of time, the digital alloys will probably rearrange to this configuration. In fact, during TEM analysis with a very high-energy electron beam on a spot for several minutes localized areas of atomic rearrangement were observed. Also, when a sample was heated to 550°C for one hour (the melting point of InSb is 525°C) with an arsenic and antimony overpressure, the surface became very rough. However, for most semiconductor device processing, specifically metal evaporation and annealing, temperatures of 300-400°C and times of 5-15 minutes are typical and no discernible degradation of the quaternary DA crystalline quality

is observed. Therefore, for temperatures lower than or equal to 480°C for several minutes, the digital alloy quaternary films are thermally stable.

Bandgap prediction

As described in another paper being prepared for publication, the bandgap of the quaternary is predicted using a model proposed by Moon¹⁶, that has been fitted to experimental data for aluminum fractions of 0.05 to 0.25 (Figure 5). As the amount of aluminum in the quaternary is increase to $x = 0.3-0.4$, the bandgap increases to values near that of GaSb, and the PL is obscured by the GaSb PL peak. At some point past 0.4 aluminum fraction, the quaternary is predicted to transition into an indirect bandgap material. No quaternary PL was observed for the 0.5 aluminum fraction sample.

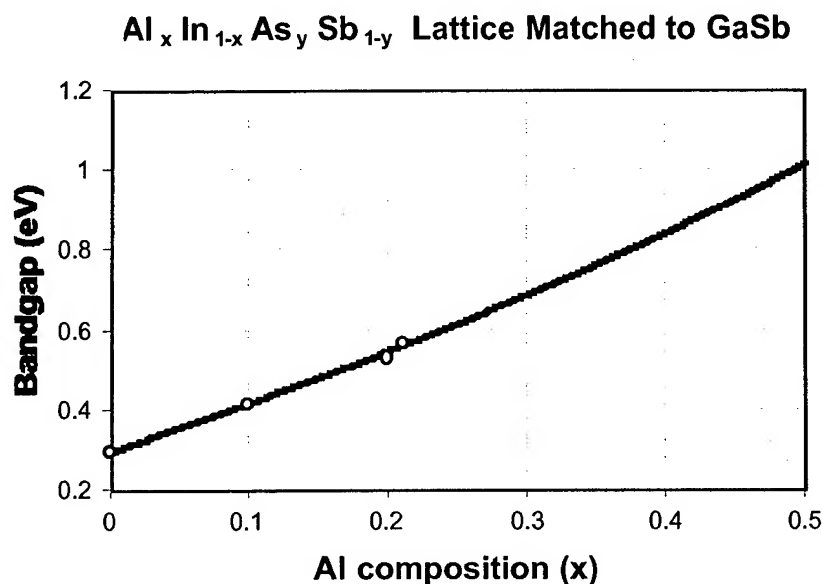
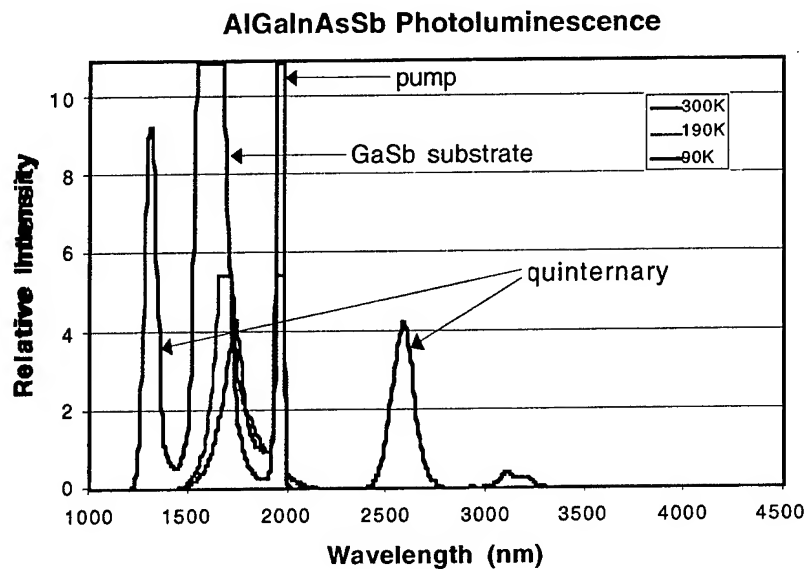


Figure 5. Bandgap prediction of AlInAsSb alloys using the Moon model fitted with experimental data.

However, PL has been observed in an $\text{Al}_{0.4}\text{Ga}_{0.15}\text{In}_{0.45}\text{As}_{0.42}\text{Sb}_{0.58}$ sample suggesting that the addition of Ga to the quaternary at high aluminum fractions causes the bandgap of the alloy to become direct. The quaternary alloy PL has two peaks (Figure 6a), one at 1.3 microns and the other at 2.6 microns, corresponding to the 1st and 2nd order reflections. As more quaternary alloys of different compositions are grown and tested, the quaternary bandgap for $x = 0.3$ to 0.5 may be deduced. The PL from the quaternary digital alloy can be seen to increase with decreasing temperature as expected when Auger is a dominant recombination mechanism. These quaternary PL peaks can also be seen in the MQW PL scans (Figure 6b). An interesting feature of the MQW PL scan is that there is a broad 4-micron peak at room temperature that decreases with decreasing temperature. This behavior is unlike that for the quaternary barrier MQW PL,

where decreasing temperature causes the 4-micron peak to increase in intensity. Further study of this phenomenon is needed.

a.



b.

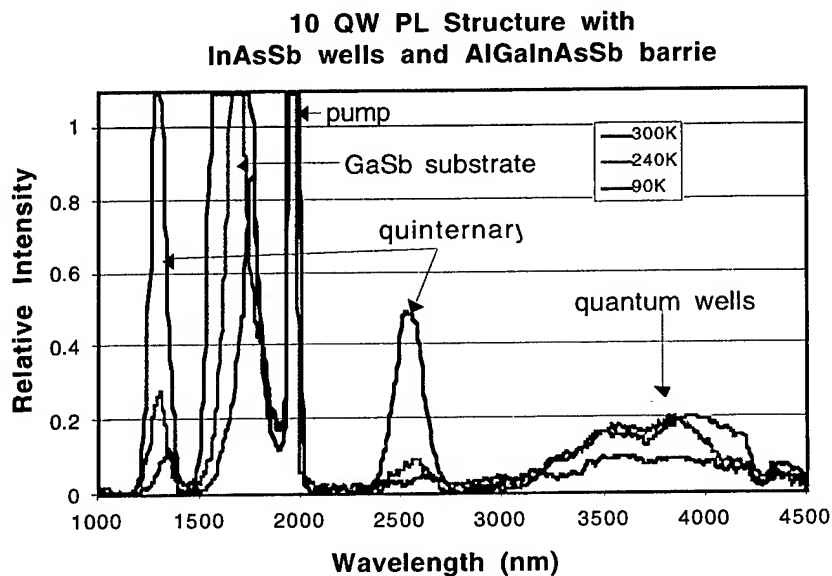


Figure 6. PL from (a) $\text{Al}_{0.4}\text{Ga}_{0.15}\text{In}_{0.45}\text{As}_{0.42}\text{Sb}_{0.58}$ 1-micron film and (b) from an MQW structure with $\text{Al}_{0.4}\text{Ga}_{0.15}\text{In}_{0.45}\text{As}_{0.42}\text{Sb}_{0.58}$ barriers and 0.9% compressively strained InAsSb wells.

Atomic ordering

Atomic ordering, where different elements naturally alternate on lattice sites during growth or anneal, has been observed in many alloys. This can be very short range ordering, as when Cu and Pt naturally alternate on the lattice sites along a particular direction in a CuPt alloy, instead of randomly distributing themselves over all of the lattice sites. It can also be like that seen in InAsSb when lamella of two very distinct compositions alternate to form a naturally occurring vertical superlattice configuration with each layer thickness on the order of a few monolayers. Atomic ordering has also been reported in other related alloys, such as InGaAs¹⁷ and GaAsSb^{18,19}.

The quaternary digital alloys were examined for atomic ordering using TEM. As seen in Figure 7, evidence of atomic ordering has been observed in the selected area electron diffraction (SAED) patterns of the quaternary alloys. The spacing of these satellite peak intensities corresponds to the thickness of the digital alloy period. For the $\text{Al}_{0.2}\text{In}_{0.8}\text{As}_{0.73}\text{Sb}_{0.27}$ sample referred to in Figure 7a, the DA period is approximately 2.3nm by design and has been confirmed from the DA thickness fringes of the DCXRD (004) scan. The bright reflections in the SAED pattern (Figure 7a) indicate the substructure of zinc blend. Satellite reflections indicate the superlattice period of the digital alloy along the (001) direction. Knowing that the spacing between the substructure spots in the diffraction pattern corresponds to 1/2 of the lattice constant, a_0 , for zinc blend structures and determining the spacing of spots between them, the atomic ordering period is determined to be 2.3nm. This is the digital alloy period. So, while there is no evidence of natural atomic ordering, there is synthetic atomic ordering imposed by the digital alloy/superlattice growth technique. A similar SAED pattern for an $\text{Al}_{0.3}\text{In}_{0.7}\text{As}_{0.64}\text{Sb}_{0.36}$ sample (DA period = 1.8nm) is shown in Figure 7b.

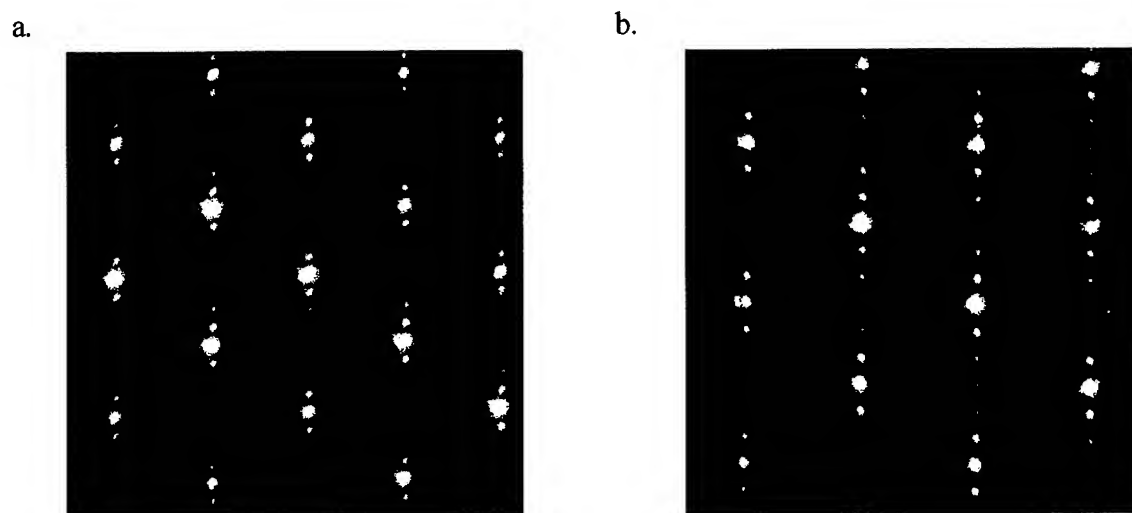


Figure 7. Atomic ordering in the growth direction (001) imposed by the DA technique is indicated in the SAED patterns for (a) $\text{Al}_{0.2}\text{In}_{0.8}\text{As}_{0.73}\text{Sb}_{0.27}$ with a DA period of 2.3nm, and (b) $\text{Al}_{0.3}\text{In}_{0.7}\text{As}_{0.64}\text{Sb}_{0.36}$ with a DA period of 1.8nm.

CONCLUSIONS

The digital alloy technique is shown to be very useful for growing stable quaternary and quinary films with compositions within the miscibility gap. These films behave as predicted for random alloy films. The quaternary digital alloy bandgap data as a function of composition has been fitted to a model so that behavior can be predicted. The addition of Ga to make a quinary alloy causes the film to transition back into direct bandgap behavior for large aluminum fractions. PL measurements of the alloys and of the MQW structures, using the alloys as barriers, demonstrate these films to be of good optical quality suitable for use in mid-IR lasers.

The films are thermally stable and are predicted to withstand semiconductor device processing temperatures and times without discernible phase segregation, certainly up to 480°C for several minutes. Also, the SAED patterns indicate that the only atomic ordering in the digital alloy is that imposed by the growth technique. TEM, Energy-filtering TEM and Z-contrast images reveal the homogeneous, regular, superlattice nature within the grown films. Finally, PL of MQW structures with quinary barriers exhibits promising room temperature 4-micron wavelength radiation. Continuing exploration and optimization of the MQW structures containing these films look promising for room temperature lasing at this wavelength.

ACKNOWLEDGEMENTS

This material is based on research sponsored by the Air Force Research Laboratory, under the agreement number F49620-99-1-0330, and on research sponsored by the Office of Naval Research, under Grant # N00014-99-1-1023. The U. S. Government is authorized to reproduce and distribute reprints for Governmental purposes notwithstanding any copyright notation thereon. The views and conclusions contained herein are those of the authors and should not be interpreted as necessarily representing the official policies, endorsements or views, either expressed or implied, of the Air Force Research Laboratory, the Office of Naval Research or the U. S. Government.

REFERENCES

1. M. E. Flatte, J. T. Olesberg, S. A. Anson, T. F. Boggess, T. C. Hasenberg, R. H. Miles and C. H. Grein, *Appl. Phys. Lett.* **70**, 3212 (1997).
2. L. A. Coldren and S. W. Corzine, in *Diode Lasers and Photonic Integrated Circuits*, (John Wiley & Sons, Inc., New York, 1995), p. 532.
3. H. K. Choi and G. W. Turner, *Appl. Phys. Lett.* **67**, 332 (1995).
4. H. K. Choi, G. W. Turner, M. J. Manfra and M. K. Connors, *Appl. Phys. Lett.* **68**, 2936 (1996).
5. G. W. Turner, M. J. Manfra, H. K. Choi and M. K. Connors, *J. Crystal Growth* **175/176**, 825 (1997).
6. M. Kudo and T. Mishima, *J. Crystal Growth* **175**, 844 (1997).
7. D. Washington, T. Hogan, P. Chow, T. Golding, C. Littler and U. Kirschbaum, *J. Vac. Sci. Technol. B* **16**, 1385 (1998).
8. J. R. Chang, Y. K. Su, D. H. Jaw, H. P. Shiao, W. Lin, *J. Crystal Growth* **203**, 481 (1999).
9. T. Y. Seong, A. G. Norman, I. T. Ferguson and G. R. Booker, *J. Appl. Phys.* **73**, 8227 (1993).

10. S. R. Kurtz and R. M. Biefeld, *Appl. Phys. Lett.* **66**, 364 (1995).
11. S. R. Kurtz, R. M. Biefeld and L. R. Dawson, *Phys. Rev. B* **51**, 7310 (1995).
12. S. R. Kurtz, R. M. Biefeld and A. J. Howard, *Appl. Phys. Lett.* **67**, 3331 (1995).
13. J. Schmitz, J. Wagner, F. Fuchs, N. Herres, P. Koidl, J. G. Ralston, *J. Cryst. Growth* **150**, 858 (1995).
14. M. Yano, T. Utatsu, Y. Iwai, M. Inoue, *J. Cryst. Growth* **150**, 868 (1995).
15. B. R. Bennett, B. V. Shanabrook and M. E. Twigg, *J. Appl. Phys.* **85**, 2157 (1999).
16. R. L. Moon, G. A. Antypas and L. W. James, *J. Electron. Mater.* **3**, 635 (1974).
17. T. S. Kuan, W. I. Wang and E. L. Wilkie, *Appl. Phys. Lett.* **51**, 51 (1987).
18. I. J. Murgatroyd, A. G. Norman and G. R. Booker, *J. Appl. Phys.* **67**, 2310 (1990).
19. Y. E. Ihm, N. Otsuka, J. F. Klem and H. Morkoc, *Appl. Phys. Lett.* **51**, 2013 (1987).



Center for High Technology Materials at the University of New Mexico

Characterization of AlInAsSb and AlGaInAsSb MBE-grown Digital Alloys

Leslie G. Vaughn, L. Ralph Dawson, Luke F. Lester
Center for High Technology Materials, UNM

Huifang Xu, Yingbing Jiang
Department of Earth and Planetary Sciences, UNM

This research was sponsored by the Office of Naval Research and the Air Force Office of Scientific Research



Center for High Technology Materials at the University of New Mexico

Outline

- *Motivation*
- *Approach and Challenges*
- *Digital Alloy Technique*
- *Growth Parameters & Crystal Structure*
- *Thermal Stability*
- *Performance in MQW Structures*
- *Summary*

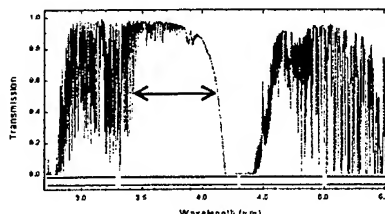


Center for High Technology Materials at the University of New Mexico

Mid Infrared Range

- Field Communications and LADAR

- Transmission window in atmosphere between 3.3 and 4.2 μm (Band IV)



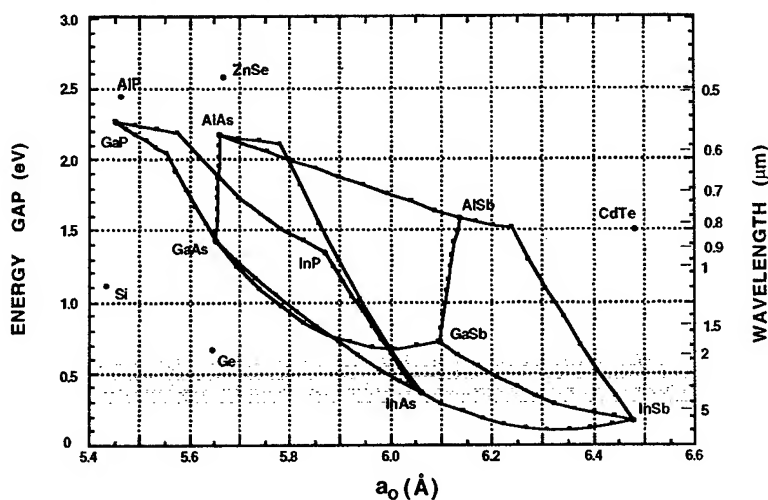
- Remote Sensing (Pollution Monitoring & Toxic Gas Detection)

- Many organic and inorganic compounds have absorption bands in 2-5 μm range (NH_3 , CN^- , CO_2 , C-H stretching, S-H, H_2O , etc.)



Center for High Technology Materials at the University of New Mexico

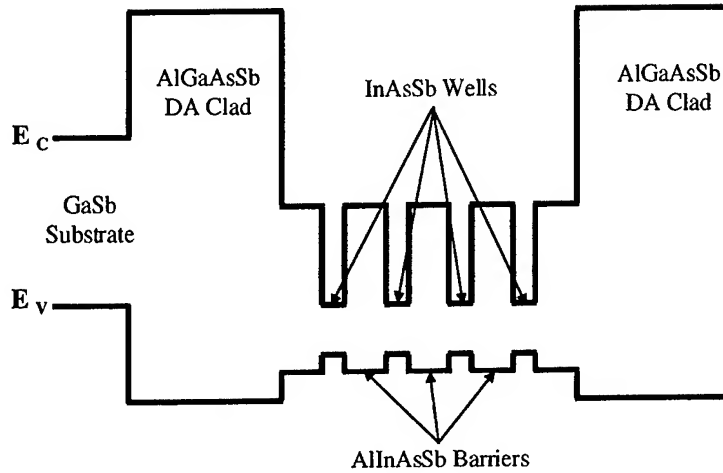
E_g versus lattice constant





Center for High Technology Materials at the University of New Mexico

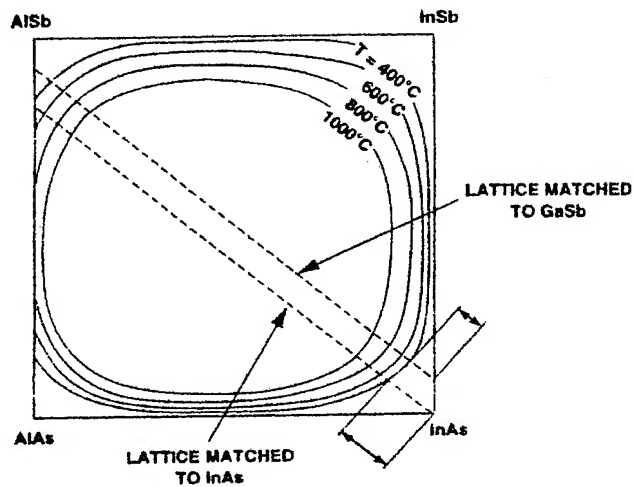
Band Alignment



Center for High Technology Materials at the University of New Mexico

Miscibility Gap

Calculated alloy stability curves for Al-In-As-Sb system

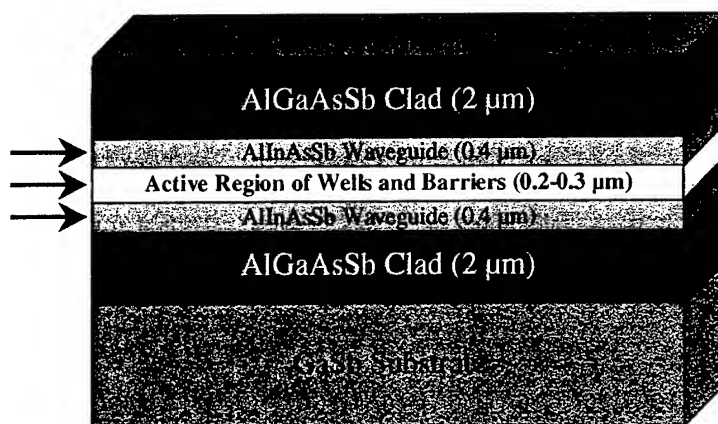


From G. W. Turner, et. al., J. Crystal Growth 175/176, 825 (1996)



Center for High Technology Materials at the University of New Mexico

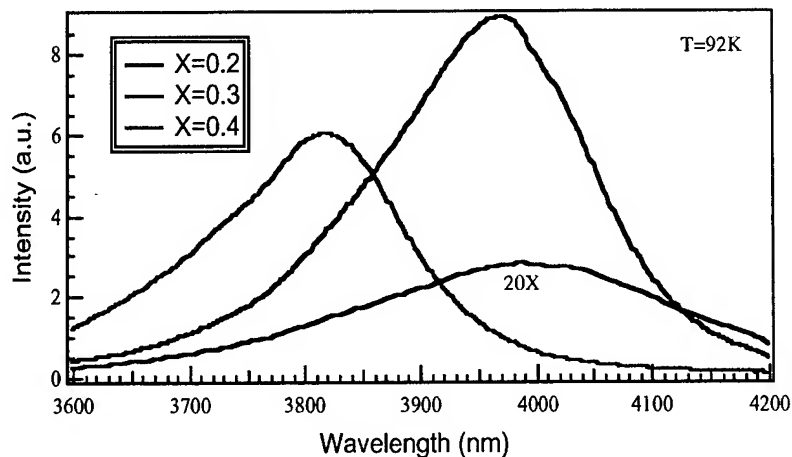
Mid-IR Laser Structure



Center for High Technology Materials at the University of New Mexico

Quaternary Alloy Performance

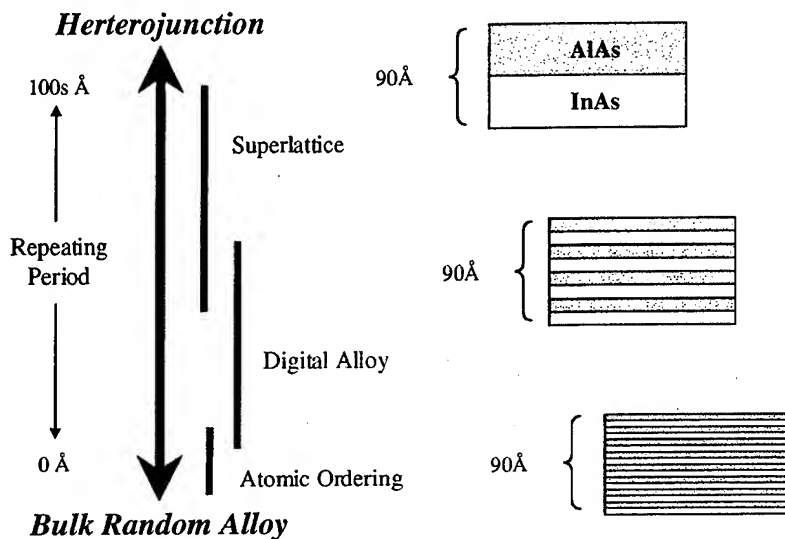
Photoluminescence of InAsSb wells/ $\text{Al}_x\text{In}_{1-x}\text{As}_y\text{Sb}_{1-y}$ barriers





Center for High Technology Materials at the University of New Mexico

Digital Alloy

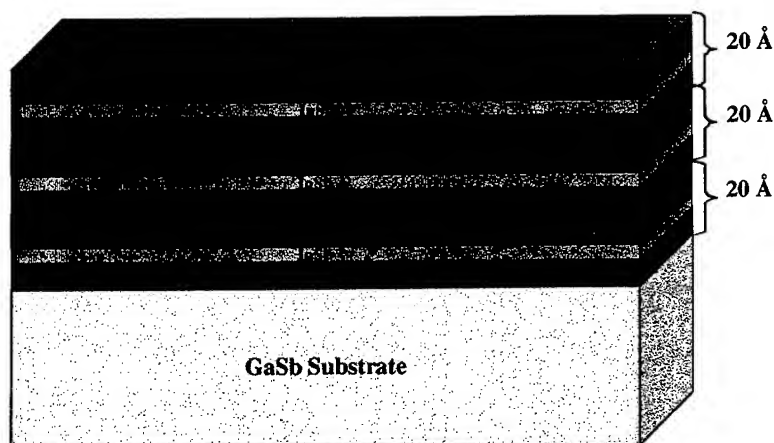


Center for High Technology Materials at the University of New Mexico

Digital Alloy Technique

AlInAsSb Quaternary Alloy

⋮ (Repeating)





Center for High Technology Materials at the University of New Mexico

Critical Growth Parameters

versus



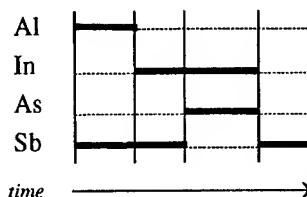
- Digital alloy period

- Want as small as possible, but below 15Å starts to phase segregate
- Components are AlSb, InSb, InAs, must pay attention to strain compensation

- Growth temperature range

- Sequence of components

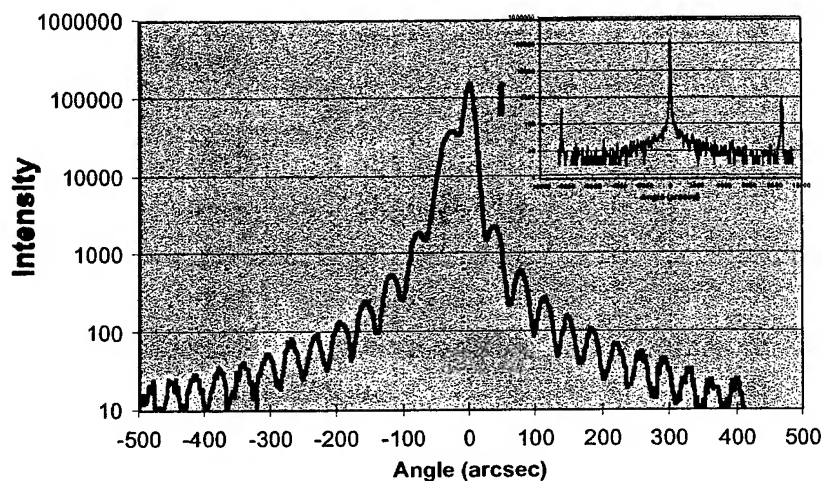
- Want smooth, abrupt interfaces, so promote Sb bonding



Center for High Technology Materials at the University of New Mexico

Typical Digital Alloy

L1-155 004 Reflection AllnAsSb (Xal=0.3)





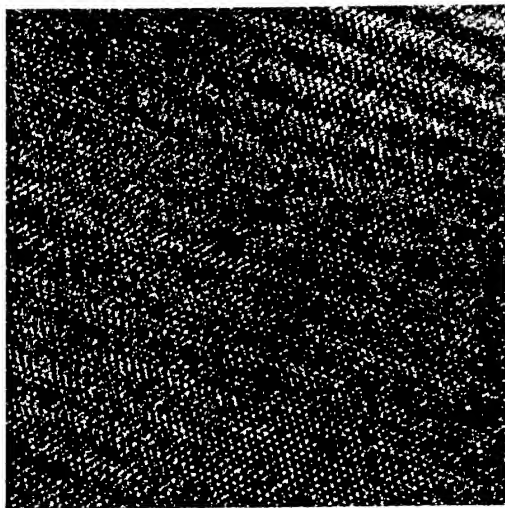
Center for High Technology Materials at the University of New Mexico

Put TEM Equipment Picture Here



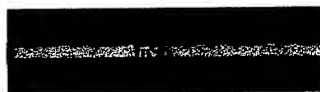
Center for High Technology Materials at the University of New Mexico

Crystal Structure



*Bright Field High Resolution
TEM image of an
 $Al_{0.2}In_{0.8}As_{0.73}Sb_{0.27}$
Sample*

- Crystalline
- Uniform atomic spacing
- Smooth, abrupt interfaces



Digital Alloy Period
~2.3nm



Center for High Technology Materials at the University of New Mexico

Interfaces



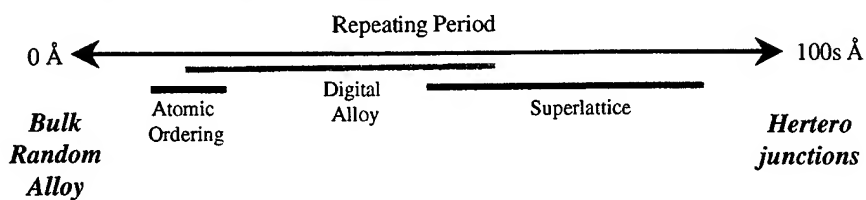
Indium Map of $Al_{0.3}In_{0.7}As_{0.64}Sb_{0.36}$ Alloy using Energy-Filtering TEM (3-window method)

No intermixing of layers--very distinct interfaces



Center for High Technology Materials at the University of New Mexico

Atomic Ordering

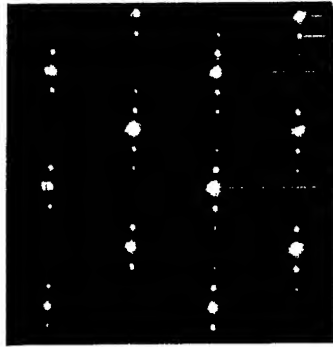


- Atomic ordering has been reported in InAsSb, InGaAs and GaAsSb alloys
- Atomic ordering can be very non-homogeneous and does affect the material bandgap



Center for High Technology Materials at the University of New Mexico

TEM Diffraction Patterns

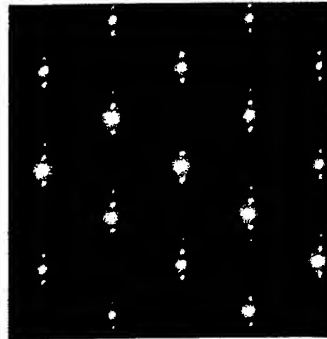


Selected Area Electron Diffraction (SAED)
Pattern for $\text{Al}_{0.3}\text{In}_{0.7}\text{As}_{0.64}\text{Sb}_{0.36}$ Alloy

- Atomic ordering is confined to the growth direction due to the imposed order of the digital alloy technique

Spacing corresponds to digital alloy period ($\sim 18\text{\AA}$)

Spacing corresponds to sublattice spacing for zinc blend, $1/2 a_0$ or 3.05\AA for GaSb

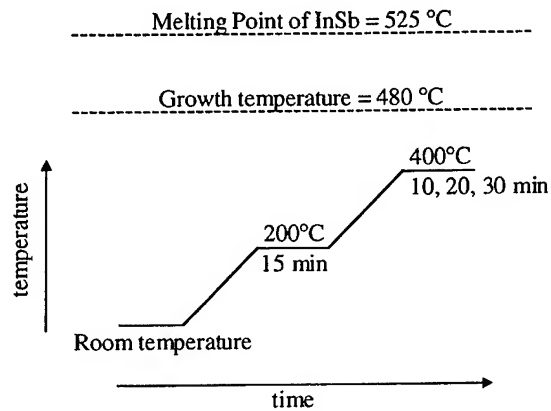


SAED Pattern for $\text{Al}_{0.2}\text{In}_{0.8}\text{As}_{0.73}\text{Sb}_{0.27}$ Alloy



Center for High Technology Materials at the University of New Mexico

Thermal Stability

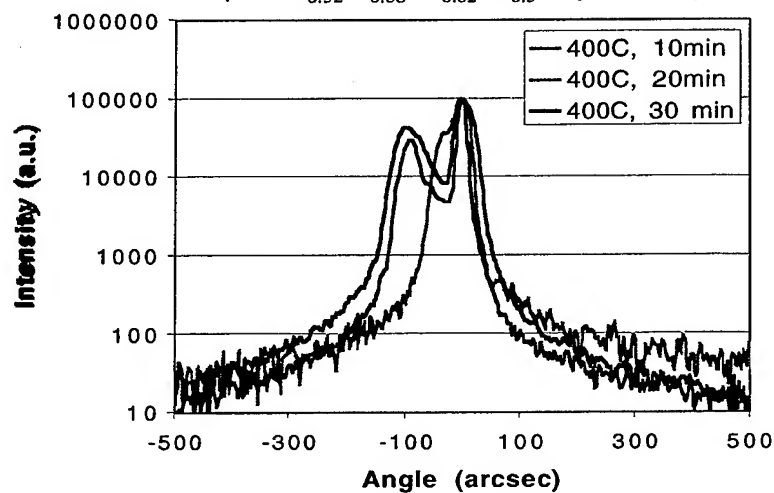




Center for High Technology Materials at the University of New Mexico

400°C Anneal Results

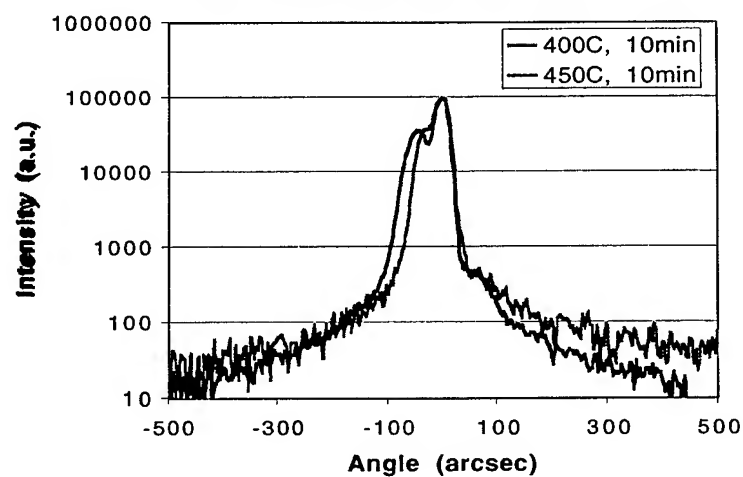
1 μ m Al_{0.32}In_{0.68}As_{0.62}Sb_{0.3} Digital Alloy



Center for High Technology Materials at the University of New Mexico

400°C versus 450°C

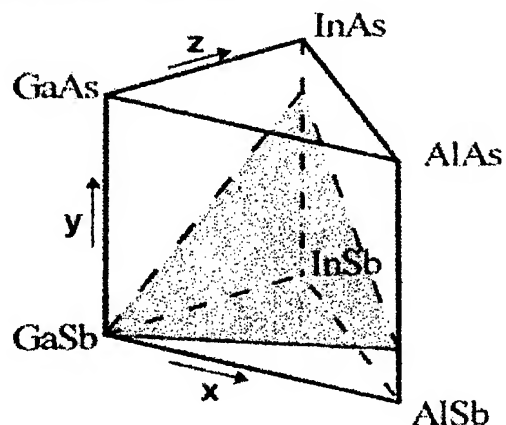
1 μ m Al_{0.32}In_{0.68}As_{0.62}Sb_{0.3} Digital Alloy





Center for High Technology Materials at the University of New Mexico

Al-Ga-In-As-Sb system



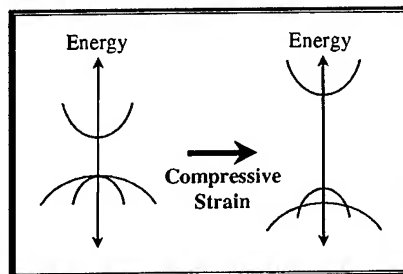
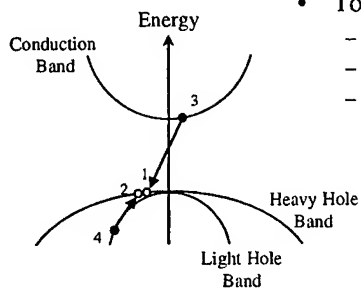
From Mishurnyi, et. al., Cryst. Res. Technol. 33 (1998) 3



Center for High Technology Materials at the University of New Mexico

Auger Recombination

- Non-radiative process
- More at longer wavelengths
- To minimize:
 - Compressively strain the well
 - Cool the laser
 - Maybe add Ga to the barrier material--QUINTERNARY!!

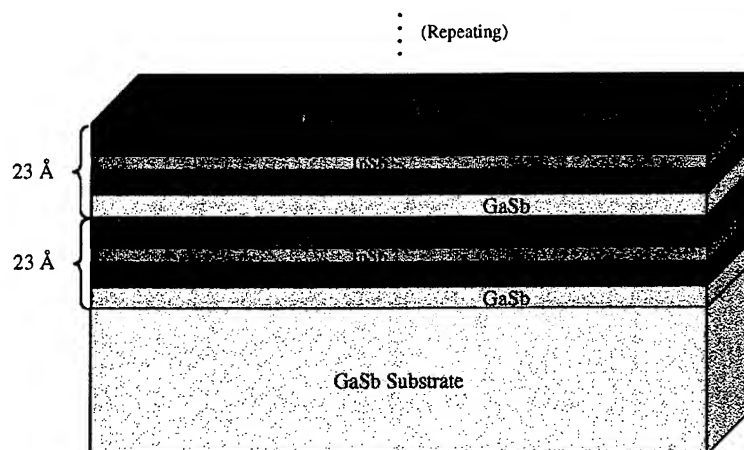




Center for High Technology Materials at the University of New Mexico

Quinternary Digital Alloy

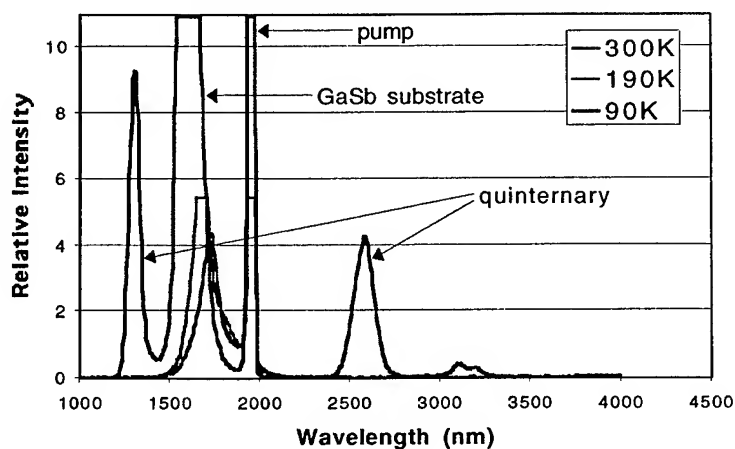
AlGaInAsSb Quinternary Alloy



Center for High Technology Materials at the University of New Mexico

Quinternary Alloy Behavior

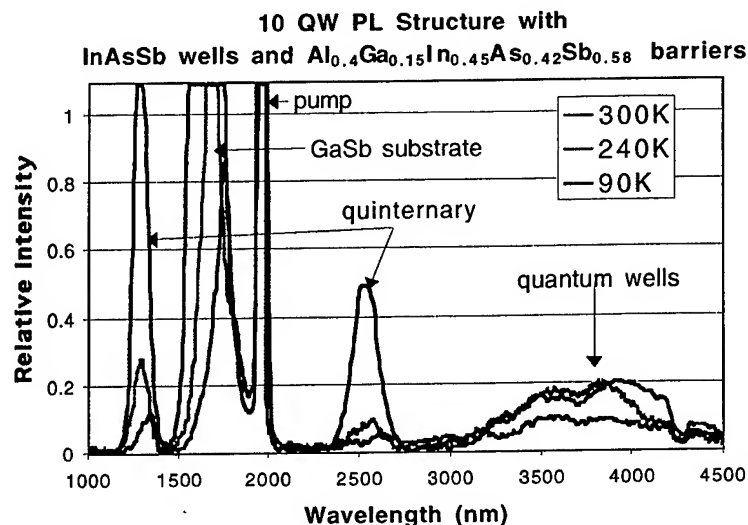
AlGaInAsSb Photoluminescence





Center for High Technology Materials at the University of New Mexico

MQW PL with Quinternary Alloy Barriers



Center for High Technology Materials at the University of New Mexico

Summary

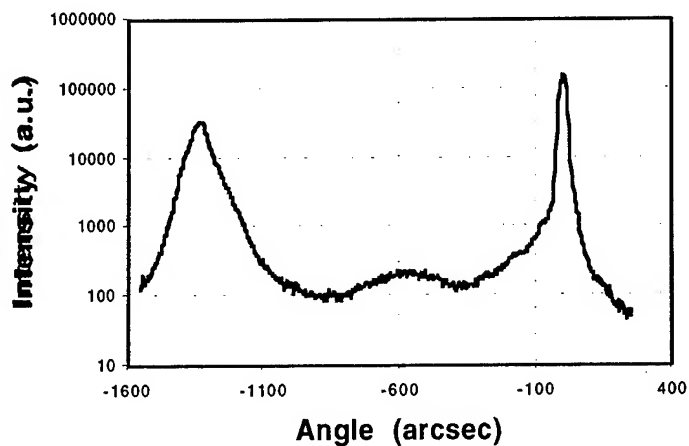
- MBE-grown quaternary and quinternary digital alloys metallurgically and electronically equivalent to bulk random alloys
- Films thermally stable up to 450°C
- Atomic ordering limited to digital alloy growth technique and is very uniform and reproducible



Center for High Technology Materials at the University of New Mexico

Best Bulk Alloy Growth

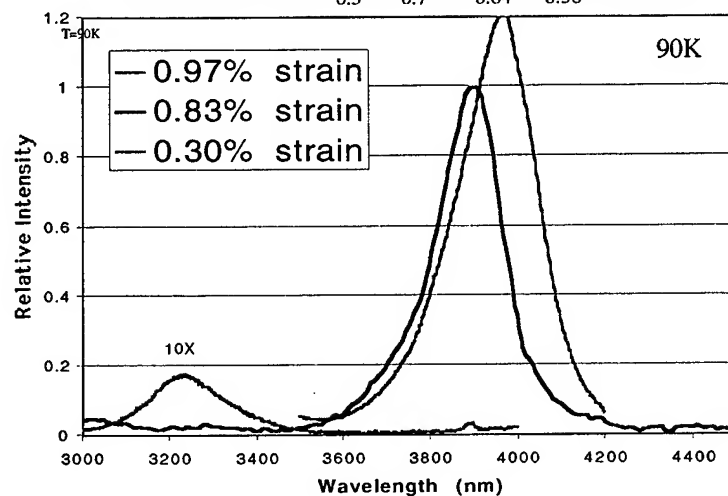
$1\mu\text{m Al}_{0.2}\text{In}_{0.8}\text{As}_{0.7}\text{Sb}_{0.3}$ Bulk Random Alloy



Center for High Technology Materials at the University of New Mexico

PL Effects of Varying Compressive Well Strain

InAsSb wells/ $\text{Al}_{0.3}\text{In}_{0.7}\text{As}_{0.64}\text{Sb}_{0.36}$ barriers



Appendix 3 — Document References (Endnotes)

References

- ¹ Arakawa, Y., and Sakai, H.: 'Multidimensional quantum well laser and temperature dependence of its threshold current', *Appl. Phys Lett.*, **40**(11), 939-941 (1982).
- ² Sch fer, F., Reithmaier, J.P., and Forchel, A.: "High-performance GaInAs/GaAs quantum-dot lasers based on a single active layer", *Appl. Phys Lett*, **74**(20), 2915-2917 (1999).
- ³ Lester, L.F., Stintz, A., Li, H., Newell, T.C., Pease, E.A. , Fuchs, B.A. and MALLOY, K.J.: "Optical characteristics of 1.24 μ m quantum dot lasers", accepted for publication in *IEEE Photonic Technology Letters*, August (1999).
- ⁴ Ustinov, V.M., Maleev, N.A., Zhukov, A.E., Kovsh, A.R., Egorov, A. Yu., Lunev, A.V., Volovik, B.V., Krestnikov, I.L., Musikhin, Yu.G., Bert, N.A., Kop Ev, P.S., Alferov, ZH.I., Ledentsov, N.N., Bimberg, D.: InAs/InGaAs quantum dot structures on GaAs substrates emitting at 1.3 μ m, *Appl. Phys. Lett.*, **74**(19), 2815-2817 (1999).
- ⁵ Sugawara, M., Mukai, K., and Shoji, H.: "Effect of phonon bottleneck on quantum-dot laser performance", *Appl. Phys. Lett.*, **71**(19), 2791-2793 (1997).
- ⁶ Huffaker, D. L., Park G., Zou, Z., Shchekin, O. B., and Deppe, D. G.: 1.3 μ m room-temperature GaAs-based quantum-dot Laser, *Appl. Phys. Lett.*, **73**(18), 2564-2566 (1998).
- ⁷ Chand, N., Becker, E.E., Van der Zeil, J.P., Chu, S.N.G., and Dutta, N.K.: "Excellent uniformity and very low (less-than-50A/cm²) threshold current density strained InGaAs quantum-well diode-lasers on GaAs substrate " *Appl. Phys. Lett.*, **58**(20), 1704-1706 (1991).
- ⁸ Turner, G.W., Choi, H.K., and Manfra, M.J.: "Ultralow-threshold (50A/cm²) strained single-quantum-well GaInAsSb/AlGaAsSb lasers emitting at 2.05 μ m", *Appl. Phys. Lett.*, **72**(8), 876-878 (1998).
- ⁹ P.J. Bennet et al., *Appl. Phys. Lett.* **73** 1787-1789, 1998.
- ¹⁰ E. Salik, D.S. Starodubov, V. Grubsky, & J. Feinberg, Thermally Stable Gratings in Optical Fibers without Temperature Annealing , *OFC 98 Tech. Digest*, paper ThD3, pp. 56-58, 1998.
- ¹¹ T4. H. Patrick, S.L. Gilbert, A. Ligard, and M.D. Gallagher, Annealing of Bragg Gratings in Hydrogen-Loaded Optical Fiber , *J. Appl. Phys.* **78** 2940-2945, 1995.
- ¹² D. Zubia and S.D. Hersee, "Nanoheteroepitaxy: A New Approach to the Heteroepitaxy of Mismatched Semiconductor Materials", *J. Appl. Phys.*, **85**, 6492 (1999).
- ¹³ S. Luryi and E. Suhir, New Approach to the High Quality Epitaxial Growth of Lattice-Mismatched Materials, *Appl. Phys. Lett.* **49**, 140 (1986).
- ¹⁴ D. Kapolnek, S. Keller, R. Vetury, R. D. Underwood, P. Kozodoy, S. P. Denbaars, U. K. Mishra, Anisotropic epitaxial lateral growth in GaN selective area epitaxy, *Appl. Phys. Lett.* **71**, 1204 (1997).
- ¹⁵ K. Linthicum, T. Gehrke, D. Thomson, E. Carlson, P. Rajagopal, T. Smith, D. Batchelor, and R. Davis, Pendeoepitaxy of gallium nitride thin films, *Appl. Phys. Lett.* **75**, 196 (1999).

- ¹⁶ J. Ramer, A. Hecht, S.D. Hersee, The Stability and Interface Abruptness of $\text{In}_x\text{Ga}_{1-x}\text{N}/\text{In}_y\text{Ga}_{1-y}\text{N}$ Multiple Quantum Well Structures Grown by MOVPE on Sapphire, *J. Electronic Matls.*, **26**, 1109 (1997).
- ¹⁷ S.D. Hersee, J.C. Ramer* and K.J. Malloy, The Microstructure of MOCVD GaN on Sapphire, *MRS Bulletin*, **22**, 45 (1997).
- ¹⁸ S. Chadda*, M. Pelcynski*, K. Malloy and S. D. Hersee, "Microstructural Study of GaN Grown on Sapphire by MOCVD", *Mat. Res. Soc. Symp. Proc.*, Growth and Process Characterization of Semiconductor Heterostructures, Vol. **326**, (1994).
- ¹⁹ D. Zubia, S. H. Zaidi, S. R. J. Brueck and S. D. Hersee, Nanoheteroepitaxial Growth of GaN on Si by Organometallic Vapor Phase Epitaxy, *Appl. Phys. Lett.* **76**, 858 (2000).
- ²⁰ T.W. Ebbesen et al., Extraordinary optical transmission through sub-wavelength hole arrays, *Nature* **391**, 667-669(1998)
- ²¹ Tae Jin Kim et al., Control of optical transmission through metals perforated with subwavelength hole arrays, *Optics Letters* **24**, 256-258(1999).
- ²² Novel composite medium exhibits reversed electromagnetic properties, *Physics Today*, May 2000.
- ²³ B. K. Minhas, W. Fan, K. Agi, S. R. J. Brueck and K. J. Malloy, Metallic inductive and capacitive grids: Theory and Experiment, submitted to *JOSA A*
- ²⁴ Shanhui et al., Manipulating light with photonic crystals, Nanoscale linear and nonlinear optics: International School on Quantum Electronics, Erice, Sicily, 2-14 July 2000, editors, M. Bertolotti, C.M. Bowden, C. Sibilia
- ²⁵ Pendry et al., Magnetism from conductors and enhanced nonlinear phenomena, *IEEE transactions on microwave theory and techniques* **47**, 2075-2084(1999)
- ²⁶ H. Kroemer, MBE Growth of GaAs on Si: Problems and Progress, *Mat. Res. Soc. Symp. Proc.* **67**, 3 (1986).
- ²⁷ M. I. Aksun, H. Morkoc, L. F. Lester, K. H. G. Duh, P. M. Smith, P. C. Chao, M. Longerbone, and L. P. Erickson, Performance of Quarter-Micron GaAs Metal-Semiconductor Field-Effect Transistors on Si Substrates, *Appl. Phys. Lett.* **49**, 1654-1655 (1986).
- ²⁸ Y. H. Lo, New Approach to Grow Pseudomorphic Structures Over the Critical Thickness, *Appl. Phys. Lett.* **59**, 2311-2313 (1991).
- ²⁹ Y. H. Lo and Z. H. Zhu, Compliant Substrates with an Embedded Twist Boundary, *Mat. Res. Soc. Proc.* **510**, 81 (1998).
- ³⁰ O. Parillaud, E. Gil-Lafon, B. Gerard, P. Etienne and D. Pribat, High Quality InP on Si by Conformal Growth, *Appl. Phys. Lett.* **68**, 2654 (1996).

- ³¹ D. Kapolnek, S. Keller, R. Vetury, R. D. Underwood, P. Kozodoy, S. P. DenBaars, and U. K. Mishra, Anisotropic Epitaxial Lateral Overgrowth in GaN Selective Area Epitaxy, *Appl. Phys. Lett.* **71**, 1204-1206 (1997).
- ³² D. Zubia and S. D. Hersee, Nanoheteroepitaxy: The Application of Nanostructuring and Substrate Compliance to the Heteroepitaxy of Mismatched Semiconductor Materials, *Jour. Appl. Phys.* **85**, 6492-6496 (1999).
- ³³ D. Zubia, S. H. Zaidi, S. R. J. Brueck and S. D. Hersee, Nanoheteroepitaxial Growth of GaN on Si by Organometallic Vapor Phase Epitaxy, *Appl. Phys. Lett.* **76**, 858-860 (2000).
- ³⁴ D. Zubia, S. H. Zaidi, S. D. Hersee and S. R. J. Brueck, *Nanoheteroepitaxy — A Nanofabrication Route to Improved Epitaxial Growth*, *Jour. Vac. Sci. Technol.* **B18** 3514-3520 (2000).
- ³⁵ D. Zubia, S. Zhang, R. Bommena, X. Sun, S. R. J. Brueck and S. D. Hersee, *Initial Nanoheteroepitaxial Growth Stages of GaAs on Si(100) by OMVPE*, *Jour. Cryst. Matl.* **30**, 812-816 (2001)
- ³⁶ For a review, see *Self-Assembled InGaAs/GaAs Quantum Dots*, ed. M. Sugawara, Academic Press (1999).
- ³⁷ S. . Jeppesen, M. S. Miller, D. Hessman, B. Kowalski, I. Maximov, and L. Samuelson, *Appl. Phys. Lett.* **68**, 2228 (1996).
- ³⁸ C. H. Hahn, Y. J. Park, E. K. Kim, D. K. Min, S. K. Jung, and J. H. Park, *Appl. Phys. Lett.* **73**, 2479 (1998).
- ³⁹ T. Ishikawa, T. Nishimura, S. Kohmoto, and K. Asakawa, *Appl. Phys. Lett.* **76**, 167 (2000).
- ⁴⁰ S. H. Lee, J. A. Johnson, M. Y. He, J. S. Speck, and P.M. Petroff, *Appl. Phys. Lett.* **78**, 105 (2001).
- ⁴¹ G. B. H. Choi, C. M. Park, S. H. Song, N. H. Son, S. W. Hwang, D. Ahn, and E. K. Kim, *Appl. Phys. Lett.* **78**, 1403 (2001).
- ⁴² D. S. Mui, D. Leonard, L. A. Coldren, and P. M. Petroff, *Appl. Phys. Lett.* **66**, 1620 (1995).
- ⁴³ M. Kitamura, M. Nishioka, J. Oshinowo, and Y. Arakawa, *Appl. Phys. Lett.* **66**, 3663 (1995).
- ⁴⁴ Y. Sugiyama, Y. Sakuma, S. Muto, and N. Yokoyama, *Appl. Phys. Lett.* **67**, 256 (1995).
- ⁴⁵ W. Seifert, N. Carlsson, A. Petersson, L.-E. Wernersson, and L. Samuelson, *Appl. Phys. Lett.* **68**, 1684 (1996).
- ⁴⁶ M. Araki, Y. Hanada, H. Fuhikura, and L. Hasegawa, *Jpn. J. Appl. Phys.* **36**, 1763 (1997).
- ⁴⁷ R. Tsui, R. Zhang, K. Shiralagi, and H. Gorokin, *Appl. Phys. Lett.* **71**, 3254 (1997).
- ⁴⁸ A. Konkar, A. Madhukar, and P. Chen, *Appl. Phys. Lett.* **72**, 220 (1998).
- ⁴⁹ S-C. Lee, K. J. Malloy and S. R. J. Brueck, *Nanoscale Selective Growth of GaAs by Molecular Beam Epitaxy*, *Jour. Appl. Phys.* (to be published)
- ⁵⁰ S. C. Lee, A. Stintz and S. R. J. Brueck, *Nanoscale Limited Area Growth of Inas Islands on Gaas(001) by Molecular Beam Epitaxy*, *Jour. Appl. Phys.* (submitted)

- ⁵¹ S.-C. Lee, L. R. Dawson, K. J. Malloy and S. R. J. Brueck, *Molecular Beam Epitaxial Growth of One-Dimensional Rows of InAs Quantum Dots on Nanoscale-Patterned GaAs*, Appl. Phys. Lett. (to be published)
- ⁵² F. Schafer, J.P. Reithmaier, A. Forchel, Appl. Phys. Lett. 74 (1999) 2915.
- ⁵³ M. Kamp, J. Hofmann, F. Schafer, M. Reinhard, T. Bleuel, J.P. Reithmaier, A. Forchel, Optical materials, 17 (2001) 19-25.
- ⁵⁴ R.C. Tiberio and P.F. Chapman, J. Vac. Sci. Technol. B 12(6), Nov/Dec 1994
- ⁵⁵ R. Schreiner, M. Korbl, H. Grabeldinger, J.L. Gentner and H. Schweizer, Electronics letters 30th March 2000 vol. 36 No. 7
- ⁵⁶ Y. Watanabe, N. Chen, K. Takei, K. Chikuma, N. Futakuchi, Y. Nakano, IEEE photonics Technology letters, Vol. 10, No. 12, December 1998
- ⁵⁷ C. L. Felix, W. W. Bewley, I. Vurgaftman, R. E. Bartolo, D. W. Stokes, J. R. Meyer, M. J. Yang, H. Lee, R. J. Menna, R. U. Martinelli, D. Z. Garbuzov, J. C. Connolly, M. Maiorov, A. R. Sugg, and G. H. Olsen, *Mid-infrared W quantum-well lasers for non-cryogenic continuous-wave operation*, Appl. Opt. 40, pp. 806-811, Feb 2001.
- ⁵⁸ W. W. Bewley, H. Lee, I. Vurgaftman, R. J. Menna, C. L. Felix, R. U. Martinelli, D. W. Stokes, D. Z. Garbuzov, J. R. Meyer, M. Maiorov, J. C. Connolly, A. R. Sugg, and G. H. Olsen, *Continuous-wave operation of $\lambda = 3.25 \mu\text{m}$ broadened-waveguide W quantum-well diode lasers up to $T = 195 \text{ K}$* , Appl. Phys. Lett. 76, pp. 256-258, Jan. 2000.
- ⁵⁹ C. Gmachl, F. Capasso, D. L. Sivco, and A. Y. Cho, *Recent progress in quantum cascade lasers and applications*, Rep. Progress Phys. 64, pp. 1533-1601, Nov. 2001.
- ⁶⁰ M. Beck, D. Hofstetter, T. Aellen, J. Faist, U. Oesterle, M. Illegems, E. Gini, and H. Melchior, *Continuous wave operation of a mid-infrared semiconductor laser at room temperature*, Science 295, pp. 301-305, Jan. 2002.
- ⁶¹ A. A. El-Emawy, H.-J. Cao, E. Zhmayev, J.-H. Lee, D. Zubia, and M. Osinski, *MOCVD growth of $\text{In}_x\text{As}_{1-x}$ on GaAs using dimethylhydrazine*, Phys. Stat. Sol. (b) 228, pp. 263-267, Nov. 2001.
- ⁶² J.-S. Wang, H.-H. Lin, L.-W. Song, and G.-R. Chen, *Growth of $\text{InAsN}/\text{InGaAs(P)}$ quantum wells on InP by gas source molecular beam epitaxy*, J. Vac. Sci. & Technol. B 19, pp. 202-206, Jan./Feb. 2001.
- ⁶³ H. Naoi, D. M. Shaw, Y. Naoi, G. J. Collins, and S. Sakai, *Growth of InNAs by low-pressure metalorganic chemical vapor deposition employing microwave-cracked nitrogen and in situ generated arsine radicals*, J. Cryst. Growth 222, pp. 511-517, 2001.
- ⁶⁴ A. A. El-Emawy, H.-J. Cao, E. Zhmayev, J.-H. Lee, D. Zubia, and M. Osinski, *MOCVD growth of $\text{In}_x\text{As}_{1-x}$ on GaAs using dimethylhydrazine*, Phys. Stat. Sol. (b) 228, pp. 263-267, Nov. 2001.
- ⁶⁵ N. Tit and M. W. C. Dharma-wardana, *Electronic structure of $\text{In}_x\text{As}_{1-x}$ alloys from tight-binding calculations*, Appl. Phys. Lett. 76, pp. 3576-3578, June 2000.

- ⁶⁶ David K , Morthier, G. Vankwikelberge, P., Baetz, R. , Wold, T., and Borchert, B.: Gain-coupled DFB lasers versus index-coupled and phase-shifted laser: a comparison based on spatial hole burning corrected yield , *IEEE J Quantum Electron*, 1991, **27**,(6), pp. 1714-1723.
- ⁶⁷ Kamp M. et al, Lateral coupling, a material independent way to complex coupled DFB laser , *Optical Materials*, (17 #1-2), pp. 19-25, JUN-JUL, 2001
- ⁶⁸ R.°A. Shelby, D.°R. Smith, and S.°Schultz, Experimental verification of a negative index of refraction., *Science*, vol. 292, no. 5514, pp. 77—79, April 2001.
- ⁶⁹ J.°B. Pendry, Negative refraction makes a perfect lens, *Physical Review Letters*, vol. 85, pp. 3966—3969, October 2000.
- ⁷⁰ Nader Engheta, An idea for thin, subwavelength cavity resonators using metamaterials with negative permittivity and permeability, *IEEE Antennas and Wireless Propagation Letters*, vol. 1, no. 1, pp. 10—13, 2002.
- ⁷¹ B.°K. Minhas, A preliminary investigation on improving the performance of microstrip antennas using left-handed materials, unpublished, 2002.
- ⁷² B.°K. Minhas, S.°R.°J. Brueck, and K.°J. Malloy, Study of grating field in the presence of negative index materials, in *Progress in Electromagnetics Research Symposium* , J.°A. Kong, Ed. July 2002, p. 755, The Electromagnetics Academy.
- ⁷³ M.°G. Moharam, Eric°B. Grann, and Drew°A. Pommet, Formulation for stable and efficient implementation of the rigorous coupled-wave analysis of binary gratings, *Journal of the Optical Society of America*, vol. 12, pp. 1068—1076, 1995.
- ⁷⁴ H.°Raether, *Surface Plasmons on smooth and rough surfaces and on gratings*, vol. 111 of *Springer Tracts in Modern Physics*, Springer-Verlag, 1988
- ⁷⁵ Ping Sheng, R.°S. Stepleman, and P.°N. Sanda, Exact eigenfunctions for square-wave gratings: Application to diffraction and surface-plasmon calculations, *Physical Review B*, vol. 26, pp. 2907—2916, September 1982.
- ⁷⁶ P.Kozodoy, J.P. Ibbetson, H. Marchand, P.T. Fini, S.Keller, J.S. Speck, S.P. Denbaars, and U.K. Mishra, Electrical Characterisation of GaN p-n Junctions with and without Threading Dislocations , *Appl. Phys. Lett.*, **73** 975 (1998)
- ⁷⁷ S. Nakamura, M. Senoh, S.I. Nagahama, N. Iwasa, T. Yamada, T. Matsushita, H. Kiyoku, Y. Sugimoto, T. Kozaki, H. Umemoto, M. Sano and K. Chocho, InGa_N/Ga_N/AlGa_N-based LaserDiodes with Modulation Doped Strained Layer Superlattices Grown on an Epitaxially Overgrown Ga_N Substrate , *Appl. Phys. Lett.*, **72** 211(1998)
- ⁷⁸ T.S. Zheleva, O.H.Nam, M.D. Bremser and R.F. Davis, Dislocation Density reduction via Lateral Epitaxy Grown Ga_N Structures , *Appl. Phys. Lett.*, **71** 2472 (1997)
- ⁷⁹ "Nanoheteroepitaxy: A New Approach to the Heteroepitaxy of Mismatched Semiconductor Materials", D. Zubia, S.D. Hersee, *J. Appl. Phys.*, **85**, (1999) 6492-6496
- ⁸⁰ D.Zubia, Ph.D. Thesis *Nanoheteroepitaxy: Theory and Application to Ga_N on Silicon* , April 2000, EECE Department, University of New Mexico

- ⁸¹ S. Luryi and E. Suhir, New approach to the high quality epitaxial growth of lattice-mismatched materials, *Appl. Phys. Lett.*, vol. **49**, pp. 140—142, 1986.
- ⁸² D. Zubia and S. D. Hersee, Nanoheteroepitaxy: The application of nanostructuring and substrate compliance to the heteroepitaxy of mismatched semiconductor materials, *J. Appl. Phys.*, vol. **85**, pp. 6492—6496, 1999.
- ⁸³ D. Zubia, S. H. Zaidi, S. R. J. Brueck, and S. D. Hersee, Nanoheteroepitaxial growth of GaN on Si by OMVPE, *Appl. Phys. Lett.*, vol. **76**, pp. 858—860, 2000.
- ⁸⁴ S. R. J. Brueck, Interferometric lithography From periodic arrays to arbitrary structures, in *Micro and Nano Eng.* 97, M. Hazatki and E. Gogolides, Eds. Amsterdam: Elsevier, 1998, pp. 145—148.
- ⁸⁵ S. C. Lee, L. R. Dawson, and S. R. J. Brueck, *J. Cryst. Growth*, **240**, 333 (2002).
- ⁸⁶ S. C. Lee, K. J. Malloy, L. R. Dawson, and S. R. J. Brueck, *J. Appl. Phys.* (to be published).
- ⁸⁷ N. Moll, A. Kley, E. Pehlke, and M. Scheffler, *Phys. Rev. B* **54**, 8844 (1996).
- ⁸⁸ J. Platen, A. Kley, C. Setzer, K. Jacobi, P. Ruggerone, and M. Scheffler, *J. Appl. Phys.*, **85**, 3597 (1999).